

STRATOSPHERIC PROCESSES  
AND THEIR ROLE IN CLIMATE  
SPARC

A project of the WMO/ICSU/IOC World Climate Research Programme

---

SPARC Report on the Evaluation of  
Chemistry Climate Models

June 2010

Prepared by the SPARC CCMVal Group under the auspices of the  
SPARC Scientific Steering Group.

Edited by V. Eyring, T. Shepherd and D. Waugh

WCRP - XXX  
WMO/TD - No. XXXX  
SPARC Report No. 5

Editing and layout: Diane Pendlebury

Citation SPARC CCMVal (2010):

SPARC CCMVal, SPARC CCMVal Report on the Evaluation of Chemistry-Climate Models, V. Eyring, T. G. Shepherd, D. W. Waugh (Eds.), SPARC Report No. 5, WCRP-X, WMO/TD-No. X, 2010.

Available at <http://www.atmosph.physics.utoronto.ca/SPARC>

# Contents

---

<b>List of Figures</b>	<b>xi</b>
<b>List of Tables</b>	<b>xxiii</b>
<b>Acknowledgements</b>	<b>xxvii</b>
<b>Executive Summary</b>	<b>xxxix</b>
Preface .....	xxxix
Overall Key Findings .....	xxxix
Overall Recommendations .....	xxxix
Key Findings by Chapter .....	xxxix
Recommendations by Chapter .....	xl
<b>Chapter 1: Introduction</b>	<b>1</b>
1.1 Rationale .....	1
1.2 CCMVal concept for model evaluation and analysis .....	3
1.3 Quantitative performance metrics.....	4
1.4 Progress beyond the state-of-the-art.....	8
1.5 Report Structure .....	9
References .....	10
<b>Chapter 2: Chemistry Climate Models and Scenarios</b>	<b>17</b>
2.1 Introduction .....	18
2.2 Climate change in CCMVal-2.....	18
2.3 Major components of chemistry climate models and their coupling by transport and radiation.....	19
2.3.1 Dynamics .....	19
2.3.1.1 Dynamical cores and model grids.....	19
2.3.1.2 Horizontal diffusion .....	23
2.3.1.3 The Quasi-Biennial Oscillation.....	24
2.3.1.4 Gravity wave drag.....	25
2.3.2 Radiation.....	27
2.3.3 Chemistry and composition .....	27
2.3.3.1 Stratospheric chemistry .....	27
2.3.3.2 Tropospheric chemistry.....	27
2.3.3.3 Mesospheric and upper atmospheric chemistry and physics .....	30

---

2.3.3.4 Time-integration of chemical kinetics .....	30
2.3.3.5 Photolysis.....	31
2.3.3.6 Heterogeneous reactions and PSC microphysics .....	31
2.3.3.7 Boundary conditions, emissions and surface sinks .....	33
2.3.4 Transport.....	35
2.3.4.1 Advection .....	35
2.3.4.2 Convective transport and turbulent mixing of chemical species .....	37
2.4 CCMVal-2 models and development since CCMVal-1 .....	37
2.4.1 AMTRAC3 (known as AMTRAC in CCMVal-1) .....	37
2.4.2 CAM3.5.....	39
2.4.3 CCSRNIES .....	39
2.4.4 CMAM.....	40
2.4.5 CNRM-ACM.....	40
2.4.6 E39CA (known as E39C in CCMVal-1).....	40
2.4.7 EMAC .....	41
2.4.8 GEOSCCM .....	41
2.4.9 LMDZrepro.....	41
2.4.10 MRI .....	41
2.4.11 SOCOL and NiwaSOCOL .....	41
2.4.12 ULAQ .....	42
2.4.13 UMETRAC .....	42
2.4.14 UMSLIMCAT .....	42
2.4.15 UМУKCA-METO and UМУKCA-UCAM .....	42
2.4.16 WACCM .....	43
2.5 Definitions of simulations and external forcings .....	43
2.5.1 Internal and external modelling uncertainties .....	45
2.5.2 CCMVal-2 simulations .....	45
2.5.2.1. REF-B0: Year 2000 time-slice simulation .....	45
2.5.2.2. REF-B1: Reproducing the past.....	45
2.5.2.3. REF-B2: Making Predictions.....	46
2.5.3 External forcings .....	47
2.5.3.1 SSTs and sea ice .....	47
2.5.3.2 Long-lived greenhouse gases and ozone-depleting substances.....	47
2.5.3.3 Ozone precursors .....	48
2.5.3.4 Stratospheric aerosol surface area densities and direct aerosol-related heating .....	48
2.5.3.5 QBO time series.....	50
2.5.3.6 Solar irradiance.....	50
2.5.4 Deviations from simulation definitions .....	50
2.6 Diagnostic output requested for CCMVal-2 .....	53
Acknowledgements .....	56
References .....	56

---

<b>Chapter 3: Radiation</b>	<b>71</b>
3.1 Introduction .....	71
3.1.1 Radiative based diagnostics .....	72
3.2 Radiative Transfer Parameterizations .....	72
3.3 Global mean temperature and temperature trends in CCMs.....	73
3.3.1 Global mean temperature climatology .....	75
3.3.2 Global mean temperature trends: Past.....	77
3.3.3 Global mean temperature trends: Future.....	78
3.4 Evaluation of the CCM radiation codes performance .....	80
3.4.1 Experimental set-up.....	82
3.4.2 Fluxes: Control experiment.....	82
3.4.3 Fluxes: Sensitivity experiments .....	85
3.4.4 Heating/Cooling rates: Control experiment.....	88
3.4.5 Heating/Cooling rates: Sensitivity experiments .....	89
3.4.6 Radiation scheme errors and model temperature biases .....	95
3.5 Solar signal in CCMs .....	97
3.5.1 Experimental Setup .....	97
3.5.2 Sensitivity of the solar signal to spectral resolution .....	98
3.6 Summary .....	99
3.6.1 Summary by model.....	101
3.6.2 Overall summary.....	105
References .....	106
<b>Chapter 4: Stratospheric Dynamics</b>	<b>109</b>
4.1 Introduction .....	109
4.2 Evaluation data sets and analyses .....	112
4.3 Mean climatology.....	113
4.3.1 Zonal-mean temperatures and eastward wind .....	113
4.3.2 Stationary waves / zonal asymmetries .....	116
4.3.3 Brewer-Dobson circulation / tropical upwelling.....	119
4.3.4 Heat flux / heat flux-temperature correlations.....	124
4.3.5 Polar stratospheric cloud threshold temperatures .....	126
4.4 Variability .....	129
4.4.1 Extra-tropical variability of the zonal-mean zonal wind.....	129
4.4.2 Tropical variability of the zonal-mean zonal wind .....	132
4.4.3 Frequency of major stratospheric sudden warmings .....	134
4.4.4 Timing of final warmings / winter-summer transition.....	136
4.5 Conclusions .....	138
4.5.1 Multi-model summary .....	138
4.5.2 Summary by model.....	139
4.5.3 Quantitative assessment / metrics.....	142
4.5.4 Future projections .....	144
Acknowledgements .....	144

---

References .....	144
<b>Chapter 5: Transport</b>	<b>149</b>
5.1 Introduction .....	149
5.2 Transport Diagnostics for the Tropics .....	150
5.2.1 Ascent .....	151
5.2.1.1 Tape Recorder Phase Speed .....	151
5.2.1.2 Ascent from Mean Age Gradients .....	155
5.2.1.3 Comparison of Vertical Velocities .....	157
5.2.2. Tropical-Midlatitude Mixing .....	159
5.2.2.1 Tape Recorder Amplitude.....	159
5.2.2.2 Tropical CH <sub>4</sub> Vertical Gradient .....	160
5.2.2.3 Tropical Mean Age .....	162
5.2.2.4 Tropical-Midlatitude N <sub>2</sub> O PDFs .....	163
5.3 Transport Diagnostics for the Extra-tropics .....	165
5.3.1 Integrated processes affecting extra-tropical composition.....	166
5.3.1.1 Mid-latitude Mean Age .....	166
5.3.1.2 Fractional Release of Cl <sub>y</sub> .....	166
5.3.1.3 Northern mid-latitude Cl <sub>y</sub> time series .....	167
5.3.1.4 N <sub>2</sub> O annual cycle in the LS .....	169
5.3.1.5 Mean age at 60°N/S .....	169
5.3.2 Polar processes .....	172
5.3.2.1 Antarctic Spring CH <sub>4</sub> PDFs .....	172
5.3.2.2 Antarctic September N <sub>2</sub> O profiles .....	174
5.3.2.3 Antarctic spring Cl <sub>y</sub> time series .....	175
5.4 Stratospheric transport changes in the 21 <sup>st</sup> Century.....	176
5.5 Summary .....	177
5.5.1 Transport Summaries by Model.....	177
5.5.2 Overall CCMVal-2 Model Transport Summary.....	184
5.5.3 Summary of 21st century transport changes .....	187
5.5.4 Comparison to CCMVal-1 model transport .....	187
5.5.5 Requirements for transport credibility .....	188
References .....	188
<b>Chapter 6: Stratospheric Chemistry</b>	<b>191</b>
6.1 Introduction .....	192
6.2 Formulation of Chemical Schemes.....	192
6.3 Evaluation of CCMs.....	192
6.3.1 Evaluation of Photolysis Rates .....	194
6.3.1.1 Introduction to PhotoComp .....	194
6.3.1.2 PhotoComp 2008 experiments .....	195
6.3.1.3 PhotoComp 2008 results and discussion .....	197
6.3.1.4 PhotoComp 2008 grading.....	202

6.3.2 Evaluation of Radical (Fast) Chemistry (Non Polar Region).....	202
6.3.2.1 Background to photochemical steady state model comparisons.....	203
6.3.2.2 Photochemical steady state model results .....	205
6.3.3 Evaluation of Reservoir and Long- Lived Chemistry.....	213
6.3.3.1 Tracer-tracer correlations.....	213
6.3.3.2 Comparison with satellite climatologies .....	217
6.3.3.3 Long-term variations .....	218
6.3.4 Evaluation of Polar Chemistry .....	227
6.3.4.1 Evolution of gas-phase HNO <sub>3</sub> , H <sub>2</sub> O, and HCl.....	227
6.3.4.2 Surface area density of PSCs.....	231
6.3.4.3 Chemical ozone depletion in the polar vortices .....	233
6.3.4.4.1 Meteorological conditions in the polar vortex.....	238
6.3.4.4.2 Evolution of Chemical Ozone Loss in the Polar Vortex .....	239
6.3.4.4.3. Polar Chemical Ozone Depletion vs. PCl and ClOx .....	242
6.4 Summary .....	243
6.4.1 Summary by model.....	243
6.4.2 Overall Summary .....	247
References .....	247

## **Chapter 7: Upper Troposphere and Lower Stratosphere** **253**

7.1 Introduction.....	253
7.2 Description of observational data sets used for CCM validation .....	254
7.2.1 Balloon data.....	256
7.2.2 Aircraft data.....	256
7.2.3 Satellite data .....	256
7.2.4 Meteorological Analyses .....	258
7.3 Metrics and Grading .....	258
7.3.1 Grading of Mean and Correlative Quantities .....	258
7.3.2 Taylor Diagram .....	259
7.4 Results: The Tropical UTLS.....	260
7.4.1. Cold Point Tropopause Temperature .....	261
7.4.2 Lapse Rate Tropopause Pressure .....	262
7.4.3 Transport in the TTL.....	263
7.4.4 Ozone .....	265
7.4.5 Water Vapour .....	266
7.4.6 Intra-seasonal Variability/ Waves.....	268
7.4.7 Vertical Thermal Structure .....	271
7.5 The Extra-tropical UTLS .....	273
7.5.1 Dynamical Structure of the Extra-tropical UTLS.....	274
7.5.1.1 Zonal mean wind.....	274
7.5.1.2 Mass of the Lowermost Stratosphere .....	275
7.5.1.3 Extra-tropical Tropopause pressure.....	276
7.5.1.4 Extra-tropical Tropopause Inversion Layer .....	277

7.5.2 Transport and mixing .....	278
7.5.2.1 Tracer seasonal cycles in the ‘background’ Lowermost Stratosphere .....	278
7.5.2.2 Meridional Tracer Gradients .....	282
7.5.2.3 Normalised Vertical Profiles of CO in Tropopause Coordinates .....	282
7.5.2.4 Vertical profiles of O <sub>3</sub> , H <sub>2</sub> O and CO relative to the tropopause height .....	284
7.5.2.5. Structure of the ExTL.....	286
7.5.5 Variability in UTLS.....	287
7.6 Trends in the UTLS.....	289
7.6.1 Tropical Tropopause Trends .....	289
7.6.2 Extra-tropical Tropopause Trends.....	292
7.7 Summary and Conclusions.....	293
7.7.1 Quantitative metrics .....	293
7.7.2 Qualitative Diagnostics Discussion.....	293
Tropical Diagnostics.....	293
Extra-tropical Diagnostics .....	294
7.7.3 Qualitative Model Discussion.....	295
7.7.4 Overall Summary .....	296
References .....	297

## **Chapter 8: Natural Variability of Stratospheric Ozone** **305**

8.1 Introduction .....	306
8.2 Data and Methodology .....	306
8.2.1 Data .....	306
8.2.2 Multiple Linear Regression Analysis .....	308
8.3 Annual Cycle in Ozone .....	309
8.3.1 Annual cycle at selected locations in the stratosphere .....	310
8.3.2 Springtime ozone values .....	312
8.3.3 Annual cycle metrics .....	312
8.4 Interannual Polar Ozone Variability .....	314
8.4.1 Heat flux and column ozone .....	316
8.4.2 Temperature and column ozone .....	318
8.4.3 Stratospheric annular mode and column ozone .....	319
8.5 Solar Cycle .....	321
8.5.1 Vertical structure of temperature and ozone signal in the tropics.....	322
8.5.2 Latitudinal structure of the solar signal in temperature and ozone .....	324
8.6 QBO in Ozone .....	326
8.6.1 Equatorial Variability and the QBO signal in the stratosphere .....	326
8.6.2 QBO signal in column ozone .....	329
8.7 ENSO Signal in Ozone .....	330
8.8 Volcanic Aerosols .....	332
8.8.1 Global mean temperature response .....	333
8.8.2 Vertical temperature response.....	334
8.8.3 Ozone response .....	334



---

8.9 Conclusions .....	335
8.9.1 Summary by process .....	336
8.9.2 Model by model summary .....	339
References .....	342
<b>Chapter 9: Long-term projections of stratospheric ozone</b>	<b>347</b>
9.1 Introduction .....	347
9.2 Analysis methods .....	349
9.2.1 Multi-Model Time Series Analysis .....	349
9.2.2 Multi-linear regression analysis .....	349
9.3 Tropical Ozone .....	350
9.3.1 From the 2006 WMO assessment: .....	350
9.3.2 Further analysis of the CCMVal-1 runs .....	350
9.3.3 Tropical TSAM analysis .....	351
9.3.4 Multiple linear regression analysis .....	354
9.3.5 The effect of upwelling on ozone .....	356
9.3.6 Brief summary .....	356
9.4 Mid-Latitude Ozone .....	356
9.4.1 From the 2006 WMO assessment: .....	356
9.4.2 Further analysis of the CCMVal-1 runs .....	356
9.4.3 Mid-Latitude TSAM analysis .....	358
9.4.4 Multiple linear regression analysis .....	359
9.4.5 Brief Summary .....	359
9.5 Polar Ozone .....	359
9.5.1 From the 2006 WMO assessment: .....	359
9.5.2 Further analysis of the CCMVal-1 runs .....	359
9.5.3 Polar TSAM analysis .....	360
9.5.4 Antarctic ozone hole diagnostics .....	362
9.5.5 Brief Summary .....	365
9.6 Ozone recovery .....	366
9.6.1 From the 2006 WMO assessment: .....	366
9.6.2 Further analysis of the CCMVal-1 runs .....	366
9.6.3 Recovery based on TSAM analysis .....	367
9.6.4 The relationship between O <sub>3</sub> and Cl <sub>y</sub> return dates .....	369
9.6.5 Ozone recovery as a function of latitude and reference year .....	370
9.6.6 The Role of transport in mid-latitude ozone recovery .....	371
9.6.7 Brief Summary .....	372
9.7 Summary .....	373
9.7.1 Summary by Model .....	373
9.7.2 Overall Summary .....	375
References .....	375
<b>Chapter 10: Effects of the stratosphere on the troposphere</b>	<b>379</b>

10.1 Introduction .....379

10.2 Validation of tropospheric and stratospheric climate .....382

    10.2.1 Multi-model mean comparison .....383

    10.2.2 CCMVal-2 performance .....385

    10.2.3 CCMVal-2 vs. CCMVal-1.....387

    10.2.4 CCMVal-2 vs. CMIP3.....387

10.3 Evaluation of Stratosphere-Troposphere Coupling in Models .....388

    10.3.1 Downward propagation of Annular Mode anomalies .....388

    10.3.2 Annular mode time scales and predictability.....391

10.4 Simulations of stratospheric influence on the troposphere in the past and future .....395

    10.4.1 Dynamical effects .....395

        10.4.1.1 Southern Hemisphere.....395

        10.4.1.2 Northern Hemisphere.....398

    10.4.2 Radiative effects .....398

        10.4.2.1 The response of surface UV radiation to stratospheric ozone changes .399

        10.4.2.2 Radiative forcing due to stratospheric ozone changes .....401

    10.4.3 Chemical effects .....402

        10.4.3.1 Stratosphere-to-troposphere ozone fluxes .....402

10.5 Summary .....405

    10.5.1 Summary by Model.....405

    10.5.2 Overall Summary .....407

References .....408

**Appendix A: List of Acronyms 413**

**Appendix B: Time Series Additive-Model Analysis 419**

B.1 Multi-Model Ensemble Analysis .....419

B.2 Nonparametric estimation of the individual model trends .....420

B.3 Baseline-adjustment of the trend estimates .....421

B.4 Multi-model trend estimates .....423

References .....426

# List of Tables

## Introduction

Table 1.1: CCMs used in the SPARC CCMVal Report. . . . .	4
Table 1.2: Overview of observations used in this report for the evaluation of CCMs. . . . .	6

## Chemistry Climate Models and Scenarios

Table 2.1: Main structure of CCMs (names of main sub-models).....	20
Table 2.2: Governing equations and horizontal discretizations of dynamical cores. ....	21
Table 2.3: Additional horizontal grids in CCMs. ....	21
Table 2.4: Transport scheme, by tracer. . . . .	22
Table 2.5: Vertical grid. ....	22
Table 2.6: Vertical resolution.....	23
Table 2.7: Horizontal diffusion . . . . .	24
Table 2.8: Usage of QBO nudging in CCMVal-2 simulations.....	25
Table 2.9: Orographic and non-orographic gravity wave drag.....	26
Table 2.10: Shortwave radiation. 2-s: Two-stream. ....	28
Table 2.11: Longwave radiation. ....	29
Table 2.12: Chlorine, bromine, and NMHC source gases . . . . .	32
Table 2.13: Species with emissions.....	34
Table 2.14: Photolysis.....	36
Table 2.15: Heterogeneous reactions.....	38
Table 2.16: Microphysics of polar stratospheric clouds (PSCs).....	39
Table 2.17: SST and sea ice data sets. ....	43
Table 2.18: Implementation of volcanic effects in REF-B1. ....	44
Table 2.19: Solar cycle by experiment with reference. ....	46
Table 2.20: Three-dimensional instantaneous diagnostics.....	52
Table 2.21: Three- and two-dimensional surface monthly-mean diagnostics.....	53
Table 2.22: Zonal-monthly-mean diagnostics produced by model . . . . .	54
Table 2.23: Surface and zonal-mean instantaneous diagnostics . . . . .	55
Table 2.24: Daily zonal-mean, and daily surface diagnostics . . . . .	56

## Radiation

Table 3.1: Summary of the radiative diagnostics and the metrics used to assess them. ....	73
Table 3.2: Model temperature climatology bias (K) with respect ERA-40.....	76
Table 3.3: Model temperature trend bias (K/decade) with respect MSU/SSU.....	80

Table 3.4: Offline radiation experiments undertaken. ....	82
Table 3.5: Near-global and diurnal mean net LW, SW and total (LW+SW) fluxes for case A and their deviation for cases B-N from reference case A. ....	83
Table 3.6: Globally and diurnally averaged flux differences at the pseudo-tropopause in W/m <sup>2</sup> for radiation models compared to reference calculations. ....	87
Table 3.7: Heating rate bias of the models with respect to LibRadtran in K/day.....	90
Table 3.8: Cooling rate bias of the models with respect to AER in K/day.. ....	91
Table 3.9: Heating rate bias of the models with respect to LibRadtran in K/day.....	92
Table 3.10: Cooling rate bias of the models with respect to AER in K/day. ....	92
Table 3.11: Heating rate bias of the models with respect to LibRadtran in K/day. ....	92
Table 3.12: Cooling rate bias of the models with respect to AER in K/day. ....	94
Table 3.13: Heating rate bias of the models with respect to LibRadtran in K/day.....	94
Table 3.14: Cooling rate bias of the models with respect to AER in K/day. ....	94
Table 3.15: Total (SW+LW) heating rates and sigmas.....	95
Table 3.16: Experimental setup for offline solar variability simulations.....	97
Table 3.17: Participating offline SW radiation codes. ....	97
Table 3.18: A summary of the metrics and gradings.....	101

## Stratospheric Dynamics

Table 4.1a: Climatological mean dynamical processes and/or phenomena validated in this chapter. ....	110
Table 4.1b: As Table 4.1a but for climate variability on intra-seasonal to interannual time scales. ....	111

## Transport

Table 5.1: Stratospheric Transport Diagnostics for CCMs.....	151
Table 5.2: CCM Age Tracer Information. ....	156

## Stratospheric Chemistry

Table 6.1: List of core processes to validate chemistry in CCMs. ....	193
Table 6.2: PhotoComp 2008 experiments. ....	195
Table 6.3: Models contributing to CCMVal PhotoComp 2008.....	195
Table 6.4: Atmospheric averaged robust standard deviation of ln(J) (x100 = RSD in %), identifying Js and conditions for which there is general agreement among the models. ....	196
Table 6.5: NAT and ICE particle properties.....	237

## Upper Troposphere and Lower Stratosphere

Table 7.1: List of core processes to validate CCMs in the UTLS.....	255
Table 7.2: The wave activity for equatorial Kelvin waves, mixed Rossby gravity (MRG) waves, and symmetric eastward-moving ISO.....	271

## Natural Variability of Stratospheric Ozone

Table 8.1: List of diagnostics employed to evaluate the modelling of natural stratospheric ozone variability by the CCMs participating in CCMVal-2. ....	307
Table 8.2: Total ozone model bias in % for different latitude ranges. ....	314
Table 8.3: Solar regression coefficient for total column ozone from 60°S to 60°N for the CCMs that impose a solar cycle compared to observations (NIWA-column). ....	322
Table 8.4: Tropical variability in the CCMVal-2 models.....	326
Table 8.5: List of metrics used in Chapter 8. ....	337

## Long-term projections of stratospheric ozone

Table 9.1: Mean low temperature areas ( $T < 195$ K) for the period July to September for the years 1980-2007 in comparison with observations for the models. ....	366
Table 9.2: Commonly used ozone hole diagnostics .....	367

## Effects of the stratosphere on the troposphere

Table 10.1: Key diagnostics.....	381
Table 10.2: Model used for model validation. ....	382
Table 10.3: Multi-model mean of the relative changes in global, northern, and southern hemispheric ozone fluxes for different time periods .....	406



# List of Figures

## Chapter 1: Introduction

- Figure 1.1: Model of the relationships between CCMVal, the CCM groups, and the WMO/UNEP Assessment.....2
- Figure 1.2: Schematic diagram of the CCMVal evaluation approach.....3

## Chapter 2: Chemistry Climate Models and Scenarios

- Figure 2.1: Basic structure of a CCM and external forcings..... 19
- Figure 2.2: HadISST1 and HadGEM1 SSTs.....47
- Figure 2.3: Surface total chlorine and total bromine as defined in the A1 scenario. Surface CO<sub>2</sub>, N<sub>2</sub>O, and CH<sub>4</sub> as defined in the SRES A1b scenario.....48
- Figure 2.4: Surface emissions of NO<sub>x</sub>, CO and CH<sub>2</sub>O as used for CCMVal-2 simulations....48
- Figure 2.5: Aerosol surface area density, reconstructed from SAGE data. ....49
- Figure 2.6: Zonal wind (u) from merged observations at Canton Island, Gan and Singapore, vertically extended.....49
- Figure 2.7: Total solar irradiance updated from Lean et al. (2005).....50

## Radiation

- Figure 3.1: Climatological global and annual mean temperature, ozone mixing ratio, and water vapour mixing ratio and biases for REF-B1 model simulations and reference data sets .....74
- Figure 3.2: Near global (70°S-70°N) and annual mean trends over 1980-1999 for (a) temperature, (b) ozone, and (c) water vapour ratio, for REF-B1 model simulations.....77
- Figure 3.3: Near global mean time series (70°S-70°N) of MSU/SSU satellite observations and REF-B1 model temperature data weighted by MSU/SSU weighting functions .....79
- Figure 3.4: Global and annual mean temperature trends from (a) REF-B1 for 1980-1999; and from REF-B2 for (b) 1980-1999, (c) 2000-2049, and (d) 2050-2099. ....81
- Figure 3.5: The global and diurnal mean SW, LW and total net flux deviations from the LBL code at the model pseudo-tropopause (200 hPa). ....83
- Figure 3.6: The global and diurnal mean SW (red circles), LW (blue circles) and total (black diamonds) net flux deviations from the LBL code (AER for LW and libRadtran for SW) at the surface.....83
- Figure 3.7: The vertical profiles of the global and diurnal mean LW downward flux from the LBL code (AER) and the absolute deviations of ECHAM4, LMDZrepro and CCSRNIIES results from the reference AER LBL scheme. ....84
- Figure 3.8: The vertical profiles of the global and diurnal mean SW downward flux from the LBL code (libRadtran) and the absolute deviations of ECHAM4, MRI and UKMO-Leeds results from the reference libRadtran LBL scheme. ....84
- Figure 3.9: The global and diurnal mean SW, LW and total net flux deviations of the radiative forcing due to CO<sub>2</sub> (case B) increase relative to the results of LBL codes at the pseudo-tropopause.....86

Figure 3.11: The global and diurnal mean SW, LW and total net flux deviations of the radiative forcing due to stratospheric ozone depletion (case H) relative to the results of LBL codes at the pseudo-tropopause.....86

Figure 3.10: The global and diurnal mean SW, LW and total net flux deviations of the radiative forcing due to LL GHG (case G) increase relative to the results of LBL codes at the pseudo-tropopause.....86

Figure 3.12: The global and diurnal mean SW, LW and total net flux deviations of the radiative forcing due to stratospheric water vapour increase (case J) relative to the results of LBL codes at the pseudo-tropopause.....86

Figure 3.13: The global and diurnal mean SW, LW and total net flux deviations of the radiative forcing due to WMGHG and stratospheric ozone changes (case L) relative to the results of LBL codes at the pseudo-tropopause.....86

Figure 3.14: Globally averaged shortwave heating rates for case A (control) and differences from that calculated with the LibRadtran. ....90

Figure 3.15: Globally averaged longwave cooling rates for case A (control) and for case L minus case A, and differences of the same cooling rate change from that calculated with the AER model.....91

Figure 3.16: The bias in the simulated global mean temperature at 2 hPa and the estimated contributions of CCM biases in: ozone climatology, water vapour climatology, and longwave/shortwave heating rates calculations.....96

Figure 3.17: Global mean, shortwave heating rate differences between minimum and maximum of the 11-year solar cycle in January (K/d), calculated offline in CCM radiation schemes and one reference LBL model. ....99

Figure 3.18: CCM grades for globally averaged climatological stratospheric temperatures and their trend.. ....102

Figure 3.19: CCM grades for globally averaged fluxes at the 200 hPa tropopause and their change (radiative forcing). ....102

Figure 3.20: CCM grades for globally averaged climatological stratospheric heating rates and their changes. ....103

Figure 3.21: A summary of the average CCM grade for temperature related metrics. ....103

**Chapter 4: Stratospheric Dynamics**

Figure 4.1: Climatological mean temperature biases for 60°N–90°N and 60°S–90°S for the winter and spring seasons. ....112

Figure 4.2: Descent of the zero zonal-mean zonal wind at 60°S based on the climatological mean annual cycle for REF-B1 simulations.....113

Figure 4.3: Zonal wind speed and latitude of the jet maximum of the NH DJF climatology, and of the SH JJA climatology in the REF-B1 simulations.. ....114

Figure 4.4: Temperature trends from 1980 to 1999, 2000 to 2049 and 2050 to 2099.....115

Figure 4.5: Latitudinal location and value of the maximum amplitude of the stationary wave field for the NH DJF climatology, and for the SH SON climatology. ....116

Figure 4.6: Seasonal variation of the maximum amplitude of the NH and SH 10 hPa climatological stationary wave.....117

Figure 4.7: Phase in degrees and amplitude (contour interval 200 m), in polar coordinates, of



wave-1 and wave-2 10 hPa stationary waves for NH DJF and SH SON. Ratio of wave-2 to wave-1 amplitude on 10 hPa for NH DJF and for SH SON.....	118
Figure 4.8: Trends in the amplitude of the seasonal-mean stationary wave for the periods 1980-1999, 2000-2049, and 2050-2099 in the REF-B2 simulations.....	119
Figure 4.9: Annual mean residual vertical velocities at 70 hPa, “turn-around” latitudes, and upward mass flux at 70 hPa calculated from residual vertical velocity. Seasonal anomalies from the annual mean are shown. ....	120
Figure 4.10: Annual mean upward mass flux averaged from 1980 to 1999 for the REF-B1 simulations and from 1992 to 2001 for the UKMO analyses. ....	121
Figure 4.11: For the REF-B2 simulations. (a) Annual mean upward mass flux at 70 hPa, calculated from $w^*$ . Also shown is the annual mean mass flux trend at 70 hPa from (b) 1980-1999, (c) 2000-2049 and (d) 2050-2099.....	122
Figure 4.12: Monthly mean climatology of the eddy meridional heat flux at 100 hPa for the months of January and July, 1980-1999.....	123
Figure 4.13: Linear trends in the mean meridional heat flux averaged between 40°N/S and 80°N/S for the winter seasons.....	125
Figure 4.14: Parameters of the linear fit to the scatter plot of the 100 hPa heat flux vs. the 50 hPa temperature. ....	126
Figure 4.15: Seasonally accumulated area at 50 hPa where daily temperatures are below 195 K and below 188 K for REF-B1 and REF-B2 simulations.....	127
Figure 4.16: Linear trend (1980-1999) for the Antarctic and the Arctic of the seasonally accumulated area at 50 hPa where daily temperatures are below 195 K and below 188 K for REF-B1 simulations.....	127
Figure 4.17: Linear trend (1980-1999, 2000-2049, 2050-2099) for the Antarctic and the Arctic of the seasonally accumulated area at 50 hPa where daily temperatures are below 195 K and below 188 K for the REF-B2 simulations.....	128
Figure 4.18: Location and amplitude of the maximum interannual standard deviation of the zonal-mean zonal wind in the NH in DJF poleward of 45°N and in the SH in JJA between 80°S and 30°S.....	130
Figure 4.19: Eigenvalue of the leading mode of variability of the 50 hPa zonal-mean zonal wind for the SH (right) and NH (left).....	131
Figure 4.20: Regression patterns (m/s) of first (top) and second (bottom) mode of the 50 hPa zonal-mean zonal wind determined for regions poleward of 45°; (left) SH and (right) NH..	131
Figure 4.21: Profiles of the standard deviation in the de-trended zonal-mean zonal wind averaged from 10°S-10°N for the REF-B1 simulations. ....	133
Figure 4.22: Profiles of the amplitude of the “QBO” in the zonal-mean zonal wind averaged between 10°S-10°N for the REF-B1 simulations. ....	133
Figure 4.23: Profiles of the amplitude of the SAO in the zonal-mean zonal wind averaged between 10°S-10°N for the REF-B1 simulations.....	133
Figure 4.24: Profiles of the amplitude of the annual-cycle in the zonal-mean zonal wind averaged between 10°S-10°N for the REF-B1 simulations. ....	134
Figure 4.25: Mean frequency of NH major SSWs per year for the REF-B1 and REF-B2 simulations between 1960 and 2000. ....	135
Figure 4.26: Histograms showing the frequency of major SSWs in the REF-B1 simulations (1960-	

2000) in comparison to ERA-40 reanalysis .....	136
Figure 4.27: Mean date of the NH and SH final warmings for REF-B1 and REF-B2 simulations (1980-1999).....	137
Figure 4.28: Linear trend in the date of the SH final warming from REF-B1 and REF-B2 simulations.....	138
Figure 4.29: Matrix showing the performance of the model ensemble in a variety of metrics described in Table 4.1a, b after Waugh and Eyring (2008).....	142

## Chapter 5: Transport

Figure 5.1: Schematic of the stratospheric circulation.....	150
Figure 5.2: Water vapour tape recorder signal from the models and the combined HALOE+MLS data set from Schoeberl et al. (2008). .....	152
Figure 5.3: Phase lag and amplitude, relative to the maximum amplitude as a function of height above the levels of maximum amplitude, of the water vapour tape recorder, averaged over 10°S-10°N. ....	153
Figure 5.4: The tape recorder phase speed versus the scale height for the TLS, and the TMS, and versus the scale height per wavelength .....	154
Figure 5.5: Mean age from 15 CCMs and the multi-model mean.....	155
Figure 5.6: Comparison of the tropical vertical velocities derived from the tape recorder (TR) and mean age gradient (AG), as well as model residual vertical velocities .....	158
Figure 5.7: Tropical (10°N-10°S) CH <sub>4</sub> profiles from all CCMs in two seasons compared to HALOE mean profiles. ....	161
Figure 5.8: Contoured probability distribution functions of N <sub>2</sub> O for 10°S-45°N for NH spring (March-April-May) for 16 CCMs. MIPAS and MLS observations are shown in the first two panels. ....	164
Figure 5.9: Probability distribution functions of N <sub>2</sub> O on the 800 K surface for NH spring (top panels) and SH spring (bottom panels). ....	165
Figure 5.10: Fractional release of inorganic Cl as a function of mean age of air .....	167
Figure 5.11: Modelled and observed Cl <sub>y</sub> times series for 1980-2006.. .....	168
Figure 5.12: Area-weighted mean over 45°S-89°S of monthly mean N <sub>2</sub> O tendencies at 50 hPa and 100 hPa. ....	170
Figure 5.13: Same as Figure 5.12, but for 45°N-89°N.....	171
Figure 5.14: Performance metrics for model mean age of air at 60°N and 60°S, 50 hPa... ..	172
Figure 5.15: Contoured PDF of HALOE CH <sub>4</sub> data and models for SH spring .....	173
Figure 5.16: The most probable values of the CH <sub>4</sub> PDFs identified from HALOE and model analyses. ....	174
Figure 5.17: 18 CCM and observed profiles of N <sub>2</sub> O, 80°S-88°S, for September.....	175
Figure 5.18: Mean age changes in the REF-B2 simulations during the 21st century.....	176
Figure 5.19: Quantitative assessment of model performance on transport diagnostics.....	183
Figure 5.20: Correlations between the average mean age grade and four fundamental diagnostic quantities .....	185
Figure 5.21: Mean age from 10 CCMs participating in CCMVal-1 and their multi-model mean. ....	186

## Chapter 6: Stratospheric Chemistry

Figure 6.1: Model deviations in $\ln(J)$ ( $\text{sec}^{-1}$ ) from the robust mean for nine selected J-values (NO, O <sub>2</sub> , O <sub>3</sub> , O <sub>3</sub> (1D), NO <sub>2</sub> , H <sub>2</sub> CO <sub>a</sub> , CFCI <sub>3</sub> , CF <sub>2</sub> Cl <sub>2</sub> , N <sub>2</sub> O) from PhotoComp experiment P1a (clear sky, SZA = 15°). .....	197
Figure 6.2: Ratio of J-values for a Pinatubo-like stratospheric aerosol layer .....	198
Figure 6.3: Ratio of J-values for a stratus cloud layer. ....	199
Figure 6.4: Model deviations in $\ln(J)$ from the robust mean for three selected J-values (NO, O <sub>2</sub> , O <sub>3</sub> ) from PhotoComp experiment P2a, and for J-NO, J-O <sub>2</sub> and J-O <sub>3</sub> and J-Cl <sub>2</sub> O <sub>2</sub> for experiments P1a, P2n, P2a, and P2m. ....	200
Figure 6.5: J-values ( $\text{sec}^{-1}$ ) vs. pressure altitude for (a) O <sub>3</sub> yielding O( <sup>1</sup> D), (b) O <sub>3</sub> total, and (c) NO <sub>2</sub> from the Photocomp P3 experiment .....	201
Figure 6.6: Matrices displaying PhotoComp grades for the nine participating CCMs. ....	202
Figure 6.7: Sulfate surface area density versus pressure and versus geometric altitude for 35°N, September 1993 and 22°N, February 1996 from eight CCMs. ....	204
Figure 6.8: Comparison of N <sub>2</sub> O profiles and the relation of radical precursors versus N <sub>2</sub> O (black) to zonal monthly mean values from various CCM models for 35°N in September 1993. ....	206
Figure 6.9: Comparison of zonal monthly mean profiles of radicals from CCM models versus 24-hour average radical profiles found using a PSS box model constrained by profiles of T, O <sub>3</sub> , H <sub>2</sub> O, CH <sub>4</sub> , CO, NO <sub>y</sub> , Cl <sub>y</sub> , Br <sub>y</sub> , and sulfate SAD from the various CCMs for 35°N in September 1993. ....	208
Figure 6.10: Metrics for radical precursors and sulfate surface area and radicals for a simulation carried out at 35°N, September 1993. ....	212
Figure 6.11: Scatter plot of metrics for the radical precursors, sulfate surface area, and fast chemistry for the simulation carried out at 35°N, September 1993 vs. metrics for the same quantities from the 22°N, February 1996 simulation .....	213
Figure 6.12: Correlation of CH <sub>4</sub> vs. N <sub>2</sub> O for zonal-mean monthly-mean output from the final 10 years of REF-B1 runs from 17 CCM runs and MIPAS data. ....	214
Figure 6.13: Correlation of CH <sub>4</sub> vs. H <sub>2</sub> O for zonal-mean monthly-mean output from the final 10 years of REF-B1 runs from 17 CCMs and MIPAS data. ....	215
Figure 6.14: Correlation of NO <sub>y</sub> vs. N <sub>2</sub> O for zonal mean monthly mean output from the final 10 years of REF-B1 runs from 16 CCMs. ....	216
Figure 6.15: Grading plot for 18 CCMs for tracer-tracer correlations, comparisons with the mean annual cycle and mean vertical profiles of a range of tracers. ....	218
Figure 6.16: Mean annual cycle for 30°N-60°N at 50 hPa for modelled CH <sub>4</sub> , H <sub>2</sub> O, CO, O <sub>3</sub> , HCl, ClONO <sub>2</sub> , HNO <sub>3</sub> , N <sub>2</sub> O <sub>5</sub> , NO <sub>2</sub> and BrO. ....	219
Figure 6.17: Mean profiles for 30°S-60°S for CH <sub>4</sub> , H <sub>2</sub> O, CO, O <sub>3</sub> , HCl, ClONO <sub>2</sub> , HNO <sub>3</sub> , N <sub>2</sub> O <sub>5</sub> , NO <sub>2</sub> and BrO compared with observations. . ....	219
Figure 6.18: Time series of modelled zonal-mean trace gas abundance in the tropical upper stratosphere for OH, H <sub>2</sub> O <sub>2</sub> , HO <sub>2</sub> , NO <sub>2</sub> , ClO, HCl, H <sub>2</sub> O, CH <sub>4</sub> and O <sub>3</sub> . ....	220
Figure 6.19: Comparison of observed column abundances (molecules cm <sup>-2</sup> ) of HCl, ClONO <sub>2</sub> , and HCl + ClONO <sub>2</sub> at Jungfraujoch (45°N) with output from REF-B1 simulations. ....	221
Figure 6.20: Comparison of observed column abundances (molecules cm <sup>-2</sup> ) of NO <sub>2</sub> at Jungfraujoch (45°N) for (a) sunrise and (b) sunset observations with output from REF-B1 simulations ..	222

Figure 6.21: Time series of total chlorine volume mixing ratio from 1960 to 2100 .....	223
Figure 6.22: As Figure 6.21 but for total bromine mixing ratio (ppbv).....	224
Figure 6.23: Time series of O <sub>3</sub> (ppmv), CH <sub>4</sub> (ppmv), N <sub>2</sub> O (ppbv), H <sub>2</sub> O (ppmv) and NO <sub>y</sub> (ppbv) annually averaged between 10°S and 10°N at 5 hPa from REF-B2 runs of 14 CCMs and the multi-model mean. ....	225
Figure 6.24: As Figure 6.23 but for an annual average between 30°N and 60°N at 70 hPa.	226
Figure 6.25: As Figure 6.23 but for a September–November average between 90°S and 60°S at 50 hPa. ....	226
Figure 6.26: Southern hemisphere profiles of HNO <sub>3</sub> versus $\theta$ from Aura MLS at mid-month from May through October .....	228
Figure 6.27: CCM climatological profiles of HNO <sub>3</sub> from mid-May through mid-October .....	229
Figure 6.28: Change in HNO <sub>3</sub> from 350 K to 600 K, relative to May, for Aura MLS (abbreviated as AMLS in legend) and 12 CCM climatologies (legend uses first 4 letters of each model) and their multi-model mean (MMM).....	230
Figure 6.29: Grades obtained for 12 CCMs and their multi-model mean (MMM) from a comparison of model versus MLS-derived climatological changes in HNO <sub>3</sub> .....	231
Figure 6.30a: Variations in average HNO <sub>3</sub> at 500 K during the course of a year in 4 EqL bins, based on climatologies from Aura MLS, 6 CCMs and their multi-model mean, and corresponding rms variability over the 5-year climatology, for each sampled day of year. ....	232
Figure 6.30b: Same as Figure 6.30a, but for Aura MLS HNO <sub>3</sub> .....	233
Figure 6.31: Climatological profiles of H <sub>2</sub> O from mid-May through mid-October.....	234
Figure 6.32: Climatological profiles of HCl from mid-May through mid-October .....	235
Figure 6.33: Summary of grades relating to SH changes in HNO <sub>3</sub> , H <sub>2</sub> O, and HCl .....	236
Figure 6.34: Comparison of model maximum SAD for NAT and ICE. ....	237
Figure 6.35: Vortex average temperatures (top), and PACI (bottom) from January through March for the Arctic (left) and from July through September for the Antarctic (right) and between 440-550K. ....	238
Figure 6.36: Chemical ozone depletion in the polar vortex from January through April and July through October between 350-550 K. ....	239
Figure 6.37: Relationship between Arctic chemical ozone loss and PACI for the years between 1990 and 2005. Model Cl <sub>x</sub> versus PACI is also shown .....	240
Figure 6.38: Relationship between Antarctic chemical ozone loss and PACI for the years between 1960 and 2005. Model Cl <sub>x</sub> versus PACI is also shown .....	241
Figure 6.39: Summary of grades, as discussed in the text.....	242

## **Chapter 7: Upper Troposphere and Lower Stratosphere**

Figure 7.1: Schematic of the UTLS. ....	257
Figure 7.2: A sample Taylor diagram. ....	259
Figure 7.3: Annual cycle of tropical (20°S-20°N) cold point tropopause temperature from models and observations, and related grades .....	262
Figure 7.4: Time series of annual mean temperature of the Cold Point Tropopause (TCPT) for 20°S-20°N from models and analyses for 1960-2007. ....	263
Figure 7.5: REF-B1 lapse rate tropopause pressure (PTP) annual zonal mean for 1980--1999	

from models and analysis systems.....	263
Figure 7.6: Annual mean time series of the Lapse Rate Tropopause Pressure (PTP) for 20°S-20°N from models and analyses for 1960-2007, and related grades. ....	264
Figure 7.7: Geographical distribution of the dehydration points for ERA-40, E39CA, and CMAM showing minimum temperatures, fractional contribution to stratospheric water vapour from different geographical areas, and longitudinal distribution of the water vapour entry value.....	265
Figure 7.8: Residence time for the trajectories in the upper part of the TTL (385-395 K) for ERA-40, CMAM, and E39CA .....	266
Figure 7.9: Annual cycle of tropical (20°S-20°N) ozone mixing ratio from models and observations, and related grades.....	267
Figure 7.10: Annual cycle of tropical (20°S-20°N) water vapour at 80 hPa from models and observations, and related grades .....	267
Figure 7.11: Correlation of minimum monthly mean water vapour with saturation vapour mixing ratio ( $Q_{\text{sat}}$ ) of the minimum monthly mean TCPT .....	268
Figure 7.12: Zonal-wavenumber-frequency spectrum of temperature at 100 hPa within 15°N-15°S for all seasons between Jan 1990 and Feb 2000 for the symmetric component for ERA-40, NCEP1, CCSRNIES, CMAM, MRI, and WACCM.....	269
Figure 7.13: Same as Figure 7.12 but for the antisymmetric component.....	270
Figure 7.14: Zonally-averaged $N^2 \times 10^4$ on the tropopause based coordinate for COSMIC/FORMOSAT-3, degraded COSMIC data and composite of 9 REF-B1 model integrations .....	272
Figure 7.15: Vertical profiles of $N^2$ in each model and observation in the tropics.....	273
Figure 7.16: Zonal-mean zonal wind $\bar{u}$ and corresponding Taylor diagrams at 200 hPa.....	275
Figure 7.17: Metrics for the zonal-mean zonal wind at 200 hPa. ....	276
Figure 7.18: Seasonal cycle in LMS mass, and corresponding Taylor diagrams of model performance .....	276
Table 7.19: Same as Figure 7.17, but for LMS mass. ....	277
Figure 7.20: Extra-tropical tropopause pressure variability for SH (left panel) and NH (right panel).....	277
Figure 7.21: Vertical profiles of $N^2$ in models and observation at (a) 50°N during DJF and (b) 80°N during JJA.....	278
Figure 7.22: Seasonal cycles in monthly mean $O_3$ , $HNO_3$ , and $H_2O$ between 40°N and 60°N and corresponding Taylor diagrams at 100 hPa and 200 hPa.....	279
Figure 7.23: Same as Figure 7.22, but for latitudes between 40°S and 60°S. ....	280
Figure 7.24: Meridional gradient in $O_3$ (ppmv/deg) at 200 hPa and corresponding Taylor diagrams.....	281
Figure 7.25: Same as Figure 7.17 but for meridional gradient in $O_3$ at 200 hPa .....	282
Figure 7.26: Profiles of normalised CO for winter/spring and summer/autumn.....	283
Figure 7.27: Ozone profiles in RALT for four seasons.....	284
Figure 7.28: Grades calculated using simplified metrics for mean ozone values in the upper troposphere and lower stratosphere.....	285
Figure 7.29: Top panels as in Figure 7.27 and bottom panels as in Figure 7.28, but for annual means of CO (left) and $H_2O$ (right). ....	286

Figure 7.30: Fraction of air parcels within the mixing layer from models for the year 2000, and from POLARIS observations for 1997 between spring and fall .....	287
Figure 7.31: Example of probability function maps at NH mid-latitudes (40°N to 50°N) during JJA season showing the relationship of O <sub>3</sub> (x-axis) and tropopause heights (y-axis) for MLS and WACCM.....	287
Figure 7.32: The temporal variation of the obtained grades on 68 hPa isobaric surfaces at mid-latitude (40°N – 50°N).....	288
Figure 7.33: Time series of O <sub>3</sub> differences (low tropopause – high tropopause) on 68 hPa isobaric surfaces.....	289
Figure 7.34: Lapse Rate Tropopause Pressure time series from 20°S-20°N for future REF-B2 scenarios.....	290
Figure 7.35: CPT time series from 20°S-20°N for future REF-B2 scenarios.....	290
Figure 7.36: 80 hPa water vapour time series from 20°S-20°N for future REF-B2 scenarios.....	291
Figure 7.37: Trends in O <sub>3</sub> and H <sub>2</sub> O in pressure and tropopause coordinates.....	291
Figure 7.38: Northern and Southern Hemisphere extra-tropical tropopause pressure time series from 90°S-60°S and 60°N-90°N for future REF-B2 scenarios.....	292
Figure 7.39: Quantitative metrics summary.....	293

## Chapter 8: Natural Variability of Stratospheric Ozone

Figure 8.1: Ozone variations for 60°S-60°N in DU estimated from ground-based measurements and individual components that comprise ozone variations, from 1964 to 2008.....	309
Figure 8.2: Monthly mean ozone mixing ratios at 1 hPa, 40°S, equator and 40°N, and 46 hPa, 72°S, equator and 72°N from MLS observations and models.....	310
Figure 8.3: Climatological zonal mean O <sub>3</sub> mixing ratios from the CCMVal-2 CCMs and HALOE in ppmv.....	311
Figure 8.4: Normalised Taylor diagram of the annual and semi-annual harmonics of the zonal-mean ozone, latitude-pressure distribution, for the NIWA-3D data set and the CCMVal-2 models.....	313
Figure 8.5: Normalised Taylor diagram of the annual cycle of the zonal-mean column ozone, latitude-month distribution, for the NIWA-column and TOMS+gb data sets and the CCMVal-2 models.....	313
Figure 8.6a: Interannual variability of polar cap averaged column ozone and corresponding normalised Taylor diagrams for NH and SH over the period onward of 1980.....	315
Figure 8.6b: Mean polar cap averaged column ozone and corresponding normalised Taylor diagrams.....	316
Figure 8.7: Slope parameter of the linear fit to the scatter plots of the Spring/Autumn ozone ratio versus the 100 hPa winter heat flux, plotted against the mean Spring/Autumn ozone ratio for each model.....	317
Figure 8.8: Slope parameter of the linear fit to the scatter plots of the polar cap averaged column ozone versus 50 hPa temperature, plotted against the column ozone value of the linear fit at T = 200 K for each model data.....	318
Figure 8.9a: Regression of column ozone on the simplified annular mode for NH March.....	319
Figure 8.9b: Regression of column ozone on the simplified annular mode for SH Nov.....	320
Figure 8.10: Normalised Taylor diagrams of the regression of column ozone on the simplified	

annular mode for NH March and SH November.....	321
Figure 8.11: Annual mean tropical (25°S-25°N) solar regression coefficients for temperature and ozone, and the relative uncertainty in temperature and ozone.....	323
Figure 8.12: Solar cycle shortwave heating rate differences in Kelvin per day in 100 units of the F10.7cm solar flux averaged between 25°S and 25°N for those CCMs that prescribed a solar cycle .....	324
Figure 8.13: Amplitude of the solar cycle in the upper stratosphere over latitude for ozone at 3 hPa in %/100 units of the F10.7cm radio flux and temperature at 1 hPa in K/100 units of the F10.7 cm radio flux .....	325
Figure 8.14: Monthly zonal-mean standard deviation of zonal-mean zonal wind (left, m/s) and ozone (right, DU/km) averaged from 5°S to 5°N .....	327
Figure 8.15: Annual mean QBO regression coefficient in ozone in percent at equatorial latitudes (5°S-5°N) from the CCMVal-2 CCMs (1960-2004) and observations.....	328
Figure 8.16: Latitudinal distribution of the annual mean QBO amplitude in column ozone from the CCMVal-2 CCMs (1960-2004) and observations .....	328
Figure 8.17: Reconstruction of the QBO contribution to the monthly zonal mean column ozone averaged from 5°S to 5°N.....	329
Figure 8.18: Annual mean tropical (25°S-25°N) ENSO regression coefficients from 1000 to 1 hPa for temperature ozone from models and observations .....	330
Figure 8.19: Scatter plot of the February-March polar cap ENSO anomaly in column ozone versus temperature (30-70 hPa average).....	332
Figure 8.20: Annual mean global mean 50 hPa temperature anomalies from pre-volcanic conditions for the Agung, El Chichón and Pinatubo eruptions.....	333
Figure 8.21: Annual mean tropical (25°S-25°N) contribution from the volcanic basis function from models and observations to temperature for Pinatubo from 1000 to 1 hPa. ....	334
Figure 8.22: Annual mean global mean column ozone anomalies from pre-volcanic conditions for the Agung, El Chichón and Pinatubo eruptions.....	334
Figure 8.23: Post volcanic eruption annual mean global mean anomalies of column ozone as a function of similarly calculated anomalies in ClO at 50 hPa .....	335
Figure 8.24: Matrix displaying the model performance.....	336

## Chapter 9: Long-term projections of stratospheric ozone

Figure 9.1: Raw time series data of annually averaged total ozone for the latitude range 25°S-25°N and initial individual model trend (IMT) estimates, and 1980 baseline-adjusted time series data and 1980 baseline-adjusted IMT estimates for the TSAM analysis.....	351
Figure 9.2: 1980 baseline-adjusted multi-model trend (MMT) estimates of annually averaged total ozone for the latitude range 25°S-25°N.....	352
Figure 9.3: Results of the MLR analysis for the CCMVal-2 models in the latitude band 25°S-25°N. Sensitivity of the model ozone to halogen, sensitivity of the model ozone amounts to temperature and sensitivity of the model ozone amounts to NO <sub>y</sub> .....	353
Figure 9.4: Results of the MLR analysis for the CCMVal-2 models for 25°S-25°N for the evolution of ozone at 5 hPa, change in 5 hPa ozone relative to 1980 levels, and the evolution of Cl <sub>y</sub> + αBr <sub>y</sub> and contribution of Cl <sub>y</sub> + αBr <sub>y</sub> to the ozone and temperature changes.....	354
Figure 9.5: Vertical profile results of the MLR analysis for the models for 25°S-25°N for ozone in	

the year 2000, ozone change from 2000 to 2100, and $Cl_y + \alpha Br_y$ change from 2000 to 2100 and contribution of the $Cl_y + \alpha Br_y$ change to the ozone, temperature and $NO_y$ change .....	355
Figure 9.6: Scatter plot showing the differences (from 1960 to 2100) in 70 hPa $\bar{w}^*$ and 50 hPa ozone for models .....	356
Figure 9.7: As in Figure 9.2 but for the latitude range 35°N-60°N. ....	357
Figure 9.8: As in Figure 9.2 but for the latitude range 35°S-60°S. ....	357
Figure 9.9: As in Figure 9.2 but for 50 hPa $Cl_y$ in the latitude range 35°N-60°N. ....	358
Figure 9.10: Vertical profiles of differences in mid-latitude (35°S-60°S and 35°N-60°N) ozone over the the 21 <sup>st</sup> century and the contributions of $Cl_y + \alpha Br_y$ , temperature, and $NO_y$ . ....	360
Figure 9.11: As in Figure 9.2 but for the month of March and the latitude range 60°N-90°N.	361
Figure 9.12: As in Figure 9.2 but for the Month of October and the latitude range 60°S-90°S..	361
Figure 9.13: As in Figure 9.2 but for 50 hPa $Cl_y$ in the latitude range 60°N-90°N. ....	363
Figure 9.14: As in Figure 9.2 but for 50 hPa $Cl_y$ in the latitude range 60°S-90°S.....	363
Figure 9.15: Total column ozone as a function of latitude, averaged for the period 1996-2005 for 10 days before and after the minimum column ozone.....	364
Figure 9.16: Meridional gradient in total column ozone averaged for the period 1996-2005 for the 10 days on either side of the ozone minimum. ....	364
Figure 9.17: Latitude of maximum meridional gradient in total column ozone, as a function of the ozone value at that latitude.....	365
Figure 9.18: Simulated and observed ozone hole areas, based on a fixed, 220 DU amount, the 1960-1965 minimum, and the value at the maximum gradient. ....	365
Figure 9.19: Ozone hole area versus cold area (50 hPa $T < 195$ K), averaged for July to September for each model compared with observations. The results were calculated from the REF-B1 simulations, and are averaged for the period 1990-2008. ....	366
Figure 9.20: Date of return to 1980 values for the annual average and spring total ozone column derived from the IMT and MMT estimates for CCMVal-1 and CCMVal-2 .....	368
Figure 9.21: Date of return to 1980 values for the annual average 50 hPa $Cl_y$ derived from the IMT and MMT estimates for CCMVal-1 and CCMVal-2 .....	368
Figure 9.22: Date of return to 1960 (left) and 1980 (right) values for the annual average (tropical and mid-latitude) and spring (polar) total ozone column derived from the IMT and MMT ]estimates for CCMVal-2.. ....	369
Figure 9.23: Date of return to 1960 and 1980 values for the annual average 50 hPa $Cl_y$ derived from the IMT and MMT estimates for CCMVal-2. ....	369
Figure 9.24: Relationship between the date of return of $Cl_y$ to the 1980 value compared with the date of return of column ozone for the selected latitude ranges in Figure 9.20.....	370
Figure 9.25: Date of return of the annual mean ozone to the value appropriate to the reference year indicated on the abscissa. ....	371
Figure 9.26: The average seasonal cycle of total column ozone over NH and SH mid-latitudes for two periods and its change.....	372
Figure 9.27: The relationship between the recovery date of mid-latitude (35°-60°) annual average ozone from the MMT analysis and the change in amplitude of the seasonal cycle of ozone averaged over the spring in each hemisphere. ....	373



## Chapter 10: Effects of the stratosphere on the troposphere

Figure 10.1: JFM multi-model errors in zonal-mean zonal wind.....	384
Figure 10.2: CCMVal-2 seasonal mean combined performance for u, v, and T..	386
Figure 10.3: Comparison between CCMVal-2 and CCMVal-1 for u and T.....	386
Figure 10.4: Median uncertainty comparison between CCMVal-2 (REF-B1) and CMIP3 (AMIP experiment) for u, v, and T combined. ....	388
Figure 10.5: Composite differences of the standardized NAM index between strong and weak stratospheric events. ....	389
Figure 10.6: Composite differences of the standardized SAM index between strong and weak stratospheric events .....	390
Figure 10.7: The RMS amplitude of the annular mode pattern of variability as a function of pressure in the NH and SH.....	391
Figure 10.8: The variance of the NAM and SAM indices as a function of seasonal and height: ECMWF reanalysis and the multi-model ensemble mean. ....	392
Figure 10.9: The e-folding time scale of the NAM and SAM indices as a function of seasonal and height: ECMWF reanalysis and the multi-model ensemble mean.....	392
Figure 10.10: The fraction of the variance of the monthly mean 850 hPa AM index, lagged by 10 days, that is linearly correlated with the instantaneous AM index as a function of season and height: ECMWF reanalysis and the multi-model ensemble mean.....	392
Figure 10.11: The annular mode e-folding time scale (left) in the lower stratosphere and (right) mid-troposphere as a function of season for the CCMVal-2 models: (top) NH, (bottom) SH.	393
Figure 10.12: Seasonal cycle of linear trends (1969-1998) in temperature and geopotential height over the Antarctic. ....	394
Figure 10.13: 30-yr trends (1969-1998) in Antarctic September-December total ozone versus the October-January temperature trend at 100-hPa.....	395
Figure 10.14: Long-term mean and linear trend of the DJF-mean zonal-mean zonal wind (a) for the time period of 1960-1999 in REF-B1 runs, and (b) for the time period of 2000-2079 in REF-B2 runs.....	396
Figure 10.15: Trend relationship between SON-December-mean ozone at 50 hPa integrated south of 64°S and variables of interest: ONDJ-mean temperature at 100 hPa integrated south of 64°S, DJF-mean extra-tropical tropopause pressure integrated south of 50°S, location of the DJF-mean zonal wind maximum at 850 hPa, and location of the SH Hadley cell boundary at 500 hPa. ....	397
Figure 10.16: SH circulation changes as simulated by the SPARC/CCMVal-2 models and four sets of the IPCC/AR4 models.....	398
Figure 10.17: REF-B1 Runs: Annual means of surface clear-sky erythemal irradiance changes (in %, relative to 1965-1979) for five latitude belts. ....	399
Figure 10.18: REF-B2 runs. Annual means of surface clear-sky erythemal irradiance changes (in %, relative to 1965-1979) for five latitude belts. ....	400
Figure 10.19: (a) Average of surface erythemal irradiance for October - November at 75°S-90°S. (b) same as in (a) but for March -April at 90°N-75°N.....	401
Figure 10.20: 20-year averages of clear-sky and all-sky erythemal irradiance changes (%) for January and July with respect to the 1965-1979 average.....	402

Figure 10.21: Calculated changes in global mean ozone-induced radiative forcing evaluated at the tropopause based on simulated ozone in 17 REF-B1 simulations and a fixed dynamical heating model.....403

Figure 10.22: Multi-model comparison of the time evolution of global, northern hemispheric, southern hemispheric stratospheric ozone flux into the troposphere between 1960 and 2100 derived from CCMVal-2 models.....405

**Appendix B: Time Series Additive-Model Analysis**

Figure B.1: CCMVal-1 time series of monthly averaged total column ozone in the latitude band 60°N-90°N for March and in the latitude band 60°S-90°S for October. ....420

Figure B.2: The initial estimate of the individual model trends  $h_j(t)$  for the raw time series displayed in Figure B.1, the 1980 baseline-adjusted time series data  $y'_{jk}$  with  $t_0 = 1980$ , and the 1980 baseline-adjusted trend estimate  $h'_j(t)$ .....421

Figure B.3: Individual model autocorrelation functions for the residuals  $\varepsilon_{jk}(t)$  for CCMVal-1 October total column ozone in the latitude band 60°S-90°S. This noise corresponds to the nonparametric model (9.8) with 1980 baseline trend estimates  $h_j(t)$  displayed in Figure B.2f.....422

Figure B.4: Individual model autocorrelation functions for the noise term  $\varepsilon_{jk}(t)$  for CCMVal-1 October total column ozone in the latitude band 60°S-90°S. This noise corresponds to the simpler nonparametric model(9.9) with a 1980 baseline trend estimate  $g(t)$  displayed in Figure B.2d. ....423

Figure B.5: Individual model notched box-and-whisker plots for the noise term  $\varepsilon_{jk}(t)$  corresponding to the simpler nonparametric additive model (B.8) and for the noise term  $\varepsilon_{jk}(t)$  corresponding to the nonparametric additive model (B.7).....424

Figure B.6: For time series of CCMVal-1 October total column ozone in the latitude band 60°S-90°S are presented the individual model fits, weights, and trend (MMT) estimate for three approaches.....425

# Acknowledgements

---

## Review Editors:

Chapter 1:  
Chapter 2:  
Chapter 3:  
Chapter 4: Neil Harris  
Chapter 5:

Chapter 6:  
Chapter 7:  
Chapter 8: Leslie Gray  
Chapter 9:  
Chapter 10:

## Author List:

Hideharu Akiyoshi  
Juan A. Añel  
John Austin  
Trevor Bailey  
Mark P. Baldwin  
Andreas Baumgaertner  
Slimane Bekki  
Huisheng Bian  
Thomas Birner  
Christian Blume  
Greg Bodeker  
Peter Braesicke  
Christoph Brühl  
Neal Butchart  
Chiara Cagnazzo  
Natalia Calvo  
Tim Canty  
Andrew J. Charlton-Perez  
Martyn Chipperfield  
Irene Cionni  
Martin Dameris  
Sandip Dhomse

Anne Douglass  
Anu Dudhia  
Veronika Eyring  
Victoria Falaleeva  
Pier Giuseppe Fogli  
Victor Fomichev  
Boris Fomin  
Piers M. Forster  
Stacey Frith  
Lucien Froidevaux  
Masatomo Fujiwara  
Ryan Fuller  
Hella Garny  
Edwin P. Gerber  
Andrew Gettelman  
Nathan Gillett  
Marco Giorgetta  
Lesley Gray  
Steven Hardiman  
Michaela Hegglin  
Peter Hoor  
Petra Huck

Michael Iacono  
Ben Johnson  
Ashley Jones  
Andreas I. Jonsson  
Alexey Karpechko  
Junsu Kim  
Doug Kinnison  
Kuni Kodera  
Stefanie Kremser  
Kirstin Krüger  
Markus Kunze  
Paul Kushner  
Jean-François Lamarque  
Ulrike Langematz  
Huikyo Lee  
Perrine Lemennais  
Jiangnan Li  
Beiping Luo  
Gloria Manney  
Elisa Manzini  
Katja Matthes  
Bernard Mayer  
Martine Michou  
Eli Mlawer  
Olaf Morgenstern  
Gunnar Myhre  
Jessica Neu  
Paul Newman  
Eric Nielsen  
Sophie Oberländer  
Luke Oman  
Cristina Pena Ortiz  
Scott M. Osprey  
Laura Pan  
Diane Pendlebury  
Judith Perlwitz  
Giovanni Pitari  
David Plummer  
Robert Portmann  
Virginie Poulain

Michael Prather  
Bill Randel  
Thomas Reichler  
Markus Rex  
Alexei Rozanov  
Eugene Rozanov  
Ross Salawich  
Michelle Santee  
Fabrizo Sassi  
John Scinocca  
Ted Shepherd  
Kiyotaka Shibata  
Michael Sigmond  
Bjorn-Martin Sinnbuer  
Dan Smale  
Seok-Woo Son  
Gera Stenchikov  
David Stephenson  
Gabriele Stiller  
Susan Strahan  
Hamish Struthers  
Susann Tegtmeier  
Wenshou Tian  
Simone Tilmes  
Claudia Timmreck  
Matthew Toohey  
Kleareti Tourpali  
Jo Urban  
Kaley Walker  
Lei Wang  
Darryn Waugh  
Don Wuebbles  
Shigeo Yoden

**Modelling Groups:****AMTRAC3**

J. Austin  
R. J. Wilson  
D. Schwarzkopf

**CAM3.5**

C. Fischer  
D. Kinnison  
F. Vitt

**CCSRNIES**

Hideharu Akiyoshi (NIES)  
Yousuke Yamashita (CCSR/NIES)  
Tetsu Nakamura (NIES)  
Jun-ichi Kurokawa (NIES)  
Tatsuya Nagashima (NIES)  
Masaaki Takahashi (CCSR)  
Takashi Imamura (NIES)  
Center for Global Environmental Research  
(NEC-SX8R super computer, NIES)

**CMAM**

Stephen Beagley  
Victor Fomichev  
Michaela Hegglin  
Andreas Jonsson  
Charles McLandress  
Michael Neish  
David Plummer  
Cathy Reader  
John Scinocca  
Kirill Semeniuk  
Larry Solheim

**CNRM-ACM**

Françoise Chéroux  
David Saint-Martin  
Martine Michou  
Dirk Olivie  
Hubert Teyssède  
Aurore Voldoire

**E39CA**

Irene Cionni  
Martin Dameris  
Veronika Eyring  
Rudolf Deckert  
Hella Garny  
Volker Grewe  
Birgit Hassler  
Sigrun Matthes  
Michael Ponater  
Andrea Stenke

**EMAC****GEOSCCM**

Richard Stolarski  
Paul Newman  
Luke Oman  
Brian Duncan  
Stacey Frith  
Eric Nielsen  
Steven Pawson  
Stephen R. Kawa  
Ann Douglass  
Feng Li  
Qing Liang

**LMDZrepro**

David Cugnet  
Marion Marchand  
Franck Lefevre  
Francois Lott  
Slimane Bekki

**MRI****NiwaSOCOL**

Dan Smale, NIWA, Lauder, NZ  
Eugene Rozanov, PMOD/WRC & ETH, Davos,  
Switzerland  
Greg Bodeker, NIWA, Lauder, NZ\*  
Irene Cionni, NIWA, Lauder, NZ\*  
Hella Garny, Oberpfaffenhofen, Germany

Olaf Morgenstern, NIWA, Lauder, NZ  
Martin Schraner, ETH, Zurich, Switzerland  
Andreas Fischer, ETH, Zurich, Switzerland  
Tatiana Egorova, PMOD/WRC & ETH, Davos,  
Switzerland  
Hamish Struthers, NIWA, Lauder, NZ\*

### **SOCOL**

#### **ULAQ**

Giovanni Pitari  
Eva Mancini  
Natalia De Luca

#### **UMETRAC**

John Austin  
Greg Bodeker  
Neal Butchart  
Irene Cionni  
Sam Dean  
Olaf Morgenstern  
Hamish Struthers

#### **UMSLIMCAT**

Martyn Chipperfield  
Sandip Dhomse  
Wenshou Tian

#### **UMUKCA-METO**

Neal Butchart  
Steven C. Hardiman  
M. Skekar Reddy  
Ian Edmond  
We also had direct help from  
Olaf Morgenstern (University of Cambridge,  
now at NIWA)

#### **UMUKCA-UCAM**

Peter Braesicke  
Andrew Bushell  
Martyn Chipperfield  
Colin Johnson  
Margaret Hurwitz  
Genevieve Millard  
Olaf Morgenstern

Fiona O'Connor  
Scott Osprey  
John Pyle  
Oliver Wild  
Glenn Carver  
Guang Zeng

### **WACCM**

Rolando R. Garcia  
Doug E. Kinnison  
Andrew Gettelman  
Dan R. Marsh  
Jadwiga H. Richter  
Hanli Liu  
Chris Fischer  
Francis Vitt

# Executive Summary

---

## Preface

Three-dimensional climate models with a fully interactive representation of stratospheric ozone chemistry — otherwise known as stratosphere-resolving chemistry-climate models (CCMs) — are key tools for the attribution and prediction of stratospheric ozone changes arising from the combined effects of changes in the amounts of greenhouse gases (GHG) and ozone-depleting substances (ODS). These models can also be used to infer potential effects of stratospheric changes on the climate of the troposphere. In order to know how much confidence can be placed in the results from the CCMs, both individually and collectively, it is necessary to assess their performance by comparison with observations and known physical constraints.

The Stratospheric Processes And their Role in Climate (SPARC) core project of the World Climate Research Programme (WCRP) initiated the CCM Validation (CCMVal) activity in 2003 to coordinate exactly such an evaluation. The CCMVal concept (see Chapter 1) takes as a starting point the premise that model performance is most accurately assessed by examining the representation of key processes, rather than just the model's ability to reproduce long-term ozone trends, as the latter can be more easily tuned and can include compensating errors. Thus a premium is placed on high-quality observations that can be used to assess the representation of key processes in the models. This Report does not provide a detailed assessment of the quality of the observational databases; the compilation and assessment of data sets suitable for model evaluation is the focus of a future SPARC activity, which has been motivated by this Report.

The first round of CCMVal (CCMVal-1) evaluated only a limited set of key processes in the CCMs, focusing mainly on dynamics and transport. This Report, which describes the second round of CCMVal (CCMVal-2), represents a more complete effort by CCMVal to assess CCM performance. As with CCMVal-1, it also includes an assessment of the extent to which CCMs are able to reproduce past observations in the stratosphere, and the future evolution of stratospheric ozone and climate under one particular scenario. A key aspect of the model evaluation within this Report is the application of observationally-based performance metrics to quantify the ability of models to reproduce key processes for stratospheric ozone and its impact on climate. The Report is targeted at a variety of users, including: (1) international climate science assessments, including the WMO/UNEP Ozone Assessments and the IPCC Assessment Reports; (2) the CCM groups themselves; (3) users of CCM simulations; (4) measurement and process scientists who wish to help improve CCM evaluation; (5) space agencies and other bodies involved in the Global Climate Observing System.

The Report was prepared by dozens of scientists and underwent several revisions and extensive peer review, culminating in a Final Review Meeting in Toledo, Spain on November 9-11, 2009. This Executive Summary outlines the overall key findings, overall recommendations, and detailed key findings and recommendations by chapter.

## Overall Key Findings

- Comprehensive process-oriented validation has led to a much better understanding of the strengths and weaknesses of CCMs. As well as identifying unphysical behaviour (*e.g.*, dehydration properties), this has led to a more precise understanding of the processes involved in CCM simulations and the connections between them. This can be used to understand some of the spread in model predictions, and will help focus model improvements.
- CCMVal-2 has provided a much more detailed assessment of model performance than CCMVal-1. For the first time, chemical and radiative processes in the CCMs have been assessed, and the upper troposphere / lower stratosphere (UTLS) has been explicitly examined. Radiation schemes have been found to be sufficient for representing the major causes of observed temperature changes in the stratosphere and the main radiative drivers of surface climate. Chemistry schemes are generally found to agree with benchmark schemes, while exceptions have been identified. Model performance in the UTLS was found to be better than might have been expected based on the spatial resolution of the models.
- The identification of model deficiencies in CCMVal-1 led to quantifiable improvements in particular models (*e.g.*, transport, Cl<sub>y</sub> abundance, tropical tropopause temperatures). CCMVal-2 has benefited from the greater number of participating models and the larger number of processes represented in those models. However, this complicates a quantitative assessment of overall model improvement between CCMVal-1 and CCMVal-2 in those diagnostics assessed by CCMVal-1.
- Compared with WRCF Coupled Model Intercomparison Project phase 3 (CMIP3) simulations, CCMVal-2 simulations have a mean stratospheric climate and variability that is much closer to that observed. In the troposphere, mean climate and synoptic variability are similarly close to the observations in both groups of simulations, while interannual variability tends to be better simulated by the CCMVal models.
- Common systematic errors in CCM results include: tropical lower stratospheric temperature, water vapour, and transport; response to volcanic eruptions; details of the Antarctic polar vortex and the ozone hole; lower stratospheric Cl<sub>y</sub>; a wide variation in values of surface area density of sulphate aerosols.
- Another systematic error in CCMs concerns the representation of the quasi-biennial oscillation (QBO), which is a dominant mode of natural stratospheric variability. Most of the current models do not simulate a QBO, and the representation of the QBO in models remains a challenge. For comparison with past observations, some modelling groups therefore choose to relax tropical winds towards observed values. This technique is fully successful in reproducing the phase of the observed QBO signal in ozone, but not its amplitude.
- Models that represent solar variability only in terms of total solar irradiance cannot properly simulate the effect of solar variability on radiative heating rates, stratospheric temperature and ozone. A spectrally resolved treatment of solar variability is required.
- Use of simulations extending through the entire period of ozone depletion and recovery (1960-2100) in CCMVal-2 has allowed a more accurate estimate of the projected long-term changes in the stratosphere and the relative contributions of ODSs and GHGs to those changes, compared with CCMVal-1. This, plus the increased number of contributing models, has reduced the statistical uncertainty in the projected future ozone changes under the scenario considered.
- The multi-model trend estimates of past ozone changes are consistent with the observed changes. Compared with CCMVal-1, the availability of model simulations from 1960 onwards together with a more robust statistical analysis has provided a more reliable estimate of the long-term ozone changes in the models.
- Widespread use of simulations beginning in 1960 has revealed that models consistently show substantial ODS-induced ozone depletion prior to 1980, especially in the SH.
- Models consistently predict an increase in tropical tropopause height and a slight warming of the tropical tropopause due to climate change. As a result, the entry value of stratospheric water vapour is predicted to increase in the future, although the magnitude of this increase is uncertain.



- Models consistently predict a strengthening of the Brewer-Dobson circulation and a decrease in mean age of air as a result of climate change, but they disagree on the relative role of resolved and parameterised wave drag.
- Models consistently predict the following changes in ozone:
  - a partial recovery of tropical ozone followed by a decrease in the second half of the 21<sup>st</sup> century, such that tropical column ozone is predicted not even to return to 1980s values within this century; the long-term decrease is mainly found in the lower stratosphere
  - a steady increase in NH mid-latitude and polar ozone, such that 1980s values are exceeded well before halogens return to 1980s values
  - a slow recovery of SH mid-latitude and polar ozone, with mid-latitude ozone returning to 1980 values slightly before halogens do, and polar ozone returning roughly in line with halogens
  - major contributors to these changes include the recovery of ozone from ODS, the strengthened Brewer-Dobson circulation, and the cooling of the upper stratosphere.
- Although Antarctic ozone is expected to recover during the 21<sup>st</sup> century, a residual intermittent ozone hole may still occur at the end of the century.
- Both models and observations indicate that Antarctic stratospheric ozone loss, together with increasing GHG concentrations, has led to a poleward shift and strengthening of the SH westerly tropospheric jet during summer. CCMVal-2 models project that in the 21<sup>st</sup> century ozone recovery will largely offset the effects of increasing GHG concentrations, so that the position of the tropospheric jet will not change significantly.
- The strengthened Brewer-Dobson circulation leads to an increased stratospheric ozone flux into the NH troposphere of ~20% between 1965 and 2095. In the SH, the change is modulated by ozone depletion and recovery, and is smaller (~10%) due to the smaller predicted change in the Brewer-Dobson circulation in that hemisphere. The model range is smaller than that obtained from tropospheric models used for the IPCC assessment, which may be attributable to a more self-consistent and comprehensive representation of the stratosphere in the CCMs.
- Stratosphere-resolving CCMs continue to evolve towards more comprehensive, self-consistent stratosphere-troposphere CCMs. In this round of CCMVal, one model was coupled to an interactive ocean, while three models included comprehensive tropospheric chemistry. These developments provide a pathway for including a better representation of stratosphere-troposphere and chemistry-climate coupling in Earth System models used for ozone and climate assessments.

## Overall Recommendations

- CCM simulations of ozone depletion/recovery should be performed seamlessly over the entire 1960-2100 period, with consistent forcings, and with data produced in a standard format to allow for multi-model inter-comparison.
- A range of different scenarios should be simulated (*e.g.*, fixed GHG, fixed ODS, different GHG projections) to allow correct attribution of the predicted changes and an understanding of the sensitivity to the scenario employed.
- Models should routinely undergo tests concerning their implementation of physical processes where benchmark comparisons are available. This is especially the case for chemistry and radiation (*e.g.*, line-by-line comparisons, PhotoComp). In the case of radiation, such comparison is facilitated if the CCM radiation codes can be run in a stand-alone offline form.
- Metrics of model performance on a wide suite of diagnostics need to be made as standard practice and calculated routinely by individual model groups and through multi-model comparisons. More analysis is needed of the robustness of the application and interpretation of metrics, and their possible use to assign relative weights to ozone projections.
- More attention needs to be paid to model development to address major persistent deficiencies, *e.g.*, the

late-spring breakdown of the Antarctic vortex, and simulations of the Antarctic ozone hole.

- Long-term vertically resolved data sets of constituent observations in the stratosphere are required to assess model behaviour and test model predictions. This includes ozone, but also other species that can be used to diagnose transport and chemistry. The current set of GCOS Essential Climate Variables is not sufficient for process-oriented validation of CCMs.
- More global vertically resolved observations are required, particularly in the UTLS. As CCMs evolve towards including tropospheric chemistry, lack of observations in this region will become a major limitation on model validation.
- A systematic comparison of existing observations is required in order to underpin future model evaluation efforts, by providing a more accurate assessment of measurement uncertainties.
- CCMs should use self-consistent formulations with the appropriate conservation properties (*e.g.*, primitive-equations dynamics, self-consistent treatment of chemistry, a unified treatment of photolysis and short-wave heating, a prognostic water vapour field, momentum-conserving gravity-wave drag).
- Development should continue towards comprehensive troposphere-stratosphere CCMs, which include an interactive ocean, tropospheric chemistry, a naturally occurring QBO, spectrally resolved solar irradiance, and a fully resolved stratosphere.
- The CCMVal assessment and projection process should be synchronized with that of CMIP to make the maximum use of human and computer resources, and to allow time for model improvements.

## Key Findings by Chapter

### CHAPTER 2

- CCMs have undergone considerable development since the CCMVal-1 inter-comparison. For CCMVal-2 there were
  - 18 models participating, with 13 models producing a total of 22 REF-B2 simulations covering the requested 1960-2100 time period. In contrast, 11 models participated in CCMVal-1, with 1 model producing 3 REF2 simulations covering the entire 1960-2100 time period.
  - 5 models using online photolysis (*vs.* 3 for CCMVal-1);
  - 3 models using comprehensive tropospheric chemistry (*vs.* 1 for CCMVal-1);
  - 3 models having implemented improved transport schemes since CCMVal-1;
  - 1 model using an interactive ocean (*vs.* 0 for CCMVal-1);
- 4 new models contributed to the CCMVal-2 activity. While it should be noted that model improvements do not necessarily translate into improvements in model performance, the developments listed above, along with numerous smaller changes across the models, demonstrate progress made in the state-of-the-art of CCM modelling over the period since CCMVal-1.
- An unprecedented level of documentation concerning the models has been achieved. This has been invaluable in understanding model behaviour.

### CHAPTER 3

- CCM global mean temperatures and their change can give an indication of errors in radiative transfer codes and/or atmospheric composition. Biases in the global mean temperature climatology are generally small, although 5 out of 18 CCMs show biases that likely indicate problems with their radiative transfer codes. Temperature trends also generally agree well with observations, although one model shows significant discrepancies that appear to be due to radiation errors.
- Heating rates and estimated temperature changes from CO<sub>2</sub>, ozone and water vapour changes are generally well modelled. Other gases (N<sub>2</sub>O, CH<sub>4</sub>, CFCs) have only played a minor role in stratospheric temperature

change but their heating rates are estimated with large fractional errors in many models.

- Models that do not account for variations in the spectrum of solar irradiance but only consider changes in total (spectrally-integrated) solar irradiance cannot properly simulate solar-induced variations in stratospheric temperature.
- The combined long-lived greenhouse gas global annual mean instantaneous net radiative forcing at the tropopause is within 30% of that from line-by-line models for all CCM radiation codes tested. Problems remain simulating radiative forcing for stratospheric water vapour and ozone changes, with a range of errors between 3% and 200% compared to line-by-line models.

#### CHAPTER 4

- Climatological mean polar temperature biases are generally small ( $< 5$  K) across the model ensemble except in the southern hemisphere (SH) lower stratosphere during spring. On average models produce the correct accumulated-area of Antarctic temperatures low enough for ice PSC formation, but too small accumulated-area for NAT PSC formation. In the Arctic, there is a large model spread in PSC area, and in general the PSC areas are smaller than reanalysis estimates.
- The model ensemble reproduces the structure of the polar night jet well, apart from the equator-ward tilt in the SH upper stratosphere. There are significant late biases in the spring-time breakup of the SH vortex. Polar night jet variability is not well reproduced by the models and has a large variation amongst the models.
- The orientation and shape of the polar vortex is well captured by the majority of models, but there are some significant outliers in the SH which are biased towards large amplitudes of zonal wavenumber 2.
- Tropical upwelling velocity is well simulated in the lower stratosphere compared to analyses, but is slightly too strong in the middle stratosphere. There is large disagreement between models on the relative contribution of resolved and parameterised (sub-grid-scale) waves to driving the Brewer-Dobson circulation.
- A common weakness of all models in the tropical upper stratosphere is a weak annual cycle in zonal-mean zonal winds, which is independent of the treatment of the QBO in models. Only a few of the CCMVal-2 models simulated a QBO-like oscillation in tropical winds. In the majority of models the QBO was absent or artificially forced.
- There is a wide spread in both the mean frequency of major stratospheric sudden warmings (SSWs) and their seasonal distribution in the models. No major SSWs were found in the SH of any of the simulations.
- Many of the persistent biases present in CCMVal-1, particularly temperature bias in the SH lower stratosphere spring and the late breakup of the Antarctic vortex, have not significantly improved in the CCMVal-2 models.
- Models simulate robust and consistent trends in southern hemisphere polar temperatures, PSC areas and final warming dates, with opposite trends during the periods of strong ozone depletion and recovery.
- In the Northern Hemisphere (NH) lower and middle polar stratosphere models on average show no significant long-term changes in winter-time temperature.
- There is a strong consensus between models that the strength of the Brewer-Dobson circulation will increase, with about a 2% per decade increase in the tropical upwelling mass flux over the 21st century. There is, however, little agreement between models on the relative contributions of resolved and parameterised waves to this trend.
- Models do not predict large changes in mid- and high-latitude 100 hPa meridional heat-flux or stratospheric stationary-wave amplitude over the 21st century.

#### CHAPTER 5

- Model tracer-derived vertical velocities tend to be faster than the observed tracer-derived vertical velocities in the tropical lower stratosphere. This appears not to be related to errors in zonal-mean upwelling. In the tropical middle stratosphere, both the modelled residual vertical velocity and the tracer-derived velocities

show better agreement with observations.

- Errors in vertical transport in models complicate the interpretation of tropical-extra-tropical mixing diagnostics that depend on the attenuation of tracer signals since the attenuation cannot be assumed to result primarily from dilution by tropical-extra-tropical mixing.
- The average of all mean age diagnostic grades provides a very useful integrated transport assessment. Comparing modelled and observed mean ages over a wide range of latitudes and altitudes is a more reliable indication of transport credibility than individual mean age diagnostics because it is difficult to match the mean age everywhere through compensating errors. Seven of 15 models performed well on average mean age grade.
- There is a positive correlation between the average mean age grade and these key diagnostics: tropical ascent, tropical-mid-latitude mixing, and Antarctic descent. Tropical ascent and polar descent are physically linked through the diabatic circulation, and the average mean age grade depends on both the diabatic circulation and quasi-horizontal mixing, particularly between the tropics and mid-latitudes. Because of the physical basis for these correlations, good performance on all of these fundamental diagnostics is essential for building model credibility.
- Lower stratospheric Antarctic vortex isolation is not correlated with the average mean age grade, suggesting that the transport barrier at the vortex edge is, to first order, independent of the overall transport circulation. Because vortex isolation is a requirement for confining perturbed chemistry and producing a realistic ozone hole, it is essential to include this transport diagnostic in evaluations of simulations predicting future ozone. Eight of 13 models evaluated for vortex isolation had adequate Antarctic vortex isolation in the lower stratosphere. Of these, only four also performed well on the average mean age grade.
- Despite the spread in model performance revealed by the transport diagnostics, all 10 CCMs running the REF-B2 future scenario predict a faster circulation (based on mean age gradients) and younger mean age at the end of the 21<sup>st</sup> century, indicating that this is a robust result.

## CHAPTER 6

- An accurate representation of photolysis rates is an essential component of any CCM chemical scheme. This chapter defined a photolysis benchmark (PhotoComp-2008) for assessing photolysis rates based on a robust mean and standard deviation for the ensemble of contributing models. PhotoComp was completed by 9 of the 18 CCMVal models of which the majority showed good agreement with the benchmark. However, there are several models that should consider improving their photolysis approach or verify photochemical data for certain species.
- Comparison of the fast (radical) photochemistry results from the CCMs with a benchmark photochemical steady state (PSS) model constrained by the abundance of long-lived species and sulfate surface area density (SAD) from each CCM generally shows very good agreement. This indicates that, for a given chemical background, most CCMs calculate the abundance of radicals that regulate ozone in a realistic manner, while exceptions were easily identified.
- Despite the stratospheric sulfate surface area density (SAD) being one of the specified forcings in the CCMVal runs, there is a wide variation in the values of SAD used inside the chemistry calculations.
- Some CCMs show a lack of conservation of tracer mixing ratios. This results in the total abundance of, for example, chlorine or bromine being larger than that specified as the time-dependent surface boundary condition and is likely due to non-conservation in the models' tracer advection. In addition, not all models followed the specified CCMVal-2 halocarbon scenarios, which complicates interpretation of long-term ozone changes. For bromine some models also included a source due to very short-lived bromocarbons, resulting in a larger inter-model variability in total inorganic bromine (Br<sub>y</sub>).
- For the distribution of source gases the most significant potential source of error in the chemistry is in the photolysis (see first bullet). Model long-lived tracer-tracer correlations, which are not necessarily sensitive to this, agree well with observations.

- For H<sub>2</sub>O there is a large spread in CCM stratospheric values. A lot of this spread is related to a spread in stratospheric entry values, but there also appear to be models with an incorrect stratospheric source from CH<sub>4</sub> oxidation. These errors in stratospheric H<sub>2</sub>O will impact on chemistry *via* HO<sub>x</sub> and heterogeneous chemistry.
- For the reservoir species CCMs generally capture the expected spatial and seasonal variations. However, there are significant discrepancies for some models and certain species. These discrepancies, for example in N<sub>2</sub>O<sub>5</sub>, ClONO<sub>2</sub> and HNO<sub>3</sub>, are larger than the expected model chemical variability. Moreover, in some cases the abundance of HCl, the main Cl<sub>y</sub> reservoir, exceeds the limit of chlorine imposed by the halocarbon scenarios. This can be due to non-conservation (see above) or differences in stratospheric entry values of inorganic chlorine due to inadequate treatment of tropospheric removal.
- Most models overestimate the abundance of gas-phase HNO<sub>3</sub> in the Antarctic winter/spring relative to observations. A few models get the minimum abundance of HNO<sub>3</sub> correct with season, but do not represent the vertical extent correctly. These discrepancies point to either biases in the model temperature or shortcomings in the denitrification scheme. CCMs tend to do a better job representing the evolution of gas-phase H<sub>2</sub>O in the same region and period. In addition, the model surface area densities for HNO<sub>3</sub> (*e.g.*, NAT) and H<sub>2</sub>O containing aerosols vary by a factor of ~10 within each PSC type. More work is needed to compare model PSCs parameters with available observations.
- The conversion of HCl to more reactive species is generally well represented in the Antarctic winter/spring. Most CCMs show near complete conversion of HCl to reactive species in the 500-600 K region between June and September. Below 500 K many models have too high abundance of HCl suggesting the process of activation is not well represented in this region. All but a few models have HCl recovering to an abundance consistent with observations by October.
- Most CCMs accurately represent chemical ozone loss in the Antarctic spring. There are clearly exceptions. Some models agree well with the loss inferred from observations, but not under the correct dynamical conditions. Some CCMs under-estimate chemical ozone loss even though the dynamics are well represented. Only a few models correctly represent the observed chemical ozone loss in the Arctic. CCMs are typically biased warm or do not have the correct variability in this region. These errors are reflected in the multi-model mean for this process, where the Antarctic is consistent with observations and the Arctic under-estimates chemical ozone loss.

## CHAPTER 7

- Several of the CCMs analysed reproduce key observed features in the UTLS (including tracer gradients across the extra-tropical tropopause) even with a fairly coarse vertical (1 km) and horizontal (200-400 km) resolution. CCMVal-2 models with semi-Lagrangian transport schemes show too much mixing across the extra-tropical tropopause.
- The tropical tropopause pressure and cold-point temperature (CPT) exhibit significant biases compared to observations and between models, although the seasonal cycles are reasonable. These biases result in a wide range of tropical lower stratospheric H<sub>2</sub>O values. Comparison of the CPT with H<sub>2</sub>O reveals in some cases unphysical simulated transport behaviour.
- Lowermost stratosphere (LMS) mass (which is an indicator of tropopause pressure) shows a wide range of skill, with a large number of models performing well, but many performing very poorly. The performance is generally better in the NH than in the SH. The difference can be explained by smaller variations in the LMS mass in the SH, which are more difficult to be captured by the models.
- The seasonal cycle of O<sub>3</sub> in the extra-tropical UTLS is for most models quite good, however the amplitude is generally too high at 100 hPa and too low at 200 hPa. The models have difficulties representing both the amplitude and phase of the seasonal cycle in H<sub>2</sub>O.
- CCMVal simulations into the future exhibit a clear signature of stratospheric O<sub>3</sub> depletion and recovery in their extra-tropical tropopause pressure trends. The signature is much stronger in the SH than in the NH,

where ozone depletion is weaker.

- Simulations show good historical fidelity with observed tropical tropopause pressure trends, and project decreases in tropical tropopause pressure in the 21<sup>st</sup> century. The rising tropopause is associated with increasing tropical tropopause temperatures and water vapour in the tropical lower stratosphere.

## CHAPTER 8

- The annual cycles in column ozone and profile ozone are quite well represented in the majority of the models. In the SH polar lower stratosphere, a few models do not reproduce the anthropogenic induced annual cycle (polar ozone depletion) that dominates the column ozone evolution in later winter and spring.
- All models show the expected minimum in polar variability in the respective summer seasons. However, in the NH active period most of the models tend to under-estimate the interannual polar ozone variability. In the SH, the models both over- and under-estimate interannual polar ozone variability.
- Most models capture the connections between the dynamical processes responsible for the interannual polar ozone variations and the ozone response. Moreover, models with poor performance in interannual polar variability also tend to perform poorly in the diagnosed dynamics-ozone connections.
- The annual mean of the solar cycle in column ozone is well represented by most models, although with some amplitude spread. The latitudinal representation of the solar response in column ozone shows improvements from earlier studies, but a large spread remains especially at mid- to high latitudes due to large interannual variability.
- The direct solar response in temperature and ozone in the upper stratosphere is well represented by most models. Large differences in the vertical structure of the solar signal occur in the tropics below 10 hPa between the models but also between different observational data sets. Uncertainties in the lower stratosphere might be related to non-linear interactions or aliasing with other signals such as the QBO, ENSO, and volcanoes.
- The technique of assimilating the QBO winds or vorticity improves the modelled variability in ozone. However, biases in the amplitude of the QBO ozone signal in the models with the assimilated QBO are comparable to those from models with an internally generated QBO.
- The observed tropical ENSO signal in temperature and ozone is evident in the models, especially in the lower stratosphere where most of the models show a cooling and an ozone reduction. Because of the large role of interannual variability, it is not possible to assess model representation of the extra-tropical ENSO signal in ozone.
- The volcanic signal in ozone differs considerably between models and depends on the method by which the direct effect of volcanic aerosols on the radiative transfer of the stratosphere is represented. This limits the ability to evaluate model performance in simulating the volcanic signal. None of the models reproduce the observed hemispheric asymmetry in post-Pinatubo ozone loss, for either full hemispheric means or for mid-latitudes.

## CHAPTER 9

- The multi-model trend estimates of past ozone changes are consistent with the observed changes. Compared with CCMVal-1, the availability of model simulations from 1960 onwards, together with a more robust statistical analysis, has provided a more reliable estimate of model behaviour.
- Models consistently show substantial ODS-induced ozone depletion prior to 1980, especially in the SH.
- Nearly all models completed simulations covering the 1960-2100 period. This provides a stronger basis from which to form an assessment of ozone projections than was previously available under CCMVal-1. This, plus the increased number of contributing models, has decreased the statistical uncertainty in the projected future ozone changes.
- Models generally predict only a small amount of chemical ozone depletion in tropical latitudes. The effect

of the expected strengthened tropical upwelling from climate change is to lower ozone column amounts, such that tropical column ozone may not return even to the values of the 1980s.

- In mid-latitudes, the future column ozone is predicted to recover faster in the NH than in the SH, due to a combination of a stronger Brewer-Dobson circulation in the NH and transport of low ozone from the Antarctic ozone hole in the SH. The projected increase in  $N_2O$  appears to play a minor role in ozone depletion for the scenario considered, in part because the impact of stratospheric climate change is to reduce the trend in reactive nitrogen amounts.
- Models consistently predict an increase in Arctic ozone from climate change, such that ozone will return to 1980 values before halogens will. This finding has resulted from the more robust statistical approach together with the longer time series, compared with those used in CCMVal-1. However, the large range in model projections, and natural variability, limit the confidence that can be placed in this conclusion.
- While many models simulate reasonably well the Antarctic ozone hole area and depth, based on the standard 220 DU threshold, most do not. This is due to a number of factors, including a large ozone bias in some models and a polar vortex that is typically too small in extent.
- In the models that simulate the current ozone hole well, a residual, *albeit* intermittent ozone hole remains at the end of the 21<sup>st</sup> century.

## CHAPTER 10

- Compared with CMIP3 simulations, CCMVal-2 simulations have a mean stratospheric climate and variability that is much closer to the observations, based on pointwise comparisons of zonal-mean winds and temperature. In the troposphere, mean climate and synoptic variability are similarly close to the observations in both groups of simulations, while interannual variability tends to be better simulated by the CCMVal models.
- CCMVal-2 models simulate a downward propagation of annular mode anomalies in both hemispheres similar to that observed, with realistic ensemble-mean annular mode variances through the troposphere and stratosphere. However, the peak in variability associated with the break-down of the vortex consistently occurs too late in the year in both hemispheres in the CCMVal-2 models. The simulated SAM tends to be too persistent through the troposphere and stratosphere in summer.
- Over the period 1960-2000 the CCMVal-2 models simulate a spring cooling of the Antarctic polar vortex, and a decrease in Antarctic geopotential height which descends to the troposphere in December-February, and is associated with an intensification and southward shift of the mid-latitude jet.
- The amount of Antarctic ozone depletion in each model is closely correlated with its shift in jet location, amount of broadening of the Hadley Cell, and its increase in SH tropopause height.
- The models indicate that in the 21<sup>st</sup> century, the effects of ozone recovery and greenhouse gas increases largely cancel leading to little change in jet location, tropopause height, or Hadley Cell width in the SH during summer. The models do not project significant trends in 21<sup>st</sup> century NH high latitude winter zonal wind.
- Erythemal ultraviolet irradiance, calculated based on CCMVal-2 ozone changes, exhibits an increase throughout the globe in the last decades of the twentieth century. In the 21<sup>st</sup> century, decreasing chemical depletion is likely to contribute to a decrease in erythemal irradiance globally, while changes in the Brewer-Dobson circulation will tend to enhance the decrease in the Arctic and slow or reverse the decrease in the tropics and Antarctic.
- In the CCMVal-2 simulations ozone depletion causes a small global decrease in the stratosphere-troposphere ozone flux in the 20<sup>th</sup> century, and its recovery contributes to the 21<sup>st</sup> century increase. However, a strengthening of the Brewer-Dobson circulation is projected to be the dominant driver of an increase in stratosphere-to-troposphere ozone fluxes in the 21<sup>st</sup> century.

## Recommendations by Chapter

### CHAPTER 2

- For future model inter-comparison an online repository for model information should be made available and kept up-to-date by model developers so that users of the model simulations are aware of the specific features of each model.

### CHAPTER 3

- CCM radiation schemes should be capable of being run independently of their host models and should regularly be involved in comparison exercises based on detailed sets of reference calculations from line-by-line models. Solar and longwave schemes should be evaluated for a range of realistic circumstances.
- Future radiation scheme comparisons should ideally evaluate the radiative effects of aerosol and cloud as well as trace gases. They should also evaluate the effect of approximations made in CCMs such as the frequency of radiative transfer calculations and the effects of plane-parallel/sphericity approximations.
- Photolysis and solar heating calculations should be merged for consistency.
- Non-local thermodynamic equilibrium effects should be accounted for above 70 km to correctly simulate heating and cooling rates in this region.
- CCMs should include spectral variations in solar irradiance when modelling solar variability in order to induce the correct stratospheric temperature change. Further work is needed to assess the level of spectral detail required.

### CHAPTER 4

- Reproducing variability on sub-seasonal time scales (*e.g.*, SSWs and final warming dates) should be regarded as an essential part of a model's ability to simulate stratospheric dynamics, since this variability can play a key role in determining the mean stratospheric climate. This assessment has shown that many models have significant over- or under-estimates in this variability.
- A key outstanding issue is understanding the cause of the robust multi-model trend in the strength of the Brewer-Dobson circulation. Further inter-comparison of models, including detailed diagnosis of the stratospheric momentum budget, should be carried out to try to understand this trend. Additional observational constraints on the processes involved are also needed.
- In order to better simulate tropical stratospheric variability and its links to the extra-tropics CCMs should move towards simulating a physically realistic, internally generated QBO.
- There are persistent dynamical weaknesses in CCMs (*e.g.*, the timing of the break-down of the polar vortex) which require further work to understand both the resolved and parameterised (gravity-wave) forcing from the troposphere.

### CHAPTER 5

- The following features are essential for realistic model transport, particularly for simulation of the Antarctic ozone hole: 1) local conservation of chemical family mixing ratios (*e.g.*,  $Cl_y$ ), 2) realistic tropical ascent in the lower stratosphere, 3) realistic mixing between the tropics and extra-tropics, 4) close agreement with *all* mean age diagnostics, and 5) generation of an isolated Antarctic vortex in the lower stratosphere. Models that reasonably represent these essential attributes have enhanced credibility for prediction of future stratospheric composition.
- Transport improvement efforts should concentrate on the tropical lower stratosphere. The ability to reproduce the observed tracer-derived vertical velocities and to maintain the correct degree of tropical isolation



seem to be key to the accurate simulation of transport throughout the stratosphere.

## CHAPTER 6

- All CCM groups should participate in the PhotoComp 2008 and PSS process diagnostics. These are fundamental diagnostics that will, after successful competition, provide confidence that these models have an accurate representation of chemical processes.
- CCM groups should monitor their sulfate SAD distributions. This chapter has shown that there is a wide variation in what models are using (even though it was prescribed).
- Models must conserve atoms of key chemical families. For example, there are several cases where the stratospheric total inorganic chlorine (or bromine) abundance is much greater than that specified at the surface. This is not necessarily a chemistry issue; it may be due to non-conservation in the CCM tracer advection scheme. However, non-conservation of ozone depleting substances will clearly affect the accuracy of modelled ozone distributions and trends.
- The community must address the issue of how to include very short-lived (VSL) organic bromine species into the boundary condition and chemical mechanism of CCMs. The measurement community has confirmed that these species are important for stratospheric inorganic bromine loading. Comparisons with measured BrO show higher abundances in the atmosphere than are found in all of the standard model simulations. Validation of model bromine chemistry and ozone loss using observations is not possible without a realistic description of the past/present atmosphere. Not including these VSL sources of inorganic bromine also makes interpretation of model derived ozone trends more uncertain. Models also need to be consistent in following the prescribed scenarios of long-lived halocarbons.
- One of the most notable differences between the models was the abundance of Cl<sub>y</sub> at the tropopause and throughout the troposphere. Some models have near zero (<< 50 ppt) values of Cl<sub>y</sub> in these regions of the atmosphere, while other models have much larger values (>> 50 ppt). Models with high levels of Cl<sub>y</sub> at the tropopause tend to have excess Cl<sub>y</sub> throughout the lower stratosphere. We postulate these differences are due to various representations of Cl<sub>y</sub> uptake and removal. In the future, attention should be devoted to model representation of Cl<sub>y</sub> in the troposphere, tropopause, and lower stratosphere regions because models with the higher values of Cl<sub>y</sub> may display a different sensitivity to future changes in stratospheric H<sub>2</sub>O and temperature (*i.e.*, more chlorine available to be activated) than models with lower values of Cl<sub>y</sub>.
- CCM groups should continue to pay attention to how water vapour is coupled to the stratospheric chemistry schemes. GCMs contain a water vapour field which should be coupled to and used by the chemistry module. The dynamics of the GCM, however, needs to be sufficiently realistic to give accurate stratospheric H<sub>2</sub>O abundances.
- The next generation of CCMs should also include a better representation of tropospheric chemical processes (*e.g.*, non-methane hydrocarbons; lightning NO<sub>x</sub> production; detail inclusion of dry and wet deposition processes). This is certainly important for science studies in the troposphere and UTLS region, but also may be important in better representing the overall climate system.

## CHAPTER 7

- The quantitative evaluation of the models has been found to be difficult for some diagnostics due to limited representativeness or low accuracy of observations in the UTLS. It will be necessary to compare the UTLS metrics with future measurements to reduce uncertainty in the model comparison associated with potential measurement errors. For this purpose, the observational database for the UTLS should be expanded by measurements with both higher spatial and temporal resolution and sampling, but also reasonable accuracy.
- New observations are needed especially for O<sub>3</sub> and H<sub>2</sub>O in the UTLS with a vertical resolution better than 1 km and a horizontal resolution better than 100 km, especially in the SH and the tropics.
- Evaluating chemical processes in the UTLS should be part of future model validation efforts, including

tropospheric CCMs used for the IPCC. However, to do this properly, future model development is needed that brings together tropospheric and stratospheric chemistry models.

- Part of this model development should include the representation of very short-lived (VSL) species that also represent major sources of bromine in the stratosphere. These VSL provide a range of lifetimes and can discriminate transport from marine and continental source regions into the UTLS.

## CHAPTER 8

- The evaluation of the sensitivity of the SH large-scale dynamics to the parameterisation of non-orographic gravity wave drag and its implication for the interannual variability in ozone should be included in future assessments.
- Models should use spectrally resolved solar irradiance data and a suitable radiation and photolysis code. More detailed inter-comparison of radiation and photolysis codes as well as sensitivity studies to understand the complex non-linear interactions of the solar signal with other natural variability signals are needed.
- The simulation of the QBO in CCMs is an outstanding challenge. It is a problem that needs to be addressed comprehensively, because of the dependence of the modelled QBO on the representation of a number of processes, ranging from convective processes to the vertical propagation of atmospheric waves. A successful simulation needs to assess both meteorological and chemical fields.
- The parameterisation of volcanic effects has to be advanced as well as the understanding of observed variations in response to volcanic eruptions.

## CHAPTER 9

- The simulation of the Antarctic ozone hole needs to be improved in most models. This can be achieved by improving the simulation of polar stratospheric clouds and their activation of chlorine, and by reducing overall ozone biases.
- The coupling of CCMs to interactive oceans is recommended in the future, in order to make the representation of climate change in the models more physically self-consistent.
- Simulations with different halogen and GHG scenarios need to be completed to complement the simulations in which these quantities are fully varying. While multi-linear regression has been effective in determining the importance of these factors in controlling ozone in the middle and upper stratosphere, the technique is less effective in the lower stratosphere where the dynamical and chemical time scales have periods of a month or more and the causality of the relationships is less clear.

## CHAPTER 10

- More CCMs should be coupled to dynamical oceans. This is necessary in order to reliably simulate the tropospheric response to stratospheric perturbations, otherwise it is constrained by the prescribed SSTs.
- Model runs with fixed ODS and both fixed and different GHG scenarios are needed to allow the influences of greenhouse gas changes and ozone depleting substances on tropospheric climate to be separated.

# Chapter 1

## Introduction

**Lead Authors:** Veronika Eyring, Ted Shepherd & Darryn Waugh

---

### 1.1 Rationale

The stratospheric ozone layer has been depleted by anthropogenic emissions of halogenated species over the last decades of the 20<sup>th</sup> century until present. Observations show that tropospheric halogen loading is now decreasing (Montzka *et al.*, 2003; WMO, 2007), which reflects the controls on production of ozone-depleting substances (ODSs) by the Montreal Protocol and its Amendments and Adjustments. Ozone is expected to continue to respond to these changes in ODSs but the timing and sensitivity of the response will depend on other changes in the atmosphere. Atmospheric concentrations of greenhouse gases (GHGs) have also increased, and are expected to increase further in the future (IPCC, 2000), with consequences for the ozone

layer. As a result of climate change, it is unlikely that the ozone layer will return to precisely its unperturbed state even if the abundance of halogens returns to background levels. Furthermore, climate change complicates the attribution of ozone recovery to the decline of halogenated species.

To predict the future evolution of stratospheric ozone and attribute its behaviour to the different forcings, models are required that can adequately represent both the chemistry of the ozone layer and the dynamics and energetics of the atmosphere, as well as their natural variability. The coupling of stratospheric chemical models with climate models has led to a new generation of models far more complex than those available when the Montreal Protocol was agreed in 1987. Such models, known as coupled Chemistry-Climate Models (CCMs), are three-dimensional atmospheric circulation models with fully coupled chemistry, *i.e.*, where chemical reactions drive changes in at-

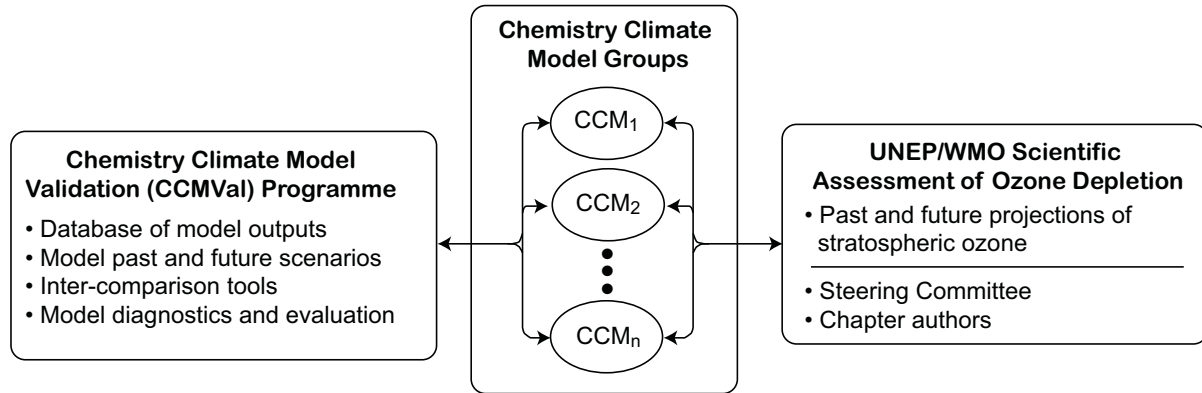


**Figure 1.1:** Model of the relationships between CCMVal, the CCM groups, and the WMO/UNEP Assessment. From Eyring *et al.* (2008).

mospheric composition which in turn change the atmospheric radiative balance and hence dynamics. Sea surface temperatures (SSTs) and sea ice distributions in CCMs are either prescribed or calculated internally if the model is interactively coupled to an ocean. CCMs are key tools for the attribution and projection of the response of stratospheric ozone to ODSs and other factors, and allow questions about future stratospheric ozone and UV radiation levels to be studied in a more comprehensive manner than could be done when the Montreal Protocol was signed. In particular, by including a representation of tropospheric climate change, they make it possible to address the coupling between climate change and ozone depletion/recovery in a comprehensive manner. However, the workings of these CCMs themselves are also much harder to fully understand, and it is therefore necessary to quantitatively assess the confidence that can be placed in their projections.

In the past there has been insufficient time to evaluate CCM performance thoroughly while preparing international ozone and climate assessments. The Chemistry-Climate Model Validation (CCMVal) Activity for WCRP’s SPARC project is producing this Report on the evaluation of CCMs so that it provides useful and timely information for the 2010 WMO/UNEP Scientific Assessment of Ozone Depletion, and the IPCC 5th Assessment Report (AR5). The Report is a response to the need to quantitatively assess the confidence that can be placed in the CCMs by a comprehensive evaluation of the ability of CCMs to represent key processes for stratospheric ozone and its impact on climate. Compared to the WMO/UNEP ozone and IPCC climate assessments, the SPARC CCMVal report allows the inclusion of a lot more detail and provides a coherent, integrated assessment of the CCMs based on the CCMVal concept (Eyring *et al.*, 2005, see also Section 1.2). The two-way communication linking the CCM groups with CCMVal and the WMO/UNEP Ozone Assessment is illustrated in **Figure 1.1**. CCMVal acts as a resource for the modelling groups and for the Ozone Assessment by developing and maintaining evaluation tools for the models,

maintaining definitions and boundary condition data for “scenario” experiments, and archiving output data from the models. The CCM groups interact with CCMVal in defining and applying the evaluation tools, using the boundary condition data, and providing model output. It is anticipated that the Ozone Assessment will make use of CCMVal resources by working with the CCM groups to help in defining relevant model scenarios, using the CCMVal data archive at the British Atmospheric Data Centre (BADC) and applying the tools and metrics derived by CCMVal in their evaluation of model results. In addition, the Assessment authors may solicit data from other model groups and, if they wish, may apply CCMVal diagnostic tools to evaluate these model results. The coordination, support, and products that SPARC CCMVal provides for the CCM community represent an important additional resource for the Assessment process.

This Report provides an up-to-date process-oriented evaluation of the ability of CCMs to represent the stratospheric ozone layer, stratospheric climate and climate variability, and the coupled ozone-climate response to natural and anthropogenic forcings. This comprehensive evaluation improves our understanding of the strengths and weaknesses of CCMs and thus increases their integrity and credibility. The evaluation of the CCMs is also used to guide the assessment of the projections of changes in ozone in the 21<sup>st</sup> century and their impact on tropospheric climate. This Report builds on previous assessments of the family of stratospheric CCMs and their General Circulation Models (GCMs) much of which have been organised under the auspices of the SPARC GCM-Reality Intercomparison Project (GRIPS) and CCMVal activities (Pawson *et al.*, 2000; Eyring *et al.*, 2005) and have contributed directly to the evaluation of CCMs during the preparation of the WMO/UNEP Scientific Assessments of Ozone Depletion (Austin *et al.*, 2003; Eyring *et al.*, 2006, 2007).

The strategy of setting up benchmarks and criteria for a process-oriented model evaluation presented in this Report could also be beneficial for the assessment of other

components of the Earth system and the development of Earth System Models that integrate our knowledge regarding the atmosphere, ocean, cryosphere and land surfaces, and account for the coupling between physical and biogeochemical processes. Developing the science of quantitative performance metrics is an emerging focus within the WCRP and will be an emphasis of the IPCC AR5.

## 1.2 CCMVal concept for model evaluation and analysis

The goal of the SPARC CCMVal activity is to improve understanding of CCMs through process-oriented evaluation and to provide reliable projections of stratospheric ozone and its impact on climate. The model evaluation is based on a set of core processes relevant for stratospheric ozone centred around four main categories (radiation, dynamics, transport, and stratospheric chemistry and microphysics), with each process associated with one or more model diagnostics and with relevant data sets that can be used for the evaluation (Eyring *et al.*, 2005, see **Figure 1.2**). The four ingredients are fundamentally interdependent and interactive and require as inputs, knowledge of human ac-

tivities and natural processes. These inputs help quantitatively define processes in the atmosphere and expectations for future changes. Trends in atmospheric constituents and parameters associated with climate forcing are examples of important inputs. The CCM output includes a wide array of parameters and diagnostics associated with the four different aspects. The distribution of stratospheric ozone is highlighted separately here because of the strong contemporary interest in halogen-based ozone depletion and the recovery of the ozone loss that has developed over recent decades. The comparisons of model diagnostics and other outputs with atmospheric observations and meteorological analyses are the key to process-oriented CCM evaluation. Finally, the results of the comparisons can be used to provide feedback to the representation of processes in CCMs in order to improve the models. In this way, the uncertainties in future changes in stratospheric ozone and other key model outputs can be reduced, and errors better quantified.

To eliminate many of the uncertainties in the conclusions of earlier multi-CCM evaluations (*e.g.*, Austin *et al.*, 2003) that resulted from differences in anthropogenic and natural forcings as well as from the experimental set-up of individual models, CCMVal has defined reference simulations for the past and for the future. The simulations used

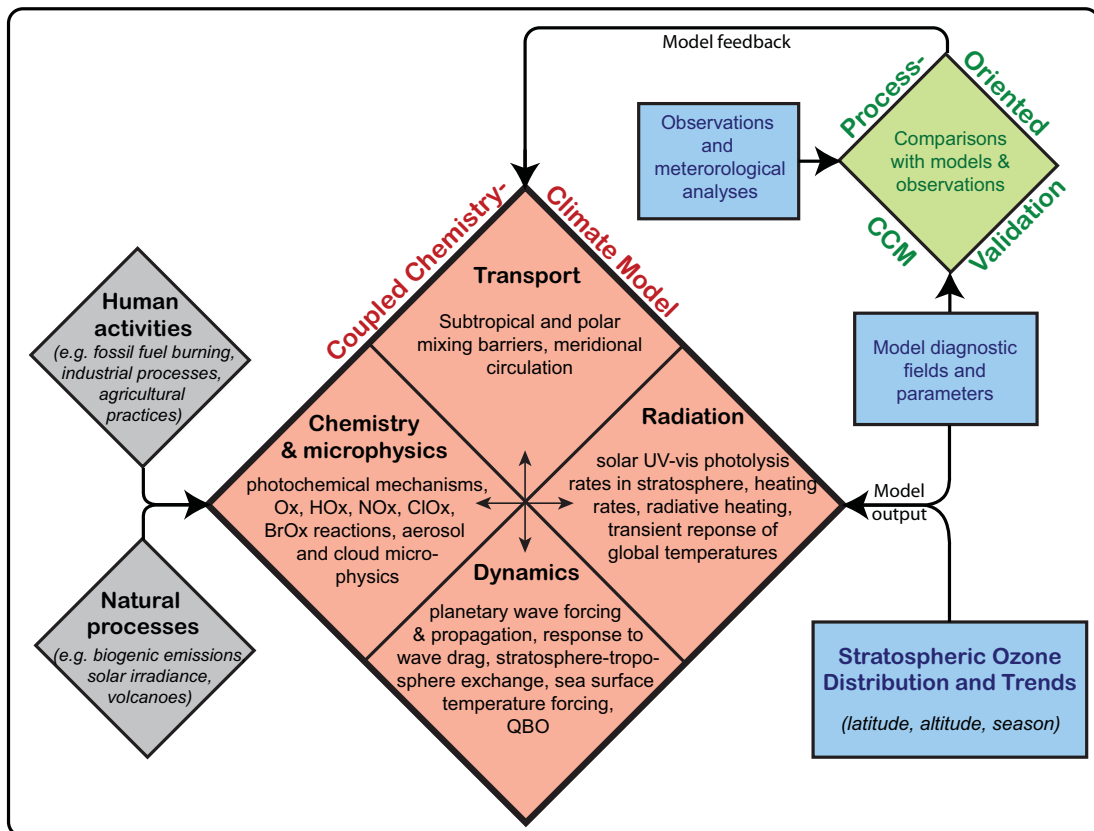


**Figure 1.2:** Schematic diagram of the CCMVal evaluation approach. The centre-piece is a CCM comprised of four basic ingredients: transport, dynamics, radiation, and stratospheric chemistry and microphysics. From Eyring *et al.* (2005), Figure 2.

**Table 1.1:** CCMs used in the SPARC CCMVal Report. The models are listed alphabetically by name.

CCM name	Institution(s)	Investigator(s)	References
AMTRAC3	GFDL, US	John Austin	<i>Austin and Wilson (2009)</i>
CAM3.5	NCAR, US	Jean-François Lamarque	<i>Lamarque et al. (2008)</i>
CCSRNIES	NIES, JP	Hideharu Akiyoshi, Yousuke Yamashita, Tetsu Nakamura	<i>Akiyoshi et al. (2009)</i>
CMAM	Univ. of Toronto/ CCCma, CA	David Plummer, John Scinocca, Ted Shepherd	<i>Scinocca et al. (2008); de Grandpré et al. (2000)</i>
CNRM-ACM (ARPEGE-Climat 4.6 Coupled MOCAGE- Climat)	CNRM/GAME, Météo- France/CNRS, FR	Martine Michou, Hubert Teyssède, Dirk Olivie	<i>Déqué (2007); Teyssède et al. (2007)</i>
E39CA	DLR, DE	Martin Dameris, Hella Garny	<i>Stenke et al. (2009); Garny et al. (2009)</i>
EMAC (version 1.6)	MPI-C, DE	Andreas Baumgärtner, Christoph Brühl, Patrick Jöckel	<i>Jöckel et al. (2006)</i>
GEOSCCM (version 2)	NASA/GSFC, US	Steven Pawson, Rich Stolarski	<i>Pawson et al. (2008)</i>
LMDZrepro	CNRS, FR	Slimane Bekki, Marion Marchand	<i>Jourdain et al. (2008)</i>
MRI (v. MJ98)	MRI, JP	Kiyotaka Shibata	<i>Shibata and Deushi (2008a, b)</i>
NiwaSOCOL	NIWA, NZ	Dan Smale, Olaf Morgenstern	<i>Schraner et al. (2008); Egorova et al. (2005)</i>
SOCOL (version 2)	PMOD/WRC, CH IAC, ETH Zürich, CH	Eugene Rozanov, Tom Peter	<i>Schraner et al. (2008)</i>
ULAQ	Univ. L'Aquila, IT	Eva Mancini, Giovanni Pitari	<i>Pitari et al. (2002); Eyring et al. (2006, 2007)</i>
UMETRAC	NIWA, NZ	Olaf Morgenstern	<i>Austin and Butchart (2003)</i>
UMSLIMCAT	Univ. Leeds, UK	Martyn Chipperfield, Sandip Dhomse, Wenshou Tian	<i>Tian and Chipperfield (2005); Tian et al. (2006)</i>
UMUKCA-METO	Met Office, UK	Steven Hardiman, Neal Butchart	<i>Morgenstern et al. (2008, 2009)</i>
UMUKCA-UCAM	Univ. Cambridge, UK	Peter Braesicke, Olaf Morgenstern, John Pyle	<i>Morgenstern et al. (2008, 2009)</i>
WACCM (version 3.5.48)	NCAR, US	Doug Kinnison, Andrew Gottelman, Rolando Garcia	<i>None yet. Based on WACCM 3.1.9 (Garcia et al., 2007)</i>

in the first round of CCMVal (CCMVal-1) were used in the 2006 WMO/UNEP Scientific Assessment of Ozone Depletion (Chapter 6 of WMO, 2007). This Report, which describes the second round of CCMVal (CCMVal-2), defines new reference simulations (see Chapter 2) in support of the 2010 Assessment and evaluates the performance of the eighteen participating CCMs (see **Table 1.1**).

The role of observations in model evaluation is crucial since both the opportunities and the limitations in the available data need to be well known. A large number of observations from a variety of different platforms and instruments are used in this Report to assess the CCMs.

These are summarized in **Table 1.2**, with further details given within individual chapters.

### 1.3 Quantitative performance metrics

A key aspect of the model evaluation within this Report is the application of observationally-based performance metrics to quantify the ability of models to reproduce key processes for stratospheric ozone. Quantitative performance metrics have been applied to evaluate the CCMVal-1 models (Waugh and Eyring, 2008), and have

also been used for the evaluation of three-dimensional chemical transport models (*e.g.*, Douglass *et al.*, 1999; Brunner *et al.*, 2003; Strahan and Douglass, 2004) and coupled atmosphere-ocean models (*e.g.*, Schmittner *et al.*, 2005; Connolley and Bracegirdle, 2007; Reichler and Kim, 2008; Gleckler *et al.*, 2008; Santer *et al.*, 2009). In contrast to most of the previous studies, the focus in this Report is, as in Waugh and Eyring (2008), on evaluating the key processes rather than the quantity of interest itself, which in this Report is stratospheric ozone. This follows the CCMVal philosophy described in Eyring *et al.* (2005), and is done partly to more accurately identify the sources of model errors, and partly to circumvent the case where an ozone metric may look good because of compensating errors in the underlying processes.

Applying quantitative performance metrics to a range of observationally-based diagnostics provides several benefits for model evaluation, including

- Easy recognition of the models' performance for multiple aspects of the simulations;
- Identification of missing or incompletely modelled processes (in the case of systematic biases in the models); and
- Quantitative assessment of model improvements, both for different versions of individual CCMs and for different generations of community-wide collections of models (*e.g.*, CCMVal-1 and CCMVal-2).

However, the application of performance metrics is still an active research topic and involves many subjective decisions, which means that caution is required with the interpretation of metrics. Important issues include the choice of diagnostics, the relative importance of different processes/diagnostics, the choice of the metric, uncertainties in observations, and the statistical limitations of the metrics.

Several different metrics have been used in previous evaluations of atmospheric models. Waugh and Eyring (2008) used the simple metric

$$g = 1 - \frac{1}{n_g} \frac{|\mu_{\text{mod}} - \mu_{\text{obs}}|}{\sigma} \quad (1.1)$$

where  $\mu_{\text{mod}}$  is the model climatological mean,  $\mu_{\text{obs}}$  is the observed climatological mean,  $\sigma$  is a measure of the uncertainty (see discussion below), and  $n_g$  is a scaling factor (typically 3). Other previously applied climatological mean state metrics include the squared difference between model and observed climatological mean values divided by the observed variance (Reichler and Kim, 2008) and the root mean squared difference between the model and observed climatological mean values (Gleckler *et al.*, 2008). Santer *et al.* (2009) applied metrics for the seasonal cycle, the variability amplitude and the variability pattern to climate models in addition to the climatological mean and combined them into three overall ranking metrics.

This Report makes use of a variety of metrics: The

metric  $g$  used by Waugh and Eyring (2008) is applied in Chapters 4, 5, 6, and 7. In Chapter 7 similar metrics to the mean metric  $g$  are additionally applied to gauge the performance of the models to simulated correlated variability and variance. Chapter 6 also applies a slightly modified version of  $g$  which considers the models' interannual variability in addition to the uncertainty in the observations in  $\sigma$  of Equation 1.1. In the extra-tropics, evaluation of Chapter 7 as well as in Chapters 8 and 10 the statistical summary of how well two patterns from a test field ( $f$ ) and a reference field ( $r$ ) match each other in terms of their correlation ( $R$ ), their root-mean-square difference ( $E'$ ), and the ratio of their variances ( $\sigma_f / \sigma_r$ ) are visualised with the help of "Taylor diagrams" (Taylor, 2001) and the correctness of phase and amplitude of the seasonal cycles quantified with the help of skill factors.

A major issue with the application and interpretation of metrics is the robustness of the scores obtained from the metrics. Grewe and Sausen (2009) have recently highlighted the statistical limitations in the metric  $g$  used by Waugh and Eyring (2008), and these limitations need to be considered when interpreting quantitative measures of performance ("grades") derived from this and other metrics. Observational uncertainties (*e.g.*,  $\sigma$  in Equation 1.1) can influence the outcome of model-data consistency tests (see, *e.g.*, Santer *et al.*, 2003), especially if there are biases in observational data sets. Wherever possible, the possibility of biases in this Report is assessed by using observations from several sources, *e.g.*, from different satellite instruments and platforms.

A possible application of metrics is to form a single model score that can be used to assign relative weights to the ozone projections from each CCM. This was explored by Waugh and Eyring (2008) for different combinations of weights for the diagnostics and metrics applied to the CCMVal-1 simulations. For the limited set of diagnostics that was used in this study there were generally only small differences between weighted and unweighted multi-model mean and variances of total ozone projections, suggesting that the multi-model mean was a robust quantity in CCMVal-1 simulations. However, there are many issues with weighting projections, including the choice and relative importance of diagnostics when forming a single score (Gleckler *et al.*, 2008). Because of this, aggregated model scores are not produced in this Report nor are the performance metrics used to weight ozone projections. However, the metrics are used to provide overall qualitative assessments of model performance and to help interpret model results that are outliers in the ozone projections. Furthermore, the robustness of the multi-model mean ozone projections and uncertainty is tested by taking out these outliers in the projections (see Chapter 9).

**Table 1.2:** Overview of observations used in this report for the evaluation of CCMs.

Species	Diagnostic (Chapter)	Instrument	Time Period	Reference
<i>Satellite Data</i>				
O <sub>3</sub> columns	Mean, variability and trends (8,9), Multiple linear regression analyses (MLR) analysis (8)	Merged satellite data	1970-2007	<i>Stolarski and Frith (2006)</i>
		NIWA	1978-2007	<i>Hassler et al. (2008)</i>
		SAGE	1978-2007	<i>updated from Miller et al. (2002); Randel and Wu (2007)</i>
		TOMS	1980-2008	<i>Stolarski and Frith (2006)</i>
O <sub>3</sub> profiles and 3D fields	Mean, annual cycle, and trends (7,8), Meridional tracer gradients @200 hPa (7), PDFs of O <sub>3</sub> variability (7), seasonal cycles (7,8), ExTL depth and width (7), MLR analysis (8), stratospheric ozone fluxes (10)	UARS HALOE	1991-2002	<i>Russell et al. (1993); Grooß and Russell (2005)</i>
		MLS	2004-2008	<i>Livesey et al. (2008)</i>
		NIWA-3D	1980-1999	<i>Hassler et al. (2008)</i>
		SAGE	1979-2005	<i>Randel and Wu (2007)</i>
		MIPAS	2004-2008	<i>von Clarmann et al. (2009)</i>
		Ozone climatology	1991-2002	<i>McPeters et al. (2007)</i>
H <sub>4</sub> , H <sub>2</sub> O, CO, O <sub>3</sub> , HCl, ClONO <sub>2</sub> , HNO <sub>3</sub> , N <sub>2</sub> O <sub>5</sub> , NO <sub>2</sub> , BrO	Mean evolution (6)	ENVISAT-MIPAS, Oxford L2	2002-2009	<i>Fischer et al. (2008)</i>
		ENVISAT-SCIAMACHY	2002-2009	<i>Rozañov et al. (2005)</i>
		ACE-FTS	2003-2009	<i>Bernath et al. (2005)</i>
		ODIN	2001-2009	<i>Murtagh et al. (2002)</i>
H <sub>2</sub> O	Dehydration in SH Polar region (6)	Aura-MLS v2.2	2004-2009	<i>Lambert et al. (2007)</i>
		UARS HALOE	1991-2002	<i>Russell et al. (1993); Grooß and Russell (2005)</i>
	Seasonal cycles@ 80, 100, 200 hPa (7), Vertical profiles in TP coordinates (7), ExTL depth and width (7), H <sub>2</sub> O tape recorder (5)	MIPAS	2004-2008	<i>von Clarmann et al. (2009)</i>
		ACE-FTS	2004-2007	<i>Hegglin et al. (2008)</i>
CH <sub>4</sub>	Tropical gradient (5)	UARS HALOE	1991-2002	<i>Russell et al. (1993); Grooß and Russell (2005)</i>
N <sub>2</sub> O	Tropical gradient (5), annual cycle (5)	ENVISAT-MIPAS	2002-2004	<i>Glatthor et al. (2005)</i>
		Aura MLS	2004-2008	<i>Lambert et al. (2007)</i>
HCl	Mean evolution in SH Polar region – surrogate for chlorine activation (6)	Aura-MLS v2.2	2004-2009	<i>Froidevaux et al. (2008)</i>
CO	Vertical profiles in TP coordinates (7)	ACE-FTS	2007	<i>Hegglin et al. (2008)</i>
Cl <sub>y</sub>	Time series (5)	Multiple Instruments (e.g., HALOE HCl, Aura MLS)	1991-2006	<i>Lary et al. (2007) and references therein</i>
HNO <sub>3</sub>	De-nitrification in SH Polar region (6)	Aura-MLS, v2.2	2004-2009	<i>Santee et al. (2007)</i>



Table 1.2 continued.

Species	Diagnostic (Chapter)	Instrument	Time Period	Reference
	Seasonal cycles@ 80, 100, and 200 hPa (7)	MIPAS	2004-2008	<i>von Clarmann et al. (2009)</i>
Temperature	TP inversion layer (7), global mean climatology and trends (3)	COSMIC GPS	2006-2008	<i>Anthes et al. (2008)</i>
		MSU/SSU	1980-1999	<i>Randel et al. (2009)</i>
Sulfate Aerosol Surface Area	Sulfate SAD (6)	Based on SAGE and SAGE II	1979-2004	<i>Thomason et al. (1997)</i>
O <sub>3</sub> , HCl	Chemical ozone loss (6)	Based on HALOE	1991-2004	<i>Russell et al. (1993); Tilmes et al. (2006)</i>
<b>Meteorological Reanalyses</b>				
Temperature	Mean and trends (3, 4, 7, 10), MLR analysis (8), PSC threshold temperatures (4)	ERA-40	1979-1999	<i>Uppala et al. (2005)</i>
		NCEP	1980-1999	<i>Kalnay et al. (1996)</i>
		ERA-Interim	1989-1999	<i>Uppala et al. (2008)</i>
		UKMO	1992-2002	<i>Swinbank and O'Neill (1994)</i>
		NCEP2	1980-1999	<i>Kanamitsu et al. (2002)</i>
		JRA25	1980-1999	<i>Onogi et al. (2007)</i>
Zonal wind	Mean, variability and long-term trends, zonal mean (4, 7,10), vertical profile of the amplitude of the QBO (4), stratospheric sudden warmings (4)	ERA-40	1979-1999	<i>SPARC (2003)</i>
		NCEP	1980-1999	<i>SPARC (2003)</i>
<i>T, u, v</i>	Potential for Activation of Chlorine (PACl). Also for the Derivation of Eqlat- $\Theta$ (6)	UKMO	1991-2005	<i>Swinbank and O'Neill (1994)</i>
		ERA-40	1958-1999	<i>Uppala et al. (2005)</i>
Geopotential height	Annular Modes (10), Annular Mode relationship to column ozone (8)	ERA-40	1980-1999	<i>Uppala et al. (2005)</i>
		NCEP	1980-1999	<i>Kalnay et al. (1996)</i>
Heat flux	Heat flux relationship with temperature (4) and ozone (8)	ERA-40	1980-1999	<i>Uppala et al. (2005)</i>
		NCEP	1980-1999	<i>Kalnay et al. (1996)</i>
		ERA-Interim	1991-2002	<i>Uppala et al. (2008)</i>
Residual vertical velocity	Brewer-Dobson circulation and tropical upwelling (4)	UKMO	1992-2001	<i>Swinbank and O'Neill (1994)</i>
	Stratospheric ozone fluxes (10)	ERA-Interim	1991-2002	<i>Uppala et al. (2008), Wohltmann and Rex (2008)</i>
<b>Ground-based Data</b>				
O <sub>3</sub> columns	Averaged over a latitude band, annual and monthly means (6)	Ground-based measurements	1964-2007	<i>updated from Fioletov et al. (2002)</i>
	Total Ozone at Halley (10)	Dobson spectrometer	1969-1998	<i>Jones and Shanklin (1995)</i>
NO <sub>2</sub> , ClONO <sub>2</sub> , HCl	Mean evolution and variability (6)	NDACC	1990-2008	<i>Rinsland et al. (2003)</i>

Table 1.2 continued.

Species	Diagnostic (Chapter)	Instrument	Time Period	Reference
<b>Balloon Flights</b>				
CO <sub>2</sub> and SF <sub>6</sub>	Mean Age (5)	Various balloon missions	1986-2005	<i>Andrews et al. (2001); Engel et al. (2009)</i>
N <sub>2</sub> O, H <sub>2</sub> O, CH <sub>4</sub> , NO <sub>y</sub> , and pressure	N <sub>2</sub> O profile and tracer-tracer correlations (6)	Mk IV FTIR	Sept. 1993	<i>Sen et al. (1998); Osterman et al. (1997)</i>
O <sub>3</sub> , N <sub>2</sub> O	Chemical ozone loss (6)	FOZAN-II, HAGAR	2005	<i>von Hobe et al. (2006)</i>
HO <sub>x</sub> , NO <sub>x</sub> , ClO, and BrO	Fast chemistry (6)	MkIV, SLS, FIRS-2, and SAOZ	Sept 1993; April and May 1997; Nov 1997	<i>Osterman et al. (1997); Jucks et al. (1998); Pundt et al. (2002); Salawitch et al. (2002, 2005)</i>
Geopotential height, <i>T</i>	Antarctic trends (10)	Radiosondes	1969-1998	<i>Thompson and Solomon (2002)</i>
<b>Aircraft Data</b>				
CO	Vertical profiles in TP coordinates (7)	SPURT	2001-2003	<i>Hoor et al. (2004)</i>
H <sub>2</sub> O	Vertical profiles in TP coordinates (7)	Climatology	1995-2005	<i>Tilmes et al. (2010)</i>
O <sub>3</sub>	Vertical profiles in TP coordinates (7), ExTL depth and width (7)	Climatology	1995-2005	<i>Tilmes et al. (2010)</i>
		POLARIS	1997	<i>Pan et al. (2007)</i>
CFC-11, CFC-12, CO <sub>2</sub> , and SF <sub>6</sub>	Fractional Release of Cl <sub>y</sub> (5)	NASA ER-2 aircraft missions	2000	<i>Schauffler et al. (2003); Douglass et al. (2008)</i>
FCs and related species, Halons, CH <sub>3</sub> Br, and N <sub>2</sub> O	Cl <sub>y</sub> vs N <sub>2</sub> O and Br <sub>y</sub> vs N <sub>2</sub> O (6)	WAS, ACATS, and ATLAS	Repeated sampling from 1992 to 2008	<i>Woodbridge et al. (1995); Wamsley et al. (1998)</i>
HO <sub>x</sub> , NO <sub>x</sub> , ClO, and BrO	Fast chemistry (6)	Harvard HO <sub>x</sub> and ClO/BrO instruments; NOAA NO <sub>x</sub> instrument	May 1993; Nov 1995; Feb 1996	<i>Wennberg et al. (1994, 1999); Salawitch et al. (1994, 2005); Wamsley et al. (1998)</i>
N <sub>2</sub> O, O <sub>3</sub> , H <sub>2</sub> O, CH <sub>4</sub> , pressure	N <sub>2</sub> O profile and tracer-tracer correlations (6)	ATLAS, NOAA O <sub>3</sub> , NOAA Lyman-Alpha Hygrometer, ACATS	Feb 1996	<i>Lanzendorf et al. (2001); Weinstock et al. (2001); Dessler (2002)</i>

## 1.4 Progress beyond the state-of-the-art

This Report describes the second round of CCMVal (CCMVal-2), which presents several advances beyond CCMVal-1. First, the number of participating CCMs has increased from thirteen to eighteen (see Table 1.1). Second, whereas the evaluation in CCMVal-1 focused mainly on diagnostics to evaluate transport and dynamics in the

CCMs, a much broader and detailed evaluation, including an assessment of chemical and radiative processes and the UTLS, has been performed in CCMVal-2. Finally, new reference simulations for the future have been performed that cover the entire period from 1960 to 2010.

The CCMVal-2 simulations are used here to answer key scientific issues, including some arising from the 2006 WMO/UNEP Ozone Assessment (Shepherd and Randel, 2007). In particular, the material in this Report aims to pro-

vide:

- **Improved understanding of process-oriented diagnostics and model evaluation.** A wider suite of process-oriented diagnostics is developed compared to that in CCMVal-1, and attempts are made to assess model skill through quantitative performance metrics. This contributes to the growing field of research in this area. The strengths and weaknesses, as well as benefits, of different approaches are analysed.
- **A better understanding of the causes of changes in observed past ozone and related variables.** CCMVal-2 contains improved versions of some of the models that participated in CCMVal-1, and also new CCMs. Together with a more detailed analysis of simulations of past changes in ozone and related variables, and an earlier starting point as compared with CCMVal-1, this allows a more thorough attribution of observed changes and a better understanding of the role of natural variability.
- **A reassessment of the projections of ozone and UV radiation through the 21<sup>st</sup> century.** In CCMVal-1 most projections only started in 1980 or later (several began only in 1995), and only three CCMs ran beyond 2050. In contrast, in CCMVal-2 the simulations begin in 1960, and most future simulations continue to 2100. The earlier starting date allows a more accurate determination of the milestone when total ozone returns to pre-1980 levels, while the extended simulations allow multi-model ozone projections and an analysis of the causes of ozone changes throughout the 21<sup>st</sup> century. In addition, improved statistical analysis allows a quantification of uncertainties in the projections.
- **A more detailed understanding of the impact of stratospheric changes on climate.** The Report contains a chapter that focuses on the effects of the stratosphere on climate. This includes the radiative forcing and UV changes from ozone changes, tropospheric effects of polar ozone depletion, and changes in the flux of ozone to the troposphere over long time scales (past and future).

## 1.5 Report Structure

This SPARC CCMVal report consists of three main parts.

**Part A** (Chapter 2) describes the CCMs and simulations to be examined in the Report. It discusses the basic ingredients in the CCMs, in terms of theoretical fundamentals, and their key approximations and uncertainties, as well as providing detailed documentation of the participating CCMs. Chapter 2 also describes the forcing scenarios (*e.g.*, ODSs, GHGs, SSTs, volcanic aerosols, and solar) used for

the CCMVal-2 runs that are analysed, and any deviations thereof for particular models assessed in this report. Since the report shows CCMVal-1 model projections in addition to the new CCMVal-2 simulations in Chapter 9, model improvements for individual CCMs that participated in both rounds are also documented here.

**Part B** (Chapters 3 to 7) evaluates the CCMs' ability to simulate core processes structured around the four categories that are displayed in Figure 1.1 plus the UTLS which is discussed separately here. All key processes in these five categories are evaluated with diagnostics and with relevant data sets, and a quantitative model assessment is made based on performance metrics that confront models with observations. Each chapter discusses the processes that contribute most to uncertainty in current coupled chemistry-climate modelling, future challenges for model developments, and measurement requirements needed to better constrain the models. The key findings per model are also summarized in each chapter, providing a qualitative synthesis of the quantitative assessment. The chapters in Part B also include analysis of long-term changes in the key processes over the past and future (*e.g.*, changes in the Brewer-Dobson circulation, PSC frequency, stratospheric sudden warmings, water vapour budget in the UTLS). This approach provides a coherent framework for the evaluation of CCMs and is used as a basis for the assessment in Part C.

**Part C** (Chapters 8 to 10) examines the coupled ozone-climate response to natural and anthropogenic forcing. Chapter 8 examines the natural variability in the CCMs, and evaluates how well CCMs represent the effects of various sources of coherent forced and unforced natural variability (seasonal cycle, quasi-biennial oscillation (QBO), volcanic, solar, El Niño Southern Oscillation (ENSO)) on stratospheric ozone. Chapter 9 examines long-term projections of stratospheric ozone from the CCMs, focusing on the simulated long-term changes in ozone and the causes of these changes (*i.e.*, their relation to changes in chemistry, dynamics, radiation, transport and UTLS discussed in Part B). Chapter 10 examines the effect of stratospheric changes on the troposphere, and includes analysis of the radiative forcing from ozone changes, tropospheric effects of polar ozone depletion, and changes in the flux of ozone to the troposphere over long time scales.

The key conclusions of the report are summarized in the Executive Summary. It is divided into overall key findings, overall recommendations, and key findings per chapter. The **overall key findings** include a synthesis of the results presented in the individual chapters to provide a coherent assessment of the current generation of CCMs based on the CCMVal concept, including a summary of the results presented in Part C. The **overall recommendations** identify the processes that contribute most to uncertainty in current coupled chemistry-climate modelling, summarize

future challenges for model development, and advocate best practices in CCM modelling and model evaluation. Key observations and key gaps needed for model evaluation are also identified.

## References

- Akiyoshi, H., L. B. Zhou, Y. Yamashita, K. Sakamoto, M. Yoshiki, T. Nagashima, M. Takahashi, J. Kurokawa, M. Takigawa, and T. Imamura, 2009. A CCM simulation of the breakup of the Antarctic polar vortex in the years 1980-2004 under the CCMVal scenarios, *J. Geophys. Res.*, **114**, doi:10.1029/2007JD009261.
- Andrews, A. E., K. A. Boering, B. C. Daube, S. C. Wofsy, M. Loewenstein, H. Jost, J. R. Podolske, C. R. Webster, R. L. Herman, D. C. Scott, G. J. Flesch, E. J. Moyer, J. W. Elkins, G. S. Dutton, D. F. Hurst, F. L. Moore, E. A. Ray, P. A. Romashkin, and S. E. Strahan, 2001. Mean ages of stratospheric air derived from in situ observations of CO<sub>2</sub>, CH<sub>4</sub>, and N<sub>2</sub>O, *J. Geophys. Res.*, **106**, 32,295–32,314.
- Anthes, R. A., R. A. Anthes, P. A. Bernhardt, Y. Chen, L. Cucurull, K. F. Dymond, D. Ector, S. B. Healy, S.-P. Ho, D. C. Hunt, Y.-H. Kuo, H. Liu, K. Manning, C. McCormick, T. K. Meehan, W. J. Randel, C. Rocken, W. S. Schreiner, S. V. Sokolovskiy, S. Syndergaard, D. C. Thompson, K. E. Trenberth, T.-K. Wee, N. L. Yen, and Z. Zeng, 2008. The COSMIC/FORMOSAT-3 mission: Early results. *Bull. Amer. Meteor. Soc.*, **89**, 313-333.
- Austin, J., and N. Butchart, 2003. Coupled chemistry-climate model simulations of the period 1980-2020: Ozone depletion and the start of ozone recovery, *Quart. J. Roy. Meteorol. Soc.*, **129**, 3225-3249.
- Austin, J., and R. J. Wilson, 2009. Sensitivity of polar ozone to sea surface temperatures and chemistry, *J. Geophys. Res.*, submitted.
- Austin, J., D. Shindell, S. R. Beagley, C. Brühl, M. Dameris, E. Manzini, T. Nagashima, P. Newman, S. Pawson, G. Pitari, E. Rozanov, C. Schnadt, and T. G. Shepherd, 2003. Uncertainties and assessments of chemistry-climate models of the stratosphere, *Atmos. Chem. Phys.*, **3**, 1-27.
- Bernath, P. F., C. T. McElroy, M. C. Abrams, C. D. Boone, M. Butler, C. Camy-Peyret, M. Carleer, C. Clerbaux, P.-F. Coheur, R. Colin, P. DeCola, M. DeMazière, J. R. Drummond, D. Dufour, W. F. J. Evans, H. Fast, D. Fussen, K. Gilbert, D. E. Jennings, E. J. Llewellyn, R. P. Lowe, E. Mahieu, J. C. McConnell, M. McHugh, S. D. McLeod, R. Michaud, C. Midwinter, R. Nassar, F. Nichitiu, C. Nowlan, C. P. Rinsland, Y. J. Rochon, N. Rowlands, K. Semeniuk, P. Simon, R. Skelton, J. J. Sloan, M.-A. Soucy, K. Strong, P. Tremblay, D. Turnbull, K. A. Walker, I. Walkty, D. A. Wardle, V. Wehrle, R. Zander, and J. Zou, 2005. Atmospheric Chemistry Experiment (ACE): Mission overview, *Geophys. Res. Lett.*, **32**, doi:10.1029/2005GL022386.
- Brunner, D., J. Staehelin, H. L. Rogers, M. O. Köhler, J. A. Pyle, D. Hauglustaine, L. Jourdain, T. K. Bernsten, M. Gauss, I. S. A. Isaksen, E. Meijer, P. van Velthoven, G. Pitari, E. Mancini, G. Grewe, and R. Sausen, 2003. An evaluation of the performance of chemistry transport models by comparison with research aircraft observations. Part 1: Concepts and overall model performance, *Atmos. Chem. Phys.*, **3**, 1609-1631.
- Connolley, W. M., and T. J. Bracegirdle, 2007. An Antarctic assessment of IPCC AR4 climate models, *Geophys. Res. Lett.*, **34**, doi:10.1029/2007GL031648.
- deGrandpré, J., S. R. Beagley, V. I. Fomichev, E. Griffioen, J. C. McConnell, A. S. Medvedev and T. G. Shepherd, 2000. Ozone climatology using interactive chemistry: Results from the Canadian Middle Atmosphere Model, *J. Geophys. Res.*, **105**, 26475-26491.
- Déqué, M., 2007. Frequency of precipitation and temperature extremes over France in an anthropogenic scenario: model results and statistical correction according to observed values. *Global and Planetary Change*, **57**, 16-26.
- Dessler, A. E., 2002. The effect of deep, tropical convection on the tropical tropopause layer, *J. Geophys. Res.*, **107**, doi:10.1029/2001JD000511.
- Douglass, A. R., M. J. Prather, T. M. Hall, S. E. Strahan, P. J. Rasch, L. C. Sparling, L. Coy, and J. M. Rodriguez, 1999. Choosing meteorological input for the global modeling initiative assessment of high-speed aircraft, *J. Geophys. Res.*, **104**, 27,545-27,564.
- Douglass, A. R., R. S. Stolarski, M. R. Schoeberl, C. H. Jackman, M. Gupta, P. A. Newman, J. E. Nielsen, and E. Fleming, 2008. Relationship of loss, mean age of air and the distribution of CFCs to stratospheric circulation and implications for atmospheric lifetimes,

- J. Geophys. Res.*, **113**, doi:10.1029/2007JD009575.
- Egorova, T., E. Rozanov, V. Zubov, E. Manzini, W. Schmutz, and T. Peter, 2005. Chemistry-climate model SOCOL: A validation of the present-day climatology, *Atmos. Chem. Phys.*, **5**, 1557-1576.
- Engel, A., T. Möbius, H. Bönisch, U. Schmidt, R. Heinz, I. Levin, E. Atlas, S. Aoki, T. Nakazawa, S. Sugawara, F. Moore, D. Hurst, J. Elkins, S. Schauffler, A. Andrews, and K. Boering, 2009. Age of stratospheric air unchanged within uncertainties over the past 30 years, *Nature Geosci.*, **2**, 28-31.
- Eyring, V., N. R. P. Harris, M. Rex, T. G. Shepherd, D. W. Fahey, G. T. Amanatidis, J. Austin, M. P. Chipperfield, M. Dameris, P. M. De F. Forster, A. Gettelman, H. F. Graf, T. Nagashima, P. A. Newman, S. Pawson, M. J. Prather, J. A. Pyle, R. J. Salawitch, B. D. Santer, and D. W. Waugh, 2005. A strategy for process-oriented validation of coupled chemistry-climate models, *Bull. Am. Meteorol. Soc.*, **86**, 1117-1133.
- Eyring, V., A. Gettelman, N. R. P. Harris, S. Pawson, T. G. Shepherd, D. W. Waugh, H. Akiyoshi, N. Butchart, M. P. Chipperfield, M. Dameris, D. W. Fahey, P. M. de F. Forster, P. A. Newman, M. Rex, R. J. Salawitch, and B. D. Santer, 2008. Report on the Third SPARC CCMVal Workshop, *SPARC Newsletter No. 30*, 17-19.
- Eyring, V., N. Butchart, D. W. Waugh, H. Akiyoshi, J. Austin, S. Bekki, G. E. Bodeker, B. A. Boville, C. Brühl, M. P. Chipperfield, E. Cordero, M. Dameris, M. Deushi, V. E. Fioletov, S. M. Frith, R. R. Garcia, A. Gettelman, M. A. Giorgetta, V. Grewe, L. Jourdain, D. E. Kinnison, E. Mancini, E. Manzini, M. Marchand, D. R. Marsh, T. Nagashima, P. A. Newman, J. E. Nielsen, S. Pawson, G. Pitari, D. A. Plummer, E. Rozanov, M. Schraner, T. G. Shepherd, K. Shibata, R. S. Stolarski, H. Struthers, W. Tian, and M. Yoshiki, 2006. Assessment of temperature, trace species and ozone in chemistry-climate model simulations of the recent past, *J. Geophys. Res.*, **111**, doi:10.1029/2006JD007327.
- Eyring, V., D. W. Waugh, G. E. Bodeker, E. Cordero, H. Akiyoshi, J. Austin, S. R. Beagley, B. Boville, P. Braesicke, C. Brühl, N. Butchart, M. P. Chipperfield, M. Dameris, R. Deckert, M. Deushi, S. M. Frith, R. R. Garcia, A. Gettelman, M. Giorgetta, D. E. Kinnison, E. Mancini, E. Manzini, D. R. Marsh, S. Matthes, T. Nagashima, P. A. Newman, J. E. Nielsen, S. Pawson, G. Pitari, D. A. Plummer, E. Rozanov, M. Schraner, J. F. Scinocca, K. Semeniuk, T. G. Shepherd, K. Shibata, B. Steil, R. Stolarski, W. Tian, and M. Yoshiki, 2007. Multimodel projections of stratospheric ozone in the 21st century, *J. Geophys. Res.*, **112**, doi:10.1029/2006JD008332.
- Fioletov, V. E., G. E. Bodeker, A. J. Miller, R. D. McPeters, and R. Stolarski, 2002. Global ozone and zonal total ozone variations estimated from ground-based and satellite measurements: 1964-2000, *J. Geophys. Res.*, **107**, doi:10.1029/2001JD001350.
- Fischer, H., M. Birk, C. Blom, B. Carli, M. Carlotti, T. von Clarmann, L. Delbouille, A. Dudhia, D. Ehnhalt, M. Endemann, J. M. Flaud, R. Gessner, A. Kleinert, R. Koopman, J. Langen, M. López-Puertas, P. Mosner, H. Nett, H. Oelhaf, G. Perron, J. Remedios, M. Ridolfi, G. Stiller, and R. Zander, 2008. MIPAS: An instrument for atmospheric and climate research, *Atmos. Chem. Phys.*, **6**, 2151-2188.
- Froidevaux L., Y. B. Jiang, A. Lambert, N. J. Livesey, W. G. Read, J. W. Waters, R. A. Fuller, T. P. Marcy, P. J. Popp, R. S. Gao, D. W. Fahey, K. W. Jucks, R. A. Stachnik, G. C. Toon, L. E. Christensen, C. R. Webster, P. F. Bernath, C. D. Boone, K. A. Walker, H. C. Pumphrey, R. S. Harwood, G. L. Manney, M. J. Schwartz, W. H. Daffer, B. J. Drouin, R. E. Cofield, D. T. Cuddy, R. F. Jarnot, B. W. Knosp, V. S. Perun, W. V. Snyder, P. C. Stek, R. P. Thurstans, and P. A. Wagner, 2008. Validation of Aura Microwave Limb Sounder HCl measurements, *J. Geophys. Res.*, **113**, doi:10.1029/2007JD009025.
- Garcia, R. R., D. R. Marsh, D. E. Kinnison, B. A. Boville, and F. Sassi, 2007. Simulation of secular trends in the middle atmosphere, 1950-2003, *J. Geophys. Res.*, **112**, doi:10.1029/2006JD007485.
- Garny, H., M. Dameris, and A. Stenke, 2009. Impact of prescribed SSTs on climatologies and long-term trends in CCM simulations, *Atmos. Chem. Phys.*, **9**, 6017-6031.
- Glatthor, N., T. von Clarmann, H. Fischer, B. Funke, U. Grabowski, M. Höpfner, S. Kellmann, M. Kiefer, A. Linden, M. Milz, T. Steck, G. P. Stiller, G. Mengistu Tsidu, and D. Y. Wang, 2005. Mixing processes during the Antarctic vortex split in September-October 2002 as inferred from source gas and ozone distri-

- butions from ENVISAT-MIPAS, *J. Atmos. Sci.*, **62**, 787-800.
- Gleckler, P. J., K. E. Taylor, and C. Doutriaux, 2008. Performance Metrics for Climate Models, *J. Geophys. Res.*, **113**, doi: 10.1029/2007JD008972.
- Grewe, V., and R. Sausen, 2009. Comment on “Quantitative performance metrics for stratospheric-resolving chemistry-climate models” by Waugh and Eyring, *Atmos. Chem. Phys.*, **9**, 9101-9110.
- Groß, J. -U. and J. M. Russell III, 2005. Technical note: A stratospheric climatology for O<sub>3</sub>, H<sub>2</sub>O, CH<sub>4</sub>, NO<sub>x</sub>, HCl and HF derived from HALOE measurements, *Atmos. Chem. Phys.*, **5**, 2797-2807.
- Hassler, B., G. E. Bodeker, and M. Dameris, 2008. Technical note: A new global data set of trace gases and aerosols from multiple sources of high resolution measurements”, *Atmos. Chem. Phys.*, **8**, 5403-5421.
- Hegglin, M. I., C. D. Boone, G. L. Manney, T. G. Shepherd, K. A. Walker, P. F. Bernath, W. H. Daffer, P. Hoor, and C. Schiller, 2008. Validation of ACE-FTS satellite data in the upper troposphere/lower stratosphere (UTLS) using non-coincident measurements, *Atmos. Chem. Phys.*, **8**, 1483-1499.
- Hoor, P., D. Brunner, M. Hegglin, Th. Peter, C. Gurk, H. Wernli, and H. Fischer, 2004. Seasonality and extent of extra-tropical TST derived from in-situ CO measurements during SPURT, *Atmos. Chem. Phys.*, **4**, 1427 - 1442.
- IPCC (Intergovernmental Panel on Climate Change), 2000. Special report on emissions scenarios: A special report of Working Group III of the Intergovernmental Panel on Climate Change, 599 pp., Cambridge University Press, Cambridge, U.K.
- Jöckel, P., H. Tost, A. Pozzer, C. Brühl, J. Buchholz, L. Ganzeveld, P. Hoor, A. Kerkweg, M. G. Lawrence, R. Sander, B. Steil, G. Stiller, M. Tanarhte, D. Taraborrelli, J. van Aardenne, and J. Lelieveld, 2006. The atmospheric chemistry general circulation model ECHAM5/MESSy1: Consistent simulation of ozone from the surface to the mesosphere, *Atmos. Chem. Phys.*, **6**, 5067– 5104.
- Jones, A. E., and J. D. Shanklin, 1995. Continued decline of total ozone over Halley, Antarctica, since 1985, *Nature*, **376**, 409-411.
- Jourdain, L., S. Bekki, F. Lott, and F. Lefèvre, 2008. The coupled chemistry-climate model LMDz-REPRO-BUS: description and evaluation of a transient simulation of the period 1980–1999, *Annales Geophysicae*, **26**, 1391-1413.
- Jucks, K. W., D. G. Johnson, K. V. Chance, W. A. Traub, J. J. Margitan, G. B. Osterman, R. J. Salawitch, and Y. Sasano, 1998. Observations of OH, HO<sub>2</sub>, H<sub>2</sub>O, and O<sub>3</sub> in the upper stratosphere: implications for HO<sub>x</sub> photochemistry, *Geophys. Res. Lett.*, **25**, 3935-3938, doi:10.1029/1998GL900009.
- Kalnay, E., M. Kanamitsu, R. Kistler, W. Collins, D. Deaven, L. Gandin, M. Iredell, S. Saha, G. White, J. Woolen, Y. Zhu, M. Chelliah, W. Ebisuzaki, W. Higgins, J. Janowiak, K. C. Mo, C. Ropelewski, J. Wang, A. Leetmaa, R. Reynolds, R. Jenne, and D. Joseph, 1996. The NCEP/NCAR 40-year reanalysis project, *Bull. Am. Meteorol. Soc.*, **77**, 437-471.
- Kanamitsu, M., W. Ebisuzaki, J. Wollen, S.-K. Yang, J. J. Hnilo, M. Fiorino, and G. L. Potter, 2002. NCEP-DEO AMIP II reanalysis (R-2), *Bull. Am. Meteorol. Soc.*, **83**, 1631–1643.
- Lamarque J.-F., D. E. Kinnison, P. G. Hess, and F. M. Vitt, 2008. Simulated lower stratospheric trends between 1970 and 2005: Identifying the role of climate and composition changes, *J. Geophys. Res.*, **113**, doi:10.1029/2007JD009277.
- Lambert A., W. G. Read, N. J. Livesey, M. L. Santee, G. L. Manney, L. Froidevaux, D. L. Wu, M. J. Schwartz, H. C. Pumphrey, C. Jimenez, G. E. Nedoluha, R. E. Cofield, D. T. Cuddy, W. H. Daffer, B. J. Drouin, R. A. Fuller, R. F. Jarnot, B. W. Knosp, H. M. Pickett, V. S. Perun, W. V. Snyder, P. C. Stek, R. P. Thurstans, P. A. Wagner, J. W. Waters, K. W. Jucks, G. C. Toon, R. A. Stachnik, P. F. Bernath, C. D. Boone, K. A. Walker, J. Urban, D. Murtagh, J. W. Elkins, and E. Atlas, 2007. Validation of the Aura microwave limb sounder middle atmosphere water vapor and nitrous oxide measurements, *J. Geophys. Res.*, **112**, doi:10.1029/2007JD008724.
- Lanzendorf, E. J., T. F. Hanisco, P. O. Wennberg, R. C. Cohen, R. M. Stimpfle, J. G. Anderson, R. S. Gao, J. J. Margitan, and T. P. Bui, 2001. Establishing the dependence of (HO<sub>2</sub>)/(OH) on temperature, halogen loading, O<sub>3</sub>, and NO<sub>x</sub> based on in situ measurements from the NASA ER-2, *J. Phys. Chem. A*, **105**, 1535–1542.
- Lary, D. J., D. W. Waugh, A. R. Douglass, R. S. Stolarski, P.

- A. Newman, and H. Mussa, 2007. Variations in stratospheric inorganic chlorine between 1991 and 2006, *Geophys. Res. Lett.*, **34**, doi:10.1029/2007GL030053.
- Livesey, N. J., M. J. Filipiak, L. Froidevaux, W. G. Read, A. Lambert, M. L. Santee, J. H. Jiang, H. C. Pumphrey, J. W. Waters, R. E. Cofield, D. T. Cuddy, W. H. Daffer, B. J. Drouin, R. A. Fuller, R. F. Jarnot, Y. B. Jiang, B. W. Knosp, Q. B. Li, V. S. Perun, M. J. Schwartz, W. V. Snyder, P. C. Stek, R. P. Thurstans, P. A. Wagner, M. Avery, E. V. Browell, J.-P. Cammas, L. E. Christensen, G. S. Diskin, R.-S. Gao, H.-J. Jost, M. Loewenstein, J. D. Lopez, P. Nedelec, G. B. Osterman, G. W. Sachse, and C. R. Webster, 2008. Validation of Aura Microwave Limb Sounder O<sub>3</sub> and CO observations in the upper troposphere and lower stratosphere, *J. Geophys. Res.*, **113**, doi:10.1029/2007JD008805.
- McPeters, R. D., G. J. Labow, and J. A. Logan, 2007. Ozone climatological profiles for satellite retrieval algorithms, *J. Geophys. Res.*, **112**, doi:10.1029/2005JD006823.
- Miller, A. J., R. M. Nagatani, L. E. Flynn, S. Kondragunta, E. Beach, R. Stolarski, R. D. McPeters, P. K. Bhartia, M. T. DeLand, C. H. Jackman, D. J. Wuebbles, K. O. Patten, and R. P. Cebula, 2002. A cohesive total ozone data set from the SBUV(2) satellite system, *J. Geophys. Res.*, **107**, doi:10.1029/2001JD000853.
- Morgenstern, O., P. Braesicke, M. M. Hurwitz, F. M. O'Connor, A. C. Bushell, C. E. Johnson, and J. A. Pyle, 2008. The world avoided by the Montreal Protocol, *Geophys. Res. Lett.*, **35**, doi:10.1029/2008GL034590.
- Morgenstern, O., P. Braesicke, F. M. O'Connor, A. C. Bushell, C. E. Johnson, S. M. Osprey, and J. A. Pyle, 2009. Evaluation of the new UKCA climate-composition model – Part 1: The stratosphere, *Geosci. Model Dev.*, **2**, 43-57.
- Montzka, S. A., J. H. Butler, B. D. Hall, D. J. Mondeel, and J. W. Elkins, 2003. A decline in tropospheric bromine, *Geophys. Res. Lett.*, **30**, doi:10.1029/2003GL017745.
- Murtagh, D., U. Frisk, F. Merino, M. Ridal, A. Jonsson, J. Stegman, G. Witt, P. Eriksson, C. Jiménez, G. Megie, J. de la Noë, P. Ricaud, P. Baron, J. R. Pardo, A. Hauchcorne, E. J. Llewellyn, D. A. Degenstein, R. L. Gattinger, N. D. Lloyd, W. F. J. Evans, I. C. McDade, C. S. Haley, C. Sioris, C. von Savigny, B. H. Solheim, J. C. McConnell, K. Strong, E. H. Richardson, G. W. Leppelmeier, E. Kyrölä, H. Auvinen, and L. Oikarinen, 2002. An overview of the Odin atmospheric mission, *Can. J. Phys.*, **80**, 309-319.
- Onogi, K., J. Tsutsui, H. Koide, M. Sakamoto, S. Kobayashi, H. Hatsushika, T. Matsumoto, N. Yamazaki, H. Kamahori, K. Takahashi, S. Kadokura, K. Wada, K. Kato, R. Oyama, T. Ose, N. Mannoji and R. Taira, 2007. The JRA-25 reanalysis. *J. Meteor. Soc. Japan*, **85**, 369-432.
- Osterman, G. B., R. J. Salawitch, B. Sen, G. C. Toon, R. A. Stachnik, H. M. Pickett, J. J. Margitan, J.-F. Blavier, and D. B. Peterson., 1997. Balloon-borne measurements of stratospheric radicals and their precursors: implications for the production and loss of ozone, *Geophys. Res. Lett.*, **24**, 1107–1110.
- Pan, L. L., J. C. Wei, D. E. Kinnison, R. R. Garcia, D. J. Wuebbles, and G. P. Brasseur, 2007. A set of diagnostics for evaluating chemistry-climate models in the extra-tropical tropopause region, *J. Geophys. Res.*, **112**, doi:10.1029/2006JD007792.
- Pawson, S., K. Kodera, K. Hamilton, T. G. Shepherd, S. R. Beagley, B. A. Boville, J. D. Farrara, T. D. A. Fairlie, A. Kitoh, W. A. Lahoz, U. Langematz, E. Manzini, D. H. Rind, A. A. Scaife, K. Shibata, P. Simon, R. Swinbank, L. Takacs, R. J. Wilson, J. A. Al-Saadi, M. Amodei, M. Chiba, L. Coy, J. de Grandpré, R. S. Eckman, M. Fiorino, W. L. Grose, H. Koide, J. N. Koshyk, D. Li, J. Lerner, J. D. Mahlman, N. A. McFarlane, C. R. Mechoso, A. Molod, A. O'Neill, R. B. Pierce, W. J. Randel, R. B. Rood, and F. Wu, 2000. The GCM-reality intercomparison project for SPARC: Scientific issues and initial results, *Bull. Am. Meteorol. Soc.*, **81**, 781-796.
- Pawson, S., R. S. Stolarski, A. R. Douglass, P. A. Newman, J. E. Nielsen, S. M. Frith, and M. L. Gupta, 2008. Goddard Earth Observing System Chemistry-Climate Model Simulations of Stratospheric Ozone-Temperature Coupling Between 1950 and 2005, *J. Geophys. Res.*, **113**, doi:10.1029/2007JD009511.
- Pitari G., E. Mancini, V. Rizi and D. T. Shindell, 2002. Impact of future climate and emission changes on stratospheric aerosols and ozone, *J. Atmos. Sci.*, **59**, 414–440.
- Pundt, I., J.-P. Pommereau, M. P. Chipperfield, M. Van Roozendaal, and F. Goutail, 2002. Climatology of the stratospheric BrO vertical distribution by bal-

- loon-borne UV–visible spectrometry, *J. Geophys. Res.*, **107**, doi:10.1029/2002JD002230.
- Randel, W. J., and F. Wu, 2006. Biases in Stratospheric and Tropospheric Temperature Trends Derived from Historical Radiosonde Data, *J. Clim.*, **19**, 2094–2104.
- Randel, W. J., K. P. Shine, J. Austin, J. Barnett, C. Claud, N. P. Gillett, P. Keckhut, U. Langematz, R. Lin, C. Long, C. Mears, A. Miller, J. Nash, D. J. Seidel, D. W. J. Thompson, F. Wu, S. Yoden, 2009. An update of observed stratospheric temperature trends. *J. Geophys. Res.*, **114**, doi:10.1029/2008JD010421.
- Reichler, T. and J. Kim, 2008. How well do coupled models simulate today’s climate?, *Bull. Am. Meteor. Soc.*, **89**, 303–311, doi:10.1175/BAMS-89-3-303.
- Rinsland, C.P., E. Mahieu, R. Zander, N. B. Jones, M. P. Chipperfield, A. Goldman, J. Anderson, J. M. Russell, P. Demoulin, J. Notholt, G. C. Toon, J.-F. Blavier, B. Sen, R. Sussmann, S. W. Wood, A. Meier, D. W. T. Griffith, L. S. Chiou, F. J. Murcray, T. M. Stephen, F. Hase, S. Mikuteit, A. Schulz, T. Blumenstock, 2003. Long-term trends of inorganic chlorine from ground-based infrared solar spectra: Past increases and evidence for stabilization, *J. Geophys. Res.*, **108**, doi:10.1029/2002JD003001.
- Rozanov, A., H. Bovensmann, A. Bracher, S. Hrechanyy, V. Rozanov, M. Sinnhuber, F. Stroh and J.P. Burrows, 2005. NO<sub>2</sub> and BrO vertical profile retrieval from SCIAMACHY limb measurements: Sensitivity studies, *Adv. Space Res.*, **36**, 846-854.
- Russell, J. M., L. L. Gordley, J. H. Park, S. R. Drayson, A. F. Tuck, J. E. Harries, R. J. Cicerone, P. J. Crutzen, and J. E. Frederick, 1993. The halogen occultation experiment, *J. Geophys. Res.*, **98**, 10,777-10,797.
- Salawitch, R. J., S. C. Wofsy, P. O. Wennberg, R. C. Cohen, J. G. Anderson, D. W. Fahey, R. S. Gao, E. R. Keim, E. L. Woodbridge, R. M. Stimpfle, J. P. Koplów, D. W. Kohn, C. R. Webster, R. D. May, L. Pfister, E. W. Gottlieb, H. A. Michelsen, G. K. Yue, J. C. Wilson, C. A. Brock, H. H. Jonsson, J. E. Dye, D. Baumgardner, M. H. Proffitt, M. Loewenstein, J. R. Podolske, J. W. Elkins, G. S. Dutton, E. J. Hintsa, A. E. Dessler, E. M. Weinstock, K. K. Kelly, K. A. Boering, B. C. Daube, K. R. Chan, and S. W. Bowen, 1994. The distribution of hydrogen, nitrogen, and chlorine radicals in the lower stratosphere: implications for changes in O<sub>3</sub> due to emission of NO<sub>y</sub> from supersonic aircraft, *Geophys. Res. Lett.*, **21**, 2543–2546.
- Salawitch, R. J., P. O. Wennberg, G. C. Toon, B. Sen, and J.-F. Blavier, 2002. Near IR photolysis of HO<sub>2</sub>NO<sub>2</sub>: Implications for HO<sub>x</sub>, *Geophys. Res. Lett.*, **29**, doi:10.1029/2002GL015006.
- Salawitch, R. J., D. K. Weisenstein, L. J. Kovalenko, C. E. Sioris, P. O. Wennberg, K. Chance, M. K. W. Ko, and C. A. McLinden, 2005. Sensitivity of ozone to bromine in the lower stratosphere, *Geophys. Res. Lett.*, **32**, doi:10.1029/2004GL021504.
- Santee, M. L., G. L. Manney, N. J. Livesey, L. Froidevaux, H. C. Pumphrey, W. G. Read, M. J. Schwartz, and J. W. Waters, 2005. Polar processing and development of the 2004 Antarctic ozone hole: First results from Aura MLS, *Geophys. Res. Lett.*, **32**, doi:10.1029/2005GL022582.
- Santer, B.D., R. Sausen, T.M.L. Wigley, J.S. Boyle, K. AchutaRao, C. Doutriaux, J.E. Hansen, G.A. Meehl, E. Roeckner, R. Ruedy, G. Schmidt, and K.E. Taylor, 2003. Behavior of tropopause height and atmospheric temperature in models, reanalyses, and observations: Decadal changes, *J. Geophys. Res.*, **108**, doi:10.1029/2002JD002258.
- Santer, B. D., K. E. Taylor, P. J. Gleckler, C. Bonfils, T. P. Barnett, D. W. Pierce, T. M. L. Wigley, C. Mears, F. J. Wentz, W. Brüggemann, N. P. Gillett, S. A. Klein, S. Solomon, P. A. Stott, and M. F. Wehner, 2009. Incorporating model quality information in climate change detection and attribution studies, *PNAS*, **106**, 14778-14783, doi: 10.1073/pnas.0901736106.
- Schauffler, S. M., E. L. Atlas, S. G. Donnelly, A. Andrews, S. A. Montzka, J. W. Elkins, D. F. Hurst, P. A. Romashkin, G. S. Dutton, and V. Stroud, 2003. Chlorine budget and partitioning during the Stratospheric Aerosol and Gas Experiment (SAGE) III Ozone Loss and Validation Experiment (SOLVE), *J. Geophys. Res.*, **108**, doi:10.1029/2001JD002040.
- Schmittner A., M. Latif, and B. Schneider, 2005. Model projections of the North Atlantic thermohaline circulation for the 21st century, *Geophys. Res. Lett.*, **32**, doi:10.1029/2005GL024368.
- Schraner, M., E. Rozanov, C. Schnadt-Poberaj, P. Kenzelmann, A. Fischer, V. Zubov, B. P. Luo, C. Hoyle, T. Egorova, S. Fueglistaler, S. Brönnimann, W. Schmutz and T. Peter, 2008. Chemistry-climate model SOCOL: version 2.0 with improved transport and



- chemistry/ microphysics schemes, *Atmos. Chem. Phys.*, **8**, 5957–5974.
- Sen, B., G. C. Toon, G. B. Osterman, J.-F. Blavier, J. J. Margitan, R. J. Salawitch, and G. K. Yue, 1998. Measurements of reactive nitrogen in the stratosphere, *J. Geophys. Res.*, **103**, 3571–3585.
- Shibata, K. and M. Deushi, 2008a. Long-term variations and trends in the simulation of the middle atmosphere 1980–2004 by the chemistry-climate model of the Meteorological Research Institute, *Annales Geophysicae*, **26**, 1299–1326.
- Shibata, K. and M. Deushi, 2008b. Simulation of the stratospheric circulation and ozone during the recent past (1980–2004) with the MRI chemistry-climate model, *CGER's Supercomputer Monograph Report*, **13**, National Institute for Environmental Studies, Japan, 154 pp.
- Scinocca, J. F., N. A. McFarlane, M. Lazare, J. Li and D. Plummer, 2008. Technical Note: The CCCma third generation AGCM and its extension into the middle atmosphere, *Atmos. Chem. Phys.*, **8**, 7055–7074.
- Shepherd, T. G., and W. J. Randel, 2007. Key issues arising from the 2006 WMO/UNEP Ozone Assessment, *SPARC Newsletter No. 29*, 20–22.
- Stenke, A., M. Dameris, V. Grewe and H. Garny, 2009. Implications of Lagrangian transport for coupled chemistry-climate simulations, *Atmos. Chem. Phys.*, **9**, 5489–5504.
- Stolarski, R. S. and S. Frith, 2006. Search for evidence of trend slow-down in the long-term TOMS/SBUV total ozone data record: the importance of instrument drift uncertainty, *Atmos. Chem. Phys.*, **6**, 4057–4065.
- Strahan, S.E., and A.R. Douglass, 2004. Evaluating the credibility of transport processes in simulations of ozone recovery using the Global Modeling Initiative three-dimensional model, *J. Geophys. Res.*, **109**, doi:10.1029/2003JD004238.
- Swinbank, R., and A. O'Neill, 1994. A stratosphere-troposphere data assimilation system, *Mon. Weather Rev.*, **122**, 686–702.
- Taylor, K. E., 2001. Summarizing multiple aspects of model performance in a single diagram. *J. Geophys. Res.*, **106**, 7183–7192.
- Teysse re H., M. Michou, H. L. Clark, B. Josse, F. Karcher, D. Olivie, V.-H. Peuch, D. Saint-Martin, D. Cariolle, J.-L. Atti e, P. N ed elec, P. Ricaud, V. Thouret, R. J. van der A, A. Volz-Thomas, and F. Cheroux, 2007. A new tropospheric and stratospheric chemistry and transport model MOCAGE-Climat for multi-year studies: Evaluation of the present-day climatology and sensitivity to surface processes, *Atmos. Chem. Phys.*, **7**, 5815–5860.
- Thomason, L. W., L. R. Poole, and T. Deshler, 1997. A global climatology of stratospheric aerosol surface area density deduced from Stratospheric Aerosol and Gas Experiment II measurements: 1984–1994, *J. Geophys. Res.*, **102**, 8967–8976.
- Thompson, D. W. J., and S. Solomon, 2002. Interpretation of recent southern hemisphere climate change, *Science*, **296**, 895–899.
- Tian, W., and M. P. Chipperfield, 2005. A new coupled chemistry-climate model for the stratosphere: the importance of coupling for future O<sub>3</sub>-climate predictions, *Quart. J. Roy. Meteor. Soc.*, **131**, 281–303.
- Tian, W., M. P. Chipperfield, L. J. Gray, and J. M. Zawodny, 2006. Quasi-biennial oscillation and tracer distributions in a coupled chemistry-climate model, *J. Geophys. Res.*, **111**, doi:10.1029/2005JD006871.
- Tilmes, S., R. M uller, A. Engel, M. Rex, and J. M. Russell III, 2006. Chemical ozone loss in the Arctic and Antarctic stratosphere between 1992 and 2005, *Geophys. Res. Lett.*, **33**, doi:10.1029/2006GL026925.
- Tilmes, S., L. Pan, P. Hoor, G. W. Sachse, M. Loewenstein, J. Lopez, C. Webster, L. E. Cristensen, M. Proffitt, R.-S. Gao, G. S. Diskin, M. A. Avery, J. R. Podolske, R. L. Herman, N. Spelten, A. Weinheimer, T. Campus, E. J. Hints, E. M. Weinstock, J. Pittman, M. A. Zondl, M. E. Paige, E. Atlas, 2010. An aircraft based upper troposphere lower stratosphere O<sub>3</sub>, CO and H<sub>2</sub>O climatology for the Northern hemisphere, *J. Geophys. Res.*, doi:10.1029/2009JD012731, in press.
- Uppala, S. M., P. W. K allberg, A. J. Simmons, U. Andrae, V. da Costa Bechtold, M. Fiorino, K. K. Gibson, J. Haseler, A. Hernandez, G. A. Kelly, X. Li, K. Onogi, S. Saarinen, N. Sokka, R. P. Allan, E. Andersson, K. Arpe, M. A. Balmaseda, A. C. M. Beljaars, L. van de Berg, J. Bidlot, N. Bormann, S. Caires, F. Chevallier, A. Dethof, M. Dragosavac, M. Fisher, M. Fuentes, S. Hagemann, E. H olm, B.J. Hoskins, L. Isaksen, P. A. E. M. Janssen, R. Jenne, A. P. McNally, J.-F. Mahfouf, J.-J. Morcrette, N. A. Rayner, R.W. Saunders, P. Simon, A. Sterl, K. E. Trenberth, A. Untch,

- D. Vasiljevic, P. Viterbo, and J. Woollen, 2005. The ERA-40 re-analysis, *Quart. J. Roy. Meteor. Soc.*, **131**, 2961-3012. doi:10.1256/qj.04.176.
- von Clarmann, T., M. Höpfner, S. Kellmann, A. Linden, S. Chauhan, B. Funke, U. Grabowski, N. Glatthor, M. Kiefer, T. Schieferdecker, G. P. Stiller, and S. Verricks, 2009. Retrieval of temperature, H<sub>2</sub>O, O<sub>3</sub>, HNO<sub>3</sub>, CH<sub>4</sub>, N<sub>2</sub>O, ClONO<sub>2</sub> and ClO from MIPAS reduced resolution nominal mode limb emission measurements, *Atmos. Meas. Tech.*, **2**, 159-175.
- von Hobe, M., A. Ulanovsky, C. M. Volk, J.-U. Groöß, S. Tilmes, P. Konopka, G. Günther, A. Werner, N. Spelten, G. Shur, V. Yushkov, F. Ravagnani, C. Schiller, R. Müller, F. Stroh, 2006. Severe ozone depletion in the cold Arctic winter 2004-05, *Geophys. Res. Lett.*, **33**, doi:10.1029/2006GL026945.
- Wamsley, P. R., J. W. Elkins, D. W. Fahey, G. S. Dutton, C. M. Volk, R. C. Myers, S. A. Montzka, J. H. Butler, A. D. Clarke, P. J. Fraser, L. P. Steele, M. P. Lucarelli, E. L. Atlas, S. M. Schauffler, D. R. Blake, F. S. Rowland, W. T. Sturges, J. M. Lee, S. A. Penkett, A. Engel, R. M. Stimpfle, K. R. Chan, D. K. Weisenstein, M. K. W. Ko, and R. J. Salawitch, 1998. Distribution of halon-1211 in the upper troposphere and lower stratosphere and the 1994 total bromine budget, *J. Geophys. Res.*, **103**, 1513-1526.
- Waugh, D. W., and V. Eyring, 2008. Quantitative performance metrics for stratospheric-resolving chemistry-climate models, *Atmos. Chem. Phys.*, **8**, 5699-5713.
- Weinstock, E. M., E. J. Hints, D. B. Kirk-Davidoff, J. G. Anderson, A. E. Andrews, R. L. Herman, C. R. Webster, M. Loewenstein, J. R. Podolske, and T. P. Bui, 2001. Constraints on the seasonal cycle of stratospheric water vapor using in situ measurements from the ER-2 and a CO photochemical clock, *J. Geophys. Res.*, **106**, 22707-22724.
- Wennberg, P.O., R. C. Cohen, R. M. Stimpfle, J. P. Koplów, J. G. Anderson, R. J. Salawitch, D. W. Fahey, E. L. Woodbridge, E. R. Keim, R. S. Gao, C. R. Webster, R. D. May, D. W. Toohey, L. M. Avallone, M. H. Profitt, M. Loewenstein, J. R. Podolske, K. R. Chan, and S. C. Wofsy, 1994. Removal of stratospheric ozone by radicals: in situ measurements of OH, HO<sub>2</sub>, NO, NO<sub>2</sub>, ClO, and BrO, *Science*, **266**, 398-404.
- Wennberg, P. O. R. J. Salawitch, D. J. Donaldson, T. F. Hanisco, E. J. Lanzendorf, K. K. Perkins, S. A. Lloyd, V. Vaida, R. S. Gao, E. J. Hints, R. C. Cohen, W. H. Swartz, T. L. Kusterer, and D. E. Anderson, 1999. Twilight observations suggest unknown sources of HOx, *Geophys. Res. Lett.*, **26**, 1373-1376.
- World Meteorological Organization (WMO)/United Nations Environment Programme (UNEP), 2007. *Scientific Assessment of Ozone Depletion: 2006*, World Meteorological Organization, Global Ozone Research and Monitoring Project, Report No. 50, Geneva, Switzerland.
- Wohlmann, I. and M. Rex, 2008. Improvement of vertical and residual velocities in pressure or hybrid sigma-pressure coordinates in analysis data in the stratosphere, *Atmos. Chem. Phys.*, **8**, 265-272.
- Woodbridge, E. L., J. W. Elkins, D. W. Fahey, L. E. Heidt, S. Solomon, T. J. Baring, T. M. Gilpin, W. H. Pollock, S. M. Schauffler, E. L. Atlas, M. Loewenstein, J. R. Podolske, C. R. Webster, R. D. May, J. M. Gilligan, S. A. Montzka, K. A. Boering, and R. J. Salawitch, 1995. Estimates of total organic and inorganic chlorine in the lower stratosphere from in situ and flask measurements during AASE II, *J. Geophys. Res.*, **100**, 3057-3064.

# Chapter 2

## Chemistry Climate Models and Scenarios

**Lead authors:** Olaf Morgenstern, Marco Giorgetta & Kiyotaka Shibata

**Contributing authors:** Hideharu Akiyoshi, John Austin, Andreas Baumgaertner, Slimane Bekki, Peter Braesicke, Christoph Brühl, Martyn Chipperfield, Martin Dameris, Sandip Dhomse, Stacey Frith, Hella Garny, Andrew Gettelman, Steven Hardiman, Michaela Hegglin, Doug Kinnison, Jean-François Lamarque, Elisa Manzini, Martine Michou, Eric Nielsen, Giovanni Pitari, David Plummer, Eugene Rozanov, John Scinocca, Dan Smale, Susan Strahan, Matthew Toohey, Wenshou Tian

### Summary

*This chapter provides ancillary information regarding the models participating in CCMVal-2, the model simulations conducted, forcings used, and diagnostics produced by the simulations. We outline the general problems associated with modelling and predicting chemistry and climate of the stratosphere. We briefly review the major components that make up modern climate-chemistry models (CCMs), addressing dynamics, radiation, chemistry, and transport. A section is devoted to introducing the 16 different models (counting nearly identical models as one) with a focus on new developments since CCMVal-1. Furthermore, we describe the reference simulations performed for CCMVal-2, the associated external forcing fields, and the deviations of the individual model setups from the definitions. We document the diagnostic output fields that modellers have produced from their simulations.*

*Morgenstern et al. (2010) have published a shortened version of this chapter.*

---

## 2.1 Introduction

CCMVal makes use of Chemistry Climate Models (CCMs) to simulate the general circulation and the chemistry of the atmosphere from 1960 to about 2100. This period is characterized by marked changes in atmospheric composition and associated climate change. There are two interconnected developments shaping these 140 years: On the one hand, during the 20<sup>th</sup> century anthropogenic activities caused an approximate 6-folding of stratospheric chlorine (WMO, 2007, assuming CH<sub>3</sub>Cl to be the only natural source of stratospheric chlorine), and an approximate doubling of bromine, which led to a thinning of the ozone layer everywhere and the occurrence of the ozone hole over Antarctica (Molina and Rowland, 1974; Farman *et al.*, 1985). When these effects were beginning to be identified, a political process was set in motion which resulted the Montreal Protocol and subsequent amendments. Thanks to these interventions, stratospheric halogen levels have peaked around the year 2000 and are anticipated to undergo a slow recovery spanning the 21<sup>st</sup> century.

On the other hand, other human activities have caused a substantial increase of greenhouse gases. Climate change has now been unambiguously identified, and with “very high confidence” (IPCC, 2007) linked to these human activities. In the stratosphere, climate change is intricately linked to ozone abundances, through a variety of feedback processes involving temperature, transport, ultraviolet (UV), and the influence of non-halogen ozone depletion cycles involving hydrogen and nitrogen radicals (Waugh *et al.*, 2009, and references therein).

Hence during the period covered by CCMVal-2, human influence on the stratosphere is thought to undergo a transition from a past dominated by ozone-depleting substances, particularly chlorofluorocarbons (CFCs), to a future increasing affected by greenhouse gases (GHGs) and climate change.

Within the CCMVal-2 project, chemistry-climate models (CCMs) are used to assess the evolution of the stratosphere under the influence of these two processes, and also taking into account natural perturbations due to volcanoes and solar variability. A comprehensive CCM would consist of a climate model and a chemistry scheme, where the climate model describes the atmosphere – ocean – land system and the different feedbacks determining the magnitude of climate change, and the chemistry scheme processes transported substances and feeds back to the circulation *via* chemical modification of radiatively active substances. One such model (see below) is participating in CCMVal-2; it is expected that in the near future more such models will reach maturity.

The first round of CCMVal (CCMVal-1), performed in 2006, produced an assessment of stratospheric climate-chemistry modelling (Eyring *et al.*, 2006, 2007) which

will form a basis of comparison for the present study, CCMVal-2 (Eyring *et al.*, 2008). Several problems were encountered during CCMVal-1. In particular, only two models covered the whole of the 21<sup>st</sup> century producing 6 simulations; other models only covered the period to 2050 or earlier (Eyring *et al.*, 2007). Considering the large differences in global ozone between models and relative to observations for the core period (1980-2025; Eyring *et al.*, 2007), the ozone forecast to 2100 produced by CCMVal-1 must be considered uncertain. Serious model problems were identified, *e.g.*, halogen non-conservation (Eyring *et al.*, 2007) leading to erroneous ozone depletion, particularly at high latitudes, temperature biases (Eyring *et al.*, 2006), and errors in the transport formulation (Eyring *et al.*, 2006). Since then, modelling groups have had a few years to address these problems. Moreover, since CCMVal-1, progress in computing capacity has enabled modellers to perform longer and more simulations or, in some cases, to expand the complexity of the models (see below). Thus now more models have completed the long simulations, some performing ensemble calculations, and the designs of many models have been improved (see below) to address the problems identified in CCMVal-1.

## 2.2 Climate change in CCMVal-2

The experimental design for this evaluation does not require interactive coupling of the atmospheric CCM to an ocean GCM. This constitutes the most important simplification in the current report, and thus all but one model do not account for changes in surface temperature caused by changes in stratospheric composition. Instead, these CCMs prescribe sea surface temperature (SST) and sea ice cover from climate model simulations that were forced by the same observed or projected GHG concentrations. All CCMVal-2 integrations of the 21<sup>st</sup> century use the middle-of-the-road Special Report on Emission Scenarios (SRES) A1b scenario (IPCC 2001; Section 2.5.3.2). Considering that A1b is only one of the possible scenarios, and that recent CO<sub>2</sub> emissions are larger than foreseen in A1b (Global Carbon Budget, 2009; Le Quéré *et al.*, 2009), the lack of consideration of other scenarios needs to be considered when interpreting the current results. Moreover, the impact of climate change on the CCMVal-2 predictions depends not only on the direct radiative impact of GHGs, but also on the realism of the associated parent AOGCM whose SSTs and sea ice are used. Biases in the ocean surface conditions (see below), as well as lacking feedback of ozone-induced climate change onto the ocean in most models, complicate the interpretation of climate change in the CCMs considered here. As noted before, the next generation of CCMs will likely comprise more models incorporating an interactive ocean.

## 2.3 Major components of chemistry climate models and their coupling by transport and radiation

The major building blocks of CCMs comprise the dynamical core, diabatic physics (*e.g.*, radiation), the transport scheme, and the chemistry and microphysics modules associated with chemical composition change. These major components are linked by feedback processes, whereby dynamics and radiation interact, radiation and chemistry interact through photolysis and GHG and aerosol forcing, and dynamics affects chemistry through the transport of chemical constituents and impacts on temperature and moisture. A schematic depiction of a CCM is given in **Figure 2.1**.

Table 1.1 (Chapter 1) introduces the models participating in CCMVal-2 with associated institutions, principal investigators, and key references. **Table 2.1** lists the main components of these models. Several models share a common heritage. For example, the E39CA, EMAC, and NiwaSOCOL models are all based on the ECHAM GCM. Likewise, the UMETRAC, UMSLIMCAT, and UМУKCA models are based on the Unified Model (UM). However, both ECHAM and the UM have undergone substantial development in recent years, such that models based on the newer versions of these models (EMAC, UМУKCA) may behave quite differently from those based on the older versions (E39CA, NiwaSOCOL, UMETRAC, UMSLIMCAT). CAM3.5 and WACCM are both based on CAM/CLM. The other models may be regarded as independent; however, models often share approaches to certain problems with other models (see below).

### 2.3.1 Dynamics

#### 2.3.1.1 Dynamical cores and model grids

Dynamical cores describe the temporal evolution of wind, temperature and pressure, or equivalent convenient variables, under the influences of inertia in a rotating framework, gravity and various diabatic forcings. The development of dynamical cores was initially strongly pushed by the needs of numerical weather prediction (NWP), with an emphasis on accurate and highly efficient numerical methods for solving, in most cases, the primitive equations (PEs). An important breakthrough was achieved by the spectral transform method (*e.g.*, Holton, 1992), which for a relatively small number of degrees of freedom allowed accurate and numerically very efficient simulations of baroclinic waves of major concern in NWP. Hence, this method is also frequently used in atmospheric general circulation models for climate research, because of its advantageous performance at low resolution; it is used by roughly half of the CCMVal-2 models (CCSRNIES, CMAM, CNRM-ACM, E39CA, EMAC, MRI, NiwaSOCOL, ULAQ; **Table 2.2**). The transport equation is however not easily treated in a spectral coordinate system, due to the occurrence of numerical artifacts, hence some “hybrid” models using the spectral transform method perform transport of chemical constituents in physical space (E39CA, EMAC, MRI, NiwaSOCOL; **Tables 2.3** and **2.4**). Likewise, parameterised and explicit physical processes are difficult to implement in spectral models.

Almost all of the remaining models use a regular

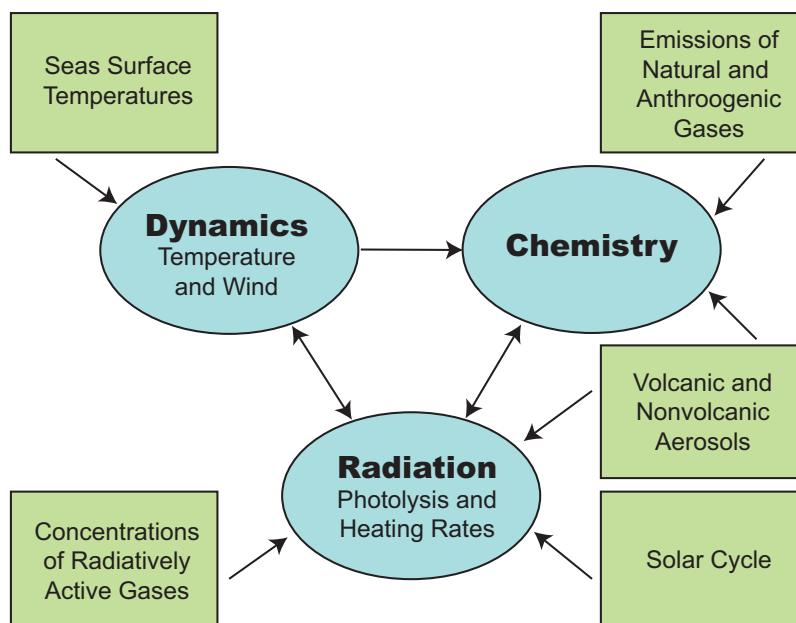


**Figure 2.1:** Basic structure of a CCM and external forcings (reproduced from WMO, 2007).

Table 2.1: Main structure of CCMs (names of main sub-models), for the atmosphere, ocean, land, transport, and chemistry. F = offline forcing.

CCM	Atmospheric GCM	Ocean GCM	Land model	Reference	Transport model for meteorol. active constituents	Transport model for chemically active constituents	Chemistry scheme
AMTRAC3	AM3	N/A	LM3		AM3	AM3	Austin (1991)
CAM3.5	CAM	N/A	CLM		CAM	CAM	WACCM + reduced HCs
CCSRNIES	CCSR/NIES AGCM 5.4g	N/A	CCSR/NIES AGCM 5.4g	Nimiguti et al. (1997)	CCSR/NIES AGCM 5.4g	CCSR/NIES AGCM 5.4g	Akiyoshi (2000), Nagashima et al. (2002) Akiyoshi et al. (2009)
CMAM	AGCM3	Modified NCOM 1.3	CLASS 2.7		AGCM3 spectral	AGCM3 spectral	deGrandpré et al. (2000) plus updates
CNRM-ACM	ARPEGE-Climate version 4.6	N/A	ISBA	Déqué (2007); Teyssèdre et al (2007)	Déqué (2007)	Williamson and Rasch (1989)	REPROBUS: Lefèvre, (1994)
E39CA	ECHAM4	N/A	ECHAM4	Roegner et al. (2004)	ECHAM4	ATTLA (Reithmeier and Sausen, 2002)	CHEM (Steil et al., 1998)
EMAC	ECHAM5	N/A	ECHAM5		ECHAM5	ECHAM5	MECCA1 (Sander et al., 2005)
GEOSCCM	GEOS5	N/A	CLSM	Koster et al. (2000)	GEOS5	GEOS5	Stratchem (Douglass et al., 1997; Kawa et al., 2002)
LMDzrepro	LMDz	N/A	ORCHIDEE (F)		Hourdin et al. (2006)	Hourdin and Armengaud (1999)	Lefèvre et al. (1998)
MRI	MJ98	N/A			MJ98	MJ98	Shibata et al. (2005)
Niwa-SOCOL SOCOL	MAECHAM4	N/A	ECHAM4		MAECHAM4	Hybrid (SLS+SOMC) Zubov et al. (1999)	MEZON (Egorova et al., 2003)
ULAQ	ULAQ-GCM	N/A	N/A		ULAQ-CTM	ULAQ-CTM	Pitari et al. (2002)
UMETRAC	HadAM3 L64	N/A	MOSES-1		UM 4.5	UM 4.5	Austin and Butchart (2003)
UMSLIMCAT	HadAM3 L64	N/A	MOSES-1		UM 4.5	UM 4.5	Tian and Chipperfield (2005)
UMUKCA-METO UMUKCA-UCAM	HadGEM-A	N/A	MOSES-2		UM 6.1	UM 6.1	Morgenstern et al. (2009)
WACCM	CAM	N/A	CLM		CAM	CAM	Kinnison et al. (2007)

**Table 2.2:** Governing equations and horizontal discretizations of dynamical cores. QG = quasi-geostrophic. PE = primitive equations, NH = non-hydrostatic. STL = spectral transform linear, STQ = spectral transform quadratic, F[D,V,E]LL = finite [difference, volume, elements] on lat-lon grid. T42 approximately corresponds to  $2.8^\circ \times 2.8^\circ$ , T30 to  $3.75^\circ \times 3.75^\circ$ .

CCM	Gov. equations	Horizontal Discretization	Truncation/ resolution	Comments
AMTRAC3	PE	FV Cubed sphere	variable, ~200 km	Most results are interpolated to $2^\circ \times 2.5^\circ$ grid.
CAM3.5	PE	FVLL	1.9 (lat) x 2.5 (lon)	
CCSRNIES	PE	STQ	T42	
CMAM	PE	STQ	T31	For dynamics
CNRM-ACM	PE	STL	T42/T63	The linear T63 and the quadratic T42 grids both have a resolution of $2.8^\circ \times 2.8^\circ$ .
E39CA	PE	STL	T30	
EMAC	PE	STQ	T42	
GEOSCCM	PE	FVLL	$2^\circ$ (lat) x $2.5^\circ$ (lon)	
LMDZrepro	PE	FVLL	$2.5^\circ$ (lat) x $3.75^\circ$ (lon)	Arakawa-C
MRI	PE	STQ	T42	
NiwaSOCOL SOCOL	PE	STL	T30	
ULAQ	QG	STL	R6 / $11.5^\circ$ (lat) x $22.5^\circ$ (lon)	Dynamical core, radiation
UMETRAC UMSLIMCAT	PE	FDLL	$2.5^\circ$ (lat) x $3.75^\circ$ (lon)	Arakawa-B
UMUKCA-METO UMUKCA-UCAM	NH	FDLL	$2.5^\circ$ (lat) x $3.75^\circ$ (lon)	Arakawa-C
WACCM	PE	FVLL	1.9 (lat) x 2.5 (lon)	

**Table 2.3:** Additional horizontal grids in CCMs. CCMs not listed here do not use additional grids.

CCM	Grid	Comments
CCSRNIES	Quadratic Gaussian	for physics and chemistry
CMAM	STL	for physics and chemistry
CNRM-ACM	T42 Gaussian T21 Gaussian	Dynamics and transport Chemistry
E39CA	T30 Gaussian	Physics, chemistry, etc.
EMAC	Quadratic Gaussian equivalent to T42	Physics, chemistry, etc.
GEOSCCM	Catchment	<i>Koster et al. (2000)</i>
MRI	Quadratic Gaussian Reduced by a quarter	Dynamics + physics + chemistry Radiation
ULAQ	$10^\circ$ (lat) x $22.5^\circ$ (lon)	Chemistry, aerosols

**Table 2.4:** Transport scheme, by tracer. FV = finite volume. FFSL = flux-form semi-Lagrangian. SL = semi-Lagrangian. STFD = spectral transform and finite difference. FFEE = flux form Eulerian explicit.

CCM	Physical tracers	Water vapour	Other chemical tracers	References
AMTRAC3	FFSL	FFSL	FFSL	<i>Lin (2004)</i>
CAM3.5	FFSL	FFSL	FFSL	<i>Lin (2004); Rasch et al. (2006)</i>
CCSRNIES	STFD	STFD	STFD	<i>Numaguti et al. (1997)</i>
CMAM	Spectral	Spectral – log(q)	Spectral	
CNRM-ACM	SL cubic	SL cubic	SL cubic	<i>Déqué (2007); Williamson and Rasch (1989)</i>
E39CA	Semi-Lagrangian	ATTILA	ATTILA	<i>Reithmeier and Sausen (2002)</i>
EMAC	FFSL	FFSL	FFSL	<i>Lin and Rood (1996)</i>
GEOSCCM	FFSL	FFSL	FFSL	<i>Lin and Rood (1996)</i>
LMDZrepro	FV	FV	FV	<i>Hourdin and Armengaud (1999)</i>
MRI	STFD	STFD	Hybrid SL quintic and PRM	<i>Shibata and Deushi (2008b)</i>
NiwaSOCOL SOCOL	semi-Lagrangian	semi-Lagrangian	Hybrid	<i>Zubov et al. (1999); Williamson and Rasch (1989)</i>
ULAQ	FFEE	FFEE	FFEE	
UMETRAC UMSLIMCAT		Quintic FV	Quintic FV	<i>Gregory and West (2002)</i>
UMUKCA-METO UMUKCA-UCAM	SL, quasi-cubic	SL. Hor.: Quasi-cubic. Vert.: quintic	Same as water vapour	<i>Priestley (1993)</i>
WACCM	FFSL	FFSL	FFSL	<i>Lin (2004)</i>

**Table 2.5:** Vertical grid: Grid type: L=Lorenz, CP=Charney Phillips, O = other. TP = terrain following hybrid pressure; TA = terrain following hybrid altitude. NTP = non-terrain following pressure.

CCM	Grid type, number of levels	Uppermost computational level	Top of model	Coordinate system
AMTRAC3	L48	0.017 hPa	0.01 hPa	TP
CAM3.5	L26	3.5 hPa	2.2 hPa	TP
CCSRNIES	L34	0.012 hPa	0.01 hPa	TP
CMAM	O71	0.00081 hPa		TP
CNRM-ACM	L60	0.07 hPa	0 hPa	TP
E39CA	L39	10 hPa	Not 0	TP
EMAC	L90	0.01 hPa	0 hPa	TP
GEOSCCM	L72	0.015 hPa	0.01 hPa	TP
LMDZrepro	L50	0.07 hPa	0 hPa	TP
MRI	L68	0.01 hPa	0 hPa	TP
NiwaSOCOL/SOCOL	L39	0.01 hPa	0 hPa	TP
ULAQ	CP26	0.04 hPa	Not 0	Log-NTP
UMETRAC/UMSLIMCAT	L64	0.01 hPa	0.0077 hPa	TP
UMUKCA-METO/UMUKCA-UCAM	CP60	84 km	84 km	TA
WACCM	L66	$5.96 \times 10^{-6}$ hPa	$4.5 \times 10^{-6}$ hPa	TP



**Table 2.6:** Vertical resolution: Number of full levels for  $p_s = 1013.25$  hPa at sea level, between  $p_s$  and 850 hPa, between 850 hPa and 300 hPa, between 300 hPa and 100 hPa, between 100 and 1 hPa, above 1 hPa.

CCM	$p_s - 850$ hPa	850 – 300 hPa	300 – 100 hPa	100 – 1 hPa	Above 1 hPa	Comments
AMTRAC3	8	9	7	15	9	
CAM3.5	4	7	7	8	0	
CCSRNIES	4	5	6	13	6	
CMAM	10	12	7	20	22	
CNRM-ACM	12	15	8	21	4	
E39CA	5	11	15	8	0	
EMAC	4	11	12	48	15	
GEOSCCM	10	18	7	23	14	
LMDZrepro	7	11	8	20	4	
MRI	6	7	6	42	7	
NiwaSOCOL/SOCOL	5	6	5	15	8	
ULAQ	1	2	3	12	8	
UMETRAC/UMSLIMCAT	4	13	9	24	14	
UMUKCA-METO/UMUKCA-UCAM	8	13	7	22	10	US standard atmosphere
WACCM	4	7	7	21	27	

latitude-longitude grid, favoured because it allows for a straightforward discretization of the governing equations on a single grid. Disadvantages are a non-uniform resolution and special treatments required at the poles (*e.g.*, Lanser *et al.*, 2000, Table 2.2). Only the AMTRAC3 model uses neither of the above discretization methods. AMTRAC3 uses a “cubed sphere” grid (Putman and Lin, 2007; Adcroft *et al.*, 2007), based on projecting the edges of a cube onto a sphere around its centre.

The dynamical cores of most CCMs are based on the primitive equations (*e.g.*, Holton, 1992), with terrain-following hybrid-pressure as the vertical coordinate (**Table 2.5**). The MetOffice’s New Dynamics Unified Model (UMUKCA-METO, UMUKCA-UCAM) solves a non-hydrostatic set of equations (Davies *et al.*, 2005), although UMUKCA is used at a resolution that would justify the hydrostatic approximation. This also results in UMUKCA being the only model using hybrid-height as the vertical coordinate system (*i.e.*, near the surface, the model levels follow the orography, but in the stratosphere are pure height levels; Tables 2.2 and 2.5). The ULAQ CCM uses a geostrophic set of equations (Pitari, 1993), resulting in stronger constraints to simulated dynamics than in the other CCMs (Table 2.2). Also ULAQ use non-terrain following pressure (Table 2.5). Vertical resolution can also play a major role in model performance, *e.g.*, in representing the QBO (see below) or transition regions such as the tropopause. CCMVal-2 models exhibit a wide range of vertical resolutions. For example, the region between 100 and 1 hPa is covered by between 8 and 48 levels (**Table 2.6**).

### 2.3.1.2 Horizontal diffusion

Diffusion is generally split into horizontal and vertical components. Horizontal diffusion is often used as closure for the discretized horizontal dynamics, which accumulates energy at the resolution limit. Depending on the dynamical core, this is achieved implicitly (GEOSCCM, UMUKCA) or explicitly using a horizontal diffusion term or a form of spectral damping (all other CCMVal-2 models). Due to the lack of a general theory of turbulence, horizontal diffusion schemes vary a lot in their characteristics, but achieve the main purpose of suppressing dynamical instabilities with the least possible impact on large scale features of the general circulation. Models with spectral transform dynamics often apply high-order diffusion operators to be scale selective (CNRM-ACM, E39CA, EMAC, (Niwa)SOCOL), while those grid-point models requiring explicit diffusion rely on low-order operators, which can be realised with small stencils (CAM3.5, LMDZrepro, WACCM; **Table 2.7**), .

“Sponges”, *i.e.* increased diffusivity near the model top, are often necessary to reduce the artificial reflection of atmospheric waves off the model top, and are used in the majority of CCMVal-2 models. Depending on the formulation of the sponge, its effects may however extend to lower layers and violate angular momentum conservation (Shepherd *et al.*, 1996; Shepherd and Shaw, 2004; Shaw *et al.*, 2009). Such effects can be avoided if the sponge does not affect the zonal-mean structures (EMAC, CMAM). Some models do not use a sponge at the model

**Table 2.7:** Horizontal diffusion

CCM	Order of diff. scheme	Linear	Damping time of smallest scales (h)	Range of sponge layer	Reference	Comment
CAM3.5	2	Yes	Wavenumber-Dependent	≤14 hPa	<i>Collins et al. (2004)</i>	Divergence Damping
CCSRNIES	4	Yes	18	Sponge	<i>Numaguti et al. (1997)</i>	
CMAM			13.9		<i>Koshyk and Boer (1995)</i>	Modified Leith diff.
CNRM-ACM	6	Yes			<i>Yessad (2001)</i>	
E39CA	10 (2 at top)		9	≤20 hPa	<i>Roeckner et al. (1996); Land et al. (2002)</i>	
EMAC	10	No	9	Sponge	<i>Roeckner et al. (2003)</i>	
GEOSCCM	N/A	N/A	N/A	No sponge		No explicit diffusion
LMDZrepro	2			Sponge	<i>Hourdin et al. (2006)</i>	
MRI	4	Yes	18 (p>150hPa) 100 (p<100hPa)	No sponge	<i>Shibata and Deushi (2008a)</i>	
NiwaSOCOL SOCOL	10	No	6	0.01 hPa (top level)	<i>Manzini and McFarlane (1998)</i>	
ULAQ	N/A	Yes	12	Sponge	<i>Pitari et al. (2002)</i>	
UMETRAC UMSLIMCAT		No		≤0.017 hPa		
UMUKCA-METO UMUKCA-UCAM	N/A	N/A	N/A	No sponge	<i>McCalpin (1988)</i>	No explicit diffusion
WACCM	2	Yes	Wavenumber-Dependent	≤1.6-5 hPa	<i>Collins et al. (2004)</i>	Divergence Damping

top (GEOSCCM, MRI, UMUKCA; Table 2.7). Further aspects of numerical diffusion are discussed below in the context of advection schemes (Section 2.3.4.1).

### 2.3.1.3 The Quasi-Biennial Oscillation

The Quasi-Biennial Oscillation (QBO) is the major dynamical mode of variability of the tropical stratosphere and gives rise to QBO signals in circulation and chemistry in many other regions of the atmosphere (Baldwin *et al.*, 2001). The QBO results from wave mean-flow interaction, which reinforces the westerly and easterly jets of the QBO and causes their downward propagation against the general upwelling in the tropical stratosphere. In recent years, a number of climate models have simulated the QBO (Takahashi, 1999; Scaife *et al.*, 2000; Giorgetta *et al.*, 2002; McLandress, 2002). However, the simulation of

the QBO in atmospheric GCMs or CCMs is still a major challenge (Giorgetta *et al.*, 2006). The major difficulty in simulating the QBO arises from the imperfect representation of tropical convection, which in reality excites a broad spectrum of vertically propagating waves. While CCMs can resolve the large-scale portion of this spectrum, if a suitable vertical resolution is used, a realistic excitation of these waves also depends strongly on the spatial and temporal characteristics of the simulated tropical convective clouds, and therefore on the parameterisation of these clouds (Horinouchi *et al.*, 2003). The contribution of unresolved waves to the wave mean-flow interaction in the QBO shear layers depends entirely on parameterisations of gravity waves. While the simulation of the wave mean-flow interaction is considered to be the biggest challenge, the tropical upwelling also needs to be well simulated, to allow for a realistic quasi-biennial period of the equatorial oscillation in zonal wind (Giorgetta *et al.*, 2006).

**Table 2.8:** Usage of QBO nudging in CCMVal-2 simulations: CCM name; experiments run with QBO nudging; variable that is nudged, '<x>' indicates that the nudging is applied on the zonal-mean of the variable x, while 'x' indicates local nudging; time scale in (days) used for the nudging in the core of the QBO domain; latitude range in °latitude where the nudging is applied; height range of the QBO nudging in hPa or km for pressure or height based vertical coordinate systems, respectively. Models not listed here do not impose a QBO but may have an internally generated QBO.

CCM	Experiments including QBO nudging	Nudged variable	Time scale (day)	Latitude range (°)	Pressure range (hPa)	Comments
CAM3.5	REF-B1	u	10	22°S-22°N	90 – 3 hPa	
CCSRNIES	REF-B1	<u>	5	Tropics	Mid-stratosphere	
E39CA	REF-B1, SCN-B2d	u	7	20°S-20°N	90 – 10 hPa	<i>Giorgetta and Bengtsson (1999)</i>
EMAC	REF-B1	u	58	7°S-7°N	50 – 15 hPa	
NiwaSOCOL SOCOL	REF-B1	u	7	10°S-10°N (full), 20°S-10°S, 10°N-20°N (tapered)	90 – 3hPa	<i>Giorgetta (1996)</i>
ULAQ	REF-B1	rel. vorticity	10	23°S–23°N	107 – 2.8 hPa	
WACCM	REF-B1	u	10	22°S-22°N	90-3 hPa	

Among the CCMs used for CCMVal-2, EMAC, the UM based models (UMETRAC, UMSLIMCAT, and UМУKCA; Scaife *et al.*, 2000), and MRI spontaneously simulate the QBO (Chapter 8). The other models either do not include QBO nudging (AMTRAC3, CMAM, LMDZrepro) and produce no QBO, or the appearance of the QBO depends entirely on the assimilation of the equatorial zonal wind to externally given QBO wind profiles (CAM3.5, CCSRNIIES, E39CA, SOCOL, NiwaSOCOL, ULAQ, WACCM; **Table 2.8**). EMAC also applies nudging in its simulations of the past, in order to synchronise its internally generated QBO with observations. The nudging time scale is typically chosen between 5 and 10 days, *i.e.*, on the time scale of large scale equatorial waves, whose unrealistic representation (due to insufficient vertical resolution and / or excitation by tropical weather) is the primary reason for the absence of a QBO in some CCMs. In EMAC, however, the time scale is 58 days, hence much longer than the time scales of the driving wave spectrum, and the nudging domain is more restricted than in the other models (**Table 2.8**).

QBO nudging has however limitations:

1. By construction, the nudging of zonal wind introduces localized momentum sources and sinks, thus violating the internal momentum budget of the atmosphere.
2. The QBO is an internal mode of variability, but nudging makes the QBO dependent on boundary conditions. This will destroy any internal variability arising

from two-way interaction with the extra-tropics (Anstey *et al.*, 2010).

3. Nudging generally results in a realistic zonally averaged structure of the QBO, but does not repair the potentially deficient wave structures. QBO nudging can therefore contribute to QBO signals related to zonal mean effects, but not to QBO signals dependent on waves, *e.g.*, eddy fluxes of tracers.
4. Simulations covering the future cannot use nudging to observations.

### 2.3.1.4 Gravity wave drag

Gravity wave drag (GWD) is among the drivers of meridional overturning in the middle atmosphere, a.k.a. the Brewer-Dobson Circulation (McIntyre, 1995), and of the QBO (Section 2.3.1.3). The small spatial scales and complications due to wave breaking require their effects to be parameterised. Gravity waves are excited by tropospheric processes, mainly flow over topography and frontal and other forms of convection. Hence GWD parameterisations are usually divided into two parts, orographic and non-orographic. CAM3.5, CNRM-ACM, and WACCM link GWD to tropospheric convection (Bossuet *et al.*, 1998; Richter *et al.*, 2009; **Table 2.9**); in the other models, this link is not incorporated. McLandress and Scinocca (2005) examine the impacts on middle-atmosphere dynamics of three different GWD schemes (Hines, 1997a,b; Alexander and Dunkerton, 1999; Warner and McIntyre, 2001), variants of

**Table 2.9:** Orographic and non-orographic gravity wave drag.

CCM	Reference for orographic GWD	Sources for nonorographic GWG	Launch level for prescribed gravity waves	Latitude range for param. gravity waves	Reference for nonorographic GWD
AMTRAC3	<i>Pierrehumbert (1986)</i>	parameterised	~tropopause	90°S-90°N	<i>Alexander and Dunkerton (1999)</i>
CAM3.5	<i>McFarlane (1987)</i>	Parameterised using deep convective heating and frontal zones	ground (orog. waves); 100 hPa (deep convection); 500 hPa (fronts)	90°S-90°N	<i>Richter et al. (2009)</i>
CCSRNIES	<i>McFarlane (1987)</i>	Parameterised	Parameterised	90°S-90°N	<i>Hines (1997b)</i>
CMAM	<i>Scinocca and McFarlane (2000)</i>	Specified generalised Desaubies	100 hPa (non-orographic)	All	<i>Scinocca (2003)</i>
CNRM-ACM	<i>Lott (1997)</i>	Convection	N/A	90°S-90°N	<i>Bossuet (1998)</i>
E39CA	<i>Miller et al. (1989)</i>	None			
EMAC	<i>Lott (1999); Lott and Miller (1997)</i>	Parameterised	640 hPa	90°S-90°N	<i>Hines (1997a,b)</i>
GEOSCCM	<i>McFarlane (1987)</i>	Parameterised	100 hPa	90°S-90°N	<i>Garcia and Boville (1994)</i>
LMDZrepro	<i>Lott and Miller, (1997); Lott (1999); Lott et al. (2005)</i>	Parameterised	Surface	90°S-90°N	<i>Lott et al. (2005) (based on Hines (1997a,b))</i>
MRI	<i>Iwasaki et al. (1989)</i>	Parameterised	Lowest level	Uniform + tropical enhancement	<i>Hines(1997b)</i>
NiwaSOCOL SOCOL	<i>McFarlane (1987), Manzini and McFarlane (1998)</i>	Parameterised	~700Pa	90°S-90°N, Tapered response based on latitude	<i>Hines (1997b); Charron and Manzini (2002)</i>
ULAQ		N/A	N/A	N/A	
UMETRAC	<i>Gregory et al. (1998)</i>	Parameterised			<i>Scaife et al. (2000)</i>
UMSLIMCAT	<i>Webster et al., (2003)</i>	Parameterised			<i>Scaife et al. (2000)</i>
UMUKCA-METO UMUKCA-UCAM	<i>Webster et al. (2003)</i>	Prescribed	Parameterised	90°S-90°N	<i>Scaife et al. (2000)</i>
WACCM	<i>McFarlane (1987)</i>	Parameterised using deep convective heating and frontal zones	ground (orog. waves); 100 hPa (deep convection); 500 hPa (fronts)	90°S-90°N	<i>Richter et al. (2009)</i>

which are widely used across the CCMVal-2 models (Table 2.9). The three schemes, when employed in a comparable way, produce very similar dynamical responses despite differences in the dissipation mechanisms. This suggests that differences in responses to GWD are mainly due to adjustable parameters in the schemes, such as the properties of the launch spectrum or the launch height, but not the dissipation mechanism. E39CA does not have a representation of non-orographic GWD because of the low top in this model. ULAQ represents the effect of GWD through Rayleigh friction (Table 2.9), which violates momentum conservation (Shepherd and Shaw, 2004). Momentum conservation can also be violated in flux-based GWD parameterisations if momentum flux is allowed to escape out the top of the model domain (Shaw and Shepherd, 2007).

### 2.3.2 Radiation

Radiative processes lead to additional challenges in the development of CCMs, especially concerning the solar UV radiation relevant for dynamics and chemistry. Traditionally separate radiative transfer schemes are used for shortwave heating and photolysis; this is the case in all CCMVal-2 models except CCSRNIES (Akiyoshi *et al.*, 2009) and WACCM (Kinnison *et al.*, 2007). Radiative transfer schemes for shortwave heating often use relatively broad spectral bands covering the solar spectrum from the near infrared to the UV, and include scattering by air molecules and cloud and aerosol particles (*e.g.*, Edwards and Slingo, 1996). Radiative transfer schemes used for photolysis (Section 2.3.3.5) need to resolve the UV spectrum much better, and scattering may be treated differently (*e.g.*, Lary and Pyle, 1991). All models use the two-stream approximation for short-wave radiation (a common simplification used in radiative transfer modeling; **Table 2.10**). An inspection of the number of spectral bands, both in the shortwave and the longwave part of the spectrum (**Table 2.11**), reveals substantial differences in spectral resolution. Models that cover the upper atmosphere (WACCM, CMAM) also include chemical heating (*i.e.* the heating produced by some exothermic / endothermic chemical reactions, which is typically ignored at lower levels; Marsh *et al.*, 2007) and non-local thermodynamical equilibrium (LTE) effects, produced *e.g.*, by excitation of vibrational states of molecules under conditions of low collision probability (low density; Kockarts, 1980; Fomichev *et al.*, 1998). A more detailed discussion on radiation in CCMVal-2 models, including an offline comparison of the models' radiation schemes, is the subject of Chapter 3.

## 2.3.3 Chemistry and composition

### 2.3.3.1 Stratospheric chemistry

**Tables 2.12** and **2.13** summarize broadly the scopes of the different chemical schemes in use for CCMVal-2. More detail is in the online supplement. All models participating in CCMVal-2 employ an inorganic chemistry scheme including chlorine chemistry; all but the E39CA model also contain an explicit representation of bromine chemistry. In the E39CA model, bromine chemistry is parameterised (supplement to Stenke *et al.*, 2009). The number and type of source gases for chlorine and bromine varies greatly between models. Lumping (*i.e.*, adding the halogen atoms of those source gases not represented in the chemistry schemes to those that are, with similar lifetimes) is used widely across the CCMVal-2 models (Section 2.5.2.2); only AMTRAC3, CCSRNIES, CNRM-ACM, NiwaSOCOL, and UMETRAC do not use it. Particularly for UMSLIMCAT and UMUKCA this has a big impact on the few halogen source gases (CFC-11, CFC-12, CH<sub>3</sub>Br) represented in their schemes (Chipperfield, 1999). AMTRAC3 and UMETRAC do not transport the halogen source species directly, but the local rates of change of inorganic chlorine and bromine are calculated using tabulated functions of the derivatives of the source molecules with respect to the age of air (Austin and Butchart, 2003). Although modellers have been asked to update their kinetics data to JPL (2006), few have done so completely and most use a mixture of different sources (Table 2.12; Chapter 6). A detailed assessment of chemistry in CCMVal-2 models, including a comparison with a benchmark photochemical steady-state (PSS) model, is the subject of Chapter 6. Also a comprehensive listing of reactions can be found there.

### 2.3.3.2 Tropospheric chemistry

The major target of CCMVal-participating models is currently not the troposphere but the stratosphere; hence tropospheric chemistry is simplified or absent in most models. This is motivated by the success *e.g.*, of stratospheric chemistry-transport models in broadly reproducing stratospheric ozone without considering tropospheric chemistry (*e.g.*, Chipperfield, 1999). However, the absence of tropospheric chemistry in most CCMVal-2 models must be regarded as a limitation. Only CAM3.5, EMAC, and ULAQ include a comprehensive representation of tropospheric chemistry (Table 2.13); these models are however characterized by low resolution (ULAQ), a low model top (CAM3.5), or few simulations (EMAC). This reflects the added cost imposed by tropospheric chemistry. In the other models, tropospheric composition is handled in a variety of ways: Introduction of background tropospheric chemis-

Table 2.10: Shortwave radiation. 2-s: Two-stream.

CCM	Reference	Description	Clouds	Spectral interval boundaries (nm)	Gas abs.
CAM3.5	<i>Briegleb et al. (1992); Collins et al. (2004)</i>	$\Delta$ -Eddington 2-s	Random / max. overlap	19 intervals (>200nm); <200nm consistent with photolysis.	O <sub>2</sub> , O <sub>3</sub> , CO <sub>2</sub> , H <sub>2</sub> O
CCSRNIES	<i>Nakajima and Tanaka (1986); Nakajima et al. (2000)</i>	2-s	random overlap	[200,217],[217,233],[233,278],[278,290],[290,303],[303,317],[317,690],[690,2500],[2500,4000]	O <sub>2</sub> , O <sub>3</sub> , CO <sub>2</sub> , H <sub>2</sub> O
CMAM	<i>Fouquart and Bonnel (1980); Fomichev et al. (2004)</i>	$\Delta$ 2-s	Maximum or random overlap	[250,690],[690,1190],[1190,2380],[2380,4000]; Separate parameterizations for near-IR CO <sub>2</sub> [1200,4300] above 1 hPa and O <sub>2</sub> absorption in SRC [125-175] and SRB [175-205] above 0.25 hPa	O <sub>2</sub> , O <sub>3</sub> , CO <sub>2</sub> , H <sub>2</sub> O
CNRM-ACM	<i>Morcrette (1990, 1991)</i>	Fourquart-Morcrette 2-s	maximum random overlap	[250,680], [680,4000]	O <sub>2</sub> , H <sub>2</sub> O, O <sub>3</sub> , CO <sub>2</sub> , CH <sub>4</sub> , N <sub>2</sub> O
E39CA	<i>Fouquart and Bonnel (1980)</i>	$\Delta$ 2-s	Maximum to random overlap	[245-685]	O <sub>2</sub> , O <sub>3</sub> , CO <sub>2</sub> , H <sub>2</sub> O
EMAC	<i>Nissen et al (2007); Fouquart and Bonnel (1980); Roeckner et al. (2003)</i>	$\Delta$ 2-s	Maximum to random overlap	[121,6],[125,175],[175,205],[206,244],[244,278],[278,362],[362,683] (49 bands), [690,1190],[1190,2380],[2380,4000]	O <sub>2</sub> , O <sub>3</sub> , CO <sub>2</sub> , H <sub>2</sub> O
GEOSSCM	<i>Chou and Suarez (1999); Sud et al. (1993); Chou et al. (1997)</i>	$\Delta$ -Eddington 2-s	Maximum random overlap	[175-225],[225-245],[245-260],[280-295],[295-310],[310-320],[320-400],[400-700],[700-1220],[1220-2270],[2270-10000]	O <sub>2</sub> , O <sub>3</sub> , CO <sub>2</sub> , H <sub>2</sub> O
LMDZrepro	<i>Fouquart and Bonnel (1980)</i>	2-s	Maximum or random overlap	[250,680], [680,4000]	O <sub>2</sub> , O <sub>3</sub> , CO <sub>2</sub> , H <sub>2</sub> O
MRI	<i>Briegleb et al. (1992); Shibata and Uchiyama (1992)</i>	$\Delta$ 2-s. DOM	Maximum to random overlap	[200,245],[245,265],[265,275],[275,285],[285,295],[295,305],[205,350],[350,700],[700,5000],[2630-2860],[4160-4550]	O <sub>2</sub> , O <sub>3</sub> , CO <sub>2</sub> , H <sub>2</sub> O
NiwaSOCOL SOCOL	<i>Fouquart and Bonnel (1980); Egorova et al. (2004)</i>	$\Delta$ 2-s	Maximum or random overlap	[250-680],[680-4000]; parameterization for O <sub>2</sub> and O <sub>3</sub> absorption in L- $\alpha$ [121-122], SRB [175-205] and HC [200-250]	O <sub>2</sub> , O <sub>3</sub> , CO <sub>2</sub> , H <sub>2</sub> O
ULAQ	<i>Lacis et al. (1992); Pitari (1993); Pitari et al. (2002)</i>	$\Delta$ -Eddington 2-s	Maximum random overlap	21 intervals [135, 175]; 14 intervals [175, 200]; 19 intervals [200, 245]; 19 intervals [245, 320]; 11 intervals [320, 690]; 16 intervals [690, 10000]	O <sub>2</sub> , O <sub>3</sub> , CO <sub>2</sub> , H <sub>2</sub> O, NO <sub>2</sub>
UMETRAC UMSLIMCAT	<i>Edwards and Slingo (1996); Zdankowski et al. (1982); Zhong et al. (2001)</i>	2-s	Maximum to random overlap	[116,175],[175,200],[200,245],[245,320],[320,690],[690,1190],[1190,2380],[2380,10000]	O <sub>2</sub> , O <sub>3</sub> , CO <sub>2</sub> , H <sub>2</sub> O
UMUKCA-METO UMUKCA-UCAM	<i>Edwards and Slingo (1996); Zdankowski et al. (1982); Zhong et al. (2008)</i>	2-s.	Maximum to random overlap	[200,320],[320,690],[690,1190],[1190,2380],[2380,10000]	O <sub>2</sub> , O <sub>3</sub> , CO <sub>2</sub> , H <sub>2</sub> O
WACCM	<i>Briegleb et al. (1992); Collins et al. (2004)</i>	$\Delta$ -Eddington 2-s	Random / max. overlap	19 intervals (>200nm); <200nm consistent with photolysis	O <sub>2</sub> , O <sub>3</sub> , CO <sub>2</sub> , H <sub>2</sub> O

Table 2.11: Longwave radiation.

CCM	Reference	Description	Spectral interval boundaries ( $\mu\text{m}$ )	Gas abs.	Chem. heating	Non-LTE
CAM3.5	<i>Collins et al. (2004)</i>	Broad Band Approach	<i>Collins et al. (2004)</i>	H <sub>2</sub> O, CO <sub>2</sub> , O <sub>3</sub> , CH <sub>4</sub> , N <sub>2</sub> O, F11, F12, NO	NO	NO
CCSRNIES	<i>Nakajima et al. (2000)</i>	Discrete ordinate and k-distribution	[4.00,5.00], [5.00,7.14], [7.14,9.09], [9.09,10.1], [10.1,13.0], [13.0,18.2], [18.2,25.0], [25.0,40.0], [40.0,200]	H <sub>2</sub> O, CO <sub>2</sub> , O <sub>3</sub> , CH <sub>4</sub> , N <sub>2</sub> O, CFCs	NO	NO
CMAM	<i>Morcrette (1991); Fomichev et al. (2004)</i>	>39 hPa: 2-s; < 6.7 hPa: Matrix param. 6.7-39: Merging region	Below 39 hPa: [6.9,8.0 : 3.5,5.3], [9.0,10.3], [10.3,12.5 : 8.0,9.0], [12.5,20.0], [20.0,28.6], [28.6,10000 : 5.3,6.9]; Above 6.7 hPa: 15 $\mu\text{m}$ CO <sub>2</sub> , 9.6 $\mu\text{m}$ O <sub>3</sub> and rotational H <sub>2</sub> O bands	Below 39 hPa: H <sub>2</sub> O, CO <sub>2</sub> , O <sub>3</sub> , CH <sub>4</sub> , N <sub>2</sub> O, F11, F12; Above 6.7 hPa: H <sub>2</sub> O, CO <sub>2</sub> , O <sub>3</sub>	YES	YES (CO <sub>2</sub> , O <sub>3</sub> , O <sub>2</sub> )
CNRM-ACM	<i>Morcrette (1990, 1991)</i>	FMR ; 2-stream	[28.6, ]+[5.3,6.9], [20.0,28.6], [12.5,20],[10.3,12.5]+[8,9],[9,10.3], [6.9,8]+[3.5,5.3]	O <sub>3</sub> , H <sub>2</sub> O, CO <sub>2</sub> , CH <sub>4</sub> , N <sub>2</sub> O, F11	NO	NO
E39CA	<i>Morcrette (1991)</i>	Broad-band flux emissivity method in six spectral intervals	[3.55,8], [8,10.31], [10.31,12.5], [12.5,20], [20,28.57], [28.57,1000]; wavenumbers 0 to 2.82 x 10 <sup>5</sup> m <sup>-1</sup>	H <sub>2</sub> O, CO <sub>2</sub> , O <sub>3</sub> , CH <sub>4</sub> , N <sub>2</sub> O, F11, F12	NO	NO
EMAC	<i>Roeckner et al. (2003); Mlawer et al. (1997)</i>	Correlated-k method, RRTM	[3.3,3.8], [3.8,4.2], [[4.2,4.4], [4.4,4.8], [4.8,5.6], [5.6,6.8], [6.8,7.2], [7.2,8.5], [8.5,9.3], [9.3,10.2], [10.2,12.2], [12.2,14.3], [14.3,15.9], [15.9,20], [20,40], [40,1000]	H <sub>2</sub> O, CO <sub>2</sub> , O <sub>3</sub> , CH <sub>4</sub> , N <sub>2</sub> O, F11, F12	NO	NO
GEOSCCM	<i>Chou et al. (2001)</i>	k-distribution and table look-up	[29.4,10000], [18.5,29.4], [16.1,18.5], [13.9,16.1], [12.5,13.9], [10.2,12.5], [9.09,10.2], [7.25,9.09], [5.26,7.25], [3.33,5.26]	H <sub>2</sub> O, CO <sub>2</sub> , O <sub>3</sub> , F11, F12, F22, CH <sub>4</sub> , N <sub>2</sub> O	NO	NO
LMDZrepro	<i>Morcrette (1991)</i>	Broad-band flux emissivity method in six spectral intervals	[3.55,8], [8,10.31], [10.31,12.5], [12.5,20], [20,28.57], [28.57,1000]; wavenumbers 0 to 2.82 x 10 <sup>5</sup> m <sup>-1</sup>	H <sub>2</sub> O, CO <sub>2</sub> , O <sub>3</sub> , CH <sub>4</sub> , N <sub>2</sub> O, F11, F12	NO	NO
MRI	<i>Shibata and Aoki (1989)</i>	Multi-parameter-random model	20-550-800-1200-2200 cm <sup>-1</sup> ; [4.55,8.33], [8.33,12.5], [12.5,18.2], [18..2,50]	H <sub>2</sub> O, CO <sub>2</sub> , O <sub>3</sub> , CH <sub>4</sub> , N <sub>2</sub> O	NO	NO

Table 2.11 continued.

CCM	Reference	Description	Spectral interval boundaries ( $\mu\text{m}$ )	Gas abs.	Chem. heating	Non-LTE
NiwaSOCOL SOCOL	<i>Morcrette (1991)</i>	Broad-band approach	[6.9-8 & 3.5-5.3], [9-10.3], [10.3-12.5 & 8-9], [12.5,20], [20,28.6], [28.6, 10000 & 5.3,6.9]	CH <sub>4</sub> , N <sub>2</sub> O, F11, F12, CO <sub>2</sub> , H <sub>2</sub> O, O <sub>3</sub>	NO	NO
ULAQ	<i>Andrews et al. (1987)</i> <i>Lacis et al. (1992)</i> ; <i>Pitari (1993)</i>	Broad Band Approach	[18.2,28.6], [12.5,18.2], [8.3,12.5], [3.3,7.5]	H <sub>2</sub> O, CO <sub>2</sub> , O <sub>3</sub>	NO	NO
UMETRAC UMSLIMCAT	<i>Edwards and Slingo (1996)</i> , <i>Zdunkowski et al. (1982)</i> , <i>Zhong and Haigh (2001)</i>	2-s.	[28.6,10000], [18.2,28.6], [12.5,18.2], [13.3,16.9], [8.33,12.5], [8.93,10.1], [6.67,8.33], [8.93,10.1], [6.67,8.33], [5.26,6.67], [3.34,5.26]	H <sub>2</sub> O, CO <sub>2</sub> , O <sub>3</sub> , CH <sub>4</sub> , N <sub>2</sub> O, F11, F12	NO	NO
UMUKCA-METO UMUKCA-UCAM	<i>Edwards and Slingo (1996)</i> , <i>Zdunkowski et al. (1982)</i>	2-s.	[25,10000], [18.2,25], [12.5,18.2], [13.3,16.9], [8.33,12.5], [8.93,10.1], [7.52,8.33], [6.67,7.52], [3.34,6.67]	H <sub>2</sub> O, CO <sub>2</sub> , O <sub>3</sub> , CH <sub>4</sub> , N <sub>2</sub> O, F11 (rescaled), F12 (rescaled)	NO	NO
WACCM	<i>Collins et al. (2004)</i>	Broad Band Approach	<i>Collins et al. (2004)</i>	H <sub>2</sub> O, CO <sub>2</sub> , O <sub>3</sub> , CH <sub>4</sub> , N <sub>2</sub> O, F11, F12, NO	<i>Marsh et al. (2007)</i>	<i>Fomichev et al. (1998)</i> , <i>Kockarts (1980)</i>

try/methane oxidation (AMTRAC3, CCSRNIES, E39CA, MRI, NiwaSOCOL, UMETRAC, UMUKCA, WACCM); relaxation of tropospheric ozone and/or other constituents to a climatology (AMTRAC3, GEOSCCM, CNRM-ACM, LMDZrepro, UMETRAC); or the treatment of chemical species as passive tracers below a level (CMAM, UMSLIMCAT; Table 2.13).

### 2.3.3.3 Mesospheric and upper atmospheric chemistry and physics

Processes specific to the upper atmosphere include ion chemistry, solar particle precipitation associated with NO<sub>x</sub> production, and other effects. Mesospheric NO<sub>x</sub> production is thought to affect NO<sub>y</sub> abundances in the stratospheric polar vortex (Vogel *et al.*, 2008) although its magnitude is uncertain and dependent on solar activity. Only WACCM has explicit representations of these upper-atmospheric processes (Garcia *et al.*, 2007). EMAC (Baumgaertner *et al.*, 2009), MRI, and WACCM treat the

production of NO<sub>x</sub> by cosmic rays and solar particles in the mesosphere; the CMAM model takes this into account by imposing an upper boundary condition (at ~95 km) for NO<sub>x</sub> of 1 ppmv.

### 2.3.3.4 Time-integration of chemical kinetics

Homogeneous reactions (*i.e.*, reactions between free-moving gas phase molecules) are represented by simultaneous first-order, first-degree, homogeneous ordinary differential equations and thus their solutions are generally not chaotic (Shepherd, 2003). This sets them apart from the chaotic properties of atmospheric dynamics. However, chemical reactions are stiff in that the lifetimes of individual species vary by many orders of magnitude (*e.g.*, Jacobson, 1999). To obtain stable and accurate solutions for such stiff chemical equations, different numerical methods have been used in atmospheric chemistry. Most popular is the family method (*e.g.*, Ramarosan *et al.*, 1992; Douglass



and Kawa, 1999), adopted by all CCMVal-2 models except CAM3.5, CMAM, EMAC, (Niwa)SOCOL, UMUKCA, and WACCM. This method relies on the fact that there are groups (families) of gases, namely the odd oxygen ( $O_x$ ), odd hydrogen ( $HO_x$ ), odd nitrogen ( $NO_x$ ), chlorine ( $ClO_x$ ), and bromine ( $BrO_x$ ) families, within which family members are linked by fast reactions (meaning that equilibrium assumptions can be made), but the lifetimes of the families as a whole are much longer. As a result, families are treated as long-lived species and can be integrated with a longer time step. Indeed, the family method is accurate for moderate- and low-stiffness systems, but, to be so, the families need to be carefully set up and validated. The grouping of species into families for chemistry does not need to correspond to any grouping adopted for transport (de Grandpré *et al.*, 1997; Dameris *et al.*, 2005).

By contrast, the non-families methods, used by CAM3.5, CMAM, EMAC, (Niwa)SOCOL, UMUKCA, and WACCM (Kinnison *et al.*, 2007; Morgenstern *et al.*, 2009), make no such *a priori* assumption about lifetimes. Advantages of non-families chemistry include the possibility to extend the chemistry scheme into the upper atmosphere (above approximately 60 km, where the chemical equilibrium assumption underlying the family formulations is not valid). Solvers in this category comprise a Rosenbrock-type predictor-corrector method (EMAC), a combined explicit-implicit backward-Euler method (CAM3.5, CMAM, WACCM), and the Newton-Raphson iterative method ((Niwa)SOCOL, UMUKCA).

### 2.3.3.5 Photolysis

There are two methods for the calculation of photolysis rates, the online and the offline (look-up table) methods. Offline methods involve filling, for every photolysis reaction included in the model, a table of photolysis rates as functions of pressure, solar zenith angle (SZA), with SZAs up to  $100^\circ$  taken into consideration, overhead ozone column, and often temperature (*e.g.*, Lary and Pyle, 1991; **Table 2.14**). SZAs larger than  $90^\circ$  are important for polar spring ozone depletion triggered by solar radiation which reaches the stratosphere earlier than the Earth's surface, due to the Earth's curvature. The tables are filled offline or once at the start of a simulation. Interpolation then yields the photolysis rates at any time and location of the model simulation. This method is computationally efficient; however, it usually limits the number and types of physical effects that can be considered. For example, surface albedo, clouds, and aerosols are often assumed uniform (*e.g.*, Chipperfield, 1999). If solar cycle effects are included, the photolysis tables need to be updated periodically, or the phase of the 11-year cycle needs to be among the interpolation parameters (AMTRAC3).

By contrast, models using online photolysis schemes

(CAM3.5, CCSRNIES, EMAC, E39CA, WACCM) evaluate the radiative transfer equation at the time of simulation, accounting in addition for variations in cloudiness, albedo, and solar output (Landgraf and Crutzen, 1998; Bian and Prather, 2002) which are usually ignored by offline photolysis methods. As noted before, CCSRNIES and WACCM treat photolysis and shortwave radiation consistently, whereas the other models calculate shortwave radiation and photolysis separately, possibly leading to inconsistencies. A detailed investigation of photolysis in CCMVal-2 models is the subject of the PHOTOCOMP study (Chapter 6).

### 2.3.3.6 Heterogeneous reactions and PSC microphysics

On the surfaces of liquid and solid particles, certain chemical reactions proceed efficiently between gas molecules and adsorbed or substrate molecules in the surface layer. Such reactions are called heterogeneous. The heterogeneous reactions are described by a first-order loss process for the gas reactant, and the rate constant is proportional to the thermal velocity of the gas molecules, the particulate surface area density, and an uptake coefficient. The uptake coefficient is dimensionless with a value between 0 and 1, and typically depends on temperature and pressure (JPL, 2006).

In the CCMVal-2 models, two types of particles, sulfate aerosols and polar stratospheric clouds (PSCs), are considered in the stratosphere. Sulfate aerosols result from oxidation of sulfur-containing precursors (*e.g.*, OCS) during volcanically clean periods; in addition, explosive volcanic eruptions can cause temporary increases in the sulfate aerosol abundance by orders of magnitude (*e.g.*, Robock, 2002). The absence of representations of stratospheric aerosol physics and chemistry in CCMVal-2 models means that sulfate aerosol needs to be externally imposed (Section 2.5.3.4). PSCs, on the other hand, are internal variables, and there are large differences among CCMs for their treatments, regarding their formation mechanisms, types, and sizes (**Tables 2.15** and **2.16**). All CCMs include water-ice PSCs and some form of sulfate aerosol; all except CMAM (Hitchcock *et al.*, 2009) furthermore include  $HNO_3 \cdot 3 H_2O$  (nitric acid trihydrate, NAT). Heterogeneous reactions also differ between CCMs. The most important reactions for chlorine activation, and  $N_2O_5$  hydrolysis leading to  $HNO_3$  formation (Table 2.15, columns 2-5) are present in all models. The treatment of reactions involving bromine is less consistent; this may be because heterogeneous activation of bromine is less important than that of chlorine due to the absence of a photochemically stable inorganic reservoir for bromine (as is HCl for chlorine; Brasseur *et al.*, 1999).

The conditions at which PSCs are condensed and evaporated vary, not only for water-ice PSCs but also for

**Table 2.12:** Chlorine, bromine, and NMHC source gases, type of chemical scheme, origin of kinetic and photolysis data. NMHC source gases are primary organic species with more than 1 carbon atom per molecule. Lumping means replacing unrepresented with represented species for chemistry. F10 =  $\text{CCl}_4$ , F11 =  $\text{CFCl}_3$ , F12 =  $\text{CF}_2\text{Cl}_2$ , F113 =  $\text{CF}_2\text{CFCFCl}_2$ , F114 =  $(\text{CF}_2\text{Cl})_2$ , F115 =  $\text{CF}_2\text{CICF}_3$ , F123 =  $\text{CHCl}_2\text{CF}_3$ , F21 =  $\text{CHFCl}_2$ , F22 =  $\text{CHF}_2\text{Cl}$ , F141b =  $\text{CH}_3\text{CFCFCl}_2$ , F142b =  $\text{CH}_3\text{CF}_2\text{Cl}$ , H1211 =  $\text{CF}_2\text{ClBr}$ , H1301 =  $\text{CF}_3\text{Br}$ .

CCM	Chlorine source gases	Bromine source gases	NMHC source gases	Chemical scheme	Origin of kinetic data	Lumping (YES/NO)
AMTRAC3	parameterised	parameterised	None	<i>Austin and Wilson (2006)</i>		NO
CAM3.5	F10, F11, F12, F113, F22, $\text{CH}_3\text{CCl}_3$ , $\text{CH}_3\text{Cl}$	$\text{CH}_3\text{Br}$ , H1211, H1301	$\text{C}_2\text{H}_6$ , $\text{C}_3\text{H}_8$ , $\text{C}_4\text{H}_{10}$ , anthropogenic VOCs	Stratosphere: WACCM Troposphere: <i>Lamarque et al. (2008)</i> , updated to <i>JPL (2006)</i>	<i>JPL (2006)</i>	YES
CCSRNIES	F11, F12, F113, F22, $\text{CH}_3\text{Cl}$ , $\text{CH}_3\text{CCl}_3$	H1211, H1301, $\text{CH}_3\text{Br}$ , $\text{CHBr}_3$	None	$\text{N}_2\text{O}$ - $\text{CH}_4$ - $\text{CO}$ - $\text{H}_2\text{O}$ -families ( $\text{O}_x$ , $\text{HO}_x$ , $\text{NO}_x$ , $\text{CHO}_x$ , $\text{ClO}_x$ , $\text{BrO}_x$ )	<i>JPL (2006)</i>	NO
CMAM	F10, F11, F12, F22, $\text{CH}_3\text{CCl}_3$ , $\text{CH}_3\text{Cl}$	$\text{CH}_3\text{Br}$	None	$\text{CH}_4$ - $\text{CO}$ - $\text{NO}_x$ - $\text{ClO}_x$ - $\text{BrO}_x$	<i>JPL (2006)</i>	YES (halocarbons)
CNRM-ACM	F10, F11, F12, F113, $\text{CH}_3\text{CCl}_3$ , $\text{CH}_3\text{Cl}$ , F22, H1211	$\text{CH}_3\text{Br}$ , H1211, H1301	N/A	REPROBUS <i>Lefèvre (1994)</i>	<i>JPL (2006)</i>	NO
E39CA	F10, F11, F12, $\text{CH}_3\text{Cl}$ , $\text{CH}_3\text{CCl}_3$	parameterisation ( <i>Stenke et al., 2009</i> )	None	CHEM ( <i>Steil et al., 1998</i> )	<i>JPL (2002)</i>	YES
EMAC	F10, F11, F12, $\text{CH}_3\text{CCl}_3$ , $\text{CH}_3\text{Cl}$ , H1211	$\text{CH}_3\text{Br}$ , H1301, H1211	$\text{C}_2\text{H}_6$ , $\text{C}_2\text{H}_4$ , $\text{C}_3\text{H}_6$ , $\text{C}_4\text{H}_{10}$ , $\text{CH}_3\text{CHO}$ , $\text{CH}_3\text{COCH}_3$ , $\text{CH}_3\text{OH}$ , $\text{HCHO}$	MECCA1	<i>JPL (2002)</i>	$\text{C}_4$ ; F113, F114, F115, F22, F141, F142 are lumped with F12
GEOSCCM	F10, F11, F12, F113, $\text{CH}_3\text{CCl}_3$ , $\text{CH}_3\text{Cl}$ , F22, F142b, F141b	$\text{CH}_3\text{Br}$ , H1301, H1211, H2402	None	<i>Dougllass et al. (1997)</i> ; <i>Kawa et al. (2002)</i>	<i>JPL (2002)</i>	YES
LMDzrepro	F10, F11, F12, F113, F22, $\text{CH}_3\text{CCl}_3$ , $\text{CH}_3\text{Cl}$	H1211, H1301, $\text{CH}_2\text{Br}_2$ , $\text{CH}_3\text{Br}$	None	$\text{CH}_4$ - $\text{CO}$ - $\text{NO}_x$ - $\text{ClO}_x$ - $\text{BrO}_x$	<i>JPL (2006)</i>	YES
MRI	F10, F11, F12, $\text{CH}_3\text{Cl}$ , H1211	$\text{CH}_3\text{Br}$ , H1211, H1301	None	$\text{CH}_4$ - $\text{CO}$ - $\text{NO}_x$ - $\text{ClO}_x$ - $\text{BrO}_x$	<i>JPL (2006)</i>	YES
NiwaSOCOL SOCOL	F10, F11, F12, F113, F114, F115, $\text{CH}_3\text{CCl}_3$ , F22, F141b, F142b, $\text{CH}_3\text{Cl}$ , F21, F123	$\text{CHBr}_3$ , $\text{CH}_2\text{Br}_2$ , $\text{CH}_3\text{Br}$ , H1211, H1301	None	$\text{CH}_4$ - $\text{CO}$ - $\text{NO}_x$ - $\text{ClO}_x$ - $\text{O}_x$ - $\text{BrO}_x$	<i>JPL (2002, 2006)</i> , <i>IUPAC (2004, 2005)</i>	No

CCM	Chlorine source gases	Bromine source gases	NMHC source gases	Chemical scheme	Origin of kinetic data	Lumping (YES/NO)
ULAQ	F10, F11, F12, F113, F114, F115, F22, F141B, F142B, F123, CH <sub>3</sub> CCl <sub>3</sub> , CH <sub>3</sub> Cl, H1211	H1211, H1301, CH <sub>3</sub> Br	C <sub>2</sub> H <sub>6</sub> , C <sub>3</sub> H <sub>8</sub> , C <sub>2</sub> H <sub>4</sub> , C <sub>3</sub> H <sub>8</sub> , C <sub>10</sub> H <sub>16</sub> , Other NMHC	N <sub>2</sub> O-CH <sub>4</sub> -CO-families (NO <sub>x</sub> , NO <sub>y</sub> , Cl <sub>y</sub> , Br <sub>y</sub> , HO <sub>x</sub> , CHO <sub>x</sub> , SO <sub>x</sub> )	JPL (2006)	YES (for other NMHCs)
UMETRAC	Parameterised	Parameterised	None	CH <sub>4</sub> -CO-NO <sub>x</sub> -ClO <sub>x</sub> -BrO <sub>x</sub>	JPL (2002)	NO
UMSLIMCAT	F11, F12 (scaled)	CH <sub>3</sub> Br (scaled)	None	CH <sub>4</sub> -CO-NO <sub>x</sub> -ClO <sub>x</sub> -BrO <sub>x</sub>	JPL (2002, 2006)	YES
UMUKCA-METO	F11, F12 (scaled)	CH <sub>3</sub> Br (scaled)	None	CH <sub>4</sub> -CO-NO <sub>x</sub> -ClO <sub>x</sub> -BrO <sub>x</sub>	JPL (2006); Chipperfield (1999)	YES
UMUKCA-UCAM	F11, F12 (scaled)	CH <sub>3</sub> Br (scaled)	None	CH <sub>4</sub> -CO-NO <sub>x</sub> -ClO <sub>x</sub> -BrO <sub>x</sub>	JPL (2002); IUPAC (2003)	YES
WACCM	F10, F11, F12, F113, F22, CH <sub>3</sub> CCl <sub>3</sub> , CH <sub>3</sub> Cl	CH <sub>3</sub> Br, H1211, H1301	None	Kinnison <i>et al.</i> (2007)	JPL (2006)	YES (for other halocarbons)

NAT and STS, between CCMs (Table 2.16). The simplest assumption is that PSCs are formed at the saturation points of HNO<sub>3</sub> over NAT and H<sub>2</sub>O over water-ice. This assumption is made in most CCMVal-2 CCMs. By contrast, the ULAQ model does not assume thermodynamic equilibrium and thus allows for supersaturation and other non-equilibrium effects. ULAQ has 9 tracers each for size-resolved NAT and ice (Pitari *et al.*, 2002). CAM3.5 and WACCM also allow for supersaturation of up to 10 times saturation but do not transport a separate NAT tracer (Garcia *et al.*, 2007). GEOSCCM accounts for non-equilibrium by using a NAT tracer. In EMAC, NAT forms only on ice or pre-existing NAT (Buchholz, 2005).

The equilibrium assumption only defines the mass of condensed PSC; assumptions about size distributions and particle shapes need to be made to derive surface area densities. The assumed size distribution affects the PSCs sedimentation velocities, *i.e.*, the rates of de-/rehydration and de-/renitrification, particularly in the case of large particles. The denitrification through PSC sedimentation contributes to the enhancement of polar stratospheric ozone loss in spring by inhibiting the formation of the ClONO<sub>2</sub> reservoir. All CCMs except CMAM include this process (Table 2.16) although sedimentation velocities differ a lot between models.

### 2.3.3.7 Boundary conditions, emissions and surface sinks

Different methods are used to impose source gases at the Earth's surface. For reproducing the past, GHGs and ODSs (CO<sub>2</sub>, N<sub>2</sub>O, CH<sub>4</sub>, CFCs, halons) are prescribed at the surface using observed global-mean surface abundances (Section 2.5.3.2). The same holds true for the future except for that here the abundances are based on future projections. This method assures the source gas abundances near the surface to be close to the desired values. Diagnosed fluxes associated with the prescribed surface abundances may however deviate substantially from those derived from emission inventories; this would indicate a mismatch in lifetime for such a species between the CCM and the assessment model used to calculate the scenario. Models with an explicit or simplified treatment of tropospheric chemistry usually impose explicit emissions (fluxes) for higher organic species (represented in CAM3.5, EMAC, and ULAQ), NO<sub>x</sub>, CO, and/or CH<sub>2</sub>O (Table 2.13). Emissions aloft by lightning (Price and Rind, 1992 or 1994, Müller and Brasseur, 1995, or Grewe *et al.*, 2001) or aircraft are also represented to a varying degree in those models (Table 2.13). Emissions of SO<sub>2</sub>, dimethyl sulfide (DMS) and NH<sub>3</sub> associated with tropospheric aerosol are represented in CAM3.5, EMAC, ULAQ, UMETRAC, and UMUKCA.

There are two types of deposition in the troposphere, dry deposition and wet deposition. Dry deposition may be

**Table 2.13:** Species with surface emissions, aircraft emissions; lightning emission of NO<sub>x</sub>, wet and dry deposition. NO = nitrogen oxide. NI = not included.

CCM	Surface emission	Aircraft em.	Lightning NO <sub>x</sub>	Wet deposition	Dry deposition	Comment
AMTRAC3	NI	NI	NI	NI	NI	Trop. NO <sub>x</sub> climatology imposed
CAM3.5	paraffin, olefin, terpene, BC, C <sub>2</sub> H <sub>4</sub> , CH <sub>2</sub> O, CH <sub>3</sub> CHO, CO, DMS, C <sub>5</sub> H <sub>8</sub> , NH <sub>3</sub> , NO, OC, SO <sub>2</sub> , C <sub>7</sub> H <sub>8</sub> , dust, SS	CO, NO	NO	Yes	Yes	
CCSRNIES	NI	NI	NI	Yes	Yes	
CMAM	NI	NI	NI	NI	Yes	
CNRM-ACM	NI	NI	NI	NI	NI	Below 577 hPa relaxation to ground values ( $\tau=7$ days)
E39CA	NO, NO <sub>2</sub>	NO, NO <sub>2</sub>	<i>Grewe et al. (2001)</i>	Yes	Yes	
EMAC	CO, NO, C <sub>2</sub> H <sub>6</sub> , C <sub>2</sub> H <sub>4</sub> , C <sub>3</sub> H <sub>6</sub> , C <sub>4</sub> H <sub>10</sub> , CH <sub>3</sub> CHO, CH <sub>3</sub> COCH <sub>3</sub> , CH <sub>3</sub> OH, CH <sub>2</sub> O, SO <sub>2</sub> , NH <sub>3</sub>	NO	<i>Tost et al. (2007); Price and Rind (1994)</i>	Yes	Yes	
GEOSCCM	NI	NI	parameterised	NI	NI	
LMDZrepro	NI	NI	NI	NI	NI	Zonally invariant composition imposed below 400 mb
MRI	CO	NO	NO	Yes	Yes	
NiwaSOCOL SOCOL	CO, NO <sub>x</sub>	NO <sub>x</sub>	<i>Müller and Brasseur (1995)</i>	Yes HNO <sub>3</sub>	Yes	Deposition: <i>Seinfeld (2006)</i> . HCl, HBr, ClONO <sub>2</sub> imposed at surface
ULAQ	NO <sub>x</sub> , CO, NMHC, SO <sub>2</sub> , DMS	H <sub>2</sub> O, NO <sub>x</sub> , CO, SO <sub>2</sub> , BC, SO <sub>4</sub>	<i>Grewe et al. (2001)</i>	Yes	Yes	
UMETRAC	SO <sub>2</sub> , DMS	NI	NI	No	No	
UMSLIMCAT	NI	NI	NI	No	No	LBCs imposed for all species
UMUKCA-METO	NO, CH <sub>2</sub> O, CO, SO <sub>2</sub> , DMS, NH <sub>3</sub>	NO	<i>Price and Rind (1992)</i>	Yes	Yes	Erroneous washout imposed for inorganic halogens
UMUKCA-UCAM	NO, CH <sub>2</sub> O, CO, SO <sub>2</sub> , DMS, NH <sub>3</sub>	NO	<i>Price and Rind (1992)</i>	Yes	Yes	0 boundary conditions for inorganic halogens imposed
WACCM	NO, CH <sub>2</sub> O, CO	NO	<i>Price and Rind (1992)</i>	Yes	Yes	Includes SPE emissions of HO <sub>x</sub> and NO <sub>x</sub>

represented by a deposition velocity for a particular surface and gas so that a deposition flux is the product of deposition velocity and abundance (*e.g.*, Walcek *et al.*, 1986). Dry deposition is an important component of the tropospheric ozone budget (*e.g.*, Hough, 1991). Wet deposition, on the other hand, involves the scavenging of gases by cloud droplets. Hydro-halogens such as HCl and HBr dissolve well in water; this makes wet depositions of these species the dominant sink for Cl<sub>y</sub> and Br<sub>y</sub>. Similarly, the wet deposition of HNO<sub>3</sub> is a major sink of NO<sub>y</sub>.

The removal of inorganic halogen is handled in different ways in the models. All models (except AMTRAC3, CMAM, CNRM-ACM, GEOSCCM, LMDZrepr, UMETRAC and UMSLIMCAT; Table 2.13) incorporate explicit washout (at least for some species). In some models removal is represented by relaxing species to a background tropospheric climatology (CNRM-ACM, LMDZrepr, UMETRAC). In the case of UMUKCA-UCAM, removal of inorganic halogens is achieved by imposing zero surface boundary conditions for these species (Morgenstern *et al.*, 2009). By contrast, UMUKCA-METO has explicit washout for these species *albeit* incorporated incorrectly. With the exception of CMAM, the same models that include washout also include dry deposition; for CMAM only dry deposition is included.

## 2.3.4 Transport

### 2.3.4.1 Advection

Advection is one of the major processes determining the distribution of chemical species, particularly in the lower stratosphere, where the chemical lifetimes of long-lived species are much longer than the dynamical (transport) lifetimes, as manifested, for example, by the tape-recorder signal of H<sub>2</sub>O in the equatorial lower stratosphere (Mote *et al.*, 1996), and by the “mixing barriers” in the subtropics and around the winter pole (*e.g.*, Shepherd, 2003). The distribution of chemical species, and the age of air, are sensitive to the details of advection schemes (*e.g.*, Eluszkiewicz *et al.*, 2000; Gregory and West, 2002; Rasch *et al.*, 2005; Chipperfield, 2006; Struthers *et al.*, 2009). In addition, inconsistencies may arise from the different discretization of the continuity equation and the tracer transport equation, as shown for example by Jöckel *et al.* (2001). Some CCMs (CNRM-ACM, E39CA, LMDZrepr, MRI, and (Niwa)SOCOL; Table 2.1) also use different advection schemes for meteorological (*i.e.*, momentum, heat, water) and chemical tracers, resulting in different numerical diffusivities for tracers advected by different schemes, and possible inconsistencies. Several types of advection schemes are used in the CCMVal-participation models, namely finite volume, spectral, semi-Lagrangian, flux-

form semi-Lagrangian, and fully Lagrangian schemes.

Spectral advection in the horizontal and finite difference advection in the vertical (CCSRNIES, CMAM) conserves species mass, but requires careful attention to avoid the development of sharp gradient in species distribution and to fill negative values (de Grandpré *et al.*, 2000).

Semi-Lagrangian schemes can be used with relatively long time steps without compromising stability. Also semi-Lagrangian schemes are advantageous when a large number of tracers needs to be advected (such as in CCMs) because a major fraction of the cost is independent of the number of tracers. However, these schemes may be overly diffusive (*e.g.*, Eluszkiewicz *et al.*, 2000) due to an interpolation step necessary to project tracers from the departure points onto the arrival points. This diffusive property can be improved through higher-order interpolation, *e.g.*, quintic (MRI, UMUKCA; Priestley, 1993; Table 2.4). However, the better accuracy of higher-order interpolation comes at the price of numerical artifacts, such as overshoots and undershoots (similar to those found in spectral advection) that require special treatment. Also, some semi-Lagrangian schemes exhibit tracer non-conservation (*e.g.*, Rasch *et al.*, 2005), requiring an unphysical correction. Flux-form semi-Lagrangian advection is considered relative accurate; however, in practice little difference has been found between flux-form semi-Lagrangian and spectral advection schemes (Eyring *et al.*, 2006; Shepherd, 2007). Flux-form schemes are used in a number of models (AMTRAC3, CAM3.5, EMAC, GEOSCCM, LMDZrepr, WACCM). They can be made to conserve tracers (Rasch *et al.*, 2005). Many models in this category (AMTRAC3, CAM3.5, EMAC, GEOSCCM, WACCM) use formulations after Lin and Rood (1996 or 1997) or Lin (2004). LMDZrepr, UMETRAC, and UMSLIMCAT use finite-volume advection schemes (Hourdin and Armengaud, 1999; Gregory and West, 2002).

The E39CA model uses a fully Lagrangian approach to constituent transport, thereby avoiding the interpolation step needed in semi-Lagrangian methods (Reithmeier and Sausen, 2002; Stenke *et al.*, 2008). This method is not subject to numerical diffusion, thus allowing for a specification of explicit, physically motivated diffusion to represent mixing between neighbouring parcels. This explicitly defined diffusion may be much smaller than numerical diffusion found in other schemes. The ATTILA scheme in E39CA does not include parcel merging or parcel splitting, implying very different concentrations of parcels in the stratosphere compared to parcels in the lower troposphere (*i.e.*, effectively decreasing resolution with height). This main disadvantage needs to be weighed against the gain of controlled diffusion.

Table 2.14: Photolysis. SZA: Solar zenith angle. OC: ozone column. L- $\alpha$ : Lyman- $\alpha$ , 121.6 nm.

CCM	Reference for scheme	References for cross section	Online	Spectral range (nm)	Average resolution (nm)	Max. SZA (degrees)	Temperature range (K)	Interpolation parameters
AMTRAC3	<i>Austin et al. (1987)</i>	<i>JPL (2006)</i>	NO	175-700, L- $\alpha$	0.5-10 (158 bands)	up to 100	200-300	T, p, SZA, OC
CAM3.5	<i>Kinnison et al. (2007)</i>	<i>JPL (2006); Burkholder et al. (1990)</i>	YES	200-750	~2-5 (200-400nm); 10-50 (>400nm).	97	150-350	T, p, SZA, OC, albedo
CCSRNIES	<i>Kurokawa et al. (2005); Akiyoshi et al. (2009)</i>	<i>JPL (2006)</i>	YES	177.5-690, L- $\alpha$	0.90-2.35 (S-R bands); 12.1-372 (>200nm)	96	195-300	N/A
CMAM	<i>de Grandpré et al. (2000)</i>	<i>JPL (2006)</i>	NO	121-852.5; 165 bands	4.4 (1.6-10)	100	Variable	p, SZA, OC
CNRM-ACM	TUV 4.1a ( <i>Madronich and Flocke, 1998</i> )	<i>JPL (2006)</i>	NO	116-850	0.01 (S-R bands); 0.1 (L- $\alpha$ ); 1 (elsewhere)	95	187-288	p, SZA, OC
E39CA	<i>Landgraf and Crutzen (1998)</i>	<i>JPL (1997)</i>	YES	175-683 (8 bands)	1-5 for pre-calculation of coefficients, 8-260 for bands (with scattering)	93 ( <i>Lamago et al., 2003</i> )	Variable	N/A
EMAC	<i>Landgraf and Crutzen (1998); Zankowski et al. (1980); Allen and Frederick (1982); Koppers and Murtagh (1996)</i>	<i>JPL (1997); Talukdar et al. (1998); Roehl et al. (2002); Blitz et al. (2004)</i>	YES	175-683 (8 bands), L- $\alpha$	1-5 for pre-calculation of coefficients, 8-260 for bands (with scattering)	94.5	Variable	Online, with clouds and ozone
GEOSCCM	<i>Douglass et al., (1997)</i>	<i>JPL (2002)</i>	YES	176.2-310 (50 bands); 310-450 (28 bands); 652.5; L- $\alpha$	176.2-310; 2.775 nm; 310-450: 5 nm	94	148-348	T, p, SZA, OC
LMDZrepro	<i>Madronich and Flocke (1998)</i>	<i>JPL (2006)</i>	NO	121-750	116-124: 0.1nm; 124-175: 1nm; 175-205: 0.01nm; 205-850: 1nm	95	Variable	Z, SZA, ozone column
MRI	<i>Shibata et al. (2005)</i>		NO	116.3-735; 171 bands	0.7-5.0	96	253-293	T, p, SZA, OC

CCM	Reference for scheme	References for cross section	Online	Spectral range (nm)	Average resolution (nm)	Max. SZA (degrees)	Temperature range (K)	Interpolation parameters
NiwaSOCOL SOCOL	Rozanov et al. (1999)	JPL (2006); IUPAC (2004, 2005)	YES (LUTs)	121-750, 73 bands	1-160; median: 5 nm	98	Variable	SZA, OC, oxygen total column
ULAQ	NASA (1993)	JPL (2006)	YES	135-850	0.7-5.0	94	Variable	Online
UMETRAC	Austin et al. (1987)		NO	175-700, L- $\alpha$	0.5-10 (158 bands)	up to 100	200-300	T, p, SZA, OC
UMSLIMCAT	Lary and Pyle (1991); Chipperfield (1999)	JPL (2002)	NO	175-850, L- $\alpha$	4.3	98	Variable	T, p, SZA, OC
UMUKCA-METO UMUKCA-UCAM	Lary and Pyle (1991); Chipperfield (1999)	Chipperfield (1999)	NO	175-850, L- $\alpha$	4.3	98	Variable	T, p, SZA, OC
WACCM	Kinnison et al. (2007)	JPL (2006); Burkholder et al. (1990)	YES	120-750	~1-2 (SRC, SRB), ~2-5 (200-400nm); 10-50 (>400nm)	97	150-350	T, p, SZA, OC, albedo

### 2.3.4.2 Convective transport and turbulent mixing of chemical species

Convection and turbulence rapidly mix air and chemical species vertically, and thus they are important for the distribution of chemical species. Such processes are of interest not just in the troposphere, but also in the middle atmosphere (*e.g.*, associated with gravity wave breaking). Turbulent mixing works predominantly within the planetary boundary layer (below ~2000m), and convective transport is the dominant process mixing air between the planetary boundary layer and the free troposphere, thereby playing a crucial role for long-range transport such as intercontinental and hemispheric transport. In particular, deep cumulus convection uplifts the chemical species in the boundary layer directly to the upper troposphere through detrainment, giving large effects on tropospheric ozone (*e.g.*, Lawrence *et al.*, 2003). Entrainment of mid-level air and downdraft associated with detrained air in a convective cell also contribute to the vertical mixing of chemical species. However, since most CCMVal-2 models do not include detailed tropospheric chemistry, sophisticated schemes are often not required for convective transport and turbulent mixing. (See online supplement for more details). Also the CCMVal-2 reference simulations (Section 2.5.2) do not consider very short-lived halogen species (VSLs) which would be sensitive to the details of convection.

## 2.4 CCMVal-2 models and development since CCMVal-1

Several models that were used for CCMVal-1 are used here again for CCMVal-2. Sometimes the name of the CCM has remained the same, although developments have taken place. In other cases, a new model name is used and a predecessor model was used for CCMVal-1. The purpose of this section is therefore to provide a basic description of each model and a detailed list of differences versus the CCMVal-1 version.

### 2.4.1 AMTRAC3 (known as AMTRAC in CCMVal-1)

AMTRAC3 is an improved version of AMTRAC (Austin and Wilson, 2006). The major model differences are incorporation of the ‘cubed sphere’ dynamical core (Putman and Lin, 2007) as well as convection (Phillips and Donner, 2006) and aerosol changes in preparation for IPCC AR5. These changes have led, in particular, to increased stratospheric water vapour amounts in much better agreement with observations. Chlorine and bromine source gases are not explicitly modelled. The parameterisation for the production of inorganic chlorine and bromine

**Table 2.15:** Heterogeneous reactions. LSA: liquid stratospheric aerosol. LTA: liquid (sulfuric) tropospheric aerosol. N: NAT. I: ice. SO<sub>4</sub>: sulfate. SAD: Sulfuric acid dihydrate. STS: supercooled ternary (H<sub>2</sub>SO<sub>4</sub> / HNO<sub>3</sub> / H<sub>2</sub>O) solution. LA: liquid aerosol

CCM	CINO <sub>3</sub> + H <sub>2</sub> O	CINO <sub>3</sub> + HCl	HOCl + HCl	N <sub>2</sub> O <sub>5</sub> + H <sub>2</sub> O	N <sub>2</sub> O <sub>5</sub> + HCl	B <sub>r</sub> NO <sub>3</sub> + H <sub>2</sub> O	HOBr + HCl	CINO <sub>3</sub> + HBr	BrNO <sub>3</sub> + HCl	HOBr + HCl	HOBr + HBr	CINO <sub>2</sub> + H <sub>2</sub> O	CINO <sub>2</sub> + HCl	HOCl + HBr
AMTRAC3 UMETRAC	SAD/N/I	SAD/N/I	SAD/N/I	SAD/ N/I	N/I	N/I	N/I				SAD/ N/I			N/I
CAM3.5	N/STS/I	N/STS/I	N/STS/I	N/STS/I		STS/I	STS/I	N/STS/I						
CCSRNIES	N/I/LSA	N/I/LSA	N/I/LSA	N/I/LSA	N/I	N/I/LSA	N/I/LSA	N/I	N/I	N/I/LSA	N/I/ LSA			N/I/ LSA
CMAM	STS/I	STS/I	STS/I	SO <sub>4</sub> / STS/I		SO <sub>4</sub> / STS	STS/I							
CNRM-ACM	N/I/LSA	N/I	N/I	N/I/LSA	N/I	N/I				N/I	N/I	N/I	N/I	
E39CA	N/I/LSA	N/I/LSA	N/I/LSA	N/I/LSA	N/I/ LSA									
EMAC	N/I/LSA	N/I/LSA	N/I/LSA	N/I/ LSA/ LTA		N/I/LSA	N/I/LSA		N/I	N/I/ LSA				
GEOSCCM	I/N/LSA	I/N/LSA	I/N/LSA	I/N/LSA	I/N/ LSA	I/N/LSA								
LMDZrepro	LA/N/I	LA/N/I	LA/N/I	LA/N/I	N/I	LA/N/I	LA/N/I				I			
MRI	N/I/SO <sub>4</sub>	N/I	N/I	N/I/SO <sub>4</sub>	N/I	SO <sub>4</sub>	N/I							
NiwaSOCOL SOCOL	LSA/N/I	LSA/N/I	LSA/N/I	LSA/ N/I		LSA/I	LSA/I							
ULAQ	N/I/SAD	N/I	N/I/SAD	N/I/ SAD	N/I	N/I/ SAD	N/I/ SAD		N/I	N/I/ SAD				
UMSLIMCAT	N/STS/I	N/STS/I	N/STS/I	N/STS/I	N/I						N/ STS/I			
UMUKCA-METO UMUKCA-UCAM	N/I/SO <sub>4</sub>	N/I	N/I/SO <sub>4</sub>	N/I/SO <sub>4</sub>	N/I									
WACCM	N/STS/I	N/STS/I	N/STS/I	N/STS/I		STS/I	STS/I	N/STS/I						



used in AMTRAC3 has been modified, *versus* AMTRAC. Essentially, the effective photolysis rates of the CFCs have been decreased in the lower stratosphere and increased in the tropical middle stratosphere. The other major change in the photochemistry is that the scattering calculation in the photolysis lookup table has been corrected (L. Horowitz, personal communication), leading to higher ozone amounts in the lower stratosphere in better agreement with observations. Finally, the positions of the model vertical levels have been adjusted to provide increased stratospheric resolution, at the expense of decreased mesospheric resolution. The new model physics and dynamics have required a new tuning (*i.e.*, a reduction) of  $\tau_{\text{oro}}$  parameterised non-orographic gravity wave forcing.

*Changes since CCMVAL-1:*

- Cubed sphere dynamics
- Improved CFC parameterisation
- Improved photolysis rates *etc.*, as in descriptive section.

## 2.4.2 CAM3.5

CAM3.5 is a version of the recently updated Community Atmosphere Model (Gent *et al.*, 2009) with interactive chemistry in the troposphere (including aerosols) and stratosphere. This setup is equivalent to CAM3 (Lamarque *et al.*, 2008). The main difference over the latter version is the inclusion of the new gravity-wave drag parameterization from Richter *et al.* (2010), similar to WACCM (see below).

CAM3.5 did not participate in CCMVal-1.

## 2.4.3 CCSRNIES

The CCSR/NIES GCM originates from an NWP model obtained from the Japan Meteorological Agency. Some improvements of the codes and an extension of the heights up to the stratosphere were made (Numaguti, 1993; Numaguti *et al.*, 1995; Takahashi, 1996, 1999; Nakajima *et al.*, 2000). The chemical module for stratospheric gas phase reactions was developed by Akiyoshi (2000) and incorporated in a CCSR/NIES GCM with a top boundary in the mesosphere (Takigawa *et al.*, 1999; Nagashima *et al.*, 2002). The heterogeneous chemistry module originates from a box model version of SLIMCAT model (Carslaw *et*

**Table 2.16:** Microphysics of polar stratospheric clouds (PSCs). EQ = thermodynamic equilibrium with gaseous  $\text{HNO}_3$  /  $\text{H}_2\text{SO}_4$  /  $\text{H}_2\text{O}$  assumed. HY = non-equilibrium / hysteresis considered.

CCM	Sedimentation velocity (mm/s)	Thermodynamics	Transported PSC tracers	References / comments
AMTRAC3 UMETRAC	NAT: 0.14; NAT/ice: 12.7	EQ	None	
CAM3.5	NAT / ice but not STS	NAT: HY; ice: EQ	None	<i>Kinnison et al. (2007)</i>
CCSRNIES	NAT/ICE, dep. on mode radius	EQ	None	
CMAM	No sedimentation	EQ	None	
CNRM-ACM	NAT/ice: mean value around 17.3	EQ	None	
E39CA	Varies by particle size ( <i>Steil et al., 1998</i> )	HY	NAT + $\text{HNO}_3$ , ice	
EMAC	<i>Buchholz (2005)</i>	NAT: HY; ice: EQ	NAT	
GEOSCCM	Varies by particle size	HY	NAT, ice	
LMDZrepro	<i>Lefèvre et al. (1998)</i>	EQ	None	
MRI	NAT: 0.17, ice: 17.4	EQ	None	
NiwaSOCOL SOCOL	<i>Schraner (2008)</i>	EQ	None	<i>Carslaw et al. (1995)</i>
ULAQ	Function of size bin	HY	9 NAT + 9 ice	
UMSLIMCAT UMUKCA-METO UKUKCA-UCAM	NAT: 0.46; NAT/ice: 17.3	EQ	None	
WACCM	NAT / ice but not STS.	NAT: HY; ice: EQ	NAT	<i>Kinnison et al. (2007)</i>

*et al.*, 1995; Sessler *et al.*, 1996). Recent updates including bromine chemistry, heterogeneous reactions, Schumann-Runge bands, atmospheric sphericity, and non-orographic GWD were made before participating in CCMVal (Akiyoshi *et al.*, 2004; Kurokawa *et al.*, 2005; Akiyoshi *et al.*, 2009).

*Changes since CCMVal-1:* None

## 2.4.4 CMAM

CMAM is an upwardly extended version of the spectral CCCma third generation atmospheric GCM (Scinocca *et al.*, 2008). The model's resolution increases monotonically from roughly 100 m near the surface to around 900 m around the extra-tropical tropopause to 2.5 km in the stratosphere and middle atmosphere. REF-B2 simulations (see below) were coupled to the NCOM 1.3 ocean general circulation model (OGCM) (Gent 1998; Arora *et al.*, 2009). The OGCM employs a horizontal resolution of 1.86° with 29 levels with a 50 m upper layer and 300 m layers in the deep ocean. CMAM includes a comprehensive representation of stratospheric chemistry with all the relevant catalytic ozone loss cycles (de Grandpré *et al.*, 1997). Sedimentation/denitrification and NAT formation are not included (Hitchcock *et al.*, 2009). The chemistry is fully interactive with the radiation code (de Grandpré *et al.*, 2000). An upper boundary condition (at ~95 km) of 1 ppmv is imposed for NO<sub>x</sub> to account for mesospheric NO<sub>x</sub> production by cosmic rays and solar particles.

*Changes since CCMVal-1:*

Probably the biggest development is that CMAM has been coupled to an ocean GCM (see above). Coupling to the ocean required retuning the model cloud and aerosol forcing for energy balance. This appears to have substantially increased the planetary wave forcing in the NH winter, such that even with observed SSTs the vortex is now too warm, SSWs are too frequent, and the Brewer-Dobson circulation is stronger. In coupled mode the troposphere warms at a rate comparable to that projected in the CMAM CCMVal-1 contribution, though the rate of acceleration of the Brewer-Dobson circulation is faster. This is the subject of further investigation. Thus, the price paid for this initial coupling to the ocean has been a degradation of the dynamical aspects of the simulations.

Further changes between CCMVal-1 and CCMVal-2 include: CCl<sub>4</sub>, CH<sub>3</sub>CCl<sub>3</sub>, HCFC-22, and CH<sub>3</sub>Cl have been added to the chemistry scheme, including lumping with non-represented source gases. Reactive chlorine (Cl<sub>y</sub>) had been advected as a single family in CMAM for CCMVal-1. For CCMVal-2, HCl was advected separately from the other Cl<sub>y</sub> species, allowing for a more realistic activation of chlorine in the polar vortex. Within the polar vortex, par-

ticularly over the Antarctic, problems were identified with the local conservation of NO<sub>y</sub> by advection due to the particular partitioning of HNO<sub>3</sub> and NO<sub>x</sub> during polar night. The sum of HNO<sub>3</sub>, NO<sub>x</sub> and HNO<sub>4</sub>, the three advected species in CMAM that carry NO<sub>y</sub>, has been constrained by the addition of an additional advected tracer (NO<sub>y</sub>) that is the sum of the three.

Gas-phase (but not heterogeneous) chemical reaction rates and photolysis rates were updated to JPL (2006). The photolysis look-up table underwent a variety of improvements which included: increased number of solar zenith angle look-up points in the table, for improved photolysis rates at twilight, the change to a more up-to-date solar flux input (SOLARIS), a revised wavelength grid for improved rates in the mesosphere, and the correction of various programming errors (fix for the excessive transmission of UV to the Earth's surface and overestimated photolysis rates for O<sub>2</sub>, CFCs, H<sub>2</sub>O, and N<sub>2</sub>O in the troposphere and lower stratosphere). An interpolation procedure in the longwave scheme was changed which caused the CCMVal-1 simulations to under-estimate the impact of the CO<sub>2</sub> increase in the recent past (Jonsson *et al.*, 2009). For REF-B1 (see below), solar variability is now included in CMAM in both J-value and solar heating calculations. To include solar variability in J-values, the look up table approach was modified. Solar variability in solar heating is calculated as an additional term and includes treatment in 8 spectral bands between 121 and 300 nm. The vertical diffusivity for tracers is enhanced in the upper stratosphere and mesosphere to crudely account for missing dissipation associated with gravity-wave breaking.

## 2.4.5 CNRM-ACM

The dynamical GCM ARPEGE-Climat 4.6 (Déqué, 2007) is coupled to the atmospheric chemistry scheme described by Teyssèdre *et al.* (2007). The composition module uses its own transport scheme. CCMVal-2 simulations have been performed with horizontal resolutions differing between dynamics and chemistry to reduce computation cost. The vertical resolutions of dynamics and chemistry are identical.

CNRM-ACM did not participate in CCMVal-1.

## 2.4.6 E39CA (known as E39C in CCMVal-1)

The coupled chemistry-climate model ECHAM4.L39(DLR)/CHEM/-ATTILA (hereafter referred to as E39CA) is an upgraded version of ECHAM4.L39(DLR)/CHEM (E39C). E39CA consists of the dynamic part ECHAM4 and the family-based chemistry module CHEM. Chemical and hydrological tracers are transported using the purely Lagrangian scheme ATTILA which is strictly mass conserving and numerically non-diffusive.

*Changes since CCMVal-1:*

- Introduction of ATTILA, see above.
- Introduction of parameterised bromine-catalysed ozone loss (Stenke *et al.*, 2009).

### 2.4.7 EMAC

The ECHAM5/MESSy Atmospheric Chemistry (EMAC) model is a numerical chemistry and climate simulation system that includes sub-models describing tropospheric and middle atmosphere processes (Jöckel *et al.*, 2006). It uses the first version of the Modular Earth Submodel System (MESSy1) to link multi-institutional computer codes. The core atmospheric model is ECHAM5 (Roeckner *et al.*, 2003). For the present study we applied EMAC (ECHAM5 version 5.3.01, MESSy version 1.6) in the T42L90MA-resolution (Giorgetta *et al.*, 2006). EMAC includes a representation of mesospheric NO<sub>x</sub> production by cosmic rays and solar particles.

EMAC replaces the MAECHAM4CHEM CCM that was used in CCMVal-1.

### 2.4.8 GEOSCCM

GEOSCCM couples the Goddard Earth Observing System (GEOS) version 5 AGCM (Reineker *et al.*, 2008) to an updated version of the Douglass *et al.* (1997) stratospheric chemistry mechanism. The GEOS-5 AGCM uses a flux-form semi-Lagrangian dynamical core (Lin, 2004) with a quasi-Lagrangian vertical coordinate (Lin and Rood, 1997) that allows for accurate computation of vertical motions. The stratospheric chemistry package includes a comprehensive suite of chemicals and chemical reactions thought to be important in the stratosphere. The photochemistry code is based on the family approach, as described by Douglass and Kawa (1999). Constituent advection also uses the Lin (2004) transport scheme. GEOSCCM does not use explicit diffusion and also does not impose a sponge at the model top. Tropospheric ozone is relaxed to a climatology (Logan, 1999).

*Changes since CCMVal-1:*

- Transition from GEOS-4 to the Earth System Modeling Framework (ESMF)-compliant GEOS-5
- New versions of several physical processes, most importantly moist physics, have been implemented (Bacmeister *et al.*, 2006; Rieneker *et al.*, 2008).
- A catchment approach (Koster *et al.*, 2000) is now used to model the land-surface.

### 2.4.9 LMDZrepro

The LMDz-REPROBUS CCM (Jourdain *et al.*, 2008)

couples interactively the vertically extended version of the LMDz 4<sup>th</sup>-generation GCM (Lott *et al.*, 2005) and the stratospheric chemistry module of the REPROBUS CTM (Lefèvre *et al.*, 1998). LMDz is the atmospheric component of the IPSL Earth System model. The chemistry module contains a detailed description of stratospheric chemistry. It calculates the chemical evolution of 55 species using 160 gas-phase reactions and 6 heterogeneous reactions with sedimentation taken into account. Radiation is based on Morcrette (1989).

*Changes since CCMVal-1:*

- Improved convection scheme (Kerry-Emmanuel)
- Improved composition climatology for NO<sub>x</sub>, CO, and O<sub>3</sub> below 400 hPa (Savage *et al.*, 2004)
- Updated chemistry to JPL (2006)
- Improved PSC scheme including a bimodal size distribution of PSC particles.

### 2.4.10 MRI

MRI-CCM is an upgraded version of the MRI-CTM (Shibata *et al.*, 2005; Shibata and Deushi, 2008). The dynamical core of MRI-CCM is based on the spectral global model MJ98 (Shibata *et al.*, 1999) at a triangular truncation of T42 used for CCM simulations. The model employs hybrid-pressure coordinates in the vertical with 68 layers, the thickness of which is about 500 m between 100 and 10 hPa with tapering off below and above the levels, respectively. Explicit bi-harmonic horizontal diffusivity is weaker in the middle atmosphere than in the troposphere to allow for a representation of the QBO (Shibata and Deushi, 2005a). Transport of chemical species is performed using a hybrid semi-Lagrangian scheme satisfying the continuity equation (see below). The chemistry module comprises full stratospheric chemistry including the relevant heterogeneous reactions on PSCs and sulfate aerosols, and also a simplified representation of tropospheric chemistry.

*Changes since CCMVal-1:*

- Implementation of a new hybrid semi-Lagrangian scheme. The new scheme is semi-Lagrangian with a quintic interpolation in the horizontal, but flux form in the vertical, wherein advection is calculated with the piecewise rational method (PRM) (Xiao and Peng, 2004).

### 2.4.11 SOCOL and NiwaSOCOL

SOCOL (Egorova *et al.*, 2005) is a combination of the GCM MA-ECHAM4 (Manzini *et al.*, 1997) and the CTM MEZON (Rozañov *et al.*, 1999; Egorova, 2003). MEZON has the same vertical and horizontal resolution as MA-ECHAM4 (used in CCMVal-1) and in addition

includes a comprehensive representation of stratospheric chemistry. An extensive evaluation of SOCOL (Egorova *et al.*, 2005; Eyring *et al.*, 2006, 2007) led to the development of SOCOL version 2.0 (Schraner *et al.*, 2008) used here.

NiwaSOCOL differs from SOCOL regarding to the lower boundary conditions and some details of photochemistry. Due to these minor differences NiwaSOCOL simulations should not be regarded as ensemble members of SOCOL.

*Changes since CCMVal-1:*

- The list of ODS is extended to 15 for chemistry, while for transport they are still clustered into three tracers;
- Inclusion of HNO<sub>3</sub> uptake by aqueous sulfuric acid aerosols;
- NAT particle number densities are limited by an upper boundary of  $5e10^{-4} \text{ cm}^{-3}$  to take into account that observed NAT clouds are often strongly supersaturated;
- All considered species are transported;
- The mass correction after the semi-Lagrangian transport step is applied to the chlorine, bromine and nitrogen families instead of their individual members, and to ozone only between 40°S and 40°N to avoid artificial mass loss in the polar areas;
- The water vapour removal by the highest ice clouds (100 hPa – CPT) is now explicitly taken into account to prevent an overestimation of stratospheric water content.

### 2.4.12 ULAQ

ULAQ-CCM is a low-resolution CCM. Dynamical fields (streamfunction, velocity potential and temperature) are taken from the output of a simplified spectral circulation model (GCM) adopting the quasi-geostrophic approximation (rhomboidal truncation with six waves and six components per wave). The effect of gravity wave breaking is simulated *via* Rayleigh friction. Pitari *et al.* (2002) describe details of the coupling between GCM and CTM (Eyring *et al.*, 2006). A flux-form Eulerian fully explicit advection scheme is used. Medium and short-lived chemical species are grouped in families (O<sub>x</sub>, NO<sub>y</sub>, NO<sub>x</sub>, HO<sub>x</sub>, CHO<sub>x</sub>, Cl<sub>y</sub>, Br<sub>y</sub>, SO<sub>x</sub>, aerosols, ice cloud particles). The size distribution of sulphate and PSCs is calculated online using an interactive and mass conserving microphysics code for aerosol formation and growth.

*Changes since CCMVal-1:*

- Inclusion of QBO nudging.
- Inclusion of upper tropospheric cirrus ice particles.
- Upgrade of tropospheric chemistry (NMHC).

### 2.4.13 UMETRAC

UMETRAC is a vertically extended version of the Met Office's HadAM3 Unified Model (UM) version 4.5, combined with a stratospheric chemistry package. Chemistry is treated in a somewhat simplified way with release of inorganic chlorine and bromine from the organic reservoir calculated as functions of age of air.

*Changes since CCMVal-1:*

- An artificial increase of CFC photolysis rates, used in CCMVal-1 to correct the inorganic chlorine loading, has been dropped.

### 2.4.14 UMSLIMCAT

UMSLIMCAT (Tian and Chipperfield, 2005) uses the stratospheric chemistry scheme from the SLIMCAT offline CTM (Chipperfield, 2006) coupled to a vertically extended version of the Met Office's HadAM3 UM version 4.5. The stratospheric water vapour is coupled to the UM's humidity field.

*Changes since CCMVal-1:*

- Chemical kinetics were updated to JPL (2006).
- The number of solar flux bands in the model's radiation scheme was changed from 3 to 6.
- A time varying solar flux with an 11-year solar cycle was incorporated.

### 2.4.15 UMUKCA-METO and UMUKCA-UCAM

UMUKCA is a vertically extended version of the Met Office's UM 6.1 in a configuration similar to HadGEM1 (Johns *et al.*, 2006) combined with the UKCA stratospheric chemistry module (Morgenstern *et al.*, 2008, 2009). The model does not use the hydrostatic approximation and uses a non-families formulation of chemistry. UMUKCA does not impose explicit diffusion and also does not have a sponge layer. Chemical water vapour production or loss is ignored in the hydrology scheme and instead a parameterisation of methane oxidation (Untch *et al.*, 1998) is used. Also water vapour is imposed at the tropical tropopause, meaning that UMUKCA does not have a tape recorder signal in the water vapour field. The two model versions used here differ in the use of some chemical kinetic data, the treatment of removal of inorganic halogen compounds in the troposphere, and stratospheric aerosol radiative heating in REF-B1 (see below). In UMUKCA-METO, wash-out of inorganic halogen is incorporated incorrectly. In UMUKCA-UCAM, instead of explicit washout inorganic halogen is forced to 0 at the surface. UMUKCA-UCAM does not have heating associated with the presence of stratospheric aerosol.

**Table 2.17:** SST and sea ice data sets. Note that CMAM has an interactive ocean.

CCM	SST/sea ice for REF-B0/B1, SCN-B1	SST/sea ice for REF-B2, SCN-B2b/c/d	Reference for SST/sea ice used in REF-B2
AMTRAC3	HadISST1		
CAM3.5	HadISST1	CCSM3	<i>Collins et al. (2006)</i>
CCSRNIES	HadISST1	MIROC / IPCC-AR4	<i>Shiogama et al. (2005); Nozawa et al. (2007)</i>
CMAM	HadISST1	Interactive	<i>Arora et al. (2009)</i>
CNRM-ACM	HadISST1	CNRM-CM3 AR4 A1B	<a href="http://www-pcmdi.llnl.gov/ipcc/subproject_publications.php">www-pcmdi.llnl.gov/ipcc/subproject_publications.php</a>
E39CA	HadISST1	HadGEM1	<i>Stott et al. (2007)</i>
EMAC	HadISST1	N/A	N/A
GEOSCCM	HadISST1	CCSM3	<i>Collins et al. (2006)</i>
LMDZrepro	AMIP-II	OPA (ocean) LIM (ice)	
MRI	HadISST1(1); MRI-CGCM2.3.2(3)	MRI-CGCM2.3.2	<i>Yukimoto et al. (2006)</i>
NiwaSOCOL	HadISST1	HadISST1:1960-2002 HadGEM1:2003-2100	HadGEM1: <i>Johns et al. (2006)</i>
SOCOL	HadISST1	ECHAM5-MPIOM	
ULAQ	HadISST1	CCSM3	<i>Collins et al. (2006)</i>
UMSLIMCAT UMUKCA-METO UKUKCA-UCAM	HadISST1	HadGEM1	<i>Johns et al. (2006)</i>
WACCM	HadISST1	CCSM3	<i>Collins et al. (2006)</i>

UMUKCA did not participate in CCMVal-1.

#### 2.4.16 WACCM

WACCM, version 3.5.48, spans the range of altitude from the Earth's surface to the lower thermosphere. WACCM is a fully interactive model with a comprehensive range of radiatively active gases (Sassi *et al.*, 2005; Tables 2.28 and 2.29). WACCM includes all of the physical parameterisations of the CAM model. A mass-conserving finite volume dynamical core (Lin, 2004) is used exclusively in WACCM. Compared to CAM3.5, only the GWD and vertical diffusion parameterisations are modified. WACCM includes chemical heating; mesospheric NO<sub>x</sub> production by cosmic rays/solar particles, mesospheric / lower thermospheric ion chemistry; ion drag and auroral processes; and parameterisations of short wave heating at extreme ultraviolet (EUV) wavelengths and NLTE infrared transfer (Garcia *et al.*, 2007; Collins *et al.*, 2004). The chemistry is based on MOZART3 (Kinnison *et al.*, 2007), involving a combined explicit and implicit backward-Euler solver. Heterogeneous processes on sulfate aerosols and polar stratospheric clouds are included following the approach of Considine *et al.* (2000).

#### Changes since CCMVal-1:

- The gas-phase chemical reaction rates and photolysis rates were updated to the recommendations of JPL (2006).
- Volcanic heating was added for the REF-B1 simulations (see below). This heating is derived from the SPARC SAD time-series.
- The wavelength dependent exo-atmospheric flux was updated following Lean *et al.* (2005).
- The GWD parameterisation was updated based on Richter *et al.* (2010).
- Relaxation of tropical winds towards observations was added for the REF-B1 simulations (see below; Table 2.9).
- The underlying tropospheric climate model has a different closure for the deep convective parameterisation and added convective momentum transport (Neale *et al.*, 2008).

## 2.5 Definitions of simulations and external forcings

In this section, we motivate and state the definitions

**Table 2.18:** Implementation of volcanic effects in REF-B1.

CCM	SADs for heterogeneous chemistry	Direct radiative effects	Comment / reference
AMTRAC3	Derived from aerosol properties used for radiation <sup>1</sup>		
CAM3.5	SPARC ASAP <sup>3</sup>	None	
CCSRNIES	SPARC ASAP	Online derived from GISS <sup>2</sup>	<i>Hansen et al. (2002); Sato et al. (1993)</i>
CMAM	SPARC ASAP	Online derived from SPARC SAD	<i>Thomason et al. (1997)</i>
CNRM-ACM	SPARC ASAP	Calculated online using monthly optical depths at 0.55 $\mu\text{m}$ of <i>Amman et al. (2003)</i>	Aerosol optical properties in REF-B1 lead to too strong sensitivity to volcanic eruptions. Different properties have been adopted since then (A. Voltaire, pers. comm.).
E39CA	CCMVal-1 <sup>4</sup>	Prescribed heating rate anomalies <sup>5</sup>	
EMAC	Derived H <sub>2</sub> SO <sub>4</sub> from SAGE measurements	Prescribed heating rate anomalies <sup>5</sup>	
GEOSCCM	Perpetual 1979 conditions (from CCMVal-1)	None	
LMDZrepro	SPARC ASAP	None	
MRI	SPARC ASAP	Online derived from GISS	
NiwaSOCOL	SAGE I and II	SAGE and GISS based offline calculations	<i>Schraner et al. (2008); Thomason and Peter (2006)</i>
SOCOL	GISS (1960-1978) SAGE (1979-2006)	GISS (1960-1978) SAGE (1979-2006)	<i>Schraner et al. (2008); Fischer et al. (2008)</i>
ULAQ	SPARC ASAP	Online using volcanic SO <sub>2</sub> estimates and gas/particle conversion	<i>Pitari (1993)</i>
UMETRAC UMUKCA-METO	SPARC ASAP	Online derived from GISS	<i>Sato et al. (1993)</i>
UMSLIMCAT UKUKCA-UCAM	SPARC ASAP	None	
WACCM	SPARC ASAP	Online derived from SPARC SAD	

## Notes:

<sup>1</sup>SADs are inferred from multi-wavelength extinction values, as in *Stenchikov et al. (2006)*.

<sup>2</sup>GISS provides optical thickness at 550 nm and effective radius from 1850–2000, available from <http://data.giss.nasa.gov/model-force/strataer/>. This data set is based on SAGE observations and was introduced by *Sato et al. (1993)*, with updates and minor improvements announced by *Hansen et al. (2002)*.

<sup>3</sup>SPARC ASAP refers to data made available through the SPARC Assessment of Stratospheric Aerosol Properties (ASAP) report (*Thomason and Peter, 2006*), based primarily on SAGE measurements. Data available at <http://www.sparc.sunysb.edu/asap/SAGE-ASAP%20Data%20Products.htm>

<sup>4</sup>CCMVal-1 SADs were specified from a monthly climatology based on satellite data, similar to that used by *Jackman et al. (1996)* and updated by *D. B. Considine (NASA Langley Research Center)*.

<sup>5</sup>The heating rates are monthly means from January 1950 to December 1999 for all-sky condition, and were calculated using GISS ModelE (*Schmidt et al. 2006*) radiative routines and volcanic aerosol parameters from the GISS data set (*Stenchikov et al., 2006*).

of the model simulations conducted for CCMVal-2, discuss the associated forcings, and list the differences between the definitions and the actual simulations conducted by the modelling groups.

### 2.5.1 Internal and external modelling uncertainties

A source of error in CCMVal integrations relates to deficiencies in model formulation. Using identical boundary conditions, differences in the formulation of CCMs will lead to differences in their common prognostic or diagnostic fields. These differences will represent the internal uncertainties in dynamics, physics and chemistry in CCMs as used here. The CCMVal-2 simulations “REF-B0” and “REF-B1” (Section 2.5.2), covering the near-present and the past, respectively, have been designed primarily to address internal modelling uncertainties since SSTs, sea ice, and other external forcings such as volcanic eruptions and variations of solar irradiation, are prescribed based on observations. By contrast, the “REF-B2” simulations, covering the past and future, also include external uncertainty because here SST and sea ice data are obtained from climate simulations, with associated biases (Section 2.5.3.1). Further external uncertainties are associated with the future GHG and ODS forcings assumed in REF-B2.

### 2.5.2 CCMVal-2 simulations

The three reference simulations noted above and six control and sensitivity experiments have been proposed (Eyring *et al.*, 2008). Most groups have completed the 3 reference simulations, some (CMAM, MRI, SOCOL, ULAQ, WACCM, for the REF-B2 simulations) with more than one ensemble member. A few of the sensitivity studies have been performed, although the coverage across the models is much less consistent than for the reference simulations (Tables O.1 – O.3 in the supplemental material). Since this report exclusively uses data from the reference simulations, only these are documented below, following Eyring *et al.* (2008).

#### 2.5.2.1. REF-B0: Year 2000 time-slice simulation

REF-B0 is a time-slice simulation for 2000 conditions, designed to facilitate the comparison of model output against constituent data sets from various high-quality observational data sources and meteorological analyses under a period of high chlorine loading. Each simulation is integrated over 20 annual cycles following 10 years of spin-up.

- **Trace gas forcings:** The surface concentrations of

GHGs are based on SRES scenario A1b of IPCC (2001) while the surface halogens are based on Table 8-5 (scenario A1) of WMO (2007) for the year 2000. Both ODSs and GHGs repeat every year.

- **Background aerosol** is prescribed from the extended SPARC (2006) SAD data set (Section 2.5.3.4) for the year 2000.
- **Solar irradiance** is averaged over one solar cycle to provide a mean solar flux for the year 2000.
- **Sea surface temperatures (SSTs) and sea ice concentrations (SICs)** in this simulation are prescribed as a mean annual cycle derived from the years 1995 to 2004 of the HadISST1 data set (Rayner *et al.*, 2003).
- The **QBO** is not externally forced.
- **Emissions of ozone and aerosol precursors** (CO, NMVOC, NO<sub>x</sub> and SO<sub>2</sub>) are averaged over the years 1998 to 2000 and are taken from an extended data set of the REanalysis of the TROpospheric chemical composition (RETRO) project (Schultz *et al.*, 2007; <http://retro.enes.org>). In case of SO<sub>2</sub>, RETRO only provides biomass burning related emissions. Therefore, this data is combined with an interpolated version of EDGAR-HYDE 1.3 (Van Aardenne *et al.*, 2001) and EDGAR 32FT2000 (Olivier *et al.*, 2005; Van Aardenne *et al.*, 2005).

#### 2.5.2.2. REF-B1: Reproducing the past

REF-B1 (1960–2006) is defined as a transient run from 1960 (with a 10-year spin-up period) to the present. All forcings in this simulation are taken from observations, and are mostly identical to those used by Eyring *et al.* (2006). This transient simulation includes all anthropogenic and natural forcings based on changes in trace gases, solar variability, volcanic eruptions, QBO, and SSTs/SICs.

- **GHGs** (N<sub>2</sub>O, CH<sub>4</sub>, and CO<sub>2</sub>) between 1950 and 1996 are taken from IPCC (2001) and merged with the NOAA observations forward through 2006. NOAA CO<sub>2</sub>, CH<sub>4</sub>, and N<sub>2</sub>O are scaled to agree on January 1996 with the historical IPCC data (Section 2.5.3.2).
- **ODSs** (CFC-10, CFC-11, CFC-12, CFC-113, CFC-114, CFC-115, CH<sub>3</sub>CCl<sub>3</sub>, HCFC-22, HCFC-141b, HCFC-142b, Halon-1211, Halon-1202, Halon-1301, and Halon-2402) are prescribed at the surface according to Table 8-5 of WMO (2007). For models that do not represent all the species listed here, the halogen content of species that are considered should be adjusted such that model inputs for total chlorine and total bromine match the time series of total chlorine and bromine given in this table (Section 2.5.3.2). This also applies to the other simulations.
- **SSTs and SICs** are prescribed as monthly-mean boundary conditions following the observed global SIC and SST data set HadISST1 (Rayner *et al.*, 2003;

Section 2.5.3.1). To correct for the loss of variance due to the time interpolation of monthly-mean data, a variance correction is applied ([http://grads.iges.org/c20c/c20c\\_forcing/karling\\_instruct.html](http://grads.iges.org/c20c/c20c_forcing/karling_instruct.html)).

- **Aerosol Surface Area Densities (SADs)** from observations are considered in REF-B1 (Section 2.5.3.4; Eyring *et al.*, 2008).
- **Stratospheric warming and tropospheric-surface cooling** due to volcanic eruptions are either calculated on line by using aerosol data or by prescribing heating rates and surface forcing (Section 2.5.3.4).
- **Solar variability.** Daily spectrally resolved solar irradiance data from 1 January 1950 to 31 Dec 2006 (in W/m<sup>2</sup>/nm) are provided at [http://www.geo.fu-berlin.de/en/met/ag/strat/research/SOLARIS/Input\\_data/index.html](http://www.geo.fu-berlin.de/en/met/ag/strat/research/SOLARIS/Input_data/index.html). The data are derived with the method described by Lean *et al.* (2005). Each modelling group is required to integrate the data over the individual wavelength intervals used in their radiation and photolysis schemes. This approach supersedes the parameterisation with the F10.7 cm radio flux previously used (Section 2.5.3.6).
- **The QBO:** Models that do not produce an internally generated QBO are asked externally impose a QBO for REF-B1 (Sections 2.3.1.3 and 2.5.3.5).
- **Ozone and aerosol precursors** (CO, NMVOC, NO<sub>x</sub> and SO<sub>2</sub>) from 1960 to 1999 are taken from the extended data set of the RETRO project (Schultz *et al.*, 2007). For the spin-up period from 1950 to 1959 the

1960 values from this data set are used cyclically. After 2000 trend estimates taken from IIASA are used to extend the data set (P. Rafaj, personal communication; [http://www.atm.ch.cam.ac.uk/~om207/Download\\_emission\\_files.html](http://www.atm.ch.cam.ac.uk/~om207/Download_emission_files.html); Section 2.5.3.3).

### 2.5.2.3. REF-B2: Making Predictions

REF-B2 is an internally consistent simulation covering 1960-2100, using only anthropogenic forcings. The objective of REF-B2 is to produce best estimates of the future ozone-climate change assuming scenario SRES A1b for GHGs and decreases in halogen emissions (adjusted Scenario A1).

- **GHGs** follow the IPCC (2001) SRES A1b scenario, as in Eyring *et al.* (2007) (Section 2.5.3.2).
- **ODSs** are based on scenario A1 from WMO (2007). However, at the 2007 Meeting of the Parties to the Montreal Protocol, the Parties agreed to an earlier phase out of HCFCs ([http://ozone.unep.org/Meeting\\_Documents/mop/19mop/Adjustments\\_on\\_HCF-Cs.pdf](http://ozone.unep.org/Meeting_Documents/mop/19mop/Adjustments_on_HCF-Cs.pdf)). Scenario A1 does not include this phase out. Hence, a new scenario has been developed that includes this phase out (hereafter referred to as the “adjusted scenario A1”). CFCs, Halons, and other non-HCFC species remain as in the original scenario A1 (Section 2.5.3.2).
- **Background aerosol** is the same as in REF-B0 (Section 2.5.2.1), *i.e.* background, non-volcanic aerosol

**Table 2.19:** Solar cycle by experiment with reference. Models not listed here do not impose a solar cycle.

CCM	REF-B0	REF-B1	REF-B2	SCN-B2d	Reference
AMTRAC3	N/A	YES	YES	N/A	
CAM3.5	YES,1996-2006 Avg	YES	Mean of Solar Cycles 19-23	N/A	Includes SPE's. Lean (2005)
CCSRNIES	NO	YES	NO	N/A	Lean <i>et al.</i> (1997) and flux at 10.7 cm (Akiyoshi <i>et al.</i> , 2009)
CMAM	NO	YES	NO	N/A	Lean (2005)
CNRM-ACM		YES	NO	N/A	GCM : Solanki and Krivova (2003). Chemistry : Lean (2005)
E39CA	N/A	YES	N/A	YES	Lean <i>et al.</i> (1997)
EMAC	N/A	YES	N/A	N/A	Nissen <i>et al.</i> (2007)
LMDZrepro	NO	YES	NO	N/A	
MRI	NO	YES	NO	N/A	
NiwaSOCOL SOCOL	NO	YES	NO	N/A	Lean (2005) as defined in CCMVal forcing data
UMSLIMCAT	NO	YES	NO	N/A	GCM: Zhong <i>et al.</i> (2001); chemistry: Lean <i>et al.</i> (1997)
WACCM	YES,1996-2006 Avg	YES	Mean of Solar Cycles 19-23	N/A	Includes SPE's. Lean (2005)



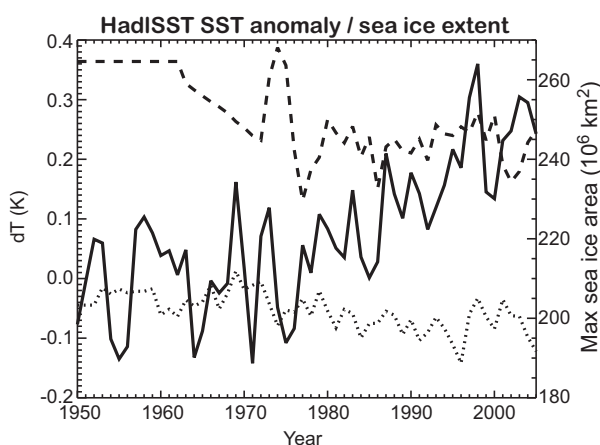
loading is assumed (Section 2.5.3.4).

- **SSTs and SICs.** Due to potential discontinuities between the observed and modelled data record, the REF-B2 runs use simulated SSTs and SICs for the entire period, using GCM simulations forced with the SRES A1b GHG scenario (Table 2.21; Section 2.5.3.1), or in the case of the CMAM model an interactive ocean.
- **Ozone and aerosol precursors** are identical to REF-B1 until 2000 and use the adjusted IIASA scenario through to 2100 (P. Rafai, personal communication). Models span a wide spectrum in how they represent tropospheric composition. Consequently, the usage of tropospheric emissions varies widely across the models (Table 2.19; Section 2.5.3.3).

## 2.5.3 External forcings

### 2.5.3.1 SSTs and sea ice

REF-B0, REF-B1, and CNTL-B0 are using the HadISST1 observational SST/sea ice data set (<http://www.metoffice.com/hadisst>; Rayner *et al.*, 2003). It covers the period of 1870-present. Climate change over the oceans documented in IPCC (2007) is largely diagnosed from the HadISST1 data set. Almost all simulations in these categories use HadISST1 (Table 2.14). There is a distinct warming trend in the HadISST1 SSTs (Figure 2.2), starting in around 1970. Since then, the sea surface has warmed by 0.2 to 0.3 K. Associated with this is a decline in the maximum monthly-mean sea-ice extent of both polar regions. For the Antarctic, sea ice coverage before 1970 is poorly known, explaining the lack of variability before 1962 and the linear trend in the late 1960s.



For the REF-B2 simulations modellers use a variety of different data sets, or, in the case of CMAM, an interactive ocean model. Mean SSTs from the HadGEM1 climate model (Johns *et al.*, 2007) are displayed in Figure 2.2, right. A cold bias of around 2 K *versus* HadISST1 is apparent. This bias, and various other biases found in other climate model data, are the reason why a seamless simulation of past and future climate and ozone, such as REF-B2, cannot be performed based on a combination of analysed and simulated SSTs. Two groups of models sharing the same ocean surface forcing in REF-B2 appear, namely CAM3.5, GEOSCCM, ULAQ, and WACCM all use CCSM3 data, and E39CA, NiwaSOCOL for parts of REF-B2, UMSLIMCAT, and the UMUKCA models use HadGEM1 data (Table 2.13). Niwa-SOCOL uses a combination of HadISST1 and HadGEM1 SSTs for its ocean forcing of REF-B2, introducing a discontinuity into this simulation.

For the LMDZrepro REF-B2 simulation, seas surface conditions are taken from the A1b simulation produced with the IPSL AOGCM (Dufresne *et al.*, 2005). Since this simulation exhibits biases with respect to the AMIP2 data set (Taylor *et al.*, 2000), the mean biases for the 1985-2005 period are first removed from the entire A1b simulation and then the corrected SST and sea ice forcing is used to force LMDZrepro.

### 2.5.3.2 Long-lived greenhouse gases and ozone-depleting substances

Figure 2.3 displays the time evolution of the major GHGs, total chlorine and total bromine, as specified in the SRES A1b (IPCC, 2001) and A1 (WMO, 2007) scenarios. The ODSs increase sharply during the 1970s and 1980s, resulting in an approximate 6-folding of organic chlorine

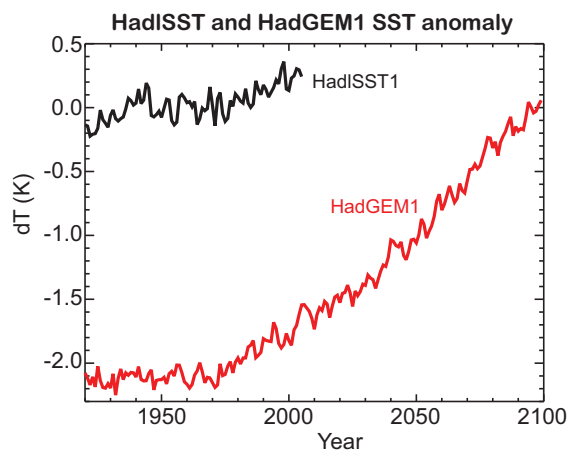


**Figure 2.2:** (left) Solid: anomaly in annual-mean, ocean-mean sea-surface temperature, relative to the 1950-1969 mean, in the HadISST1 data set. Dashed and dotted: Antarctic and Arctic maximum monthly-mean sea ice coverage ( $10^6 \text{ km}^2$ ). (right) HadISST1 and HadGEM1 SSTs, relative to the 1950-1969 mean of HadISST1, from 1920 to 2099.

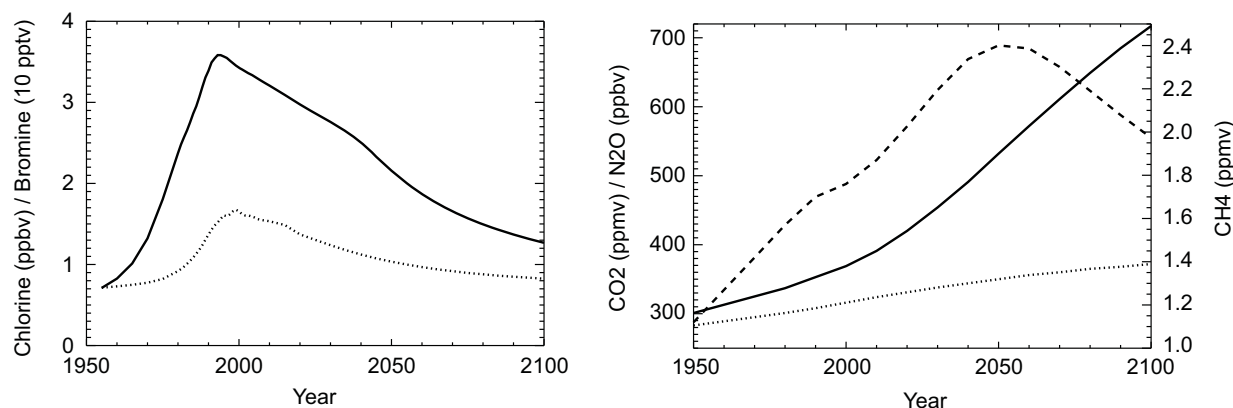


**Figure 2.3:** (left) Surface total chlorine (solid) and total bromine (dotted) as defined in the A1 scenario. (right) Surface  $\text{CO}_2$  (solid),  $\text{N}_2\text{O}$  (dotted), and  $\text{CH}_4$  (dashed) as defined in the SRES A1b scenario.

and a doubling of organic bromine at peak abundances in the 1990, relative to pre-industrial times. For the 21<sup>st</sup> century, a continuous decline, in accordance with the Montreal Protocol, is anticipated. The decline is substantially slower than the increase in the 20<sup>th</sup> century. By contrast, for the leading greenhouse gas  $\text{CO}_2$  a steady increase is anticipated, leading to a more than doubling by 2100, compared to 1950.  $\text{N}_2\text{O}$  follows a similar trend, *albeit* with smaller growth rates.  $\text{CH}_4$ , by contrast, is anticipated to undergo a trend reversal around 2050.

### 2.5.3.3 Ozone precursors

Surface emissions of  $\text{NO}_x$ , CO, and  $\text{CH}_2\text{O}$ , as used by many models, are displayed in **Figure 2.4**. For the period from 1960 to 1999 the data are from the RETRO database ([http://retro.enes.org/reports/D1-6\\_final.pdf](http://retro.enes.org/reports/D1-6_final.pdf)). Note the general increase of  $\text{NO}_x$ , CO, and  $\text{CH}_2\text{O}$  emissions during the 20<sup>th</sup> century. During the 21<sup>st</sup> century, however, the IIASA SRES A1b scenario forecasts a general reduction in CO emissions and a trend reversal for  $\text{NO}_x$  around 2020, followed by a sharp decrease. Emissions of  $\text{CH}_2\text{O}$  are forecast to increase then stabilize during the second half of the century. Evidently the interannual variability characterizing the RETRO emissions is absent in the 21<sup>st</sup> century. The IIASA emissions are courtesy of Peter Rafaj, IIASA ([http://www.atm.ch.cam.ac.uk/~om207/Download\\_emission\\_files.html](http://www.atm.ch.cam.ac.uk/~om207/Download_emission_files.html)). Not included in Figure 2.4 is lightning-produced  $\text{NO}_x$  which is included in most models and is determined using a variety of different parameterisations (Section 2.3.3.7; Table 2.12).

### 2.5.3.4 Stratospheric aerosol surface area densities and direct aerosol-related heating

The SPARC aerosol data set is constructed from SAGE profile measurements of aerosols, beginning in

1983. Unlike in IPCC modelling, stratospheric CCMs require height-resolved aerosol forcing data due to the importance of heterogeneous chemical processing. Four big volcanic events are obvious, Agung in 1963, El Chichón in 1982, Nevado del Ruiz in 1985 and Mt Pinatubo in 1991 (**Figure 2.5**). Also some smaller events are apparent. Data before 1983 are constructed based on assumptions of background aerosol and, in the case of Agung, assuming a similar distribution of aerosol as after later volcanic eruptions. A problem is apparent at high latitudes in the Southern Hemisphere, where the satellite sensor cannot distinguish between sulfate aerosols and PSCs. In these areas, sometimes a very low SAD of sulfate aerosol is assumed. With the exception of (Niwa)SOCOL (using a combination of SAGE and GISS data), all models use this data set for the REF-B1 simulations. For REF-B0 and REF-B2, background (year-2000) data are used cyclically throughout the simulations.

Aerosols cause a perturbation to the heating/cooling

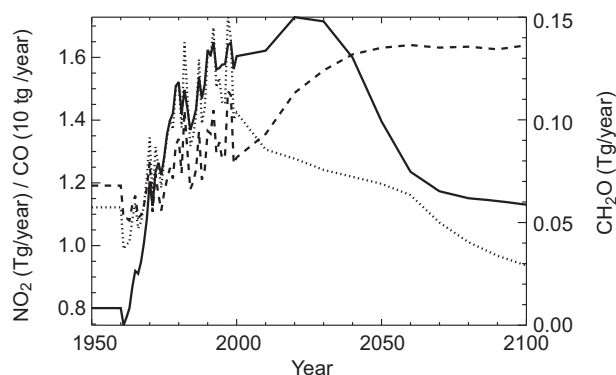


**Figure 2.4:** Surface emissions of (solid)  $\text{NO}_x$  (displayed as Tg/year of  $\text{NO}_2$ ), CO (dotted) and  $\text{CH}_2\text{O}$  (dashed) as used for CCMVal-2 simulations. From 1960 to 1999, data are from the RETRO emissions database (see text), after 1999 they are extrapolated using an IIASA scenario. Before 1960 they are repeated 1960 RETRO emissions.

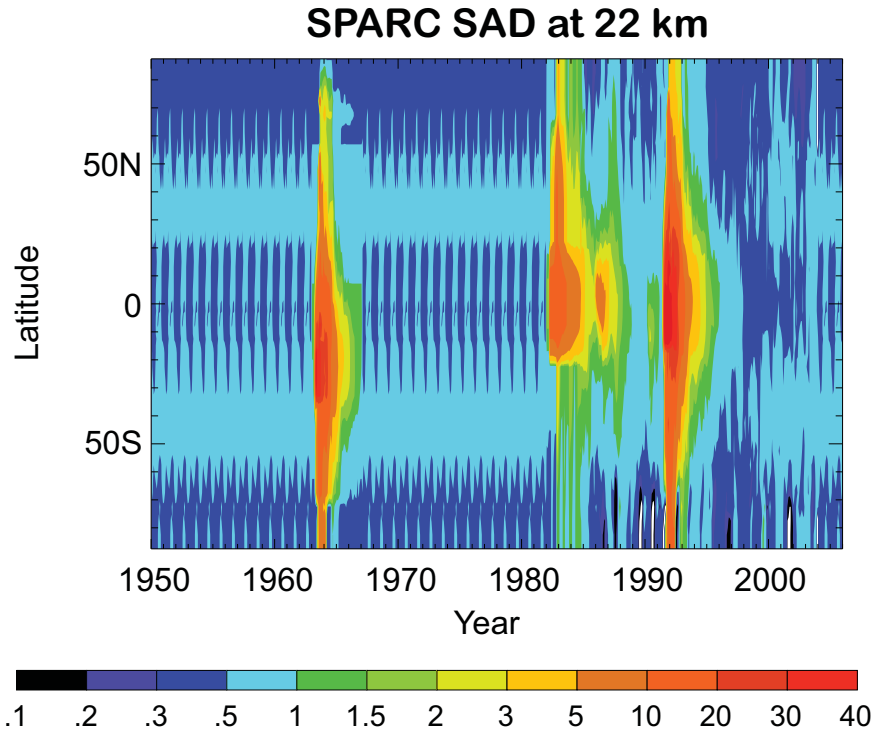


**Figure 2.5:** Aerosol surface area density ( $\mu\text{m}^2/\text{cm}^3$ ) at 22 km, reconstructed from SAGE data.

profiles of the troposphere and stratosphere, particularly during volcanic periods, and also cause the Earth's surface to warm or cool (Sato *et al.*, 1993; Robock, 2002). Several different approaches have been taken by the CCMVal-2 models regarding this effect: Two models derive heating rates consistent with the prescribed SAD data set (CMAM, WACCM). Others use independent data sets such as the GISS data (CCSRNIES, MRI, UMETRAC, UМУKCA-METO). E39CA and EMAC use precalculated rates (Stenchikov *et al.*, 2006; Eyring *et al.*, 2008). The

SOCOL models use a mixture of different sources. One (of 4) ULAQ REF-B1 simulation uses estimates of volcanic injections of  $\text{SO}_2$ , and an interactive aerosol calculation to infer heating rates. CNRM-ACM reports problems with their calculation, which is based on observed optical depth (Table 2.10, and references therein). Five CCMVal-2 models do not represent heating due to volcanic aerosol.

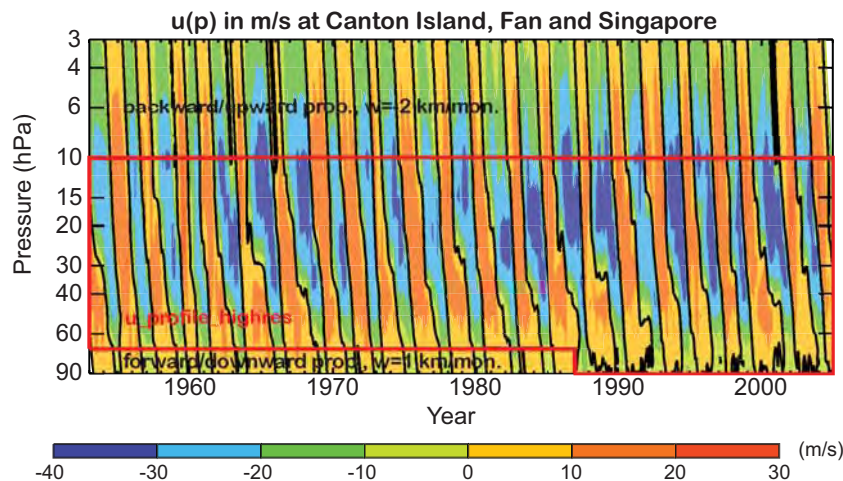


**Figure 2.6:** Zonal wind ( $u$ ) from merged observations at Canton Island, Gan and Singapore, vertically extended. ([http://www.pa.op.dlr.de/CCMVal/Forcings/qbo\\_data\\_ccmval/u\\_profile\\_195301\\_200412.html](http://www.pa.op.dlr.de/CCMVal/Forcings/qbo_data_ccmval/u_profile_195301_200412.html)). The violet box denotes the area constrained by the observations. In the areas outside the box the data are extrapolated, assuming a phase speed of 2 km/month (above 10 hPa) and 1 km/month (below 70 hPa, before 1987).

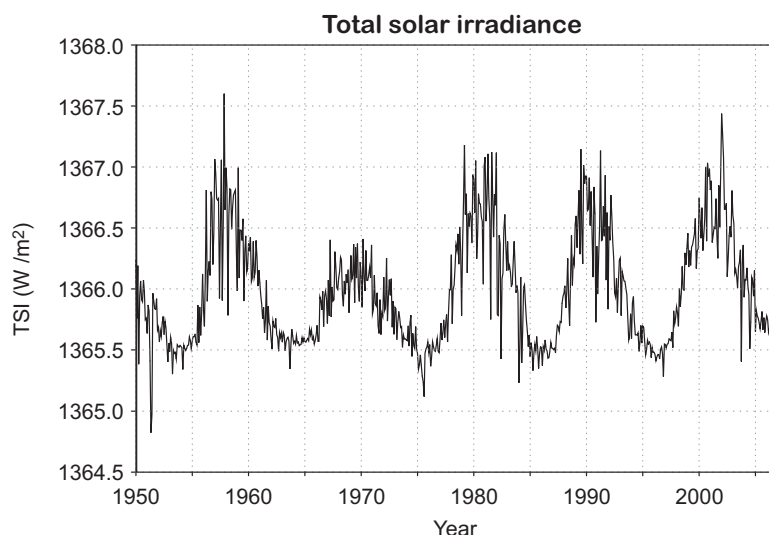


**Figure 2.7:** Total solar irradiance ( $\text{W}/\text{m}^2$ ) updated from Lean et al. (2005).

### 2.5.3.5 QBO time series

In the REF-B1 simulations, the QBO is imposed in the tropical region in various models. **Figure 2.6** shows a depiction of the QBO. Table 2.5 summarizes the different ways in which these models impose the QBO (Section 2.3.1.3).

### 2.5.3.6 Solar irradiance

Solar output varies with sunspot numbers and other parameters. Most of the atmospherically relevant variability is in the 11-year solar cycle. CCMVal-2 modellers have been asked to use the data by Lean *et al.* (2005) for their REF-B1 simulations. **Figure 2.7** shows total solar irradiance; it varies by about  $1 \text{ W}/\text{m}^2$  on a background of around  $1366 \text{ W}/\text{m}^2$ . However, most of the variability is at short wavelengths, where the solar cycle is relatively more important than for the spectrally integrated solar output (the “solar constant”).

### 2.5.4 Deviations from simulation definitions

The following is a model-by-model listing of the various ways in which model setups deviate from the definitions (Eyring *et al.*, 2008) as summarized above:

#### AMTRAC3:

- REF-B2 includes an 11-year solar cycle.
- In REF-B1 there is no nudging of the QBO.

#### CAM3.5

- Direct radiative forcing by volcanic aerosols (impact heating and photolysis) is not implemented in

#### REF-B1.

- No variance correction is applied to the SSTs.

#### CCSRNIES:

- $1.8 \text{ pptv}$  of  $\text{CHBr}_3$  is assumed at the surface.
- Some photolysis cross sections stem from JPL (2002) and JPL (1997).
- The variance correction for SSTs is not applied.

#### CMAM:

- The REF-B1 simulations did not include a spontaneous or nudged QBO.
- The variance correction for SSTs was not performed.
- Heterogeneous reaction rates have not been updated to JPL (2006).

#### CNRM-ACM:

- There is no QBO in REF-B1.
- The variance correction for SSTs was not performed.

#### E39CA:

- In REF-B1 halogen loadings from WMO (2003) are used.
- In REF-B1: for 2000-2004, stratospheric aerosol from 1999 is used, otherwise as CCMVal definitions.
- In SCN-B2d, the future scenario of  $\text{NO}_x$  emissions from industry and traffic is set up as follows:
- 8 different regions (Europe, USA, Australia, Asia, India, South America, Africa) are defined. They are broken up into two categories: Industrialized (Europe, USA, Australia) and developing (Africa, Asia, India, South America). For the industrialized countries the linear trend between 1990 and 2000 is extrapolated until 2015, and constant  $\text{NO}_x$  emissions are assumed from 2015. For the developing countries a linear trend

between 1990 and 2000 is extrapolated until 2030, and constant NO<sub>x</sub> emissions are assumed from 2030. This scenario assumes that developing countries will adopt technological advance 15 years later than industrialized countries.

#### EMAC:

- Chemical kinetics are mostly based on JPL (2002).
- Lumping is not performed for organic bromine, meaning there is slightly less bromine due to non-representation of compounds other than CH<sub>3</sub>Br, Halon-1211, and Halon-1301.
- Stratospheric aerosol is as in CCMVal-1.

#### GEOSCCM:

- All runs use JPL(2002) chemical kinetics.
- All runs use trace gas forcings prescribed for CCMVal-1 (*i.e.*, they are not updated to CCMVal-2). For ODSs, annual means were prescribed following scenario Ab (WMO, 2003, Table 1-16).
- All runs use background (1979) surface area densities from a data set created by D. Considine.
- Direct radiative forcing by volcanic aerosol (on heating and photolysis) is not implemented in REF-B1.
- All runs ignore the solar cycle for photolysis.
- The REF-B1 run does not include QBO forcing.

#### LMDZrepro:

- No heating from volcanic aerosol was imposed in REF-B1.
- No QBO was imposed in REF-B1.
- REF-B0 and REF-B1 are forced with AMIP-II sea surface conditions.
- Halon-1211 and Halon-1301 surface mixing ratios are set to 1 pptv where the A1 scenario implies less than 1 pptv (before about 1980 and after about 2040).
- A constant surface mixing ratio of 3 pptv is imposed for CH<sub>2</sub>Br<sub>2</sub>.

#### MRI:

- Members 1, 2, and 3 of REF-B1 use SST and sea-ice modelled by MRI-CGCM 2.3.2.
- These simulations also do not include the CH<sub>4</sub> changes after 2002.

#### NiwaSOCOL:

- The parameters associated with sulfate aerosol are as in Schraner *et al.* (2008), covering 1975-2002. The only change to this data set was to set the single-scattering albedo to 0.995 instead of 1.0 in the solar/short-wave spectral region, as recommended by Fischer *et al.* (2008).
- For REF-B1 and SCN-B1 the SAD data set is defined as follows:

- 1950-1962 and 1967-1974: 1975 annual mean of SAD data set
- 1963-1966: 1991-1994 SAD data (to simulate the Agung volcano event, similar to Pinatubo)
- 2003-2005: 2002 SAD data set.
- For REF-B0, REF-B2 and SCN-B2x the 2000 annual mean of the SAD data is used cyclically.
- For CTL0: The 1975 annual mean of SAD data set is used cyclically.
- Volcanic aerosol does not affect the photolysis rates.
- The Niwa-SOCOL halogen chemistry includes CHBr<sub>3</sub> and CH<sub>2</sub>Br<sub>2</sub> at 1.63 and 1.21 pptv in 2000, respectively.

#### SOCOL:

- The future scenarios for CO and NO<sub>x</sub> emissions differ from those recommended. Future CO and NO<sub>x</sub> emissions use the RETRO data set scaled by the SRES prediction of the future anthropogenic activities.
- JPL (2006) rates were used where applicable. Also data from earlier JPL versions, IUPAC (2005) and analytic expressions were used.
- SAD (background aerosol): see Niwa-SOCOL. The influence of stratospheric sulfate aerosol on the short- and longwave radiation has been directly taken into account, *i.e.*, the model radiation code calculates online the changes in the radiation fields due to stratospheric aerosol.
- Photolysis rates are not affected by volcanic aerosol.
- The SOCOL halogen chemistry includes CHBr<sub>3</sub> and CH<sub>2</sub>Br<sub>2</sub> at 1.63 and 1.21 pptv in 2000, respectively.

#### ULAQ:

- Three REF-B1 integrations do not include diabatic heating rates from volcanoes.
- A fourth REF-B1 run includes the volcanic forcing, calculated online from the aerosol microphysics code of the ULAQ-CCM.

#### UMETRAC:

- There is no solar cycle in UMETRAC.
- The photochemistry has not been updated to JPL (2006).
- The SSTs have not been manipulated to account for a loss of variance.
- Photolysis rates do not account for the presence of volcanic aerosol.

#### UMSLIMCAT:

- Direct radiative (on photolysis and heating) due to volcanic impacts is not represented in REF-B1.
- The photolysis cross-section data was not updated to JPL (2006).
- The REF-B1 and REF-B2 simulations use an extra 6

**Table 2.20:** Three-dimensional instantaneous (T3I) diagnostics produced by model, for REF-B2. Models not listed did not produce any T3I diagnostics. For the meaning of names see Table 1 of [http://www.pa.op.dlr.de/CCMVal/DataRequests/CCMVal-2\\_Datarequest\\_FINAL.pdf](http://www.pa.op.dlr.de/CCMVal/DataRequests/CCMVal-2_Datarequest_FINAL.pdf).

CCM	T3I diagnostics
AMTRAC3 (REF-B1)	va, ua, ta, ps, plev, O3, N2O, H2O, CO, CH4
CCSRNIES	zg, wap, vorpot, va, ua, tntsw, tntlw, ta, sad-sulf, sad-nat, sad-ice, plev, OH, OCIO, O3P, O3, NOy, NO2, NO, N2O5, N2O, N, HOCl, HOBr, HO2, HNO4, HNO3, HNO3s, HCl, HBr, H2O2, H2O, CO, Cly, ClONO2, ClO, Cl2O2, CHBr3, CH3OOH, CH3Cl, CH3Br, CH2O, CFC13, CF2Cl2, Bry, BrONO2, BrO, BrCl, Br
CMAM	zg, wap, va, ua, tntsw, tntlw, ta, plev, OH, OCIO, O3P, O3, O1D, NOy, NO2, NO, N2O5, N2O, N, mean_age, HOCl, HOBr, HO2, HNO4, HNO3, HCl, HBr, H2O2, H2, CO, Cly, clt, ClONO2, CO, Cl2O2, Cl, CH4, CH3OOH, CH3OOH, CH3Cl, CH3Br, CH2O, CFC13, CF2Cl2, Bry, BrONO2, BrO, BrCl, Br
CNRM-ACM	sad-sulf, sad-nat, sad-ice, psc, OH, OCIO, O3P, O3, O1D, NOy, NO, NO2, N, N2O, N2O5, jO2, jCl2O2, HOCl, HOBr, HO2, HNO4, HNO3, HCl, HBr, H2SO4, H2O, H2O2, CO, Cly, ClONO2, ClO, Cl, Cl2O2, CH4, CH3OOH, CH3Cl, CH3Br, CH2O, CFC13, CF2Cl2, CCl4, CCl2FCCl2F, CBrF3, CBrClF2, Bry, BrONO2, BrO, BrCl, Br
EMAC (REF-B1)	zg, vorpot, va, ua, ta, OH, OCIO, O3P, O3, O1D, NOy, NO2, NO, N2O5, N2O, ice, HO2, HNO3_NAT, HNO3_liq, HNO3, HCl, H2O, CO2, CO, Cly, ClO, ClONO2, Cl2O2, CH4, CFC13, CF2Cl2, Bry, BrO, BrNO3
GEOSCCM	zg, wap, va, ua, tntsw, tntlw, ta, plev, OH, OCIO, O3, O(3P), O(1D), NOy, NO2, NO, N2O5, N2O, N, mean_age, HOCl, HOBr, HO2, HNO4, HNO3, HCl, HBr, H2O2, H2O, CO, Cly, ClONO2, ClO, Cl2O2, Cl, CH4, CH3OOH, CH3Cl, CH3Br, CH2O, CFC13, CF2Cl2, Bry, BrONO2, BrO, BrCl, Br
LMDZrepro	zg, wap, vorpot, va, ua, tntsw, tntlw, ta, sad-sulf, sad-nat, sad-ice, plev, OH, OCIO, O3s, O3, NOy, NO2, NO, N2O5, N2O, N, mean_age, HOCl, HOBr, HO2, HNO3, HCl, HBr, H2O2, H2O, convclt, CO, Cly, clt, ClONO2, ClO, Cl2O2, Cl, CH4, CH3OOH, CH3Cl, CH3Br, CH2O, CH2Br2, CFC13, CF2Cl2, Bry, BrONO2, BrO, BrCl, Br
MRI	OH, OCIO, O3, NOy, NO2, NO, N2O5, N2O, N, HOCl, HOBr, HO2, HNO4, HNO3, HCl, HBr, H2O2, H2O, CO2, CO, Cly, ClONO2, ClO, Cl2O2, Cl, CH4, CH3Cl, CH3Br, CFC13, CF2Cl2, Bry, BrONO2, BrO, BrCl, Br Niwa-SOCOL (REF-B1) va, ua, ta, O3, NAT-SAD, NAT, N2O, ICE-SAD, ICE, HNO3, HCl, H2O, CO, ClO, Cl2O2, CH4
UMUKCA-METO	zg, va, ua, tntsw, tntlw, ta, plev, OH, OCIO, O3s, O3P, O3, NOy, NOx, NO, N2O, N2O5, mean_age, HOCl, HOBr, HO2, HNO4, HNO3, HCl, HBr, H2O, H2O2, H2, CO, Cly, ClONO2, ClO, Cl, Cl2O2, CH4, CH3Br, CFC13, CF2Cl2, Bry, BrONO2, BrO, BrCl, Br
WACCM	zg, wap, va, ua, tntsw, ta, sad-sulf, sad-nat, sad-ice, OH, OCIO, O3, O1D, NOy, NO, NO2, N, N2O, N2O5, mean_age, JCl2O2, HOCl, HOCl, HOBr, HO2, HNO3, HCl, HBr, H2O, H2O2, H2, convclt, CO, CO2, Cly, clt, ClONO2, ClO, Cl, Cl2O2, CH4, CH3OOH, CH3Cl, CH3Br, CH2O, CFC13, CF2Cl2, Bry, BrONO2, BrO, BrCl, Br

pptv of Br<sub>y</sub>.

- The SSTs have not been manipulated to account for a loss of variance.

#### UMUKCA-METO:

- There is no solar cycle in the UMUKCA-METO simulations.
- SSTs are not manipulated to increase day-to-day variability.
- Photolysis cross sections and heterogeneous reaction

data are not updated to JPL (2006).

- Photolysis rates are not affected by volcanic aerosol.
- For ODSs, in REF-B2 the unadjusted scenario A1 (WMO, 2006) is used.

#### UMUKCA-UCAM:

- UMUKCA-UCAM does not have a representation of the solar cycle.
- There is no direct volcanic aerosol effect implemented in UMUKCA-UCAM for REF-B1 (neither on

**Table 2.21:** Three- and two-dimensional surface monthly-mean (T3M, T2Ms) diagnostics produced by model, for REF-B2.

CCM	T3M diagnostics	T2Ms diagnostics
AMTRAC3 (REF-B1)	zg, ua, tntsw, ta, H2O	toz,slp
CAM3.5	zg, va, ua, ta	toz, sic, ps, hfss, hfsl
CCSRNIES	zg, wap, va, ua, TRACER, tntsw, tntlw, ta, O3, NO2, N2O, HCl, H2O, CO, CH4	ztp, toz, tatp, ptp, ps, nuffl
CMAM	zg, wa, va, ua, tntsw, tntlw, ta, O3P, O3, O1D, NO2, NO, N2O, mean_age, HCl, H2O, CO, clt, CH4	ztp, toz, tatp, ptp, ps, nuffl
CNRM-ACM	zg, wap, va, ua, ta, O3, NO, NO2, N2O, mean_age, HCl, H2O, CO, CH4	toz, tatp, ptp, ps, pr, hfss, hfls, conclt, clt
E39CA (REF-B1)	va, ua, ta, O3, H2O	toz
EMAC (REF-B1)	zg, va, ua, ta, O3, HNO3, H2O, CO, Cly, CH4, Bry	toz
GEOSCCM	zg, va, ua, tntsw, tntlw, ta, O3, N2O, mean_age, inst_wap, inst_NOx, inst_HCl, inst_CO, H2O, convclt, clt, CH4	ztp, toz, tatp, ptp, ps, pr, clt
LMDZrepro	zg, wa, va, ua, tntsw, tntlw, ta, O3, NO2, NO, N2O, mean_age, HCl, H2O, convclt, CO, clt, CH4	toz, tatp, ptp, ps, pr, ogw_flux, nuffl, hfss, hfls
MRI	zg, wa, va, ua, tntsw, tntlw, ta, O3, N2O, HCl, H2O, CH4	toz, rdsdcs, rsds, ps
NiwaSOCOL (REF-B1)	zg, va, ua, ta, O3, NO2, NO, N2O, HCl, H2O, CO, ClONO2, CH4	toz, ps
SOCOL	zg, wap, va, ua, ta, O3, NOx, N2O, mean_age, HCl, H2O, CO, CH4	ztp, toz, tatp, ptp, ps, pr, hfss, hfls, clt
ULAQ	zg, va, ua, ta, O3, N2O, mean_age, H2O, CO2, CO, CH4	toz
UMSLIMCAT	zg, wa, va, ua, ta, OH, OCIO, O3, NOy, NO, NO3, NO2, N2O, N2O5, HOCl, HOBr, HO2, HNO4, HNO3, HCl, HBr, H2O, H2O2, CO, Cly, ClONO2, ClO, Cl2O2, CH4, CH3Br, CH2O, BrONO2, BrCl	toz, tos, snd, rdsdcs, rsds, ps, nuffl, convclt, clt
UMETRAC (REF-B1)	ua, ta, O3, NOy, mean_age, HOCl, HOBr, HCl, HBr, H2O, CO, Cly, ClONO2, CH3OOH, Bry, BrONO	ztp, toz, tatp, ptp, ps, clt
UMUKCA-METO	zg, wa, ua, tntsw, tntlw, ta, O3, NOx, N2O, mean_age, HCl, CO, Cly, CH4	ztp, toz, tatp, ptp, ps
UMUKCA-UCAM	zg, wa, va, ua, tntsw, tntlw, ta, O3, N2O, mean_age, H2O, CO, Cly, ClONO2, CH4	toz
WACCM	zg, wa, va, ua, tntsw, tntlw, ta, O3, N2O, mean_age, H2O, CO, Cly, ClONO2, CH4	toz, sic, ps, precl, precc, nuffl, hfss, hfls

heating nor photolysis).

- SSTs are not manipulated to increase day-to-day variability.
- Kinetic data are not updated to JPL (2006).
- For ODSs, in REF- B2 the unadjusted scenario A1 (WMO, 2006) is used.

#### WACCM

- No variance correction is applied to the SSTs.

## 2.6 Diagnostic output requested for CCMVal-2

In comparison with CCMVal-1, a much more comprehensive list of diagnostics has been requested ([http://www.pa.op.dlr.de/CCMVal/DataRequests/CCMVal-2\\_Datarequest\\_FINAL.pdf](http://www.pa.op.dlr.de/CCMVal/DataRequests/CCMVal-2_Datarequest_FINAL.pdf)). In particular, the process-oriented validation approach envisaged for CCMVal means that a lot of instantaneous fields have been produced; this class of diagnostics is missing in CCMVal-1. Monthly- and daily-mean diagnostics are given on 31 standard

**Table 2.22:** Zonal-monthly-mean (T2Mz) diagnostics produced by model, for REF-B2.

CCM	T2Mz diagnostics
AMTRAC3 (REF-B1)	va, ua, ta, O3, NOy, N2O, mean_age, HNO3, HCl, H2O, Cly, CH4, Bry
CAM3.5	zg, wstar, vstar, va, ua, ta, OH, OCIO, O3, NOy, NO, NO2, N, N2O, N2O5, mean_age, HOCl, HOBr, HO2, HNO3, HCl, HBr, H2O, H2O2, H2, Cly, ClONO2, ClO, Cl, Cl2O2, Cl2, CHClF2, CH4, CH3Cl, CH3CCl3, CFC13, CF2Cl2, CCl4, BrONO2, BrO, BrCl, Br
CCSRNIES	zg, wstar, vstar, va, ua, TRACER, ta, OH, OCIO, O3, NOy, NO, NO2, N, N2O, N2O5, HOCl, HOBr, HO2, HNO4, HNO3, HCl, HBr, H2O, H2O2, fz, fy, CO, Cly, ClONO2, ClO, Cl2O2, CHClF2, CHBr3, CH4, CH3OOH, CH3Cl, CH3CCl3, CH3Br, CH2O, CFC13, CF2Cl2, CCl4, CCl2FCClF2, CBrF3, CBrClF2, Bry, BrO, BrCl, Br, accel_ogw, accel_gw, accel_divf
CMAM	zg, wstar, vstar, va, ua, ta, OH, ogw_flux, OCIO, O3P, O3, O1D, NOy, nogw_w_flux, nogw_e_flux, NO, NO2, N, N2O, N2O5, mean_age, HOCl, HOBr, HO2, HNO4, HNO3, HCl, HBr, H2O, H2O2, H2, fz, fy, CO, Cly, ClONO2, ClO, Cl2O2, Cl, CHF2Cl, CH4, CH3OOH, CH3Cl, CH3CCl3, CH3Br, CH2O, CFC13, CF2Cl2, CCl4, Bry, BrONO2, BrO, BrCl, Br, accel_ogw, accel_nogw, accel_gw, accel_divf
CNRM-ACM	zg, wstar, va, ua, ta, OH, OCIO, O3, NOy, NO, NO2, N, N2O, N2O5, mean_age, HOCl, HOBr, HO2, HNO4, HNO3, HCl, HBr, H2O, H2O2, CO, Cly, ClONO2, ClO, Cl2O2, Cl, CH4, CH3OOH, CH3Cl, CH3CCl3, CH3Br, CH2O, CFC13, CF2Cl2, CCl4, CCl2FCClF2, CBrF3, CBrClF2, Bry, BrONO2, BrO, BrCl, Br
E39CA (REF-B1)	zg, wstar, vstar, va, ua, ta, O3, NO2, N2O, HNO3, HCl, H2O, fz, fy, CO, Cly, ClONO2, CH4, accel_divf
EMAC (REF-B1)	zgm, zg, wstar, vstar, va, ua, tntsw, ta, SF6, OH, O3P, O3, NOy, NO2, NO, N2O5, N2O, HO2, HNO3, HCl, H2O, fz, fy, CO, Cly, ClONO2, ClO, CH4, CFC13, CF2Cl2, Bry, BrO, accel_divf
GEOSCCM	zg, wstar, va, ua, ta, OH, OCIO, O3, NOy, NO, NO2, N, N2O, N2O5, mean_age, HOCl, HOBr, HO2, HNO4, HNO3, HCFC-22, HCl, HBr, H2O, H2O2, fz, fy, Cly, ClONO2, ClO, Cl2O2, Cl, CH4, CH3Cl, CH3CCl3, CH3Br, CFC13, CF2Cl2, CCl4, CBrF3, Bry, BrONO2, BrO, BrCl, Br, accel_ogw, accel_nogw, accel_gw, accel_divf
LMDZrepro	g, wstar, vstar, va, ua, ta, OH, OCIO, O3, NOy, NO, NO2, N, N2O, N2O5, mean_age, HOCl, HOBr, HO2, HNO3, HCl, HBr, H2O, H2O2, fz, fy, CO, Cly, ClONO2, ClO, Cl2O2, Cl, CH4, CH3OOH, CH3Cl, CH3Br, CH2O, CH2Br2, CFC13, CF2Cl2, CCl4, CBrF3, CBrClF2, Bry, BrONO2, BrO, BrCl, Br, accel_ogw, accel_nogw, accel_gw, accel_divf
MRI	zg, wstar, vstar, va, ua, ta, OH, OCIO, O3, NOy, NO, NO2, N, N2O, N2O5, mean_age, HOCl, HOBr, HO2, HNO4, HNO3, HCl, HBr, H2O, H2O2, fz, fy, CO2, CO, Cly, ClONO2, ClO, Cl2O2, Cl, CH4, CH3Cl, CH3Br, CFC13, CF2Cl2, Bry, BrONO2, BrO, BrCl, Br, accel_ogw, accel_gw, accel_divf
NiwaSOCOL (REF-B1)	zg, wstar, vstar, va, ua, ta, sad-sulf, sad-nd, OH, odscls, odscll, O3, NOy, NO, NO2, N, N2O, N2O5, mean_age, HOCl, HOBr, HO2, HNO4, HNO3, HCl, HBr, H2O, H2O2, H2, fz, fy, CO, Cly, ClONO2, ClO, Cl2O2, Cl2, Cl, CH4, Bry, BrONO2, BrO, BrCl, Br, accel_divf
SOCOL	zg, wstar, vstar, va, ua, ta, OH, O3, NOy, NO, NO2, N, N2O, N2O5, mean_age, HOCl, HOBr, HO2, HNO4, HNO3, HCl, HBr, H2O, H2O2, H2, fz, fy, CO, Cly, ClONO2, ClO, Cl2O2, Cl2, Cl, CH4, CH3OOH, CH2O, CFC13, CF2Cl2, CBry, Bry, BrONO2, BrO, BrCl, Br, accel_ogw, accel_nogw, accel_gw, accel_divf
ULAQ	zg, wstar, vstar, va, ua, ta, OH, O3, NOy, NO, NO2, N2O, N2O5, mean_age, HO2, HNO4, HNO3, HCl, HBr, H2O, H2O2, H2, fz, fy, Cly, ClONO2, ClO, CHClF2, CH4, CH3Cl, CH3CCl3, CH3Br, CFC13, CF2Cl2, ClF2CF3, ClF2CClF2, CCl4, CCl2FCClF2, CBrF3, CBrClF2, Bry, BrO, Br, accel_divf



Table 2.22 continued.

CCM	T2Mz diagnostics
UMSLIMCAT	zg, wstar, wa, vstar, va, ua, ta, OH, OCIO, O3, NOy, NO, NO3, NO2, N2O, N2O5, HOCl, HOBr, HO2, HNO4, HNO3, HCl, HBr, H2O, H2O2, fz, fy, divf, CO, Cly, CIONO2, ClO, Cl2O2, CH4, CH3Br, CH2O, CFC-12, CFC-11, Bry, Brx, BrONO2, BrCl
UMETRAC (REF-B1)	zg, ua, ta, O3, NOy, N2O5, N2O, mean_age, HOCl, HOBr, HCl, HBr, H2O, CO, Cly, CIONO2, CH4, CH3OOH, Bry, BrONO2
UMUKCA-METO	zg, wstar, vstar, va, ua, ta, OH, ogw_flux, O3, NOy, NOx, nogw_w_flux, nogw_e_flux, NO, NO2, N, N2O, N2O5, mean_age, HOCl, HOBr, HO2, HNO4, HNO3, HCl, HBr, H2O, fz, fy, CO, Cly, CIONO2, ClO, Cl2O2, Cl, CH4, CH3Br, CH2Br2, CFC13, Bry, BrONO2, BrO, BrCl, Br, accel_ogw, accel_nogw, accel_divf
UMUKCA-UCAM	zg, wstar, vstar, va, ua, ta, O3, NOy, N2O, N2O5, mean_age, HNO3, H2O, Cly, CIONO2, CH4, accel_divf
WACCM	zg, wstar, vstar, va, ua, ta, OH, OCIO, O3, NOy, NO, NO2, N, N2O, N2O5, mean_age, HOCl, HOBr, HO2, HNO3, HCl, HBr, H2O, H2O2, H2, Cly, CIONO2, ClO, Cl2O2, Cl, CHClF2, CH4, CHCl3, CH3CCl3, CFC13, CF2Cl2, CCl4, Bry, BrONO2, BrO, BrCl, Br

Table 2.23: Surface and zonal-mean instantaneous (T2Is, T2Iz) diagnostics produced by model, for REF-B2.

CCM	T2Is diagnostics	T2Iz diagnostics
CAM3.5	toz, ta50	
CMAM	zg500, zg100, zg10, va100, va10, ua100, ua10, toz, ta100, ta10, ps	zg, ua, ta
CNRM-ACM	zg500, zg10, zg100, zg1000, vp_840K, vp_460K, va_10, va_100, va_1000, ua_10, ua_100, ua1000, toz, tasmin, tasmax, tas, ta_10, ta_100, ta_1000, ps, clt	zg, va, ua, ta
E39CA (REF-B1)	tas	zg
NiwaSOCOL (REF-B1)	rsdscs, rsds	
UMSLIMCAT	zg500, zg10, zg100, va10, va100, ua10, ua100, toz, tos, ta10, ta100, snd, rsdscs, rsds, ps, nuff, convclt, clt	zg, va, ua, ta
UMUKCA-METO	zg500, zg10, zg100, zg1000, vorpot_840K, vorpot_460K, va10, va100, va1000, ua10, ua100, ua1000, toz, tasmin, tasmax, tas, ta10, ta100, ta1000, ps, nuff	

CCMVal-2 levels (1000, 850, 700, 500, 400, 300, 250, 200, 170, 150, 130, 115, 100, 90, 80, 70, 50, 30, 20, 15, 10, 7, 5, 3, 2, 1.5, 1, 0.5, 0.3, 0.2, and 0.1 hPa), whereas 3-dimensional instantaneous fields are given on model levels. In the horizontal, the data are requested on the native model grid. AMTRAC3 data are interpolated onto a regular latitude-longitude grid because of the unusual grid used in this model. The monthly-mean diagnostics fall into the categories T3M (3-dimensional), T2Ms (latitude-longitude), and T2Mz (zonal-mean). Instantaneous diagnostics likewise come in the categories T3I, T2Is, and T2Iz. For the T3I category, to reduce data volume, the diagnostics have been requested for specified periods, namely all years between 1990-2005, every 3-years before 1989, and every three years from 2005. Some diagnostics were requested as daily means (T2Ds, T2Dz). Finally, a few more diag-

nostics were 1- or 0-dimensional. **Tables 2.20-2.24** list the 3- and 2-dimensional diagnostics. (Note that the database (<ftp://ftp.badc.rl.ac.uk>) is updated frequently, so the reader is referred there for the most up-to-date listing.) CCMVal-1 data has originally been requested in ASCII format. This format is now considered outdated. For CCMVal-2, diagnostic output has been requested in Climate- and Forecast (CF)-compliant NetCDF format (<http://www.unidata.ucar.edu/software/netcdf>), and the CCMVal-1 data have also been reprocessed into the same format for easier comparison with CCMVal-2. CF also defines the names for meteorological and chemical diagnostics which are generally used in CCMVal-2. See [http://www.pa.op.dlr.de/CCMVal/DataRequests/CCMVal-2\\_Datrequest\\_FINAL.pdf](http://www.pa.op.dlr.de/CCMVal/DataRequests/CCMVal-2_Datrequest_FINAL.pdf) for a list of the names of diagnostics listed here.

Special (offline) diagnostics have been requested for

**Table 2.24:** Daily zonal-mean (T2Dz), and daily surface (T2Ds) diagnostics produced by model, for REF-B2.

CCM	T2Dz diag.	T2Ds diagnostics
AMTRAC3 (REF-B1)	vptp, ua, ta	toz
CCSRNIES	zg, ua, ta	zg500, zg1000, zg100, zg10, vorpot840, vorpot460, va1000, va100, va10, ua1000, ua100, ua10, toz, ta1000, ta100, ta10, ps, nuffl
CMAM		tasmin, tasmax, tas, snd, rdsdcs, rsds
E39CA (REF-B1)		toz
EMAC (REF-B1)		va100, ua10, toz, tas, ta100
GEOSCCM	zg, ua, ta	zg500, zg1000, zg100, zg10, toz, tas, ta1000, ta100, ta10, ps, clt
LMDZrepro	zg, ua, ta	zg500, zg100, zg10, vorpot840, vorpot480, va100, va10, ua100, ua10, toz, tasmin, tasmax, tas, ta100, ta10, ps, nuffl
MRI	zg, ua, ta	va100, va10, ua100, ua10, toz
Niwa-SOCOL (REF-B1)	zg, ua, ta	zg500, vorpot840, vorpot480, va100, va10, ua100, ua10, toz, tas, ta100, ta10, ps
SOCOL	zg, ua, ta	zg500, zg100, zg10, va100, va10, ua100, ua10, toz, tasmin, tasmax, tas, ta100, ta10, snd, rdsdcs, rsds, ps, nuffl, clt
ULAQ		toz
UMETRAC (REF-B1)		zg500, zg100, zg10, vorpot_840K, vorpot_460K, va100, va10, ua100, ua10, toz, tas, ta100, ta10, snw, rsds, ps, clt
UMUKCA-METO	zg, ua, ta	snw
UMUKCA-UCAM		ua10, toz, ta50
WACCM	zg, ua, ta	ps

the photolysis and radiation chapters, using stand-alone versions of the photolysis and radiation modules used in the models (Chapters 3 and 6).

## Acknowledgements

We would like to thank the 7 anonymous reviewers and José Rodriguez for constructive comments.

## References

- Adcroft, A., J.-M. Campin, C. Hill, and J. Marshall, 2007. Implementation of an atmosphere–ocean general circulation model on the expanded spherical cube, *Mon. Wea. Rev.*, **132**, 2845–2863.
- Allen, M., and J. E. Frederick, 1982. Effective photodissociation cross sections for molecular oxygen and nitric oxide in the Schumann-Runge bands, *J. Atmos. Sci.*, **39**, 2066–2075.
- Akiyoshi, H., 1997. Development of a global 1-D chemically radiatively coupled model and an introduction to the development of a chemically coupled general circulation model, GGER’s supercomputer monograph report, 4, ISSN 1341-4356, 69pp.
- Akiyoshi, H., 2000. Modeling of chemistry and chemistry-radiation coupling process for the middle atmosphere and a numerical experiment on CO<sub>2</sub> doubling with a 1-D coupled model, *J. Meteorol. Soc. Jpn.*, **78**, 563–584.
- Akiyoshi, H., T. Sugita, H. Kanzawa, and N. Kawamoto, 2004. Ozone perturbations in the Arctic summer lower stratosphere as a reflection of NO<sub>x</sub> chemistry and planetary scale wave activity, *J. Geophys. Res.*, **109**, doi:10.1029/2003JD003632.
- Akiyoshi, H., L. B. Zhou, Y. Yamashita, K. Sakamoto, M. Yoshiki, T. Nagashima, M. Takahashi, J. Kurokawa, M. Takigawa, and T. Imamura, 2009. A CCM simulation of the breakup of the Antarctic polar vortex in the years 1980–2004 under the CCMVal scenarios, *J. Geophys. Res.*, **114**, doi:10.1029/2007JD009261.
- Alexander, M. J., and T. J. Dunkerton, 1999. A spectral parameterization of mean flow forcing due to breaking gravity waves, *J. Atmos. Sci.*, **56**, 4167–4182.
- Andrews, D. G., J. R. Holton, and B. Leovy, 1987. *Middle Atmospheric Dynamics*, Acad.Press.
- Anstey, J. A., T. G. Shepherd, J. F. Scinocca (2010), In-

- fluence of the Quasi-Biennial Oscillation on the extratropical winter stratosphere in an atmospheric general circulation model and in reanalysis data. *J. Atmos. Sci.*, in press.
- Arakawa, A., and W. H. Schubert, 1974. Interactions of cumulus cloud ensemble with the large-scale environment. Part I, *J. Atmos. Sci.*, **31**, 671-701.
- Arora, V. K., G. J. Boer, J. R. Christian, C. L. Curry, K. L. Denman, K. Zahariev, G. M. Flato, J. F. Scinocca, W. J. Merryfield, and W. G. Lee, 2009. The effect of terrestrial photosynthesis down regulation on the twentieth-century carbon budget simulated with the CCCma Earth System model, *J. Clim.*, **22**, 6066-6088.
- Austin, J., R. C. Pallister, J. A. Pyle, A. F. Tuck, and A. M. Zavody, 1987. Photochemical model comparisons with LIMS observations in a stratospheric trajectory coordinate system, *Quart. J. Roy. Meteorol. Soc.*, **113**, 361-392.
- Austin J., 1991. On the explicit versus family solution of the fully diurnal photochemical equations of the stratosphere, *J. Geophys. Res.*, **96**, 12,941-12,975.
- Austin, J., and N. Butchart, 2003. Coupled chemistry-climate model simulations of the period 1980-2020: Ozone depletion and the start of ozone recovery, *Quart. J. Roy. Meteorol. Soc.*, **129**, 3225-3249.
- Austin, J. and R.J. Wilson, 2006. Ensemble simulations of the decline and recovery of stratospheric ozone, *J. Geophys. Res.*, **111**, doi: 10.1029/2005JD006907.
- Austin, J., J. Wilson, F. Li, and H. Vömel, 2007. Evolution of Water Vapor Concentrations and stratospheric age of air in coupled chemistry-climate model simulations. *J. Atmos. Sci.*, **64**, 905-921.
- Bacmeister, J. T., M. J. Suarez, and F. R. Robertson, 2006. Rain re-evaporation, boundary layer convection interactions, and Pacific rainfall patterns in an AGCM. *J. Atmos. Sci.*, **8**, SRef-ID: 1607-7962/gra/EGU06-A-08925.
- Baldwin, M. P., L. J. Gray, T. J. Dunkerton, K. Hamilton, P. H. Haynes, W. J. Randel, J. R. Holton, M. J. Alexander, I. Hirota, T. Horinouchi, D. B. A. Jones, J. S. Kinnersley, C. Marquardt, K. Sato, and M. Takahashi, 2001. The Quasi-Biennial Oscillation, *Rev. Geophys.*, **39**, 179-229.
- Baumgaertner, A. J. G., P. Jöckel, and C. Brühl, 2009. Energetic particle precipitation in ECHAM5/MESSy1 – Part 1: Downward transport of upper atmospheric NO<sub>x</sub> produced by low energy electrons, *Atmos. Chem. Phys.*, **9**, 2729-2740.
- Bian, H., and M. J. Prather, 2002. Fast-J2: Accurate simulation of stratospheric photolysis in global chemical models, *J. Atmos. Chem.*, **41**, 281-296.
- Blitz, M. A., D. E. Heard, M. J. Pilling, S. R. Arnold, and M. P. Chipperfield, 2004. Correction to pressure and temperature-dependent quantum yields for the photodissociation of acetone between 279 and 327.5 nm, *Geophys. Res. Lett.*, **31**, 2.
- Bonan, G. B., K. W. Oleson, M. Vertenstein, S. Levis, X. Zeng, Y. Dai, R. E. Dickinson, and Z.-L. Yang (2002), The land surface climatology of the Community Land Model coupled to the NCAR Community Climate Model, *J. Clim.*, **15**, 3123-3149.
- Blondin, C. and H. Böttger, 1987. The surface and subsurface parameterisation scheme in the ECMWF forecasting system. Revision and operational assessment of weather elements, *ECMWF Tech. Memo.*, **135**, 48 pp.
- Bossuet C., M. Déqué, and D. Cariolle, 1998. Impact of a simple parameterization of convective gravity-wave drag in a stratosphere-troposphere general circulation model and its sensitivity to vertical resolution. *Ann. Geophys.*, **16**, 238-249.
- Bougeault, P., 1985. A simple parameterization of the large-scale effects of cumulus convection, *Mon. Wea. Rev.*, **113**, 2108-2121.
- Brasseur, G. P., J. J. Orlando, and G. S. Tyndall, 1999. Atmospheric Chemistry and Climate Change, Oxford University Press, 688 pp.
- Briegleb, B. P., 1992. Delta-Eddington approximation for solar radiation in the NCAR Community Climate Model, *J. Geophys. Res.*, **97**, 7603-7612.
- Brinkop, S., Inclusion of cloud processes in the ECHAM PBL parameterization; In: R. Sausen (Ed.) Studying Climate with the ECHAM Atmospheric Model. Large Scale Atmospheric Modelling, Report No. 9, 5-14, Meteorologisches Institut der Universität Hamburg, 1991.
- Brinkop, S., 1992. Parameterisierung von Grenzschichtwolken für Zirkulationsmodelle; Berichte aus dem Zentrum für Meeres- und Klimaforschung, Reihe A: Meteorologie, Nr. 2, Meteorologisches Institut der Universität Hamburg, 77 pp.

- Brinkop, S., and E. Roeckner, 1995. Sensitivity of a general circulation model to parameterizations of cloud-turbulence interactions in the atmospheric boundary layer, *Tellus*, **47A**, 197–220.
- Brinkop, S., and R. Sausen, 1997. A modified mass-flux scheme for convection which maintains positive tracer concentrations, *Beitr. Phys. Atmos.*, **70**, 245–248.
- Buchholz, J., 2005. Simulations of physics and chemistry of polar stratospheric clouds with a general circulation model, Ph.D. thesis, University of Mainz, Germany, <http://nbn-resolving.de/urn/resolver.pl?urn=urn:nbn:de:hebis:77-8187>.
- Burkholder, J. B., J. J. Orlando, and C. J. Howard, 1990. Ultraviolet absorption cross-sections of Cl<sub>2</sub>O<sub>2</sub>, between 210 and 410nm, *J. Phys. Chem.*, **94**, 687–695.
- Carslaw, K. S., B. Luo, and T. Peter, 1995. An analytic expression for the composition of aqueous HNO<sub>3</sub>-H<sub>2</sub>SO<sub>4</sub> stratospheric aerosols including gas phase removal of HNO<sub>3</sub>, *Geophys. Res. Lett.*, **22**, 1877–1880.
- Charron M., and E. Manzini, 2002. Gravity waves from fronts: Parameterization and middle atmosphere response in a general circulation model, *J. Atmos. Sci.*, **59**, 923–941.
- Chipperfield, M. P., 1999. Multiannual simulations with a three-dimensional chemical transport model. *J. Geophys. Res.*, **104**, 1781–1805.
- Chipperfield, M. P., 2006. New version of the TOMCAT/SLIMCAT off-line chemical transport model: Intercomparison of stratospheric tracer experiments, *Quart. J. Roy. Meteorol. Soc.*, **132**, 1179–1203, doi:10.1256/qj.05.51.
- Chou, M.-D., M. J. Suarez, C.-H. Ho, M. M.-H. Yan, K.-T. Lee, (1997), Parameterizations for cloud overlapping and short-wave single-scattering properties for use in general circulation and cloud ensemble members, *J. Clim.*, **11**, 202–214.
- Chou, M.-D., and M. J. Suarez, 1999. A Solar Radiation Parameterization for Atmospheric Studies, NASA Technical Report Series on Global Monitoring and Data Assimilation, 104606, v15, 40pp.
- Chou, M.-D., M. J. Suarez, X. Z. Liang, and M. M.-H. Yan (2001), A thermal infrared radiations parameterization for atmospheric studies. NASA Technical Report Series on Global Monitoring and Data Assimilation, 104606, v19, 56pp.
- Collins, W. D., P. J. Rasch, B. A. Boville, J. R. McCaa, D. L. Williamson, J. T. Kiehl, B. P. Briegleb, C. M. Bitz, S.-J. Lin, , M. Zhang, and Y. Dai, 2004. Description of the NCAR community atmosphere model (CAM3.0). Technical Report NCAR/TN-464+STR, National Center for Atmospheric Research, Boulder, CO, USA.
- Collins, W. D., P. J. Rasch, B. A. Boville, J. J. Hack, J. R. McCaa, D. L. Williamson, B. P. Briegleb, C. M. Bitz, S.-J. Lin, and M. Zhang, 2006. The formulation and atmospheric simulation of the Community Atmosphere Model: CAM3. *J. Clim.*, **19**, 2122–2161.
- Considine, D. B., A. R. Douglass, D. E. Kinnison, P. S. Connell, and D. A. Rotman, 2000. A polar stratospheric cloud parameterization for the three dimensional model of the global modeling initiative and its response to stratospheric aircraft emissions, *J. Geophys. Res.*, **105**, 3955–3975.
- Cox, P., R. Betts, C. Bunton, R. Essery, P.R. Rowntree, and J. Smith, 1999. The impact of new land surface physics on the GCM simulation of climate and climate sensitivity. *Clim. Dyn.*, **15**, 183–203.
- Cusack S., A. Slingo, J. M. Edwards, and M. Wild, 1998, The radiative impact of a simple aerosol climatology on the Hadley Centre GCM. *Quart. J. Roy. Meteorol. Soc.*, **124**, 2517–2526.
- Dameris, M., V. Grewe, M. Ponater, R. Deckert, V. Eyering, F. Mager, S. Matthes, C. Schnadt, A. Stenke, B. Steil, C. Brühl, and M. Giorgetta, 2005. Long-term changes and variability in a transient simulation with a chemistry-climate model employing realistic forcing, *Atmos. Chem. Phys.*, **5**, 2121–2145.
- Davies, T, M. J. P. Cullen, A. J. Malcolm, M. H. Mawson, A. Staniforth, A. A. White, and N. Wood, 2005. A new dynamical core for the Met Office’s global and regional modelling of the atmosphere. *Quart. J. Roy. Meteorol. Soc.*, **131**, 1759–1782.
- de Grandpré, J., J. W. Sandilands, J. C. McConnell, S. R. Beagley, P. C. Croteau, and M. Y. Danilin, 1997. Canadian Middle Atmosphere Model: Preliminary results from the Chemical Transport Module, *Atmos. Ocean*, **35**, 385–431.
- deGrandpré, J., S. R. Beagley, V. I. Fomichev, E. Griffioen, J. C. McConnell, A. S. Medvedev and T. G. Shepherd, 2000. Ozone climatology using interactive

- chemistry: Results from the Canadian Middle Atmosphere Model, *J. Geophys. Res.*, **105**, 26,475-26,491.
- DeMore, W. B., Sander, S. P., Golden, D. M., Hampson, R. F., Kurylo, M. J., Howard, C. J., Ravishankara, A. R., Kolb, C. E., and Molina, M. J. (1997), Chemical kinetics and photochemical data for use in stratospheric modeling. Evaluation number 12, JPL Publication 97-4, Jet Propulsion Laboratory, Pasadena, CA, (referred to as JPL, 1997).
- Delworth, T. L., A. Rosati, R. J. Stouffer, K. W. Dixon, J. Dunne, K. L. Findell, P. Ginoux, A. Gnanadesikan, C. T. Gordon, S. M. Griffies, R. Gudgel, M. J. Harrison, I. M. Held, R. S. Hemler, L. W. Horowitz, S. A. Klein, T. R. Knutson, S.-J. Lin, V. Ramaswamy, M. D. Schwarzkopf, J. J. Sirutis, M. J. Spelman, W. F. Stern, Michael Winton, A. T. Wittenberg, B. Wyman, A. J. Broccoli, V. Balaji, J. Russell, R. Zhang, J. A. Beesley, Jian Lu, William F. Cooke, J. W. Durachta, A. R. Langenhorst, H.-C. Lee, F. Zeng, K. A. Dunne, P. C. D. Milly, P. J. Kushner, Sergey L. Malyshev, E. Shevliakova, 2006. GFDL's CM2 global coupled climate models – Part 1: Formulation and simulation characteristics, *J. Clim.*, **19**, 643-674.
- Déqué, M., 2007. Frequency of precipitation and temperature extremes over France in an anthropogenic scenario: model results and statistical correction according to observed values. *Global and Planetary Change*, **57**, 16-26.
- Douglass, A. R., R. B. Rood, S. R. Kawa and D. J. Allen (1997), A three-dimensional simulation of the evolution of middle latitude winter ozone in the middle stratosphere, *J. Geophys. Res.*, **102**, 19,217-19,232.
- Douglass, A. R., and S. R. Kawa, 1999. Contrast between 1992 and 1997 high-latitude spring Halogen Occultation Experiment observations of lower stratospheric HCl, *J. Geophys. Res.*, **104**, 18,739-18,754.
- Douville H., S. Planton, J. F. Royer, D. B. Stephenson, S. Tyteca, L. Kergoat, S. Lafont, and R. A. Betts, 2000. Importance of vegetation feedbacks in doubled-CO2 climate experiments, *J. Geophys. Res.*, **105**, 14841-14861.
- Dufresne, J.-L., J. Quaas, O. Boucher, F. Denvil, and L. Fairhead, 2005. Contrasts in the effects on climate of anthropogenic sulfate aerosols between the 20th and the 21st century, *Geophys. Res. Lett.*, **32**, doi:10.1029/2005GL023619.
- Dümenil, L., and E. Todini, 1992. A rainfall-runoff scheme for use in the Hamburg climate model, in: Advances in Theoretical Hydrology, A Tribute to James Dooge, edited by Kane, J. O., European Geophysical Society Series on Hydrological Sciences, pp. 129–157. Elsevier, Amsterdam.
- Edwards, J.M. and A. Slingo, 1996. Studies with a flexible new radiation code. I: Choosing a configuration for a large scale model. *Quart. J. Roy. Meteorol. Soc.*, **122**, 689-719.
- Egorova, T., E. Rozanov, V. Zubov, and I. Karol, 2003. Model for investigating ozone trends, *Isv. Atm. Ocean. Phys.*, **39**, 277-292.
- Egorova T., E. Rozanov, E. Manzini, M. Haberreiter, W. Schmutz, V. Zubov, and T. Peter, 2004. Chemical and dynamical response to the 11-year variability of the solar irradiance simulated with a chemistry-climate model, *Geophys. Res. Lett.*, **31**, L06119.
- Egorova, T., E. Rozanov, V. Zubov, E. Manzini, W. Schmutz, and T. Peter, 2005. Chemistry-climate model SOCOL: a validation of the present-day climatology, *Atm. Chem. Phys.*, **5**, 1557-1576.
- Eluszkiewicz, J., R. S. Hemler, J. D. Mahlman, L. Bruhwiler and L. L. Takacs, 2000 Sensitivity of age-of-air calculations to the choice of advection scheme. *J. Atmos. Sci.*, **57**, 3185-3201.
- Eyring, V., N. Butchart, D. W. Waugh, H. Akiyoshi, J. Austin, S. Bekki, G. E. Bodeker, B. A. Boville, C. Brühl, M. P. Chipperfield, E. Cordero, M. Dameris, M. Deushi, V. E. Fioletov, S. M. Frith, R. R. Garcia, A. Gettelman, M. A. Giorgetta, V. Grewe, L. Jourdain, D. E. Kinnison, E. Mancini, E. Manzini, M. Marchand, D. R. Marsh, T. Nagashima, P. A. Newman, J. E. Nielsen, S. Pawson, G. Pitari, D. A. Plummer, E. Rozanov, M. Schraner, T. G. Shepherd, K. Shibata, R. S. Stolarski, H. Struthers, W. Tian, and M. Yoshiki, 2006. Assessment of temperature, trace species and ozone in chemistry-climate model simulations of the recent past, *J. Geophys. Res.*, **111**, doi:10.1029/2006JD007327.
- Eyring, V., D. W. Waugh, G. E. Bodeker, E. Cordero, H. Akiyoshi, J. Austin, S. R. Beagley, B. Boville, P. Braesicke, C. Brühl, N. Butchart, M. P. Chipperfield, M. Dameris, R. Deckert, M. Deushi, S. M. Frith, R. R. Garcia, A. Gettelman, M. Giorgetta, D. E. Kinnison, E. Mancini, E. Manzini, D. R. Marsh, S. Mat-

- thes, T. Nagashima, P. A. Newman, J. E. Nielsen, S. Pawson, G. Pitari, D. A. Plummer, E. Rozanov, M. Schraner, J. F. Scinocca, K. Semeniuk, T. G. Shepherd, K. Shibata, B. Steil, R. Stolarski, W. Tian, and M. Yoshiki, 2007. Multimodel projections of stratospheric ozone in the 21st century, *J. Geophys. Res.*, **112**, doi:10.1029/2006JD008332.
- Eyring, V., M. P. Chipperfield, M. A. Giorgetta, D. E. Kinnison, E. Manzini, K. Matthes, P. A. Newman, S. Pawson, T. G. Shepherd, and D. W. Waugh (2008), Overview of the New CCMVal Reference and Sensitivity Simulations in Support of Upcoming Ozone and Climate Assessments and the Planned SPARC CCMVal Report, *SPARC Newsletter No. 30*, 20-26.
- Farman, J. C., B. G. Gardiner, and J. D. Shanklin (1985), Large losses of total ozone in Antarctica reveal seasonal ClO<sub>x</sub>/NO<sub>x</sub> interaction, *Nature*, **315**, 207–210.
- Fischer, A. M., M. Schraner, E. Rozanov, P. Kenzelmann, C. S. Poberaj, D. Brunner, A. Lustenberger, B. P. Luo, G. E. Bodeker, T. Egorova, W. Schmutz, T. Peter, and S. Brönnimann, 2008. Interannual-to-decadal variability of the stratosphere during the 20th century: Ensemble simulations with a chemistry-climate model. *Atmos. Chem. Phys.*, **8**, 7755-7777.
- Fomichev, V. I., J. P. Blanchet, and D. S. Turner, 1998. Matrix parameterization of the 15 μm CO<sub>2</sub> band cooling in the middle and upper atmosphere for variable CO<sub>2</sub> concentration, *J. Geophys. Res.*, **103**, 11505–11528.
- Fomichev, V. I., C. Fu, J. de Grandpré, S. R. Beagley, V. P. Ogibalov, and J. C. McConnell, 2004. Model thermal response to minor radiative energy sources and sinks in the middle atmosphere, *J. Geophys. Res.*, **109**, doi:10.1029/2004JD004892.
- Fouquart, Y. and B. Bonnel, 1980. Computations of solar heating of the Earth's atmosphere: A new parameterization, *Beitr. Phys. Atmos.*, **53**, 35–62.
- Garcia, R. R. and B. A. Boville, 1994. Downward control of the mean meridional circulation and temperature distribution of the polar winter stratosphere, *J. Atmos. Sci.*, **51**, 2238–2245.
- Garcia, R. R., D. Marsh, D. E. Kinnison, B. Boville, and F. Sassi, 2007. Simulations of secular trends in the middle atmosphere, 1950-2003, *J. Geophys. Res.*, **112**, doi:10.1029/2006JD007485.
- Garny, H., M. Dameris, and A. Stenke, 2009. Impact of prescribed SSTs on climatologies and long-term trends in CCM simulations, *Atmos. Chem. Phys.*, **9**, 6017-6031.
- Gent, P. R., F. O. Bryan, G. Danabasoglu, S. C. Doney, W. R. Holland, W. G. Large, and J. C. McWilliams, 1998. The NCAR Climate System Model global ocean component, *J. Clim.*, **11**, 1287-1306.
- Gent, P. R., S. G. Yeager, R. B. Neale, S. Levis, and D. A. Bailey, 2009. Improvements in a half degree atmosphere/land version of the CCSM, *Clim. Dyn.*, in press, doi:10.1007/s00382-009-0614-8
- Giorgetta, M. A., 1996. Der Einfluss der quasi-zweijährigen Oszillation: Modellrechnungen mit ECHAM4, Max-Planck-Institut für Meteorologie, Hamburg, Examensarbeit Nr. 40, MPI-Report 218.
- Giorgetta, M., and L. Bengtsson, 1999. Potential role of the Quasi-Biennial Oscillation in the stratosphere-troposphere exchange as found in water vapor in general circulation model experiments, *J. Geophys. Res.*, **104**, 6003-6019.
- Giorgetta, M. A., E. Manzini, and E. Roeckner (2002), Forcing of the Quasi-Biennial Oscillation from a broad spectrum of atmospheric waves, *Geophys. Res. Lett.*, **29**, doi:10.1029/2002GL014756.
- Giorgetta, M. A., E. Manzini, E. Roeckner, M. Esch, and L. Bengtsson, 2006. Climatology and forcing of the quasi-biennial oscillation in the MAECHAM5 model, *J. Clim.*, **19**, 3882-3901.
- Global Carbon Budget, 2009. Carbon budget and trends 2008. [www.globalcarbonproject.org/carbonbudget](http://www.globalcarbonproject.org/carbonbudget), released on 17 November 2009.
- Gregory, D., R. Kershaw, and P. M. Inness, 1997. Parameterization of momentum transport by convection. II: Tests in single column and general circulation models. *Quart. J. Roy. Meteorol. Soc.*, **123**, 1153-1183.
- Gregory, D., G. J. Shutts, and J. R. Mitchell, 1998. A new gravity wave drag scheme incorporating anisotropic orography and low level wave breaking: Impact upon the climate of the UK Meteorological Office Unified Model. *Quart. J. Roy. Meteorol. Soc.*, **124**, 463-493.
- Gregory, A. R., and V. West, 2002. The sensitivity of a model's stratospheric tape recorder to the choice of advection scheme. *Quart. J. Roy. Meteorol. Soc.*, **128**, 1827-1846.
- Grewe, V., D. Brunner, M. Dameris, J. Grenfell, R. Hein, D. Shindell, J. Staehelin, 2001. Origin and variability of upper tropospheric nitrogen oxides and ozone at

- northern mid-latitudes, *Atmos. Env.*, **35**, 3421-3433.
- Hack, J. J., 1994. Parameterization of moist convection in the NCAR community climate model (CCM2), *J. Geophys. Res.*, **99**, 5551-5568.
- Hansen, J., M. Sato, L. Nazarenko, R. Ruedy, A. Lacis, D. Koch, I. Tegen, T. Hall, D. Shindell, B. Santer, P. Stone, T. Novakov, L. Thomason, R. Wang, Y. Wang, D. Jacob, S. Hollandsworth, L. Bishop, J. Logan, A. Thompson, R. Stolarski, J. Lean, R. Willson, S. Levitus, J. Antonov, N. Rayner, D. Parker, and J. Christy, 2002. Climate forcings in Goddard Institute for Space Studies SI2000 simulations, *J. Geophys. Res.*, **107**, 4347, doi:10.1029/2001JD001143.
- Hines, C. O., 1997a. Doppler spread parameterization of gravity wave momentum deposition in the middle atmosphere. Part I: Basic formulation. *J. Atmos. Solar Terr. Phys.*, **59**, 371-386.
- Hines, C. O., 1997b. Doppler spread parameterization of gravity wave momentum deposition in the middle atmosphere. Part II: Broad and quasi monochromatic spectra and implementation. *J. Atmos. Solar Terr. Phys.*, **59**, 387-400.
- Hitchcock, P., T. G. Shepherd and C. McLandress, 2009. Past and future conditions for polar stratospheric cloud formation in the Canadian Middle Atmosphere Model. *Atmos. Chem. Phys.*, **9**, 483-495.
- Holstag, A., and B. A. Boville, 1993. Local versus nonlocal boundary-layer diffusion in a global climate model, *J. Clim.*, **6**, 1825-1842.
- Holton, J. R., 1992. An Introduction to Dynamical Meteorology, 3rd ed., Academic Press, San Diego, CA, 511pp.
- Horinouchi, T., S. Pawson, K. Shibata, U. Langematz, E. Manzini, M. A. Giorgetta, F. Sassi, R. J. Wilson, K. Hamilton, J. de Grandpré, and A. A. Scaife, 2003. Tropical Cumulus Convection and Upward-Propagating Waves in Middle-Atmospheric GCMs, *J. Atmos. Sci.*, **60**, 2765-2782.
- Hough, A. M., 1991. Development of a 2-dimensional global tropospheric model - Model chemistry, *J. Geophys. Res.*, **96**, 7325-7362.
- Hourdin, F., and A. Armengaud, 1999. The use of finite-volume methods for atmospheric advection trace species: 1. Tests of various formulations in a general circulation model, *Mon. Weather Rev.*, **127**, 822-837.
- Hourdin, F., I. Musat, S. Bony, P. Braconnot, F. Codron, J. L. Dufresne, L. Fairhead, M. A. Filiberti, P. Friedlingstein, J. Y. Grandpeix, G. Krinner, P. Levan, Z. X. Li and F. Lott, 2006. The LMDZ4 general circulation model: Climate performance and sensitivity to parametrized physics with emphasis on tropical convection, *Clim. Dyn.*, **27**, 787-813.
- Hoyle, C. R., 2005. Three dimensional chemical transport model study of ozone and related gases 1960-2000, ETH Zürich, Dissertation No. 16271.
- Intergovernmental Panel on Climate Change (IPCC) (2001), Climate Change 2001, The Scientific Basis, J. T. Houghton et al. (editors), Cambridge University Press, Cambridge UK and New York, USA, 881 pp.
- IPCC, 2007: Climate Change 2007: The Physical Science Basis. Contribution of Working Group I to the Fourth Assessment Report of the Intergovernmental Panel on Climate Change [Solomon, S., D. Qin, M. Manning, Z. Chen, M. Marquis, K.B. Averyt, M. Tignor and H.L. Miller (eds.)]. Cambridge University Press, Cambridge, United Kingdom and New York, NY, USA, 996 pp.
- International Union of Pure and Applied Chemistry (IUPAC) (various years), Evaluated kinetic data, <http://www.iupac-kinetic.ch.cam.ac.uk/index.html>.
- Iwasaki, T., S. Yamada, and K. Tada, 1989. A parameterization scheme of orographic gravity wave drag with the different vertical partitioning, part 1: Impact on medium range forecasts. *J. Meteor. Soc. Japan*, **67**, 11-41.
- Jackman, C. H., E. L. Fleming, S. Chandra, D. B. Conditine, and J. E. Rosenfield, 1996. Past, present, and future modeled ozone trends with comparisons to observed trends, *J. Geophys. Res.*, **101**, doi:10.1029/96JD00577.
- Jacobson, M. Z., 1999. Fundamentals of Atmospheric Modeling, Cambridge Univ. Press, 656pp.
- Jöckel, P., R. von Kuhlmann, M. G. Lawrence, B. Steil, C. A. M. Brenninkmeijer, P. J. Crutzen, P. J. Rasch, and B. Eaton, 2001. On a fundamental problem in implementing flux-form advection schemes for tracer transport in 3-dimensional general circulation and chemistry transport models. *Quart. J. Roy. Meteorol. Soc.*, **127**, 1035-1052.
- Jöckel, P., H. Tost, A. Pozzer, C. Brühl, J. Buchholz, L. Ganzeveld, P. Hoor, A. Kerkweg, M. G. Lawrence, R. Sander, B. Steil, G. Stiller, M. Tanarhte, D. Tarabor-

- relli, J. van Aardenne, and J. Lelieveld, 2006. The atmospheric chemistry general circulation model ECHAM5/MESSy1: Consistent simulation of ozone from the surface to the mesosphere, *Atmos. Chem. Phys.*, **6**, 5067–5104.
- Johns, T. C., C. F. Durman, H. T. Banks, M. J. Roberts, A. J. McLaren, J. K. Ridley, C. A. Senior, K. D. Williams, A. Jones, G. J. Rickard, S. Cusack, W. J. Ingram, M. Crucifix, D. M. H. Sexton, M. M. Joshi, B.-W. Dong, H. Spencer, R. S. R. Hill, J. M. Gregory, A. B. Keen, A. K. Pardaens, J. A. Lowe, A. Bodas-Salcedo, S. Stark, and Y. Searl, 2006. The new Hadley Centre climate model HadGEM1: Evaluation of coupled simulations, *J. Clim.*, **19**, 1327–1353.
- Jonsson, A. I., V. I. Fomichev, and T. G. Shepherd, 2009. The effect of nonlinearity in CO<sub>2</sub> heating rates on the attribution of stratospheric ozone and temperature changes, *Atmos. Chem. Phys.*, **9**, 8447–8452.
- Jourdain, L., S. Bekki, F. Lott, and F. Lefèvre, 2008. The coupled chemistry-climate model LMDz-REPROBUS: description and evaluation of a transient simulation of the period 1980–1999, *Ann. Geophys.*, **26**, 1391–1413.
- Kanae, S., K. Nishio, T. Oki, and K. Musiaka, 1995. Hydrograph estimation by flow routing modeling from AGCM output in major basins of the world, *Proceedings of Hydraulic Engineering*, **39**, 97–102 (in Japanese with English abstract).
- Kärcher, B., and U. Lohmann, 2001. The parameterization of cirrus cloud formation: homogeneous freezing of supercooled aerosols, *J. Geophys. Res.*, **108**, 4402–4415.
- Kawa, S. R., R. M. Bevilacqua, J. J. Margitan, A. R. Douglass, M. R. Schoeberl, K. W. Hoppel, and B. Sen, 2002. Interaction between dynamics and chemistry of ozone in the setup phase of the Northern Hemisphere polar vortex, *J. Geophys. Res.*, **107**, doi:10.1029/2001JD001527.
- Kinnison, D. E., G. P. Brasseur, S. Walters, R. R. Garcia, F. Sassi, B. A. Boville, D. Marsh, L. Harvey, C. Randall, W. Randel, J. F. Lamarque, L. K. Emmons, P. Hess, J. Orlando, J. Tyndall, and L. Pan, 2007. Sensitivity of chemical tracers to meteorological parameters in the MOZART-3 chemical transport model, *J. Geophys. Res.*, **112**, doi:10.1029/2006JD007879.
- Kockarts, G. (1980), Nitric oxide cooling in the terrestrial thermosphere, *Geophys. Res. Lett.*, **7**, 137–140.
- Koepke, P., M. Hess, I. Schult, and E. P. Shettle, 1997. Global Aerosol Data Set, Report No. 243, Max-Planck-Institut für Meteorologie, Hamburg, ISSN 0937-1060.
- Koppers, G. A. A., and D. P. Murtagh, 1996. Model studies of the influence of O<sub>2</sub> photodissociation parameterizations in the Schumann-Runge bands on ozone related photolysis in the upper atmosphere, *Ann. Geophys.*, **14**, 68–79.
- Koshyk, J. N. and G. J. Boer, 1995. Parameterization of dynamical subgrid-scale processes in a spectral GCM, *J. Atmos. Sci.*, **52**, 965–976.
- Koster, R. D., M. J. Suarez, A. Ducharne, M. Stieglitz, and P. Kumar, 2000. A catchment-based approach to modeling land surface processes in a general circulation model: 1. Model structure, *J. Geophys. Res.*, **105**, 24,809–24,822.
- Kraus, E. B., and J. S. Turner, 1967. A one dimensional model of the seasonal thermocline. Part II, *Tellus*, **19**, 98–105.
- Kurokawa, J., H. Akiyoshi, T. Nagashima, H. Masunaga, T. Nagajima, M. Takahashi, and H. Nakane, 2005. Effects of atmospheric sphericity on stratospheric chemistry and dynamics over Antarctica, *J. Geophys. Res.*, **110**, doi:10.1029/2005JD005798.
- Lacis, A., J. E. Hansen, and M. Sato, 1992. Climate forcing by stratospheric aerosols, *Geophys. Res. Lett.*, **19**, 1607–1610.
- Land, C., J. Feichter, and R. Sausen, 2002. Impact of vertical resolution on the transport of passive tracers in the ECHAM4 model, *Tellus*, **54B**, 344–360.
- Lamarque J.-F., D. E. Kinnison, P. G. Hess, and F. M. Vitt, 2008. Simulated lower stratospheric trends between 1970 and 2005: Identifying the role of climate and composition changes, *J. Geophys. Res.*, **113**, doi:10.1029/2007JD009277.
- Landgraf, J., and P. J. Crutzen, 1998. An efficient method for online calculations of photolysis and heating rates. *J. Atmos. Sci.*, **55**, 863–878.
- Lanser, D., J. G. Blom and J. G. Verwer, 2000. Spatial discretization of the shallow water equations in spherical geometry using Osher's Scheme, *J. Comp. Phys.*, **165**, 542–565.
- Lary, D. and J. A. Pyle, 1991. Diffuse-radiation, twilight, and photochemistry. 1., *J. Atmos. Chem.*, **13**, 393–



- 406.
- Lawrence, M. G., R. von Kuhlmann, M. Salzmann, and P. J. Rasch, 2003. The balance of effects of deep convective mixing on tropospheric ozone, *Geophys. Res. Lett.*, **30**, doi:10.1029/2003GL017644.
- Lean, J. L., G. J. Rottman, H. L. Kyle, T. N. Woods, J. R. Hickey, and L. C. Puga, 1997. Detection and parameterization of variations in solar mid and near ultraviolet radiation (200 to 400 nm), *J. Geophys. Res.*, **102**, 29,939-29,956.
- Lean, J., G. Rottman, J. Harder, and G. Kopp, 2005. Source contributions to new understanding of global change and solar variability, *Solar Phys.*, **230**, 27-53.
- Lefèvre, F., G. P. Brasseur, I. Folkins, A. K. Smith, and P. Simon, 1994. Chemistry of the 1991-1992 stratospheric winter: Three-dimensional model simulations, *J. Geophys. Res.*, **99**, 8183-8195.
- Lefèvre, F., F. Figarol, K. S. Carslaw, and T. Peter, 1998. The 1997 Arctic ozone depletion quantified from three-dimensional model simulations, *Geophys. Res. Lett.*, **25**, 2425-2428, 10.1029/98GL51812.
- Le Quééré, C., M. R. Raupach, J. G. Canadell, G. Marland, L. Bopp, P. Ciais, T. J. Conway, S. C. Doney, R. A. Feely, P. Foster, P. Friedlingstein, K. Gurney, R. A. Houghton, J. I. House, C. Huntingford, P. E. Levy, M. R. Lomas, J. Majkut, N. Metzler, J. P. Ometto, G. P. Peters, I. C. Prentice, J. T. Randerson, S. W. Running, J. L. Sarmiento, U. Schuster, S. Sitch, T. Takahashi, N. Viovy, G. R. van der Werf, F. I. Woodward, 2009. Trends in the sources and sinks of carbon dioxide. *Nature Geosci.*, **2**, 831 - 836 doi: 10.1038/ngeo689.
- Le Treut, H. and Z.-X. Li, 1991. Sensitivity of an atmospheric general circulation model to prescribed SST changes: feedback effects associated with the simulation of cloud optical properties, *Clim. Dyn.*, **5**, 175-187.
- Lin, S.-J., and R. Rood, 1996. Multi-dimensional flux-form semi-Lagrangian transport schemes, *Mon. Wea. Rev.*, **124**, 2046-2070.
- Lin, S.-J., and R. B. Rood, 1997. An explicit flux-form semi-Lagrangian shallow water model on the sphere, *Quart. J. Roy. Meteorol. Soc.*, **123**, 2477-2498.
- Lin, S.-J. (2004), A "vertically Lagrangian" finite volume dynamical core for global models. *Mon. Wea. Rev.*, **132**, 2293-2307.
- Logan, J. A., 1999. An analysis of ozonesonde data for the troposphere: Recommendations for testing 3-D models and development of a gridded climatology for tropospheric ozone, *J. Geophys. Res.*, **104**, 16115-16150.
- Lock, A. P., A. R. Brown, M. R. Bush, G. M. Martin, and R. N. B. Smith, 2000. A new boundary layer mixing scheme. Part 1: Scheme description and single-column model tests. *Mon. Wea. Rev.*, **138**, 3187-3199.
- Lott, F. and M. J. Miller, 1997. A new-subgrid-scale orographic drag parameterization: Its formulation and testing. *Quart. J. Roy. Meteor. Soc.*, **123**, 101-12.
- Lott, F., 1999. Alleviation of stationary biases in a GCM through a mountain drag parameterization scheme and a simple representation of mountain lift forces. *Mon. Wea. Rev.*, **127**, 788-801.
- Lott, F., L. Fairhead, F. Hourdin and P. Levan, 2005. The stratospheric version of LMDz: Dynamical climatologies, Arctic Oscillation, and impact on the surface climate. *Clim. Dyn.*, **25**, 851-868, doi: 10.1007/s00382-005-0064.
- Louis, J., 1979. A parametric model of vertical eddy fluxes in the atmosphere, *Bound. Layer Meteor.*, **17**, 187-202.
- Louis, J., M. Tiedtke, and J. Geleyn, 1982. A short history of the PBL parameterization at ECMWF. Proc. ECMWF Workshop on Planetary Boundary Layer Parameterization, Reading, United Kingdom, ECMWF, 59-80.
- Madronich, S., and S. Flocke, 1998. The role of solar radiation in atmospheric chemistry, pp. 1-26, Springer-Verlag, New York.
- Manabe, S., J. Smagorinski, and R. F. Strickler, 1965. Simulated climatology of a general circulation model with a hydrologic cycle, *Mon. Wea. Rev.*, **93**, 769-798.
- Manzini, E., N. A. McFarlane, and C. McLandress, 1997. Impact of the Doppler spread parameterization on the simulation of the middle atmosphere circulation using the MA/ECHAM4 general circulation model, *J. Geophys. Res.*, **102**, 25,751-25,762.
- Manzini, E., and N. McFarlane, 1998. The effect of varying the source spectrum of a gravity wave parameterization in the middle atmosphere general circulation model, *J. Geophys. Res.*, **103**, 31,523-31,539.
- Marsh, D. R., R. R. Garcia, D. E. Kinnison, B. A. Boville, S. Walters, K. Matthes, and S.C. Solomon, 2007.

- Modeling the whole atmosphere response to solar cycle changes in radiative and geomagnetic forcing, *J. Geophys. Res.*, **112**, doi:10.1029/2006JD008306.
- Martin, G. M., M. R. Bush, A. R. Brown, A. P. Lock, and R. N. B. Smith, 2000. A new boundary layer mixing scheme. Part II: Tests in climate and mesoscale models. *Mon. Wea. Rev.*, **128**, 3200-3217.
- Martin, G. M., M. A. Ringer, V. D. Pope, A. Jones, C. Dearden, and T. J. Hinton, 2006. The physical properties of the atmosphere in the new Hadley Centre Global Environment Model (HadGEM1). Part I: Model description and global climatology. *J. Clim.*, **19**, 1274-1301.
- Mascart P., J. Noilhan, and H. Giordani, 1995. A modified parameterization of flux profile relationships in the surface layer using different roughness length values for heat and momentum. *Bound. Layer Meteorol.*, **72**, 331-344.
- McCalpin, J. D., 1988. A quantitative analysis of the dissipation inherent in semi-Lagrangian advection, *Mon. Wea. Rev.*, **116**, 2330-2336.
- McIntyre, M. E., 1995. The stratospheric polar vortex and sub-vortex: fluid dynamics and midlatitude ozone loss, *Phil. Trans. Roy. Soc.*, **352**, 227-240.
- McFarlane, N. A., 1987. The effect of orographically excited gravity wave drag on the general circulation of the lower stratosphere and troposphere, *J. Atmos. Sci.*, **44**, 1775 – 1800.
- McLandress, C., 2002. Interannual variations of the diurnal tide in the mesosphere induced by a zonal-mean wind oscillation in the tropics, *Geophys. Res. Lett.*, **29**, doi:10.1029/2001GL014551.
- McLandress, C., and J. F. Scinocca, 2005. The GCM response to current parameterizations of non-orographic gravity wave drag, *J. Atmos. Sci.*, **42**, 2394-2413.
- Mellor, G. L., and T. Yamada, 1974. A hierarchy of turbulence closure models for planetary boundary layers. *J. Atmos. Sci.*, **31**, 1791-1806.
- Miller, M. J., T. N. Palmer, and R. Swinbank, 1989. Parameterization and influence of sub-grid scale orography in general circulation and numerical weather prediction models, *Meteorol. Atmos. Phys.*, **40**, 84-109.
- Mlawer, E. J. S. Taubman, P. Brown, M. Iacono, and S. Clough, 1997. Radiative transfer for inhomogeneous atmospheres: RRTM, a validated correlated-k model for the longwave. *J. Geophys. Res.*, **102**, 16,663-16,682.
- Molina, M. J., and F. S. Rowland, 1974. Stratospheric sink for chlorofluoromethanes — Chlorine atomic-catalyzed destruction of ozone, *Nature*, **249**, 810-812.
- Moorthi, S., and M. J. Suarez, 1992. Relaxed Arakawa-Schubert: A parameterization of moist convection for general circulation models, *Mon. Wea. Rev.*, **120**, 978-1002.
- Morcrette, J.-J., 1989. Description of the radiative scheme in the ECMWF model, Technical Report, No. 260165, ECMWF, Reading, United Kingdom, 26 pp.
- Morcrette, J.-J., 1990. Impact of changes to the radiation transfer parameterizations plus cloud optical properties in the ECMWF model. *Mon. Wea. Rev.*, **118**, 847-873.
- Morcrette, J.-J., 1991. Radiation and cloud radiative properties in the ECMWF operational weather forecast model, *J. Geophys. Res.*, **96**, 9121– 9132.
- Morgenstern, O., P. Braesicke, M. M. Hurwitz, F. M. O'Connor, A. C. Bushell, C. E. Johnson, and J. A. Pyle, 2008. The World Avoided by the Montreal Protocol, *Geophys. Res. Lett.*, **35**, doi: 10.1029/2008GL034590.
- Morgenstern, O., P. Braesicke, F. M. O'Connor, A. C. Bushell, C. E. Johnson, S. M. Osprey, and J. A. Pyle, 2009. Evaluation of the new UKCA climate-composition model. Part 1: The stratosphere. *Geosci. Model Dev.*, **1**, 43-57.
- Morgenstern, O., M. A. Giorgetta, K. Shibata, V. Eyring, D. W. Waugh, T. G. Shepherd, H. Akiyoshi, J. Austin, A. J. G. Baumgaertner, S. Bekki, P. Braesicke, C. Brühl, M. P. Chipperfield, D. Cugnet, M. Dameris, S. Dhomse, S. M. Frith, H. Garny, A. Gettelman, S. C. Hardiman, M. I. Hegglin, P. Jöckel, D. E. Kinnison, J.-F. Lamarque, E. Mancini, E. Manzini, M. Marchand, M. Michou, T. Nakamura, J. E. Nielsen, D. Olivié, G. Pitari, D. A. Plummer, E. Rozanov, J. F. Scinocca, D. Smale, H. Teyssèdre, M. Toohey, W. Tian, Y. Yamashita, 2010. Review of the formulation of present-generation stratospheric chemistry-climate models and associated external forcings, *J. Geophys. Res.*, in press.
- Mote, P. W., K. H. Rosenlof, M. E. McIntyre, E. S. Carr, J. C. Gille, J. R. Holton, J. S. Kinniersley, H. C. Pumphrey, J. M. Russell, and J. W. Waters, 1996. An atmospheric tape recorder: The imprint of tropical tro-

- popause temperatures on stratospheric water vapor, *J. Geophys. Res.*, **101**, 3989-4006.
- Müller, J.-F., and G. Brasseur, 1995. IMAGES: A three dimensional chemical transport model of the global troposphere, *J. Geophys. Res.*, **100**, 16,445-16,490.
- Nissen, K. M., K. Matthes, U. Langematz, and B. Mayer, 2007. Towards a better representation of the solar cycle in general circulation models, *Atmos. Chem. Phys.*, **7**, 5391-5400.
- Nagashima, T., M. Takahashi, M. Takigawa, and H. Akiyoshi, 2002. Future development of the ozone layer calculated by a general circulation model with fully interactive chemistry, *Geophys. Res. Lett.*, **29**, doi:10.1029/2001GL014026.
- Nakajima, T., and M. Tanaka, 1986. Matrix formulation for the transfer of solar radiation in a plane-parallel scattering atmosphere, *J. Quant. Spectrosc. Radiat. Transfer*, **35**, 13-21.
- Nakajima, T., M. Tsukamoto, Y. Tsumi, A. Numaguti, and T. Kimura, 2000. Modeling of the radiative process in an atmospheric general circulation model, *Appl. Opt.*, **39**, 4869-4878.
- NASA, 1993. The atmospheric effects of stratospheric aircraft: Report of the 1992 Models and Measurements Workshop, NASA Publ. 1292.
- Neale, R. B., J. H. Richter and M. Jochum, 2008. The impact of convection on ENSO: From a delayed oscillator to a series of events, *J. Clim.*, **21**, 5904-5924.
- Noilhan, J. and S. Planton, 1989. A simple parameterization of land surface processes for meteorological models. *Mon. Wea. Rev.*, **117**, 536-549.
- Nozawa, T., T. Nagashima, T. Ogura, T. Yokohata, N. Okada, and H. Shiogama, 2007. Climate change simulations with a coupled ocean-atmosphere GCM called the model for interdisciplinary research on climate: MIROC, CGER's supercomputer monograph report, 12, ISSN 1341-4356, 79pp.
- Numaguti, A., 1993. Dynamics and energy balance of the Hadley circulation and the tropical precipitation zones: Significance of the distribution of evaporation, *J. Atmos. Sci.*, **50**, 1874-1887.
- Numaguti, A., M. Takahashi, T. Nakajima, and A. Sumi, 1995. Development of an atmospheric general circulation model, in *Reports of a New Program for Creative Basic Research Studies, Studies of Global Environment Change to Asia and Pacific Regions*, Rep. I-3, pp. 1 - 27, CCSR, Tokyo.
- Numaguti, A., S. Sugata, M. Takahashi, T. Nakajima, A. Sumi, 1997. Study on the climate system and mass transport by a climate model, *CGER's supercomputer monograph report*, **3**, CGER-I025-'97, NIES, Tsukuba, Japan, 91pp.
- Olivier, J., et al., 2005. Recent trends in global greenhouse gas emissions: regional trends and spatial distribution of key sources, In: "Non-CO2 Greenhouse Gases (NCGG-4)", van Amstel, A. (coord.), 325-330, Millpress, Rotterdam, ISBN 90 5966 043 9.
- Pawson, S., R. S. Stolarski, A. R. Douglass, P. A. Newman, J. E. Nielsen, S. M. Frith, and M. L. Gupta, 2008. Goddard Earth Observing System chemistry-climate model simulations of stratospheric ozone-temperature coupling between 1950 and 2005, *J. Geophys. Res.*, **113**, doi:10.1029/2007JD009511.
- Phillips, V. T., and L. J. Donner, 2006. Cloud microphysics, radiation and vertical velocities in two- and three-dimensional simulations of deep convection, *Quart. J. Roy. Meteorol. Soc.*, **132**, doi:10.1256/qj05.171.
- Pierrehumbert, R.T., 1986. An essay on the parameterization of orographic gravity wave drag. Proc. ECMWF 1986 Seminar, Vol. I, Reading, U.K., ECMWF, 251-282.
- Pitari, G., 1993. A numerical study of the possible perturbation of stratospheric dynamics due to Pinatubo aerosols: Implications for tracer transport, *J. Atmos. Sci.*, **50**, 2443-2461.
- Pitari G., E. Mancini, V. Rizi and D. T. Shindell, 2002. Impact of future climate and emission changes on stratospheric aerosols and ozone, *J. Atmos. Sci.*, **59**.
- Price, C., and D. Rind, 1992. A simple parameterization for calculating global lightning distributions, *J. Geophys. Res.*, **97**, 9919-9933.
- Price, C., and D. Rind, 1994. Modeling global lightning distributions in a general-circulation model, *Mon. Wea. Rev.*, **122**, 1930-1.
- Priestley, A., 1993. A quasi-conservative version of the semi-Lagrangian advection scheme, *Mon. Wea. Rev.*, **121**, 621-629. doi:10.1175/1520-0493.
- Putman, W. M., and S.-J. Lin, 2007. Finite-volume transport on various cubed-sphere grids, *J. Comp. Phys.*, **227**, 55-78.
- Ramaroson, R., M. Pirre, and D. Cariolle, 1992. A box model for online computations of diurnal variations

- in a 1-D model – Potential for application in multidimensional cases, *Ann. Geophys.*, **10**, 416-428.
- Rasch, P. J., N. M. Mahowald, and B. E. Eaton, 1997. Representations of transport, convection, and the hydrological cycle in chemical transport models: Implications for the modeling of short-lived and soluble species, *J. Geophys. Res.*, **102**, 28,127-28,138.
- Rasch, P. J., and J. E. Kristjánsson, 1998. A comparison of the CCM3 model climate using diagnosed and predicted condensate parameterizations, *J. Clim.*, **11**, 1587-1614.
- Rasch, P. J., D. B. Coleman, N. Mahowald, D. L. Williamson, S.-J. Lin, B. A. Boville, and P. Hess, 2006. Characteristics of atmospheric transport using three numerical formulations for atmospheric dynamics in a single GCM framework, *J. Clim.*, **19**, 2243-2266.
- Rayner, N. A., P. Brohan, D. E. Parker, C. K. Folland, J. J. Kennedy, M. Vanicek, T. Ansell, and S. F. B. Tett, 2006. Improved analyses of changes and uncertainties in sea surface temperature measured in situ since the mid-nineteenth century: The HadISST2 data set, *J. Clim.*, **19**, 3, 446-469.
- Reithmeier, C., and R. Sausen, 2002. ATTILA: atmospheric tracer transport in a Lagrangian model, *Tellus B*, **54**, 278-299.
- Ricard, J.-L., and J.-F. Royer, 1993. A statistical cloud scheme for use in a AGCM, *Ann. Geophys.*, **11**, 1095-1115.
- Richter, J. H., F. Sassi, and R. R. Garcia, 2010. Towards a physically based gravity wave source parameterization in a general circulation model, *J. Atmos. Sci.*, **67**, 136-156.
- Rienecker M. M., et al. (2008) The GEOS-5 Data Assimilation System—Documentation of versions 5.0.1, 5.1.0, and 5.2.0. NASA/TM-2008-104606, Vol. 27, Tech. Rep. Series on Global Modeling and Data Assimilation, 118 pp. (available at <http://gmao.gsfc.nasa.gov/systems/geos5/>)
- Robock, A., 2002. Pinatubo eruption: The climatic aftermath, *Science*, **295**, 1242-1244.
- Roeckner, E., K. Arpe, L. Bengtsson, S. Brinkop, L. Dümenil, M. Esch, E. Kirk, F. Lunkeit, M. Ponater, B. Rockel, R. Sausen, U. Schleese, S. Schubert, and M. Windelband, 1992. Simulation of the present-day climate with the ECHAM model: Impact of model physics and resolution, Max-Planck-Institut für Meteorology, MPI-Report No. 93.
- Roeckner, E., 1995. Parameterization of cloud radiative properties in the ECHAM4 model, in Cloud microphysics parameterizations in global circulation models, Proceedings of the WCRP Workshop, WCRP Report No. 93, WMO/TD–No. 713, 105–116.
- Roeckner, E., K. Arpe, L. Bengtsson, M. Christoph, M. Clausen, L. Dümenil, M. Esch, M. Giorgetta, U. Schleese, and U. Schulzweida, 1996. The atmospheric general circulation model ECHAM-4: Model description and simulation of present-day climate, Rep. 218, Max-Planck-Inst. für Meteorol., Hamburg, Germany.
- Roeckner, E., et al., 2003. The atmospheric general circulation model ECHAM5. Part I: Model description, MPI Report No. 218, Max-Planck-Institut für Meteorologie, Hamburg, Germany, 90pp.
- Roeckner, E., R. Brokopf, M. Esch, M. Giorgetta, S. Hagemann, L. Kornblüeh, E. Manzini, U. Schleese, and U. Schulzweida, 2004. The atmospheric general circulation model ECHAM5 Part II: Sensitivity of simulated climate to horizontal and vertical resolution, Max-Planck-Institute for Meteorology, MPI-Report No. 354, 2004.
- Roehl, C. M., S. A. Nizkorodov, H. Zhang, G. A. Blake, and P. O. Wennberg, 2002. Photodissociation of peroxyacetic acid in the near-IR, *J. Phys. Chem. A*, **106**, 3766-3772.
- Rossow, W. B., B. L. Garder, P. J. Lu, and A. W. Walker, 1987. Satellite cloud climatology project (ISCCP), Documentation on cloud data, WMO/TD-266, WMO, Geneva, 78.
- Roazanov, E., M. E. Schlesinger, V. Zubov, F. Yang, and N. G. Andronova, 1999. The UIUC three-dimensional stratospheric chemical transport model: Description and evaluation of the simulated source gases and ozone, *J. Geophys. Res.*, **104**, 11,755-11,781.
- Sander, S. P., R. R. Friedl, A. R. Ravishankara, D. M. Golden, C. E. Kolb, M. J. Kurylo, R. E. Huie, V. L. Orkin, M. J. Molina, G. K. Moortgat, and B. J. Finlayson-Pitts, 2002. Chemical kinetics and photochemical data for use in atmospheric studies, JPL Publications 02-25 (referred to as JPL, 2002)
- Sander, S. P., R. R. Friedl, D. M. Golden, M. J. Kurylo, R. E. Huie, V. L. Orkin, G. K. Moortgat, A. R. Ravishankara, C. E. Kolb, M. J. Molina, and B. J. Finlay-

- son-Pitts (2006), Chemical Kinetics and Photochemical Data for Use in Atmospheric Studies, Evaluation Number 15, JPL Publication, 06-2, Jet Propulsion Laboratory, Pasadena (referred to as JPL, 2006).
- Sander, R., A. Kerkweg, P. Jöckel, and J. Lelieveld, 2005. Technical note: The new comprehensive atmospheric chemistry module MECCA, *Atmos. Chem. Phys.*, **5**, 445–450.
- Sassi, F., B. A. Boville, D. Kinnison, and R. R. Garcia, 2005. The effects of interactive ozone chemistry on simulations of the middle atmosphere, *Geophys. Res. Lett.*, **32**, doi:10.1029/2004GL022131.
- Sato, M., J. E. Hansen, M. P. McCormick, and J. B. Pollack, 1993. Stratospheric aerosol optical depths, 1850-1990, *J. Geophys. Res.*, **98**, 22,987-22,994.
- Savage, N. H., K. S. Law, J. A. Pyle, A. Richter, H. Nuss, and J. P. Burrows, 2004. Using GOME NO<sub>2</sub> satellite data to examine regional differences in TOMCAT model performance, *Atm. Chem. Phys.*, **4**, 1895-1912.
- Scaife, A., N. Butchart, C. D. Warner, D. Stainforth, W. Norton, and J. Austin, 2000. Realistic Quasi-Biennial Oscillations in a simulation of the global climate. *Geophys. Res. Lett.*, **27**, 3481-3484.
- Scaife, A. A., N. Butchart, C. D. Warner, and R. Swinbank, 2002. Impact of a spectral gravity wave parameterization on the stratosphere in the Met Office Unified Model. *J. Atmos. Sci.*, **59**, 1473-1489.
- Schraner, M., E. Rozanov, C. Schnadt-Poberaj, P. Kenzelmann, A. Fischer, V. Zubov, B. P. Luo, C. Hoyle, T. Egorova, S. Fueglistaler, S. Brönnimann, W. Schmutz, and T. Peter, 2008. Technical Note: Chemistry-climate model SOCOL: Version 2.0 with improved transport and chemistry/microphysics schemes. *Atmos. Chem. Phys.*, **8**, 5957-5974.
- Schultz, M., et al., 2007. Emission data sets and methodologies for estimating emissions ([http://retro.enes.org/reports/D1-6\\_final.pdf](http://retro.enes.org/reports/D1-6_final.pdf)), REanalysis of the Tropospheric chemical composition over the past 40 years, A long-term global modeling study of tropospheric chemistry funded under the 5th EU framework programme, EU-Contract No. EVK2-CT-2002-00170.
- Scinocca, J. F., and N. A. McFarlane (2000), The parameterization of drag induced by stratified flow over anisotropic orography, *Quart. J. Roy. Meteorol. Soc.*, **126**, 2353-2393.
- Scinocca, J.F., 2003. An accurate spectral nonorographic gravity wave drag parameterization for General Circulation Models, *J. Atmos. Sci.*, **60**, 667-682.
- Scinocca, J. F., N. A. McFarlane, M. Lazare, J. Li and D. Plummer, 2008. Technical note: The CCCma third generation AGCM and its extension into the middle atmosphere, *Atmos. Chem. Phys.*, **8**, 7055-7074.
- Seinfeld, J.H., and S. N. Pandis, 2006. Atmospheric Chemistry and Physics - From Air Pollution to Climate Change (2nd Edition).. John Wiley & Sons., ISBN: 0471720186.
- Sellers, P. J., Y. Mintz, Y. C. Sud, and A. Dalcher, 1986. A simple biosphere model (Sib) for use within general circulation models, *J. Atmos. Sci.*, **43**, 505-531.
- Sessler, J., P. Good, A. R. MacKenzie, and J. A. Pyle, 1996. What role do type I polar stratospheric cloud and aerosol parameterizations play in modeled lower stratospheric chlorine activation and ozone loss?, *J. Geophys. Res.*, **101**, 28,817-28,835.
- Shaw, T. A., and T. G. Shepherd, 2007 Angular momentum conservation and gravity wave drag parameterization: Implications for climate models. *J. Atmos. Sci.*, **64**, 190-203.
- Shaw, T. A., M. Sigmond, T. G. Shepherd, and J. F. Scinocca, 2009. Sensitivity of simulated climate to conservation of momentum in gravity wave drag parameterization, *J. Clim.*, **22**, 2726-2742.
- Shepherd, T. G., K. Semeniuk, and J. N. Koshyk, 1996. Sponge layer feedbacks in middle-atmosphere models, *J. Geophys. Res.*, **101**, 23,447–23,464.
- Shepherd, T. G., 2003. Large-scale atmospheric dynamics for atmospheric chemists, *Chem. Revs.*, **103**, 4509-4531.
- Shepherd, T. G., and T. A. Shaw, 2004. The angular momentum constraint on climate sensitivity and downward influence in the middle atmosphere, *J. Atmos. Sci.*, **61**, 2899-2908.
- Shepherd, T. G., 2007. Transport in the middle atmosphere, *J. Meteorol. Soc. Japan*, **85B**, 165-191.
- Shibata, K., and T. Aoki, 1989. An infrared radiative scheme for the numerical models of weather and climate, *J. Geophys. Res.*, **94**, 14,923-14,943.
- Shibata, K., and A. Uchiyama, 1994. An application of the discrete ordinate method to terrestrial radiation in climate models, *J. Atmos. Sci.*, **51**, 3531-3538.
- Shibata, K., M. Deushi, T. T. Sekiyama, and H. Yoshimura

- (2005), Development of an MRI chemical transport model for the study of stratospheric chemistry, *Papers Meteorol. Geophys.*, **55**, 75-119.
- Shibata, K., and M. Deushi (2008a), Long-term variations and trends in the simulation of the middle atmosphere 1980-2004 by the chemistry-climate model of the Meteorological Research Institute, *Ann. Geophys.*, **26**, 1299-1326.
- Shibata, K., and M. Deushi, 2008b. Simulation of the stratospheric circulation and ozone during the recent past (1980-2004) with the MRI chemistry-climate model, *CGER's Supercomputer Monograph Report*, **13**, NIES, Japan, 154 pp.
- Shiogama, H., M. Watanabe, M. Kimoto, and T. Nozawa, 2005. Anthropogenic and natural forcing impacts on ENSO-like decadal variability during the second half of the 20th century, *Geophys. Res. Lett.*, **32**, doi:10.1029/2005GL023871.
- Slingo, J. M., 1987. The development and verification of a cloud prediction scheme for the ECMWF model, *Quart. J. Roy. Meteorol. Soc.*, **113**, 899-927.
- Smith, R. N. B., 1990. A scheme for predicting layer clouds and their water content in a general circulation model. *Quart. J. Roy. Meteorol. Soc.*, **116**, 435-460.
- Solanki S. K. and N. A. Krivova, 2003. Can solar variability explain global warming since 1970?, *J. Geophys. Res.*, **108**, doi:10.1029/2002JA009753.
- Steil, B., M. Dameris, C. Brühl, P. J. Crutzen, V. Grewe, M. Ponater, and R. Sausen, 1998. Development of a chemistry module for GCMs: First results of a multi-annual integration, *Ann. Geophys.*, **16**, 205-228.
- Stenchikov, G., K. Hamilton, R. J. Stouffer, A. Robock, V. Ramaswamy, B. Santer, and H.-F. Graf, 2006. Arctic Oscillation response to volcanic eruptions in the IPCC AR4 climate models, *J. Geophys. Res.*, **111**, D7, doi:10.1029/2005JD006286, 2006
- Stenke, A., V. Grewe, and M. Ponater, 2008a. Lagrangian transport of water vapor and cloud water in the ECHAM4 GCM and its impact on the cold bias, *Clim Dyn.*, **31**, 491-506.
- Stenke, A., M. Dameris, V. Grewe, and H. Garny, 2008b. Implications of Lagrangian transport for coupled chemistry-climate simulations, *Atmos. Chem. Phys.*, **9**, 5489-5504.
- Stott, P., G. Jones, J. Lowe, P. Thorne, C. Durman, T. Johns, and J. Thelen, 2006. Transient climate simulations with the HadGEM1 climate model: Causes of past warming and future climate change, *J. Clim.*, **19**, 2763-2782.
- Struthers, H., G. E. Bodeker, D. Smale, E. Rozanov, M. Schraner, and T. Peter, 2009. Evaluating how photochemistry and transport determine stratospheric inorganic chlorine in coupled chemistry-climate models. *Geophys. Res. Lett.*, **36**, doi:10.1029/2008GL036403.
- Sud, Y. C., W. C. Chao, and G. K. Walker, 1993. Dependence of rainfall on vegetation: Theoretical consideration, simulation experiments, observations, and inferences from simulated atmospheric soundings, *J. Arid. Environ.*, **25**, 5-18.
- Sud, Y. and G. K. Walker, 1999. Microphysics of clouds with the Relaxed Arakawa Schubert Scheme (McRAS). Part 1: Design and Evaluation with GATE Phase III Data. *J. Atmos. Sci.*, **56**, 3196-3220.
- Sundqvist, H., 1978. A parameterization scheme for non-convective condensation including prediction of cloud water content, *Quart. J. Roy. Meteorol. Soc.*, **104**, 677-690.
- Sundqvist, H., E. Berge, and J. E. Kristjansson, 1989. Condensation and cloud parameterization studies with a mesoscale numerical weather prediction model, *Mon. Wea. Rev.*, **117**, 1641-1657.
- Takahashi, M., 1996. Simulation of the stratospheric quasi-biennial oscillation using a general circulation model, *Geophys. Res. Lett.*, **23**, 661-664.
- Takahashi, M., 1999. Simulation of the quasi-biennial oscillation in a general circulation model, *Geophys. Res. Lett.*, **26**, 1307-1310.
- Takigawa, M., M. Takahashi, and H. Akiyoshi, 1999. Simulation of ozone and other chemical species using a Center for Climate System Research/National Institute for Environmental Studies atmospheric GCM with coupled stratospheric chemistry, *J. Geophys. Res.*, **104**, 14003-14018.
- Talukdar, R. K., C. A. Longfellow, M. K. Gilles, and A. R. Ravishankara, 1998. Quantum yields of O(1D) in the photolysis of ozone between 289 and 329 nm as a function of temperature, *Geophys. Res. Lett.*, **25**, 143-146.
- Teyssède H., M. Michou, H. L. Clark, B. Josse, F. Karcher, D. Olivie, V.-H. Peuch, D. Saint-Martin, D. Cariolle, J.-L. Attié, P. Nédélec, P. Ricaud, V. Thouret, R. J. van der A, A. Volz-Thomas, and F. Cheroux, 2007.

- A new tropospheric and stratospheric chemistry and transport model MOCAGE-Climat for multi-year studies: Evaluation of the present-day climatology and sensitivity to surface processes, *Atmos. Chem. Phys.*, **7**, 5815-5860.
- Tian, W., and M. P. Chipperfield, 2005. A new coupled chemistry-climate model for the stratosphere: the importance of coupling for future O<sub>3</sub>-climate predictions, *Quart. J. Roy. Meteorol. Soc.*, **131**, 281-303.
- Tian, W., and M. P. Chipperfield, 2006. Stratospheric water vapor trends in a coupled chemistry-climate model, *Geophys. Res. Lett.*, **33**, doi:10.1029/2005GL024675.
- Tiedtke, M., 1989. A comprehensive mass flux scheme for cumulus parameterization in large-scale models, *Mon. Wea. Rev.*, **117**, 1779-1800.
- Thomason, L. W., L. R. Poole, and T. Deshler, 1997. A global climatology of stratospheric aerosol surface area density deduced from Stratospheric Aerosol and Gas Experiment II measurements: 1984-1994, *J. Geophys. Res.*, **102**, 8967-8976.
- Thomason, L., and T. Peter, 2006. Assessment of Stratospheric Aerosol Properties (ASAP), SPARC Report No. 4., WCRP-124, WMO/TD-No. 1295.
- Tompkins, A., 2002. A prognostic parameterization for the subgrid-scale variability of water vapor and clouds in large-scale models and its use to diagnose cloud cover. *J. Atmos. Sci.*, **59**, 1917-1942.
- Tost, H., P. Jöckel, and J. Lelieveld, 2007. Lightning and convection parameterisations – uncertainties in global modeling, *Atmos. Chem. Phys.*, **7**, 4553-4568.
- Untch, A., A. Simmons, et al., 1998. Increased stratospheric resolution in the ECMWF forecasting system, ECMWF Newsletter, 82, 2-8.
- Uno, I., X.-M. Cai, D. G. Steyn, and S. Emori (1995), A simple extension of the Louis method for rough surface layer modeling, *Bound. Layer Meteorol.*, **76**, 395-409.
- Van Aardenne, J., et al., 2005. The EDGAR 3.2 Fast Track 2000 dataset (32FT2000), Technical documentation, <http://www.mnp.nl/edgar/model/v32ft2000edgar>.
- Vogel, B., P. Konopka, J.-U. Grooss, R. Müller, B. Funke, M. Lopez-Puertas, T. Reddmann, G. Stiller, T. von Clarmann, and M. Riese (2008), Model simulations of stratospheric ozone loss caused by enhanced mesospheric NO<sub>x</sub> during Arctic winter 2003/2004, *Atmos. Chem. Phys.*, **8**, 5279-5293.
- Walcek, C. J., R. A. Brost, J. S. Chang, and M. L. Wesely (1986), SO<sub>2</sub>, sulfate and HNO<sub>3</sub> deposition velocities computed using regional landuse and meteorological data, *Atmos. Env.*, **20**, 949-964.
- Warner, C. D., and M. E. McIntyre, 2001. An ultrasimple spectral parameterization for non-orographic gravity waves, *J. Atmos. Sci.*, **58**, 1837-1857.
- Warrilow, D.A., A. B. Sangster, and A. Slingo, 1986. Modelling of land surface processes and their influence on European climate; Meteorological Office, Met O 20 Tech. Note DCTN 38, Bracknell, U.K..
- Waugh, D. W., L. Oman, S. R. Kawa, R. S. Stolarski, S. Pawson, A. R. Douglass, P. A. Newman, and J. E. Nielsen. 2009. Impacts of climate change on stratospheric ozone recovery, *Geophys. Res. Lett.*, **36**, doi:10.1029/2008GL036223.
- Webster, S., A. R. Brown, D. R. Cameron, and C. P. Jones, 2003. Improvements to the representation of orography in the Met Office Unified Model. *Quart. J. Roy. Meteorol. Soc.*, **129**, 1989-2010. doi:10.1256/qj.02.133.
- Williamson, D. L., and P. J. Rasch, 1989. Two-dimensional semi-Lagrangian transport with shape-preserving interpolation, *Mon. Wea. Rev.*, **117**, 102-129.
- World Meteorological Organisation Scientific assessment of ozone depletion, Global Ozone Res. Monit. Rep. 16, Geneva, 1992.
- World Meteorological Organization (WMO)/United Nations Environment Programme (UNEP), 2007. *Scientific Assessment of Ozone Depletion: 2006*, World Meteorological Organization, Global Ozone Research and Monitoring Project, Report No. 50, Geneva, Switzerland.
- Xiao, F., and X. Peng, 2004. A convexity preserving scheme for conservative advection transport, *J. Comput. Phys.*, **198**, 389-402, doi:10.1016/j.jcp.2004.01.013.
- Yessad, K., 2001. Horizontal diffusion computations in the cycle 24T1 of ARPEGE/IFS. ARPEGE Technical Documentation, 96pp.
- Yukimoto, S., A. Noda, A. Kitoh, M. Hosaka, H. Yoshimura, T. Uchiyama, K. Shibata, O. Arakawa, and S. Kusunoki, 2006. Present-day climate and climate sensitivity in the Meteorological Research Institute coupled GCM version 2.3 (MRI-CGCM2.3), *J. Meteorol. Soc. Japan*, **84**, 333-363.
- Zdunkowski, W. G., R. M. Welch, and G. Korb, 1980. An

investigation of the structure of typical two-stream-methods for the calculation of solar fluxes and heating rates in clouds. *Contr. Phys. Atmos.*, **53**, 147-166.

Zhong, W. and J. D. Haigh, 2001. An efficient and accurate correlated-k parameterization of infrared radiative transfer for troposphere-stratosphere-mesosphere GCMs, *Atmos. Sci. Lett.*, **1**, doi:10.1006/asle.2000.0022.

Zhong, W, J. D. Haigh, D. Belmiloud, R. Schermail, and J. Tennyson, 2001. The impact of new water vapour spectral line parameters on the calculation of atmospheric absorption, *Quart. J. Roy. Meteorol. Soc.*, **127**, 1615-1626.

Zhong, W., S. M. Osprey, L. J. Gray, and J. D. Haigh, 2008. Influence of the prescribed solar spectrum on calculations of atmospheric temperature. *Geophys. Res. Lett.*, **35**, doi:10.1029/2008GL035993.

Zubov, V., E. Rozanov, and M. Schlesinger, 1999. Hybrid scheme for three-dimensional advective transport, *Mon. Wea. Rev.*, **127**, 1335-1346.



Table O-1: Number of reference simulations by model

CCM	REF-B0: 2000 time slice	REF-B1: 1960-2006	REF-B2: 1960-2100
AMTRAC3	0	1 (to 2007)	1
CAM3.5	1	1	1
CCSRNIES	1	1	1
CMAM	1	3	3
CNRM-ACM	2 (20, 17 years)	2 (1960-2005)	1
E39CA	0	1 (to 2004)	0
EMAC	0	1 (to 2000)	0
GEOSCCM	1	1	1 (from 2000)
LMDZrepro	0	3	1
MRI	1/36yrs	4	2
Niwa-SOCOL	1	1	1
SOCOL	1	3	3
ULAQ	1	4	3
UMETRAC	1	1	0
UMSLIMCAT	1 (15 years)	1 (45 years)	1
UMUKCA-METO	1	1	1 (to 2083)
UMUKCA-UCAM	1	1	1
WACCM	1	3	3

Table O-2: Control and sensitivity simulations, number of simulations per CCM.

CCM	CTL-B0 1960 time slice	SCN-B1 incl. brominated VLS	SCN-B2a 2000- 2100 Diff. GHG scen.
CCSRNIES	1	0	0
MRI	1	0	0
Niwa-SOCOL	1	1	0
ULAQ	1	0	0

Table O-2, continued.

CCM	SCN-B2b: 1960-2100, fixed halogens	SCN-B2c: 1960-2100, no climate ch.	SCN-B2d: 1960-2100, nat. forcing
CCSRNIES	1 (in Dec 2009)	0	0
E39CA	0	0	1 (to 2049)
ULAQ	0	1	0



Table O-4: References for physical parameterizations. LMDZrepro is investigating a problem with tropical UTLS water vapour. Table O-4 continues next page.

<b>CCM</b>	<b>Turbulent vertical fluxes, dry convection</b>	<b>Moist convection</b>	<b>Cloud microphysics</b>
CAM3.5	Holtslag and Boville (1993)	Neale et al. (2008) (deep) Hack (1994) (shallow)	Rasch and Kirstjánsson (1998)
CCSRNIES	Mellor and Yamada (1974)	Arakawa and Schubert (1974) Moorthi and Suarez (1992)	Large-scale condensation with prognostic cloud water scheme
CMAM	Scinocca et al. (2008)	Scinocca et al. (2008)	Scinocca et al. (2008)
CNRM-ACM	Ricard and Royer (1993)	Bougeault (1985)	Ricard and Royer (1993)
E39CA	Louis (1979); Brinkop and Roeckner (1995)	Tiedtke (1989) Brinkop and Sausen (1997)	Sundquist (1978)
EMAC	Tost et al. (2007)	Tost et al. (2007)	Lohmann and Roeckner (1996)
GEOSCCM	Louis et al. (1982) (stable PBL); Lock et al. (2000) unstable or cloud-topped PBL	Relaxed Arakawa-Schubert (RAS) (Moorthi and Suarez, 1992)	Sud and Walker (1999)
LMDZrepro	Hourdin et al. (2006)	Hourdin et al. (2006)	Hourdin et al. (2006)
MRI	Level2, no dry convection	Arakawa and Schubert (1974)	None
SOCOL Niwa-SOCOL	Tiedtke (1989) Louis (1979)	Brinkop (1991, 1992)	Sundqvist (1978); Tiedtke (1989)
ULAQ	Müller and Brasseur (1995)	Müller and Brasseur (1995)	Kärcher and Lohmann (2001)
UMETRAC UMSLIMCAT	Gordon et al. (1999)	Gregory et al. (1997, 1998)	Smith (1990)
UMUKCA-METO UMUKCA-UCAM	Martin et al. (2000)	Martin et al. (2000)	Martin et al. (2000)
WACCM	Holtslag and Boville (1993)	Neale et al. (2008) (deep) Hack (1994) (shallow)	Rasch and Kirstjánsson (1998)

Table O-4, continued

<b>CCM</b>	<b>Aerosol microphysics</b>	<b>Cloud cover</b>	<b>Cloud microphysics</b>
CAM3.5	N/A	Slingo (1987); Collins et al. (2004)	Collins et al. (2004)
CCSRNIES	N/A	Numaguti et al. (1997)	Le Treut and Li (1991)
CMAM	Scinocca et al. (2008)	Scinocca et al. (2008)	Scinocca et al. (2008)
CNRM-ACM	N/A	Strati: Ricard and Royer (1993) Conv: Bougeault (1985)	Ricard and Royer (1993)
E39CA	N/A	Sundquist (1978)	Sundqvist et al. (1989); Roeckner (1995)
EMAC	N/A	Tompkins (2002)	Lohmann and Roeckner (1996) with some revisions
GEOSCCM	N/A	Rienecker et al. (2008)	Sud and Walker (1999)
LMDZrepro	N/A	Hourdin et al. (2006)	Hourdin et al. (2006)
MRI	None	Relative humidity dependent	None
SOCOL Niwa-SOCOL	Koepke et al. (1997)	Sundqvist (1978)	Manzini and McFarlane (1998) Sundqvist (1978)
ULAQ	Pitari et al. (2002)	Rossow et al. (1987)	N/A
UMETRAC	Cussack et al. (1998)	Smith (1990)	Smith (1990)
UMSLIMCAT	N/A	Smith (1990)	Smith (1990)
UMUKCA-METO UMUKCA-UCAM	Martin et al. (2000)	Martin et al. (2000)	Martin et al. (2000)
WACCM	N/A	Slingo (1987); Collins et al. (2004)	Collins et al. (2004)

Table O-5: Surface, soil, and boundary layer schemes

CCM	Land surface scheme (reference)	Soil moisture (reference)	Planetary boundary layer scheme (reference)
CAM3.5	Bonan et al. (2002)	Bonan et al. (2002)	Holtslag and Boville (1993)
CCSRNIES	Kanae et al. (1995)	Manabe et al. (1965) Numaguti et al. (1997)	Louis (1979), Uno et al. (1995)
CMAM	CLASS 2.7 (Scinocca et al., 2008)	Scinocca et al. (2008)	Scinocca et al. (2008)
CNRM-ACM	ISBA, Noilhan and Planton (1989) – Douville et al. (2000)	ISBA, Noilhan and Planton (1989) – Douville et al. (2000)	Boundary layer based on Louis (1982) modified by Mascart et al. (1995)
E39CA	Dümenil and Todini (1992) Roeckner et al. (1992)	Roeckner et al. (1996)	Louis (1979); Roeckner et al. (1996)
EMAC	Roeckner et al. (2003)	Dümenil and Todini (1992)	Roeckner et al. (2003)
GEOSCCM	Koster et al. (2000)	Koster et al. (2000)	Lock et al. (2000)
LMDZrepro	Hourdin et al. (2006)	Hourdin et al. (2006)	Hourdin et al. (2006)
MRI	Improved SiB, 3 layers (Shibata et al., 2005)	Improved SiB, 3 layers (Shibata et al., 2005)	Mellor and Yamada (1974) level 2 Louis et al. (1982) surface layer
SOCOL Niwa-SOCOL	Blondin and Böttger (1987) Sellers et al. (1986) Fischer et al. (2008)	Warrilow et al. (1986)	Louis (1979)
ULAQ	N/A	N/A	Specification of emissions and deposition velocities: Müller and Brasseur (1995)
UMETRAC UMSLIMCAT	Cox et al. (1999)	Cox et al. (1999)	Cox et al. (1999)
UMUKCA-METO UMUKCA-UCAM	Martin et al. (2000)	Martin et al. (2000)	Martin et al. (2000)
WACCM	Bonan et al. (2002)	Bonan et al. (2002)	Holtslag and Boville (1993)

# Chapter 3

## Radiation

**Lead Authors:** Victor Fomichev & Piers M. Forster

**Co-authors:** Chiara Cagnazzo  
Andreas I. Jonsson  
Ulrike Langematz  
Eugene Rozanov

**Contributors:** Victoria Falaleeva, Boris Fomin, Nathan Gillett, Michael Iacono, Alexey Karpechko, Jiangnan Li, Perrine Lemennais, Bernard Mayer, Eli Mlawer, Olaf Morgenstern, Gunnar Myhre, Sophie Oberländer, Robert Portmann, Michael Sigmund

---

### 3.1 Introduction

Understanding and quantifying radiative processes is of fundamental importance to the study of climate and its change. Radiative processes drive global climate change and play a key role in establishing the temperature structure of the atmosphere. The thermal regime of the middle atmosphere is determined to a great extent by the balance between the incoming solar and outgoing infrared radiation. The radiative heating changes brought on by changes in carbon dioxide and ozone can cause large trends in

stratospheric temperatures as well as affect surface climate (WMO, 2003). Given the prime importance of radiative processes for understanding the atmosphere and its evolution, the development and improvement of radiation schemes is obviously one of the crucial points in the ongoing development and maintenance of atmospheric models. The purpose of this chapter is to evaluate key radiative processes in the CCMVal models.

This chapter covers a number of topics. Current radiative parameterisation architecture is assessed in Section 3.2. Global mean temperature profiles and long-term trends provided by CCMVal models are analysed in Section 3.3. In Section 3.4, radiative transfer schemes of different CCMVal models are compared with each other and compared against line-by-line (LBL) calculations. The

incoming solar irradiance at short wavelengths significantly varies with the solar cycle, leading to strong ozone and temperature solar signals in the stratospheric climate. The ability of CCMval models' radiation schemes to reproduce the solar signal is analysed in Section 3.5. The last four sections present metric summaries (3.6), model by model analysis (3.7), recommendations (3.8) and the executive summary (3.9).

### 3.1.1 Radiative based diagnostics

**Table 3.1** presents the details of the radiative diagnostics and the metrics used to assess them.

Throughout the chapter we have tried to explain differences between CCMs. However, in many instances appropriate diagnostics were not available and interpretation is lacking, so a full assessment of differences has not been possible.

Several radiative processes are not assessed in this chapter. A representation of photolysis is of fundamental importance for CCMs: this aspect of radiation is discussed in Chapter 6. Above 70 km, local thermodynamic equilibrium (LTE) begins to breakdown (see Fomichev 2009 for a detailed review of non-LTE effects). At present only two CCMs include these effects (CMAM and WACCM), and both employ the same parameterisation (Fomichev *et al.*, 1998; Ogibalov and Fomichev, 2003). Clouds and aerosols (both stratospheric and tropospheric) also have important effects on stratospheric heating rates and on radiative forcing but these effects are not evaluated here. We also do not assess the effects of the plane parallel atmosphere approximation that is typically employed in radiation codes. This approximation fails to give any solar heating at zenith angles larger than 90°. Lastly we do not assess the way the radiation scheme is implemented within the CCM. Important considerations here are the frequency of full radiative calculations compared to the model time step; sub-grid-scale variations and the order of the radiation call in relation to the call to other physical parameterisations.

## 3.2 Radiative Transfer Parameterizations

Accurate methods of solving radiative transfer within the Earth's atmosphere exist. However, such schemes are too computationally expensive to currently be employed within a climate modelling context. Parameterisations were designed to approximate more exact treatments with sufficient enough accuracy for the problem being considered. A good example of this is one of the earliest parameterisations of solar radiative transfer (Lacis and Hansen, 1974). Their approximations provide useful insights into more complex ones used today. Even their simple param-

eterisation accounted for Rayleigh scattering, cloud, solar zenith angle, water vapour and ozone absorption, but like many shortwave codes today, it ignored minor absorption by CO<sub>2</sub> and CH<sub>4</sub> (see Collins *et al.*, 2006). For its purpose the code was extremely accurate and only increased the computer time overhead in the parent model by 0.3%; variants of this code were employed in climate models until very recently. Much of their original paper was concerned with finding measurements of input properties to test their code and they made the point that uncertainties in water vapour or cloud radiative properties are likely to be a bigger source of error than their approximate radiative transfer solution – this still remains true today.

Radiative transfer approximations within climate models encompass three broad categories of 1) the radiative transfer solution, 2) input parameters and 3) implementation. These are described briefly below

1. *Radiative transfer solution.* The most important choice here is the number of spectral bands to employ and how to account for overlapping within bands. Also important are the number of streams used for scattering approximations. In the CCM context it is also worth considering the choice of a plane parallel atmosphere: nearly all climate models including CCMs adopt this approximation, even when the photolysis codes in CCMs adopt spherical geometry. Most CCMs would therefore not have any solar heating at zenith angles greater than 90°, but still have photolysis of ozone in the stratosphere, creating an inconsistency.
2. *Input parameters.* Important choices include line databases and cross-sections for the absorbing gases and the water vapour continuum; the extra-terrestrial solar spectrum; and cloud and aerosol optical properties.
3. *Implementation.* CCMs and climate models also have to make pragmatic choices about how often to call the radiative transfer code, as calling the code every time step is often impractical and unnecessary. Also choices of cloud overlap and sub-grid-scale variability need to be made. Ways of calculating solar zenith angle and Earth-Sun distance can also cause differences between models. Differences in the underlying model's vertical resolution can also affect the radiation scheme.

Several previous inter-comparisons of climate model radiative transfer codes have been undertaken (*e.g.*, Forster *et al.*, 2001; Collins *et al.*, 2006; Goldblatt *et al.*, 2009; Myhre *et al.*, 2009). Most of these studies have found very significant differences between radiation codes, even when considering only clear skies and constraining many of the input parameters. Common problems identified have been the use of radiation codes beyond their original limitations



**Table 3.1:** Summary of the radiative diagnostics and the metrics used to assess them.

Process	Diagnostic	Variables	Data	Metric	Section
Stratospheric temperatures	Comparing 1980-1999 climatological global mean temperature profiles	Temperature, Atmospheric composition	(Re)analyses	Maximum difference between ERA-40 and either UKMO or NCEP analysis	3.3
Stratospheric temperature change	Comparing 1980-1999 global mean temperature trends	Temperature, Atmospheric composition	MSU/SSU trends	MSU/SSU trend uncertainty 95% confidence interval	3.3
Radiative fluxes	Comparing climatological fluxes in offline radiation schemes	Shortwave, longwave up/down/net fluxes for global daily average	LBL and other sophisticated offline radiation models	Maximum difference between sophisticated radiation models	3.4
Radiative forcing	Comparing forcings in offline radiation schemes for a variety of atmospheric composition changes	Global and diurnal mean shortwave, longwave up/down/net instantaneous forcings.	LBL and other sophisticated offline radiation models	Maximum difference between sophisticated radiation models	3.4
Stratospheric heating/cooling	Comparing climatological heating/cooling rates in offline radiation schemes	Global and diurnal mean shortwave, longwave/net heating rates	LBL and other sophisticated offline radiation models	Maximum difference between sophisticated radiation models	3.4
Changes in stratospheric heating/cooling	Comparing changes in heating/cooling rates in offline radiation schemes	Global and diurnal mean changes in shortwave, longwave, net heating rates	LBL and other sophisticated offline radiation models	Maximum difference between sophisticated radiation models	3.4
Solar variability	Comparing SW heating rates in offline radiation schemes with prescribed solar spectrum variations and ozone change	Shortwave heating rates	Sophisticated offline radiation model	Whether or not radiation code reproduces sophisticated model signal	3.5

and/or using outdated input data for, for example, spectral line databases.

Some details of the CCM radiation codes employed are presented in Chapter 2 Tables 2.10 and 2.11. All employ versions of the two stream approximation for solving scattering and have an order of 10 spectral bands in the shortwave and longwave. Although all codes include the main absorbers, minor absorbers differ between codes. They also employ different spectral line databases.

### 3.3 Global mean temperature and temperature trends in CCMs

In this section the performance of the models in terms

of their global mean temperature climatology and global mean temperature trends is assessed. On a globally averaged basis the temperature in the middle atmosphere below about 70 km is controlled mainly by radiative processes. This means that long-term global mean temperature biases between models and observations are mainly due to either inaccuracies in the model treatments of radiative processes or due to inaccurate distributions of radiatively active gases in the models. Below 70 km the major contributions to the radiative energy budget are provided by ozone, carbon dioxide, and water vapour. For CCMVal, carbon dioxide is specified identically in all models so its abundance should not contribute to any model differences. However, the distributions of ozone and water vapour, which are affected by the transport and chemistry schemes

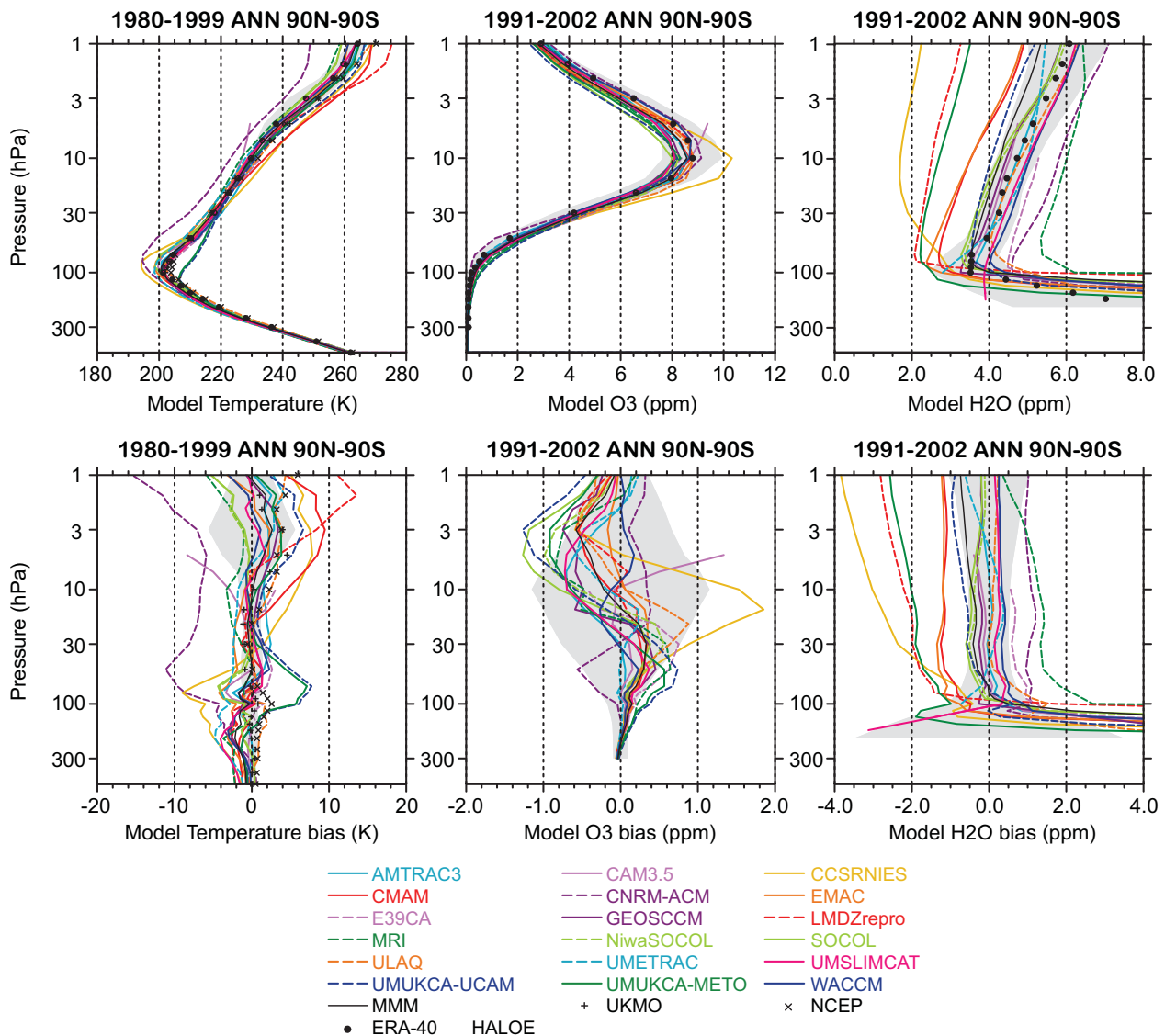


**Figure 3.1:** Climatological global and annual mean (a) temperature, (b) ozone mixing ratio, and (c) water vapour mixing ratio for REF-B1 model simulations and reference data sets; and (d) temperature bias, (e) ozone bias and (f) water vapour bias with respect to reference data sets. Reference data sets include ERA-40, NCEP and UKMO reanalyses for temperature and HALOE observations for ozone and water vapour. For temperature, the climatological means and biases are calculated for 1980-1999 except for UKMO reanalyses which are shown for 1992-2001. Biases are calculated relative to the ERA-40 reanalyses. For ozone and water vapour, the climatological means and biases are calculated for 1991-2002 except for EMAC and UMETRAC which are shown for 1991-2000. The grey areas show ERA-40 and HALOE plus and minus two standard deviations about the climatological means. The solid black lines indicate the multi-model mean results. For other data sets, see legend. Model acronyms are described in Table 1.1 and details for each model are given in Chapter 2.

of each individual model, affect the calculated temperature biases. Overestimation of ozone should generally lead to a warm bias (due to larger ozone solar heating) while overestimation of water vapour should generally lead to a cold bias (due to larger infrared cooling), and *vice versa*. Thus, inter-comparison of model results for temperature on the one hand and ozone and water vapour on the other hand provides some guidance as to whether model temperature

biases are due to biases in the abundance of these chemical species or due to inaccuracies in the radiation schemes.

A model's ability to reproduce the observed temperature climate does not ensure an accurate sensitivity to perturbations, such as increasing GHGs and ozone depletion. Therefore, we assess model temperatures and model temperature trends separately. The model temperature climatologies are discussed in Section 3.3.1 and the model

temperature trends for the past and future are discussed in Sections 3.3.2 and 3.3.3, respectively.

The analyses presented for the climatology and the past trends are based on model results from the REF-B1 scenario, including observed surface forcings of sea surface temperatures (SSTs), greenhouse gases (GHGs) and ozone depleting substances (ODSs), and variations in volcanic aerosols and solar forcing. To assess future trends, however, model results for the REF-B2 scenario are used. The REF-B2 experiments include the same surface forcing of GHGs and ODSs as REF-B1 but do not include variations in volcanic aerosol and solar forcing. For a complete description of the REF-B1 and REF-B2 scenarios see Chapter 2. For models that have provided multiple ensemble members (for REF-B1: CMAM, CNRM-ACM, LMDZrepro, MRI, SOCOL and WACCM) the results presented show the ensemble mean values, unless stated otherwise.

### 3.3.1 Global mean temperature climatology

Figure 3.1a shows global mean vertical temperature profiles averaged over 1980-1999 for both the REF-B1 model experiments and for three reanalyses data sets, the latter including ERA-40, NCEP and UKMO (note that the UKMO climatology is derived for 1992-2001). The grey shaded area shows ERA-40 plus and minus two standard deviations about the climatological mean, indicating the interannual variability of this data set. All models capture the large scale features of the troposphere and stratosphere, with decreasing temperatures with height in the troposphere, a distinct temperature minimum at the tropopause around 100 hPa and increasing temperature with height in the stratosphere. The spread between the models is larger in the stratosphere than in the troposphere. Figure 3.1d shows model biases with respect to the ERA-40 climatology. NCEP and UKMO are generally close to ERA-40, but are up to 3 K warmer around the tropopause (near 100 hPa) and up to 6 K warmer in the upper stratosphere. Most models agree well with the observations and are generally within  $\pm 5$  K of the ERA-40 temperatures. Exceptions are the temperatures from CAM3.5, CCSRNIES, CMAM, CNRM-ACM, LMDZrepro, UMUKCA-METO and UMUKCA-UCAM. CAM3.5, with an upper model boundary at 3 hPa, provides data only up to 5 hPa where it under-estimates temperatures by up to 9 K. CCSRNIES has a cold bias around the tropopause that maximises at -9 K near 70 hPa, and a positive bias of up to 8 K in the middle and upper stratosphere. CMAM displays a similar positive bias of up to 9 K in the middle and upper stratosphere. CNRM-ACM has a cold bias throughout the stratosphere with maximum values of -11 K and -15 K in the lower and upper stratosphere, respectively. LMDZrepro has a warm bias of up to 15 K in the upper stratosphere. UMUKCA-METO and UMUKCA-

UCAM both display a distinct warm bias of up to 7-8 K in the lower stratosphere, and UMUKCA-UCAM has a warm bias of up to 6 K in the upper stratosphere. Finally it can be noted that the multi-model mean results fall within the ERA-40 interannual variability limits above about 70 hPa, *i.e.*, throughout most of the stratosphere. Below 70 hPa, particularly in the upper troposphere between 300 and 100 hPa, there is a general tendency for the models to have a cold bias. These results are roughly in agreement with the previous multi-model temperature assessment, performed for CCMVal-1 (Austin *et al.*, 2009).

Below follows a qualitative assessment that attempts to identify which features of the temperature biases highlighted above are associated with biases in ozone and water vapour. Models without a clear connection between temperature biases on the one hand, and ozone and water vapour biases on the other, are as discussed earlier likely to have deficiencies in their radiation scheme. Note that the focus here is on explaining features in the temperature fields, not in ozone or water vapour, which are dealt with separately in Chapter 6. Also note that inferences in this section are suggestive. The methodology cannot rule out unknown reasons for model biases. For example, effects of different treatments of clouds and aerosols may have a significant impact on the results in the lower stratosphere, but are not considered in the following analysis.

A more detailed assessment of the radiation scheme performances based on radiative fluxes and heating rates is given in Section 3.4. The combined effect of errors in heating rates and distribution of radiatively active gases on biases in the global mean temperature climatology is analysed in Section 3.4.6.

Figures 3.1b and 3.1c show global mean vertical ozone and water vapour profiles averaged over 1991-2002 for the REF-B1 model experiments and for HALOE observations. Figure 3.1e and 3.1f show model biases with respect to the HALOE climatology. The grey shaded areas show the HALOE plus and minus two standard deviations about the climatological mean.

For ozone, model values are generally within  $\pm 1$  ppm of the observations, with a tendency for the models to overestimate ozone in the lower stratosphere and to underestimate ozone in the upper stratosphere. The multi-model mean results fall well within the HALOE interannual variability limits throughout the stratosphere and upper troposphere. For water vapour, the inter-model spread is much larger, and biases with respect to the observed climatology are in some cases in excess of 50% of the climatological values themselves. The multi-model mean results underestimate the observations by about 1 ppm in the stratosphere, but are within the HALOE interannual variability limits in this region. Generally, ozone biases are expected to have a larger impact on the temperature than biases in water vapour, since the longwave radiative effect of water

vapour generally is overshadowed by that from CO<sub>2</sub> (an exception is the lower stratosphere, see *e.g.*, Fomichev 2009). However, water vapour biases as large as those presented here can have a significant effect on the radiative balance throughout the stratosphere. For example, in CMAM the inclusion of water vapour cooling in the upper stratosphere leads to a temperature reduction of about 5 K in this region (Fomichev *et al.*, 2004), which suggests that large water vapour biases could have a significant impact throughout the stratosphere. Notably, all the models with a significant warm bias in the middle to upper stratosphere (CCSRNIES, CMAM and LMDZrepro) display significant negative biases in water vapour.

CAM3.5 water vapour biases are small (Figure 3.1f), and a large overestimation of ozone mixing ratios in excess of 1 ppm near the model upper boundary (Figure 3.1e), which should lead to overestimated solar heating, seems inconsistent with the CAM3.5 cold bias in this region. Hence the cold bias for this model above 10 hPa is likely to be due to inaccuracies in the model's radiative scheme or possibly associated with the low upper boundary.

CCSRNIES displays the largest bias in water vapour of all models. The model under-estimates the observed values by 2-4 ppm in the middle and upper stratosphere, which likely explains a significant fraction of the model's warm bias in this region. CCSRNIES also overestimates ozone near its peak in the middle stratosphere by almost 2 ppm, which should also contribute to the warm bias. Thus, it is possible that the warm bias in the middle stratosphere is due to biases in ozone and water vapour alone, while in the upper stratosphere, where the model simulation of ozone is quite adequate, the water vapour bias is unlikely to be responsible for the entire 8 K bias there. Also, the

cold bias in the lower stratosphere and upper troposphere, cannot be linked to biases in ozone and water vapour, and thus is likely due to inaccuracies in the model's radiative scheme.

CMAM displays a similar positive temperature bias to that of CCSRNIES in the middle and upper stratosphere. While CMAM under-estimates water vapour by about 1 ppm throughout the stratosphere, which should lead to somewhat under-estimated infrared cooling, this can only explain a small fraction of the CMAM warm bias. Furthermore, the fact that CMAM under-estimates ozone slightly in this region, which should lead to reduced solar heating, suggests that the CMAM warm bias in this region is likely to be primarily due to inaccuracies in the model's radiative scheme.

CNRM-ACM ozone biases are small, and although a 1 ppm positive bias in water vapour throughout the stratosphere should contribute to a somewhat overestimated infrared cooling, the bulk of the cold bias in this model is likely to be due to inaccuracies in the model's radiative scheme.

LMDZrepro displays similar biases as CMAM, with overestimated upper stratospheric temperatures, a slight low ozone bias in the upper stratosphere, and a negative bias in water vapour throughout the stratosphere. Although the water vapour bias for LMDZrepro is significantly stronger than for CMAM, amounting to 2-3 ppm, this bias is not sufficient to explain the large warm bias in the upper stratosphere. This and the fact that LMDZrepro agrees well with observed temperatures below 5 hPa (despite a large water vapour bias there) suggests that inaccuracies in the model's radiative scheme should be the main cause for the LMDZrepro temperature bias.

**Table 3.2:** Model temperature climatology bias (K) with respect ERA-40 for 1980-1999 at 70, 15 and 2 hPa. Values in parentheses show the bias in units of ERA-40 one standard deviation interannual variability (70 hPa: 0.65 K; 15 hPa: 0.65 K; 2 hPa: 2.20 K). Sigma values for grading purposes are defined as the maximum differences between the reanalyses data sets and are presented in the last line.

	70 hPa	15 hPa	2 hPa		70 hPa	15 hPa	2 hPa
AMTRAC3	-0.98 (-1.51)	1.81 (2.77)	1.64 (0.74)	SOCOL	-4.39 (-6.73)	-0.29 (-0.44)	-2.54 (-1.15)
CAM3.5	-3.04 (-4.67)	-1.35 (-2.07)	NA	ULAQ	0.71 (1.09)	1.24 (1.89)	2.80 (1.27)
CCSRNIES	-7.45 (-11.4)	4.49 (6.88)	6.00 (2.73)	UMETRAC	-2.97 (-4.56)	-1.91 (-2.93)	2.83 (1.29)
CMAM	1.29 (1.98)	2.28 (3.49)	8.30 (3.78)	UMSLIMCAT	1.37 (2.11)	-0.46 (-0.70)	-0.88 (-0.40)
CNRM-ACM	-9.64 (-14.8)	-6.76 (-10.4)	-10.30 (-4.69)	UMUKCA-UCAM	7.74 (11.87)	0.85 (1.31)	5.39 (2.45)
EMAC	-3.19 (-4.89)	-1.49 (-2.27)	0.40 (0.18)	UMUKCA-METO	7.13 (10.95)	-0.34 (-0.51)	2.62 (1.19)
E39CA	1.99 (3.05)	1.74 (2.67)	NA	WACCM	-0.59 (-0.90)	-0.13 (-0.21)	-0.03 (-0.01)
GEOSCCM	0.53 (0.82)	0.49 (0.75)	2.77 (1.26)	MMM	-0.92 (-1.41)	-0.19 (-0.29)	1.54 (0.70)
LMDZrepro	0.10 (0.15)	-0.65 (-0.99)	11.10 (5.05)	NCEP	0.74 (1.13)	0.95 (1.46)	3.23 (1.47)
MRI	-0.99 (-1.53)	-2.88 (-4.41)	-2.60 (-1.18)	UKMO	-0.18 (-0.27)	-0.99 (-1.51)	1.30 (0.59)
NiwaSOCOL	-4.14 (-6.36)	-0.01 (-0.01)	-2.85 (-1.29)	Sigma	0.74 (1.13)	-0.99 (-1.51)	3.23 (1.47)

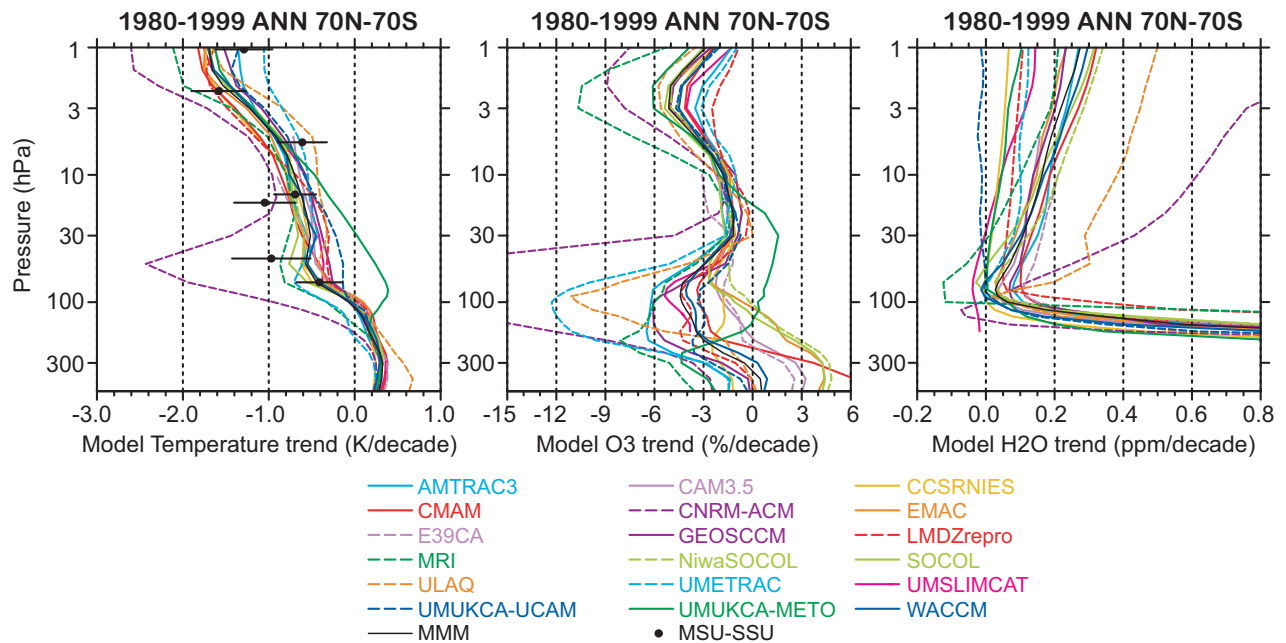


**Figure 3.2:** Near global (70°S-70°N) and annual mean trends over 1980-1999 for (a) temperature, (b) ozone, and (c) water vapour ratio, for REF-B1 model simulations. Panel (a) includes satellite observed MSU/SSU trends and 95% confidence intervals. MSU/SSU data points include channels: MSU-4 (at 70 hPa), SSU25 (15 hPa), SSU26 (5 hPa), SSU27 (2 hPa), SSU15X (45 hPa), SSU26X (15 hPa) and SSU36X (1 hPa), where the specified pressure levels represent the approximate weighted mean heights derived from the MSU/SSU vertical weighting functions for each channel (see Randel *et al.*, 2009), negative portions of the weighting functions excluded. The solid black lines indicate the multi-model mean (MMM) results. For other data sets, see legend.

UMUKCA-METO and UМУKCA-UCAM overestimates ozone in the lower stratosphere, which should lead to overestimated radiative heating. This provides a plausible explanation for the UМУKCA-METO and UМУKCA-UCAM warm biases in this region, although other effects cannot be ruled out.

**Table 3.2** shows model temperature climatology biases with respect ERA-40 for 1980-1999 at 70, 15 and 2 hPa. Sigma values for grading purposes are defined as the maximum differences between the reanalyses data sets and are also presented in Table 3.2 (see Sections 3.6 and 3.7).

### 3.3.2 Global mean temperature trends: Past

**Figure 3.2** shows near global mean trends for temperature, ozone and water vapour from 1980-1999 for the REF-B1 model experiments. Trends were calculated from linear fits to the annual mean time series from each model. Figure 3.2a also shows the observed stratospheric temperature trend over this period, indicated by the MSU/SSU dataset. The horizontal error bars for MSU/SSU indicate the 95% confidence intervals for the fitted trends. Note that MSU/SSU data are also associated with uncertainty in the vertical due to the vertical distribution of its weighting functions (see Randel *et al.*, 2009). Here the MSU/

SSU data was simply plotted at the weighted mean heights (negative portions of the weighting functions excluded). Since the focus in this analysis is on temperature no observations are included in Figure 3.2 for ozone and water vapour, and thus the following qualitative assessment will use the multi-model mean as a reference for these species.

The observed temperature trend is associated with emission of CO<sub>2</sub> and ozone depleting substances (Jonsson *et al.*, 2009) and is driven radiatively by increases in CO<sub>2</sub> and water vapour and decreases in ozone (Shine *et al.*, 2003). All models capture the large scale features of the observed temperature trend, with warming in the troposphere (not shown) and cooling in the stratosphere. Furthermore, the vertical structure of the stratospheric trend, with cooling maxima in the upper and lower stratosphere that are consistent with decreases in ozone (Figure 3.2b), is generally well captured. The following discussion will primarily focus on the stratospheric results. Disregarding the main model outliers in the stratosphere, CNRM-ACM and UМУKCA-METO, the model spread varies between 0.4 K/decade and 0.8 K/decade. In the deep troposphere (below 300 hPa) the models agree better, and except for the main outlier there, ULAQ, the model spread is within 0.2 K/decade. The multi-model mean results overlap with, or are very close to overlapping with, the MSU/SSU uncer-

tainty estimates, and the disagreements are largest for the so called SSU X-channels that are not as reliable as the regular SSU channels. Note that many models with significant biases in the temperature climatology (see Section 3.3.1), including CCSRNIES, CMAM, LMDZrepro and CAM3.5, do not show a significant disagreement with the observed trends. Some models, however, and most notably CNRM-ACM and UMUKCA-METO, but also MRI, UMETRAC, UMUKCA-UCAM and ULAQ, display trends that are in sufficient disagreement with the observations and the multi-model mean trend that they warrant some further investigation.

CNRM-ACM overestimates the observed cooling trend throughout most of the stratosphere and exhibits cooling, rather than warming, in the upper troposphere (Figure 3.2a). The discrepancies are particularly severe near the stratopause and in the lower stratosphere and upper troposphere, between 200 and 20 hPa, where the modelled trend is a roughly factor of 1.5 and 4, respectively, greater than the multi-model mean trend. The overestimated temperature trend is quite clearly associated with a significantly overestimated negative ozone trend (Figure 3.2b) and a significantly overestimated positive water vapour trend (Figure 3.2c), both leading to overestimated cooling. A particularly strong temperature response to volcanic eruptions in 1982 and 1991 (Figure 3.3) appears to be partly responsible for these anomalous trends.

MRI also overestimates the temperature trend near the stratopause and in the lower stratosphere and upper troposphere, although to a lesser degree than CNRM-ACM. This appears to be associated with too strong negative ozone trends.

UMETRAC displays a stronger temperature trend than most models in the upper troposphere and lower stratosphere and a weaker trend than most models in the upper stratosphere. This seems consistent with slightly stronger and weaker ozone trends than most models in these regions.

UMUKCA-METO displays an anomalous feature with a weaker than average temperature trend in the middle stratosphere and a positive trend of up to 0.4 K/decade in the lower stratosphere. This behaviour seems directly related to an anomalous ozone trend with positive, rather than negative, values throughout the lower and middle stratosphere.

While UMUKCA-UCAM and UMUKCA-METO showed very similar results for the temperature and ozone climatologies and biases (Figure 3.1), this is not the case for temperature trends. UMUKCA-UCAM performs well throughout the domain, except for a slightly weaker than average trend in the lower stratosphere, which appears consistent with the absence of a significant negative water vapour trend and a slightly weaker than average negative ozone trend in this region.

ULAQ displays somewhat weaker negative temperature trends than the other models at 20-2 hPa, despite showing reasonable ozone trends in this region and an overestimated water vapour trend. As the latter would lead to more cooling, not less, this suggests that the lower than average sensitivity for this model at 20-2 hPa could be due to inaccuracies in the model's radiative scheme. Also, although the focus here is on the stratosphere, it can be noted that the upper tropospheric warming in ULAQ is much stronger than for other models (by roughly a factor of 2 below 300 hPa). This appears to be related to an upper tropospheric increase in water vapour that is about twice as strong as for the multi-model mean (not shown).

Figure 3.3 shows the full time series of global mean temperature anomalies compared to satellite data weighted over specific vertical levels (see Randel *et al.*, 2009). Most of the models capture the observed trends and variability. In particular many CCMs capture the levelling of the temperature since the late 1990s. The impact of the prescribed SSTs in the troposphere is also apparent as MSU-4 and model temperatures are particularly well correlated compared to other levels.

A disagreement between the models and observations is clearly seen in SSU26 over the last decade. SSU26 has a maximum weight at about 5 hPa and a considerable contribution from the lower stratosphere. In contrast the agreement is better in SSU27 which peaks at 2 hPa with less contribution from the lower stratosphere.

Table 3.3 shows the CCM temperature trend bias (K/decade) with respect MSU/SSU for 1980-1999 at 70, 15 and 2 hPa. 95% Confidence intervals in the MSU/SSU trend are used for grading purposes (see Sections 3.6 and 3.7). These are also presented in the table.

### 3.3.3 Global mean temperature trends: Future

To assess the model simulations of future changes Figures 3.4c and d show global mean vertical temperature trend profiles for 2000-2049 and 2050-2099 for the REF-B2 model experiments. For reference, the global mean trends for 1980-1999 for REF-B1 and REF-B2 are shown in Figures 3.4a and b. We first compare the REF-B2 and REF-B1 results for 1980-1999. The REF-B2 results are generally very similar to the REF-B1 results in the stratosphere, as should be expected since the prescribed changes of GHGs and ODSs are the same in both scenarios. The multi-model mean trends for REF-B1 and REF-B2 are very close. However, there are a few important differences that are discussed below.

While the focus here is on the stratospheric results it can be noted that three models show significantly different temperature trends in the upper troposphere for REF-B2 than for REF-B1. CMAM and UMUKCA-UCAM REF-B2

trends are roughly 1.5 and 2 times as strong as the multi-model mean trend in this region. For CMAM this is related to its coupled ocean implementation, which is documented elsewhere in the report. CCSRNIES shows the opposite behaviour, *i.e.*, under-estimating the multi-model trend, showing a near zero trend throughout the troposphere for REF-B2.

For the stratosphere, the REF-B2 trends show slightly better agreement between the various models than for REF-B1 (but note that not all models provided data for REF-B2). This is not surprising as the variation in model response to volcanic eruptions and solar variability contributes to different temperature responses in the REF-B1 simulations, while those effects are not considered for

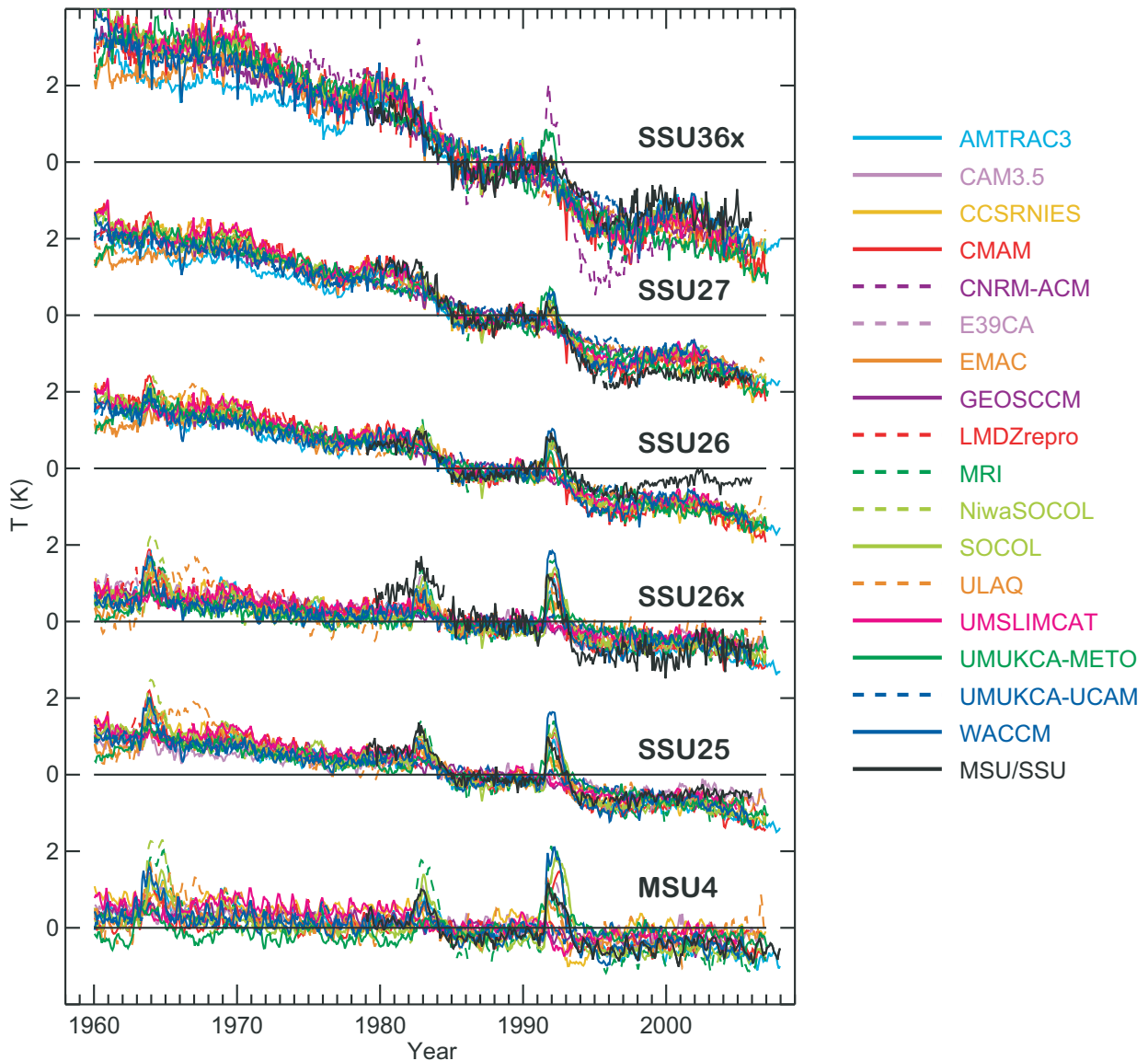


**Figure 3.3:** Near global mean time series ( $70^{\circ}\text{S}$ - $70^{\circ}\text{N}$ ) of MSU/SSU satellite observations and REF-B1 model temperature data weighted by MSU/SSU weighting functions. MSU/SSU channels include: MSU-4 (at 70 hPa), SSU25 (15 hPa), SSU26 (5 hPa), SSU27 (2 hPa), SSU26x (15 hPa) and SSU36x (1 hPa), where the specified pressure levels represent the approximate weighted mean heights derived from the MSU/SSU vertical weighting functions for each channel (see Randel et al., 2009), negative portions of the weighting functions excluded. For each model only the first ensemble member from the REF-B1 simulations is shown. The anomalies are calculated with respect to the period 1980-1994, as in the provided SSU anomalies. Note that UMETRAC is not included in this figure. CNRM-ACM is only shown in the highest SSU36x level due to its too strong sensitivity to volcanoes. UMUKCA-UCAM is not shown after year 2000. Low top models CAM3.5 and E39CA (the lids are at 3 hPa and 10 hPa respectively) are shown only in the MSU4, SSU25 and SSU26x panels.

**Table 3.3:** Model temperature trend bias (K/decade) with respect MSU/SSU for 1980-1999 at 70, 15 and 2 hPa. Values in parentheses show biases in units of the MSU/SSU 95% confidence intervals (70 hPa: 0.27 K/decade; 15 hPa: 0.24 K/decade; 2 hPa: 0.32 K/decade). The Sigma values used for grading purposes are presented in the last line.

	70 hPa	15 hPa	2 hPa		70 hPa	15 hPa	2 hPa
AMTRAC3	0.02 (0.08)	-0.03 (-0.14)	0.31 (0.99)	NiwaSOCOL	0.03 (0.10)	0.01 (0.03)	0.16 (0.49)
CAM3.5	0.14 (0.53)	0.11 (0.47)	NA	SOCOL	-0.14 (-0.52)	-0.03 (-0.14)	0.16 (0.51)
CCSRNIES	-0.09 (-0.33)	0.03 (0.12)	-0.01 (-0.02)	ULAQ	0.08 (0.31)	0.29 (1.18)	0.43 (1.34)
CMAM	0.10 (0.37)	-0.08 (-0.34)	-0.01 (-0.04)	UMETRAC	-0.30 (-1.10)	0.17 (0.68)	0.62 (1.94)
CNRM-ACM	-1.53 (-5.66)	-0.22 (-0.91)	-0.57 (-1.79)	UMSLIMCAT	0.03 (0.13)	0.19 (0.78)	0.18 (0.56)
EMAC	0.01 (0.04)	-0.07 (-0.28)	0.07 (0.21)	UMUKCA-METO	0.77 (2.85)	0.38 (1.54)	0.20 (0.62)
E39CA	0.09 (0.35)	-0.12 (-0.48)	NA	UMUKCA-UCAM	0.27 (1.01)	0.22 (0.88)	0.31 (0.97)
GEOSCCM	0.15 (0.57)	0.18 (0.75)	0.27 (0.86)	WACCM	0.00 (0.01)	0.07 (0.30)	0.19 (0.58)
LMDZrepro	0.12 (0.46)	0.19 (0.78)	-0.06 (-0.18)	MMM	-0.03 (-0.13)	0.07 (0.28)	0.12 (0.38)
MRI	-0.40 (-1.49)	-0.05 (-0.20)	-0.28 (-0.88)	Sigma	0.27 (1.0)	0.24 (1.0)	0.32 (1.0)

REF-B2.

CNRM-ACM shows the most dramatic difference in temperature trends between REF-B1 and REF-B2 of all models. The considerably overestimated cooling trends for 1980-1999 for REF-B1 are much reduced in REF-B2, particularly in the lower stratosphere. This confirms the earlier speculations that the CNRM-ACM temperature trend biases for REF-B1 are largely due to effects of volcanic eruptions, since the REF-B2 simulation does not include those. It can be speculated that the particularly large model spread for REF-B1 in the lower stratosphere, including significant deviations also for MRI, UMETRAC, UMUKCA-METO and UMUKCA-UCAM, could be related to different responses to volcanic eruptions. Note that for REF-B2, except for UMUKCA-METO and UMUKCA-UCAM, the model spread is quite small. Further work is needed to understand this better. MRI shows better agreement with the multi-model mean for REF-B2 than for REF-B1, particularly in the upper troposphere and lower stratosphere. UMUKCA-UCAM on the other hand showed better agreement with the multi-model mean (and with the observations) for REF-B1 than for REF-B2. For REF-B2, UMUKCA-UCAM follows the anomalous results of UMUKCA-METO, showing a strong positive bias in its temperature trend throughout the lower and middle stratosphere.

The future global mean temperature trend is attributable primarily to CO<sub>2</sub> increase, although the expected gradual recovery of ozone over the 21<sup>st</sup> century will reduce the CO<sub>2</sub> induced cooling somewhat in the upper stratosphere (Jonsson *et al.*, 2009). A hint of this can be seen in Figures 3.4c and d. For 2000-2049 (Figure 3.4c) only two models can be considered as significant outliers: MRI under-estimates the multi-model cooling trend in the upper stratosphere and ULAQ overestimates the multi-model warming trend in the upper troposphere. In particular the anomalous

behaviour of UMUKCA-METO and UMUKCA-UCAM in the lower stratosphere is not present in this period. CMAM and UMUKCA-UCAM tropospheric trends are also closer to the multi-model mean trend. MRI did not include CH<sub>4</sub> changes after 2002 (see Chapter 2) which would explain weaker temperature trend for MRI in the upper stratosphere than for other models (CH<sub>4</sub> is the main source of upper stratospheric water vapour and odd hydrogen that control ozone loss rates in this region). For 2050-2099 (Figure 3.4d) the same level of agreement between the models is achieved in the stratosphere. In the troposphere, however, the model spread is larger during 2050-2099 than during 2000-2049. In particular, SOCOL shows a more anomalously warm trend during 2050-2099 than during 2000-2049.

### 3.4 Evaluation of the CCM radiation codes performance

There is a long history of international efforts aimed on the evaluation of the radiation codes of climate models. After several national projects in Europe, Russia and US (*e.g.*, Feigelson and Dmitrieva, 1983; Luther *et al.*, 1988) the first international comparison of radiation codes for climate models (ICRCCM) campaign was launched in 1984. ICRCCM resulted in a series of publications (Ellingson *et al.*, 1991; Fouquart *et al.*, 1991) that evaluated the performance of the existing radiation codes and inspired further progress. ICRCCM also established a framework for the subsequent campaigns, based on the comparison of the radiation codes against reference high-resolution line-by-line (LBL) codes. This approach was justified by the unavailability of reliable observations of the radiation fluxes and heating rates in the atmosphere. There were several



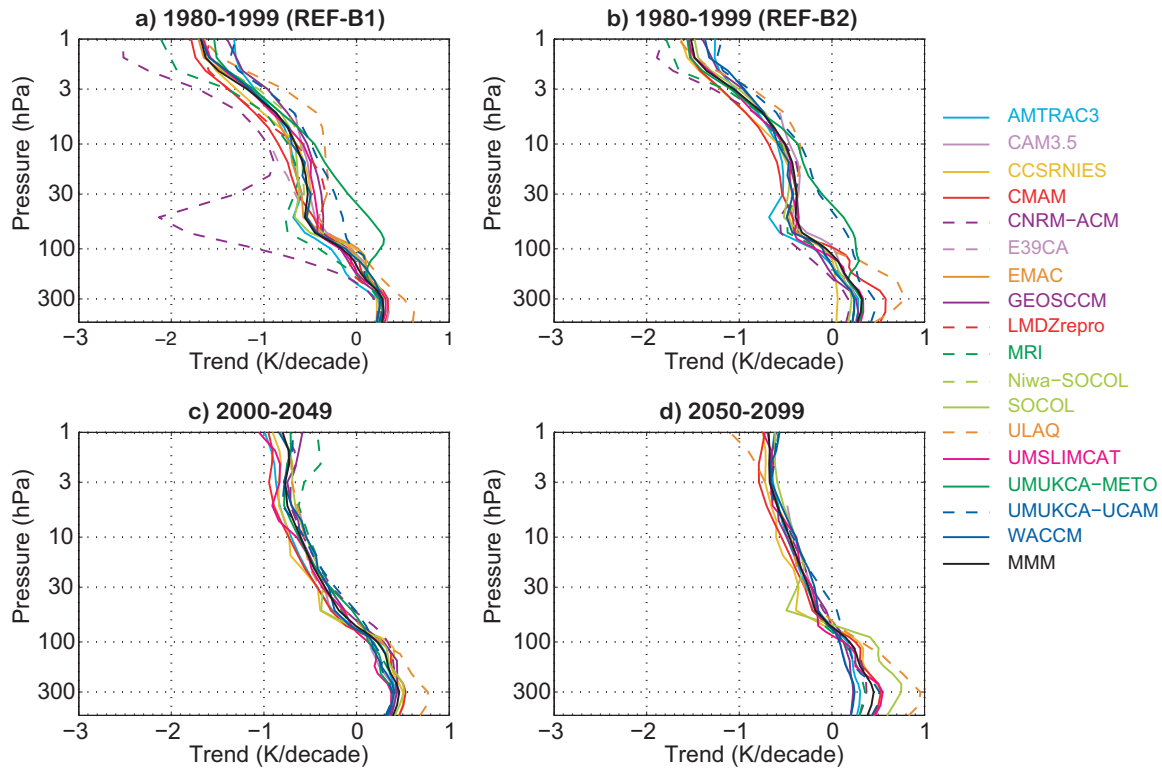


**Figure 3.4:** Global and annual mean temperature trends from (a) REF-B1 for 1980-1999; and from REF-B2 for (b) 1980-1999, (c) 2000-2049, and (d) 2050-2099. Note that UMETRAC is not included in this plot and that four models shown for REF-B1 (EMAC, E39CA, LMDZrepro and NiwaSOCOL) did not supply data for REF-B2. The solid black lines indicate the multi-model mean (MMM) results.

other attempts to evaluate radiation codes for climate models. The representation of clouds was analysed by Barker *et al.*, (2003). An evaluation of clear sky radiation codes used by IPCC AR4 GCMs was performed by Collins *et al.*, (2006), employing a single profile and solar zenith angle. These evaluations were also based on the comparison of operational radiation codes with reference LBL schemes. Such tests can provide a useful, if incomplete, understanding of potential sources of uncertainty and error, because the state-of-the-art LBL radiation codes are used as a base for the judgment. A more complete picture can be obtained by comparing radiation codes directly implemented to a single climate model (*e.g.*, Feigelson and Dmitrieva, 1983; Cagnazzo *et al.*, 2007). However, it would not be feasible to apply this approach using the LBL reference codes due to their high computational costs and, moreover, the results of offline experiments allow clear evaluation of the model performance and interpretation of the underlying causes of error.

Most of the previous campaigns were aimed at the radiation fluxes and tropospheric heating/cooling rates evaluation. In this comparison we focus on two aspects of radiation code output: stratospheric heating/cooling rates and instantaneous radiative fluxes. The heating/cooling rates are necessary to understand the biases and trends in the

global mean stratospheric temperature, while the instantaneous radiative fluxes can help to interpret global climate change, including surface temperature change. It should be noted that the evaluation of radiation codes in cloudy conditions and in the presence of different atmospheric aerosols will not be performed here, because of high uncertainties in aerosol optical properties and limited availability of proper reference codes. Nevertheless, these issues are very important and should be addressed in future work.

In this section we analyse the performance of the CCM radiation codes presented in Section 3.2 and described in Chapter 2 using the results of offline calculations. Section 3.4.1 describes the cases required for this analysis. Sections 3.4.2 and 3.4.4 evaluate the performance of CCM radiation codes for the control case (case A, see Section 3.4.1), for fluxes and heating/cooling rates, respectively, which can help to explain the possible causes of the biases in the CCM simulated climatological temperature discussed in Section 3.3. Sections 3.4.3 and 3.4.5 evaluate the response of the simulated radiation fluxes and heating rates, respectively, to the changes of atmospheric gas composition and Section 3.4.6 discusses the effect of errors in heating rates and distribution of ozone and water vapour on biases in the global mean temperature climatology.

### 3.4.1 Experimental set-up

We perform a number of clear sky and aerosol free tests using zonally averaged profiles of the atmospheric state parameters compiled from ECMWF ERA-40 output and ozone data provided by Randel and Wu (2007). These profiles represent January atmosphere and are given for five latitudes (80°S, 50°S, 0°, 50°N, and 80°N). The solar fluxes in the atmosphere were calculated for three solar zenith angles, allowing one to evaluate the radiation code performance for diurnal means as well as for different solar positions. Where possible the extra-terrestrial spectral solar irradiance was prescribed with ~1 nm resolution from Lean *et al.* (2005) compilation. Surface albedo was set to 0.1 for all cases. We also asked participants to use solar irradiance for 1 AU Sun-Earth distance. The set of reference vertical profiles and the description of the test cases are presented at [www.env.leeds.ac.uk/~piers/ccmvalrad.shtml](http://www.env.leeds.ac.uk/~piers/ccmvalrad.shtml). These tests were designed to very crudely approximate the radiative forcing evolution since 1980 due to ozone and greenhouse gases. **Table 3.4** describes the experiments undertaken. Case A represents the control experiment and is based on the concentration of radiatively active species for 1980. The cases B-L are based on the observed changes of gas abundances in the atmosphere from 1980 to 2000 and allow us to evaluate the radiation code response to these climate forcings.

As a base for comparison we use the results of five LBL codes: AER (Clough and Iacono, 1995; Clough *et al.*, 2005); FLBLM (Fomin and Mazin, 1998; Fomin, 2006; Halthore *et al.*, 2005); LibRadtran (Mayer and Kylling, 2005); NOAA (Portmann *et al.*, 1997) and OSLO (Myhre and Stordal, 1997, 2001; Myhre *et al.*, 2006). AER, FLBLM, NOAA and OSLO provided longwave (LW) fluxes, while shortwave (SW) fluxes were calculated with FLBLM, LibRadtran and OSLO codes. Therefore, for most of the cases the results of at least three independent LBL codes are available. The complete set of the test calculations was submitted by the following thirteen CCMs: AMTRAC3, CCSRNIES, CMAM, E39CA, EMAC, GEOSCCM, LMDZrepro, MRI, SOCOL, NiwaSOCOL (identical to SOCOL), UMSLIMCAT, UMUKCA-METO, and UMUKCA-UCAM. Five CCMs (CAM3.5, CNRM-ACM, ULAQ, UMETRAC, and WACCM) did not participate in the radiation code comparison. Two CCMs have radiation codes based on ECHAM4 (E39CA and SOCOL). In addition to the operational codes, we also analysed the results of four perspective radiation codes: ECHAM5, LMDZ-new, UKMO-HADGEM3 and UKMO-Leeds, which will be used in the new generation of CCMs or GCMs.

### 3.4.2 Fluxes: Control experiment

The global and diurnal mean net (downward minus upward) LW, SW and total (SW+LW) fluxes for case A calculated with AER (LW) and LibRadtran (SW) at 200 hPa (the pseudo-tropopause) are presented in **Table 3.5**. The differences between the fluxes calculated with all participating models and two particular LBL codes (AER for LW and LibRadtran for SW) at the pseudo-tropopause are illustrated in **Figure 3.5**. For this particular case the accuracy of the calculated SW fluxes is very good. The scatter among the LBL codes is within 1 W/m<sup>2</sup>. Most of the participating CCMs show a net SW flux error smaller than 2.5 W/m<sup>2</sup>. Only the SW radiation scheme of MRI produces a larger error, ~4 W/m<sup>2</sup>. For LW and total radiation the situation is slightly worse. While LBL codes are in a very good agreement, total flux errors for GEOSCCM, LMDZrepro and CCSRNIES exceed 4 W/m<sup>2</sup>, primarily due to errors in LW calculations. MRI and UMSLIMCAT also display a total flux error of ~4 W/m<sup>2</sup>, which is due to either SW errors (for MRI) or a combination of SW and LW errors (for UMSLIMCAT). In general, an error of ~4 W/m<sup>2</sup> could lead to ~4 K error in the global mean surface temperature, unless this error is compensated by some other bias in the concentrations of radiatively active gases or physical parameterisations in the core CCM. It is interesting to note, that for UMUKCA-METO, UMUKCA-UCAM and UKMO-Leeds the SW and LW errors compensate each other making the model performance for the total net flux better than for its individual components. From the results presented, it can be concluded that the performance of the majority of participating models in the simulation of the

**Table 3.4:** Offline radiation experiments undertaken.

A) 1980 Control experiment
B) CO <sub>2</sub> from 338 ppm to 380 ppm
C) CH <sub>4</sub> from 1600 ppb to 1750 ppb
D) N <sub>2</sub> O from 300 ppb to 320 ppb
E) CFC-11 from 150 ppt to 250 ppt
F) CFC-12 from 300 ppt to 550 ppt
G) All long-lived greenhouse gas changes combined (B-F)
H) 10% stratospheric ozone depletion, for pressures less than 150 hPa
I) 10% tropospheric ozone increase, for pressures greater 150 hPa
J) 10% stratospheric water vapour increase, for pressures less than 150 hPa
K) 10% tropospheric water vapour increase, for pressures greater than 150 hPa
L) Combined stratospheric ozone depletion and greenhouse gas changes (G and H)

net fluxes at the pseudo-tropopause is very good.

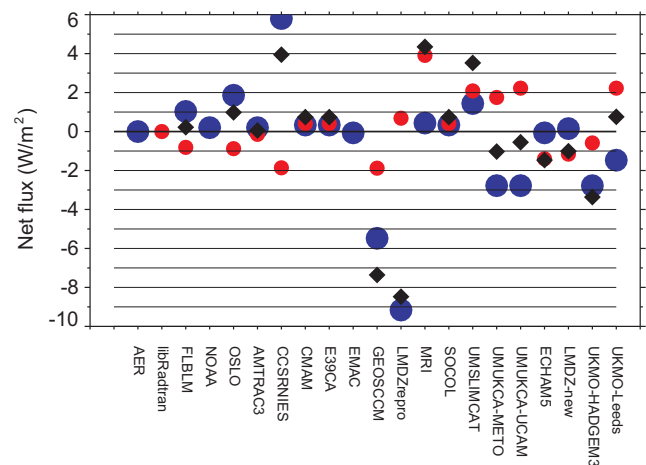
The global and diurnal mean net (downward minus upward) LW, SW and total (SW+LW) fluxes for case A calculated with AER (LW) and LibRadtran (SW) at the surface are presented in the first line of Table 3.5. Deviations from the LBL code are shown in Figure 3.6. In general, the model accuracy at the surface is similar to the results at the pseudo-tropopause for LW fluxes. All models except the ECHAM4 family of models (E39CA and SOCOL), CMAM, LMDZrepro and CCSRNIES have relatively small ( $< 2 \text{ W/m}^2$ ) biases.

Figure 3.7 illustrates the errors in downward LW fluxes simulated with three of these models relative to the reference AER LBL scheme. The SOCOL radiation scheme overestimates the downward LW flux at the surface by more than  $7.5 \text{ W/m}^2$ , which leads to an overestimation of the net LW flux, because the upward LW flux is constrained by the prescribed surface temperature and emission efficiency. The overestimation of the downward flux in SOCOL starts from  $\sim 250 \text{ hPa}$  and its magnitude increases towards the surface, which suggests some problems with the emission by water vapour or its continuum in

**Table 3.5:** Near-global and diurnal mean net LW, SW and total (LW+SW) fluxes for case A and their deviation for cases B-N from reference case A at the pseudo-tropopause calculated with AER (LW) and LibRadtran (SW). The first line also shows surface fluxes for reference. LW fluxes are positive upwards, and SW and total fluxes are positive downwards.

Case	LW flux ( $\text{W/m}^2$ )	SW flux ( $\text{W/m}^2$ )	Total flux ( $\text{W/m}^2$ )
A (reference surface)	71.88	223.77	151.89
A (reference trop)	234.076	282.444	48.368
B (CO <sub>2</sub> )	0.815	-0.052	0.763
C (CH <sub>4</sub> )	0.072	-0.006	0.066
D (N <sub>2</sub> O)	0.073	-0.0026	0.0704
E (CFC-11)	0.0251	0.0	0.0251
F (CFC-12)	0.078	0.0	0.078
G (LLGHG)	1.063	-0.061	1.002
H (O <sub>3</sub> strat)	-0.094	0.34	0.246
I (O <sub>3</sub> trop)	0.164	0.006	0.170
J (H <sub>2</sub> O strat)	0.072	-0.013	0.059
K (H <sub>2</sub> O trop)	2.258	0.089	2.347
L (LLGHG&O <sub>3</sub> )	0.971	0.278	1.248
M (T strat)	0.0945	0.0184	0.113
N (T trop)	-0.830	0.012	-0.824

the atmospheric transparency window. Similar behaviour (perfect agreement in the stratosphere and rising overestimation in the troposphere) is also characteristic for the CCSRNIES model up to  $\sim 300 \text{ hPa}$ , however, in the lower troposphere CCSRNIES dramatically under-estimates LW downward fluxes, which leads to substantial errors at the surface and potential implications for the surface energy budget in the core CCM. This model deficiency can be connected to some problems in the representation of the strong emission from H<sub>2</sub>O rotational ( $\lambda > 15 \mu\text{m}$ ) or vibrational ( $\sim 6.3 \mu\text{m}$ ) bands. The accuracy of the LMDZrepro LW downward flux is reasonable in the stratosphere and upper troposphere, but in the lower troposphere, and at the surface the model error exceeds  $5 \text{ W/m}^2$ . It should be noted also that this model generates a jump in the downward LW



**Figure 3.5:** The global and diurnal mean SW (red circles), LW (blue circles) and total (black diamonds) net flux deviations from the LBL code (AER for LW and libRadtran for SW) at the model pseudo-tropopause (200 hPa).

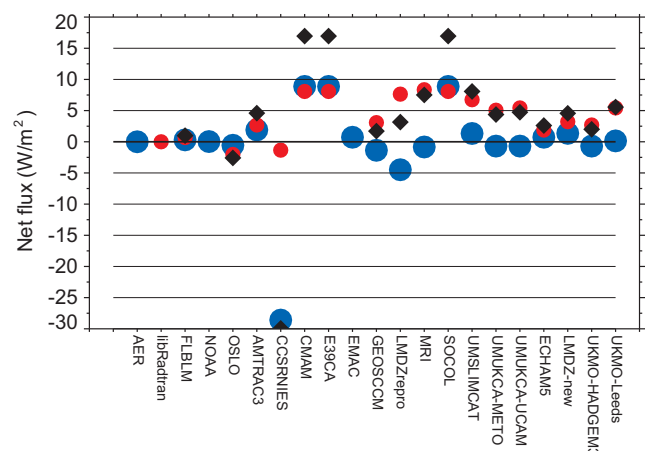


**Figure 3.6:** The global and diurnal mean SW (red circles), LW (blue circles) and total (black diamonds) net flux deviations from the LBL code (AER for LW and libRadtran for SW) at the surface.

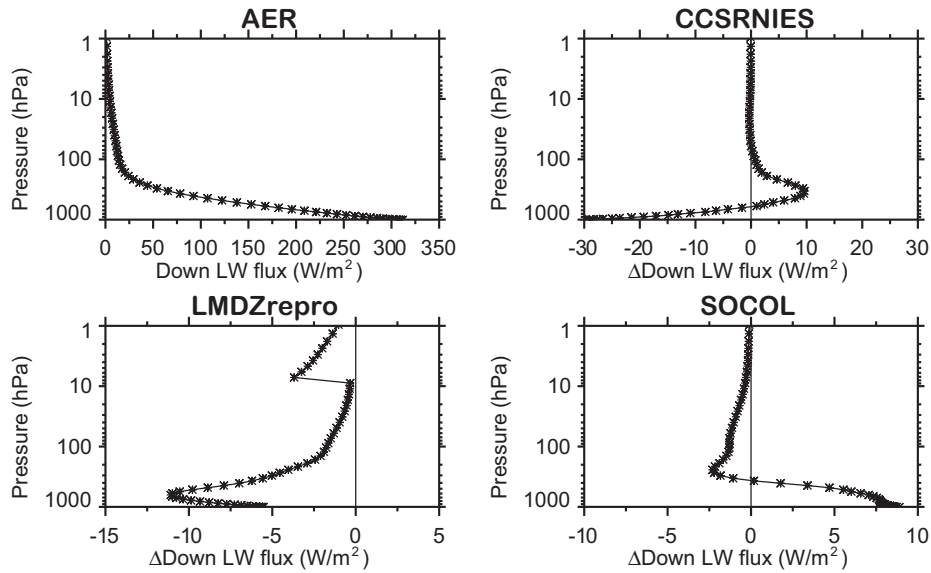


**Figure 3.7:** The vertical profiles of the global and diurnal mean LW downward flux from the LBL code (AER) and the absolute deviations of ECHAM4, LMDZrepro and CCSRNIIES results from the reference AER LBL scheme.

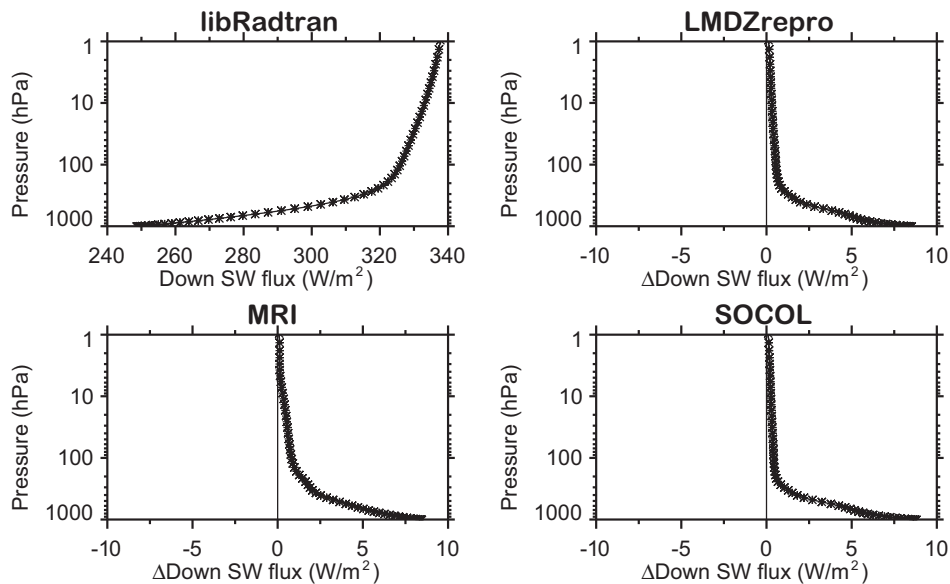


**Figure 3.8:** The vertical profiles of the global and diurnal mean SW downward flux from the LBL code (libRadtran) and the absolute deviations of ECHAM4, MRI and UKMO-Leeds results from the reference libRadtran LBL scheme.

fluxes around 10 hPa.

The accuracy of the calculated SW net fluxes at the surface (Figure 3.6) is generally not as good as at the pseudo-tropopause. For this case only six models (AMTRAC3, CCSRNIIES, GEOSCCM, ECHAM5, LMDZ-new and UKMO-HADGEM3) perform well. All other models are biased high compared to the reference LibRadtran results. The magnitude of the bias varies from about 5 to 8 W/m<sup>2</sup> with larger biases for the ECHAM4 family, CMAM, LMDZrepro and MRI. The bias in the SW net fluxes mostly comes from the errors in the downward SW fluxes, because the upward SW fluxes are smaller and constrained

by the prescribed surface albedo. The downward SW flux errors in most of the above-listed models have similar behaviour. As illustrated in **Figure 3.8**, the errors are small in the stratosphere, but start to increase around ~200 hPa reaching the maximum value near the surface. Because the main absorber of the solar irradiance in the cloud and aerosol free troposphere is water vapour, it can be tentatively concluded that H<sub>2</sub>O absorption in the near-infrared spectral region is under-estimated by these models, although under-estimating O<sub>3</sub> absorption in the visible spectral region also can contribute. The errors in the total net radiation fluxes (Figure 3.6) coincide with the errors in SW net fluxes for

most of the models. The exceptions are ECHAM4 family of models, LMDZrepro and CCSRNIES. In ECHAM4 based models the errors in SW and LW net fluxes are almost equal in magnitude providing a substantial deviation of the surface radiation balance from the reference results. The total net flux error for CCSRNIES is very large ( $\sim 30$  W/m<sup>2</sup>) and is dominated by the problems in the LW part of the code. The error in total net surface flux for LMDZrepro is rather small due to compensation of the errors in SW and LW calculations.

### 3.4.3 Fluxes: Sensitivity experiments

The analysis of the radiation flux responses to the observed changes of gas abundances in the atmosphere from 1980 to 2000 is an important part of the radiation code evaluation, because the accuracy of past climate change simulations depends on the ability of the radiation codes to properly simulate the effects of the main climate drivers (Collins *et al.*, 2006). In Table 3.5 we present the near-global and diurnal mean net LW, SW and total flux changes for cases B-L relative to reference case A (for case definitions see Table 3.4) at the pseudo-tropopause simulated with reference LBL codes (AER for LW fluxes and LibRadtran for SW fluxes). The calculated effects of different atmospheric perturbations are generally close to the previous estimates (Collins *et al.*, 2006; Forster *et al.*, 2007).

The global and diurnal mean net SW, LW and total flux deviations of the radiative forcing due to CO<sub>2</sub> increase relative to the results of the LBL codes at the pseudo-tropopause are presented in **Figure 3.9**. The accuracy of the LW radiation codes is generally very good and is within 10% for most of the participating models. Slightly larger underestimation of the CO<sub>2</sub> forcing is visible for the ECHAM4 family, CMAM and LMDZrepro, but it does not exceed 20%.

The relatively weak SW solar CO<sub>2</sub> forcing is more difficult to simulate. Only the AMTRAC3 and MRI results are in good agreement with the reference code, while most of the models (except CCSRNIES) overestimate its magnitude. The accuracy is still reasonable (<20%) for the UKMO family of models (UMSLIMCAT, UMUKCA-METO, UMUKCA-UCAM, UKMO-HADGEM3 and UKMO-Leeds), but several other models overestimate the solar CO<sub>2</sub> forcing by up to 80%. CCSRNIES does not include CO<sub>2</sub> in the solar part of the code and therefore underestimates SW forcing by 100%. The total (SW+LW) forcing is dominated by LW forcing. Therefore, the accuracy of the total forcing calculation almost completely coincides with the accuracy of LW forcing. Similar conclusions can be drawn for the accuracy of radiative forcing due to increase of all long-lived greenhouse gases (LL GHG) (**Figure 3.10**) since the forcing magnitude is mostly defined by the CO<sub>2</sub> increase. However, for this case the ac-

curacy of the LW forcing calculations is slightly lower for MRI and LMDZ-new and much higher for CMAM. It can be explained by the error compensation in the latter model, which under-estimates LW CO<sub>2</sub> forcing but overestimates the LW forcing by N<sub>2</sub>O and CFCs (see **Table 3.6**). It should be noted, that the CCSRNIES code does not take into account all LL GHG in the solar part of the spectrum (Table 2.11).

**Figure 3.11** shows the accuracy of the considered radiation codes for case H (10% decrease of stratospheric ozone). In contrast to the previously considered cases the SW forcing for this case plays a major role and all models are able to simulate its magnitude with an accuracy of 20% or better. The performance of some models in the LW part, however, is poor. The accuracy of AMTRAC3, CCSRNIES, CMAM, EMAC, GEOSCCM, LMDZrepro, MRI, ECHAM5 and LMDZ-new is only around 30% or worse, which has important implications for the total forcing of stratospheric ozone although the SW component dominates the total effect.

The accuracy of the LW radiative forcing due to tropospheric ozone and water vapour increase (cases I and K, not shown) is within 10% for all models except CCSRNIES, which has a problem with the H<sub>2</sub>O treatment in the LW part of the spectrum and under-estimates the LW forcing for case K by  $\sim 20\%$ . The solar forcing for these cases does not play a substantial role. The results for the case J (stratospheric water vapour increase) are shown in **Figure 3.12**. For this case it is interesting to note  $\sim 100\%$  overestimation of the LW stratospheric water vapour forcing by all models from the UKMO family and by  $\sim 200\%$  by CCSRNIES. The large spread in stratospheric water vapour forcings was also noticed by Myhre *et al.* (2009). It is even more interesting that the SW forcing by stratospheric water vapour is also roughly two times higher in the UKMO family (except for UMSLIMCAT) than for the reference model.

The accuracy of the forcing calculations for case L (all LL GHG and stratospheric ozone depletion) is illustrated in **Figure 3.13**. This forcing represents the sum of the main climate drivers (except water vapour and tropospheric ozone) for the considered period and its reasonable accuracy is a prerequisite for successful simulation of tropospheric climate changes. The results reveal that most of the models have accuracy of forcing calculations within 10%. The outliers are ECHAM4 based models, LMDZ-new and MRI, which under-estimate the total forcing by more than  $\sim 10\%$ .

**Table 3.6** presents a summary of total flux and forcing differences compared to the total forcing of the reference case (LibRadtran + AER). The table shows all the individual forcings analysed. Also shown are sigma values for the total cases that are used for grading. One sigma corresponds to the maximum absolute SW difference between

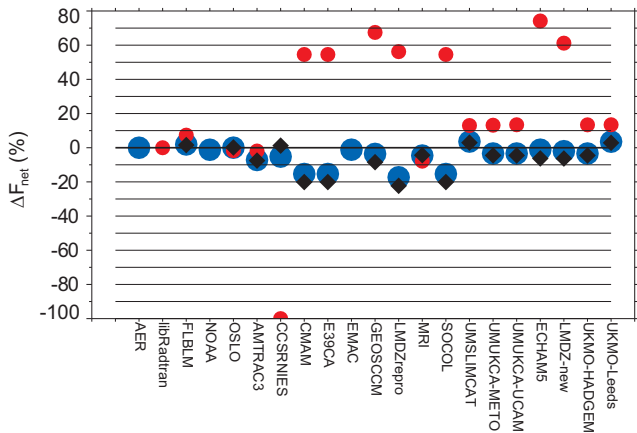


**Figure 3.9:** The global and diurnal mean SW (red circles), LW (blue circles) and total (black diamonds) net flux deviations of the radiative forcing due to CO<sub>2</sub> (case B) increase relative to the results of LBL codes (AER for LW and libRadtran for SW) at the pseudo-tropopause.

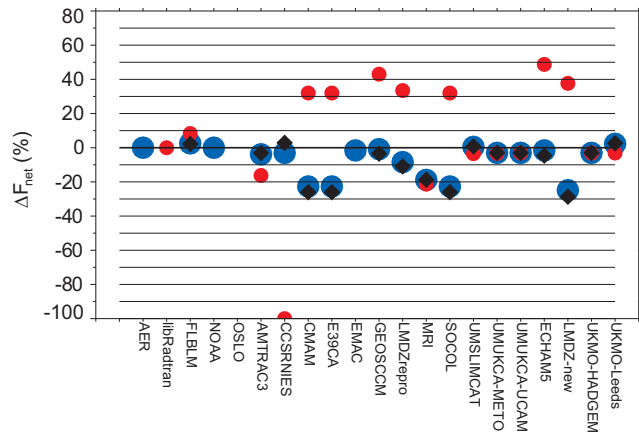


**Figure 3.10:** The global and diurnal mean SW (red circles), LW (blue circles) and total (black diamonds) net flux deviations of the radiative forcing due to LL GHG (case G) increase relative to the results of LBL codes (AER for LW and libRadtran for SW) at the pseudo-tropopause.

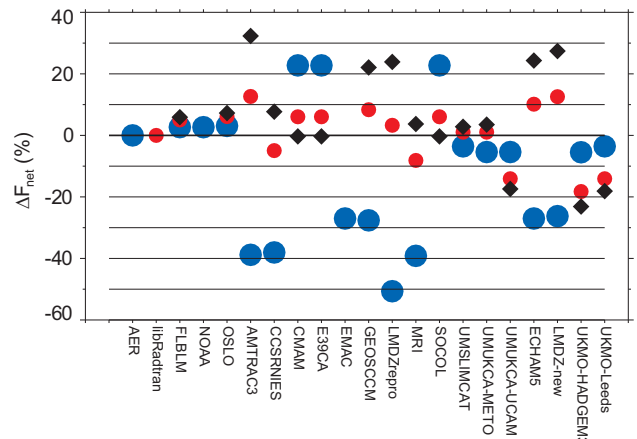


**Figure 3.11:** The global and diurnal mean SW (red circles), LW (blue circles) and total (black diamonds) net flux deviations of the radiative forcing due to stratospheric ozone depletion (case H) relative to the results of LBL codes (AER for LW and libRadtran for SW) at the pseudo-tropopause.

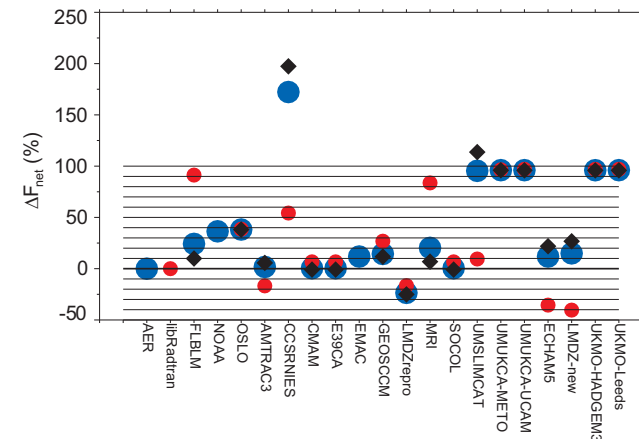


**Figure 3.12:** The global and diurnal mean SW (red circles), LW (blue circles) and total (black diamonds) net flux deviations of the radiative forcing due to stratospheric water vapour increase (case J) relative to the results of LBL codes (AER for LW and libRadtran for SW) at the pseudo-tropopause.

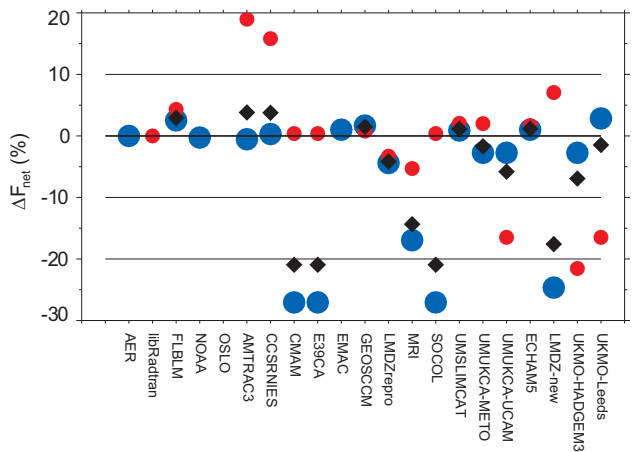


**Figure 3.13:** The global and diurnal mean SW (red circles), LW (blue circles) and total (black diamonds) net flux deviations of the radiative forcing due to WMGHG and stratospheric ozone changes (case L) relative to the results of LBL codes (AER for LW and libRadtran for SW) at the pseudo-tropopause.

**Table 3.6:** Globally and diurnally averaged flux differences at the pseudo-tropopause in  $W/m^2$  for radiation models compared to reference calculations. AER is used for the LW reference and LibRadtran is used for the SW reference. The control simulation and individual forcing cases are shown. Also shown are sigma values for the total cases that are used for grading. One sigma corresponds to the maximum absolute SW difference between the LBL models and LibRadtran added to the absolute maximum LW difference between AER and the other LBL models.

All units $W/m^2$		Control	CO <sub>2</sub>	CH <sub>4</sub>	N <sub>2</sub> O	CFC11	CFC12	Strat O <sub>3</sub>	Trop O <sub>3</sub>	Strat H <sub>2</sub> O	Trop H <sub>2</sub> O
Model	CASE	A	B-A	C-A	D-A	E-A	F-A	H-A	I-A	J-A	K-A
FLBLM	Lw	1.0326	0.0156	0.0005	0.0009	0.0029	0.007	0.0025	0.0013	0.0175	0.0409
FLBLM	Sw	0.8118	0.0038	0.0138	0.0004	0	0	0.017	0.0061	0.0116	0.0011
FLBLM	Tot	0.2207	0.0117	0.0132	0.0005	0.0029	0.007	0.0145	0.0074	0.0059	0.0398
NOAA	Lw	0.1995	0.0097	0.0004	0.0006	0.0026	0.006	0.0025	0.0016	0.0263	0.0073
OSLO	Lw	1.8617	0.0002	0.0033	-	-	-	0.0029	0.0007	0.0276	0.0532
OSLO	Sw	0.8783	0.0009	0.0047	-	-	-	0.0207	-	0.0049	-
OSLO	Tot	0.9834	0.0011	0.008	-	-	-	0.0178	-	0.0227	-
AMTRAC3	Lw	0.1977	0.0585	0.002	0.0025	0.0058	0.007	0.0364	0.018	0.0012	0.0183
AMTRAC3	Sw	0.1441	0.001	0.0063	0.0026	0	0	0.0429	0.0053	0.0021	0.0202
AMTRAC3	Tot	0.0535	0.0575	0.0083	0.005	0.0058	0.007	0.0793	0.0127	0.0034	0.0385
CCSRNIES	Lw	5.806	0.0425	0.0224	0.0071	0.001	0.0054	0.0357	0.0166	0.1246	0.4197
CCSRNIES	Sw	1.8613	0.0519	0.0063	0.0026	0	0	0.0168	0.0019	0.0069	0.1091
CCSRNIES	Tot	3.9447	0.0093	0.0287	0.0045	0.001	0.0054	0.0189	0.0147	0.1177	0.5289
CMAM	Lw	1.0954	0.1498	0.0084	0.0354	0.0204	0.0752	0.0397	0.0203	0.0054	0.1210
CMAM	Sw	0.0583	0.0178	0.0063	0.0026	0	0	0.0230	0.0004	0.0050	0.0001
CMAM	Tot	1.1537	0.1676	0.0147	0.0380	0.0204	0.0752	0.0626	0.0199	0.0004	0.1211
E39CA	Lw	0.5306	0.1255	0.0028	0.0165	0.0042	0.0022	0.0212	0.0196	0.0003	0.0765
E39CA	Sw	0.4057	0.0283	0.0063	0.0026	0	0	0.0205	0.003	0.0008	0.0317
E39CA	Tot	0.9363	0.1538	0.0091	0.0139	0.0042	0.0022	0.0007	0.0227	0.0005	0.0448
EMAC	Lw	0.067	0.0094	0.0379	0.0366	0.003	0.0065	0.0253	0.0108	0.0086	0.0443
GEOSCCM	Lw	5.4807	0.0296	0.0088	0.0033	0.0017	0.0067	0.0259	0.0008	0.0104	0.0317
GEOSCCM	Sw	1.8803	0.035	0.0063	0.0026	0	0	0.0283	0.0003	0.0034	0.0102
GEOSCCM	Tot	7.361	0.0646	0.015	0.0059	0.0017	0.0067	0.0542	0.0011	0.007	0.0215
LMDZrepro	Lw	9.1617	0.141	0.0199	0.0073	0.0041	0.0199	0.0475	0.0333	0.0171	0.049
LMDZrepro	Sw	0.685	0.0292	0.0063	0.0026	0	0	0.0111	0.0007	0.0021	0.0284
LMDZrepro	Tot	8.4767	0.1702	0.0262	0.0099	0.0041	0.0199	0.0586	0.034	0.015	0.0773
MRI	Lw	0.4369	0.0374	0.0117	0.049	-	-	0.0367	0.0023	0.0147	0.1326
MRI	Sw	3.91	0.0041	0.0063	0.0026	-	-	0.0276	0.0035	0.0106	0.0196
MRI	Tot	4.3469	0.0333	0.0054	0.0464	-	-	0.0091	0.0058	0.0041	0.113
SOCOL	Lw	0.3341	0.1253	0.0028	0.0165	0.025	0.078	0.0213	0.0199	0.0003	0.0803
SOCOL	Sw	0.4057	0.0283	0.0063	0.0026	0	0	0.0205	0.003	0.0008	0.0317
SOCOL	Tot	0.7399	0.1536	0.0091	0.0139	0.025	0.078	0.0008	0.0229	0.0005	0.0486
UMSLIMCAT	Lw	1.4382	0.0293	0.0181	0.0046	0.0018	0.0002	0.0033	0.0025	0.069	0.1614
UMSLIMCAT	Sw	2.0846	0.0067	0.0063	0.0026	0	0	0.0035	0.0043	0.0012	0.0639

Table 3.6 continued.

All units W/m <sup>2</sup>		Control	CO <sub>2</sub>	CH <sub>4</sub>	N <sub>2</sub> O	CFC11	CFC12	Strat O <sub>3</sub>	Trop O <sub>3</sub>	Strat H <sub>2</sub> O	Trop H <sub>2</sub> O
Model	CASE	A	B-A	C-A	D-A	E-A	F-A	H-A	I-A	J-A	K-A
UMSLIMCAT	Tot	3.5228	0.0226	0.0118	0.0021	0.0018	0.0002	0.0069	0.0018	0.0678	0.2252
UMUKCA-METO	Lw	2.7772	0.0276	0.0023	0.0021	0.0011	0.0067	0.0051	0.001	0.0695	0.1623
UMUKCA-METO	Sw	1.7498	0.0068	0.0063	0.0026	0	0	0.0035	0.0043	0.0122	0.0103
UMUKCA-METO	Tot	1.0274	0.0344	0.0086	0.0005	0.0011	0.0067	0.0086	0.0032	0.0572	0.1725
UMUKCA-UCAM	Lw	2.7772	0.0276	0.0023	0.0021	0.0011	0.0067	0.0051	0.001	0.0695	0.1623
UMUKCA-UCAM	Sw	2.2267	0.007	0.0063	0.0026	0	0	0.0478	0.0005	0.0123	0.0115
UMUKCA-UCAM	Tot	0.5505	0.0345	0.0086	0.0005	0.0011	0.0067	0.0427	0.0016	0.0572	0.1737
ECHAM5	Lw	0.067	0.0094	0.0379	0.0366	0.003	0.0065	0.0253	0.0108	0.0086	0.0443
ECHAM5	Sw	1.3982	0.0385	0.0063	0.0026	0	0	0.0344	0.0002	0.0045	0.0369
ECHAM5	Tot	1.4652	0.0479	0.0316	0.0392	0.003	0.0065	0.0597	0.011	0.0131	0.0812
LMDZ-new	Lw	0.1507	0.0166	0.0723	0.0733	0.0251	0.0783	0.0246	0.0105	0.0108	0.0142
LMDZ-new	Sw	1.1596	0.0317	0.0063	0.0026	0	0	0.0427	0.0008	0.0051	0.0469
LMDZ-new	Tot	1.0088	0.0483	0.066	0.0707	0.0251	0.0783	0.0673	0.0098	0.0159	0.0327
UKMO-HADGEM3	Lw	2.7797	0.0277	0.0023	0.0021	0.0011	0.0067	0.0051	0.001	0.0694	0.162
UKMO-HADGEM3	Sw	0.5848	0.0069	0.0063	0.0026	0	0	0.0619	0.002	0.0123	0.0122
UKMO-HADGEM3	Tot	3.3645	0.0346	0.0086	0.0005	0.0011	0.0067	0.0568	0.003	0.0572	0.1742
UKMO-Leeds	Lw	1.471	0.0288	0.0022	0.0021	0.0011	0.0068	0.0033	0.0031	0.0695	0.142
UKMO-Leeds	Sw	2.2267	0.007	0.0063	0.0026	0	0	0.0478	0.0005	0.0123	0.0115
UKMO-Leeds	Tot	0.7557	0.0218	0.0085	0.0005	0.0011	0.0068	0.0445	0.0036	0.0572	0.1535
Sigma	Tot	2.7401	0.0194	0.0171	0.0013	0.0029	0.007	0.0236	0.0078	0.0392	0.0543

the LBL models and LibRadtran added to the absolute maximum LW difference between AER and the other LBL models. See Sections 3.6 and 3.7 for grading details.

#### 3.4.4 Heating/Cooling rates: Control experiment

In this section vertical profiles of total clear sky SW global mean heating rates (diurnally averaged) and LW cooling rates for the relevant cases are discussed. **Figure 3.14** (top panels) and **Table 3.7** show global mean SW heating rates for the control (case A) and their deviations

with respect to LibRadtran. Results at three specific levels located in the lower (70 hPa), middle (15 hPa) and upper (2 hPa) stratosphere are shown in all tables of this section. The chosen levels are similar to those at which the observed temperature trends are available (Section 3.3.2). **Figure 3.15** (top panels) and **Table 3.8** show global mean LW cooling rates for case A and their deviations with respect to AER. **Tables 3.9** and **3.10** show heating and cooling rates, respectively, for a CO<sub>2</sub> increase. **Tables 3.11** and **3.12** show heating and cooling rates, respectively, for stratospheric ozone decrease. **Tables 3.13** and **3.14** show heating and cooling rates, respectively, for a stratospheric water vapour increase.



From Figure 3.14 it is evident that the correlations among the heating rate profiles in the stratosphere are very high, mainly due to the fact that heating rate patterns strongly depend on the gases input profiles, identical for all the models.

For case A, two sophisticated LBL heating rate calculations other than LibRadtran are available, namely OSLO and FLBLM. OSLO heating rates are in better agreement with LibRadtran below 2 hPa (see Figure 3.14 and Table 3.7). In particular, FLBLM heating rate biases at 70 hPa and 15 hPa are larger than for the OSLO model.

At 2 hPa, most of the models tend to overestimate the LibRadtran heating rates. Specifically, the biases found for LMDZ-new (15%), CMAM (9%), UMUKCA-UCAM (9%), the two UKMO models (8%) and ECHAM5 (8%) are more than a factor of two larger than the FLBLM bias ( $\sim 0.18$  K/day). The error at this level is consistent with an overestimation of the ozone solar heating as can be seen from Table 3.11 (case H minus case A – the instantaneous change from 10% stratospheric ozone depletion). For case H, these models report the largest negative bias at 2 hPa indicating a too large sensitivity to the ozone changes. For case A only three models present a negative bias in the heating rates larger than 0.18 K/day at this level (E39CA, LMDZrepro, SOCOL) even though they overestimate the ozone heating (Table 3.11). This under-estimation of the heating rate around the stratopause is however consistent with an under-estimation of the CO<sub>2</sub> heating as can be seen from Table 3.9 (case B minus case A, the instantaneous change due to CO<sub>2</sub> increase from 338 ppmv to 380 ppmv). However, it should be noted that the LibRadtran SW heating rates at these heights cannot be considered a good benchmark due to the differences between LBL schemes.

In the middle stratosphere (15 hPa), a better agreement is found between the models and LibRadtran, with all the models in a closer agreement with LibRadtran than FLBLM.

In the lower stratosphere (70 hPa), the biases for the majority of the models (except CCSRNIES and GEOSCCM) are also smaller than the bias found for FLBLM. In this region, the long radiative relaxation time in the lower stratosphere allows small heating and cooling rate changes to induce substantial temperature changes, therefore a heating/cooling rate bias of few tenths of a degree per day would be able to potentially warm or cool the lower stratosphere by several degrees. Specifically, for GEOSCCM the heating rate positive bias is consistent with an overestimation of the ozone absorption (see Table 3.11).

Figure 3.15 (top panels) illustrates global mean cooling rates for case A and their deviations with respect to AER. Note that the cooling rate is defined to be a positive quantity. The strong cooling peak in the upper stratosphere at about 1 hPa is due to the radiative effects of CO<sub>2</sub> and, by a lesser degree, O<sub>3</sub> and H<sub>2</sub>O. At 1 hPa, the majority of the

models under-estimate the cooling rate with a maximum negative bias of more than 3 K/day (LMDZrepro). As for the heating rates, the correlations among the cooling rate profiles in the stratosphere are high, as the cooling rates profiles strongly depend on the temperature input profiles, identical for all the models.

Table 3.8 reports the cooling rate biases for case A. Cooling rates from four LBL models are available (AER, FLBLM, NOAA and OSLO). In the lower stratosphere (70 hPa), the biases for the three LBL models with respect to AER are negative and smaller than the biases for the other models, with the exception of MRI, GEOSCCM and EMAC. The largest bias is found for CCSRNIES, partly due to an overestimation of the CO<sub>2</sub> and H<sub>2</sub>O cooling (see Tables 3.10 and 3.14). At 15 hPa there is a better agreement among models and LBLs. At 2 hPa, only LMDZrepro presents a bias (17%) larger than the bias of FLBLM, consistent with a too high sensitivity to CO<sub>2</sub> cooling (see Table 3.10).

### 3.4.5 Heating/Cooling rates: Sensitivity experiments

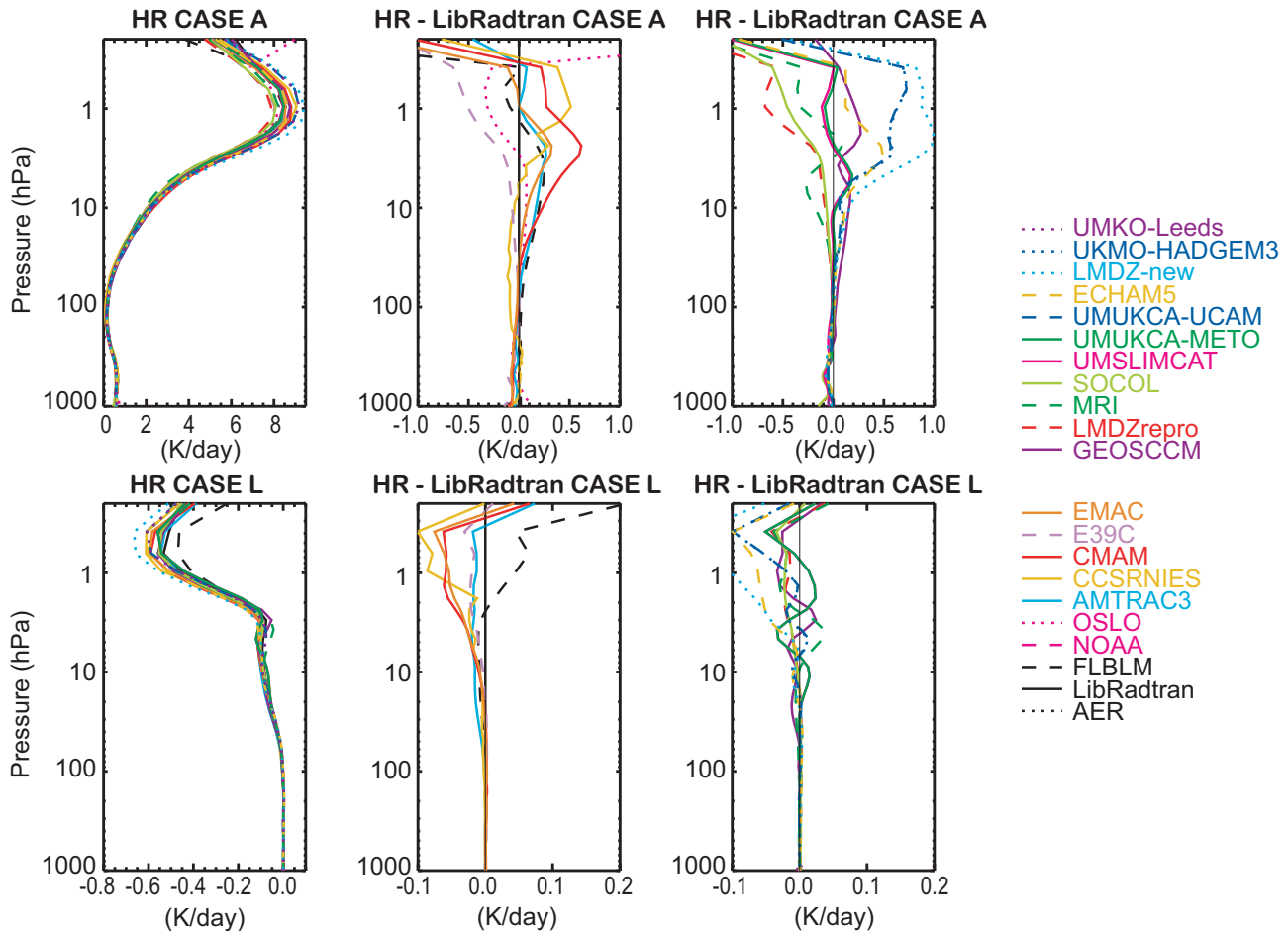
The lower panels of Figure 3.14 report the heating rate profiles and their biases with respect to LibRadtran for case L (the instantaneous change from combined 10% stratospheric ozone depletion and 1980-2000 LL GHG changes). The LibRadtran profile shows a decreased heating rate with respect to case A, maximum above 1 hPa of  $\sim 0.6$  K/day, almost entirely due to ozone change. Between 1 hPa and 0.2 hPa the majority of the models overestimate the cooling associated with imposed ozone depletion (maximum 25%, LMDZ-new). However, it should be noted that the LBL calculations presented here cannot be considered accurate at these heights due to the strong non-LTE effects for O<sub>3</sub> and CO<sub>2</sub> solar heating in the mesosphere (*e.g.*, Fomichev, 2009).

Table 3.11 shows that in the middle and upper stratosphere almost all the models are too sensitive to imposed ozone change (negative biases) with a better agreement at 15 hPa (the maximum overestimation at this level is found for AMTRAC3) and larger biases at 2 hPa (maximum biases are found for LMDZ-new, ECHAM5 and CMAM). The maximum heating rate biases for reduced ozone at 2 hPa implies a bias in the temperature change of about 0.35 K (see Section 3.4.6). At 70 hPa AMTRAC3 and GEOSCCM are too sensitive to ozone reduction.

The second and third largest heating rate changes in the stratosphere are found for increased CO<sub>2</sub> from 338 to 380 ppm (case B) and 10% stratospheric water vapour increase (case J). The absorption of solar radiation by CO<sub>2</sub> in the near-infrared spectrum contributes to atmospheric heating of the entire atmosphere, maximising in the upper stratosphere and mesosphere (*e.g.*, Fomichev, 2009).

**Table 3.7:** Heating rate bias of the models with respect to LibRadtran in K/day. The LibRadtran heating rate values are 0.24 K/day, 1.68 K/day and 6.6 K/day at 70 hPa, 15 hPa and 2 hPa respectively.

CASE A	70 hPa	15 hPa	2 hPa	CASE A	70 hPa	15 hPa	2 hPa
FLBLM	0.031	0.170	0.177	MRI	-0.009	-0.119	0.087
NOAA	-	-	-	SOCOL	-0.00003	-0.058	-0.200
OSLO	-0.003	0.065	-0.072	UMSLIMCAT	-0.014	-0.020	-0.013
AMTRAC3	0.003	0.146	0.255	UMUKCA-METO	-0.007	-0.004	0.011
CCSRNIES	-0.091	-0.076	0.289	UMUKCA-UCAM	-0.007	0.070	0.567
CMAM	-0.004	0.165	0.617	ECHAM5	0.015	0.101	0.471
E39CA	-0.00004	-0.058	-0.220	LMDZ-new	0.013	0.126	0.974
EMAC	-0.0127	0.0511	0.322	UKMO-HADGEM3	-0.006	0.091	0.583
GEOSCCM	0.035	0.137	0.206	UKMO-Leeds	-0.007	0.070	0.567
LMDZrepro	-0.003	-0.065	-0.226				



**Figure 3.14:** The top figures show the globally averaged shortwave heating rates for case A (control) (left) and differences in this heating rate from that calculated with the LibRadtran (middle and right). The bottom figures show the globally averaged shortwave heating rate changes for case L minus case A (the instantaneous change from combined 10% stratospheric ozone depletion and 1980-2000 LL GHG changes) (left) and differences of the same heating rate change from that calculated with the LibRadtran (middle and right).

**Table 3.8:** Cooling rate bias of the models with respect to AER in K/day. Results for case A (control). The AER cooling rate values are 0.3 K/day, 2.0 K/day and 6.1 K/day at 70 hPa, 15 hPa and 2 hPa respectively.

CASE A	70 hPa	15 hPa	2 hPa	CASE A	70 hPa	15 hPa	2 hPa
FLBLM	-0.009	0.112	0.454	MRI	0.011	-0.039	0.181
NOAA	-0.020	-0.011	0.092	SOCOL	-0.019	-0.216	-0.002
OSLO	-0.017	0.026	0.199	UMSLIMCAT	-0.057	-0.133	-0.030
AMTRAC3	-0.043	-0.161	0.089	UMUKCA-METO	-0.044	-0.077	-0.442
CCSRNIES	0.141	-0.080	-0.045	UMUKCA-UCAM	-0.044	-0.077	-0.442
CMAM	-0.038	0.108	-0.451	ECHAM5	-0.025	0.026	0.089
E39CA	-0.019	-0.216	-0.002	LMDZ-new	-0.027	0.028	0.092
EMAC	-0.012	0.118	0.402	UKMO-HADGEM3	-0.044	-0.077	-0.442
GEOSCCM	-0.018	-0.162	-0.379	UKMO-Leeds	-0.052	-0.115	0.014
LMDZrepro	-0.033	-0.015	-0.944				

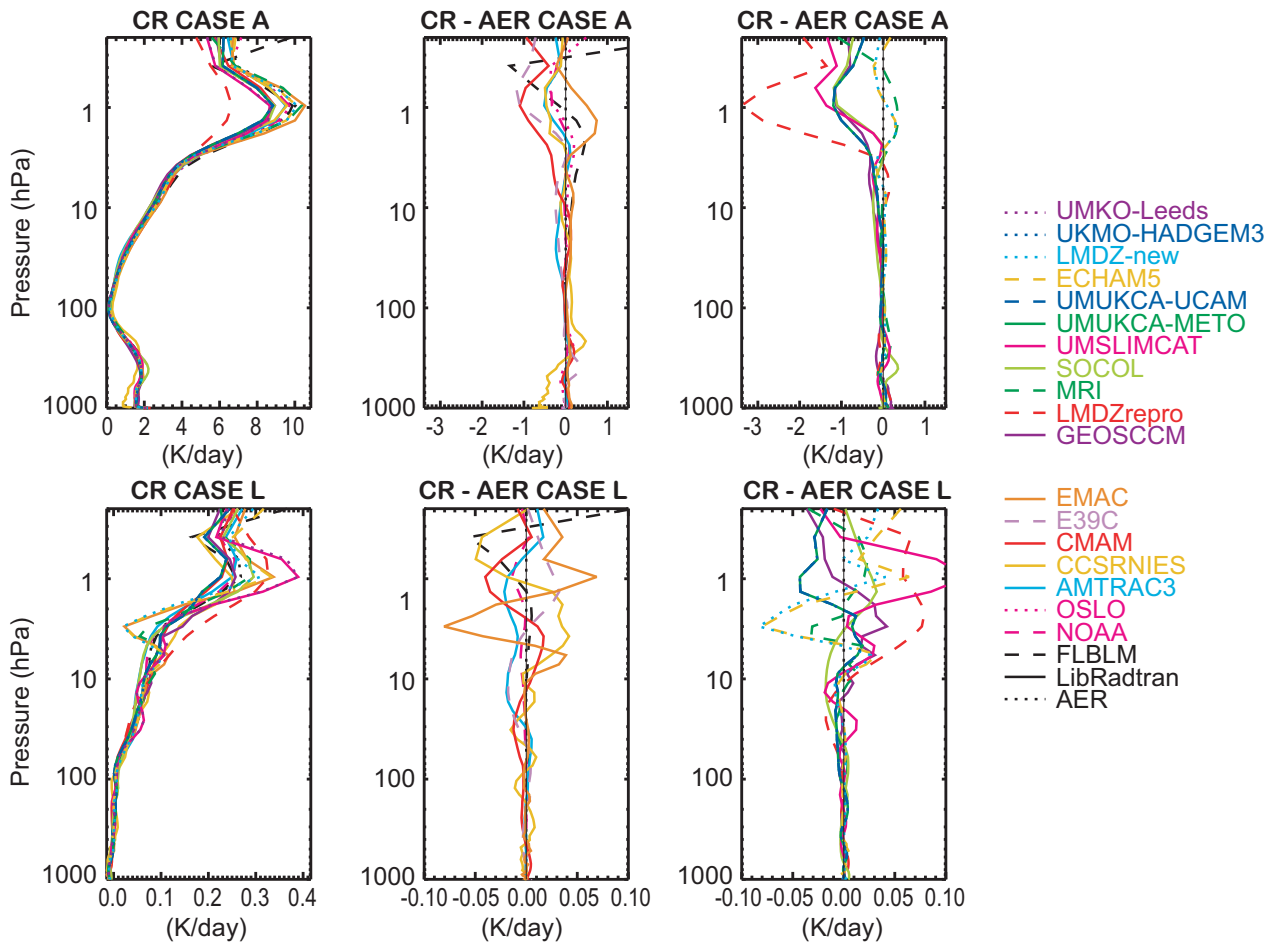


**Figure 3.15:** The top figures show the globally averaged longwave cooling rates for case A (control) (left) and differences in this cooling rate from that calculated with the AER model (middle and right). The bottom figures show the globally averaged longwave cooling rate changes for case L minus case A (the instantaneous change from combined 10% stratospheric ozone depletion and 1980-2005 LL GHG changes) (left) and differences of the same cooling rate change from that calculated with the AER model (middle and right).

**Table 3.9:** Heating rate bias of the models with respect to LibRadtran in K/day. Results are for case B minus case A (i.e., a CO<sub>2</sub> increase from 338 ppm to 380 ppm).

CASE B - CASE A	70 hPa	15 hPa	2 hPa	CASE B - CASE A	70 hPa	15 hPa	2 hPa
FLBLM	0.0003	0.0004	0.0004	MRI	-0.0003	-0.0009	-0.0034
NOAA	-	-	-	SOCOL	0.0030	0.0014	-0.0060
OSLO	0.0002	0.0001	0.0004	UMSLIMCAT	0.0010	0.0038	0.0104
AMTRAC3	-0.0002	0.0005	0.0033	UMUKCA-METO	0.0010	0.0037	0.0104
CCSRNIES	-0.0022	-0.0050	-0.0114	UMUKCA-UCAM	0.0010	0.0038	0.0105
CMAM	0.0021	0.0041	-0.0023	ECHAM5	0.0028	0.0034	-0.0069
E39CA	0.0030	0.0014	-0.0060	LMDZ-new	0.0026	0.0025	-0.0068
EMAC	0.0016	0.0011	-0.0078	UKMO-HADGEM3	0.0010	0.0038	0.0105
GEOSCCM	0.0013	0.0016	0.0024	UKMO-Leeds	0.0010	0.0038	0.0105
LMDZrepro	0.0031	0.0012	-0.0060				

**Table 3.10:** Cooling rate bias of the models with respect to AER in K/day. Results are for case B minus case A (i.e., a CO<sub>2</sub> increase from 338 ppm to 380 ppm).

CASE B - CASE A	70 hPa	15 hPa	2 hPa	CASE B - CASE A	70 hPa	15 hPa	2 hPa
FLBLM	0.0016	0.0010	0.0134	MRI	0.0039	-0.0080	0.0023
NOAA	0.0002	-0.0020	0.0010	SOCOL	0.0039	-0.0108	0.0252
OSLO	0.0003	0.0004	0.0131	UMSLIMCAT	0.0006	-0.0069	0.0044
AMTRAC3	0.0008	-0.0046	0.0028	UMUKCA-METO	-0.0035	0.0015	-0.0036
CCSRNIES	0.0066	0.0055	0.0021	UMUKCA-UCAM	-0.0035	0.0015	-0.0036
CMAM	0004	-0.0013	0.0190	ECHAM5	-0.0012	-0.0033	-0.0579
E39CA	0.0039	-0.0108	0.0252	LMDZ-new	-0.0010	-0.0045	-0.0579
EMAC	-0.0013	0.0015	-0.0442	UKMO-HADGEM3	-0.0035	0.0015	-0.0037
GEOSCCM	0.0004	0.0049	0.0108	UKMO-Leeds	0.0006	-0.0068	0.0045
LMDZrepro	0.0004	-0.0093	0.0228				

**Table 3.11:** Heating rate bias of the models with respect to LibRadtran in K/day. Results are for case H minus case A (i.e., a 10% stratospheric ozone depletion).

CASE H - CASE A	70 hPa	15 hPa	2 hPa	CASE H - CASE A	70 hPa	15 hPa	2 hPa
FLBLM	-0.00123	-0.00923	-0.00046	MRI	-0.00096	-0.00411	-0.00294
NOAA	-	-	-	SOCOL	-0.00006	-0.00194	-0.01317
OSLO	-0.00082	-0.00501	0.00513	UMSLIMCAT	0.00041	0.00792	-0.00034
AMTRAC3	-0.00224	-0.01569	-0.01924	UMUKCA-METO	0.00040	0.00790	-0.00032
CCSRNIES	-0.00056	-0.00002	-0.01239	UMUKCA-UCAM	0.00064	-0.00620	-0.02986
CMAM	0.00013	-0.00919	-0.04148	ECHAM5	0.00075	-0.01238	-0.04441
E39CA	-0.00006	-0.00194	-0.01488	LMDZ-new	0.00077	-0.01144	-0.04453
EMAC	0.00002	-0.0062	-0.02905	UKMO-HADGEM3	0.00053	-0.00756	-0.03098
GEOSCCM	-0.00161	-0.00826	0.01489	UKMO-Leeds	0.00064	-0.00620	-0.02986
LMDZrepro	0.00038	-0.00172	-0.01541				

The LibRadtran vertical profile shows positive heating rate changes in the entire atmosphere, with values ranging between +0.3% above 10 hPa and +0.6% between 100 and 10 hPa due to CO<sub>2</sub> increasing (not shown). The majority of contributing models overestimate the absorption of near-infrared radiation below 4 hPa (see Table 3.9). From analysis of other cases it is evident that none of the models consider absorption in the SW spectral range by LL GHG other than CO<sub>2</sub>.

For cooling rates, the strongest cooling rate change in the stratosphere is associated with CO<sub>2</sub> increase (case B) and ozone depletion (case H). Figure 3.15 (lower panels) reports the cooling rate profiles and the biases with respect to AER for case L minus case A (*i.e.*, a combined effect of all LL GHG change and 10% ozone depletion). Due to combined 10% ozone depletion and LL GHG changes, an increased cooling rate of about 0.25 K/day with respect to the reference case A is found at 1 hPa for AER (Figure 3.15). The model responses deviate between 2% (AMTRAC3) and 40% (UMSLIMCAT and UMUKCA-Leeds) from this value. The FLBLM deviation is about 3% at this level.

The maximum cooling rate bias with respect to AER for imposed CO<sub>2</sub> increase at 70 hPa is found for CCSRNIES (Table 3.10), this value is more than a factor of four larger than the LBL bias. Also E39CA, MRI and SOCOL cooling rate biases are more than twice as large as the LBL bias. UMUKCA-METO, UMUKCA-UCAM and UKMO-HADGEM3 under-estimate the cooling rates by the same factor at this level. At 15 hPa, most of the models tend to under-estimate cooling rates due to the imposed CO<sub>2</sub> increase, with the maximum bias found for SOCOL and E39CA, except CCSRNIES and GEOSCCM which are too sensitive to CO<sub>2</sub> emission by a factor of five. At 2 hPa, EMAC, ECHAM5 and LMDZ-new present the largest negative biases in the cooling rates under-estimating the effect of CO<sub>2</sub> increase. These biases are of the same order of magnitude as the biases for the same models in the heating rates found for a reduction in stratospheric ozone (case H, Table 3.11).

With respect to AER the majority of the CCMVal models and other LBLs under-estimate the cooling rate decrease associated with stratospheric ozone decrease at 70 hPa and 15 hPa (Table 3.12), whereas about half of the models overestimate it at 2 hPa.

Finally, CCSRNIES significantly overestimates the cooling rate associated with stratospheric H<sub>2</sub>O increase at 70 hPa and 15 hPa (Table 3.14), followed by UMUKCA-METO, UMUKCA-UCAM and the two UKMO models at 70 hPa and by E39CA and SOCOL at 15 hPa, whereas LMDZrepro is not sensitive enough to H<sub>2</sub>O change at 15 hPa. CCSRNIES and the UKMO/UMUKCA based models also report too high sensitivity to H<sub>2</sub>O change in the upper stratosphere.

A summary of heating and cooling rates biases by model is presented below. Only biases larger than the largest LBL bias are discussed.

### Heating rates

EMAC slightly overestimates the heating rate in the upper stratosphere. This is consistent with an overestimation of the ozone absorption at 2 hPa.

CCSRNIES largely under-estimates heating rates at 70 hPa, whilst it overestimates them at 2 hPa (~4%), consistently with too high sensitivity of absorption of solar radiation by ozone. This model is also too sensitive to the absorption of solar radiation by H<sub>2</sub>O at 15 hPa and 2 hPa in the infrared spectral region.

GEOSCCM overestimates heating rates at 70 hPa and 2 hPa, which is at 70 hPa consistent with an overestimation of absorption of solar radiation by ozone.

AMTRAC3, ECHAM5, LMDZ-new, CMAM, UMUKCA-UCAM, UMUKCA-HADGEM3 and the two UKMO models overestimate heating rates at 2 hPa, consistent with too large sensitivity to absorption of solar radiation by ozone. All these models, except AMTRAC3 and UMUKCA-UCAM, are not sensitive enough to absorption of solar radiation by H<sub>2</sub>O in the infrared at 70 and 15 hPa.

E39CA, LMDZrepro and SOCOL under-estimate heating rates at 2 hPa (~3%), consistently with an under-estimation of CO<sub>2</sub> absorption.

In general, almost all the models tend to overestimate the weak absorption of solar radiation by CO<sub>2</sub> in the lower and middle stratosphere, consistently with results in Section 3.4.4.

### Cooling rates

CCSRNIES largely overestimates the cooling rates in the lower stratosphere (~50%). This overestimation is consistent with too high a sensitivity to emission due to CO<sub>2</sub> and to H<sub>2</sub>O.

UMSLIMCAT and AMTRAC3 under-estimate the cooling rates in the lower and middle stratosphere by around ~20% and ~15%, respectively. At 15 hPa there is a competing effect of a too small a sensitivity to CO<sub>2</sub> emission and a too high sensitivity to O<sub>3</sub> and/or H<sub>2</sub>O emission.

UMUKCA-METO, UMUKCA-UCAM, UKMO-HADGEM3 and UKMO-Leeds under-estimate cooling rates in the lower stratosphere by ~15%. For the first three models, this under-estimation is consistent with a too small sensitivity to CO<sub>2</sub> emission. All four models tend to be too sensitive to both O<sub>3</sub> and H<sub>2</sub>O emission.

LMDZrepro overestimates the cooling rates at 70 hPa by ~10% and at 2 hPa by ~17%, showing too large a sensitivity to O<sub>3</sub> emission in the lower stratosphere and to CO<sub>2</sub> and H<sub>2</sub>O emission in the upper stratosphere.

**Table 3.12:** Cooling rate bias of the models with respect to AER in K/day. Results are for case H minus case A (i.e., a 10% stratospheric ozone depletion).

CASE H - CASE A	70 hPa	15 hPa	2 hPa	CASE H - CASE A	70 hPa	15 hPa	2 hPa
FLBLM	0.0005	-0.0015	-0.0082	MRI	-0.0021	0.0063	0.0002
NOAA	-0.00003	-0.0008	-0.0015	SOCOL	-0.0013	-0.0066	-0.0056
OSLO	-0.000008	-0.0002	-0.0017	UMSLIMCAT	-0.0008	-0.0103	0.0028
AMTRAC3	0.0021	-0.0145	-0.0165	UMUKCA-METO	-0.0012	-0.0054	0.0203
CCSRNIES	-0.0004	0.0034	0.0348	UMUKCA-UCAM	-0.0012	-0.0054	0.0203
CMAM	-0.0016	0.0011	-0.0142	ECHAM5	-0.0003	-0.0001	-0.0039
E39CA	-0.0013	-0.0066	-0.0056	LMDZ-new	0.0006	-0.0002	-0.0042
EMAC	-0.0008	-0.0012	-0.0022	UKMO-HADGEM3	-0.0012	-0.0054	0.0202
GEOSCCM	-0.0015	-0.0006	0.0245	UKMO-Leeds	-0.0008	-0.0102	0.0029
LMDZrepro	-0.0033	0.0013	0.0577				

**Table 3.13:** Heating rate bias of the models with respect to LibRadtran in K/day. Results are for case J minus case A (i.e., a 10% stratospheric water vapour increase).

CASE J - CASE A	70 hPa	15 hPa	2 hPa	CASE J - CASE A	70 hPa	15 hPa	2 hPa
FLBLM	0.00016	0.00065	0.00285	MRI	0.00022	0.00001	0.00050
NOAA	-	-	-	SOCOL	0.00007	-0.00057	-0.00043
OSLO	-0.00005	0.00039	0.00299	UMSLIMCAT	-0.00025	-0.00057	0.00014
AMTRAC3	0.00013	-0.00029	-0.00010	UMUKCA-METO	0.00036	0.00094	0.00252
CCSRNIES	0.00015	0.00112	0.00313	UMUKCA-UCAM	0.00037	0.00094	0.00250
CMAM	-0.00036	-0.00102	-0.00047	ECHAM5	-0.00035	-0.00099	-0.00042
E39CA	0.00007	-0.00057	-0.00043	LMDZ-new	-0.00040	-0.00113	0.00250
EMAC	-0.00036	-0.00098	-0.00042	UKMO-HADGEM3	0.00036	0.00094	0.00250
GEOSCCM	0.00010	-0.00080	-0.00051	UKMO-Leeds	0.00037	0.00094	0.00250
LMDZrepro	0.00007	-0.00058	0.00025				

**Table 3.14:** Cooling rate bias of the models with respect to AER in K/day. Results are for case J minus case A (i.e., a 10% stratospheric water vapour increase).

CASE J - CASE A	70 hPa	15 hPa	2 hPa	CASE J - CASE A	70 hPa	15 hPa	2 hPa
FLBLM	0.000799	0.000979	0.00204	MRI	0.003412	-0.000488	0.00023
NOAA	0.000261	-0.000408	0.00014	SOCOL	-0.001729	-0.005009	-0.00739
OSLO	0.000759	-0.000051	-0.00018	UMSLIMCAT	0.003696	0.002172	0.01682
AMTRAC3	0.000792	0.000714	0.00234	UMUKCA-METO	0.004084	0.003070	0.02056
CCSRNIES	0.009523	0.016349	0.01829	UMUKCA-UCAM	0.004084	0.003070	0.02056
CMAM	-0.000042	0.000615	-0.00076	ECHAM5	-0.000254	0.000774	0.00561
E39CA	-0.001729	-0.005009	-0.00739	LMDZ-new	-0.000316	0.001125	0.00573
EMAC	0.000188	0.001315	0.00501	UKMO-HADGEM3	0.004078	0.003060	0.02066
GEOSCCM	-0.000533	0.000485	-0.00107	UKMO-Leeds	0.004086	0.003072	0.02058
LMDZrepro	-0.001918	-0.005194	-0.01124				

CMAM under-estimates the cooling rates in the lower stratosphere by ~13%. The model biases show an increased sensitivity to O<sub>3</sub> emission.

SOCOL and E39CA, under-estimate the cooling rates in the middle stratosphere by ~10%. At 15 hPa they report a too small sensitivity to CO<sub>2</sub> and H<sub>2</sub>O emission and a too high sensitivity to O<sub>3</sub> emission.

LMDZrepro overestimates the cooling rates at 2 hPa by ~17%, showing too large a sensitivity to CO<sub>2</sub> and O<sub>3</sub> emission at this level.

EMAC cooling rate response to CO<sub>2</sub> increase (case B) substantially deviates from LBL model results above 10 hPa. The same behaviour is also observed for ECHAM5 and LMDZ-new models which exploit similar LW codes.

**Table 3.15** shows total (SW+LW) heating rates and sigmas used for the three cases used for grading, analysed at the three levels. One sigma corresponds to the maximum absolute SW difference between LBL models and

**Table 3.15:** Total (SW+LW) heating rates and sigmas used for the three cases used for grading, analysed at the three levels: 70, 15 and 2 hPa. One sigma corresponds to the maximum absolute SW difference between LBL models and LibRadtran added to the absolute maximum LW difference between AER and the other LBL models.

All units K/day	Control (CASE A)			CO2 increase (CASE B-A)			10% stratospheric ozone depletion		
	70 hPa	15 hPa	2 hPa	70 hPa	15 hPa	2 hPa	70 hPa	15 hPa	2 hPa
FLBLM	0.04	0.058	-0.277	-0.0013	-0.0006	-0.013	-0.00173	-0.00773	0.00774
OSLO	0.014	0.039	-0.271	0.0005	-0.0003	-0.0127	-0.00081124	-0.00481	0.00683
AMTRAC3	0.046	0.307	0.166	-0.001	0.0051	0.0005	-0.00434	-0.00119	-0.00274
CCSRNIES	-0.232	0.004	0.334	-0.0088	-0.0105	-0.0135	-0.00016	-0.00342	-0.04719
CMAM	0.034	0.057	1.068	0.0017	0.0054	-0.0213	0.00173	-0.01029	-0.00928
E39CA	0.019	0.158	-0.218	-0.0009	0.0122	-0.0312	0.00124	0.00466	-0.00928
EMAC	-0.0007	-0.0669	-0.08	0.0029	-0.0004	0.0364	0.00082	-0.005	-0.02685
GEOSCCM	0.053	0.299	0.585	0.0009	-0.0033	-0.0084	-0.00011	-0.00766	-0.00961
LMDZrepro	0.03	-0.05	0.718	0.0027	0.0105	-0.0288	0.00368	-0.00302	-0.07311
MRI	-0.02	-0.08	-0.094	-0.0042	0.0071	-0.0057	0.00114	-0.01041	-0.00314
SOCOL	0.018965	0.158	-0.198	-0.0009	0.0122	-0.0312	0.00124	0.00466	-0.00757
UMSLIMCAT	0.043	0.113	0.017	0.0004	0.0107	0.006	0.00121	0.01822	-0.00314
UMUKCA-METO	0.037	0.073	0.453	0.0045	0.0022	0.014	0.0016	0.0133	-0.02062
UMUKCA-UCAM	0.037	0.147	1.009	0.0045	0.0023	0.0141	0.00184	-0.0008	-0.05016
ECHAM5	0.04	0.075	0.382	0.004	0.0067	0.051	0.00105	-0.01228	-0.04051
LMDZ-new	0.04	0.098	0.882	0.0036	0.007	0.0511	0.00017	0.01124	-0.04033
UKMO-HADGEM3	0.038	0.168	1.025	0.0045	0.0023	0.0142	0.00173	-0.00216	-0.05118
UKMO-Leeds	0.045	0.185	0.553	0.0004	0.0106	0.006	0.00144	0.004	-0.03276
Sigmas	0.05	0.18	0.631	0.0019	0.0024	0.0139	0.00183	0.01073	0.01333

LibRadtran added to the absolute maximum LW difference between AER and the other LBL models. See Sections 3.6 and 3.7 for grading discussion.

### 3.4.6 Radiation scheme errors and model temperature biases

In this section the assessment of the heating and cooling rates from Section 3.4 is applied to the analysis of the stratospheric temperatures biases simulated by the CCMs. Biases in the global mean temperature climatology (reported in Section 3.3.1) are compared with the temperature errors arising both from the inaccuracy of the radiative heating rate calculations and from the biases in simulated ozone and water vapour mixing ratios (see Section 3.3.1).

The potential errors in the temperature simulations from errors in heating and cooling rates are estimated by

converting the results from the offline heating and cooling rate calculations for reference case A to temperature using pre-calculated relaxation times. Relaxation times represent the thermal inertia due to radiative transfer and are estimated from the cooling rate response to a constant (with height) 1 K temperature change using the correlated k-distribution scheme by Li and Barker (2004). At three considered levels in the lower (70 hPa), middle (15 hPa) and upper (2 hPa) stratosphere, the estimated global mean relaxation times are 180, 25 and 8 days respectively.

The contribution from the ozone and water vapour biases is estimated using biases from Section 3.3.1 to scale the radiative response to the stratospheric ozone depletion and water vapour increase (cases H and J) simulated by the participating models. The obtained errors in the heating and cooling rates associated with the model's ozone and water vapor biases are also converted to an equivalent temperature bias using the relaxation time. This procedure provides temperature errors for all participating models related both to the errors in the LW and SW radiation codes and to the errors in the simulated ozone and water vapour fields.

The analysis has been carried out for the upper, middle and lower stratosphere (pressure levels 2, 15 and 70 hPa) and the conclusions drawn in this section generally confirm the qualitative assessment of the upper stratospheric model performance in Section 3.3.1. The results for the upper stratosphere (2 hPa) are shown in **Figure 3.16**. At this level the total temperature errors derived from the inaccuracy of the radiation schemes and the biases in ozone and water vapour abundances are very close to the temperature biases simulated by the CCMs for most of the participating models (black diamonds and black circles, respectively). For AMTRAC3 the small positive temperature bias is explained by overestimated solar heating rates. The large temperature bias for CCSRNIES results from under-estimated longwave cooling rates, overestimated solar heating rates, and a negative bias in the simulated water vapour mixing ratio, with all three factors contributing about equally. The large warm bias for CMAM is explained both by overestimation of solar heating rates and under-estimation of cooling rates. The small temperature bias for EMAC is due to its overestimated cooling rates. For GEOSCCM the warm bias is produced by overestimated heating rates and under-estimated cooling rates and is partially compensated by under-estimated ozone mixing ratios. The very large temperature bias for LMDZrepro is dominated by a massive under-estimation of the cooling rates. The negative temperature bias for MRI is mainly due to slightly overestimated cooling rates, while the same sized bias in SOCOL is primarily due to under-estimated solar heating rates and a negative bias in the ozone mixing ratio. UMSLIMCAT has only a very small cold bias, for which a small under-estimation of the cooling rates is com-

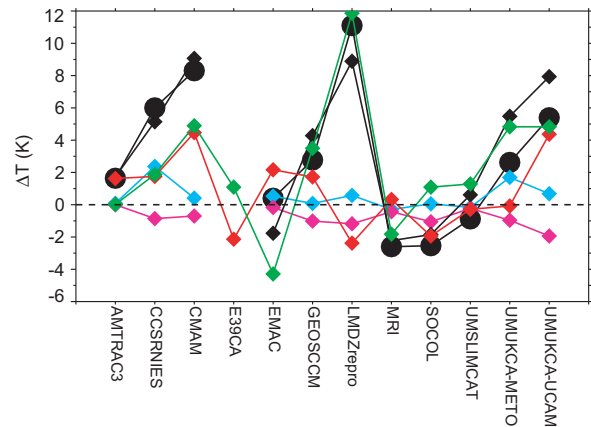


**Figure 3.16:** The bias in the simulated global mean temperature at 2 hPa from Section 3.3 (black circles) and the estimated contributions of CCM biases in: ozone climatology (pink diamonds); water vapour climatology (light blue diamonds); and longwave/shortwave heating rates calculations (green/red diamonds). The total CCM bias is represented by black diamonds. See text for details.

pensated by the cumulative effects of small errors in solar heating and water vapour and ozone mixing ratios. Warm biases in UMUKCA-METO and UMUKCA-UCAM result primarily from under-estimated cooling rates, although under-estimated water vapour mixing ratios for UMUKCA-METO and overestimated solar heating rates and under-estimated ozone mixing ratios for UMUKCA-UCAM also contribute significantly.

Four models were singled out in the analysis of simulated temperature climatologies in Section 3.3.1 as likely to have deficiencies in their radiation schemes in the upper stratosphere: CCSRNIES, CMAM, CNRM-ACM and LMDZrepro. While CNRM-ACM is not analysed here, the present analysis confirms the qualitative assessment made in Section 3.3.1 for the other three models.

In the middle stratosphere (15 hPa) and in the lower stratosphere (70 hPa) the temperature biases and estimated errors (not shown) are generally well correlated but significant discrepancies between the two values exist, making a similar analysis less useful for these heights. This is probably due to a number of reasons. First, using relaxation time for the conversion heating rate to temperature is a rough approach which works better in the vicinity of the stratopause than in the middle and lower stratosphere where the relaxation time depends more strongly on the shape of the perturbation and has a strong latitudinal dependence. Second, the effect of errors in  $O_3$  and  $H_2O$  mixing ratios has been estimated based on the local biases. However, non-locality plays an important role in the middle and lower stratosphere for both solar heating and longwave cooling rate calculations. Third, the temperature biases reported in Section 3.3.1 are based on the annually averaged glo-



bal mean climatology, whereas heating rates used to estimate errors are global values based on calculations at five latitudes for January conditions. And finally, the effect of clouds and volcanic aerosol which is important in the lower and middle stratosphere, was not evaluated in the framework of this exercise.

### 3.5 Solar signal in CCMs

The incident solar radiation at the top of Earth's atmosphere varies on different time scales. Observational studies, *e.g.*, Randel *et al.* (2009), found a statistically significant decadal signal in annual mean upper stratospheric temperature of up to 1 K, associated with the 11-year solar activity cycle. While the total solar irradiance (TSI), *i.e.*, the spectrally integrated solar irradiance at the top of Earth's atmosphere, varies only by about 0.1% over the 11-year cycle, larger variations occur in the ultraviolet (UV) part of the spectrum, reaching several percent in the ozone absorption bands that are responsible for the SW heating of the stratosphere. However, given the much lower intensity in the UV spectral region compared to the visible (VIS) and near-infrared (IR) parts of the solar spectrum, and because of the historical focus of numerical global modelling on the troposphere where absorption of solar UV radiation by ozone plays only a very minor role, SW radiation codes in GCMs and CCMs do not consider the solar irradiance for the wavelengths shorter than  $\sim 250$  nm and quite often exploit broad-band parameterisations using TSI as an input variable. Depending on the radiation scheme, fractions of TSI are then used to calculate solar fluxes and heating rates in one or two SW absorption bands from the top of the atmosphere to the surface. More sophisticated SW radiation codes designed for applications to the middle atmosphere usually consider extended spectral range and include more spectral bands in the UV/VIS. Egorova *et al.* (2004) and Nissen *et al.* (2007) compared the performance of SW radiation codes with different spectral resolution and showed that the observed solar temperature signal in the stratosphere can only be reproduced in models that allow for the effects of spectral variations between solar minimum and maximum.

In this section we will address the following questions:

1. How sensitive are the CCM SW radiation codes to changes in solar irradiance and ozone?
2. How well is the 11-year radiative solar signature reproduced by the participating SW radiation codes in comparison with reference LBL codes?
3. Can the grade of the simulated solar signature in temperature in the REF-B1 simulations, discussed in Chapter 8 of this report, be explained in terms of the characteristics of the SW radiation codes?

#### 3.5.1 Experimental Setup

Heating rate differences between the minimum and maximum phases of the 11-year solar cycle have been calculated in stand-alone versions of the CCM shortwave radiation parameterisations and in LBL models for prescribed spectral flux and solar induced ozone differences between the minimum and maximum phases of the 11-year solar cycle.

The spectral solar irradiance (SSI) and TSI data to be used in this comparison are based on the method described in Lean *et al.* (2005). Extra-terrestrial spectral solar irradiance for the spectral range 120 – 100,000 nm were provided with a spectral resolution ranging from 1 to 50 nm as well as the spectral integral over all wavelengths, *i.e.*, TSI. The monthly mean solar irradiance of September 1986 and November 1989 has been selected for solar minimum and solar maximum conditions, respectively. For mean solar conditions average data were derived from the period 1950 to 2006. Depending on the individual SW radiation codes the modelling groups were requested to either use the suggested TSI for solar minimum and maximum conditions, or to integrate the provided high resolution spectral irradiances to match the broader spectral intervals of their own SW radiation codes and to adapt the total solar irradiance to be consistent with the integral over all intervals.

**Table 3.16:** Experimental setup for offline solar variability simulations.

Experiment	Solar irradiance	Ozone
A	mean	1980 climatology
O	max	1980 climatology
P	min	1980 climatology
R	mean	max
S	mean	min

**Table 3.17:** Participating offline SW radiation codes and ways of prescribing solar variability.

CCM	TSI	Spectral
CCSRNIES		✓
CMAM		✓
ECHAM4	✓	
ECHAM5	✓	
EMAC		✓
LMDZrepro	✓	
SOCOL		✓
UMSLIMCAT		✓
UMUKCA-METO	✓	
UMUKCA-UCAM	✓	

To study the effect of solar induced ozone variations on heating rates, experiments with mean solar irradiance and prescribed ozone changes between solar minimum and maximum were carried out. The ozone changes have been derived from 2-dimensional, photochemical model calculations (Haigh, 1994) to ensure smooth distributions of the changes.

Further settings of the experiments were identical to the 1980 control simulation (case A, Table 3.4). **Table 3.16** gives an overview of the recommended experiments.

The participating CCM SW radiation codes and the provided SW radiative heating rates are summarized in **Table 3.17**. Further it is indicated whether the radiation codes are forced with TSI or spectral irradiance data. More details of the radiation codes including references can be found in Chapter 2.

The results of the offline calculations have been evaluated against reference calculations from the LBL radiation code LibRadtran (Meyer and Kylling, 2005).

### 3.5.2 Sensitivity of the solar signal to spectral resolution

**Figure 3.17** shows global mean profiles of the differences in SW heating rates between solar minimum and maximum in January. In the left panel only solar irradiance variations are taken into account and in the middle panel the effects of prescribed solar induced ozone changes only. The right panel shows the total effects of solar irradiance and prescribed solar induced ozone changes between solar minimum and maximum. The largest response to 11-year solar irradiance changes (experiments O-P, left panel) occurs in the stratopause region with global mean heating rate changes from solar minimum to maximum of about 0.12 K/d in the LibRadtran reference model (black line). The results of the CCM radiation schemes can be grouped into three categories: a) schemes that closely follow the reference heating rate change profile, *i.e.*, CMAM, EMAC and CCSRNIES, and with some minor deviations SOCOL, b) two schemes that reproduce about half of the reference heating rate differences (ECHAM5 and UMSLIMCAT) and c) schemes that have an almost negligible radiative response to solar irradiance changes of less 0.02 K/day, like ECHAM4, LMDZrepro, UMUKCA-METO, and UMUKCA-UCAM.

Differences between the three groups can be explained by the spectral resolution of the prescribed solar irradiance change between solar minimum and maximum. With 44 spectral intervals between 121 and 683 nm the EMAC scheme reproduces the reference profile over the whole stratosphere very well; similarly the CMAM code with 8 bands between 121 and 305.5 nm and only 3 bands for ozone absorption between 206 and 305.5 nm. SOCOL (4 spectral intervals between 120 and 680 nm) overesti-

mates the maximum SW heating rate difference in the lower mesosphere by about 10%, associated with an under-estimation in the lower stratosphere. In contrast, the SW radiation codes in LMDZrepro, UMUKCA-METO, UMUKCA-UCAM, and ECHAM4 that are driven by TSI changes between solar minimum and maximum only, are not able to capture the magnitude of the SW heating rate changes between solar minimum and maximum.

The SW radiation scheme of the Unified Model (UM) model series can also be driven by spectral irradiance changes, as was done for example in the REF-B1 simulation of UMSLIMCAT. This allows for a direct assessment of the effect of spectral irradiance versus TSI input data. As seen in Figure 3.17 (left panel), the SW heating rate response of the spectrally forced offline calculation with UMSLIMCAT is stronger than in the TSI forced UMUKCA-METO and UMUKCA-UCAM models. However with a SW heating rate difference of  $\sim 0.07$  K/day, UMSLIMCAT reproduces only about 50% of the LBL model result. A similar result to that of UMSLIMCAT is obtained for ECHAM5. The ECHAM5 offline radiation code was included into this comparison to investigate the effect of adding two bands in the UV to the single UV/VIS absorption band used in the ECHAM4 code (Cagnazzo *et al.*, 2007). Although with the additional absorption bands (185–690 nm) the full spectral range of ozone absorption is resolved, only 50% of the heating rate differences between solar minimum and maximum can be simulated.

The global mean SW heating rate response to prescribed solar induced ozone changes (experiments R-S, middle panel of Figure 3.17) in the reference model reaches about 0.07 K/d from solar minimum to maximum, that is approximately 65% of the response to the solar irradiance variations. The strongest response occurs in the upper stratosphere, about 10 km lower than the strongest response to irradiance changes. This behaviour is qualitatively well reproduced by the different CCM radiation codes. Deviations from the LBL code are much smaller than for the irradiance changes, as mean solar irradiance was prescribed to isolate the clean ‘ozone effect’. Differences between the models occur due to the band width adopted and generally correspond to the differences encountered in case A. Note that the ‘ozone effect’ exceeds the effect of solar irradiance variations below 10 hPa emphasising the importance of considering the feedback of changes in ozone photochemistry during a solar cycle on the SW radiation budget.

The total SW heating rate change between solar minimum and maximum, *i.e.*, due to both solar irradiance changes and the solar induced ozone changes, (right panel in Figure 3.17) clearly illustrates that those CCM SW radiation codes that use only TSI variations under-estimate the solar radiative signal by about 50%.

The response to solar variability obtained with the CCM SW radiation codes in offline mode is generally

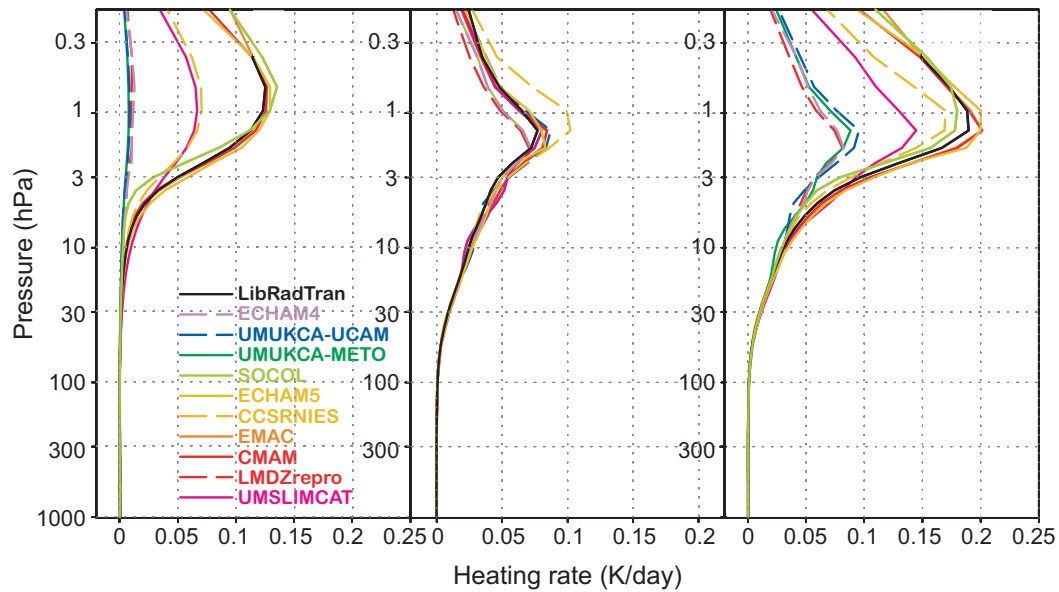


**Figure 3.17:** Global mean, shortwave heating rate differences between minimum and maximum of the 11-year solar cycle in January (K/d), calculated offline in CCM radiation schemes and one reference LBL model. Left panel: Radiative response to prescribed solar irradiance change (experiments O-P, Table 3.16), middle panel: radiative response to solar induced ozone change (experiments R-S, Table 3.16), right panel: total radiative response (experiments (O-P)+(R-S), Table 3.16).

consistent with the solar response in the transient REF-B1 simulations discussed in Chapter 8. The REF-B1 solar heating rate differences for those models, which also provided off-line heating rates (CCSRNIIES, CMAM, EMAC, and LMDZrepro) range between 0.07 and 0.17 K per day per 100 units of the F10.7cm solar flux around the tropical stratopause (Figure 8.12). By multiplying these values by a factor 1.3 we obtain an estimate of the SW heating rate differences between solar minimum and maximum that can be compared with the offline calculations. There is good agreement between online and offline calculated heating rate differences for the four CCMs (not shown). For example, we find an annual mean tropical heating rate difference of 0.20 K per day in the REF-B1 run of CMAM and a heating rate difference of 0.22 K per day at the equator in January from the CMAM offline code.

In Chapter 8, the temperature response to decadal solar forcing in the CCMs was derived by a multiple linear regression analysis (Figure 8.11). The strongest solar temperature signal is found consistently in the tropical upper stratosphere/lower mesosphere, indicating that the direct mechanism of heating by absorption of enhanced UV radiation at solar maximum is well captured by the spectrally resolving SW radiation schemes. The reduced decadal temperature signal in LMDZrepro can be explained by the under-estimation of the spectral solar forcing that was identified in the offline calculations. However, while the responses to solar irradiance changes in the spectrally resolving radiation codes of CCSRNIIES, CMAM, EMAC, and SOCOL are close to each other (Figure 3.17, left pan-

el), the solar temperature responses in the corresponding REF-B1 simulations of these models show a considerable spread in the upper stratosphere and mesosphere (Figure 8.11a), which cannot be explained by a direct radiative effect alone. Similarly, indirect dynamical processes seem to contribute to the strong solar response of mesospheric temperature in the UMSLIMCAT REF-B1 simulation, as the offline calculation shows that its SW radiation code underestimates the heating rate response to UV-variations.

### 3.6 Summary

In this section, as in other chapters, we employ the concepts of metrics and grades to help synthesize the discussions of the preceding sections. A metric can be seen as a way for assessing a model and comparing it to an objective benchmark. For example we compare a model's globally averaged temperature to an observed climatological mean. In this case the metric would be temperature difference, and the benchmark given as the observed climatological mean temperature. A grading is then applied to this temperature difference according to how big a difference is deemed acceptable without down-grading the model performance. For our example, we compare the model temperature difference to the observed interannual variability in temperature, and say that a model with an error smaller than the interannual variability is performing well, and assign the model a “good” grade.

We adopt the above approach in a quantitative way.

Each CCM is graded between zero and one, with a grade of one representing a “perfect” result and a grade of zero representing no skill. The gradings are based on a standard deviation approach where, nominally, one sigma ( $\sigma$ ) away from the reference diagnostic reduces the grade by 0.33. A grade ( $G$ ) is given by

$$G = 1 - 0.33 X/\sigma, \quad (3.1)$$

Therefore, three or more sigmas away from the reference diagnostic would give a grade of zero. For most metrics, a sigma value could not be calculated from statistics so the choice of sigma values and grading has been somewhat subjective. Table 3.1 summarizes the metrics and gradings used to evaluate each processes. **Table 3.18** gives details of each grading used and tables in the chapter that give the diagnostics and sigma values that are used to calculate the grades for each process.

Three sets of gradings are shown in Figures 3.18 to 3.21. These refer to temperature based diagnostics (**Figure 3.18**), flux diagnostics (**Figure 3.19**) and heating rate diagnostics (**Figure 3.20**). Sigma values used are based on interannual variability measures for temperature trend metrics. For other metrics sigmas are based on the maximum difference between CCMs and either reference analyses or reference calculations. Therefore, a model grade above 0.66 is as good as can be expected with current knowledge. We class grades as 0.66 or higher “good”, grades between 0.33 and 0.66 as “adequate” and grades below 0.33 as “poor”. Note that many caveats exist in grade representation and these grades should not be seen as definitive or over interpreted. A different choice of diagnostic, reference model and/or sigma can lead to different answers. We have tried to be pragmatic with these choices, picking metrics that we believe to be most relevant to the CCM community, although a degree of subjectivity will still exist.

By deriving sigma values from differences between reference calculations a poor grading does not necessarily mean a large source of model error. Take, for example, the CO<sub>2</sub> and stratospheric water vapour forcing grades in Figure 3.19. The stratospheric water vapour forcing has errors of over 100% between models (Figure 3.12), yet model grades are adequate or good. Whereas, the error in CO<sub>2</sub> forcing is estimated to be within 20% (Figure 3.9) yet several CCMs are given a poor grade. This, perhaps unintuitive, grading results from the CO<sub>2</sub> forcing being much better constrained between the reference sets of calculations, compared to the reference calculations for stratospheric water vapour. Our choice of metric can therefore be seen as an indicator of how close a model is to “state of the art” rather than how accurate a model is.

General grading features are discussed here. Individual model grades and performance are summarized in Section 3.7.

Many CCMs have poor representation of lower strat-

ospheric temperatures yet are able to produce a good simulation of temperature trends throughout the stratosphere (Figure 3.18). This likely is, in part, due to temperature changes depending largely on carbon dioxide and ozone changes, whereas many other factors such as clouds can affect temperature climatologies in the lower stratosphere. The multi-model mean has a higher grade than all but one model (WACCM) which indicates the value of multi-model studies.

CO<sub>2</sub> and N<sub>2</sub>O forcings are generally less well modelled by CCMs than by LBLs, so CCMs typically have a poor grader for these forcings, indicating potential areas for radiation scheme improvement (Figure 3.19). When gradings are combined with knowledge of radiation scheme errors (see above), a good grade for stratospheric water vapour changes suggests that at least some of the sets of reference calculations should be improved.

Stratospheric heating rate based metrics for the climatology, CO<sub>2</sub> increases and ozone depletion are shown in Figure 3.20. These grades are generally good across CCMs, meaning that CCMs should be able to provide good estimates of temperature change. Hence these grades corroborate the temperature trend based grade results in Figure 3.18.

The aim of Section 3.5 was to validate the ability of the CCM SW radiation codes to reproduce the radiative effects of decadal solar variability. Therefore, the basis for allotting grades to the different SW radiation codes (Table 3.17) is their response or sensitivity to solar irradiance changes that vary increasingly towards shorter wavelengths between solar minimum and maximum, reaching several percent in the UV. The comparison described here clearly revealed that only CCM radiation codes that are designed to take prescribed spectral irradiance data into account are able to reproduce the magnitude and vertical profile shape of the heating rate differences between solar minimum and maximum (Figure 3.17, left panel). These models (CCSRNIES, CMAM, EMAC, and SOCOL) simulate the reference heating rate difference profile within a few percent and are therefore graded as 0.9 (see Table 3.17). Another class of models fails to reproduce the solar signal in SW heating rates due to their neglect of spectral irradiance changes. These models (ECHAM4, LMDZrepo, UMUKCA-METO, and UMUKCA-UCAM) are graded as 0.1. Two models (ECHAM5 and UMSLIMCAT) are able to alleviate the bias to some extent by considering spectral irradiance changes in a simplified way. They reproduce about half the variability in SW heating rates, and are therefore graded as 0.5.

This grading also applies to the total effects of solar variability (Figure 3.17, right panel) including the effects of solar induced ozone changes, as the heating rate changes due to prescribed solar induced ozone changes (Figure 3.17, middle panel), are well captured by most models. As

**Table 3.18:** A summary of the metrics and gradings used to evaluate each processes.

Process	Metric	Metric sigma basis	Grading basis
Stratospheric temperatures	Comparing 1980-1999 climatological global mean temperature profiles	Maximum difference between ERA 40 and either UKMO or NCEP analysis. Evaluated at 70 hPa, 15 hPa and 2 hPa	See Table 3.2
Stratospheric temperature change	Comparing 1980-1999 global mean temperature trends	MSU/SSU trend uncertainty (95% confidence interval). Evaluated at 70 hPa, 15 hPa and 2 hPa	See Table 3.3
Radiative fluxes	Comparing global mean total (SW+LW) climatological fluxes in offline radiation schemes with LBL models	Maximum difference between sophisticated radiation models for globally annually averaged total (SW+LW). Evaluated at the tropopause	See Table 3.6
Radiative forcing	Comparing global mean instantaneous total forcings (SW+LW) in offline radiation schemes for a variety of atmospheric composition changes with LBL models	Maximum difference between sophisticated radiation models for globally annually averaged total (SW+LW). Evaluated at the tropopause	See Table 3.6
Stratospheric heating/cooling	Comparing global mean total (SW+LW) climatological heating rates in offline radiation schemes with LBL models	Maximum difference between sophisticated radiation models for globally annually averaged total (SW+LW). Evaluated at 70 hPa, 15 hPa and 2 hPa	See Table 3.15
Changes in stratospheric heating/cooling	Comparing changes in globally averaged total (SW+LW) heating rates in offline radiation schemes with LBL models	Maximum difference between sophisticated radiation models for globally annually averaged total (SW+LW). Evaluated at 70 hPa, 15 hPa and 2 hPa	See Table 3.15
Solar variability	Comparing globally averaged SW heating rates in offline radiation schemes with prescribed solar spectrum variations and ozone change	Whether or not radiation code reproduces sophisticated model signal. A subjective grade based on how similar their signal is to LibRadtran results	See Table 3.17

the outcome of this inter-comparison clearly suggests three categories of SW radiation codes, we abstain from a more detailed grading.

Throughout the chapter we have tried to explain differences between CCMs. However, in many instances appropriate diagnostics were not available and interpretation is lacking, so a full assessment of differences has not been possible.

### 3.6.1 Summary by model

We class grades as 0.66 or higher “good”, grades

between 0.33 and 0.66 as “adequate” and grades below 0.33 as “poor”. We employ this standard terminology to the model summaries below. For English clarity respective adverb forms of “well”, “adequately” and “poorly” are also employed,

**AMTRAC3:** This CCM has an adequate representation of climatological global mean temperatures in the lower and middle stratosphere, and a good representation of temperatures in the upper stratosphere. Global mean temperature trends throughout the stratosphere are well reproduced. Climatological total radiative flux at the tropopause is well modelled. Radiative forcings at the tropopause are well modelled for water vapour changes, both in the stratosphere and troposphere, and for CH<sub>4</sub>, CFC forcings and

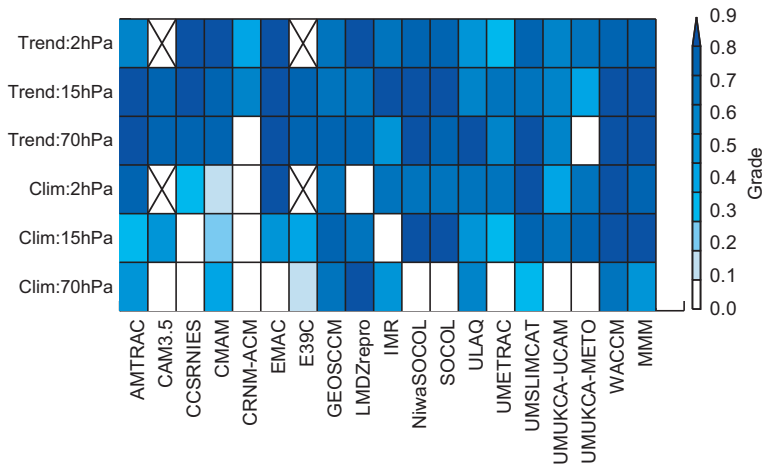


**Figure 3.18:** CCM grades for globally averaged climatological stratospheric temperatures and their trend. See Table 3.18 for details.

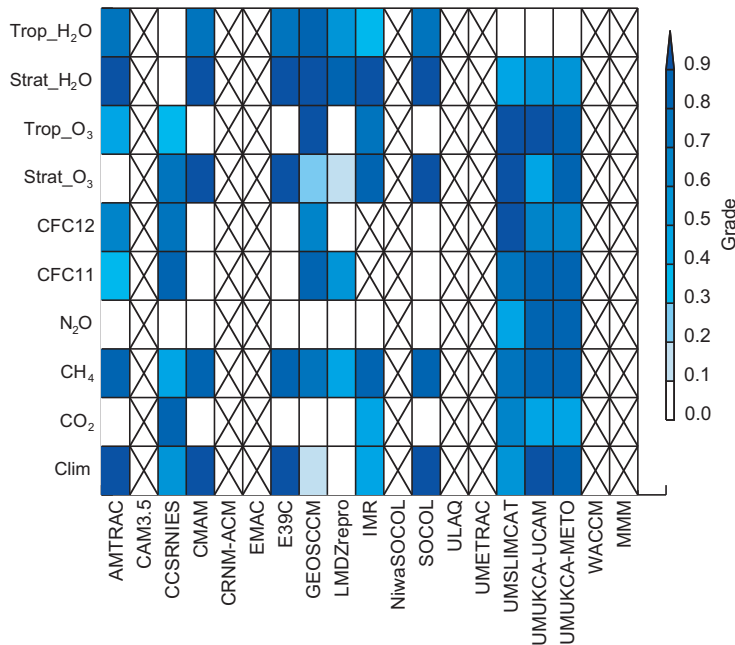


**Figure 3.19:** CCM grades for globally averaged fluxes at the 200 hPa tropopause and their change (radiative forcing). See Table 3.18 for details.

tropospheric O<sub>3</sub> forcings are adequately modelled. CO<sub>2</sub>, stratospheric O<sub>3</sub> and N<sub>2</sub>O forcings are poorly modelled. Climatological heating rates and their change from CO<sub>2</sub> and stratospheric O<sub>3</sub> perturbations are either adequate or better. The CCM’s representation of solar variability is not assessed.

**CAM3.5:** This CCM has a low model lid so upper stratospheric levels were not assessed. This CCM has an adequate representation of climatological global mean temperatures in the middle stratosphere, and a poor representation of temperatures in the lower stratosphere. Global mean temperature trends throughout the CCM’s stratosphere are well reproduced. The CCM’s representation of fluxes,

heating rates and solar variability is not assessed.

**CCSRNIIES:** This CCM has an adequate representation of climatological global mean temperatures in the upper stratosphere, and a poor representation of temperatures in the lower and middle stratosphere. Global mean temperature trends throughout the stratosphere are well reproduced. Climatological total radiative flux at the tropopause is adequately modelled. CO<sub>2</sub>, stratospheric O<sub>3</sub> and CFC forcings are well modelled. CH<sub>4</sub> and tropospheric ozone forcings are adequately modelled. Radiative forcings at the tropopause are poorly modelled for water vapour changes, both in the stratosphere and troposphere, and for N<sub>2</sub>O. Climatological heating rates are well represented, except

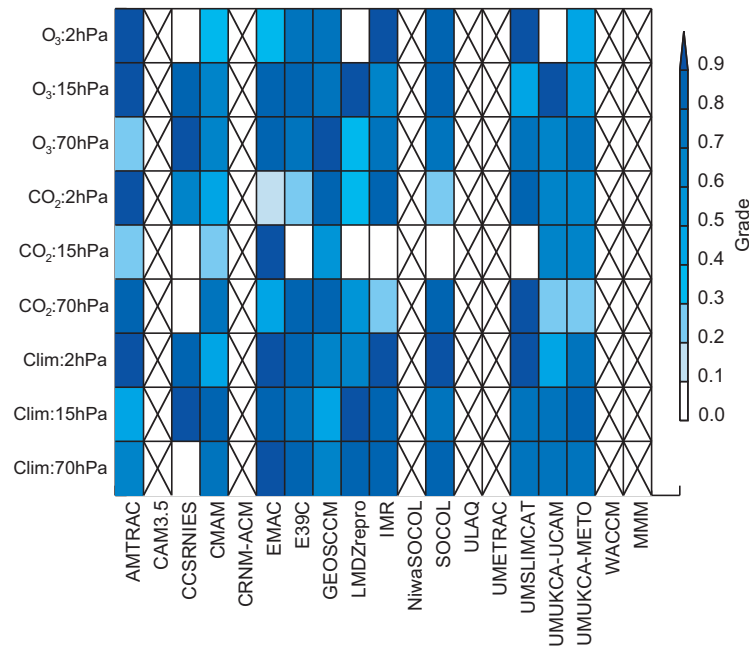


**Figure 3.20:** CCM grades for globally averaged climatological stratospheric heating rates and their changes. See Table 3.18 for details.

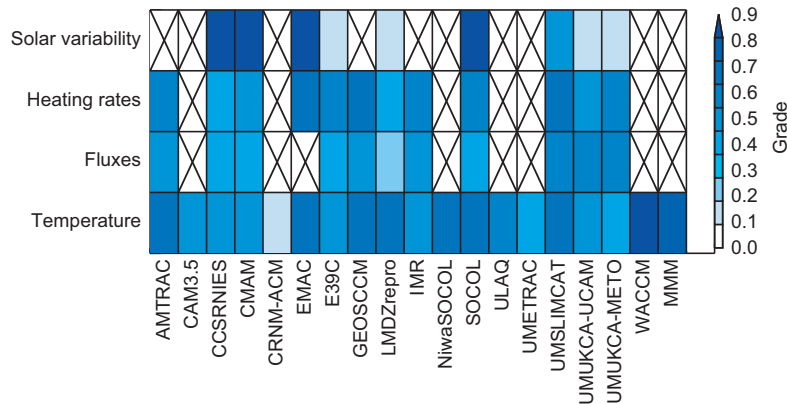


**Figure 3.21:** A summary of the average CCM grade for temperature related metrics (Figure 3.18), flux related metrics (Figure 3.19), heating rate related metrics (Figure 3.20) and the solar heating metric (Table 3.17).

in the lower stratosphere which is poorly represented. Changes in heating rates are well modelled for ozone in the lower and middle stratosphere and for CO<sub>2</sub> in the upper stratosphere. Middle and lower stratospheric heating rate changes due to CO<sub>2</sub> are poorly modelled, as are upper stratospheric ozone heating rate changes. The CCM’s representation of solar variability is good.

**CMAM:** This CCM has an adequate representation of climatological global mean temperatures in the lower stratosphere, and a poor representation of temperatures in the middle and upper stratosphere. Global mean temperature trends throughout the stratosphere are well reproduced. Climatological total radiative flux at the tropopause is well modelled. Radiative forcings at the tropopause are well

modelled for CH<sub>4</sub> and stratospheric water vapour changes, while stratospheric O<sub>3</sub>, CFC, CO<sub>2</sub>, N<sub>2</sub>O and tropospheric O<sub>3</sub> forcings are poorly modelled. Climatological heating rates and their change from CO<sub>2</sub> and stratospheric O<sub>3</sub> perturbations are either adequate or better. The CCM’s representation of solar variability is good.

**CNRM-ACM:** This CCM has a poor representation of climatological global mean temperatures throughout stratosphere. Global mean temperature trends reproduction in the middle and upper stratosphere are adequate. Reproduction of temperature trends in the lower stratosphere is poor. The CCM’s representation of fluxes, heating rates and solar variability is not assessed.

**EMAC:** This CCM has a good representation of climatological global mean temperatures in the upper stratosphere, adequate representation in the middle stratosphere and poor representation in lower stratosphere. Global mean temperature trends throughout the stratosphere are well reproduced. Climatological total radiative flux at the tropopause is not assessed. Climatological heating rates are well represented. Changes in heating rates from stratospheric O<sub>3</sub> perturbations are good, except at upper stratospheric levels where they are adequate. Heating rate changes from CO<sub>2</sub> perturbations are adequate or better, except in the upper stratosphere where they are poor. The CCM's representation of solar variability is good.

**E39CA:** This CCM has a low model lid so upper stratospheric levels were not assessed. This CCM has an adequate representation of climatological global mean temperatures in the middle stratosphere, and a poor representation of temperatures in the lower stratosphere. Global mean temperature trends throughout the CCM's stratosphere are well reproduced. Climatological total radiative flux at the tropopause is well modelled. Radiative forcings at the tropopause are well modelled for CH<sub>4</sub>, CFC, stratospheric O<sub>3</sub> and water vapour changes, both in the stratosphere and troposphere, for tropospheric O<sub>3</sub> and for CO<sub>2</sub>, N<sub>2</sub>O and tropospheric O<sub>3</sub> forcings are poorly modelled. Climatological heating rates and their change from CO<sub>2</sub> and stratospheric O<sub>3</sub> perturbations are either adequate or better. The CCM's representation of solar variability is poor.

**GEOSCCM:** This CCM has a good representation of climatological global mean temperatures throughout the stratosphere. Global mean temperature trends throughout the stratosphere are well reproduced. Climatological total radiative flux at the tropopause is poorly modelled. Radiative forcings at the tropopause are well modelled for water vapour changes, both in the stratosphere and troposphere, and for CH<sub>4</sub>, the CFCs, and for tropospheric O<sub>3</sub>. Stratospheric O<sub>3</sub> forcing is adequately modelled while CO<sub>2</sub> and N<sub>2</sub>O forcings are poorly modelled. Climatological heating rates and their change from CO<sub>2</sub> and stratospheric O<sub>3</sub> perturbations are either adequate or better. The CCM's representation of solar variability is not assessed.

**LMDZrepro:** This CCM has a good representation of climatological global mean temperatures in the lower and middle stratosphere, and a poor representation of temperatures in the upper stratosphere. Global mean temperature trends throughout the stratosphere are well reproduced. Climatological total radiative flux at the tropopause is poorly modelled. Radiative forcings at the tropopause are well modelled for water vapour changes, both in the stratosphere and troposphere. CH<sub>4</sub> and CFC12 forcings are adequately modelled. CFC11, CO<sub>2</sub>, tropospheric O<sub>3</sub> and stratospheric

O<sub>3</sub> forcings are all poorly modelled. Climatological heating rates and their change from CO<sub>2</sub> and stratospheric O<sub>3</sub> perturbations are either adequate or better, except in the middle troposphere for CO<sub>2</sub> changes and the upper troposphere for ozone changes where representation is poor. The CCM's representation of solar variability is poor.

**MRI:** This CCM has a good representation of climatological global mean temperatures in the upper stratosphere, an adequate representation of temperatures in the lower stratosphere, and a poor representation in the middle stratosphere. Global mean temperature trends in the upper and middle stratosphere are well reproduced, whilst temperature trends in the lower stratosphere are adequately reproduced. Climatological total radiative flux at the tropopause is adequately modelled. Radiative forcings at the tropopause are well modelled for water vapour changes in the stratosphere, for O<sub>3</sub> changes both in the stratosphere and troposphere, and for CH<sub>4</sub>, CO<sub>2</sub> and water vapour forcings in the troposphere are adequately represented. The forcings from N<sub>2</sub>O is poorly represented. CFC forcings are not assessed. Climatological heating rates and their change from CO<sub>2</sub> and stratospheric O<sub>3</sub> perturbations are either adequate or better, except in the mid- and low troposphere for CO<sub>2</sub> changes where representation is poor. The CCM's representation of solar variability is not assessed.

**NiwaSOCOL:** This CCM has a good representation of climatological global mean temperatures in the middle and upper stratosphere and a poor representation in the lower stratosphere. Global mean temperature trends are well reproduced throughout the stratosphere. The CCM's representation of fluxes, heating rates and solar variability is not assessed.

**SOCOL:** This CCM has a good representation of climatological global mean temperatures in the middle and upper stratosphere and a poor representation in the lower stratosphere. Global mean temperature trends are well reproduced throughout the stratosphere. Climatological total radiative flux at the tropopause is well modelled. Radiative forcings at the tropopause are well modelled for water vapour changes in the stratosphere and troposphere, for O<sub>3</sub> changes in the stratosphere, for CFCs and CH<sub>4</sub>. Forcings from CO<sub>2</sub>, N<sub>2</sub>O, and O<sub>3</sub> changes in the troposphere are poorly represented. Climatological heating rates and their change from CO<sub>2</sub> and stratospheric O<sub>3</sub> perturbations are either adequate or better, except in the middle and upper troposphere for CO<sub>2</sub> changes where representation is poor. The CCM's representation of solar variability is good.

**ULAQ:** This CCM has a good representation of climatological global mean temperatures in the lower and upper stratosphere and an adequate representation in the middle



stratosphere. Global mean temperature trends are well reproduced throughout the stratosphere. The CCM's representation of fluxes, heating rates and solar variability is not assessed.

**UMETRAC:** This CCM has a good representation of climatological global mean temperatures in the upper stratosphere, an adequate representation in the middle stratosphere, and a poor representation in the lower stratosphere. Global mean temperature trends are well reproduced in the lower and middle stratosphere and adequately reproduced in the upper stratosphere. The CCM's representation of fluxes, heating rates and solar variability is not assessed.

**UMSLIMCAT:** This CCM has a good representation of climatological global mean temperatures in the middle and upper stratosphere, and an adequate representation of temperatures in the lower stratosphere. Global mean temperature trends throughout the stratosphere are well reproduced. Climatological total radiative flux at the tropopause is adequately modelled. Radiative forcings at the tropopause are well modelled for ozone changes both in the stratosphere and troposphere,  $\text{CH}_4$  and the CFCs. Forcings are adequately modelled for  $\text{CO}_2$ ,  $\text{N}_2\text{O}$  and stratospheric water vapour. Tropospheric water vapour forcing is poorly modelled. Climatological heating rates and their change from  $\text{CO}_2$  and stratospheric  $\text{O}_3$  perturbations are either adequate or better, except in the middle troposphere for  $\text{CO}_2$  changes where representation is poor. The CCM's representation of solar variability is adequate.

**UMUKCA-METO:** This CCM has a good representation of climatological global mean temperatures in the middle and upper stratosphere, and a poor representation of temperatures in the lower stratosphere. Global mean temperature trends in the upper stratosphere are well reproduced, middle stratospheric trends are adequately reproduced and lower stratospheric trends are poorly reproduced. Climatological total radiative flux at the tropopause is well modelled. Radiative forcings at the tropopause are well modelled for stratospheric and tropospheric  $\text{O}_3$  changes,  $\text{N}_2\text{O}$ , CFC11 and  $\text{CH}_4$ . Forcings are adequately modelled for  $\text{CO}_2$ , CFC12 and stratospheric water vapour. Tropospheric water vapour forcing is poorly modelled. Climatological heating rates and their change from  $\text{CO}_2$  and stratospheric  $\text{O}_3$  perturbations are either adequate or better. The CCM's representation of solar variability is poor.

**UMUKCA-UCAM:** This CCM has a good representation of climatological global mean temperatures in the middle and upper stratosphere, and a poor representation of temperatures in the lower stratosphere. Global mean temperature trends throughout the stratosphere are well reproduced. Climatological total radiative flux at the tro-

popause is well modelled. Radiative forcings at the tropopause are well modelled for tropospheric  $\text{O}_3$  change,  $\text{N}_2\text{O}$ , CFC11 and  $\text{CH}_4$ . Forcings are adequately modelled for  $\text{CO}_2$ , CFC12, stratospheric  $\text{O}_3$  and stratospheric water vapour. Tropospheric water vapour forcing is poorly modelled. Climatological heating rates and their change from  $\text{CO}_2$  and stratospheric  $\text{O}_3$  perturbations are either adequate or better, except in the upper troposphere for  $\text{O}_3$  changes where representation is poor. The CCM's representation of solar variability is poor.

**WACCM:** This CCM has a good representation of climatological global mean temperatures throughout the stratosphere. Global mean temperature trends are well reproduced throughout the stratosphere. The CCM's representation of fluxes, heating rates and solar variability is not assessed.

### 3.6.2 Overall summary

The work in this chapter has shown that CCM global mean temperatures and their change can give an indication of errors in radiative transfer codes and/or atmospheric composition. Biases in the global temperature climatology are generally small, although five out of 18 CCMs shows biases in their climatology that likely indicate problems with their radiative transfer codes. Temperature trends also generally agree well with observations, although one model shows significant discrepancies that appear to be due to radiation errors. Heating rates and estimated temperature changes from  $\text{CO}_2$ , ozone and water vapour changes are generally well modelled. Other gases ( $\text{N}_2\text{O}$ ,  $\text{CH}_4$ , CFCs) have only played a minor role in stratospheric temperature change but their heating rates are estimated with large fractional errors in many models. Models that do not account for variations in the spectrum of solar irradiance but only consider changes in total (spectrally-integrated) solar irradiance (TSI) cannot properly simulate solar-induced variations in stratospheric temperature. The combined LL GHG global-annual-mean instantaneous net radiative forcing at the tropopause is within 30% of LBL models for all CCM radiation codes tested. Problems remain simulating radiative forcing for stratospheric water vapour and ozone changes with a range of errors between 3% and 200% compared to LBL models.

Performing a comparison of radiation schemes has been challenging. This work would have benefitted from more CCM radiation schemes being run independently of their host models. We suggest that in future radiation schemes should regularly be involved in comparison exercises based on detailed sets of reference calculations from LBL models. Ideally, solar and longwave schemes should be evaluated for a range of realistic circumstances. Future

radiation scheme comparisons should also ideally evaluate the radiative effects of aerosol and cloud as well as trace gases. They should also evaluate the effect of approximations made in CCMs such as the frequency of radiative transfer calculations and the effects of plane-parallel/sphericity approximations. Photolysis and solar heating calculations should be merged for consistency. Non-local thermodynamic equilibrium effects should be accounted for above 70 km to correctly simulate heating and cooling rates in this region. CCMs should include spectral variations in solar irradiance when modelling solar variability in order to induce the correct stratospheric temperature change. Further work is needed to assess the level of spectral detail required.

## References

- Austin, J., R. J. Wilson, H. Akiyoshi, S. Bekki, N. Butchart, C. C. Chou, V. I. Fomichev, P. Forster, R. R. Garcia, N. P. Gillett, P. Keckhut, U. Langematz, E. Manzini, T. Nagashima, W. J. Randel, E. Rozanov, K. Shibata, K. P. Shine, H. Struthers, D. W. J. Thompson, F. Wu, S. Yoden, 2009. Coupled chemistry climate model simulations of stratospheric temperatures and their trends for the recent past. *Geophys. Res. Lett.*, **36**, doi:10.1029/2009GL038462.
- Barker, H. W., G. L. Stephens, P. T. Partain, J. W. Bergman, B. Bonnel, K. Campana, E. E. Clothiaux, S. Clough, S. Cusack, J. Delamere, J. Edwards, K. F. Evans, Y. Fouquart, S. Freidenreich, V. Galin, Y. Hou, S. Kato, J. Li, E. Mlawer, J. J. Morcrette, W. O'Hirok, P. Raisanen, V. Ramaswamy, B. Ritter, E. Rozanov, M. Schlessinger, K. Shibata, P. Sporyshev, Z. Sun, M. Wendisch, N. Wood, F. Yang, 2003. Assessing 1D atmospheric solar radiative transfer models: Interpretation and handling of unresolved clouds. *J. Clim.*, **16**, 2676–2699.
- Cagnazzo, C., E. Manzini, M. A. Giorgetta, P. M. D. Forster, J. J. Morcrette, 2007. Impact of an improved shortwave radiation scheme in the MAECHAM5 General Circulation Model. *Atmos. Chem. Phys.*, **7**, 2503-2515.
- Clough, S.A., and M. J. Iacono, 1995. Line-by-line calculations of atmospheric fluxes and cooling rates. II: Application to carbon dioxide, ozone, methane, nitrous oxide, and the halocarbons. *J. Geophys. Res.*, **100**, 16,519-16,535.
- Clough, S. A., M. W. Shephard, E. J. Mlawer, J. S. Delamere, M. J. Iacono, K. Cady-Pereira, S. Boukabara, P. D. Brown, 2005. Atmospheric radiative transfer modeling: a summary of the AER codes, Short Communication, *J. Quant. Spectrosc. Radiat. Transfer*, **91**, 233-244.
- Collins, W. D., V. Ramaswamy, M. D. Schwarzkopf, Y. Sun, R. W. Portmann, Q. Fu, S. E. B. Casanova, J. L. Dufresne, D. W. Fillmore, P. M. D. Forster, V. Y. Galin, L. K. Gohar, W. J. Ingram, D. P. Kratz, M. P. Lefebvre, J. Li, P. Marquet, V. Oinas, Y. Tsushima, T. Uchiyama, W. Y. Zhong, 2006. Radiative forcing by well-mixed greenhouse gases: Estimates from climate models in the Intergovernmental Panel on Climate Change (IPCC) Fourth Assessment Report (AR4). *J. Geophys. Res.*, **111**, doi:10.1029/2005JD006713.
- Egorova, T., E. Rozanov, E. Manzini, M. Haberreiter, W. Schmutz, V. Zubov, and T. Peter, 2004. Chemical and dynamical response to the 11-year variability of the solar irradiance simulated with a chemistry-climate model, *Geophys. Res. Lett.*, **31**, doi:10.1029/2003GL019294.
- Ellingson, R. G., S. J. Ellis, S. B. Fels, 1991. The intercomparison of radiation codes used in climate models - Long-wave results, *J. Geophys. Res.*, **96**, 8929–8953.
- Feigelson, E. M., and L. R. Dmitrieva (eds.), 1983. Radiative algorithms in the atmospheric general circulation models: A review, Inf. VNIGMI-MCD, issue 1, Obninsk.
- Fomichev, V. I., 2009. The radiative energy budget of the middle atmosphere and its parameterizations in general circulation models. *J. Atmos. Solar-Terr. Phys.*, **71**, 1577-1585.
- Fomichev, V. I., J.-P. Blanchet, D. S. Turner, 1998. Matrix parameterization of the 15  $\mu\text{m}$  CO<sub>2</sub> band cooling in the middle and upper atmosphere for variable CO<sub>2</sub> concentration. *J. Geophys. Res.*, **103**, 11505 - 11528.
- Fomichev, V. I., C. Fu, J. de Grandpré, S. R. Beagley, V. P. Ogibalov, J. C. McConnell, 2004. Model thermal response to minor radiative energy sources and sinks in the middle atmosphere. *J. Geophys. Res.*, **109**, doi:10.1029/2004JD004892.
- Fomin, B.A., 2006. Monte-Carlo algorithm for line-by-line calculations of thermal radiation in multiple scattering layered atmospheres. *J. Quant. Spectrosc. Rad.*

- Transfer*, **98**, 107-115.
- Fomin, B.A., and I. P. Mazin, 1998. Model for an investigation of radiative transfer in cloudy atmosphere. *Atmospheric Research*, **48**, 127-153.
- Forster, P. M. D., M. Ponater, W. Y. Zhong, 2001. Testing broadband radiation schemes for their ability to calculate the radiative forcing and temperature response to stratospheric water vapour and ozone changes. *Meteorol. Z.*, **10**, 387-393.
- Forster, P., V. Ramaswamy, P. Artaxo, T. Berntsen, R. Betts, D.W. Fahey, J. Haywood, J. Lean, D.C. Lowe, G. Myhre, J. Nganga, R. Prinn, G. Raga, M. Schulz, R. Van Dorland, 2007. Changes in Atmospheric Constituents and in Radiative Forcing. In: *Climate Change 2007: The Physical Science Basis. Contribution of Working Group I to the Fourth Assessment Report of the Intergovernmental Panel on Climate Change*. Cambridge University Press, Cambridge, United Kingdom and New York, NY, USA.
- Fouquart, Y., B. Bonnel, V. Ramaswamy, 1991. Intercomparing shortwave radiation codes for climate studies. *J. Geophys. Res.*, **96**, 8955-8968.
- Goldblatt, C., T. M. Lenton, A. J. Watson, 2009. An evaluation of the long-wave radiative transfer code used in the Met Office Unified Model. *Quart. J. Roy. Meteorol. Soc.*, **135**, 619-633.
- Haigh, J. D., 1994. The role of stratospheric ozone in modulating the solar radiative forcing of climate. *Nature*, **370**, 544-546.
- Halhore, R. N., D. Crisp, S. E. Schwartz, G. P. Anderson, A. Berk, B. Bonnel, O. Boucher, F. L. Chang, M. D. Chou, E. E. Clothiaux, P. Dubuisson, B. Fomin, Y. Fouquart, S. Freidenreich, C. Gautier, S. Kato, I. Laszlo, Z. Li, J. H. Mather, A. Plana-Fattori, V. Ramaswamy, P. Ricchiuzzi, Y. Shiren, A. Trishchenko, W. Wiscombe, 2005. Intercomparison of shortwave radiative transfer codes and measurements. *J. Geophys. Res.*, **110**, doi:10.1029/2004JD005293.
- Jonsson, A. I., V. I. Fomichev, T. G. Shepherd, 2009. The effect of nonlinearity in CO<sub>2</sub> heating rates on the attribution of stratospheric ozone and temperature changes. *Atmos. Chem. Phys.*, **9**, 8447-8452.
- Kiehl, J. T., C. Bruhl, T. Yamanouchi, 1985. A parameterization for the absorption due to the near infrared bands of CO<sub>2</sub>. *Tellus*, **37B**, 189-196.
- Lacis, A. A., and J.E. Hansen, 1974. A parameterization for the absorption of solar radiation in the Earth's atmosphere. *J. Atmos. Sci.*, **31**, 118-133.
- Lean, J. L., G. Rottman, J. Harder, G. Kopp, 2005. SORCE contributions to new understanding of global change and solar variability. *Solar Phys.*, **230**, 27-53.
- Li, J., and H. W. Barker, 2005. A radiation algorithm with correlated-k distribution. Part I: Local thermal equilibrium. *J. Atmos. Sci.*, **62**, 286-309.
- Luther, F. M., R.G. Ellingson, Y. Fouquart, S. Fels, N. A. Scott, W. J. Wiscombe, 1988. Intercomparison of radiation codes in climate models (ICRCCM) - Long-wave clear-sky results - A workshop summary. *Bull. Am. Meteorol. Soc.*, **69**, 40-48.
- Mayer, B., and A. Kylling, 2005. Technical Note: The LibRadtran software package for radiative transfer calculations: Description and examples of use. *Atmos. Chem. Phys.*, **5**, 1855-1877.
- Myhre, G., and F. Stordal., 1997. Role of spatial and temporal variations in the computation of radiative forcing and GWP. *J. Geophys. Res.*, **102**, 11181-11200.
- Myhre, G., and F. Stordal, 2001. On the tradeoff of the thermal and solar radiative impact of contrails. *Geophys. Res. Lett.*, **28**, 3119-3122.
- Myhre, G., F. Stordal, I. Gausemel, C. Nielsen, and E. Mahieu, 2006. Line-by-line calculations of thermal infrared radiation representative for global condition: CFC-12 as an example. *J. Quant. Spec. Rad. Trans.*, **97**, 317-331.
- Myhre, G., M. Kvalevåg, G. Rädel, J. Cook, K. P. Shine, H. Clark, F. Karcher, K. Markowicz, A. Kardas, P. Wolkenberg, Y. Balkanski, M. Ponater, P. Forster, A. Rap, R. R. de Leon, 2009. Intercomparison of radiative forcing of stratospheric water vapour and contrails. *Meteorol. Z.*, **18**, 585-596.
- Nissen, K., K. Matthes, U. Langematz, B. Mayer, 2007. Towards a better representation of the solar cycle in general circulation models. *Atmos. Chem. Phys.*, **7**, 5391-5400.
- Ogibalov, V. P., and V. I. Fomichev, 2003. Parameterization of solar heating by the near IR CO<sub>2</sub> bands in the mesosphere. *Adv. Space Res.*, **32**, 759-764.
- Portmann, R., S. Solomon, J. Fishman, J. Olson, J. Kiehl, B. Briegleb, 1997. Radiative forcing of the Earth's climate system due to tropical tropospheric ozone production. *J. Geophys. Res.*, **102**, 9409-941.
- Randel, W. J., and F. Wu, 2007. A stratospheric ozone profile data set for 1979-2005: Variability, trends, and comparisons with column ozone data. *J. Geophys. Res.*, **112**, doi:10.1029/2006JD007339
- Randel, W. J., K. P. Shine, J. Austin, J. Barnett, C. Claud,

- N. P. Gillett, P. Keckhut, U. Langematz, R. Lin, C. Long, C. Mears, A. Miller, J. Nash, D. J. Seidel, D. W. J. Thompson, F. Wu, S. Yoden, 2009. An update of observed stratospheric temperature trends. *J. Geophys. Res.*, **114**, doi:10.1029/2008JD010421.
- Shine, K. P., M. S. Bourqui, P. M. Forster, S. H. E. Hare, U. Langematz, P. Braesicke, V. Grewe, M. Ponater, C. Schnadt, C.A. Smiths, J. D. Haigh, J. Austin, N. Butchart, D. T. Shindell, W. J. Randel, T. Nagashima, R. W. Portmann, S. Solomon, D. J. Seidel, J. Lanzante, S. Klein, V. Ramaswamy, M. D. Schwarzkopf, 2003. A comparison of model-simulated trends in stratospheric temperatures. *Quart. J. Roy. Meteor. Soc.*, **129**, 1565–1588.
- Taylor, K. E., 2001. Summarizing multiple aspects of model performance in a single diagram. *J. Geophys. Res.*, **106**, 7183–7192.
- WMO, 2003. Scientific assessment of ozone depletion: 2002. Tech. Rep. 47, Global Ozone Research and Monitoring Project, World Meteorological Organization, Geneva, Switzerland, 498 pp.
- World Meteorological Organization (WMO)/United Nations Environment Programme (UNEP), 2007. *Scientific Assessment of Ozone Depletion: 2006*, World Meteorological Organization, Global Ozone Research and Monitoring Project, Report No. 50, Geneva, Switzerland.

# CHAPTER 4

## Stratospheric Dynamics

**Lead Authors:** Neal Butchart & Andrew J. Charlton-Perez

**Co-authors:** Irene Cionni  
Steven C. Hardiman  
Kirstin Krüger  
Paul Kushner  
Paul Newman  
Scott M. Osprey  
Judith Perlwitz  
Fabrizo Sassi  
Michael Sigmond  
Lei Wang

---

### 4.1 Introduction

This chapter assesses and compares the abilities of the Climate-Chemistry Models (CCMs) to reproduce the climate, circulation and associated variability of the stratosphere, though not the coherent naturally occurring variability such as that resulting from El-Niño Southern Oscillation (ENSO) events, big volcanic eruptions and variations in solar irradiance. This coherent natural variability is assessed separately in Chapter 8. The assessment in this chapter is process based, *i.e.*, the underlying dynamical

processes occurring in the model stratospheres are evaluated as well as the simulation of the basic meteorological quantities such as winds and temperature. The processes and quantities considered (see **Table 4.1a, b** for a full list) are those relevant for modelling the long-term behaviour of stratospheric ozone (*e.g.*, temperature and the Brewer-Dobson circulation) and the impact of stratospheric change on surface climate (*e.g.*, annular modes). The chapter also looks at the predicted effects of climate change and ozone depletion/recovery on these modelled dynamical quantities and processes. In particular linear trends are calculated for many of the diagnostics assessed for the periods of ozone depletion (1980-1999), strong ozone recovery (2000-2049) and longer-term ozone and climate changes (2050-2099). Because of limited space, the dynamical meteorology

**Table 4.1a:** Climatological mean dynamical processes and/or phenomena validated in this chapter. The first column lists the processes and phenomena plus the subsection where the analysis can be found. Diagnostics used in the validation are listed in column 2 while columns 3 and 4 indicate which diagnostics will be used as quantitative metrics for the overall model assessment (see Section 4.5.3). All the diagnostics are validated against one or more of the reanalysis data sets introduced in Section 4.2. Abbreviations: NH=Northern Hemisphere; SH=Southern Hemisphere; DJF=December-January-February; MAM=March-April-May; JJA=June-July-August; SON=September-October-November; EP=Eliassen-Palm; PSC=polar stratospheric cloud; NAT=nitric acid trihydrate.

Mean climate			
Phenomena Process	Diagnostic	Metric Name	Metric Description
4.3.1 Zonal mean climatology	DJF & MAM temperatures 60–90°N	<b>nhtemp</b>	DJF value at 50 hPa
	JJA & SON temperatures 60–90°S	<b>shtemp</b>	SON value at 50 hPa
	Date of the transition from eastward to westward winds at 60°S		
	Latitude & maximum wind speed of the NH jet in DJF	<b>umax_djf</b>	Maximum DJF eastward wind at 10 hPa
	Latitude & maximum wind speed of the SH jet in JJA	<b>umax_jja</b>	Maximum JJA eastward wind at 10 hPa
4.3.2 Stationary waves Zonal asymmetries	Location & maximum amplitude of the stationary wave field for the NH DJF & SH SON climatology		
	Phase & amplitude of wave-1 & wave-2 10 hPa NH DJF & SH SON stationary waves		
	Seasonal variation of the maximum amplitude of the NH & SH 10 hPa climatological stationary waves		
4.3.3 Brewer-Dobson circulation Tropical upwelling	70 hPa residual vertical velocity $\bar{w}^*$ : annual mean 40°S–40°N, seasonal cycle in the turn-around latitudes where $\bar{w}^* = 0$ & tropical upwelling mass flux		
	Tropical upwelling mass flux at 70 & 10 hPa and downward control estimates of the driving from resolved (~EP-flux divergence) & parameterised (gravity) waves	<b>upwell_70</b> <b>upwell_10</b>	Annual mean upwelling mass flux at 70 hPa Annual mean upwelling mass flux at 10 hPa
4.3.4 Extra-tropical wave driving	100 hPa meridional heat flux for January in the NH & July in the SH		
	Regression (slope & intercept) of the February & March 50 hPa temperatures 60°N–90°N on the 100 hPa January and February heat flux 40°N–80°N	<b>PW_nh</b>	Slope of the regression fit
	Regression (slope & intercept) of the August & September 50 hPa temperatures 60°S–90°S on the 100 hPa July and August heat flux 40°S–80°S	<b>PW_sh</b>	Slope of the regression fit
4.3.5 PSC threshold temperatures	Seasonally accumulated area at 50 hPa where temperatures are below 195 K (threshold for NAT clouds) & below 188 K (threshold for ice clouds)		

**Table 4.1b:** As Table 4.1a but for climate variability on intra-seasonal to interannual time scales. Abbreviations: EOF=empirical orthogonal function; SAO=semi-annual oscillation; QBO=quasi-biennial oscillation.

<b>Climate variability (intraseasonal - interannual)</b>			
<b>Phenomena Process</b>	<b>Diagnostic</b>	<b>Metric Name</b>	<b>Metric Description</b>
4.4.1 Extra-tropical variability	Latitude & amplitude of the maximum interannual standard deviation of the zonal-mean zonal wind in DJF poleward of 45°N & in JJA from 30°S to 80°S		
	Eigenvalue of the leading mode of variability of the 50 hPa zonal-mean zonal wind for the NH & SH	<b>firsteval_nh</b>	Amplitude of first EOF in the NH
		<b>firsteval_sh</b>	Amplitude of first EOF in the SH
	Fraction of the total variance explained by EOF1 & EOF2		
Regression patterns of first and second mode of variability of the 50 hPa zonal-mean zonal wind for the NH & SH regions poleward of 45°			
4.4.2 Tropical variability	Vertical profile of the interannual standard deviation of the zonal-mean zonal wind, 10°S – 10°N		
	Vertical profile of the amplitude of the annual cycle in the zonal-mean zonal wind, 10°S – 10°N	<b>tann</b>	Amplitude at 2 hPa
	Vertical profile of the amplitude of the SAO in the zonal-mean zonal wind, 10°S – 10°N	<b>sao</b>	Amplitude at 1 hPa
	Vertical profile of the amplitude of “QBO” in the zonal-mean zonal wind, 10°S – 10°N	<b>qbo</b>	Amplitude at 20 hPa
4.4.3 Stratospheric sudden warmings	Frequency per year of NH major stratospheric sudden warmings, defined using reversal of the zonal-mean zonal wind at 10 hPa, 60°N	<b>SSW</b>	Mean frequency at 10 hPa, 60°N
	Monthly-distribution of NH major stratospheric sudden warmings		
4.4.4 Final warming	Mean date of the NH & SH final warmings defined using the criteria of Black and McDaniel (2007a, b)	<b>final_nh</b>	Mean date at 50 hPa, 60°N
		<b>final_sh</b>	Mean date at 50 hPa, 70°S

of the troposphere *per se* is not considered in any detail. Nonetheless, the stratosphere can have a direct impact on the mean climate and variability of the troposphere, and this is considered in Chapter 10.

## 4.2 Evaluation data sets and analyses

Although the diagnostics in this chapter are varied in their scope and time scale, their common theme is that they consider stratospheric and tropospheric dynamics on long, climate-relevant time scales, and on large spatial scales. With this in mind, a short survey of the data sets available to validate the models is useful. Individual diagnostic studies will use the data set most appropriate to their needs. Where possible at least two different data sets will be used to validate each diagnostic, so that some indication of the level of agreement between the data sets, and uncertainty in the observations, can be ascertained.

A previous SPARC report undertook an extensive comparison of middle atmosphere climatologies derived from the different data sets (Randel *et al.*, 2004; SPARC, 2002). That report is used as a guide for determining biases in particular data sets. In addition to the data sets considered by Randel *et al.* (2004), a further reanalysis conducted by the Japanese Meteorological Agency (JRA-25) is now available and extends to 0.4 hPa. General conclusions from

Randel *et al.* (2004) can be summarized as follows:

1. Reanalysis data sets with high model tops (ECMWF ERA-40 (Uppala *et al.*, 2005) and Met Office (UKMO) Stratospheric Analyses (Swinbank and O'Neill, 1994)) have the best overall performance in comparison to rocketsonde and lidar measurements.
2. Particular uncertainties occur in the lower stratosphere and near the stratopause, and more care should be taken here.
3. The Quasi-Biennial and Semi-Annual Oscillations (QBO and SAO) are poorly captured in many of the available data sets when compared to Singapore radiosonde data.

Aspects of stratospheric data sets not considered by Randel *et al.* (2004) include the variability on both daily and interannual time scales. A brief inter-comparison of this variability in five reanalysis data sets (ECMWF ERA-40, NCEP/NCAR reanalysis, Met Office operational analyses, JRA-25, and ERA-Interim) shows a remarkable agreement between the different data sets. This agreement suggests that choosing any of the five reanalysis data sets would be appropriate when validating variability in the models.

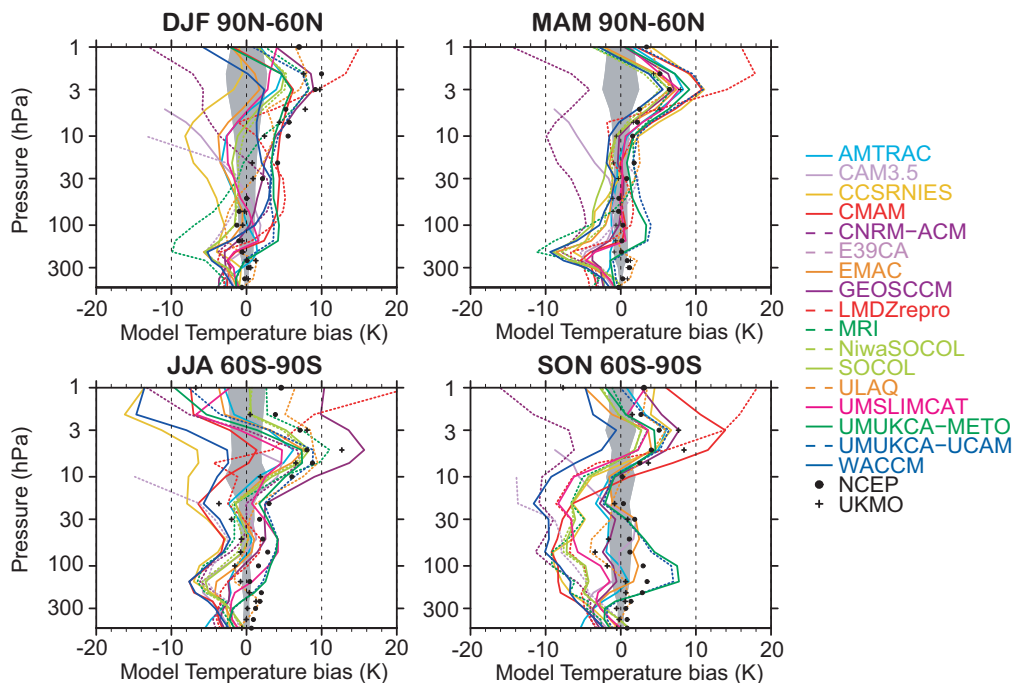


**Figure 4.1:** Climatological mean temperature biases for 60°N–90°N (upper panels) and 60°S–90°S (lower panels) for the winter (left) and spring (right) seasons. The climatological means for the model REF-B1 simulations and NCEP data from 1980 to 1999, and for UKMO analyses from 1992 to 2001 are included. Biases are calculated relative to ERA-40 reanalyses for 1980–1999. The grey area shows a 95% confidence interval for the 20-year mean from the ERA-40 reanalyses based on a t-distribution.



## 4.3 Mean climatology

### 4.3.1 Zonal-mean temperatures and eastward wind

In this section the zonal-mean temperature and eastward wind climatologies from the REF-B1 simulations are compared to ERA-40 and NCEP reanalyses (Uppala *et al.*, 2005; Kalnay *et al.*, 1996), the UKMO stratospheric analyses (Swinbank and O'Neill, 1994) and the Randel *et al.* (2004) stratospheric climatology.

Firstly, two key diagnostics of the previous CCMVal-1 inter-comparison (Eyring *et al.*, 2006) are reproduced for the new CCMVal-2 simulations. **Figure 4.1** shows climatological temperature biases over the polar cap in winter and spring in the Northern (NH) and Southern (SH) Hemispheres. Eyring *et al.* (2006) highlighted the contrast between the upper and lower stratosphere in CCMVal-1. In the upper stratosphere in both hemispheres most models lie within the large range of temperatures shown in the different analyses, though there is also a very large spread between models. In the lower stratosphere, where the range of the analyses is much smaller, strong contrasts exist between the two hemispheres, with a clear cold bias for most of the models in the SH spring, and a more vertically confined cold bias between 300 and 100 hPa in the NH spring.

The results from the CCMVal-2 inter-comparison (Figure 4.1) are broadly similar to the previous Eyring *et al.* (2006) inter-comparison. The largest biases between models and observations occur in the SH spring in the lower stratosphere. For most models these biases are of the order of 5 K, though some models have biases of

slightly more than 10 K. In CCMVal-1 typical biases were also around 5 K, but with two outliers with biases greater than 15 K in some places (Eyring *et al.*, 2006). Both these outliers (E39CA and LMDZrepro) have reduced biases in the CCMVal-2 assessment. One new feature in the CCMVal-2 data set, in comparison to CCMVal-1, is the presence of three simulations (EMAC, UMUKCA-METO and UMUKCA-METO) with positive temperature biases between 30 and 300 hPa in the SH spring.

**Figure 4.2** shows the descent of the climatological zero-wind line at 60°S (*e.g.*, Scaife *et al.*, 2002, Figure 7) in the models. Although this result is based on the monthly mean climatology with the transition date obtained by linear interpolation between months (assuming the monthly mean is valid for the 15<sup>th</sup> Hardiman *et al.* (2010b) have shown that remarkably similar conclusions are obtained when the climatologies are constructed from daily data. Results from the CCMVal-1 and CCMVal-2 inter-comparisons are very similar, both showing a delayed or missing (below 10hPa) transition to westward winds in the zonal wind climatology in the SH spring. Eleven of the sixteen CCMVal-2 models analysed exhibited this delay, which is consistent with the spring-time temperature biases noted above. The date of the final warming is examined in more detail in Section 4.4.2. The large temperature biases in the lower stratosphere are strongly linked to the behaviour of ozone. Strong cold biases would tend to allow the ozone hole to persist for longer into the SH spring, and indeed the extended duration of the ozone hole is consistent with the stratospheric cooling trends seen in Chapter 10, Figure 10.12, which tend to persist well into the SH summer.

Further dynamical analysis of the basic stratospheric state in the REF-B1 simulations can be conducted by considering the structure of the zonal-mean zonal wind clima-

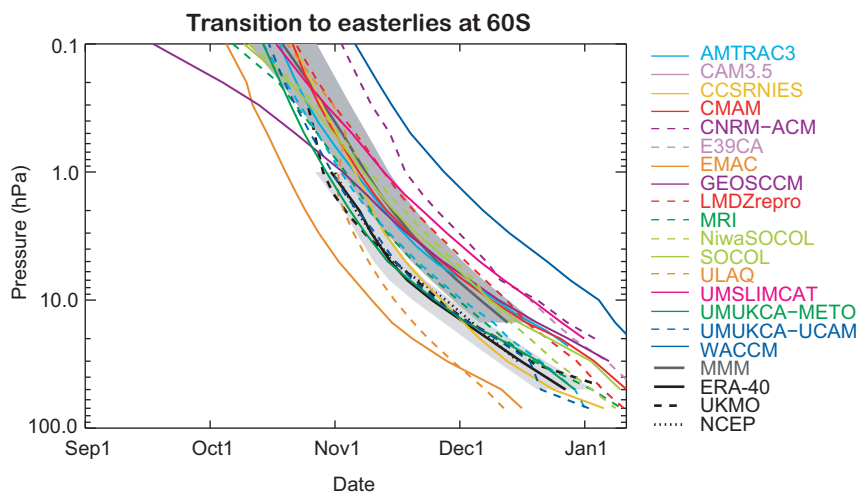


**Figure 4.2:** For the REF-B1 simulations. Descent of the zero zonal-mean zonal wind at 60°S based on the climatological mean annual cycle calculated from the monthly and zonal-mean zonal winds. The grey area shows a 95% confidence interval for the 20-year mean ERA-40 transition, based on a t-distribution. Climatological means are calculated for the same period as in Figure 4.1. -dark grey shading?

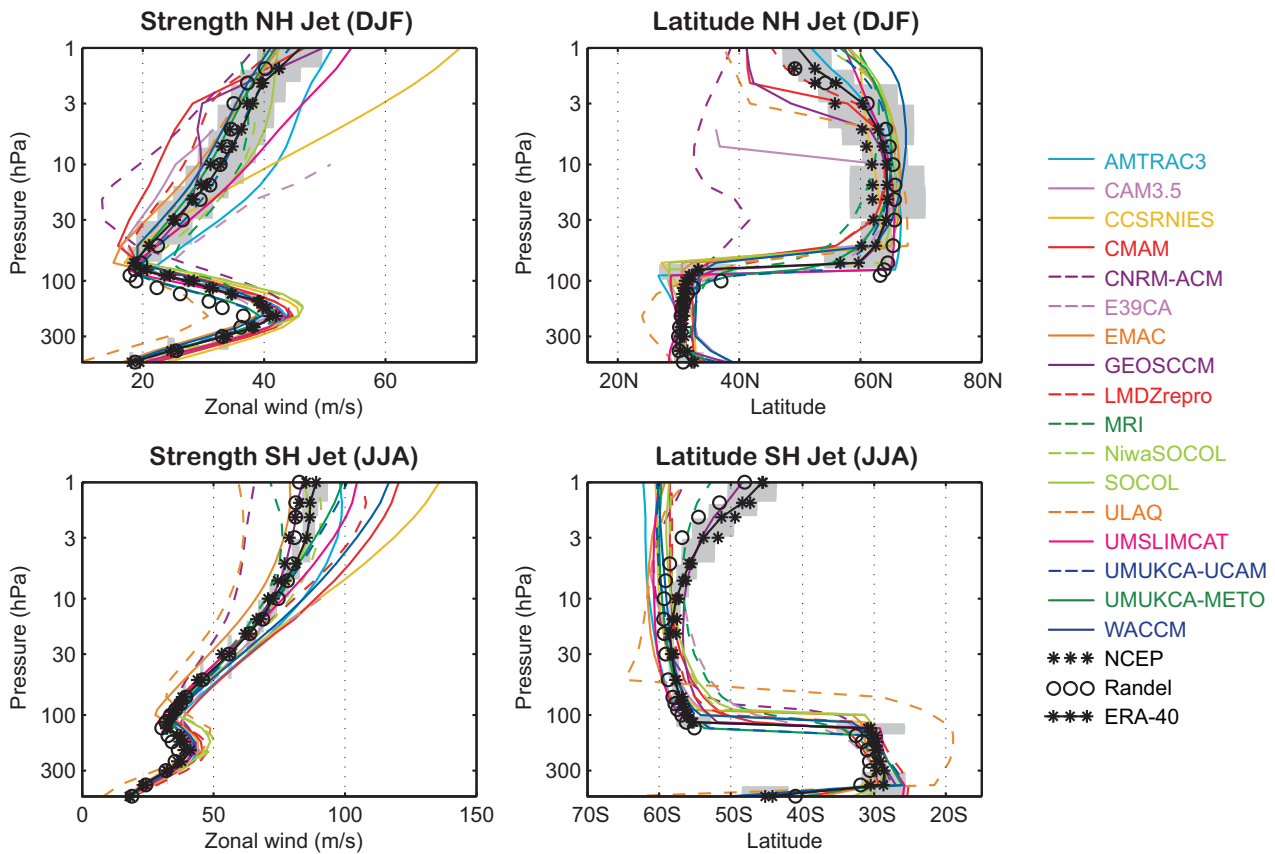


**Figure 4.3:** Zonal wind speed and latitude of the jet maximum of the NH DJF climatology (top), and of the SH JJA climatology (bottom) in the REF-B1 simulations. Data are based on climatological means for the models, ERA-40 and NCEP data from 1980 to 1999 and for the Randel et al. (2004) climatology that represents the time period 1992-1997. The grey area indicates a 95% confidence interval for the 20-year mean ERA-40 climatology based on a  $t$ -distribution. Where an ensemble of simulations is available, quantities are calculated for the ensemble mean zonal-mean zonal wind field.

tology. Instead of simply analysing the zonal wind biases of the models, two aspects of the zonal wind climatology are considered: the strength of the stratospheric or polar night jet and its latitudinal position. These two diagnostics are shown for the NH and SH winters in **Figure 4.3**. Very similar results are obtained for the REF-B2 simulations for the same period (not shown).

Most of the models performed extremely well in these diagnostics. In the NH the jet is generally both well positioned and of the correct strength in almost all models with the exception of the CNRM-ACM, which has its jet positioned too close to the equator with too weak winds in the lower stratosphere, the CCSRNIIES model, which has a very strong jet in the upper stratosphere, and the E39CA model, which has a too strong jet near its relatively low upper boundary (10 hPa). Although the NH jet in the ULAQ model seems quite accurate in terms of position and strength, its width is too large (not shown). In the SH winter, clear biases exist for the majority of models in the upper stratosphere. Almost all the models fail to capture the

observed tilt of the jet toward the equator between 10 and 1 hPa, most producing a jet with an un-tilted profile. There is a large model spread in the strength of the mid-winter jet in the SH upper stratosphere. A large number of models produce jets which are too strong, while the CNRM-ACM and ULAQ model produce jets which are too weak. The ULAQ results also show a large misplacement of the SH jet in the upper troposphere/lower stratosphere.

Predicted trends in latitudinally averaged stratospheric temperatures are also compared between the models. Since many of the more complex diagnostics later in the chapter examine changes to key stratospheric process over the 21<sup>st</sup> century, it is necessary to establish the broad context to these changes by examining changes to the stratospheric mean state. While the annual-mean global-mean temperature trends were discussed in Chapter 3, this chapter focuses on the latitudinal and seasonally averaged temperature trends. The seasonal cycle of the SH temperature trends averaged over all CCMVal-2 models is discussed in Chapter 10. **Figure 4.4** shows the trends for the three time

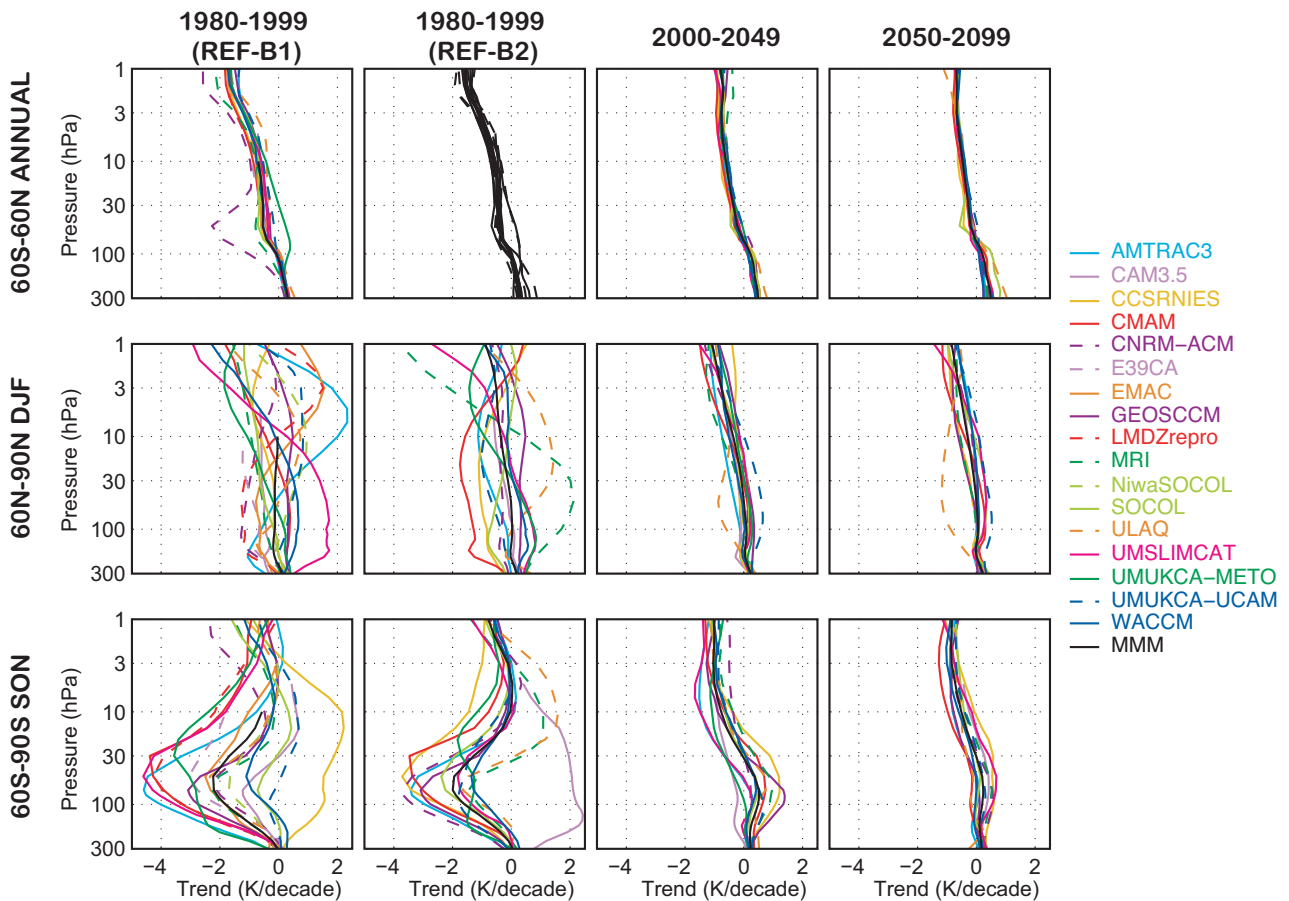


**Figure 4.4:** Temperature trends from 1980 to 1999 (first column for REF-B1 simulations, second column for REF-B2 simulations), from 2000 to 2049 (third column, REF-B2 simulation) and from 2050 to 2099 (fourth column, REF-B2 simulations). Top row: annual mean 60°S-60°N; middle row: December-January-February mean 60°N-90°N; lower row September-October-November mean 60°S-90°S.

periods: 1980-1999, 2000-2049, and 2050-2099, for the regions 60°S-60°N (annual mean, first row), 60°N-90°N (December-January-February (DJF) mean, second row) and 60°S-90°S (September-October-November (SON) mean, third row). For the past, trends from both the REF-B1 (first column) and REF-B2 (second column) simulations are shown. However, due to the shorter time-period, there is a larger spread between the models for the past than for the future trends. The inter-model spread in past trends over the longer period (1960-2000, not shown) is comparable to the spread in the future trends.

For the global-mean trends, a stratospheric cooling (maximising in the upper stratosphere) occurred in all three time-periods, consistent with radiative changes due to increasing greenhouse gas (GHG) amounts. For the past, relatively large cooling trends were found in the lower stratosphere due to ozone depletion (see Chapter 3). The first row of Figure 4.4 shows that the 60°S-60°N annual mean temperature trends are very similar to the global temperature trends (*c.f.*, Figures 4.4 and 3.4), except that the lower

stratospheric cooling is smaller due to the smaller ozone depletion in this region which excludes the poles. For the past, the lower stratospheric cooling in the CNRM-ACM is a factor of four larger than the multi-model mean (in REF-B1, but not REF-B2), whereas the UМУKCA-METO shows a small warming in the lower stratosphere. There is a small spread in the model trends for the future.

The second row of Figure 4.4 shows the winter-time stratospheric temperature trends averaged over 60°N-90°N. In the lower and middle stratosphere, models on average show no significant long-term changes in the winter-time temperatures, in contrast to the small cooling that was found in the near-global, annual mean temperatures (top row of Figure 4.4). This indicates that the radiative cooling due to increasing GHG amounts is largely counterbalanced by dynamical heating resulting from stronger adiabatic compression (see Section 4.3.3). For the future, the ULAQ model shows lower stratospheric cooling that is inconsistent with the other models, whereas the UМУKCA-UCAM shows a larger than average lower stratospheric warming

trend. Temperature trends in NH spring (not shown) are similar to those in winter, except for the past when the models, on average, show small cooling trends, presumably related to the extra radiative cooling due to stratospheric ozone depletion, and possibly the absence of dynamical heating.

The last row of Figure 4.4 shows SON mean temperature trends over 60°S–90°S. Temperature trends in this region and season are clearly affected by ozone depletion in the past (1980–1999), resulting in lower stratospheric cooling, while the slower ozone recovery between 2000–2050, results in a small warming of the lower stratosphere in many of the models. Interestingly, the past cooling trends tend to be larger in the REF-B1 than in the REF-B2 simulations, reflecting the effects of different surface boundary conditions. For the past, the CCSRNIES REF-B1 and the CAM3.5 REF-B2 simulations do not show the lower stratospheric cooling. Trends in the second part of the 21<sup>st</sup> century are generally in line with the global-mean trends and are dominated by changes in GHG amounts with ozone changes having only a small impact in this period.

To summarize, the model climatological temperature biases are generally small (< 5 K) apart from in the SH lower stratosphere in spring. In addition, the structure of the polar night jets is well simulated by the models with the

exception of the equator-ward tilt in the SH upper stratosphere. A recurring problem from previous generations of the models is the delay in the spring-time break-down of the southern polar vortex and concomitant cold bias in the Antarctica lower stratosphere. Models predict consistent trends in the SH polar temperatures with opposite trends during the periods of strong ozone depletion (1980–1999) and ozone recovery (2000–2049). In the NH lower and middle polar stratosphere, models show no significant long-term change to the mean winter-time temperature.

### 4.3.2 Stationary waves / zonal asymmetries

The stationary wave field, *i.e.*, the time mean zonally asymmetric part of the circulation, is a key dynamical quantity that contributes significantly to the flux of wave activity (“EP-Flux” - see Andrews *et al.*, 1987, Chapter 3) from the troposphere to the stratosphere and to the driving of the Brewer-Dobson circulation. The stationary wave field can be used to characterize the vertical and meridional structure of zonal asymmetries, the shape and position of the polar vortex, and long-term trends in the zonally asymmetric flow. The climatological stationary wave field, *i.e.*, the zonally asymmetric part of the climatological

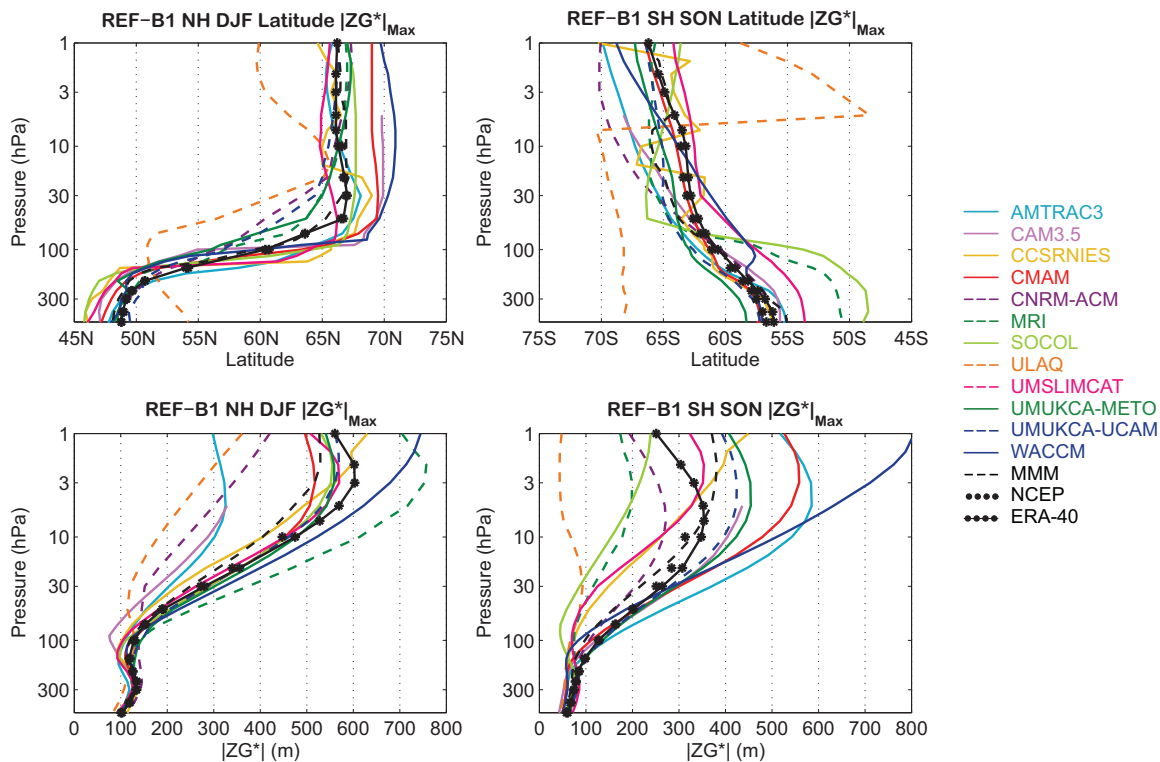


**Figure 4.5:** Latitudinal location and value of the maximum amplitude of the stationary wave field for the NH DJF climatology (left), and for the SH SON climatology (right). Data are based on climatological means for the models, ERA-40 and NCEP data from 1980 to 1999. Cubic spline interpolation is used to determine the latitude of the maximum and its value from the gridded data. The black dashed curve is the mean of all the model curves.

mean circulation, is observed to have a well-defined maximum in latitude at each altitude in the extra-tropical troposphere and stratosphere. **Figure 4.5** shows the simulated (REF-B1) and observed maximum amplitude in latitude of the climatological stationary wave in geopotential, and the latitudinal location of this maximum for the NH in DJF and the SH in SON. The latitudinal location of the maximum is generally well simulated by all the models, with the exception of the ULAQ model, in both hemispheres. The main biases that are robust between the REF-B1 and REF-B2 simulations (not shown) include an equator-ward bias in the upper troposphere for many of the models, a group of models with a poleward bias throughout the stratosphere, and a group of models with an equator-ward bias in the lower stratosphere. These groupings do not involve the same models for the two hemispheres, indicating that the biases are occurring for distinct reasons in each case. The models have more difficulty in simulating the observed stationary wave amplitude, with a tendency for the waves to be too weak in the NH winter and for the amplitudes to be very variable among the models in the SH spring. A systematic bias in the NH winter extends throughout the year, as seen in **Figure 4.6**, which shows the seasonal cycle of the climatological stationary wave amplitude at 10 hPa; the simulated NH stratospheric stationary waves are typically weak and have a relatively weak seasonal cycle. **Figure 4.6** also shows that the amplitude and seasonal cycle of this quantity in the SH is too large and reaches its maximum amplitude too early for many of the models; differences in the seasonal timing account for the large spread in the simulations in **Figure 4.5**. For many of the models, the maximum NH stationary wave amplitude is weaker than the maximum SH stationary wave amplitude, in qualitative contrast to the observations. The bias toward small stationary wave amplitudes in the NH winter are consistent with the negative bias in the heat flux at 100 hPa in January (Section 4.3.4, **Figure 4.12**), probably because the clima-

tological stationary wave contributes significantly to the NH heat flux (as in observations); this suggests that the NH heat flux errors are at least partially linked to problems with the stationary wave amplitude. In the SH in July, the climatological stationary wave contributes less to the SH heat flux, and this probably explains why the stationary-wave to heat-flux connection is not as straightforward: the stationary wave amplitudes are biased large (**Figure 4.6**) but the heat fluxes vary widely among the models (**Figure 4.12**).

The structure of the polar vortex is reflected in the stratospheric stationary wave field when decomposed into its dominant wave-1 component, which describes the location of the centre of the vortex relative to the pole, and its weaker wave-2 component, which describes the orientation and distortion of the vortex. **Figures 4.7a, b** show in polar coordinates the amplitude and phase of these components for the 50°-70° latitude climatological stationary wave at 10 hPa, for DJF in the NH and SON in the SH (the wave-2 amplitude is multiplied by a factor of four for graphical display). The amplitude biases in the figure are consistent with **Figures 4.5** and **4.6**. In the observations, the NH wave-1 component leads to a polar vortex centred off the pole between 0 and 30°E. Most of the models simulate this, although the UMSLIMCAT rotates the structure, and hence the polar vortex, significantly to the west, and the ULAQ simulation is almost 180° out of phase with the observations. The SH wave-1 component is more poorly simulated, corresponding to the fact that the orientation of the Antarctic polar vortex varies significantly among the models. For the NH and SH, the wave-2 component is more variable among the models, and exhibits significant differences between the REF-B1 and REF-B2 simulations (not shown). The ratio of the wave-2 to wave-1 amplitudes, which is one measure of the distortion of the vortex from a simple shifting off the pole, is shown in **Figures 4.7c, d**, and in the observations is about 25% in the NH and 10%

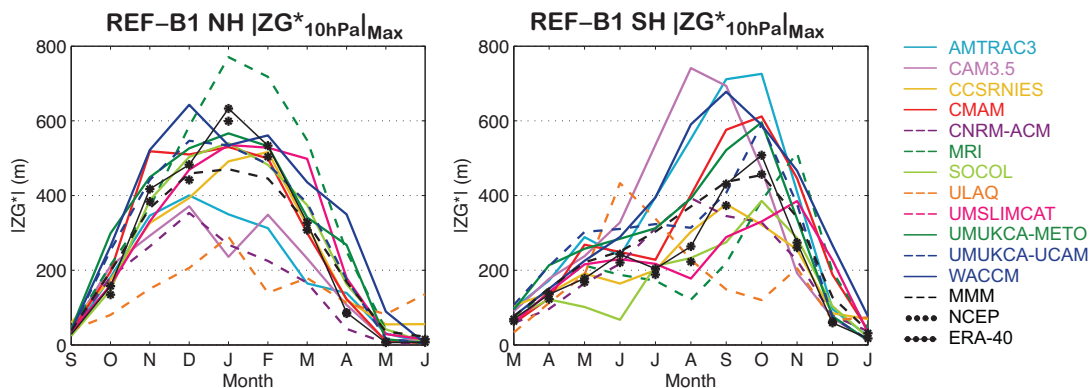


**Figure 4.6:** Seasonal variation of the maximum amplitude of the NH (left) and SH (right) 10 hPa climatological stationary wave. Data are based on climatological means for the model REF-B1 simulations, ERA-40 and NCEP data from 1980 to 1999. Cubic spline interpolation is used to determine the maximum value, as in **Figure 4.5**. The black dashed curve is the mean of all the model curves.

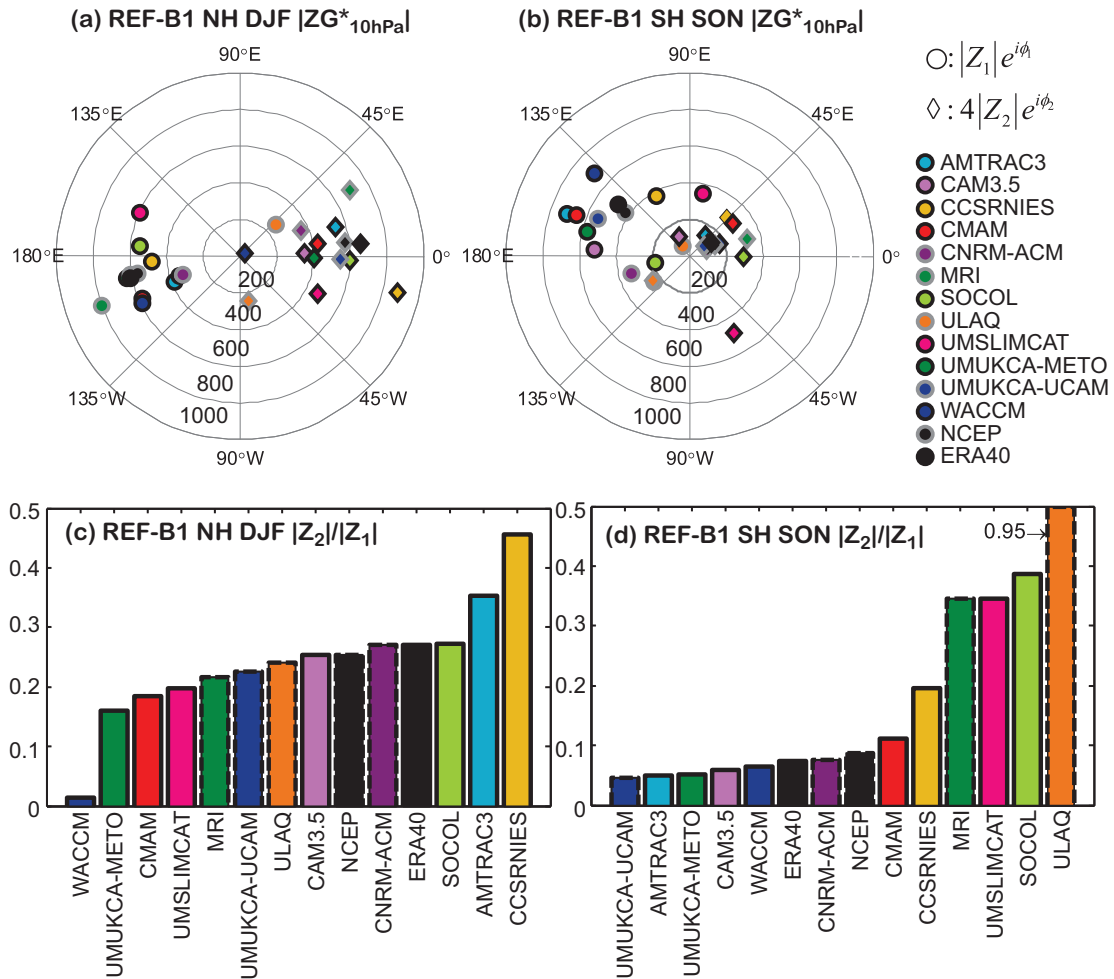


**Figure 4.7:** a) Phase in degrees and amplitude (contour interval 200 m), in polar coordinates, of wave-1 (circles) and wave-2 (diamonds) 10 hPa stationary waves for NH DJF. The wave-2 amplitude has been multiplied by a factor of 4. b) As in a), for SH SON. c) Ratio of wave-2 to wave-1 amplitude on 10 hPa for NH DJF. d) As in c), for SH SON. Data are based on climatological means for the model REF-B1 simulations, ERA-40 and NCEP data from 1980 to 1999.

in the SH. This ratio is generally well simulated in the NH, with a moderate bias towards small values, but is generally overestimated in the SH (the small value of the ratio in the WACCM simulation is found to increase from REF-B1 to REF-B2), suggesting that the SH vortex in the models is unrealistically distorted from circularity.

The seasonal stationary wave field is the zonally asymmetric part of the circulation for a given season and year. Trends derived from the interannual variations in this field in the period 1980-1999 of the REF-B2 simulations showed that there was no significant trend in the latitudinal location of the maximum amplitude in the NH in DJF and the SH in SON.

In the period after 2000, very few of the models project significant trends in this statistic with no significant trend in the multi-model mean. An absence of observed and simulated trends also holds for the amplitude of the

NH DJF wave. However, **Figure 4.8**, shows that there is an observed significant trend in the maximum amplitude of the seasonal SH SON wave in the period 1980-1999, and that almost all models simulate trends of the same sign, although the simulated trends are generally statistically insignificant, as is the trend for the multi-model mean. Nevertheless there is a consistency between the simulations and observations suggesting that the changes to the stationary wave field in the SH are caused by ozone depletion *via* two independent, but not mutually exclusive, mechanisms. The change in the stationary wave could be a direct response to zonally asymmetric trends in the SH ozone depletion (Crook *et al.*, 2009); for this mechanism, a strengthening of a displaced Antarctic vortex associated with photochemical ozone loss within the vortex would enhance the stationary wave field. This effect would reverse under ozone recovery and in all the models the positive

trend in Figure 4.8 weakens or switches sign from 1980-1999 to 2050-2099; though again, few of these trends are statistically significant. Alternatively, the impact of ozone depletion on the zonal-mean stratospheric circulation, which could also reverse as ozone recovers, could indirectly affect planetary wave properties *via* linear planetary wave dynamics.

To summarize, the models simulate the meridional and zonal location of the stationary wave field, but exhibit a bias towards weak amplitudes in the NH and a seasonal cycle that reaches its maximum too early and at too large a value in the SH. The stationary wave analysis shows that the orientation and shape of the stratospheric polar vortex is generally well captured by the models. Finally, few significant trends in the seasonal stationary wave field are found, apart from a trend towards stronger zonal asymmetry in the SH, which would be associated with either, or both of, the zonally symmetric and zonally asymmetric features of ozone radiative forcing.

### 4.3.3 Brewer-Dobson circulation / tropical upwelling

The Brewer-Dobson circulation plays an important role in transporting chemical species into and within the stratosphere, and also in determining the thermal structure of the stratosphere through adiabatic warming or cooling. A useful proxy for the Brewer-Dobson circulation in the models is the Transformed Eulerian Mean (TEM) residual velocity ( $\bar{v}^*$ ,  $\bar{w}^*$ ) (Hardiman *et al.*, 2010a, Equations 22 and 23). In particular the residual vertical velocity,  $\bar{w}^*$ , just above the tropical tropopause can be used to deduce the mass flux entering the stratosphere and thereby provide a measure of the overall strength of the overturning meridional mass circulation in the model stratospheres (Butchart and Scaife, 2001). The rate of tropical upwelling also gives a good indication of the mean age of stratospheric air – the time elapsed since a stratospheric parcel of air was last in contact with the troposphere (Austin and Li, 2006; Butchart *et al.*, 2010; also see Chapter 5).

In the REF-B1 simulations at 70 hPa there is good agreement between nine out of the fourteen models in the climatological residual vertical velocities,  $\bar{w}^*$ , between

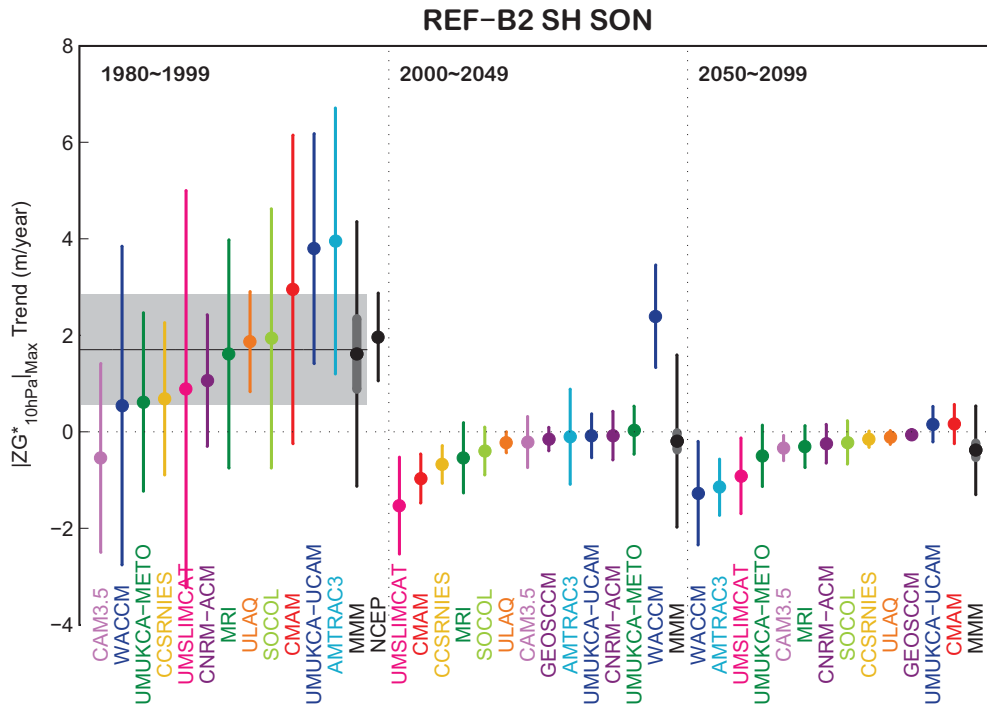


**Figure 4.8:** Trends in the amplitude of the seasonal-mean stationary wave for the periods 1980-1999, 2000-2049, and 2050-2099 in the REF-B2 simulations. Data are based on seasonal means for the models, ERA-40 (shaded) and NCEP data from 1980 to 1999. The linear trend is calculated using least square estimates, and the t-distribution is used to test the two-sided hypothesis that the true trend is within the estimated trend plus or minus an uncertainty for a given significance level ( $p = 0.05$  here). The multi-model mean trend is simply the average of the trends of individual models, where its thin error bar indicates the inter-model spread (twice of the standard deviation of the trends of all models) and its thick error bar in deep grey represents the uncertainty due to the confidence intervals of individual models.

40°S and 40°N (**Figure 4.9a**). As found by Butchart *et al.* (2006, Figure 2) for a different multi-model ensemble, the latitudinal distributions of the model residual vertical velocities are remarkably similar to that derived from the UKMO analyses (Figure 4.9a). All the models apart from the Socol model have the characteristic local minimum in  $\bar{w}^*$  at the equator with local maximum 15°-20° either side of this. Although  $\bar{w}^*$  is notoriously difficult to derive from reanalysis data, these basic features were also present in the residual vertical velocities derived from ERA-40 for 1994-2002 (Randel and Wu, personal communication, 2009) hence it is possible to have some confidence that the models are behaving at least qualitatively correctly. The NiwaSOCOL model has too strong upwelling in the tropics, and the CNRM-ACM and E39CA model have downwelling there. An apparent deficiency in all the simulation occurs in the SH subtropics where the annual mean upward residual velocities ( $\bar{w}^* > 0.0$ ) extend 10°-15° further poleward than in the UKMO analyses, though there is rather

good agreement (little spread) between the models at these latitudes. There is also too little upwelling in the models between 10°N and 20°N. In general model residual vertical velocities are more symmetric across the equator than those derived from the UKMO analyses (or ERA-40 – not shown).

Similar features are seen in the REF-B2 simulations (not shown), though the Socol results are now in better agreement with the UKMO analyses. For the multi-model mean, there is more upwelling equator-ward of ~13° and less poleward of ~13° (up to the turn-around latitudes) in the REF-B2 simulations compared to the REF-B1 simulations, but on average the total tropical upwelling is the same in both sets of simulations to within 1%.

When the seasonal movement of the tropical upwelling region toward the summer hemisphere is taken into account all the models with the exception of the NiwaSOCOL, Socol and ULAQ models correctly reproduce, with respect to the UKMO analyses, the locations

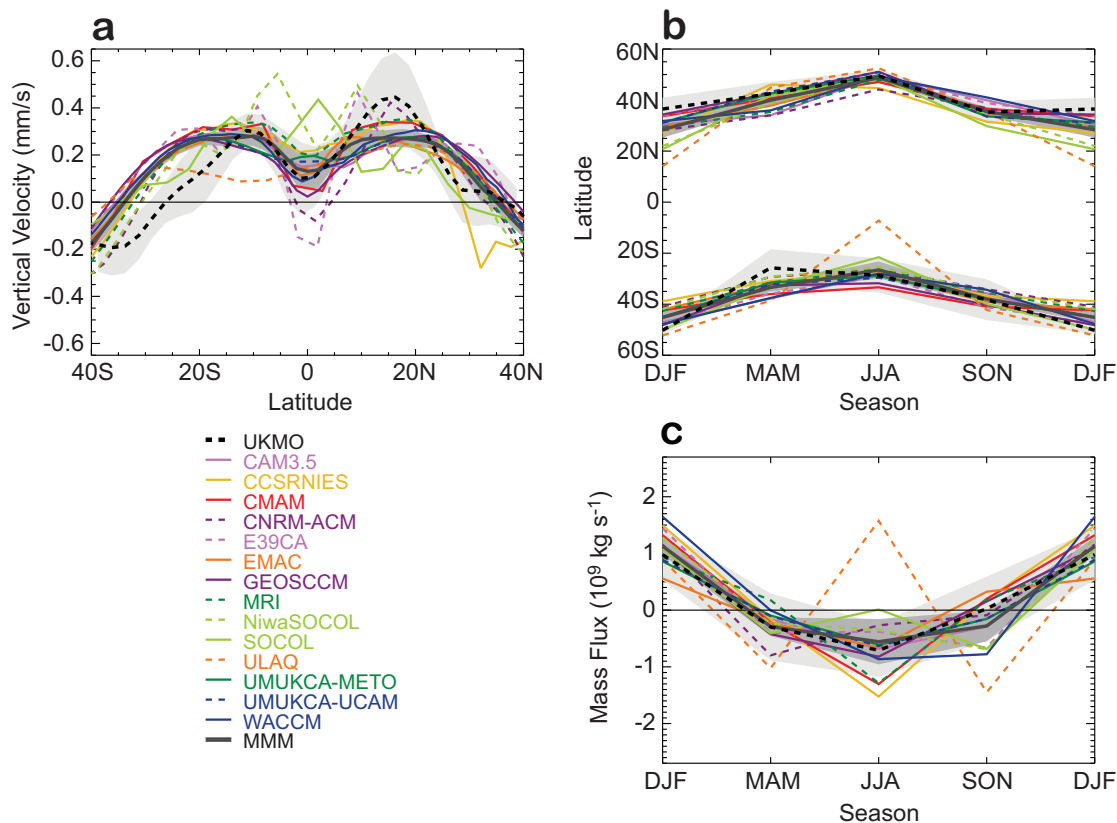


**Figure 4.9:** (a) Annual mean residual vertical velocities  $\bar{w}^*$  at 70 hPa. (b) “Turn-around” latitudes, defined as the latitudes within 50°S-50°N where  $\bar{w}^* = 0$ . (c) Upward mass flux at 70 hPa calculated from residual vertical velocity  $\bar{w}^*$ . Seasonal anomalies from the annual mean are shown. All panels show averages from 1980-1999 for REF-B1 simulations. The thick dark grey solid line shows the multi-model mean. Where data from an ensemble of runs is available, the ensemble mean is used. The thick black dashed line shows the UKMO stratospheric analysis (averaged from 1992-2001; the averaging period is found not to matter). Light grey shading shows the 95% confidence interval for the 10 year mean from the UKMO analyses and dark grey shading shows the inter-model standard error.



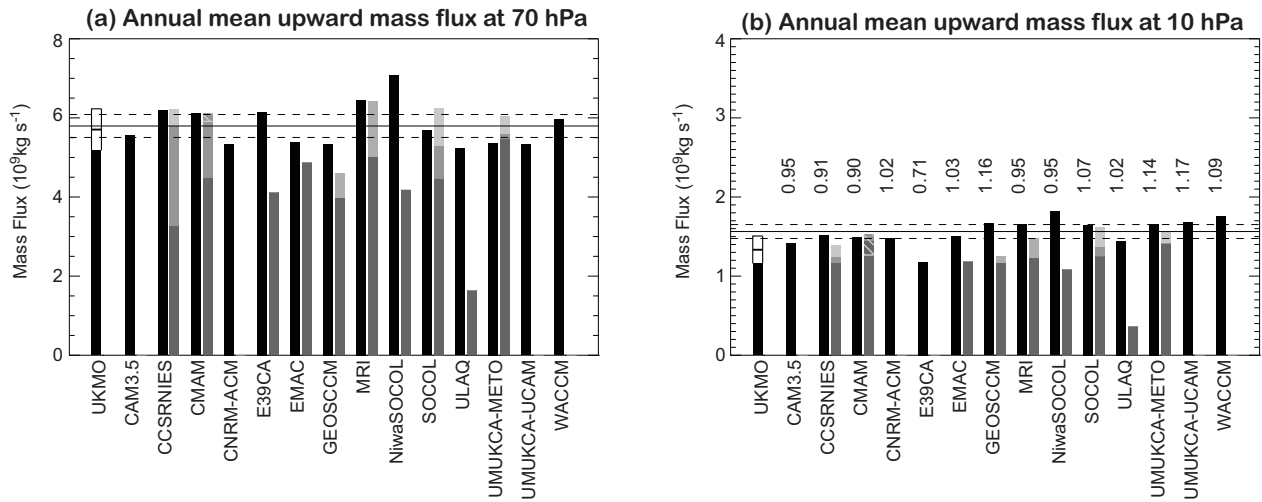


**Figure 4.10:** Annual mean upward mass flux averaged from 1980 to 1999 for the REF-B1 simulations and from 1992 to 2001 for the UKMO analyses. Averaging the modelled upwelling from 1992-2001 gives very similar values to those shown for 1980-1999. Upwelling calculated from  $w^*$  is shown by black bars. Upwelling calculated by downward control is split into contributions from: resolved waves (dark grey), orographic gravity wave drag (OGWD) (grey), and non-orographic gravity wave drag (NOGWD) (light grey). OGWD and NOGWD are shown combined for the GEOSCCM and MRI model. For some models only the resolved wave contributions are shown due to the unavailability of gravity wave drag diagnostics. In the CMAM, NOGWD produces a negative upwelling and so cancels some of the upwelling produced by the OGWD and the resolved waves. This cancellation is shown by diagonal lines. The black horizontal lines show the multi-model mean and the inter-model standard error. The 95% confidence interval for the UKMO analyses is shown by the unshaded part of the bar with the horizontal line at the mid-point being the multi-year (10-year) mean. Values shown at (a) 70 hPa, and (b) 10 hPa. The numbers above the bars in (b) are the ratio for that model of the upwelling mass flux (normalised by the multi-model mean) at 10 hPa to upwelling mass flux (normalised by the multi-model mean) at 70 hPa.

of the “turn-around latitudes” where  $\bar{w}^*$  is zero (*i.e.*, the latitudes where the tropical upwelling changes to extratropical downwelling – Figure 4.9b). The annual cycle in the integrated upward mass flux between these turn-around latitudes was also generally well reproduced, though again the SOCOL and ULAQ models did not perform as well as the other models (Figure 4.9c). In the REF-B2 simulations, the turn-around latitudes are, on average, the same as in the REF-B1 simulations to within  $0.5^\circ$ . The multi-model mean REF-B2 upwelling is 0.1-0.2 mm/s greater in DJF and SON and 0.1-0.2mm/s less in March-April-May (MAM) and June-July-August (JJA) than that for REF-B1, though the annual mean upwelling is the same in both sets of simulations to within 1%.

On average the annual-mean tropical upwelling mass fluxes in the REF-B1 simulations, calculated between the turn-around latitudes at 70 hPa and following the seasonal movement of those latitudes, agrees with the mass fluxes derived from the UKMO analysis (Figure 4.10a, black bars). The standard error in the multi-model mean is less than the interannual variability in the analysed mass fluxes (not shown). The contributions of resolved and parameterised wave drag in driving this upward mass flux can be es-

timated using the Haynes *et al.* (1991) Downward Control Principle (*e.g.*, Butchart *et al.*, 2010). These contributions are shown by the grey bars in Figure 4.10a. With the exception of the UMUKCA-METO there is a significant contribution from the parameterised orographic gravity wave drag (OGWD) (for those models that supplied OGWD data), which on average accounts for 21.1% of the driving of the upwelling at 70 hPa decreasing to 4.7% at 10 hPa (Figure 4.10b). At 70 hPa the resolved waves accounted for 70.7% (71.6% at 10 hPa) and non-orographic gravity wave drag (NOGWD) 7.1% (10.9% at 10 hPa) of the driving again averaged over those models which provided these diagnostics. In general, however, there was a wide spread between the models in the contributions from the wave drags. At 70 hPa, the contributions from the resolved waves ranged from 31.4 % (ULAQ) to 102.1% (UMUKCA-METO), while the range for OGWD and NOGWD was 2.0 (UMUKCA-METO) to 40.9% (CCSRNIES) and -3.4 (CMAM) to 16.8% (SOCOL), respectively. It is also worth noting that the models generally overestimate the 100 hPa heat flux ( $\sim$ vertical component of the EP-Flux) between  $20^\circ\text{S}$  and  $40^\circ\text{S}$  (Section 4.3.4, Figure 4.12), which includes the southern latitude (*i.e.*, the turn-around latitude, *c.f.*,

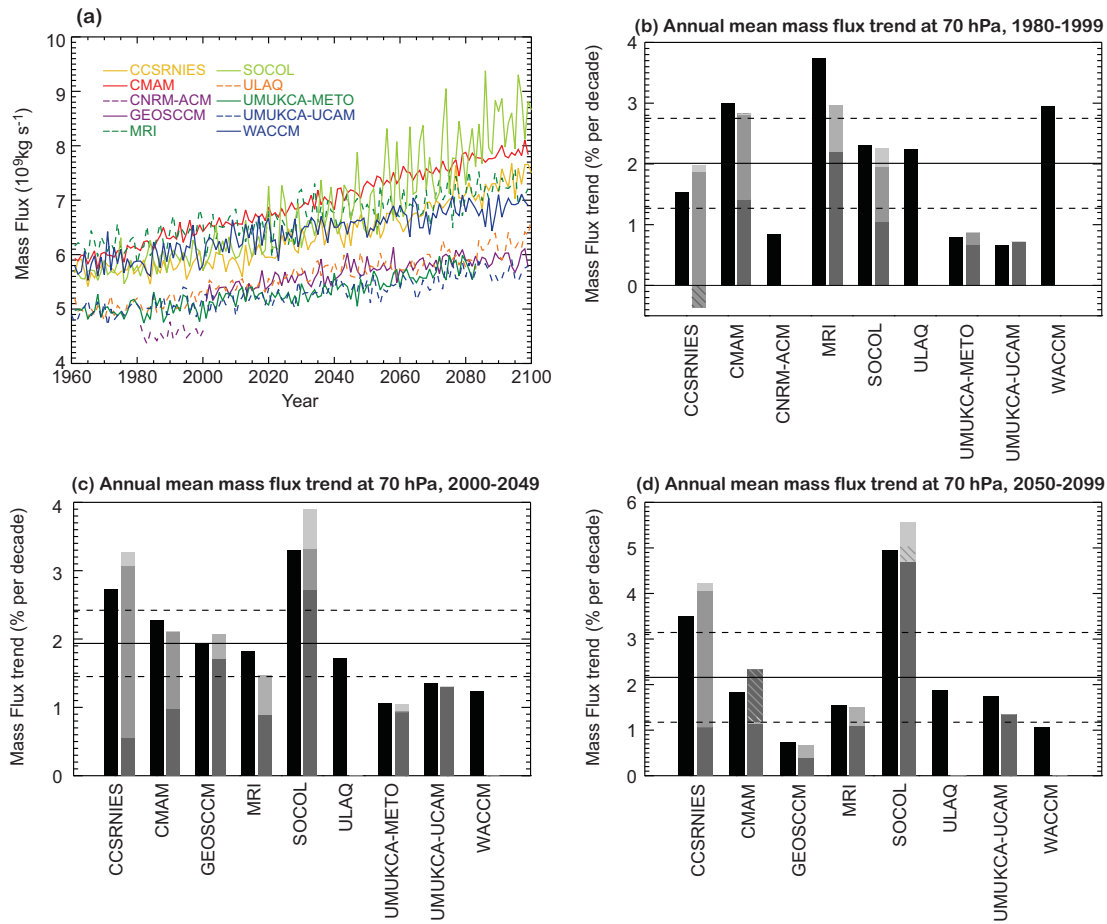


**Figure 4.11:** For the REF-B2 simulations. (a) Annual mean upward mass flux at 70 hPa, calculated from  $\bar{w}^*$ . Also shown is the annual mean mass flux trend at 70 hPa from (b) 1980-1999, (c) 2000-2049 and (d) 2050-2099. The grey shading and diagonal lines are as in Figure 4.10. The values are calculated from a linear fit to the annual mean mass flux from (b) 1980-1999 shown as a percentage of 1980 mass flux values, (c) 2000-2049 and (d) 2050-2099 shown as a percentage of 2000 mass flux values. The horizontal lines show the multi-model mean and the inter-model standard error.

Figure 4.9b) at which the downward control integral is performed, though it is unclear what impact this would have on the upwelling estimated from the EP-flux divergence.

Similar results were obtained for the REF-B2 simulations (not shown) with the multi-model mean upwelling within 3% of that in the REF-B1 simulations. The largest differences occurred for the CNRM-ACM which had over 15% less upwelling for the REF-B2 than for the REF-B1 simulation.

In REF-B1 simulation, the ratio of the upwelling (as calculated from  $\bar{w}^*$ ) at 10 hPa to that at 70 hPa (weighted by the multi-model means) gives some indication of the relative leakiness of the tropical pipe in the lower stratosphere with respect to the multi-model mean (Neu and Plumb, 1999; see also Chapter 5, Section 5.2.1.2). This ratio is shown in Figure 4.10b (see figure caption for details). The UMUKCA and GEOSCCM simulations show too little upwelling at 70 hPa and too much upwelling at

10hPa, with the ratio of upwelling at 10 hPa to that at 70 hPa being around 115% of that of the multi-model average. Conversely, the CCSRNIES model, and the CMAM show too much upwelling at 70 hPa and too little upwelling at 10 hPa, with a ratio of 90% or less of that of the multi-model average.

For all the models the annual mean upward mass flux at 70 hPa increased from the start (1960) to the end of the REF-B2 simulations (see Figure 4.11). On average the trend in the upward mass flux was about 2% per decade (Figure 4.11b, c, d) with the largest trends occurring in JJA (not shown). With the exception of the Socol model, interannual variability in the annual mean upward mass flux is less than the multi-model spread (Figure 4.11a). For the end of the 20<sup>th</sup> century (1980-1999) the trends predicted by the REF-B2 simulations (Figure 4.11) were very similar to those for the REF-B1 simulations (not shown). The largest difference was found for the CCSRNIES model, which had

a negative trend from the resolved waves in the REF-B2 simulation but not for the REF-B1 simulation. The multi-model mean trend for the period 1980-1999, was 2% per decade for REF-B2, and 2.3% per decade for REF-B1. It should also be noted that the partitioning of the downward control estimate of the trends into resolved and parameterised drag contributions (grey bars in Figure 4.11b, c, d) is rather sensitive to the calculation of the location of the turn-around latitudes (McLandsres and Shepherd, personal communication, 2009). This sensitivity results from the strong latitudinal dependence of the OGWD in the NH subtropics (*i.e.*, near the turn-around latitudes) and will most likely impact the calculations for models with a coarse horizontal resolution.

To summarize, the strength of tropical upwelling and position of the turn-around latitudes are well represented in general, but in all models the annual mean upwelling in the SH extends  $10^{\circ}$ - $15^{\circ}$  further poleward than in the analysis, and there is too little upwelling between  $10^{\circ}$ N and  $20^{\circ}$ N. Tropical upwelling at 70 hPa is within observational uncertainty whilst at 10 hPa there is slightly too much upwelling. There is disagreement across models as to the relative contributions from resolved waves and parameterised gravity waves to driving this upwelling, through apart from one model there was a significant contribution from orographic gravity wave drag at 70 hPa. The strength of tropical upwelling, and thus the Brewer-Dobson circulation is projected to increase throughout the 21<sup>st</sup> century by

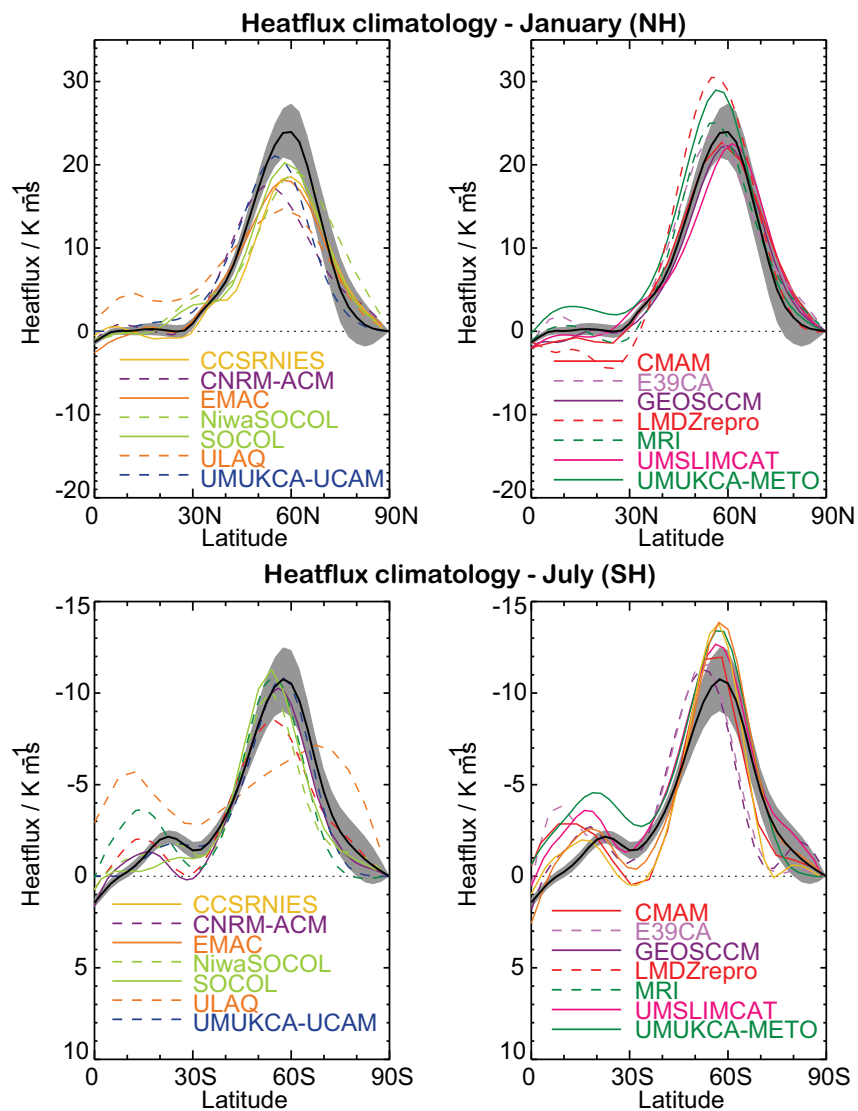


**Figure 4.12:** Monthly mean climatology of the eddy meridional heat flux at 100 hPa for the months of January and July, 1980-1999. Data from ERA-40 reanalysis is shown in the black line. Grey shading shows the 95% uncertainty estimate for the 20-year mean of the ERA-40 based on a t-distribution. Where ensemble simulations are available, the climatology is derived by taking the mean across all ensemble members.

around 2% per decade.

#### 4.3.4 Heat flux / heat flux-temperature correlations

In this section the climatology of the eddy meridional heat flux at 100 hPa and the relationship between year-to-year variability of this quantity and spring-time polar cap temperatures is assessed. The meridional heat flux is the zonal-mean of the product of the eddy components of temperature and meridional wind. For studies of stratospheric dynamics, it is a useful proxy for the vertical component of the EP-flux (see Andrews *et al.*, 1987) due to planetary-scale Rossby waves. Newman *et al.* (2001) noted the strong correlation between the eddy meridional heat flux at 100 hPa, averaged over a band between 40°N–80°N during January and February, and the subsequent temperature of the polar cap at 50 hPa in February and March. A simple linear fit to a scatter plot of 100 hPa heat flux and 50 hPa polar temperature provides information about the way in which the polar stratosphere responds to anomalous tropospheric wave activity propagating into the stratosphere.

**Figure 4.12** shows the monthly mean climatological heat flux for mid-winter in the NH and SH in the REF-B1 simulations. In the NH, most models reproduce the latitudinal distribution of the mid-winter heat flux climatology well, with a strong peak located around 55°N. However, in many of the models, including all those in the top left panel, the maximum heat flux is substantially smaller than that seen in the ERA-40 reanalysis data, with peak values well outside the estimated 95% confidence interval for the reanalysis data. The ULAQ model has a particularly low heat flux maximum. In the top right panel, most of the models perform well in simulating the heat flux climatology, although the LMDZrepro model and UMUKCA-METO have peak values larger than in the ERA-40 reanalysis.

In contrast in the SH, the climatological heat flux tends to be close to or slightly larger than that derived from the ERA-40 reanalysis. There are also some significant differences in the structure of the mid-winter heat flux climatology between the models and the reanalysis. In particular, models seem to over-emphasize the heat flux in the region between 20°S and 40°S associated with the subtropical jet. This is a particular problem in the ULAQ model which also mis-positions and under-estimates the strength of the main region of large negative meridional heat flux centred around 60°S.

Linear trends in meridional heat flux in the three periods 1980–1999, 2000–2049 and 2050–2099 of the REF-B2 simulations are shown in **Figure 4.13**. For this calculation, the mean heat flux between 40°N/S and 80°N/S during the northern and southern mid-winter is considered. Although there is a great deal of variability between models in each period, overall there is little sign of a consistent trend in the

mid-winter heat flux in any of the three periods in either hemisphere. The only period with a statistically significant trend in the multi-model mean heat flux is the period 2050–2099 in the NH. However, sensitivity tests of the multi-model mean show that if either the strong negative trends present in the ULAQ model or the UMUKCA-METO are removed, the multi-model trend is no longer significant. This indicates the multi-model trend should be treated with caution, particularly since the UMUKCA-METO REF-B2 simulation ends in the mid-2080s. Similar analyses were also performed for the REF-B1 simulations and for heat flux trends in the meteorological spring, but neither produced significant, consistent trends in the multi-model average.

Finally, the response of stratospheric temperatures to variations in heat flux is considered. This analysis follows directly from the work of Newman *et al.* (2001) and was reproduced by the CCMVal-1 inter-comparison (Eyring *et al.*, 2006). Here, to provide a more succinct way of comparing different models, only the parameters of the linear fits to the scatter plots of 100 hPa heat flux vs. 50 hPa temperatures are presented. **Figure 4.14** shows these for the REF-B1 simulations. The slope and intercept of the regression lines diagnose different properties of the model stratosphere. The intercept of the regression line (x-axis) gives an indication of the temperature that the polar cap would have if no resolved wave-driving were present. The slope of the regression line (y-axis) gives an indication of the strength of the stratospheric temperature response to a unit amount of resolved tropospheric wave-driving.

In the NH, almost all of the models produce linear fit parameters within the sampling uncertainty of the linear fit parameters in the ERA-40 reanalysis. Only the UMSLIMCAT and UMUKCA-UCAM, which has a significantly large stratospheric temperature response to the 100 hPa heat flux, are outliers in this diagnostic. It is interesting however, that the 95% confidence limits for the two UMUKCA simulations (UMUKCA-UCAM and UMUKCA-METO) overlap, and the UMUKCA-METO has linear fit parameters that are not significantly different from the ERA-40 reanalysis. In general in the NH, the cluster of model points is shifted toward the upper left quadrant of the plot, indicating a tendency toward lower polar temperatures and an enhanced response of the lower stratosphere to tropospheric wave-driving. The tendency towards a cold bias in the lower stratosphere during spring is consistent with previous model assessments (*e.g.*, Eyring *et al.*, 2006) and with Figure 4.1.

In the SH, there is a similar spread in the properties of the linear fit to the NH. Several of the models show properties statistically distinct from those in the ERA-40 reanalysis, including the EMAC model, which shows both a cold bias and an enhanced sensitivity to tropospheric wave-driving, the AMTRAC3, which has an enhanced sensitivity

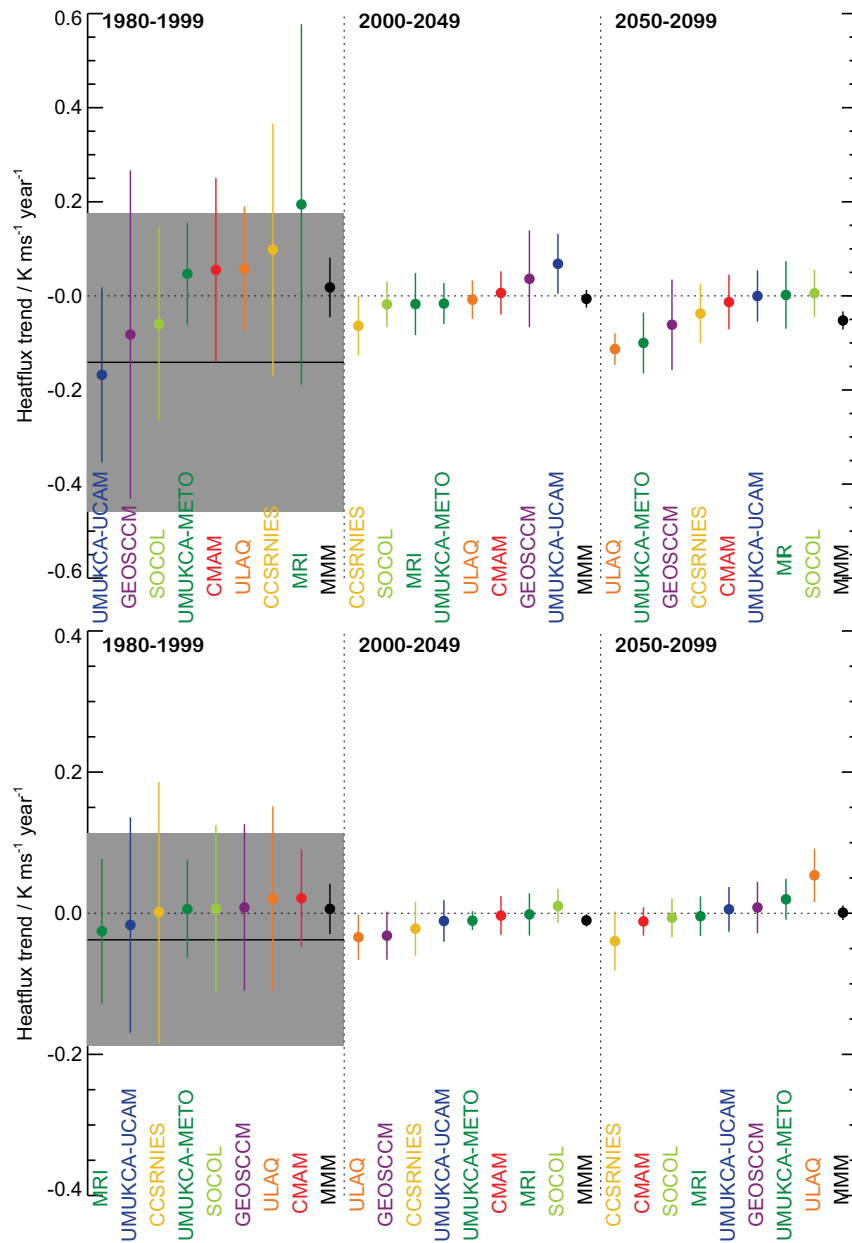


**Figure 4.13:** Linear trends in the mean meridional heat flux averaged between 40°N/S and 80°N/S for the winter seasons. Top panel shows trends for the January heat flux in the NH. Each section shows trends for a different time period, 1980-1999 in the leftmost panel, 2000-2049 in the middle panel and 2050-2099 in the right panel. Each model is represented by its mean trend shown by a dot and an estimate of the 95% confidence estimate on the trend, shown by plotting two standard errors either side of the mean estimate. In the 1980-1999 panel, trends and confidence limits for the ERA-40 reanalysis are shown by the solid black line and grey shading. In each panel, a multi-model mean estimate is given. The multi-model mean is calculated by weighting each model's trend by its uncertainty. The bottom panel shows the same information for the trends in the SH in July.

to tropospheric wave-driving, the CMAM, which displays a cold bias, and the GEOSCCM, which displays a warm bias. As an aside, it is important to remember that in this analysis (in both the NH and SH), results from the CMAM are from a three member ensemble average while many of the other models supplied only one realization, which

can be observed from the relatively small error bars for the CMAM fit parameters in Figure 4.14.

In contrast, the CNRM-ACM has very large error bars on its fit parameters because only 10 years of heat flux data were supplied by this model. Given the difference in the amount of data considered it is therefore easier to distin-

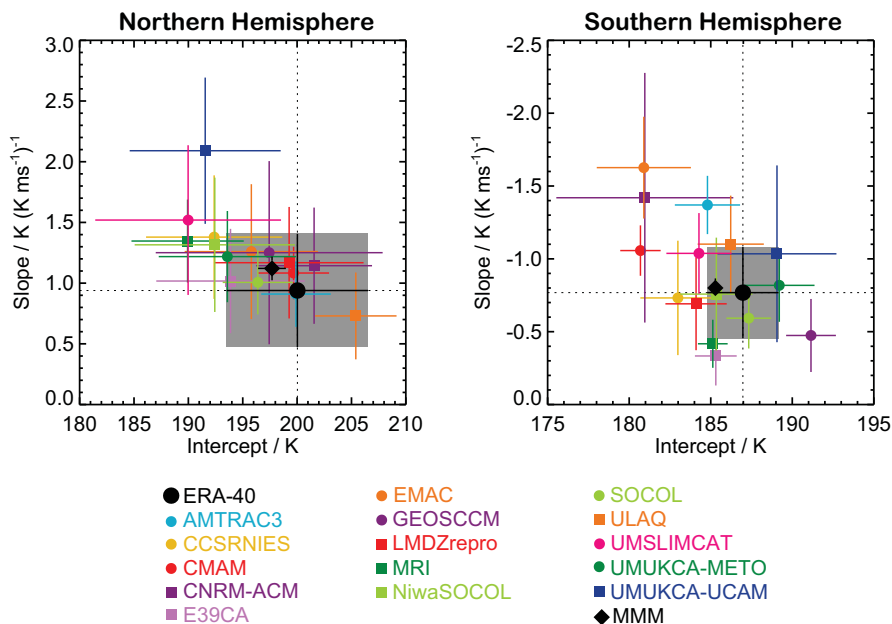


**Figure 4.14:** Parameters of the linear fit to the scatter plot of the 100 hPa heat flux vs. the 50 hPa temperature (for more details of procedure see Newman *et al.* (2001) and Eyring *et al.* (2006)). The panels show the intercept of the linear fit (x-axis) plotted against the slope of the regression line (y-axis) for the NH and the SH. Black symbols show the same diagnostic for the ERA-40 reanalysis data. Estimates of 95% confidence limits for the two parameters are included for each estimate in the thin coloured lines. Grey shading indicates the 95% confidence estimates for the ERA-40 reanalysis data.

guish significant differences between models and reanalysis for those models which supplied multiple realizations.

To summarize, the models reproduce the observed connection between lower stratospheric heat flux and temperature reasonably well in both the NH and SH, and the generally good performance of models in this diagnostic is consistent with the previous CCMVal-1 generation of models (Eyring *et al.*, 2006). In Chapter 8 the relationship between heat flux and the seasonal ozone gain/loss is diagnosed in more detail and shows larger spread between models than is evident from the heat flux vs. temperature correlations diagnosed here, because of the additional model spread introduced by the chemistry and transport.

### 4.3.5 Polar stratospheric cloud threshold temperatures

Changes in stratospheric temperatures are expected to have a large impact on polar ozone loss through their influence on the formation and occurrences of polar stratospheric clouds (PSCs). Polar stratospheric cloud formation is related to both the mean climatological structure of the polar vortex and its variability. To broadly assess the ability of models to reproduce mean conditions suitable for the formation of nitric acid trihydrate (NAT) and ice PSCs, the accumulated area where temperatures are below the appropriate thresholds (195 K for NAT and 188 K for ice) are

calculated. Although these diagnostics provide a useful estimate of the potential for PSC formation they do not take into account microphysical factors which are considered in more detail in Chapter 6. However, the simple diagnostics based on accumulated areas as described here are used in Chapter 9 when assessing the amounts of polar ozone depletion in the models (Section 9.5.4).

Following Pawson *et al.* (1999) and Austin *et al.* (2003), the potential for PSC formation in the models and ERA-40 reanalysis is estimated by calculating, each day, the percentage of the horizontal area of the hemisphere where the 50 hPa temperatures poleward of 50° are below the NAT and ice PSC formation thresholds. These daily percentage areas are then accumulated over the course of the winter and spring (92 days from July to September in the SH; and 90 days from December to February in the NH) to provide, for that year, an estimate of the total amount of NAT ( $\tilde{A}_{\text{NAT}}$ ) and ice ( $\tilde{A}_{\text{ice}}$ ) PSCs in units of %-days.

The climatological mean  $\tilde{A}_{\text{NAT}}$  and  $\tilde{A}_{\text{ice}}$  for the REF-B1 simulations for 1980-1999 are shown in **Figure 4.15**. The linear trends for the same period are shown in **Figure 4.16**, though there is considerable uncertainty in the trend estimates due to the large interannual variability in  $\tilde{A}_{\text{NAT}}$  and  $\tilde{A}_{\text{ice}}$ , particularly in the Arctic. In the Antarctic, the multi-model mean  $\tilde{A}_{\text{ice}}$  (grey bars) agrees well with the ERA-40 estimate, but the multi-model mean  $\tilde{A}_{\text{NAT}}$  is significantly smaller than the ERA-40 estimate over the same

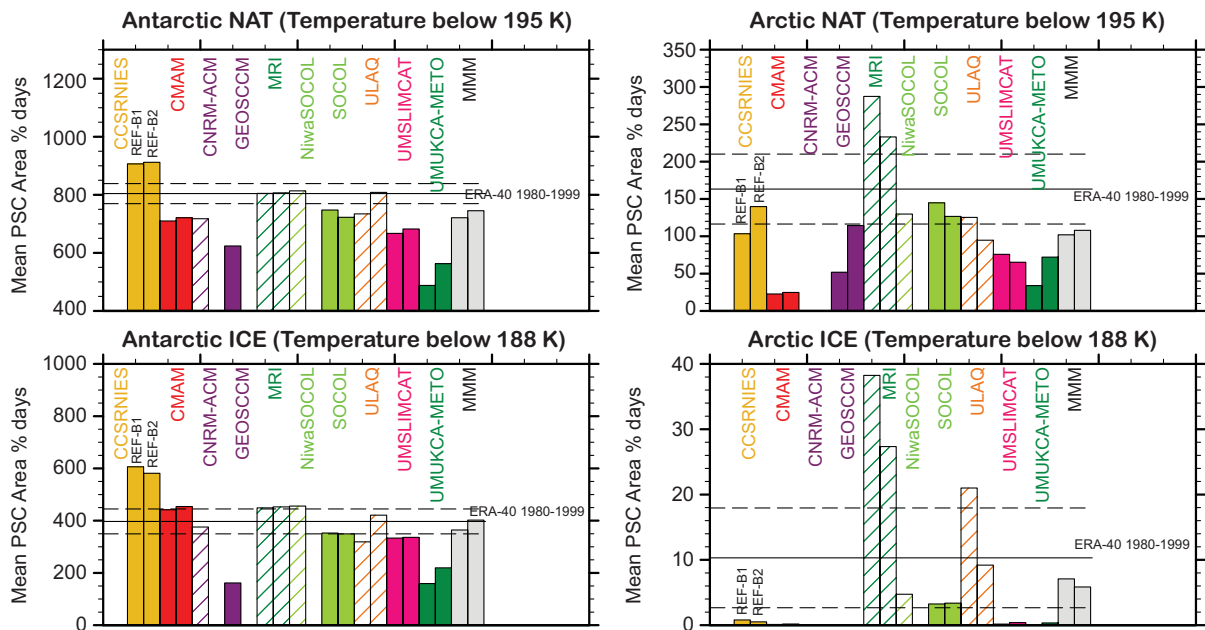


**Figure 4.15:** Mean (1980-1999) for the Antarctic (left) and the Arctic (right) of the seasonally accumulated area at 50 hPa where daily temperatures are below 195 K (approximate threshold temperature for NAT formation, top panels) and below 188 K (approximate threshold temperature for ice formation, bottom panels) for REF-B1 (first column) and REF-B2 (second column) simulations. The dashed black line is for the ERA-40 reanalysis (1980-1999). The units are the percentage of the hemisphere where the daily temperature is below the threshold multiplied by the duration in days.

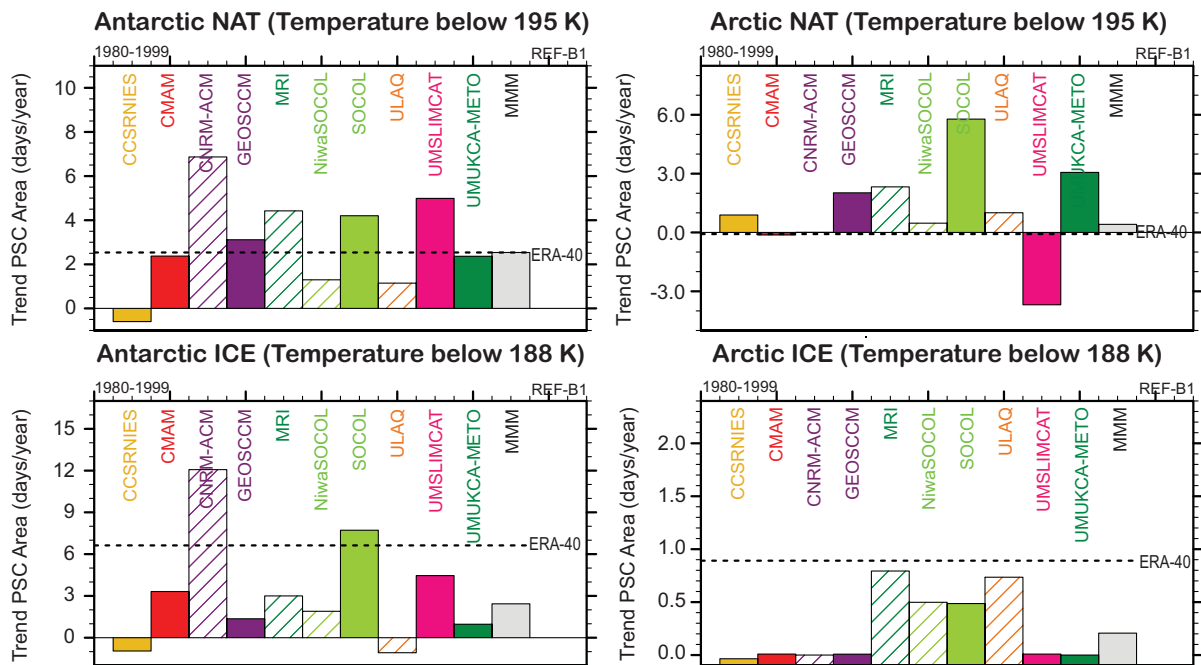


**Figure 4.16:** Linear trend (1980-1999) for the Antarctic (left) and the Arctic (right) of the seasonally accumulated area at 50 hPa where daily temperatures are below 195 K (approximate threshold temperature for NAT formation, top panels) and below 188 K (approximate threshold temperature for ice formation, bottom panels) for REF-B1 simulations. The dashed black line is the trend for the ERA-40 reanalysis (1980-1999).

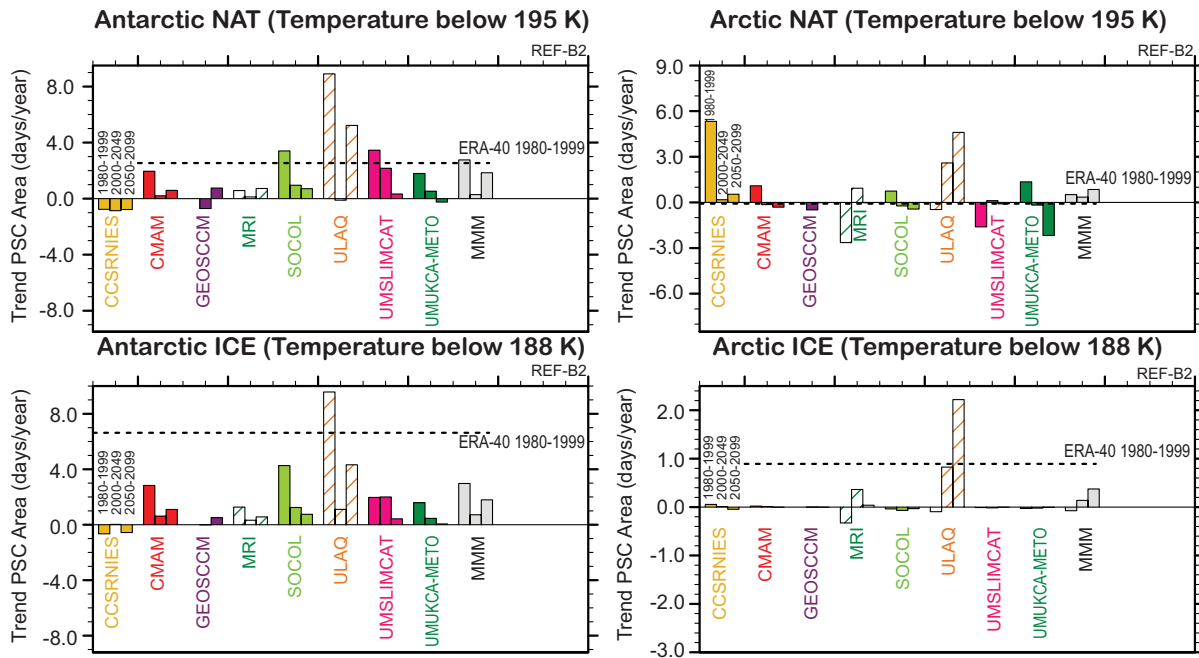


**Figure 4.17:** Linear trend (1980-1999, first column; 2000-2049, second column; 2050-2099 third column) for the Antarctic (left) and the Arctic (right) of the seasonally accumulated area at 50 hPa where daily temperatures are below 195 K (approximate threshold temperature for NAT formation, top panels) and below 188 K (approximate threshold temperature for ice formation, bottom panels) for the REF-B2 simulations. The dashed black line is the trend for the ERA-40 reanalysis (1980-1999).

period. There is a large spread among the models, with the UMUKCA-METO and the GEOSCCM being particular outliers with low values of both  $\tilde{A}_{\text{NAT}}$  and  $\tilde{A}_{\text{ice}}$  (consistent with the warm bias at this height in both models — see Figure 4.1). The majority of the models simulate an increase in  $\tilde{A}_{\text{NAT}}$  and  $\tilde{A}_{\text{ice}}$  throughout the time period (Figure 4.16) leading to a positive trend of 2.5 and 2 %-days per year respectively, for the multi-model mean. In the case of  $\tilde{A}_{\text{NAT}}$ , this is close to the trend estimate from ERA-40, but for  $\tilde{A}_{\text{ice}}$  is significantly smaller than the ERA-40 trend. Again there is a large model spread in the trends with some models indicating zero or small negative trends over the 1980-1999 period, and others simulating large positive trends.

In the Arctic there are large differences among the simulations in both the climatological mean values (Figure 4.15) of  $\tilde{A}_{\text{NAT}}$  and  $\tilde{A}_{\text{ice}}$  and the trends (Figure 4.16) for the period 1980-1999. In general, the models simulate lower values of  $\tilde{A}_{\text{NAT}}$  and  $\tilde{A}_{\text{ice}}$  than those derived from the ERA-40 reanalysis with the exception of the MRI and ULAQ models, which both have large cold biases in the NH winter (see Figure 4.1). Although the multi-model mean estimate of  $\tilde{A}_{\text{ice}}$  is not significantly different from the ERA-40 reanalysis, there is large uncertainty in the ERA-40 estimate because of the large NH variability, and the multi-model mean estimate is dominated by the two significant outliers

(MRI and ULAQ) with above average  $\tilde{A}_{\text{ice}}$ . The Arctic multi-model mean trend reflects almost no trend in  $\tilde{A}_{\text{NAT}}$ , whereas for  $\tilde{A}_{\text{ice}}$ , a positive trend is simulated by all the models.

Trends in PSC quantities are hard to derive from global assimilation data and estimates of  $\tilde{A}_{\text{NAT}}$  and  $\tilde{A}_{\text{ice}}$  can be quite different depending on the analysis or reanalysis data sets used (*e.g.*, Manney *et al.*, 2003, 2005a, b; Austin and Wilson, 2009). Therefore, those based on the ERA-40 reanalyses have to be interpreted cautiously. The ERA-40 reanalyses also show unrealistic vertical temperature oscillations in the Antarctic lower stratosphere in recent years, affecting PSC area calculations (Manney *et al.*, 2005a, b). In the Arctic, such behaviour is much less pronounced, and limited to the upper stratosphere and the last few years of the ERA-40 time series. For Arctic winters, ERA-40 temperatures also have a cold bias compared to Freie Universitat Berlin data, which are able to capture the temperature extremes relevant for the PSC derived quantities (Manney *et al.*, 2003). Nonetheless, the time evolution and the positive trend between 1980 and 1999 for  $\tilde{A}_{\text{NAT}}$  at 50 hPa exist in both observational data sets (Manney *et al.*, 2005a). Trends in  $\tilde{A}_{\text{NAT}}$  and  $\tilde{A}_{\text{ice}}$  for the REF-B2 simulations are shown in **Figure 4.17**. The trends for the period 1980-1999 can be compared with the corresponding trends in the REF-B1 simulations shown in Figure 4.16. With the



exception of the CCSRNIES model, all the other models which provided output from the REF-B2 simulations show an increase in Antarctic  $\tilde{A}_{\text{NAT}}$  and  $\tilde{A}_{\text{ice}}$  over the period 1980-1999. A positive, statistically significant trend of  $\tilde{A}_{\text{NAT}}$  of 2.5 %-days per year is simulated for the multi-model mean. This positive trend has a similar size to the trend calculated from the ERA-40 reanalysis, however the trend in the ERA-40 data is not significant at 95% confidence using a standard t-test for the regression slope. For the period 2000-2049, all the models project a smaller positive or slightly negative trend in  $\tilde{A}_{\text{NAT}}$  and  $\tilde{A}_{\text{ice}}$ ; these trends are statistically significant only for the SOCOL model and the UMSLIMCAT. In the following 50 years (2050-2099) all models, except for the CCSRNIES model and UMUKCA-METO, simulate a positive trend for Antarctic  $\tilde{A}_{\text{NAT}}$  and  $\tilde{A}_{\text{ice}}$ , leading to a multi-model mean trend for both quantities of 2 %-days per year with 95% significance. These trends are smaller than the observed trend in 1980-1999. The change in magnitude and sign of the trend for the different time periods is consistent with the radiative effects of simulated ozone depletion between 1980 and 1999 and slower ozone recovery in the 21<sup>st</sup> century (see Chapter 9), in addition to continued cooling of the stratosphere due to the prescribed increases in GHG amounts (Section 4.3.1; Eyring *et al.*, 2007; Butchart *et al.*, 2010).

In the Arctic there are large differences among the models in the trends in  $\tilde{A}_{\text{NAT}}$  and  $\tilde{A}_{\text{ice}}$  obtained from the REF-B2 simulations. Over the period 1980-2099 only a few of the REF-B2 simulations show an increase in  $\tilde{A}_{\text{NAT}}$  and  $\tilde{A}_{\text{ice}}$ , reflecting the role of interannual variability in influencing temperatures over the polar cap during Arctic winters (see Section 4.4). During the period 2050-2099, the CMAM, GEOSCCM, SOCOL and UMUKCA-METO time series show a decrease in  $\tilde{A}_{\text{NAT}}$ , whereas the CCSRNIES and ULAQ models simulate an increase, leading to a non-significant positive trend of 1 %-days per year in the multi-model mean. All of the models simulate a decrease in the magnitude of the trend in  $\tilde{A}_{\text{NAT}}$  from 1980-1999 to 2050-2099. In contrast, most models show an increase in the magnitude of the trend in  $\tilde{A}_{\text{NAT}}$  from 2000-2049 to 2050-2099. Trends in Arctic  $\tilde{A}_{\text{ice}}$  are very small in most models, with only those with large cold biases (ULAQ and MRI) showing a significant trend over the period 2000-2099.

To summarize, the multi-model mean predicts a significant increase in  $\tilde{A}_{\text{NAT}}$  and  $\tilde{A}_{\text{ice}}$  for the Antarctic and no significant changes for the Arctic during the 1980-2099 period. On average in the Antarctic, the models show greater agreement in their climatological estimates of  $\tilde{A}_{\text{NAT}}$  and  $\tilde{A}_{\text{ice}}$  and their estimates of trends from 1980-1999. This gives confidence in model future projection for the SH. There is little agreement between the models concerning future Arctic amounts of  $\tilde{A}_{\text{NAT}}$  and  $\tilde{A}_{\text{ice}}$ . This is almost certainly related to the large spread in climatological accumulated PSC amounts between the models. Much of this spread

in the model ensemble is likely related to the differences in variability between the models (see Section 4.4) which has a strong influence on both the mean temperature climatology and year-to-year variability which is important for  $\tilde{A}_{\text{NAT}}$  and  $\tilde{A}_{\text{ice}}$ .

## 4.4 Variability

### 4.4.1 Extra-tropical variability of the zonal-mean zonal wind

A realistic simulation of the winter-time extra-tropical stratospheric circulation indicates a more realistic description of dynamical troposphere-stratosphere coupling with implications for chemistry-climate interactions. The variability of the winter-time extra-tropical stratospheric circulation is mainly characterized by variations in the strength and location of the polar night jet. As with the climatological zonal-mean state (Section 4.3.1), the zonal wind variability is first assessed in terms of the strength and latitude of the maximum interannual standard deviation in the zonal-mean zonal wind. Results for the extra-tropical regions (see Section 4.4.2 for tropical variability), 45°N-90°N for the Boreal winter, and 30°S-80°S for the Austral winter are shown in **Figure 4.18**. Most models do not simulate the variability as well as they do the mean climatology. For the NH, the reanalyses show maximum variability close to the climatological mean jet maximum. All the models fail to capture the equator-ward tilt with height, and the maximum variability in the AMTRAC3 and the GEOSCCM occurs too far equator-ward in the upper stratosphere. The CNRM-ACM has too little stratospheric variability, whereas the MRI model, UMUKCA-UCAM and WACCM show too much variability, especially in the upper stratosphere. For the REF-B2 simulations for the same period (not shown), the results are very similar, except for the CAM3.5 and ULAQ model which have too little variability, and the UMUKCA-METO and UMSLIMCAT which have too much variability compared to the reanalysis. For the SH, the reanalysis shows the maximum variability occurs on the equator-ward side of the jet, fairly close to the QBO region. Most of the models have variability that is too weak and located too far poleward compared to the reanalyses. The REF-B2 simulations (not shown) have very similar biases.

The nature of the variability of the polar night jet can be further investigated by applying an Empirical Orthogonal Function (EOF) analysis to the extra-tropical zonal-mean zonal wind (*e.g.*, Feser *et al.*, 2000; Black and McDaniel, 2009). Here, an EOF analysis of the 50 hPa zonal-mean zonal wind is used to provide a more detailed assessment of the lower stratospheric variability in the

REF-B1 simulation than that obtained above using the interannual standard deviation. Furthermore, by considering all months, this EOF analysis captures seasons when the variability maximises. In the reanalysis data, variability of extra-tropical zonal-mean zonal wind in the stratosphere maximised during January to March in the NH, and during mid-October to mid-December in the SH (Thompson and Wallace, 2000). In general, the models capture this seasonality reasonably well, though the period when there is large variability is extended in several of the models compared to the reanalysis (not shown, but see Chapter 10, Section 10.3.2 and Figure 10.10 for the multi-model mean seasonal cycle in the annular mode variance).

In both the reanalysis and the models, the extra-tropical variability of the zonal-mean zonal wind in the stratosphere can be mainly described by two modes, with the first mode dominating. In the reanalysis data the leading mode clearly dominates in the NH, explaining 87% of the variance. In the SH, both modes contribute explaining 59% and 35% of the variance, respectively. **Figure 4.19** shows the eigenvalues of the first mode which is a measure of the variance described by this mode. The error bars indi-

cate sampling error (see figure caption for details). **Figure 4.20** shows the spatial regression patterns of the first and second mode. The leading mode describes the variations in the strength of the eastward polar night jet while the second mode represents the meridional shift of the jet (Figure 4.20).

In the NH, nine of the sixteen models agree well with the reanalysis after allowing for the uncertainties given by the error bars, while two (five) models have larger (smaller) values (Figure 4.19). The two models with the largest low-bias (CNRM-ACM, ULAQ) also show the smallest maximum variability of the zonal-mean wind in mid-latitudes (Figure 4.20). Furthermore, the results for the ULAQ model are consistent with that model having the lowest frequency of stratospheric sudden warmings (SSWs) (see Section 4.4.3, Figure 4.25). The SSW frequency was not diagnosed for the CNRM-ACM due the absence of the appropriate data. A comparison of Figures 4.19 and 4.20 (top right also indicates that the two models with the largest positive bias in the eigenvalue of the leading EOF (MRI, UMUKCA-UCAM) show larger than average maximum in the zonal wind variability in mid-latitudes, but more im-

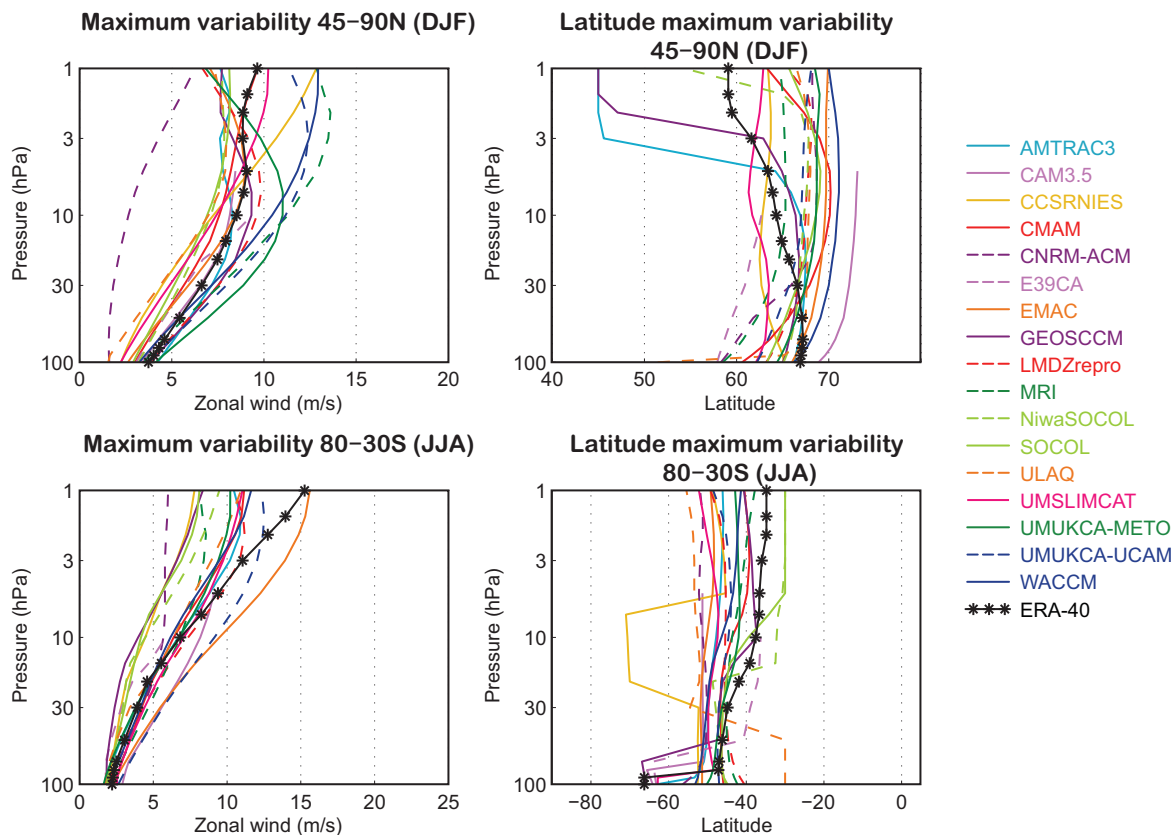


**Figure 4.18:** Location and amplitude of the maximum interannual standard deviation of the zonal-mean zonal wind in the NH in DJF poleward of 45°N (top) and in the SH in JJA between 80°S and 30°S (bottom). Data are based on the period 1980–1999 for the REF-B1 simulations and the ERA-40 reanalysis. Where an ensemble of simulations is available, the time series of the different members are concatenated before the calculation of the interannual standard deviation field.

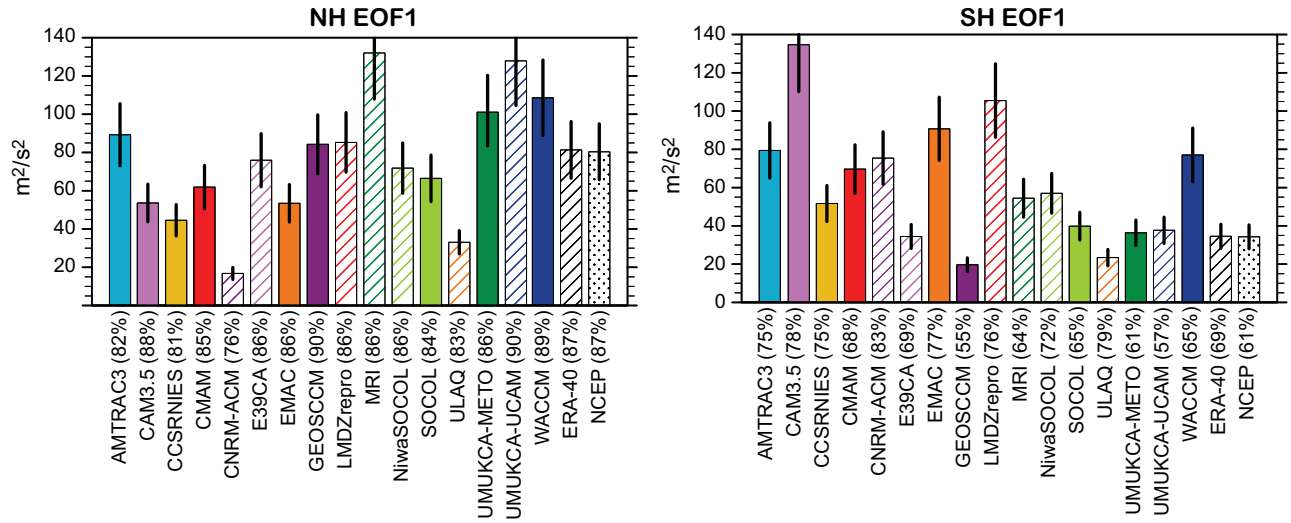


**Figure 4.19:** Eigenvalue of the leading mode of variability of the 50 hPa zonal-mean zonal wind ( $m^2/s^2$ ) for the SH (right) and NH (left). Numbers in brackets (tick labels of the x-axes) indicate the fraction of the total variance explained by the leading mode. Error bars  $2\Delta\lambda$  indicate the sampling error determined after North et al. (1982):  $\Delta\lambda = \sqrt{(2/N)}$ , where  $N$  is the sample size. With  $N = 60$ , a conservative estimate of the effective sample size is used considering long persistence (two months) in the stratosphere and weak zonal wind variations during 50% of the year. The EOF analysis was carried out for the NH (SH) 50 hPa zonal-mean zonal wind anomalies poleward of  $45^\circ N$  ( $^\circ S$ ). Monthly mean fields for all months from 1980 to 1999 are included with seasonal cycle and linear trends removed. Data are also weighted with the square root of the cosine of latitude.

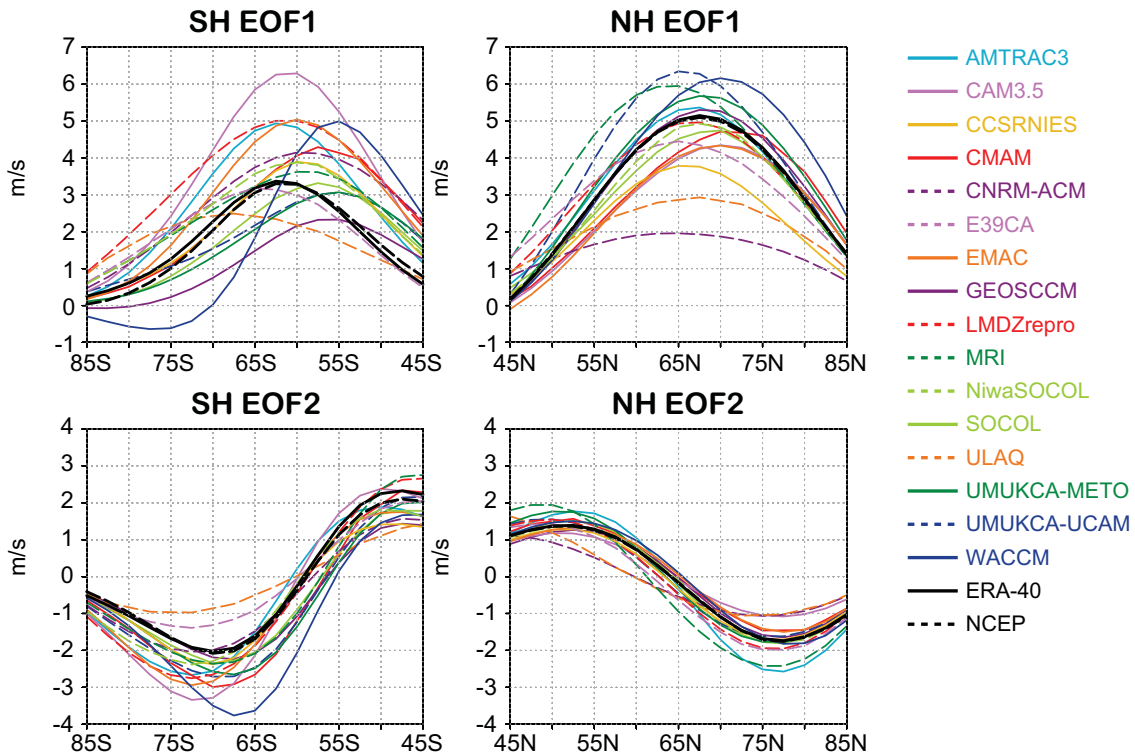


**Figure 4.20:** Regression patterns (m/s) of first (top) and second (bottom) mode of the 50 hPa zonal-mean zonal wind determined for regions poleward of  $45^\circ$ ; (left) SH and (right) NH.

portantly, the variability of the jet maximises at a lower latitude than in the reanalysis, by up to  $\sim 5^\circ$ .

The situation is quite different in the SH where only five models agree with observations in respect to the magnitude of the leading eigenvector (Figure 4.19). Ten models overestimate the variations in the strength of the polar night jet and two under-estimate this parameter. Figure 4.20 reveals a large spread both in the magnitude and location of maximum zonal wind variability between the models. The bias in the magnitude (and eigenvalue) is largest and positive in the CAM3.5. Several models show maximum zonal wind variations  $10^\circ$  further equator-ward than the reanalysis, while the ULAQ model shows maximum zonal wind anomalies shifted poleward by about  $8^\circ$ .

In summary, the analysis of the structure of the monthly mean zonal wind variability in the lower stratosphere reveals that most models simulate well both the magnitude and zonal structure of the variability in the NH. The largest biases result from an under-estimation of variability of the jet in the CNRM-ACM and ULAQ model, and a shift in the location of the maximum variability to lower latitudes in the UMUKCA-UCAM and MRI model. In the SH, most models exhibit large biases in the leading mode of variability of the zonal-mean zonal wind with subsequent implications for the second mode. Positive biases in the magnitude of the leading coupled mode and, hence, the variability of the polar jet, are related to a delayed break-up of the polar vortex in spring (Fogt *et al.*, 2009) which is a common problem in most of the models (see Section 4.3.1). Several models also overestimate the variability in the SH compared to the NH.

#### 4.4.2 Tropical variability of the zonal-mean zonal wind

A faithful representation of tropical variability above the tropopause has broad scientific relevance. In the tropical middle and upper stratosphere, the direction of the zonal-mean zonal winds, *e.g.*, phase of the quasi-biennial oscillation (QBO), has been linked with the frequency of a disturbed polar vortex (Holton and Tan, 1980; Lu *et al.*, 2008) and the rate of transport to higher latitudes of trace gases such as ozone (Li *et al.*, 2008). Tropical variability can also influence processes thought to be relevant for maintaining the extra-tropical mean stratospheric climate and its variability.

Tropical variability in the REF-B1 simulations is first assessed in terms of the vertical profile of the interannual standard deviation in the de-trended zonal-mean zonal wind averaged between  $10^\circ\text{S}$  and  $10^\circ\text{N}$  (Figure 4.21). Below  $\sim 48$  km ( $\sim 1$  hPa) all the models under-estimate tropical variability in comparison to ERA-40, with the exception of the WACCM at levels below 20 hPa. Five models exhibit particularly low stratospheric variability, largely

due to the absence of either an internally generated or explicitly prescribed QBO.

Figure 4.22 shows the vertical profile of the amplitude of the variability in zonal wind at periods between 2 and 5 years (see figure caption for details). This range of periods captures possible QBO-like variability and it is evident from the figure which models neither prescribe nor internally-generate a QBO (*c.f.*, Chapter 2, Table 2.8; Chapter 8, Table 8.4). Interestingly enough, there are still differences seen between those models that prescribe a QBO, possibly related to the fact that these models do not include any feedback mechanisms between the simulated ozone and the imposed artificial forcings. Furthermore, all models show a weaker peak amplitude for the QBO compared with ERA-40 (1980-1999).

The representation of the semi-annual oscillation (SAO) in the models can be seen in Figure 4.23. This shows the amplitude of the SAO, calculated using the same method as in Figure 4.22 but now including only the 6-month harmonic. Unlike for the QBO, the models show a spread in peak amplitude of the SAO about the amplitude seen for ERA-40. The CAM3.5 and ULAQ model, exhibit SAO amplitudes significantly less than that obtained for ERA-40. On the other hand the GEOSCCM and LMDZrepro model have peak SAO amplitudes significantly larger than that for ERA-40 (*c.f.*, Figure 4.29). Most likely this is due to a lack of a QBO in these models: the QBO in the lower stratosphere winds would act periodically to filter out parts of the model's resolved and/or parameterised gravity waves, responsible for driving the eastward phase of the SAO. The significance of any net model bias above  $\sim 32$  km (10 hPa) must, however, be treated with caution due to the paucity of observations assimilated there by ERA-40.

The amplitude of annual cycle in tropical zonal-mean zonal wind in the REF-B1 simulations is shown in Figure 4.24, again derived using the same method as for Figure 4.22, but now including only the 12-month harmonic. The amplitude of the ERA-40 annual cycle shows two peaks; in the upper troposphere and at the stratopause. All the models exhibit a peak in the amplitude in the upper troposphere, with the ULAQ model and the CNRM-ACM having unrealistically large and small amplitudes, respectively.

All the models significantly under-estimate the amplitude of the annual cycle near the stratopause, although the MRI and EMAC models and the UMSLIMCAT perform better than the others. A weak annual cycle in the models may be linked with the overly strong SAO. Similar features are referred to in Osprey *et al.* (2010), using the a high-top version of the Met Office's global climate model. They link a reduced annual cycle at the tropical stratopause to an overly strong SH summer jet and stronger than observed westward circulation during JJA.

A brief comparison of the tropical zonal wind variability in the REF-B1 and REF-B2 simulations from 1980-

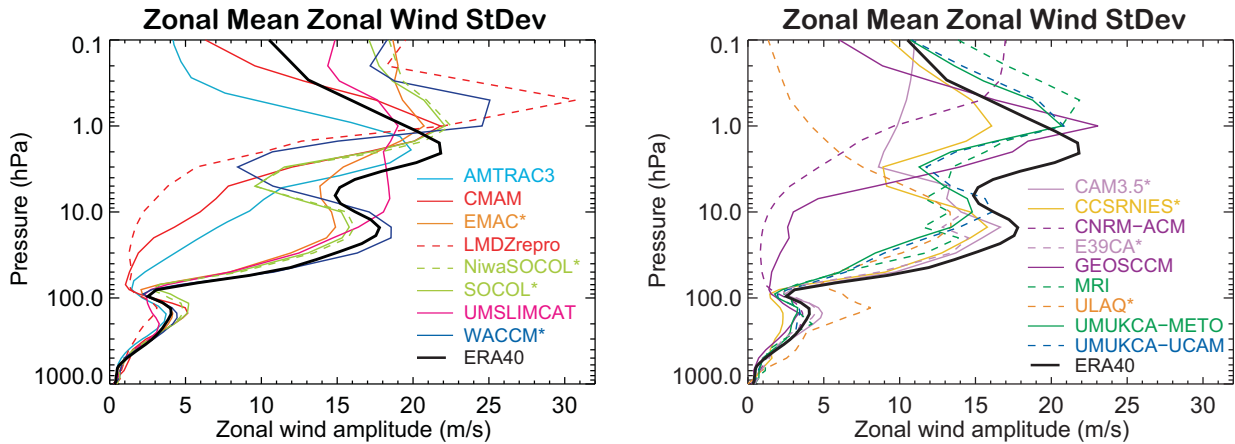


**Figure 4.21:** Profiles of the standard deviation in the de-trended zonal-mean zonal wind averaged from 10°S-10°N for the REF-B1 simulations. An asterisk after a model name indicates that that model has an externally forced (i.e., artificial) QBO.

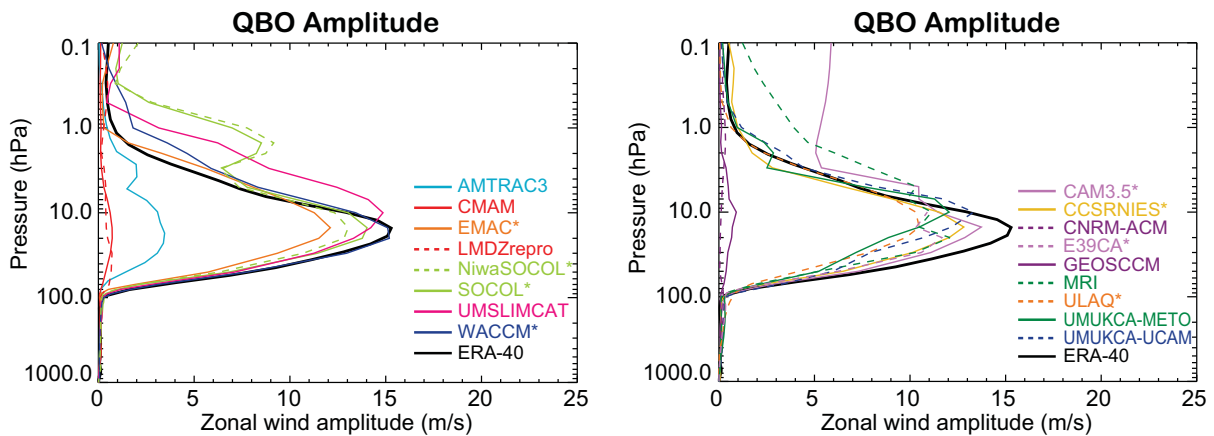


**Figure 4.22:** Profiles of the amplitude of the “QBO” (i.e., variability with periods between 2 and 5 years) in the zonal-mean zonal wind averaged between 10°S-10°N for the REF-B1 simulations. Methodology follows that of Pascoe et al., (2005). The amplitude is the ratio of the definite integral of the zonal wind power spectrum (between periods of 2 and 5 years) to the standard deviation of the zonal-mean zonal wind. The data was first detrended by removing the linear fit. An asterisk after a model name indicates that that model has an externally forced (i.e., artificial) QBO.

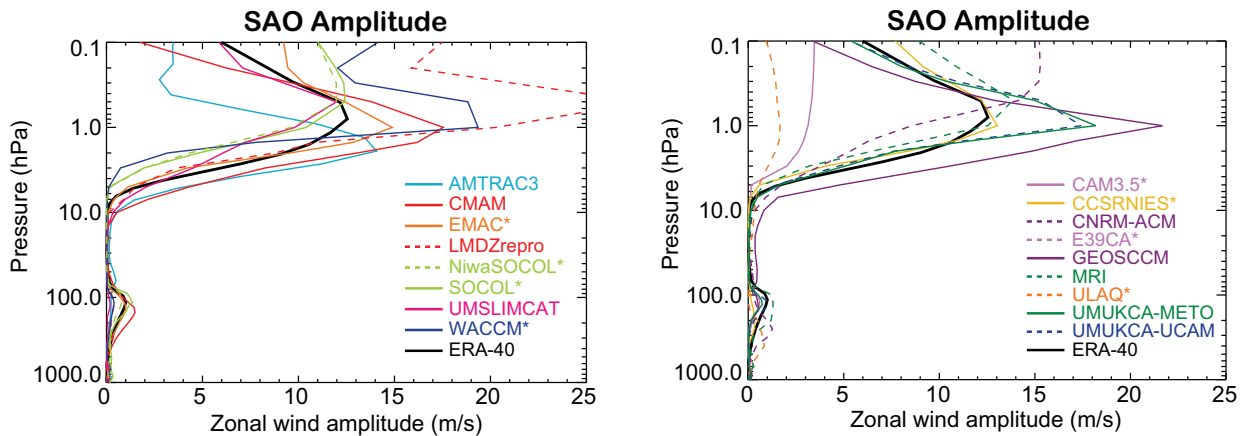


**Figure 4.23:** Profiles of the amplitude of the SAO in the zonal-mean zonal wind averaged between 10°S-10°N for the REF-B1 simulations. Method as for Figure 4.22, but including only the 6-month harmonic. An asterisk after a model name indicates that that model has an externally forced (i.e., artificial) QBO.

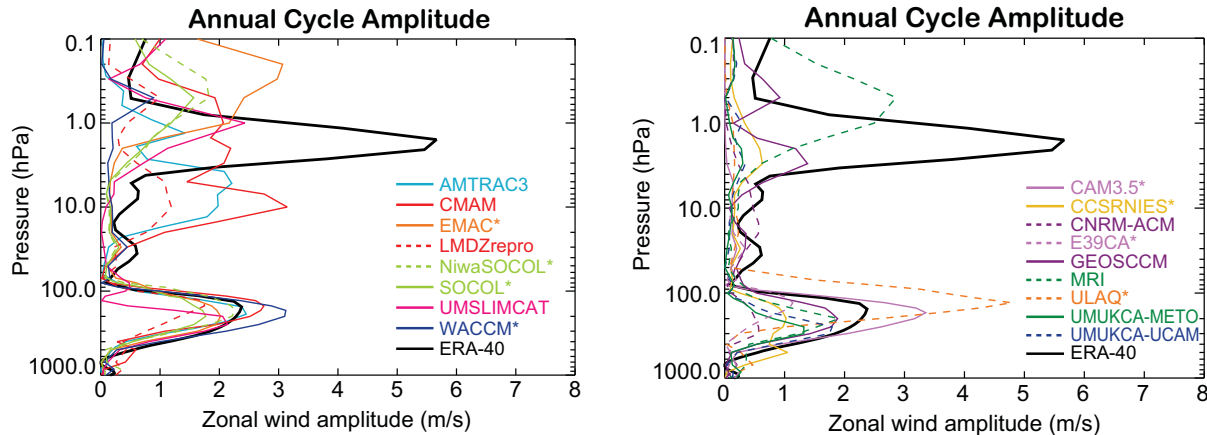


**Figure 4.24:** Profiles of the amplitude of the annual-cycle in the zonal-mean zonal wind averaged between  $10^{\circ}\text{S}$ - $10^{\circ}\text{N}$  for the REF-B1 simulations. Method as for Figure 4.22, but including only the 12-month harmonic. An asterisk after a model name indicates that that model has an externally forced (i.e., artificial) QBO.

2000 shows differences throughout the stratosphere, which are associated with a lack of a QBO in most of the REF-B2 simulations and a strengthened SAO (not shown). For those models with an internally generated QBO, only the UMUKCA-METO shows a slightly weaker QBO and SAO in the REF-B2 simulations. Neither the UMSLIMCAT nor MRI model show significant differences. As with the REF-B1 simulations, all the REF-B2 simulations exhibit a poor annual cycle in the upper stratosphere. Little systematic change or trend is seen in the magnitude of the tropical variability in the zonal wind in the stratosphere across the REF-B2 simulations. However, of the ten models compared, six showed a larger amplitude SAO from 2050-2099 compared with 2000-2049 (two smaller amplitude and two no change).

In summary, considering the large fraction of REF-B1 simulations that included nudging toward observations, there was an unexpected spread in tropical zonal wind variability. Most models under represented the amplitude of the QBO, while there was a large spread in the multi-model ensemble in the amplitude of the SAO. An excessively weak stratospheric annual cycle was common across all models. Finally, little trends were seen in the future REF-B2 simulations, although a significant fraction of the models showed an increase in the amplitude of the SAO.

#### 4.4.3 Frequency of major stratospheric sudden warmings

Sections 4.4.1. and 4.4.2 considered interannual variability in monthly and seasonal mean fields. However a novel feature of this assessment compared to most previous assessments of stratosphere resolving models is the evaluation of variability on sub-monthly time scales using daily data. This is an important advance since much of the variability of the stratospheric polar vortex occurs

on short time scales and spans the boundary between months. Moreover this intra-seasonal variability is known to contribute significantly to the interannual variability in the monthly and seasonal means. Its main manifestations are mid-winter major stratospheric sudden warmings and variability in the timing of the final warming or transition from winter to summer conditions. The simulation of these two phenomena is considered here and in Section 4.4.4, respectively.

In the extra-tropics major stratospheric sudden warmings (SSWs) play a key role in determining the mean climate and chemistry of the region. Obvious differences exist between the northern and southern winters due to the differences in the number of major SSWs. For the models and ERA-40 major SSWs are identified using the methodology of Charlton and Polvani (2007), based on reversals of the zonal-mean zonal wind at  $60^{\circ}\text{N}$  and 10 hPa, for the months November to March. **Figure 4.25** shows the mean frequency of major SSWs for both the REF-B1 and REF-B2 simulations (where results were available) compared to the frequency of major SSWs in the ERA-40 reanalysis. In contrast to a previous inter-comparison of stratosphere resolving general circulation models (Charlton *et al.*, 2007) most of the CCMs produce approximately the correct number of major SSWs over the second half of the 20<sup>th</sup> century (1960-1999). This result should not be taken to mean that models with interactive chemistry produce better dynamical variability (although a detailed investigation of this idea would be interesting), merely that this selection/generation of models appears to produce an improved simulation of major SSWs than those without interactive chemistry analysed in Charlton *et al.* (2007).

The only models with a significantly different frequency of major SSWs (at 95% confidence) when compared to the ERA-40 reanalysis are the AMTRAC3 and SOCOL and ULAQ models (which have a lower frequency of SSWs than the reanalysis) and the CMAM (which

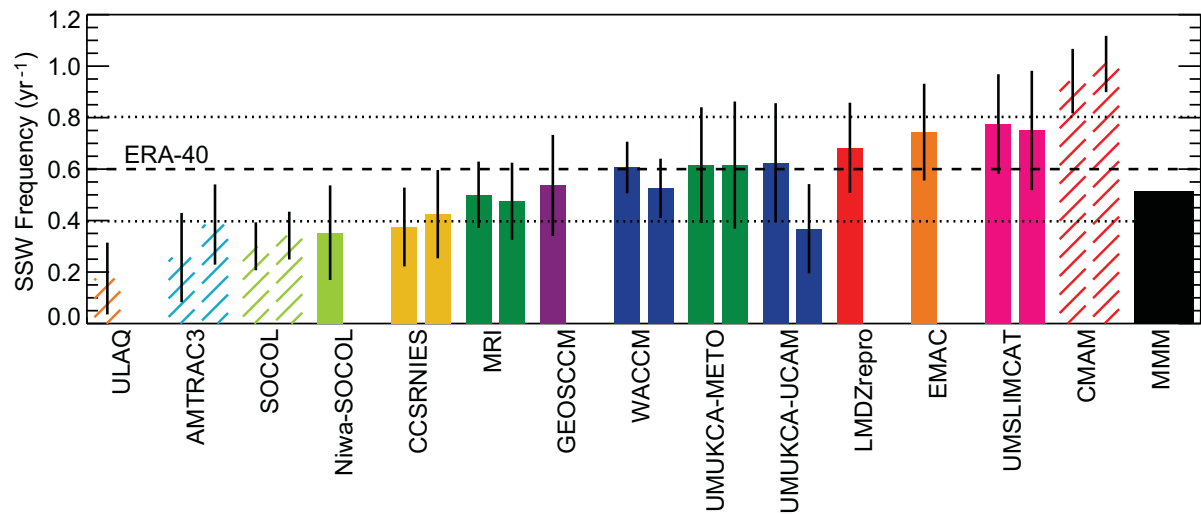


**Figure 4.25:** Mean frequency of NH major SSWs per year for the REF-B1 and REF-B2 simulations between 1960 and 2000. Dashed black line shows the mean frequency in the ERA-40 data set and 95% confidence interval (dotted lines). For each model, bars to the left of the model name indicate REF-B1 simulations and bars to the right of the model name indicate REF-B2 simulations. Where ensemble simulations are available, the mean frequency is calculated by combining all ensemble members. Bars are sorted according to major SSW frequency in the REF-B1 simulations. Where the frequency of major SSWs in the model and ERA-40 data set is significantly different at 95% confidence the bars are shown with hatched shading. Whiskers on each bar indicate a 95% confidence interval for the major SSW frequency.

has a higher frequency of SSWs than the reanalysis). The CMAM, which has a large number of major SSWs also has a mid-winter stratospheric jet with significantly reduced strength (see Figure 4.3). There is no significant difference between the REF-B1 (with prescribed sea-surface temperatures (SSTs)) and REF-B2 (with an interactive ocean) simulations of the CMAM, which suggests that coupling that model to an interactive ocean does not have a large impact on SSW variability. It should, however, also be noted that the version of the CMAM used for CCMVal-1 produced a realistic simulation of the number of major SSWs (McLandress and Shepherd, 2009).

A useful comparison of the impact of the full observed variability in SST forcing on SSW frequency can be made by comparing models which have REF-B1 and REF-B2 simulations available for the 1960-2000 period (REF-B1 simulations are run with observed SSTs while REF-B2 simulations, apart from those from the CMAM, are run with SSTs generated by atmosphere-ocean general circulation models). In Figure 4.25 models with two plotted bars show the frequency of major SSWs in the REF-B1 simulations in the left bar and in the REF-B2 simulations in the right bar. There appears to be little systematic difference between the number of major SSWs in the REF-B1 and REF-B2 simulations, except for the UМУKCA-UCAM. In all cases however, 95% confidence intervals for the SSW frequency (shown in black lines extending from the top of each bar) overlap for the REF-B1 and the REF-B2 simu-

lations, suggesting that the differences largely result from sampling variations, even in the case of the UМУKCA-UCAM. For the SH winter period between 1960 and 2000 in the REF-B1 simulations no examples of a major SSW, similar to that observed during September 2002 (Shepherd *et al.*, 2005), were found for any of the models based on the same criteria for major SSW occurrence as used for the NH.

A more detailed comparison of SSW variability in the models and the ERA-40 reanalysis can be made by plotting histograms of major SSW frequency in each month from November to March. **Figure 4.26** shows the climatology of major SSW events for the REF-B1 simulations. In general, models which produce SSWs with a frequency close to that of the reanalysis also tend to produce more realistic SSW climatologies, although there are some notable exceptions. In particular, the EMAC and LMDZrepro models tend to produce lots of dynamical variability at the start of winter and little during the mid-winter period. Further analysis of these events for the EMAC model, suggests that they occur after the initial spin-up of the vortex in mid-September, although during the period in which the vortex is still relatively weak. In several other models, noticeably the CCSRNIIES and two SOCOL models, the climatology of major SSWs is shifted toward the end of winter. This problem was noted in previous studies of SSW climatologies in models (Charlton *et al.*, 2007) and may be related to the late final warming, which occurs in some of the models

(particularly SOCOL and NiwaSOCOL).

Any significant trends in SSW frequency in the NH, could have important consequences for both ozone chemistry and the signal of climate change in the lower stratosphere. Recently, Charlton-Perez *et al.* (2008) showed that simulations of the AMTRAC predicted a small increase in major SSW frequency over the 21<sup>st</sup> century. McLandress and Shepherd (2009) also note a similar trend in the CMAM, but suggest that this trend may simply reflect the change in stratospheric climatology rather than a real increase in stratospheric variability. In general, when comparing the frequency of major SSWs in the period 1960-2000 with the frequency of major SSWs in the period 2060-2100 projected by the models, a mixed result is found. The majority of models simulate either no change in the SSW frequency or a small increase in the late 21<sup>st</sup> century. The multi-model mean projection is therefore for a slight increase in the SSW frequency in the later half of the 21<sup>st</sup> century, although the trends in heat flux (January, 100 hPa) over the 21<sup>st</sup> century show a slight decrease between 2050-2099 (see Section 4.3.4). However, it is emphasized that some caution should be exercised when considering projected trends in heat flux since the majority of models do not suggest a significant trend. In addition, the subset of models considered here is not the same as the subset used for the heat flux comparison in Section 4.3.4 due to data availability. It is also important to note that changes in the SSW frequency are likely to be strongly influenced by changes in heat flux variability rather than just by changes to the mean heat flux climatology.

#### 4.4.4 Timing of final warmings / winter-summer transition

The timing of the final warming (the date at which the winter-time polar vortex breaks down and is replaced by the summer-time stratospheric westward circulation (Andrews *et al.*, 1987)) is an important diagnostic related both to the climatological vortex breakdown shown in Figure 4.2 and the study of stratospheric variability in Section 4.4.3. Studies by Black and McDaniel (2007a, b) and Black *et al.* (2006) have shown that there is an important dynamical link between the stratosphere and troposphere as the final warming takes place and that the timing of the final warming is highly variable from year to year. In addition, there is a clear trend toward later final warming dates over the 22 years between 1979 and 2001 (Waugh *et al.*, 1999; Waugh and Rong, 2002) in the SH which is related to coupling between dynamics and ozone depletion and therefore should be captured by the CCMs.

Final warming dates in both the NH and SH are calculated using the method of Black and McDaniel (2007a, b) and 5-day low-pass filtered zonal-mean zonal wind data at 50 hPa from the models and reanalysis. This method

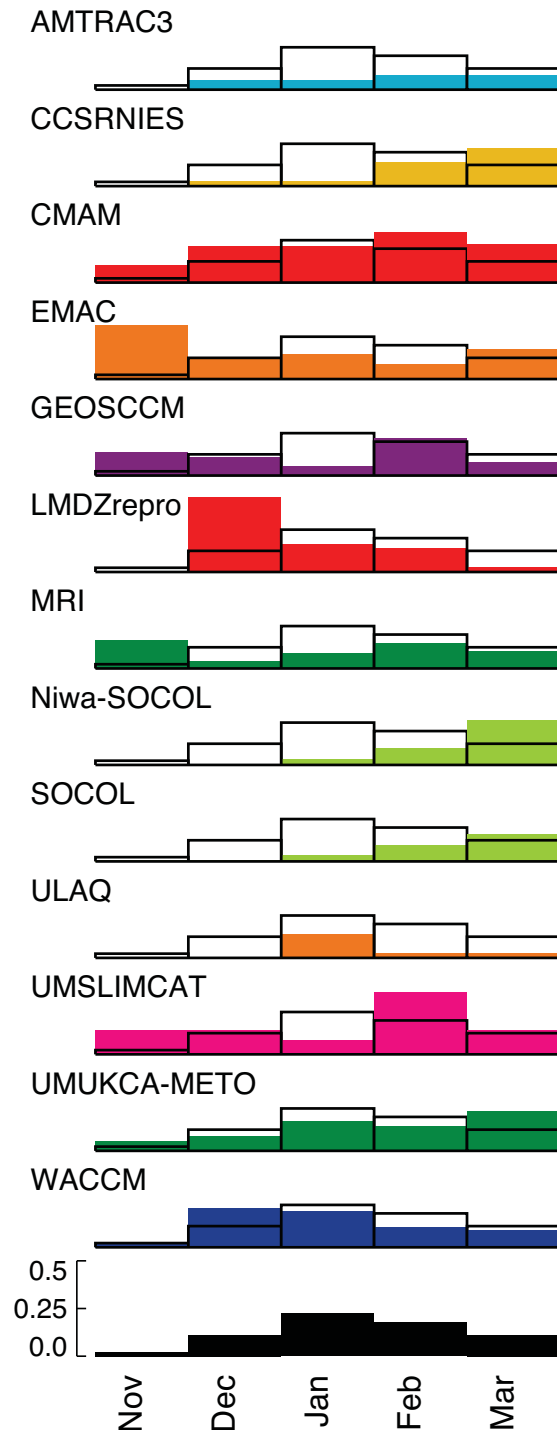


**Figure 4.26:** Histograms showing the frequency of major SSWs (in events per year) in the REF-B1 simulations (1960-2000, coloured bars) in comparison to ERA-40 reanalysis (open bars). Where an ensemble of simulations is available, the plot reflects major SSWs observed in all ensemble members. ERA-40 reanalysis climatology is reproduced at the bottom of the plot for comparison.



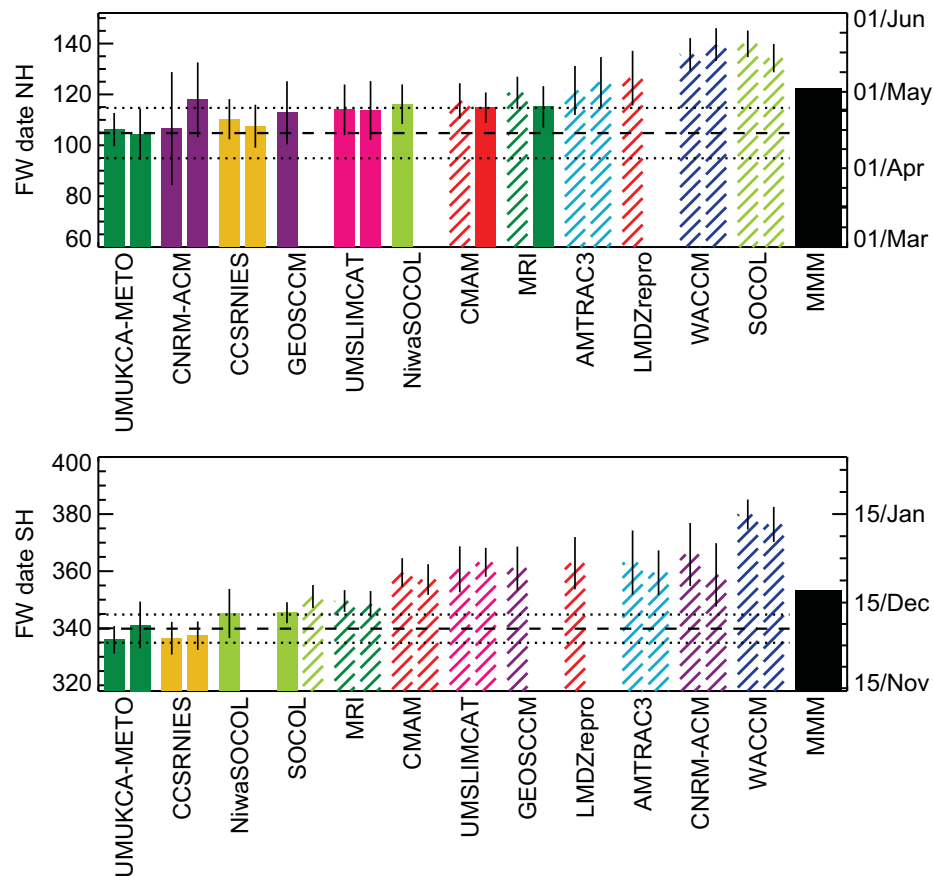


**Figure 4.27:** Mean date of the NH and SH final warmings (day number) for REF-B1 (leftmost bars for each model) and REF-B2 (rightmost bars for each model) simulations (1980-1999). Black dashed line shows the mean final warming date for the ERA-40 data with 95% confidence estimates shown in dotted lines. Models are ordered by the mean date of their final warming in the REF-B1 simulation. Where a significant difference between models and the ERA-40 reanalysis estimate is observed, the bar is plotted with a hatched shading. Where an ensemble of simulations is available, the statistic reflects the mean of all three ensemble members. Black whiskers on each bar indicate twice the standard error for each estimate. Approximate comparable calendar dates for a non-leap year are included on the right-hand axis.

defines the final warming as occurring when the zonal-mean zonal winds at a specified latitude cross a low-wind threshold (0.0 m/s in the NH and 10 m/s in the SH) and do not return to eastward values before the next winter (see Black and McDaniel (2007a, b) for further details). For some models, zonal-mean zonal winds never cross the low-wind threshold in some years, these years are ignored in the analysis. The occurrence of these years is not frequent enough in any of the models (typically of the order 1 or 2 winters in a given 20 year period) that it would impose a significant bias requiring modification of the identification technique.

**Figure 4.27** shows the mean date of the final warming for the NH and SH for the REF-B1 and REF-B2 simulations over the period (1980-1999). The black dashed line shows an estimate of the final warming date for the ERA-40 reanalysis data set for the same period. Figure 4.27

shows that models have final warming dates in both the NH and SH which are generally either at or later than the date of the final warming in the reanalysis data. This result is consistent with the diagnoses in Figure 4.2 of the descent of the mean, climatological zero-wind line. Of the models considered, in both hemispheres, more than half have mean final warming dates significantly later than those in the ERA-40 reanalysis. There are particularly large differences in the SOCOL model and the WACCM in the NH and the CNRM-ACM and the WACCM in the SH.

Trends in the date of the final warming in the SH for the three periods 1980-1999, 2000-2049 and 2050-2099 are shown in **Figure 4.28** along with the multi-model trend estimate for each period. Although there is some spread between models, the multi-model mean trend shows the expected pattern of large positive values over the recent past ( $\sim +1$  day per year, consistent with the ERA-40 estimate)

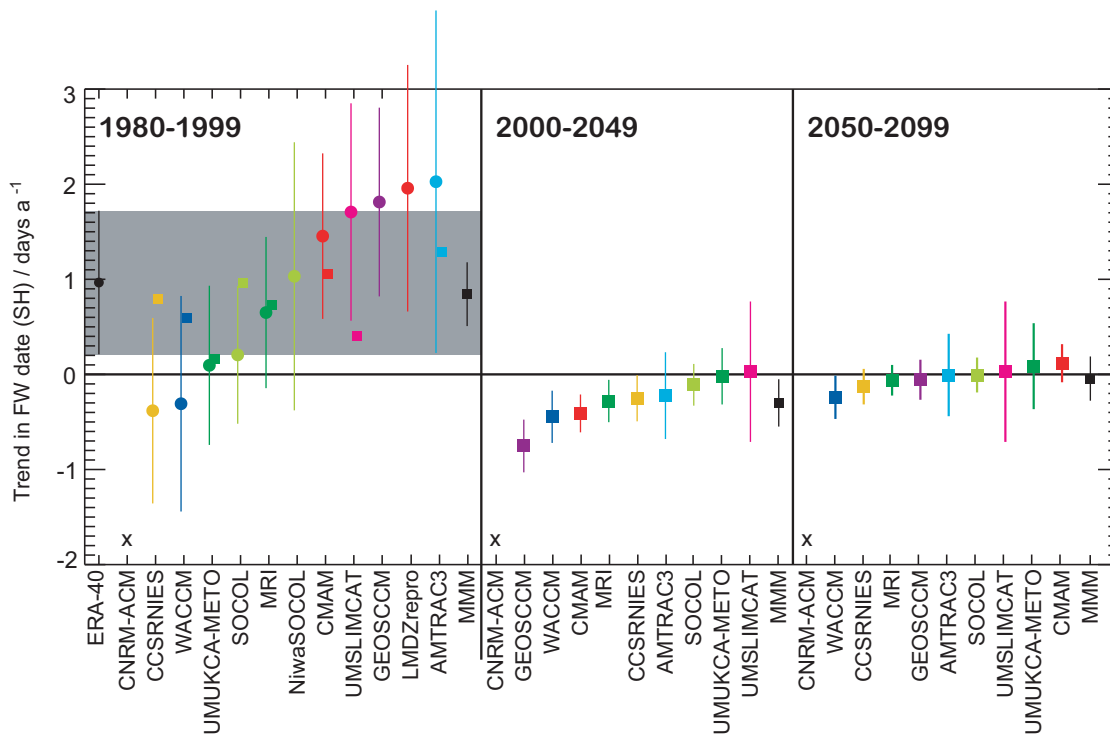


**Figure 4.28:** Linear trend in the date of the SH final warming from REF-B1 and REF-B2 simulations. Where an ensemble of simulations is available the trend is calculated for the ensemble mean final warming date in each year. Grey shading shows 95% confidence limits for the ERA-40 estimate. Whiskers on each point show respective 95% confidence limits. Left panel shows trends for the period 1980-1999, middle panel shows trends for 2000-2049 and right panel shows trends for 2050-2099. If not enough data exists to estimate a consistent trend, model is plotted with an X near to the x-axis. Models are shown in order of the trends for the REF-B1 simulations in the left panel and the REF-B2 simulations in the middle and right panels. Where both REF-B1 and REF-B2 simulations are available for the 1980-1999 period, REF-B1 trends are shown with a circle and REF-B2 trends shown with a square. Multi-model means are calculated by weighting each trend with its standard error.

and smaller negative values ( $\sim -0.3$  days per year) during the period of ozone recovery and is statistically significant at 95% confidence in both cases.

Part of the inter-model spread in the estimated final warming trend may be related to mean final warming biases over the same period. Of the models which fail to capture a strong trend in the recent past (**Figure 4.28**), two of them (SOCOL and WACCM) have very late mean final warming dates (see Figure 4.27). During the period of ozone recovery (2000-2049) there is reduced inter-model variability in the trend estimate, almost all the models show a reversed negative trend in the SH final warming date, toward earlier final warmings (Figure 4.28). These results reinforce the idea that the spring-time ozone concentration plays a large role in determining the final warming date and that the models are able to capture this coupling between chemistry and climate satisfactorily. In the following period (2050-2099), when the rate of ozone recovery is smaller in most models and the effects of changes in GHG forcing are larger, trends in the final warming date are much smaller and not statistically significant. In the NH (not shown),

during the period 1980-1999, a significant, positive multi-model trend is simulated similar to that seen in the SH, however this trend is not consistent with the corresponding, observed reanalysis trend for the same diagnostic. In the two future periods, no significant individual or multi-model trends were simulated in the NH.

## 4.5 Conclusions

### 4.5.1 Multi-model summary

In Sections 4.3 and 4.4 the reproduction by the climate-chemistry models of those stratospheric dynamical processes and phenomena that are considered important for modelling the long term evolution of stratospheric ozone and the impact of the stratosphere on climate, have been assessed by comparison with observation and/or through model inter-comparisons. The response and robustness of the response (*i.e.*, model independence) of the various

dynamical processes and phenomena to climate and long-term ozone changes was also noted (see Section 4.4.4).

For the mean climate there was generally good agreement among the majority of the models both in their strengths and weaknesses when evaluated against the reanalysis data sets. Overall the models reproduce the extra-tropical temperature and zonal-mean climatology very well with the notable exception of some key phenomena. Common problems for many of the models were a SH polar night jet that is too strong, lacks the observed equatorward tilt with height, and that persists too long into spring before changing to the summer-time westward circulation. Concomitantly, many models had a cold bias in the Antarctic lower stratosphere in spring. These problems in the SH are almost certainly inter-related and existed in earlier versions of many of the models (*e.g.*, Eyring *et al.*, 2006). On the other hand the causes of the weaknesses are not well understood. Possibly they are related to a deficiency in the wave driving from the troposphere though, in both hemispheres the climatological upward flux of resolved wave activity entering the stratosphere in mid-winter was remarkably well reproduced in nearly all the models. Moreover, most models displayed, more or less, the correct temperature response to variations in this wave flux. Again the majority of models accurately reproduce the strength of the Brewer-Dobson circulation, or at least the tropical upwelling mass flux at 70 hPa, though there was considerable uncertainty across the models as regards the contribution of the different wave drags (*i.e.*, EP-flux divergence and parameterised orographic and non-orographic gravity wave drag) driving the upwelling. The models also showed, on average, less inter-hemispheric asymmetry than is observed in both the wave driving and also the stationary waves.

Variability in the stratosphere on all time scales from the intra-seasonal to interannual was, in general, less well reproduced by the models, with a large inter-model spread for some diagnostics. Most obviously, many models place the transition between winter and spring conditions significantly later than observed. This deficiency is seen in both hemispheres and in diagnostics of the mean climate (see above) and individual final warming dates. In the northern winter, although most models accurately simulate the frequency of major stratospheric sudden warmings, the climatology of these key events is poorly simulated with the worst performing models producing only early and late winter warmings. Nonetheless in mid-winter in both hemispheres the polar night jet has the correct modes (EOFs) of variability in the lower stratosphere in all the models. However, in agreement with the other diagnostics, there is considerable inter-model spread in the amount of variability in the strength of the polar night jet (the first EOF of the zonal-mean zonal wind).

In the tropics, there remains a large divergence between model design and/or experimental setup and the sub-

sequent ability to simulate tropical variability, particularly the QBO. Models can be split into three groups: those that have very little or no stratospheric variability, those that impose an artificial QBO and therefore can not be considered as free running climate-chemistry models, and those with an internally generated QBO. Even with a QBO (artificial or not), the variability in the models is less than observed. An assessment of the impact of these modelling choices on the extra-tropical stratospheric variability or the variability of ozone is presented in Chapter 8.

An implicit assumption of the above assessment is that any dynamical biases in the models are the result of a poor representation of dynamical processes in the models. However, because the models considered are coupled climate-chemistry models, errors in the simulated radiatively active gases and, in particular, ozone can lead to an apparent error in the dynamical fields when evaluated against observations where no dynamical bias in the model exists. The representation of other dynamical process in the models such as the QBO may also be quite sensitive to details of the simulated ozone (*e.g.*, Bushell *et al.*, 2010), even if this lies within the observational errors. In general however, it is thought that any errors in ozone are unlikely to affect the overall conclusions of this chapter apart from over Antarctica where there is rapid ozone change and significant model spread in ozone behaviour (see Chapter 9). Because the Antarctic ozone change projects strongly on to the Southern Annular Mode (SAM), uncertainties in the simulated ozone can lead to uncertainties in the representation and behaviour of the SAM in the models. Quantitative uncertainties in the projected long-term trends of ozone (Chapter 9) will also introduce quantitative uncertainties in the long-term trends in some of the dynamical fields and processes reported in this chapter.

#### 4.5.2 Summary by model

In this section, a summary of the performance of each model in the range of dynamical processes assessed in the chapter is provided. This summary and, in particular, the overall assessment at the end of each paragraph is subjective and thereby gives a more complete picture of the overall dynamical performance of each model than can be obtained from a limited number of metrics. In the next section this subjective assessment is complemented by a quantitative summary of several key processes in terms of appropriately chosen metrics.

The **AMTRAC3** simulates the stratospheric mean temperatures in winter and spring well in both hemispheres, but the strength of its mid-winter jet is significantly stronger than the reanalysis climatology in both hemispheres, and the model is an outlier in the multi-model ensemble in the NH. The mean meridional circulation was not assessed.

Stratospheric variability in the AMTRAC3 is somewhat weaker than observed, particularly in terms of the number of major SSWs and is consistent with its stronger than average winter jet in the NH. The final warming is significantly late in both hemispheres. In the tropics the AMTRAC3 exhibits weak, internally generated variability in the QBO region but simulates well the variability in the SAO region. Overall, the AMTRAC3 simulates stratospheric dynamics adequately, but has some dynamical biases particularly in the SH.

The **CAM3.5** provided only limited diagnostics. In the diagnostics produced, the CAM3.5 has significant biases in its mean state close to the upper boundary at 3.5 hPa, particularly in the NH. The mean meridional circulation is adequately simulated. In the tropics the model imposes a QBO *via* external forcing.

The **CCSRNIES** model has significant large biases in its mean state during winter and spring in both hemispheres. In general, the stratospheric vortex in this model is too strong and has very low temperatures at its core. The CCSRNIES model produces an accurate simulation of the mean meridional circulation. Stratospheric variability in the NH is slightly weaker than the multi-model mean which may be related to the relatively weak meridional heat flux climatology at 100 hPa in the model. In the tropics the model imposes a QBO *via* external forcing. Overall, the CCSRNIES model has an adequate representation of stratospheric dynamics.

The **CMAM** suffers from significant biases in its mean state of opposite sign in the two hemispheres. In the NH, the mid-winter polar vortex is too weak above 30 hPa and is too dynamically active. In the SH, the mid-winter polar vortex is too strong, and breaks up too late in the spring season. The mean meridional circulation is consistent with that derived from meteorological analyses. In the tropics, the CMAM does not simulate a QBO, but has an SAO of large amplitude. Overall, the CMAM has a mixed dynamical performance, and is sometimes an outlier in the multi-model distribution.

The **CNRM-ACM** produces a stratospheric mean state with significant biases in temperature and jet strength and position. It has particularly large biases in the NH, positioning its mean jet too far equator-ward. The meridional circulation has generally the correct strength but has an unusual structure, with downwelling seen at the equator, and a seasonal cycle with a minimum in MAM as opposed to JJA. Only a limited assessment of stratospheric variability was possible, but significant problems, including a lack of 100 hPa heat flux during the NH mid-winter and a late break-up of the vortex in the SH were identified. In the

tropics, the CNRM-ACM does not simulate a QBO, but has an SAO of large amplitude. Overall, the CNRM-ACM has significant dynamical problems, particularly in the SH and is frequently an outlier from the multi-model mean.

The **E39CA** model provided only limited diagnostics. In the diagnostics produced, the E39CA model has a large cold bias in its mean state in the middle stratosphere of both the NH and SH near the rather low model top (~10 hPa) and large biases in the spring SH lower stratosphere. Linked to these biases, the model has very strong jets during both NH and SH winters. The mean meridional circulation is weaker than the multi-model mean and that derived from analysis data and exhibits mean downwelling at the equator. Limited diagnosis of stratospheric variability in the extra-tropics was carried out. In the tropics the model imposes a QBO through external forcing, although the model has a top boundary at 10 hPa. Overall, the E39CA model has significant dynamical biases in both hemispheres and is a particular outlier in the multi-model ensemble in the middle stratosphere, especially near the model top.

The **EMAC** model simulates the stratospheric mean state in winter and autumn well in both hemispheres, despite relatively small values of 100 hPa heat flux in the NH mid-winter and large values of 100 hPa heat flux in the SH mid-winter. In the SH, the EMAC model exhibits a stronger relationship between heat flux and spring polar temperatures than most models or observations, and a very cold bias for undisturbed vortex conditions. This suggests compensating errors help to produce its accurate SH mean state. The EMAC model simulates stratospheric variability well, although with too much dynamical variability in November in the NH. In the tropics the model imposes a QBO through external forcing. Overall, the EMAC model has an adequate representation of stratospheric dynamics.

The **GEOSCCM** simulates the stratospheric mean state in winter and autumn well in both hemispheres. Its meridional circulation in the middle stratosphere is somewhat weaker than the circulation estimated from observations. Stratospheric variability in the GEOSCCM is generally well simulated, although it does exhibit a late SH vortex break up. In the tropics, the model does not produce a QBO but has a large amount of variability in the SAO region. Overall, the GEOSCCM simulates stratospheric dynamics well, with better performance than the multi-model mean in most diagnostics.

The **LMDZrepro** model simulates the stratospheric jet strength in NH mid-winter well, but has significant warm biases in winter and spring in the upper stratosphere and in winter in the lower stratosphere. In the SH, the LMDZrepro model has similar warm biases in winter and spring above

5 hPa and a strong bias in jet strength above and at 10 hPa. The mean meridional circulation was not assessed. Mid-winter variability in the stratosphere is well simulated, but vortex break-up in both hemispheres is too late. In the tropics, no QBO is simulated but the SAO region has a large amount of variability. Overall, the LMDZrepro model produces an adequate representation of stratospheric dynamics.

The **MRI** model simulates the stratospheric mean state in winter and spring well in the middle and upper stratosphere but has a significant cold bias in the lower stratosphere (below 50 hPa) in all seasons. The structure of the mean meridional circulation is well represented in the MRI model, although it is one of the strongest in the multi-model ensemble. Stratospheric variability is also well simulated by the model but the final warming is slightly too late in both hemispheres. In the tropics, the model has an internally generated QBO with an amplitude comparable to the observations and has a large amount of variability in the SAO region. Overall, the MRI model simulates stratospheric dynamics well with better than or similar performance to the multi-model mean in most diagnostics.

**SOCOL** and **NiwaSOCOL** simulations are considered together, since they use versions of the same model. However, in several diagnostics there are considerable differences between simulations by the two model versions. An important point to note here is that many of the SOCOL diagnostics are based on the mean performance of a three member ensemble, whereas for NiwaSOCOL there was only one realization, which may explain some of the discrepancy. The SOCOL models simulate the stratospheric mean state in winter and spring well in both hemispheres although they both have significant biases in the SH lower stratosphere in spring. Tropical upwelling in the SOCOL model shows a maximum on the equator, and the annual cycle of the mean meridional circulation is also qualitatively wrong. The NiwaSOCOL model does little better, and shows the strongest circulation in the multi-model ensemble. Stratospheric variability in the model is weak, perhaps linked to the small amounts of heat flux at 100 hPa and to the late final warming in the NH. In the SH the relationship between heat flux and lower stratospheric temperatures is well simulated. In the NH, the final warming simulated by the SOCOL model is significantly later than that observed. In the tropics, the model imposes a QBO through external forcing. Overall, the SOCOL model has a moderate representation of stratospheric dynamics with notable shortcomings.

The **ULAQ** model has significant biases both in the position and strength of the stratospheric jet in the SH and is a large outlier in the multi-model ensemble. Its meridional

circulation is too weak and exhibits an incorrect seasonal cycle. Stratospheric variability is generally too weak. In the tropics, the model imposes a QBO through external forcing. Overall, the ULAQ model has limited success in simulating stratospheric dynamics and is an outlier in the multi-model ensemble for some diagnostics.

The **UMSLIMCAT** simulates the stratospheric mean state in winter and spring well in the NH but has a slight strong bias in the strength of the winter jet in the upper stratosphere of the SH. It also has a large cold bias in the middle stratosphere in SH spring. The mean meridional circulation was not assessed. The model produces a good simulation of stratospheric variability, although its final warming in the SH is significantly too late. In the tropics, the model internally generates a good simulation of the QBO and SAO. Overall, the UMSLIMCAT simulates stratospheric dynamics well, with better performance than the multi-model mean in most diagnostics.

The **UMUKCA-METO** and **UMUKCA-UCAM** have the same dynamical core. Although the two models only had small differences in the experimental setup there are considerable differences between the simulations for several of the diagnostics. In general, however, the UMUKCA models simulate the stratospheric mean state in winter and spring well in both hemispheres, apart from a large warm-bias near 100 hPa in the SH spring. The mean meridional circulation is well simulated by the models, although weaker than the multi-model mean. Unlike the other models, parameterised orographic gravity wave drag does not contribute significantly to driving the meridional circulation. Stratospheric variability is well simulated by the model in all diagnostics. In the tropics, the model internally generates a good simulation of the QBO and SAO. Overall, the UMUKCA models simulate stratospheric dynamics well, with better performance than the multi-model mean in most diagnostics.

The **WACCM** simulates the stratospheric mean state well in the NH but has a very large cold bias throughout much of the stratosphere in the SH spring and a very strong stratospheric jet in the SH in winter. This cold bias is linked to a very late break-down of the vortex in both the climatological annual cycle and final warming diagnostics, causing the model to be a significant outlier in the multi-model ensemble. The model has a good simulation of the mean meridional circulation. Stratospheric variability in the NH is well simulated by the model. In the tropics, the model imposes a QBO through external forcing. Overall, the WACCM simulates a great deal of stratospheric dynamics well but has a significant problem in simulating the SH vortex break-down.

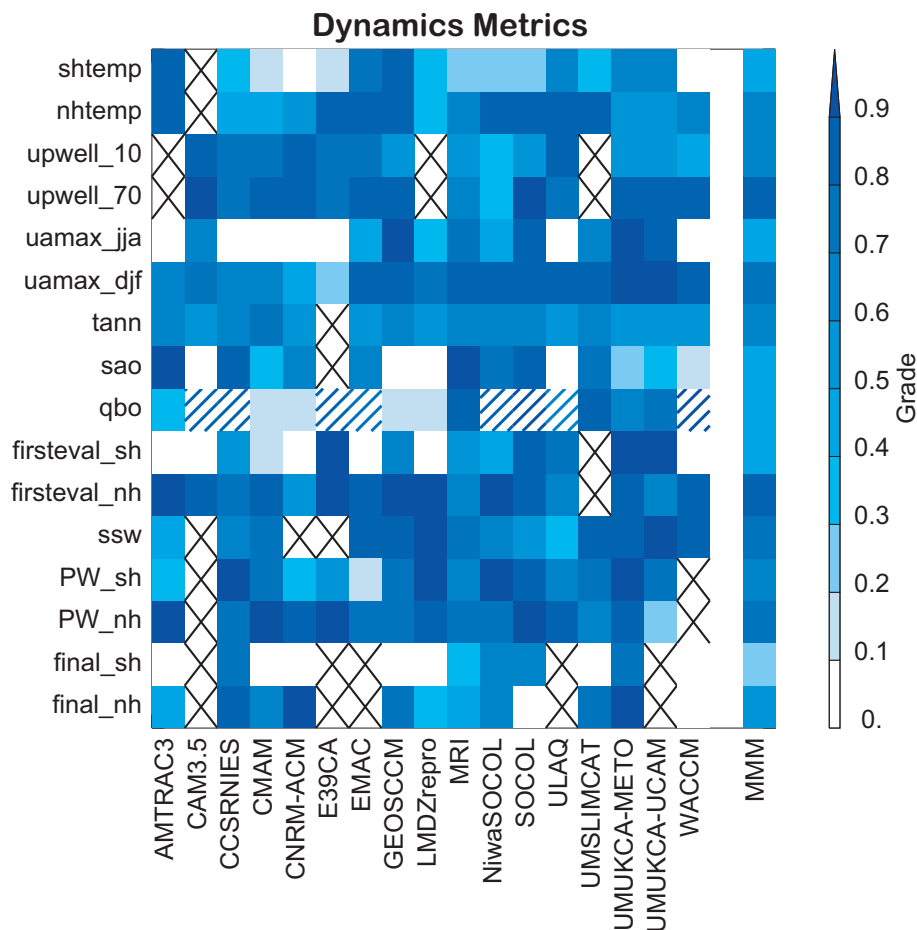


**Figure 4.29:** Matrix showing the performance of the model ensemble in a variety of metrics described in Table 4.1a, b after Waugh and Eyring (2008). See text for details of the matrix calculation. Each pixel represents the performance of a model in a given metric, darker colours indicate better performance. Crosses in a pixel indicate the metric was not evaluated for that model. On the right of the diagram the average metric score for each diagnostic is shown. Hatching in the QBO metric indicates the model uses a relaxation scheme to produce QBO variability, models with a relaxation scheme are not included in the calculation of the mean metric.

**4.5.3 Quantitative assessment / metrics**

To establish the fidelity and quantify the assessment of the simulation of stratospheric dynamics by the models, “metrics” representing most of the dynamical diagnostics analysed in Sections 4.3 and 4.4 have been identified. The full list of metrics is presented in Tables 4.1a and b. The list has some metrics in common with the study of Waugh and Eyring (2008), but also extends that list, particularly in the area of stratospheric variability.

This list captures the main dynamical processes in the stratosphere. A pragmatic approach has, however, been used and for many diagnostics the metric opted for requires the least input of dynamical fields or complex analysis. There are a number of cases where diagnostics might be replaced with more dynamically meaningful alternatives if more data from more model runs were available. For example, the diagnostics “shtemp” and “nhtemp” might be

replaced by the area of temperatures below PSC formation thresholds. Metrics are calculated as listed in the table and normalised using Equation 4 of Waugh and Eyring (2008). In order to maintain some consistency with the Waugh and Eyring analysis, scores are standardized using the standard deviation of the observed quantity in question. For the tropical variability, estimating the uncertainty in the ERA-40 reanalysis is more complex. To estimate the uncertainty, the data set was re-sampled for several 10-year periods, and the range of possible values for the amplitudes of the annual cycle, SAO and QBO was used in the metric calculation. An attempt is also made to assess where a model’s performance (as assessed by the metric) is different from the observations and different from the multi-model mean.

**Figure 4.29** shows the metric portrait of the models. For each model, every metric is assigned a box on the diagram, and the box is shaded according to model performance. Darker colours indicate that a metric is closer to 1,

*i.e.*, a very good performance in that metric. Black crosses indicate that insufficient data was available to calculate the metric for that model. On the right of the diagram, mean metrics across the multi-model ensemble are calculated for each metric. For the QBO metrics, models which relaxed the tropical winds to the observed QBO are shown hatched. The calculation of the mean metric for the QBO does not include those models with tropical wind relaxation.

As well as impacting on the QBO metric (“qbo”), constraining the winds in the tropics towards observations in some models is likely to impact on many of the other processes and phenomena considered in this chapter and, indeed, other chapters too (*e.g.*, Chapter 8). With the data and simulations available it was not possible to quantify what effect this would then have on the other metrics though there is the possibility that prescribing the QBO in a model will artificially enhance the score for some of these metrics. Consequently there is a risk that the confidence that is placed in the future projections made with these models will also be overestimated since the observational constraints can not be included in simulations for the future, for obvious reasons.

A broad conclusion which can be drawn from the metric portrait is that all models have deficient performance in some metrics. No model produces an excellent simulation of stratospheric dynamics in all metrics. However, it is also clear that both the performance of the multi-model ensemble in some metrics is better than in others and that the overall performance of some models in these metrics is better than others (note that some caution should be exercised here since some of the differences between metrics can arise from the different diagnostics used to produce them). Particularly poor performance is seen across models in metrics for the SH temperature bias, the tropical annual cycle and diagnostics of the final warming date in both the NH and SH. One obvious point to note is the difference in model performance in the NH and SH. In general, metrics for the SH circulation (shtemp, ummax\_jja, firstevl\_sh, PW\_sh and final\_sh — see Tables 4.1a and b for a description of the metrics) have lower values and more outliers than those for the NH circulation. In general, metrics of tropical variability highlight the significant difference in performance related to the different choices for model design described in Section 4.3.2 (see also Chapter 2). Improvement of the simulation of tropical dynamics, particularly the QBO, remains a pressing need for the models.

A more detailed examination of the performance of the models in terms of the metrics in Tables 4.1a and b clearly indicates that, when considering the multi-model ensemble performance as a whole, the assessment of poor metric performance can be further refined. For some metrics in which model performance is generally poor, model biases tend to have the same sign indicating a systematic difference between the models and the observations.

For the metrics considered here,

- metrics with a systematic negative bias are those for the SH temperature, tropical annual cycle and the QBO (excluding models with a nudged QBO, although some caution is necessary for the tropical diagnostics),
- metrics with a systematic positive bias are those for upwelling at 10 hPa, the final warming date in the NH, the final warming date in the SH, the amplitude of the first EOF in the SH and the slope of the fit between lower stratospheric heat flux and lower stratospheric temperature in the NH.

For other metrics, there are large numbers of models with significant biases, but these tend to be evenly distributed between positive and negative signs and hence while indicating poor performance for individual models, they do not indicate systematic biases amongst the multi-model ensemble.

Additionally, it is also possible to examine the statistical distribution of models within individual metrics to determine those models which perform significantly differently from the multi-model mean. In general, this tends to indicate particularly poor performance of a model for that metric (although this conclusion assumes that the multi-model mean performance is good). There are some models which are outliers in significantly more diagnostics than others, *e.g.*, ULAQ (5; 35% of the model’s submitted metrics), CAM3.5 (3; 33%), CNRM-ACM (5; 33%).

One concern about the assignment of metrics, also noted by Waugh and Eyring (2008), is that they may not be independent measures of dynamical performance. Following Waugh and Eyring (2008), the correlation between metrics was examined as a simple measure of this non-independence. Of the 120 possible correlations between the 16 metrics considered, only 7 had correlations above 0.5, suggesting that there is not a large degree of dependence between these metrics. The highest correlation between metrics was 0.7, between metrics for the amplitude of the first EOF in the SH and the final warming date in the SH. The amplitude of the first EOF in the SH also had large correlations with several other metrics, including the slope of the fit between lower stratospheric heat flux and lower stratospheric temperature in the SH and strength of the winter jet in the SH.

Due to the large diversity in the formulation of the models (see Chapter 2) it is difficult to systematically assess what role resolution by itself plays in the qualitative and quantitative performance of the models. Nonetheless, a brief subjective assessment of the results presented in the chapter suggests that no systematic improvement in the ability to represent the stratospheric dynamical processes and/or phenomena was obtained with finer horizontal or vertical resolution, or the position of the model top.

However, it is clear that some of the models with very coarse horizontal resolution, or a rather low upper boundary in the middle stratosphere, have worse performance than the multi-model average. For models with upper boundaries above the stratopause and horizontal resolution greater than a moderate threshold (which might tentatively be set at  $4^\circ$  or a spectral truncation at T30) there is no obvious link between increased model resolution and dynamical performance in stratosphere. This suggests that beyond this threshold, the suitability of other model components dominates model performance, though some of these other components, such as tropospheric dynamics or tracer transport, are highly likely to be resolution dependent.

#### 4.5.4 Future projections

For many of the dynamical quantities and processes assessed in this chapter, past and future trends were calculated for the periods 1980-1999, 2000-2049 and 2050-2099. Using these three periods gave some indication of the different roles of ozone depletion/recovery and GHG induced climate change on the long-term secular changes in stratospheric dynamics. In general, and as expected, the signal of ozone depletion/recovery on the trends in dynamical quantities is broadly stronger in the SH than in the NH, particularly over the Antarctic. This is reflected both in the strength and significance of the trends in individual models and in the consistency of the trends across the multi-model ensemble. Particularly strong trends in the periods 1980-1999 and 2000-2049 were found in diagnostics of stratospheric polar temperatures, and final warming dates. In both these cases, opposite trends were found in the ozone depletion and recovery periods. Strong positive trends in Antarctic accumulated PSC area diagnostics were found during the 1980-1999 and 2050-2099 periods, consistent with the above trends in temperature, but trends during the 2000-2049 period were small, consistent with the changing influence of ozone concentrations on lower stratospheric temperatures. In the NH both past and predicted trends become more uncertain as the region of interest becomes smaller or the diagnostic more complex. Nonetheless, in the lower and middle Arctic stratosphere the models, on average, projected no significant long-term change to the mean winter-time temperature in contrast to the predicted annual global mean cooling at these levels shown in the previous chapter.

It is also clear that there is a strong consensus amongst the models that the strength of the Brewer-Dobson circulation is simulated to have increased over the recent past and will continue to increase in strength by about 2% per decade over the 21<sup>st</sup> century. However, there is little consensus amongst the models about the contribution of different types of tropospheric wave-forcing toward this trend. Similarly there was no significant multi-model trend

in the extra-tropical mid-winter meridional heat flux at 100 hPa or in the amplitude of the stationary wave field in the upper troposphere. In contrast, a recent analysis of a few observations from the NH mid-latitude lower stratosphere ( $32\text{--}51^\circ\text{N}$  and 24-35 km) shows a weak increase in estimates of the age-of-air (Engel *et al.*, 2009) implying a deceleration of the Brewer-Dobson circulation, though the large uncertainties in this observational trend estimate mean it is not inconsistent with the model trends (Engel *et al.*, 2009). Differences between the Engel *et al.* (2009) results and the models are considered in more detail in the following chapter.

### Acknowledgements

The chapter authors thank John Austin, Mark Baldwin, Natalia Calvo, Ed Gerber, Gloria Manney, Elisa Manzini, Katja Matthes, Charles McLandress, Jessica Neu, Dieter Peters, Adam Scaife, John Scinocca, Ted Shepherd, and Susan Strahan for helpful discussions.

Also rather helpful were the written reviews from Martin Dameris, Marv Geller, Nathan Gillett, Peter Haynes, John Thuburn, nine anonymous reviewers and various model PIs.

Bill Randel/Paul Newman and Fei Wu very kindly provided Transformed Eulerian Mean diagnostics derived from ERA-40 data.

### References

- Andrews, A. G., J. R. Holton, and C. B. Leovy, 1987. *Middle Atmosphere Dynamics*, Academic, 489pp.
- Austin, J., and F. Li, 2006. On the relationship between the strength of the Brewer-Dobson circulation and the age of stratospheric air, *Geophys. Res. Lett.*, **33**, doi:10.1029/2006GL026867.
- Austin, J., and R. J. Wilson, 2009. Polar ozone: sensitivity to sea surface temperature and bromine amounts, *J. Geophys. Res.*, submitted.
- Austin, J., D. Shindell, S. R. Beagley, C. Brühl, M. Dameris, E. Manzini, T. Nagashima, P. Newman, S. Pawson, G. Pitari, E. Rozanov, C. Schnadt, and T. G. Shepherd, 2003. Uncertainties and assessments of chemistry-climate models of the stratosphere, *Atmos. Chem. Phys.*, **3**, 1-27.
- Black, R. X., and B. A. McDaniel, 2009. Submonthly polar vortex variability and stratosphere-troposphere coupling in the Arctic, *J. Clim.*, **22**, 5886-5901.
- Black, R. X., and B. A. McDaniel, 2007a. The dynamics



- of Northern Hemisphere stratospheric final warming events, *J. Atmos. Sci.*, **64**, 2932-2946.
- Black, R. X., and B. A. McDaniel, 2007b. Interannual variability in the Southern Hemisphere circulation organized by stratospheric final warming events, *J. Atmos. Sci.*, **64**, 2968-2974.
- Black, R. X., B. A. McDaniel, and W. A. Robinson, 2006. Stratosphere-troposphere coupling during spring onset, *J. Clim.*, **19**, 4891-4901.
- Bushell, A. C., N. Butchart, S. C. Hardiman, T. J. Hinton, D. R. Jackson, S. M. Osprey, and L. J. Gray, 2010. Sensitivity of GCM tropical middle atmosphere variability and climate to ozone and parameterized gravity wave drag changes, *J. Geophys. Res.*, accepted subject to revision.
- Butchart, N., and A. A. Scaife, 2001. Removal of chlorofluorocarbons by increased mass exchange between the stratosphere and troposphere in a changing climate, *Nature*, **410**, 799-802.
- Butchart, N., A. A. Scaife, M. Bourqui, J. de Grandpré, S. H. E. Hare, J. Kettleborough, U. Langematz, E. Manzini, F. Sassi, K. Shibata, D. Shindell, and M. Simmond, 2006. Simulations of anthropogenic change in the strength of the Brewer-Dobson circulation. *Climate Dyn.*, **27**, 727-741.
- Butchart, N., I. Cionni, V. Eyring, T. G. Shepherd, D. W. Waugh, H. Akiyoshi, J. Austin, C. Brühl, M. P. Chipperfield, E. Cordero, M. Dameris, R. Deckert, S. Dhomse, S. M. Frith, R. R. Garcia, A. Gettelman, M. A. Giorgetta, D. E. Kinnison, F. Li, E. Mancini, C. McLandress, S. Pawson, G. Pitari, D. A. Plummer, E. Rozanov, F. Sassi, J. F. Scinocca, K. Shibata, B. Steil, and W. Tian, 2010. Chemistry-climate model simulations of the 21st century stratospheric climate and circulation changes, *J. Clim.*, accepted.
- Charlton, A. J., and L. M. Polvani, 2007. A new look at stratospheric sudden warmings. Part I. Climatology and modelling benchmarks, *J. Clim.*, **20**, 449-469.
- Charlton, A. J., L. M. Polvani, J. Perlwitz, F. Sassi, E. Manzini, K. Shibata, S. Pawson, J. E. Nielsen, and D. Rind, 2007. A new look at stratospheric sudden warmings. Part II. Evaluation of numerical model simulations, *J. Clim.*, **20**, 470-488.
- Charlton-Perez, A. J., L. M. Polvani, J. Austin, and F. Li, 2008. The frequency and dynamics of stratospheric sudden warmings in the 21st century, *J. Geophys. Res.*, **113**, doi:10.1029/2007JD009571.
- Crook, J. A., N. P. Gillett, and S. P. E. Keeley, 2008. Sensitivity of Southern Hemisphere climate to zonal asymmetry in ozone, *Geophys. Res. Lett.*, **35**, doi:10.1029/2007GL032698.
- Engel, A. T. Möbius, H. Bönisch, U. Schmidt, R. Heinz, I. Levin, E. Atlas, S. Aoki, T. Nakazawa, S. Sugawara, F. Moore, D. Hurst, J. Elkins, S. Schauffler, A. Andrews, and K. Boering, 2009. Age of stratospheric air unchanged within uncertainties over the past 30 years, *Nature Geosci.*, **2**, 28-31.
- Eyring, V., N. Butchart, D. W. Waugh, H. Akiyoshi, J. Austin, S. Bekki, G. E. Bodeker, B. A. Boville, C. Brühl, M. P. Chipperfield, E. Cordero, M. Dameris, M. Deushi, V. E. Fioletov, S. M. Frith, R. R. Garcia, A. Gettelman, M. A. Giorgetta, V. Grewe, L. Jourdain, D. E. Kinnison, E. Mancini, E. Manzini, M. Marchand, D. R. Marsh, T. Nagashima, P. A. Newman, J. E. Nielsen, S. Pawson, G. Pitari, D. A. Plummer, E. Rozanov, M. Schraner, T. G. Shepherd, K. Shibata, R. S. Stolarski, H. Struthers, W. Tian, and M. Yoshiki, 2006. Assessment of temperature, trace species, and ozone in chemistry-climate model simulations of the recent past, *J. Geophys. Res.*, **111**, doi:10.1029/2006JD007327.
- Eyring, V., D. W. Waugh, G. E. Bodeker, E. Cordero, H. Akiyoshi, J. Austin, S. R. Beagley, B. A. Boville, P. Braesicke, C. Brühl, N. Butchart, M. P. Chipperfield, M. Dameris, R. Deckert, M. Deushi, S. M. Frith, R. R. Garcia, A. Gettelman, M. A. Giorgetta, D. E. Kinnison, E. Mancini, E. Manzini, D. R. Marsh, S. Matthes, T. Nagashima, P. A. Newman, J. E. Nielsen, S. Pawson, G. Pitari, D. A. Plummer, E. Rozanov, M. Schraner, J. F. Scinocca, K. Semeniuk, T. G. Shepherd, K. Shibata, B. Steil, R. S. Stolarski, W. Tian, and M. Yoshiki, 2007. Multi-model projections of ozone recovery in the 21st century, *J. Geophys. Res.*, **112**, doi:10.1029/2006JD008332.
- Feser, F., H.-F. Graf, and J. Perlwitz, 2000. Secular variability of the coupled tropospheric and stratospheric circulation in the GCM ECHAM 3/LSG, *Theor. Appl. Climatol.*, **65**, 1-15.
- Fogt, R. L., J. Perlwitz, S. Pawson, and M. A. Olsen, 2009. Intra-annual relationships between polar ozone and the SAM, *Geophys. Res. Lett.*, **36**, doi:10.1029/2008GL036627.

- Hardiman, S. C., D. G. Andrews, A. A. White, N. Butchart, and I. Edmond, 2010a. Using different formulations of the transformed Eulerian-mean equations and Eliassen-Palm diagnostics in general circulation models, *J. Atmos. Sci.*, accepted for publication.
- Hardiman, S. C., N. Butchart, S. M. Osprey, L. J. Gray, A. C. Bushell, and T. J. Hinton, 2010b. The climatology of the middle atmosphere in a vertically extended version of the Met Office's climate model. Part I: Mean state, *J. Atmos. Sci.*, accepted for publication.
- Haynes, P. H., C. J. Marks, M. E. McIntyre, T. G. Shepherd, and K. P. Shine, 1991. On the "downward control" of the extratropical diabatic circulation by eddy-induced mean zonal forces, *J. Atmos. Sci.*, **48**, 651-678.
- Holton, J. R., and H.-C. Tan, 1980. The influence of the equatorial quasi-biennial oscillation on the global circulation at 50 mb, *J. Atmos. Sci.*, **37**, 2200-2208.
- Kalnay, E., M. Kanamitsu, R. Kistler, W. Collins, D. Deaven, L. Gandin, M. Iredell, S. Saha, G. White, J. Woolen, Y. Zhu, A. Leetmaa, R. Reynolds, M. Chelliah, W. Ebisuzaki, W. Higgins, J. Janowiak, K. C. Mo, C. Ropelewski, J. Wang, R. Jenne, and D. Joseph, 1996. The NCAR/NCEP 40-year reanalysis project, *Bull. Am. Meteor. Soc.*, **77**, 437-471.
- Li, F., J. Austin, and J. Wilson, 2008. The strength of the Brewer-Dobson circulation in a changing climate: Coupled chemistry-climate model simulations, *J. Clim.*, **21**, 40-57.
- Lu, H., M. P. Baldwin, L. J. Gray, and M. J. Jarvis, 2008. Decadal-scale changes in the effect of the QBO on the northern stratospheric polar vortex, *J. Geophys. Res.*, **113**, doi:10.1029/2007JD009647.
- Manney, G. L., J. L. Sabutis, S. Pawson, M. L. Santee, B. Naujokat, R. Swinbank, M. E. Gelman, and W. Ebisuzaki, 2003. Lower stratospheric temperature differences between meteorological analyses in two cold Arctic winters and their impact on polar processing studies, *J. Geophys. Res.*, **108**, doi:10.1029/2001JD001149.
- Manney, G. L., K. Krüger, J. L. Sabutis, S. A. Sena, and S. Pawson, 2005a. The remarkable 2003-2004 winter and other recent warm winters in the Arctic stratosphere since the late 1990s, *J. Geophys. Res.*, **110**, doi:10.1029/2004JD005367.
- Manney, G. L., D. R. Allen, K. Krüger, J. L. Sabutis, S. Pawson, R. Swinbank, C. E. Randall, A. J. Simmons, and C. Long, 2005b. Diagnostic comparison of meteorological analyses during the 2002 Antarctic winter, *Mon. Wea. Rev.*, **133**, 1261-1278.
- McLandress, C., and T. G. Shepherd, 2009. Impact of climate change on stratospheric sudden warmings as simulated by the Canadian middle atmosphere model, *J. Clim.*, **22**, 5449-5463.
- Neu, J. L., and R. A. Plumb, 1999. Age of air in a "leaky pipe" model of stratospheric transport, *J. Geophys. Res.*, **104**, 19,243-19,255.
- Newman, P. A., E. R. Nash, and J. E. Rosenfield, 2001. What controls the temperature of the Arctic stratosphere during spring? *J. Geophys. Res.*, **106**, 19,999-20,010.
- North, G. R., T. L. Bell, R. F. Cahalan, and F. J. Moeng, 1982. Sampling errors in the estimation of empirical orthogonal functions, *Mon. Wea. Rev.*, **110**, 699-706.
- Osprey, S., L. Gray, A. Bushell, N. Butchart, S. Hardiman, and T. Hinton, 2009. The climatology of the middle atmosphere in a vertically extended version of the Met Office's climate model. Part II: Variability, *J. Atmos. Sci.*, accepted subject to revision.
- Pascoe, C. L., L. J. Gray, S. A. Crooks, M. N. Juckes and M. P. Baldwin, 2005. The quasibiennial oscillation: Analysis using ERA-40 data, *J. Geophys. Res.*, **110**, doi:10.1029/2004JD004941.
- Pawson, S., K. Krüger, R. Swinbank, M. Bailey, and A. O'Neill, 1999. Intercomparison of two stratospheric analyses: temperatures relevant polar stratospheric cloud formation, *J. Geophys. Res.*, **104**, 2041-2050.
- Randel, W., P. Udelhofen, E. Fleming, M. Gelman, K. Hamilton, D. Karoly, D. Ortland, R. Swinbank, M.-L. Chenin, P. Keckhut, K. Labitzke, E. Remsberg, A. Simmons, D. Wu, M. Geller, S. Pawson, F. Wu, and M. Baldwin, 2004. The SPARC Intercomparison of Middle-Atmosphere Climatologies, *J. Clim.*, **17**, 986-1003.
- Scaife, A. A., N. Butchart, C. D. Warner, and R. Swinbank, 2002. Impact of a spectral gravity wave parametrization on the stratosphere in the Met Office Unified Model, *J. Atmos. Sci.*, **59**, 1473-1489.
- Shepherd, T. G., R. A. Plumb, and S. C. Wofsy (Eds.), 2005. *J. Atmos. Sci.*, **62**, Issue #3.
- SPARC, 2002. , SPARC Intercomparison of Middle Atmosphere Climatologies, W. Randel, M.-L. Chanin and

- C. Michaut (Eds.), SPARC Report No. 3, WCRP-116, WMO/TD-No. 1142, 96pp.
- Swinbank, R., and A. O'Neill, 1994. A stratosphere-troposphere data assimilation system, *Mon. Wea. Rev.*, **122**, 686-702.
- Thompson, D. W. J., and J. M. Wallace, 2000. Annular modes in the extratropical circulation. Part I: Month-to-month variability, *J. Clim.*, **13**, 1000-1016.
- Uppala, S. M., P. W. Kållberg, A. J. Simmons, U. Andrae, V. da Costa Bechtold, M. Fiorino, K. K. Gibson, J. Haseler, A. Hernandez, G. A. Kelly, X. Li, K. Onogi, S. Saarinen, N. Sokka, R. P. Allan, E. Andersson, K. Arpe, M. A. Balmaseda, A. C. M. Beljaars, L. van de Berg, J. Bidlot, N. Bormann, S. Caires, F. Chevallier, A. Dethof, M. Dragosavac, M. Fisher, M. Fuentes, S. Hagemann, E. Hólm, B. J. Hoskins, L. Isaksen, P. A. E. M. Janssen, R. Jenne, A. P. McNally, J.-F. Mahfouf, J.-J. Morcrette, N. A. Rayner, R. W. Saunders, P. Simon, A. Sterl, K. E. Trenberth, A. Untch, D. Vasiljevic, P. Viterbo, and J. Woollen, 2005. The ERA-40 re-analysis, *Quart. J. Roy. Meteor. Soc.*, **131**, 2961-3012. doi:10.1256/qj.04.176.
- Waugh, D. W., and V. Eyring, 2008. Performance metrics for stratosphere-resolving chemistry-climate models, *Atmos. Chem. Phys.*, **8**, 5699-5713.
- Waugh, D. W., and P. P. Rong, 2002. Interannual variability in the decay of lower stratospheric Arctic vortices, *J. Meteor. Soc. Japan*, **80**, 997-1012.
- Waugh, D. W., W. J. Randel, S. Pawson, P. A. Newman, and E. R. Nash, 1999. Persistence of lower stratospheric polar vortices, *J. Geophys. Res.*, **104**, 27,191-27,201.



# Chapter 5

## Transport

**Lead Authors:** Jessica Neu & Susan Strahan

**Co-Authors:** Peter Braesicke

Anne Douglass

Petra Huck

Luke Oman

Diane Pendlebury

Susann Tegtmeier

---

### 5.1 Introduction

The distribution of long-lived trace gases in the stratospheric overworld is controlled mainly by the balance between the diabatic circulation, which acts to create equator-to-pole gradients in tracer isopleths, and quasi-horizontal mixing, which acts to flatten tracer isopleths in mixing regions while sharpening gradients at the locations of mixing barriers. Three important barriers to transport are the subtropical barrier (*i.e.*, the tropical “pipe”), the edge of the polar vortex, and the extra-tropical tropopause. A schematic of the stratospheric circulation and transport barriers

is shown in **Figure 5.1**. Both the strength of the diabatic circulation and that of the transport barriers are linked to wave activity in the stratosphere and thus vary with height and season.

In this chapter, model representation of stratospheric transport processes is evaluated using process-oriented diagnostics derived from observations. In many cases it is impossible to create a diagnostic that uniquely assesses a single process because most have contributions from multiple transport mechanisms. For example, the age of air in the tropics depends on integrated vertical advection, vertical mixing, and mixing between the tropics and extratropics across the subtropical transport barrier. However, combining the diagnostics and, where possible, using the information from diagnostics that do uniquely assess a

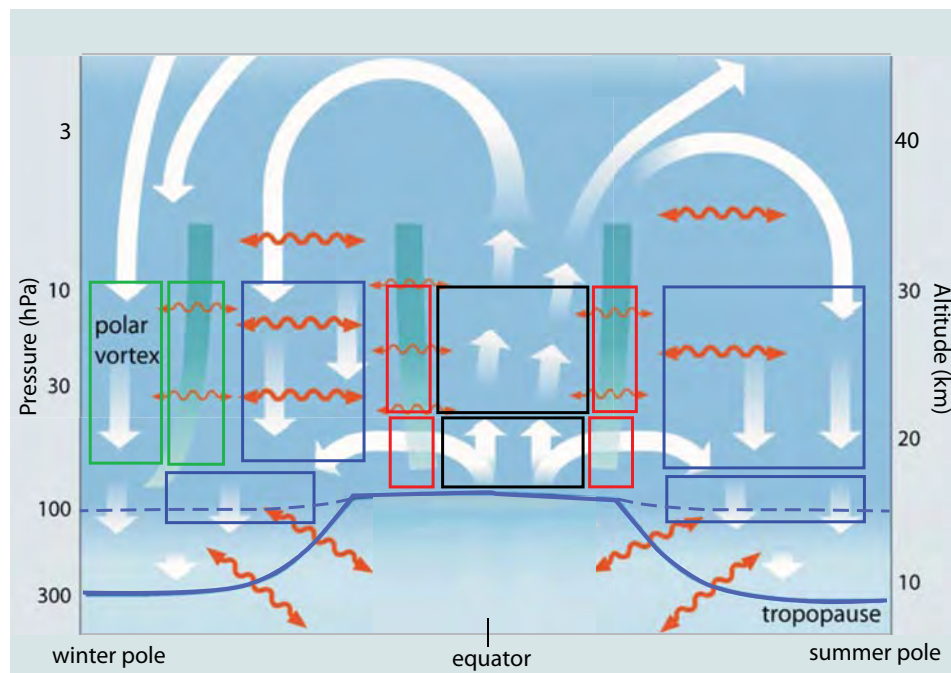


**Figure 5.1:** Schematic of the stratospheric circulation (courtesy of Harald Boenisch). The blue dashed line shows the boundary between the overworld and the lowermost stratosphere (380 K = ~100 hPa, 16 km). White arrows indicate the direction of the residual circulation in the winter and summer hemispheres. Transport barriers are shown as dark blue shaded regions. Red two-headed arrows indicate mixing, with smaller arrows showing weaker mixing across transport barriers. The boxes indicate regions where transport processes are evaluated in this chapter, with the colour of the box corresponding to the Region/Process column of Table 5.1 and the chapter sections (Black = Tropical ascent, Red = Tropical-extra-tropical mixing, Blue = Integrated processes affecting mid-latitude composition, Green = Polar processes) The lowermost stratosphere is not evaluated in this chapter. A complete list of transport diagnostics can be found in Table 5.1.

single process allows model behaviour to be broken down and assessed in a physically-meaningful way. The suite of diagnostics chosen for this chapter (**Table 5.1**) is intended to cover the major processes controlling stratospheric trace gas distributions in the overworld (above 380 K, ~100 hPa), from entry in the tropical lower stratospheric to exit through the extra-tropical 100 hPa surface. The diagnostics emphasize transport processes below 10 hPa because the goal of this report is to understand 21<sup>st</sup> century O<sub>3</sub> in the WMO reference simulations. The present day (~1990-2006) behaviour of CCMs is evaluated and compared to observations, using the REF-B1 simulations for all models except UMETRAC. For UMETRAC, REF-B0, the present day time slice simulation, was used because REF-B1 was unavailable. Diagnostics are calculated from 10-15 years of model output whenever possible. Future changes in a few key diagnostics are presented by comparing changes between the recent past (1990-2006) and the future (2080-2099) from the REF-B2 simulations.

More than a dozen diagnostics are applied here but many have overlap in the processes they evaluate. The results presented in this chapter are grouped by process and region in the same order as listed in Table 5.1. The proc-

esses evaluated include tropical ascent, mixing between the tropics and mid-latitudes (*i.e.*, the “leakiness” of the subtropical barriers), and descent and isolation in the polar region. As a connection to the upper troposphere/lower stratosphere (UTLS) region evaluated in Chapter 7, the influence of seasonal variations in transport on air leaving the stratosphere is also examined. Unless otherwise noted, model performance on the diagnostics presented here has been quantified using the metric described in Waugh and Eyring (2008), hereafter referred to as WE08, using  $3\sigma$  of the observational uncertainty in the denominator. Because there are significant differences in model performance between the lower ( $\geq 50$  hPa) and middle stratosphere ( $\leq 50$  hPa) (LS and MS, respectively), many of the diagnostics are applied separately to the two regions.

## 5.2 Transport Diagnostics for the Tropics

Most air enters the stratosphere in the tropics, so transport in this region is critical to determining stratospheric composition. Only by simulating the correct balance be-

**Table 5.1:** Stratospheric Transport Diagnostics for CCMs. Gray highlights indicate diagnostics that are used as quantitative metrics for the overall model performance.

Diagnostic	Variables	Observations	References
<b>Tropical Ascent</b>			
H <sub>2</sub> O tape recorder phase	H <sub>2</sub> O and CH <sub>4</sub>	UARS HALOE and Aura MLS	<i>Mote et al. (1996; 1998); Hall et al. (1999); Schoeberl et al. (2008)</i>
Tropical-Mid-latitude Mean Age Gradient	CO <sub>2</sub> and SF <sub>6</sub>	Various balloon missions	<i>Andrews et al. (2001); Engel et al. (2009)</i>
<b>Tropical-Extratropical Mixing</b>			
H <sub>2</sub> O tape recorder amplitude	H <sub>2</sub> O and CH <sub>4</sub>	UARS HALOE and Aura MLS	<i>Mote et al. (1996; 1998); Hall et al. (1999); Schoeberl et al. (2008)</i>
Tropical Mean Age profile	CO <sub>2</sub> and SF <sub>6</sub>	OMS balloon profiles	<i>Andrews et al. (2001)</i>
Tropical CH <sub>4</sub> vertical gradient	CH <sub>4</sub>	UARS HALOE	<i>Eyring et al. (2006)</i>
Tropical-Mid-latitude N <sub>2</sub> O PDFs	N <sub>2</sub> O, potential temperature	ENVISAT-MIPAS and Aura MLS	<i>Douglass et al. (1999); Sparling (2000)</i>
<b>Integrated Processes Affecting Extratropical Composition</b>			
NH Mid-latitude Mean Age profile	CO <sub>2</sub> and SF <sub>6</sub>	Various balloon missions	<i>Engel et al. (2009)</i>
Fractional Release of Cly	CFC-11, CFC-12, CO <sub>2</sub> , and SF <sub>6</sub>	NASA ER-2 aircraft missions	<i>Schauffler et al. (2003); Douglass et al. (2008)</i>
NH Mid-latitude Cly time series	Cly	UARS HALOE and Aura MLS	<i>Lary et al. (2007); Waugh and Eyring (2008)</i>
N <sub>2</sub> O annual cycle in the LS	N <sub>2</sub> O	Aura MLS	
Mean Age at 60°N/S	CO <sub>2</sub>	NASA ER-2 aircraft missions	<i>Andrews et al. (2001); Boering et al. (1996)</i>
<b>Polar Processes</b>			
Antarctic spring CH <sub>4</sub> PDFs	CH <sub>4</sub> , potential temperature	UARS HALOE	<i>Strahan and Polansky (2006)</i>
Antarctic September N <sub>2</sub> O profile	N <sub>2</sub> O	Aura MLS	
Antarctic spring Cly time series	Cly	UARS HALOE and Aura MLS	<i>Douglass et al. (1995); Santee et al. (1996); Lary et al. (2007)</i>

tween ascent and mixing across the subtropical barriers can a model get the correct balance of pathways necessary for accurate simulation of photochemically active species.

## 5.2.1 Ascent

### 5.2.1.1 Tape Recorder Phase Speed

Air entering the stratosphere through the tropics slowly ascends with limited horizontal mixing. The vertical propagation of annual variations in tropical tropopause water vapour, known as the “tape recorder” signal (*e.g.*,

*Mote et al., 1998; Hall et al., 1999, Waugh and Hall, 2002, Schoeberl et al., 2008*), provides striking visual evidence of this isolated ascent. **Figure 5.2** shows the deviation of the water vapour mixing ratio from the monthly mean profile averaged over 10°S to 10°N for combined HALOE and MLS observations, and for the available models (data courtesy of Mark Schoeberl). UMETRAC, UMUCA-METO, and UMUCA-UCAM use water vapour climatologies, so no tape recorder diagnostics can be calculated for these models. The model-to-model differences in the amplitude of the anomalies, propagation speed, and attenuation rate are quite large. There are also significant differences in the location of the base of the tape recorder (*i.e.*, the minimum

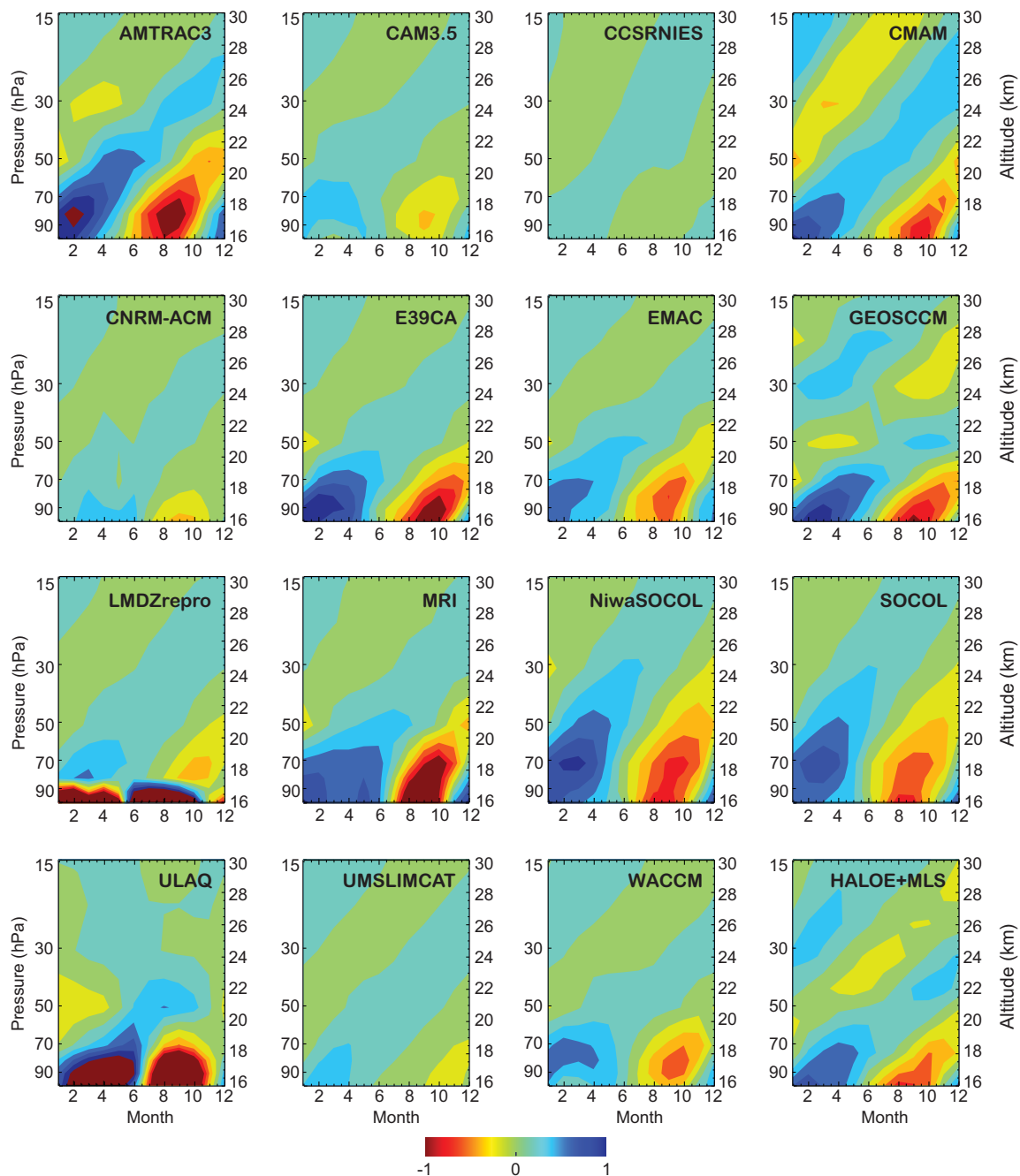


**Figure 5.2:** Water vapour tape recorder signal from the models and the combined HALOE+MLS data set from Schoeberl *et al.* (2008). Plots show the deviation in water vapour mixing ratio (ppmv) from the time-mean average profile averaged over  $10^{\circ}\text{N}$ - $10^{\circ}\text{S}$ . The contour interval is the same on all plots and is given next to the observations.

in water vapour) near the tropical tropopause, but most of the models fall within the range indicated by MLS (3.5 km vertical resolution, tape recorder base at  $\sim 80$  hPa) and HALOE (2 km vertical resolution, tape recorder base at  $\sim 100$  hPa). The morphology of the water vapour anomalies is significantly different than observed in several models.

**Figure 5.3** compares the phase lag of the tape recorder signal from the models, calculated as the average

propagation of the maximum and minimum water vapor anomalies, to the HALOE-derived phase lag (Hall *et al.*, 1999; Eyring *et al.*, 2006). The phase lag is set to zero at the level of maximum amplitude,  $Z_o$ , for the observations and for each model, and is plotted as a function of altitude above  $Z_o$ . The slope of the phase lag (the phase speed,  $c$ ) of the tape recorder signal is a measure of the net vertical transport in the tropics (large-scale ascent +



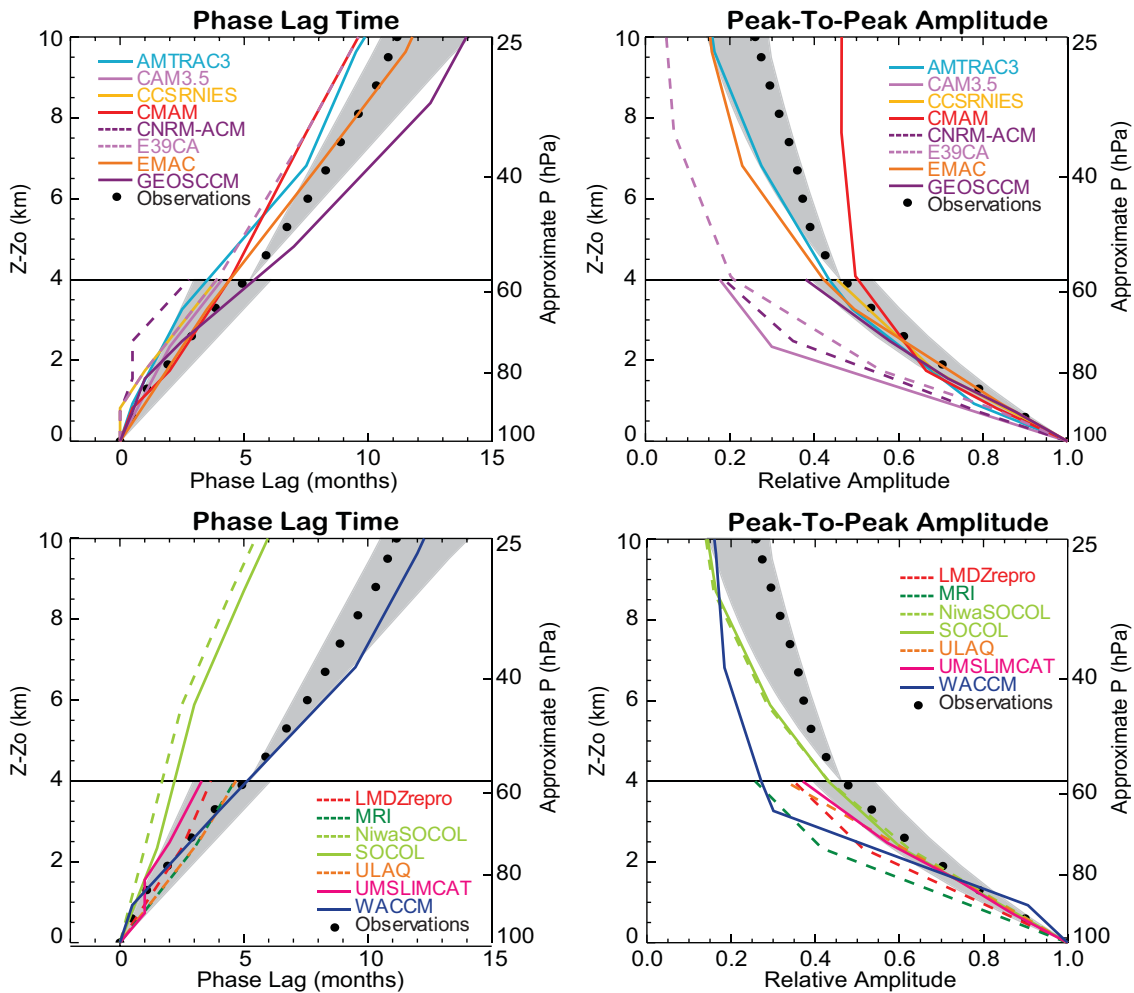


**Figure 5.3:** Left Panels: Phase lag of the water vapour tape recorder, averaged over  $10^{\circ}\text{S}$ - $10^{\circ}\text{N}$ . The phase lag is set to zero at the level of maximum amplitude, and the vertical coordinate is the distance from that level. The phase lag is the average of the propagation of the maxima and the minima. The models are split into two panels for clarity. Solid circles are HALOE observations. Grey shaded areas indicate the minimum and maximum slopes  $\pm$  the estimated measurement uncertainty used to evaluate the models in the TLS and TMS. Note that the shaded areas do not represent the uncertainty of the phase lag, but of the phase speed (slope of the phase lag). Right Panels: Amplitude of the tape recorder signal relative to the maximum amplitude as a function of height above the level of maximum amplitude. The grey shaded areas indicate the range of scale heights that can be fit to the observations ( $\pm$  estimated measurement uncertainty).

vertical diffusion) (Mote *et al.*, 1996; Mote *et al.*, 1998; Hall *et al.*, 1999), and the HALOE phase speed has been shown to agree quite well with estimates of the residual vertical velocity in the 16-26 km range (Mote *et al.*, 1998; Schoeberl *et al.*, 2008). The phase speed in the tropical LS (TLS,  $Z - Z_o \leq 4$  km) and tropical MS (TMS,  $Z - Z_o > 4$  km) is evaluated using a linear fit to the phase lag for both the observations and the models. The phase lag is ill-defined when the amplitude of the water vapour maxima or minima is less than 0.1 ppmv, so it is not analysed if the amplitude falls below this threshold. All of the models have sufficient amplitude for evaluation in the TLS, but only eight do in the TMS. The 0.1 ppmv threshold precludes evaluation of

CAM3.5, CCSRNIES, CNRM-ACM, LMDZrepro, MRI, ULAQ, and UMSLIMCAT in the TMS.

**Figure 5.4** shows the phase speed calculated from the observations and from the models along the y-axis for the TLS (top panels) and TMS (bottom panels). The mean phase speed derived from a linear fit to the observations is 0.34 mm/s in the TLS and 0.35 mm/s in the TMS. WE08 estimated a standard deviation of 0.05 mm/s for the phase speed derived from the entire altitude range of the observations, but a larger uncertainty is used here since the analysis is split into the TLS and TMS, thus reducing the number of points for obtaining the linear fit. The maximum and minimum phase speeds that can be derived from the obser-

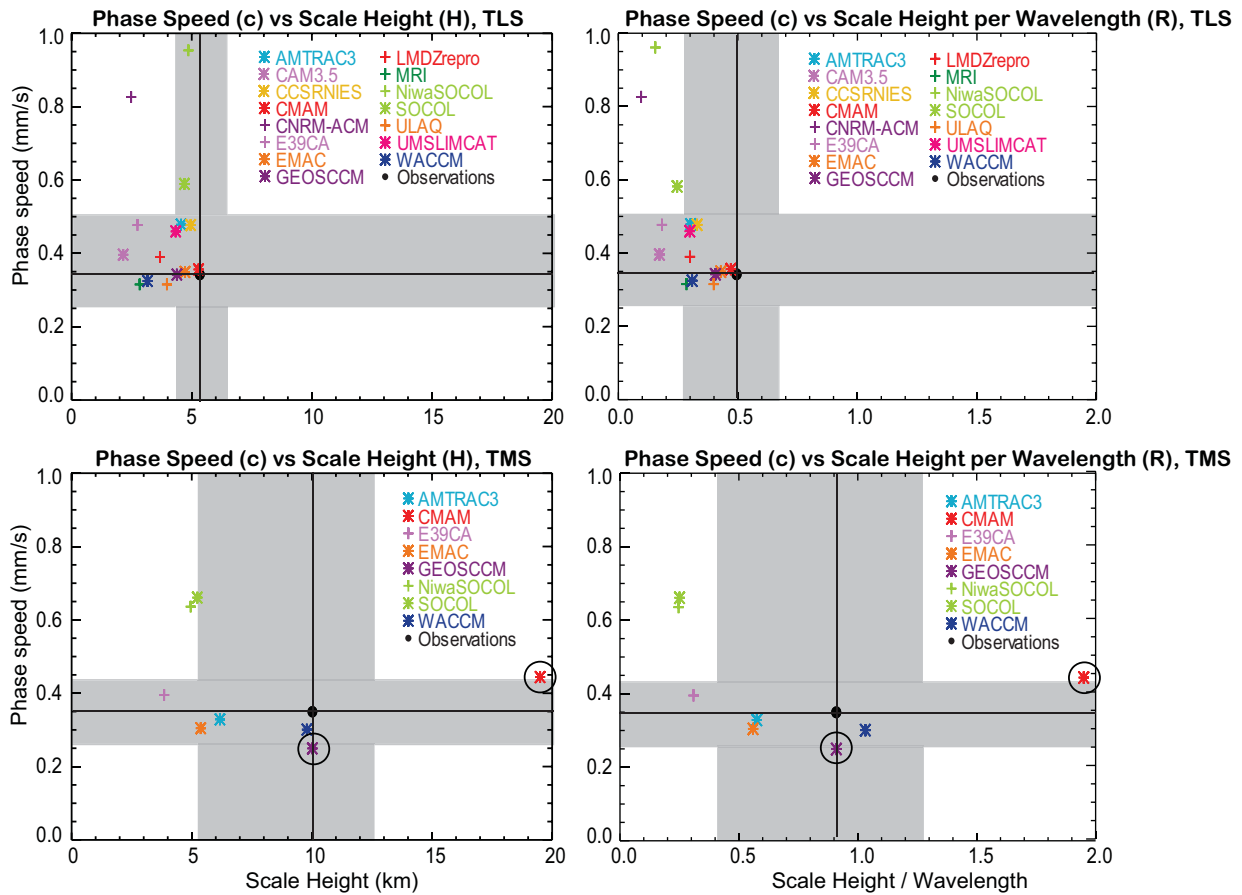


**Figure 5.4:** Left panels: The tape recorder phase speed,  $c$ , calculated as the slope of a linear least squares fit to the phase lag, versus the scale height,  $H$ , that satisfies the equation  $A=A_0 \exp(-z/H)$ , where  $A/A_0$  is the relative amplitude of the tape recorder signal. Top panel shows the values for the TLS, bottom panel shows the values for the TMS. The solid black circle shows the observations, and the horizontal and vertical lines show the observed phase speed and scale height, respectively. Horizontal grey shaded regions are bounded by the maximum and minimum slopes that can be fit to the phase lag observations  $\pm 1\sigma$  measurement uncertainty, and the vertical grey shaded regions are bounded by the maximum and minimum scale heights that can be fit to the observations  $\pm 1\sigma$ . Right panels: Same as the left panels, except that the scale height per wavelength,  $R=H/c \cdot 1\text{year}$ , is plotted along the x-axis. Vertical grey shaded regions are bounded by  $H_{\text{max}}/c_{\text{min}}$  and  $H_{\text{min}}/c_{\text{max}} \pm 1\sigma$ . Note that the faster the phase speed, the larger the difference between  $R$  and  $H$ . GEOSCCM is circled in the bottom panels because its scale height could not be evaluated in the TMS; the amplitude increases with height due to evaporation of precipitable water. CMAM is circled because its scale height is off the scale of the plot:  $H=72 \text{ km}$ ,  $R=5.2$  for CMAM in the TMS.

observations are used as an additional measure of uncertainty, so that the denominator of the WE08 metric becomes  $(c_{\text{max}} - c_{\text{min}}) + 3\sigma$ , with the maximum and minimum values of  $c$  determined by a linear fit through the observations with the largest least squares residual values in each region, and  $\sigma = 0.05 \text{ mm/s}$  as in WE08. The light grey shaded areas in Figures 5.3 and 5.4 show the maximum and minimum slope  $\pm 1\sigma$  in each region.

As in CCMVal-1, most of the model phase speeds are greater than observed, indicating too rapid net vertical motion in the tropics. However, the total model spread over the range of observations has decreased since CCMVal-1,

as has the difference between modelled and observed phase speeds, suggesting improvements in tropical transport in the models. This will be discussed further in Section 5.5.4. The models that most closely match the observed TLS phase speed are CMAM, EMAC, GEOSCCM, MRI, ULAQ, and WACCM. AMTRAC3, CAM3.5, CCSRNIES, E39CA, LMDZrepro, and UMSLIMCAT all have fast phase speeds relative to the observations, but are within the estimated uncertainties. Three models fall well outside the range of uncertainty in the TLS, with extremely fast phase speeds: CNRM-ACM, NiwaSOCOL, and SOCOL. Of the 8 models evaluated in the TMS, AMTRAC3,

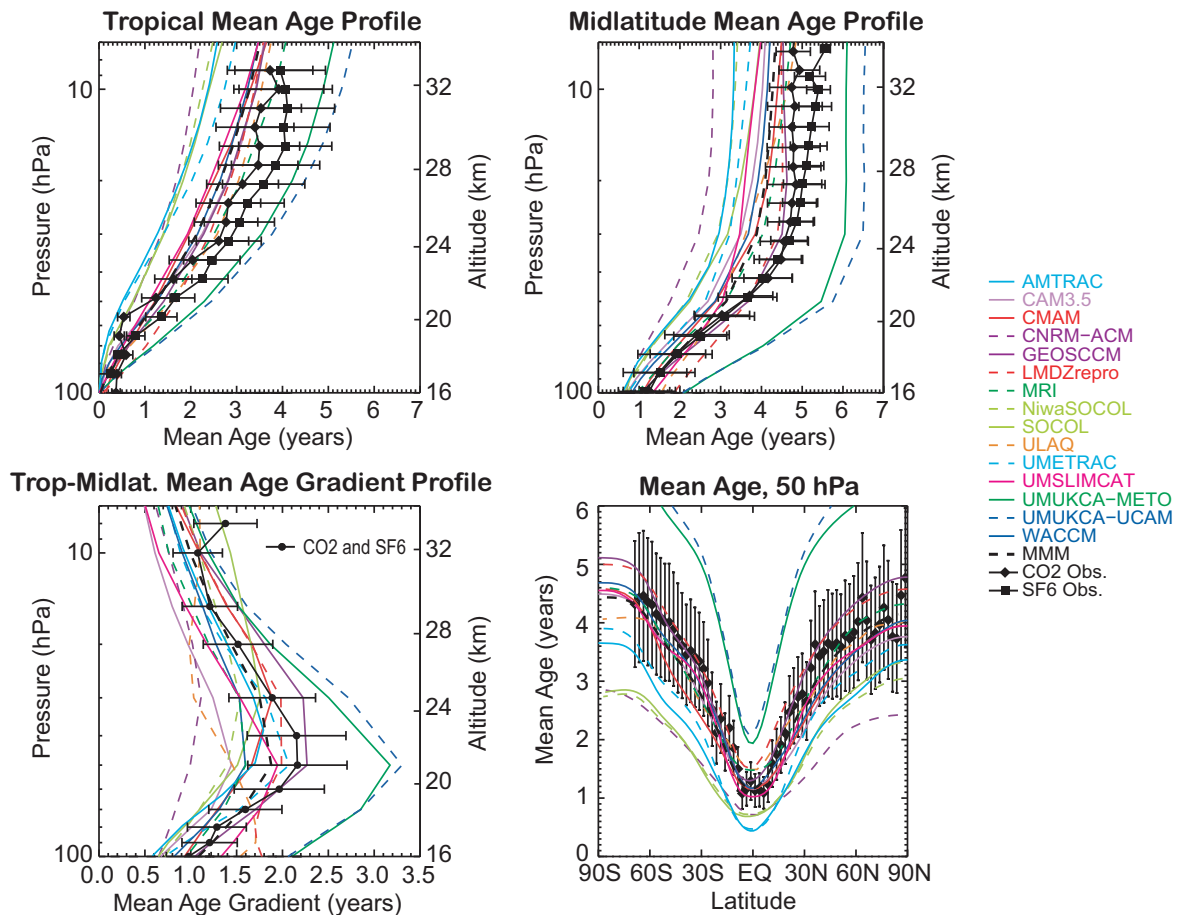


**Figure 5.5:** Mean age from 15 CCMs and the multi-model mean. Black symbols are the observed mean age profiles derived from  $\text{CO}_2$  (diamonds) and  $\text{SF}_6$  (squares) for the tropics ( $10^\circ\text{N}$  -  $10^\circ\text{S}$ , upper left panel (Andrews et al. (2001))) and mid-latitudes ( $35^\circ\text{N}$  -  $45^\circ\text{N}$ , upper right panel (Engel et al., 2009)), as well as the latitudinal distribution of mean age at 50 hPa (bottom right panel, Andrews et al., (2001)). The bottom left panel shows the difference between the average of the observed tropical profiles and midlatitude profiles on pressure surfaces. All uncertainties shown are  $1\sigma$ .

E39CA, EMAC, and WACCM fall within the uncertainties of the observed phase speed. CMAM, NiwaSOCOL, and SOCOL have faster than observed TMS phase speeds and the TMS phase speed in GEOSCCM is too slow compared to observations.

### 5.2.1.2 Ascent from Mean Age Gradients

The mean age of air is the time elapsed since a stratospheric parcel of air was last in contact with the troposphere, and it can be calculated from observations of conserved tracers whose concentrations increase approximately linearly over time. Observations of  $\text{CO}_2$  and  $\text{SF}_6$  have been used in previous studies to derive empirical estimates of the mean age and to qualitatively evaluate model representations of the residual circulation and mixing (Hall et al., 1999; Eyring et al., 2006).

Neu and Plumb (1999) demonstrated that for a sim-

plified “tropical leaky pipe” model in steady equilibrium, the age difference between the tropics and mid-latitudes along surfaces parallel to the age isopleths depends only on the local tropical vertical velocity and the air mass overhead, assuming that the cross-isopleth diffusion of age is negligible. The age difference is independent of path and of mixing across the edge of the tropics. Any horizontal mass flux from the tropics into mid-latitudes (which acts to decrease the age in mid-latitudes) will be balanced by a decrease in the tropical vertical mass flux (thus increasing the mid-latitude age). In the case of recirculation of air through the tropics, multiple circuits act to age both the tropics and mid-latitudes equally. The result that the age gradient depends only on the ascent rate when diffusion is negligible does not depend on the artificial construct of discontinuities between the tropics and extra-tropics; it applies in general, except in the singular case where the mixing between tropics and mid-latitudes is infinitely fast, as

**Table 5.2:** CCM Age Tracer Information.

CCM	Tracer Type <sup>1</sup>	Reference Location <sup>2</sup>
AMTRAC3	Stratospheric source	N/A
CAM3.5	Linearly increasing	Equator (0.95°N), 139 hPa
CCSRNIES	Linearly increasing	PBL
CMAM	Stratospheric source	N/A
CNRM-ACM	Linearly increasing	8°S-8°N, below 700 hPa
GEOSCCM	Linearly increasing	Equator at 100 hPa
LMDZ-repro	Linearly increasing	Tropical Thermal Tropopause
NiwaSOCOL	Linearly increasing	PBL
MRI	Linearly increasing	Equator (1.4°S-1.4°N) at 100 hPa
SOCOL	Linearly increasing	PBL
ULAQ	Linearly increasing	15°S-15°N, below 132 hPa
UMSLIMCAT	Pulse source	N/A
UMUKCA-METO	Linearly increasing	PBL
UMUKCA-UCAM	Linearly increasing	PBL
WACCM	Linearly increasing	Equator (0.95°N) at 139 hPa

<sup>1</sup> Linearly increasing - an inert tracer whose concentration grows linearly with time below a given lower boundary; Stratospheric source - direct 'age of air' tracer, where the value of the tracer field in the stratosphere increases by  $\Delta t$  every model  $\Delta t$ ; Pulse tracer - given a value of 1.0 during the first month of model simulations and then set to 0.0 afterwards.

<sup>2</sup> Reference location refers to the location used to calculate the mean age fields archived at British Atmospheric Data Centre. For all plots shown the mean age fields were normalised so that mean age = 0 at Equator, 100 hPa.

long as the age difference is taken to be between upwelling and downwelling regions (R. A. Plumb, personal communication). Thus, the difference in mean age between tropics and mid-latitudes can be used to assess tropical ascent independently of quasi-horizontal mixing, which cannot be done using the age itself.

A recent study by Engel *et al.* (2009) used 27 balloon-

borne CO<sub>2</sub> and SF<sub>6</sub> profiles measured over 30 years to derive the loss-corrected mean age of air from 35°N-45°N, between 15 and 32 km. Combining these newly available mid-latitude age profiles (Figure 5.5, top right panel) with existing tropical profiles from 10°N to 10°S (Figure 5.5, top left panel) (Boering *et al.*, 1996; Andrews *et al.*, 2001) provides the necessary data to calculate a profile of the tropical-mid-latitude age gradient (Figure 5.5, bottom left panel). The observational uncertainty in the mid-latitude mean ages reflects a combination of the trace gas uncertainties and the variability of mean age over the 30 year period (Engel *et al.*, 2009). The fact that the Engel *et al.* (2009) data reflect little or no trend in the Northern Hemisphere (NH) mean age above 24 km is discussed further in Section 5.4. For the purposes of this discussion, the absence of a trend allows for a meaningful comparison between observations collected over the past three decades and present-day model output. The tropical data (Andrews *et al.*, 2001) were not reported with uncertainties, but the variability in the published CO<sub>2</sub> and SF<sub>6</sub> profiles suggests that an uncertainty of  $\pm 0.5$  year for mean ages above 20 km spans the range of observed variability (*e.g.*, Eyring *et al.*, 2006). Stiller *et al.* (2008) report mean ages derived from global measurements of SF<sub>6</sub> but they cannot be used for this diagnostic because the effects of mesospheric losses were not used in the mean age calculation. Age derived from SF<sub>6</sub> assuming no loss results in mean ages that are up to 1.5 years older than CO<sub>2</sub>-derived mean ages in the LS, with much greater differences in the MS.

Table 5.2 describes the type of age tracer used in each model and the reference location used to normalise the mean age where applicable. For the mean age diagnostics, all modelled mean ages were renormalised to 0 on the 100 hPa surface at the equator. The comparison of modelled and observed age difference between the tropics and mid-latitudes is shown in Figure 5.5 (bottom left panel), and the metrics are calculated as an average of the scores at 90, 80, 70, and 50 hPa for the TLS, and as an average of the scores at 30, 20, 15, and 10 hPa for the TMS. There is no standard model output level between 50 hPa and 30 hPa, and so the models' ability to capture the maximum age gradient between these levels cannot be assessed.

In agreement with the results for the tape recorder phase speed, most models have smaller than observed age gradients in the TLS, indicating fast ascent. However, as with the tape recorder, most models lie within the observational uncertainty. Only AMTRAC3, CAM3.5, CNRM-ACM, NiwaSOCOL, and SOCOL have age gradients that are smaller than observed and lie outside the observational uncertainty over most of the TLS. Both UMUCKA models, which were not included in the tape recorder analysis, have much larger than observed age gradients (well outside the observational uncertainty), indicating very slow tropical ascent. The age difference profiles in ULAQ

and LMDZrepro have a significantly different shape than observed in the TLS. In the TMS the agreement between the models and the observations is improved, with only CAM3.5, CNRM-ACM, and ULAQ having age gradients smaller than the observational uncertainty over most of the region. Again, the ULAQ age difference profile shape is much different than observed in the TMS. The UMUCCA models are closer to observations in the TMS, but are still the only models with age gradients that are significantly larger than observed.

### 5.2.1.3 Comparison of Vertical Velocities

The tape recorder phase speed and tropical-mid-latitude age gradient are fully independent measures of the tropical upwelling, and tracer-derived vertical velocities can only be expected to agree with one another when the tracer-dependent terms of the continuity equation are small and the transport circulation closely approximates the residual circulation. Processes that can lead to significant differences in tracer-derived vertical velocities include vertical diffusion, horizontal and vertical eddy tracer fluxes, and rectifier effects between tracer variability and the seasonal or interannual variability of the circulation (see Andrews, *et al.* (1987) for a discussion of the differences between the transport and residual circulation). In models, numerical errors in transport can also lead to significant differences in tracer-derived vertical velocities.

The top left panel of **Figure 5.6** shows a comparison between the tropical vertical velocity calculated from the observed tropical-mid-latitude age gradient (from Figure 5.5, bottom left panel), the vertical velocity calculated by Schoeberl *et al.* (2008) for the combined HALOE-MLS water vapour tape recorder, and the vertical velocity calculated as a simple vertical derivative of the phase lag of the HALOE water vapour observations (from Figure 5.3, left panels). Assuming that age isopleths are roughly parallel to pressure surfaces in the tropics and in the well-mixed portion of the mid-latitudes, the age gradient estimate of the vertical velocity is given by

$$(1+\alpha)H/\alpha \Delta\Gamma, \quad (5.1)$$

where  $H$  is a constant scale height (7 km),  $\alpha$  is the ratio of the mass of air in the tropics to the mass of air in mid-latitudes, and  $\Delta\Gamma$  is the tropical-mid-latitude age difference on pressure surfaces (Neu and Plumb, 1999). The boundaries of the tropical upwelling region used to calculate  $\alpha$  are  $\pm 25^\circ$ . The Schoeberl *et al.* (2008) tape recorder vertical velocities were calculated from the phase-lagged correlation coefficient between adjacent levels, and give a much smoother  $w$  profile than a simple vertical derivative of the tape recorder phase lag. The three observational tracer-derived estimates of the tropical upwelling show remark-

able consistency. Below 26 km, the tape recorder vertical velocity has been shown to agree very well with estimates of the residual circulation (Mote *et al.*, 1998; Schoeberl *et al.*, 2008). The agreement between the observed age gradient and tape recorder vertical velocities provides further evidence that the transport circulation is a very good approximation to the residual circulation and that the tracer-dependent transport terms are small in the real atmosphere.

The remaining panels of Figure 5.6 show the residual vertical velocity,  $\overline{w^*}$ , averaged over  $\pm 20^\circ$ , and the age gradient and tape recorder vertical velocities for all of the models. The age gradient velocities are calculated in the same way as for the observations, and the tape recorder velocities are a simple vertical derivative of the phase lag from Figure 5.3. The tape recorder velocities are plotted starting at the level of maximum amplitude for each model tape recorder rather than normalised to a common height as in Figure 5.3. The solid black line in each panel is the mean of the observed age gradient vertical velocity and the Schoeberl *et al.* (2008) tape recorder vertical velocity from  $\sim 90$ -25 hPa. Above and below that region the age gradient vertical velocity is used. The grey shaded region shows the corresponding uncertainties.

Of the ten models that have all three vertical velocity estimates, there is relatively good agreement between the three different upwelling calculations and good agreement with the observations for CMAM, GEOSCCM, MRI (which only has tape recorder results in the TLS), and WACCM. The differences between the tracer-derived vertical velocities and  $\overline{w^*}$  are relatively small for LMDZrepro and ULAQ, but as noted in Section 5.2.1.2, both show age gradient profiles that are significantly different than observed (though LMDZrepro agrees well with observations in the TMS). CNRM-ACM has very fast tracer-derived vertical velocities, which differ significantly from  $\overline{w^*}$ . CAM3.5 shows significant differences between the age gradient vertical velocity, which is considerably faster than observed, and the tape recorder and residual circulation vertical velocities, which compare well to the observations. SOCOL and NiwaSOCOL also have large differences between the tracer-derived velocities; the tape recorder velocity is much faster than observed, while the age gradient velocity is just outside the range of observational uncertainty in the TLS and compares fairly well to the observations in the TMS. Despite very similar tracer-derived vertical velocities, SOCOL and NiwaSOCOL have very different  $\overline{w^*}$  profiles, with SOCOL's  $\overline{w^*}$  agreeing very well with the observed tracer velocities and NiwaSOCOL's  $\overline{w^*}$  being much faster than any other model's; see also Figure 4.9. EMAC and E39CA do not have an age tracer. EMAC shows very good agreement between its tape recorder vertical velocity and  $\overline{w^*}$  as well as very good agreement with the observations. The E39CA tape recorder has a layer of infinite phase speed (zero phase lag) above the tropopause, but shows rel-

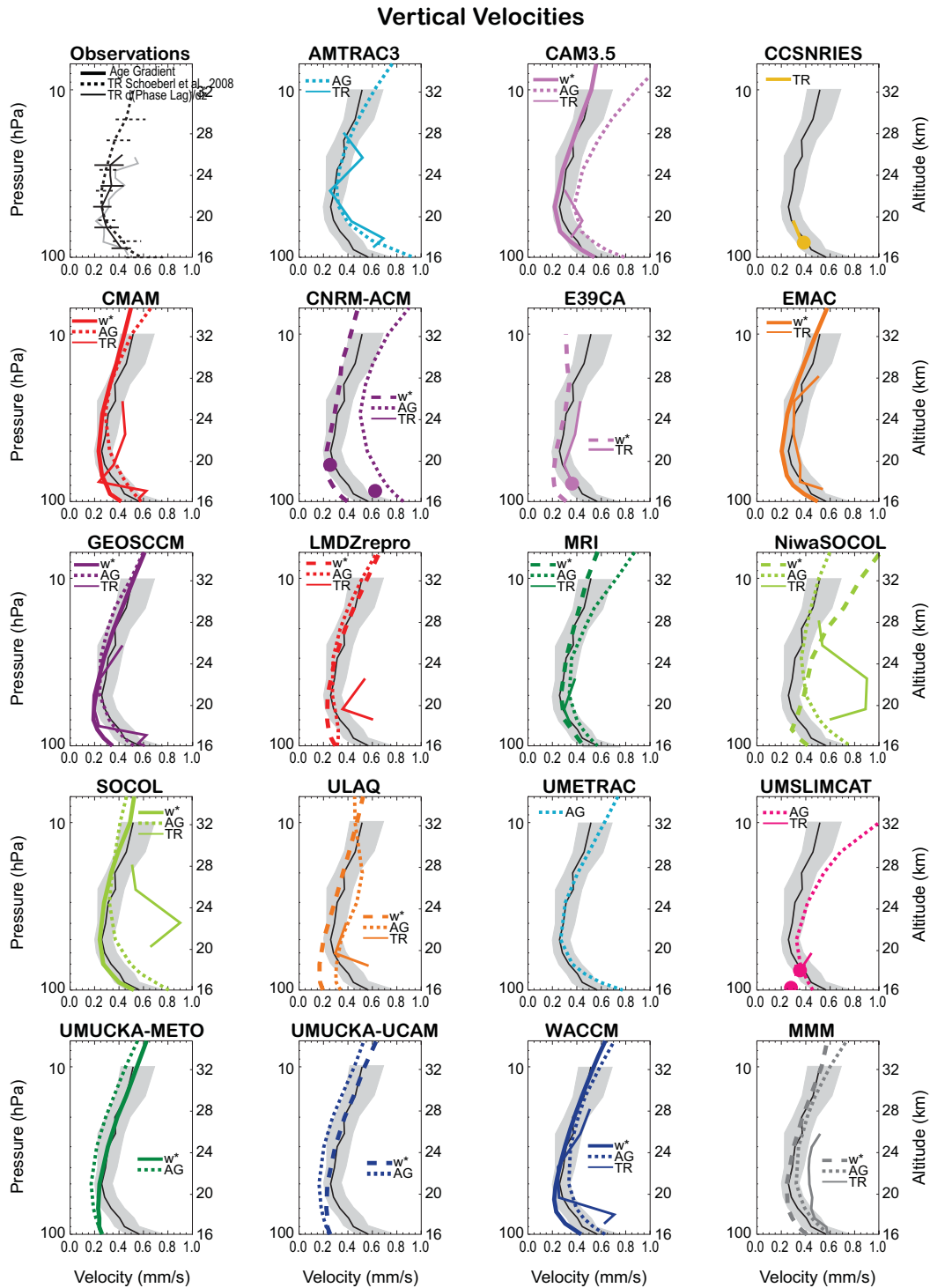


**Figure 5.6:** Comparison of the tropical vertical velocities derived from the tape recorder (TR) and mean age gradient (AG), as well as model residual vertical velocities,  $w^*$ . The top left panel shows  $w$  calculated from the observed AG with uncertainties,  $w$  calculated by Schoeberl et al. (2008) for the combined HALOE-MLS TR with uncertainties, and  $w$  calculated as a simple vertical derivative of the phase lag of the HALOE TR. The remaining panels show  $w^*$ , averaged over  $\pm 20^\circ$ , and the AG and TR  $w$ 's where available for all of the models. Tape recorder  $w$ 's are represented by large dots where the adjacent levels give infinite phase speeds. The solid black lines and grey shaded regions in the model panels are an average between the observed AG and Schoeberl et al. (2008) TR  $w$ 's and uncertainties between 90 and 25 hPa. Above and below those levels, the observed AG  $w$  and uncertainties are used.

atively good agreement with the observations and with  $\overline{w^*}$  above 80 hPa. UMUCCA-METO and UMUCCA-UCAM do not have tape recorder signals, but show relatively close agreement between their age gradient vertical velocities and  $\overline{w^*}$ , both of which are very slow in the TLS relative to the observations. The residual vertical velocity could not be obtained for AMTRAC3, CCSRNIES, UMETRAC, and UMSLIMCAT. The tape recorder and age gradient vertical velocities agree very well in AMTRAC3, and are very fast compared to the observations in the TLS. The age gradient vertical velocity is also too fast in UMETRAC just above the tropopause, but then agrees very well with observations throughout the rest of the domain. UMSLIMCAT has a layer of infinite phase speed, but overall there is reasonable agreement between the tape recorder, age gradient, and observed velocities in the TLS. In the TMS the age gradient vertical velocity in UMSLIMCAT is much faster than observed. The only vertical velocity available from CCSRNIES is from the TLS tape recorder, which has a layer of infinite phase speed below 90 hPa but then agrees well with observations.

The multi-model mean (MMM) residual vertical velocity and age gradient vertical velocity are fairly consistent with each other and agree closely with observations. The MMM tape recorder vertical velocity was calculated using only the 8 models whose tape recorders could be analysed throughout both the TLS and TMS (the infinite phase speed at the lowest level in E39CA is not included in the mean). It reflects the very fast tape recorder velocities of SOCOL and NiwaSOCOL, and is significantly faster than observations and than the other models' vertical velocities. Overall, the models present a consistent, coherent picture with respect to the transport circulation: when the tracer-derived vertical velocities agree with one another, they also agree with the observed residual vertical velocity; when there are differences between the tracer-derived vertical velocities, they also differ substantially from the residual circulation, indicating a substantial role for tracer-dependent terms in the transport circulation.

## 5.2.2. Tropical-Midlatitude Mixing

### 5.2.2.1 Tape Recorder Amplitude

The tape recorder amplitude decays with height due to both vertical diffusion and dilution by mid-latitude air. Vertical diffusion plays a modest role in the decay from 19–24 km, where ascent rates are slow and the tropics are relatively isolated, but dilution accounts for most of the attenuation of the observed signal (Mote *et al.*, 1998; Hall *et al.*, 1999). However, Hall *et al.* (1999) showed that diffusion can play a significant role in the attenuation of the water vapour tape recorder in models. Three of the models shown

here (CNRM-ACM, SOCOL, and NiwaSOCOL) have tape recorder phase speeds that are considerably faster than  $w^*$ , indicating that they may be in the “high diffusion” regime described by Hall *et al.* (1999), in which case diffusion can account for a large portion of the amplitude attenuation. Nevertheless, most of the models have  $c \approx w^*$ , indicating that they are in the “low diffusion” regime and thus the attenuation is a measure of dilution by mid-latitude air.

Figure 5.3 shows the vertical profile of the decrease in the peak-to-peak amplitude of the tape recorder water vapour anomalies relative to the maximum peak-to-peak amplitude for the models and for HALOE observations. For a given dilution profile, rapid ascent will result in less attenuation of the signal than slower ascent. To isolate the effect of mixing between the tropics and mid-latitudes as much as possible, the influence of the phase speed on the amplitude attenuation is removed by evaluating the scale height of the amplitude decay,  $H$ , relative to the vertical wavelength ( $\lambda=c*1$  year), so that the metric is  $R=H/\lambda$ , which provides a better measure of the dilution rate than  $H$  itself. As in WE08,  $H$  is determined by an exponential fit to the HALOE observations and the models, with the relative amplitude  $A/A_0$  described by  $\exp(-z/H)$ . As with the phase speed, separate fits are applied in the TLS and TMS and the maximum and minimum values of  $R$  are used as an additional measure of uncertainty so that the denominator of the WE08 metric becomes  $(R_{max} - R_{min}) + 3\sigma$ .  $R_{max}$  is given by  $H_{max}/C_{min}$ , where  $H_{max}$  is the maximum scale height that can be fit to the observations (*i.e.*, the exponential passes through the largest residual of the fit in each region), and  $c_{min}$  is as defined in Section 5.2.1.1.  $R_{min}$  is likewise equal to  $H_{min}/C_{max}$ . An observational uncertainty of 20% is estimated for  $R$ , similar to the value used by WE08.

Figure 5.4 shows  $H$  (left panels) and  $R$  (right panels) for the observations and for the models. The observational values of  $H$  are 5.3 km in the TLS and 10.0 km in the TMS, corresponding to  $R$  values of 0.5 and 0.9, respectively. These values are in good agreement with Hall *et al.* (1999). The light grey shaded areas in Figures 5.3 and in the left panels of 5.4 show  $H_{max}$  and  $H_{min} \pm 1\sigma$  in each region (with  $\sigma$  estimated as 20%, as for  $R$ ). The shaded regions in the right panels of Figure 5.4 show  $R_{max}$  and  $R_{min} \pm 1\sigma$ .  $R$  was not calculated for the CCMVal-1 models in Eyring *et al.* (2006), and it is difficult to compare the differences in the amplitude attenuation given the differences in phase speed. However, most CCMVal-1 models attenuated the tape recorder signal too strongly despite all having fast phase speeds, indicating too much dilution by mid-latitude air and/or too much vertical diffusion. Here also, most of the models attenuate the signal too quickly in the TLS compared to the observations ( $R < R_{obs}$ ). CMAM, EMAC, GEOSCCM, and ULAQ are the best performing models. All other models have values of  $R$  near or outside of the range of uncertainty in the measurements. For mod-

els with  $c \approx \bar{w}^*$ , this indicates too much mixing across the subtropics. In the TMS, WACCM is the best performing model. CMAM has extremely isolated ascent relative to the observations, with an  $R$  value of 5.2. All of the other models have  $R$  values less than the observations, ranging from  $\sim 0.6$  (AMTRAC3 and EMAC) to less than 0.35 (E39CA, NiwaSOCOL, and SOCOL), again indicating too much tropical-extra-tropical mixing and/or vertical diffusion for this limited set of models. The GEOSCCM tape recorder amplitude was not evaluated in the TMS because it increases with height over part of this region. GEOSCCM carries precipitable water too high into the stratosphere, and the increase in amplitude results from re-evaporation of condensed water.

### 5.2.2.2 Tropical CH<sub>4</sub> Vertical Gradient

Methane is long-lived in the lower and middle stratosphere but is destroyed by O(<sup>1</sup>D), OH and Cl radicals in the upper stratosphere; its annual-average photochemical lifetime is one year at 3 hPa and increases rapidly with decreasing altitude. Thus, below 3 hPa there is almost no photochemical loss and the profile's vertical gradient is primarily controlled by the balance between ascent and quasi-horizontal mixing across the subtropics. This diagnostic tests the ability of the models to represent the observed balance between these two processes, but, like the tape recorder amplitude, it is sensitive to vertical diffusion. The models are evaluated in two seasons using 9 years of HALOE CH<sub>4</sub> from 10°S-10°N. At the lowest level of the HALOE observations (68 hPa), 10 years of seasonal mean model output are normalised to the 9-year tropical mean CH<sub>4</sub> from HALOE. Model output is interpolated to the 9 HALOE vertical levels (68-3 hPa, or  $\sim 18$ -42 km with 3 km spacing) and the gradients are evaluated over three regions: TLS (68-31 hPa), TMS (31-10 hPa), and tropical upper stratosphere (TUS) (10-3 hPa). The ratio of the mixing ratios at the top and bottom of each altitude range is evaluated and compared to the observations. The HALOE uncertainties are calculated from deviations from the seasonal mean gradients, averaged over 9 years of observations, and include the effects of QBO and interannual variability.

The mixing ratio vertical gradient is evaluated rather than the mixing ratio itself so that poor transport at one level will not affect the score of the levels above it. For example, if a model has too much subtropical mixing and/or ascent in the TLS, but the right amount above, the profile in the TMS will be offset from the HALOE profile but it will have the same vertical gradient. Each model's grade is the average of the score for the gradients in the TLS, TMS, and TUS, for two seasons, January, February, March (JFM) and July, August, September (JAS).

Although the quantitative assessment is based on the gradients, for consistency with previous work (Eyring *et*

*al.*, 2006) **Figure 5.7** shows HALOE and model CH<sub>4</sub> tropical seasonal mean profiles. Many models reproduce the profiles fairly well. The bottom panel of Figure 5.7 shows that the models perform about equally well in the TLS and TMS. The spread of model performance is greater during JAS than during JFM, especially in the middle and upper stratosphere. A direct comparison to CCMVal-1 is difficult because Eyring *et al.* (2006) showed CH<sub>4</sub> profiles for March. However, it appears that the spread in model performance has decreased. Approximately the same percentage of the models show good agreement with the observations in the two assessments, but the worst-performing models are much closer to the observations in CCMVal-2 than in CCMVal-1.

It is possible to infer information about mixing in the models and compare it to the results from the tape recorder attenuation by using the ascent rate information from Section 5.2.1 and accounting for the tendency for rapid (slow) vertical transport to decrease (increase) the vertical gradient of CH<sub>4</sub> for a given tropical-mid-latitude mixing profile. The TLS and TMS definitions used here ( $\sim 18$ -24 km and  $\sim 24$ -32 km) differ somewhat from the altitude ranges used in the tape recorder attenuation analysis ( $\sim 17$ -21 km and 21-27 km, respectively, depending on the location of the water vapour minimum), but in most cases the overall behaviour of the CH<sub>4</sub> profile in each region does not depend strongly on the exact altitudes used and there is consistency between the two diagnostics. CNRM-ACM, SOCOL, and NiwaSOCOL match the observed CH<sub>4</sub> gradients well. This is not necessarily inconsistent with their very strong attenuation of the tape recorder signal, given that they may have significant vertical diffusion. However, the comparison between mixing diagnostics is difficult, both because of the direct impact of vertical mixing on tracers and because diffusion generates inconsistencies in the estimates of vertical velocity. Of the remaining 12 models that have output for both diagnostics in the TLS, all but two (EMAC and ULAQ) show qualitative agreement between the tape recorder and CH<sub>4</sub> mixing diagnostics. In both EMAC and ULAQ, the TLS CH<sub>4</sub> gradients are much stronger than observed, indicating too much mixing, while the tape recorder signal closely matches the observations. The differences in the diagnostics do not appear to be related to the differences in TLS altitudes. Three models (AMTRAC3, CMAM, and E39CA) show significant differences between the mixing inferred from the CH<sub>4</sub> gradients and that inferred from the tape recorder signal in the TMS. The tape recorder analysis implies too much mixing for AMTRAC3 and E39CA and almost no mixing for CMAM. The CH<sub>4</sub> gradients, on the other hand, indicate that CMAM and E39CA have good mixing and AMTRAC3 has too little. For AMTRAC3 and CMAM, which have the output available for the tropical age and N<sub>2</sub>O PDF mixing diagnostics, the results of the CH<sub>4</sub> analysis are supported by the



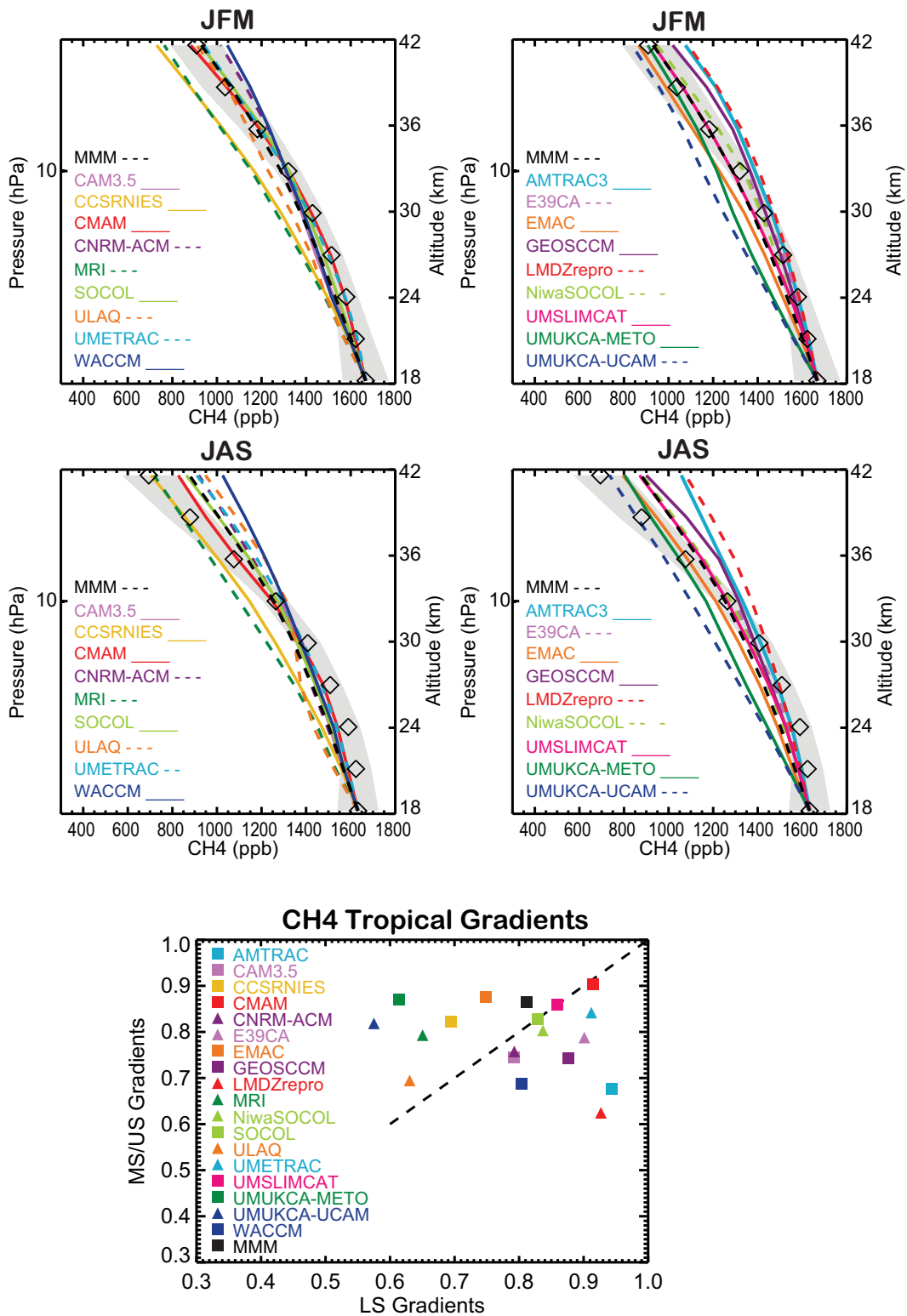


**Figure 5.7:** Tropical ( $10^{\circ}\text{N}$ - $10^{\circ}\text{S}$ )  $\text{CH}_4$  profiles from all CCMs in two seasons compared to HALOE mean profiles. Diamonds show the HALOE mean  $\text{CH}_4$  profile for Jan-Feb-Mar (top panels) and Jul-Aug-Sep (bottom panels). The black dashed line is the profile from the multi-model mean (MMM). The grey shading shows the  $1\sigma$  range of the observations. The bottom panel compares the model scores for the gradient of the  $\text{CH}_4$  profile in the LS versus the scores in the MS.

other mixing diagnostics.

Three models did not have the output for the tape recorder analysis (UMETRAC, UMUCCA-METO, and UMUCCA-UCAM) and eight others have tape recorder output but could not be evaluated in the TMS (CAM3.5, CCSRNIES, CNRM-ACM, GEOSCCM, LMDZrepro, MRI, ULAQ, and UMSLIMCAT). CNRM-ACM is discussed above. UMETRAC was found to have very good ascent using the age gradient diagnostic, and its  $\text{CH}_4$  gradients are good in both the TLS and TMS, indicating good mixing across the subtropics in both regions. The  $\text{CH}_4$  profiles in the UMUCCA models fall off very rapidly in the TLS, consistent with their very slow ascent. No additional information can be inferred about their tropical-extra-tropical mixing. In the TMS their  $\text{CH}_4$  profiles show much better agreement with observations, indicating too little mixing given their slow circulations. GEOSCCM, LMDZrepro, and MRI have good TMS tracer-derived ascent rates. The TMS  $\text{CH}_4$  gradients are too weak in GEOSCCM and LMDZrepro, indicating too little mixing, and too strong in MRI, indicating too much mixing. ULAQ has relatively fast age gradient ascent in the TMS. Its  $\text{CH}_4$  profile matches the observations in JFM, suggesting too much mixing, but the gradient is much weaker in JAS, which is consistent with the fast ascent. CAM3.5 and UMSLIMCAT have very fast TMS age gradient ascent rates. The  $\text{CH}_4$  gradients are very weak in CAM3.5, while UMSLIMCAT matches the observations fairly well. This suggests too much tropical-extra-tropical mixing (particularly in CAM3.5) given the rapid tropical ascent. However, while the residual vertical velocity was not available for UMSLIMCAT, the difference between the age gradient ascent and  $\bar{w}^*$  is large in CAM3.5, which points to the possible importance of vertical diffusion. CCSRNIES has no TMS ascent diagnostics. Its  $\text{CH}_4$  profiles fall off too quickly with height in the TMS, indicating too much mixing across the subtropics unless the ascent is very slow. The MMM  $\text{CH}_4$  gradient is slightly strong in the TLS and slightly weak in the TMS but shows overall good agreement with the observations, suggesting only small net biases in tropical-extra-tropical mixing.

### 5.2.2.3 Tropical Mean Age

The top left panel of Figure 5.5 shows the tropical ( $10^\circ\text{S}$ - $10^\circ\text{N}$ ) annual mean age profile for the CCMs, plotted with the mean age derived from  $\text{CO}_2$  (black squares) and  $\text{SF}_6$  (black diamonds with  $\pm 25\%$  error bars) (Andrews *et al.*, 2001). The tropical mean age reflects the combined effects of large-scale ascent, vertical diffusion, and horizontal mixing across the subtropics. In the TLS, the mean age is a relatively local diagnostic of the circulation and mixing, but understanding a model's age becomes more complicated higher up in the tropics, where the integrated effects of transport below make it more difficult to diagnose

reasons for deviations from the observations. Furthermore, the influence of in-mixing of mid-latitude air varies with height since the age difference increases in the TLS and decreases in the TMS.

The models are evaluated at four pressure levels in the TLS (90, 80, 70, 50 hPa) and TMS (30, 20, 15, 10 hPa), and the score for each region is the average of the scores and individual pressure levels. Most of the models have younger mean ages than the observations; they do not reproduce the rapid increase in mean age from 60 to 30 hPa, which causes an offset in the profiles throughout the TMS. Seven models fall outside the range of observational uncertainty (AMTRAC3, UMETRAC, CNRM-ACM, NiwaSOCOL, SOCOL, UMUCCA-METO, and UMUCCA-UCAM). The UMUCCA models have older than observed air throughout the tropical stratosphere, reflecting their very slow tracer ascent rates. However, they match the shape of the observed profile from 60 to 15 hPa, suggesting, in agreement with the  $\text{CH}_4$  profiles, that their mean ages in this region reflect a balance between slow ascent and very little mixing. The remaining five models have very young mean ages, and all except UMETRAC have very fast tracer-derived vertical velocities over some or all of the altitude range considered. Furthermore, there are indications that three of these models (CNRM-ACM, NiwaSOCOL, and SOCOL) may have excessive vertical diffusion. AMTRAC3's young mean ages in the TLS are consistent with its apparently rapid ascent, but it becomes progressively younger than the observations all the way up to 20 hPa despite very good ascent rates in the TMS. The  $\text{CH}_4$  gradients from AMTRAC3 suggest, in disagreement with the tape recorder analysis, that there is too little in-mixing from mid-latitudes in the TMS. The age profile supports that conclusion. UMETRAC, which diverges from AMTRAC3 in the TMS and maintains a relatively constant offset from the observations, has  $\text{CH}_4$  gradients that are much closer to observed than AMTRAC3.

Of the eight models that generally fall within the range of observational uncertainty, CAM3.5 and UMSLIMCAT have relatively good tropical mean ages that must reflect a balance between rapid net vertical transport and excessive tropical-extra-tropical mixing. LMDZrepro and ULAQ have fairly complicated ascent and mixing profiles and the tropical ages do not provide any clear indication of mixing. CMAM, GEOSCCM, MRI, and WACCM have both good tropical mean age and good ascent rates. GEOSCCM and WACCM have too little tropical-extra-tropical mixing in the TMS, which likely contributes to their slightly young ages. As with AMTRAC3, the CMAM age profile shows agreement with the  $\text{CH}_4$  gradients rather than the tape recorder analysis. The complete lack of TMS mixing implied by the tape recorder attenuation would likely yield considerably younger ages than seen here. MRI has the best tropical mean age profile despite diagnostics that indicate that it

has significantly greater than observed tropical-extra-tropical mixing. However, the fact that MRI has older ages than any of the other models with good ascent is consistent with it having more mixing than the other models. The MMM tropical mean age profile closely matches the profile of this cluster of models with good performance; the models with poor performance largely cancel each other out.

### 5.2.2.4 Tropical-Midlatitude N<sub>2</sub>O PDFs

N<sub>2</sub>O is a long-lived tracer that decreases with height in the stratosphere. Its distribution is controlled by a balance between the large-scale circulation, which acts to steepen its isopleths, and stirring by wave activity, which acts to flatten its isopleths in the stirring region but produces very strong gradients at its edges. Probability distribution functions of satellite measurements of long-lived tracers such as N<sub>2</sub>O show multiple modes, with three modes in the winter hemisphere corresponding to the tropics, the well-mixed surf zone, and the polar vortex, and two modes in the summer hemisphere corresponding to the tropics and the extra-tropics (Sparling, 2000; Neu *et al.*, 2003). The minima between the modes correspond to the strong tracer gradients marking the transitions between tropical and extra-tropical air and between the mid-latitudes and the polar vortex. PDFs of N<sub>2</sub>O have been used to assess the ability of models to reproduce tropical isolation in the middle and upper stratosphere (Douglass *et al.*, 1999; Strahan and Douglass, 2004; Gray and Russell, 1999). Douglass *et al.* (1999) used CLAES data on isentropic surfaces between 10°S and 45°N to construct N<sub>2</sub>O PDFs to benchmark the performance of the GMI-CTM. An inability to maintain the separation and the depth of the minimum between the tropical and mid-latitude modes indicates that a model has too much tropical-extra-tropical mixing, which acts to homogenize the distribution.

Recent MIPAS and MLS observations of N<sub>2</sub>O are used to determine the ability of the models to maintain the correct tropical isolation. The MIPAS N<sub>2</sub>O data are a product of the Institute of Meteorology and Climate Research in Karlsruhe (IMK), updated from Glatthor *et al.* (2005) for the period July 2002 to March 2004. The data has a small positive bias below 25 km (Gabriele Stiller, personal communication). The MLS data cover the years 2004 to present (Lambert *et al.*, 2007). Because the observational periods are relatively short and do not overlap, there are differences between the two data sets that are related primarily to QBO variability. By combining the data and using the differences between the observations to define the uncertainty, the influence of the QBO on the analysis is minimised. The models are evaluated at three isentropic levels (600 K, 800 K, and 1000 K; ~24-34 km) in each hemisphere using seasonally-averaged PDFs at the locations and seasons that MIPAS and MLS both indicate a bimodal distribution. The

quantitative assessment of the PDFs is based on how well they reproduce the observed separation and relative amplitudes of the modes of the distribution.

Observations and model output are processed in the same way. Instantaneous profiles are binned according to season and isentropic level for each hemisphere (NH: 10°S-45°N; SH: 45°S-10°N). All available data for the observational periods of each instrument are used. The model analyses use instantaneous data from the most recent 4-5 years of the REF-B1 integrations. The characteristics of the PDFs do not tend to be very sensitive to the chosen period. To remove any bias in the N<sub>2</sub>O mixing ratio, the PDFs are re-scaled to give a mean value of zero for the distribution. The relative maximum on each side of zero is determined. To determine whether the maxima are well separated, the sensitivity of the location of the maxima to small offsets with respect to zero are tested. If the same maxima are detected, it is assumed that the maxima are well separated, and the relative amplitude (ratio of the right hand peak over left hand peak amplitude) and peak-to-peak separation (difference between the N<sub>2</sub>O values for the right peak minus the left peak) are calculated.

The uncertainty is estimated by calculating the relative difference between MIPAS and MLS, so that the metric is

$$1 - \frac{|X_{mod} - X_{obs}|}{n|X_{MIPAS} - X_{MLS}|}, \quad (5.2)$$

with  $X_{obs} = (X_{MIPAS} + X_{MLS})/2$ , for each hemisphere at each isentropic level during each season. The separation is generally easier to capture than the relative amplitude and can be tested more stringently, so  $n=1$  is used for the separation and  $n=2$  for the relative amplitude. If the model does not have a bimodal PDF, it scores zero. The final grade of the model is averaged over both hemispheres for all of the isentropic levels and seasons in which MIPAS and MLS both show unambiguously bimodal distributions (12 out of a possible 24).

**Figure 5.8** shows the N<sub>2</sub>O distribution as a function of potential temperature in the NH spring for the MIPAS and MLS observations and the 16 models that submitted the necessary output for this diagnostic. While this figure illustrates model behaviour for only one season and hemisphere, it provides a good example of model performance. CAM3.5 and ULAQ do not show a good barrier to subtropical mixing. All other models have clearly bimodal distributions at most levels 600 K-1000 K. However, CCSRNIES, EMAC, and UMSLMCAT do not show enough separation between the tropical and mid-latitude peaks at many levels, while GEOSCCM, UMUCKA-UCAM, UMUCKA-METO, and WACCM show too much separation. **Figure 5.9** shows the PDFs for NH and SH spring at a single level (800K, ~10 hPa). While there are significant differences between the NH and SH in both the

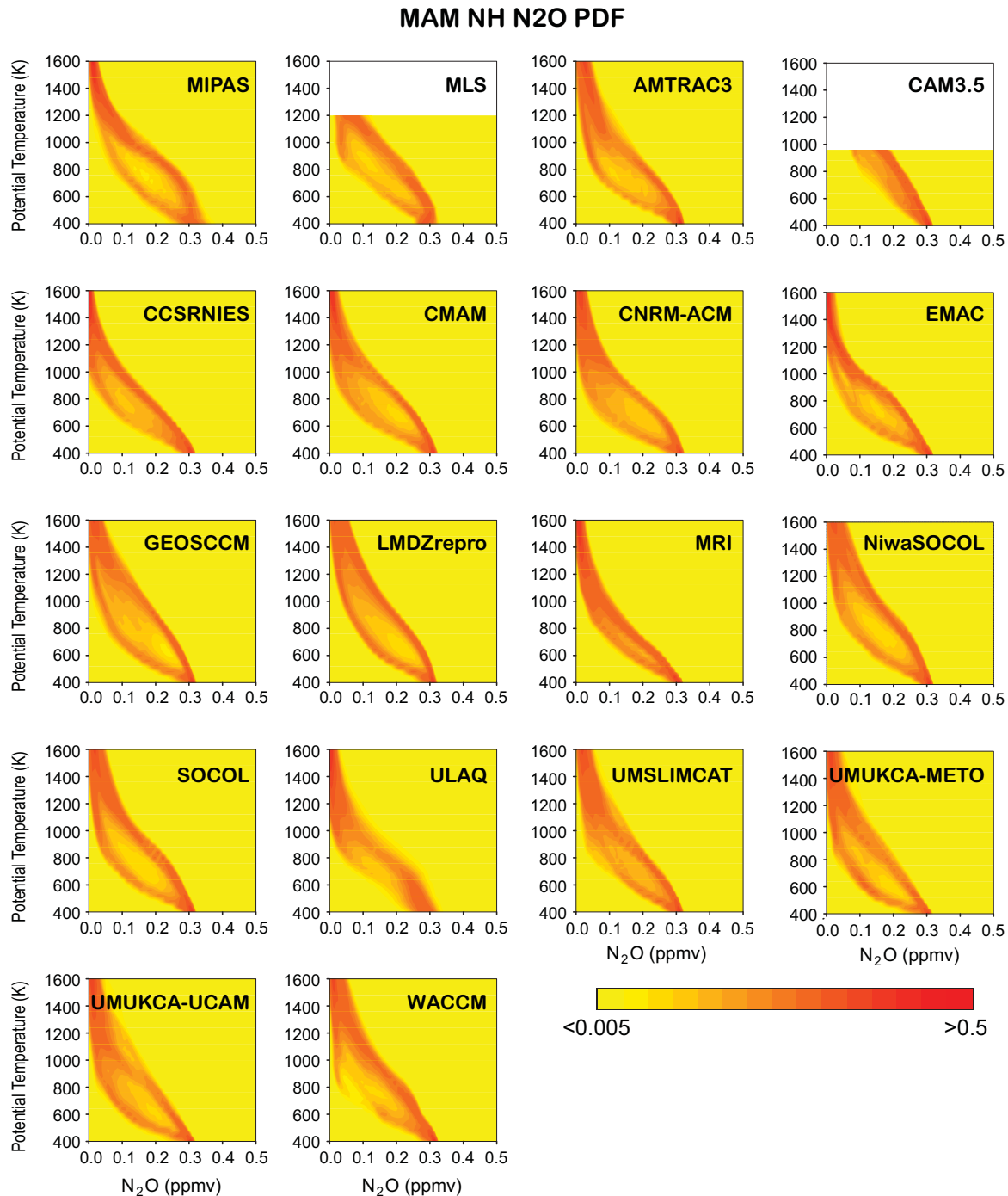


**Figure 5.8:** Contoured probability distribution functions of  $N_2O$  for  $10^{\circ}S-45^{\circ}N$  for NH spring (March-April-May) for 16 CCMs. MIPAS and MLS observations are shown in the first two panels. The contour interval is the same for all plots, and is given with the observations. Deep orange shows the mixing ratio of the most probable  $N_2O$  values. Both MIPAS and MLS show a deep minimum (yellow) in their bimodal PDFs for levels 600 K-1000 K ( $\sim 24-34$  km). This indicates a strong barrier to tropical-mid-latitude mixing in the NH during this season.

observations and the models, the model behaviour is generally consistent in the two hemispheres. Exceptions are CAM3.5, which does not have a bimodal distribution in the NH but shows a clearly bimodal distribution in the SH (though the peaks are not well-separated); LMDZrepro,

which shows good separation between the peaks in the NH but too much separation in the SH; and WACCM, which shows too much separation between the peaks in the NH but very good agreement with observations in the SH. On average, AMTRAC3, CMAM, GEOSCCM, LMDZrepro,

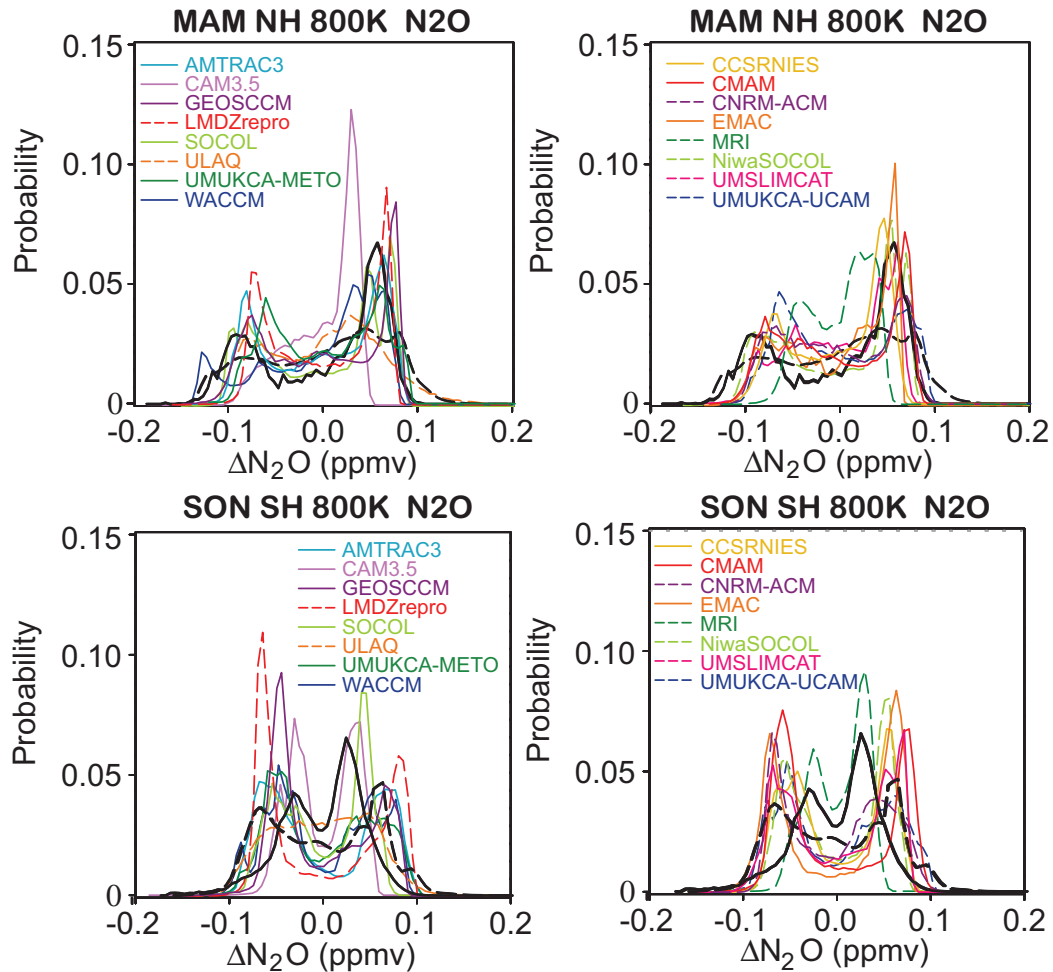


**Figure 5.9:** Probability distribution functions of  $N_2O$  on the 800 K surface for NH spring (top panels) and SH spring (bottom panels). The models are split into two panels for clarity. For the observations and each CCM,  $N_2O$  values have been scaled so that the mean value of the distribution is zero. MIPAS observations are black solid lines, MLS observations are black dashed lines. MIPAS and MLS data are from different years. Although they do not show the same separation, both sets of observations are clearly bimodal at these levels in these seasons.

SOCOL, NiwaSOCOL, and WACCM show very good performance and CAM3.5, MRI, and ULAQ show the poorest performance on this diagnostic. The results for SOCOL and NiwaSOCOL are somewhat surprising given that these two models were shown to have serious transport problems below  $\sim 26$  km. However, the  $N_2O$  PDFs are evaluated from  $\sim 24$ – $34$  km, where these models show much better agreement with other observations.

### 5.3 Transport Diagnostics for the Extra-tropics

Trace gas composition in the extra-tropics is affected by many seasonally varying processes. At 70 hPa, the net vertical motion of the annually-averaged Brewer-Dobson circulation equatorward of  $40^\circ$  is upward while poleward

of  $40^\circ$  it is downward (Rosenlof, 1995). Young air ascending in the tropics is exported to the mid-latitudes by extra-tropical planetary wave activity, which varies in strength with height and season. In summer, mixing between the mid- and high latitudes is weak because stirring by planetary wave activity is at a minimum. From late fall through early spring, the polar vortex forms, creating a barrier to transport between the mid- and high latitudes. Inside the vortex there is strong, largely unmixed descent, particularly in the Antarctic. In the mid-latitudes, meridional gradients are weak as a result of mixing by strong planetary wave activity (the ‘surf zone’), particularly in the NH. The extra-tropical diagnostics presented here cannot isolate and evaluate the effects of a single process, rather, they evaluate the net effect of multiple transport processes. Taken together, these diagnostics evaluate the integrated effects of transport on extra-tropical trace gas composition.

### 5.3.1 Integrated processes affecting extra-tropical composition

#### 5.3.1.1 Mid-latitude Mean Age

Mid-latitude mean age is influenced by the ascent rate in the tropics, the strength of mixing across the subtropical barrier, and the strength of polar descent and degree of vortex isolation. In Section 5.2.1.2, mid-latitude mean ages between 10-90 hPa derived from balloon-borne  $\text{CO}_2$  and  $\text{SF}_6$  profiles from 35°N-45°N (Engel *et al.*, 2009) were combined with tropical mean age profiles to assess tropical ascent rates. The NH mid-latitude mean age is evaluated on 4 levels in the LS (50-90 hPa) and 4 in the MS (30-10 hPa). In the SH, the only mid-latitude mean age data available are for ~50 hPa (Figure 5.5, lower right panel); these data are used in the calculation of the average mean age grade, defined in the Section 5.5.2.. The essential features of the NH mid-latitude mean age profile are a rapid increase in age from 1 to 4.5 years through the LS and nearly constant age from 24-32 km (~30-7 hPa). Below 70 hPa, most models fall within the uncertainties of the observed mean age, but above 40 hPa, 10 CCMs have ages completely outside the  $1\sigma$  uncertainty range. Eight are too young and two are too old.

AMTRAC3, CNRM-ACM, NiwaSOCOL, and SOCOL have the youngest LS mid-latitude age profiles. CAM3.5, UMETRAC, and UMSLIMCAT are slightly older but still 1-1.5 years younger than the observationally-derived profiles shown in Figure 5.5. Many of these models have been diagnosed with fast tracer-derived tropical ascent and some have indications of excessive vertical diffusion, both of which likely play a role in their young mean ages here. CMAM, GEOSCCM, and MRI have the best agreement over the entire altitude range. WACCM is slightly young and ULAQ shows mixed agreement with altitude. The two UMUKCA models are 1-1.5 years older than observed, and their age is explained by slow tropical ascent.

The agreement between models and observations in the SH mid-latitudes is very similar: The same four models plus UMETRAC have the youngest ages as in the NH mid-latitude comparison. The two UMUKCA models are ~2 years older than the observations indicate. CMAM is slightly young, but the remainder of the models show good agreement. Mid-latitude mean age grades play an important role in calculating each model's globally averaged mean age grade (Section 5.5.2).

#### 5.3.1.2 Fractional Release of $\text{Cl}_y$

The fractional release of a long-lived source gas such as  $\text{CF}_2\text{Cl}_2$  (CFC-12) or  $\text{CFCl}_3$  (CFC-11) is a measure of

how much of the source gas has been photolysed or oxidised since entry in the stratosphere. It is defined as  $f_r = (1 - X/X_{\text{entry}})$  where  $X$  is the mixing ratio at a particular location and  $X_{\text{entry}}$  is the value at the time of stratospheric entry. As CFC photolysis rates are a function of altitude and latitude, fractional release depends strongly on transport pathways in a model. Schauffler *et al.* (2003), using trace gas measurements made by instruments on the ER-2 during the NASA SOLVE campaign, show a compact relationship between the mean age of air and the fractional release for  $\text{CF}_2\text{Cl}_2$  and  $\text{CFCl}_3$ . This compact relationship is robust in the lower stratosphere, and does not depend on the latitude and altitude of the measurements up to the maximum altitude of the ER-2 (~50 hPa). The mean age of a parcel is the average over all of the elements (*i.e.*, transport pathways) that contribute to the parcel in question. Hall (2000) shows that in general, elements with older ages have ascended to higher altitudes, experiencing more rapid photolysis of long-lived gases than elements that have not been transported above the ozone maximum. Douglass *et al.* (2008) show that the local mixing ratio (and thus the fractional release) depends on the maximum altitude obtained by various elements of the age spectrum. The simulated relationship between fractional release and mean age thus depends on several aspects of the simulation, including the age spectrum, the maximum altitude reached by the older elements in the age spectrum, and the photolysis field.

The simulations analysed by Douglass *et al.* (2008) all used the same photolysis code, and differences in the simulated relationships between fractional release and mean age were clearly the result of differences in transport. Because the simulations analysed here did not use a common set of photolysis rates, and some use a parameterised fractional release rate based on age of air, a quantitative transport diagnostic cannot be calculated; differences in photolysis and transport both contribute to differences in the fractional release relationship. In general, simulations with greater values of fractional release for a given mean age can be thought of as having more photolytic loss, and, since the atmospheric burden of CFCs is almost completely controlled by the tropospheric burden and the boundary conditions, these simulations are associated with shorter CFC lifetimes. The evolution of active chlorine in these models would differ widely if they employed flux boundary conditions (controlling the atmospheric input) rather than mixing ratio boundary conditions (controlling the atmospheric burden).

Ten CCMs had the necessary CFC and mean age output for this diagnostic. The simulated relationship between fractional release and mean age is shown for  $\text{CF}_2\text{Cl}_2$  and  $\text{CFCl}_3$  in Figure 5.10. For CNRM-ACM, MRI, SOCOL, and WACCM, the simulated values of fractional release for  $\text{CF}_2\text{Cl}_2$  are significantly greater than observed for a specified mean age. Since fractional release is strongly altitude

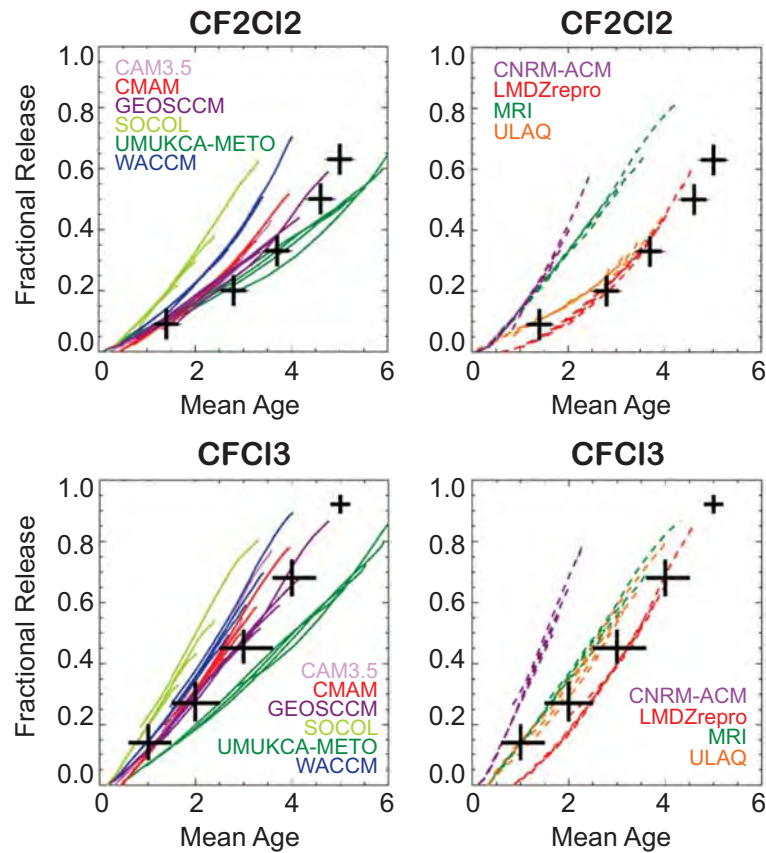


**Figure 5.10:** Fractional release of inorganic Cl ( $Cl_y$ ) as a function of mean age of air in the lower stratosphere, where mean age was derived from  $CO_2$  measurements. The observations used include a large suite of chlorine-containing organics and  $CO_2$ , measured simultaneously by ER-2 instruments. Schauffler et al. (2003) derived the empirical relationship between fractional release of Cl from these species and mean age and their results, including uncertainties, are plotted with large crosses. Model curves that are steeper than observed indicate that more  $Cl_y$  is released for a given mean age than observed. If all models use the same photolysis rates, this diagnostic reflects only differences in transport.

dependent, the curves falling to the left of the observations suggest that these models quickly transported air to high altitudes. For CNRM-ACM and SOCOL, this is consistent with diagnoses of fast net vertical transport in Section 5.2. However, LS ascent in MRI and WACCM was found to be fairly good, so differences in photolysis rates may play a role; see Chapter 6.3.1 for details. Interestingly, MRI is the only model to have nearly identical fractional release curves for  $CF_2Cl_2$  and  $CFCl_3$ , while the empirical curves (Figure 5.10) show  $CFCl_3$  to be released at much younger mean ages than  $CF_2Cl_2$ . This suggests that MRI may use the  $CFCl_3$  photolysis rate for  $CF_2Cl_2$ .

Models that have young mean age at all latitudes in the lower stratosphere do not span the same range of observed mean ages (1-4.5 years); this is seen in CAM3.5, CMAM, CNRM-ACM, and SOCOL. Only UМУKCA-METO has curves falling to the right of the observations, meaning less photolysis of CFCs for a given mean age. This is consistent with the diagnosis of slow ascent, implying long trans-

port times to high altitudes. The models that best show the observationally-derived relationship between fractional release and mean age are CMAM, GEOSCCM, LMDZrepro, and ULAQ. It is interesting that LMDZrepro agrees poorly at young ages – this is consistent with very slow ascent rates diagnosed from the age gradient in the lowest levels of the tropics. For  $CFCl_3$ , all of the models except MRI respond in the correct sense, *i.e.*, fractional release values for a given mean age are larger than for  $CF_2Cl_2$ , given the more rapid photolysis rate for  $CFCl_3$ .

### 5.3.1.3 Northern mid-latitude $Cl_y$ time series

This diagnostic evaluates the time evolution of the annual mean inorganic chlorine ( $Cl_y$ ) in the NH mid-latitude LS. As described in the previous section,  $Cl_y$  in the mid-latitude lower stratosphere depends on the photolysis rates of the major organic species, such as CFC-11 and CFC-12, and on the mean age of air because it is an indicator of the

maximum altitude to which a parcel has travelled. If the same photolysis rates were used in all CCMs,  $Cl_y$  would be a diagnostic that compares only transport between the models; however, this is not the case for all the CCMVal-2 models. The disagreement between the models and the observations depends on both the photolysis fields and transport differences.

The estimates of observed  $Cl_y$  are based on an analysis of UARS HALOE and Aura MLS HCl measurements (Lary *et al.*, 2007). The observed mean values and uncertainties are the same as those used in WE08. The vortex grade is the average of the comparisons in October 1992 and 2005, and the mid-latitude grade is the average of 7 annual means. In the models, all chlorine comes from long-lived source gases emitted at the surface, primarily  $CF_2Cl_2$  and  $CFCl_3$ , but other HCFC and CFC species contribute nearly 50% of the total Cl emitted. Maximum Cl emissions occurred in the mid-1990s and equaled roughly 3.7 ppb Cl.

**Figure 5.11** shows the time series of annual mean zonal mean ( $35^{\circ}N$ - $60^{\circ}N$ )  $Cl_y$  at 50 hPa for 18 models and

the observations. All models show increasing  $Cl_y$  from 1960-1990, and all but UMUKCA-METO show  $Cl_y$  leveling off by the mid- or late 1990s in the lower stratosphere. (The UMUKCA-METO increase in the late 1990s and its high  $Cl_y$  mixing ratio are caused by a known error in the model's HCl washout; see Chapter 2.) The observations cover the time period from 1992 until 2004 with values between 1.7 and 1.9 ppb. There is considerable model spread, but nearly all models fall within the uncertainty of the measurements. CAM3.5 is the only model that is consistently below the uncertainty range of the observations; it has young mid-latitude mean age but a good fractional release curve, so the low  $Cl_y$  may simply reflect young age. Young mid-latitude mean age may also be to blame for low  $Cl_y$  in AMTRAC3. CMAM  $Cl_y$  is also quite low, only getting within the uncertainty range for a few years, which is surprising given its good mean age and reasonable fractional release curves. MRI and UMUCKA-UCAM are the only models with  $Cl_y$  consistently higher than observed, lying outside the uncertainty range in most years. For the

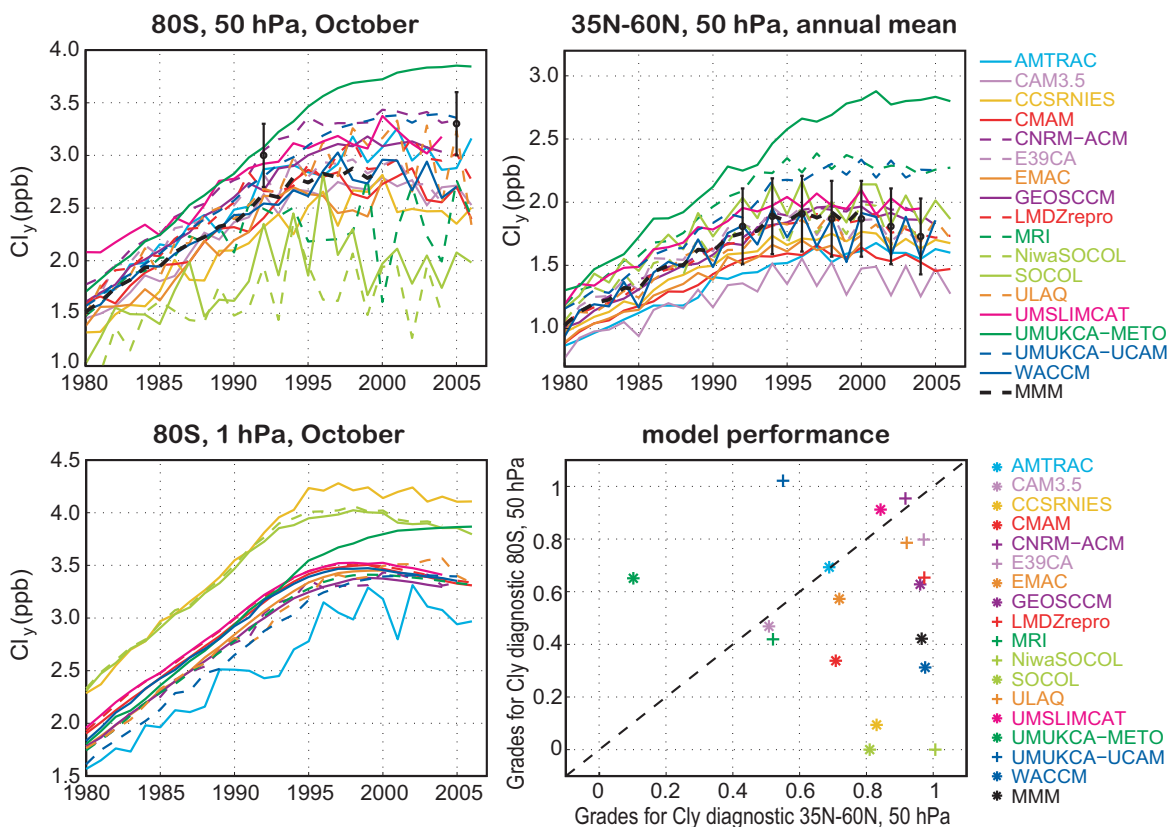


**Figure 5.11:** Modelled and observed  $Cl_y$  times series for 1980-2006. Estimated observational uncertainties are shown by the vertical black bars. Upper left:  $80^{\circ}S$  October  $Cl_y$  time series, 50 hPa. Upper right: NH mid-latitude  $Cl_y$  time series,  $35^{\circ}N$ - $60^{\circ}N$ , 50 hPa. Lower left:  $80^{\circ}S$  October  $Cl_y$  at 1 hPa. Lower right: grading summary for mid- and high latitude  $Cl_y$  diagnostics.  $Cl_y$  at 1 hPa is not a graded diagnostic but is included as a check for maximum  $Cl_y$  in a model. At 1 hPa, nearly all Cl-containing organics have been photolysed.  $Cl_y$  at this level should never be greater than the total Cl emitted at the surface. The prescribed REF-B1 and REF-B2 source gas boundary conditions do not exceed  $\sim 3.8$  ppb in any year.



latter this may be related to very old mid-latitude mean age that has permitted air parcels more time for photolysis, but for MRI, which has good mid-latitude mean age, the high  $Cl_y$  may indicate a chemical problem. The MRI CFC-12 fractional release curve (Figure 5.10) lies well to the left of the observations, indicating much greater photochemical release of Cl for a given mean age.

This diagnostic was applied to CCMVal-1 models in WE08. CCSRNIES, LMDZrepro, and UMSLIMCAT have virtually the same mid-latitude  $Cl_y$  as they did in CCMVal-1. CMAM, SOCOL, ULAQ, and WACCM all increased a few tenths of a ppb since CCMVal-1, improving their agreement with observations. GEOSCCM also increased slightly but its agreement is the same. In CCMVal-1, MRI was too high and its  $Cl_y$  increased in the 2000's instead of levelling off. Now it levels off appropriately but it is still too high by  $\sim 0.5$  ppb in the 2000's. AMTRAC3 was unrealistically high, 3 ppb, but is now slightly lower than observed ( $\sim 1.6$  ppb). E39CA was  $\sim 1$  ppb low in CCMVal-1 but now agrees very well with observations. However, E39CA's  $Cl_y$  can not be evaluated as a transport diagnostic because the abundance is influenced by the  $Cl_y$  boundary condition imposed at the model lid (10 hPa).

### 5.3.1.4 $N_2O$ annual cycle in the LS

This diagnostic assesses whether a model represents the observed balance of seasonally varying transport processes affecting the mean composition of air in the descending branch of the Brewer-Dobson circulation at 50 and 100 hPa. In the extra-tropics, increasing  $N_2O$  in spring and summer is the result of quasi-horizontal transport of young air from low latitudes, while decreasing  $N_2O$  in fall and winter shows the influence from descending, photochemically aged air. The balance of these transport processes is evaluated using monthly mean changes in the mean extratropical  $N_2O$ . Monthly tendencies are computed using the zonal monthly area-weighted means of Aura MLS  $N_2O$  at 50 and 100 hPa between  $45^\circ$ - $89^\circ$  in each hemisphere, averaged over a 4-year period (9/2004-8/2008). The models' outputs are normalised to a surface value of 320 ppb for consistency with the Aura MLS data set used. Because MLS  $N_2O$  has a vertical resolution of  $\sim 3$  km, it was uncertain whether a model diagnostic calculated from only a single level would accurately reflect the vertical sensitivity of the MLS measurements. As an experiment, model levels above and below the MLS levels were combined in a weighted average reflecting the sensitivity of MLS retrieval to nearby pressure levels (Livesey *et al.*, 2007). It was found that this averaging was unnecessary and that models' monthly trends were nearly the same as when calculated using a weighted mean on a single pressure level (50 or 100 hPa). Model behaviour is evaluated with monthly ten-

dencies and the overall grade reported is the mean of 12 monthly grades. The standard deviations were calculated for each monthly mean from daily data and include inter-annual variability for the 4 years of MLS data used.

The  $N_2O$  monthly tendencies for 50 hPa and 100 hPa from the models and MLS with  $1\sigma$  uncertainty are shown in **Figure 5.12** (SH) and **Figure 5.13** (NH). The models' performance at 50 hPa is remarkable: in both hemispheres, all models are able to realistically simulate the seasonal cycle. At 100 hPa in the NH, 15 models perform well while UMUKCA-METO, UMUKCA-UCAM, and GEOSCCM cycles indicate too much low latitude influence too early in spring. In the SH at 100 hPa, all models perform adequately in most months, although nearly all models miss the decrease in  $N_2O$  in spring and the large increase that follows in early summer (December), suggesting that low  $N_2O$  from the Antarctic vortex does not have enough impact at 100 hPa. The two UMUKCA models, EMAC, and ULAQ are the only models that produce the sharp rise in  $N_2O$  seen in early summer, but they all start to increase two months early. The UMUKCA models may capture this feature because of the very old air found in the Antarctic vortex, which gives them unrealistically low  $N_2O$ . When the vortex breaks down in late spring/early summer, the much younger low latitude air (*i.e.*, with high  $N_2O$ ) has a larger impact on the mean value due to the large contrast in mixing ratios.

Overall, models behave very well at 50 hPa, and although they do not perform as well at 100 hPa, all models perform roughly the same there. The seasonal cycles are worst in the SH at 100 hPa, where most models lack a low latitude (quasi-horizontal) influence in early fall, as well as strong downward influence in mid-spring. This suggests that the strength of the circulation is too weak in the lowest levels of the SH stratosphere. While this diagnostic may be useful for identifying large problems in the seasonality or strength of the Brewer-Dobson circulation, in the case of the 18 CCMs evaluated here, this diagnostic shows that seasonality of the LS circulation is quite similar in all models.

### 5.3.1.5 Mean age at $60^\circ$ N/S

The mean age of air at  $60^\circ$  is influenced both by descent of older air (during fall and winter) and by horizontal mixing with mid-latitude (younger) air at a latitude that is generally outside the vortex. The observations used to derive the  $60^\circ$ N mean age were collected in all seasons and reflect both of these transport processes. The  $60^\circ$ S mean age was derived from observations between April and October, and thus has less influence from younger, low latitude air. The diagnostic is based on the mean ages and uncertainties from Andrews *et al.* (2001), and model mean ages are averaged over  $55^\circ$ - $65^\circ$  in each hemisphere. Low mean age

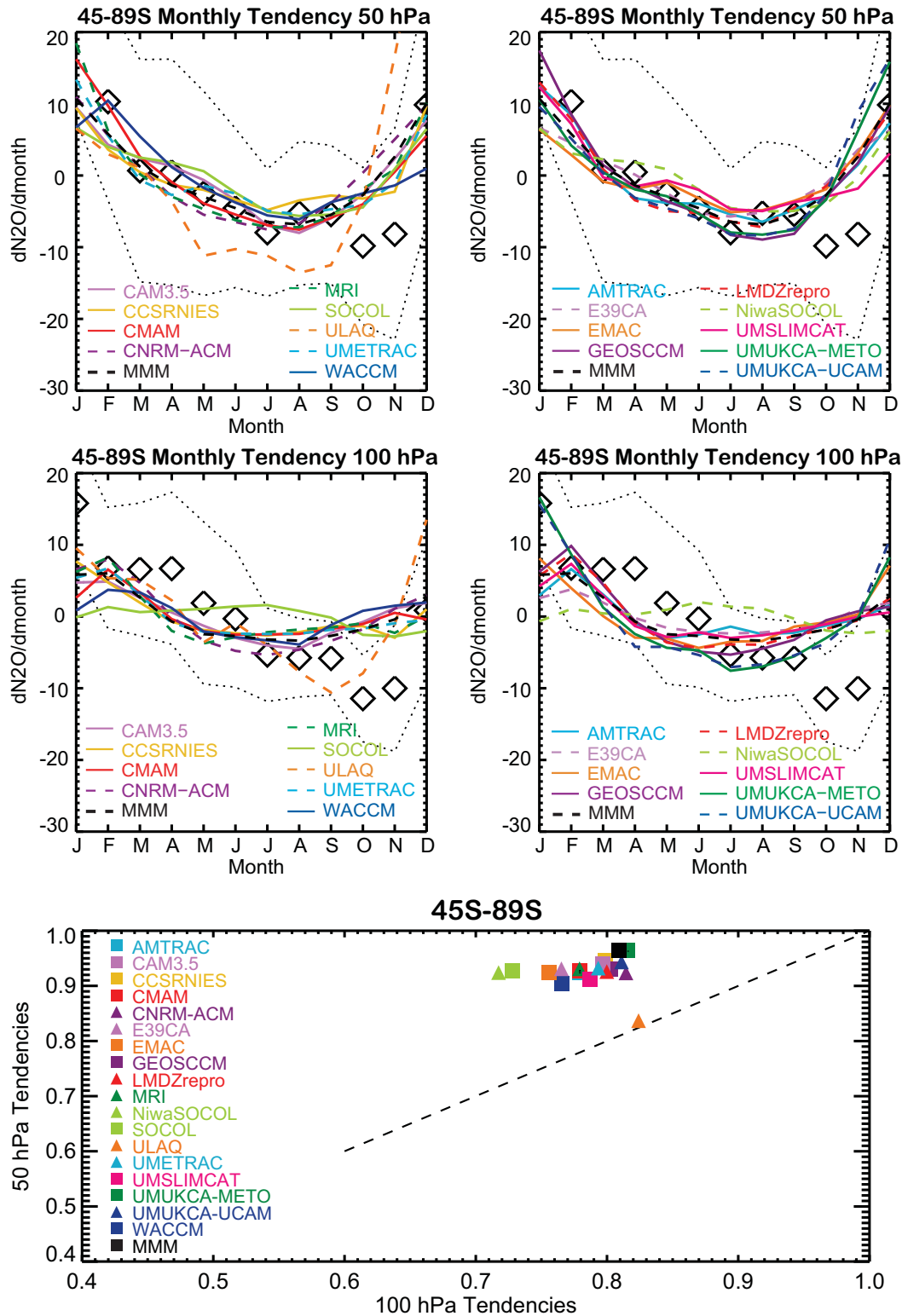


**Figure 5.12:** Area-weighted mean over 45°S-89°S of monthly mean N<sub>2</sub>O tendencies at 50 hPa and 100 hPa. The monthly means and 1σ uncertainties for the observations, shown with black diamonds and dotted lines, are calculated from 4 years of Aura MLS N<sub>2</sub>O observations. The mean annual cycle in the extra-tropics shows the seasonally varying balance between descent due to the Brewer-Dobson circulation and quasi-horizontal transport of young (high N<sub>2</sub>O) air from the tropics. All models perform well for most of the year but show deficiencies in the austral spring.

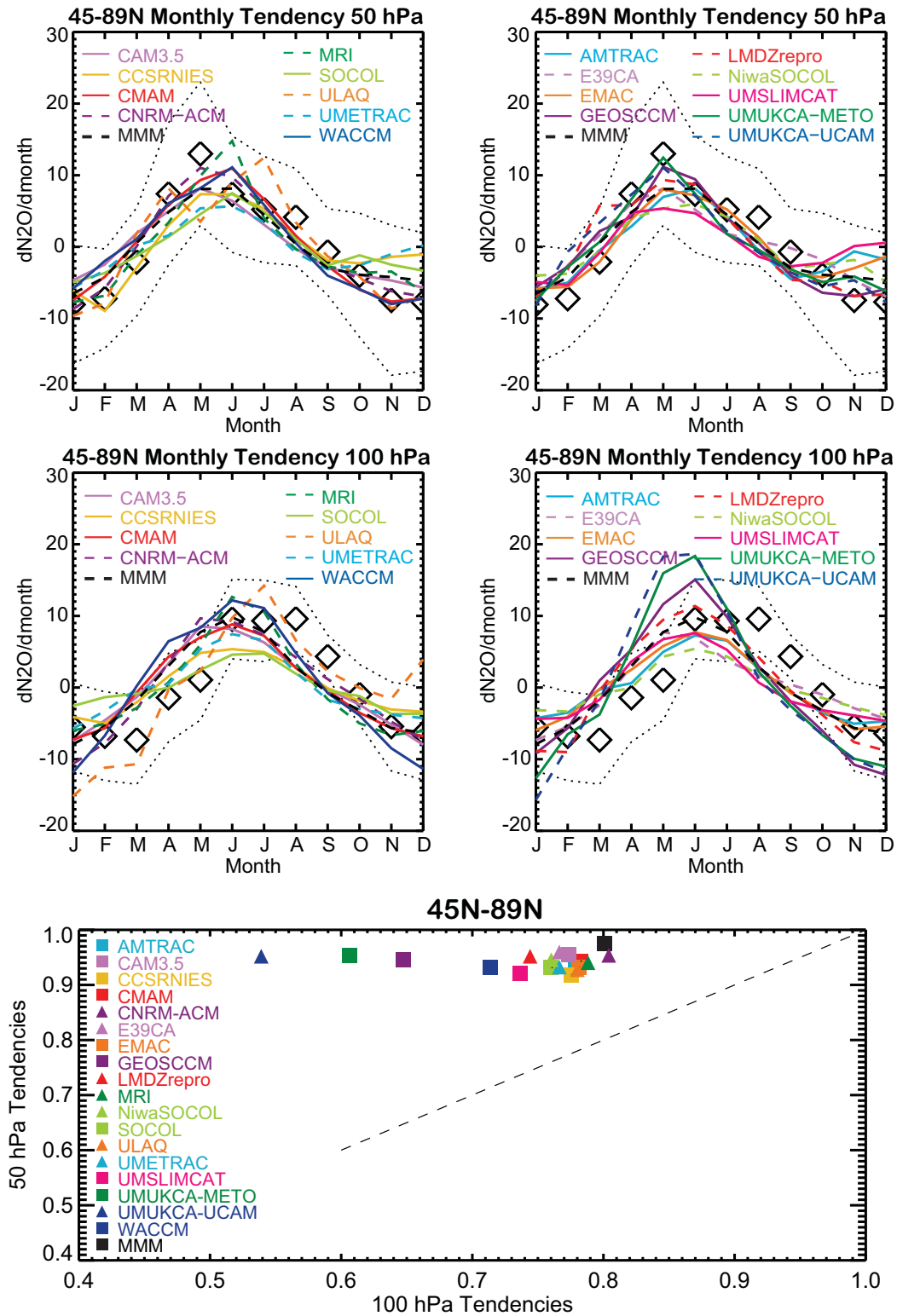


**Figure 5.13:** Same as Figure 5.12, but for 45°N-89°N. All models perform very well at 50 hPa in the NH, but not as well at 100 hPa. The late winter/spring  $N_2O$  increase occurs earlier than observed in several models and all show a summer time decrease that occurs two months too soon. This may impact the seasonally varying composition of the lowermost stratosphere.

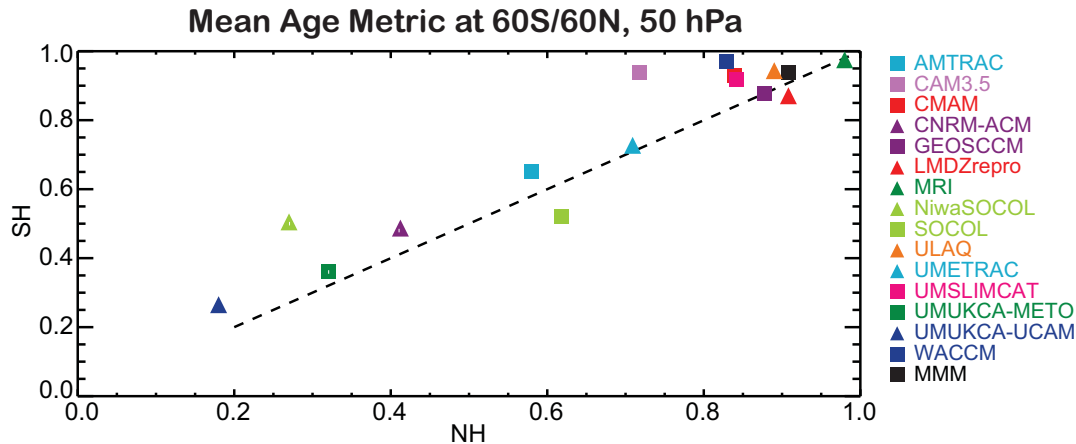


**Figure 5.14:** Performance metrics for model mean age of air at 60°N and 60°S, 50 hPa. About half the CCMs have mean age in close agreement with the observations. Most models perform equally well in both hemispheres.

at high latitudes may be an indication of weak descent, poor vortex isolation, or fast circulation, all of which can lower mean age everywhere. The models' results, shown in **Figure 5.14**, illustrate that the models perform equally well in both hemispheres.

Model and empirically derived mean age as a function of latitude at 50 hPa is shown in **Figure 5.5**. CNRM-ACM has the youngest age, 3 years or less at all latitudes. NiwaSOCOL, SOCOL, and AMTRAC3 are slightly older but are 1–1.5 years younger than observed at 60°. All four have polar ages outside the uncertainties and all except AMTRAC3 have indications of excessive vertical diffusion. The two UМУKCA models have been diagnosed with slow circulations and their mean ages are much greater than observed in both polar regions (> 6 years). The nine remaining models that can be evaluated fall within the uncertainty of the observations most of the time. The best mean ages are found in CAM3.5, CMAM, GEOSCCM, LMDZrepro, MRI, ULAQ, UMSLIMCAT, and WACCM.

Mean age at 60°N/S was not explicitly evaluated in CCMVal-1, however, comparison to **Figure 10** in Eyring *et al.* (2006) shows that the bulk of the models have 60°N/S mean ages very similar to the age shown in this evaluation (**Figure 5.5**). The models with the most noticeable change at these latitudes are UMETRAC (was ~3 years, now has increased by ~0.5 year), MRI (decreased from ~6 years to ~4.5 years), and UMSLIMCAT (was > 5 years at 60°S but it now just under 4 years). These changes improved the agreement with observations for UMETRAC and MRI.

### 5.3.2 Polar processes

#### 5.3.2.1 Antarctic Spring CH<sub>4</sub> PDFs

This diagnostic uses 9 years of Antarctic UARS

HALOE CH<sub>4</sub> and temperature profiles to examine the degree of vortex isolation in early spring at 13 levels from 400 to 2000K (~68–1 hPa); it is similar to the vortex isolation diagnostic developed in Strahan and Polansky (2006). The HALOE data set used spans the period 1993 to 2001 and includes profiles from 68°S–78°S from October to mid-November. Because of HALOE's small daily spatial coverage it is not possible to calculate an area-weight probability distribution function (PDF). The HALOE data shown are simply distributions of the observed mixing ratios within the noted latitude range, which is not uniformly sampled. The months chosen for this evaluation are constrained by the sampling pattern of the HALOE instrument and the UARS orbit; latitudes poleward of 60° are sampled only in two seasons per year in each hemisphere. The models are evaluated over a relatively large latitude range (50°–80°), so that a model having a particularly large vortex will not get a low score simply because the location of the barrier is equator-ward of 68°S. All models except EMAC show a transition to easterlies at 60°S occurring after October (see **Figure 4.2**), so this evaluation is made before vortex breakdown occurs. For EMAC, the October transition to easterlies occurs only in the upper stratosphere.

All HALOE high latitude CH<sub>4</sub> data from the 9-year period were interpolated to 13 isentropic surfaces and then binned to create the contoured distributions shown in **Figure 5.15**. Where the distributions are bimodal, the peak with the lower mixing ratio indicates vortex air, and the other peak identifies the most probable mid-latitude mixing ratio in this latitude range. PDFs for the models are calculated at each of 13 isentropic levels and are defined as bimodal if both peaks have a Gaussian shape. In **Figure 5.15**, the key features shown by the HALOE vortex distribution at 700 K and above are a lack of a vertical gradient, a narrow distribution, and low mixing ratios, all of which indicate very isolated descent and little interannual

variability. Below 700 K, bimodal distributions have deep minima, indicating that the vortex is isolated, but vortex air found at these levels has greater influence from younger air (*i.e.*, higher  $\text{CH}_4$ ).

The HALOE most probable value (MPV) profiles and those from 14 CCMs are shown in **Figure 5.16**. Grading is based on the difference between mid-latitude and vortex MPVs (MPV2-MPV1, or  $\Delta\text{MPV}$ ). When a model distribution has a single peak,  $\Delta\text{MPV}$  is set to zero. Because

interannual variability in the vortex is low, and the quantity evaluated is the difference between two measurement means, the HALOE  $\Delta\text{MPV}$  uncertainty is quite low, probably less than 10%. The diagnostic identifies whether the mid-spring Antarctic vortex has an appropriate barrier to transport at 13 levels from 450-1300 K, based on the separation of the mid-latitude and vortex MPV profiles. At 400 K and above 1300 K, the distribution has only 1 peak and  $\Delta\text{MPV}$  is zero. At 400 K the single peak distribution is

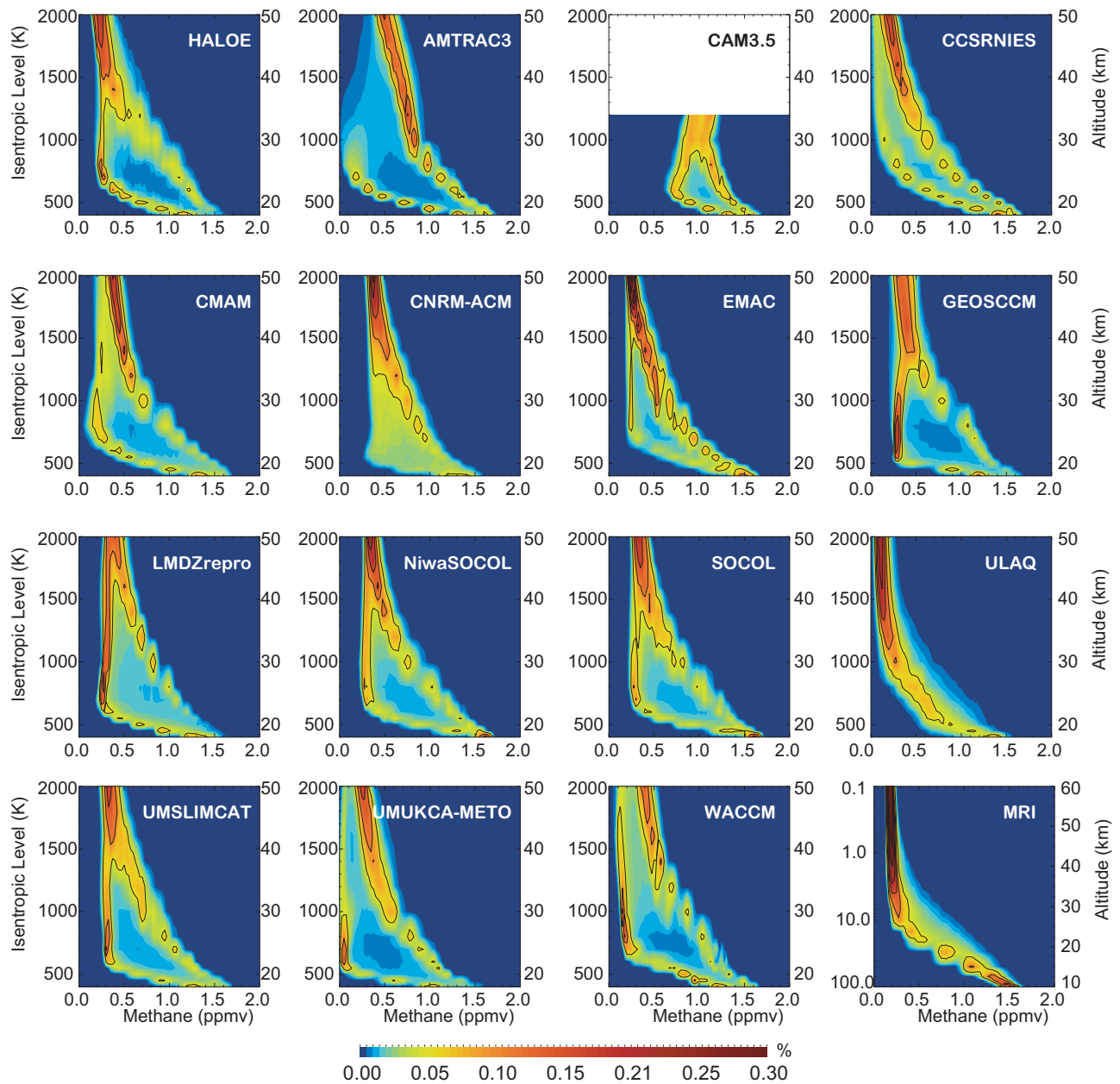


**Figure 5.15:** Contoured PDF of HALOE  $\text{CH}_4$  data,  $68^\circ\text{S}$ - $78^\circ\text{S}$ , for the period mid-October to mid-November (first panel). Model PDFs are calculated from  $50^\circ\text{S}$ - $80^\circ\text{S}$  (see text). Yellow and red indicate the most probable values, blue is the least probable value. The HALOE distributions are bimodal from 450-1300 K, indicating low- $\text{CH}_4$  vortex air that is isolated from the mid-latitudes (the high  $\text{CH}_4$  branch of the PDF). MRI model results (bottom right panel) are shown on pressure surfaces.

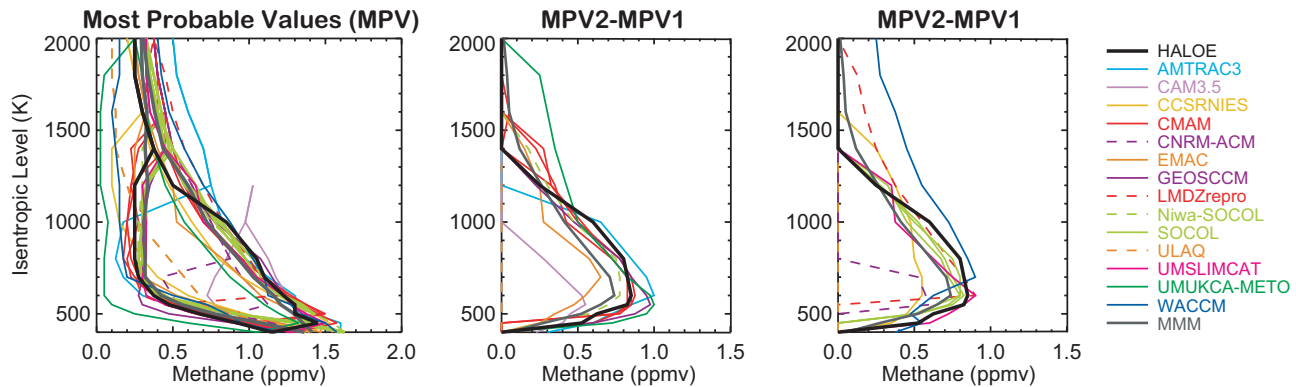


**Figure 5.16:** The most probable values (MPVs) of the  $\text{CH}_4$  PDFs identified from HALOE and model analyses (left panel). The grading metric for this diagnostic is based on a model's agreement with difference between the MPVs in the mid-latitudes and vortex (MPV2-MPV1, or  $\Delta\text{MPV}$ ). The centre and right panels show the  $\Delta\text{MPV}$  profile from HALOE, 14 CCMs (split into two panels), and the multi-model mean (MMM).

characteristic of vortex air, and at levels 1400 K and above,  $\Delta\text{MPV}=0$  implies that spring planetary wave activity has eliminated the transport barrier, mixing vortex and mid-latitude air together. Vortex isolation is particularly important at levels where large spring-time  $\text{O}_3$  loss occurs, so grading is divided into a LS grade for PSC-forming levels (400–700 K) and a middle and upper stratospheric grade above that (800–2000 K).

The  $\text{CH}_4$  PDFs from 15 CCMs are shown in Figure 5.15. In the LS, CNRM-ACM, MRI, ULAQ show no evidence of a transport barrier. (MRI could only be evaluated on pressure surfaces, but its PDFs show single mode behaviour at all levels. It is highly unlikely the evaluation would be any different on isentropic surfaces.) CAM3.5, CCSRNIES, and EMAC show an LS barrier but with too little separation between MPVs. NiwaSOCOL and SOCOL have reasonable LS barriers at 500 K and above, but do not extend to 450 K. Poor agreement in the 450–550 K range can have a serious impact on a model's ability to sequester high  $\text{Cl}_y$  inside the vortex. LMDZrepro has some LS barrier but the predominance of low  $\text{CH}_4$  suggests the vortex is extremely large. A good LS barrier is found in AMTRAC3, CMAM, GEOSCCM, UMSLIMCAT, UMUKCA-METO, and WACCM.

In upper stratosphere around 1400 K, the observations show a shift from bimodal to single mode PDF. Some models do not maintain a vortex barrier to high enough levels (AMTRAC3 and CAM3.5) and some have a vortex that persists to very high levels in the upper stratosphere or lower mesosphere (CCSRNIES, LMDZrepro, UMUKCA-METO, and WACCM). The AMTRAC3 PDF is single mode above 1000 K, but the mixing ratios are much higher than observed, suggesting that the vortex above 1000 K broke down and became well-mixed with mid-latitude air by October. Although UMUKCA-METO did not submit the required output for this test, its circulation is very similar to UMUKCA-METO and probably has very similar

vortex representation.

Because of large interannual variability in the Arctic vortex size and duration, the HALOE high northern latitude observations, primarily from March and April, do not regularly sample the vortex when it is well-isolated. These data cannot be used to derive a robust diagnostic of Arctic vortex isolation in late winter.

### 5.3.2.2 Antarctic September $\text{N}_2\text{O}$ profiles

This diagnostic assesses the integrated effects of descent and mixing deep in the vortex during the late austral winter. It uses 5 years of Aura MLS v2.2  $\text{N}_2\text{O}$  September observations from 80°S–88°S between 10–100 hPa (Livesey *et al.*, 2007). From 10–68 hPa, the  $\text{N}_2\text{O}$  accuracy is 9–14%, but 25% at 100 hPa. September was chosen for the analysis because descent that has been occurring since autumn is essentially complete, but in the lower stratosphere the vortex is still very strong and un-influenced by recent transport from lower latitudes. The observational uncertainties used are calculated from measurement accuracy and the interannual variability in the  $\text{N}_2\text{O}$  data. The diagnostic is calculated on 7 pressure levels between 100 and 10 hPa; the reported grade is the average of grades from these levels.

**Figure 5.17** shows the observed and model  $\text{N}_2\text{O}$  September mean profiles in the Antarctic. Most of the CCMs fall within the one sigma uncertainty for many or all parts of the profile. Seven CCMs lie significantly further from the observations. CAM3.5, CCSRNIES, E39CA, NiwaSOCOL, and SOCOL have  $\text{N}_2\text{O}$  mixing ratios much higher than observed, suggesting either insufficient vortex descent and/or insufficient isolation from mid-latitudes. In the cases of E39CA and CAM3.5, the high  $\text{N}_2\text{O}$  is likely a consequence of their low lids (10 and 3 hPa, respectively). Insufficient isolation has been diagnosed for CAM3.5 and CCSRNIES. NiwaSOCOL and SOCOL show very good isolation except at 450 K, so their high  $\text{N}_2\text{O}$  may be the

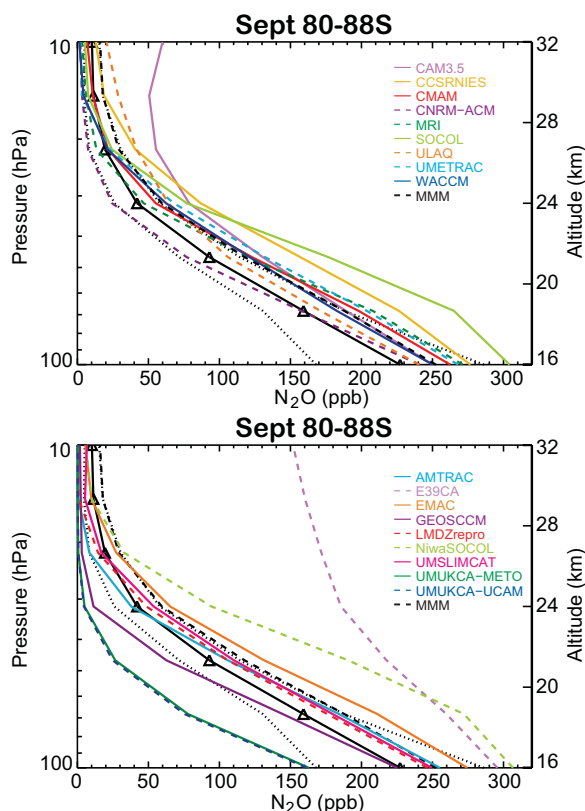


**Figure 5.17:** 18 CCM and observed profiles of  $N_2O$ ,  $80^\circ S$ – $88^\circ S$ , for September. The observed mean profile (triangles) was derived from 5 years of September Aura MLS observations; the combined effects of measurement uncertainty and interannual variability ( $1\sigma$ ) are shown by the black dotted lines. The September  $N_2O$  profile at these latitudes reflects the net effect of descent and mixing that occurred in the vortex during winter.

related to their overall low mean ages and may again reflect excessive vertical diffusion. Both of the UMUKCA models have  $N_2O$  much lower than observed, consistent with very old mean age in the vortex.

### 5.3.2.3 Antarctic spring $Cl_y$ time series

The time evolution of  $Cl_y$  for the Antarctic in October was evaluated in WE08. The estimates of observed  $Cl_y$  in the Antarctic stratosphere are based on HCl measurements from HALOE in 1992 (Douglass *et al.*, 1995; Santee *et al.*, 1996) and from MLS on the Aura satellite in 2005 (WMO, 2007); the observations show evidence for the complete conversion of  $Cl_y$  (HCl and  $ClONO_2$ ) to  $ClO_x$  in the deep vortex by early October. By the end of October,  $ClO_x$  has converted back to HCl, not  $ClONO_2$ , because the vortex is denitrified. Thus, the observed HCl mixing ratio in late October can be used as an estimate of vortex  $Cl_y$  (Douglass *et al.*, 1995). The uncertainties used for the  $Cl_y$  estimates

are discussed in Eyring *et al.* (2006). Because the dates and latitudes sampled by HALOE change every year, the estimation of  $Cl_y$  from HCl was only possible in 1992. In all other years deep vortex air was not sampled during the brief period when all  $ClO_x$  has been converted to HCl. October vortex  $Cl_y$  was estimated from Aura MLS HCl data for 2005 only because of a radiometer failure in 2006.

The upper left panel of Figure 5.11 shows the evaluation of October monthly mean model  $Cl_y$  at  $80^\circ S$  in 1992 and 2005. The results reported represent the average of the grades for both years, or only for the 1992 grade if the simulation did not continue to 2005. Low  $Cl_y$  in the vortex can result from insufficient vortex isolation that allows low  $Cl_y$  from the mid-latitudes to mix into vortex, or from a circulation that does not transport source gases to high enough altitudes for the CFC photolysis necessary for  $Cl_y$  production.

Except the two UMUKCA models, all models show a  $Cl_y$  increase beginning in the 1980s that levels off by the late 1990s. UMUKCA-UCAM flattens in the early 2000's, consistent with its mean age being several years older than the other models, and UMUKCA-METO appears to peak in 2005. The unusually high  $Cl_y$  seen in UMUKCA-METO ( $\sim 3.9$  ppb in 2006) is a result of a known bug involving the treatment of HCl washout. MRI, NiwaSOCOL, and SOCOL show extremely large interannual variability and fall well below the observations. In the case of NiwaSOCOL and SOCOL, both show good vortex isolation except at 450 K, but have low mean ages due to rapid net vertical transport, which could explain their low  $Cl_y$ . MRI has very good mean age, but its lack of a vortex barrier (Figure 5.16) could explain the low  $Cl_y$ . Most of the models under-estimate the observations, but CNRM-ACM, GEOSCCM, ULAQ, UMSLIMCAT, and UMUKCA-UCAM fall within the uncertainty at both data points. The very good agreement of CNRM-ACM with observations is quite surprising given its poor Antarctic vortex isolation (Figure 5.15) and very young age of air at high latitudes (Figure 5.5). However, this CNRM-ACM result is consistent with their fractional release behaviour (Figure 5.10), which shows unusually large fractional release for a given mean age. E39CA's  $Cl_y$  is slightly below the observations, but as discussed in Section 5.3.1.3, E39CA  $Cl_y$  cannot be evaluated as a transport diagnostic.

Nearly all organic Cl from source gases has been converted to  $Cl_y$  by the time it reaches the upper stratosphere, thus the  $Cl_y$  time series at 1 hPa should be less than or equal to the surface organic Cl time series lagged by several years. In the REF-B1 scenario the maximum surface Cl is less than 3.8 ppb. The bottom left panel of Figure 5.11 shows model  $Cl_y$  time series at 1 hPa,  $80^\circ S$ . CCSRNIIES, NiwaSOCOL, SOCOL, and UMUKCA-METO all have maximum  $Cl_y$  greater than the surface boundary condition. The UMUKCA problem is reported to be caused by a

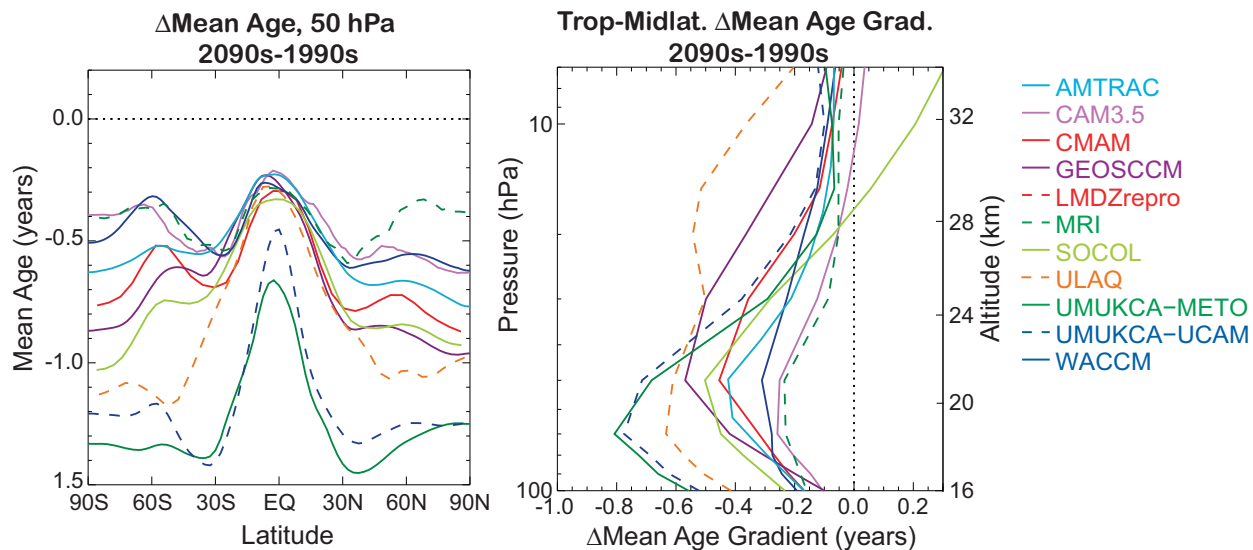


**Figure 5.18:** Mean age changes in the REF-B2 simulations during the 21<sup>st</sup> century. The mean age difference is the difference between an average of the last 10 years of the REF-B2 run, usually 2090-2099, and an average over 1990-1999. Ten CCMs submitted mean age for the REF-B2 scenario. The left panel shows the change in mean age at 50 hPa for the CCMs, all of which predict younger age at all latitudes at the end of the 21<sup>st</sup> century. All ten CCMs also predict that tropical ascent rates based on the age gradient will increase in the lower stratosphere (right panel), and most models predict a slight increase in age gradient ascent rates in the middle stratosphere as well.

known HCl washout problem. If the source gas boundary conditions for Cl are correctly implemented in the other three models, these results imply a lack of local mass conservation for the Cl<sub>y</sub> family.

Antarctic Cl<sub>y</sub> was evaluated for 13 CCMs for CCMVal-1 using the same data sets shown here and was reported in WE08. Six models have essentially the same behaviour as seen in CCMVal-1: CCSRNIIES, CMAM, EMAC, LMDZrepro, MRI, and UMSLIMCAT. AMTRAC3 was significantly too high in mid-latitudes and in the Antarctic but is now much lower and agrees much better with the mid-latitude observations. Five models, GEOSCCM, E39CA, SOCOL, ULAQ, and WACCM, all have higher Cl<sub>y</sub> and improved comparisons with observations. E39CA prescribes an upper boundary condition for Cl<sub>x</sub> at 10 hPa, so this diagnostic is not a true transport test for this model. For SOCOL and WACCM, the Cl<sub>y</sub> improvement is most confined to the mid-latitudes; their polar Cl<sub>y</sub> is still low. The UMETRAC REF-B1 simulation was not available for this analysis.

## 5.4 Stratospheric transport changes in the 21<sup>st</sup> Century

Several diagnostics that reveal fundamental characteristics of stratospheric transport have been evaluated for the REF-B2 scenario. In this section, model simulation of the recent past, 1990-2006, is contrasted with simulation

of the late 21<sup>st</sup> century, roughly 2080-2099. The diagnostics evaluated are mean age in the lower stratosphere, the tropical-mid-latitude mean age gradient, the water vapour tape recorder, and Antarctic vortex isolation.

The mean age of the lower stratosphere shows a striking and consistent change among the 10 CCMs that ran the REF-B2 scenario. **Figure 5.18** shows the difference in mean age at 50 hPa between the future and the recent past. All 10 models predict a decrease in mean age. The models also show similar latitudinal structure. All show the smallest age decrease in the tropics, and most show the second smallest decrease near 60°N/S and the greatest decreases at 30°N/S. Except for the two UМУKCA models that have by far the slowest circulation, all models make nearly identical predictions between 15°S-15°N. In the extra-tropics, the bulk of the models predict age decreases of 0.5-1.0 year.

The decrease in mean age in the lower stratosphere is consistent with faster ascent rates predicted for the end of the century, indicated by a decrease in the tropical-mid-latitude mean age gradient (right panel of Figure 5.18). All models predict an increase in the speed of the circulation in the LS, extending as low as 100 hPa, with maximum increases in ascent between 50-30 hPa. Ascent rates at 10 hPa show only a slight increase in the future. The mean age and age gradient results are consistent with Chapter 4 results showing a strong consensus among models that there will be a stronger circulation in the 21<sup>st</sup> century and with results from analyses of the future changes in the circulation and age of air from the CCMVal-1 simulations



(Li *et al.*, 2007; McLandress and Shepherd, 2008; Garcia and Randel, 2008; Oman *et al.*, 2009). However, the CCMVal-1 models that provided age output (AMTRAC, CMAM, GEOSCCM, and WACCM) also all simulated a decrease in the mean age of air between 1960 and the present (Waugh, 2009). These results are contradicted by the Engel *et al.* (2009) data, which show little or no trend in the age in the NH above 24 km. Nevertheless, there is indirect evidence of an increase in the tropical upwelling in the past few decades from trends in lower stratospheric ozone, water vapour, and temperature (Randel *et al.*, 2006). The differences between observed and modelled age trends could result from errors in simulating compensating circulation changes (such as an increase in poleward transport in the lowermost stratosphere) or changes in mixing (which could offset a decrease in age from the circulation) and will continue to be an important area of research.

Of the 10 models that submitted REF-B2 water vapour, only six had water vapour anomalies with a clearly identifiable and easily analysed tape recorder signal in the TLS (CAM3.5, CCSRNIES, CMAM, LMDZrepro, SOCOL, and WACCM). Of these, only three had sufficient amplitude to be analysed in the TMS as well (CMAM, SOCOL, and WACCM). The base of the tape recorder is higher at the end of the 21<sup>st</sup> century than during present day in all but one model. The changes in the tape recorder phase speed (ascent rate) provide a less clear picture of changes in the circulation than the age gradient, but nevertheless all models but one (SOCOL) predict an increase in the phase speed over most of the tape recorder altitude range. It is interesting that SOCOL predicts a decrease in the phase speed when it has one of the fastest phase speeds in the present-day simulation and has indications of excessive vertical diffusion. The models also generally predict less rapid attenuation of the tape recorder signal in the future, which is consistent with the increase in phase speed and the decrease in mean age gradient.

Antarctic vortex isolation at the end of the 21<sup>st</sup> century has been examined for the five CCMs that submitted the output necessary to calculate Antarctic CH<sub>4</sub> PDFs. These models are CCSRNIES, CMAM, GEOSCCM, UMUKCA-METO, and WACCM. CCSRNIES, GEOSCCM, and UMUKCA-METO show increased mixing between the vortex and mid-latitudes above 1000 K in the future, suggesting that winter planetary wave activity may have increased, stirring the vortex and mid-latitudes together earlier in the season. Chapter 4 notes that SH final warmings occur earlier in the 2000-2049 period, though there was no consensus among models on the type of tropospheric wave forcing responsible. WACCM shows less vortex and more mid-latitude air in the PDFs above 1500 K, which indicates some increased mixing at high altitudes. CMAM showed a similar shift from vortex to mid-latitude values from 1000-1500 K in only 1 of its 3 ensemble members.

The only thing that all of the models had in common in the future was a slightly deeper minimum separating the vortex and mid-latitude peaks in the MS (~600-1000 K). The predicted change in LS vortex size, as judged by the area under the vortex peak in the PDF, varied between the models. In CMAM and GEOSCCM, the LS vortex is predicted to increase in size, while UMUKCA-METO and WACCM each have a smaller vortex in the future. CCSRNIES did not have a clear change in size. These 5 CCMs provide no consensus as to how the Antarctic vortex size and depth may change in the future.

## 5.5 Summary

### 5.5.1 Transport Summaries by Model

**Multi-Model Mean (MMM).** The multi-model mean tape recorder signal was not quantitatively assessed, but the vertical velocity inferred from the mean tape recorder phase speed, which includes only the eight models for which the tape recorder could be analysed in both the TLS and TMS (and does not include E39CA at the lowest level, where its phase speed is infinite), is considerably faster than the observed tracer-derived ascent at all levels. However, it is strongly influenced by two models with very fast tape recorder phase speeds (NiwaSOCOL and SOCOL). The age gradient vertical velocity was calculated from 15 models and includes two models with very slow ascent (UMUCKA-METO and UMUCKA-UCAM), which were not available for the tape recorder analysis and which balance out the models with very fast ascent. The age gradient vertical velocity is much closer to the observations and suggests no overall bias in the CCMVal-2 models' ascent rates. The tropical CH<sub>4</sub> gradients indicate slightly too much mixing below ~25 hPa and slightly too little mixing in the SH winter above. Mean age at 50 hPa matches the observations closely at all latitudes. The tropical mean age profile is within the uncertainty of the observations at all altitudes while the mid-latitude mean age profile is slightly too young in the MS. These comparisons suggest, at most, only small biases in tropical ascent and tropical-mid-latitude mixing in the CCMVal-2 models as a whole.

It is interesting that the mean of all models' average mean age (AMA) grade and the AMA grade of the MMM are quite different. When averaging the mean age of all CCMs together, young mean ages compensate for old mean age to produce a multi-model mean age that scores a very high AMA grade (0.85). However, the average of individual model AMA grades is only 0.57. This quantity is a more meaningful indication of the overall transport credibility in CCMs than the grade for the physically unmean-

ingful MMM. It indicates that the average transport fidelity of the 15 CCMs is only fair.

In the Antarctic, three independent diagnostics point to insufficient vortex isolation in the mean model. The Antarctic  $N_2O$  profile is about  $1\sigma$  higher than the observations,  $Cl_y$  inside the vortex in October about  $1\sigma$  lower than the observations, and the lower stratospheric separation between mid- and high latitude most probable  $CH_4$  values in October is less than observed. Overall, while the tropical and mid-latitude transport diagnostics do not indicate any obvious biases, the average of all model AMA grades suggests that transport deficiencies exist in most models. The mean model is unable to produce a sufficiently isolated, chemically perturbed lower stratospheric vortex in austral spring.

**AMTRAC3:** The tape recorder and age gradient vertical velocities are too fast in the TLS, but close to observed in the TMS. The tape recorder attenuation and  $CH_4$  gradients indicate somewhat rapid mixing in the TLS, but there are significant tracer-dependent differences in mixing diagnostics in the TMS, with the tape recorder attenuation indicating somewhat too much mixing while the  $CH_4$  profiles have very weak vertical gradients, indicating too little in-mixing from mid-latitudes. The tropical age is very young and the shape of the age profile also suggests too little mixing in the TMS. The  $N_2O$  PDFs generally agree well with the observations in the TMS, with somewhat stronger than observed separation above 800 K. The  $60^\circ N/S$  mean ages are about a year too young. Antarctic September  $N_2O$  agrees well from 100-20 hPa but is too old above that, and the vortex isolation looks good in the LS up to 1000 K. No fractional release could be calculated. The  $Cl_y$  time series in the mid-latitudes is lower than observed, consistent with mean age that is more than 1 year too young. The Antarctic 50 hPa  $Cl_y$  is only slightly low but it is higher than its value at 1 hPa in some years. This is consistent its mean age in the Antarctic LS being older than in the US. Furthermore, vortex PDFs above 1000 K ( $\sim 8$  hPa) show strong mixing between mid- and high latitudes, consistent with a reversed vertical age gradient and lower  $Cl_y$  at 1 hPa. Overall, the model is characterized by a somewhat fast circulation in the LS and good circulation in the MS. Tropical-mid-latitude (T-M) mixing is a little strong in the TLS and too weak in the TMS, although the TMS diagnostics are mixed. The AMA grade is low. There is reasonable LS vortex isolation, but the lack of a vortex above 1000 K and the inverted  $Cl_y$  and mean age vertical gradients hint at strong high altitude wave activity in the late Austral winter.

**CAM3.5:** The tape recorder signal could only be analysed in the TLS. The tape recorder shows somewhat rapid ascent in the TLS, consistent with the age gradient vertical velocities. The age gradient ascent is also fast in the TMS,

with increasing divergence from the observations and from the residual vertical velocity with height. Most T-M mixing diagnostics support too much mixing in the TLS and TMS. The  $60^\circ N/S$  ages are fairly good, but Antarctic  $N_2O$  suggests there is slightly young air in the LS vortex.  $CH_4$  and  $N_2O$  are too high in the vortex just above the LS, suggesting a problem with getting sufficient descent with isolation. The model does not show a distinct vortex above 900 K – the branches of the PDFs are merged. Mid-latitude  $Cl_y$  is considerably lower than the observations and is the lowest of the CCMs. Vortex  $Cl_y$  is also too low. The fractional release curves are in good agreement with observations. Overall, the tracer-derived circulation is somewhat fast in the LS, and more so in the MS, and T-M mixing is too strong at all levels. This model has reasonable mean age in the LS but the fast circulation gives ages that are too young in the MS in spite of the strong T-M mixing. The AMA is better than the average CCMVal-2 model. The fast vertical transport may be responsible for the low  $Cl_y$  in the mid-latitudes and vortex. It is likely that deficiencies in the circulation and mixing can be at least partially attributed to the model's low lid ( $\sim 40$  km).

**CCSRNIES:** The mean age could not be evaluated for this model. The tape recorder signal could only be analysed in the TLS. The tape recorder phase lag is zero above the tropopause and then agrees quite well with observations, so the overall ascent rate in the TLS is somewhat fast. The tape recorder attenuation indicates fairly rapid mixing in the TLS, and this is supported by the  $CH_4$  profiles that fall off quite rapidly. The  $CH_4$  gradients and  $N_2O$  PDFs also indicate too much T-M mixing in the MS. The Antarctic  $N_2O$  profile, which is too high at all levels from 100-10 hPa, is consistent with fast ascent, but this cannot be confirmed because there are no TMS ascent diagnostics. The Antarctic vortex shows some barrier to mixing between 500-1500 K, but high values of  $CH_4$  inside the vortex (and low values outside) suggest a weak barrier. The mid-latitude  $Cl_y$  time series agrees well with observations, but in the vortex,  $Cl_y$  is too low by about 1 ppb. CFC-11 and CFC-12 J-values are well outside expected values (see Chapter 6).  $Cl_y$  at 1 hPa is greater than 4 ppb after 1994, which is higher than the total Cl prescribed by the boundary conditions in any year of this simulation. Overall this model has a slightly fast LS circulation with too much T-M mixing in the LS and MS. Antarctic composition is consistent a fast circulation.  $Cl_y$  family mixing ratios are not conserved.

**CMAM:** In the TLS the tape recorder phase speed is variable but overall agrees well with observations. The age gradient vertical velocity is slightly fast, but within the range of observational uncertainty. Relatively good consistency was found between the three estimates of vertical velocity in the TLS. In the TMS, the age gradient ascent rate agrees

quite well with the residual vertical velocity and with observations, but the tape recorder ascent rate is somewhat fast. The tape recorder attenuation indicates very good mixing rates in the TLS, corroborated by good  $\text{CH}_4$  gradients and tropical mean ages. In the TMS there are significant tracer-dependent differences in the mixing diagnostics, with the tape recorder amplitude indicating far too little mixing, despite the fact that the  $\text{CH}_4$  gradients are very close to observed and the tropical mean ages are only slightly young. The  $\text{N}_2\text{O}$  PDFs agree very well with the observations, also indicating good tropical-extra-tropical mixing. The  $60^\circ\text{N/S}$  mean ages are good. The Antarctic  $\text{N}_2\text{O}$  profile is a little high in the LS but agrees with observations at and above 30 hPa. The vortex isolation diagnostic shows a very good LS vortex barrier. Both descent and isolation in the Antarctic LS appear reasonable. Fractional release curves are a little higher than the observations, meaning that for a given mean age this model produces more  $\text{Cl}_y$  than observed. In spite of this,  $\text{Cl}_y$  in the mid-latitudes and vortex are both  $\sim 1\sigma$  lower than the observations. Overall, this model has reasonable ascent and good T-M mixing in the LS. T-M mixing in the MS looks very good using three diagnostics while the tape recorder attenuation shows no mixing at all. Consistent with good circulation and mixing, the AMA is better than most. The reasons for low  $\text{Cl}_y$  are undiagnosed.

**CNRM-ACM:** The tape recorder signal could only be analysed in the TLS. The tape recorder and the age gradient both indicate very rapid ascent in the TLS. The age gradient also indicates very rapid ascent in the TMS, and the differences between the tracer-derived velocities and the residual vertical velocity are very large, suggesting, along with other diagnostics, that there may be excessive vertical diffusion. The mean ages are very young everywhere, consistent with very fast net vertical transport. The tape recorder is very rapidly attenuated in the TLS, and the  $\text{CH}_4$  gradients agree reasonably well with observations despite the fast tracer ascent rates, suggesting either too much mixing or vertical diffusion or a combination of both. However, the  $\text{N}_2\text{O}$  PDFs compare well to the observations, indicating that mixing may be reasonable in the TMS. The  $60^\circ\text{N/S}$  mean ages are the youngest of any CCM, and all extra-tropical mean ages are  $\sim 1.5$  years too young. Surprisingly, the Antarctic  $\text{N}_2\text{O}$  profile agrees well with observations in the LS and is lower than observed in the MS - the opposite of what is expected with young air. The vortex is not isolated at any level. The fractional release curves are much steeper than the observations, meaning that even very young air has undergone significant photolysis; the fast vertical transport may explain this. (This model did not participate in the photochemical inter-comparison reported in Chapter 6.) The large fractional release explains the good agreement with the mid-latitude and vortex  $\text{Cl}_y$  time series. In the Antarctic,  $\text{Cl}_y$  at 1 hPa is about the same

as it is at 50 hPa. The lack of vertical gradient is consistent with all CFC photolysis occurring at relatively low altitudes in the stratosphere. Overall, in spite of a very fast tracer-derived circulation, indications of significant vertical diffusion, and the absence of a high latitude transport barrier, compensating errors allow this model to produce realistic levels  $\text{Cl}_y$  in the Antarctic LS. The AMA grade is among the lowest of the CCMVal-2 models.

**E39CA:** Mean age was not available for this evaluation, however, Stenke *et al.* (2009) present mean ages at 25 hPa that are nearly a year older than E39C and close to observed values. The tape recorder phase lag is zero above the tropopause and then agrees fairly well with observations, so that the overall ascent rate is somewhat fast in the TLS. The tape recorder ascent rate is fairly close to observations throughout the TMS. There are some tracer-dependent differences in the mixing diagnostics. The tape recorder attenuation indicates very rapid mixing in both the TLS and TMS. However, the  $\text{CH}_4$  gradients indicate relatively good mixing throughout the year in the TMS. Output for the  $\text{N}_2\text{O}$  PDF diagnostic was unavailable. The Antarctic  $\text{N}_2\text{O}$  profile is extremely high, which probably reflects the 10 hPa lid. The output for evaluating vortex isolation was unavailable, but October zonal mean meridional gradients of  $\text{N}_2\text{O}$  and  $\text{CH}_4$  at 50 hPa are nearly flat in the SH, suggesting that this model is not likely to have a high latitude transport barrier. The mid-latitude  $\text{Cl}_y$  time series agrees well with the observations; the vortex  $\text{Cl}_y$  agrees in 1992 but is too low in 2005. Overall, the circulation is slightly fast in the TLS but good in the TMS. There is too much T-M mixing in the TLS, but the diagnostics are contradictory in the TMS. The low lid likely impacts high-latitude descent.  $\text{Cl}_y$  is reasonable in the mid-latitudes but low in high latitudes, but as this model uses an upper boundary condition for  $\text{Cl}_y$ ,  $\text{Cl}_y$  cannot be used to diagnose transport.

**EMAC:** Mean age is not available for this model. The tape recorder phase speed indicates good agreement with the observations throughout most of the TLS and TMS. The tape recorder attenuation shows very good mixing in the TLS, but the  $\text{CH}_4$  gradients show strong mixing in the this region. The tape recorder and  $\text{CH}_4$  diagnostics are consistent in showing somewhat strong mixing where they overlap in the TMS, but the  $\text{CH}_4$  indicates that the mixing is good overall from 24-32 km. The  $\text{N}_2\text{O}$  PDFs generally agree well with the observations in the SH but do not agree as well in the NH. The vortex isolation diagnostic indicates good separation at 800 K and above, but below 600 K the vortex is not strongly isolated from the mid-latitudes. Consistent with that, the Antarctic  $\text{N}_2\text{O}$  profile is too high from 30-100 hPa, indicating young air inside the vortex. Mid-latitude  $\text{Cl}_y$  is slightly lower than observations. Vortex  $\text{Cl}_y$  in 1992 is too low, and although this run did not continue to 2005,

its time series in the late 1990's shows that  $Cl_y$  has already peaked at  $\sim 2.6$  ppb, more than 0.5 ppb lower than the 2005 observations. Overall, tropical ascent rates are about right, but there is too much T-M mixing in the TMS. The polar vortex barrier is too weak throughout the LS and thus the vortex lacks the necessary isolation to produce realistic  $Cl_y$  levels. Low mid-latitude  $Cl_y$  may contribute to this.

**GEOSCCM:** The tape recorder phase speed is variable in the TLS, but the average value compares well to observations, as does the age gradient ascent rate. Both the tape recorder and age gradient ascent rates are somewhat faster than the residual vertical velocity in the TLS, but all three agree in the TMS and are relatively close to the observed velocities. In the TLS the tape recorder attenuation indicates very good mixing rates, supported by reasonable  $CH_4$  gradients and good mean ages. In the TMS, the  $CH_4$  gradients are weak, which suggests too little mixing given the good ascent rates. The tropical mean age is slightly young, also indicating somewhat weak mixing given the good ascent. The  $N_2O$  PDFs show slightly too much separation above 600 K, especially in the NH. The  $60^\circ N/S$  mean ages agree very well with observations. The Antarctic  $N_2O$  profile agrees well in the LS but is too low above 50 hPa, suggesting descent may occur with too much isolation. The  $CH_4$  PDFs support this, showing very low  $CH_4$  in the vortex, persisting to below at 400 K, lower than observed. The fractional release curves and age range spanned agree very closely with the empirical curves. The mid-latitude  $Cl_y$  time series matches the observations very well and the vortex  $Cl_y$  is slightly lower than observed. Overall, the stratospheric circulation appears to be quite realistic in the tropics as well as in the high latitudes. Transport barriers may be somewhat strong in the MS. The AMA grade is the highest of the CCMVal-2 models. Although the vortex is somewhat too strong, this does not hinder its ability maintain realistic levels of  $Cl_y$  in the Antarctic spring.

**LMDZrepro:** The tape recorder signal could only be analysed in the TLS. The tape recorder phase speed is variable, but is overall slightly fast in the TLS. The age gradient ascent is too slow in the TLS and does not have the correct profile – the ascent is essentially constant between the tropopause and 50 hPa. The residual vertical velocity is similar to the age gradient but shows a slight minimum at  $\sim 75$  hPa. In the TMS, the age gradient ascent agrees very well with both the observed tracer ascent and the residual vertical velocity. The tape recorder amplitude and  $CH_4$  gradients indicate somewhat too much mixing in the TLS. In the TMS, where the ascent rates appear to be very good, the  $CH_4$  profiles indicate too little mixing. The  $N_2O$  PDFs agree well with the observations but occasionally show too much separation between the tropics and extra-tropics. The  $60^\circ N/S$  mean ages are in good agreement with observa-

tions. The Antarctic  $N_2O$  agrees with observations from 100-20 hPa but is too low above. The vortex isolation diagnostic, which evaluates composition from  $50^\circ S$ - $80^\circ S$ , finds little mid-latitude air below 700 K, suggesting either a very large vortex or insufficient isolation. Above 700 K, strong vortex isolation is found but the isolation extends too high (2000 K), suggesting a lack of wave activity at high altitudes in this season. Fractional release curves agree very closely in slope and range with the observations. The mid-latitude  $Cl_y$  time series agrees closely with the observations. The vortex  $Cl_y$  is slightly low (by  $\sim 1\sigma$ ) for both years evaluated. Overall, the unusual shape of the age gradient profile and the structure of the tape recorder water vapour anomalies below 17 km indicate problems with TLS transport. There is too much T-M mixing in the LS, but good ascent and slightly weak T-M mixing in the MS. Except for the tropical LS, mean ages are very good and the average mean age is better than most models. Antarctic descent may be reasonable, but the LS vortex appears to be too large or insufficiently isolated in spring.

**MRI:** The tape recorder signal could only be analysed in the TLS. The tape recorder phase speed is variable, but overall agrees well with the observations in the TLS. The age gradient ascent rates also agree well with observations and both ascent rates are close to the residual vertical velocity. In the TMS, the age gradient ascent agrees well with the observed tracer ascent up to 30 hPa but is somewhat fast above. The tape recorder attenuation indicates that TLS subtropical mixing is a bit strong, but the tropical  $CH_4$  gradients and  $N_2O$  PDFs indicate very strong mixing in the TLS and TMS. The mean age profiles in the tropics and mid-latitudes are both in excellent agreement with the observations, yet MRI is older than all other models with good ascent rates. The  $60^\circ N/S$  mean ages are also in excellent agreement with observations. The Antarctic  $N_2O$  profile is slightly high in the LS but is in good agreement above. The  $CH_4$  PDFs calculated on pressure surfaces (temperature was unavailable) have no bimodal structure whatsoever for latitudes poleward of  $50^\circ S$ . The  $CH_4$  mixing ratios in the LS are characteristic of mid-, not high latitudes, in contrast with the LS  $N_2O$  which is more characteristic of vortex air. The fractional release rates of CFC-11 and CFC-12 are the same, and only the CFC-11 curve is in good agreement with the observations. The CFC-12 slope is much steeper than observed, indicating a larger release of Cl occurring at younger ages which may explain the higher than observed mid-latitude  $Cl_y$  time series. The CFC results and inconsistencies between photochemical and non-photochemical tracer diagnostics indicate that there may be problems with photolysis rates, but this model did not submit results for the photochemical inter-comparison in Chapter 6. Vortex  $Cl_y$  is much lower than observations, shows no increasing trend in the 1990's, and has very large interannual vari-

ability. The low vortex  $Cl_y$  is consistent with high  $CH_4$  (*i.e.*, non-vortex) mixing ratios seen in the high latitude PDFs. Overall, the tropical diagnostics indicate good ascent below 30 hPa with somewhat fast ascent above. MRI has an AMA that is among the highest of all CCMs yet T-M mixing is too strong in both the TLS and TMS. This suggests that problems with ascent (fast) and mixing (strong) act to offset each other, producing good mean ages. Fractional release discrepancies, the lack of vortex isolation, and inconsistencies between indicators of high latitude composition all raise red flags.

**NiwaSOCOL:** There are large differences in the tropical upwelling velocities, which, along with other diagnostics, suggests excessive vertical diffusion. The tape recorder ascent rates are much faster than the observed tracer ascent rates in both the TLS and TMS. The age gradient ascent rates are also quite fast below  $\sim 40$  hPa. Above 40 hPa the age gradient velocities agree well with observations. The residual vertical velocity, however, is much faster than the observed tracer-based velocities above 50 hPa. The mean age is young everywhere, consistent with rapid net vertical transport. The tape recorder signal is rapidly attenuated, and the  $CH_4$  gradients agree well with the observations despite the fast tracer-derived ascent. Taken together, they suggest either too much T-M mixing, too much vertical diffusion, or both. Above 20 hPa, however, the  $CH_4$  and  $N_2O$  diagnostics suggest very good T-M mixing. The  $60^\circ N/S$  mean ages are the 2<sup>nd</sup> youngest of any CCM, and the extra-tropical mean age is too low by at least 1 year at all levels. The Antarctic  $N_2O$  profile is much higher than observed at all levels below  $\sim 14$  hPa. The vortex isolation diagnostic shows very good vortex barriers at appropriate levels from 500-1500 K, but the isolation does not persist at 450 K. Both of these diagnostics suggest too much low latitude influence in the LS vortex. While the mid-latitude  $Cl_y$  time series is in excellent agreement with observations, the vortex  $Cl_y$  is the lowest of all the CCMs, more than 1 ppb lower than observed. The  $Cl_y$  1 hPa time series raises concerns because its maximum value is  $\sim 4$  ppb, a value greater than total Cl prescribed at the surface. Overall, the model vertical transport is too fast throughout much of the tropics and there is inconsistency between the three vertical velocity estimates, suggesting excessive vertical diffusion. The polar transport barrier is too weak below 500 K. The AMA grade is among the lowest of all models. The model is unable to maintain high  $Cl_y$  levels in the vortex and  $Cl_y$  family mixing ratios are not conserved. The good agreement with mid-latitude  $Cl_y$  could result from compensating errors ( $Cl_y$  non-conservation and LS circulation issues).

**SOCOL:** In general, the diagnostics are very similar to NiwaSOCOL. The tape recorder and, to a lesser degree, age gradient ascent rates both indicate very rapid ascent

in the TLS. In the TMS the age gradient ascent is much closer to observations than the tape recorder ascent. The mean ages are slightly older than NiwaSOCOL in the TMS, consistent with slightly slower ascent there (as diagnosed by the age gradients). As in NiwaSOCOL, the age gradient and tape recorder ascent rates show large deviations from the residual vertical velocities in the TLS, but unlike NiwaSOCOL, the age gradient agrees well with the residual vertical velocity above  $\sim 40$  hPa. The tape recorder attenuation and  $CH_4$  gradients both indicate too much mixing and/or too much vertical diffusion below 20 hPa given the fast ascent rates. As with NiwaSOCOL, the  $CH_4$  and  $N_2O$  diagnostics indicate that T-M mixing is much better above 20 hPa. The  $60^\circ N/S$  mean ages are 1 year or more too young. The vortex isolation diagnostic shows very good vortex barriers at appropriate levels from 500-1500 K, but the isolation does not persist at 450 K. Mid-latitude  $Cl_y$  agrees closely with the observations. Vortex  $Cl_y$  is  $\sim 0.2$  ppb higher than NiwaSOCOL but remains well below the observations and shows large interannual variability. The  $Cl_y$  1 hPa time series also increases unrealistically to  $\sim 4$  ppb. While SOCOL shows overall slightly higher mean ages than Niwa-SOCOL, this does not significantly change the transport conclusions. Overall, the model circulation is too fast in the LS, there are indications of excessive vertical diffusion, the polar transport barrier below 500 K is too weak, and the LS vortex is unable to maintain high  $Cl_y$  levels. The AMA grade is among the lowest of all models.  $Cl_y$  family mixing ratios are not conserved. The good agreement with midlatitude  $Cl_y$  could result from compensating errors ( $Cl_y$  non-conservation and LS circulation issues).

**ULAQ:** The tape recorder signal could only be analysed in the TLS. The phase speed is variable but shows overall good agreement with the observed tracer-derived ascent rates. The age gradient ascent is slower than observed below 60 hPa and then faster than observed from 60 to 15 hPa. The age gradient vertical velocities are somewhat faster than the residual vertical velocities, but both have the same profile, with the minimum ascent near 90 hPa instead of 50 hPa as in the observed tracer derived profile. The tape recorder attenuation indicates reasonable mixing in the TLS. The  $CH_4$  gradients, however, are very strong in the TLS, indicating rapid mixing. In the TMS, the  $CH_4$  profile shows good agreement with observations in JFM (indicating too much mixing given the fast ascent) but much more slowly in JAS (consistent with the ascent). The  $N_2O$  PDFs are only weakly bimodal, further suggesting too much mixing in the TMS. The  $60^\circ N/S$  mean ages agree very well with observations and Antarctic  $N_2O$  agrees very well with observations in the LS but is too high above 30 hPa. The vortex isolation diagnostic shows no evidence of a vortex barrier to mixing at any level. In the LS,  $CH_4$  values are intermediate between the observed vortex and

mid-latitude mixing ratios, consistent with a lack of vortex isolation. Fractional release for CFC-11 and CFC-12 both agree well with observations although they span a slightly lower mean age range. The mid-latitude  $Cl_y$  time series agrees very well with observations but the vortex  $Cl_y$  is slightly low. Overall, the tropical ascent is somewhat slow above the tropopause and somewhat fast in the TMS, and the shape of the age gradient ascent profile is significantly different than observed. There is reasonable T-M mixing in the TLS, but it is too strong above. The AMA grade is quite high, but given the ascent rate profile and the lack of a tape recorder signal in the MS, the AMA may not be a good indicator of this model's transport credibility. The vortex either extends equator-ward of 50°S or has no transport barrier; either way, an important feature of the Antarctic stratosphere is not well-represented.

**UMETRAC.** A water vapour climatology is used; no tape recorder diagnostics can be evaluated. The age gradient ascent rates show very good agreement with observations. The  $CH_4$  gradients compare well with observations in the TLS and TMS, indicating good mixing. The ages are young despite good ascent and mixing. There are no  $N_2O$  PDF diagnostics for this model. The 60°N/S mean ages are both slightly low, and, consistent with this, the Antarctic  $N_2O$  profile is a little high. The vortex isolation diagnostic could not be applied, and as the REF-B0 (time slice) experiment was evaluated, no  $Cl_y$  time series was possible. In spite of realistic tropical ascent rates, the average mean age grade is only fair, suggesting transport barriers (subtropical and/or polar) may be affecting mean age in the MS. There is insufficient output to draw more specific conclusions about the credibility of transport, particularly in the high latitudes.

**UMSLIMCAT.** The tape recorder signal could only be analysed in the TLS. The tape recorder phase lag is variable and is zero (*i.e.*, infinite phase speed) over a portion of the TLS, so that the average ascent is considerably faster than observed. The age gradient ascent, however, agrees fairly well with the observations in the TLS. In the TMS, the age gradient ascent becomes progressively faster than observed. The tape recorder attenuation and  $CH_4$  gradients indicate somewhat too much mixing in the TLS. TMS  $CH_4$  gradients match the observations fairly well, indicating too much mixing given the fast ascent rates. The fact that the tropical mean ages are relatively good while the mid-latitude mean ages are too young also suggests rapid ascent with too much in-mixing of mid-latitude air in the TMS. The  $N_2O$  PDFs show weak bimodality in the LS but somewhat stronger bimodality in the MS. The 60°N mean age is very good and the 60°S age is slightly low. The Antarctic  $N_2O$  profile is realistic in the LS and MS, and the vortex isolation diagnostic shows excellent vortex barriers at the

appropriate levels. Both the mid-latitude and vortex  $Cl_y$  agree very well with observations, however, CFC-11 and CFC-12 J-values are well outside the expected range (see Chapter 6). Overall, this model has a fast circulation in the TMS along with too much T-M mixing throughout the TLS and TMS. As these attributes have opposite effects on mean age, the AMA is fairly high. Vortex isolation and  $Cl_y$  are realistic, but the CFC J-values are significantly different from other models.

**UMUKCA-METO.** A water vapour climatology is used; no tape recorder diagnostics can be evaluated. The age gradient ascent rates are much slower than observed in the TLS. They are also slower than observed in the TMS, but the difference between the observations and the model is smaller. The UMUCKA models are the only models for which the age gradient ascent rates are considerably slower than the residual vertical velocity throughout the tropical stratosphere. The mean ages are very old, consistent with the slow age-derived circulation. The shape of the tropical age profile, the  $CH_4$  gradients, and the  $N_2O$  PDFs all indicate too little mixing in the TMS. The 60°N/S mean ages are 2 or more years too old. This is consistent with the Antarctic  $N_2O$  profile, which is much lower than observed. The  $CH_4$  PDFs show a very strong vortex extending to higher than observed levels (at least 2000 K). The PDFs also show that the vortex has no influence from lower latitude air down to ~550 K while observations indicate the influence of lower latitude air at 700 K and below. The fractional release curves are less steep than observed, meaning that for a given mean age they have released less Cl than expected. This is consistent with the very slow circulation: slow ascent allows old mean ages to occur at lower altitudes where photolysis rates are lower. Both the vortex and mid-latitude  $Cl_y$  time series are much higher than observed. There is a known bug in this simulation related to wet deposition of HCl, and this has been reported to increase  $Cl_y$  levels in the stratosphere. Overall, this model has a very slow circulation leading to very old mean ages throughout the stratosphere. The AMA grade is among the lowest of all models. The Antarctic vortex is too strong in the LS and in the US/lower mesosphere.

**UMUKCA-UCAM.** A water vapour climatology is used; no tape recorder diagnostics can be evaluated. Dynamics are reported to be identical to UMUKCA-METO. The diagnostics for this model are very similar to those for UMUCKA-METO, and indicate a very slow age-derived circulation in the TLS with somewhat better agreement with observations in the TMS. UMUCKA-UCAM has slightly slower age-based ascent and slightly older (0.3-0.4 years) tropical and mid-latitude mean age profiles than UMUCKA-METO. As in UMUCKA-METO, the tropical age profile,  $CH_4$  gradients, and  $N_2O$  PDFs indicate too lit-

tle mixing in the TMS. The Antarctic N<sub>2</sub>O behaviour is the same, and although output was not available to calculate the CH<sub>4</sub> PDFs, there is no reason to expect that vortex behaviour would be different from UMUKCA-METO. The mid-latitude Cl<sub>y</sub> time series is higher than observed and the vortex Cl<sub>y</sub> is in good agreement. The high mid-latitude Cl<sub>y</sub> could be related to the very old mean ages found in the mid-latitude LS. Overall, this model has a very slow circulation, leading to very old mean ages throughout the stratosphere. The AMA grade is the lowest of all models. The Antarctic vortex is probably too strong in the LS and above.

**WACCM.** The tape recorder phase speed is variable but overall shows quite good agreement with observations in both the TLS and TMS. The age gradient vertical velocities also show good agreement with the observations, and both the age gradient and the tape recorder ascent are relatively close to the residual vertical velocity. The tape recorder attenuation indicates somewhat too much mixing in the TLS, but slightly weak mixing in the TMS. The CH<sub>4</sub> gradients

also indicate too much mixing in the TLS and too little in the TMS. The N<sub>2</sub>O PDFs indicate too much tropical isolation in some seasons. The tropical mean age profile is quite good in the LS and MS, but the mid-latitude mean age profile is too young above 50 hPa, consistent with too little T-M mixing in the MS. The 60°N/S mean ages are in very good agreement with observations. The Antarctic N<sub>2</sub>O profile has overall good agreement with observations in the LS and MS, and the vortex isolation in the LS has excellent agreement with observations, including the appearance of lower latitude influence in vortex air at 700 K and below. However, a strong vortex extends all the way to the lower mesosphere instead of ending at ~1400 K. Fractional release curves have steeper slopes than observed, especially for CFC-12. This means more CI is released for a given mean age than expected, although CFC-11 and CFC-12 J-values are in the expected range (see Chapter 6). The mid-latitude Cl<sub>y</sub> time series has excellent agreement with observations but vortex Cl<sub>y</sub> is lower than observed for reasons that are not clear. Overall, the circulation is fairly realistic, with minor T-M mixing issues, and the LS polar transport

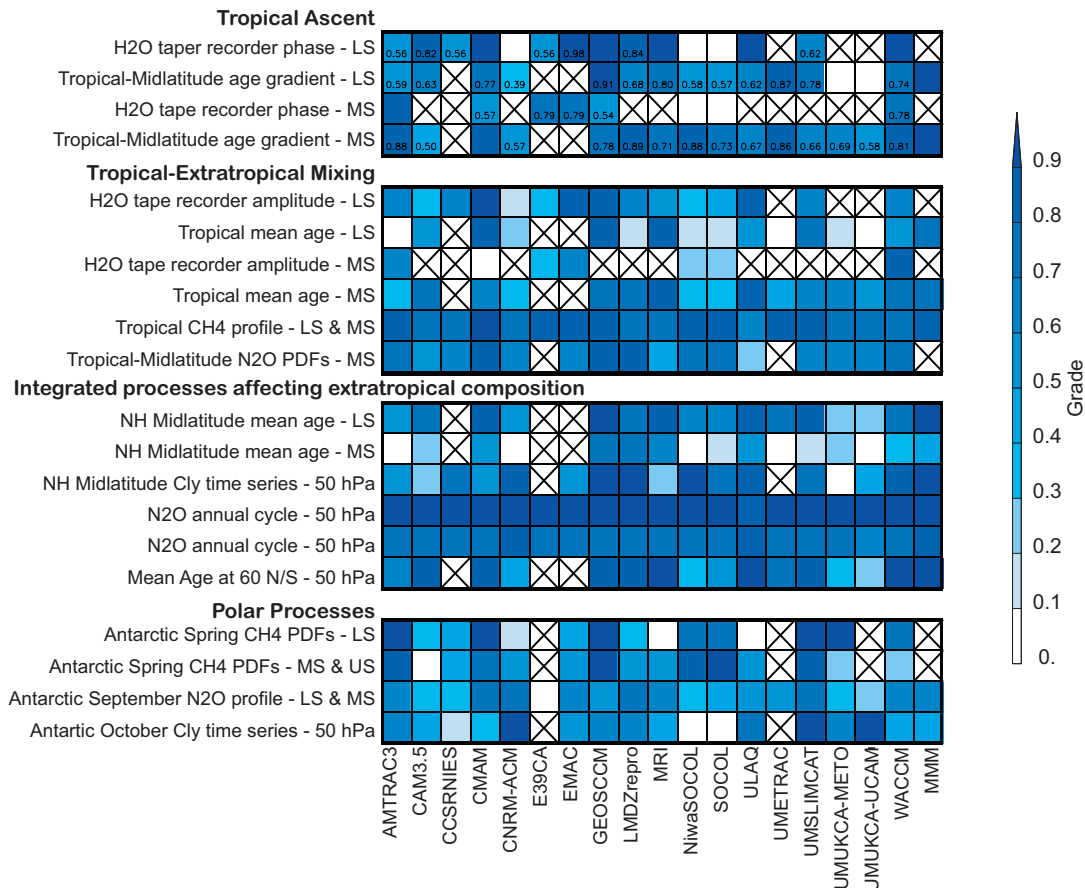


**Figure 5.19:** Quantitative assessment of model performance on transport diagnostics. The colour bar indicates the grade on each diagnostic test discussed in the chapter, with deeper blue indicating better agreement with observations. 'X' indicates no diagnostic could be calculated. LS, MS, and US refer to the lower stratosphere, middle stratosphere, and upper stratosphere, respectively.

barrier is very good. The AMA grade is fairly high.

### 5.5.2 Overall CCMVal-2 Model Transport Summary

A summary of the quantitative evaluation of the transport diagnostics is given in **Figure 5.19**. There are significant problems with simulation of the tropical stratosphere in the CCMVal-2 models. Tropical ascent and mixing across the subtropics are crucial to distributing ozone depleting substances in the stratosphere, and these transport deficiencies affect modelled abundances of  $\text{Cl}_y$ . Of the 12 models with both tape recorder and age output, only four score higher than 0.7 (*i.e.*, are within  $\sim 1\sigma$  of the observations) on both measures of tropical ascent in the tropical lower stratosphere. Of the remaining eight models, six have faster-than-observed ascent according to at least one diagnostic and two fail to reproduce the shape of the observed profile in the age gradient. Of the six models with only one available ascent diagnostic, two score higher than 0.7, two show fast tracer-derived ascent relative to observations, and two have slow ascent. The performance in the middle stratosphere is somewhat better, with eight models showing improvement in at least one ascent diagnostic. However, the fraction of models that score better than 0.7 on both diagnostics is the same as in the lower stratosphere: 1/3. The models that perform well on both tracer ascent diagnostics also tend to show good consistency between their tracer-derived upwelling and the tropical residual vertical velocity,  $\bar{w}^*$ . Lack of consistency between these measures of ascent may indicate numerical errors in transport or problems with vertical diffusion, horizontal or vertical eddy tracer fluxes, or phasing between temporal variability in tracers and in the circulation.

The tape recorder amplitude is the only tropical-extra-tropical mixing diagnostic that is fully independent of the circulation, but the other mixing diagnostics are independent of one another and are affected by the circulation in different ways. Thus, the performance relative to the suite of diagnostics as a whole is a more accurate assessment of subtropical mixing than performance on any single mixing diagnostic. The range of model performance here is smaller than the range on the tropical ascent diagnostics: no model has an average mixing grade higher than 0.8 or lower than 0.4 (the range for the average of the ascent diagnostics, on the other hand, is 0.15 to 1.0). Only five models have an average mixing score higher than 0.7 (all of them also performed well on the ascent diagnostics). The remaining models all have too much tropical-extra-tropical mixing and/or too much vertical diffusion in the lower stratosphere.

Excessive subtropical mixing would tend to increase the mean age in the models and is a likely explanation for

the fact that most models have good mean ages in the tropical lower stratosphere despite having relatively fast circulations. However, a rapid circulation coupled with an inability to maintain tropical isolation will lead to inadequate conversion of CFCs to  $\text{Cl}_y$ . In the middle stratosphere, six models had at least some indication of too little mixing. This may contribute to the young modelled mean ages in the tropical middle stratosphere, though the error in mean age at a given level depends on the integrated errors in transport below that level and thus the relative dependence on local processes decreases with height above the tropopause.

The mean age is a sensitive function of both the circulation and mixing and the distribution of mean ages throughout the stratosphere reflects the balance between these two transport processes and their variations with height. The average of mean age grades evaluated at a wide range of latitudes and altitudes can be used to assess a model's overall transport fidelity. While it is theoretically possible to achieve the correct mean age everywhere through compensating errors in ascent and quasi-horizontal mixing, in practice it is unlikely to happen because it would require the two to perfectly offset each other throughout the stratosphere. The average mean age (AMA) grade should give a more reliable indication of transport credibility than individual mean age diagnostics and should be evaluated in addition to the individual mean age diagnostics.

The AMA metric is calculated from seven mean age grades: tropical LS (90-50 hPa), tropical MS (30-10 hPa), NH mid-latitude LS (90-50 hPa), NH mid-latitude MS (30-10 hPa), SH mid-latitude LS (50 hPa), 60°N (50 hPa), and 60°S (50 hPa). **Figure 5.20** illustrates the relationship between the AMA metric and several key diagnostic quantities: tropical LS ascent, tropical-mid-latitude mixing, Antarctic descent, and LS vortex isolation. Tropical LS ascent is the average of the two independent diagnostics for ascent, and the tropical-mid-latitude mixing quantity plotted is the average over all mixing grades available for each model (as many as six). (See Table 5.1 for a complete list of diagnostics.) The AMA shows a positive correlation with all the key diagnostics except for vortex isolation. The grey-shaded area shows models that score greater than 0.6 for the diagnostics plotted.

The relationship between a model's AMA and mean LS ascent grade is particularly powerful (**Figure 5.20**). Models falling in the grey-shaded upper right quadrant have successfully simulated tropical LS ascent and mean age at all locations, implying that tropical-mid-latitude mixing is probably good as well. (This is borne out by **Figure 5.20b** which shows that nearly the same set of models performs well on the mixing diagnostics.) A model that falls in the lower right quadrant has successfully simulated the tropical ascent, but not mean age; thus it must have a good circulation but too much or too little mixing



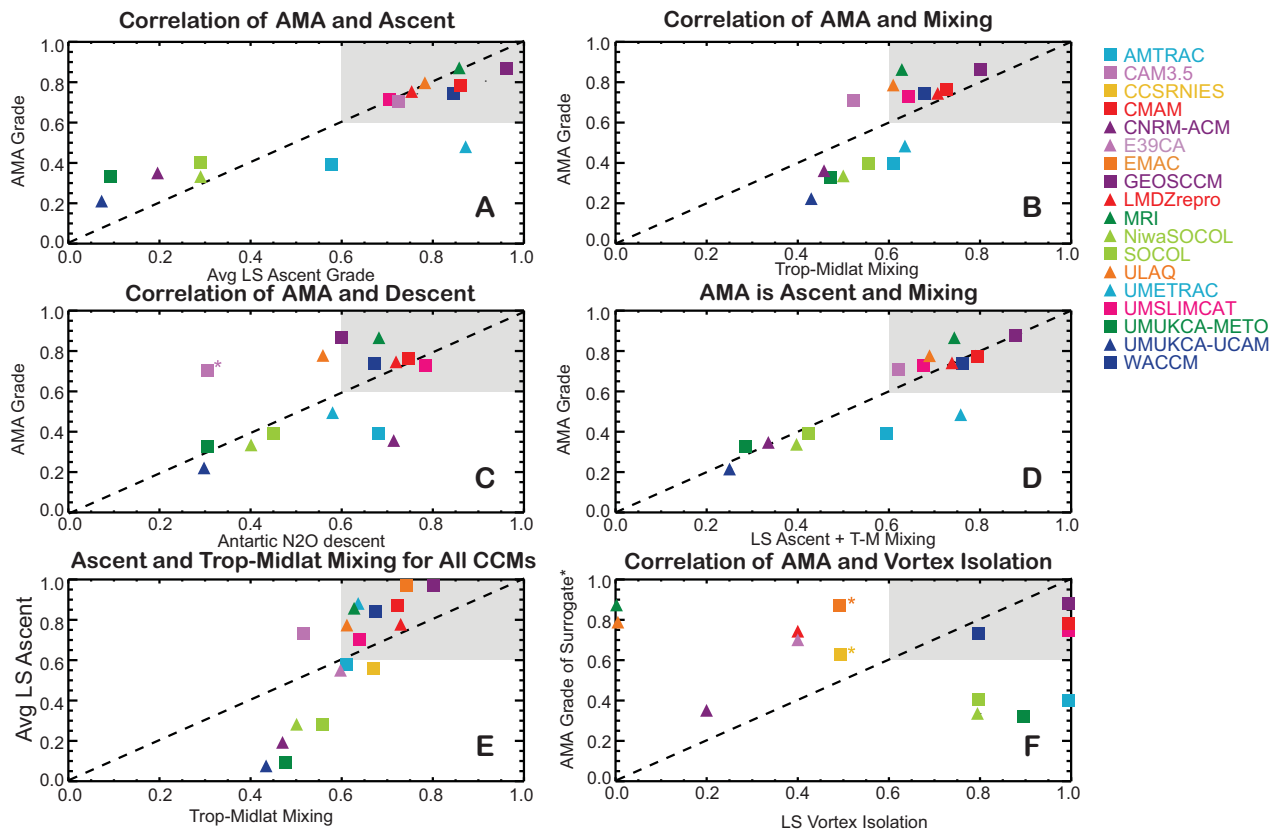


**Figure 5.20:** Correlations between the average mean age (AMA) grade and four fundamental diagnostic quantities: tropical LS ascent (A), tropical-mid-latitude mixing (B), vortex descent (C), and LS vortex isolation (F). The grey shaded area identifies realistic model performance for the metrics shown in that panel. The AMA is calculated from 7 mean age diagnostic scores (see text). The average LS ascent grade (panel A) is the average of the tape recorder and mean age gradient tropical ascent grades in the LS. The tropical-extra-tropical mixing grade (panel B) is the average of all tropical-extra-tropical mixing grades in the LS (Section 2 of Figure 5.19). The vortex descent grade (panel C) is taken from the Antarctic  $N_2O$  profiles. CAM3.5 has a lid of  $\sim 3$  hPa that affects vortex descent; this is noted by an asterisk in panel C. Panel D shows that the AMA is a strong function of both tropical LS ascent and tropical-mid-latitude mixing. Because of this relationship, a surrogate for AMA can be calculated for models that did not submit age of air output. This allows their vortex isolation behaviour to be plotted in panel F; the models with AMA surrogate are labelled with an asterisk. Panel E shows the tropical ascent and tropical-mid-latitude mixing performance for all CCMs participating in this evaluation.

across the subtropics. UMETRAC is the only model that falls in the lower right quadrant. Unfortunately, it does not have output for the tape recorder or  $N_2O$  diagnostics, so it is difficult to draw conclusions about its mixing, but the  $CH_4$  gradients do independently suggest that it may have too little mixing in the TMS in some seasons. The upper left quadrant indicates a poor circulation and incorrect mixing; the mixing would have to be compensating for the circulation to give reasonable ages. The lower left quadrant indicates problems with tropical ascent, but nothing can be inferred about the mixing across the subtropics since the circulation alone could be responsible for the poor mean age grades. However, note that the models in the lower quadrants do, in fact, have low mean values on the tropical-extra-tropical mixing diagnostics, as seen in

Figure 5.20b. This correlation between the ascent and mixing diagnostics is not surprising, given that both depend on the strength and distribution of wave activity in the extratropics. Figure 5.20c shows the relationship between polar descent and the AMA. Tropical ascent and polar descent are physically linked through the diabatic circulation, thus most of the models that do well Figure 5.19a also do well in Figure 5.20c (except CAM3.5, which has a low lid and cannot fully simulate Antarctic descent). Because there is a physical basis for the correlations shown, evaluation of these fundamental diagnostics, including the AMA, is essential for building model credibility.

While the AMA grade is a very useful quantity for evaluating a model's overall transport fidelity, the age of air output necessary for this calculation was not available

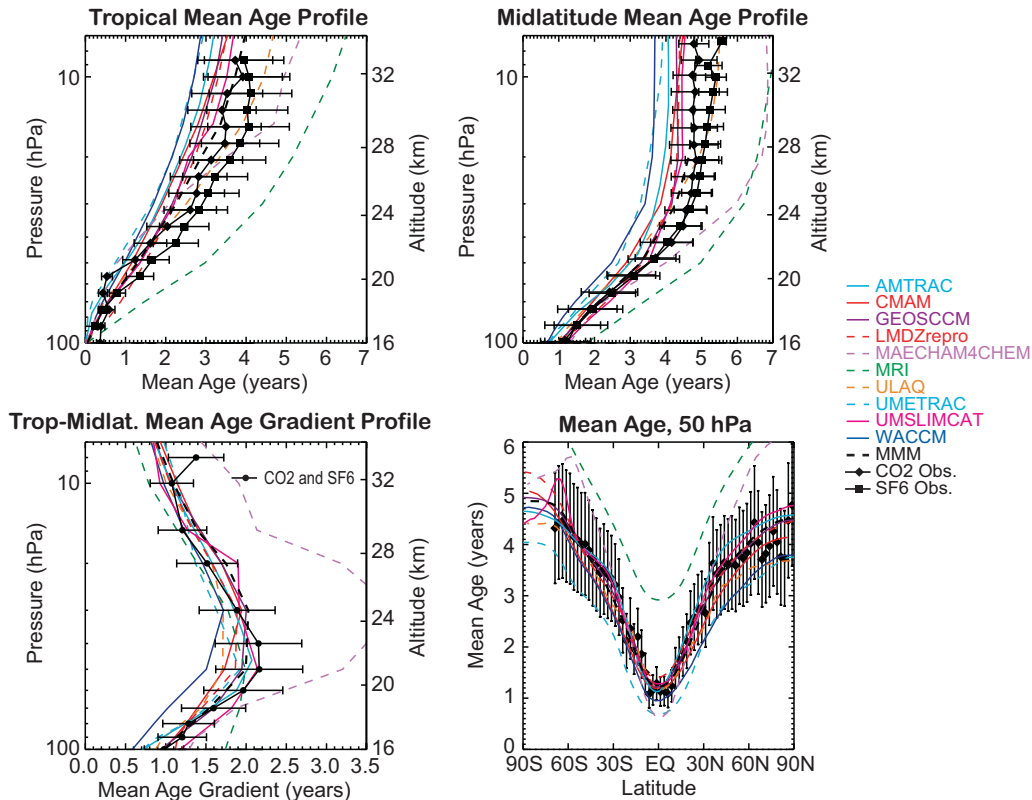


**Figure 5.21:** Mean age from 10 CCMs participating in CCMVal-1 and their multi-model mean (MMM). Black symbols are the observed mean age profiles derived from  $\text{CO}_2$  (diamonds) and  $\text{SF}_6$  (squares) for the tropics ( $10^\circ\text{N}$ – $10^\circ\text{S}$ ) and mid-latitudes ( $35^\circ\text{N}$ – $45^\circ\text{N}$ ), and the latitudinal distribution of mean age at 50 hPa; the same as in Figure 5.5. The bottom left panel shows the difference between the average of the observed tropical profiles and mid-latitude profiles on pressure surfaces. All uncertainties shown are  $1\sigma$ .

from all models. Nevertheless, the strong correlations between AMA, LS ascent, and tropical-mid-latitude mixing allow a surrogate for AMA to be calculated for the models without age of air (CCSRNIES, E39CA, and EMAC). Figure 5.20d shows a roughly 1:1 relationship between the mean of the average LS ascent and average T-M mixing grades and the AMA grade for the 15 models with age output. Figure 5.20e shows the relationship between LS ascent and tropical-mid-latitude mixing for all 18 CCMs participating in this evaluation. The three models that have no AMA grade (CCSRNIES, E39CA, and EMAC) fall along the same line as the other CCMs, suggesting that the average of their LS ascent and T-M mixing grades can be used as a surrogate for AMA. This plot shows that EMAC, which could not be evaluated using the AMA, also performs very well on the ascent and mixing diagnostics.

Figure 5.20f shows correlation between LS vortex

isolation and the AMA (or its surrogate) for all 18 models. The lack of correlation suggests that the transport barrier at the vortex edge is to first order independent of the overall transport circulation. Because it is not correlated with other key diagnostics and because it is a required feature for producing a realistic ozone hole, it is important to include this transport diagnostic for simulations predicting future ozone.

Figure 5.20 shows that nine of the 18 CCMs perform acceptably ( $> 0.6$ ) on the AMA metric or its surrogate (CAM3.5, CMAM, EMAC, GEOSCCM, LMDZrepro, MRI, ULAQ, UMSLIMCAT, and WACCM), and eight of these also have reasonable tropical ascent and tropical-midlatitude mixing (all but CAM3.5). Of these eight models, six also perform well on the diagnostic of Antarctic descent (models CMAM, GEOSCCM, LMDZrepro, MRI, ULAQ, and WACCM). Of these six, LMDZrepro and MRI

do not create an isolated vortex in the Antarctic lower stratosphere. Only CMAM, GEOSCCM, UMSLIMCAT, and WACCM, demonstrate credible transport performance in all key areas.

Grewe and Sausen (2009) proposed that the grading metric and observational data sets used in WE08 are unlikely to be able to distinguish between realistic and unrealistic model behaviour due to uncertainties and interannual variability in the data sets; that is, they believe there is a high potential for the grades to be meaningless. Figure 5.20 demonstrates the overall credibility of the diagnostics, as well as the WE08 grading metric used, by showing strong correlations between the grades for average mean age and the average of the tropical LS ascent and tropical-mid-latitude mixing grades. If the individual grades that make up the combined grades were meaningless, that is, if a grade of 1 were not statistically different from a grade of 0, the average of those grades would be a random number bearing no relation to model transport behaviour. In that case, plotting those metrics against each other (Figures 5.20 a-e) would produce random scatter. On the contrary, Figure 5.20 shows a remarkable degree of correlation between the grades for these fundamental transport diagnostics. The relationship between these diagnostics demonstrates that the observations used to create them are physically meaningful and have statistically significant information, and that the grading metric itself is not a random, statistically insignificant quantity.

### 5.5.3 Summary of 21st century transport changes

REF-B2 output was analysed from 10 CCMs. Despite the spread in model performance revealed by the transport diagnostics, all of these models predict a faster circulation and younger mean age at the end of the 21<sup>st</sup> century, indicating that this is a robust result that depends on large-scale forcing. Only six of these models had water vapour anomalies with a clearly identifiable tape recorder signal in the TLS (CAM3.5, CCSRNIES, CMAM, LMDZrepro, SOCOL, and WACCM), and only three had a tape recorder that persisted in the TMS (CMAM, SOCOL, and WACCM). The changes in the tape recorder ascent rate provide a less clear picture of changes in the circulation than the age gradient, but all models but one (SOCOL) predict an increase in the phase speed over most of the tape recorder altitude range. The base of the tape recorder is higher at the end of the 21<sup>st</sup> century than during present day in all but one model. The models also generally predict less rapid attenuation of the tape recorder signal in the future, which is consistent with the predicted changes in circulation.

Comparisons of the future Antarctic vortex predicted by 5 CCMs showed no agreement on whether the vor-

tex would be larger or smaller in the future. All showed a slightly deeper minimum in the LS/MS PDFs (*i.e.*, a stronger barrier) and all showed some indication of increased horizontal mixing in the upper stratosphere.

### 5.5.4 Comparison to CCMVal-1 model transport

Mean age can be used to examine differences in transport performance between CCMVal-1 and CCMVal-2. Figure 5.21 shows tropical and mid-latitude mean age profiles, the mean age gradient, and 50 hPa mean age for CCMVal-1 models in the same format as the CCMVal-2 models shown in Figure 5.5. The multi-model mean (MMM) ascent rate as assessed by the tropical-mid-latitude age gradients is nearly identical for both sets of models, but the spread of the CCMVal2 models is much greater. At 50 hPa, the age gradients of only 2 of 10 CCMVal-1 models fall outside the observational uncertainty while 7 of 15 CCMVal-2 models do. The same is true for all 50 hPa mean ages. CCMVal-1 models are tightly clustered with only 2 models frequently outside the uncertainties and the MMM agrees very closely with the observations. The CCMVal-2 MMM is in almost as good agreement in spite of a much larger spread. This is largely due to a fortuitous balance of models with very old age cancelling the effects of models with very young age.

In contrast to the age diagnostics, the CCMVal2 tape recorder phase speed shows improvement in both the difference between the MMM and observations and in the spread of model performance relative to CCMVal-1. This at first seems contradictory, but of the seven models with both diagnostics available for both CCMVal-1 and CCMVal-2, six (CMAM, GEOSCCM, WACCM, LMDZrepro, MRI, and ULAQ) scored better than 0.7 on at least one tropical ascent diagnostic in this assessment. The changes between CCMVal-1 and CCMVal-2 varied for these six models, and also varied for the two tropical ascent diagnostics from a single model, but all performed relatively well on these diagnostics in both assessments. (The tape recorder performance was only considered for the TLS for LMDZrepro, MRI, and ULAQ.) Four of the five CCMVal-2 models with the worst performance on the tropical ascent diagnostics did not participate in CCMVal-1 (NiwaSOCOL, UMUCCA-METO, UMUCCA-UCAM, and CNRM-ACM).

The mid-latitude mean age profile comparison reveals some interesting differences between the sets of models. While both sets of models have young and old outliers, most of the CCMVal-1 models form a fairly compact cluster underneath the observational uncertainties. The CCMVal-2 models form a looser cluster, and relatively few fall under the observations above 30 hPa (25 km); overall they are about 0.5 years younger than CCMVal-1

models in the middle stratosphere. Although the tropical mean profiles show the same spread for both sets of models, the CCMVal-2 MMM mean age is younger than the CCMVal-1 MMM and does not agree as well with the observations.

It is not clear that there has been any improvement in performance among the models that participated in both CCMVal-1 and CCMVal-2. Two of the best-performing models from this assessment showed better agreement with the observations in CCMVal-1 (GEOSCCM and CMAM), and the other models show mixed results depending on the diagnostic. However, eight of the 11 models that participated in both assessments appear in the upper-right corner of Figure 5.20e, indicating reasonable performance on the tropical ascent and mixing diagnostics. The addition of four new models, all appearing in the lower left corner of Figure 5.20e, accounts for a good deal of the increase in model spread between Figure 5.21 and Figure 5.5. It is only the fortuitous cancellation of the models that perform poorly that gives a CCMVal-2 MMM in good agreement with the observations. This fact reinforces the importance of the goals of this report, namely, to reduce uncertainties in model predictions by using observationally-based diagnostics to understand model performance and determine model credibility. A multi-model mean calculated only from models with proven transport credibility would represent a step forward in reducing uncertainties in chemistry climate model predictions.

### 5.5.5 Requirements for transport credibility

Realistic representation of several key aspects of transport should be considered essential for credibility. They are

1. local conservation of chemical family mixing ratios (*e.g.*,  $Cl_y$ ),
2. realistic tropical ascent in the LS,
3. realistic mixing between the tropics and extra-tropics in the LS and MS,
4. close agreement with *all* mean age diagnostics, that is, a high score for the average mean age grade, and
5. generation of an isolated lower stratospheric Antarctic vortex.

All of these aspects of transport are necessary for the simulation of realistic levels of vortex  $Cl_y$ . Models that reasonably represent these essential physical processes have demonstrated the credibility necessary for prediction of future stratospheric composition.

The evaluations presented in this chapter indicate transport improvement efforts in CCMs should concentrate on the simulation of the tropical lower stratosphere. Improvements are needed in the ascent rate profile below 50 hPa in the tropics and in the rate of mixing between the tropics and mid-latitudes, which is currently too strong in

most models. In addition, discrepancies between a model's residual vertical velocity in the tropics and its tracer-derived velocities suggests possible problems with vertical diffusion or numerics.

## References

- Andrews, D.G., Holton, J.R., and Leovy, C.B., 1987. *Middle Atmospheric Dynamics*, 489 pp. Academic, San Diego, CA.
- Andrews, A. E., K. A. Boering, B. C. Daube, S. C. Wofsy, M. Loewenstein, H. Jost, J. R. Podolske, C. R. Webster, R. L. Herman, D. C. Scott, G. J. Flesch, E. J. Moyer, J. W. Elkins, G. S. Dutton, D. F. Hurst, F. L. Moore, E. A. Ray, P. A. Romashkin, and S. E. Strahan, 2001. Mean ages of stratospheric air derived from in situ observations of  $CO_2$ ,  $CH_4$ , and  $N_2O$ , *J. Geophys. Res.*, **106**, 32,295–32,314.
- Boering, K. A., Wofsy, S. C., Daube, B. C., Schneider, H. R., Loewenstein, M., Podolske, J. R., and Conway, T. J., 1996. Stratospheric Mean Ages and Transport Rates from Observations of Carbon Dioxide and Nitrous Oxide, *Science*, **274**, doi: 10.1126/science.274.5291.1340.
- Douglass, A. R. Schoeberl, M. R., Stolarski, R. S., Waters, J. W., Russell, J. M., Roche, A. E., and Massie, S.T., 1995. Interhemispheric differences in springtime production of HCl and ClONO<sub>2</sub> in the polar vortices, *J. Geophys. Res.*, **100**, 13,967-13,978.
- Douglass, A. R., Prather, M. J., Hall, T. M., Strahan, S. E., Rasch, P. J., Sparling, L. C., Coy, L., and Rodriguez, J. M., 1999. Choosing meteorological input for the global modeling initiative assessment of high-speed aircraft, *J. Geophys. Res.*, **104**, 27,545-27,564.
- Douglass, A. R., Stolarski, R.S., Schoeberl, M.R., Jackman, C.H., Gupta, M., Newman, P.A., Nielsen, J.E., and Fleming, E., 2008. Relationship of loss, mean age of air and the distribution of CFCs to stratospheric circulation and implications for atmospheric lifetimes, *J. Geophys. Res.*, **113**, doi:10.1029/2007JD009575.
- Engel, A., T. Möbius, H. Bönisch, U. Schmidt, R. Heinz, I. Levin, E. Atlas, S. Aoki, T. Nakazawa, S. Sugawara, F. Moore, D. Hurst, J. Elkins, S. Schauffler, A. Andrews, and K. Boering, 2009. Age of stratospheric air unchanged within uncertainties over the past 30 years, *Nat. Geosci.*, **2**, 28-31.
- Eyring, V., N. Butchart, D. W. Waugh, H. Akiyoshi, J.

- Austin, S. Bekki, G. E. Bodeker, B. A. Boville, C. Brühl, M. P. Chipperfield, E. Cordero, M. Dameris, M. Deushi, V. E. Fioletov, S. M. Frith, R. R. Garcia, A. Gettelman, M. A. Giorgetta, V. Grewe, L. Jourdain, D. E. Kinnison, E. Mancini, E. Manzini, M. Marchand, D. R. Marsh, T. Nagashima, P. A. Newman, J. E. Nielsen, S. Pawson, G. Pitari, D. A. Plummer, E. Rozanov, M. Schraner, T. G. Shepherd, K. Shibata, R. S. Stolarski, H. Struthers, W. Tian, and M. Yoshiki, 2006. Assessment of temperature, trace species, and ozone in chemistry-climate model simulations of the recent past, *J. Geophys. Res.*, **111**, doi:10.1029/2006JD007327.
- Garcia, R. R., and Randel, W. J., 2008. Acceleration of the Brewer-Dobson circulation due to increases in greenhouse gases, *J. Atmos. Sci.*, **65**, 2731-2739, doi:10.1175/2008JAS2712.1.
- Glatthor, N., T. von Clarmann, H. Fischer, B. Funke, U. Grabowski, M. Höpfner, S. Kellmann, M. Kiefer, A. Linden, M. Milz, T. Steck, G. P. Stiller, G. Mengistu Tsidu, and D-Y. Wang, 2005. Mixing processes during the Antarctic vortex split in September-October 2002 as inferred from source gas and ozone distributions from ENVISAT-MIPAS, *J. Atmos. Sci.*, **62**, 787-800.
- Gray, L.J. and Russell, J.M., 1999. Interannual variability of trace gases in the subtropical winter stratosphere, *J. Atmos. Sci.*, **56**, 977-993.
- Grewe, V. and Sausen, R., 2009. Comment on “Quantitative performance metrics for stratospheric-resolving chemistry-climate models” by Waugh and Eyring, *Atmos. Chem. Phys.*, **9**, 9101-9110.
- Hall, T. M., 2000. Path histories and time scales in stratospheric transport: Analysis of an idealized model, *J. Geophys. Res.*, **105**, 22,811-22,823.
- Hall, T. M., and R. A. Plumb, 1994. Age as a diagnostic of stratospheric transport, *J. Geophys. Res.*, **99**, 1059-1070, doi:10.1029/93JD03192.
- Hall, T.M., Waugh, D.W., Boering, K.A., and Plumb, R.A. (1999), Evaluation of transport in stratospheric models, *J. Geophys. Res.*, **104**, 18815-18839.
- Lambert, A., W. G. Read, N. J. Livesey, M. L. Santee, G. L. Manney, L. Froidevaux, D. L. Wu, M. J. Schwartz, H. C. Pumphrey, C. Jimenez, G. E. Nedoluha, R. E. Cofield, D. T. Cuddy, W. H. Daffer, B. J. Drouin, R. A. Fuller, R. F. Jarnot, B. W. Knosp, H. M. Pickett, V. S. Perun, W. V. Snyder, P. C. Stek, R. P. Thurstans, P. A. Wagner, J. W. Waters, K. W. Jucks, G. C. Toon, R. A. Stachnik, P. F. Bernath, C. D. Boone, K. A. Walker, J. Urban, D. Murtagh, J. W. Elkins, and E. Atlas, 2007. Validation of the Aura Microwave Limb Sounder middle atmosphere water vapor and nitrous oxide measurements, *J. Geophys. Res.*, **112**, doi:10.1029/2007JD008724.
- Lary, D. J., Waugh, D. W., Douglass, A. R., Stolarski, R. S., Newman, P. A., and Mussa, H., 2007. Variations in stratospheric inorganic chlorine between 1991 and 2006, *Geophys. Res. Lett.*, **34**, doi:10.1029/2007GL030053.
- Li, F., Austin, J., and Wilson, J., 2008. The strength of the Brewer-Dobson circulation in a changing climate: Coupled chemistry-climate model simulations, *J. Clim.*, **21**, 40-57, doi:10.1175/2007JCLI1663.1.
- Livesey, N.J., et al., (2007). Earth Observing System (EOS) Aura Microwave Limb Sounder (MLS) Version 2.2 Level 2 data quality and description document, JPL D-33509, 2007.
- McLandress, C. and Shepherd, T. G., 2009. Simulated anthropogenic changes in the Brewer-Dobson circulation, including its extension to high latitudes, *J. Clim.*, **22**, 1516-1540, doi:10.1175/2008JCLI2679.1.
- Mote, P. W., Rosenlof, K. H., McIntyre, M. E., Carr, E. S., Gille, J. C., Holton, J. R. Kinnersley, J. S., Pumphrey, H. C., Russell, J. M., and Waters, J. W., 1996. An atmospheric tape recorder: The imprint of tropical tropopause temperatures on stratospheric water vapor, *J. Geophys. Res.*, **101**, 3989-4006.
- Mote, P. W., Dunkerton, T., McIntyre, M., Ray, E., Haynes, P., and Russell, J., 1998. Vertical velocity, vertical diffusion, and dilution by midlatitude air in the tropical lower stratosphere, *J. Geophys. Res.*, **103**, 8651-8666.
- Neu, J. L. and Plumb, R. A., 1999. Age of air in a ‘leaky pipe’ model of stratospheric transport, *J. Geophys. Res.*, **104**, 19,243-19,255.
- Neu, J. L., Sparling, L.C., and Plumb, R.A. (2003), Variability of the subtropical ‘edges’ in the stratosphere, *J. Geophys. Res.*, **108**, doi:10.1029/2002JD002706.
- Oman, L., Waugh, D. W., Pawson, S., Stolarski, R. S., and Newman, P. A., 2009. On the influence of anthropogenic forcings on changes in the stratospheric mean age, *J. Geophys. Res.*, **114**,

- doi:10.1029/2008JD010378.
- Randel, W. J., Wu, F., Vomel, H., Nedoluha, G. E., and P. Forster, 2006. Decreases in stratospheric water vapor after 2001: Links to changes in the tropical tropopause and the Brewer-Dobson circulation, *J. Geophys. Res.*, **111**, doi:10.1029/2005JD006744.
- Read, W., A. Lambert, J. Bacmeister, R. E. Cofield, L. E. Christensen, D. T. Cuddy, W. H. Daffer, B. J. Drouin, E. Fetzer, L. Froidevaux, R. Fuller, R. Herman, R. F. Jarnot, J. H. Jiang, Y. B. Jiang, K. Kelly, B. W. Knosp, L. J. Kovalenko, N. J. Livesey, H.-C. Liu, G. L. Manney, H. M. Pickett, H. C. Pumphrey, K. H. Rosenlof, X. Sabouchi, M. L. Santee, M. J. Schwartz, W. V. Snyder, P. C. Stek, H. Su, L. L. Takacs, R. P. Thurstans, H. Vömel, P. A. Wagner, J. W. Waters, C. R. Webster, E. M. Weinstock, and D. L. Wu, 2007. Aura Microwave Limb Sounder upper tropospheric and lower stratospheric H<sub>2</sub>O and relative humidity with respect to ice validation, *J. Geophys. Res.*, **112**, doi:10.1029/2007JD008752.
- Rosenlof, K., 1995. Seasonal cycle of the residual mean meridional circulation in the stratosphere, *J. Geophys. Res.*, **100**, 5173-5191.
- Santee, M. L., Froidevaux, L., Manney, G. L., Read, W. G., Waters, J. W., Chipperfield, M. P., Roche, A. E., Kumer, J. B., Mergenthaler, J. L., and Russell III, J. M., 1996. Chlorine deactivation in the lower stratospheric polar regions during late winter: Results from UARS, *J. Geophys. Res.*, **101**, 18,835-18,859.
- Schauffler, S.M., E. L. Atlas, S. G. Donnelly, A. Andrews, S. A. Montzka, J. W. Elkins, D. F. Hurst, P. A. Romashkin, G. S. Dutton, V. Stroud, 2003. Chlorine budget and partitioning during the Stratospheric Aerosol and Gas Experiment (SAGE) III Ozone Loss and Validation Experiment (SOLVE), *J. Geophys. Res.*, **108**, doi:10.1029/2001JD002040.
- Sparling, L.C., 2000. Statistical perspectives on stratospheric transport, *Rev. Geophys.*, **38**, 417-436.
- Schoeberl, M.R., Douglass, A.R., Stolarski, R.S., Pawson, S., Strahan, S., and Read, W., 2008. Comparison of lower stratospheric tropical mean vertical velocities, *J. Geophys. Res.*, **113**, doi:10.1029/2008JD010221.
- Stenke, A., Dameris, M., Grewe, V., and Garny, H., 2009. Implications of Lagrangian transport for simulations with a coupled chemistry-climate model, *Atmos. Chem. Phys.*, **9**, 5489-5504.
- Stiller, G.P., T. von Clarmann, M. Höpfner, N. Glatthor, U. Grabowski, S. Kellmann, A. Kleinert, A. Linden, M. Milz, T. Reddmann, T. Steck, H. Fischer, B. Funke, M. López-Puertas, and A. Engel, 2008. Global distribution of mean age of stratospheric air from MIPAS SF<sub>6</sub> measurements, *Atmos. Chem. Phys.*, **8**, 677-695.
- Strahan, S. E. and Douglass, A. R., 2004. Evaluating the credibility of transport processes in simulations of ozone recovery using the Global Modeling Initiative three-dimensional model, *J. Geophys. Res.*, **109**, doi:10.1029/2003JD004238.
- Strahan, S. E., and Polansky, B. C., 2006. Meteorological implementation issues in chemistry and transport models, *Atmos. Chem. Phys.*, **6**, 2895-2910.
- Waugh, D., 2009. Atmospheric dynamics: The age of stratospheric air, *Nature Geo.*, **2**, 14-16, doi:10.1038/ngeo397.
- Waugh, D. W. and Hall, T. M., 2002. Age of stratospheric air: Theory, observations, and models, *Rev. Geophys.*, **40**, doi:10.1029/2000RG000101.
- Waugh, D.W., and Eyring, V., 2008. Quantifying performance metrics for stratospheric-resolving chemistry-climate models, *Atmos. Chem. Phys.*, **8**, 5699-5713.
- World Meteorological Organization (WMO)/United Nations Environment Programme (UNEP), 2007. *Scientific Assessment of Ozone Depletion: 2006*, World Meteorological Organization, Global Ozone Research and Monitoring Project, Report No. 50, Geneva, Switzerland.

# Chapter 6

## Stratospheric Chemistry

**Lead Authors:** Martyn Chipperfield & Douglas Kinnison

**Co-Authors:** Slimane Bekki  
Huisheng Bian  
Christoph Brühl  
Tim Canty  
Irene Cionni  
Sandip Dhomse  
Lucien Froidevaux  
Ryan Fuller  
Rolf Müller  
Michael Prather  
Ross Salawich  
Michelle Santee  
Wenshou Tian  
Simone Tilmes

**Acknowledgements:** Anu Dudhia, Ben Johnson, Ashley Jones, Perrine Lemennais, Beiping Luo, Alexei Rozanov, Virginie Poulain, Bjorn-Martin Sinnbuer, Jo Urban, Kaley Walker

---

## 6.1 Introduction

An accurate representation of atmospheric chemistry is a key component of a coupled CCM. Clearly, a realistic chemistry scheme is a requirement for reliable predictions of key trace gases, but it is also essential for realistic climate simulations. Aside from CO<sub>2</sub>, the stratospheric distribution of the other major GHGs is partly determined by atmospheric chemistry.

CCMs are comprised of an underlying general circulation model (GCM) coupled to a chemistry module. The inclusion of detailed chemistry tends to add significantly to the computational cost both through the expense of solving the chemistry and the cost of additional tracers. The expense and complexity of the CCMs mean that evaluation of the models is difficult and time consuming. This is particularly true if the chemistry scheme has been developed ‘on-line’ within the CCM. A useful strategy for many CCMs is to use the same chemistry module in simpler models, *e.g.*, 3-D chemical transport models or 2-D models, so that more simulations can be performed. In any case, the evaluation of the climatological CCM simulations with observations is problematic. If enough observations exist then mean distributions can be compared but this is not generally possible with campaign data. Therefore, alternative approaches to evaluation are needed.

The aim of this chapter is to evaluate the chemical schemes of current CCMs using, where possible, a process-based approach or otherwise climatological observations. This builds on the proposals for chemical validation contained in Eyring *et al.* (2005), which are summarized in **Table 6.1**. The proposed processes to evaluate CCMs can be separated into the four areas of (i) photolysis rates, (ii) fast radical chemistry, (iii) reservoir and longer-lived species and (iv) polar chemistry. The remainder of this chapter is therefore structured along these lines. Section 6.2 describes some relevant aspects of how CCMs are formulated. The main results of the evaluation are contained in Section 6.3, which is divided into the 4 areas listed above and summarized in Table 6.1. Each subsection summarizes the performance of the models in the form of a grading. The overall performance of each model is then summarized in Section 6.4.

## 6.2 Formulation of Chemical Schemes

Details of the chemistry schemes included in the CCMs are given in Chapter 2. Although there are differences in detail, all of the models essentially contain a description of the main chemical species of relevance for stratospheric ozone, contained in the O<sub>x</sub>, HO<sub>y</sub>, Cl<sub>y</sub>, NO<sub>y</sub>, Br<sub>y</sub> chemical families (where x or y denotes the total components for the given family) and the relevant source gases

(except E39CA does not include bromine chemistry). The models also contain a treatment of heterogeneous chemistry on sulfate aerosols and polar stratospheric clouds (PSCs). However, these aerosol/PSC schemes are based on an equilibrium approach where the models condense gas-phase species (*e.g.*, H<sub>2</sub>O, HNO<sub>3</sub>) onto a specified distribution of particle number density or size. Therefore, the models evaluated here do not contain explicit microphysics. The surface area density of sulfate aerosols in the CCMVal runs is specified from a provided climatology.

As stratospheric CCMs have evolved by a number of different pathways, a full chemistry evaluation needs to consider the explicit reactions schemes contained in the model. Clearly all CCMs aim to have a chemistry scheme sufficient to model stratospheric ozone accurately, but comparisons presented in this chapter, and elsewhere, can show very different model behaviour. Tables 6S.1, 6S.2 and 6S.3 in the Supplementary Material list the chemical species, gas-phase reactions and photolytic reactions, respectively, for each CCM and the photostationary state (PSS) model used in Section 6.3.2. The species and reactions listed are those important enough to be considered for inclusion in a global stratospheric CCM. Where individual models have ignored species and/or reactions the implications of this should be investigated further. Specific cases where the simplifications in the chemistry scheme have clearly affected model performance are mentioned below. Note that the description of the heterogeneous chemistry in the CCMs is provided in Chapter 2.

## 6.3 Evaluation of CCMs

This section evaluates the performance of the CCMs in four principal areas (see Table 6.1). Subsection 6.3.1 deals with photolysis rates. Subsection 6.3.2 covers fast radical chemistry outside of the polar winter/spring. Subsection 6.3.3 investigates reservoir species and long-lived tracers. Finally, Subsection 6.3.4 evaluates the performance of the models for chemistry related to polar ozone depletion. Throughout this analysis, output is taken from either the CCMVal-2 REF-B1 or REF-B2 simulations.

Throughout this chapter, quantitative estimates of CCM performance for a range of diagnostics have been obtained by using a formula based on the grades from Douglass *et al.* (1999) and Waugh and Eyring (2008):

$$g = 1 - \left( \frac{1}{N} \left[ \sum \frac{|\mu_{CCM}^i - \mu_{obs}^i|}{n\sigma} \right] \right) \quad (6.1)$$

where  $N$  is an averaging factor,  $\mu_{CCM}$  is the model climatological mean and  $\mu_{obs}$  is the observed climatological mean and  $\sigma$  is a measure of the uncertainty. The value of  $n$  can be chosen to give a spread in  $g$ ; if  $n = 3$  then a value of  $g = 0$  indicates the model mean is three times the error away from the observed mean. More discussion of this approach



**Table 6.1:** List of core processes to validate chemistry in CCMs with a focus on their ability to accurately model stratospheric ozone. The diagnostics which are used as quantitative metrics for the overall model assessment are highlighted in gray.

Process	Diagnostic	Variables	Data	References <sup>a</sup>
<b>Photolysis Rates</b>				
Accuracy of high-sun photolysis rates	Single profiles (0-80 km), also with clouds and aerosols	$J_s^b$	None	<i>Prather and Remsberg (1993)</i>
Accuracy of low-sun photolysis rates (spherical atmospheres, polar chemistry)	Noon, midnight & average profiles	$J_s$	None	
Accuracy of wavelength binning (290-400 nm)	Single profile (0-24 km)	$J-O_3(^1D)$ , $J-O_3$ , and $J-NO_2$	IPMMI transfer std with TUV	
<b>Short time scale chemical processes</b>				
Offline box model comparisons of fast chemistry	Profiles and tracer-tracer correlations of radical precursors	$N_2O$ , $O_3$ , $NO_y^b$ , $Cl_y^b$ , $Br_y^b$	Balloon, shuttle, aircraft, and satellite obs.	<i>Gao et al. (2001); Salawitch et al. (1994a)</i>
	Profiles, tracer-tracer correlations, and partitioning of radicals	$O(^3P)$ , $O(^1D)$ , $HO_x^b$ , $NO_x^b$ , $ClO$ , $BrO$ , $Cl_y$ , $Br_y$ , $NO_y$	Same as above	<i>Pierson et al. (2000); Park et al. (1999)</i>
<b>Long time scale chemical processes</b>				
Comparisons of source gases and reservoir species to observational climatologies	Tracer-tracer correlations	$NO_y$ , $N_2O$ , $CH_4$ , $H_2O$	Balloon, aircraft and MIPAS obs.	<i>Chang et al. (1996); Fahey et al. (1996); Müller et al. (1997)</i>
	Mean annual cycle @ 1hPa and 50hPa	$BrO$ , $CO$ , $HCl$ , $ClONO_2$ , $N_2O_5$ , $N_2O$ , $HNO_3$ , $CH_4$ , $H_2O$ , $O_3$	ACE-FTS, MIPAS, ODIN, SCIAMACHY	<i>Millard et al. (2002); Salawitch et al. (2002); Sen et al. (1998)</i>
	Mean Profiles @ 30°-60°S	Same as above	Same as above	Same as above
Long-term variation of reservoir and radical species	Comparison of total column at selected ground based stations	$HCl$ , $ClONO_2$ , $NO_2$	NDACC	<i>Rinsland et al. (2003)</i>
	Evolution of model results from 1960-2100; PoLS; EqUS; ExtrpLS	$NO_y$ , $Cl_y$ , $Br_y$ , $N_2O$ , $CH_4$ , $O_3$ , $H_2O$	None, model/model comparison	<i>Eyring et al. (2007)</i>
	Summation of total organic and inorganic bromine and chlorine	$TCl_y^b$ , $TBr_y^b$	None, model/model comparison	
<b>Polar Processes</b>				
Denitrification / dehydration	Comparison of gas-phase $HNO_3$ and $H_2O$ on Eqlat / theta grid	$HNO_3$ and $H_2O$ (gas-phase) [ $u,v,T$ for Eqlat- $\theta^b$ ]	Aura-MLS	<i>Manney et al. (2007); Santee et al. (2007); Lambert et al. (2007)</i>
Chlorine activation	Comparison of $HCl$ on Eqlat / theta grid (loss of $HCl$ is proportional to $Cl_x$ activation)	$HCl$ [ $u,v,T$ for Eqlat- $\theta$ ]	Aura-MLS	<i>Froidevaux et al. (2008)</i>

Table 6.1 continued.

Process	Diagnostic	Variables	Data	References <sup>a</sup>
Stratospheric aerosol processes	Abundance of NAT <sup>b</sup> and ICE <sup>b</sup> SAD	SAD-NAT; SAD-ICE	None, model/model comparison	
Chemical ozone depletion	Tracer-tracer chemical ozone loss	O <sub>3</sub> , N <sub>2</sub> O, [u,v,T for Eqlat/θ]	HALOE-UARS	Rex <i>et al.</i> (2004); Tilmes <i>et al.</i> (2004); Tilmes <i>et al.</i> (2007)
	PACI <sup>b</sup>	T, EESC	UKMETO; ERA-40	Tilmes <i>et al.</i> (2007)

<sup>a</sup> Listed references only provide examples.

<sup>b</sup> Abbreviations:  $J_s$ =photolysis rate constants ( $\text{sec}^{-1}$ ); IPMMI = International Photolysis Frequency Measurement and Modeling Intercomparison campaign; SAD = surface area density;  $\text{NO}_y$  = total reactive nitrogen;  $\text{Cl}_y$  = total inorganic chlorine;  $\text{Br}_y$  = total inorganic bromine;  $\text{TCl}_y$  = total chlorine (inorganic + organic);  $\text{TBr}_y$  (inorganic+organic);  $\text{HO}_x = \text{OH} + \text{HO}_2$ ;  $\text{NO}_x = \text{NO} + \text{NO}_2$ ; NAT = nitric acid trihydrate; ICE = water ice; Eqlat- $\theta$  = Equivalent latitude - potential temperature coordinate system; PoLS = polar lower stratosphere; EqUS = equatorial upper stratosphere; ExtrpLS = extratropical lower stratosphere; PACI = potential for chlorine activation.

is given in Chapter 1.

### 6.3.1 Evaluation of Photolysis Rates

The accurate calculation of photolysis (J) rates is an essential component of any atmospheric chemical model. However, this calculation is complex and there are likely many causes for the differences between models. Models may differ in their treatment of radiative transfer, aerosols and clouds. Models may update the photolysis rates at a different time resolution. Although all CCM photolysis modules use standard absorption cross-sections (*e.g.*, Sander *et al.*, 2006, hereafter JPL-2006), they likely differ in how they are implemented in terms of wavelength integration or temperature dependence.

For these reasons it is important to compare photolysis rates calculated by CCMs using a standard set of prescribed conditions (*e.g.*, O<sub>3</sub>, temperature, and pressure profiles). Modelling groups need to use the code actually employed in the CCM for this comparison, which is based only on the final J-values – the quantity actually relevant for the chemical comparisons – and not on the separate components of the calculation. For example, it is not useful to plot and compare cross-sections since each model has their own algorithm for number of wavelength bins, the method of averaging the cross-sections with solar flux, and how to include temperature dependencies.

#### 6.3.1.1 Introduction to PhotoComp

This photolysis benchmark (PhotoComp 2008) is a component of SPARC CCMVal and has been designed to evaluate how models calculate photolysis rates (and indirectly heating rates) in the stratosphere and troposphere.

The primary goal is to improve model performance due to better calibration against laboratory and atmospheric measurements, and to provide more accurate numerical algorithms for solving the equation of radiative transfer. As with specific components of any major model comparison (*e.g.*, Prather and Remsberg, 1993), there may be numerous mistakes due to a different interpretation of the experiment, simple mistakes in model coding, different sources of physical data (solar fluxes, cross-sections, quantum yields) or different approximations of the exact solution. Any of these can make a model an “outlier” for one particular test, and thus the analysis must strive to identify these outliers as quickly as possible and provide clues as to the cause. This does not always mean that the majority rules, but in most cases, singularly unusual J-value profiles for a model are in error. The PhotoComp experiments are summarized in **Table 6.2**.

The PhotoComp 2008 participating models and the experiments they submitted are listed in **Table 6.3**. Details of the model photolysis schemes are given in the Supplementary Material in Table 6S-4. A total of 12 models (11 groups) performed at least some of the experiments and these included some stand-alone photolysis codes that have participated in other comparisons with models and measurements. Unfortunately, only 9 of the 18 CCMVal CCMs are represented. The missing CCMs should perform these tests in the future.

For PhotoComp 2008 we do not establish a single model as a reference standard, but instead define a robust mean and standard deviation from the ensemble of contributing models (see **Table 6.4**). The J-values ( $\text{sec}^{-1}$ ) are converted to the natural logarithm of the J-value ( $\ln(J)$ ) and averaged. A lower altitude cutoff is made where  $J < 10^{-10} \text{ sec}^{-1}$  (or  $10^{-14} \text{ sec}^{-1}$  for  $J\text{-O}_2$ ). Models that fall more than

**Table 6.2:** PhotoComp 2008 experiments. The diagnostics which are used as quantitative metrics for the overall model assessment are highlighted in gray.

Simulation	ALB	SZA	RS	CLD	AER	Figure	Comments
<b>High Sun</b>							
P1a	0.1	15°	Y	N	N	6.1, 6.4	Clear sky, with Rayleigh scattering
P1b	0.1	15°	Y	N	Y	6.2	Pinatubo aerosol in stratosphere
P1c	0.1	15°	Y	Y	N	6.3	Stratus cloud in troposphere
<b>Low Sun</b>							
P2a	0.1	84-96°	Y	N	N	6.4	24-hour average
P2n	0.1	84°	Y	N	N	6.4	Noontime
P2m	0.1	96°	Y	N	N	6.4	Midnight
<b>Wavelength Binning</b>							
P3	0.0	15°	N	N	N	6.5	Beer's Law extinction only, test wavelength binning for J-O <sub>3</sub> and J-NO <sub>2</sub>

Abbreviations: *J*s=photolysis rate constants ( $\text{sec}^{-1}$ ); SZA = solar zenith angle; ALB = surface albedo; RS= Rayleigh scattering; AER = aerosol; CLD = cloud.

**Table 6.3:** Models contributing to CCMVal PhotoComp 2008. The eight CCMs are indicated in bold.

Group	Model	Label	P1a	P1b	P1c	P2a	P2n	P2m	P3	Participants
GFDL, USA	<b>AMTRAC</b>	AMTR	✓			✓	✓	✓		J. Austin
NIES, Japan	<b>CCSRNIES</b>	CCSR	✓	✓		✓	✓	✓		H. Akiyoshi
MPI-C, Ger.	<b>EMAC</b>	EMAC	✓		✓	✓	✓			R. Sander, C. Brühl
GSFC, USA	FastJX	GFJX	✓	✓	✓	✓	✓	✓	✓	H. Bian
GSFC, USA	<b>GEOSCCM</b>	Gtbl	✓			✓	✓	✓		R. Kawa, R. Stolarski
CNRS, France	<b>LMDZrepro (TUV4.1)</b>	LMDZ	✓	✓	✓	✓	✓	✓	✓	S. Lefebvre, S. Bekki
NIWA, NZ	<b>NiwaSOCOL</b>	NIWA	✓		✓	✓	✓	✓		D. Smale, E. Rozanov
PMOD-WRC / ETH, CH	SOCOL	SOCOL	✓			✓	✓	✓		E. Rozanov
NCAR, USA	TUV	TUVM	✓	✓	✓	✓	✓	✓	✓	S. Madronich
UCI, USA	FastJX & UCiref	UCIJ UCIr	✓	✓	✓	✓	✓	✓	✓	M. Prather
U. Leeds, UK, U. Bremen, Ger.	<b>UMSLIMCAT</b>	SLIM	✓			✓	✓	✓		M. Chipperfield, M. Sinnhuber
NCAR, USA	<b>WACCM</b>	WACC	✓			✓	✓	✓	✓	D. Kinnison

2 standard deviations (in  $\ln(J)$ ) from the mean for levels starting 3 levels above the lowest altitude (step 2) up to ~74 km are dropped, and we recalculate this 'robust' mean  $\ln(J)$  and standard deviation for the remaining models. The atmospheric average robust standard deviation (RSD) for the 60 J-values are reported in Table 6.4 and the profiles of the model deviations from the robust mean  $\ln(J)$  for selected J-values are shown in Figures 6.1 and 6.4. This method

quickly identified outlying models with obvious mistakes, and it also identifies specific J-values for which there is clearly a large uncertainty, even among the best models.

### 6.3.1.2 PhotoComp 2008 experiments

There were 3 parts to the photolysis comparison which are summarized below. Complete experimental details are

**Table 6.4:** Atmospheric averaged robust standard deviation of  $\ln(J)$  ( $\times 100 = \text{RSD in } \%$ ), identifying  $J_s$  and conditions for which there is general agreement among the models. Results are shown for high sun (P1a), polar noontime (P2n) and 24-hour average (P2a).

No.	J-value	P1a	P2n	P2a	No.	J-value	P1a	P2n	P2a
1	NO	19	30	34	31	F115	15	20	26
2	O2	7	9	10	32	CCl4	4	5	6
3	O3	18	14	16	33	CH3Cl	8	5	6
4	O3 (1D)	9	10	13	34	MeCCl3	8	8	12
5	H2COa	12	32	45	35	CHF2Cl	24	31	33
6	H2COt	28	53	71	36	F123	13	-	9
7	H2O2	7	6	20	37	F141b	7	4	5
8	CH3OOH	7	10	22	38	F142b	24	13	13
9	NO2	7	7	17	39	CH3Br	3	6	8
10	NO3	7	10	19	40	H1211	5	4	5
11	N2O5	13	11	14	41	H1301	3	4	5
12	HNO2	3	4	-	42	H2402	4	4	4
13	HNO3	9	10	16	43	CH2Br2	8	6	10
14	HNO4	15	47	63	44	CHBr3	8	28	34
15	CINO3a	10	18	26	45	CH3I	-	-	-
16	CINO3t	7	17	28	46	CF3I	-	-	-
17	Cl2	11	9	22	47	OCS	-	-	-
18	HOCl	5	16	24	48	PAN	6	9	16
19	OCIO	8	8	13	49	CH3NO3	-	-	-
20	Cl2O2	16	15	21	50	ActAld	41	45	49
21	ClO	-	-	-	51	MeVK	5	-	-
22	BrO	3	15	24	52	MeAcr	21	-	-
23	BrNO3	6	9	15	53	GlyAld	24	-	-
24	HOBr	7	6	12	54	MEKeto	-	-	-
25	BrCl	10	6	15	55	EAld	-	-	-
26	N2O	3	5	13	56	MGlyxl	21	25	38
27	CFCl3	4	4	10	57	Glyxla	74	-	-
28	CF2Cl2 9	10	14	58	58	Glyxlt	39	-	-
29	F113	10	8	9	59	Acet-a	12	35	36
30	F114	5	-	6	60	Acet-t	11	34	36

available in the Supplementary Material for Chapter 6.

Part 1 is a basic test of all  $J$ -values for high sun (SZA =  $15^\circ$ ) over the ocean (albedo = 0.10, Lambertian). Part 1a: Clear sky (only Rayleigh scattering) and no aerosols. Part 1b: Pinatubo aerosol in the stratosphere. Part 1c: Stratus cloud in the troposphere. The primary atmosphere was specified in terms of pressure layers, mean temperature, and column  $O_3$  in each layer. Absorption by  $NO_2$  or other species was not included in calculating optical depths.

Part 2 tests the simulation of a spherical atmosphere

and twilight conditions that are critical to the polar regions. It used the same atmosphere as Part 1 without clouds or aerosols and assumed equinox (solar declination =  $0^\circ$ ) and latitude of  $84^\circ N$ . The surface SZA (not including refraction) therefore varies from  $84^\circ$  (noon) to  $96^\circ$  (midnight).  $J$ -values were reported at noon, midnight, and the 24-hour average (integrating as done in the CCM).

Part 3 tests the accuracy of wavelength binning in the critical region 290-400 nm that dominates tropospheric photolysis. Rayleigh scattering and surface reflection were

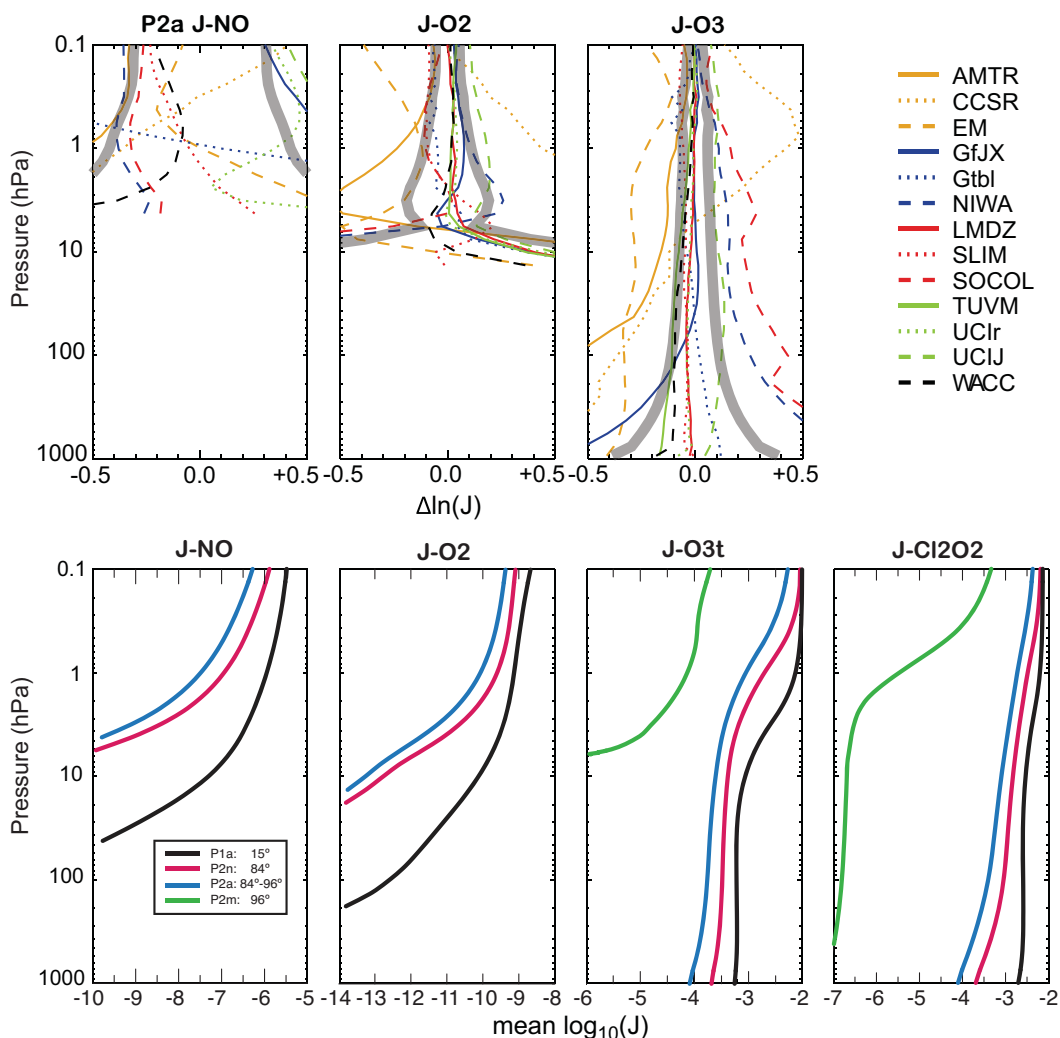


**Figure 6.1:** Model deviations in  $\ln(J)$  ( $\text{sec}^{-1}$ ) from the robust mean for nine selected J-values ( $\text{NO}$ ,  $\text{O}_2$ ,  $\text{O}_3$ ,  $\text{O}_3(^1\text{D})$ ,  $\text{NO}_2$ ,  $\text{H}_2\text{COa}$ ,  $\text{CFCl}_3$ ,  $\text{CF}_2\text{Cl}_2$ ,  $\text{N}_2\text{O}$ ) from PhotoComp experiment P1a (clear sky,  $\text{SZA} = 15^\circ$ ). The robust mean and standard deviation are derived as follows: (1) calculate the mean  $\ln(J)$  from all contributing models; (2) drop all lower altitudes where mean  $J < 1 \times 10^{-10}$  (or  $< 1 \times 10^{-14}$  for  $\text{J-O}_2$ ); (3) drop any model outside two standard deviations for levels starting 3 levels above the lowest altitude (step 2) up to  $\sim 74$  km; (4) recalculate this robust mean  $\ln(J)$  and standard deviation for the remaining models. The  $\pm 1$  standard deviations are plotted as wide gray bands.

switched off (albedo = 0) giving effectively a simple Beer's Law calculation. The calculation repeated Part 1, but report only J-values for  $\text{J-O}_3$  (*i.e.*, total),  $\text{J-O}_3(^1\text{D})$  [ $\text{O}_3 \rightarrow \text{O}_2 + \text{O}(^1\text{D})$ ], and  $\text{J-NO}_2$  [ $\text{NO}_2 \rightarrow \text{NO} + \text{O}$ ]. These are the two critical J-values for the troposphere, and they both have unusual structures in absorption cross-section and quantum yields. Reference runs were done using very high resolution ( $< 0.1$  nm) cross-sections and solar fluxes and for different options (*e.g.*, JPL-2006 vs. IUPAC cross-sections) to provide a benchmark. Results for Part 3 focus on J-values below 24 km.

A standard atmosphere was specified, whose primary definition is in terms of the air mass (pressure thickness), ozone mass, and mean temperature in each layer. This cho-

sen atmosphere is typical of the tropics with total ozone column of 260 DU. The use of JPL-2006 data (same as main CCM runs) was encouraged. High-resolution solar fluxes as a reference (sun-earth distance = 1.0 astronomical unit, averaged over the 11-year solar cycle) were also provided.

### 6.3.1.3 PhotoComp 2008 results and discussion

**Figure 6.1** shows the deviations in  $\ln(J)$  from the robust mean for nine selected J-values from experiment P1a. The agreement among the core models (those within 2

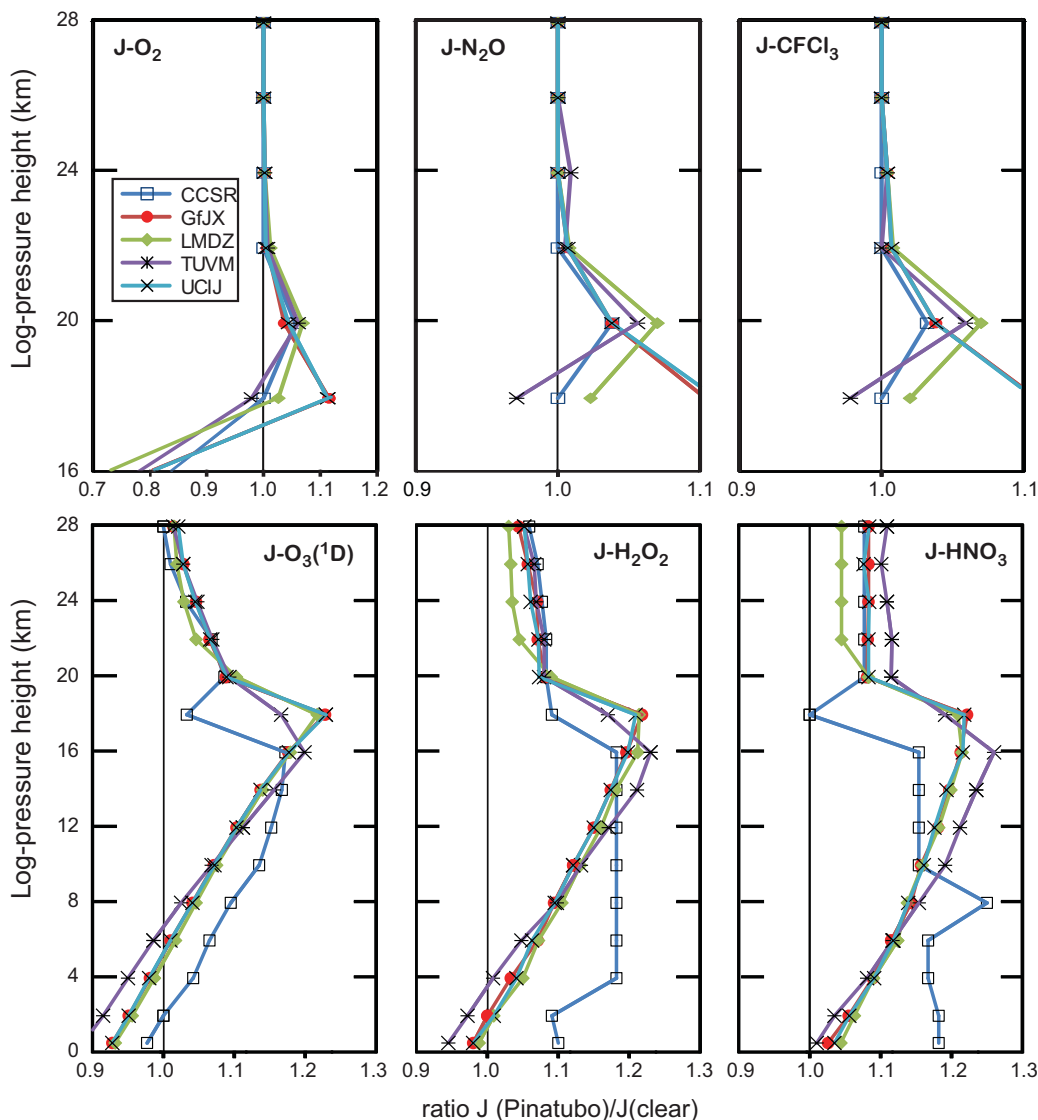


**Figure 6.2:** Ratio of J-values for a Pinatubo-like stratospheric aerosol layer (P1b: 17–19 km, optical depth 1.0 at 600 nm) to those for clear sky vs. pressure altitude (km). Five models contributed results and selected J-values are shown ( $\text{O}_2$ ,  $\text{N}_2\text{O}$ ,  $\text{CFCl}_3$ ,  $\text{O}_3(^1\text{D})$ ,  $\text{H}_2\text{O}_2$ ,  $\text{HNO}_3$ ) for altitudes of relevance to atmospheric chemistry.

standard deviations) is really excellent for many J-values. Some models consistently fall outside this core and it appears to be due to the method of solving the radiative transfer equation (*e.g.*, look-up tables). The robust standard deviation in J-NO is less than 20% above 1 hPa, but for the region 1–10 hPa where most of the  $\text{NO}_y$  is destroyed by J-NO, the models diverge with the fast-JX based models being almost a factor of 2 larger than the others. This discrepancy may reflect the failure of some models (*e.g.*, UCI) to account for NO self-absorption above 0.1 hPa, or else the very different treatments of the Schumann-Runge bands.

For  $\text{N}_2\text{O}$  and  $\text{CFCl}_3$ , the robust standard deviation is very small. Surprisingly, it is much larger for  $\text{CF}_2\text{Cl}_2$  which photolyses in the same wavelength region, and possibly the

cross-sections for  $\text{CF}_2\text{Cl}_2$  are effectively different in several models. Other oddities stand out, *e.g.*, the relatively large  $\pm 15\%$  range in J- $\text{H}_2\text{CO}_a$  ( $a = \text{radical-radical product channel, H} + \text{HCO}$ ). Another feature is the generally worse agreement between J- $\text{O}_3$  and J- $\text{O}_3(^1\text{D})$  within the troposphere compared with the stratosphere, and is probably caused by inadequate treatment of Rayleigh scattering. In general, most J-values that fall outside the  $\pm 2$  standard deviation test show unusual structures with altitude, implying errors in the radiative transfer solution rather than the cross-sections.

**Table 6.4** summarizes the RSD of the model J-values averaged over altitudes of interest for case studies P1a, P2n and P2a (see table text). For many J-values we find exceedingly good agreement (10% or less), but there are surpris-

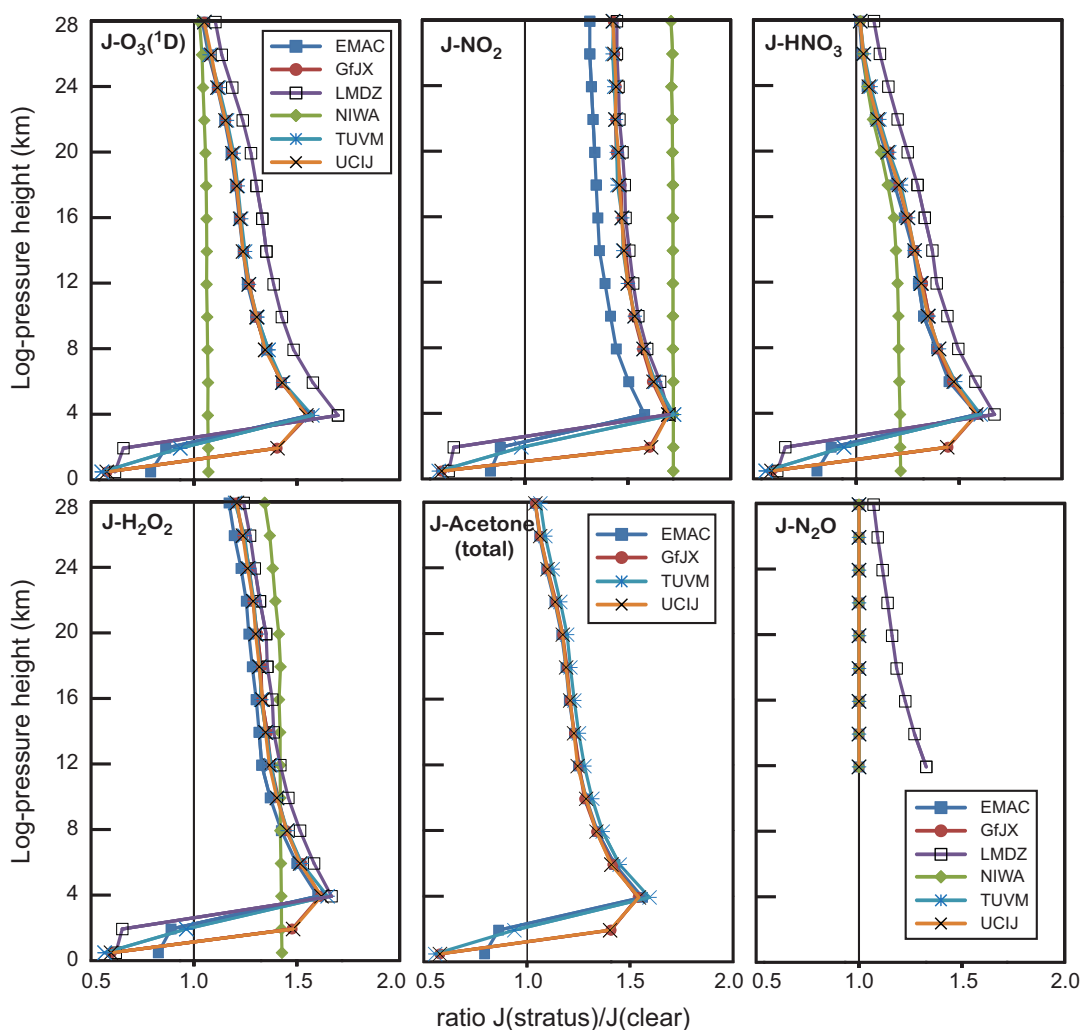


**Figure 6.3:** Ratio of J-values for a stratus cloud layer (P1c: 1-3 km, optical depth 20.0 at 600 nm) to those for clear sky vs. pressure altitude (km). Six models contributed results and selected J-values are shown ( $O_3(^1D)$ ,  $NO_2$ ,  $HNO_3$ ,  $H_2O_2$ , acetone (total, only 4 models),  $N_2O$ ).

ingly large RSDs for  $J-O_3$  ( $t = \text{sum of all product channels}$ ),  $J-H_2CO$  (a and t),  $J-HNO_4$ ,  $J-Cl_2O_2$ , a couple fluorocarbons, and many of the volatile organic compounds (VOCs) (few contributing models). For  $J-HNO_4$  the near-IR photolysis may not be included (Evans *et al.*, 2003).  $J-O_3$  is a key heating rate term: Three models show aberrant profiles at high sun (see Figure 6.1), but six models are obviously outside the RSD for polar conditions (see Figure 6.4). These discrepancies are worrisome and may impact the model circulations. However, note that in most cases CCM photolysis schemes are not linked to heating rate calculations.

The RSD is a single iteration that identifies and removes models more than  $\pm 2$  standard deviations from the mean of  $\ln(J)$ . This method was chosen to avoid having extreme outliers influence the mean. The process can be iterated again and again to remove those outside the new smaller standard deviation range. For example, if we focus on  $J-O_2$ , the initial RSD over the stratospheric range

of interest (18-70 km) is 7.1% with AMTR and CCSR and Gtbl removed. A second iteration removes EMAC, NiwaSOCOL, UMSLIMCAT and SOCOL, and cuts the standard deviation to 3.2%. Thus, a core group (GfJX, LMDZrepro, TUVM, UCIr, UCIJ, WACCM) shows remarkable agreement in the calculation of  $J-O_2$ . Similarly for  $J-O_3(^1D)$ , if we focus on the stratosphere and mesosphere (12-74 km), then the first iteration drops CCSR and Gtbl, resulting in an RSD of 7.6%. The next iteration drops NiwaSOCOL and SOCOL, reducing the standard deviation to 4.0%; and a further iteration drops AMTRAC, leaving a core group (EMAC, Gfjx, LMDZrepro, TUVM, UCIJ, WACCM, UMSLIMCAT) with a standard deviation of only 2.8%.

Figure 6.2 shows the change in J-values for a Pinatubo-like aerosol layer (P1b). The enhanced aerosol scattering of the Mt. Pinatubo layer was predicted to alter the photolysis rates in the stratosphere and troposphere

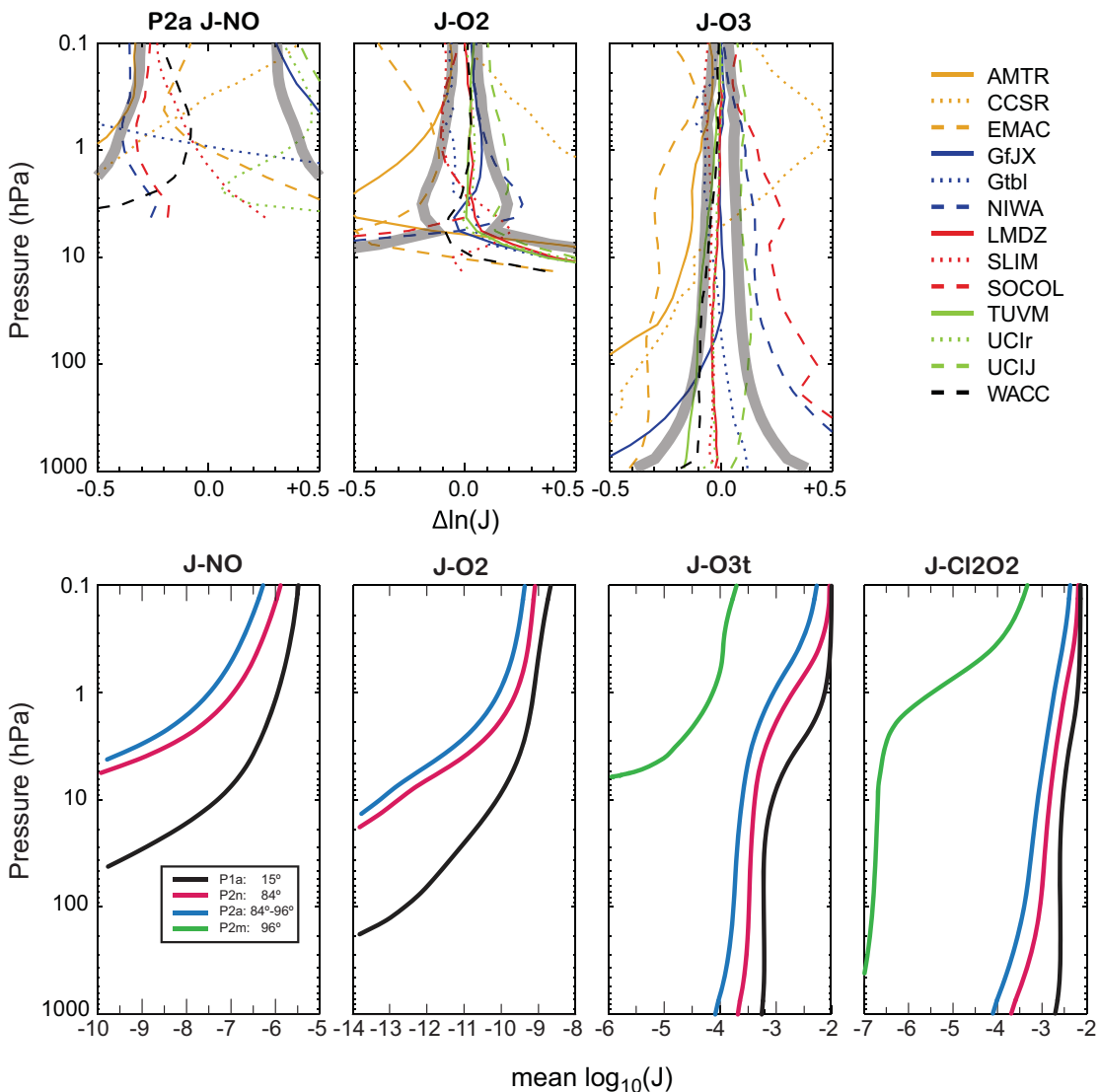


**Figure 6.4:** (top) Model deviations in  $\ln(J)$  ( $\text{sec}^{-1}$ ) from the robust mean for three selected J-values ( $\text{NO}$ ,  $\text{O}_2$ ,  $\text{O}_3(\text{total})$ ) from PhotoComp experiment P2a (24-hour average, polar,  $\text{SZA} = 84^\circ\text{-}96^\circ$ ). (bottom) The robust mean  $\ln(J)$  ( $\text{sec}^{-1}$ ) for J- $\text{NO}$ , J- $\text{O}_2$  and J- $\text{O}_3(\text{total})$  and J- $\text{Cl}_2\text{O}_2$  for experiments P1a, P2n, P2a, and P2m.

(Michelangeli *et al.*, 1989). Five models (only two of which are CCMVal models) submitted results. All models agree on the 4-7% increase at short wavelengths ( $\sim 205$  nm, J- $\text{O}_2$ , J- $\text{N}_2\text{O}$ , J- $\text{CFCl}_3$ ) in the layer immediately above the aerosols (20 km), but there is a large disparity in the middle of the aerosol layer at 18 km. UCII and GfJX (both based on fast-JX codes) predict a further increase to 11% above clear sky, whereas CCSRNIES, LMDZrepro, and TUVM predict a decrease in the ratio. Given the optical depth of 0.5 at mid-layer, one would expect that the J-values relative to clear sky would continue to increase in the aerosol layer, but this discrepancy may reflect the different ways of implementing a scattering layer relative to the CTM layers. Some models may have reported mid-aerosol-layer J-values; and others, the bottom of aerosol-layer (similar

analysis applies to the stratus cloud layer (Figure 6.3). For J-values of interest throughout the atmosphere (*e.g.*, J- $\text{O}_3(^1\text{D})$ , J- $\text{H}_2\text{O}_2$ , J- $\text{HNO}_3$ ) the models are in reasonable agreement, showing up to 20% enhancements through most of the troposphere, except for CCSRNIES for which there may be a mistake in submission as the pattern of change in the troposphere is inexplicable. The offset of TUVM below the cloud from the GfJX-LMDZ-UCII curves is probably due to differences in aerosol layer placement, but needs to be clarified.

**Figure 6.3** is similar to Figure 6.2 but for a thick stratus cloud (P1c). The enhanced scattering above a thick stratus cloud layer increases photolysis rates above and reduces them at the surface. Six models submitted results, and five models have the correct pattern. Once again, as in



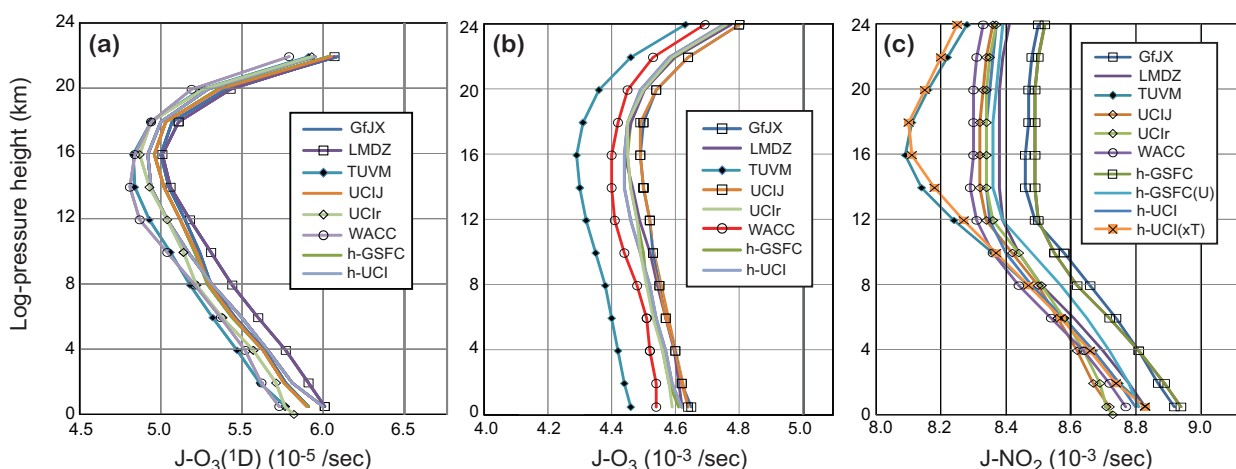


**Figure 6.5:** J-values ( $\text{sec}^{-1}$ ) vs. pressure altitude (km) for (a)  $\text{O}_3$  yielding  $\text{O}(^1\text{D})$ , (b)  $\text{O}_3$  total, and (c)  $\text{NO}_2$  from the Photocomp P3 experiment ( $\text{SZA} = 15^\circ$ , no Rayleigh scattering, no surface albedo, see text). In addition to the standard coarse wavelength resolution models already described, Bian (GfJX) and Prather (UCIr, UCIJ) contributed very-high wavelength resolution ( $\sim 0.1$  nm) calculations (h-GSFC and h-UCI) using the same cross-section, quantum yield and solar data as in their coarse models. For  $\text{J-NO}_2$ , the h-GSFC(U) also contributed a high-resolution J using the UCI tables for cross-section and quantum yield, and the h-UCI(xT) also included a log-extrapolation of both tables below their lower temperature limits.

P1b, the placement of cloud in the second layer appears to differ with UCIJ-GfJX having 50% enhancements in the middle of the CTM layer, but TUVM-LMDZrepro-EMAC having reductions, possibly representing the bottom of the cloud. All five of these models have large (20% to 40%) reductions in the lowest layer, below the cloud. NiwaSOCOL apparently has a very simple and inaccurate parameterisation of clouds. LMDZrepro reproduces the expected tropospheric patterns, but calculates large, incorrect enhancements in the 205 nm wavelength region, thus predicting enhanced photolysis of species such as  $\text{O}_2$ ,  $\text{N}_2\text{O}$ , and  $\text{CFCl}_3$  above clouds.

**Figure 6.4** shows (*bottom*) the robust mean  $\ln(\text{J})$  for  $\text{J-NO}$ ,  $\text{J-O}_2$ ,  $\text{J-O}_3(\text{t})$  and  $\text{J-Cl}_2\text{O}_2$  for experiments P1a and P2 (n, a, m), and (*top*) the deviations from the mean for the 24-hour polar average rates P2a for  $\text{J-NO}$ ,  $\text{J-O}_2$ ,  $\text{J-O}_3(\text{t})$ . As expected, averaging over polar twilight conditions increases the spread in the models as compared with high sun (P1a).

**Figure 6.5** shows results from the high-wavelength-resolution experiment P3 ( $\text{SZA}=15^\circ$ , no Rayleigh scattering, no surface albedo, see figure caption). Six models contributed results from their standard models and two (h-GSFC, h-UCI) also contributed high-resolution wavelength integrations of the J-values. These two high-resolution models also included an additional high-resolution calculation for  $\text{J-NO}_2$  that explored different approaches to using the  $\text{NO}_2$  cross-sections and quantum yields (see figure caption). The calculation of  $\text{J-O}_3(^1\text{D})$  from the ten different submissions is in good agreement, with a min-max range of  $\pm 4\%$ . An estimate of the error in adopting the coarser

wavelength resolution of UCIJ's fast-JX (7 nm) instead of the UCIr's J-ref code (1 to 2 nm bins over 295-324 nm) is seen to be small (2%) and is consistent with the very high resolution of h-UCI (0.05 nm bins) using the same solar flux and physics. Thus we conclude that 5 groups agree on the calculation of  $\text{J-O}_3(^1\text{D})$  within 5% and that the various wavelength resolutions and quadratures have small errors.

The  $\text{J-O}_3(\text{t})$  values, with the exception of TUVM are much tighter, with a  $\pm 2.5\%$  min-to-max range. The TUVM values are surprisingly about 3% below the mean of models and may reflect a difference in the Chappuis-band photolysis ( $> 400$  nm).

The  $\text{J-NO}_2$  values are in excellent agreement with a core group of models having a  $\pm 1\%$  min-max range. The two Goddard models (GfJX and h-GSFC) are inexplicably, uniformly greater by almost 3%. In the upper troposphere and lower stratosphere at temperatures below 240 K there is ambiguity in how to calculate  $\text{NO}_2$  photolysis given the recommended tables for cross-sections (220 K and 294 K) and quantum yields (248 K and 298 K). The UCI models (UCIJ, UCIr, h-UCI) interpolate linearly with temperature between the two tabulated values and do not extrapolate; whereas the h-UCI(xT) model (and apparently the TUVM model) extrapolates the log of both values to temperatures beyond the table range. This modest extrapolation is probably valid and thus there is a bias error in most standard models for  $\text{J-NO}_2$  in the upper troposphere/lower stratosphere (UTLS) of about +3%.

Overall, the agreement among the participating models in experiment P3 (Figure 6.5) is excellent. Even the potential biases identified are below 3%. In terms of grading,

Complete		Accurate			
trop Js	strat Js	P1a	P2n	P2a	
	■	■	■	■	AMTRAC3
	■	■	■	■	CCSRNIES
■	■	■	■	■	EMAC
	■	■	■	■	GEOSCCM
	■	■	■	■	LMDZrepro
	■	■	■	■	NiwaSOCOL
	■	■	■	■	SOCOL
	■	■	■	■	UMSLIMCAT
	■	■	■	■	WACCM

**Figure 6.6:** Matrices displaying PhotoComp grades for the nine participating CCMs. Two grades were given for the completeness of reported J-values relevant to the stratosphere (~45 out of 60) and the troposphere (~15, mostly VOCs). Accuracy for the J-values was based on the number of Js (out of the 45 stratospherically relevant ones) that were not eliminated by the initial  $\pm 2$  standard deviation test for P1a, P2n, and P2a. The stand-alone photolysis codes (GfJX, TUVM, UCIJ, UCIr) all received grades of 0.9 to 1.0 in all tests.

we could give all the participating models a good score for this part, but more importantly, this experiment shows that calculation of J-values using coarse resolution - providing the wavelength averaging is done correctly (see Wild *et al.*, 2000) - does not induce errors above 2%.

**Models and Measurements.** An earlier version of TUVM participated in the International Photolysis Frequency Measurement and Modeling Intercomparison (IPMMI; Cantrell *et al.*, (2003); Hofzumahaus *et al.*, (2004)) and performed excellently in calculating the clear-sky  $J\text{-NO}_2$ ,  $J\text{-O}_3(\text{total})$ , and  $J\text{-O}_3(^1\text{D})$  at the ground over the full range of SZA during the day. Thus TUVM provides a transfer standard for the P3 experiments (at least near the surface) and indicates that those participating models do match measured tropospheric J-values. Several campaigns measured J-values in the lower stratosphere (*e.g.*, POLARIS, and SOLVE) and it may be possible in the future to find a suitable transfer standard, such as the APL model, for these measurements.

### 6.3.1.4 PhotoComp 2008 grading

One major issue of model comparison is to grade models objectively. For photolysis we consider both the completeness of the reported J-values and the accuracy compared with the robust mean. While it is possible to calculate the abundance of stratospheric ozone *without* all the requested J-values, their inclusion in the CCM allows for that species to be simulated and evaluated against observations. Thus we include completeness of J-values relevant to stratosphere and troposphere separately. For accuracy, we consider only the 45 J-values with stratospheric relevance and the grades (in %) represent roughly the fraction of J-values that passed the RSD test. These grades are slightly generous for models that did not report all 45 J-values as only the reported outlying J-values were counted as inaccurate. Grades for the stand-alone (non-CCM) models were all in the 0.9 – 1.0 (90-100%) range.

The reporting CCMs showed a wide range of skill in calculating Js (**Figure 6.6**). EMAC, GEOSCCM, LMDZrepro, UMSLIMCAT and WACCM were consistently in the 0.9 – 1.0 (90-100%) range. EMAC was unusual in having trouble with the 24-hour average polar Js, and given the rest of its performance, this looks like a mistake in averaging for the PhotoComp reporting. NiwaSOCOL and SOCOL have some occasional problems that could be either the radiative transfer solutions or cross-sections. AMTRAC and CCSRNIES appear to have serious flaws in the radiative transfer solution with large errors in key J-values. Unfortunately, we have no information on the other nine CCMs. If the lack of participation was due to the difficulty of running PhotoComp experiments with the CCM J-value code, then this is worrisome as it points to the lack of ability to test the components of the CCMs or have a traceability to independent codes. Overall, given the good comparison of many CCMs with the detailed benchmark codes, we can conclude that it is possible to incorporate an accurate but computationally efficient photolysis scheme in a global CCM.

### 6.3.2 Evaluation of Radical (Fast) Chemistry (Non Polar Region)

The fast photochemistry within the CCMs has been evaluated by comparison of radical species in the  $\text{O}_x$ ,  $\text{HO}_x$ ,  $\text{NO}_x$ ,  $\text{ClO}_x$ , and  $\text{BrO}_x$  families to results from a photochemical steady state (PSS) box model, constrained by values of radical precursors specific to each CCM. In the past the PSS box model has been compared exhaustively to observed abundances of radicals and radical precursors (*e.g.*, Salawitch *et al.*, 1994a,b, 2002; Wennberg *et al.*, 1994, 1998; Osterman *et al.*, 1997, 1999; Sen *et al.*, 1998, 1999; Jucks *et al.*, 1998, 1999; Christensen *et al.*, 2002; Kovalenko *et al.*, 2007). The approach described below has

been used previously in the evaluation of 2D and 3D models sponsored by the NASA Models and Measurements Intercomparison II (NASA/TM-1999-209554).

### 6.3.2.1 Background to photochemical steady state model comparisons

We computed zonal, monthly mean values of the radical precursors  $O_3$ ,  $H_2O$ ,  $CH_4$ ,  $CO$ ,  $NO_y$ ,  $Cl_y$ , and  $Br_y$  (hereafter precursors) as a function of pressure and radicals ( $O(^3P)$ ,  $O(^1D)$ ,  $OH$ ,  $HO_2$ ,  $NO_x/NO_y$ ,  $ClO/Cl_y$ , and  $BrO/Br_y$ ) from the REF-B1 T3I files. Zonal, monthly mean profiles of  $T$ ,  $N_2O$  and sulfate surface area density (SAD) were also found. The profiles of  $T$ ,  $O_3$ ,  $H_2O$ ,  $CH_4$ ,  $CO$ ,  $NO_y$ ,  $Cl_y$ ,  $Br_y$ , and sulfate SAD were input to the PSS box model. The model is used to compute the diel variation of  $O(^3P)$ ,  $O(^1D)$ ,  $OH$ ,  $HO_2$ ,  $NO_x$ ,  $ClO$ , and  $BrO$  on a 15 minute time grid using an implicit integration scheme that converges to steady state (production and loss of each chemical species = 0 when integrated over a 24 hr period) using a Newton-Raphson solver. If the CCM model has used the same chemical mechanism (reaction scheme, rate constants, and absorption cross-sections) as the PSS model, then 24-hour average profiles of radicals found from the PSS simulation should closely approximate the zonal monthly mean profiles of radicals from the CCM. A close level of agreement should occur because the T3I files upon which the zonal monthly mean CCM profiles are based provide an instantaneous snapshot for a specific value of GMT at all longitudes. There are possible non-linearities in the chemistry due to zonal asymmetry. We provide a quantitative evaluation of the impact of these non-linearities on the comparisons by calculating the standard deviation, about the zonal monthly mean, of temperature and radical precursor abundances. The PSS model is re-run, varying each of the quantities, with the results factoring into the uncertainty calculation. In this manner, we provide a first-order estimate of the impact of these non-linearities on the fast chemistry.

We have chosen to analyse time periods for which observations of precursors and radicals are available from balloon and aircraft campaigns. We compare zonal, monthly mean profiles of radical precursors from each CCM to measured values to assess how accurately these fields are simulated. Rather than compare CCM profiles of radicals to measured radicals, we instead compare to profiles of radicals from the PSS model, which are calculated in the same manner using precursor fields from each CCM. It has been established that the PSS box model provides a reasonably accurate description of measured  $OH$ ,  $HO_2$ ,  $NO$ ,  $NO_2$ , and  $BrO$  (e.g., Salawitch *et al.*, 1994a,b, 2002, 2005; Wennberg *et al.*, 1994, 1998; Osterman *et al.*, 1997, 1999; Sen *et al.*, 1998, 1999; Jucks *et al.*, 1998, 1999; Christensen *et al.*, 2002; Pundt *et al.*, 2002; Kovalenko *et al.*, 2007).

Therefore, our presumption is that a CCM provides a reasonable representation of fast photochemical processes if:

- the CCM specifies the abundance of radical precursors reasonably well compared to observations and;
- the CCM calculates the abundance of radicals species in a manner that agrees reasonably well with the output of the PSS box model, when the PSS model is constrained to precursor profiles from the CCM.

Unfortunately, we lack observations of  $O(^3P)$  and  $O(^1D)$ . For these species, the PSS box model is used to place the CCM output on a common scale; models that compare well to the PSS output can be inferred to have similar representations of the chemical processes that control these  $O_x$  species, whereas models that differ significantly from the PSS output can be inferred to have a representation of  $O_x$  chemistry that differs from the other CCMs. It would be difficult to reach such a meaningful conclusion based on comparisons of profiles of  $O(^3P)$  and/or  $O(^1D)$  from individual CCMs, due to the non-linear dependence of  $O_x$  on local  $O_3$  and density as well as overhead  $O_3$  and pressure.

For the results shown in this chapter, we focus on comparisons for two time periods. The first is for volcanically perturbed conditions at northern hemisphere (NH) mid-latitudes; the second is for moderate aerosol loading conditions in the subtropical NH. Observations during the first time period in the analysis were obtained by the JPL Fourier Transform InfraRed (FTIR) Interferometer (<http://mark4sun.jpl.nasa.gov/>), which flew on the NASA Observations of the Middle Stratosphere (OMS) balloon payload launched from Ft. Sumner, New Mexico (35°N, 104°W) on September 25 and 26, 1993 (e.g., Osterman *et al.* 1997; Sen *et al.*, 1998; Jucks *et al.*, 1998; Salawitch *et al.*, 2002). Observations during the second time period were obtained by instruments on board the NASA ER-2 aircraft, on a flight based out of Barbers Point, Hawaii (21°N, 158°W) during the STRAT campaign ([http://www.espo.nasa.gov/strat/status/summary\\_jan96.html](http://www.espo.nasa.gov/strat/status/summary_jan96.html)) on February 21, 1996 (e.g., Lanzendorf *et al.*, 2001; Weinstock *et al.*, 2001; Dessler, 2002).

There are two other important details of the PSS comparisons that require explanation. One involves chemical kinetics; the other involves sulfate SAD. The PSS model is well suited to mimic the chemical kinetics used by each CCM group (Table 6S.2). For the 2 CCM groups (EMAC and GEOSCCM) that used kinetics parameters from JPL-2002 (Sander *et al.*, 2003) in the REF-B1 simulation, we conducted the PSS comparison using JPL-2002 kinetics. For the other 12 CCMs, JPL-2006 (Sander *et al.*, 2006) kinetics were used both in the REF-B1 simulation and the PSS evaluation. Of these 12 groups, only 3 CCMs (LMDZrepro, UM-SLIMCAT, and WACCM) included the chemical reaction  $BrONO_2+O$ , new for JPL-2006, within

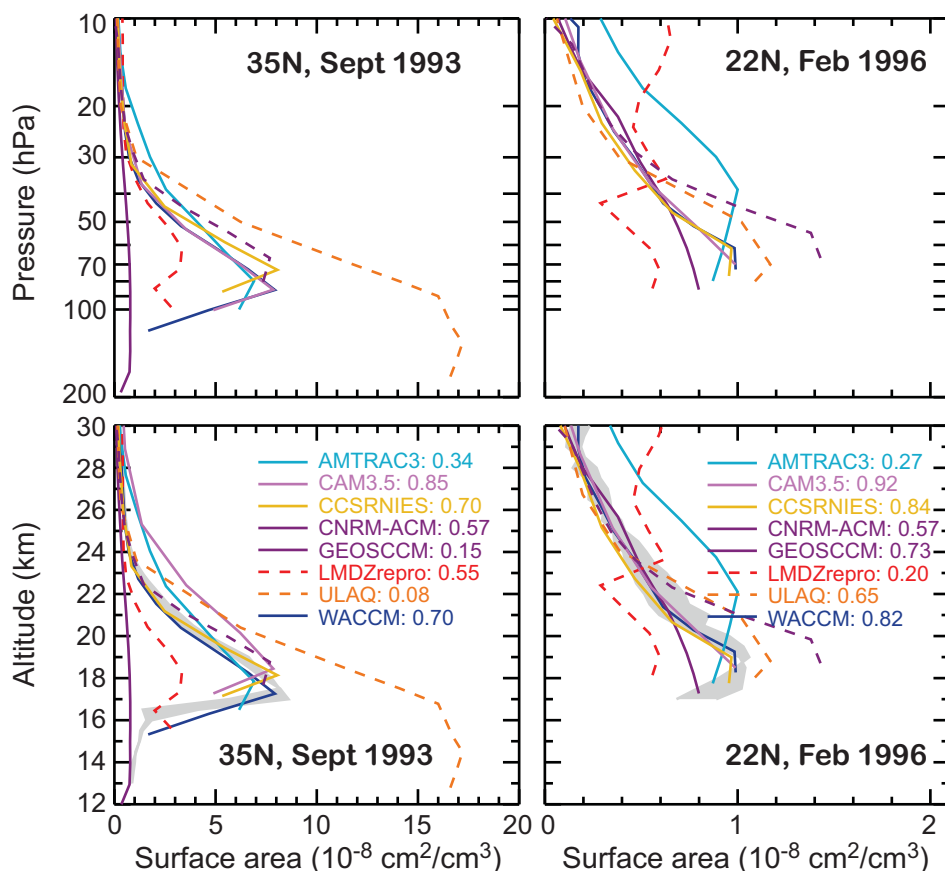


**Figure 6.7:** Sulfate surface area density versus pressure (top two panels) and versus geometric altitude (bottom two panels) for 35°N, September 1993 (left) and 22°N, February 1996 (right) from eight CCMs. The grey shaded region on the bottom two panels shows the climatology for sulfate surface area specified for the REF-B1 simulation (grey bounds values for 32.5° to 37.5°N for September 1993 and for 17.5° to 27.5°N for February 1996). The GEOSCCM REF-B1 calculation was carried out for background sulfate aerosol conditions. The variability among the other models reflects differences with respect to the prescribed climatology that occur for reasons either related to a difficulty in using a prescribed value of surface area given as a function of geometric altitude, or some other unknown cause.

their model. The other 9 CCM teams that used JPL-2006 kinetics neglected this reaction. Inclusion of this reaction increases the  $\text{BrO}/\text{Br}_y$  ratio (Sinnhuber *et al.*, 2002) and has an important effect on the evaluation of CCM chemistry. Indeed, in preliminary versions of this exercise, we provided our own “assessment” of which CCM teams had overlooked this reaction in their implementation of JPL-2006 kinetics that proved to be remarkably accurate. Finally, one group, MRI, neglected the production of HCl by the reaction  $\text{ClO}+\text{OH}$ . Neglect of this product channel, which has been well quantified in the laboratory (Lipson *et al.*, 1999), results in an overestimate of model ClO (McElroy and Salawitch, 1989) and an overestimate of the impact of halogens on future levels of upper stratospheric ozone (Müller and Salawitch, 1999). For the ClO evaluation of the MRI model, the PSS model was run with and without this product channel.

The other detail requiring explanation is sulfate SAD.

For the REF-B1 simulation, each CCM group was supposed to use specified values of sulfate SAD, as a function of altitude and latitude, based on the climatology reported by Thomason *et al.* (1997) (updated to near present times). Six CCM teams submitted T3I files for sulfate SAD to the archive. One model team, GEOSCCM, provided their value of sulfate SAD *via* private communication. Another team, AMTRAC, submitted time slices of sulfate SAD for the two evaluation periods. **Figure 6.7** shows profiles of sulphate SAD from these 8 CCMs, as a function of altitude and pressure, for the two fast chemistry evaluation periods. The profiles exhibit tremendous differences. The top panels of Figure 6.7 compare sulphate SAD versus pressure. The bottom panels compare sulfate SAD versus geometric altitude; on these plots, the climatological values of sulfate SAD are shown by the grey shaded region. For September 1993, the grey shaded region corresponds to the Thomason *et al.* (1997) climatology at 32.5°N and 37.5°N;

for February 1996, the grey region corresponds to the climatology at 17.5°N and 27.5°N. To show the results from the CCM models as a function of altitude, we integrated the hypsometric equation starting at the surface, using the zonal monthly mean CCM values of  $T$  versus pressure (none of the models archived altitude information). The bottom panel indicates values of  $g$  for each model, found using Equation 6.1 with  $n = 3$ , where  $\sigma_{obs}$  was based on either the width of the grey shaded region at a particular altitude or 10% of the climatological value of sulfate SAD, whichever is largest. The vertical lines in all panels extend to the tropopause.

The values of sulfate SAD archived by the various CCMs exhibit tremendous variability, despite the aim that the REF-B1 be conducted using the same prescribed aerosol climatology in all models. The lowest value of sulfate SAD was used by GEOSCCM, which ran REF-B1 for background (non-volcanic) aerosol conditions. The other 7 CCMs display large differences in SAD for both altitude and pressure coordinates. With the exception of AMTRAC, which provided profiles of sulfate SAD for only a few specified time slices, we have examined time series of sulfate SAD at various altitudes to confirm that we properly interpreted the time coordinate of each model. Results are shown in Figure 6S.1 of the Supplementary Material. All of the models show a peak in sulfate SAD at about the time that aerosol from the eruption of Mt. Pinatubo reached the stratosphere. However, two of the models (LMDZrepro and ULAQ) have archived values of sulfate SAD that are quite different from the prescribed climatology. Furthermore, 6 CCM groups (CMAM, EMAC, MRI, SOCOL, UMSLIMCAT, and UMUKCA-METO) submitted enough T3I files from the REF-B1 for the fast chemistry to be evaluated, but neglected to archive sulfate SAD. The goal of the REF-B1 simulation was for each model to simulate, as closely as possible, the sensitivity of ozone to halogens and volcanic aerosol during the past half century. The large difference between the archived values of sulfate SAD and the climatology suggests this goal has not been achieved. One difficulty in achieving this goal may be that the aerosol climatology was specified as a function of geometric altitude, a coordinate not native to most CCMs.

The profile of sulfate SAD has a profound impact on the abundance of  $\text{NO}_x$ ,  $\text{HO}_x$ , and  $\text{ClO}/\text{Cl}_y$  in the lowermost stratosphere. We chose September 1993 as a first case for examination due to the perturbation to the chemical radicals by the Pinatubo aerosol. Provided each model archives the actual profiles of sulfate SAD used in their REF-B1 run, the fact that there is so much model to model variability is not central to our evaluation of the CCM fast chemistry. For the 6 CCM groups that did not archive sulfate SAD, we have estimated this quantity by calculating a value of geometric altitude at each CCM pressure level and interpolating the sulfate SAD climatology for the precise CCM

latitude. We associated the uncertainty in these values of sulfate SAD based on a  $\pm 0.2$  km uncertainty in the altitude and a  $5^\circ$  uncertainty in the latitude used in the interpolation. In the grading table that summarizes the results of the fast chemistry evaluation, we include an asterisk within the “total grade” cell for the 6 CCMs that did not archive sulfate SAD, reflecting the importance of this parameter to the fast chemistry evaluation.

### 6.3.2.2 Photochemical steady state model results

**Figure 6.8** compares the zonal monthly mean profile of radical precursor from 14 CCMs, for September 1993 and the closest model latitude to 35°N, to the profile of  $\text{N}_2\text{O}$  measured by the balloon-borne MkIV instrument on 25 Sept 1993 at 35°N. Comparisons are also conducted for correlations of  $\text{O}_3$  vs.  $\text{N}_2\text{O}$ ,  $\text{H}_2\text{O} + 2\text{CH}_4$  ( $\text{H}_{\text{tot}}$ ) vs.  $\text{N}_2\text{O}$ ,  $\text{NO}_y$  vs.  $\text{N}_2\text{O}$ , where all observed values of all quantities are based on MkIV measurements. Comparisons are made for  $\text{Cl}_y$  vs.  $\text{N}_2\text{O}$  and  $\text{Br}_y$  vs.  $\text{N}_2\text{O}$  as well. Here, the estimates of  $\text{Cl}_y$  and  $\text{Br}_y$  are based on the Woodbridge *et al.* (1995) and Wamsley *et al.* (1998) relations, respectively. These relations were derived from aircraft observations that sampled stratospheric air masses, and have been scaled to mid-latitude conditions appropriate for September 1993 using well known time variations of organic halocarbons (*e.g.*, Table 8-5, WMO 2007). The  $\text{Br}_y$  relation was scaled to remove the influence of  $\text{CH}_2\text{Br}_2$ , a species known to provide  $\sim 2.2$  ppt to the stratosphere (Wamsley *et al.*, 1998) that was not prescribed in the REF-B1 simulation.

For a quantitative evaluation of the radical precursor fields within the CCMs, we used Equation 6.1 with  $n=3$  to find  $g_{\text{precursor}}$  for each model (numerical values given on Figure 6.8). Here,  $\mu_{\text{CCM}}$  is the zonal-mean value from each CCM,  $\mu_{\text{obs}}$  is the precursor value from either MkIV or the  $\text{Cl}_y$  (Woodbridge) or  $\text{Br}_y$  (Wamsley) relation, and  $\sigma = \sqrt{(\sigma_{\text{CCM}}^2 + \sigma_{\text{obs}}^2)}$ , where  $\sigma_{\text{CCM}}$  is the average value of the standard deviation about the zonal-mean for all of the CCM days that were used to describe the zonal, monthly mean (the number of days used varies from model to model, but is typically between 3 and 5),  $\sigma_{\text{obs}}$  is the uncertainty of the observation, and the summation is carried out over the  $N$  CCM model levels between the tropopause and 1 hPa. Negative values of  $g$  were set to zero. For the  $\text{N}_2\text{O}$  comparison, the MkIV profile was interpolated versus log-pressure to the pressure of each model. For the other comparisons, the “observed relation” of each species versus  $\text{N}_2\text{O}$  is interpolated to the CCM value of  $\text{N}_2\text{O}$  at each model level. The tropopause for each model was determined from the zonal monthly mean temperature versus pressure profile, using the WMO definition of the thermal tropopause. We averaged between the tropopause and 1 hPa to focus on the part of the stratosphere relevant for ozone loss and

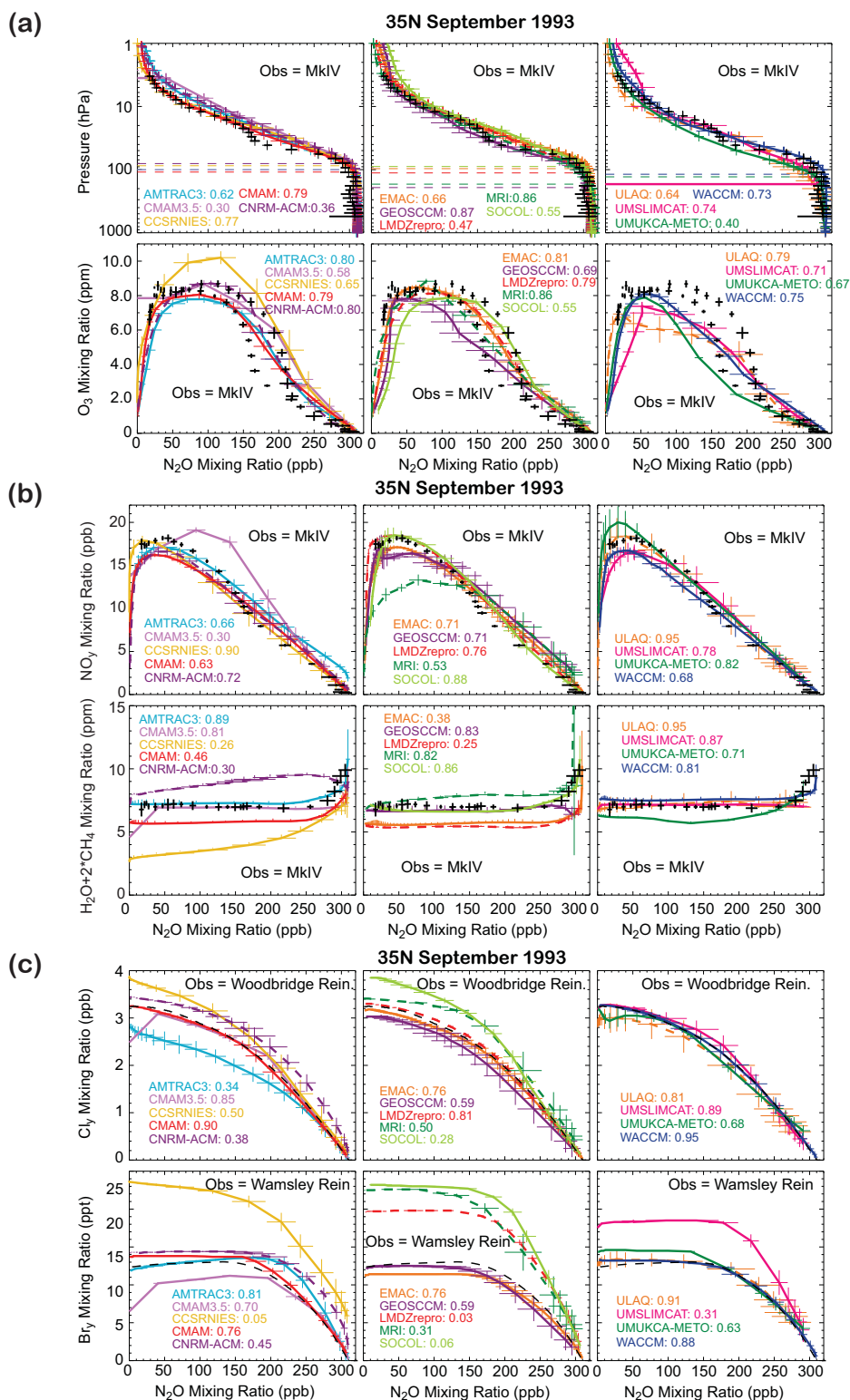


**Figure 6.8:** Comparison of N<sub>2</sub>O profiles and the relation of radical precursors versus N<sub>2</sub>O (black) to zonal monthly mean values from various CCM models (coloured lines and symbols, as indicated) for 35°N in September 1993. CCM output is for the closest model latitude to 35°N, as indicated. Numerical values of *g* (see text) are also noted. Comparisons of N<sub>2</sub>O vs. pressure and O<sub>3</sub> vs. N<sub>2</sub>O are shown in panel (a); comparisons of NO<sub>y</sub> vs. N<sub>2</sub>O and H<sub>2</sub>O+2CH<sub>4</sub> vs. N<sub>2</sub>O are shown in panel (b); comparisons of Cl<sub>y</sub> vs. N<sub>2</sub>O and Br<sub>y</sub> vs. N<sub>2</sub>O are shown in panel (c).

recovery calculations.

For the calculation of  $g_{precursor}$  we have added an additional constraint on  $\sigma_{obs}$ : it can never fall below 5%, 10%, 5%, 10%, 2.5%, or 10% of  $\mu_{obs}$  for  $N_2O$ ,  $O_3$ ,  $NO_y$ ,  $H_{tot}$ ,  $Cl_y$ , or  $Br_y$ , respectively. A “floor” on  $\sigma_{obs}$  is essential, because otherwise the quantitative evaluation of  $g_{precursor}$  is biased by altitudes where a measurement team might claim to have extraordinarily high accuracy, causing small differences between  $\mu_{obs}$  and  $\mu_{CCM}$  to be magnified by the low value of the denominator of Equation 6.1. The numerical values given above are based on our assessment, based on many years of working with atmospheric chemistry measurements, of how well each parameter is really known. The “floor” on  $\sigma_{obs}$  is analogous to “error inflation”, a process whereby the uncertainty of meteorological observations is increased prior to assimilation within Numerical Weather Prediction models (*e.g.*, Whitaker *et al.*, 2008; Hamill and Whitaker, 2005). It is reassuring that after application of this additional constraint on  $\sigma_{obs}$ , the resulting values of  $g_{precursor}$  represent the visual impression gleaned from examination of many model/data comparison plots. The high value of 10% for  $O_3$  reflects the difficulty inherent in the comparison of the  $O_3$  vs.  $N_2O$  relation measured at a single location, which is sensitive to the dynamical histories of the sampled air parcels, to a relation based on zonal monthly mean profiles from the CCMs. Also, for 35°N, Sept 1993, the MkIV instrument obtained observations on a successive sunset and sunrise (Sen *et al.*, 1998). The observations were similar, except for  $O_3$  vs.  $N_2O$  (Figure 6.8a). Atmospheric observations have revealed that the other tracer relations are much less sensitive to recent air mass history, owing to the longer photochemical lifetimes for  $NO_y$ ,  $H_{tot}$ ,  $Cl_y$ , and  $Br_y$  compared to that for  $O_3$ . The uncertainty in the observed value of  $O_3$  at a particular value of  $N_2O$ , used to compute  $g_{precursor}$ , is based on whichever is larger: 10% of the mean value of  $O_3$  or the range of  $O_3$ , defined as one-half of the measurement difference.

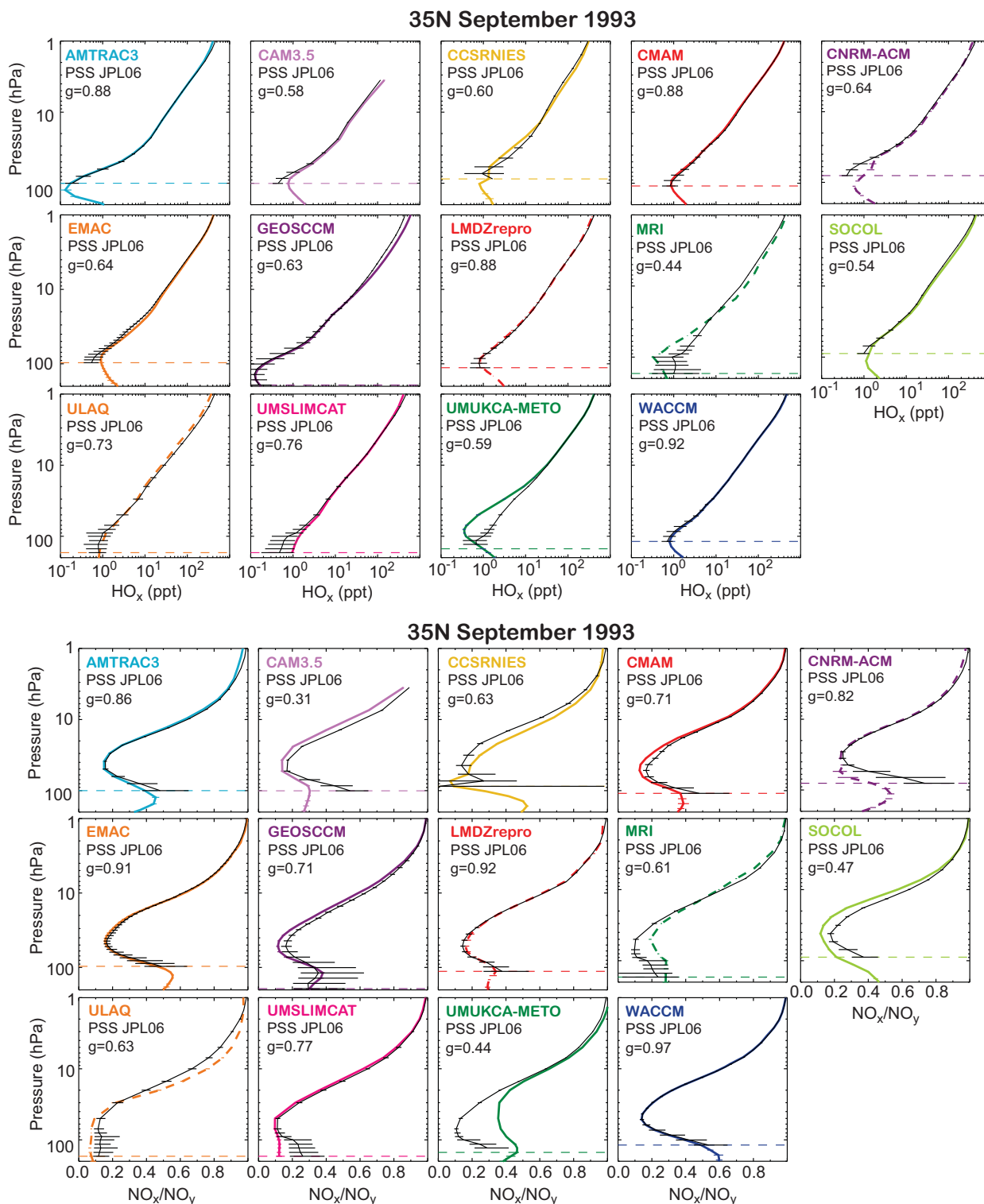
As noted above, Figure 6.8 shows the evaluation of the radical precursor fields at ~35°N for September 1993. The models have a range of skill for representation of radical precursors, with some models (*i.e.*, WACCM and ULAQ) providing extremely realistic overall specifications. The measured profile of  $N_2O$  is represented reasonably well by all models, with some indicating somewhat more (or less) descent than implied by the observation. The GEOSCCM and MRI models exhibit best agreement with this metric. The models exhibit a range of values for  $O_3$  vs.  $N_2O$ , reflecting the sensitivity of this metric to recent air mass history. Nonetheless, ten of the models demonstrate very good agreement (*i.e.*,  $g_{precursor} > 0.70$ ) with the observed range of  $O_3$  vs.  $N_2O$  relation. The  $NO_y$  vs.  $N_2O$  relation is represented quite well by most of the models, with the exception of CAM3.5 ( $NO_y$  much larger than observation) and MRI ( $NO_y$  much less observation).

The models exhibit a range of values for  $H_{tot}$ , with some models (especially CCSRNIES) exhibiting a too dry stratosphere and other models (especially CNRM-ACM) exhibiting excess moistness. Best simulations of  $H_{tot}$  are achieved by AMTRAC, CAM3.5, GEOSCCM, MRI, SOCOL, ULAQ, UMSLIMCAT, and WACCM. The range of values for  $H_{tot}$  may reflect the sensitivity of stratospheric  $H_2O$  to small differences in tropopause temperature (see Section 6.3.3).

The CCMs exhibit a substantial range in the  $Cl_y$  vs.  $N_2O$  relation, which is surprising because the loss processes of the source gases are well known and the surface abundances have been specified for the REF-B1 simulation. Best agreement is achieved by CAM3.5, CMAM, EMAC, LMDZrepro, ULAQ, UMSLIMCAT, and WACCM. Simulated values of  $Cl_y$  at the top of the stratosphere for September 1993 range from a low of ~2.8 ppb (AMTRAC) to a high of ~3.8 ppb (CCSRNIES and SOCOL); observations suggest an actual value of ~3.25 ppb, as indicated. The chlorine loading of the CCM runs is discussed in more detail in Section 6.3.3.

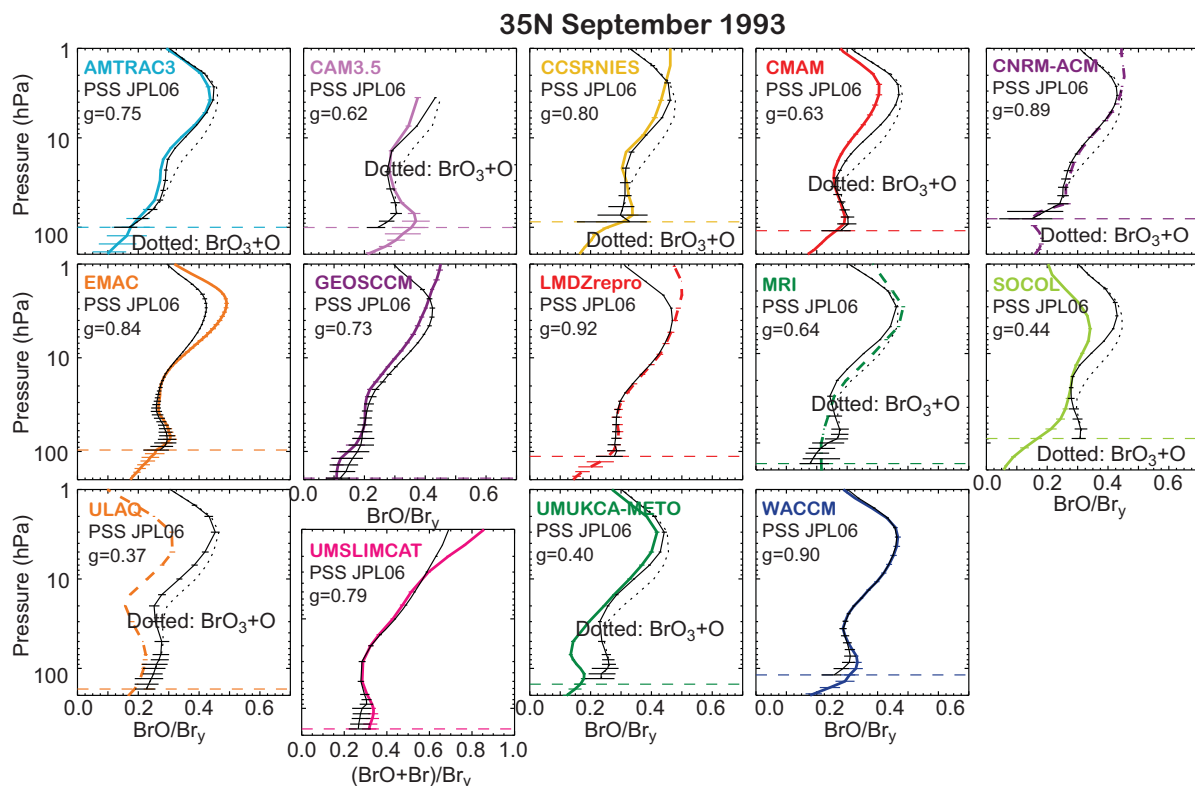
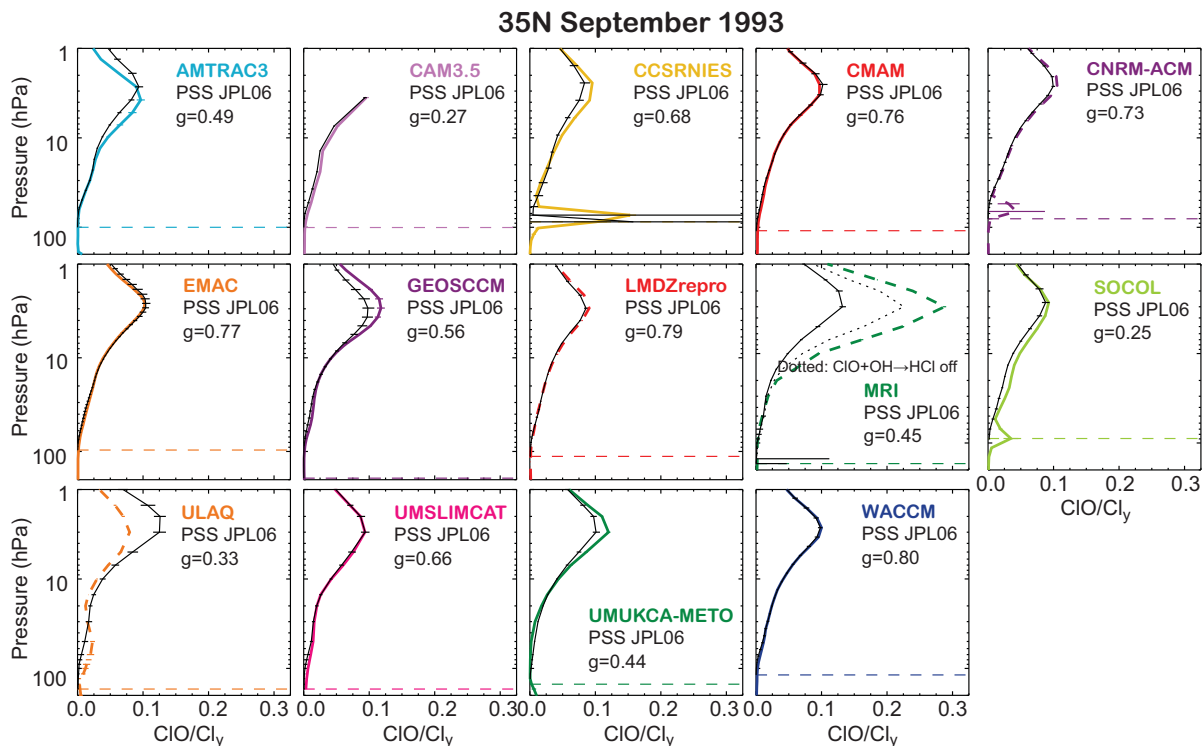
Inorganic bromine ( $Br_y$ ) is the radical precursor field that varies the most among the CCMs. The  $Br_y$  vs.  $N_2O$  relation exhibits a large amount of model to model variability. The REF-B1 calculation was supposed to be carried out with stratospheric bromine supplied only by  $CH_3Br$  and halons. Some models (*i.e.*, CCSRNIES, LMDZrepro, MRI, SOCOL, and UMSLIMCAT) also apparently allow for the influence of very short-lived bromocarbons on stratospheric  $Br_y$  (see Section 6.3.3 for a full discussion). Other models (*i.e.*, CAM3.5 and EMAC) archived lower values of  $Br_y$  than should be present in the mid-latitude stratosphere during September 1993.

Figure 6.9 shows a comparison of zonal monthly mean values of radicals ( $HO_x$ ,  $NO_x/NO_y$ ,  $ClO/Cl_y$ , and  $BrO/Br_y$ ) from each CCM to the 24-hour average value of the radicals found using the PSS box model, constrained by profiles of T,  $O_3$ ,  $H_2O$ ,  $CH_4$ , CO,  $NO_y$ ,  $Cl_y$ ,  $Br_y$ , and sulfate SAD from the various CCMs. (Similar plots for  $O(^3P)$  and  $O(^1D)$  are provided in Figure 6S.2 of the Supplementary Material). Metrics, in this case  $g_{RADICAL}$  (numerical values given on each panel) are again found using Equation 6.1, with  $n = 3$ ,  $\sigma = \sqrt{(\sigma_{CCM}^2 + \sigma_{PSS}^2)}$ , and the other CCM terms described as above. Here,  $\mu_{obs} = \mu_{PSS}$  and represents 24-hour abundance of radicals found using the latitude, solar declination angle for each CCM from a full diel simulation, and the summation is carried out for the  $N$  CCM model levels between the tropopause and 1 hPa (between the tropopause and 5 hPa for  $BrO/Br_y$ ). Again, negative values of  $g$  are set to zero. The quantity  $\sigma_{PSS}$  represents the variability of the PSS output found by perturbing, relative to the baseline run, values of nine input parameters given above by the standard deviation, about the zonal mean, of these quantities from each CCM. This variability is represented by the



**Figure 6.9:** Comparison of zonal monthly mean profiles of radicals from CCM models (coloured lines and symbols) versus 24-hour average radical profiles found using a PSS box model constrained by profiles of T, O<sub>3</sub>, H<sub>2</sub>O, CH<sub>4</sub>, CO, NO<sub>y</sub>, Cl<sub>y</sub>, Br<sub>y</sub>, and sulfate SAD from the various CCMs for 35°N in September 1993. The PSS model was run for CCM model levels from the tropopause (dashed lines) to 1 hPa. The PSS model uses the latitude of the CCM output that is closest to 35°N and solar declination corresponding to the mid point of the monthly mean. Numerical values of g and the chemical kinetics in the simulation are given (see text). The





coloured error bars represent the standard deviation about the zonal monthly mean for various days used to compute the mean. The black error bars represent the sensitivity of PSS output to variability in the CCM profiles of radical precursors. Results for  $\text{HO}_x$ ,  $\text{NO}_x/\text{NO}_y$ ,  $\text{ClO}/\text{Cl}_y$ , and  $\text{BrO}/\text{Br}_y$  are shown, respectively, in panels (a), (b), (c), and (d). For the MRI model, results are shown with and without production of HCl by the chemical reaction  $\text{ClO} + \text{OH}$  (see text). For AMTRAC, CAM3.5, CCSRNIES, CMAM, CNRM-ACM, MRI, SOCOL, ULAQ, and UMUKCA-METO, results are shown with and without consideration of the reaction  $\text{BrONO}_2 + \text{O}$  (see text).

black error bars in Figures 6.9. Typically,  $\sigma_{PSS}$  peaks in the lowermost stratosphere, reflecting the sensitivity of radicals to zonal asymmetry in this region of the atmosphere. For the calculation of  $g_{RADICAL}$ , the value of  $\sigma_{PSS}$  is floored at 5% of the value of  $\mu_{PSS}$  (the figures show  $\sigma_{PSS}$  before this floor is imposed). Flooring  $\sigma_{PSS}$  at a modest, non-zero value is crucial to the proper use of the PSS model to assess the chemical mechanism within CCMs, because often the radical profiles found from a CCM model will follow the general shape of the PSS profile, but be 3 to 5% systematically high (or low) at many levels. If we allowed  $\sigma_{PSS}$  to reflect only the propagation of variability in the precursors through the PSS model, the calculation of  $g_{RADICAL}$  would be biased whenever the variance about the zonal-mean of the radical precursors (from the CCM) leads to very small perturbations in radical fields (*i.e.*, whenever an unduly small value for the denominator of Equation 6.1 is found).

We chose O(<sup>3</sup>P), O(<sup>1</sup>D), HO<sub>x</sub>, NO<sub>x</sub>/NO<sub>y</sub>, ClO/Cl<sub>y</sub>, and BrO/Br<sub>y</sub> as our basis for comparison because these species participate in the crucial rate limiting steps for loss of ozone and/or other long-lived stratospheric gases. The ratios NO<sub>x</sub>/NO<sub>y</sub>, ClO/Cl<sub>y</sub>, and BrO/Br<sub>y</sub> are used because these quantities are less sensitive to dynamical variability than values of NO<sub>y</sub>, ClO, and BrO. Presumably, if the PSS model, using precursor fields from the CCM, accurately simulates the values of O(<sup>3</sup>P), O(<sup>1</sup>D), HO<sub>x</sub>, NO<sub>x</sub>/NO<sub>y</sub>, ClO/Cl<sub>y</sub>, and BrO/Br<sub>y</sub> found by the CCM, then both models represent a “chemical mechanism” in a similar manner.

Figure 6S.2a shows comparisons for O(<sup>3</sup>P). With the exception of the MRI model, the comparisons are uniformly very good to excellent (note: three of the CCM groups failed to archive fields of O(<sup>3</sup>P)). Larger differences are found for O(<sup>1</sup>D) (Figure 6S.2b). The values of  $g_{RADICAL}$  range from a high of 0.83 (CAM3.5) to a low of 0.23 (MRI), with four CCM groups failing to archive fields of O(<sup>1</sup>D).

The shape and magnitude of the HO<sub>x</sub> profile found by the PSS simulation agrees well with the profile found by most CCMs (Figure 6.9a). Differences are typically largest in the lower stratosphere, where the influence of zonal asymmetry is largest (highest values of  $\sigma_{PSS}$ ). Profiles of HO<sub>x</sub> reported by AMTRAC, CMAM, LMDZrepro, ULAQ, UMSLIMCAT, and WACCM are simulated in a very good to excellent manner. The shape and magnitude of the NO<sub>x</sub>/NO<sub>y</sub> ratio from the various CCMs, as for HO<sub>x</sub>, is generally simulated quite well by the PSS model (Figure 6.9b). Excellent agreement is achieved for EMAC, LMDZrepro, and WACCM. The large differences between the PSS simulation and the value of NO<sub>x</sub>/NO<sub>y</sub> archived in the lower stratosphere by a few of the CCMs suggests either misrepresentation of sulfate SAD within the PSS model (fields of sulfate SAD were not archived by CCM groups with some of the largest differences) or else the effect of volcanic aerosols on chemical composition is represented in a different

manner by the respective models compared to the representation in the PSS model. In general, when the value of NO<sub>x</sub>/NO<sub>y</sub> in the lower stratosphere from the PSS model exceeds the value from a CCM (*i.e.*, UMSLIMCAT), then the value of HO<sub>x</sub> from the PSS model falls below the value from the CCM (UMSLIMCAT). When NO<sub>x</sub>/NO<sub>y</sub> from PSS falls below that from a CCM (*i.e.*, UMUKCA-METO and MRI), then generally HO<sub>x</sub> from PSS exceeds that of the CCM. This interplay between the two radical families is “as expected” (*e.g.*, Wennberg *et al.*, 1994); it is reassuring to see this characteristic of the comparisons shown in Figures 6.9a and 6.9b.

Figure 6.9c shows the comparison for ClO/Cl<sub>y</sub>. In nearly all cases, the PSS and CCM profiles follow a similar shape. However, for some CCMs, the magnitudes are quite different. Best agreement is achieved for CMAM, CNRM-ACM, EMAC, LMDZrepro, UMSLIMCAT, and WACCM. The peak value of ClO/Cl<sub>y</sub> is highly overestimated, with respect to the PSS simulation, by the MRI model. This overestimate is due in part to the neglect of the ClO + OH → HCl product channel in the MRI model (Table 6S.1). We have conducted another PSS simulation neglecting this product channel, to better approximate the chemical mechanism used by MRI. Neglecting this product channel results in a profile for ClO/Cl<sub>y</sub> that lies closer to the MRI profile (dotted line, MRI panel, Figure 6.9c), but the MRI value of ClO/Cl<sub>y</sub> still exceeds the PSS value. For the computation of the  $g_{RADICAL}$ , we have used the PSS simulation that includes the HCl product channel, because production of HCl by ClO+OH is a key component of the “standard” stratospheric photochemical mechanism in use for the past decade. The profile of ClO/Cl<sub>y</sub> is somewhat overestimated by GEOSCCM, near the peak, for reasons that are unclear. For ULAQ, values of ClO/Cl<sub>y</sub> are strongly under-estimated in the upper stratosphere and strongly overestimated in the lower stratosphere. Use of a linear coordinate for the horizontal axis obscures some important differences in the lower stratosphere, such as the presence of quite large values of ClO/Cl<sub>y</sub> by the CNRM-ACM and SOCOL models.

Figure 6.9d shows the comparison for BrO/Br<sub>y</sub>. For the 2 CCMs that use JPL-2002 kinetics (EMAC and GEOSCCM) as well as the 3 CCMs that use JPL-2006 kinetics and include the BrONO<sub>2</sub>+O reaction (LMDZrepro, UMSLIMCAT, and WACCM), one PSS curve is shown. For the other 7 CCMs, the results of PSS simulations both including and neglecting this reaction are shown. The numerical value of  $g_{RADICAL}$  in all cases, represents the best PSS representation of the CCM chemistry, as given in Table 6S.3. Since the PSS simulation diverges from many (but not all) of the CCMs at low pressure, where bromine chemistry is not important, we use 5 hPa as the maximum altitude for the calculation of  $g_{RADICAL}$  for this ratio. Finally, the UMSLIMCAT group has archived BrO + Br, rather

than BrO, resulting in the display of a different quantity for this CCM.

The CCMs exhibit a wide range of variability for the representation of BrO/Br<sub>y</sub> (Figure 6.9d). Best agreement with the PSS model is achieved for CCSRNIIES, CNRM-ACM, EMAC, LMDZrepro, MRI, UMSLIMCAT, and WACCM. Some of the other models (*i.e.*, SOCOL, ULAQ, and UMUKCA-METO) exhibit considerable differences with respect to the PSS simulation.

**Figure 6.10** represents grades for  $g_{\text{PRECURSOR}}$  and  $g_{\text{RADICAL}}$  for the 35°N, Sept 1993 simulation from all of the models. The values of these metrics shown in Figures 6.7, 6.8 and 6.9 are represented by the shaded squares, as indicated. Two new pieces of information are represented in Figure 6.10:

1. An additional metric, a measure of the tropospheric abundance of Cl<sub>y</sub> in each CCM (termed Cl<sub>y</sub> Tropos), has been added;
2. the cell for BrO/Br<sub>y</sub> has been split, with the left side representing the metric when the BrONO<sub>2</sub>+O reaction is included (if JPL-2006 kinetics are used in the CCM) and the right side representing the metric when this reaction is excluded (if JPL-2006 kinetics are used in the CCM and this reaction was not included in the chemical mechanism, as shown in Table 6S.2).

The additional metric for Cl<sub>y</sub> Tropos was assessed by examination of the value of Cl<sub>y</sub> at 500 hPa archived by each CCM for 35°N, Sept 1993. Some of the CCM models have high (*i.e.*, >> 50 ppt) levels of Cl<sub>y</sub> extending from the surface to the tropopause that impacts the model value of Cl<sub>y</sub> throughout the lowermost stratosphere (LMS); these models will undoubtedly have a different sensitivity of O<sub>3</sub> to changes in temperature in the LMS compared to models with near zero (<< 50 ppt) of Cl<sub>y</sub> from the surface to the tropopause. Models with high values of Cl<sub>y</sub> Tropos have the potential for chlorine activation in the extra-polar LMS as temperature approaches 198 K that will affect ozone much more strongly than for the models with Cl<sub>y</sub> Tropos ≈ 0. The metric for Cl<sub>y</sub> Tropos assumed  $\mu_{\text{obs}} = 0$  and  $\sigma_{\text{obs}} = 50$  ppt, which proved to be an excellent discriminate between models with Cl<sub>y</sub> Tropos ≈ 0 and models with excessive Cl<sub>y</sub> Tropos (which is clearly associated with elevated levels of Cl<sub>y</sub> in the LMS within these models). The CCSRNIIES, CNRM-ACM, MRI, SOCOL, ULAQ, and UMUKCA-METO models have Cl<sub>y</sub> >> 50 ppt at the tropopause and throughout the troposphere, whereas the AMTRAC, CAM, EMAC, GEOSCCM, LMDZrepro, and WACCM models have Cl<sub>y</sub> << 50 ppt for these regions of the atmosphere. In general, models with high values of Cl<sub>y</sub> in the troposphere also archived high values of Br<sub>y</sub> (>> 2 ppt) in the troposphere (we did not develop a metric for Br<sub>y</sub> Tropos).

The metric for BrO/Br<sub>y</sub> in Figure 6.10 was split to

indicate the sensitivity of the fast chemistry evaluation to a single chemical reaction and to incorporate, into the overall total fast chemistry metric, a quantification of the failure of some CCM groups to properly represent the JPL-2006 chemical mechanism. It is important to note that the same numerical value is given on both sides of the BrO/Br<sub>y</sub> grading cell for CCMs that either used JPL-2002 kinetics (the BrONO<sub>2</sub>+O reaction was not included in JPL-2002) or else used JPL-2006 kinetics and represented this reaction. The values on the left and right side of the BrO/Br<sub>y</sub> grading cell thus differ only for CCMs that used JPL-2006 kinetics and neglected this new reaction. For 7 of the 8 models that neglected the BrONO<sub>2</sub>+O reaction, the metric on the right hand side of the BrO/Br<sub>y</sub> cell improves when this reaction is neglected within the PSS simulation (the exception is MRI, a model for which the simulation of NO<sub>x</sub> is not matched by PSS). This behaviour suggests that the fast chemistry evaluation has the fidelity to assess the inclusion (or neglect) of a single chemical reaction within a complex CCM.

The last column of Figure 6.10 represents the total fast chemistry metric for the 35°N, Sept 1993 simulation. The numerical value is the mean of all available metrics (precursors, radicals, and sulfate SAD). The mean of the two BrO/Br<sub>y</sub> values is used, representing a compromise to take into consideration the neglect of an important new chemical reaction by the CCM groups that used JPL-2006 kinetics but omitted this BrONO<sub>2</sub>+O reaction, while at the same time factoring into the grade how well the CCM fares when this reaction is also neglected within the PSS simulation. The total metric includes a demarcation if sulfate SAD was not reported (\*), if the CCM did not use JPL-2006 kinetics (◇), and if the CCM group failed to provide adequate information to participate in the fast chemistry evaluation (×). Overall, the CMAM, EMAC, UMSLIMCAT, and WACCM models fared best in the fast chemistry metric for Sept 1993, with the AMTRAC, GEOSCCM and LMDZrepro models not far behind.

We conclude this section with a brief, *albeit* very important summary of the fast chemistry evaluation for 22°N, February 1996. Data used for this evaluation were obtained by instruments aboard the NASA ER-2 aircraft during the STRAT campaign (*e.g.*, Lanzendorf *et al.*, 2001; Weinstock *et al.*, 2001; Dessler, 2002). Figure 6.7 shows profiles of sulfate SAD for this period. As is well known, the highly perturbed volcanic aerosol characteristic of September 1993 had fallen considerably by February 1996 (note the different scales used for the horizontal axes in Figure 6.7).

We have repeated the entire analysis (precursors and radicals) for February 1996. Figures analogous to those shown for the September 1993 time period can be found in the Supplementary Material (Figures 6S.3, 6S.4, and 6S.5). Here, in **Figure 6.11**, we show only scatter diagrams of the values of:  $g_{\text{PRECURSOR}}$  (N<sub>2</sub>O profiles; O<sub>3</sub>, NO<sub>y</sub>, H<sub>tot</sub>, Cl<sub>y</sub>,

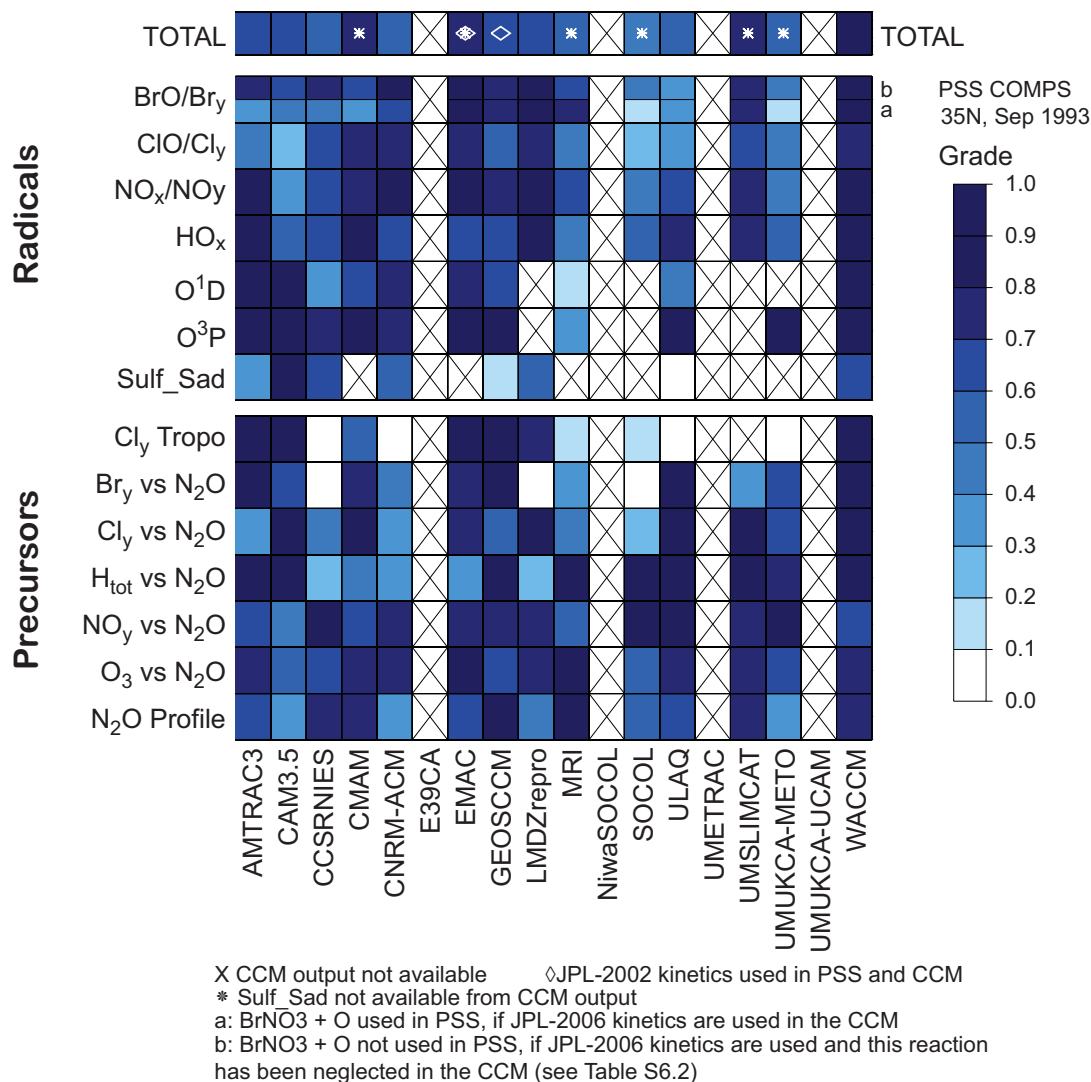


**Figure 6.10:** Metrics for (a, left) radical precursors and (b, right) sulfate surface area and radicals for a simulation carried out at 35°N, September 1993. The same dark shade of blue is used for  $0.8 < g < 1.0$ , reflecting that there is little significance in differences that fall within this range of values. The symbol X denotes CCM output not archived;  $\diamond$  denotes use of JPL-2002 kinetics, and \* denotes sulfate SAD not archived (see text). For model that used JPL-2006 kinetics and neglected the BrONO<sub>2</sub>+O reaction, two grades are given for the evaluation of BrO/Br<sub>y</sub> (see text).

and Br<sub>y</sub> all vs. N<sub>2</sub>O; Cl<sub>y</sub> Tropos) for the Feb 1996 vs. Sept 1993 evaluations (top panel);  $g_{\text{RADICAL}}$  (sulfate SAD, O(<sup>3</sup>P), O(<sup>1</sup>D), HO<sub>x</sub>, NO<sub>x</sub>/NO<sub>y</sub>, ClO/Cl<sub>y</sub>, and BrO/Br<sub>y</sub>) for the Feb 1996 vs. Sept 1993 evaluations (middle panel); and total fast chemistry metric for the Feb 1996 vs. Sept 1993 evaluations (bottom panel). Numerical values of the respective metrics (mean of the Feb 1996 and Sept 1993 evaluations) are given in the list to the right of each figure, placed in order of the total overall fast chemistry metric (bottom panel). In all cases, the metrics scatter about the 1:1 line. For the precursors, the notable outliers are the N<sub>2</sub>O profile and the O<sub>3</sub> vs. N<sub>2</sub>O relation for MRI (this model exhibits much better agreement with Sept 1993 observations than

with Feb 1996 data). Removing these two outliers results in a value for  $r^2$  of 0.67 and a slope of 1.01, for the rest of the evaluation points. Therefore, the metric for a particular precursor from a specific CCM for the first time period is generally a good predictor of the metric for the second time period. For the radicals, the notable outliers are sulfate SAD for GEOSCCM and ULAQ as well as O(<sup>1</sup>D), HO<sub>x</sub>, and O(<sup>3</sup>P) from ULAQ. The outlier for sulfate SAD from GEOSCCM is due to use of background aerosol loading at all times. The sulfate SAD used by ULAQ bears a closer relation to the climatology for Feb 1996 than for Sept 1993, for reasons that are unclear. It is also not clear why the good to very good ability of the PSS model to simulate

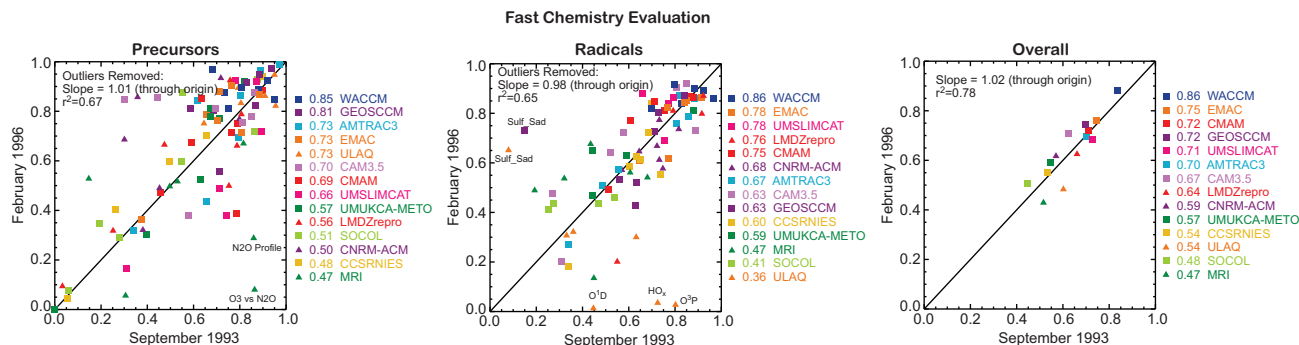


**Figure 6.11:** (Top panel): Scatter plot of metrics for the radical precursors for the simulation carried out at 35°N, September 1993 (horizontal axis) vs. metrics for the same quantities from the 22°N, February 1996 simulation (vertical axis). (Middle panel): Scatter plot of metrics for sulfate surface area and radicals for the simulation carried out at 35°N, September 1993 vs. metrics for the same quantities from the 22°N, February 1996 simulation. For models that archived all quantities, points represent the metrics for sulfate SAD, O(<sup>3</sup>P), O(<sup>1</sup>D), HO<sub>x</sub>, NO<sub>x</sub>/NO<sub>y</sub>, ClO/Cl<sub>y</sub>, and BrO/Br<sub>y</sub> from both time periods. The geophysical quantity associated with the various outliers is denoted (see text). (Bottom panel): Scatter plot of the total fast chemistry metric (last column of Figure 6.10 and Figure 6S.5) for the simulation carried out at 35°N, September 1993 vs. metrics for the same quantities from the 22°N, February 1996 simulation. The metric points, excluding the outliers, have a variance ( $r^2$ ) of 0.67, 0.65, and 0.78 for the three panels, respectively, indicating that about two-thirds of the variance in the precursor and radical metrics, and almost 80% of the variance of the overall fast chemistry metrics is common between both time periods. Slopes of a linear least squares fit are also indicated; for the precursor and radical evaluations, these slopes have been forced to pass through the origin.

O(<sup>3</sup>P), O(<sup>1</sup>D), and HO<sub>x</sub> within ULAQ for Sept 1993 is not reflected in the Feb 1996 comparisons (see Figure 6S.4). Removal of these five outliers results in a value of  $r^2$  of 0.65 and a slope of 0.98.

The total fast chemistry metrics (cells titled “Total” in Figure 6.10 and Figure 6S.5) exhibit a strong correlation ( $r^2 = 0.78$ ; slope = 1.02) considering all of the evaluation points (bottom panel, Figure 6.11). This scatter diagram demonstrates the robustness of the conclusions of the fast chemistry evaluation. Some of the models (WACCM, EMAC, GEOSCCM, CMAM, UMSLIMCAT, AMTRAC) have implemented a more realistic representation of fast chemistry than the models that rank on the low end of this metric. In all cases, performance in the Sept 1993 evaluation is an excellent predictor (78% of the variance) of the performance in the Feb 1996 evaluation.

### 6.3.3 Evaluation of Reservoir and Long-Lived Chemistry

#### 6.3.3.1 Tracer-tracer correlations

A concise way of inter-comparing important aspects of CCM results, and identifying model-model differences, is by plotting correlations of long-lived tracer fields. These correlations can be used to investigate transport properties (see Chapter 5), but also reveal some chemical information. Section 6.3.2 used correlations to analyse

radical precursors near the locations of balloon flights, but in this section we use them to condense multi-annual global data sets. Figures 6.12 to 6.14 show the CH<sub>4</sub>:N<sub>2</sub>O, CH<sub>4</sub>:H<sub>2</sub>O and NO<sub>y</sub>:N<sub>2</sub>O correlations from the last 10 years of the REF-B1 runs of 17 CCMs (no data was provided from UMETRAC). Figures 6.12 to 6.14 also show corresponding ENVISAT Michelson Interferometer for Passive Atmospheric Sounding (MIPAS) data. This data was produced using the University of Oxford Retrieval (A. Dudhia, personal communication, 2009). Other MIPAS retrievals exist but the choice of data set should not be critical for the comparisons (species and spatial averaging) performed here.

For CH<sub>4</sub>:N<sub>2</sub>O (Figure 6.12) most CCMs produce a compact correlation in good agreement with the straight-line fit inferred from ER-2 and MIPAS data down to 50 ppbv N<sub>2</sub>O. The ER-2 data corresponds to the lower stratosphere and so represents a sub-sample of the global MIPAS data. The altitude variation of the correlation (indicated by the colours) is also quite similar between many models. The lower resolution ULAQ model gives a larger spread in the correlation than other models, but then so does the MIPAS data. The low-lid E39CA model diverges from the straight line correlation at the lowest values of CH<sub>4</sub> and N<sub>2</sub>O, although the other model with a relatively low lid, CAM3.5, performs well.

Figure 6.13 is a similar plot for CH<sub>4</sub> and H<sub>2</sub>O. In the stratosphere, the oxidation of CH<sub>4</sub> will lead to the production of up to 2 molecules of H<sub>2</sub>O (the alternative minor

ultimate product is  $H_2$ ). In contrast to  $N_2O$ , there is therefore a direct chemical link between these two tracers. As expected the CCMs generally show large mixing ratios of water vapour in the troposphere (*i.e.*, for large  $CH_4$ ), a minimum in the lower stratosphere followed by an increase in the stratosphere as  $CH_4$  decreases. The variation in stratospheric maximum  $H_2O$  as a function of  $CH_4$  in most models tends to follow the line  $H_{tot} = 7$  ppmv (although the

MIPAS data indicates  $H_{tot}$  may be 0.5-1.0 ppmv larger than this). Notable exceptions to this behaviour are: CCSRNIIES which shows small lower stratosphere  $H_2O$  mixing ratios and only a small stratospheric increase (*i.e.*, less than 2 molecules  $H_2O$  per  $CH_4$  oxidised); UMUKCA-METO, which shows similar smaller stratospheric  $H_2O$  and a smaller stratospheric production, and also LMDZrepro. A failure of a model to reproduce this slope of 2 indicates a failing

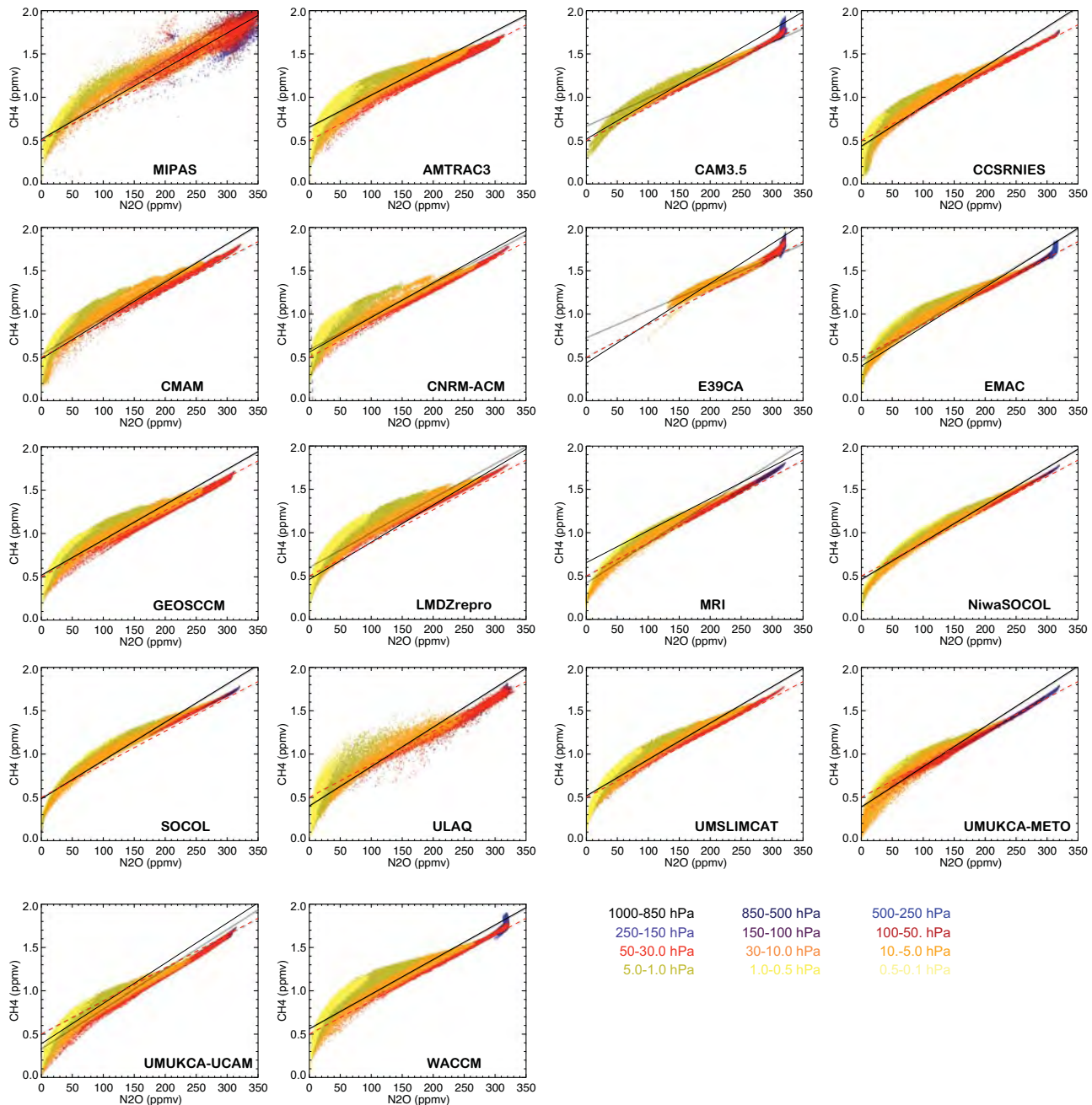
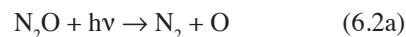


**Figure 6.12:** Correlation of  $CH_4$  (ppmv) vs.  $N_2O$  (ppbv) for zonal-mean monthly-mean output from the final 10 years of REF-B1 runs from 17 CCM runs and MIPAS data. The solid line is the best fit to the model/satellite data sampled between  $60^\circ N$ - $60^\circ S$ , 70-0.5 hPa. The dashed line shows the equation  $N_2O$  (ppbv) =  $261.8CH_4$  (ppmv) – 131, which is a fit from lower stratospheric ER-2 data (see Kawa et al., 1993).

of the chemistry. The CNRM-ACM model appears to have a slope slightly larger than 2 and a stratosphere that is too moist. Other models reproduce the stratospheric slope of 2 but have lower stratospheric H<sub>2</sub>O overall due presumably to different input at the tropical tropopause. This is not a failing of the chemistry scheme, which is being evaluated here, but these low H<sub>2</sub>O mixing ratios will have an impact on calculated model HO<sub>x</sub> for example.

N<sub>2</sub>O is the main source of stratospheric NO<sub>y</sub> and in

the CCMVal runs the only source considered. Overall, stratospheric N<sub>2</sub>O has 3 destruction channels:



Section 6.3.2 examined the NO<sub>y</sub>:N<sub>2</sub>O correlation for a specific location in September 1993. **Figure 6.14** shows

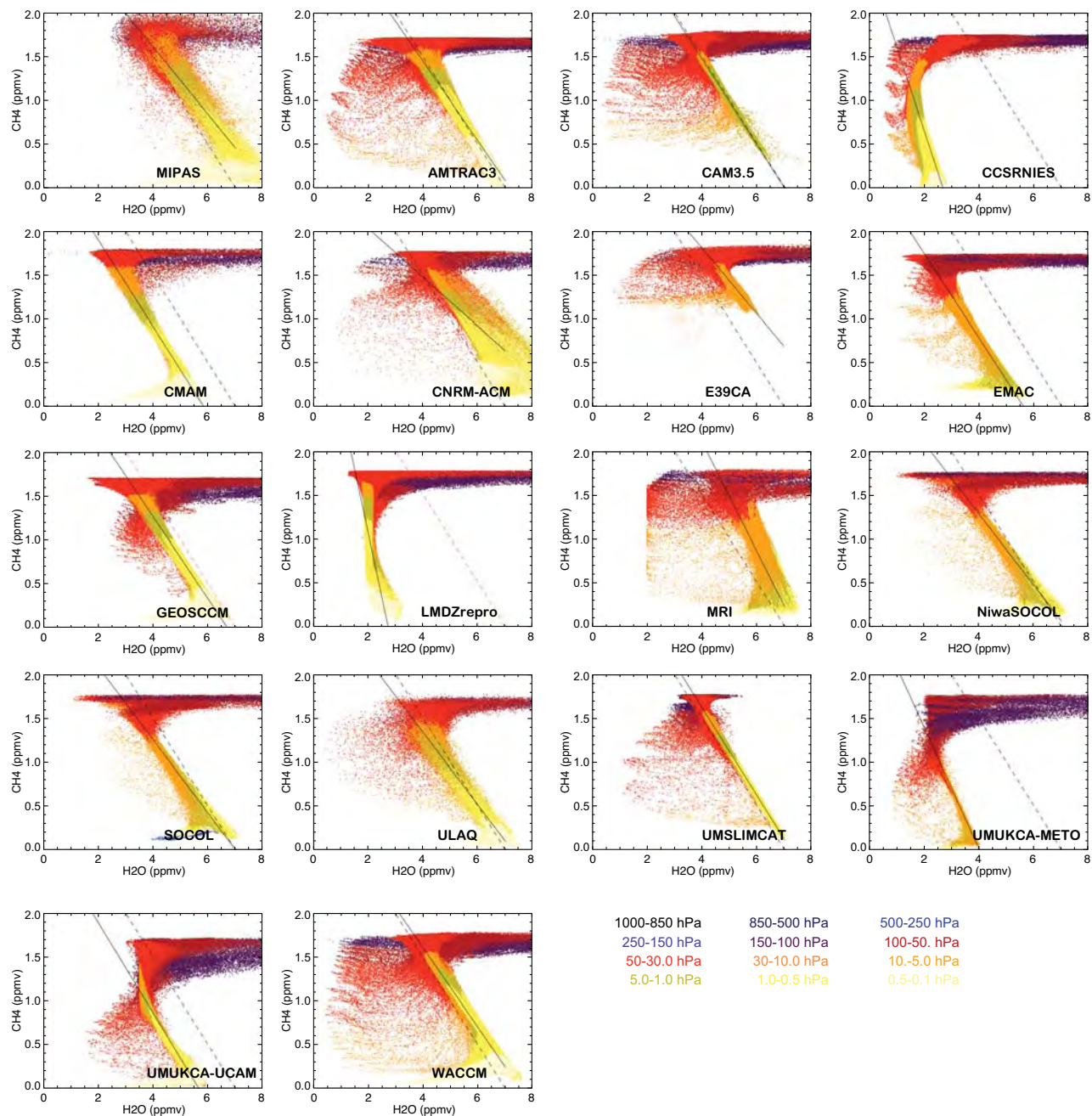
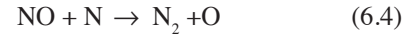


**Figure 6.13:** Correlation of CH<sub>4</sub> (ppmv) vs. H<sub>2</sub>O (ppmv) for zonal-mean monthly-mean output from the final 10 years of REF-B1 runs from 17 CCMs and MIPAS data. The solid line is the best fit to the model/satellite data sampled between 60°N-60°S, 70-0.5 hPa. The dashed line shows the equation H<sub>2</sub>O + 2CH<sub>4</sub> = 7 ppmv.

the global correlation of these two species. MIPAS  $\text{NO}_y$  has been calculated using observed night-time  $\text{NO}_2$ ,  $\text{HNO}_3$ ,  $\text{N}_2\text{O}_5$  and  $\text{ClONO}_2$ . At lower altitudes (high  $\text{N}_2\text{O}$ ) there is generally a straight line correlation. The slope of this depends on the modelled yield of  $\text{NO}_y$  from  $\text{N}_2\text{O}$  (6.2b, around 6%), compared to the loss by the other channels (mainly 6.2a, but also 6.2c). For some models there is a variation of this slope at high  $\text{N}_2\text{O}$  with, for example,



SOCOL, UMUKCA-UCAM, UMUKCA-METO and CAM3.5 giving a higher yield. Consequently the range of peak  $\text{NO}_y$  in the mid-stratosphere in these models varies from 17 to 25 ppbv. The turn-over of the correlation and low  $\text{N}_2\text{O}$  is caused by loss of  $\text{NO}_y$  through:

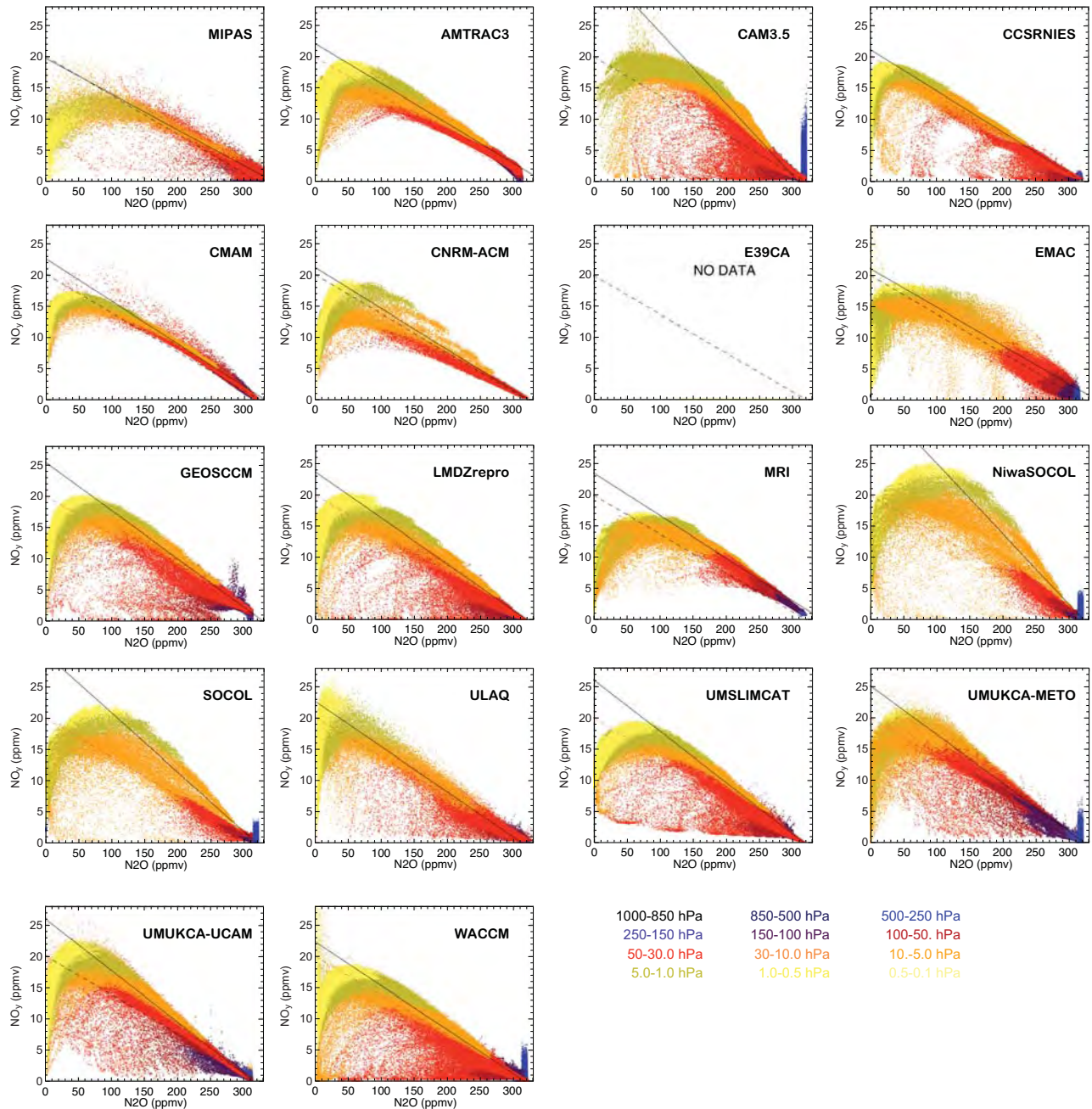


**Figure 6.14:** Correlation of  $\text{NO}_y$  (ppbv) vs.  $\text{N}_2\text{O}$  (ppbv) for zonal mean monthly mean output from the final 10 years of REF-B1 runs from 16 CCMs (no E39CA results). The solid line is the best fit to the model/satellite data sampled between  $30^\circ\text{N}$ - $30^\circ\text{S}$ , 70-10 hPa. The dashed line shows the equation  $\text{NO}_y$  (ppbv) =  $20.0 - 0.0625\text{N}_2\text{O}$  (ppbv), based on mid-latitude balloon profiles and ER-2 data (see Kondo et al., 1996).



There is a large variation in the shape of this turn-over. This will be partly related to large differences in J-NO (see Section 6.3.1). Figure 6.14 also reveals the impact of Antarctic denitrification. All models show this, but the denitrification appears larger in some models, *e.g.*, WACCM appears to have the most extensive denitrification, while some models have little or none. This is discussed in more detail in Section 6.3.4.

The agreement of these tracer-tracer correlations with observations in the stratosphere has been quantified in the following way:

1. The difference between the fitted stratospheric slopes between a model and observations (see figures) is calculated.
2. If this difference is larger than 3x the observed slope then the score = 0.1.
3. If this difference is greater than 2x the observed slope, but less than 3x, then the score = 0.2.
4. Otherwise the score is calculated using Equation (6.1) with  $n = 2$  and error (s) in the estimated slope = 1%.

The multi-model mean is calculated by summing the slopes from all the models and following the same procedure as steps (2)-(4). **Figure 6.15** shows the results of this grading for the 3 tracer-tracer correlations. The grades for  $\text{CH}_4:\text{N}_2\text{O}$  are uniformly high showing that this is well modelled. For most models, the score for  $\text{CH}_4:\text{H}_2\text{O}$  is also high, but lower scores apply to the models which do a poor job of stratospheric  $\text{H}_2\text{O}$ . For  $\text{NO}_y:\text{N}_2\text{O}$  the scores are again generally good with lower scores for CAM3.5, NiwaSOCOL and SOCOL.

### 6.3.3.2 Comparison with satellite climatologies

This section compares climatologies of long-lived and reservoir species from the CCMs with satellite data. We compare the mean annual cycle at two altitudes (1 hPa and 50 hPa) and 3 latitude bands (30°S-60°S, 15°N-15°S, 60°N-30°N) and mean annual profiles in the same regions. Satellite climatologies of relevant species have been provided from MIPAS (Oxford retrieval, A. Dudhia, personal communication, 2009), the Atmospheric Chemistry Experiment FTS instrument (ACE-FTS) (A. Jones and K. Walker, personal communication 2009; Bernath *et al.*, 2005), ODIN (J. Urban, personal communication 2009, Murtagh *et al.*, 2002) and SCIAMACHY (A. Rozanov and B. M. Sinnhuber, personal communication, 2009; Rozanov *et al.*, 2005; Sinnhuber *et al.*, 2005). We do not have space here to show all comparisons; the Supplementary Material contains further plots (Figures 6S.6 to 6S.9).

**Figures 6.16 and 6.17** compare the mean annual cycles at 50hPa, 30°N-60°N, and annual mean profiles at 30°S-60°S, respectively for a range of species. For  $\text{CH}_4$

UMUKCA-METO and UMUKCA-UCAM give values which are only around 1.0 ppmv at 50 hPa compared to the observed 1.4 ppmv, presumably as a consequence of their slow stratospheric circulation (Chapter 5). The two models with relatively low lids, E39CA, and to a lesser extent CAM3.5, overestimate lower stratosphere  $\text{CH}_4$ , probably as they do not treat loss at higher levels. The  $\text{H}_2\text{O}$  comparisons again show the large variation seen in CCMs discussed earlier. For CO the majority of models overestimate the observations in the mid-lower stratosphere with CCSRNIES being particularly large, followed by MRI, SOCOL, CNRM-ACM, NiwaSOCOL, UMUKCA-METO, LMDZrepro, and CMAM. For HCl there is, overall, a larger than expected spread in the model results, bearing in mind that this is the largest contributor to inorganic chlorine, which in itself should be well constrained in the REF-B1 experiment. At 50 hPa the UMUKCA-METO model has very large values (over 2 ppbv), although the agreement with the profile is reasonable at higher altitudes. The CCSRNIES, NiwaSOCOL, and SOCOL models also have larger mixing ratios than observed. These upper stratospheric mixing ratios exceed that possible based on the REF-B1 halocarbon scenarios (see discussion of total chlorine below). For ClONO<sub>2</sub> models tend to capture the mid-latitude seasonal cycle *albeit* with a spread of values. The MRI model gives significantly larger values than the other models. The picture is similar for HNO<sub>3</sub>, although in this case the UMUKCA-UCAM model has anomalously large values, *e.g.*, ~10 ppbv at 50 hPa in the mid-latitudes. For N<sub>2</sub>O<sub>5</sub> UMUKCA-METO this time has large values in the lower stratosphere and upper troposphere. A detailed comparison for this species would have to allow for its diurnal cycle, but this discrepancy, which is not shown by other models, is much larger than any issue to do with that. While the differences in HCl between the two versions of UMUKCA can be explained by different assumptions of tropospheric HCl loss (see Chapter 2), it is not clear why these two models should differ for other chemical species and their relative partitioning. Figures 6.16 and 6.17 also show comparisons of CCM climatologies of NO<sub>2</sub> and BrO, averaged over 24-hours in the TM2z output, with satellite observations made at a fixed local time but converted to a 24-hour mean using a photochemical model (B. M. Sinnhuber, personal communication, 2009). Despite this approximation the comparisons indicate whether the models capture the observed seasonal cycles in these species. (A detailed evaluation of the radicals is provided in Section 6.3.2). For NO<sub>2</sub> models do capture the shape of the seasonal cycle, with ULAQ spanning the models and observations at the high end and SOCOL at the low end. For BrO the comparison is complicated by the fact that the REF-B1 scenario is defined without bromine from very short-lived species. Therefore, the models should under-estimate stratospheric Br<sub>y</sub> by around 5 pptv (WMO, 2007), although

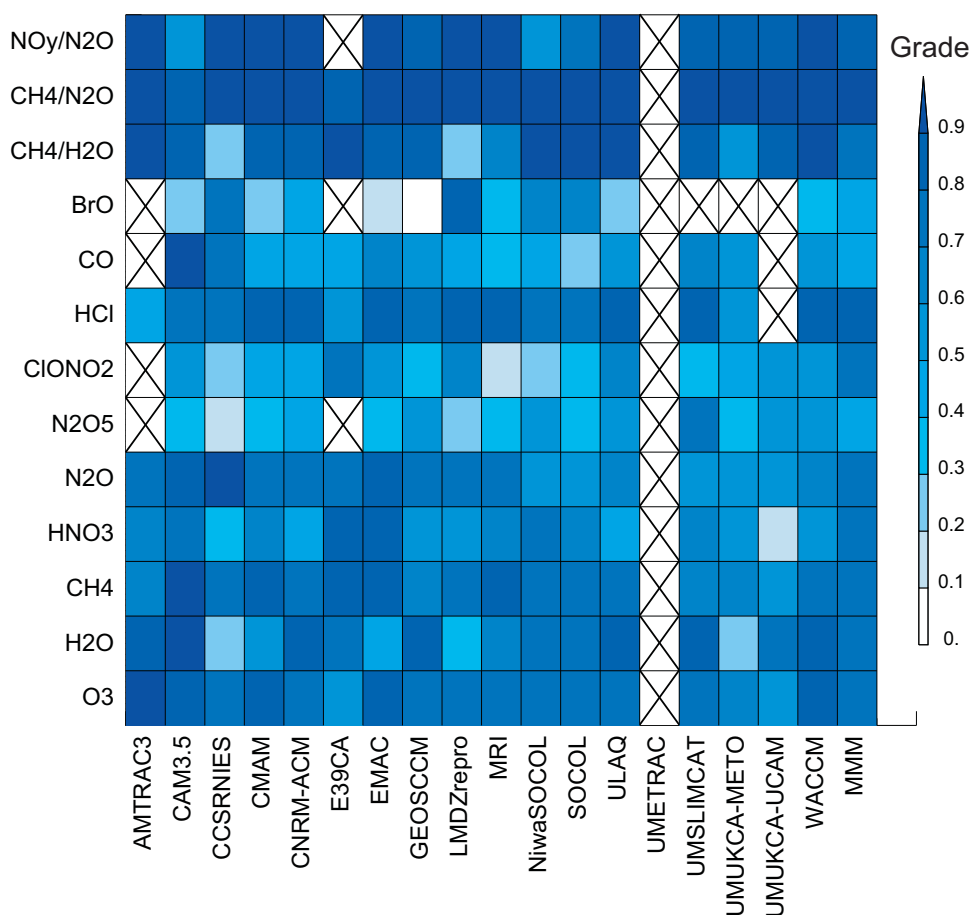


**Figure 6.15:** Grading plot for 18 CCMs (although no grades for UMETRAC) for tracer-tracer correlations, comparisons with the mean annual cycle (at 1 hPa and 50 hPa) and mean vertical profiles of a range of tracers in 3 latitude bands. Also shown is the score of the multi-model mean (MMM).

many CCMs included extra bromine (see below). The figure shows that the CCMs have a wide range in average BrO. Many models under-estimate the observed 24-hour mean values.

The comparison between the CCMs and satellite data for the selected altitudes and latitude regions was quantified as follows:

1. For every month, we calculated absolute differences (model-observation) on two levels, 1 hPa and 50 hPa.
2. If this difference is more than 3x the observational mean we assign a score = 0.1.
3. If this difference is more than 2x the observational mean, but less than 3x, we assign a score = 0.2.
4. If this difference is less than the observational mean we calculate the score using Equation (6.1) assuming all the observational data have 10% error ( $\sigma$ ) and  $n = 3$  (scaling factor).

We then average all the scores for all the months and latitude bands for 50 hPa and 1 hPa. Multi-model means are calculated by summing monthly mean values from all the CCMs and then calculating the differences between multi-

model mean - observational mean and then following steps (2) – (4).

Figure 6.15 shows the results of the grading for the comparison with the satellite climatologies. There are some tests for which all of the models tend to score lower, *e.g.*, ClONO<sub>2</sub> and N<sub>2</sub>O<sub>5</sub>, which may indicate some bias in the observations.

### 6.3.3.3 Long-term variations

Long-term observations provide data to test another component of the chemical models. Multi-annual satellite missions provide global altitude-resolved observations of trace gases from the early 1990s. In addition, observations from the Network for the Detection of Atmospheric Composition Change (NDACC) provide long-term data sets at certain ground-based sites which extend from the 1980s or 1990s to the present day. These data can be used to check the modelled variability (*e.g.*, annual cycle, volcanic influence) of key species which control stratospheric ozone.

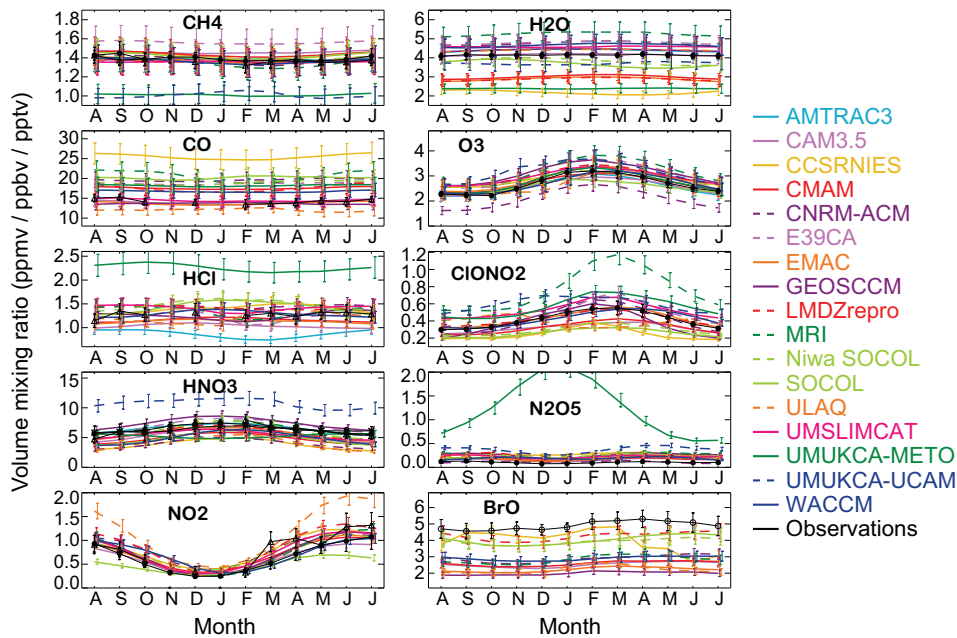


**Figure 6.16:** Mean annual cycle for 30°N-60°N at 50 hPa for modelled CH<sub>4</sub> (ppmv), H<sub>2</sub>O (ppmv), CO (ppbv), O<sub>3</sub> (ppmv), HCl (ppbv), ClONO<sub>2</sub> (ppbv), HNO<sub>3</sub> (ppbv), N<sub>2</sub>O<sub>5</sub> (ppbv), NO<sub>2</sub> (ppbv) and BrO (pptv). The CCM data is taken from the T2Mz files (2000-2004, except for the E39CA model 1996-2000). Also shown are corresponding satellite observations from MIPAS (CH<sub>4</sub>, H<sub>2</sub>O, O<sub>3</sub>, ClONO<sub>2</sub>, HNO<sub>3</sub>, N<sub>2</sub>O<sub>5</sub>, NO<sub>2</sub>; filled circles), ACE (NO<sub>2</sub>, HNO<sub>3</sub>, CO, HCl; triangles), ODIN (HNO<sub>3</sub>, crosses) and SCIAMACHY (BrO; open circles). The error bars are the standard deviations in the monthly-mean values (except for ACE data).

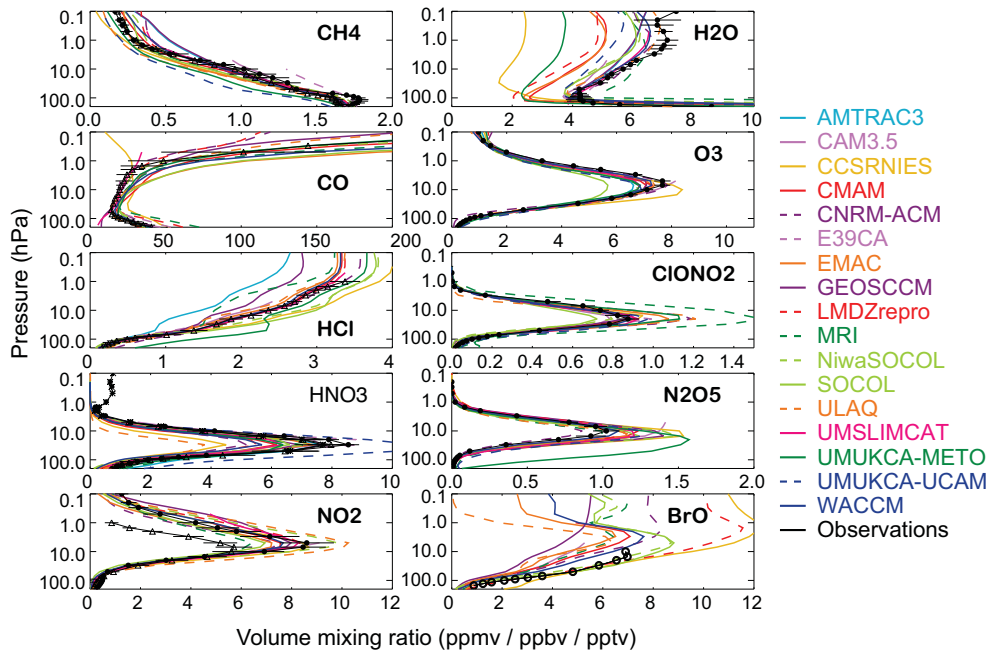


**Figure 6.17:** Mean profiles for 30°S-60°S for modelled CH<sub>4</sub> (ppmv), H<sub>2</sub>O (ppmv), CO (ppbv), O<sub>3</sub> (ppmv), HCl (ppbv), ClONO<sub>2</sub> (ppbv), HNO<sub>3</sub> (ppbv), N<sub>2</sub>O<sub>5</sub> (ppbv), NO<sub>2</sub> (ppbv) and BrO (pptv). The CCM data is taken from the T2Mz files (2000-2004, except for the E39CA model 1996-2000). Also shown are corresponding satellite observations from MIPAS (CH<sub>4</sub>, H<sub>2</sub>O, O<sub>3</sub>, ClONO<sub>2</sub>, HNO<sub>3</sub>, N<sub>2</sub>O<sub>5</sub>, NO<sub>2</sub>; filled circles), ACE (NO<sub>2</sub>, HNO<sub>3</sub>, CO, HCl; triangles), ODIN (HNO<sub>3</sub>, crosses) and SCIAMACHY (BrO; open circles). The error bars are the standard deviations in the annual mean values (except for ACE data).

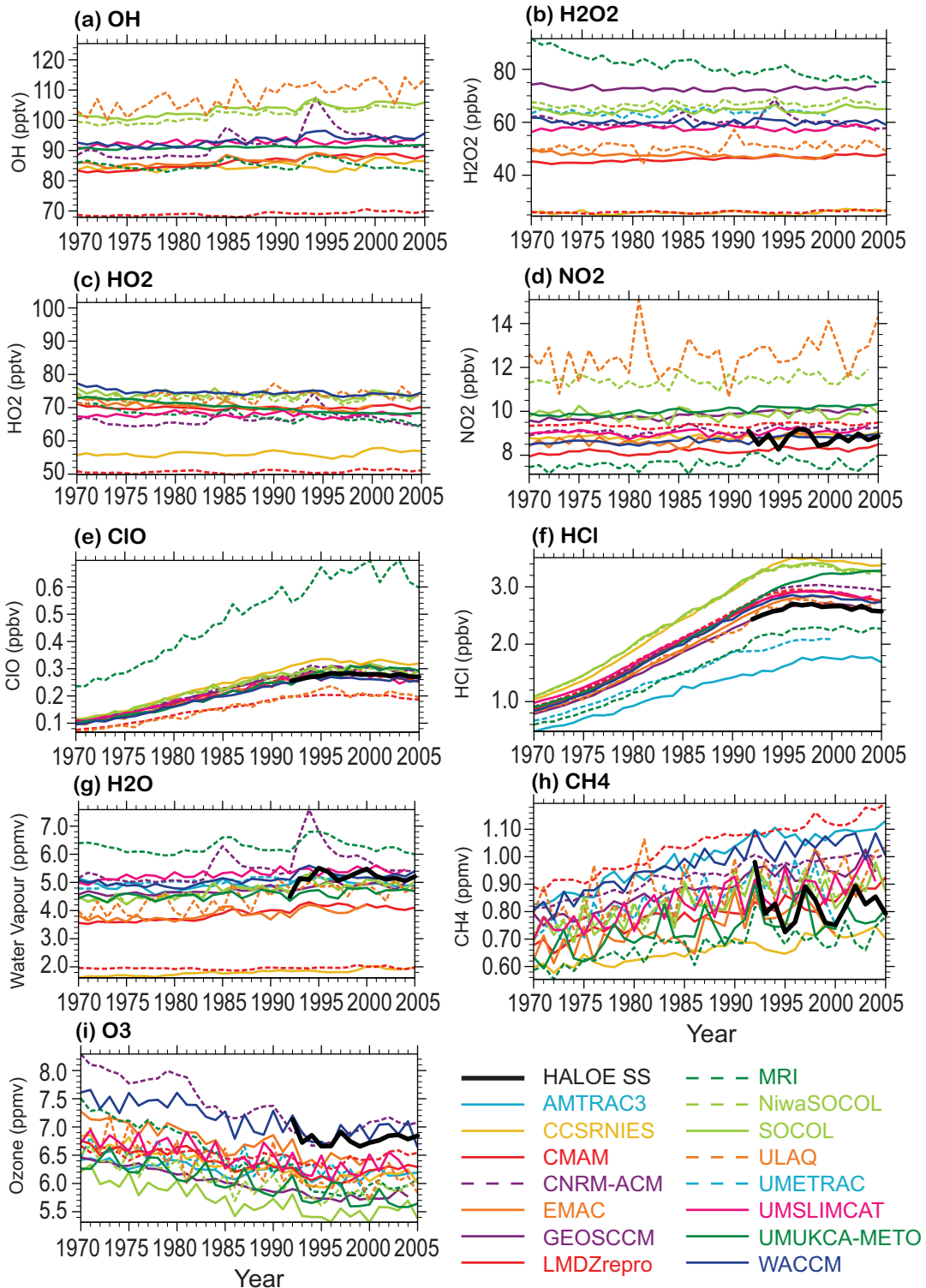


**Figure 6.18:** Time series of modelled zonal-mean (24-hour mean) trace gas abundance in the tropical upper stratosphere (3 hPa, 5°S-5°N) for (a) OH (pptv), (b) H<sub>2</sub>O<sub>2</sub> (pptv), (c) HO<sub>2</sub> (pptv), (d) NO<sub>2</sub> (ppbv), (e) ClO (ppbv), (f) HCl (ppbv), (g) H<sub>2</sub>O (ppmv), (h) CH<sub>4</sub> (ppmv) and (i) O<sub>3</sub> (ppmv). Also shown (1991 onwards) are HALOE satellite observations for NO<sub>2</sub>, HCl, H<sub>2</sub>O, CH<sub>4</sub> and O<sub>3</sub>. In panel (d) the twilight HALOE observations are converted to a 24-hour mean by using the ratio NO<sub>2</sub>/NO<sub>x</sub> from the EMAC model. Panel (e) also shows ClO derived from HALOE HCl by using the ratio of HCl/ClO from the EMAC model.

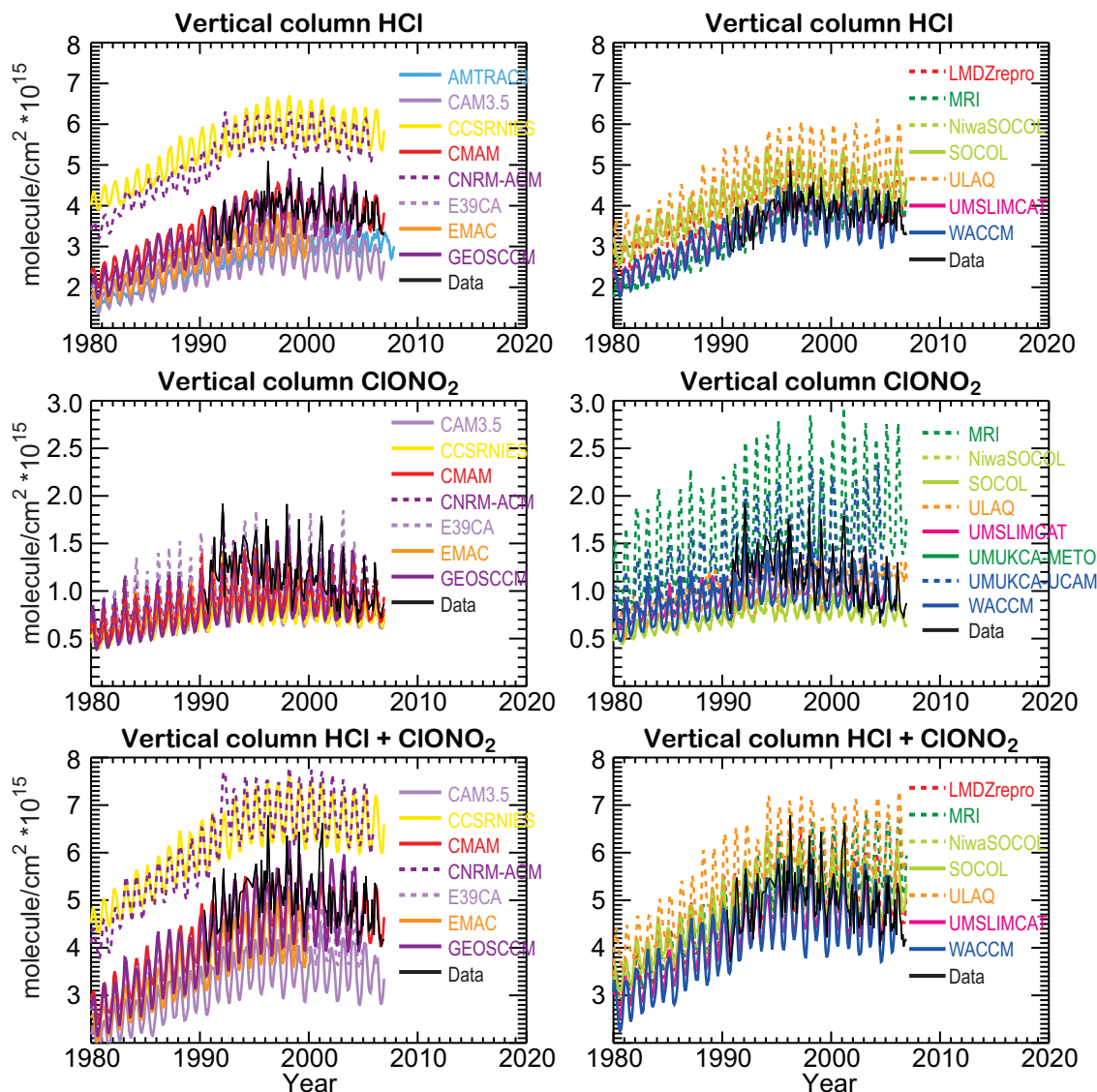


**Figure 6.19:** Comparison of observed column abundances (molecules  $\text{cm}^{-2}$ ) of HCl,  $\text{ClONO}_2$ , and HCl +  $\text{ClONO}_2$  at Jungfraujoch ( $45^\circ\text{N}$ ) with output from REF-B1 simulations.

**Figure 6.18** shows modelled mean tracer variations in the tropical upper stratosphere (3 hPa) for selected species. The model zonal mean output was averaged between  $5^\circ\text{S}$  and  $5^\circ\text{N}$ . Also shown are observations from the HALOE instrument starting in 1991. For  $\text{H}_2\text{O}$  this figure again shows the variation between the CCMs. The majority of models do agree fairly well with the observed 5 ppmv at this altitude. The CCSRNIES and LMDZrepro models, however, are very dry (only 2 ppmv  $\text{H}_2\text{O}$  at this altitude), while EMAC and CMAM are slightly dry. In contrast, the MRI model is too moist (over 6 ppmv). CNRM-ACM is exceptional among the models for showing significant enhancements in  $\text{H}_2\text{O}$  around 1985 and 1994, following the volcanic eruptions. For OH and  $\text{HO}_2$  the models tend to show similar values with little interannual variability, though the spread in OH is larger. The very dry models

(CCSRNIES and LMDZrepro) show the smallest values of  $\text{HO}_2$ , but only LMDZrepro has correspondingly low OH. ULAQ, SOCOL and NiwaSOCOL have the largest values of OH. For  $\text{CH}_4$  the models show a lot of model-model differences (*e.g.*, due to different circulation rates) and there is a large degree of interannual variability, presumably due to the equatorial QBO. For  $\text{NO}_2$ , ULAQ (which also has large interannual variability) and NiwaSOCOL show relatively large values. For HCl the CCMs reproduce the increasing trend through to 1997, followed by the turn-over and decrease. However, the AMTRAC3 model, for which we cannot assess the source gas loading and distribution, has significantly lower HCl than HALOE. The models with the highest HCl (*i.e.*, over 3 ppmv at this altitude in the early 2000s – UMUKCA-METO, CCSRNIES, SOCOL, NiwaSOCOL) are those that have spurious excess chlorine

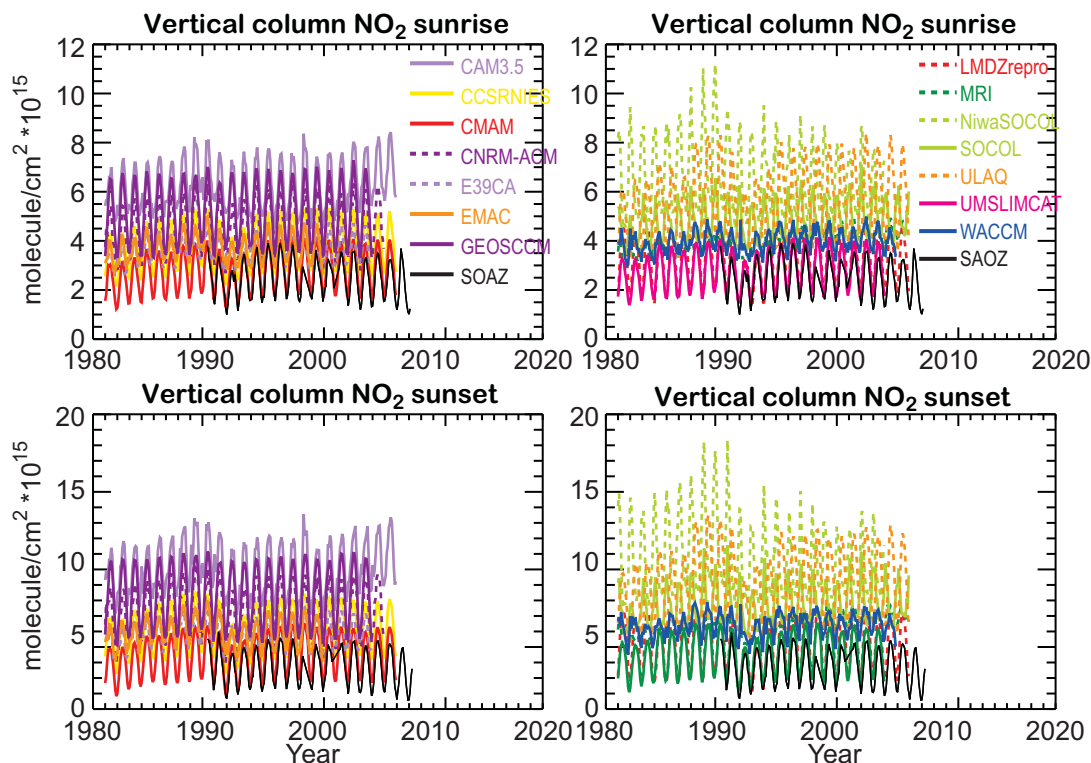


**Figure 6.20:** Comparison of observed column abundances (molecules  $\text{cm}^{-2}$ ) of  $\text{NO}_2$  at Jungfraujoch ( $45^\circ\text{N}$ ) for (a) sunrise and (b) sunset observations with output from REF-B1 simulations. The modelled 24-hour mean output (from zonal-mean files) have been converted to sunrise and sunset values using ratios of sunrise and sunset columns to 24-hour mean columns from the SLIMCAT 3D chemical transport model.

(see discussion of Figure 6.21 below). For ClO a notable outlier is the MRI model, which has significantly too much ClO. This will be due to the omission in this model of the  $\text{ClO} + \text{OH} \rightarrow \text{HCl} + \text{O}_2$  reaction (see Table 6S.2) which is important for the partitioning of inorganic chlorine ( $\text{Cl}_y$ ) at this altitude. This means that the MRI model will have a much larger sensitivity of ozone to  $\text{Cl}_y$  increases in the upper stratosphere. For  $\text{O}_3$  itself, all of the models tend to produce a decrease through the 1970s and 1980s, although there is a spread of values in the models. This spread, in the region where ozone is photochemically controlled, will be due to differences in the abundance of radicals which destroy ozone at this altitude, differences in the production rate from  $\text{O}_2$  photolysis, and differences in model temperatures. Further comparisons of  $\text{HO}_2$ ,  $\text{NO}_2$  and ClO at lower altitudes are provided in the supplementary material in Figure 6S.10.

**Figure 6.19** shows observations of column HCl,  $\text{ClONO}_2$ , and their sum, at the Jungfraujoch station ( $45^\circ\text{N}$ ) along with CCM results for  $45^\circ\text{N}$  (from zonally averaged output). These two species are the main reservoirs for stratospheric inorganic chlorine. The observations show an increase in column  $\text{HCl} + \text{ClONO}_2$  until about 1998 followed by a decrease. The stratospheric trend in inorganic chlorine is expected to follow the tropospheric loading of organic

chlorine (see Chapter 2) with a lag due to stratospheric transport time scales. Interestingly, at this station  $\text{ClONO}_2$  appears to be decreasing relatively faster than HCl over the past decade in the observations, whereas the models do not show such a marked difference. Further analysis of this apparent discrepancy is not possible here. There is a large variation in the magnitude of the column  $\text{HCl} + \text{ClONO}_2$  predicted by the models. The CCSRNIES and CNRM-ACM models predict much larger columns (by about 40%) than the observations. This will be due, at least in part, to the larger chlorine loading in these models although column comparisons also depend sensitively on the shape of the model profiles in the lower stratosphere (where higher pressures mean a potentially large contribution to the column). In contrast, the CAM3.5 model under-estimates column  $\text{HCl} + \text{ClONO}_2$ . Despite these differences in magnitude, most models predict a similar long-term behaviour with a peak in inorganic chlorine in the late 1990s. The ULAQ and MRI models, however, maintain high chlorine until the end of the REF-B1 run. There are further differences between the models in terms of the partitioning of HCl and  $\text{ClONO}_2$ . The MRI and UMUKCA-UCAM models compare well for HCl but overestimate  $\text{ClONO}_2$  while SOCOL and NiwaSOCOL under-estimate this species.

**Figure 6.20** compares column  $\text{NO}_2$  observed at

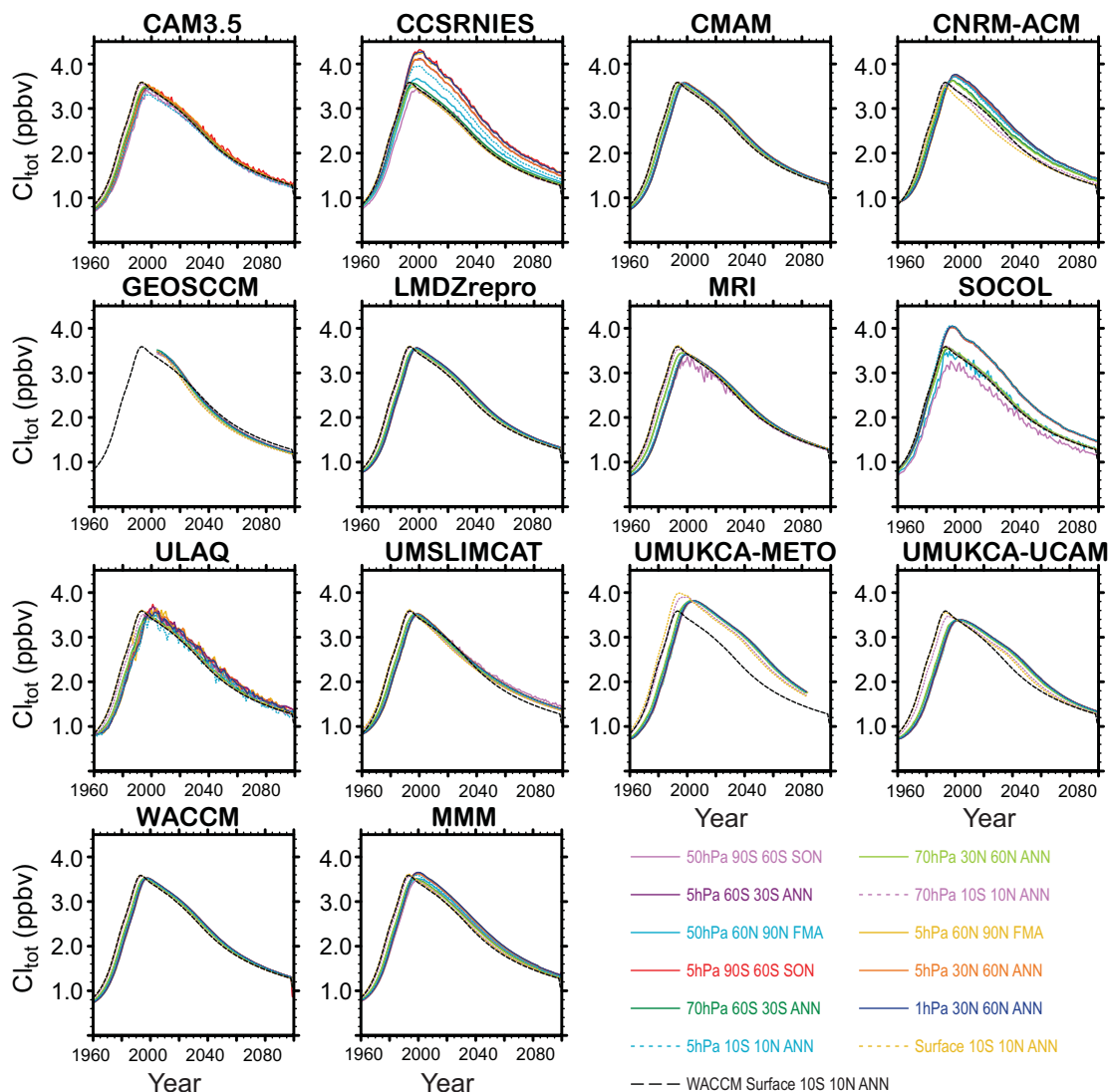


**Figure 6.21:** Time series of total chlorine volume mixing ratio (sum of all inorganic and organic chlorine tracers) (ppbv) from 1960 to 2100 from 13 REF-B2 CCM simulations and the multi-model mean. A selection of averages within different latitude bands and at different altitudes are plotted. For reference, each panel also includes the total chlorine curve from the WACCM model at the surface (black dashed line).

Jungfraujoch with the available CCM output. As  $\text{NO}_2$ , which is a key ozone-destroying radical, has a strong diurnal cycle the CCM zonal mean (*i.e.*, 24-hour mean over different local times and different longitudes) output had to be converted to the time of the observations (sunrise and sunset) using output from the SLIMCAT chemical transport model. Note that this conversion is not necessarily self-consistent because a different model is used in the conversion of daily means into sunset/sunrise values. Again, there is a large variation in the magnitude of the column predicted by the models. While some models agree quite well, many other models overestimate the observations. In particular, column  $\text{NO}_2$  derived from CAM3.5, GEOSCCM, CNRM-ACM, NiwaSOCOL, ULAQ and SOCOL are up to a factor 2 larger than observations. WACCM appears

to severely under-estimate the magnitude of the  $\text{NO}_2$  annual cycle. The eruption of Mt Pinatubo in 1991 led to a decrease in column  $\text{NO}_2$  followed by an increase through the mid-1990s. Since almost all the models use prescribed sulphate surface area density, they are able to capture this long-term variation. This is not the case for GEOSCCM which was run with constant aerosol. The long-term trend in  $\text{NO}_y$  and hence in  $\text{NO}_2$  (expected from the trend in its source gas,  $\text{N}_2\text{O}$ ) is too small to be visible in the time series of observations and model calculations.

We now analyse results from the REF-B2 simulations from 1960 to 2100. The aim here is not to evaluate against observations but to check the CCMs for internal consistency in their chemical schemes and to verify that the models have used the recommended source gas bound-

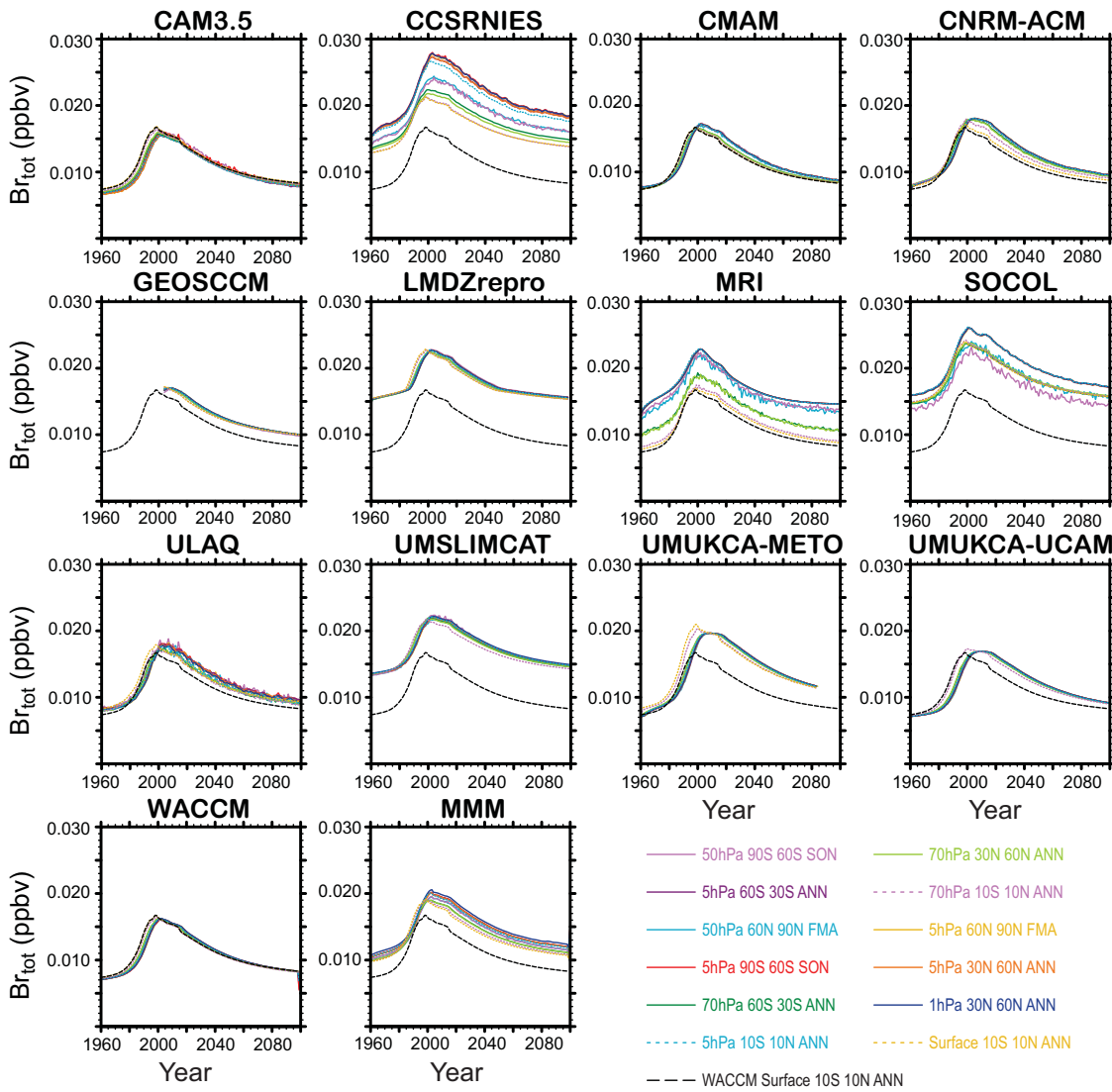


**Figure 6.22:** As Figure 6.21 but for total bromine mixing ratio (ppbv).

ary conditions. **Figures 6.21 and 6.22** plot the time series of total chlorine ( $Cl_{tot}$ ) and total bromine ( $Br_{tot}$ ), respectively, from the available models in selected latitude bins and at selected altitudes. These model curves have been constructed by summing all of the organic and inorganic chlorine or bromine species in the model. Many models employ a lumping scheme for minor halocarbons (see Chapter 2), but in these cases the contribution of chlorine and bromine is added to the tracers that are carried, and so this will not affect the total abundance. Therefore, ideally the total chlorine and bromine curves for all models at the surface should be consistent with the specified scenario. For any model, the total chlorine and bromine curves at high altitudes in the stratosphere should mimic the surface (tropospheric) variation with a delay and smoothing reflecting the model mean age-of-air (see Chapter 5) and atmospheric mixing. Similar plots for just organic chlorine and bromine are provided in the Supplementary Material,

Figures 6S.11 and 6S.12.

For total chlorine (Figure 6.21) many models show the expected behaviour but there are some notable deviations. The models which perform well are CAM3.5, CMAM, LMDZrepro, UMSLIMCAT, and WACCM. These models show a compact set of curves which are very similar at all locations with a slight delay between the tropospheric values and higher altitudes. The GEOSCCM and UMUKCA-UCAM models also appear intrinsically well behaved but the models' total chlorine scenarios appear to differ from that specified in the forcing data. MRI, and to a greater extent ULAQ, show fairly good consistency between different model levels except that in some locations total chlorine variations appear to be more noisy. Figure 6.21 also reveals that some models have stratospheric  $Cl_{tot}$  variations which are inconsistent with the specified tropospheric forcing. In the CCSRNIIES, model the tropospheric  $Cl_{tot}$  follows the specified scenario. However, on going to higher



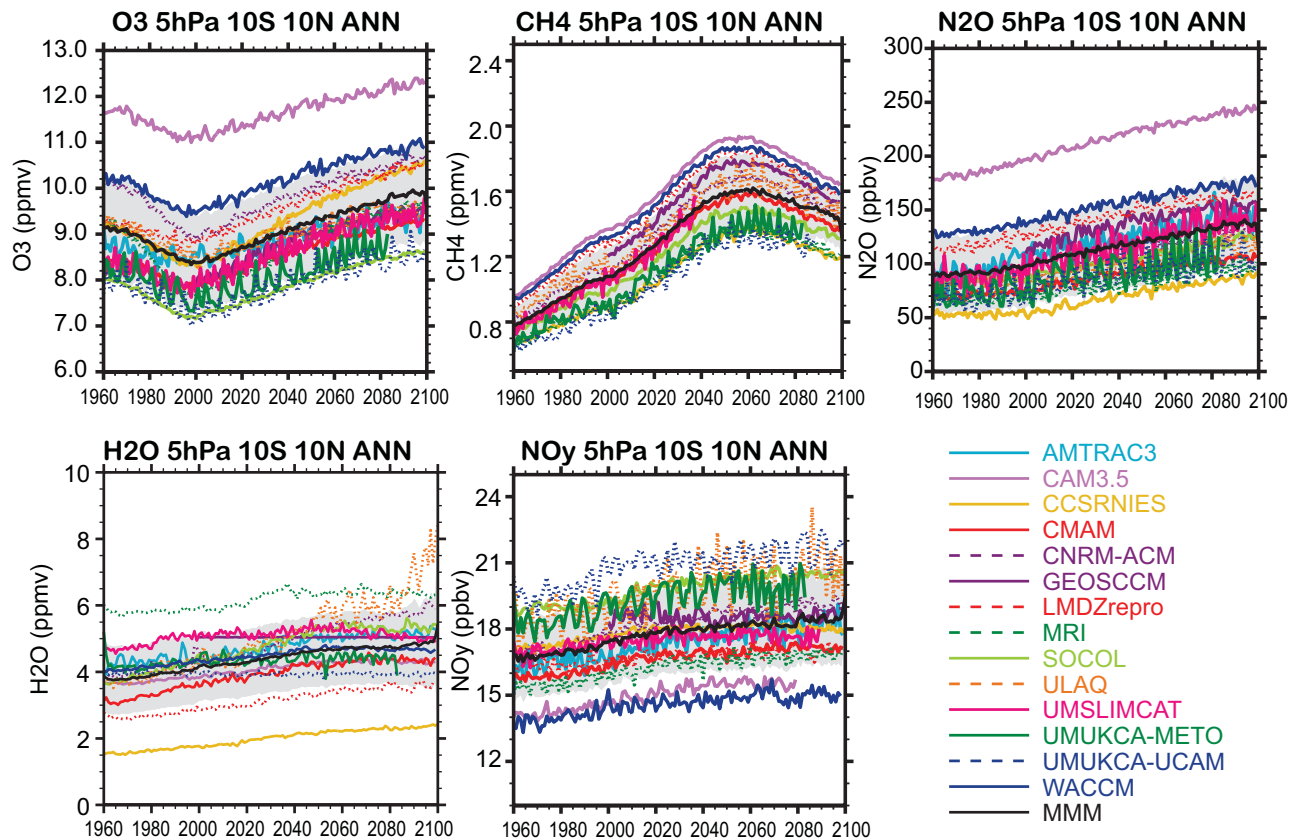


**Figure 6.23:** Time series of  $O_3$  (ppmv),  $CH_4$  (ppmv),  $N_2O$  (ppbv),  $H_2O$  (ppmv) and  $NO_y$  (ppbv) annually averaged between  $10^\circ S$  and  $10^\circ N$  at 5 hPa from REF-B2 runs of 14 CCMs and the multi-model mean.

altitudes  $Cl_{tot}$  increases until it peaks at over 4 ppbv at 5 hPa around 2000. Evidently this model does not conserve the total chlorine mixing ratio. This effect is also seen, but to a much smaller extent, in CNRM-ACM. SOCOL shows a similar behaviour to CCSRNIIES but in this case there is an apparent separation between the lower curves (50 hPa, 70 hPa) which follow the specified  $Cl_{tot}$  scenario and the higher curves (1hpa, 5 hPa) which have unrealistically high  $Cl_{tot}$ . The UMUKCA-METO model has  $Cl_{tot}$  that is too high because of the reported mistreatment of tropospheric removal of species, in this case HCl (see Chapter 2). Otherwise UMUKCA-METO behaves similarly to UMUKCA-UCAM. Finally, we could not plot  $Cl_{tot}$  from AMTRAC because it does not carry organic halocarbons. We analysed total inorganic chlorine ( $Cl_y$ ) from AMTRAC and noted that even in the upper stratosphere  $Cl_y$  was significantly less than  $Cl_{tot}$  from other realistic models (see also comparison with HALOE HCl in Figure 6.18). Therefore, it seems likely that the AMTRAC treatment of chlorine causes an under-estimate in total chlorine.

Figure 6.22 shows the evolution of model  $Br_{tot}$ . In general for bromine the CCMs show more differences compared to the planned scenario than for chlorine. The specifications for the CCMval runs only considered long-

lived bromine source gases. Therefore, model tropospheric  $Br_{tot}$  should have peak at around 16 pptv just before the year 2000. The models CAM3.5, CMAM and WACCM follow this scenario with consistent variations in the stratosphere. Other models appear to conserve bromine but have been run with different scenarios: UMUSLIMCAT and LMDZrepro assumed an extra  $\sim 6$  pptv bromine from short-lived sources; UMUKCA-UCAM has larger  $Br_{tot}$  after 2000, as does ULAQ and GEOSCCM. CCSRNIIES includes a short-lived source of bromine (bromoform) hence its tropospheric  $Br_{tot}$  variation peaks around 21 pptv. However, bromine increases at higher levels in a similar way to the model's  $Cl_{tot}$  indicating conservation problems. SOCOL also appears to include additional bromine sources but also has mid-stratospheric  $Br_{tot}$  larger than expected, again similar to  $Cl_{tot}$ . UMUKCA-METO has larger bromine than UMUKCA-UCAM, suggesting that the tropospheric washout problem (Chapter 2) is also affecting the abundance of total bromine. The MRI model generally performed well for  $Cl_{tot}$  but show an increase in  $Br_{tot}$  with altitude.

**Figure 6.23** shows the evolution of  $O_3$ ,  $CH_4$ ,  $N_2O$ ,  $H_2O$  and  $NO_y$  at 5 hPa in the tropics from the REF-B2 runs. **Figures 6.24** and **6.25** are similar plots for 70 hPa

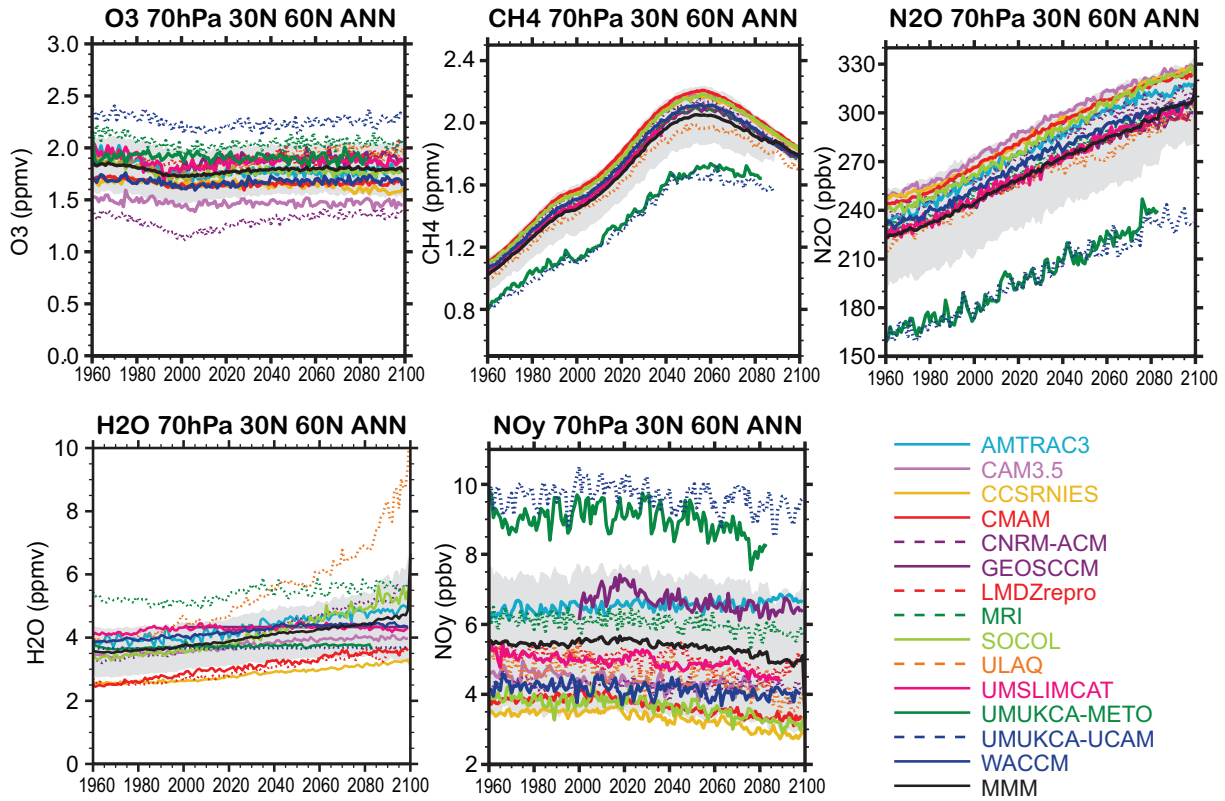


Figure 6.24: As Figure 6.23 but for an annual average between 30°N and 60°N at 70 hPa.

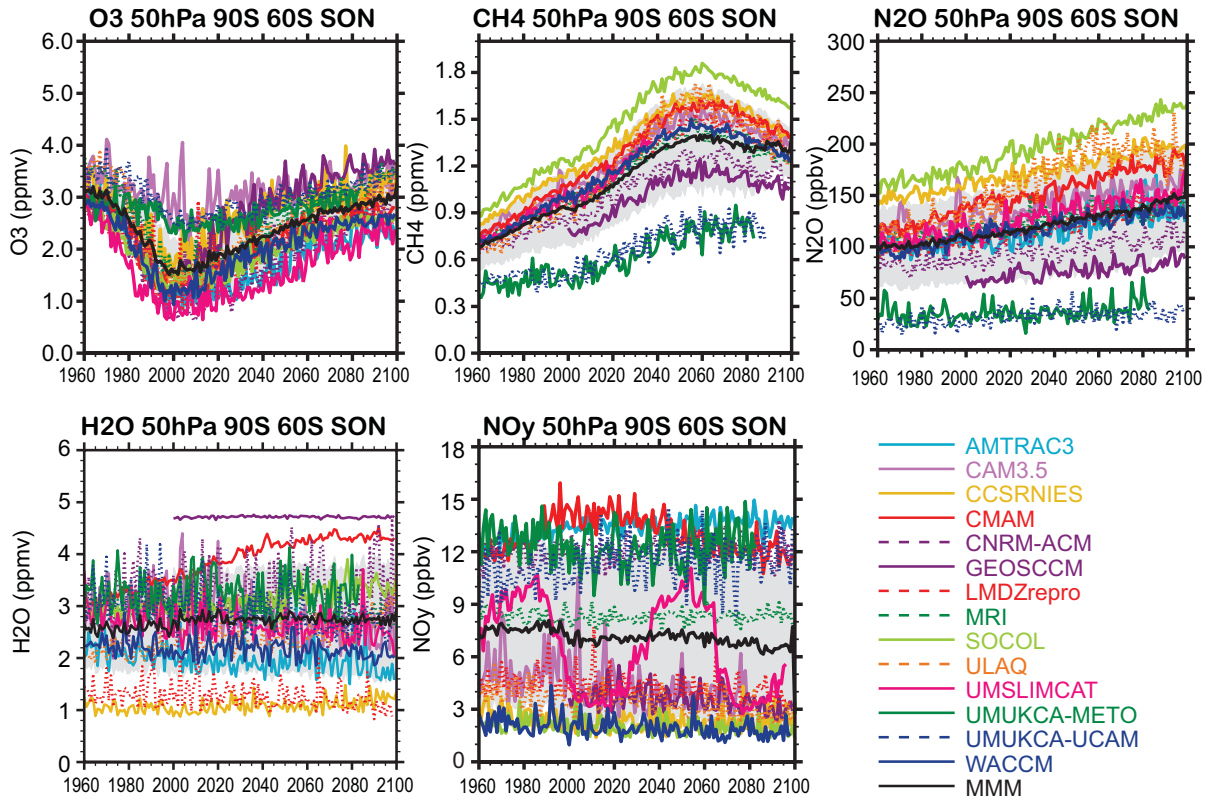


Figure 6.25: As Figure 6.23 but for a September–November average between 90°S and 60°S at 50 hPa.

in the mid-latitudes and 50 hPa in the polar region, respectively. The modelled distribution of long-lived tracers will be affected by both transport and chemistry. Chapter 5 contains a detailed evaluation of transport in the models and will not be repeated here. Clearly a lot of the variations in, for example, tropical mid-stratosphere  $\text{N}_2\text{O}$  will be due to differences in the strength of the model circulation. Other differences will be due to chemistry, *e.g.*, photolysis loss rates (see Section 6.3.1). In this section we show these long-term variations to provide an overview of the long-term variations in the sources of  $\text{NO}_x$  and  $\text{HO}_x$  radicals, which, in conjunction with halogens, will be driving ozone changes (see Chapters 8 and 9). Overall, the models show similar variations in  $\text{CH}_4$  and  $\text{N}_2\text{O}$ , both of which are specified as tropospheric surface boundary conditions. At 5 hPa CAM3.5 is an outlier but this is near the model's top boundary. At mid- to high latitudes, the two UMUKCA models are significantly lower but this will be a consequence of the slow stratospheric circulation in this model (Chapter 5). The model spread in  $\text{NO}_y$ , which is derived from  $\text{N}_2\text{O}$ , is at least as large as the source gas. High  $\text{N}_2\text{O}$  will correlate with low  $\text{NO}_y$  and *vice versa*. In the polar region in winter/spring (*e.g.*, Figure 6.25) there is also the additional variability caused by denitrification. Compared to other source gases, there are larger variations (and differences in sign) in the modelled trends in  $\text{H}_2\text{O}$ , which depends both on the input to the stratosphere and production from methane oxidation. The CCSRNIES and LMDZrepro models are relatively dry, while the MRI model is moist. GEOSCCM uses constant water vapour in the stratosphere (note: this was a run time error and the simulation is being repeated). A number of models produce an increasing trend in  $\text{H}_2\text{O}$  towards the later decades on this century, notably ULAQ at low and mid-latitudes and CMAM in the polar region.

### 6.3.4 Evaluation of Polar Chemistry

#### 6.3.4.1 Evolution of gas-phase $\text{HNO}_3$ , $\text{H}_2\text{O}$ , and HCl

In this section we evaluate aspects of polar winter/spring chemical processing in the southern hemisphere (SH), by comparing the time evolution of CCM lower stratospheric abundances to global observations (from mid-2004 through mid-2009) by the Microwave Limb Sounder aboard the Aura satellite. The processes involved include denitrification (or at least a decrease in gaseous  $\text{HNO}_3$ ) as a result of heterogeneous reactions that occur on PSCs when temperatures in the lower stratosphere polar vortex dip below about 195 K, as well as dehydration (or at least a decrease in gaseous  $\text{H}_2\text{O}$ ) and chlorine activation (the sunlight-driven release of active chlorine, following

a decrease in the HCl and  $\text{ClONO}_2$  reservoir abundances *via* heterogeneous reactions). We investigate polar changes in  $\text{HNO}_3$ ,  $\text{H}_2\text{O}$ , and HCl, in order to assess how models compare to each other and to observations. We use a decrease in HCl as an indication of chlorine activation, rather than an increase in ClO, because of the added complications that ClO poses in terms of time of day sampling and comparisons to model values that are more representative of 24-hr averages (and therefore significantly lower than midday values). Model grades are provided as a quantitative guide to the MLS comparison, and to illustrate the range of variations between the models. We also comment briefly on the extent of model variations in space and time, for “outliers” in particular, in comparison to the “typical” behaviour from observations (and models).

In order to investigate such complex processes in free-running models, which are likely to vary significantly in their representation and parameterisation of heterogeneous chemistry and related polar processing and dynamics, and without unduly focusing on a specific year, we have compared climatologies of volume mixing ratio (VMR) *versus* potential temperature ( $\theta$ ) as a function of equivalent latitude (EqL). The model values were obtained from REF-B1 simulations, typically from 1950 to 2006 (although the exact start and end dates vary between models, with some models ending in 2004 and some in 2006). The models were all converted from gridded 10-day instantaneous results to mean profiles on a vertical  $\theta$ -grid, in EqL bins spaced every  $2.5^\circ$ ; 15 of 18 total CCMs provided the necessary results for analysis. The Aura MLS data were also transferred to this coordinate system (more appropriate for analyses of polar winter processes) by using UKMO analysis files and related “Derived Meteorological Products” from the work of Manney *et al.* (2007). Five years of MLS data (from August, 2004 through July, 2009) were used to construct the climatological averages. These files were all produced in the same format (netCDF), for ease of use. The last 5 years of each model run were used to compare to the MLS 5-year climatological profiles. Based on our analysis of model variability (from year to year), using 10-15 years rather than 5 years for the model climatologies is not expected to generally change the main results, as model variability is typically fairly small compared to average model values (or model changes during polar winter/spring). Relevant references for the Aura MLS data include Waters *et al.* (2006) for a description of the limb emission microwave measurement technique, as well as detailed validation papers for the species mentioned here (and for MLS version 2.2 retrievals), namely Santee *et al.* (2007) for  $\text{HNO}_3$ , Froidevaux *et al.* (2008) for HCl, and Lambert *et al.* (2007) for stratospheric  $\text{H}_2\text{O}$ .

Figure 6.26 shows the climatological average evolution of Aura MLS  $\text{HNO}_3$  profiles (on a  $\theta$ -grid) between mid-May and mid-October, for 4 EqL ranges centred at

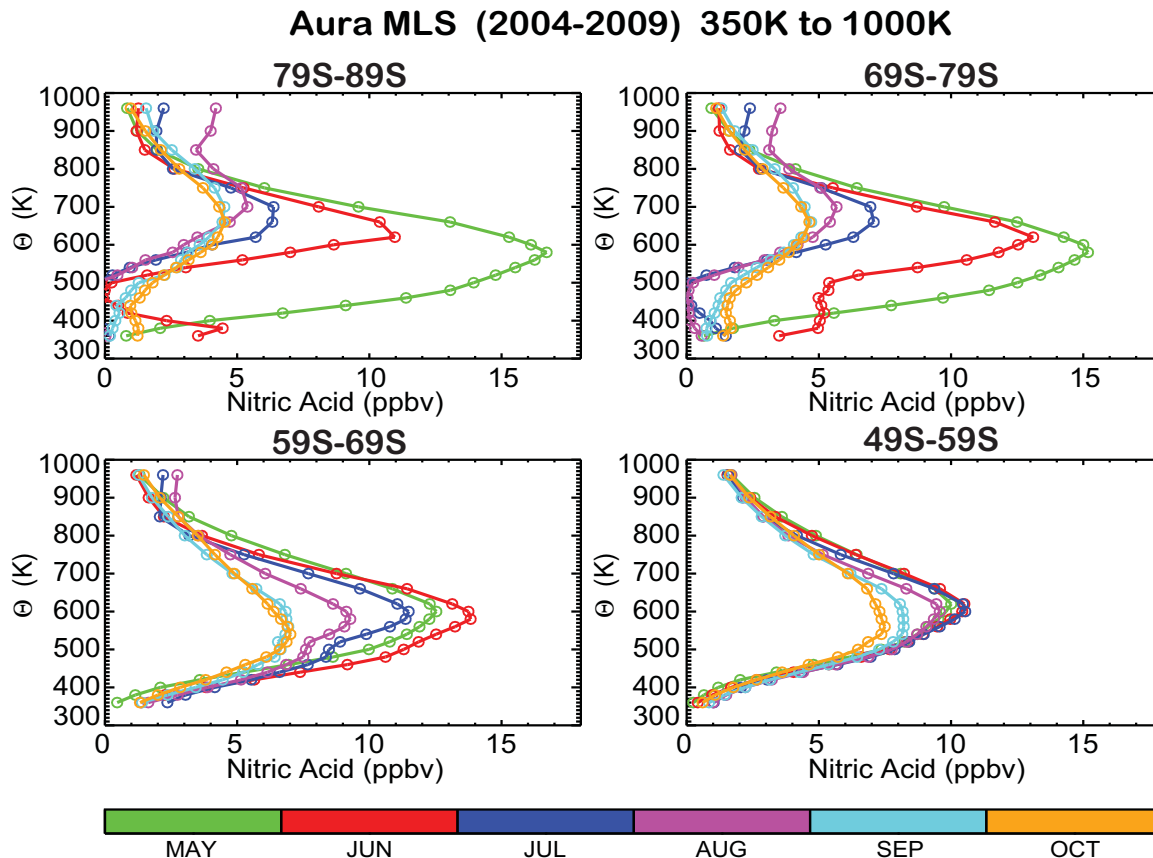


**Figure 6.26:** Southern hemisphere profiles of  $\text{HNO}_3$  versus  $\theta$  from Aura MLS at mid-month (on the 15<sup>th</sup> day of each month shown in colour bar), from May through October, based on a 5-year MLS climatology (mid-2004 to mid-2009). Profiles are averaged over the EqL ranges shown above each panel.

about 85°S, 75°S, 65°S, and 55°S. **Figure 6.27** shows similar profile distributions, but only for the southernmost EqL bin, and includes all the available CCM climatological monthly changes, as well as a multi-model mean result (labelled “MMM”). The mid-month values are obtained by using the day closest to the 15<sup>th</sup> of each month; while this falls on the 15<sup>th</sup> day for MLS (daily) data, this will not be exactly the case for the model climatologies (models usually provided output every ten days). Most of the decreases in MLS  $\text{HNO}_3$  are seen to occur for  $\theta < 800$  K, with the lowest  $\text{HNO}_3$  values occurring between July and September for  $\theta < 550$  K in the two southernmost EqL bins. A more rapid/extensive lower stratospheric nitric acid decrease is observed by Aura MLS than in most of the models, although some models show decreases in  $\text{HNO}_3$  at higher altitudes ( $\theta$ ) than observed. To summarize the evolution of lower stratospheric CCM  $\text{HNO}_3$  distributions over the high SH latitudes, **Figure 6.28** shows a comparison of the various model (5-year) climatological monthly changes in  $\text{HNO}_3$  (relative to mid-May) over the 350 K–600 K  $\theta$  range versus the MLS climatology in four EqL bins.

Grades indicating the quality of the model fits to the data over this time period are obtained by using Equation

(6.1), evaluating the average absolute separation (over  $N$  months, with  $N = 5$  here) between model ( $\mu_{model}^i$ ) and observed ( $\mu_{obs}^i$ ) climatological values, divided by a measure of uncertainty (or variability) in the data, so that the grade is

$$g = 1 - \frac{1}{N} \sum_i \frac{|\mu_{model}^i - \mu_{obs}^i|}{n\sigma}. \quad (6.5)$$

In order to check such fits, a value for  $n\sigma$  in the above equation needs to be provided, with  $n = 3$  used in previous recommendations (Vaugh and Eyring, 2008). Given the fairly large spread of models about the data in Figure 6.28 for  $\text{HNO}_3$  (and to some extent for other species discussed below), we would obtain low-grade values (or negative grades) for many of the models if  $\sigma$  values corresponding only to data variability or (especially) knowledge were used. Instead, we have arrived at grades that provide a range of values between 0 and 1, so that model differences can be fairly well discerned. Therefore, this is more a *relative* indication of model fits to the data than a rigorous statistical test. Some changes to the values of  $n\sigma$  have been explored (*e.g.*, variations by a factor of 2 or more). While the absolute grades can certainly be affected (by several tenths), the main results regarding the best or poorest fit-

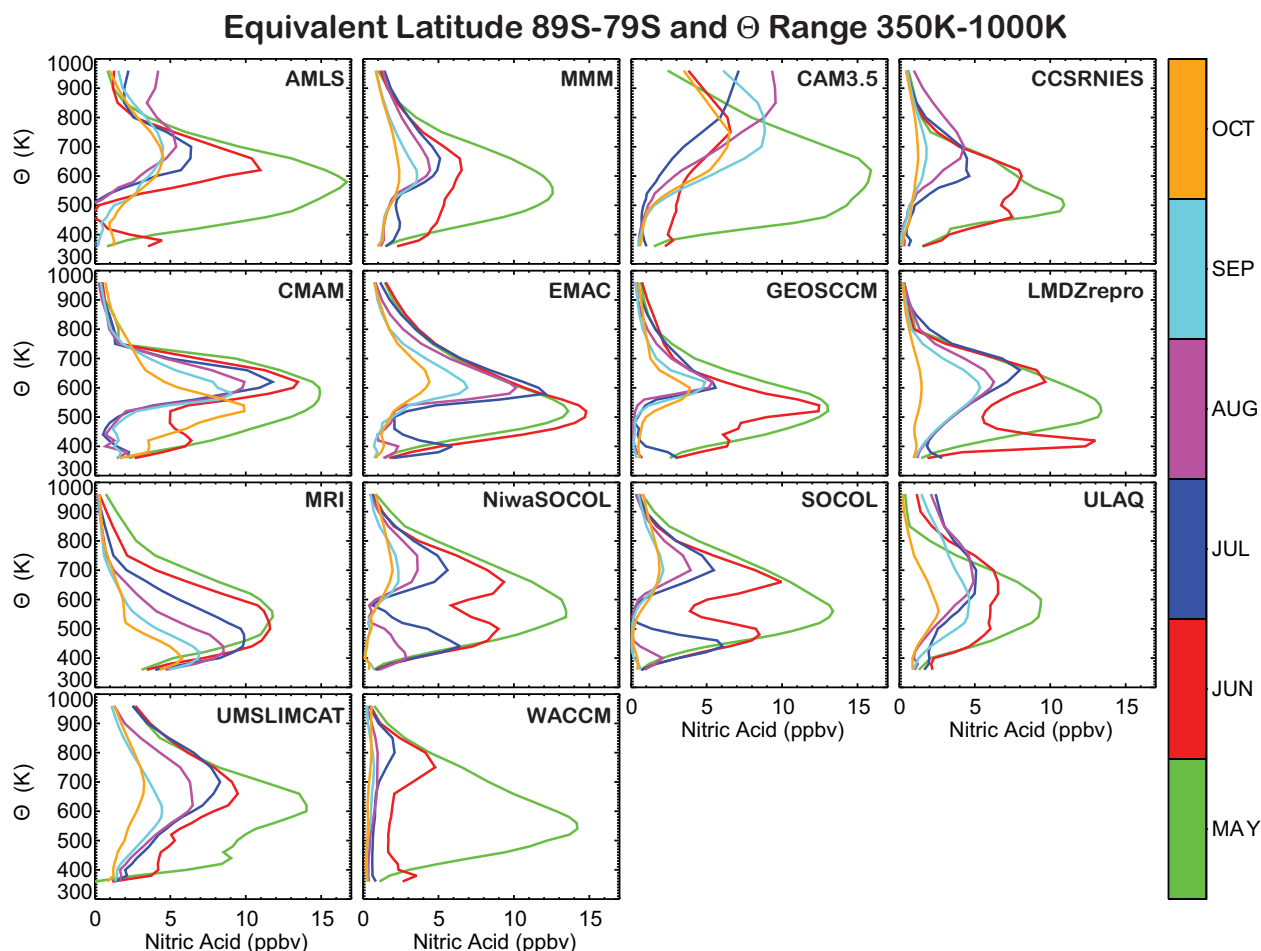


**Figure 6.27:** CCM climatological profiles of  $\text{HNO}_3$  from mid-May through mid-October (same colour bar as in Figure 6.26) for 12 CCMs and multi-model mean (MMM). Only the southernmost EqL bin from Figure 6.26 is displayed here.

ting models do not change much, and this will be the main focus of our discussion. For reference, values of  $n\sigma$  used in this study are 5 ppbv, 1.5 ppmv, 1 ppbv, and 1.5 ppmv for  $\text{HNO}_3$ ,  $\text{H}_2\text{O}$ ,  $\text{HCl}$ , and  $\text{O}_3$ , respectively. **Figure 6.29** displays the resulting model grades for  $\text{HNO}_3$  versus EqL for each of the three  $\theta$  bins. This methodology is then repeated for changes in  $\text{H}_2\text{O}$ ,  $\text{HCl}$ , and  $\text{O}_3$ , discussed below in more detail.

We see from Figure 6.27 that the various CCMs develop significantly different average profiles for  $\text{HNO}_3$  as a function of month, despite the evidence for fairly similar distributions during May (prior to the vortex formation and the presence of low enough temperatures for significant polar processing). Aura MLS  $\text{HNO}_3$  data at 350 K to 600 K show (Figure 6.28) significant decreases (by 8 to 10 ppbv) at 69°S to 89°S from May to October. The steepness and magnitude of these (climatological) changes are best reproduced by CAM3.5 and WACCM, leading to high scores (Figure 6.29) for these models in this respect. These models' performances drop somewhat at 65°S, where the model decreases are larger than observed. Also, both of

these models exhibit (Figure 6.27) a large vertical extent of low  $\text{HNO}_3$  values (probably accompanied by low  $T$ ), and thus get lower grades in the 600 K-800 K range, where the MLS data do not indicate such a rapid drop from May to July. In contrast, many models under-estimate the  $\text{HNO}_3$  decrease in the 350 K - 600 K range especially in early winter, resulting in poor grades; these models perform better in the 600 K - 800 K range. More detailed views of the  $\text{HNO}_3$  evolution can be studied from plots at each  $\theta$  level, as shown in **Figures 6.30a** and **6.30b** for the 500 K level; each of these figures displays only half of the available models, for clarity. However, assigning model grades from such plots (for each  $\theta$  level) would create a difficult task to summarize. Averaging over a range of  $\theta$  is thus chosen as the preferred approach. Similar figures at 500 K, but for  $\text{H}_2\text{O}$  and  $\text{HCl}$ , are provided in the Supplementary Material for reference (Figures 6S.13 and 6S.14).

Considering now the evolution of the SH polar  $\text{H}_2\text{O}$  in a similar manner, we refer to **Figure 6.31** and Figures 6S.15 and 6S.17 in the Supplementary Material. For EqL values larger (more poleward) than 69°S, the Aura MLS

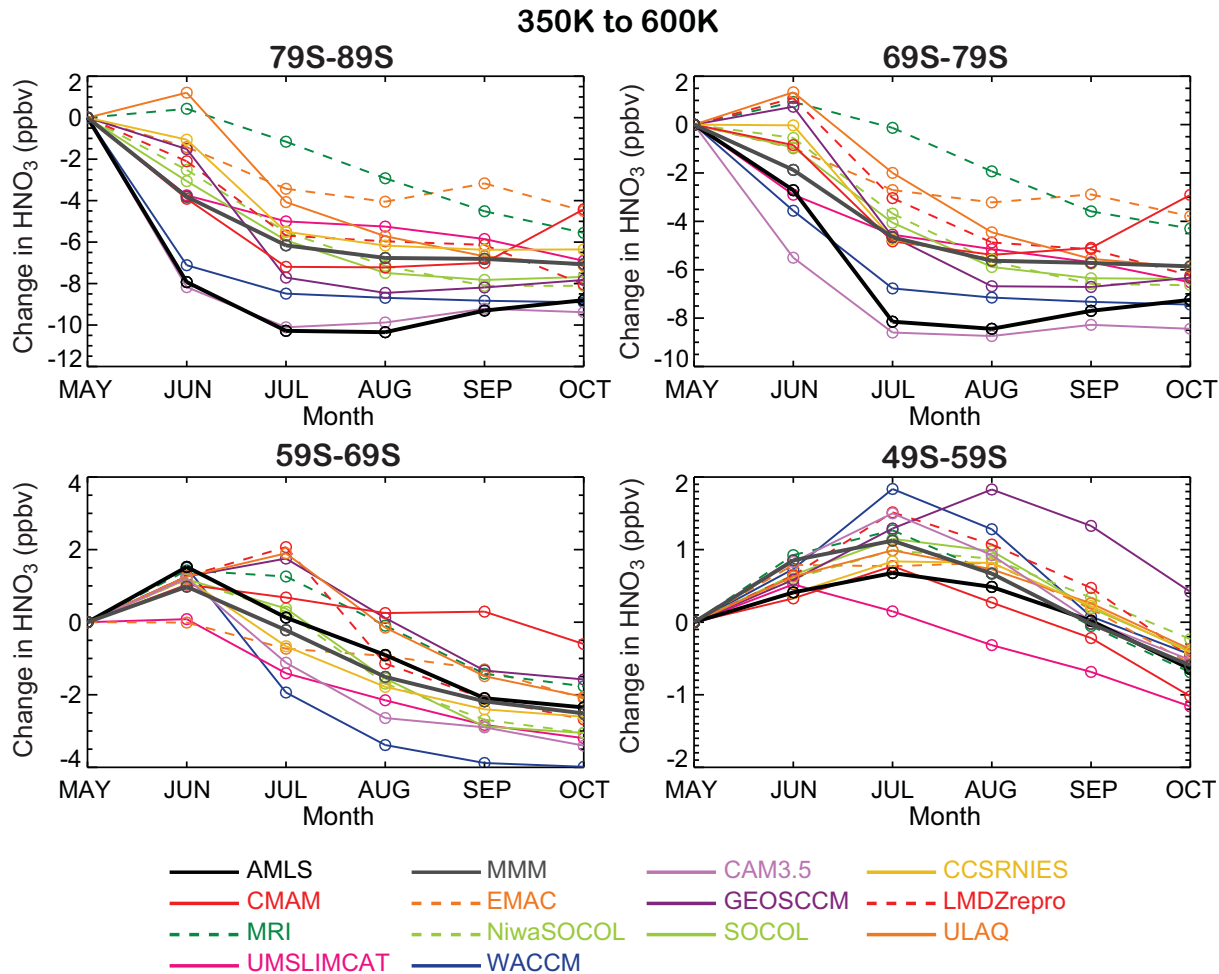


**Figure 6.28:** Change in  $\text{HNO}_3$  from 350 K to 600 K, relative to May, for Aura MLS (abbreviated as AMLS in legend) and 12 CCM climatologies (legend uses first 4 letters of each model) and their multi-model mean (MMM).

climatology indicates that  $\text{H}_2\text{O}$  decreases by 1 to 2 ppmv from May to August, with a mild increase from August to October. Models tend to follow this behaviour very well in the mean, and the multi-model mean (MMM) performs quite well. There are a few models that depart more from the average behaviour: AMTRAC, MRI, and WACCM exhibit significantly larger decreases in  $\text{H}_2\text{O}$  (about 3 ppmv or more), leading to poorer grades for this process, whereas at the other extreme, GEOSCCM shows very little change in  $\text{H}_2\text{O}$  during May to October. Other plots (not shown here) indicate that for some models (*e.g.*, WACCM), the low  $\text{H}_2\text{O}$  values cover a wide vertical range and that this “dehydration” also happens for a significantly more extended time period than observed in the MLS data. As in the case of  $\text{HNO}_3$ , the spread in model distributions and model grades (see Figure 6S.17) decreases at the lower (equivalent) latitudes as well as at the higher altitudes (larger  $\theta$  values); these regions are less influenced by winter polar chemical processes.

Similar observations hold for the chlorine activa-

tion fits, exemplified by the decrease and recovery in HCl, shown in **Figure 6.32** and in the Supplementary Material in Figures 6S.16 and 6S.20, with related model grades given in Figure 6S.18. Models tend to represent fairly well, on average, the observed climatological decreases in HCl (associated with chlorine activation on PSCs) in the Antarctic winter lower stratosphere. The observed HCl changes between May and August are slightly larger than 1.5 ppbv, for the EqL bins used here. On average, the models show smaller decreases (by about 0.5 ppbv) than observed, and only one model (UMUKCA-METO) produces a larger decrease than the observed climatological HCl decrease. The observed average HCl recovery from September to October is not followed quite as steeply in the models, although in some cases (*e.g.*, UMSLIMCAT), this recovery tends to happen faster and earlier than the MLS data suggest. Based on these average results, we might expect that chemical ozone loss arising from chlorine activation in the Antarctic would be fairly well modelled, although the somewhat smaller model activation could lead to an under-

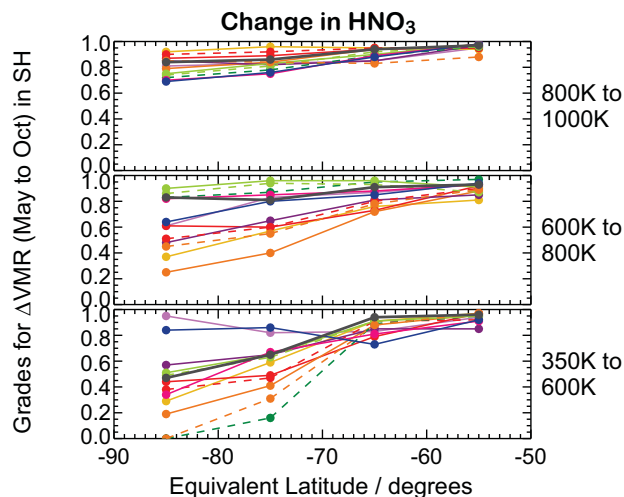


**Figure 6.29:** Grades obtained for 12 CCMs and their multi-model mean (MMM) from a comparison of model versus MLS-derived climatological changes in  $\text{HNO}_3$  (see text and Figure 6.28). Grades are calculated for 4 EqL bins and 3 ranges of  $\theta$  values. Colours and linestyles correspond to those shown in Figure 6.28.

estimation of the net chemical ozone loss (all other factors, *e.g.*, bromine, transport effects, being equal). However, the slightly longer time period for activation (in the CCMs) could, to some extent, counteract the magnitude of the activation itself (in a month when there are more day-time hours for ozone loss as well).

All the model grades discussed in this section are summarized in **Figure 6.33**, as a function of  $\theta$  range and EqL. While the range of model results may be somewhat disconcerting (even with no observations), there are several instances of good to excellent fits *versus* the Aura MLS climatology. However, there is no model that fits the MLS VMR changes best all the time (May to October) and for all EqL bins, or for all species studied here. Also, a well-known factor relating to heterogeneous polar chemistry is the vertical/temporal extent of low temperature regions. We have seen in past work (*e.g.*, comparisons between MLS data and WACCM model values) that significant differences between model and data temperature values can lead to overestimates (or under-estimates) of “denitrification”, “dehydration”, and chlorine activation. However, more detailed studies of such differences for each CCM are beyond the scope of this report. It is hoped that the comparisons and grades given here can lead to some re-examination of the representation of dynamical and chemical processes in many, if not all, the CCMs used in this study, so that improvements in model performances can be obtained in the future.

### 6.3.4.2 Surface area density of PSCs

In this section we show nitric acid trihydrate (NAT) and water-ice (ICE) SAD results from 8 CCMs that submitted T3I output (instantaneous output; 10-day frequency). The aim of this section is to show the magnitude and variability between a small set of CCMs, not to grade their SAD distributions. In fact, currently there are limited observations available to grade the CCM SADs; however, we show these results with the hope of encouraging the observational community to assemble data sets for such comparisons and eventual diagnostic grading.

As in the previous section, the model results were translated from a latitude-pressure grid to a potential temperature ( $\theta$ ) - equivalent latitude (EqL) grid. **Figure 6.34** is one example of the model-derived distribution of SAD NAT and ICE at 480 K and  $77.5^\circ$  EqL. The SADs shown in this figure are the maximum abundance (binned per month) over a 15-year period (1990-2004). In addition, when the SADs were binned to the EqL- $\theta$  grid, only values of NAT and ICE SADs that were  $\sim 1.0 \times 10^{-10} \text{ cm}^2 \text{ cm}^{-3} (\text{cm}^{-1})$  were used in the transformation from pressure-latitude to  $\theta$ -EqL. The goal here was to examine SAD magnitudes where PSCs were present for a given EqL- $\theta$  condition. If there were no PSC particles present in the given EqL- $\theta$  bin, the SADs were set to zero. In Figure 6.34, the model results were divided into two groups: 1) with a maximum NAT SAD  $< 10 \times 10^{-9} \text{ cm}^{-1}$  (panel a); 2) with NAT SAD between  $\sim 10$ - $50 \times 10^{-9} \text{ cm}^{-1}$  (panel b). Out of the eight CCMs, three of the models have maximum NAT SAD distributions that strongly peak in June (CAM3.5, LMDZrepro, and WACCM); with three models showing a broad peak that is nearly constant in June, July, and August (ULAQ, NiwaSOCOL, SOCOL); and one model shows a broad peak between June and July (CCSRNIES). The NAT SAD from CNRM-ACM is similar in magnitude between June and September. In the previous section, the CAM3.5 and WACCM models do a nice job of representing the evolution of gas-phase  $\text{HNO}_3$  poleward of  $70^\circ\text{S}$  for June through August relative to observations of  $\text{HNO}_3$  from Aura MLS (Figure 6.28). Because these models show substantial denitrification from June through August, the subsequent NAT SAD also decreases rapidly over this period. CCSRNIES, ULAQ, NiwaSOCOL, SOCOL, and LMDZrepro all tend to overestimate the  $\text{HNO}_3$  abundance in June relative to Aura MLS; again consistent with NAT SAD peaking in July and August for these models. The CNRM-ACM did not submit gas-phase  $\text{HNO}_3$  to CCMVal and therefore was not evaluated in the previous section. However, examination of the total  $\text{HNO}_3$  (gas-phase plus condensed phase) for this model showed little irreversible denitrification. This result is consistent with this model having the largest SAD. A large SAD implies smaller particles and therefore less sedimentation (see discussion below).

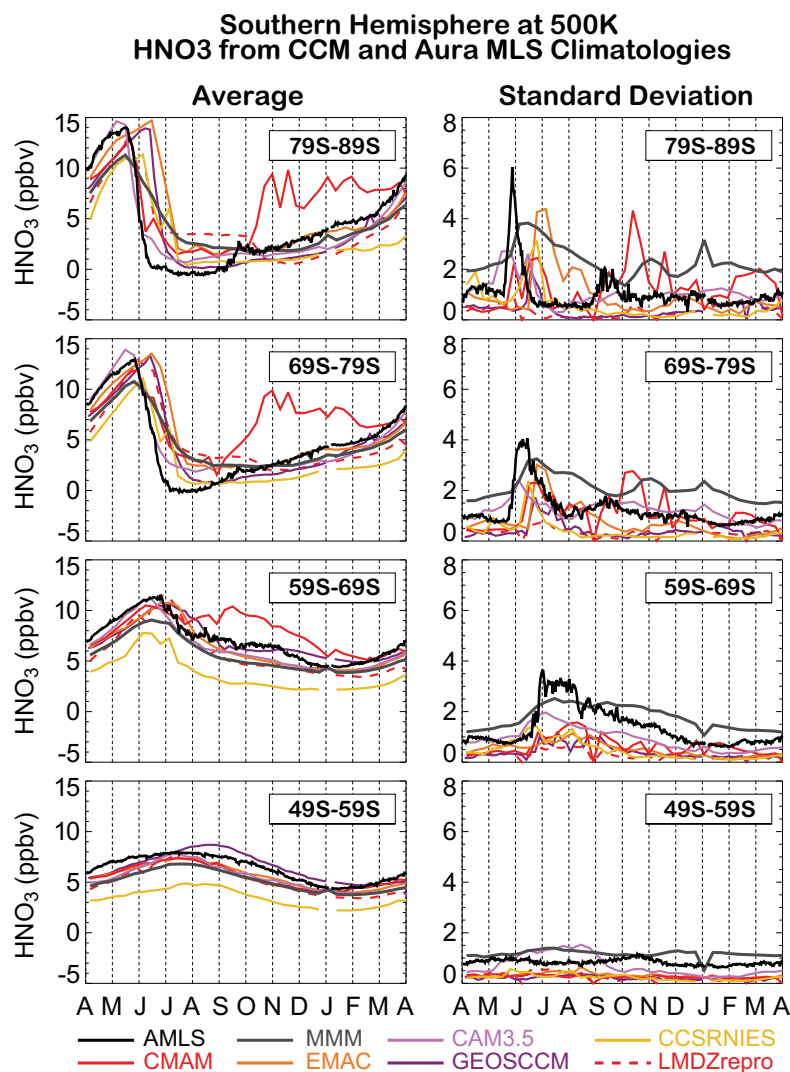


**Figure 6.30a:** Left panels display variations in average HNO<sub>3</sub> at 500 K during the course of a year in 4 EqL bins, based on climatologies from Aura MLS (black, solid lines) and 6 CCMs and their multi-model mean (with model sources shown in bottom legend). Right panels show the corresponding rms variability over the 5-year climatology, for each sampled day of year.

The large variability in the magnitude of SAD NAT between the CCMs is most likely due to assumptions made on the number of particles per cm<sup>3</sup>. For example, the WACCM model assumes 0.01 particles per cm<sup>3</sup> and the maximum NAT SAD is shown to be  $\sim 3 \times 10^{-9}$  cm<sup>-1</sup> (not shown) - with a maximum over this period of approximately  $\sim 8\text{--}10 \times 10^{-9}$  cm<sup>-1</sup>. In **Table 6.5**, examples are shown of what the idealized NAT SAD (and radius) would be under different assumptions of HNO<sub>3</sub> abundance and NAT number density. As expected, the WACCM NAT SAD is consistent with those shown in **Table 6.5** for particle densities between 0.01-0.001 particles cm<sup>-3</sup>. In **Figure 6.34**, the SOCOL and NiwaSOCOL models derive one of the smallest mean NAT SAD abundances. These two models use an equilibrium NAT approach that does not fix the number of particles per cm<sup>3</sup>, instead, the mean radius is fixed (at 5 m). Therefore,

according to **Table 6.5**, the NAT SAD should be  $\sim 1\text{--}2 \times 10^{-9}$  cm<sup>-1</sup>. This is again consistent with the magnitude of NAT SAD that is derived by the SOCOL and NiwaSOCOL models. For the models shown in panel b), *i.e.*, the CNRM-ACM and LMDZrepro models, the maximum NAT SADs is in the range  $10\text{--}40 \times 10^{-9}$  cm<sup>-1</sup>, which would imply a much larger particle number density ( $\sim 1$  cm<sup>-3</sup>) and smaller particle radius. A smaller NAT radius would therefore give less irreversible denitrification.

The ICE SAD is shown in the bottom row of **Figure 6.34**. Here, as in the NAT SAD comparisons, the models are grouped into two ranges: 1) where the maximum ICE SAD is  $< 50 \times 10^{-9}$  cm<sup>-1</sup> (panel c); 2) with ICE SAD between  $\sim 50\text{--}250 \times 10^{-9}$  cm<sup>-1</sup> (panel d). For this PSC type, one model has a maximum ICE SAD distribution that peaks in June (WACCM); six models peak in July (CAM3.5, CNRM-



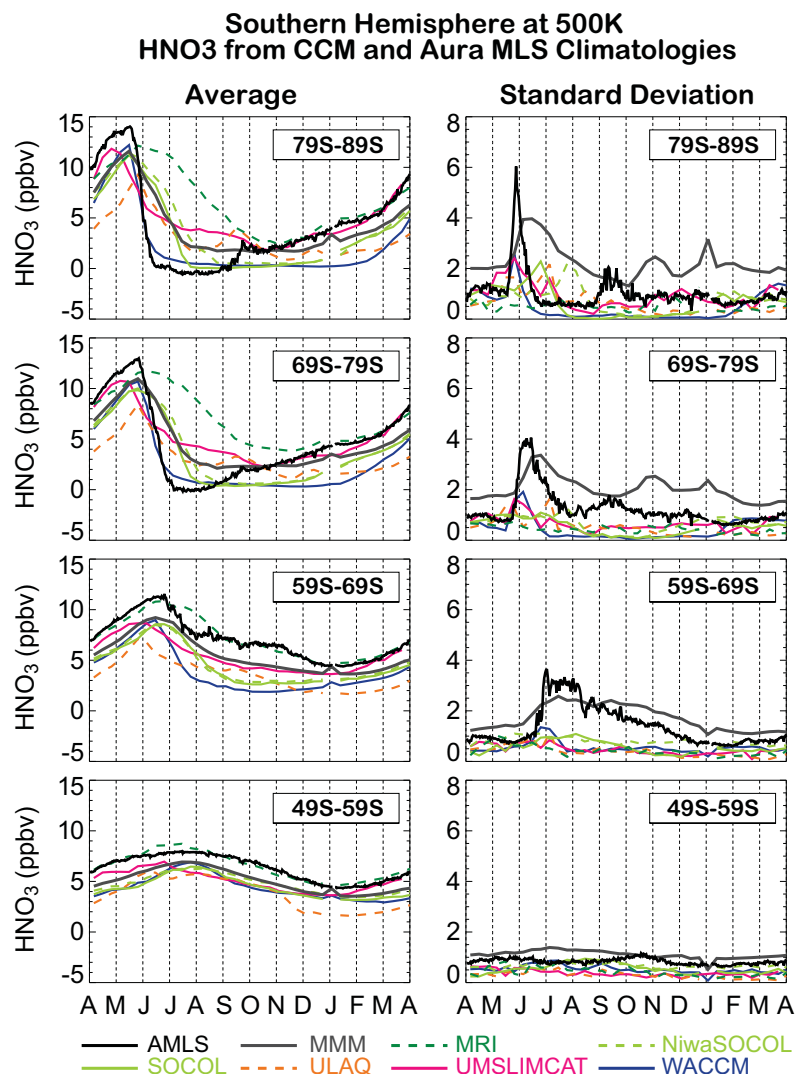


**Figure 6.30b:** Same as Figure 6.30a, but for Aura MLS HNO<sub>3</sub> (and its rms variability) compared to the 6 other available CCM distributions of HNO<sub>3</sub> versus time of year.

ACM, LMDZrepro, NiwaSOCOL, SOCOL, ULAQ), and one model peaks in August (CCSRNIES). Similar to the NAT discussion above, the range in ICE SAD magnitude can be attributed to assumptions regarding particle density. For example, it is known that the particle density is 0.001 and 0.1 cm<sup>-3</sup> for the WACCM and SOCOL models, respectively. Therefore, it is not surprising that there is over a factor of six difference in the derived ICE SAD between these models. These derived SADs are also consistent with the idealized ICE SAD as listed in Table 6.5.

In summary, more work is needed to evaluate NAT and ICE aerosols. In addition to evaluating the SAD, the radius, and size distribution of these aerosols should be examined. Comparison to observations is clearly needed; currently there are not any global data sets available that can be used to evaluate these constituents. In addition, future CCM aerosol evaluations should examine the model distributions and reactivity of sulfate aerosols. In CCMVal-2, the

sulfate SAD fields are prescribed, but modelling groups are beginning to couple microphysical models to their CCMs; these types of couplings will allow scientist to examine the future aerosol loading based on assumptions of the evolution of tropospheric sulfate species.

#### 6.3.4.3 Chemical ozone depletion in the polar vortices

Heterogeneous processes in the polar lower stratosphere initiate large chemical ozone depletion during late winter and spring in the Antarctic and during cold winters in the Arctic. Within the isolated polar vortex, very cold temperatures result in the formation of polar stratospheric clouds (PSCs). Heterogeneous reactions that convert halogen reservoir species to more active forms occur on the surfaces of PSCs, *e.g.*, nitric acid trihydrate (NAT) particles (Hansen and Mauersberger, 1988), water-ice particles,

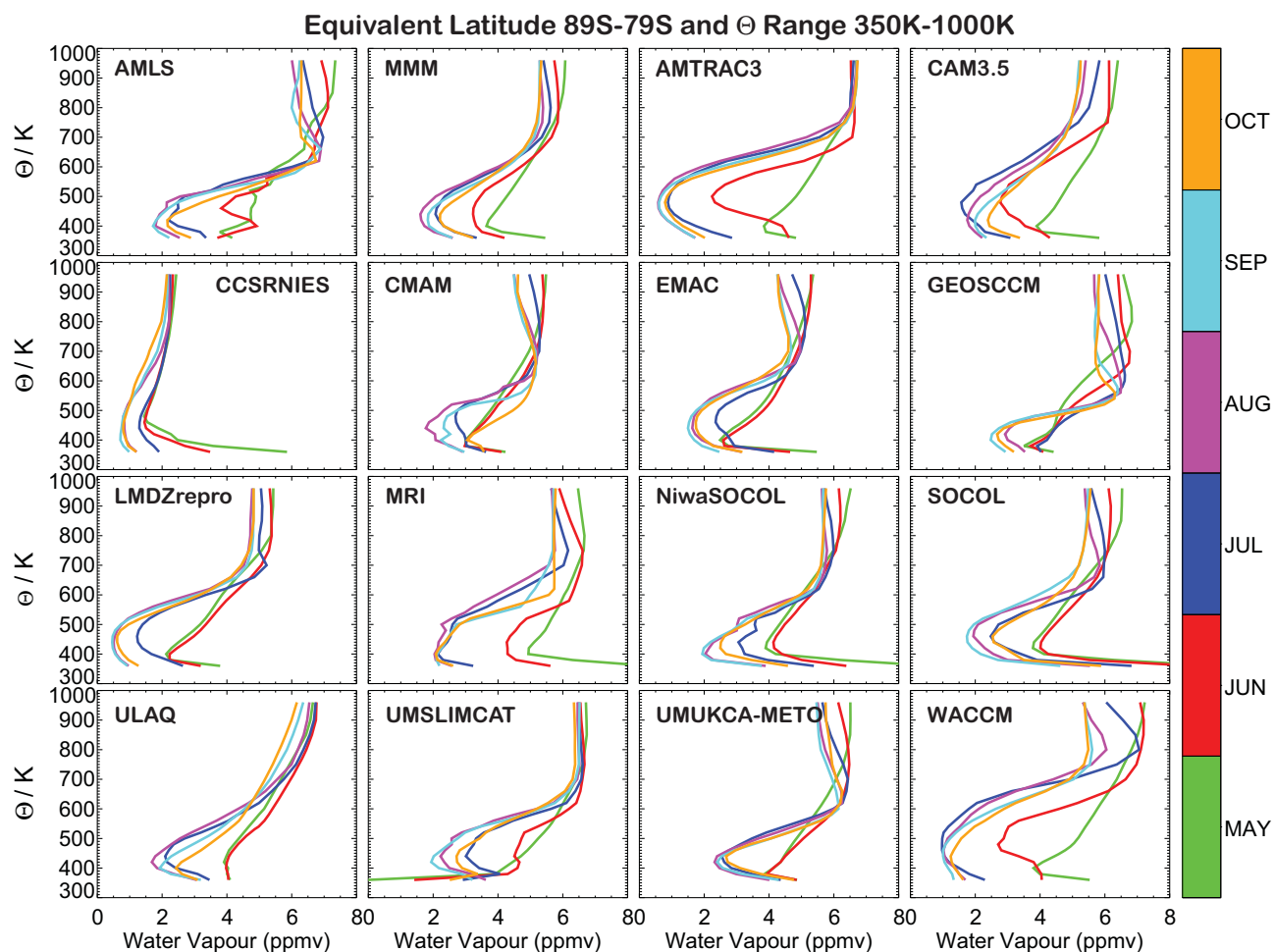


**Figure 6.31:** Climatological profiles of  $\text{H}_2\text{O}$  from mid-May through mid-October for Aura MLS, 14 CCMs, and the multi-model mean.

as well as on liquid sulfate aerosols (*e.g.*, Solomon *et al.*, 1986; Peter 1997). During late winter/spring, the increasing solar illumination of the vortex region increases the photolysis rate of the ClO dimer, enhancing ozone depletion (*e.g.*, Solomon, 1999). This process continues until the vortex temperatures warm past the threshold of PSC formation and/or there is a major stratospheric warming.

### TRAC Method

The extent of chemical ozone depletion occurring in the polar vortex during the polar winter and spring depends strongly on: 1) The dynamical conditions in the polar vortex, 2) temperature, 3) the degree of isolation of the vortex, and 4) the duration of chlorine activation. In addition, the abundance of inorganic halogens in the polar stratosphere is also important for determining ozone depletion within the vortex (*e.g.*, Newman *et al.*, 2007). Other important factors that influence chemical ozone depletion include the extent of denitrification and dehydration by sedimentation of PSC particles.

The diagnosis of chemical ozone depletion in the polar regions is not straightforward. Decreasing ozone mixing ratios in spring, as a result of chemical depletion are often masked by the descent of ozone-rich air at high latitudes, especially in the NH. The tracer-tracer correlation method (TRAC) was developed to quantify chemical ozone depletion in absence of transport processes within an isolated polar vortex (*e.g.*, Proffitt *et al.*, 1993; Müller *et al.*, 1997; Tilmes *et al.*, 2004). This method has the advantage in that it does not rely on any additional model simulations to quantify the passive ozone (*i.e.*, ozone in the absence of chemical loss), which can lead to uncertainties as a result of the simulated transport. The vortex average depth of chemical depletion in column ozone between 350 K - 550 K potential temperature was derived for the period between early winter and spring. For this purpose, we used satellite observations from the HALOE/UARS, ILAS/ADEOS, and ILAS-2/ADEOS-2 instruments, combined with balloon and aircraft observations (Tilmes *et al.*, 2006). The edge of the polar vortex was defined using the criterion of Nash *et al.* (1996). The results derived using the tracer-

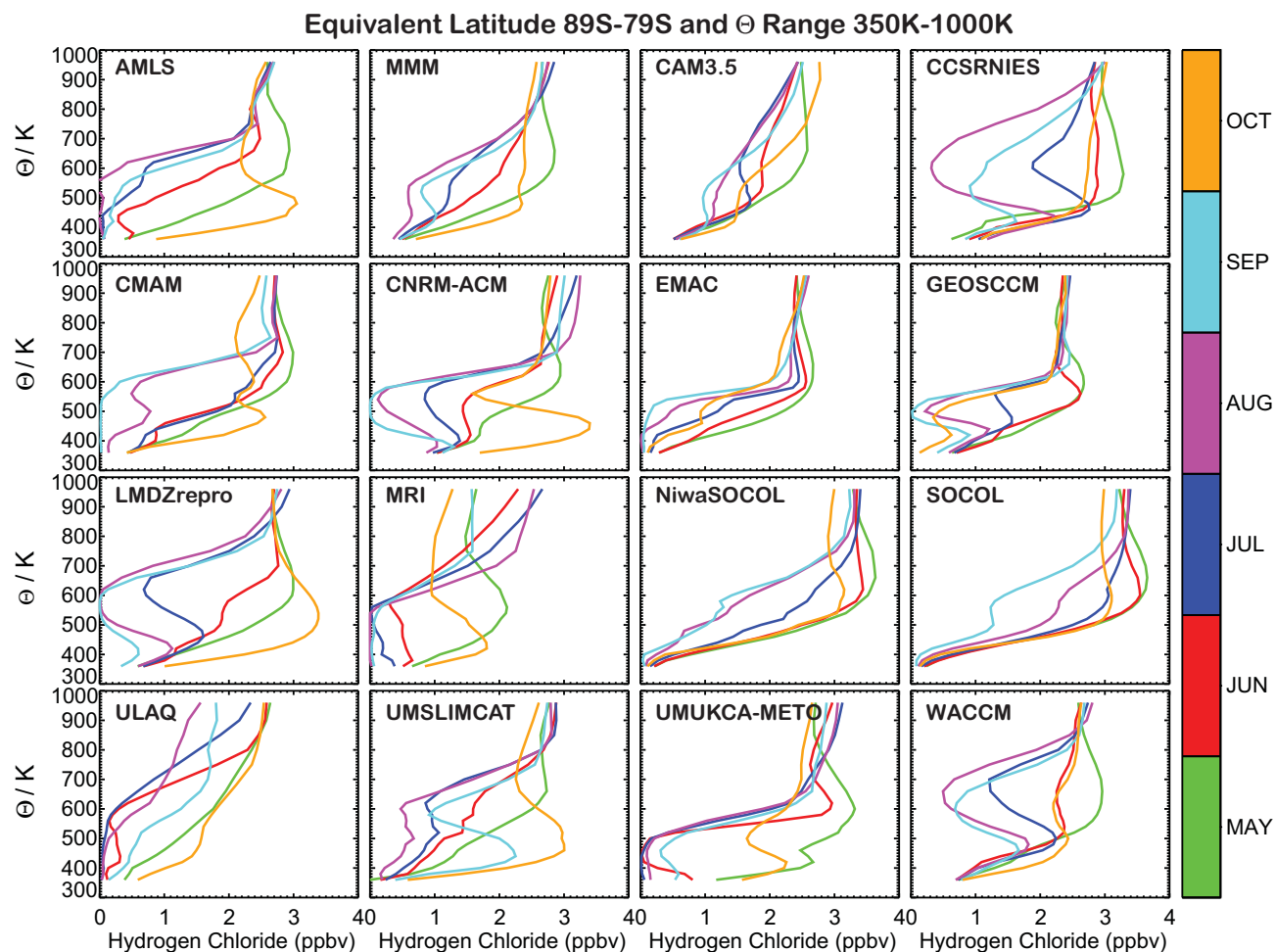


**Figure 6.32:** Climatological profiles of HCl from mid-May through mid-October for Aura MLS, 14 CCMs, and the multi-model mean.

tracer correlation method (TRAC) are in good agreement with results from other established methods (Tilmes *et al.*, 2004; WMO, 2007). There are clearly uncertainties in all ozone depletion approaches, however, the TRAC method has been shown to result in an under-estimation of chemical ozone depletion rather than in overestimation in cases of a less isolated polar vortex, as summarized in Müller *et al.* (2005, 2008).

### Potential for Activation of Chlorine

Chemical ozone loss depends on temperature conditions in the vortex. However, the averaged vortex temperature is not linearly related to chemical ozone depletion. For example, very cold temperatures in a very small area of the vortex can result in very different amount of ozone depletion than homogeneously distributed moderately cold temperatures over the entire vortex. In addition, the temperature evolution during winter and spring is an important factor. A temperature-based measure was developed that describes the fraction of the vortex where temperatures

are low enough to allow the activation of chlorine during winter and spring. This measure is called the potential for chlorine activation (PACI) and details can be found in Tilmes *et al.* (2008). PACI is a measure that quantifies to what amount meteorological conditions allow chlorine to be activated, and therefore ozone depletion to occur. This measure however does not necessarily imply that the model vortex size and temperature distribution are simulated correctly.

$PACI_{met}$  is defined as:  $V_{ACI}/V_{vortex}$ , where the  $V_{vortex}$  is the volume of the vortex derived using the Nash criterion and  $V_{ACI}$  is volume of the vortex where the temperature is below a threshold temperature for chlorine activation. This threshold temperature is calculated based on pressure, altitude, surface area densities of liquid sulfate aerosol, and water vapour abundance (Tilmes *et al.*, 2007). If the SAD of liquid sulfate aerosols is not available for the given CCM, we use the SAD climatology as specified for the REF-B1 scenario. PACI is averaged over a given potential temperature range and the period considered. This measure allows the comparison of polar vortices with vary-

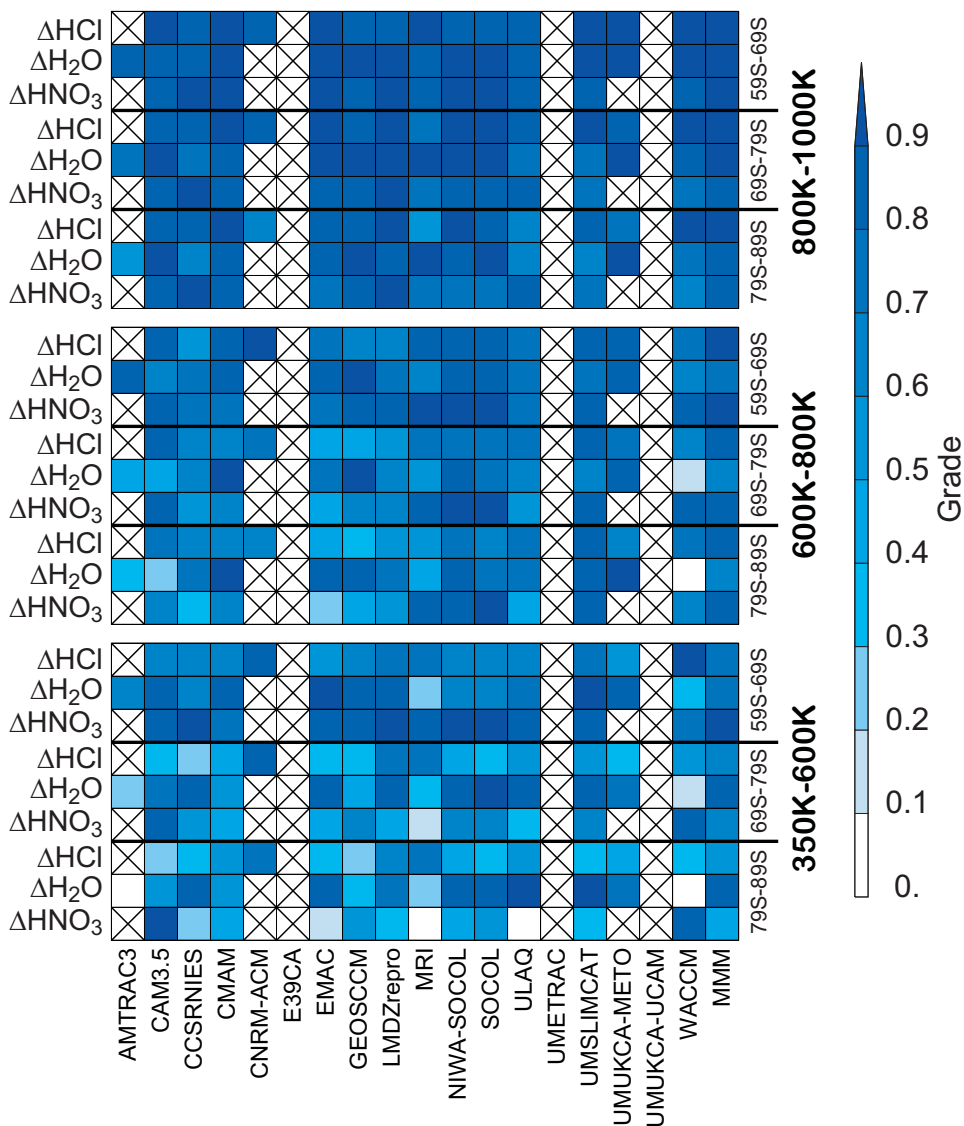


**Figure 6.33:** Summary of grades (shown previously in this section) relating to SH changes in  $\text{HNO}_3$ ,  $\text{H}_2\text{O}$ , and  $\text{HCl}$  (from May to October) for 3 EqL bins (centred at  $85^\circ\text{S}$ ,  $75^\circ\text{S}$ , and  $65^\circ\text{S}$ ). Each plot refers to a different  $\theta$  range (see legend at bottom).

ing vortex volume, for example the Arctic and Antarctic. It is also useful to evaluate the polar chemistry of various CCMs with varying vortex volumes in both hemispheres, even though models might not reproduce the size of the polar vortex correctly.

A linear relation between Arctic chemical ozone loss and PACI was established based on observations between 1991 and 2005 for a period with maximum stratospheric halogen loading. To consider varying halogen loading in the stratosphere (e.g., Newman *et al.*, 2006), the  $\text{PACI}_{\text{net}}$  value is extended to a measure that includes the impact of changing EESC. Therefore,  $\text{PACI} = \text{PACI}_{\text{net}} \times \text{EESC}_n$ , where  $\text{EESC}_n$  is the normalised EESC for year  $n$  (assuming an age-of-air of 5.5 years). A linear relationship between

ozone loss and PACI can then be derived for the SH as well, and can be used to summarize the performance of different CCMs (Tilmes *et al.*, 2007). To evaluate the representation of heterogeneous processes in CCMs, the dynamical and chemical conditions for chemical ozone depletion will be compared with available observations. In particular, we consider the ability of the models to reproduce the potential of chlorine activation that is necessary to match observed chemical polar ozone loss.

*Evaluation of CCM PACI and Chemical Ozone Loss*

The performance of the models is again graded by deriving  $g$  values, following Equation (6.1). Here,  $\mu$  is the

**Table 6.5:** NAT and ICE particle properties derived for different assumptions of the particle number density and precursor molecule abundances. For NAT particles the radius and SAD are derived for 1 and 5 ppbv  $\text{HNO}_3$  (left and right numbers in the radius and SAD columns). For ICE particles the radius and SAD are derived for 1 and 3 ppmv  $\text{H}_2\text{O}$  (left and right numbers in the radius and SAD columns). The SAD was derived assuming spherical particles. These conditions are only valid inside NAT and ICE clouds. Both particle properties were derived at 30 hPa and 190 K (Thomas Peter and Beiping Luo, personal communication, 2009).

SAD Type	Number Density ( $\text{cm}^{-3}$ )	Radius ( $\mu\text{m}$ )	Surface Area Density ( $\times 10^{-9} \text{cm}^2 \text{cm}^{-3}$ )
<b>NAT</b>			
	10	0.15 / 0.26	28 / 83
	1	0.32 / 0.55	13 / 38
	0.1	0.70 / 1.2	6.1 / 18
	0.001	3.2 / 5.5	1.3 / 3.8
	0.0001	7.0 / 12	0.6 / 1.8
<b>ICE</b>			
	10	0.96 / 1.4	1200 / 2480
	1	2.1 / 3.0	540 / 1120
	0.1	4.5 / 6.5	250 / 520
	0.01	9.6 / 14	120 / 250

mean value of ozone loss or PACI over the years between 1990 and 2005. Furthermore, instead of using the standard deviation  $\sigma$  of the observations, we use the mean error of the ozone loss in particular years. This is because the standard deviation of the considered distributions in the Arctic

is of the same magnitude as the observed values; for the Antarctic,  $\sigma$  is much smaller than the uncertainty of the measurements. We use a value 3 for  $n_g$ .

The following grade ( $g$ ) values for Arctic and Antarctic conditions are employed here:

- $g_{\text{pac1}}$  the grading of the models to reproduce conditions for chlorine activation.
- $g_{\text{O}_3}$  the grading of the models to describe chemical polar ozone depletion.

Both these grades together allow the quantification of the ability of models to reproduce chemical ozone depletion and chlorine activation with regard to observations and, therefore, the ability to reproduce observed chemical ozone depletion as a result of a reasonable representation of meteorological conditions in the polar vortex.

A good grade in PACI does not necessarily lead to a good grade in ozone depletion and *vice versa*. The ability of a model to reproduce the observed chemical ozone depletion is not independent of the simulated volume of the vortex, nor the isolation of the vortex. A smaller vortex will in general lead to less ozone depletion than a larger vortex, since in spring the sun reaches the cold vortex area at a later time. In addition, the location of the vortex relative to the pole is important. Therefore, it is important to evaluate the vortex volume if diagnostics such as ozone hole area are considered. Further, if the polar vortex is not well isolated, the TRAC method will result in an under-estimation of chemical ozone depletion. However, this problem is reduced here by considering only ozone loss in the vortex core (as described in the next section).

For this analysis we use results from the REF-B1 simulations to evaluate the evolution of chemical ozone

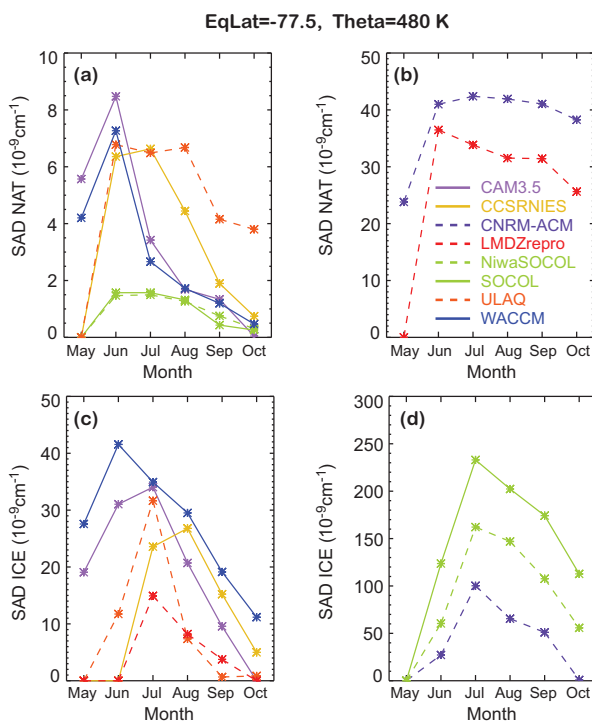


**Figure 6.34:** Comparison of model maximum surfaces area density (SAD) for (a, b) NAT (top row) and (c, d) ICE (bottom row). See text for details on binning procedure.

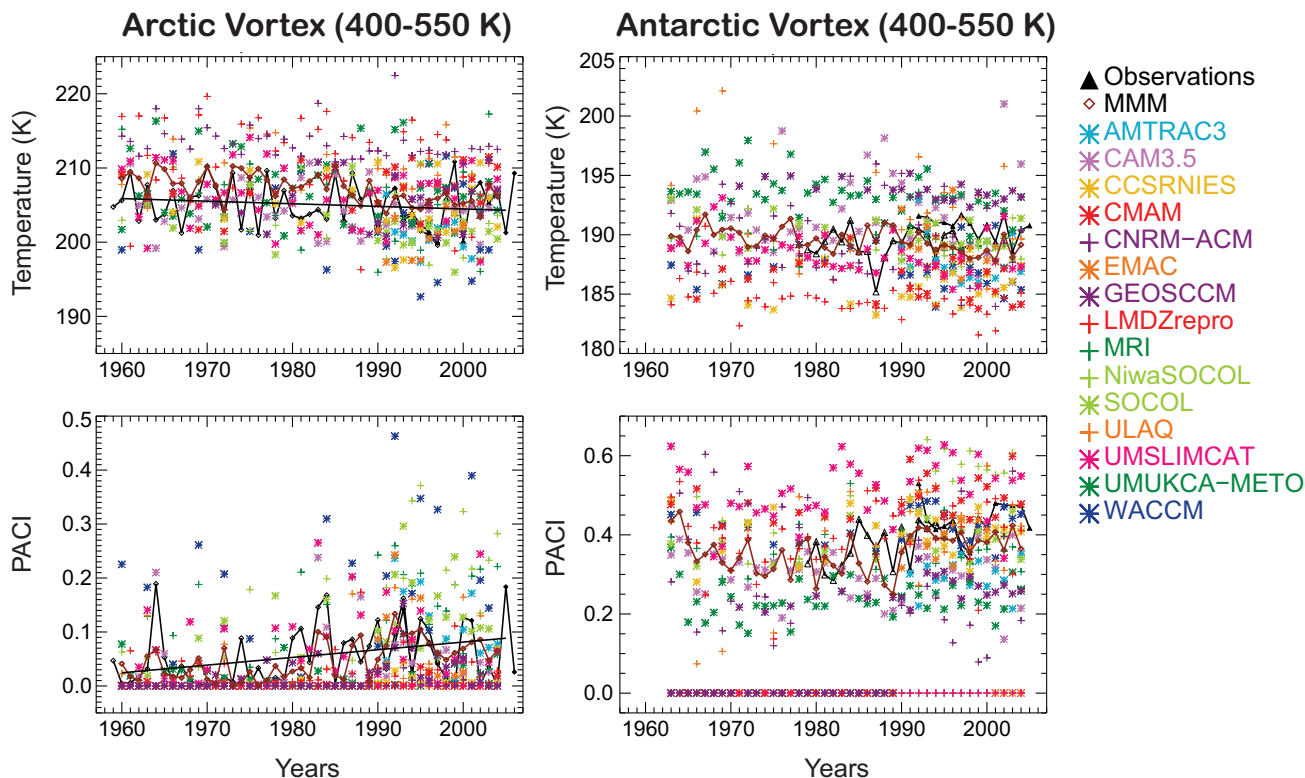


**Figure 6.35:** Vortex average temperatures (top), and PACI (bottom) from January through March for the Arctic (left) and from July through September for the Antarctic (right) and between 440-550K. Values derived from meteorological analyses (UK Met Office between 1991-2005 and ERA-40 1958-1999) are shown in black. The multi-model mean is shown in brown. Model results are shown in different symbols and colours.

depletion with changing atmospheric halogen content between 1960 and 2005. The period between 1990 and 2005, for which sufficient observational information is available, will be graded. We use T3I output for this diagnostic and all model results are transformed to EqLat/ $\theta$  surfaces.

#### 6.3.4.4.1 Meteorological conditions in the polar vortex

##### *Vortex Temperatures*

Average vortex temperatures for a period between January through March (Arctic) and July through September (Antarctic) were derived between 1960 and 2005 and we use the criterion derived by Nash *et al.* (1996) to identify the edge of the polar vortex. **Figure 6.35** (top panel) compares Arctic and Antarctic temperatures for models and observations. For the Arctic, the majority of models are able to simulate Arctic temperatures in the range of ERA-40 and UK Met Office analyses. In general, models do follow the observed decreasing trend in temperatures between 1960 and 2005. A few models scatter well above or below the observed range. The models that

simulate warmer temperatures than the observations are not expected to simulate significant chemical ozone depletion in the Arctic polar vortex; the required threshold temperature where chlorine activation and therefore ozone depletion can be expected will likely not be reached. For the Antarctic, models show a larger spread in polar vortex temperatures than for the Arctic.

##### *Meteorological Potential for chlorine activation*

$PACI_{met}$  was derived between 1960 and 2005 (Arctic) and 1979 and 2005 (Antarctic) for a period between January through March (Arctic) and July through September (Antarctic). Different meteorological analyses (ERA-40 and UK Met Office, Figure 6.35, bottom panel) result in an uncertainty of observed  $PACI_{met}$  values of  $\sim 10\%$  for the Antarctic and  $\sim 20\%$  for the Arctic. We apply the grading (Equation 6.1) to both, the mean values of the  $PACI_{met}$  distribution ( $g_{pacI_{mean}}$ ) and the standard deviation of the distribution ( $g_{pacI_{std}}$ ) derived from models and observations for the Antarctic and the Arctic between 1990 and 2005. This is then consistent with the period chosen for the grading of ozone loss. Both these values are equally important to quantify the representativeness of the models, because the standard deviation of the distribution is a meas-

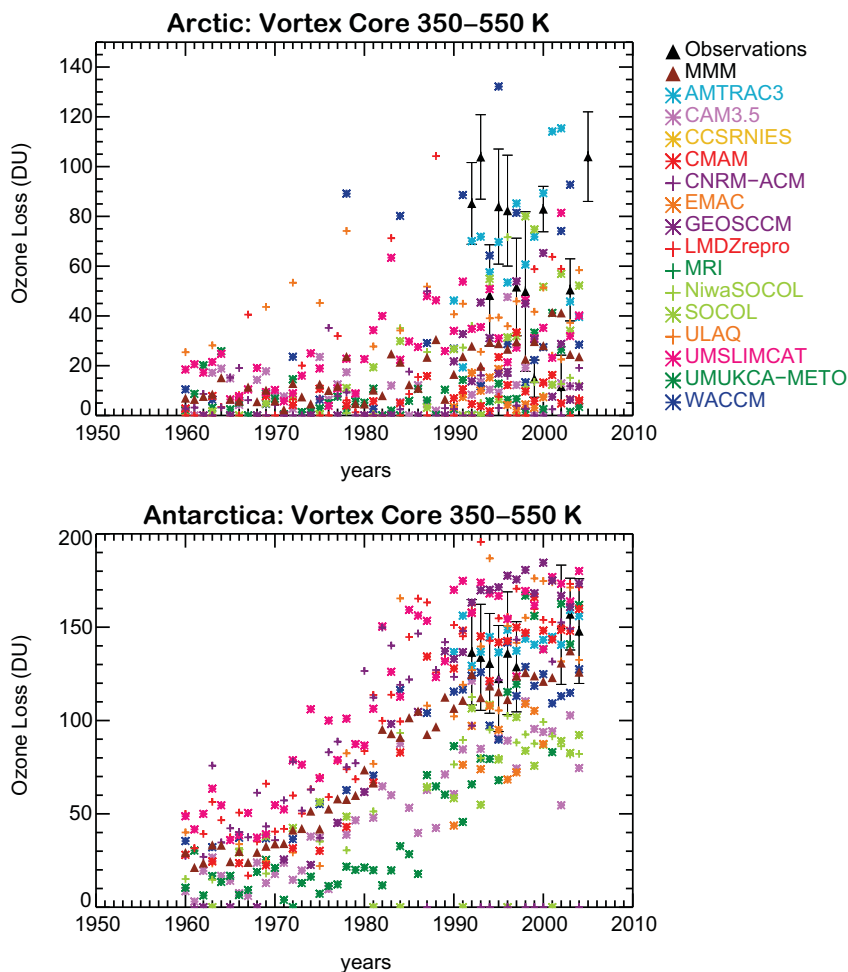


**Figure 6.36:** Chemical ozone depletion in the polar vortex from January through April (top panel) and July through October (bottom panel) between 350–550 K. Results from observations (black triangles) were derived from HALOE/UARS (Tilmes et al., 2006) for the polar vortex core. The multi-model mean (MMM) is shown in brown. Model results are shown in different colours and calculated within EqLat  $> 80^\circ$ .

ure for the interannual variability of  $\text{PACI}_{\text{met}}$ . Both grades are combined to give the overall grading for  $\text{PACI}_{\text{met}}$ :  $g_{\text{pacI}} = (g_{\text{pacI}_{\text{mean}}} + g_{\text{pacI}_{\text{std}}})/2$  (Figure 6.39, first and third columns).

For the Antarctic, only two models (out of 14) show  $g$  values smaller 0.5. Meteorological conditions in most of the models provide the conditions for the occurrence of observed chemical ozone loss (however, as mentioned previously, the temperature distribution and vortex size might still be wrong). In many cases, the standard deviation of the distribution (*i.e.*, the variability) is better represented than the mean values. For the Arctic, about half of the models are able to reproduce PACI values with a grade of 0.5 or better. As for the SH, in general, models reproduce the value of the standard deviation better than the mean values of the distribution.

#### 6.3.4.4.2 Evolution of Chemical Ozone Loss in the Polar Vortex

The tracer-tracer correlation method was applied consistently to the output of all CCMs to derive the depth of chemical ozone depletion in the Arctic between January through April and the Antarctic between July through October as shown in **Figure 6.36**. The impact of potential underestimation of chemical ozone depletion, as a result of a less isolated polar vortex in the models will be especially strong at the vortex edge. This impact is reduced by considering the area of the vortex within EqLat  $> 80^\circ$ , *i.e.*, within the vortex core. In case of very diffusive models, a strong underestimation of chemical ozone depletion in the polar vortex core points to the inability to reproduce realistic ozone values for that particular CCM. Therefore, the low grades that emerge for excessively diffusive models are appropriate. Possible shortcomings of the models in reproducing the entire polar vortex are not considered here.

All models that are able to simulate chemical ozone loss in the Arctic polar vortex show an increase of ozone depletion in the Arctic between 1960-2005, as expected due to the increasing halogen content in the stratosphere and the increasing PACI as a result of decreasing temperatures with time (Figure 6.36). To evaluate the models with regard to observations, we consider the period between 1991

and 2005. The mean values of chemical ozone loss for this period, as well as the standard deviation of chemical ozone depletion of the model results, are graded compared to observations. As above, we combine the two grades for ozone depletion as follows:  $g_{O_3} = (g_{O_3\_mean} + g_{O_3\_std})/2$  (Figure 6.39, second and fourth columns).

For the Antarctic, most of the models that obtained a

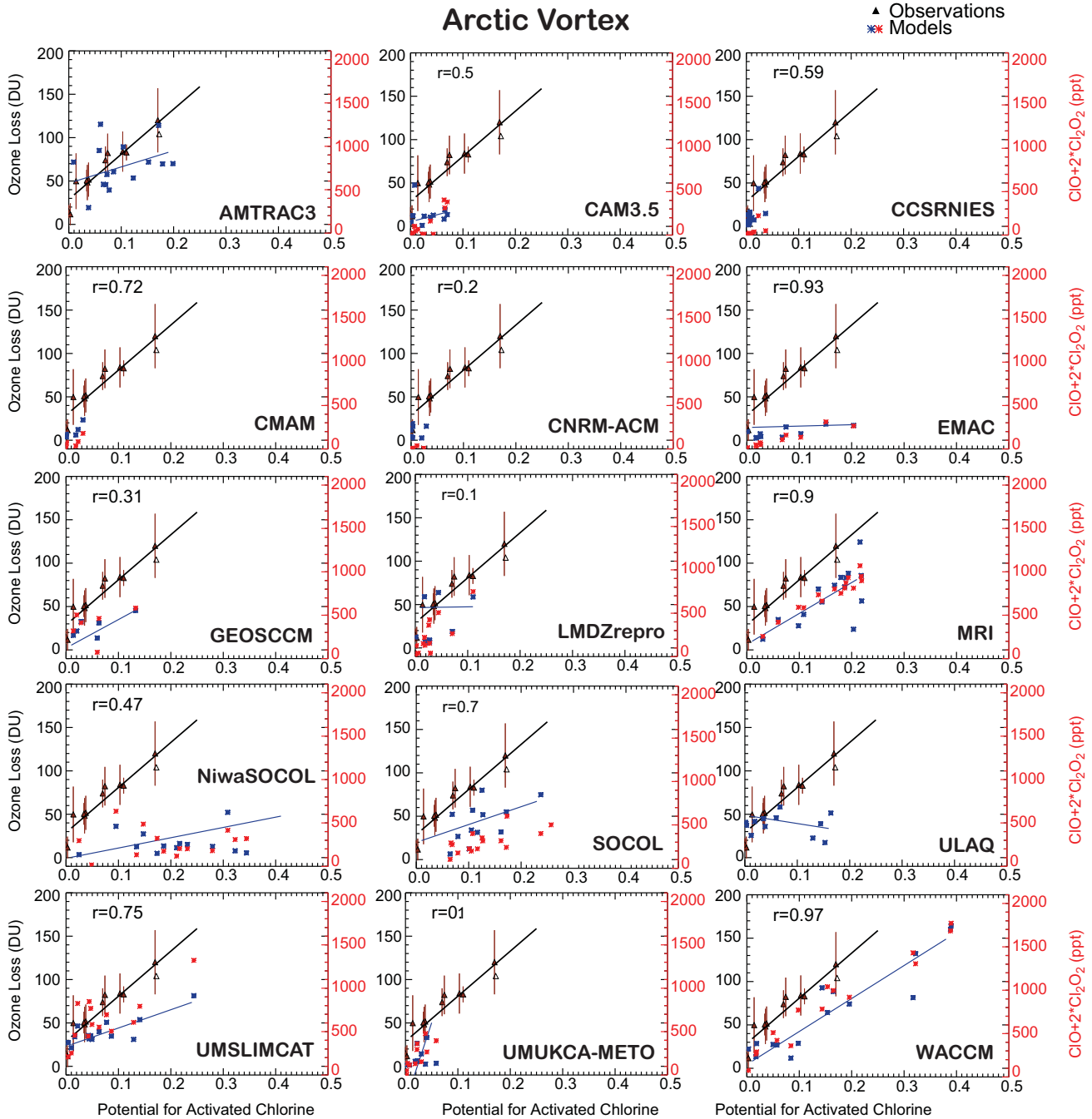


**Figure 6.37:** Relationship between Arctic chemical ozone loss (Figure 6.36) and the potential for activated chlorine (PACI) for the years between 1990 and 2005. Both observations (black triangle) and model results (blue asterisk) are shown. Model  $Cl_x$  ( $ClO + 2Cl_2O_2$ ) versus PACI is also shown (red asterisk). The correlation coefficient ( $r$ ) between model  $Cl_x$  and chemical ozone loss is shown in each panel.



high PACI grading also have a high score for the ozone depletion grading. This outcome of the grading is reassuring in so far as the two diagnostics should be connected. Some models do show differences between the two diagnostics. These differences are discussed in the next section. For the Arctic, the grade of the PACI and ozone depletion in the

models often varies widely. This points to the uncertainty of models in reproducing Arctic chemical ozone depletion as a result of reasonably reproduced meteorological conditions. Less than half the models reach grades of  $g_{O_3}$  above 0.5. Only, two models reach grades above 0.8.

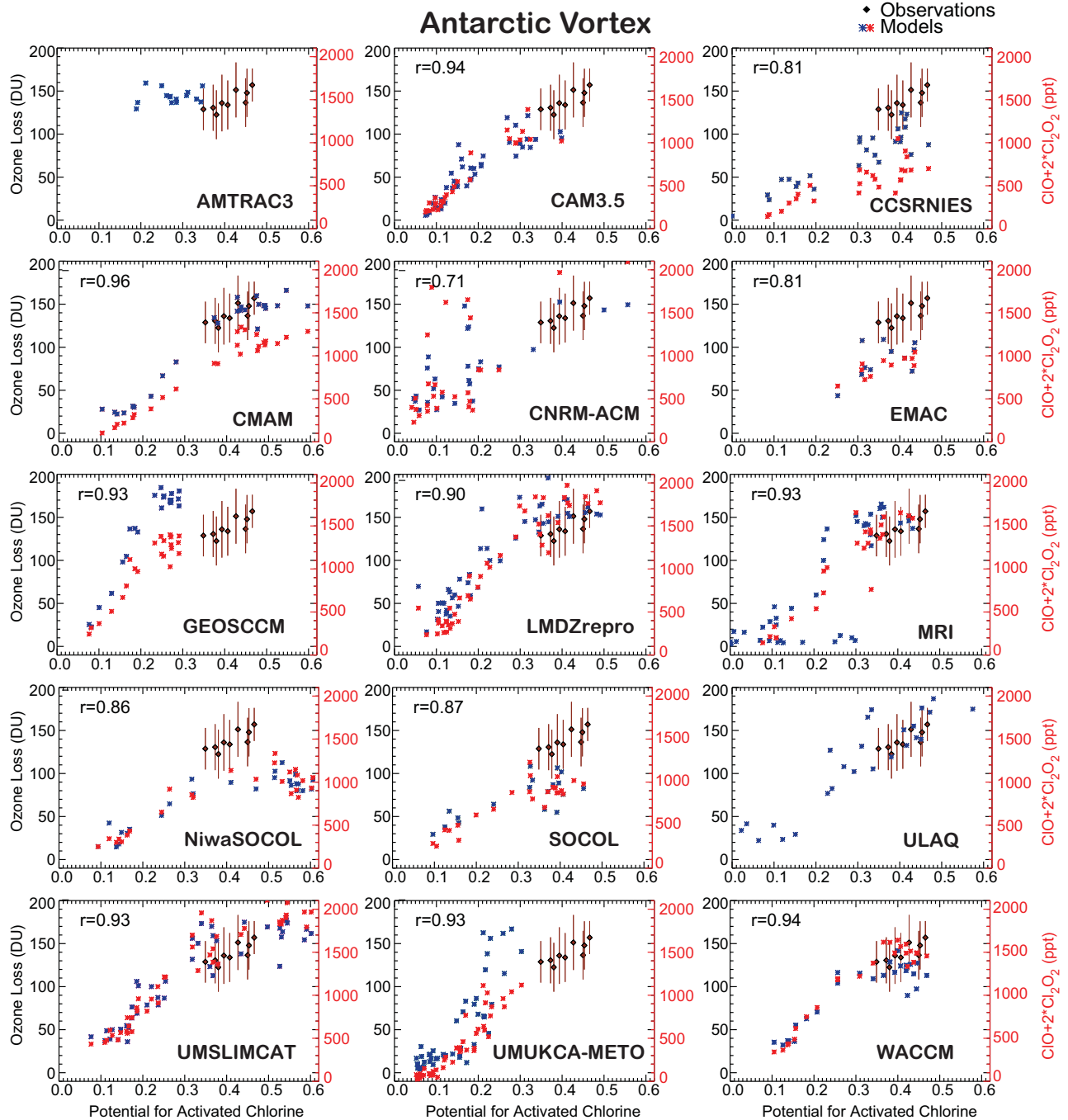


**Figure 6.38:** Relationship between Antarctic chemical ozone loss (Figure 6.36) and the potential for activated chlorine (PACI) for the years between 1960 and 2005 (blue asterisk). Model  $Cl_x$  ( $ClO + 2Cl_2O_2$ ) versus PACI for the same period is also shown (red asterisk). The observed chemical ozone loss versus PACI are between 1990 and 2005 (black triangle). The correlation coefficient ( $r$ ) between model  $Cl_x$  and chemical ozone loss is shown in each panel.

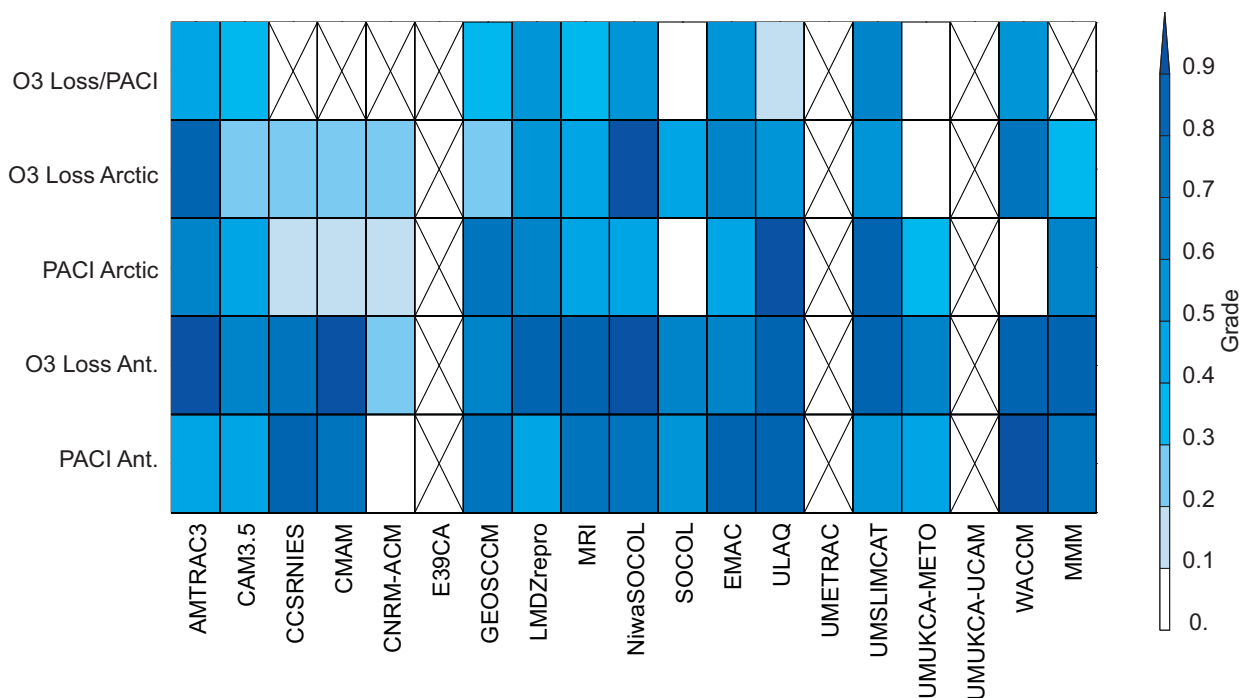


**Figure 6.39:** Summary of grades, as discussed in the text. Crosses indicate those models that could not be evaluated for a specific grade. O<sub>3</sub>/PACI grading was performed for only those models with at least 2 values larger than 0.03.

#### 6.3.4.4.3. Polar Chemical Ozone Depletion vs. PACI and Cl<sub>x</sub>

The relationship between ozone loss and PACI summarizes the performance of the model with regard to heterogeneous processes and chemical ozone depletion (Figures 6.37 and 6.38). In addition we show simulated Cl<sub>x</sub> (= ClO + 2Cl<sub>2</sub>O<sub>2</sub>) averaged over the entire vortex between 400 K - 550 K (if the model output is available). There are no Cl<sub>x</sub> observations available for various years in the polar vortex to evaluate the models. Nevertheless, the amount of Cl<sub>x</sub> in the models provides further information to what degree PACI and Cl<sub>x</sub> are related in each model, since PACI is based on meteorological conditions and not on the actual simulated chlorine loading. Most models describe a tight relationship between Cl<sub>x</sub> and PACI. The different slopes of the relationship between ozone loss and PACI and ozone loss and Cl<sub>x</sub> are a result of different sensitivity of Cl<sub>x</sub> to PACI in the models. In Figures 6.37 (Arctic) and 6.38 (Antarctic) we present a model-to-model inter-comparison of these relationships between Cl<sub>x</sub> and PACI. For the Arctic, available observations allow the evaluation of the polar chemistry in comparing the slope of the relationship between chemical ozone depletion and the PACI. If a model reproduces the slope of this relationship, the meteorology in the model results in appropriate ozone depletion. Therefore, models which show either too much chlorine activation, or too little (to a certain degree if at

least two years show PACI values are larger than 0.03) can be still tested for the quality of their chemical mechanism. The uncertainty of the slope of this relationship cannot be estimated precisely, so the outcome of the grading is a matter of the choice of the uncertainty and is therefore rather unreliable. Here we chose an error for the observed slope of 33% to grade the models (Figure 6.39, fifth column). The graded slope of the model includes the y-axis intercept, as well as the ratio between ozone loss and PACI. Qualitatively, the slope of the relationship between ozone loss and PACI is well reproduced in some models. For example, for WACCM, the PACI values are not graded high, although a reasonable slope shows that the mechanism for chemical ozone loss is reliable even though the meteorology might not allow the observed amount of ozone depletion. For most of the models PACI and Cl<sub>x</sub> values correlate well. UMSLIMCAT shows slightly higher Cl<sub>x</sub> values and SOCOL slightly lower values with respect to PACI than other models.

For the Antarctic, the slope between ozone depletion and PACI cannot be graded, because chemical ozone loss in the period where observations are available is saturated and no significant change in ozone loss with changing PACI is expected (Tilmes *et al.*, 2006). No significant dependence of ozone loss on PACI values is observed for the years between 1991 and 2005. Most models agree with observed Antarctic ozone loss, although a larger spread exists in the PACI values between the models. Some models show a rather poor representation of PACI with grades be-

low 0.5, although chemical ozone depletion is well within the range of the observations. These models indicate too little chlorine activation. On the other hand, models such as UMSLIMCAT, CMAM and NiwaSOCOL have a larger potential of chlorine activation than observed. Since Antarctic ozone loss is saturated in these models, ozone loss values do not exceed the range of observations. As for the Arctic,  $Cl_x$  and PACl are well correlated for most of the models. Some models show a lower sensitivity of  $Cl_x$  for a given PACl value compared other models, like CCSRNIES, CMAM and GEOSCCM. On the other hand UMSLIMCAT shows a slightly higher sensitivity of  $Cl_x$  for a given PACl values. Note, chemical ozone loss was derived between July and mid-October. Continuous ozone depletion during the first weeks of October in the models might result in better agreement with observed ozone depletion, even if chemical ozone loss is delayed during winter/spring in some models.

In this section, only polar chemical ozone loss in the vortex core was evaluated to eliminate the impact on the inhomogeneous distributed ozone depletion in the entire vortex. Derived inhomogeneous ozone loss can be a result of an under-estimation of chemical ozone depletion at the vortex edge, caused by mixing across a too weak polar vortex edge. On the other hand, PACl was evaluated for the entire polar vortex.

## 6.4 Summary

This section gives a summary of the performance of the 18 CCMs, and the multi-model mean, in the comparisons described in Section 6.3. In the following summary, unless stated otherwise, “polar region” is defined as 79°S-89°S EqL and 350 K - 600 K. Note: One needs to be careful in comparing the HCl grades (Section 6.3.4.1) with the PACl grades below. A low grade for PACl does not mean that there was little chlorine activation. One can get a low grade for PACl with too much chlorine activation (see Section 6.3.4.3). In addition, the PACl is grade over the entire vortex, between 400 K - 550 K, where HCl is examined in the “polar region” (as defined above).

### 6.4.1 Summary by model

**Multi-Model Mean:** There are some chemistry diagnostics where the notion of the multi-model mean (MMM) is not useful or where the mean cannot be graded. Our photolysis comparison compared individual model results with a ‘robust’ model mean, rather than observations, and so the model mean already provided the benchmark. The PSS comparison is performed model by model; running the PSS code using the mean of the individual chemical species in the CCM schemes would not have any value given their

different complexity, rate constants *etc.* Chemical schemes (and other CCM modules) are expected to conserve tracer families. Most CCMs exhibit this desirable behaviour while some others do not. For an analysis of this property, any mean which combines ‘correct’ models with ‘incorrect’ models is clearly going to be worse than the ‘correct’ models. The metrics where the MMM could be analysed are the following. For tracer-tracer correlations the MMM, like most of the CCMs, was good. For the reservoir chemistry the MMM scored relatively well; however, no model scored better than the MMM for all species and the MMM avoids any relatively low values. The MMM would also smooth out any errors in the partitioning of families in the individual CCMs. In the polar region, the MMM did a good job of representing the evolution of  $HNO_3$ ,  $H_2O$ , and HCl. Most CCMs accurately represent chemical ozone loss in the Antarctic spring. There are clearly exceptions. Only a few models correctly represent the observed chemical ozone loss in the Arctic. This is reflected in the multi-model mean for this process, where the Antarctic is consistent with observations and the Arctic under-estimates chemical ozone loss.

**AMTRAC:** This model generally had a good performance on the photolysis inter-comparison; however there were exceptions for several important odd-oxygen production and loss Js (*e.g.*,  $J-O_2$  and  $J-Cl_2O_2$ ). This model did a very good job of representing the radical precursors and the radicals in the PSS section, with the exception of the  $Cl_y$  vs.  $N_2O$  relation and the  $ClO/Cl_y$  ratio. Otherwise, it produced excellent tracer-tracer correlations. The model parameterises total chlorine and bromine loadings, so these could not be evaluated. The reservoir chemistry was generally well simulated except for HCl which appeared low. This may be due to a problem with the parameterised halogen loading. AMTRAC did not submit  $HNO_3$  and HCl for the polar studies, so these species could not be evaluated there.  $H_2O$  was included but was not well simulated in the lower polar region (model too low) although the model did better in the 600 K - 800 K range. The model’s polar chemical ozone loss was well simulated in both the Antarctic and Arctic. However, for the Antarctic the chemical ozone loss matched observations at a lower PACl abundance relative to reanalyses. The SAD for the polar ozone loss analysis was not supplied and therefore based on the REF-B1 sulfate time-series. Profiles of SAD provided for the PSS comparisons showed significant differences compared to profiles used by other models, particularly at higher altitudes.

**CAM3.5:** This model did not participate in the photolysis inter-comparison; however, CAM3.5 uses the same LUT approach as WACCM (see comments below). This model did a good job of representing the radical precursors, with

the exception of  $\text{NO}_y$  vs.  $\text{N}_2\text{O}$ . In the PSS comparison the model had a good representation of  $\text{O}_x$ ,  $\text{HO}_x$  and  $\text{BrO}/\text{Br}_y$ , with slightly poorer results for the  $\text{NO}_x/\text{NO}_y$  and  $\text{ClO}/\text{Cl}_y$  ratios. It had good tracer-tracer correlations except for  $\text{NO}_y$  vs.  $\text{N}_2\text{O}$  and  $\text{Br}_y$  vs.  $\text{N}_2\text{O}$ . The reservoir chemistry was generally well simulated except for  $\text{ClONO}_2$  and  $\text{N}_2\text{O}_5$ . CAM3.5 did well in representing  $\text{HNO}_3$  in the polar region although less well in the 600 K - 800 K range (model too low). The model over dehydrates in the 350 K - 800 K region. This model also exhibited problems in the evolution of  $\text{HCl}$  (model too high) in the same high polar latitudes, suggesting it under-estimates chlorine activation. The model under-estimated polar chemical ozone loss in both the Antarctic and Arctic, consistent with too low chlorine activation. The sulfate SAD for the polar ozone loss calculation was supplied.

**CCSRNIES:** This model showed discrepancies (*versus* the multi-model mean) for all photolysis rates examined. The model did well in representing the precursors in the PSS section, with the exception of  $\text{Cl}_y$  in the middle troposphere, and the abundance of total hydrogen *versus*  $\text{N}_2\text{O}$ . This model did well in representing most of the PSS radical diagnostics. This model has very good tracer-tracer correlations except for  $\text{CH}_4$  vs.  $\text{H}_2\text{O}$ . This model had excessive levels of  $\text{Br}_y$  in the troposphere and throughout the stratosphere due to inclusion of  $\text{CHBr}_3$  in boundary conditions. Model levels of  $\text{Cl}_y$  in the troposphere and lowermost stratosphere are quite high. The model has more inorganic chlorine and bromine in the stratosphere than expected based on the prescribed surface source gases. This indicates a lack of conservation in the model. The reservoir chemistry comparisons showed variable results. In particular, the upper stratosphere loading of  $\text{HCl}$  is very large due to the excess chlorine. This model had problems representing polar  $\text{HNO}_3$ . The model showed too much  $\text{HNO}_3$  early in the winter and too little  $\text{HNO}_3$  later in the winter/spring. The PACI analysis was good for the Antarctic but not for the Arctic. The polar chemical ozone loss was underestimated in the Antarctic. Little chemical ozone loss was derived in the Arctic. The sulfate SAD for the polar ozone loss calculation was supplied.

**CMAM:** Did not participate in the photolysis inter-comparison. The model did very well in representing the radical precursors and radicals in the PSS diagnostic. It also has very good tracer-tracer correlations, although values of total hydrogen ( $\text{H}_{\text{tot}}$ ) tend to be lower than observation and most of the other models. The reservoir chemistry species appear to be well represented. It should be noted that this model does not represent the sedimentation of  $\text{HNO}_3$  and  $\text{H}_2\text{O}$  containing particles, but does represent an equilibrium partitioning of these species before they are used in the chemistry solver. This model does well in representing  $\text{HCl}$

in the polar region. The PACI analysis showed good results for the Antarctic but poorer agreement in the Arctic. The polar chemical ozone loss was also very well represented in the Antarctic. Little chemical ozone loss was derived in the Arctic, consistent with PACI in this region. The sulfate SAD for the polar chemical ozone loss was supplied.

**CNRM-ACM:** Did not participate in the photolysis inter-comparison. This model did a very good job in representing the radical precursors in the PSS section, with the exception of  $\text{Cl}_y$  in the troposphere and lowermost stratosphere (model values too high) and  $\text{H}_{\text{tot}}$  (model has higher values than observed and than found in most other models). The model consistently did a very good job of representing radicals. The model has good tracer-tracer correlations and the reservoir chemistry appears to be well represented. The model shows a slight lack of conservation of total chlorine and total bromine in the mid- to upper stratosphere. This model did a good job representing  $\text{H}_2\text{O}$  and  $\text{HCl}$  in the Antarctic polar region. However, the PACI analysis revealed large disagreement for both the Antarctic and Arctic, because of a very large variability in the PACI for the Antarctic and too warm temperatures in the Arctic. Chemical ozone loss was generally low in the Antarctic, even though the evolution of polar evolution  $\text{HCl}$  was adequately represented. Little chemical ozone loss was derived in the Arctic, consistent with PACI in this region. The sulfate SAD for the polar ozone loss calculation was supplied.

**E39CA:** Did not participate in the photolysis inter-comparison, the PSS comparison or the polar studies. The model has good tracer-tracer correlations, although we could not evaluate  $\text{NO}_y$  vs.  $\text{N}_2\text{O}$ . The model appears to have a good representation of chlorine and nitrogen reservoir chemistry. This model does not include an explicit treatment of bromine chemistry, but we were unable to evaluate if and how this affects the performance of the model (*e.g.*, for polar ozone loss).

**EMAC:** This model performed well in the photolysis inter-comparison. The model did a very good job of representing the radical precursors in the PSS section with the exception that the model under-estimated the abundance of  $\text{H}_{\text{tot}}$ . This model also did a good job of representing the radicals in the PSS evaluation. The model simulates good tracer-tracer correlations. The model simulates reservoir chemistry well. The model did not simulate polar  $\text{HNO}_3$  well (model too high early in the winter) although  $\text{H}_2\text{O}$  and  $\text{HCl}$  in the same region were better. The model's PACI analysis was good for both the Antarctic and Arctic. The polar chemical ozone loss was well represented in the Antarctic but slightly less loss in the Arctic. Large PACI values in the Arctic did not lead to apparent chemical ozone loss - this may be due to the vortex edge not being isolated and

resulting in mixing processes adding to the uncertainties in the tracer-tracer correlation method. This would result in an under-estimation of chemical ozone loss. This model under-estimated the chemical ozone loss in the Antarctic. The sulfate SAD was supplied for the polar ozone analysis.

**GEOSCCM:** This model performed very well in the photolysis inter-comparison. The model did a good job of representing precursors and radicals in the PSS evaluation. However, the model overestimated the ClO/Cl<sub>y</sub> ratio in the upper stratosphere and under-estimates the Cl<sub>y</sub> vs. N<sub>2</sub>O relation. The REF-B1 simulation was run using volcanically clean background aerosol loading, rather than the prescribed sulfate SAD climatology. This model produces good tracer-tracer correlations and appears to have a good description of reservoir chemistry. GEOSCCM did a good of representing the polar evolution of HNO<sub>3</sub>, however it tended to overestimate HNO<sub>3</sub> abundances early in winter (June). This model did a very good job of representing H<sub>2</sub>O in the same region. HCl in the polar region was adequately represented, with the exception that the model had too much HCl in the 400 K - 425 K region relative to MLS. Overall, the model's Antarctic chemical ozone loss was consistent with observations. However, in this region, the chemical ozone loss was too large near the end of the winter, likely due to too large of ozone loss during the first half of October. The model did derive some chemical ozone loss in the Arctic, but less than observations would suggest.

**LMDZrepro:** This model performed very well in the photolysis inter-comparison. This model did a good job of representing the radical precursors in the PSS section, with the exceptions of the abundance of H<sub>tot</sub> versus N<sub>2</sub>O (model values low) and the Br<sub>y</sub> versus N<sub>2</sub>O diagnostic, which is due to the inclusion of a very short-lived source of Br<sub>y</sub>. The model did an excellent job of representing the radical partitioning diagnostics in PSS section, although comparisons could not be performed for O(<sup>1</sup>D) and O(<sup>3</sup>P). The model produces good tracer-tracer correlations, except for CH<sub>4</sub> vs. H<sub>2</sub>O which illustrated a problem in modelled H<sub>2</sub>O. The model has a reasonable representation of reservoir chemistry. In the polar region the modelled HNO<sub>3</sub> was too high but H<sub>2</sub>O was more realistic. In this same region the model did a good job representing the evolution of HCl. The PACl analysis gave good results for the Antarctic and Arctic. The modelled polar chemical ozone loss was also very good for both polar regions. The sulfate SAD for the polar chemical ozone loss calculation was supplied.

**MRI:** Did not participate in the photolysis inter-comparison. This model performed well in the radical precursor PSS section, with the exception that there was too much Br<sub>y</sub> present in the troposphere and throughout the stratosphere and too much Cl<sub>y</sub> in the troposphere and lowermost

stratosphere. While the modelled stratospheric total chlorine loading followed the prescribed scenario, the model appeared to produce more inorganic bromine than expected based on specified halocarbons. The N<sub>2</sub>O vs. NO<sub>y</sub> diagnostic showed that model values of NO<sub>y</sub> are high in the lower stratosphere and low in the upper stratosphere. The model provided a good representation of NO<sub>x</sub>/NO<sub>y</sub> and BrO/Br<sub>y</sub> in the PSS evaluation, a fair representation of O(<sup>1</sup>D), O(<sup>3</sup>P), and HO<sub>x</sub>, and a poor representation of ClO/Cl<sub>y</sub>. The large overestimate of ClO/Cl<sub>y</sub> by this model is due, in part, to the neglect of HCl production by the ClO + OH reaction. Overall, this model received the lowest numerical score in the fast chemistry evaluation. However, tracer-tracer correlations were well simulated. This model performed relatively poorly in representing the evolution of HNO<sub>3</sub>, but did a much better job of representing H<sub>2</sub>O and HCl in the polar region. The polar chemical ozone loss was very well simulated in both hemispheres. The sulfate SAD was not supplied for the polar chemical ozone loss calculation and therefore based on the REF-B1 sulfate time-series.

**NiwaSOCOL:** NiwaSOCOL provided joint results with SOCOL for the photolysis inter-comparison (see below). Did not participate in the PSS inter-comparisons. The model produced good tracer-tracer correlations except for NO<sub>y</sub> vs. N<sub>2</sub>O. The model performed well for the reservoir chemistry. Modelled polar HNO<sub>3</sub> was good while the simulation of H<sub>2</sub>O was better. In the same region, overall, the model did a good job in representing the evolution of HCl. However, the model overestimated HCl in the 500 K - 600 K region. The PACl analysis was good for the Antarctic but poorer for the Arctic. The Arctic PACl values were very high in the vortex as a result of too large H<sub>2</sub>O in the NH for some winters. Polar chemical ozone loss was well simulated in the Antarctic but, to a lesser extent, the Arctic where only very little ozone loss was derived. The sulfate SAD was not supplied for the polar chemical ozone loss analysis and therefore based on the REF-B1 sulfate time-series.

**SOCOL:** This model performed well in the photolysis inter-comparison. This model did well in representing the H<sub>tot</sub> vs. N<sub>2</sub>O diagnostics in the PSS section. However, it performed much less well in representing the Br<sub>y</sub> vs. N<sub>2</sub>O relation in the stratosphere. Model values of Cl<sub>y</sub> and Br<sub>y</sub> are large throughout the troposphere and stratosphere, and in the upper stratosphere exceed the values expected from the prescribed halocarbon scenarios. This indicates a lack of mass conservation. The model did a good job for HO<sub>x</sub> diagnostic in the PSS section; model values of NO<sub>x</sub>/NO<sub>y</sub>, ClO/Cl<sub>y</sub>, and BrO/Br<sub>y</sub> differ considerably from the benchmark (comparison for O(<sup>3</sup>P) and O(<sup>1</sup>D) could not be performed). Overall, the model did not fare well in the PSS evaluation. The model simulated good tracer-tracer correlations, except for NO<sub>y</sub> vs. N<sub>2</sub>O, and has a good represen-

tation of reservoir chemistry. Modelled polar  $\text{HNO}_3$  was good, while the simulation of  $\text{H}_2\text{O}$  was better. In the same region, overall, the model did a good job in representing the evolution of HCl. However, the model overestimated HCl in the 500 K - 600 K region. The PACI analysis was good for the Antarctic but slightly less so for the Arctic. The simulation of polar chemical ozone loss was good for both regions. The sulfate SAD was not supplied for the polar chemical ozone loss analysis and therefore based on the REF-B1 sulfate time-series.

**ULAQ:** Did not participate in the photolysis inter-comparison. This model did a good job in representing the radical precursors in the PSS section with the exception of exhibiting large  $\text{Cl}_y$  in the troposphere and throughout the lower stratosphere. The model also used a different sulfate SAD than what was prescribed for REF-B1. This model did a good job of representing  $\text{O}(^3\text{P})$ ,  $\text{O}(^1\text{D})$ ,  $\text{HO}_x$ , and  $\text{NO}_x/\text{NO}_y$  for one time period of the PSS evaluation (Sept 1993), and a poor job of representing these species for the other time period (Feb 1996). The model did a fair job for the representation of the partitioning of  $\text{ClO}/\text{Cl}_y$  and  $\text{BrO}/\text{Br}_y$  for both time periods. It is not clear why this model represented fast chemistry much better for one time period than another time period; no other model exhibited such behaviour. The model simulated good tracer-tracer correlations. The model has a good description of reservoir chemistry though results for  $\text{HNO}_3$  showed a larger disagreement. For the polar region the model performed fairly for  $\text{HNO}_3$  (model too high) but better for  $\text{H}_2\text{O}$ . In the same region the model did well in representing the evolution of HCl. The PACI analysis was good for both the Antarctic and Arctic, and the simulated polar chemical ozone loss was also good for both regions. The sulfate SAD was supplied for the polar chemical ozone loss analysis.

**UMETRAC:** Did not participate in any of the Chapter 6 chemistry diagnostics. Some tracer fields were supplied late in the CCMVal process and were included in reservoir species figures where possible.

**UMSLIMCAT:** Performed well in the photolysis inter-comparison. This model did a good job in the radical and radical precursor diagnostics for the PSS section, except for the  $\text{Br}_y$  vs.  $\text{N}_2\text{O}$  relation. Values of  $\text{Br}_y$  were higher than found by other models due to the inclusion of a source of very short-lived  $\text{Br}_y$  (an additional 6 pptv of  $\text{Br}_y$  was added). Comparisons could not be performed for  $\text{O}(^3\text{P})$  and  $\text{O}(^1\text{D})$ . The model produced good tracer-tracer correlations. The model has a good description of reservoir chemistry although a slightly larger discrepancy existed for  $\text{ClONO}_2$ . This model had a good representation of  $\text{HNO}_3$  (though model was too high) and  $\text{H}_2\text{O}$  in the polar region. In the same region the model performed fairly well

for HCl. The PACI results were good for the Antarctic and Arctic. The simulation of polar chemical ozone loss was also good for both regions (though note that the model run has larger  $\text{Br}_y$ ). The sulfate SAD was not supplied for the polar chemical ozone loss analysis and therefore based on the REF-B1 sulfate time-series.

**UMUKCA-METO:** Did not participate in the photolysis inter-comparison. This model compared well in the radical precursor diagnostics in the PSS section with the exception that this model had too much  $\text{Cl}_y$  at the tropopause and throughout the troposphere, due to errors in treating the rainout of HCl. This led to an excess of total chlorine throughout the stratosphere. The model did a good job of representing radicals in the PSS diagnostics. The model tended to overestimate stratospheric  $\text{NO}_x/\text{NO}_y$  by a large amount and under-estimate stratospheric  $\text{HO}_x$  also by a large amount. The comparisons for  $\text{O}(^1\text{D})$  could not be performed. The model produced good tracer-tracer correlations, except for  $\text{CH}_4$  vs.  $\text{H}_2\text{O}$ . The model generally did a fair job of reservoir chemistry. In the polar region the model did a fair job of  $\text{HNO}_3$  (model too high) but better for  $\text{H}_2\text{O}$ . In the same region the model was good at representing the evolution of HCl. The PACI analysis gave relatively poor results for the Antarctic and Arctic. The simulation of polar chemical ozone loss was good for the Antarctic but poorer for the Arctic. The sulfate SAD was not supplied for the polar chemical ozone loss and therefore based on the REF-B1 sulfate time-series. This model ran with a slightly different surface chlorine and bromine scenario to that prescribed for the REF-B2 run.

**UMUKCA-UCAM:** Did not participate in the photolysis inter-comparison, the PSS inter-comparison or the polar studies. However, this model is very similar to UMUKCA-METO and the performance of the chemical scheme should therefore be expected to be very similar. Chemical output could be analysed for the climatological comparisons. The model produced good tracer-tracer correlations. For the reservoir chemistry the model performed reasonably with the notable exception of  $\text{HNO}_3$ . An outstanding issue is the apparent differences in chemical behaviour with the METO version of UMUKCA for these climatological comparisons. Like UMUKCA-METO, this model ran with a slightly different surface chlorine and bromine scenario to that prescribed for the REF-B2 run.

**WACCM:** This model performed very well in the photolysis inter-comparison. The model did an excellent job representing radicals and radical precursors. Peak values of  $\text{NO}_y$  are a bit lower than found in most of the other models and observed during Sept 1993. This model received the highest overall score in the fast chemistry metric. The model produced good tracer-tracer correlations and appears to

have a good description of reservoir chemistry. In the polar region WACCM was performed well in its representation of  $\text{HNO}_3$  but less well for  $\text{H}_2\text{O}$  (model too low). It should be noted that this model stayed denitrified too long into spring. In the same region the model was good in representing the evolution of  $\text{HCl}$ . The  $\text{PACl}$  comparison was good for the Antarctic but poorer for the Arctic where the  $\text{PACl}$  values were too large. The simulation of polar chemical ozone loss was very good for both the Antarctic and Arctic. The sulfate SAD was supplied for the polar chemical ozone loss analysis.

## 6.4.2 Overall Summary

This chapter is the first *major* attempt at quantifying the accuracy of different components of the stratospheric chemistry modules contained within global 3D CCMs. This work has shown some very good agreement, but at times significant discrepancies, in how the state-of-the-art CCMs represent radicals and their precursors.

A wide range of chemical observations are available for testing CCMs. However, the effective use of these observations sometime requires specific temporal sampling of the model runs. For example, satellite observations of key radicals for ozone loss are now available over many years but these species tend to have strong diurnal variations. Uncertainties in modelled polar ozone loss could be reduced by critical comparison with climatologies of polar  $\text{ClO}$ . Future CCM runs should look to sample the model to produce output files directly comparable to such observations.

## References

- Bernath, P. F., C. T. McElroy, M. C. Abrams, C. D. Boone, M. Butler, C. Camy-Peyret, M. Carleer, C. Clerbaux, P.-F. Coheur, R. Colin, P. DeCola, M. DeMazière, J. R. Drummond, D. Dufour, W. F. J. Evans, H. Fast, D. Fussen, K. Gilbert, D. E. Jennings, E. J. Llewellyn, R. P. Lowe, E. Mahieu, J. C. McConnell, M. McHugh, S. D. McLeod, R. Michaud, C. Midwinter, R. Nassar, F. Nichitiu, C. Nowlan, C. P. Rinsland, Y. J. Rochon, N. Rowlands, K. Semeniuk, P. Simon, R. Skelton, J. J. Sloan, M.-A. Soucy, K. Strong, P. Tremblay, D. Turnbull, K. A. Walker, I. Walkty, D. A. Wardle, V. Wehrle, R. Zander, and J. Zou, 2005. Atmospheric Chemistry Experiment (ACE): Mission overview, *Geophys. Res. Lett.*, **32**, doi:10.1029/2005GL022386.
- Cantrell, C. A., J. G. Calvert, A. Bais, R. E. Shetter, B. L. Lefer, and G. D. Edwards, Overview and conclusions of the International Photolysis Frequency Measurement and Modeling Intercomparison (IPMMI) study, *J. Geophys. Res.*, **108**, 8542, 2003.
- Chang, A., R. J. Salawitch, H. A. Michelsen, M. R. Gunson, M. C. Abrams, R. Zander, C. P. Rinsland, M. Loewenstein, J. R. Podolske, M. H. Proffitt, J. J. Margitan, D. W. Fahey, R.-S. Gao, K. K. Kelly, J. W. Elkins, C. R. Webster, R. D. May, K. R. Chan, M. M. Abbas, A. Goldman, F. W. Irion, G. L. Manney, M. J. Newchurch and G. P. Stiller, 1996. A Comparison of Measurements from ATMOS and Instruments Aboard the ER-2 Aircraft: Tracers of Atmospheric Transport, *Geophys. Res. Lett.*, **23**, 2389-2392.
- Christensen, L. E., M. Okumura, S. P. Sander, R. J. Salawitch, G. C. Toon, B. Sen, J.-F. Blavier, and K. W. Jucks, 2002. Kinetics of  $\text{HO}_2 + \text{HO}_2 \rightarrow \text{H}_2\text{O}_2 + \text{O}_2$ : Implications for stratospheric  $\text{H}_2\text{O}_2$ , *Geophys. Res. Lett.*, **29**, 10.1029/2001GL014525.
- Dessler, A. E., 2002. The effect of deep, tropical convection on the tropical tropopause layer, *J. Geophys. Res.*, **107**, doi:10.1029/2001JD000511.
- Douglass, A., M. Prather, T. Hall, S. Strahan, P. Rasch, L. Sparling, L. Coy, and J. Rodriguez, 1999. Choosing meteorological input for the global modeling initiative assessment of high-speed aircraft, *J. Geophys. Res.*, **104**, 27545-27564.
- Evans, J.T., M.P. Chipperfield, H. Oelhaf, M. Stowasser, and G. Wetzel, 2003. Effect of near-IR photolysis of  $\text{HO}_2\text{NO}_2$  on stratospheric chemistry, *Geophys. Res. Lett.*, **30**, doi:10.1029/2002GL016470.
- Eyring, V., N. R. P. Harris, M. Rex, T. G. Shepherd, D. W. Fahey, G. T. Amanatidis, J. Austin, M. P. Chipperfield, M. Dameris, P. M. De F. Forster, A. Gettelman, H. F. Graf, T. Nagashima, P. A. Newman, S. Pawson, M. J. Prather, J. A. Pyle, R. J. Salawitch, B. D. Santner, and D. W. Waugh, 2005. A strategy for process-oriented validation of coupled chemistry-climate models, *Bull. Am. Meteorol. Soc.*, **86**, 1117-1133.
- Eyring, V., D. W. Waugh, G. E. Bodeker, E. Cordero, H. Akiyoshi, J. Austin, S. R. Beagley, B. Boville, P. Braesicke, C. Brühl, N. Butchart, M. P. Chipperfield, M. Dameris, R. Deckert, M. Deushi, S. M. Frith, R. R. Garcia, A. Gettelman, M. Giorgetta, D. E. Kinison, E. Mancini, E. Manzini, D. R. Marsh, S. Mat-

- thes, T. Nagashima, P. A. Newman, J. E. Nielsen, S. Pawson, G. Pitari, D. A. Plummer, E. Rozanov, M. Schraner, J. F. Scinocca, K. Semeniuk, T. G. Shepherd, K. Shibata, B. Steil, R. Stolarski, W. Tian, and M. Yoshiki, 2007. Multimodel projections of stratospheric ozone in the 21st century, *J. Geophys. Res.*, **112**, doi:10.1029/2006JD008332.
- Fahey, D. W., S. G. Donnelly, E. R. Keim, R. S. Gao, R. C. Wamsley, L. A. Del Negro, E. L. Woodbridge, M. H. Proffitt, K. H. Rosenlof, M. K. W. Ko, D. K. Weisenstein, C. J. Scott, C. Nevison, S. Solomon and K. R. Chan, 1996. In situ observations of NO<sub>y</sub>, O<sub>3</sub>, and the NO<sub>y</sub>/O<sub>3</sub> ratio in the lower stratosphere, *Geophys. Res. Lett.*, **23**, 1653-1656.
- Froidevaux L., Y. B. Jiang, A. Lambert, N. J. Livesey, W. G. Read, J. W. Waters, R. A. Fuller, T. P. Marcy, P. J. Popp, R. S. Gao, D. W. Fahey, K. W. Jucks, R. A. Stachnik, G. C. Toon, L. E. Christensen, C. R. Webster, P. F. Bernath, C. D. Boone, K. A. Walker, H. C. Pumphrey, R. S. Harwood, G. L. Manney, M. J. Schwartz, W. H. Daffer, B. J. Drouin, R. E. Cofield, D. T. Cuddy, R. F. Jarnot, B. W. Knosp, V. S. Perun, W. V. Snyder, P. C. Stek, R. P. Thurstans, and P. A. Wagner, 2008. Validation of Aura Microwave Limb Sounder HCl measurements, *J. Geophys. Res.*, **113**, doi:10.1029/2007JD009025.
- Gao, R.S., L. A. Del Negro, W. H. Swartz, R. J. Salawitch, S. A. Lloyd, M. H. Proffitt, D. W. Fahey, S. G. Donnelly, J. A. Neuman, R. M. Stimpfle, and T. P. Bui, 2001. J at high solar zenith angle in the lower stratosphere, *Geophys. Res. Lett.*, **28**, 2405-2408.
- Hamill, T. M., J. S. Whitaker, 2005. Accounting for the error due to unresolved scales in ensemble data assimilation: A comparison of different approaches, *Mon. Wea. Rev.*, **133**, 3132 - 3147.
- Hanson, D. R., and K. Mauersberger, 1998. Laboratory studies of the nitric acid trihydrate: Implications for the south polar stratosphere, *Geophys. Res. Lett.*, **15**, 855-858, doi:10.1029/88GL00209.
- Hofzumahaus, A., B. L. Lefer, P. S. Monks, S. R. Hall, A. Kylling, B. Mayer, R. E. Shetter, W. Junkermann, A. Bais, J. G. Calvert, C. A. Cantrell, S. Madronich, G. D. Edwards, A. Kraus, M. Müller, B. Bohn, R. Schmitt, P. Johnston, R. McKenzie, G. J. Frost, E. Griffioen, M. Krol, T. Martin, G. Pfister, E. P. Röth, A. Ruggaber, W. H. Swartz, S. A. Lloyd, and M. Van Weele, 2004. Photolysis frequency of O<sub>3</sub> to O(1D): Measurements and modeling during the International Photolysis Frequency Measurement and Modeling Intercomparison (IPMMI), *J. Geophys. Res.*, **109**, doi:10.1029/2003JD004333.
- Jucks, K. W., D. G. Johnson, K. V. Chance, W. A. Traub, J. J. Margitan, G. B. Osterman, R. J. Salawitch, and Y. Sasano, 1998. Observations of OH, HO<sub>2</sub>, H<sub>2</sub>O, and O<sub>3</sub> in the upper stratosphere: implications for HO<sub>x</sub> photochemistry, *Geophys. Res. Lett.*, **25**, 3935-3938, doi:10.1029/1998GL900009.
- Jucks, K. W., D. G. Johnson, K. V. Chance, W. A. Traub, and R. J. Salawitch, 1999. Nitric acid in the middle stratosphere as a function of altitude and aerosol loading, *J. Geophys. Res.*, **104**, 26,715-26,723.
- Kawa, S.R., R.A. Plumb, and U. Schmidt, 1993. Simultaneous observations of long-lived species, Chapter H, The atmospheric effects of stratospheric aircraft: Report of the 1992 models and measurements workshop, NASA Ref. Publ. 1292, 352pp, NASA Goddard Space Flight Center, Greenbelt, MD,.
- Kondo, Y., U. Schmidt, T. Sugita, A. Engel, M. Koike, P. Amedieu, M.R. Gunson, and J. Rodriguez, 1996. NO<sub>y</sub> correlation with N<sub>2</sub>O and CH<sub>4</sub> in the midlatitude stratosphere, *Geophys. Res. Lett.*, **23**, 2369-2372.
- Kovalenko, L. J., K. W. Jucks, R. J. Salawitch, G. C. Toon, J.-F. Blavier, D. G. Johnson, A. Kleinböhl, N. J. Livesey, J. J. Margitan, H. M. Pickett, M. L. Santee, B. Sen, R. A. Stachnik, and J. W. Waters, 2007. Observed and modeled HOCl profiles in the midlatitude stratosphere: Implications for ozone loss, *Geophys. Res. Lett.*, **34**, doi:10.1029/2007GL031100.
- Lanzendorf, E. J., T. F. Hanisco, P. O. Wennberg, R. C. Cohen, R. M. Stimpfle, J. G. Anderson, R. S. Gao, J. J. Margitan, and T. P. Bui, 2001. Establishing the dependence of [HO<sub>2</sub>]/[OH] on temperature, halogen loading, O<sub>3</sub>, and NO<sub>x</sub> based on in situ measurements from the NASA ER-2, *J. Phys. Chem. A*, **105**, 1535-1542.
- Lambert A., W. G. Read, N. J. Livesey, M. L. Santee, G. L. Manney, L. Froidevaux, D. L. Wu, M. J. Schwartz, H. C. Pumphrey, C. Jimenez, G. E. Nedoluha, R. E. Cofield, D. T. Cuddy, W. H. Daffer, B. J. Drouin, R. A. Fuller, R. F. Jarnot, B. W. Knosp, H. M. Pickett, V. S. Perun, W. V. Snyder, P. C. Stek, R. P. Thurstans, P. A. Wagner, J. W. Waters, K. W. Jucks, G. C. Toon,



- R. A. Stachnik, P. F. Bernath, C. D. Boone, K. A. Walker, J. Urban, D. Murtagh, J. W. Elkins, and E. Atlas, 2007. Validation of the Aura Microwave Limb Sounder middle atmosphere water vapor and nitrous oxide measurements, *J. Geophys. Res.*, **112**, doi:10.1029/2007JD008724.
- Lipson, J. B., T. W. Beiderhase, L. T. Molina, M. J. Molina, and M. Olzmann, 1999. Production of HCl in the OH + ClO reaction: Laboratory measurements and statistical rate theory calculations, *J. Phys. Chem. A*, **103**, 6540–6551.
- Manney G. L., W. H. Daffer, J. M. Zawodny, P. F. Bernath, K. W. Hoppel, K. A. Walker, B. W. Knosp, C. Boone, E. E. Remsberg, M. L. Santee, V. L. Harvey, S. Pawson, D. R. Jackson, L. Deaver, C. T. McElroy, C. A. McLinden, J. R. Drummond, H. C. Pumphrey, A. Lambert, M. J. Schwartz, L. Froidevaux, Sean McLeod, L. L. Takacs, M. J. Suarez, Charles R. Trepte, D. C. Cuddy, N. J. Livesey, R. S. Harwood, and J. W. Waters, 2007. Solar occultation satellite data and derived meteorological products: Sampling issues and comparisons with Aura Microwave Limb Sounder, *J. Geophys. Res.*, **112**, doi:10.1029/2007JD008709.
- McElroy, M. B., and R. J. Salawitch, 1989. Changing composition of the global stratosphere, *Science*, **243**, 763–770.
- Michelangeli, D. V., M. Allen, and Y. L. Yung, 1989. El Chichon volcanic aerosols: impact of radiative, thermal, and chemical perturbations, *J. Geophys. Res.*, **94**, 18,429–18,443.
- Millard, G. A., A. M. Lee, and J. A. Pyle, 2002. A model study of the connection between polar and midlatitude ozone loss in the Northern Hemisphere lower stratosphere, *J. Geophys. Res.*, **107**, doi:10.1029/2001JD000899.
- Müller, R., P. J. Crutzen, J.-U. Grooss, C. Bruehl, J. M. Russell II, H. Gernandt, D. S. McKenna and A. F. Tuck, 1997. Severe chemical ozone loss in the Arctic during the winter of 1995–1996, *Nature*, **389**, 709–712.
- Müller, R. and R. J. Salawitch (lead authors), P. J. Crutzen, W. A. Lahoz, G. L. Manney, and R. Toumi, Chapter 6: Upper Stratospheric Processes, Scientific Assessment of Ozone Depletion: 1998, World Meteorological Organization, Global ozone research and monitoring project, Report No. 44, Geneva, Switzerland, 1999.
- Müller, R., S. Tilmes, P. Konopka, J.-U. Grooß, and H.-J. Jost, 2005. Impact of mixing and chemical change on ozone-tracer relations in the polar vortex, *Atmos. Chem. Phys.*, **5**, 3139–3151.
- Müller, R., J.-U. Grooß, C. Lemmen, D. Heinze, M. Dameris, and G. Bodeker, 2008. Simple measures of ozone depletion in the polar stratosphere, *Atmos. Chem. Phys.*, **8**, 251–264.
- Murtagh, D., U. Frisk, F. Merino, M. Ridal, A. Jonsson, J. Stegman, G. Witt, P. Eriksson, C. Jiménez, G. Megie, J. de la Noë, P. Ricaud, P. Baron, J. R. Pardo, A. Hauchcorne, E. J. Llewellyn, D. A. Degenstein, R. L. Gattinger, N. D. Lloyd, W. F. J. Evans, I. C. McDade, C. S. Haley, C. Sioris, C. von Savigny, B. H. Solheim, J. C. McConnell, K. Strong, E. H. Richardson, G. W. Leppelmeier, E. Kyrölä, H. Auvinen, and L. Oikarinen, 2002. An overview of the Odin atmospheric mission, *Can. J. Phys.*, **80**, 309–319.
- Nash, E. R., P. A. Newman, J. E. Rosenfield, and M. R. Schoeberl, 1996. An objective determination of the polar vortex using Ertel's potential vorticity, *J. Geophys. Res.*, **101**, 9471–9478.
- Newman, P. A., E. R. Nash, S. R. Kawa, S. A. Montzka, and S. M. Schauffler, 2006. When will the Antarctic ozone hole recover?, *Geophys. Res. Lett.*, **33**, doi:10.1029/2005GL025232.
- Newman, P. A., J. S. Daniel, D. W. Waugh, and E. R. Nash, 2007. A new formulation of equivalent effective stratospheric chlorine (EESC), *Atmos. Chem. Phys.*, **7**, 4537–4552.
- Osterman, G. B., R. J. Salawitch, B. Sen, G. C. Toon, R. A. Stachnik, H. M. Pickett, J. J. Margitan, J.-F. Blavier, and D. B. Peterson, 1997. Balloon-borne measurements of stratospheric radicals and their precursors: implications for the production and loss of ozone, *Geophys. Res. Lett.*, **24**, 1107–1110.
- Osterman, G. B., B. Sen, G. C. Toon, R. J. Salawitch, J. J. Margitan, J.-F. Blavier, D. W. Fahey, and R. S. Gao, 1999. Partitioning of NO<sub>y</sub> species in the summer Arctic stratosphere, *Geophys. Res. Lett.*, **26**, 1157–1160.
- Park, J.H., et al., Models and Measurements Intercomparison II, NASA/TM-1999-209554, 1999.
- Peter, T., 1997. Microphysics and heterogeneous chemistry

- of polar stratospheric clouds, *Ann. Rev. Phys. Chem.*, **48**, 785-822.
- Pierson, J., S. Kawa, R. Salawitch, T. Hanisco, E. Lanzaendorf, K. Perkins, and R. Gao, 2000. Influence of air mass histories on radical species during the Photochemistry of Ozone Loss in the Arctic Region in Summer (POLARIS) mission, *J. Geophys. Res.*, **105**, 15,185-15,199.
- Prather, M.J. and E.E. Remsberg, (eds.), 1993. Report of the 1992 Stratospheric Models and Measurements Workshop, Satellite Beach, FL, February 1992, NASA Ref. Publ. 1292, 144+268+352 pp.
- Proffitt, M. H., K. Aikin, J. J. Margitan, M. Loewenstein, J. R. Podolske, A. Weaver, K. R. Chan, H. Fast, and J. W. Elkins, 1993. Ozone loss inside the northern polar vortex during the 1991-1992 winter, *Science*, **261**, 1150-1154.
- Pundt, I., J.-P. Pommereau, M. P. Chipperfield, M. Van Roozendaal, and F. Goutail, 2002. Climatology of the stratospheric BrO vertical distribution by balloon-borne UV-visible spectrometry, *J. Geophys. Res.*, **107**, doi:10.1029/2002JD002230.
- Rex, M., R. J. Salawitch, P. von der Gathen, N. R. Harris, M. P. Chipperfield, and B. Naujokat, 2004. Arctic ozone loss and climate change, *Geophys. Res. Lett.*, **31**, doi:10.1029/2003GL018844.
- Rinsland, C.P., E. Mathieu, R. Zander, N.B. Jones, M.P. Chipperfield, A. Goldman, J. Anderson, J.M. Russell, P. Demoulin, J. Notholt, G.C. Toon, J.F. Blavier, B. Sen, R. Sussmann, S.W. Wood, A. Meier, D.W.T. Griffith, L.S. Chiou, F.J. Murcray, T.M. Stephen, F. Hase, S. Mikuteit, A. Schulz, and T. Blumenstock, 2003. Long-term trends of inorganic chlorine from ground-based infrared solar spectra: Past increases and evidence for stabilization, *J. Geophys. Res.*, **108**, doi:10.1029/2002JD003001.
- Rozanov, A., H. Bovensmann, A. Bracher, S. Hrechanyy, V. Rozanov, M. Sinnhuber, F. Stroh and J.P. Burrows, 2005. NO<sub>2</sub> and BrO vertical profile retrieval from SCIAMACHY limb measurements: Sensitivity studies, *Adv. Space Res.*, **36**, 846-854.
- Salawitch, R. J., S. C. Wofsy, P. O. Wennberg, R. C. Cohen, J. G. Anderson, D. W. Fahey, R. S. Gao, E. R. Keim, E. L. Woodbridge, R. M. Stimpfle, J. P. Koplów, D. W. Kohn, C. R. Webster, R. D. May, L. Pfister, E. W. Gottlieb, H. A. Michelsen, G. K. Yue, J. C. Wilson, C. A. Brock, H. H. Jonsson, J. E. Dye, D. Baumgardner, M. H. Proffitt, M. Loewenstein, J. R. Podolske, J. W. Elkins, G. S. Dutton, E. J. Hintsá, A. E. Dessler, E. M. Weinstock, K. K. Kelly, K. A. Boering, B. C. Daube, K. R. Chan, and S. W. Bowen, 1994a. The distribution of hydrogen, nitrogen, and chlorine radicals in the lower stratosphere: implications for changes in O<sub>3</sub> due to emission of NO<sub>y</sub> from supersonic aircraft, *Geophys. Res. Lett.*, **21**, 2543-2546.
- Salawitch, R. J., S. C. Wofsy, P. O. Wennberg, R. C. Cohen, J. G. Anderson, D. W. Fahey, R. S. Gao, E. R. Keim, E. L. Woodbridge, R. M. Stimpfle, J. P. Koplów, D. W. Kohn, C. R. Webster, R. D. May, L. Pfister, E. W. Gottlieb, H. A. Michelsen, G. K. Yue, J. C. Wilson, C. A. Brock, H. H. Jonsson, J. E. Dye, D. Baumgardner, M. H. Proffitt, M. Loewenstein, J. R. Podolske, J. W. Elkins, G. S. Dutton, E. J. Hintsá, A. E. Dessler, E. M. Weinstock, K. K. Kelly, K. A. Boering, B. C. Daube, K. R. Chan, and S. W. Bowen, 1994b. The diurnal variation of hydrogen, nitrogen, and chlorine radicals: implications for the heterogeneous production of HNO<sub>2</sub>, *Geophys. Res. Lett.*, **21**, 2547-2550.
- Salawitch, R. J., P. O. Wennberg, G. C. Toon, B. Sen, and J.-F. Blavier, 2002. Near IR photolysis of HO<sub>2</sub>NO<sub>2</sub>: Implications for HOx, *Geophys. Res. Lett.*, **29**, doi:10.1029/2002GL015006.
- Salawitch, R. J., D. K. Weisenstein, L. J. Kovalenko, C. E. Sioris, P. O. Wennberg, K. Chance, M. K. W. Ko, and C. A. McLinden, 2005. Sensitivity of ozone to bromine in the lower stratosphere, *Geophys. Res. Lett.*, **32**, doi:10.1029/2004GL021504.
- Sander, S. P., et al., Chemical Kinetics and Photochemical Data for Use in Atmospheric Studies, Evaluation No. 14, JPL Publication 02-25, Jet Propulsion Lab, Pasadena, CA, 2003.
- Sander, S. P. et al., Chemical Kinetics and Photochemical Data for Use in Atmospheric Studies, Evaluation Number 15, JPL Publication 06-02, Jet Propulsion Laboratory, Pasadena, Calif., 2006.
- Santee M. L., A. Lambert, W. G. Read, N. J. Livesey, R. E. Cofield, D. T. Cuddy, W. H. Daffer, B. J. Drouin, L. Froidevaux, R. A. Fuller, R. F. Jarnot, B. W. Knosp, G. L. Manney, V. S. Perun, W. V. Snyder, P. C. Stek, R. P. Thurstans, P. A. Wagner, J. W. Waters, G. Muscari, R. L. de Zafra, J. E. Dibb, D. W. Fahey, P. J. Popp, T. P. Marcy, K. W. Jucks, G. C. Toon, R. A. Stachnik,

- P. F. Bernath, C. D. Boone, K. A. Walker, J. Urban, and D. Murtagh, 2007. Validation of the Aura Microwave Limb Sounder HNO<sub>3</sub> measurements, *J. Geophys. Res.*, **112**, doi:10.1029/2007JD008721.
- Sen, B., G. C. Toon, G. B. Osterman, J.-F. Blavier, J. J. Margitan, R. J. Salawitch, and G. K. Yue, 1998. Measurements of reactive nitrogen in the stratosphere, *J. Geophys. Res.*, **103**, 3571-3585.
- Sen, B., G. B. Osterman, R. J. Salawitch, G. C. Toon, J. J. Margitan, J.-F. Blavier, A. Y. Chang, R. D. May, C. R. Webster, R. M. Stimpfle, G. P. Bonne, P. B. Voss, K. K. Perkins, J. G. Anderson, R. C. Cohen, J. W. Elkins, G. S. Dutton, D. F. Hurst, P. A. Romashkin, E. L. Atlas, S. M. Schauffler, and M. Loewenstein, 1999. The budget and partitioning of stratospheric chlorine during the 1997 Arctic summer, *J. Geophys. Res.*, **104**, 26,653-26,665.
- Sinnhuber, B.-M., A. Rozanov, N. Sheode, O. T. Afe, A. Richter, M. Sinnhuber, F. Wittrock, J. P. Burrows, G. P. Stiller, T. von Clarmann, and A. Linden, 2005. Global observations of stratospheric bromine monoxide from SCIAMACHY, *Geophys. Res. Lett.*, **32**, doi:10.1029/2005GL023839.
- Solomon, S., R. R. Garcia, F.S. Rowland and D.J. Wuebbles, 1998. On the depletion of Antarctic ozone, *Nature*, **321**, 755-758.
- Solomon, S., Stratospheric ozone depletion: A review of concepts and history, *Rev. Geophys.*, **37**, 275-316, 1999.
- Thomason, L. W., L. R. Poole, and T. Deshler, A global climatology of stratospheric aerosol surface area density deduced from Stratospheric Aerosol and Gas Experiment II measurements: 1984-1994, *J. Geophys. Res.*, **102**, 8967-8976, 1997.
- Tilmes, S., R. Müller, J.-U. Grooß, and J. M. Russell, 2004. Ozone loss and chlorine activation in the Arctic winters 1991-2003 derived with the tracer-tracer correlations, *Atmos. Chem. Phys.*, **4**, 2181-2213.
- Tilmes, S., R. Müller, A. Engel, M. Rex, and J. M. Russell III, 2006. Chemical ozone loss in the Arctic and Antarctic stratosphere between 1992 and 2005, *Geophys. Res. Lett.*, **33**, doi:10.1029/2006GL026925.
- Tilmes, S., E. D. Kinnison, R. R. Garcia, R. Mueller, B. A. Boville, F. Sassi, D. R. Marsh, 2007. Evaluation of heterogeneous processes in the polar lower stratosphere in WACCM3, *J. Geophys. Res.*, **112**, doi:10.1029/2006JD008334.
- Tilmes, S., R. Müller, and R. Salawitch, 2008. The sensitivity of polar ozone depletion to proposed geo-engineering schemes, *Science*, **320**, 1201-1204, doi:10.1126/science.1153966.
- Wamsley, P. R., J. W. Elkins, D. W. Fahey, G. S. Dutton, C. M. Volk, R. C. Myers, S. A. Montzka, J. H. Butler, A. D. Clarke, P. J. Fraser, L. P. Steele, M. P. Lucarelli, E. L. Atlas, S. M. Schauffler, D. R. Blake, F. S. Rowland, W. T. Sturges, J. M. Lee, S. A. Penkett, A. Engel, R. M. Stimpfle, K. R. Chan, D. K. Weisenstein, M. K. W. Ko, and R. J. Salawitch, 1998. Distribution of halon-1211 in the upper troposphere and lower stratosphere and the 1994 total bromine budget, *J. Geophys. Res.*, **103**, 1513-1526.
- Waters, J. W., et al., The Earth Observing System Microwave Limb Sounder (EOS MLS) on the Aura Satellite, *IEEE Trans. Geosci. Remote Sensing*, **44**, no. 5, 1075-1092, 2006.
- Waugh, D. and V. Eyring, 2008. Quantitative performance metrics for stratospheric-resolving chemistry-climate models, *Atmos. Chem. Phys.*, **8**, 5699-5713.
- Weinstock, E. M., E. J. Hints, D. B. Kirk-Davidoff, J. G. Anderson, A. E. Andrews, R. L. Herman, C. R. Webster, M. Loewenstein, J. R. Podolske, and T. P. Bui, 2001. Constraints on the seasonal cycle of stratospheric water vapor using in situ measurements from the ER-2 and a CO photochemical clock, *J. Geophys. Res.*, **106**, 22,707-22,724.
- Wennberg, P.O., R. C. Cohen, R. M. Stimpfle, J. P. Koplów, J. G. Anderson, R. J. Salawitch, D. W. Fahey, E. L. Woodbridge, E. R. Keim, R. S. Gao, C. R. Webster, R. D. May, D. W. Toohey, L. M. Avallone, M. H. Proffitt, M. Loewenstein, J. R. Podolske, K. R. Chan, and S. C. Wofsy, 1994. Removal of stratospheric ozone by radicals: in situ measurements of OH, HO<sub>2</sub>, NO, NO<sub>2</sub>, ClO, and BrO, *Science*, **266**, 398-404.
- Wennberg, P. O. R. J. Salawitch, D. J. Donaldson, T. F. Hanisco, E. J. Lanzendorf, K. K. Perkins, S. A. Lloyd, V. Vaida, R. S. Gao, E. J. Hints, R. C. Cohen, W. H. Swartz, T. L. Kusterer, and D. E. Anderson, 1999. Twilight observations suggest unknown sources of HO<sub>x</sub>, *Geophys. Res. Lett.*, **26**, 1373-1376.
- Whitaker, J.S., T.M. Hamill, X. Wei, Y. Song and Z. Toth, 2008. Ensemble data assimilation with the NCEP global forecast system, *Mon. Wea. Rev.*, **136**, 463-

482.

Wild, O., X. Zhu, M.J. Prather, 2000. Fast-J: Accurate simulation of in- and below-cloud photolysis in tropospheric chemical models, *J. Atmos. Chem.*, **37**, 245-282.

World Meteorological Organization (WMO)/United Nations Environment Programme (UNEP), 2007. *Scientific Assessment of Ozone Depletion: 2006*, World Meteorological Organization, Global Ozone Research and Monitoring Project, Report No. 50, Geneva, Switzerland.

Woodbridge, E. L., J. W. Elkins, D. W. Fahey, L. E. Heidt, S. Solomon, T. J. Baring, T. M. Gilpin, W. H. Pollock, S. M. Schauffler, E. L. Atlas, M. Loewenstein, J. R. Podolske, C. R. Webster, R. D. May, J. M. Gilligan, S. A. Montzka, K. A. Boering, and R. J. Salawitch, 1995. Estimates of total organic and inorganic chlorine in the lower stratosphere from in situ and flask measurements during AASE II, *J. Geophys. Res.*, **100**, 3057–3064.

1 • **Stratospheric Chemistry**

---

2

3

4

5 **Chapter 6 Supplementary Material**

6

7 **Includes:**

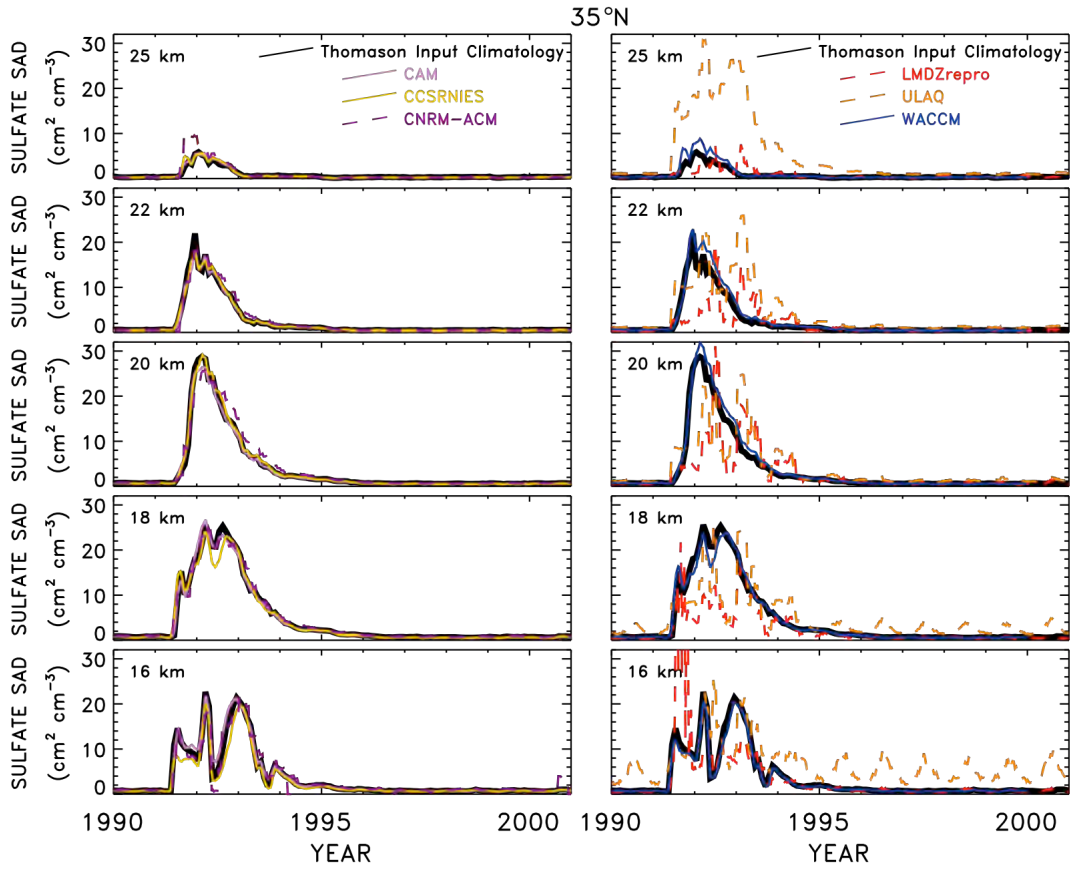
8 • 6S Supplementary Figures (6S-1 through 6S-20)

9 • 6S Tables (6S-1 through 6S-4)

10 • Photocomp 2008 Experiment

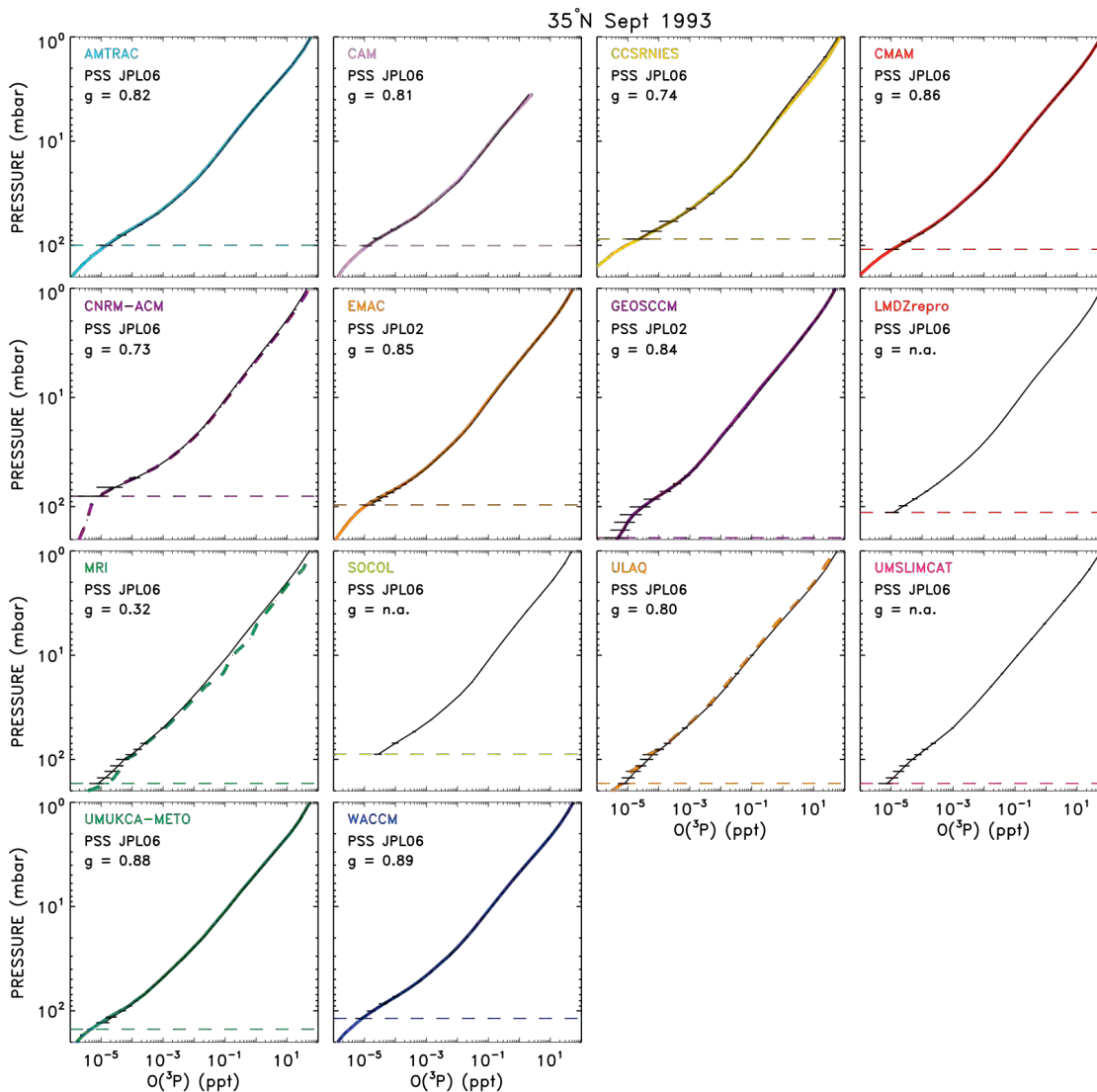
11

12 **6S Supplemental Figures**

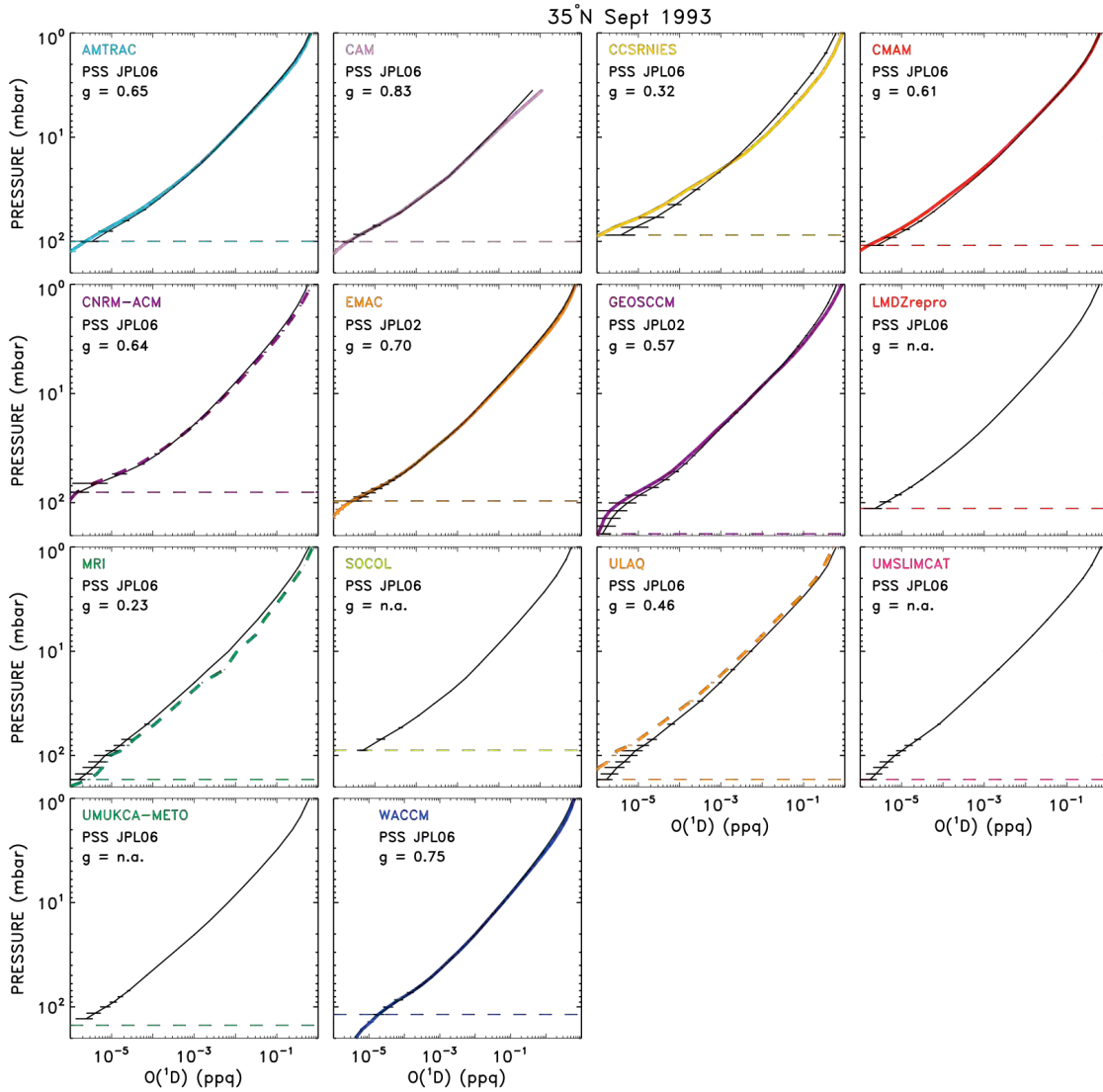


13

14 **Figure 6S-1:** Sulfate surface area density ( $\text{cm}^2 \text{cm}^{-3}$ ) time series at  $35^\circ\text{N}$  and 25km,  
15 22km, 20km, 18km, and 16km for CAM3.5, CCSRNIES, CNRM-ACM, LMDZrepro,  
16 ULAQ, and WACCM.



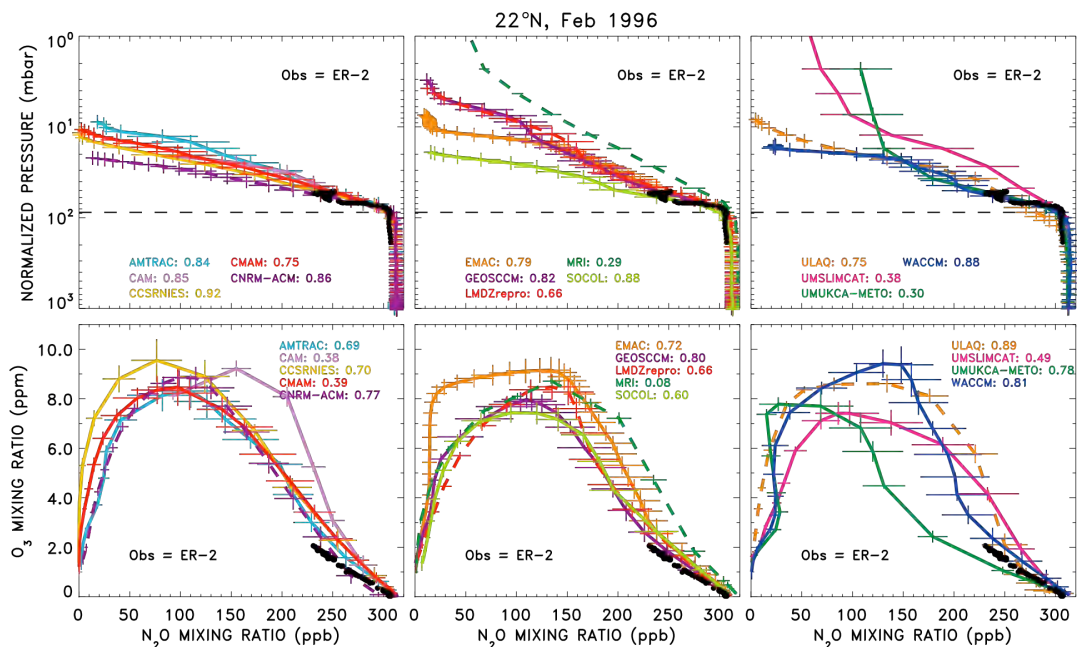
17  
 18 **Figure 6S-2a:** Comparison of zonal, monthly mean profiles of  $O(^3P)$  radicals from CCM  
 19 models (coloured lines and symbols) versus 24-hour average radical profiles found using  
 20 a PSS box model constrained by profiles of T,  $O_3$ ,  $H_2O$ ,  $CH_4$ , CO,  $NO_Y$ ,  $Cl_Y$ ,  $Br_Y$ , and  
 21 sulfate SAD from the various CCMs for 35°N in **September 1993**. The PSS model was  
 22 run for CCM model levels from the tropopause (dashed lines) to 1 hPa. The PSS model  
 23 uses the latitude of the CCM output that is closest to 35°N and solar declination  
 24 corresponding to the mid point of the monthly mean. Numerical values of g and the  
 25 chemical kinetics in the simulation are given (see main chapter text). The coloured error  
 26 bars represent the standard deviation about the zonal monthly mean for various days used  
 27 to compute the mean. The black error bars represent the sensitivity of PSS output to  
 28 variability in the CCM profiles of radical precursors.  
 29



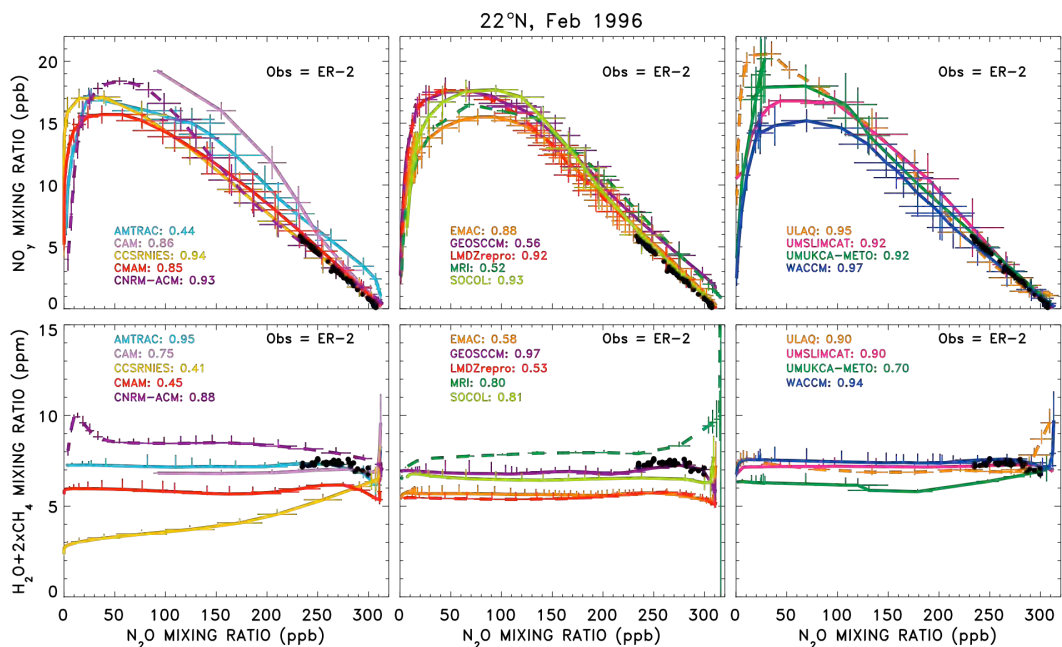
30  
31  
32

Figure 6S-2b: same as Figure 6S-2a, except  $O(^1D)$  is shown.

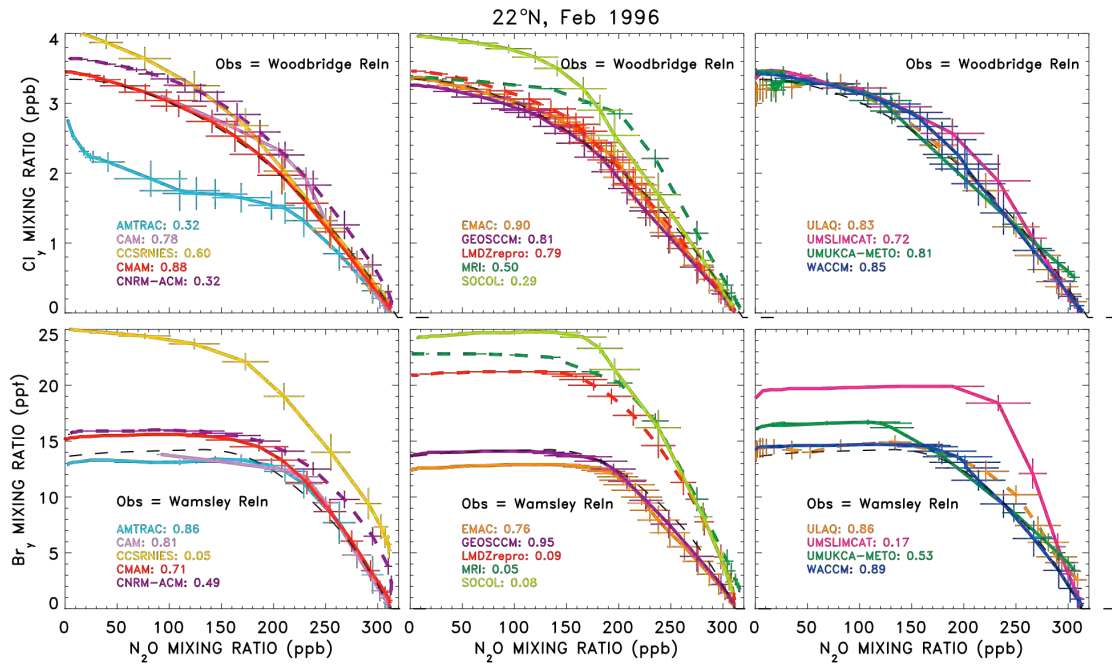




33  
 34 **Figure 6S-3a:** Comparison of N<sub>2</sub>O profile and the relation of radical precursors versus  
 35 N<sub>2</sub>O (black) to zonal, monthly mean values from various CCM models (coloured lines  
 36 and symbols, as indicated) for **February 1996**. CCM output is for the closest model  
 37 latitude to 22°N, as indicated. Numerical values of g (see main chapter text) are also  
 38 noted. Comparisons of N<sub>2</sub>O vs pressure and O<sub>3</sub> vs N<sub>2</sub>O are shown.

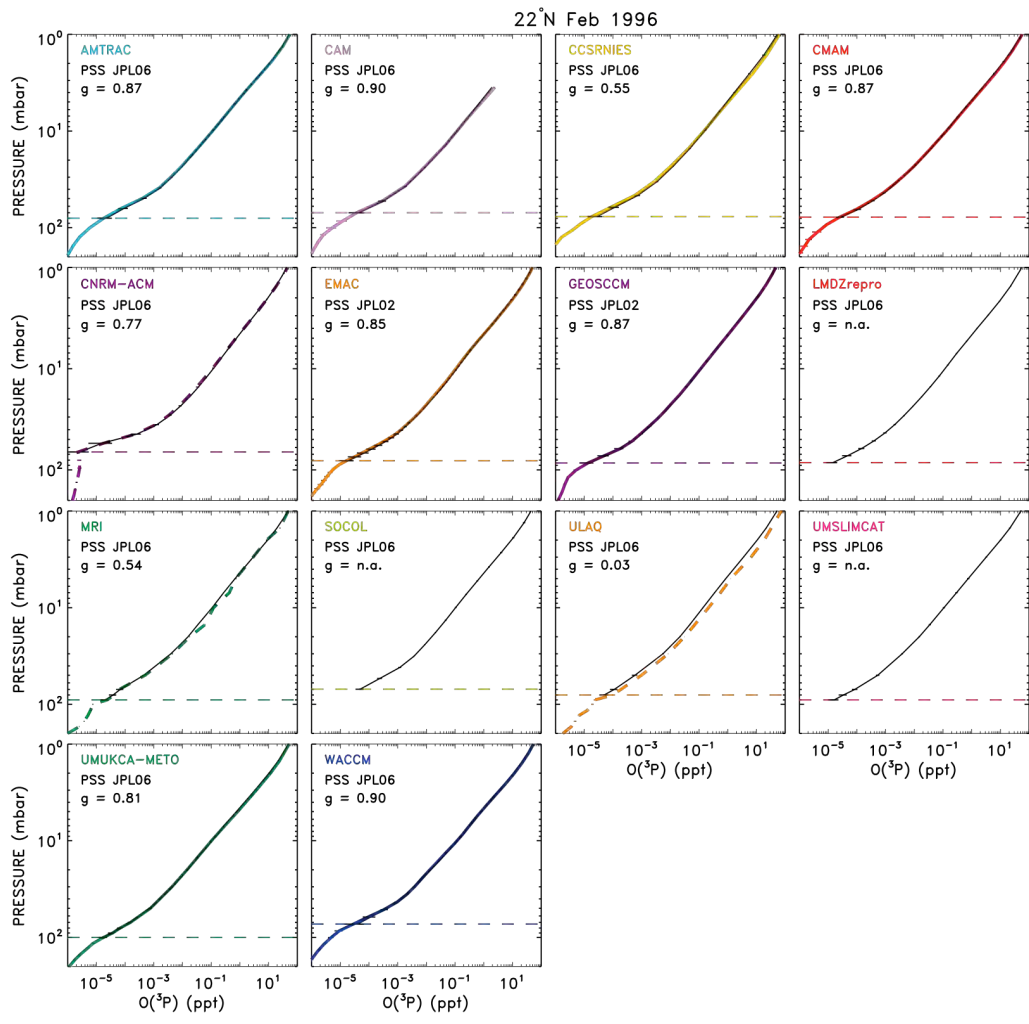


39  
 40 **Figure 6S-3b:** Same as Figure 6S-3a, except comparisons of NO<sub>Y</sub> vs N<sub>2</sub>O and  
 41 H<sub>2</sub>O+2×CH<sub>4</sub> vs N<sub>2</sub>O are shown.



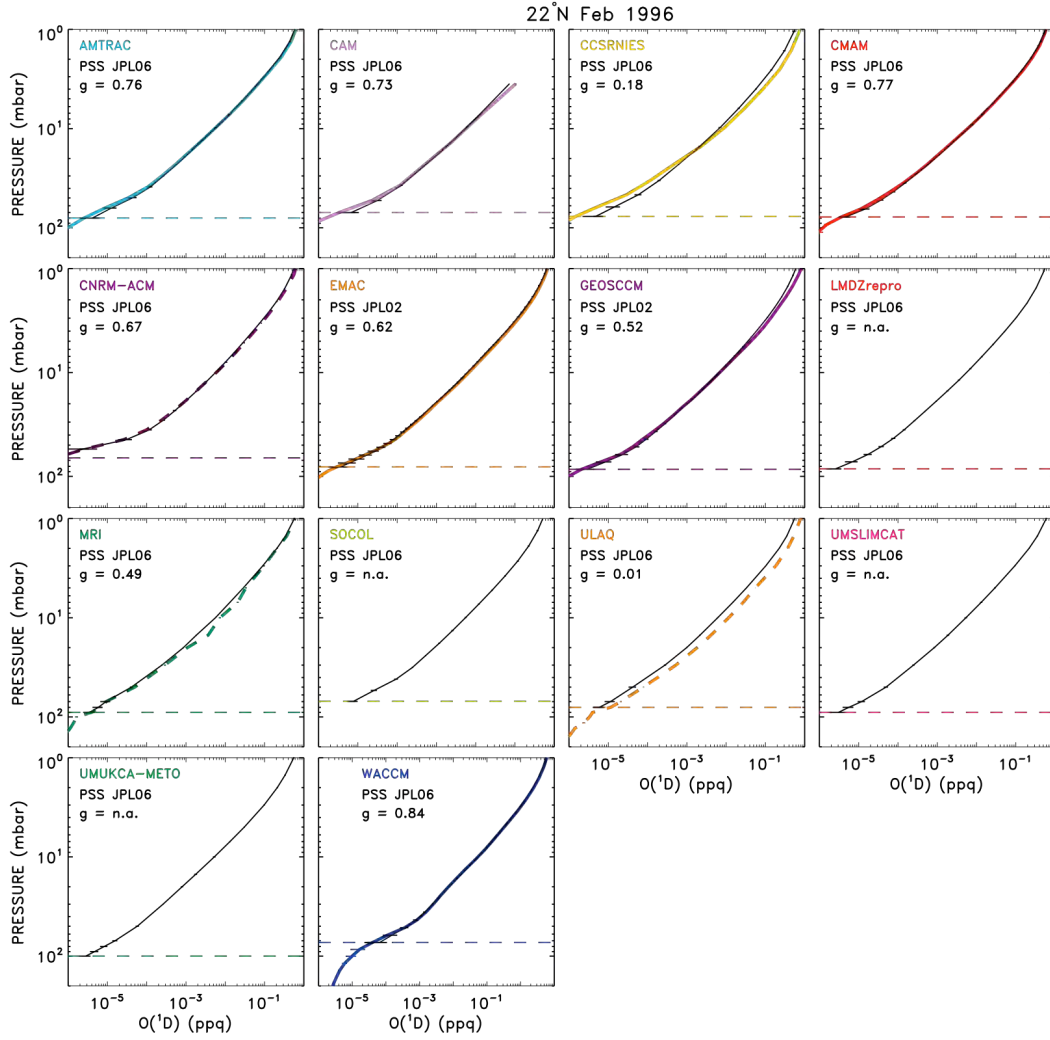
42  
43  
44  
45

**Figure 6S-3c:** same as Figure 6S-3a, except comparisons of  $Cl_Y$  vs  $N_2O$  and  $Br_Y$  vs  $N_2O$  are shown.



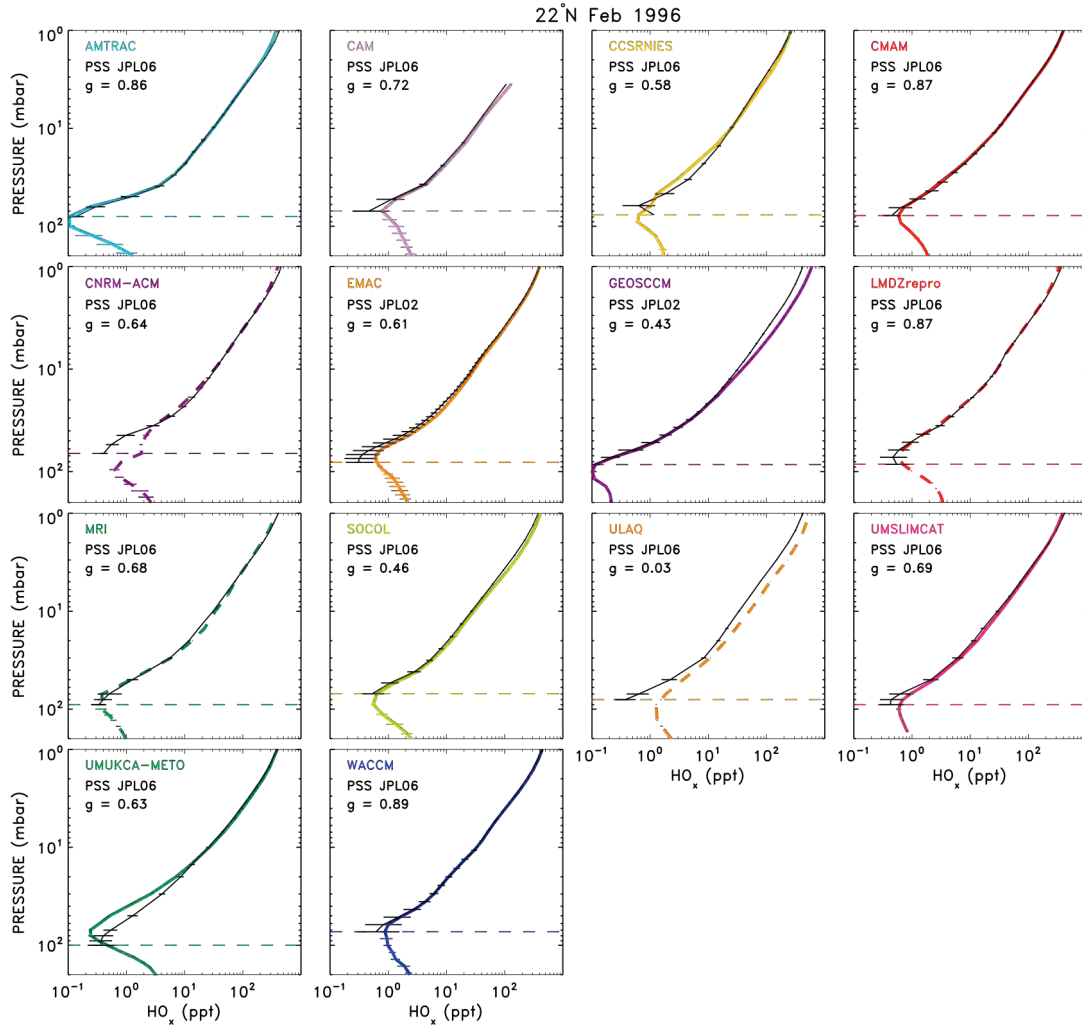
46  
 47  
 48  
 49  
 50  
 51  
 52  
 53  
 54  
 55  
 56  
 57  
 58

**Figure 6S-4a:** Comparison of zonal, monthly mean profiles of  $O(^3P)$  radicals from CCM models (coloured lines and symbols) versus 24-hour average radical profiles found using a PSS box model constrained by profiles of T,  $O_3$ ,  $H_2O$ ,  $CH_4$ , CO,  $NO_Y$ ,  $Cl_Y$ ,  $Br_Y$ , and sulfate SAD from the various CCMs for  $22^\circ N$  in **February 1996**. The PSS model was run for CCM model levels from the tropopause (dashed lines) to 1 hPa. The PSS model uses the latitude of the CCM output that is closest to  $22^\circ N$  and solar declination corresponding to the mid point of the monthly mean. Numerical values of g and the chemical kinetics in the simulation are given (see main chapter text). The coloured error bars represent the standard deviation about the zonal monthly mean for various days used to compute the mean. The black error bars represent the sensitivity of PSS output to variability in the CCM profiles of radical precursors.



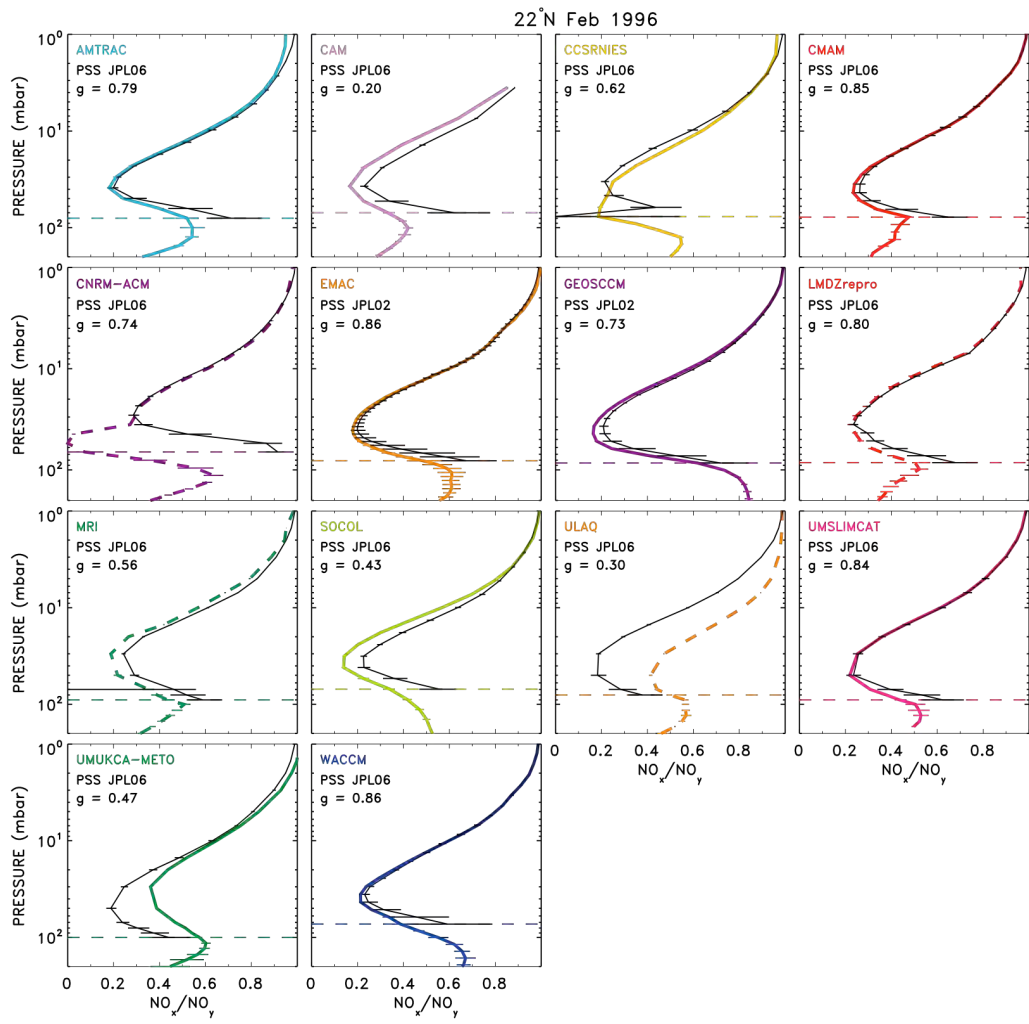
59  
60

Figure 6S-4b: same as Figure 6S-4a, except  $O(^1D)$  is shown.



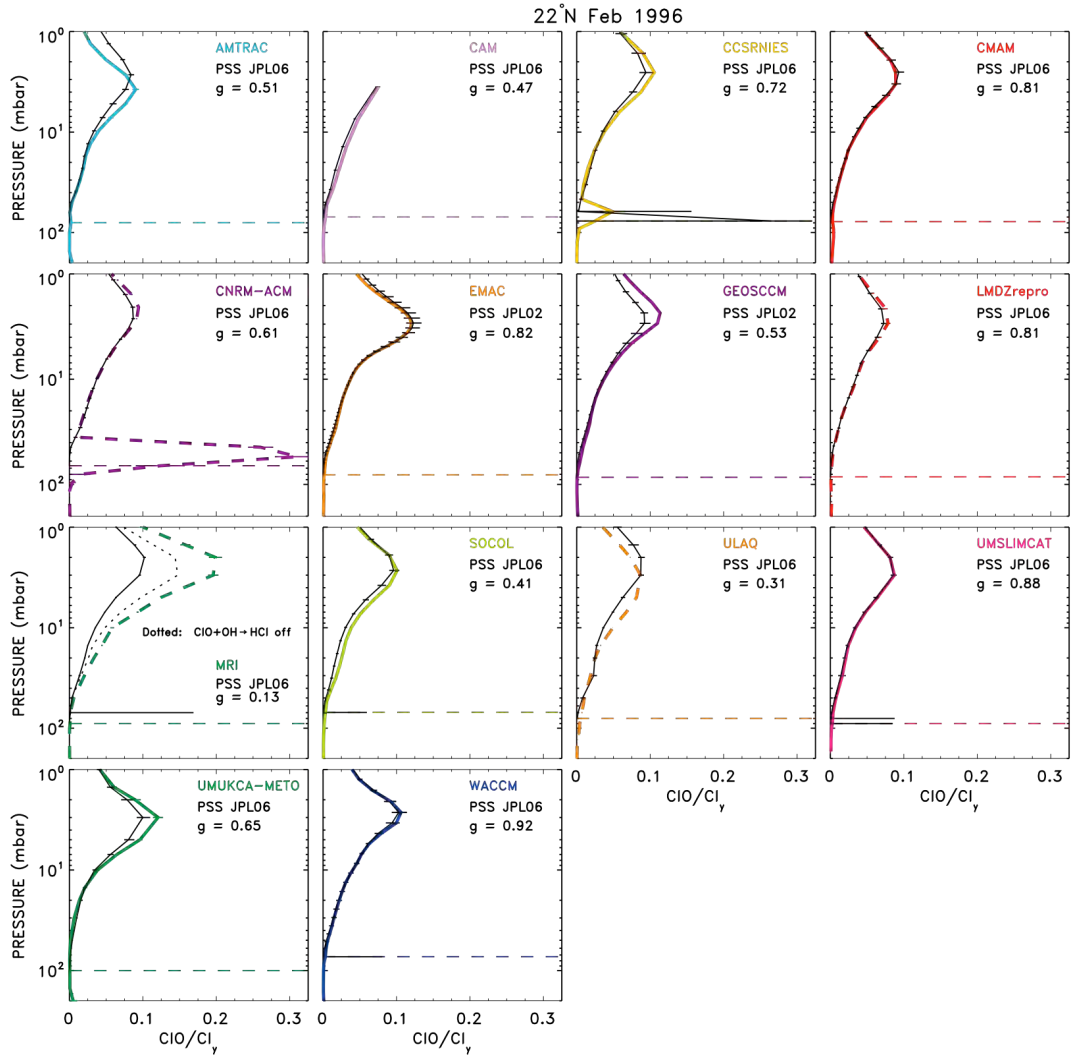
61  
62

Figure 6S-4c: same as Figure 6S-4a, except  $\text{HO}_x$  is shown.



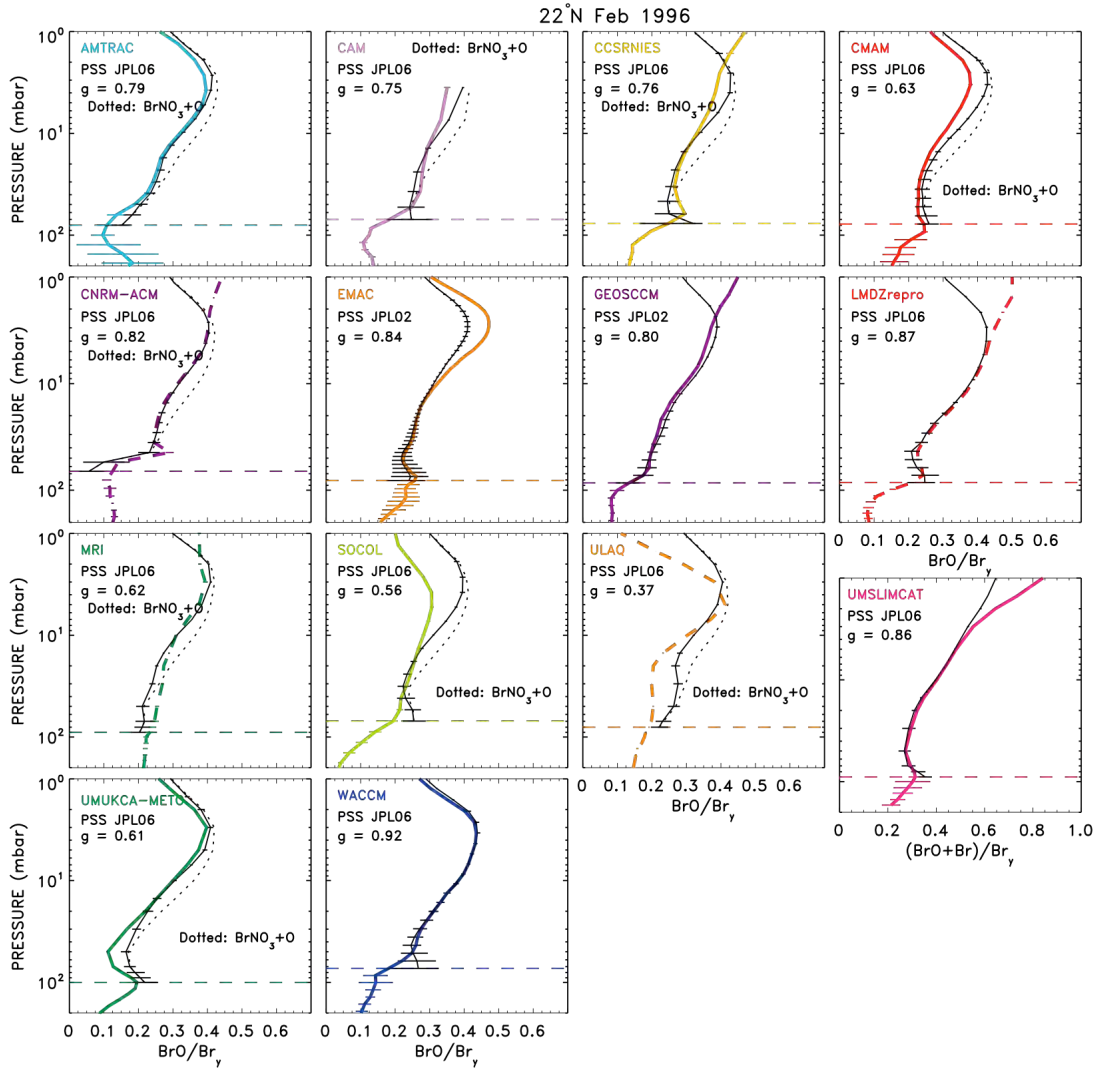
63  
64

Figure 6S-4d: same as Figure 6S-4a, except  $\text{NO}_x/\text{NO}_y$  is shown.



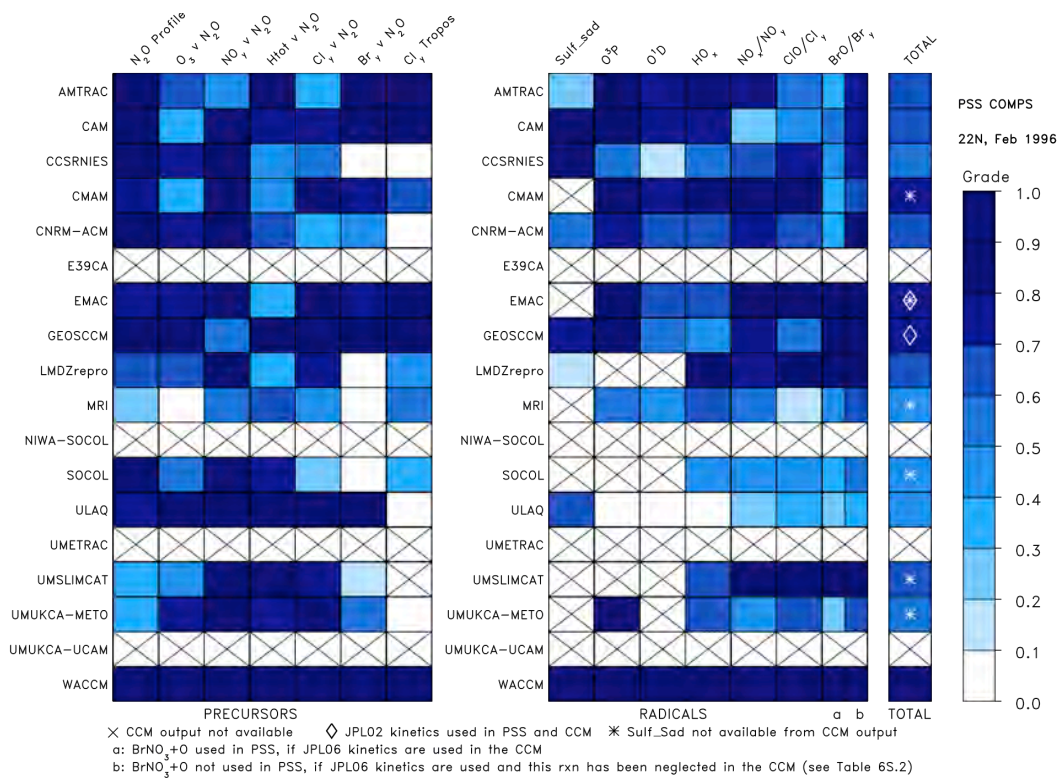
65  
66

Figure 6S-4e: same as Figure 6S-4a, except  $\text{ClO}/\text{Cl}_y$  is shown.

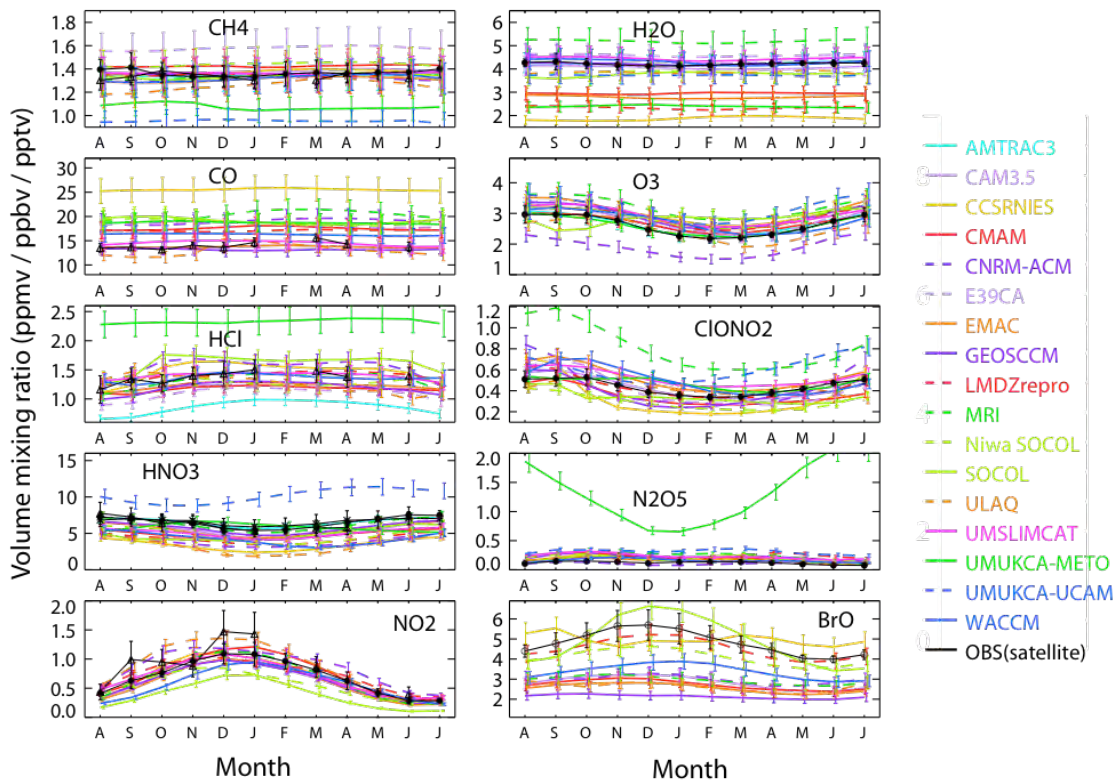


67  
68 **Figure 6S-4f:** same as Figure 6S-4a, except  $\text{BrO}/\text{Br}_y$  is shown.

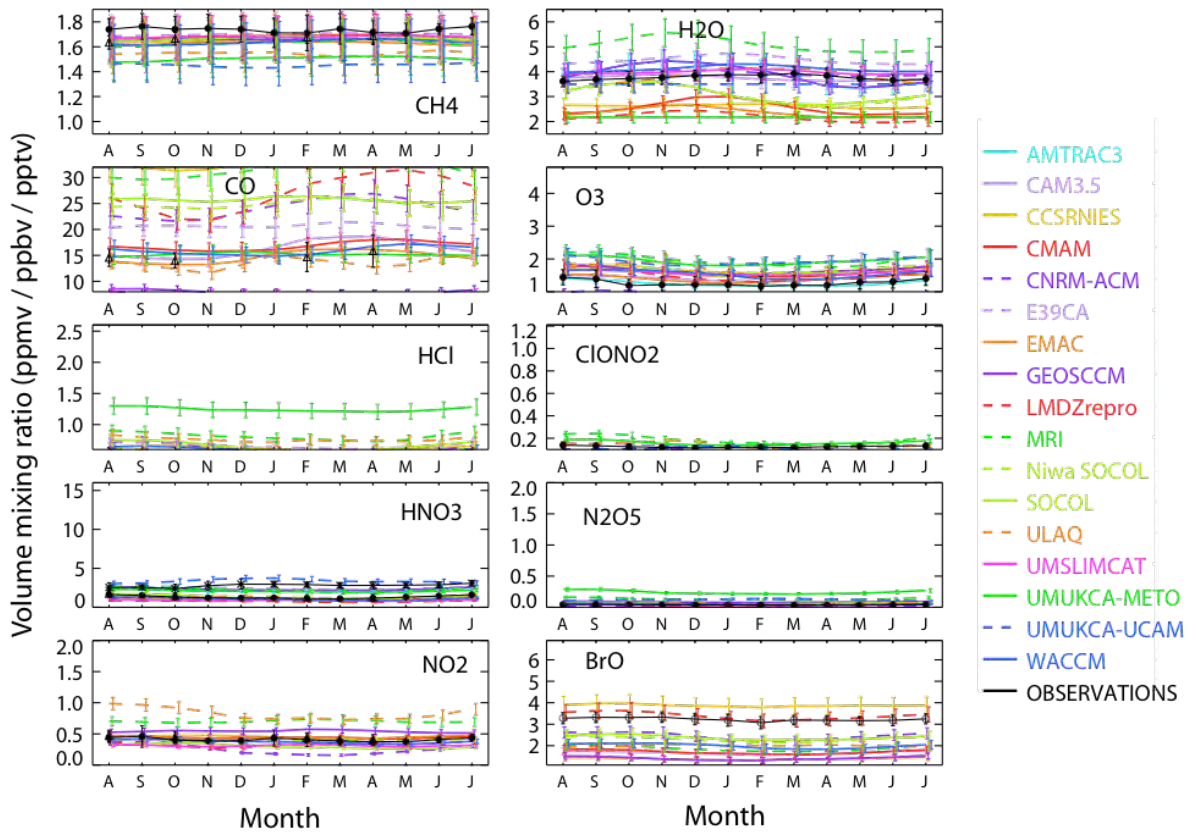




69  
 70 **Figure S6-5:** Metrics for (a, left) radical precursors and (b, right) sulfate surface area and  
 71 radicals for a simulation carried out at 22°N February 1996. The same dark shade of blue  
 72 is used for  $0.8 < g < 1.0$ , reflecting that there is little significance in differences that fall  
 73 within this range of values. The symbol X denotes CCM output not archived; ◇ denotes  
 74 use of JPL-2002 kinetics, and \* denotes sulfate SAD not archived (see main chapter text).  
 75 For models that used JPL-2006 kinetics and neglected the BrONO<sub>2</sub>+O reaction, two  
 76 grades are given for the evaluation of BrO/Br<sub>γ</sub> (see text).  
 77  
 78

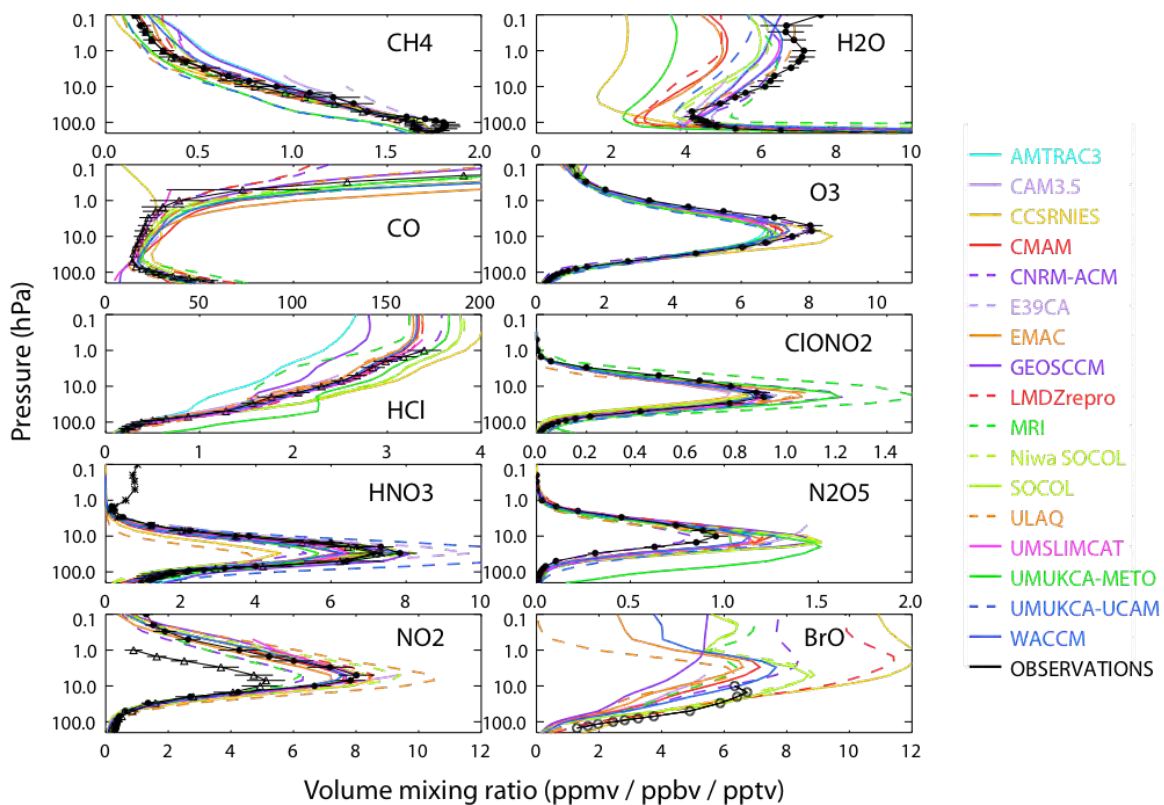


79  
 80 **Figure 6S-6:** Mean annual cycle for 30°S-60°S at 50 hPa for modelled (a) CH<sub>4</sub>, (ppmv)  
 81 (b) H<sub>2</sub>O (ppmv), (c) CO (ppbv), (d) O<sub>3</sub> (ppmv), (e) HCl (ppbv), (f) ClONO<sub>2</sub> (ppbv), (g)  
 82 HNO<sub>3</sub> (ppbv), (h) N<sub>2</sub>O<sub>5</sub> (ppbv), (i) NO<sub>2</sub> (ppbv) and (j) BrO (pptv). The CCM data is  
 83 taken from the T2Mz files (2000-2004, except E39CA model 1996-2000). Also shown  
 84 are corresponding satellite observations from MIPAS (CH<sub>4</sub>, H<sub>2</sub>O, O<sub>3</sub>, ClONO<sub>2</sub>, HNO<sub>3</sub>,  
 85 N<sub>2</sub>O<sub>5</sub>, NO<sub>2</sub>), ACE (CO, HCl), ODIN (HNO<sub>3</sub>) and SCIAMACHY (BrO). The error bars  
 86 are the standard deviations in the monthly mean values (except for ACE data).



87  
88  
89

**Figure 6S-7:** As Figure 6S-6 but for the tropics 30°S-30°N.



90  
91  
92  
93  
94  
95  
96  
97  
98

**Figure 6S-8:** Mean profiles for 30°N-60°N for modelled (a) CH<sub>4</sub>, (ppmv) (b) H<sub>2</sub>O (ppmv), (c) CO (ppbv), (d) O<sub>3</sub> (ppmv), (e) HCl (ppbv), (f) ClONO<sub>2</sub> (ppbv), (g) HNO<sub>3</sub> (ppbv), (h) N<sub>2</sub>O<sub>5</sub> (ppbv), (i) NO<sub>2</sub> (ppbv) and (j) BrO (pptv). The CCM data is taken from the T2Mz files (2000-2004, except E39CA model 1996-2000). Also shown are corresponding satellite observations from MIPAS (CH<sub>4</sub>, H<sub>2</sub>O, O<sub>3</sub>, ClONO<sub>2</sub>, HNO<sub>3</sub>, N<sub>2</sub>O<sub>5</sub>, NO<sub>2</sub>), ACE (CO, HCl), ODIN (HNO<sub>3</sub>) and SCIAMACHY (BrO). The error bars are the standard deviations in the annual mean values (except for ACE data).

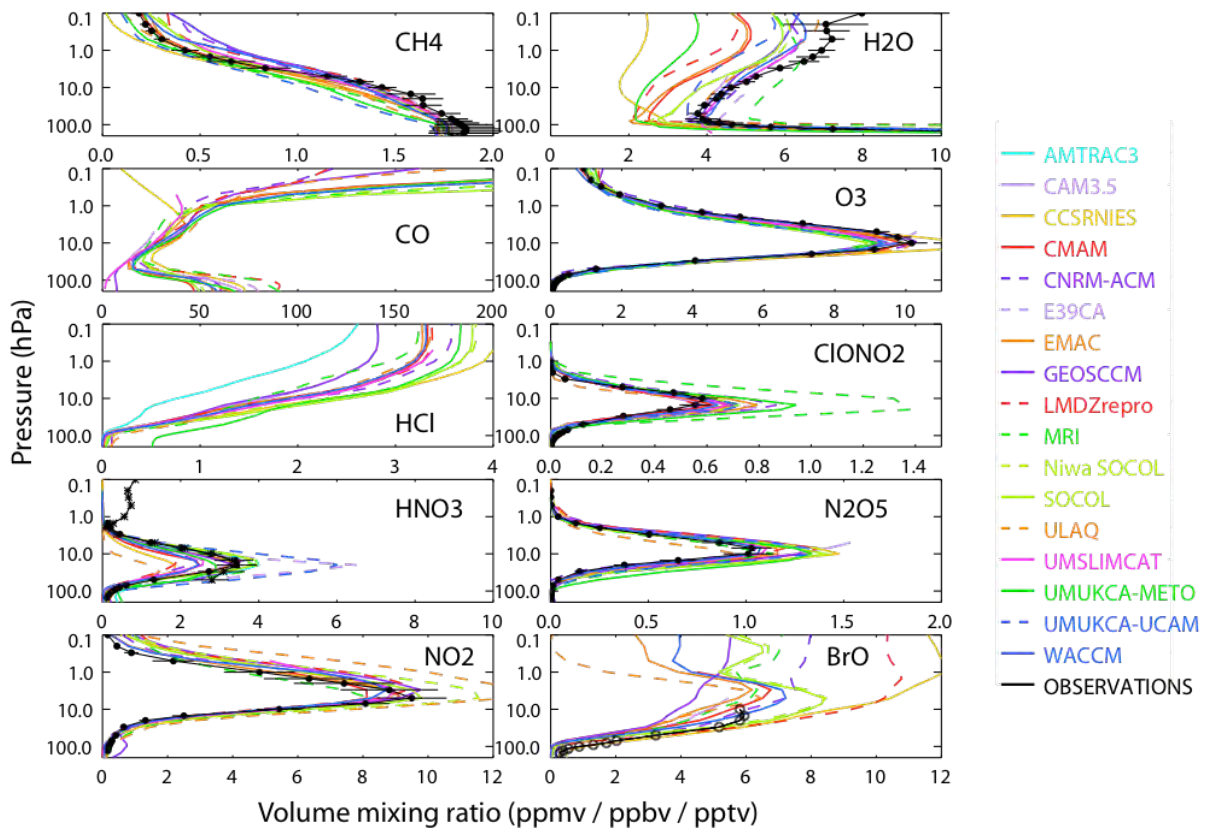
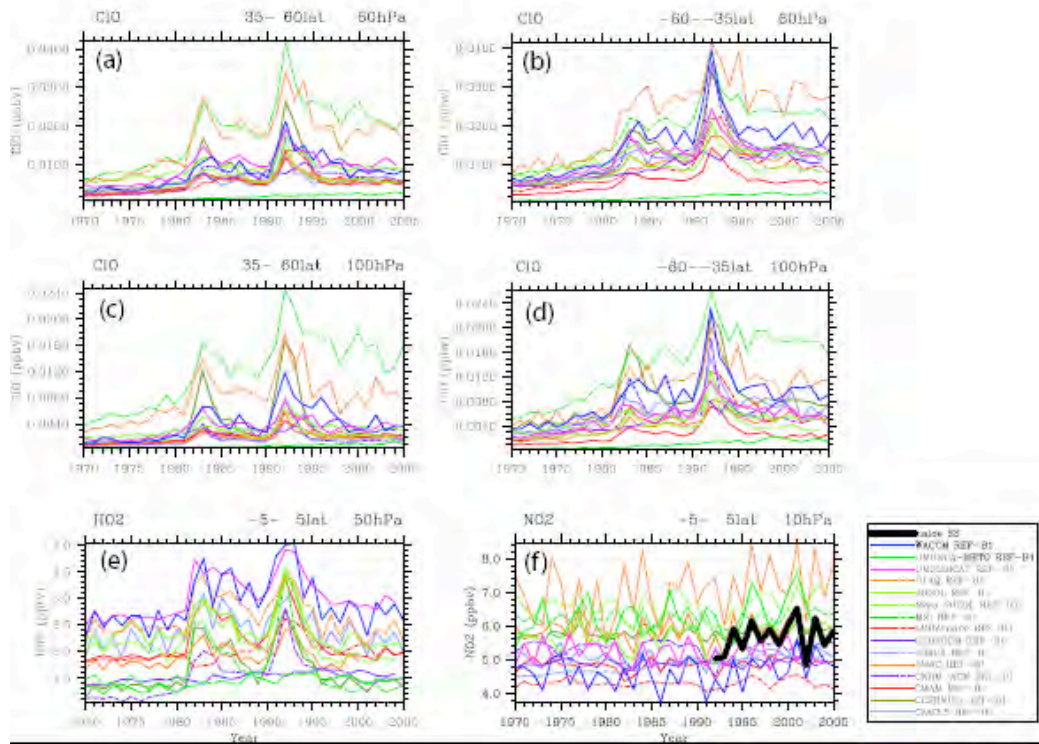


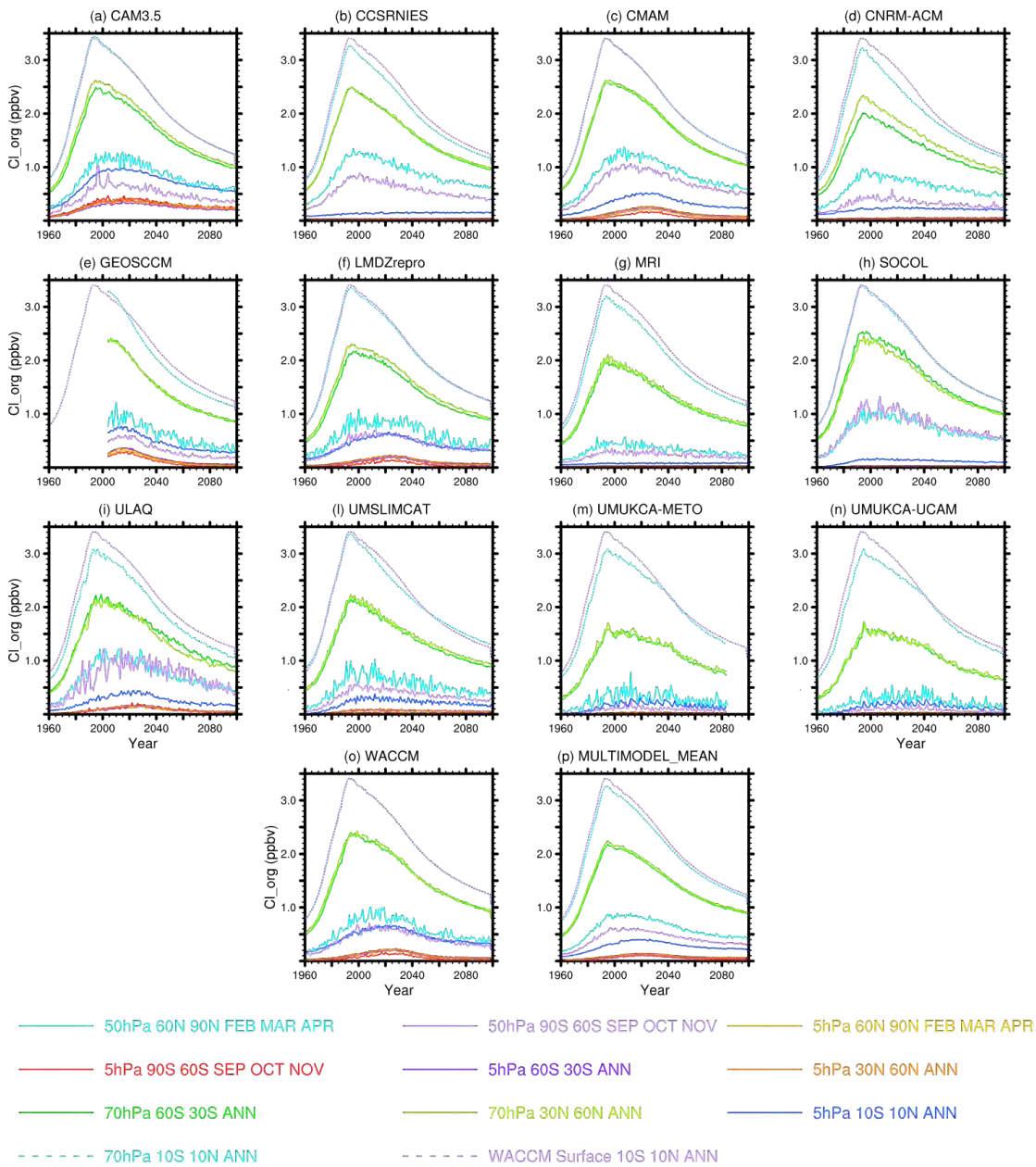
Figure 6S-9: As Figure 6S-8 but for the tropics 30°S-30°N.

99  
 100  
 101  
 102



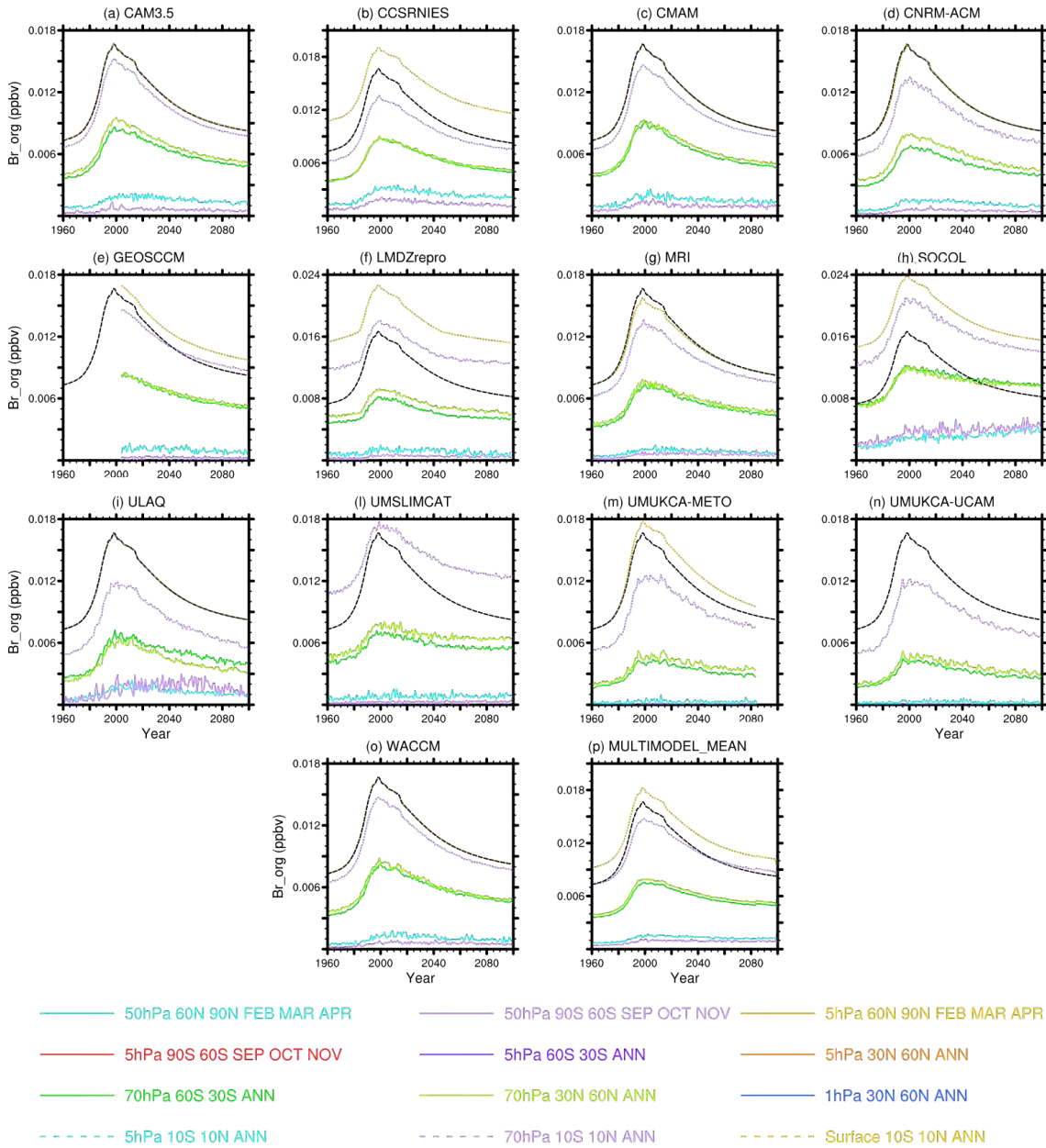
103  
 104  
 105  
 106  
 107  
 108  
 109  
 110  
 111  
 112

**Figure 6S-10.** Time series of mean tracer mixing ratios for (a) ClO (ppbv) 35°N-60°N at 60 hPa, (b) ClO (ppbv) 35°S-60°S at 60 hPa, (c) ClO (ppbv) 35°N-60°N at 100 hPa, (d) ClO (ppbv) 35°S-60°S at 100 hPa, (e) HO<sub>2</sub> (pptv) 5°S-5°N at 50 hPa, and (f) NO<sub>2</sub> (ppbv) 5°S-5°N at 10 hPa. Also shown for NO<sub>2</sub> are HALOE sunset observations converted to 24-hr mean using output from the EMAC model.



113  
 114  
 115  
 116  
 117  
 118  
 119  
 120  
 121

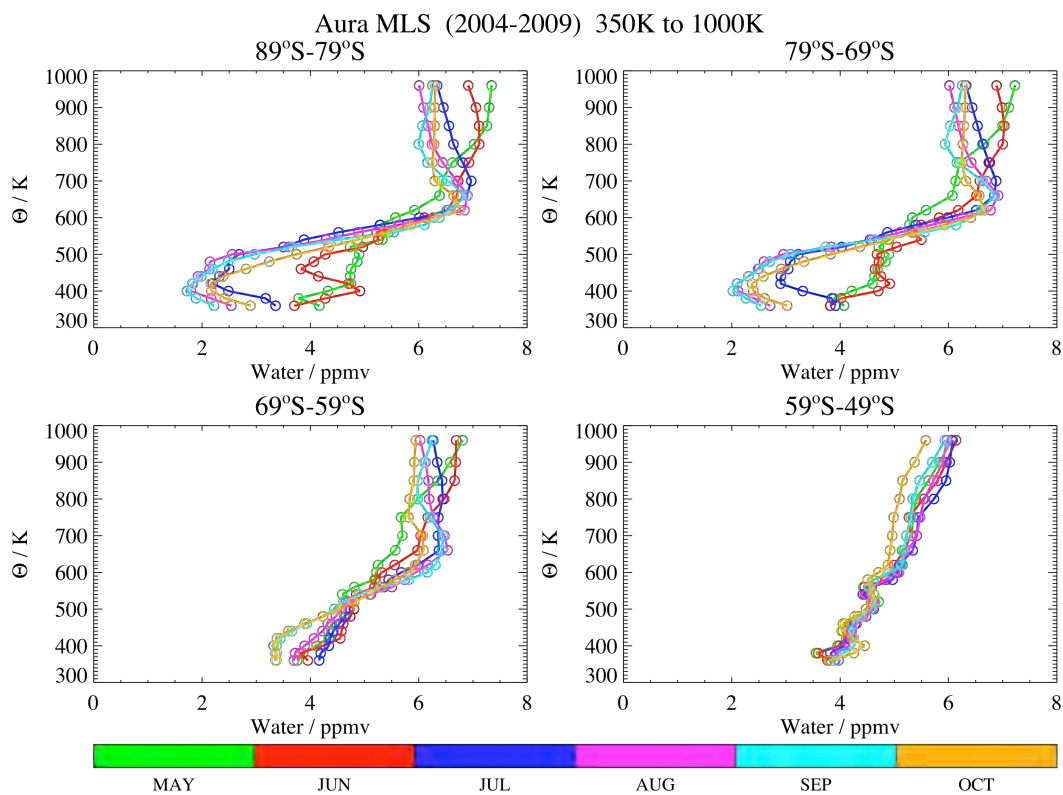
**Figure 6S-11:** Time series of organic chlorine volume mixing ratio (organic chlorine tracers) (ppbv) from 1960 to 2100 from 13 **REF-B2** CCM simulations and the multimodel mean. A selection of averages within different latitude bands and at different altitudes are plotted. For reference, each panel also includes the total chlorine curve from the WACCM model at the surface (black dashed line).



122  
 123  
 124  
 125

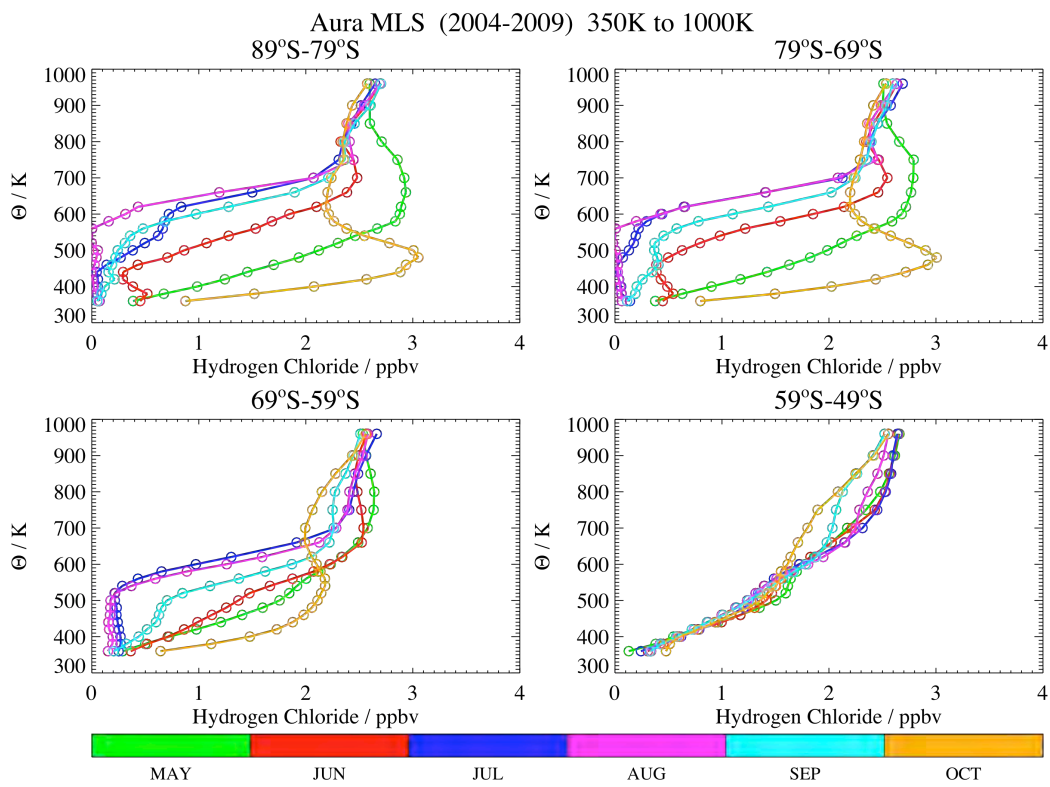
**Figure 6S-12:** As Figure 6S-11 but for organic bromine mixing ratio (pptv).





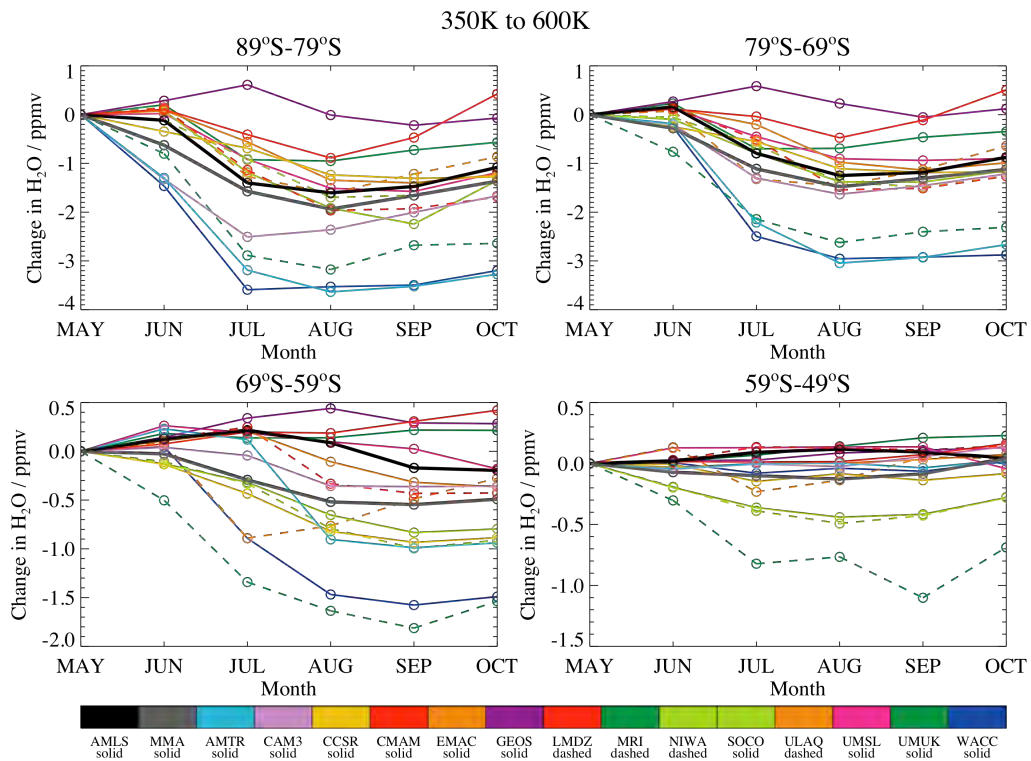
126  
127  
128  
129  
130  
131

**Figure 6S-13.** Southern hemisphere profiles of H<sub>2</sub>O versus  $\theta$  from Aura MLS at mid-month (on the 15<sup>th</sup> day of each month shown in colour bar), from May through October, based on a 5-yr MLS climatology (mid-2004 to mid-2009). Profiles are averaged over the EqL ranges shown above each panel.



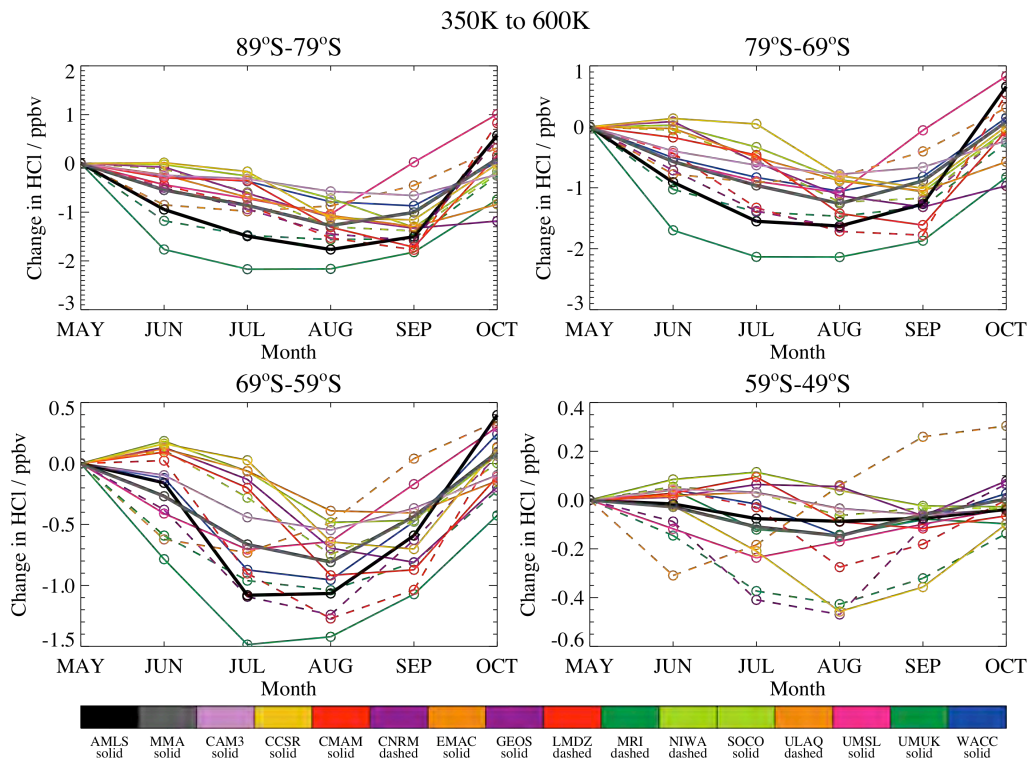
132  
133

**Figure 6S-14.** Same as Figure 6S-13, except for HCl.



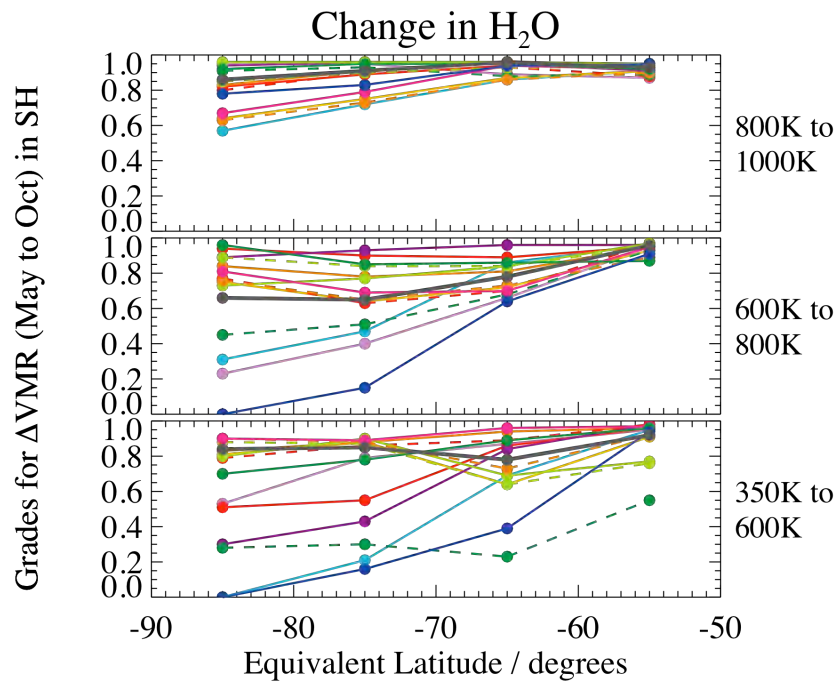
134  
 135  
 136  
 137  
 138

**Figure 6S-15:** Change in H<sub>2</sub>O from 350K to 600K, relative to May, for Aura MLS (abbreviated as AMLS in legend) and 14 CCM climatologies (legend uses first 4 letters of each model) and multimodel mean.



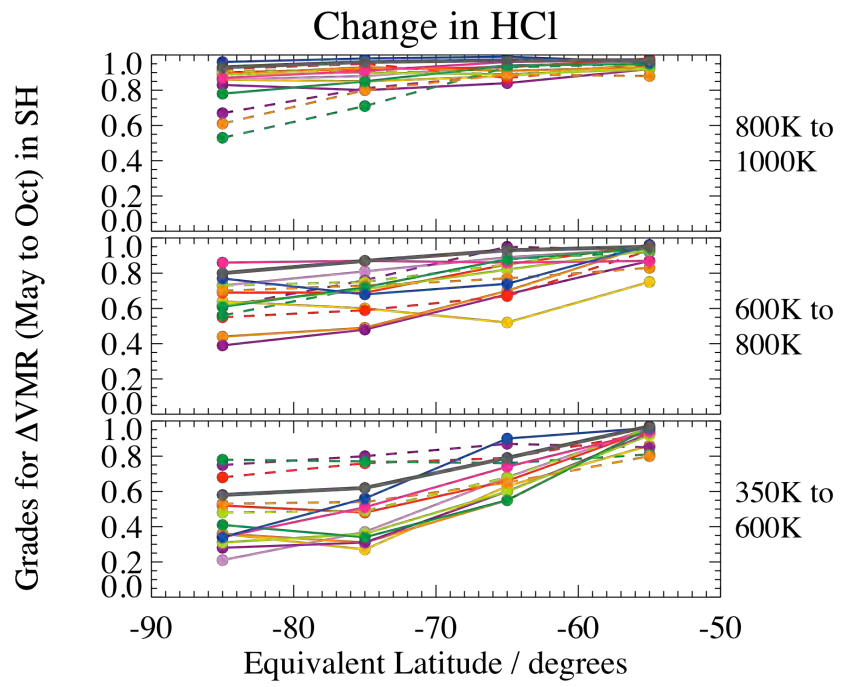
139  
140  
141

**Figure 6S-16:** As Figure 6S-15 but for HCl.



142  
 143  
 144  
 145  
 146  
 147

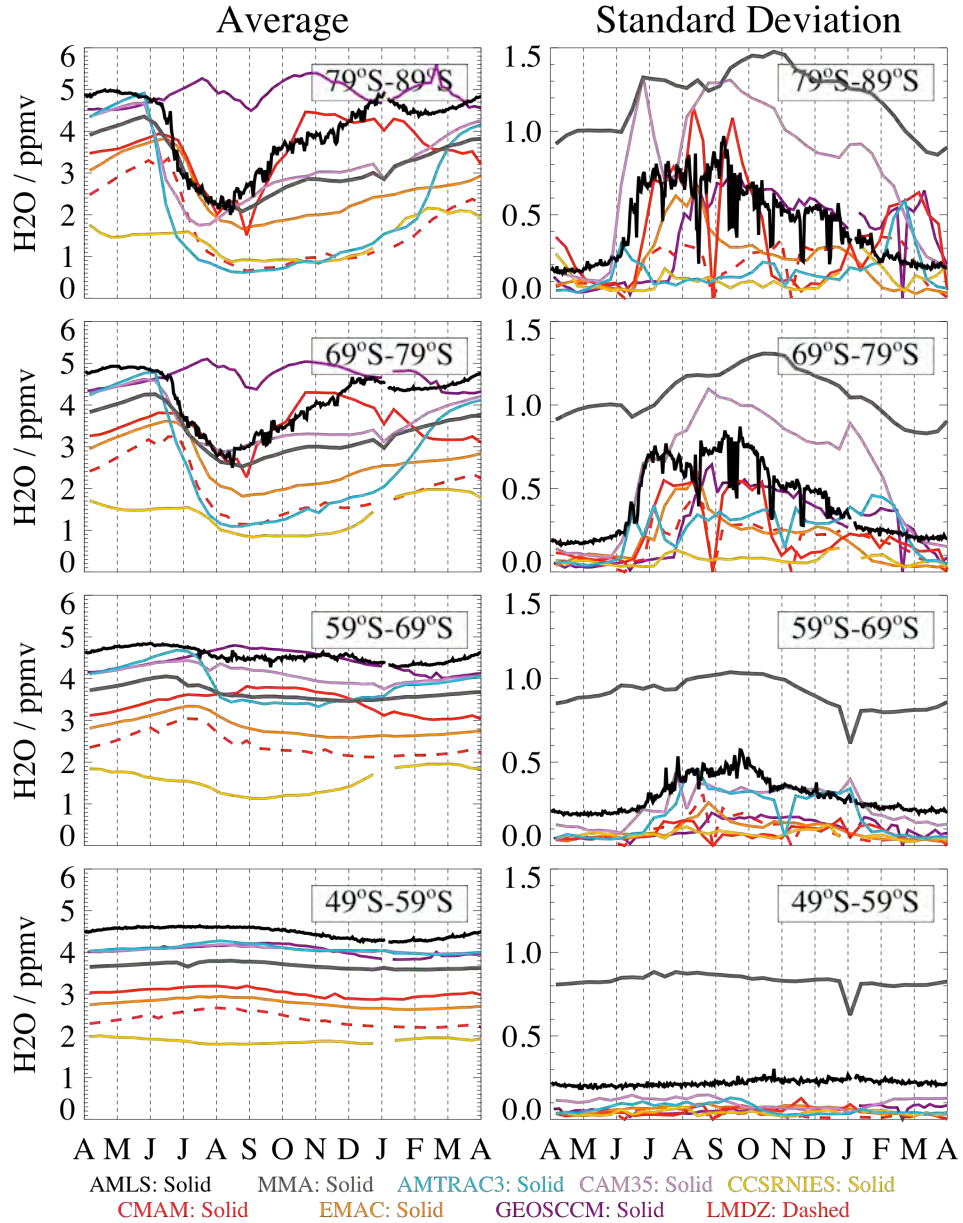
**Figure 6S-17:** Grades obtained for 14 CCMs from a comparison of model versus MLS-derived climatological changes in H<sub>2</sub>O (see main chapter text and Figure 6S-12). Grades are calculated for 4 EqL bins and 3 ranges of  $\theta$  values. Colours and linestyles correspond to those shown in Figure 6S-16.



148  
 149  
 150

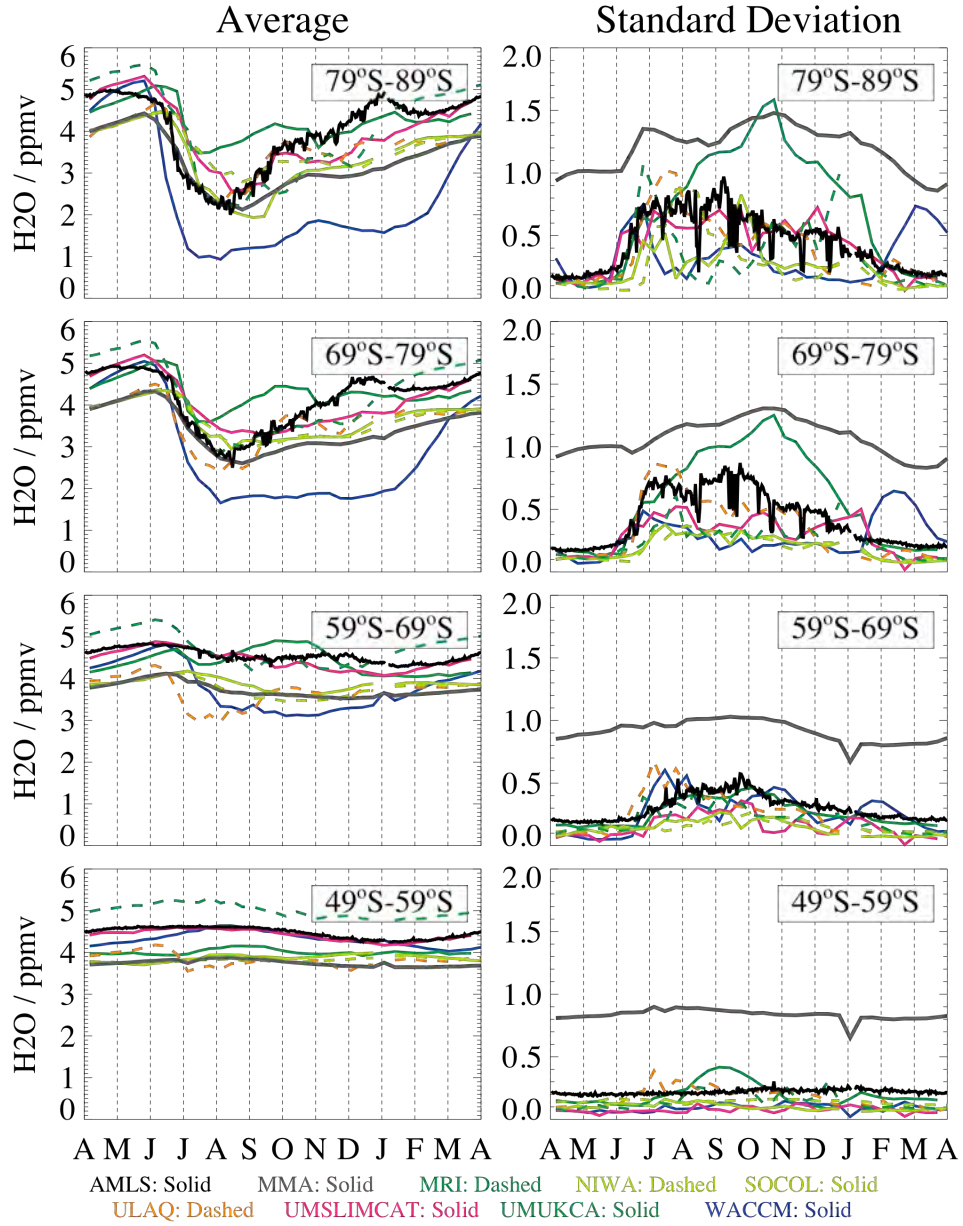
**Figure 6S-18:** As Figure 6S-17 but for HCl.

Southern Hemisphere at 500K  
H<sub>2</sub>O from CCM and Aura MLS Climatologies



151  
 152 **Figure 6S-19a:** Left panels display variations in average H<sub>2</sub>O at 500K during the course  
 153 of a year in 4 EqL bins, based on climatologies from Aura MLS (black, solid lines) and 7  
 154 CCMs (with model sources shown in bottom legend). Right panels show the  
 155 corresponding rms variability over the 5-year climatology, for each sampled day of year.  
 156

Southern Hemisphere at 500K  
H<sub>2</sub>O from CCM and Aura MLS Climatologies

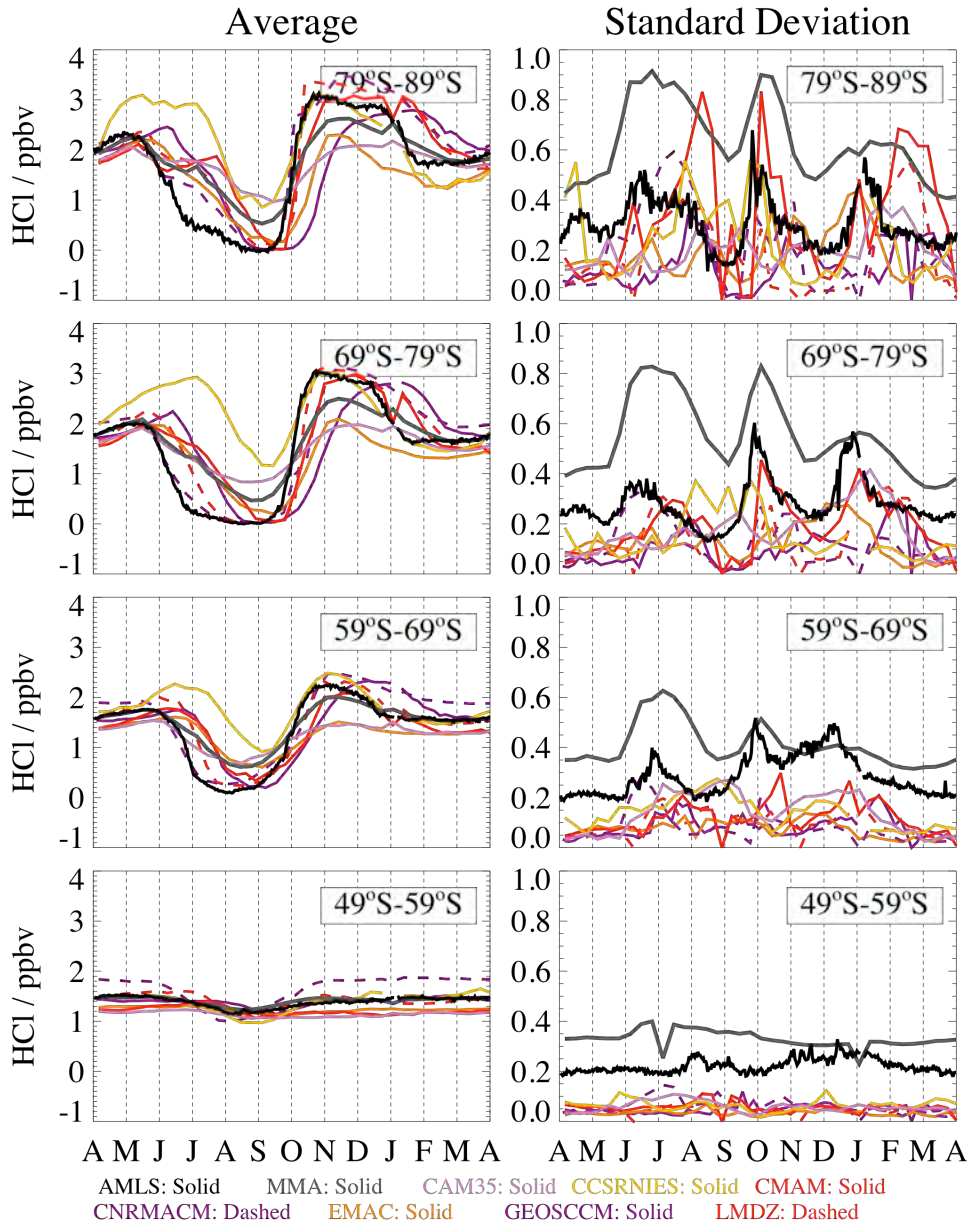


157  
158  
159  
160

**Figure 6S-19b:** Same as Figure 6S-16a, but for Aura MLS H<sub>2</sub>O (and its rms variability) compared to the 7 other available CCM distributions of H<sub>2</sub>O versus time of year.

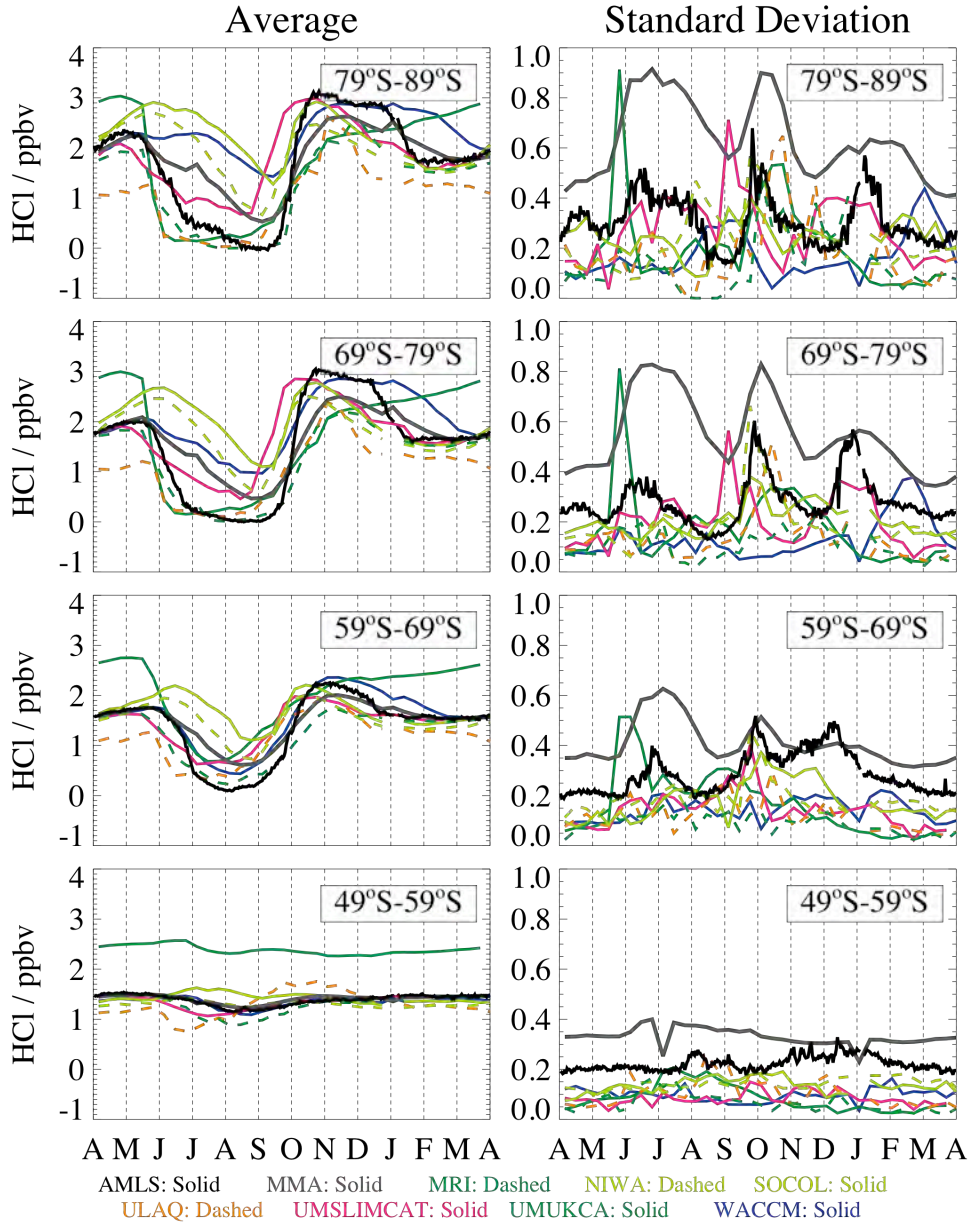


Southern Hemisphere at 500K  
HCl from CCM and Aura MLS Climatologies



161  
162 **Figure 6S-20a:** Left panels display variations in average HCl at 500K during the course  
163 of a year in 4 EqL bins, based on climatologies from Aura MLS (black, solid lines) and 7  
164 CCMs (with model sources shown in bottom legend). Right panels show the  
165 corresponding rms variability over the 5-year climatology, for each sampled day of year.  
166

Southern Hemisphere at 500K  
HCl from CCM and Aura MLS Climatologies



167  
168  
169  
170

**Figure 6S-20b:** Same as Figure 6S-20a, but for Aura MLS HCl (and its rms variability) compared to the 7 other available CCM distributions of HCl versus time of year.

171 **Chapter 6 Supplemental Tables 1-4 and Photocomp 2008 Instructions**

172

173 **Table 6S-1. Chemical Species in CCMs** (1=AMTRAC3; 2=CAM3.5; 3=CCSRNIES; 4=CMAM; 5=CNRM-ACM; 6=E39CA;  
 174 7=EMAC; 8=GEOSCCM; 9=LMDZrepro; 10=MRI; 11=NIWA-SOCOL; 12=SOCOL; 13=ULAQ; 14=UMETRAC;  
 175 15=UMSLIMCAT; 16=UMUKCA-METO; 17=UMUKCA-UCAM; 18=WACCM; 19= PSS model).

#		1	2	3	4	5	6	7	8	9	10	11	12	13	14	15	16	17	18	19	
1	O( <sup>3</sup> P)	Y	Y	Y	Y	Y	Y	Y	Y*	Y	Y	Y	Y	Y	Y	Y	Y	Y	Y	Y	Y
2	O( <sup>1</sup> D)	Y	Y	Y	Y	Y	Y	Y	Y*	Y	Y	Y	Y	Y	Y	Y	Y	Y	Y	Y	Y
3	O <sub>3</sub>	Y	Y	Y	Y	Y	Y	Y	Y*	Y	Y	Y	Y	Y	Y	Y	Y	Y	Y	Y	Y
4	O <sub>2</sub>	Y	Y	Y	Y	Y	Y	Y	Y	Y	Y	Y	Y	Y	Y	Y	Y	Y	Y	Y	Y
5	H	Y	N	Y	Y	Y	Y	Y	Y*	Y	Y	Y	Y	Y	Y	Y	Y	Y	Y	Y	Y
6	OH	Y	Y	Y	Y	Y	Y	Y	Y*	Y	Y	Y	Y	Y	Y	Y	Y	Y	Y	Y	Y
7	HO <sub>2</sub>	Y	Y	Y	Y	Y	Y	Y	Y*	Y	Y	Y	Y	Y	Y	Y	Y	Y	Y	Y	Y
8	H <sub>2</sub>	N	Y	Y	Y	N	Y	Y	N	N	Y	Y	Y	Y	N	Y	Y	Y	Y	Y	Y
9	H <sub>2</sub> O <sub>2</sub>	Y	Y	Y	Y	Y	Y	Y	Y	Y	Y	Y	Y	Y	Y	Y	Y	Y	Y	Y	Y
10	N	Y	Y	Y	Y	Y	Y	Y	Y*	Y	Y	Y	Y	Y	Y	Y	Y	Y	Y	Y	Y
11	NO	Y	Y	Y	Y	Y	Y	Y	Y*	Y	Y	Y	Y	Y	Y	Y	Y	Y	Y	Y	Y
12	NO <sub>2</sub>	Y	Y	Y	Y	Y	Y	Y	Y*	Y	Y	Y	Y	Y	Y	Y	Y	Y	Y	Y	Y
13	NO <sub>3</sub>	Y	Y	Y	Y	Y	Y	Y	Y*	Y	Y	Y	Y	Y	Y	Y	Y	Y	Y	Y	Y
14	N <sub>2</sub> O <sub>5</sub>	Y	Y	Y	Y	Y	Y	Y	Y	Y	Y	Y	Y	Y	Y	Y	Y	Y	Y	Y	Y
15	HONO	Y	N	N	N	N	Y	Y	N	N	N	N	N	N	Y	N	N	N	N	N	Y
16	HNO <sub>3</sub>	Y	Y	Y	Y	Y	Y	Y	Y	Y	Y	Y	Y	Y	Y	Y	Y	Y	Y	Y	Y
17	HO <sub>2</sub> NO <sub>2</sub>	Y	Y	Y	Y	Y	Y	Y	Y	Y	Y	Y	Y	Y	Y	Y	Y	Y	Y	Y	Y
18	Cl	Y	Y	Y	Y	Y	Y	Y	Y*	Y	Y	Y	Y	Y	Y	Y	Y	Y	Y	Y	Y
19	ClO	Y	Y	Y	Y	Y	Y	Y	Y*	Y	Y	Y	Y	Y	Y	Y	Y	Y	Y	Y	Y
20	Cl <sub>2</sub>	N	Y	Y	Y	Y	Y	Y	Y	Y	N	Y	Y	N	N	N	N	N	N	Y	Y
21	OCIO	N	Y	Y	Y	Y	Y	Y	Y	Y	Y	N	N	N	N	Y	Y	Y	Y	Y	Y
22	Cl <sub>2</sub> O <sub>2</sub>	Y	Y	Y	Y	Y	Y	Y	Y*	Y	Y	Y	Y	Y	Y	Y	Y	Y	Y	Y	Y
23	HCl	Y	Y	Y	Y	Y	Y	Y	Y	Y	Y	Y	Y	Y	Y	Y	Y	Y	Y	Y	Y
24	HOCl	Y	Y	Y	Y	Y	Y	Y	Y	Y	Y	Y	Y	Y	Y	Y	Y	Y	Y	Y	Y

#		1	2	3	4	5	6	7	8	9	10	11	12	13	14	15	16	17	18	19
25	ClONO <sub>2</sub>	Y	Y	Y	Y	Y	Y	Y	Y	Y	Y	Y	Y	Y	Y	Y	Y	Y	Y	Y
26	Br	Y	Y	Y	Y	Y	Y*	Y	Y*	Y	Y	Y	Y	Y	Y	Y	Y	Y	Y	Y
27	BrO	Y	Y	Y	Y	Y	Y*	Y	Y*	Y	Y	Y	Y	Y	Y	Y	Y	Y	Y	Y
28	HOBr	Y	Y	Y	Y	Y	Y*	Y	Y	Y	Y	Y	Y	Y	Y	Y	Y	Y	Y	Y
29	HBr	Y	Y	Y	Y	Y	Y*	Y	Y	Y	Y	Y	Y	Y	Y	Y	Y	Y	Y	Y
30	BrONO <sub>2</sub>	Y	Y	Y	Y	Y	Y*	Y	Y	Y	Y	Y	Y	Y	Y	Y	Y	Y	Y	Y
31	BrCl	Y	Y	Y	Y	Y	Y*	Y	Y	Y	Y	Y	Y	N	Y	Y	Y	Y	Y	Y
32	Br <sub>2</sub>	N	N	Y	N	N	Y*	N	N	N	N	N	N	N	N	N	N	N	N	N
33	CH <sub>4</sub>	Y	Y	Y	Y	Y	Y	Y	Y	Y	Y	Y	Y	Y	Y	Y	Y	Y	Y	Y
34	CH <sub>3</sub> O <sub>2</sub>	Y	Y	Y	Y	Y	Y	Y	Y*	Y	N	Y	Y	Y	Y	Y	Y	Y	Y	Y
35	CH <sub>3</sub> OOH	Y	Y	Y	Y	Y	Y	Y	Y	Y	N	Y	Y	Y	Y	Y	Y	Y	Y	Y
36	CH <sub>2</sub> O	Y	Y	Y	Y	Y	Y	Y	Y*	Y	N	Y	Y	Y	Y	Y	Y	Y	Y	Y
37	CO	Y	Y	Y	Y	Y	Y	Y	Y	Y	Y	Y	Y	Y	Y	Y	Y	Y	Y	Y
38	H <sub>2</sub> O	Y	Y	Y	Y	Y	Y	Y	Y	Y	Y	Y	Y	Y	Y	Y	Y	Y	Y	Y
39	N <sub>2</sub> O	Y	Y	Y	Y	Y	Y	Y	Y	Y	Y	Y	Y	Y	Y	Y	Y	Y	Y	N
40	CO <sub>2</sub>	N	N	N	a	N	Y	Y	N	N	Y	Y	Y	Y	N	Y	Y	Y	Y	N
41	C <sub>2</sub> H <sub>6</sub>	N	N	N	N	N	N	Y	N	N	N	N	N	Y	N	N	N	N	N	Y
42	CH <sub>3</sub> Cl	N	Y	Y	Y	Y	Y	Y	Y	Y	Y	Y	Y	Y	N	N	N	N	Y	N
43	CFC-11	N	Y	Y	Y	Y	Y	Y	Y	Y	Y	Y	Y	Y	N	Y	Y	Y	Y	N
44	CFC-12	N	Y	Y	Y	Y	Y	Y	Y	Y*	Y	Y	Y	Y	N	Y	Y	Y	Y	N
45	CFC-113	N	Y	Y	N	Y	N	*	Y	Y	N	Y	Y	Y	N	N	N	N	Y	N
46	HCFC-22	N	Y	Y	Y	Y	N	*	Y	Y	N	Y	Y	Y	N	N	N	N	Y	N
47	HCFC141b	N	a	N	N	N	N	*	a	a	N	Y	Y	a	N	N	N	N	a	N
48	HCFC142b	N	b	N	N	N	N	*	a	b	N	Y	Y	b	N	N	N	N	b	N
49	CCl <sub>4</sub>	N	Y	Y	Y	Y	Y	Y	Y	Y	Y	Y	Y	Y	N	N	N	N	Y	N
50	CH <sub>3</sub> CCl <sub>3</sub>	N	Y	Y	Y	Y	Y	Y	Y	Y	N	Y	Y	Y	N	N	N	N	Y	N
51	H-1202	N	c	N	N	N	N	N	N	c	N	N	N	c	N	N	N	N	c	N

#		1	2	3	4	5	6	7	8	9	10	11	12	13	14	15	16	17	18	19
52	H-1211	N	Y	Y	N	Y	N	Y	b	Y	Y	Y	Y	Y	N	N	N	N	Y	N
53	H-1301	N	Y	Y	N	Y	N	Y	Y	Y	Y	Y	Y	Y	N	N	N	N	Y	N
54	H-2402	N	d	N	N	N	N	N	b	d	N	Y	Y	d	N	N	N	N	d	N
55	CH <sub>3</sub> Br	N	Y	Y	Y	Y	Y*	Y	Y	Y	Y	Y	Y	Y	N	Y	Y	Y	Y	N
56	NMHCs	N	e	N	N	N	N	Y	N	N	N	N	N	Y	N	N	N	N	N	N

176

177 **Notes:**

178 Y = this species is explicitly derived. (O<sub>2</sub> specified as a constant volume mixing ratio).

179 N = this species is not explicitly derived.

180 NMHCs = the chemical mechanism includes a detailed representation of Non-Methane Hydrocarbons.

181

182 **Notes specific to each model:**

183 1: The halogen source molecules are parameterized to give realistic Cly and Bry.

184 2a-d: These species are not explicitly derived in CAM3.5. The time-dependent VMR lower boundary conditions for these species are added to surrogates with similar chemical lifetimes.

185 2e: CAM3.5 has a reduced NMHC mechanism for better representation of tropospheric chemistry.

186 3: The CCSRNIES model includes CHBr<sub>3</sub> with a constant surface mixing ratio of 1.8 pptv.

187 4a: For CMAM, photolysis of CO<sub>2</sub> is included (yielding CO + O(<sup>3</sup>P)) though the concentration of CO<sub>2</sub> is globally constant.

188 5: CNRM-ACM also includes ClNO<sub>2</sub> species.

189 6\*: E39CA uses parameterization of bromine-catalyzed ozone loss (Appendix in Stenke *et al.*, 2009).

190 7\*: Lumped into CFC-12 using weighting by amount of chlorine atoms.

191 8: GEOSCCM variables denoted by Y\* are inferred from transported chemical families. CO<sub>2</sub>, and H<sub>2</sub> are specified in the model.

192 8a: The surface boundary conditions of HCFC141b and HCFC142b are combined into one species defined as HCFC142b + 2\*HCFC141b to account for total chlorine atoms involved.

193 8b: The surface boundary conditions of H-1211 and H-2402 are combined into one species defined as H-1211 + 2\*H-2402 to account for the total bromine atoms involved.

194 9\*: CFC-114 and CFC-115 are lumped into CFC-12 using weighting by number of chlorine atoms.

195 9a: Lumped into CH<sub>3</sub>CCl<sub>3</sub> using weighting by number of chlorine atoms.

196 9b: Lumped into HCFC-22 using weighting by number of chlorine atoms.

200 9c: Lumped into CH<sub>3</sub>Br using weighting by number of bromine atoms.  
201 9d: Lumped into H-1301 using weighting by number of bromine atoms.  
202 12: In the CCMVal SOCOL runs chlorine source gases were lumped in CFC-11 and CFC-12 (based on lifetimes) and bromine  
203 source gases lumped into CH<sub>3</sub>Br.  
204 13: NMHC chemistry is included in ULAQ with a limited number of species (6), using lumping technique.  
205 15-17: In the CCMVal UMSLIMCAT and UMUKCA runs chlorine source gases were lumped in CFC-11 and CFC-12 (based on  
206 lifetimes) and bromine source gases lumped into CH<sub>3</sub>Br.  
207 18a-d: These species are not explicitly derived in WACCM. The time-dependent VMR lower boundary conditions for these species  
208 are added to surrogates with similar chemical lifetimes.  
209 19: The PSS model also includes: ClNO<sub>2</sub>, ClONO, ClOO, HOONO; ClNO<sub>2</sub> is produced by N<sub>2</sub>O<sub>5</sub>+HCl(het) & Cl+NO<sub>2</sub>; ClONO is  
210 also produced by Cl+NO<sub>2</sub> and ClONO<sub>2</sub> photolysis; ClOO is produced by ClO+ClO; HOONO is produced by NO<sub>2</sub>+OH. In this  
211 model, Cl<sub>y</sub>, NO<sub>y</sub>, and Br<sub>y</sub> are specified, rather than being produced from the organic source gases and N<sub>2</sub>O. C<sub>2</sub>H<sub>6</sub> from tracer  
212 relations, with the focus on its production of HOx radicals and HCl, via reaction with OH and Cl, respectively.  
213

213

214 **Table 6S-2. Gas-phase Reactions in CCMs** (1=AMTRAC3; 2=CAM3.5; 3=CCSRNIES; 4=CMAM; 5=CNRM-ACM; 6=E39CA;  
 215 7=EMAC; 8=GEOSCCM; 9=LMDZrepro; 10=MRI; 11=NIWA-SOCOL; 12=SOCOL; 13=ULAQ; 14=UMETRAC;  
 216 15=UMSLIMCAT; 16=UMUKCA-METO; 17=UMUKCA-UCAM; 18=WACCM; 19= PSS model).

#	Reactions	1	2	3	4	5	6	7	8	9	10	11	12	13	14	15	16	17	18	19
Oxygen Reactions																				
1	O + O <sub>2</sub> + M	J6	J6	J6	J6	J6	J2	J2	J2	J6	J6	J6	J6	J6	J2	J6	J6	14	J6	J6
2	O + O <sub>3</sub>	J6	J6	J6	J6	J6	J2	J2	J2	J6	J6	J6	J6	J6	J2	J6	J6	14	J6	J6
3	O + O + M	N	N	J6	J6	N	N	N	J2	J6	J6	J6	J6	J6	N	J6	N	N	J6	J6
4	O( <sup>1</sup> D) + N <sub>2</sub>	J6	J6	J6	J6	J6	J2	J2	J2	J6	J6	J6	J6	J6	J2	J6	J6	14	J6	J6
5	O( <sup>1</sup> D) + O <sub>2</sub>	J6	J6	J6	J6	J6	J2	J2	J2	J6	J6	J6	J6	J6	J2	J6	J6	14	J6	J6
6	O( <sup>1</sup> D) + O <sub>3</sub>	N	J6	J6	J6	J6	J2	J2	J2	N	N	J6	J6	J6	N	J6	J6	14	J6	J6
7	O( <sup>1</sup> D) + H <sub>2</sub> O	J6	J6	J6	J6	J6	J2	J2	J2	J6	J6	J6	J6	J6	J2	J6	J6	14	J6	J6
8	O( <sup>1</sup> D) + N <sub>2</sub> O (NO)	J6	J6	J6	J6	J6	J2	J2	J2	J6	J6	J6	J6	J6	J2	J6	J6	J2	J6	N
9	O( <sup>1</sup> D) + N <sub>2</sub> O (N <sub>2</sub> )	J6	J6	J6	J6	J6	J2	J2	J2	J6	J6	J6	J6	J6	J2	J6	J6	J2	J6	N
10	O( <sup>1</sup> D) + CH <sub>4</sub> (tot)	J6	J6	J6	J6	J6	J2	J2	J2	J6	N	J6	J6	J6	J2	J6	J6	14	J6	J6
11	O( <sup>1</sup> D) + H <sub>2</sub>	N	J6	J6	J6	J6	J2	J2	J2	N	J6	J6	J6	J6	N	J6	J6	14	J6	J6
12	O( <sup>1</sup> D) + HCl	N	J6	N	N	J6	N	N	N	N	N	J6	J6	N	N	N	J6	14	J6	N
13	O( <sup>1</sup> D) + HBr	N	N	J6	N	J6	N	N	N	J6	N	J6	J6	N	N	J6	J6	J2	J6	J6
14	O( <sup>1</sup> D) + CFC-11	N	J6	J6	J6	J6	J2	J2	J2	J6	J6	J6	J6	J6	N	J6	J6	J2	J6	N
15	O( <sup>1</sup> D) + CFC-12	N	J6	J6	J6	J6	J2	J2	J2	J6	J6	J6	J6	J6	N	J6	J6	J2	J6	N
16	O( <sup>1</sup> D) + CFC-113	N	J6	J6	N	J6	N	N	J2	J6	N	J6	J6	J6	N	N	N	N	J6	N
17	O( <sup>1</sup> D) + CFC-114	N	N	N	N	N	N	N	J2	N	N	J6	J6	J6	N	N	N	N	J6	N
18	O( <sup>1</sup> D) + CFC-115	N	N	N	N	N	N	N	J2	N	N	J6	J6	J6	N	N	N	N	J6	N
19	O( <sup>1</sup> D) + HCFC22	N	J6	J6	J6	J6	N	N	N	J6	N	J6	J6	J6	N	N	N	N	J6	N
20	O( <sup>1</sup> D) + HCFC-141b	N	N	N	N	N	N	N	N	N	N	J6	J6	N	N	N	N	N	N	N
21	O( <sup>1</sup> D) + HCFC-142b	N	N	N	N	N	N	N	N	N	N	J6	J6	N	N	N	N	N	N	N
22	O( <sup>1</sup> D) + CCl <sub>4</sub>	N	N	J6	J6	J6	J2	J2	J2	J6	J6	J6	J6	J6	N	N	N	N	J6	N
23	O( <sup>1</sup> D) + CH <sub>3</sub> Br	N	N	J6	J6	J6	N	N	J2	J6	J6	J6	J6	J6	N	N	J6	J2	J6	N



#	Reactions	1	2	3	4	5	6	7	8	9	10	11	12	13	14	15	16	17	18	19
24	O( <sup>1</sup> D) + H-1211	N	N	J6	N	J6	N	N	J2	J6	J6	J6	J6	J6	N	N	N	N	J6	N
25	O( <sup>1</sup> D) + H-1301	N	N	J6	N	J6	N	N	J2	J6	J6	J6	J6	J6	N	N	N	N	J6	N
26	O( <sup>1</sup> D) + H-1202	N	N	N	N	N	N	N	N	N	N	N	N	N	N	N	N	N	N	N
Nitrogen Radicals																				
27	H + NO <sub>2</sub>	N	N	N	J6	J6	N	N	J2	N	N	J6	J6	N	N	N	J6	J2	N	J6
28	N + O <sub>2</sub>	J6	J6	J6	J6	J6	J2	J2	J2	J6	J6	J6	J6	J6	J2	J6	J6	J2	J6	J6
29	N + NO	J6	J6	J6	J6	J6	J2	J2	J2	J6	J6	J6	J6	J6	J2	J6	J6	J2	J6	N
30	N + NO <sub>2</sub>	J6	N	N	N	J6	J2	J2	J2	J6	N	J6	J6	N	J2	N	J6	J2	J6	N
31	N + O <sub>3</sub>	N	N	J6	N	J6	N	N	N	N	N	N	N	N	N	J6	N	N	N	N
32	NO + O + M	N	N	N	J6	J6	N	N	J2	N	N	J6	J6	N	J2	N	J6	J2	J6	J6
33	NO + OH + M (HONO)	J6	N	N	N	N	J2	J2	N	J6	N	N	N	N	J2	N	N	N	N	J6
34	NO + HO <sub>2</sub>	J6	J6	J6	J6	J6	J2	J2	J2	J6	J6	J6	J6	J6	J2	J6	J6	J2	J6	J6
35	NO + O <sub>3</sub>	J6	J6	J6	J6	J6	J2	J2	J2	J6	J6	J6	J6	J6	J2	J6	J6	14	J6	J6
36	NO <sub>2</sub> + O	J6	J6	J6	J6	J6	J2	J2	J2	J6	J6	J6	J6	J6	J2	J6	J6	14	J6	J6
37	NO <sub>2</sub> + O + M	N	N	N	N	J6	N	N	J2	N	N	J6	J6	N	N	N	J6	14	J6	J6
38	NO <sub>2</sub> + O <sub>3</sub>	J6	J6	J6	J6	J6	J2	J2	J2	J6	J6	J6	J6	J6	J2	J6	J6	14	J6	J6
39	NO <sub>2</sub> + NO <sub>3</sub> + M	J6	J6	J6	J6	J6	J2	J2	J2	J6	J6	J6	J6	J6	J2	J6	J6	14	J6	J6
40	N <sub>2</sub> O <sub>5</sub> + M	J6	J6	J6	J6	J6	J2	J2	J2	J6	J6	J6	J6	J6	J2	J6	J6	14	J6	J6
41	NO <sub>2</sub> + OH + M	J6	J6	J6	J6	J6	J2	J2	J2	J6	J6	J6	J6	J6	J2	J6	J6	14	J6	J6
42	NO <sub>2</sub> + HO <sub>2</sub> + M	J6	J6	J6	J6	J6	J2	J2	J2	J6	J6	J6	J6	J6	J2	J6	J6	14	J6	J6
43	NO <sub>3</sub> + NO	J6	J6	N	N	J6	J2	J2	J2	N	N	J6	J6	N	J2	J6	J6	14	J6	J6
44	NO <sub>3</sub> + O	N	N	N	J6	N	N	N	N	N	N	J6	J6	N	N	J6	J6	14	J6	J6
45	NO <sub>3</sub> + OH	N	N	N	N	J6	N	N	N	N	N	J6	J6	N	N	N	J6	J2	J6	J6
46	NO <sub>3</sub> + HO <sub>2</sub>	N	J6	N	N	N	J2	J2	N	N	N	J6	J6	N	N	N	J6	14	J6	J6
47	HONO + OH	J6	N	N	N	N	J2	J2	N	N	N	N	N	N	J2	N	N	N	N	J6
48	HO <sub>2</sub> NO <sub>2</sub> + OH	N	J6	J6	J6	J6	J2	J2	J2	J6	J6	J6	J6	J6	J2	J6	J6	J2	J6	J6
49	HO <sub>2</sub> NO <sub>2</sub> + M	J6	J6	J6	J6	J6	J2	J2	J2	J6	J6	J6	J6	J6	J2	J6	J6	14	J6	J6

#	Reactions	1	2	3	4	5	6	7	8	9	10	11	12	13	14	15	16	17	18	19
50	HNO <sub>3</sub> + OH	J6	J6	J6	J6	J6	J2	J2	J2	J6	J6	J6	J6	J6	J2	J6	a	14	J6	J6
	Hydrogen Radicals																			
51	H + O <sub>2</sub> + M	J6	N	J6	J6	J6	J2	J2	J2	J6	J6	J6	J6	J6	J2	J6	J6	J2	J6	J6
52	H + O <sub>3</sub>	J6	N	J6	J6	J6	J2	J2	J2	J6	J6	J6	J6	J6	J2	J6	J6	14	J6	J6
53	H + HO <sub>2</sub> (OH)	N	N	J6	J6	J6	J2	a	J2	J6	J6	J6	J6	J6	N	J6	J6	J2	J6	J6
54	H + HO <sub>2</sub> (H <sub>2</sub> O)	N	N	J6	J6	J6	J2	a	J2	J6	J6	N	N	J6	N	J6	J6	J2	J6	J6
55	H + HO <sub>2</sub> (H <sub>2</sub> )	N	N	J6	J6	J6	J2	a	J2	J6	J6	J6	J6	J6	N	J6	J6	J2	J6	J6
56	OH + O	J6	J6	J6	J6	J6	J2	J2	J2	J6	J6	J6	J6	J6	J2	J6	J6	14	J6	J6
57	OH + O <sub>3</sub>	J6	J6	J6	J6	J6	J2	J2	J2	J6	J6	J6	J6	J6	J2	J6	J6	14	J6	J6
58	OH + HO <sub>2</sub>	J6	J6	J6	J6	J6	J2	J2	J2	J6	J6	J6	J6	J6	J2	J6	J6	14	J6	J6
59	OH + OH (tot)	J6	J6	J6	J6	J6	N	N	J2	J6	N	J6	J6	J6	J2	J6	J6	J2	J6	J6
60	OH + OH + M	J6	J6	N	J6	J6	N	N	J2	N	N	J6	J6	J6	J2	J6	J6	14	J6	J6
61	OH + H <sub>2</sub>	J6	J6	J6	J6	J6	J2	J2	J2	J6	J6	J6	J6	J6	J2	J6	J6	14	J6	J6
62	OH + H <sub>2</sub> O <sub>2</sub>	J6	J6	J6	J6	J6	J2	J2	J2	J6	J6	J6	J6	J6	J2	J6	J6	14	J6	J6
63	HO <sub>2</sub> + O	J6	J6	J6	J6	J6	J2	J2	J2	J6	J6	J6	J6	J6	J2	J6	J6	14	J6	J6
64	HO <sub>2</sub> + O <sub>3</sub>	J6	J6	J6	J6	J6	J2	J2	J2	J6	J6	J6	J6	J6	J2	J6	J6	14	J6	J6
65	HO <sub>2</sub> + HO <sub>2</sub>	J6	J6	J6	J6	J6	J2	b	J2	J6	J6	J6	J6	J6	J2	J6	J6	14	J6	J6
66	H <sub>2</sub> O <sub>2</sub> + O	N	N	N	J6	N	N	N	J2	N	N	J6	J6	N	N	N	J6	14	J6	J6
	Chlorine Radicals																			
67	Cl + O <sub>3</sub>	J6	J6	J6	J6	J6	J2	J2	J2	J6	J6	J6	J6	J6	J2	J6	J6	14	J6	J6
68	Cl + H <sub>2</sub>	N	J6	J6	J6	J6	J2	J2	J2	J6	J6	J6	J6	J6	N	J6	J6	14	J6	J6
69	Cl + H <sub>2</sub> O <sub>2</sub>	N	J6	J6	J6	N	J2	J2	J2	N	N	J6	J6	N	N	J6	J6	14	J6	J6
70	Cl + HO <sub>2</sub> (HCl)	J6	J6	J6	J6	J6	J2	J2	J2	J6	J6	J6	J6	J6	J2	J6	J6	14	J6	J6
71	Cl + HO <sub>2</sub> (ClO)	N	J6	J6	J6	J6	J2	J2	J2	N	N	J6	J6	J6	N	J6	J6	14	J6	J6
72	Cl + CH <sub>2</sub> O	J6	J6	J6	J6	J6	J2	J2	J2	J6	N	J6	J6	J6	J2	J6	J6	14	J6	J6
73	Cl + CH <sub>4</sub>	J6	J6	J6	J6	J6	J2	J2	J2	J6	J6	J6	J6	J6	J2	J6	J6	14	J6	J6
74	ClO + O	J6	J6	J6	J6	J6	J2	J2	J2	J6	J6	J6	J6	J6	J2	J6	J6	14	J6	J6

#	Reactions	1	2	3	4	5	6	7	8	9	10	11	12	13	14	15	16	17	18	19
75	ClO + OH (Cl)	J6	J6	J6	J6	J6	J2	J2	J2	J6	J6	J6	J6	J6	J2	J6	J6	J2	J6	J6
76	ClO + OH (HCl)	J6	J6	J6	J6	J6	J2	J2	J2	J6	N	J6	J6	J6	N	J6	J6	J2	J6	J6
77	ClO + HO <sub>2</sub>	J6	J6	J6	J6	J6	J2	J2	J2	J6	J6	J6	J6	J6	J2	J6	J6	14	J6	J6
78	ClO + NO	J6	J6	J6	J6	J6	J2	J2	J2	J6	J6	J6	J6	J6	J2	J6	J6	14	J6	J6
79	ClO + NO <sub>2</sub> + M	J6	J6	J6	J6	J6	J2	J2	J2	J6	J6	J6	J6	J6	J2	J6	J6	14	J6	J6
80	ClO + ClO (Cl <sub>2</sub> )	N	J6	J6	J6	J6	N	N	N	J6	N	J6	J6	J6	N	J6	J6	14	J6	J6
81	ClO + ClO (ClOO)	J6	J6	N	N	a	N	N	N	N	N	N	N	J6	N	J6	J6	14	J6	J6
82	ClO + ClO (OCIO)	N	J6	J6	N	J6	N	N	N	N	N	N	N	J6	N	J6	J6	14	J6	J6
83	ClO + ClO + M	N	J6	J6	J6	J6	J2	15	J2	J6	J6	J6	J6	J6	J2	J6	J6	14	J6	J6
84	OCIO + O	N	N	J6	J6	N	N	N	N	N	J6	N	N	N	N	N	J6	14	N	J6
85	OCIO + NO	N	N	J6	J6	N	N	N	N	N	J6	N	N	N	N	N	J6	14	N	J6
86	OCIO + Cl	N	N	J6	J6	N	N	N	N	N	J6	N	N	N	N	N	J6	14	N	J6
87	Cl <sub>2</sub> O <sub>2</sub> + M	J6	J6	J6	J6	J6	J2	J2	J2	J6	J6	J6	J6	J6	J2	J6	J6	14	J6	J6
88	Cl <sub>2</sub> O <sub>2</sub> + Cl	N	N	N	N	N	N	N	N	N	N	J6	J6	N	N	J6	J6	14	N	J6
89	HCl + OH	J6	J6	J6	J6	J6	J2	J2	J2	J6	J6	J6	J6	J6	J2	J6	J6	14	J6	J6
90	HCl + O	N	J6	J6	J6	N	N	N	N	N	N	J6	J6	N	N	N	J6	J2	J6	J6
91	HOCl + O	N	N	J6	J6	J6	N	N	N	J6	J6	J6	J6	N	N	J6	J6	14	J6	J6
92	HOCl + Cl	N	J6	J6	J6	J6	N	N	N	J6	N	J6	J6	N	N	J6	J6	J2	J6	J6
93	HOCl + OH	N	N	J6	J6	J6	J2	J2	J2	J6	J6	J6	J6	J6	N	J6	J6	J2	J6	J6
94	ClONO <sub>2</sub> + O	J6	J6	J6	J6	J6	J2	J2	J2	J6	J6	J6	J6	J6	J2	J6	J6	J2	J6	J6
95	ClONO <sub>2</sub> + OH	N	J6	N	N	N	N	N	J2	N	N	J6	J6	N	N	J6	J6	J2	J6	J6
96	ClONO <sub>2</sub> + Cl	N	J6	N	N	N	J2	J2	N	N	N	J6	J6	N	N	J6	J6	J2	J6	J6
Bromine Radicals																				
97	Br + O <sub>3</sub>	J6	J6	J6	J6	J6	*	J2	J2	J6	J6	J6	J6	J6	J2	J6	J6	14	J6	J6
98	Br + HO <sub>2</sub>	J6	J6	J6	J6	J6	*	J2	J2	J6	J6	J6	J6	J6	J2	J6	J6	14	J6	J6
99	Br + CH <sub>2</sub> O	J6	J6	J6	N	J6	*	J2	J2	J6	N	J6	J6	N	J2	J6	J6	J2	J6	J6
100	BrO + O	J6	J6	J6	J6	J6	*	J2	J2	J6	J6	J6	J6	J6	N	J6	J6	14	J6	J6
101	BrO + OH	N	J6	J6	J6	J6	*	N	N	N	N	J6	J6	J6	N	J6	J6	14	J6	J6

#	Reactions	1	2	3	4	5	6	7	8	9	10	11	12	13	14	15	16	17	18	19	
102	BrO + HO <sub>2</sub>	J6	J6	J6	J6	J6	*	J2	J2	J6	J6	J6	J6	J6	J2	J6	J6	J2	J6	J6	
103	BrO + NO	J6	J6	J6	J6	J6	*	J2	J2	J6	N	J6	J6	J6	J2	J6	J6	14	J6	J6	
104	BrO + NO <sub>2</sub> + M	J6	J6	J6	J6	J6	*	J2	J2	J6	J6	J6	J6	J6	J2	J6	J6	14	J6	J6	
105	BrO + ClO (OCIO)	N	J6	J6	J6	J6	*	J2	J2	J6	J6	J6*	J6*	J6	N	J6	J6	14	J6	J6	
106	BrO + ClO (ClOO)	J6	J6	J6	a	b	*	J2	J2	N	J6	J6*	J6*	J6	J2	J6	J6	14	J6	J6	
107	BrO + ClO (BrCl)	J6	J6	J6	J6	J6	*	J2	J2	J6	J6	J6	J6	J6	J2	J6	J6	14	J6	J6	
108	BrO + BrO	N	J6	J6	J6	J6	*	N	J2	N	N	J6	J6	J6	N	J6	J6	J2	J6	J6	
109	BrO+BrO → Br <sub>2</sub> + O <sub>2</sub>	N	N	J6	N	c	*	N	N	J6	N	N	N	J6	N	N	N	N	N	J6	
110	Br <sub>2</sub> + OH	N	N	N	N	N	*	N	N	N	N	N	N	N	N	N	N	N	N	N	J6
111	HBr + O	N	N	J6	N	N	*	N	N	N	N	J6	J6	J6	N	J6	J6	J2	J6	J6	
112	HBr + OH	J6	J6	J6	J6	J6	*	J2	J2	J6	J6	J6	J6	J6	J2	J6	J6	14	J6	J6	
113	HOBr + O	J6	N	N	N	J6	*	J2	N	J6	N	J6	J6	J6	J2	J6	N	N	J6	J6	
114	BrONO <sub>2</sub> + O	N	N	N	N	N	*	N	N	J6	N	N	N	N	N	J6	N	N	J6	J6	
	Organic Halogen Reactions																				
115	CH <sub>3</sub> Cl + Cl	N	J6	N	J6	N	N	N	N	N	N	N	N	N	N	N	N	N	J6	N	
116	CH <sub>3</sub> Cl + OH	N	J6	J6	J6	J6	J2	J2	J2	J6	J6	J6	J6	J6	N	N	N	N	J6	N	
117	CH <sub>3</sub> CCl <sub>3</sub> + OH	N	J6	J6	J6	J6	J2	J2	J2	J6	N	J6	J6	J6	N	N	N	N	J6	N	
118	HCFC22 + OH	N	J6	N	J6	J6	N	N	J2	J6	N	J6	J6	J6	N	N	N	N	J6	N	
119	CH <sub>3</sub> Br + OH	N	J6	J6	J6	J6	N	J2	J2	J6	N	J6	J6	J6	N	J6	J6	J2	J6	N	
	CH <sub>4</sub> and Derivatives																				
120	CH <sub>4</sub> + OH	J6	J6	J6	J6	J6	J2	c	J2	J6	J6	J6	J6	J6	J2	J6	J6	14	J6	J6	
121	CH <sub>3</sub> O <sub>2</sub> + NO	J6	J6	J6	J6	J6	J2	J2	J2	J6	N	J6	J6	J6	J2	J6	J6	14	J6	J6	
122	CH <sub>3</sub> O <sub>2</sub> + HO <sub>2</sub>	J6	J6	J6	J6	J6	J2	J2	J2	J6	N	J6	J6	J6	J2	J6	J6	14	J6	J6	
123	CH <sub>3</sub> O <sub>2</sub> + ClO	N	N	J6	J6	J6	J2	J2	N	N	N	N	N	N	N	J6	J6	J2	N	J6	
124	CH <sub>3</sub> O <sub>2</sub> + CH <sub>3</sub> O <sub>2</sub>	J6	J6	J6	J6	J6	J2	J2	N	J6	N	J6	J6	J6	J2	J6	J6	J2	N	J6	
125	CH <sub>3</sub> OOH + OH	J6	J6	J6	J6	J6	J2	J2	J2	J6	N	J6	J6	J6	J2	J6	J6	14	J6	J6	
126	CH <sub>2</sub> O + NO <sub>3</sub>	N	J6	N	N	J6	J2	J2	N	N	N	J6	J6	N	J2	N	J6	14	J6	J6	

#	Reactions	1	2	3	4	5	6	7	8	9	10	11	12	13	14	15	16	17	18	19
127	CH <sub>2</sub> O + OH	J6	J6	J6	J6	J6	J2	d	J2	J6	N	J6	J6	J6	J2	J6	J6	I4	J6	J6
128	CH <sub>2</sub> O + O	N	N	J6	J6	J6	N	N	J2	J6	N	J6	J6	J6	N	J6	J6	I4	J6	J6
128	CO + OH +M (CO <sub>2</sub> )	J6	J6	N	J6	J6	J2	e	J2	J6	N	J6	J6	J6	J2	J6	I4	I4	J6	J6
129	CO + OH +M (HOCO)	N	N	N	b	J6	N	N	N	N	N	N	N	N	N	N	N	N	J6	J6
C <sub>2</sub> H <sub>6</sub> chemistry																				
130	C <sub>2</sub> H <sub>6</sub> +OH	N	N	N	N	N	N	c	N	N	N	N	N	J6	N	N	N	N	N	J6
131	C <sub>2</sub> H <sub>6</sub> +Cl	N	N	N	N	N	N	N	N	N	N	N	N	N	N	N	N	N	N	J6

217

218

219 **Notes:**

220 I4 = IUPAC, 2004.

221 I5 = IUPAC, 2005.

222 J2 = Chemical Kinetics and Photochemical Data for Use in Atmospheric Studies, Eval#14 (JPL-02).

223 J6 = Chemical Kinetics and Photochemical Data for Use in Atmospheric Studies, Eval#15 (JPL-06).

224 N = This reaction is not explicitly represented.

225

226 **Notes specific to each model:**

227 3: rxn#101: BrO + OH → Br + HO<sub>2</sub> (98%), → HBr + O<sub>2</sub> (2%) is assumed.

228 3: rxn#108: BrO + BrO → 2Br + O<sub>2</sub> is assumed.

229 3: The CCSRNIES model includes the reactions Cl + O<sub>2</sub> + M → ClOO + M, OClO + OH → HOCl + O<sub>2</sub>, CHBr<sub>3</sub> + OH → 3Br + products, and CO + OH → H + CO<sub>2</sub>.

231 4a: JPL-06 but forms Cl + O<sub>2</sub>

232 4b: Both channels of OH + CO included, but both yield CO<sub>2</sub> + H.

233 5: "a" produces OClO; "b" produces OClO; "c" produces 2xBr instead of Br<sub>2</sub>.

234 6\*: Uses parameterization of bromine-catalyzed ozone loss (Appendix in Stenke *et al.*, 2009).

235 7a: Hack *et al.* (1978), listed in JPL-02.

236 7b: Christensen *et al.* (2002), Kircher and Sander (1984).

237 7c: Atkinson (2003).

238 7d: Sivakumaran *et al.* (2003).

239 7e: McCabe *et al.* (2001).  
240 12: The products of 105 and 106 are Cl + Br + O<sub>2</sub>.  
241 16a: The OH + HNO<sub>3</sub> reaction rate is amalgamated from JPL-06 and IUPAC (2002).  
242 17: The IUPAC 2004 (I4) reference is used for many of the reactions; however, the rate constants were set in 2002 using the  
243 online version of IUPAC.  
244

244  
245  
246  
247  
248

**Table 6S-3. Photolytic Reactions in CCMs** (1=AMTRAC3; 2=CAM3.5; 3=CCSRNIES; 4=CMAM; 5=CNRM-ACM; 6=E39CA; 7=EMAC; 8=GEOSCCM; 9=LMDZrepro; 10=MRI; 11=NIWA-SOCOL; 12=SOCOL; 13=ULAQ; 14=UMETRAC; 15=UMSLIMCAT; 16=UMUKCA-METO; 17=UMUKCA-UCAM; 18=WACCM; 19= PSS model).

#	Reaction	1	2	3	4	5	6	7	8	9	10	11	12	13	14	15	16	17	18	19	
1	O <sub>2</sub> + hv (O <sup>1</sup> D)	N	N	N	N	N	N	N	J2	N	N	La	La	N	N	N	J	J	J6	N	
2	O <sub>2</sub> + hv (O <sup>3</sup> P)	J6	J6	J6	J6	J6	a	a	J2	J6	J6	Af	Af	J6	Y	Mi	J	J	J6	J6	
3	1.0 O <sub>3</sub> + hv (O <sup>1</sup> D)	J6	J6	J0	J6	J6	b	b	J2	J6	J6	J0	J0	J6	Y	J2	J	J	J6	J6	
4	O <sub>3</sub> + hv (O <sup>3</sup> P)	J6	J6	J0	J6	J6	b	b	J2	J6	J6	J0	J0	J6	Y	J2	J	J	J6	J6	
5	N <sub>2</sub> O + hv	J6	J6	J6	J6	J6	J7	J7	J2	J6	J6	J2	J2	J6	Y	J0	J	J	J6	N	
6	NO + hv	J6	Mi	Af	Mi	J6	c	c	J2	J6	J6	Ni	Ni	J6	Y	Mi	J	J	Mi	J6	
7	NO <sub>2</sub> + hv	J6	J6	J2	J6	J6	J7	J7	J2	J6	J6	J2	J2	J6	Y	J0	J	J	J6	J6	
8	N <sub>2</sub> O <sub>5</sub> + hv (NO)	N	N	N	N	A	N	N	N	N	N	N	N	N	N	N	N	N	N	J6	N
9	N <sub>2</sub> O <sub>5</sub> + hv (NO <sub>2</sub> )	J6	J6	J2	J6	A	J7	J7	J2	J6	J6	J6	J6	J6	Y	J0	J	J	J6	J6	
10	HONO + hv	J6	N	N	N	N	J7	J7	N	J6	N	N	N	N	Y	N	N	N	N	J6	
11	HNO <sub>3</sub> + hv	J6	J6	J6	J6	J6	J7	J7	J2	J6	J6	J6	J6	J6	Y	J0	J	J	J6	J6	
12	NO <sub>3</sub> + hv (NO)	J6	J6	J2	J6	J6	J7	J7	J2	J6	J6	J2	J2	J6	Y	J0	J	J	J6	J6	
13	NO <sub>3</sub> + hv (NO <sub>2</sub> )	J6	J6	J2	J6	J6	J7	J7	J2	J6	J6	J2	J2	J6	Y	J0	J	J	J6	J6	
14	HO <sub>2</sub> NO <sub>2</sub> + hv (NO <sub>2</sub> )	J6	a	J2	J6	J6	d	d	J2	J6	J6	J6	J6	J6	Y	J0	J	J	a	J6	
15	HO <sub>2</sub> NO <sub>2</sub> + hv (NO <sub>3</sub> )	N	a	J2	N	J6	N	N	N	N	N	N	N	N	N	N	J	J	a	J6	
16	CH <sub>3</sub> OOH + hv	J6	J6	J6	J6	J6	J7	J7	J2	J6	N	J6	J6	J6	Y	J0	J	J	J6	J6	
17	CH <sub>2</sub> O + hv (H)	J6	J6	J2	J6	J6	J7	J7	J2	J6	N	J2	J2	J6	Y	J0	J	J	J6	J6	
18	CH <sub>2</sub> O + hv (H <sub>2</sub> )	J6	J6	J2	J6	J6	J7	J7	J2	J6	N	J2	J2	J6	Y	J0	J	J	J6	J6	
19	H <sub>2</sub> O + hv	J6	N	a	J	J6	J7	J7	J2	J6	J6	La	La	J6	Y	J	J	J	b	J6	
20	HO <sub>2</sub> + hv	N	N	N	N	N	N	N	N	N	N	N	N	N	N	N	N	N	N	N	J6
21	H <sub>2</sub> O <sub>2</sub> + hv	J6	J6	J6	J6	J6	J7	J7	J2	J6	J6	J2	J2	J6	Y	J0	J	J	J6	J6	
22	Cl <sub>2</sub> + hv	Y	J6	J2	J6	J6	J7	J7	N	J6	J6	J6	J6	N	N	N	N	N	J6	J6	
23	ClO + hv	N	N	N	N	N	N	N	N	N	N	N	N	N	N	N	N	N	J6	J6	

24	OCIO + hv	N	J6	J2	J6	J6	e	e	J2	J6	J6	N	N	N	N	J	J	J	J6	J6
25	Cl <sub>2</sub> O <sub>2</sub> + hv	J6	b	J6	J6	J6	f	f	J2	J6	J6	J6	J6	a	Y	a	a	a	c	J6
26	HOCl + hv	J6	J6	J2	J6	J6	J7	J7	J2	J6	J6	J6	J6	J6	Y	J0	J	J	J6	J6
27	2.0 HCl + hv	J6	J6	J2	J6	J6	J7	J7	J2	J6	J6	J6	J6	J6	N	J0	J	J	J6	J6
28	ClONO <sub>2</sub> + hv ClONO)	N	J6	J6	N	B	N	N	N	J6	N	N	N	N	N	N	N	N	J6	J6
29	ClONO <sub>2</sub> + hv (NO <sub>3</sub> )	J6	J6	J6	J6	J6	J7	J7	J2	J6	J6	J6	J6	J6	Y	J0	J	J	J6	J6
30	BrCl + hv	J6	J6	J6	J6	J6	N	J7	N	J6	J6	J6	J6	N	Y	J0	J	J	J6	J6
31	BrO + hv	J6	J6	J2	J6	J6	N	N	J2	J6	N	J6	J6	J6	Y	J0	J	J	J6	J6
32	HOBr + hv	J6	J6	J2	J6	J6	N	J2	J2	J6	J6	J6	J6	J6	Y	J0	J	J	J6	J6
33	HBr + hv	N	N	b	J6	N	N	N	N	N	N	N	N	N	N	N	N	N	N	J6
34	Br <sub>2</sub> + hv	N	N	J6	N	N	N	N	N	N	N	N	N	N	N	N	N	N	N	J6
35	BrONO <sub>2</sub> + hv (NO <sub>2</sub> )	N	J6	J2	N	N	N	N	J2	N	J6	J6	J6	N	N	N	J	J	J6	J6
36	BrONO <sub>2</sub> + hv (NO <sub>3</sub> )	J6	J6	J2	J6	J6	N	J7	N	J6	J6	J6	J6	J6	Y	J0	J	J	J6	J6
37	CH <sub>4</sub> + hv	J6	J	N	J	N	N	N	J2	J6	J6	La	La	N	N	J	J	J	J	J6
38	CO <sub>2</sub> + hv	N	N	N	J	J6	J7	J7	J2	J6	J6	La	La	J6	N	J	J	J	J	N
39	CH <sub>3</sub> Cl + hv	N	J6	J0	J6	J6	J7	J7	J2	J6	J6	15	15	J6	N	N	N	N	J6	N
40	CCl <sub>4</sub> + hv	N	J6	J0	J6	J6	J7	J7	J2	J6	J6	15	15	J6	N	N	N	N	J6	N
41	CH <sub>3</sub> CCl <sub>3</sub> + hv	N	J6	J0	J6	J6	J7	J7	J2	J6	N	15	15	J6	N	N	N	N	J6	N
42	CFC-11 + hv	N	J6	J0	J6	J6	J7	J7	J2	J6	J6	15	15	J6	N	J0	J	J	J6	N
43	CFC-12 + hv	N	J6	J0	J6	J6	J7	J7	J2	J6	J6	J2	J2	J6	N	J0	J	J	J6	N
44	CFC-113 + hv	N	J6	J0	N	J6	N	N	J2	J6	N	15	15	J6	N	N	N	N	J6	N
45	CFC-114 + hv	N	N	N	N	N	N	N	J2	N	N	15	15	J6	N	N	N	N	N	N
46	CFC-115 + hv	N	N	N	N	N	N	N	J2	N	N	15	15	J6	N	N	N	N	N	N
47	HCFC-22 + hv	N	J6	J6	J6	J6	N	N	J2	J6	N	15	15	J6	N	N	N	N	J6	N
48	HCFC-141b + hv	N	N	N	N	N	N	N	N	N	N	15	15	N	N	N	N	N	J6	N
49	HCFC-142b + hv	N	N	N	N	N	N	N	N	N	N	15	15	N	N	N	N	N	J6	N
50	CH <sub>3</sub> Br + hv	N	J6	J0	J6	J6	N	J7	J2	J6	J6	14	14	J6	N	J0	J	J	J6	N
51	H-1202 + hv	N	N	N	N	N	N	N	N	N	N	N	N	N	N	N	N	N	N	N



52	H-1211 + hv	N	J6	J6	N	J6	N	J7	J2	J6	J6	I4	I4	J6	N	N	N	N	J6	N
53	H-1301 + hv	N	J6	J6	N	J6	N	J7	J2	J6	J6	J2	J2	J6	N	N	N	N	J6	N
54	H-2402 + hv	N	N	N	N	N	N	N	N	N	N	I4	I4	N	N	N	N	N	N	N

249

250 **Notes:**

251 J7 = Chemical Kinetics and Photochemical Data for Use in Atmospheric Studies, Eval#12 (JPL-97).

252 J0 = Chemical Kinetics and Photochemical Data for Use in Atmospheric Studies, Eval#13 (JPL-00).

253 J2 = Chemical Kinetics and Photochemical Data for Use in Atmospheric Studies, Eval#14 (JPL-02).

254 J6 = Chemical Kinetics and Photochemical Data for Use in Atmospheric Studies, Eval#15 (JPL-06).

255 I4 = IUPAC, 2004.

256 I5 = IUPAC, 2005.

257

258 J = Data taken from a variety of sources.

259 N = This reaction is not explicitly represented.

260

261 **Notes specific to each model:**

262 1: Cl<sub>2</sub> is photolysed, but lumped with Cl<sub>2</sub>O<sub>2</sub>.

263 2a: CAM3.5 does not include the near-IR photolysis of HO<sub>2</sub>NO<sub>2</sub>.

264 2b: JCl<sub>2</sub>O<sub>2</sub> uses Burkholder *et al.*, (1990) [with log-linear extrapolation to 450nm].

265 2Mi: On-line calculation of J<sub>NO</sub> using parameterization of Minschwaner and Siskind (1993).

266

266

267 3Af: Allen and Frederick (1982).

268 3a: Equations (4.98) and (4.99) on p.157, Brasseur and Solomon (1986).

269 3b: Assumed to be the same values as those for  $J_{\text{HCl}}$ .

270 4Mi: On-line calculation of  $J_{\text{NO}}$  using parameterization of Minschwaner and Siskind (1993).

271 5a: Produces 2x  $\text{NO}_x$  according to JPL-06.

272 5b: Produces  $\text{ClO} + \text{NO}_2$  according to JPL-06.

273 6a/7a: JPL-97 + Koppers and Murtagh (1996) + Chabrilla and Kockarts (1997).

274 6b/7b: JPL-97 + Talukdar *et al.* (1998).

275 6c/7c: Allen and Frederick (1982).

276 6d/7d: JPL-97 + Roehl *et al.* (2002).

277 6e/7e: Wahner *et al.* (1987).

278 6f/7f: JPL-97, j-value scaled by 1.4 (close to Burkholder *et al.* 1990). See PhotoComp. Some values marked with N can be

279 calculated by the model but are not used.

280 11Af: Allen and Frederick (1982).

281 12Af: Allen and Frederick (1982).

282 12Ni: Nicolet (1979); Nicolet and Cieslik, (1980).

283 14: The code contains no information on when the rates were last updated, so only existence or not could be established.

284 15Mi: Minschwaner *et al.* (1993), Minschwaner and Siskind (1993);

285 15a: Burkholder *et al.*, (1990) [with log-linear extrapolation to 450nm].

286 16-17: Photolysis in UMUKCA (both versions) is based on an earlier version of the SLIMCAT CTM but the cross sections have not

287 been updated. Exceptions are the photolysis of  $\text{HO}_2\text{NO}_2$ ,  $\text{ClONO}_2$ , and  $\text{BrONO}_2$ . Here the cross sections are unchanged but

288 new information on branching ratios has been adopted. Also we have introduced a reaction  $\text{O}_2 + h\nu \Rightarrow \text{O}(^1\text{D}) + \text{O}(^3\text{P})$  with a

289 branching ratio following JPL-06. The cross sections and quantum yields for oxygen photolysis follow WMO (1985).

290 18 For  $\text{JO}_2$ , the Ly-a and SRB is derived using Chabrilat and Kockarts (1997) and Kopper and Murtagh (1996), respectively.

291 18a: WACCM does not include the near-IR photolysis of  $\text{JHO}_2\text{NO}_2$ .

292 18b:  $\text{JH}_2\text{O}$  cross sections are taken from JPL-06, plus Lyman alpha photolysis.

293 18c:  $\text{JCl}_2\text{O}_2$  uses Burkholder *et al.*, (1990) [with log-linear extrapolation to 450nm].

294 18Mi: On-line calculation of  $J_{\text{NO}}$  using parameterization of Minschwaner and Siskind (1993).

295

295  
296 **References:**  
297 Allen, M., and J. E. Frederick, Effective photodissociation cross sections for molecule oxygen and nitric oxide in the Schumann-  
298 Runge bands, *J. Atmos. Sci.*, 39, 2066-2075, 1982.  
299 Atkinson, R. Kinetics of the gas-phase reactions of OH radicals with alkanes and cycloalkanes, *Atmos. Chem. Phys.*, 3, 2233-2307,  
300 2003.  
301 Brasseur, G., and S. Solomon, Aeronomy of the middle atmosphere, D. Reidel Publishing Company, 1986.  
302 Burkholder, J. B., J. J. Orlando, and C. J. Howard, Ultraviolet-Absorption Cross-Sections of Cl<sub>2</sub>O<sub>2</sub> between 210 and 310nm, *J. Phys.*,  
303 *Chem.*, 94(2), 687-695, 1990.  
304 Chabrillat, S. and G. Kockarts, Simple parameterization of the absorption of the solar Lyman-alpha line, *Geophys. Res. Lett.*, 24(21),  
305 2659-2662, 1997.  
306 Christensen, L. E., M. Okumura, S. P. Sander, R. J. Salawitch, G. C. Toon, B. Sen, J. -F. Blavier, and K. W. Jucks, Kinetics of HO<sub>2</sub> +  
307 HO<sub>2</sub> => H<sub>2</sub>O<sub>2</sub> + O<sub>2</sub>: Implications for stratospheric H<sub>2</sub>O<sub>2</sub>, *Geophys. Res. Lett.*, 29(9), 10.1029/2001GL014525, 2002.  
308 Hack, W., H. Gg. Wagner, K. Hoyermann, *Ber. Bunsen-Ges. Phys. Chem.*, 82, 713, 1978.  
309 IUPAC 2004: Atkinson R, Baulch DL, Cox RA, et al., Evaluated kinetic and photochemical data for atmospheric chemistry: Volume I  
310 - gas phase reactions of Ox, HOx, NOx and SOx species, *Atmos. Chem. Phys.*, Volume: 4 Pages: 1461-1738, Sept. 1, 2004.  
311 IUPAC 2005: Atkinson, R. D. L. Baulch, R. A. Cox, J. N. Crowley, R. F. Hampson, Jr., J. A. Kerr, M. J. Rossi, and J. Troe,  
312 "Summary of evaluated kinetic and photochemical data for atmospheric chemistry," Web Version March 2005, updated: 15th  
313 December 2000. **Also see:** Atkinson, R., D. L. Baulch, R. A. Cox, J. N. Crowley, R. F. Hampson, R. G. Hynes, M. E. Jenkin,  
314 M. J. Rossi, J. Troe, and T. J. Wallington, "Evaluated kinetic and photochemical data for atmospheric chemistry: Volume IV -  
315 gas phase reactions of organic halogen species", *Atmos. Chem. Phys.*, 8, 4141-4496, 2008.  
316 JPL97: DeMore W. B., S P. Sander, D. M. Golden, R. F. Hampson, M. J. Kurylo, C. J. Howard, A. R. Ravishankara, C. E. Kolb, and  
317 M. J. Molina, Chemical Kinetics and Photochemical Data for Use in Atmospheric Studies, **Eval #12**, JPL Publications 97-4,  
318 January, 15, 1997.  
319 JPL00: Sander, S. P., R. R. Friedl, W. B. DeMore, D. M. Golden, M. J. Kurylo, R. F. Hampson, R. E. Huie, G. K. Moortgat, A. R.  
320 Ravishankara, C. E. Kolb, M. J. Molina, Chemical Kinetics and Photochemical Data for Use in Atmospheric Studies, **Eval #13**,  
321 JPL Publications 00-003, March 8, 2000.  
322 JPL02: Sander, S. P., R. R. Friedl, D. M. Golden, M. J Kurylo, R. E. Huie, V. L. Orkin, G. K. Moortgat, A. R. Ravishankara, C. E.  
323 Kolb, M. J. Molina, B. J. Finlayson-Pitts, Chemical Kinetics and Photochemical Data for Use in Atmospheric Studies, **Eval**  
324 **#14**, JPL Publications 02-25, February 1, 2003.  
325 JPL06: Sander, S. P., R. R. Friedl, D. M. Golden, M. J Kurylo, G. K. Moortgat, H. Keller-Rudek, P. H. Wine, A. R. Ravishankara, C.

326 E. Kolb, M. J. Molina, B. J. Finlayson-Pitts, R. E. Huie, V. L. Orkin, Chemical Kinetics and Photochemical Data for Use in  
327 Atmospheric Studies, **Eval #15**, JPL Publications 06-2, July 10, 2006.

328 Kircher, C. C., and S. P. Sander, Kinetics mechanism of HO<sub>2</sub> and DO<sub>2</sub> disproportionations, *J. Phys. Chem.*, 88, 2082-2091, 1984.

329 Koppers, G. A. A., and D.P. Murtagh, Model studies of the influence of O<sub>2</sub> photodissociation parameterizations in the Schumann-  
330 Runge bands on ozone related photolysis in the upper atmosphere, *Ann. Geophysicae*, 14, 68-79, 1996.

331 McCabe, D. C., T. Gierczak, R. K. Talukdar, and A. R. Ravishankara, *Geophys. Res. Lett.*, 28, 3135-3138, 2001.

332 Minschwaner, K., G. P. Anderson, L. A. Hall, and K. Yoshino, Polynomial coefficients for calculating O<sub>2</sub> Schumann-Runge cross  
333 sections at 0.5cm<sup>-1</sup> resolution, *J. Geophys. Res.*, 98, 10,543-10,561, 1993.

334 Minschwaner, K. and D. E. Siskind, A new calculation of nitric oxide photolysis in the stratosphere, mesosphere, and lower  
335 thermosphere, *J. Geophys. Res.*, 98, 20,401-20,412, 1993.

336 Nicolet, M., Photodissociation of nitric oxide in the stratosphere and mesosphere: Simplified numerical relations for atmospheric  
337 model calculations, *Geophys. Res. Lett.*, 6, 866-868, 1979.

338 Nicolet, M. and S. Cieslik, The photodissociation of nitric oxide in the mesosphere and stratosphere, *Planet Space Sci.*, 28, 105-115,  
339 1980.

340 Roehl, C. M., S. A. Nizkorodov, H. Zhang, G. A. Blake, P. O. Wennberg, Photodissociation of peroxyxynitric acid in the near-IR, *J.*  
341 *Phys. Chem. A*, 106, 3766-3772, 2002.

342 Sivakumaran, M., K. L. Demerjian, N. M. Donahue, and J. G. Anderson, Reaction between OH and HCHO: temperature dependent  
343 rate coefficients (202-399 K) and product pathways (298 K), *Phys. Chem. Chem. Phys.*, 4, 4821-4827, 2003.

344 Talukdar, R. K., C. A. Langfellow, M. K. Gilles, and A. R. Ravishankara, Quantum yields of O(<sup>1</sup>D) in the photolysis of ozone  
345 between 289 and 329 nm as a function of temperature, *Geophys. Res. Lett.*, 25, 143-146, 1998.

346 Wahner, A., G. S. Tyndall, and A. R. Ravishankara, Absorption cross sections for OCIO as a function of temperature in the  
347 wavelength range 240-480 nm, *J. Phys. Chem.*, 91, 2734, 1987.

348

348  
349

**Table 6S-4. Description of models in PhotoComp 2008.**

Label	Model	Method	Bins	Scattering code	SR Bands	Solar Irradiance and CS/QY comments	Low Sun	Cloud (P1c)	Aerosol(P1b)
AMTR	AMTRAC	LUT from Groves & Tuck 1980	?	?	?	JPL 2002	Spherical solar rays, no refraction.		
CCSR	CCSRNIES	Inline RT	16 [200 – 690nm] + 2 [>690 nm], SR param for O <sub>2</sub> &NO	Two-stream, plane-parallel	O <sub>2</sub> : M93 NO: AF82	Sep86+Nov89 from L97	Spherical solar rays, no refraction.		Own aerosol scattering, same tau
EMAC	EMAC	Inline RT (v1.5)	7 [202-682 nm] + Ly-alpha + SR param.	Delta 2-stream (PIFM) + LUT	O <sub>2</sub> : KM96 NO: AF82	JPL1997 + updates: O( <sup>1</sup> D), HNO <sub>4</sub> , acetone, OCIO, HOBr, ...	Extrapolation when SZA 88–94.5° (L03)	OD match PC08, LWC and scattering from EMAC	
GFJX	UCI Fast-JX (v6.2)	Standalone RT	18 [177.4 - 850nm], not contiguous.	8-stream, asymmetric Feautrier, plane-parallel	Redo SR ODFs in UCIR by BP02	JPL 2002, IUPAC 2005 + updates (O <sup>1</sup> D, HNO <sub>4</sub> , acetone, NO <sub>2</sub> (JPL O3 from AFGL/Molina. SUSIM solar fluxes (Mar 92+Nov 94)	Spherical solar rays, no refraction.	per PC08	per PC08
Gtbl	GEOSCCM	LUT (p,col-O <sub>3</sub> ,SZA, λ)	79 [176.215-652.5 nm] +Lyman-alpha	Matrix inversion, isotropic scattering	KM96	JPL 2002	Spherical solar rays with refraction		
LMDZ	LMDZRepro	LUT from TUV 4.1		LUT (p, col-O <sub>3</sub> , SZA, λ)	See TUV	See TUV 4.1	See TUV	?	?
NIWA	NIWA-SOCOL v2.0	LUT from Mezon CTM	73 total [120-750 nm] with Lyman-alpha	LUT (XO <sub>2</sub> & XO <sub>3</sub> )	O <sub>2</sub> and NO: AF82	Mostly JPL 2006 + IUPAC. Solar: CCMVal2 see Lean 2005.	Spherical solar rays, no refraction	OD match PC08, LWC and scattering from S78	

SLIM	UMSLIMCAT	LUT(p,col-O <sub>3</sub> ,SZA, T)	203 total [120-850 nm] with Lyman-alpha	Plane parallel isotropic multiple scattering.	O <sub>2</sub> : M93 NO: MS93	JPL 2002. Solar: WMO (1985) for PhotoComp. Lean (2005) for CCMVal runs.	Spherical solar rays, no refraction.		
SOCL	SOCOL v2.0	Inline RT (Mezon CTM)	73 [120-750nm]	Delta-Eddington, plane-parallel	NO & O <sub>2</sub> : AF82	Mostly JPL 2006 + IUPAC. Solar: CCMVal2 see Lean 2005	Spherical solar rays, no refraction		
TUVM	NCAR TUV (v4.6)	Standalone RT	For campaign: fixed bins SR and 8 bins [208-735 nm], with <b>L<math>\alpha</math></b>	4-stream discrete-ordinates, plane-parallel, St88.	KM96	mostly JPL06 Solar irradiance: SUSIM: $\lambda < 150$ nm Atlas 3: 150 ~ 400 nm Neckel and Labs 1984: $> 400$ nm	Spherical solar rays, no refraction	per PC08	per PC08
UCIJ	UCI Fast-JX (v6.5)	Standalone RT	18 [177.4 - 850nm], not contiguous	8-stream, asymmetric Feautrier, plane-parallel	Redo SR ODFs in UCIR by BP02	JPL 2002, IUPAC 2005 + updates (O <sup>1</sup> D, HNO <sub>4</sub> , acetone, NO <sub>2</sub> (JPL O <sub>3</sub> from AFGL/Molina. SUSIM solar fluxes (Mar 92+Nov 94)	Spherical solar rays, no refraction	per PC08	per PC08
UCIr	UCI ref J-code (2005)	Standalone RT	62 [202-850 nm] +83 ODFs [177-202 nm]	6-stream, symmetric Feautrier, plane-parallel	O <sub>2</sub> & NO ODFs derived from M93 & MS93	JPL 2002, IUPAC 2005, hi-res O <sub>3</sub> + updates (O <sup>1</sup> D, HNO <sub>4</sub> , acetone, NO <sub>2</sub> ). SUSIM solar fluxes (Mar 92+Nov 94)	Spherical solar rays, no refraction		
WACC	WACCM	LUT [SZA, ALB, colO <sub>3</sub> , temp, press]	100 total [120-750 nm]  33: [120-200 nm] 67: [200-750 nm] with <b>L<math>\alpha</math></b>	4-stream discrete-ordinates, St98.	In line: O <sub>2</sub> : KM96 NO: MS93	CS and QY: mostly JPL06 Solar irradiance model of Lean <i>et al.</i> (2005) interpolated to the 100 bins used in WACCM. A solar average file was used for the photocomp 2008.	Spherical solar rays, no refraction ; SZA $\leq 97^\circ$		

350

351

**Abbreviations:**

352

CS = Cross Sections; QY= Quantum yield; SZA: Solar zenith angle; ALB = surface albedo; RT=radiative transfer; SR = Schumann-Runge; L $\alpha$  =

353

Lyman-Alpha; LUT: Lookup Table,  $\lambda$ : wavelength

- 354  
355 **Abbr. References:**  
356 **AF82:** Allen, M., and J. E. Frederick, Effective photodissociation cross sections for molecule oxygen and nitric oxide in the Schumann-Runge  
357 bands, *J. Atmos. Sci.*, 39, 2066-2075, 1982.  
358 **BP02:** Bian, B., and M. J. Prather, Fast-J2: Accurate Simulation of Stratospheric Photolysis in Global Chemical Models *Journal of Atmospheric*  
359 *Chemistry* **41**: 281–296, 2002.  
360 **I05:** IUPAC 2005: Atkinson, R. D. L. Baulch, R. A. Cox, J. N. Crowley, R. F. Hampson, Jr., J. A. Kerr, M. J. Rossi, and J. Troe, "Summary of  
361 evaluated kinetic and photochemical data for atmospheric chemistry," Web Version March 2005, updated: 15th December 2000. **Also**  
362 **see:** Atkinson, R., D. L. Baulch, R. A. Cox, J. N. Crowley, R. F. Hampson, R. G. Hynes, M. E. Jenkin, M. J. Rossi, J. Troe, and T. J.  
363 Wallington, "Evaluated kinetic and photochemical data for atmospheric chemistry: Volume IV - gas phase reactions of organic halogen  
364 species", *Atmos. Chem. Phys.*, 8, 4141-4496, 2008.  
365 **KM96:** Koppers, G. A. A., and D.P. Murtagh, Model studies of the influence of O<sub>2</sub> photodissociation parameterizations in the Schumann-Runge  
366 bands on ozone related photolysis in the upper atmosphere, *Ann. Geophysicae*, 14, 68-79, 1996.  
367 **L03:** Lamago, D., M. Dameris, C. Schnadt, V. Eyring, and C. Brühl, Impact of large solar zenith angles on lower stratospheric dynamical and  
368 chemical processes in a coupled chemistry- climate model, *Atmos. Chem. Phys.*, **3**, 1981-1990, 2003.  
369 **MS93:** Minschwaner, K. and D. E. Siskind, A new calculation of nitric oxide photolysis in the stratosphere, mesosphere, and lower  
370 thermosphere, *J. Geophys. Res.*, 98, 20,401-20,412, 1993.  
371 **M93:** Minschwaner, K., Salawitch, R. J., and McElroy, M. B. (1993), Absorption of solar radiation by O<sub>2</sub>: Implications for O<sub>3</sub> and lifetimes of  
372 N<sub>2</sub>O, CFCl<sub>3</sub>, and CF<sub>2</sub>Cl<sub>2</sub>, *J. Geophys. Res.*, 98(D6), 10543-10561.  
373 **S78:** Stephens G. L., Ackerman S., Smith E. A., Radiation Profiles in extended water clouds. II: Parameterization schemes, **J.Atmos.Sci**, vol  
374 35, no11, pp2123-2132, 1978.  
375 **St88:** Stamnes, K., S. Tsay, W. Wiscombe, and K. Jayaweera, A numerically stable algorithm for discrete-ordinate-method radiative transfer in  
376 multiple scattering and emitting layered media, *Appl. Opt.*, 27, 2502-2509, 1988.  
377 **T98:** Talukdar, R. K., C. A. Langfellow, M. K. Gilles, and A. R. Ravishankara, Quantum yields of O(<sup>1</sup>D) in the photolysis of ozone between  
378 289 and 329 nm as a function of temperature, *Geophys. Res. Lett.*, 25, 143–146, 1998.  
379  
380 **Other References:**  
381 Lean, J., G. Rottman, J. Harder, and G. Kopp, Source contributions to new understanding of global change and solar variability, *Solar Phys.*, 230,  
382 27-53, 2005.  
383  
384

384  
385  
386  
387  
388  
389  
390  
391  
392  
393  
394  
395  
396  
397  
398  
399  
400  
401  
402  
403  
404  
405  
406  
407  
408  
409  
410  
411  
412  
413

**SPARC CCMVal PhotoComp-2008** (1 June 2008, MJP)

**GOALS.** Evaluate how models calculate photolysis (and indirectly heating) rates in the stratosphere and troposphere with the incentive of locating errors or biases and identifying improved and practical methods. There are three basic parts to PhotoComp2008:

(1) Basic test of *all* J- values for high sun (SZA=15°), w/ & w/o additional scattering layers (stratiform clouds & stratospheric volcanic aerosols).

(2) Test of twilight, sphericity, and 24-hour averages (SZA = 84° - 96°).

(3) Test of wavelength integration w/o scattering (SZA = 15°).

There will be one standard atmosphere, whose primary definition will include air mass, ozone mass, and temperature in each layer. This atmosphere is typical of the tropics, ozone column = 260 DU. For efficiency, we will use this same atmosphere in all sections, even the low-sun, polar cases.

**PARTICIPATION.** This study is designed to aid development and testing of the photolysis and short-wave heating codes used in chemistry-transport models and coupled chemistry-climate models. This project is open: any research group can participate by running the experiments and reporting the results as specified below. We also encourage participation from groups (without CTMs or CCMs) who have participated in other model-measurement studies (e.g., IPMMI, POLARIS). Many CTM/CCMs will be using “the same” photolysis scheme (e.g., fast-TUV, fast-J) and think their participation redundant – this is false. The implementation of a standard scheme into any CTM/CCM will likely alter (intended or inadvertent) how the J-values are calculated: thus it is very important when you perform these tests that the photolysis module that is as close a possible to that embedded within the CTM/CCM and not the original, standalone version that you used to derive your inline model.

**EXPERIMENTS.**

**Part 1** is a basic test of all J-values for high sun (SZA = 15°) over the ocean (albedo = 0.10, Lambertian). **Part 1a: Clear sky** (only Rayleigh scattering) and no aerosols. **Part 1b: Pinatubo aerosol** in the stratosphere (layer 10). **Part 1c: Stratus cloud** (layer 2). The primary atmosphere (Table 1a) is specified in terms of pressure layers, mean temperature, and column O<sub>3</sub> in each layer. Please do not include absorption by NO<sub>2</sub> or other species in calculating optical depths. For 1b and 1c we recommend that you use the specified optical properties in Table 1c, interpolating across the 5 specified wavelengths.



414 **Part 2** tests the simulation of a spherical atmosphere and twilight conditions that are critical to the polar regions. Use the same  
415 atmosphere as Part 1 without clouds or aerosols. Assume equinox (solar declination = 0°) and a latitude of 84°N. The surface SZA  
416 (not including refraction) varies from 84° (noon) to 96° (midnight). Report all J-values at noon, midnight, and the 24-hour average  
417 (integrating as you would in your CTM/CCM). With a spherical atmosphere, the local solar zenith angle changes with altitude and if  
418 refraction is included it will change the surface angle. Please note how you treat the solar ray path in your model description.  
419

420 **Part 3** tests the accuracy of wavelength binning in the critical region 290-400 nm that dominates tropospheric photolysis. Shut off all  
421 Rayleigh scattering and surface reflection (albedo = 0) giving effectively a simple Beer's Law calculation. Repeat the calculation in  
422 Part 1, but report only J-values for J-O3 (i.e., total), J-O3(1d) [ $O_3 \Rightarrow O_2 + O(^1D)$ ], and J-NO2 [ $NO_2 \Rightarrow NO + O$ ]. These are the two  
423 critical J-values for the troposphere, and they both have unusual structures in absorption cross section and quantum yields. The  
424 organizers will make these calculations using very high resolution (0.05 nm) cross sections and solar fluxes and for different options  
425 (e.g., JPL-06 vs. IUPAC cross sections) to provide a benchmark. NOTE that we will only use results below 20 km (L=1:11) for this  
426 comparison.  
427

## 428 **DIAGNOSTICS.**

430  
431 **Model Documentation** should include a brief outline of the methods and any references (limit: one page). Please include brief notes  
432 on: how you treat sphericity and refraction, the Schumann-Runge bands (J-O<sub>2</sub> and J-NO), Rayleigh scattering, multiple scattering,  
433 clouds and aerosols, seasonal changes in sun-earth distance, solar variability, and any specific parameterizations. Default cross  
434 sections are JPL-2006, please note if you are using alternate.  
435

436 **Report** all J-values and all standard model layers since this is a check on all modeled J-values, not just the radiative transfer solution.  
437 See Appendix for data formatting. We are not specifying the day-of-the-year, so use solar fluxes for sun-earth distance = 1.0 au and  
438 average over the 11-yr solar cycle if possible. UCI's high-resolution solar spectrum used in these experiments is the average of two  
439 high and low SUSIM spectra (29 Mar 1992 and 11 Nov 1994), this is not meant to be the 11-yr average. It will be provided at 0.05  
440 nm resolution, but we encourage you to use your own solar fluxes for the primary tests since changing solar fluxes will mostly likely  
441 require a complete re-averaging of all cross-sections (see Fast-J paper, Wild, Zhu, Prather, 2000). Please report in model  
442 documentation what you are using for the solar spectrum and how the solar cycle is represented in your submissions, and if possible  
443 submit it as a separate file so that it may be used to address differences later. (With different wavelength binning, this will not be  
444 trivial.) Reported photolysis rates should be calculated for the mass mid-point of each layer, this brings PhotoComp closer to current

445 CTM usage rather than the original grid-point formulation used in M&M. Results in the form of clearly labeled ascii text files should  
446 be sent to the organizers (see web posting for specific details).

447

448

## 449 **DISCUSSION.**

450

451 Implementation into a particular model's code will up to the participant. For example, at UCI we have two models that we will use in  
452 PhotoComp: a fast-JX model within the CTM that uses layers of uniform composition defined by mass ( $\text{kg/m}^2$ ); and a stand-alone  
453 photochemical box model that defines altitude (in cm) as the vertical grid and uses number densities for air and ozone. For the latter,  
454 we have re-mapped the primary atmosphere (Table 1a) onto a grid-point structure (Table 1b) that has the same mid-layer properties as  
455 the layer mean value and the same columns of  $\text{O}_2$  and  $\text{O}_3$ .

456 One question will be: What is the correct answer? In some cases we may be able to define a "best" answer based on obvious physics  
457 or convergence of some of the more resolved models, but in others we may not. Thus in all of our proposed experiments we will  
458 begin with a "standard model" result (not necessarily the best answer) from one of the models and then determine a best answer, if  
459 possible, after analysis of the results.

460

461 One approach to defining the correct answer would be to merge observed radiation fields or photolysis rates (e.g., IPMMI, POLARIS,  
462 see references below), but we feel this may be too difficult to match the exact observing conditions. One way to include the  
463 knowledge gained by these field studies is to ensure participation from some of the models (e.g., NCAR-TUV, APL).

464

465 We do not recommend reporting detailed actinic fluxes as a function of wavelength since everyone selects different ways of  
466 integrating over wavelength (e.g., bins) and trying to reconcile the different wavelength scales is not worthwhile. If major problems  
467 show up, then a subgroup of models can consider how to resolve the differences.

468

469 Another major issue with photolysis and heating rates is the treatment of clouds and cloud fraction. This is very important, but  
470 probably beyond the current PhotoComp. It would require a special workshop. We do include an option for a plane-parallel volcanic  
471 aerosol layer (aka Pinatubo) and a stratiform cloud.

472

## 473 **APPENDIX**

474

### Standard Atmosphere & Other Specifications

475

476

477

478

479

480

481

482

483

484

485

486

487

488

489

490

491

492

493

494

495

496

497

498

499

500

501

502

503

504

505

506

507

508

509

510

511

512

=====  
**Table 1a.** PhotoComp 2008 standard atmosphere =====

	L	edge p(hPa)	T	O3(mass/mass)	DU(**redundant)
	1	1000.0	299.9	3.844E-08	2.4532
	2^^	866.0	289.5	4.704E-08	4.8514
	3	649.4	278.8	4.720E-08	3.6498
	4	487.0	267.2	4.972E-08	2.8831
	5	365.2	253.9	5.551E-08	2.4140
	6	273.8	239.7	5.977E-08	1.9491
	7	205.4	224.6	6.390E-08	1.5627
	8	154.0	209.4	9.012E-08	1.6527
	9	115.5	198.2	1.486E-07	2.0441
	10**	86.60	195.8	3.885E-07	4.0065
	11	64.94	203.1	1.533E-06	11.8582
	12	48.70	209.9	3.790E-06	21.9783
	13	36.52	215.5	6.849E-06	29.7855
	14	27.38	220.1	1.034E-05	33.7361
	15	20.54	224.5	1.326E-05	32.4219
	16	15.40	228.9	1.577E-05	28.9124
	17	11.55	233.3	1.653E-05	22.7293
	18	8.660	237.8	1.670E-05	17.2239
	19	6.494	242.6	1.578E-05	12.2053
	20	4.870	248.3	1.363E-05	7.9054
	21	3.652	254.1	1.236E-05	5.3734
	22	2.738	259.5	9.733E-06	3.1740
	23	2.054	262.9	8.158E-06	1.9951
	24	1.540	265.1	6.721E-06	1.2325
	25	1.155	266.9	5.511E-06	0.7578
	26	0.8660	264.7	4.810E-06	0.4960
	27	0.6494	261.8	4.009E-06	0.3100
	28	0.4870	259.7	3.325E-06	0.1928
	29	0.3652	254.3	2.820E-06	0.1226
	30	0.2738	247.0	2.323E-06	0.0758
	31	0.2054	239.4	1.909E-06	0.0467
	32	0.1540	234.4	1.585E-06	0.0291
	33	0.1155	232.7	1.335E-06	0.0184
	34	0.08660	226.4	1.102E-06	0.0114

513 35 0.06494 216.4 8.927E-07 0.0069  
514 36 0.04870 210.8 7.372E-07 0.0043  
515 37 0.03652 208.0 6.168E-07 0.0027  
516 38 0.02738 205.2 5.162E-07 0.0017  
517 39 0.02054 202.4 4.317E-07 0.0011  
518 40 0.01540 199.4 3.607E-07 0.00066  
519 41 0.01155 197.6 3.032E-07 0.00042  
520 42 0.00866  
521 above model top layer=41 @ 0.0866 hPa, assume uniform T & O3  
522 42 0.00866 197.6 3.032E-07 0.00125  
523 43 0.00000

524 =====  
525 ^^ layer for stratiform cloud: OD (600 nm) = 20.0  
526 \*\* layer for Pinatubo sulfate aerosol: OD(600 nm) = 1.00  
527 see Table 1c.  
528 =====

529  
530  
531 **Table 1b.** Standard atmosphere shown mapped into grid points  
532 =====

L	alt(km)	air(#/cm <sup>3</sup> )	O3(#/cm <sup>3</sup> )	T(K)
533	1	2.416E+19	5.611E+11	299.9
534	2	1.877E+19	5.335E+11	289.5
535	3	1.462E+19	4.169E+11	278.8
536	4	1.144E+19	3.436E+11	267.2
537	5	9.025E+18	3.027E+11	253.9
538	6	7.169E+18	2.589E+11	239.7
539	7	5.737E+18	2.215E+11	224.6
540	8	4.615E+18	2.513E+11	209.4
541	9	3.656E+18	3.283E+11	198.2
542	10	2.775E+18	6.514E+11	195.8
543	11	2.006E+18	1.858E+12	203.1
544	12	1.456E+18	3.334E+12	209.9
545	13	1.063E+18	4.399E+12	215.5
546	14	7.807E+17	4.879E+12	220.1
547	15	5.740E+17	4.598E+12	224.5
548	16	4.222E+17	4.022E+12	228.9
549	17	3.106E+17	3.102E+12	233.3
550	18	2.285E+17	2.306E+12	237.8
551	19	1.680E+17	1.602E+12	242.6
552				

553	20	37.5	1.231E+17	1.014E+12	248.3
554	21	39.6	9.018E+16	6.732E+11	254.1
555	22	41.7	6.622E+16	3.894E+11	259.5
556	23	43.9	4.902E+16	2.416E+11	262.9
557	24	46.2	3.645E+16	1.480E+11	265.1
558	25	48.4	2.715E+16	9.039E+10	266.9
559	26	50.6	2.053E+16	5.966E+10	264.7
560	27	52.8	1.557E+16	3.771E+10	261.8
561	28	55.0	1.177E+16	2.364E+10	259.7
562	29	57.2	9.011E+15	1.535E+10	254.3
563	30	59.3	6.957E+15	9.766E+09	247.0
564	31	61.4	5.383E+15	6.210E+09	239.4
565	32	63.4	4.123E+15	3.949E+09	234.4
566	33	65.3	3.114E+15	2.512E+09	232.7
567	34	67.3	2.400E+15	1.597E+09	226.4
568	35	69.1	1.883E+15	1.016E+09	216.4
569	36	70.9	1.450E+15	6.458E+08	210.8
570	37	72.7	1.102E+15	4.107E+08	208.0
571	38	74.4	8.374E+14	2.612E+08	205.2
572	39	76.1	6.367E+14	1.661E+08	202.4
573	40	77.8	4.846E+14	1.056E+08	199.4
574	41	79.5	3.667E+14	6.717E+07	197.6

```

=====
576 above-top extend with 6.3-km scale-height for air & O3
577     columns:  air(#/cm^2)  O3(#/cm^2)
578             2.129E+25   6.985E+18
579 =====

```

**Table 1c.** Scattering properties of Pinatubo and stratus layers

```

=====
585 Definitions:
586     W = wavelength (nm)
587
588     Q = scattering efficiency (average of cross-section / (pi * r**2) )
589         typically Q ~ 2 for large clouds and large aerosols
590         fn of aerosol size distrib N(r), index of refraction, wavelength.
591
592     K = extinction (m2/g), the cross-sectional area per gram of material

```

593  $K(m^2/g) = Q / [4/3 * Reff(micron) * Rho(g/cm^3)]$   
594  
595 Reff = effective radius (microns)  
596 = Average[N(r) \* r\*\*3] / Average[N(r) \* r\*\*2]  
597  
598 Rho = density of particles (g/cm3)  
599  
600 n = index of refraction  
601  
602 OD = optical depth (column) = column mass (g/m2) \* K (m2/g)  
603  
604 SSA = single scattering abledo  
605  
606 LG(1:8) = coefficients of Legendre expansion of scattering phase fn.  
607 both polarizations are added. By definition SLEG(1) = 1.  
608 Fast-JX uses these first 8 terms to define the scattering.  
609  
610 g = asymmetry factor = LG(2) / 3.  
611  
612  
613 Pinatubo: OD = 1.0 in layer 10 (86.6 to 64.9 hPa)  
614 =====  
615 Stratospheric aerosol composed of 75%-wt H2SO4.  
616 Rho = 1.630  
617 n = 1.514 + 0.000i (200 nm)  
618 1.473 + 0.000i (300 nm)  
619 1.459 + 0.000i (400 nm)  
620 1.448 + 0.000i (600 nm)  
621 1.435 + 0.000i (999 nm)  
622 Log-normal distribution with R0 = 0.08 micron & sigma = 0.800  
623 \*\*check that you are using the right log-normal by deriving Reff  
624 Reff = 0.386 micron  
625  
626 K (600nm) = 2.610  
627 OD (@600nm) = 1.00 ==> aerosol = 1.00/K = 0.3832 g/m2  
628  
629 W Q SSA LG(2) LG(3) LG(4) LG(5) LG(6) LG(7) LG(8)  
630 200 2.5935 1.0000 2.092 2.914 2.880 3.295 3.185 3.430 3.379  
631 300 2.6669 1.0000 2.121 2.861 2.792 2.936 2.733 2.703 2.568  
632 400 2.5588 1.0000 2.144 2.813 2.711 2.695 2.425 2.257 2.069

```

633      600 2.1893 1.0000 2.149 2.713 2.547 2.362 2.018 1.740 1.499
634      999 1.4540 1.0000 2.118 2.537 2.277 1.951 1.555 1.229 0.972
635      (fast-JX v61 scatter #15)
636
637      Stratus: OD = 20.0 in layer 2 (866 to 649 hPa)
638      =====
639      Pure water cloud
640      Rho = 1.000
641      n = 1.335 + 0.000i (assumed 200-999 nm)
642      Deirmendjian Cumulus C1 (Gamma, n(r) = a r**alpha exp[-b r**gamma])
643      mode radius Rc = 4 microns, alpha=6, b=3/2, gamma = 1
644      Reff = 6.00 micron
645
646      K (600nm) = 0.2668
647      OD (@600nm) = 20.0 ==> aerosol = 20.0/K = 75.0 g/m2
648
649      W   Q   SSA LG(2) LG(3) LG(4) LG(5) LG(6) LG(7) LG(8)
650      200 2.0650 1.0000 2.610 3.998 4.771 5.450 6.196 6.829 7.721
651      300 2.0835 1.0000 2.596 3.973 4.725 5.406 6.129 6.751 7.607
652      400 2.1064 1.0000 2.571 3.936 4.660 5.345 6.056 6.670 7.492
653      600 2.1345 1.0000 2.557 3.902 4.596 5.263 5.923 6.507 7.267
654      999 2.1922 1.0000 2.499 3.799 4.418 5.081 5.667 6.213 6.851
655      (fast-JX v61 scatter #08)
656      =====
657
658
659      =====
660      Table 2. Standard diagnostics and file names
661      =====
662      Ascii tables will be fine given small data sets.
663      Report J-values at the mid-point of Layers 1 through 40.
664      File names: PC08_{model name + version if need be}_{PhotoPart#}
665      Write format: J-title, J-value(1:41) '(a8,1x,41e9.2)'
666
667      File Examples:
668      PC08_UCIref_doc.txt (or .pdf or .doc if need formatting)
669      UCI old reference code, documentation
670      PC08_UCI-JX_doc.txt
671      UCI version of fast-JX, documentation
672      PC08_UCIref_P1a.txt

```

673 PC08\_UCIref\_P1b.txt  
674 PC08\_UCIref\_P1c.txt  
675 UCI-ref results for Part 1 clear, Pinatubo & stratus (see sample below)  
676 PC08\_UCIref\_P2n.txt  
677 PC08\_UCIref\_P2m.txt  
678 PC08\_UCIref\_P2a.txt  
679 UCI-ref results for Part 2 noon, midnight and average  
680 PC08\_UCIref\_P3.txt  
681 UCI-ref results for Part 3 (J-O3(1d) and J-NO2 only).  
682  
683 PC08\_UCIref\_P1.txt  
684 -----file: PC08\_UCIref\_P1a.txt -----  
685 PhotoComp2008: UCI pratmo P1a '(a8,1x,41e9.2)' \*\* note that UCIref does not calculate L=1(933) but at surface(1000)  
686 pressure 933.\*\* 750. 562. .... .0237 .0178 .0133 .0100  
687 J-NO 7.02E-31 6.85E-28 7.42E-25 ..... 4.71E-06 4.91E-06 5.10E-06 5.26E-06  
688 J-O2 1.16E-23 6.49E-22 4.67E-20 ..... 4.80E-09 5.57E-09 6.45E-09 7.51E-09  
689 J-O3 4.55E-04 5.09E-04 5.37E-04  
690 J-O3(1D) 4.84E-05 7.00E-05 8.02E-05  
691 J-H2COa 3.08E-05 4.43E-05 5.22E-05  
692 .....  
693 J-Acet-b 4.26E-07 3.94E-07 2.79E-07 .....

=====  
**Table 3. Standard J-value names.**  
=====

700 Please use these abbreviations (if possible in the following order) so that J's can be sorted. For new J's please add with unique name. (available as PC08\_J-  
701 labels.txt)

702 Note that for some J's, the branching ratios do not have different cross-sections associated with them and the branching ratios are fixed, hence we report only  
703 one J.

704 For many organics, the quantum yields are complex and have been incorporated into  
705 these J's. If you do not calculate one of these, please keep that row in your table with zero or blank values.

- =====  
707 1 J-NO NO =N+O  
708 2 J-O2 O2 =O+O  
709 3 J-O3 O3 =O+O2 (total = both O(3P) and O(1D))\*  
710 4 J-O3(1d) O3 =O(1D)+O2  
711 5 J-H2COa H2COa =H+HCO  
712 6 J-H2COb H2COb =H2+CO



713 7 J-H2O2 H2O2 =OH+OH  
714 8 J-CH3OOH CH3OOH =CH3O+OH  
715 9 J-NO2 NO2 =NO+O  
716 10 J-NO3 NO3 =NO+O2(11.4%) & NO2+O(88.6%)\*  
717 11 J-N2O5 N2O5 =NO2+NO3  
718 12 J-HNO2 HONO =OH+NO  
719 13 J-HNO3 HNO3 =OH+NO2  
720 14 J-HNO4 HO2NO2 =OH+NO3  
721 15 J-ClNO3a ClNO3a =Cl+NO3  
722 16 J-ClNO3b ClNO3b =ClO+NO2  
723 17 J-Cl2 Cl2 =Cl+Cl  
724 18 J-HOCl HOCl =OH+Cl  
725 19 J-OCIO OCIO =O+ClO  
726 20 J-Cl2O2 Cl2O2 =Cl+Cl+O2  
727 21 J-ClO ClO =Cl+O  
728 22 J-BrO BrO =Br+O  
729 23 J-BrNO3 BrNO3 =Br+NO3(29%) & BrO+NO2(71%)\*  
730 24 J-HOBr HOBr =OH+Br  
731 25 J-BrCl BrCl =Br+Cl  
732 26 J-N2O N2O =N2+O  
733 27 J-CFCl3 CFCl3 =...  
734 28 J-CF2Cl2 CF2Cl2 =...  
735 29 J-F113 CF2ClCFCl2=...  
736 30 J-F114 CF2ClCF2Cl=...  
737 31 J-F115 CF3CF2Cl=...  
738 32 J-CCl4 CCl4 =...  
739 33 J-CH3Cl CH3Cl =CH3+Cl  
740 34 J-MeCCl3 CH3CCl3=...  
741 35 J-CH2Cl2 CH2Cl2 =...  
742 36 J-CHF2Cl CHF2Cl =...  
743 37 J-F123 CF3CHCl2=...  
744 38 J-F141b CH3CFCl2=...  
745 39 J-F142b CH3CF2Cl=...  
746 40 J-CH3Br CH3Br =CH3+Br  
747 41 J-H1211 CF2ClBr=...  
748 42 J-H1301 CF3Br =...  
749 43 J-H2402 C2F4Br2=...  
750 44 J-CH2Br2 CH2Br2 =...  
751 45 J-CHBr3 CHBr3 =...  
752 46 J-CH3I CH3I =CH3+I

753 47 J-CF3I CF3I =CF3+I  
 754 48 J-OCS OCS =CO+S  
 755 49 J-PAN CH3C(O)O2NO2 =CH3C(O)O2+NO2(60%) & CH3C(O)O+NO3(40%)\*  
 756 50 J-CH3NO3 CH3ONO2=CH3O+NO2  
 757 51 J-ActAld CH3CHO =CH3+HCO  
 758 52 J-MeVK CH3C(O)CH=CH2 =C3H6+CO(60%) & CH2=CHCO+CH3(40%)\*  
 759 53 J-MeAcr CH2C(CH3)CHO =CH2=C(CH3)+HCO  
 760 54 J-GlyAld HOCH2CHO =HOCH2+HCO  
 761 55 J-MEKeto CH3COC2H5 =CH3+C2H5CO(15%) & C2H5+CH3CO(85%)\*  
 762 56 J-EAld C2H5CHO =C2H5+HCO  
 763 57 J-MGlyxl CH3COCHO =CH3CO+HCO  
 764 58 J-Glyxla (CHO)2 =HCO+HCO  
 765 59 J-Glyxlb (CHO)2 =H2+CO+CO  
 766 61 J-Acet-a C3H6O =CH3CO+CH3  
 767 62 J-Acet-b C3H6O =CH3+CH3+CO

=====

\* In preliminary comparisons, we have found it best to compare  
 the total O3 photolysis rate and the rate leading to O(1D),  
 skipping the O(3P) path. When branching paths with % are  
 indicated in the table, they indicate the values derived for  
 fast-JX, please just report the total J-value.

# Chapter 7

## Upper Troposphere and Lower Stratosphere

**Lead Authors:** Andrew Gettelman & Michaela Hegglin

**Co-authors:** Seok-Woo Son  
Masatomo Fujiwara  
Simone Tilmes  
Laura Pan  
Peter Hoor  
Huikyo Lee  
Gloria Manney  
Thomas Birner  
Gabriele Stiller  
Markus Rex  
Stefanie Kremser  
Don Wuebbles  
Kaley Walker  
Juan A. Añel

---

### 7.1 Introduction

The upper troposphere/lower stratosphere (UTLS) plays a key role in radiative forcing and chemistry-climate

coupling (see Shepherd (2007) for a recent review). The UTLS is the region lying between the lower troposphere and the middle stratosphere, from roughly 5 to 22 km altitude. The dynamical, chemical, and radiative properties of the UTLS are in many ways distinct from both the lower troposphere and the middle stratosphere. The coupling between dynamics, chemistry, and radiation is especially strong in the UTLS, controlled by complex processes on

a wide range of spatial and time scales. UTLS processes depend crucially on the distribution of greenhouse gases (GHGs), especially  $O_3$  and  $H_2O$ , as well as aerosols and clouds. Perturbations to the distributions of these atmospheric constituents can lead to direct forcing of surface climate through both radiative and dynamical mechanisms. The extra-tropical tropopause region is an important source of baroclinic instabilities that impact surface weather. In turn, climate change, through changing temperatures and transport patterns, has the potential to affect the chemical composition and structure of the UTLS.

In order to investigate the mechanisms determining the structure of the UTLS and to quantify future changes using CCMs, it is important that CCMs accurately represent the dynamical, radiative, and chemical properties of the UTLS. In this chapter, we present the first comprehensive validation of CCMs in the UTLS, using a wide range of process-oriented model diagnostics. To achieve this goal, new data sets are compiled and analysed in order to test their usefulness in serving as observational references. Many of the diagnostics are based on seasonal cycles, a long-established tool for validating models. Many other diagnostics presented here are used for the first time, and may require further development. The different diagnostics are used to grade model skill, which are summarized at the end of the chapter into a qualitative overall assessment of each model's performance. Some of the more complex diagnostics are applied only to a subset of the CCMVal-2 models that provided temporally higher-resolved instantaneous chemical and dynamical fields. These evaluations add additional information on key aspects of transport and dynamics in the UTLS, and may be regarded as examples of how future validation efforts could be expanded, but are not at this time comprehensive quantitative metrics of model performance. Some of the analyses are compared to recently published studies using the CCMVal-1 models. Also, past and future trends of key dynamical and chemical quantities are presented at the end of the chapter.

In many cases, a different balance of processes and structures exists in the tropics and at higher latitudes, providing a natural separation between the tropical UTLS, which also contains the Tropical Tropopause Layer (TTL), and the extra-tropical UTLS. We use this distinction as a natural break, but do not neglect the interactions across latitudes, and processes in the subtropics. **Table 7.1** provides an overview of the model diagnostics described in this chapter organised according to the key processes the diagnostics are testing for both the tropical and the extra-tropical UTLS.

The different diagnostics are explained in detail in the tropical and extra-tropical UTLS sections, but here a short summary is given:

**Tropical UTLS diagnostics:** For the tropical UTLS, or

Tropical Tropopause Layer (TTL), we focus on several diagnostics of temperature, transport and water vapour. The TTL is the source of almost all stratospheric air, and water vapour in the stratosphere is regulated by tropopause temperatures (Brewer 1949). Tropopause temperature is an important aspect of model representation of the TTL since it has strong implications for the water vapour distribution. Other diagnostics focus on variability in the TTL, both for examining large scale and long term variability in tropopause temperature, as well as intra-seasonal variability and the representation of tropical wave modes in the models. Quantitative grades are reported for diagnostics for water vapour, tropopause temperature and tropopause pressure.

**Extra-tropical UTLS diagnostics:** For the extra-tropical UTLS, we focus on several diagnostics of dynamics, transport, mixing and variability. The mass flux into the lowermost stratosphere (LMS, see **Figure 7.1**) from above and the seasonality in LMS mass determine the amount and temporal variability of stratospheric ozone transported into the troposphere, thereby having a crucial impact on the radiative budget of the upper troposphere, but also on tropospheric chemistry. The distributions of radiatively active species such as ozone and water vapour influence temperatures, winds, and dynamics in the extra-tropical UTLS.  $O_3$  and  $H_2O$  are key in determining the models' capabilities to represent stratosphere-troposphere coupling accurately. Several diagnostics therefore focus on how well the models represent the dynamical and chemical structure of the extra-tropical UTLS, especially the distributions of temperature,  $O_3$  and  $H_2O$ .

The chapter starts with a description of the data sets used in the comparisons (Section 7.2), followed by an introduction to the diagnostics used in this chapter (Section 7.3). The main validation exercise is divided into two sections discussing UTLS characteristics of the tropics (Section 7.4) and the extra-tropics (Section 7.5) separately. In Section 7.6, we discuss past and future changes simulated in the models, before we summarize our findings and provide an overall assessment of the models' performance in the UTLS in Section 7.7.

## 7.2 Description of observational data sets used for CCM validation

High quality measurements in the global UTLS for the use of model validation are difficult to obtain due to major challenges for the available measurement platforms. *In situ* instruments on balloons or aircraft are challenged by the low pressure and low temperature conditions. Remote sensing techniques used to observe the stratosphere are challenged by saturation of the measured radiances in the

**Table 7.1:** List of core processes to validate CCMs in the UTLS. Gray highlights the diagnostics that will be used as quantitative metrics for the overall model assessment.

Process	Diagnostic	Variables	Data	References <sup>a</sup>	Section
<b>Tropical UTLS</b>					
Dynamics	Seasonal cycle in CPT <sup>b</sup>	$T$	NCEP, ERA-40	<i>Eyring et al. (2006)</i>	7.4.1
	TP inversion layer	$T$	GPS	<i>Gettelman et al. (2010)</i>	7.4.7
Dehydration	Seasonal cycle in H <sub>2</sub> O above CPT (80 hPa)	H <sub>2</sub> O	HALOE	<i>Eyring et al. (2006)</i>	7.4.5
	H <sub>2</sub> O – CPT correlations	H <sub>2</sub> O	NCEP, ERA-40, HALOE	<i>Gettelman et al. (2010)</i>	7.4.5
	Lagrangian CPT	$u, v, T,$ Heating	NCEP, ERA-40	<i>Kremser et al. (2009)</i>	7.4.3
Variability	Interannual CPT anomalies	$T$	NCEP, ERA-40	<i>Gettelman et al. (2009)</i>	7.4.1
	Wave analyses	$T, u, v,$ OLR <sup>b</sup>	ERA-40, ERA-Interim, NCEP, NCEP2, JRA25	<i>Wheeler and Kiladis (1999)</i>	7.4.1
Transport & mixing	O <sub>3</sub> seasonal cycle (100 hPa)	O <sub>3</sub>	O <sub>3</sub> -sondes	<i>Eyring et al. (2006)</i>	7.4.4
	Lagrangian Transport Time	$u, v, T,$ Heating	NCEP, ERA-40	<i>Kremser et al. (2009)</i>	7.4.3
<b>Extra-tropical UTLS</b>					
Dynamics	Zonal mean zonal wind @200 hPa	$u$	ERA-40, NCEP	<i>Hegglin et al. (2010)</i>	7.5.1.1
	Seasonal cycle in LMS mass	$M$	NCEP	<i>Appenzeller et al. (1996)</i>	7.5.1.2
	TP pressure anomalies	pressure	ERA-40, NCEP	<i>Gettelman et al. (2010)</i>	7.5.1.3
	TP inversion layer	$T$	GPS	<i>Birner (2006)</i>	7.5.1.4
Transport & mixing	Seasonal cycle in O <sub>3</sub> , HNO <sub>3</sub> , H <sub>2</sub> O @100 and 200 hPa	O <sub>3</sub> , HNO <sub>3</sub> , H <sub>2</sub> O	MIPAS, ACE-FTS, MLS	<i>Logan (1999)</i>	7.5.2.1
	Meridional tracer gradients @200 hPa	O <sub>3</sub>	MLS	<i>Shepherd (2002)</i>	7.5.2.2
	Normalised CO relative to TP	CO	SPURT	<i>Hoor et al. (2004, 2005); Hegglin et al. (2010)</i>	7.5.2.3
	Vertical profiles in TP coordinates	H <sub>2</sub> O, CO, O <sub>3</sub>	Aircraft, ACE-FTS	<i>Pan et al. (2004, 2007) Tilmes et al. (2010)</i>	7.5.2.4
	ExTL <sup>b</sup> depth	H <sub>2</sub> O/O <sub>3</sub>	Aircraft, ACE-FTS	<i>Pan et al. (2007) Hegglin et al. (2009)</i>	7.5.2.5
Variability	PDFs of O <sub>3</sub> variability	O <sub>3</sub>	MLS	<i>Lee et al. (2010)</i>	7.5.2.6

<sup>a</sup>Listed references provide information on the diagnostic and/or the observations used for the evaluation

<sup>b</sup>Abbreviations: CPT=cold point temperature; TP=tropopause; OLR=outgoing long-wave radiation; ExTL=extra-tropical tropopause transition layer

UTLS in many commonly used wavelengths. Additional difficulties arise from the small vertical and horizontal length scales found in the chemical and dynamical fields in the UTLS – the result of the large dynamical activity in the tropopause region.

Here, an overview is given of the observational data sets used for the model-measurement comparisons in the UTLS in order to provide critical information about their accuracy, precision, and potential sampling issues. Note that the list below is not a comprehensive compilation of currently available data sets which may be useful for model evaluation in the UTLS.

### 7.2.1 Balloon data

The global radiosonde network provides a comprehensive view of the thermal structure of the UTLS. High vertical resolution radiosondes have provided a wealth of information about TTL structure. However, inhomogeneities in radiosonde records over time often make use of raw records problematic for trend analysis, and care must be taken when trends are analysed (Seidel and Randel, 2006).

### 7.2.2 Aircraft data

As with balloon measurements, aircraft observations provide mostly high accuracy, high precision, and high resolution data in the UTLS, but may be restricted in their representativeness due to limited sampling in time and space.

Data from various NASA, NSF, and some German aircraft campaigns between 1995 and 2008 have recently been compiled into a high resolution aircraft based UTLS climatology of ozone, CO and H<sub>2</sub>O (Tilmes *et al.*, 2010). The data set covers a broad altitude range up to 22 km. The spatial coverage ranges over all latitudes in the NH for most of the four seasons, but coverage is predominantly over North America and Europe. The precision and accuracy of the ozone data is  $\pm 5\%$ . CO observations taken by different instruments have a precision of  $< 1\%$  and an accuracy of  $< 3\%$ . The precision of H<sub>2</sub>O data is estimated to be  $< 5\%$  and the accuracy is between 0.3 ppmv and values of 10% depending on the instrument. The aircraft climatology is especially designed to serve as a tool to evaluate the representation of chemistry and transport by CCMs in the UTLS.

A subset of these high-resolution and high-precision observations is used separately in this chapter and stem from the German SPURT aircraft campaign (SPUREnstofftransport in der Tropopausenregion, or trace gas transport in the tropopause region). The campaign consisted of 8 deployments distributed seasonally over the course of three years (2001-2003), with a total of 36 flights, each yielding around 2-5 hours of observations. The flights were carried out between around 35°N and

75°N over Europe and reached potential temperature levels between 370 K and 375 K. A campaign overview is given by Engel *et al.* (2006). The CO measurements used in this study typically showed total uncertainties of 1.5% (Hoor *et al.*, 2004).

Another subset of high-resolution data used separately in this chapter stems from the NASA POLARIS (Photochemistry of Ozone Loss in the Arctic Region in Summer) campaign (Newman *et al.*, 1999). During the campaign, 35 flights were deployed between March and September 1997 using the NASA ER-2 research aircraft from three locations: Moffett Field, California (~37°N), Fairbanks, Alaska (~65°N), and Barbers Point, Hawaii (~21°N). The flights covered a latitude range of approximately 20°N-70°N and a vertical range of 5-18 km. For the O<sub>3</sub> and H<sub>2</sub>O data used in this study, the estimated accuracies are ~3% and 5%, respectively (Proffitt and McLaughlin, 1983; Hints *et al.*, 1999). The use of these data to characterize the ExTL has been described in Pan *et al.* (2004; 2007).

### 7.2.3 Satellite data

Recently, satellite instruments have achieved the technological maturity to remotely sound the UTLS from space, offering an unprecedented temporal and spatial coverage of this region. To determine the accuracy and precision of these measurements is the focus of intensive validation efforts. While more data sets will become available in the near future, here we describe only the data from instruments used in this chapter.

#### *ACE-FTS on SCISAT-1*

The Atmospheric Chemistry Experiment Fourier Transform Spectrometer (ACE-FTS) on Canada's SCISAT-1 satellite features high resolution (0.02 cm<sup>-1</sup>) and broad spectral coverage in the infrared (750 to 4400 cm<sup>-1</sup>) (Boone *et al.*, 2005; Bernath *et al.*, 2005). The instrument has operated since February 2004 in solar occultation mode providing seasonally varying coverage of the globe, with an emphasis on mid-latitudes and the polar regions. Up to 30 occultation events occur per calendar day. The very high signal-to-noise ratio characterizing the ACE-FTS infrared spectra makes it possible to measure more than 30 chemical trace gas species with high accuracy and precision (Clerbaux *et al.*, 2008; Dupuy *et al.*, 2008; Hegglin *et al.*, 2008). The derived overall measurement uncertainties in the observations for the UT and LS were  $\pm 9\%$  and  $\pm 12\%$  for CO,  $\pm 30\%$  and  $\pm 18\%$  for H<sub>2</sub>O, and  $\pm 18\%$  and  $\pm 8\%$  for O<sub>3</sub>, respectively (Hegglin *et al.*, 2008). This, together with vertical sampling ranging from about 3 km to less than 1 km in the UTLS, provides the first global view of tracer distributions in the extra-tropical tropopause re-

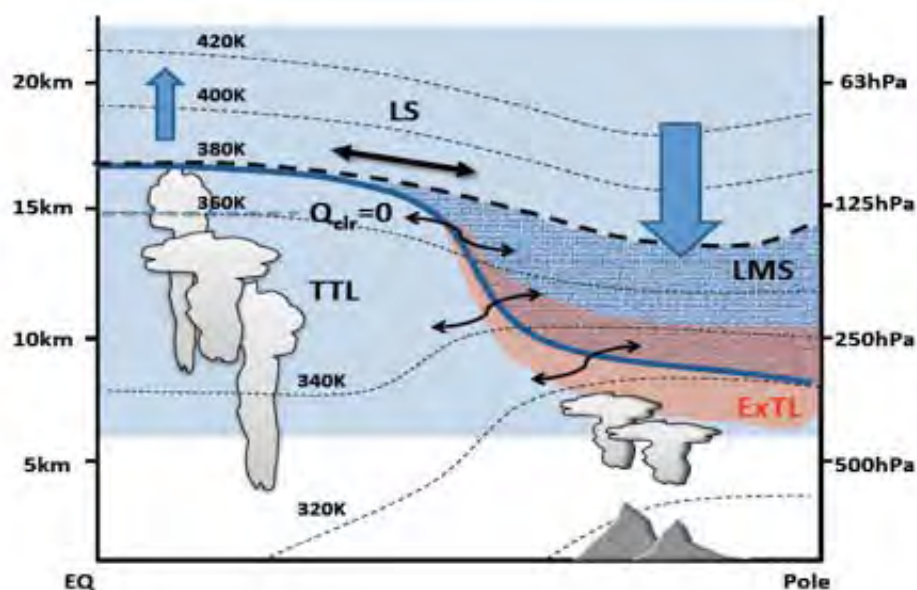


**Figure 7.1:** Schematic of the UTLS illustrating the Tropical Tropopause Layer (TTL) extending from the level of deep convective outflow, through the level of zero clear-sky radiative heating ( $Q_{clr}=0$ ) up to the cold point and the tropopause (thick blue line). The lower stratospheric (LS) branch of the Brewer-Dobson wave driven circulation is shown by the blue arrows. Faster and seasonally dependent meridional transport between the tropics and extra-tropics is found within the 380–420 K layer (black straight arrow). The extra-tropical UTLS contains the lowermost stratosphere (LMS) between the 380 K potential temperature surface and the tropopause. Also illustrated (in red) is the Extra-tropical Transition Layer (ExTL) which represents a mixing layer in which air has partly tropospheric, partly stratospheric chemical characteristics.

gion (Hegglin *et al.*, 2009).

### Aura MLS

The Microwave Limb Sounder (MLS) on the EOS Aura satellite measures millimeter- and submillimeter-wavelength thermal emission from the limb of Earth's atmosphere (Waters *et al.*, 2006). Aura MLS has data coverage from 82°S to 82°N latitude on every orbit, providing comprehensive information on UTLS tracer distributions. Vertical profiles are measured every 165 km along the sub-orbital track and have a horizontal resolution of ~200–300 km along-track and ~3–9 km across-track. Vertical resolution of the Aura MLS data is typically ~3–4 km in the lower and middle stratosphere (Livesey *et al.*, 2007).  $O_3$  has been used successfully in studies to examine transport in the UTLS, although some biases still exist in the version 2.2 retrieval used in the evaluations presented here. Validation of stratospheric  $O_3$  is discussed by Livesey *et al.* (2008). The MLS v2.2  $O_3$  retrieval has an accuracy of 0.02 ppmv and 0.05 ppmv at 214 hPa and 100 hPa, respectively, and a precision of 0.04 ppmv at both levels.

### MIPAS

MIPAS is a limb-viewing Fourier transform emission

spectrometer on board Envisat in a sun-synchronous polar orbit. MIPAS covers the mid-infrared spectral region between 685 and 2410  $\text{cm}^{-1}$  (Fischer *et al.*, 2008). MIPAS has provided data since 2002 at about 1000 geo-locations per day from pole to pole during day and night. MIPAS covers the atmosphere from the upper troposphere to the mesosphere (6 to 70 km), and provides global distributions of a large number of species. In its original observation set-up from July 2002 to March 2004 it measured one limb radiance profile every 500 km along track with a vertical sampling of 3 km and a spectral resolution of 0.035  $\text{cm}^{-1}$ . Validation of these data products can be found in Milz *et al.* (2005, 2009), Wang *et al.* (2007), and Steck *et al.* (2007). Since January 2005, the observation set-up has been changed to slightly reduced spectral resolution (0.0625  $\text{cm}^{-1}$ ), but improved vertical (1.5 km) and horizontal along-track (400 km) sampling. Description of these data products can be found in von Clarmann *et al.* (2009). The accuracy (including contributions of precision and systematic errors) of the MIPAS data has been found to be 9.6% (at 15 km) and 17% (at 10 km) for  $O_3$ , 4.4% (at 15 km) and 6.0% (at 10 km) for  $\text{HNO}_3$ , and 17.7% (at 20 km) and 8.3% (at 15 km) for  $\text{H}_2\text{O}$ , respectively (von Clarmann *et al.*, 2009). All data used within this study have been processed at the Institute for Meteorology and Climate Research (IMK) (von Clarmann *et al.*, 2003).

## HALOE

We also use water vapour observations from the Halogen Occultation Experiment (HALOE) on the UARS satellite (Russell III *et al.*, 1993). HALOE H<sub>2</sub>O observations have been extensively validated (*e.g.*, Kley *et al.*, 2000). HALOE validation and a 13-year record (1992-2004) gives us high confidence in HALOE performance. The random and systematic errors in HALOE H<sub>2</sub>O at 100 hPa are 11% and 28%, and for O<sub>3</sub> 14% and 24%, respectively.

## COSMIC

The Global Positioning System (GPS) Radio Occultation (RO) data used in this study were obtained from the COSMIC (Constellation Observing System for Meteorology, Ionosphere, and Climate)/FORMOSAT-3 (Formosa Satellite Mission 3) mission, which is a collaborative project between Taiwan and the United States (Anthes *et al.*, 2008). The mission placed six micro-satellites in different orbits at 700-800 km above the ground. These satellites form a low-orbit constellation that receives signals from US GPS satellites, providing approximately 2500-3000 soundings per day almost evenly distributed over the globe. The mission has a relatively short data record since its mission launch was only in 2006. In this study, we use data between 2006 and 2009.

### 7.2.4 Meteorological Analyses

Operational meteorological analyses are produced on a daily basis by weather forecast centres. These analyses (or ‘reanalyses’ if they are produced by consistent forecast models over time) are very valuable for model comparison, since they provide complete fields that are closely tied to observations, but with similar space scales and statistics as global models. Here we use analyses from the National Center for Environmental Prediction and National Center for Atmospheric Research (NCEP) described by Kalnay *et al.* (1996), the NCEP and Department of Energy (NCEP2) described by Kanamitsu *et al.* (2002), the Japanese Re-Analysis (JRA25) described by Onogi *et al.* (2007), the European Centre for Medium Range Weather Forecasts (ECMWF) 40 year reanalysis (ERA-40) described by Uppala *et al.* (2005) and ‘interim’ analysis (ERA-Interim) described by Uppala (2008). For information on the different reanalyses (ERA-40, NCEP, JRA25) the reader is referred to Randel *et al.* (2002) and references therein. A few distinct caveats common to reanalyses have to be noted. Because of the inhomogeneity of input data, specifically the introduction of significant assimilation of satellite observations starting in the late 1970’s, estimating trends from reanalysis systems is difficult, and in general not scientifically justified across the late-1970’s. Trend analysis since

the late-1970’s does usually have utility. We will use these data to estimate ‘observed’ trends in the UTLS. Second, re-analysis systems can have systemic biases. Perhaps most notable as an example is a significant warm bias to NCEP/NCAR reanalysis tropopause temperatures, caused by the selection of assimilated data (Pawson and Fiorino, 1998). Thus, the reanalyses need to be treated with some caution (Randel *et al.*, 2002). For comparison purposes with temperature and the tropopause, we will use the ERA-40 reanalysis, because of their high quality and a relatively long (20 year) record for comparison.

## 7.3 Metrics and Grading

Metrics are diagnostics with quantitative grading (a ‘grade’) applied, and are used to quantitatively assess model behaviour for some of the diagnostics. For example, mean values of a certain quantity or the amplitude and phase of a seasonal cycle can be used as a metric. We introduce below the two main approaches that were used in this chapter to lead from those metrics to a grading of the models. If a different grading approach is used for a diagnostic, it will be explained in the respective sections. Section 7.7 discusses how these approaches are applied and what values are ‘acceptable’.

### 7.3.1 Grading of Mean and Correlative Quantities

Some metrics (*e.g.*, in the tropics for the cold point tropopause temperature, water vapor annual cycle and tropopause pressure, and in the extra-tropics for the zonal mean wind) are defined following Douglass *et al.* (1999) and Waugh and Eyring (2008), with extensions to look at variability. Metrics are based on defining monthly means after spatial averaging. Douglass *et al.* (1999) define a metric based on mean differences:

$$g_m = \max(0, 1 - \frac{1}{n} \sum_{i=0}^n \frac{|\mu_{obs} - \mu_{mod}|}{n_g \sigma_{obs}}). \quad (7.1)$$

Here,  $\mu$  is a monthly mean quantity and  $n_g$  a scaling factor representing a number of standard deviations ( $\sigma$ ), often taken to be 3 (Waugh and Eyring, 2008). We also define a metric based on correlated variability where  $\mu'$  are anomalies from a mean quantity and  $C$  is the linear correlation coefficient:

$$g_c = (Cor(\mu'_{mod}, \mu'_{obs}) + 1)/2. \quad (7.2)$$

For the analysis here, the correlation is taken on annual mean values, and thus reflects correlations of interannual variability between a model and observations.

We can also define a metric based on the magnitude of the variance of a quantity, where  $\sigma$  is calculated each



month:

$$g_v = \max(0, 1 - \frac{1}{n} \sum_{i=0}^n \frac{|\sigma_{obs} - \sigma_{mod}|}{n_g \sigma_{obs}}). \quad (7.3)$$

A single metric is then the linear combination:

$$G_{mod} = (g_m + g_c + g_v) / 3. \quad (7.4)$$

This was found to yield reasonable results and encapsulate more than just the difference in means. The composite grade is designed to better represent uncertainty and forced variability. This partly (but not completely or rigorously) addresses shortcomings in the application of metrics recently identified by Grewe and Sausen (2009).

We have evaluated grades using several different measures of  $\sigma_{obs}$  and  $\mu_{obs}$  from different reanalysis systems, or using  $\sigma_{obs}$  and  $\mu_{obs}$  estimated from an ensemble of reanalysis systems. While the quantitative grades do change, the relative grades between models and the spread are robust across the different methods examined. For clarity, we will report grades against one set of observations, and grade other observational data sets against that for some idea of the potential spread. We also examine the multi-model mean, calculated by summing model outputs to generate a multi-model  $\mu_{obs}$ . The multi-model grades and averages are also shown. The goal of applying grades is to quantitatively determine model deficiencies with sufficient detail to understand where models perform well and why models do not perform well.

### 7.3.2 Taylor Diagram

Taylor diagrams (Taylor, 2001) are used as an alternative to the above metrics in the extra-tropics and visualise the statistical summary of how well two patterns from a test field ( $f$ ) and a reference field ( $r$ ) match each other in terms of their correlation ( $R$ ), their root-mean-square (RMS) difference ( $E'$ ), and the ratio of their variances ( $\sigma_f / \sigma_r$ ). These quantities can be used to quantify the correctness of phase and amplitude of seasonal cycles, which are often used in model-measurement comparisons.

The ratio between the variances of the test and reference field  $\sigma_f / \sigma_r$  is the normalised variance of the test field and given as the radial coordinate in the Taylor diagram. It therefore corresponds to the distance between  $f$  and the origin of the plot (see **Figure 7.2**).

The correlation  $R$  is defined by

$$R = \frac{\frac{1}{N} \sum_{n=1}^N (f_n - \bar{f})(r_n - \bar{r})}{\sigma_f \sigma_r}, \quad (7.5)$$

and is given as the azimuthal coordinate in the Taylor diagram. In principle,  $R$  could be negative and represented in a Taylor diagram (see Taylor, 2001 for an example). The

RMS difference is defined by

$$E' = \sqrt{\frac{1}{N} \sum_{n=1}^N [(f_n - \bar{f}) - (r_n - \bar{r})]^2} \quad (7.6)$$

and can be determined once the correlation  $R$  and  $\sigma_f / \sigma_r$  are known. Smaller  $E'$  represents a better fit between the test field and the reference field. Taylor diagrams can be used to test various aspects of model performance and to specify the relative skill of many different models (Taylor, 2001) as for example used in the Houghton *et al.* (2001) or the chemistry transport model inter-comparison by Brunner *et al.* (2003; 2005). The skill factor ( $S$ ) can be defined using

$$S = \frac{4(1+R)}{(\hat{\sigma}_f + 1/\hat{\sigma}_r)^2(1+R_0)}. \quad (7.7)$$

Here,  $\sigma_f$  is the standard deviation of the test field normalised by the standard deviation of the reference field ( $\sigma_f / \sigma_r$ ).  $R_0$  is the maximum correlation models can achieve. Choosing  $R_0 < 1$  allows us to account for uncertainty in the observations or model limitations such as spatial and temporal resolution. The skill approaches unity as the model

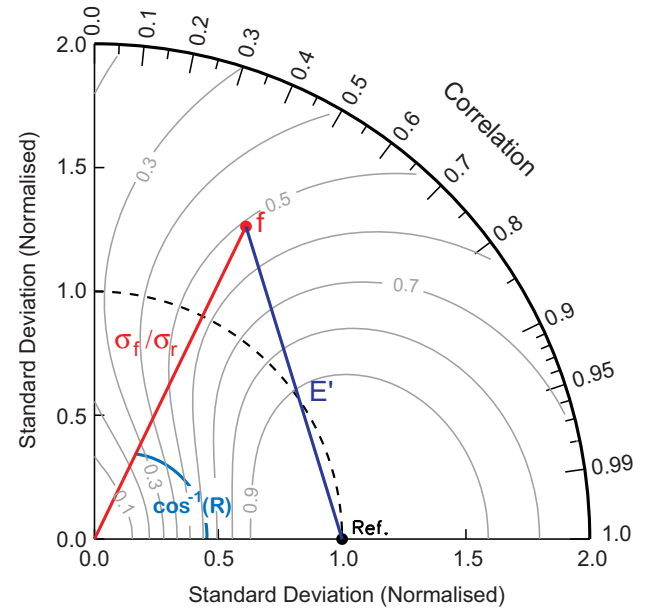


**Figure 7.2:** A sample Taylor diagram.  $f$  indicates the test or model field, and  $Ref.$  (or  $r$ ) a reference field. The inverse cosine of the correlation  $R$  between the test and reference field (indicated in light blue) determines the location on the azimuthal axis. The radial distance of  $f$  from the origin corresponds to the standard deviation of the test field normalised by the standard deviation of the reference field ( $\sigma_f / \sigma_r$ , red line). The RMS difference ( $E'$ , dark blue line) between test and reference field is proportional to the distance between the two fields on the diagram. Grey thin lines indicate the skill score ( $S$ ) of the test field, which obtains in this example a value of 0.51.

variance approaches the observed variance (*i.e.*, as  $\sigma_f \rightarrow 1$ ) and as  $R \rightarrow R_0$ .

For another illustrative example of how to read a Taylor diagram see also Hegglin *et al.* (2010). Finally, Taylor diagrams do not yield information on how close the mean of a given test field is to that of the reference field. Equation 1 is therefore used in addition to the skill to grade the simulated mean value ( $g_m$ ). A single grade for a model is then the linear combination of the skill and the mean:

$$G_{tot} = (S + g_m) / 2. \quad (7.8)$$

## 7.4 Results: The Tropical UTLS

The tropical UTLS region is usually known as the Tropical Tropopause Layer (TTL). The TTL is the region in the tropics within which air has characteristics of both the troposphere and the stratosphere. The tropical tropopause layer sets the lower boundary condition for the stratosphere (Brewer, 1949). Representing the TTL correctly in global models is critical for simulating the future of the TTL and its effects on climate and chemistry of the stratosphere.

The TTL is the layer in the tropics between the level of main convective outflow and the cold point, about 12–19 km (Gettelman and Forster 2002). The TTL has also been defined as a shallower layer between 15–19 km (Fueglistaler *et al.*, 2009). We will use the deeper definition of the TTL here because we seek to understand not just the stratosphere, but the tropospheric processes that contribute to TTL structure (see below), and it is more representative of the tropical UTLS. The TTL is maintained by the interaction of convective transport, convectively generated waves, radiation, cloud microphysics and the large-scale stratospheric circulation. The TTL is the source region for most air entering the stratosphere, and therefore the chemical boundary conditions of the stratosphere are set in the TTL. Clouds in the TTL, both thin cirrus clouds and convective anvils, have a significant impact on the radiation balance (Gettelman *et al.*, 2004; Corti *et al.*, 2006).

Here we will explore the representation of the TTL in global models, and assess potential changes to the TTL over time in Section 7.6.2.

### Detailed Description of Tropical Diagnostics

The following diagnostics also have quantitative metrics defined as noted in Section 7.3. We set  $n_g = 3$  ( $3\sigma$  threshold) for temperature and water vapour, and set the grading threshold ( $3\sigma n_g$ ) to 10 hPa for tropopause pressure, because it represents 1<sup>st</sup> CCMVal-2 level around the tropopause.

- **Diagnostic 1:** Temperature of the Cold Point Tropopause (Amplitude and Phase of Annual Cycle):

It is critical that models reproduce the amplitude and phase of the annual cycle of Temperature at the Cold Point Tropopause (TCPT), the coldest point in a UTLS profile. Because of the non-linearity of the Clausius-Clapeyron equation regulating water vapour saturation, the annual cycle is as important as the annual mean. This is a simplified metric of the true ‘Lagrangian Cold Point’, which we can examine in only a few models.

- **Diagnostic 2:** Tropopause Pressure: Lapse rate tropopause pressure (PTP) and its interannual variability should reflect the interannual variability in the observations. In particular, responses to major forcing events (*e.g.*, ENSO and volcanoes) should resemble observations. Anomalies of PTP have been shown to be more robust (*i.e.*, there is better agreement between observations) than tropopause temperature (Gettelman *et al.*, 2009). Simulated anomalies can be compared to reanalysis and radiosonde observations. A metric for this diagnostic is the correlation with interannual anomalies and the mean values from reanalysis systems in similar coordinates. A measure of the uncertainty is the variability of the grade of reanalysis systems compared to each other, which gives a sense of the unforced variation between analysis models.
- **Diagnostic 3:** Water vapour above the CPT (80 hPa): In conjunction with the CPT, the water vapour concentration above the CPT is the dominant term in the total hydrogen budget of the stratosphere. Models should simulate appropriately the annual cycle of the water vapour concentration in the lower tropical stratosphere, and its interannual variability.
- **Diagnostic 4:** Ozone in the TTL: Ozone in the TTL is affected by both transport and chemistry. TTL ozone is an important indicator of TTL processes. Models should represent the vertical structure of ozone and its annual cycle. The ozone concentration at a fixed level in the TTL (100 hPa) is used as a proxy for the ozone gradient. Ozone is also radiatively important in the TTL, and thus important for getting the thermal structure correct. Since ozone is chemically produced in the TTL by various processes, it is also an integrated measure of TTL chemistry processes and TTL transport time. Differences in ozone may be due to different chemical processes (for example  $\text{NO}_x$  production by lightning), which may or may not be present in a given model, but this needs to be understood.

### Diagnostics not used as quantitative metrics in the overall model assessment

These diagnostics are not used as quantitative metrics because they either do not yet have clear and robust quantitative relevance that fits the grading methodology

(Diagnostics 5 and 8), or are not produced for a large fraction of the models (Diagnostics 6 and 7).

- **Diagnostic 5:** H<sub>2</sub>O Correlations with TCPT: H<sub>2</sub>O at 80 hPa and TCPT can be combined by translating TCPT into water vapour by a saturation vapour mixing ratio. There should be a correlation between H<sub>2</sub>O and TCPT. This can also be expressed as the saturation vapour mixing ratio of the CPT ( $Q_{SAT}(T_{CPT})$ ) and the ratio  $H_2O / Q_{SAT}(T_{CPT})$  should reflect physical mixing processes (*e.g.*,  $H_2O / Q_{SAT}(T_{CPT}) > 1$  is physically implausible based on observations). Monthly anomalies with a 1 month lag or interannual anomalies can also be compared.
- **Diagnostic 6:** Tropical Waves: The structures seen in transport times, chemistry and water vapour are not just consequences of large-scale processes on zonal or monthly scales. Waves and intra-seasonal variability in the TTL are critical for properly representing structures in the TTL. Here we use detailed high-resolution information to examine intra-seasonal variability and wave modes in a subset of models that provided high temporal frequency output (every 6 hours). Wave activity metrics are defined, but only a few models are analysed.
- **Diagnostic 7:** TTL transport time: The transport time through the TTL is a complex, emergent diagnostic reflecting a mix of transport processes, including large-scale advection by radiation and waves, as well as rapid convective motion in the vertical. Representing the transport time through the TTL is critically important for short-lived species, whose lifetimes are less than a small multiple of the transport time. Several studies have attempted to assess the transport time, and here we will use Lagrangian trajectory studies to estimate transport times from a subset of models with high temporal resolution output to drive a trajectory model, and compare them to similar calculations with a reanalysis system.
- **Diagnostic 8:** Tropopause Inversion Layer: The Tropopause Inversion Layer (TIL) is a layer exhibiting an increase in the static stability that occurs just above the tropopause (Birner, 2006). The TIL provides an integrated look at the dynamical structure of the TTL in the vertical. It not only shows the separation between the stratosphere and troposphere, but also provides insights into the correct dynamical results of convection in the upper troposphere, and transport and dynamics in the lower stratosphere. The static stability structure is sensitive to the radiative balance of the TTL, and hence transport of H<sub>2</sub>O and O<sub>3</sub>, as well as large-scale dynamics. Here we analyse the TIL in models that provided 3D instantaneous output.

### 7.4.1. Cold Point Tropopause Temperature

The TCPT is analysed from models and reanalyses vertically interpolated to CCMVal-2 levels. This provides a slightly blurred picture of the true cold point relevant for H<sub>2</sub>O condensation experienced by a simulated air parcel, but it is a useful baseline for comparisons. The annual cycle of tropical cold point temperature (or cold point tropopause temperature) is illustrated in **Figure 7.3** using the REF-B1 CCMVal-2 model fields. In addition to the models, several analysis systems are also shown (ERA-40, NCEP, NCEP2, JRA25, ERA-Interim). All analyses use monthly means interpolated to CCMVal-2 standard levels, so the models and analyses systems are on the same temporal and vertical grids. The gray region is 3 standard deviations ( $\sigma$ ) from the ERA-40 observations. In general, almost all models are able to reproduce the annual cycle. There are significant differences between the models, but the monthly averages of 8 models and the multi-model mean are clustered within  $3\sigma$  of the mean of ERA-40, as seen in the quantitative grades ( $g_m$ ) in Figure 7.3. The quantitative metrics of the cold point are based on Equation 7.4. ERA-40 is taken as the base observation for the mean ( $\mu_{obs}$ ) and the standard deviation ( $\sigma_{obs}$ ). The reanalyses themselves do not all compare well (*i.e.*, score highly) compared to ERA-40, largely due to the warm bias of NCEP, and lack of correlated interannual variability.

The multi-model mean is very close to ERA-40, closer than some other analysis systems. These results are also better than CCMVal-1 models reported by Gettelman *et al.* (2009). Note that there is general quantitative agreement between the reanalyses, with ‘grades’ (compared to ERA-40) ranging from 0.6-0.8 (Figure 7.3). This is largely due to mean offsets between the analysis systems, the amplitude and phase of the annual cycle are in good agreement. NCEP and NCEP2 have a known warm bias (Pawson and Fiorino, 1998).

Most models do not show strong long-term trends in cold point temperatures, as indicated in **Figure 7.4**. NCEP and NCEP-2 reanalyses show strong cooling, which is not seen in the ERA-40, JRA25 and ERA-Interim analyses, as noted by Zhou *et al.* (2001). Note that these trends differ from other cooling trends reported from radiosondes (Gettelman and Forster, 2002; Seidel and Randel, 2006). This may be due to the gridding and interpolation to a standard set of vertical levels. Thus, if there is cooling of the cold point, it is not clear that this appears significantly in coarse resolution analyses. However, the lack of agreement among observations highlights the uncertainty in interannual and long-term changes in the TCPT.

Interannual variability is also illustrated in **Figure 7.4**. Most models show significant warming of the cold point in 1991 of a degree or so, likely associated with the eruption of Mt. Pinatubo. Most models and the multi-mod-

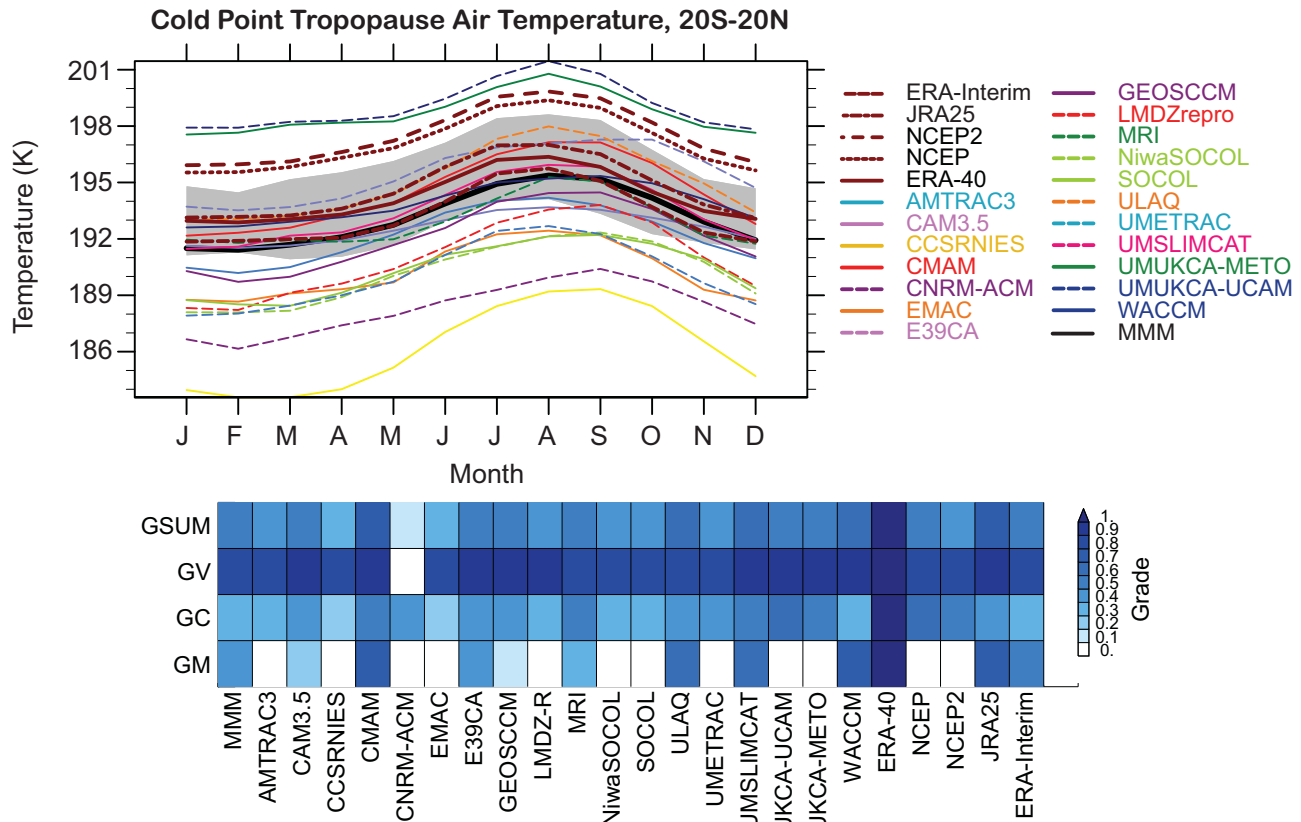


**Figure 7.3:** (Above) Annual cycle of tropical (20°S-20°N) cold point tropopause temperature from models and observations. Output and observations are from the period 1980-1999. Gray shaded region is 3σ variability from ERA-40 analyses. Multi-model mean is the thick black line, JRA25 (brown dot-dash), NCEP (brown dotted), NCEP2 (brown dashed), ERA-40 (brown solid), ERA-Interim (brown short-dash). (Below): Quantitative metrics summary of Cold Point Tropopause Temperature (TCPT) for mean (GM), correlation (GC), variance (GV) and the average of all three grades (GSUM).

el mean show warming of the TCPT after volcanic events (especially El Chichón in 1983 and Mt. Pinatubo in 1991). This warming is not as clear in analysis systems. Some models have a warming that is much too large (CNRM-ACM, NiwaSOCOL, SOCOL, MRI). This is factored into the metrics for variability ( $g_v$ ) as described above. Models with large variability will have a lower score on the  $g_v$  metric component (Figure 7.3). Also, the effect of the El-Niño Southern Oscillation (ENSO) and the Quasi-Biennial Oscillation (QBO) on the tropical tropopause (Zhou *et al.*, 2001) are not clear in these low vertical resolution analyses. Interannual anomalies are not correlated between models and analyses, or between analyses themselves.

### 7.4.2 Lapse Rate Tropopause Pressure

The pressure of the lapse rate tropopause (PTP) has been shown to be a more robust metric than the cold point temperature (Gettelman *et al.*, 2009). PTP is more sensitive to increasing thickness (vertically integrated temperature) below, and the temperature response is a more verti-

cally confined. It is easier to get bulk thickness (latent heat release) right than TCPT details. This is evidenced by a high (0.8-0.9 or 1) correlation ( $g_c$ ) among most analysis systems compared to ERA-40 (Figure 7.6). Grades are determined based on Equation (7.4). The meridional structure of tropopause pressure from models and analysis systems is shown in **Figure 7.5**. The models all broadly reproduce the observed tropopause structure. There are some differences in the pressure of the tropical tropopause, which all analysis systems place at the 90 hPa level (when interpolated to CCMVal levels). Several models shift the tropopause up or down by a level. There are large differences, however, in the diagnosed tropopause at high latitudes, again due to potential shifts by a level or so in the thermal structure. CCMVal-2 levels are noted on Figure 7.5

Long-term changes in the tropopause pressure from 20°S-20°N are shown in **Figure 7.6**. There is good agreement between the interannual anomalies of most of the models, as well as trends in tropopause pressure. The simulated variability in models is higher than the observations. Most models and analysis systems show decreases in tro-

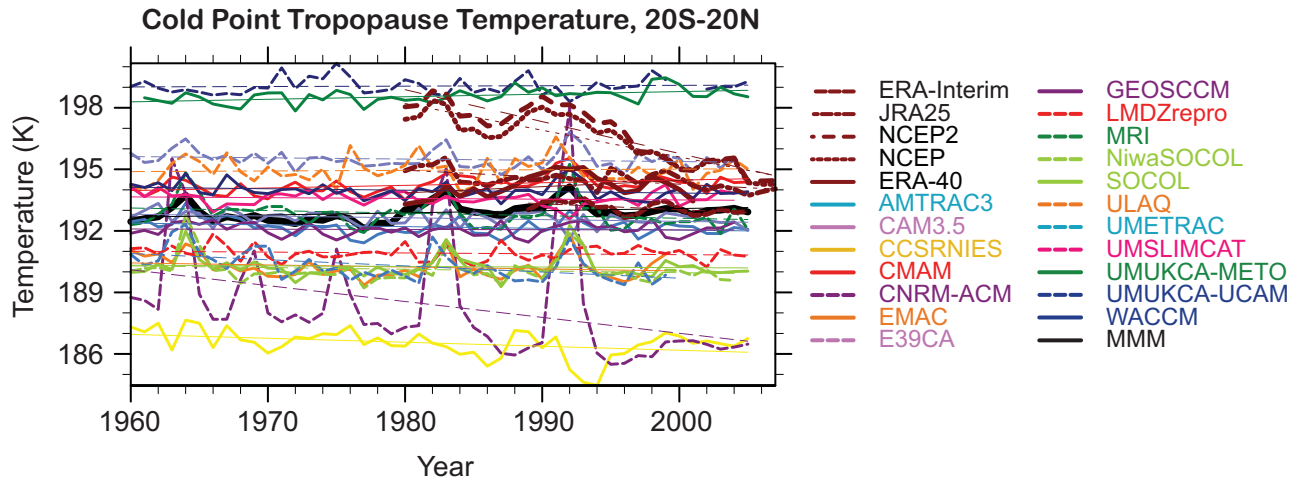


**Figure 7.4:** Time series of annual mean temperature of the Cold Point Tropopause (TCPT) for 20°S-20°N from models and analyses for 1960-2007. Thin lines are linear fits. Multi-model mean (MMM) is the thick black line.

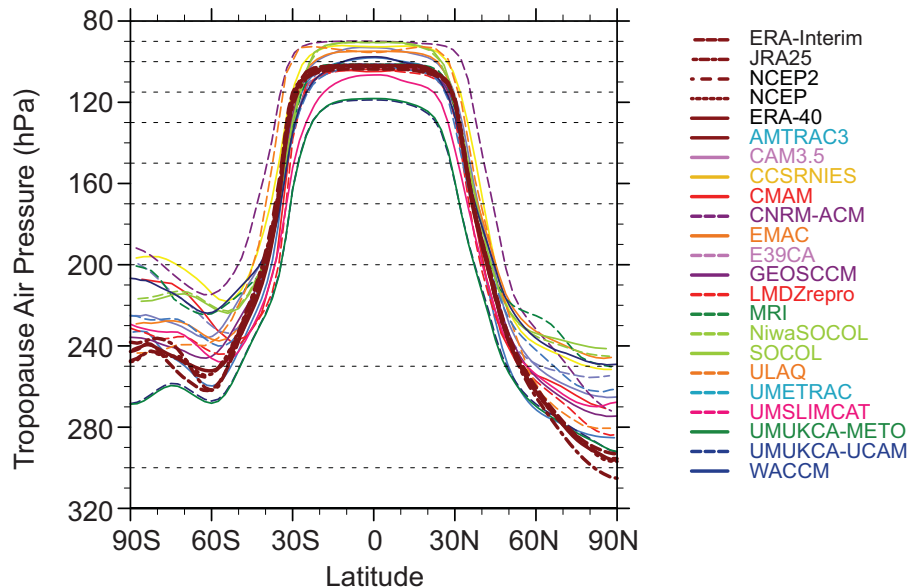


**Figure 7.5:** REF-B1 lapse rate tropopause pressure (PTP) annual zonal mean for 1980-1999 from models and analysis systems. Dotted lines represent CCMVal-2 vertical level structure in the UTLS, with levels at 400, 300, 250, 200, 170, 150, 130, 115, 100, 90, 80, 70, 50 hPa.

popause pressure associated with volcanic events, though model variability is larger. In particular, it is too large for CNRM-ACM, which jumps 2 levels (90 to 115hPa). Metrics for tropopause pressure indicate a high degree of consistency among the analysis systems as noted above. CCMVal models can broadly reproduce trends and variability, but with too much variance.

### 7.4.3 Transport in the TTL

Lagrangian trajectory studies are established tools for studying transport processes in the tropical tropopause, and in particular the transport from the troposphere to the stratosphere (*e.g.*, Hatsushika and Yamazaki, 2003, Bonazzola

and Haynes, 2004, Fueglistaler *et al.*, 2004). Stratospheric water vapour is strongly correlated with the Lagrangian Cold Point (Fueglistaler *et al.*, 2005). We analyse the minimum temperature ( $T_{min}$ ) and TTL residence time of two CCMVal-2 models, CMAM and E39CA and compare them to ERA-40 following the methodology of Kremser *et al.* (2009). These models provided the necessary instantaneous 6-hourly fields of temperature, winds and heating rates needed to perform the calculation. Two sets of  $T_{min}$  calculations were performed using ERA-40. A ‘standard’ calculation used 3D winds, and a diabatic calculation used vertical winds based on heating rates following Wohltmann and Rex (2008). The latter set of calculations (using diabatic calculations) is referred to as the ‘reference’ calculation.

The trajectories were analysed to determine the geographical distribution of points where individual air masses encounter their minimum temperature ( $T_{min}$ ) and thus minimum water vapour mixing ratio (referred to as dehydration points) during their ascent through the TTL into the stratosphere. In addition, the residence times of air parcels in the TTL were derived.

For all years analysed, both CCMs have a warm bias in the temperatures of the dehydration points of about 6 K (E39CA) and 8 K (CMAM) in NH winter, and about 2 K (E39CA) and 4 K (CMAM) in NH summer compared to the ERA-40 reference calculation. This is not the same as the temperature bias in the models (Figure 7.3). The Eulerian mean tropical  $T$  is about 3 K low for E39CA and 1 K high for CMAM. Thus, the overall degree of dehydration during transport of air into the stratosphere should be significantly too low, a known shortcoming of simulations with CCMs (Eyring *et al.*, 2006). The reasons for the warm bias are probably deficiencies in transport, given differences from the model Eulerian TCPT.

Figure 7.7 shows that the overall geographical distribution of dehydration points in the simulation based on

ERA-40 data are fairly well reproduced by both CCMs in NH winter 1995-1996. This suggests that the geographical distribution of dehydration points in winter is fairly robust. A closer look at the figure reveals that in E39CA, the region of the main water vapour flux is shifted eastwards compared to ERA-40 and the model shows excessive water vapour transport through warm regions over Africa. The CMAM model compares very well with the reference calculations, and if anything slightly overestimates the water vapour transport over the warm regions of South America. These overestimates in warm regions, however, are sufficient to create a significant warm bias to the Lagrangian cold point estimates.

In NH summer for 1996, the reference calculations show that the water vapour transport into the stratosphere is clearly dominated by the Indian monsoon and downwind regions (not shown), similar to Fueglistaler *et al.* (2005). This result is largely reproduced by the CMAM model, which also reproduces the location of this feature nicely. But the water vapour flux through the warm region over Africa is overestimated. In E39CA, the impact of the Indian monsoon is not well reproduced, and dehydration

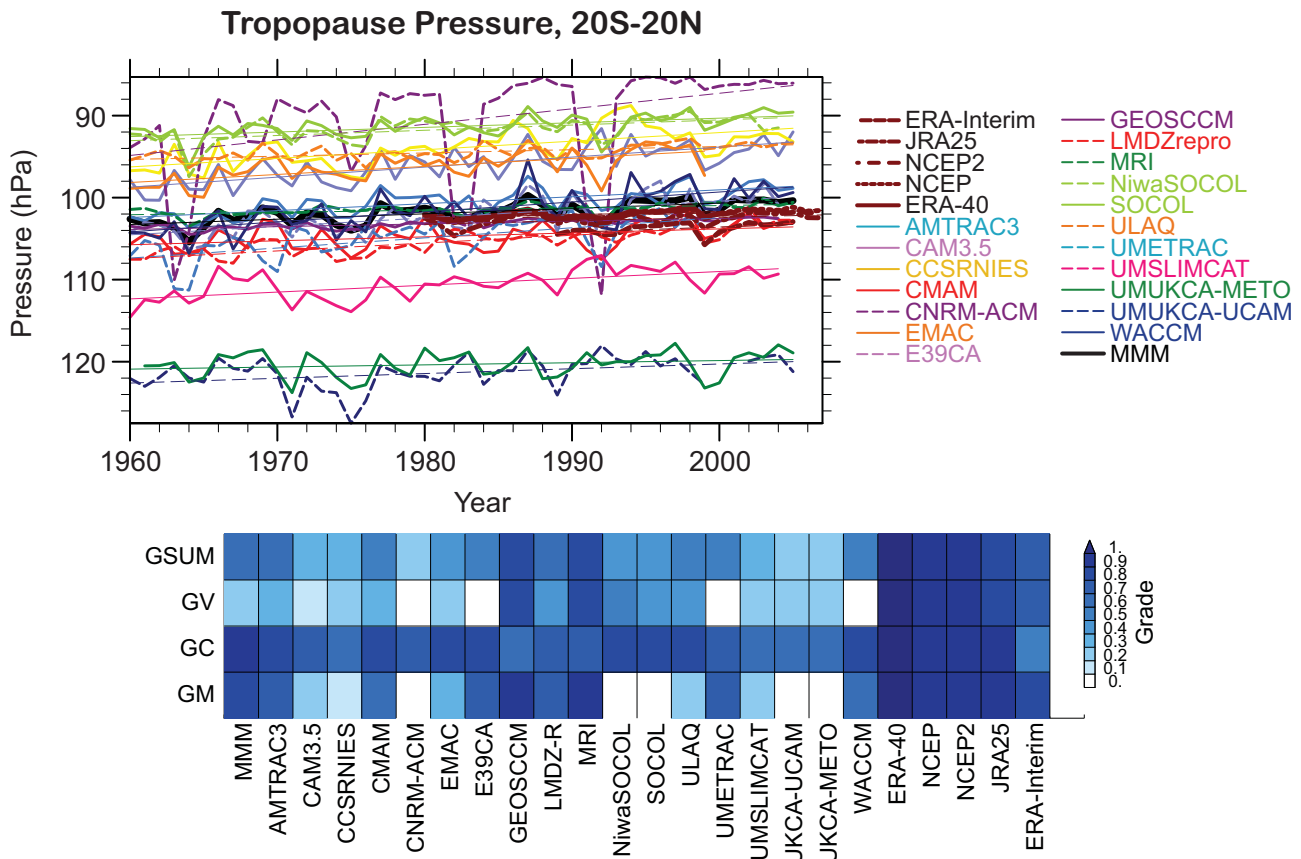
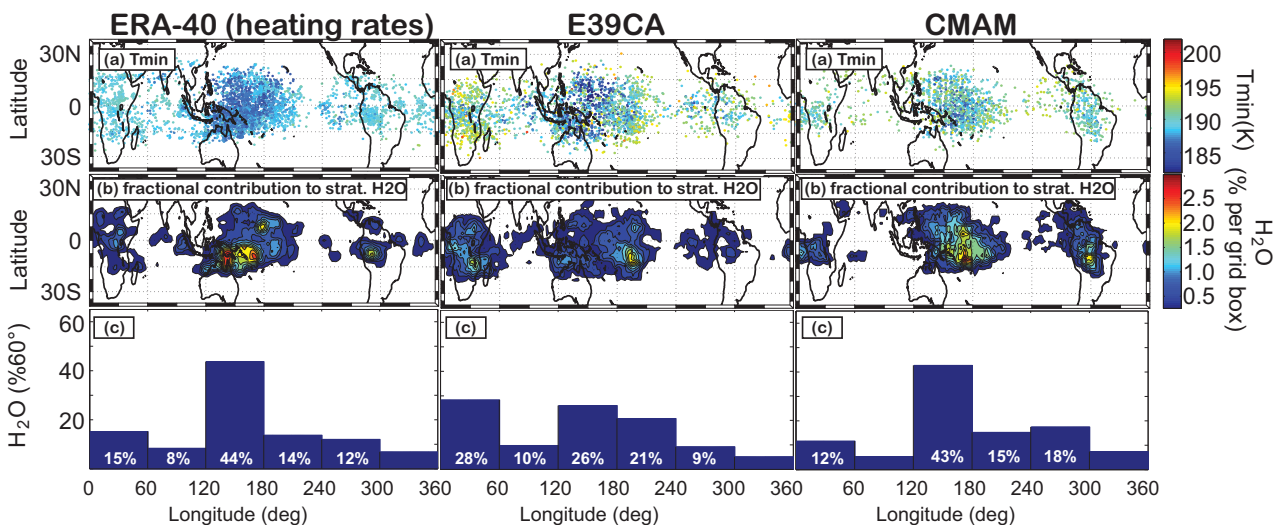


Figure 7.6: (Above): Annual mean time series of the Lapse Rate Tropopause Pressure (PTP) for 20°S-20°N from models and analyses for 1960-2007. Thin lines are linear fits. The multi-model mean (MMM) is the thick black line. (Below): Quantitative metrics summary of lapse rate tropopause pressure (PTP) for the mean (GM), the correlation (GC), the variance (GV), and the average of all three grades (GSUM).



**Figure 7.7:** NH winter 1995-1996. The scatter plots (panel a) show the geographical distribution of the dehydration points for ERA-40 (left), E39CA (middle), and CMAM (right). Colour code in (a) shows the minimum temperatures experienced by the trajectories. Panel (b) illustrates the fractional contribution to stratospheric water vapour from different geographical areas, expressed as percentage contribution per individual  $10 \times 5$  grid boxes (the sum is 100%). Panel (c) shows longitudinal distribution of the water vapor entry value, i.e., the value from (b) integrated over latitude ( $30^{\circ}\text{N}$ - $30^{\circ}\text{S}$ ) per  $60^{\circ}$  longitude (where the sum is 100%).

in NH summer for 1996 occurs mostly over the central Pacific rather than over India and the westernmost Pacific.

The residence times in the upper part of the TTL ( $\theta = 385$ – $395$  K) were derived from the trajectory calculations to examine the time scales of transport processes through the TTL. The residence time is a key parameter for chemical transformation of air before it gets into the stratosphere. **Figure 7.8** shows histograms of the probability density function (PDF) of the residence times obtained from the calculations in the upper part of the TTL for NH winter 1995-1996 and NH summer 1996.

Figure 7.8 indicates that on average the reference trajectories stay a few days longer in the upper part of the TTL than the kinematic trajectories, except in NH winter, where the kinematic trajectories calculated with the CMAM data on average stay longer in the TTL than the reference trajectories. In the latter case more kinematic trajectories stay longer than 10 days in the upper part of the TTL than in the reference calculations. The difference between the reference trajectories and the kinematic trajectories is most pronounced based on ERA-40 data, which is consistent with the notion of Schoeberl *et al.* (2003) that assimilation models tends to produce noisier vertical wind fields than free running GCMs. The most important difference between the different panels is the shape of the PDF. The majority of the reference trajectories reside 9-10 days in the upper TTL before they leave this layer. Only very few air masses pass through this layer in less than 5 days. In contrast, for transport that is based on vertical winds (*i.e.*, the transport in the CCMs) more trajectories reside 0-5 days in this layer

than in the reference calculations, in particular the calculations based on E39CA data result in residence times that are shorter than 5 days for the majority of the trajectories. The percentage of kinematic trajectories based on CMAM data that reside longer than 10 days in the upper part of the TTL is higher than in the reference for both NH winter and NH summer. This is a crucial influence on the transport of short-lived chemical species through the TTL. In E39CA, more short-lived compounds should be able to reach the stratosphere chemically unaltered compared to CMAM and the reference calculation.

The seasonal cycle of the residence time (with slower ascent and longer residence times in NH summer) is represented in the reference calculations (solid bars compared to lines). This is expected from the seasonal variation of the Brewer-Dobson circulation. Both CCMs fail to reproduce the seasonal variation of ascent rates through the TTL.

#### 7.4.4 Ozone

The annual cycle of ozone at 100 hPa in the tropics is illustrated in **Figure 7.9**. The annual cycle of  $\text{O}_3$  near the tropical tropopause is determined by chemical production, vertical transport, and any mixing with stratospheric air from higher latitudes that contains more ozone. Air with higher ozone is likely to have either (a) ascended more slowly or (b) mixed with more high-latitude air. The seasonal cycle reflects these processes (chemical production and transport). Ozone is compared to the combined and processed NIWA observational data set (Hassler *et al.*,

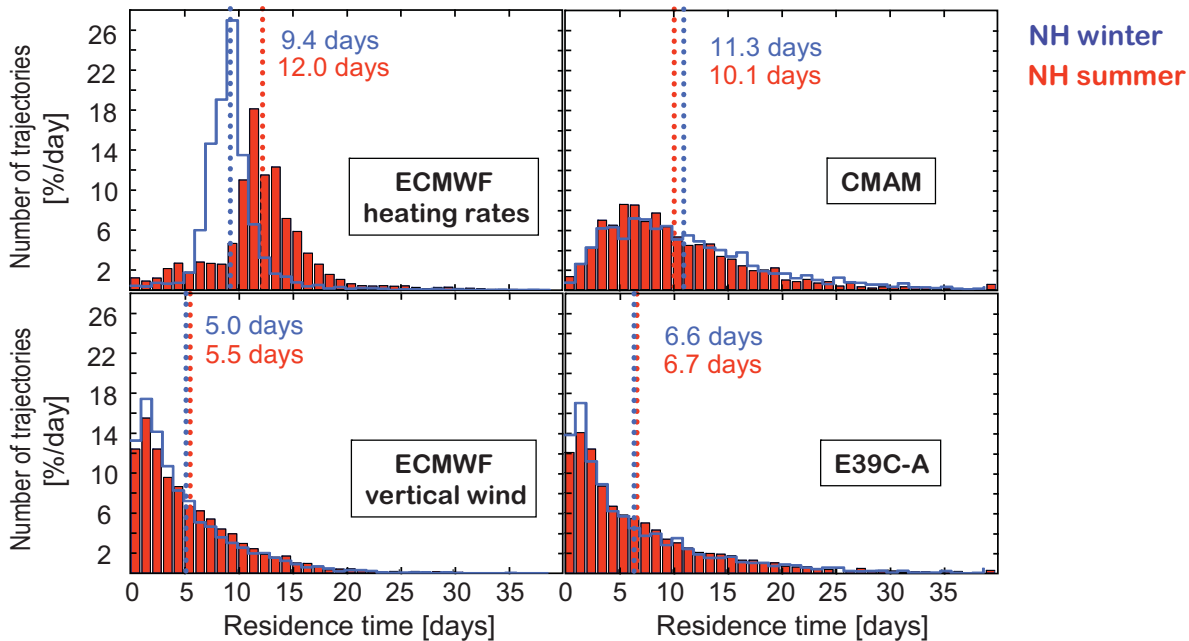


**Figure 7.8:** NH winter 1995–1996 and NH summer 1996. Residence time for the trajectories in the upper part of the TTL (385–395 K) for ERA-40, using heating rates as the vertical velocity (top left), ERA-40 using vertical wind as the vertical velocity (bottom left), CMAM (top right), and E39CA (bottom right). JJA solid red, DJF blue outline. Dotted vertical lines indicate the mean residence time.

2008), and grades are based on the annual cycle, variance and anomalies for this data set. Most models reproduce the phase of the annual cycle of ozone correctly in the tropics. Two models (UMSLIMCAT and CNRM-ACM) have a significantly different annual cycle of ozone. Many models have lower amplitude (and mean), while ULAQ, UMUKCA-METO and UMUKCA-UCAM have higher amplitude (and mean), indicating perhaps slow transport times in the TTL.

#### 7.4.5 Water Vapour

Water vapour in the lower stratosphere is critical for the chemistry and climate of the stratosphere, affecting both stratospheric chemistry by regulating total hydrogen as well as affecting UTLS temperatures through the radiative impact of water vapour (Kley *et al.*, 2000). Thus reproducing the transport of water vapour through the tropical tropopause is a critical requirement of CCMs in the TTL. Representing the appropriate relationships between cold point temperature and water vapour is also critical, as it requires the appropriate representation of processes that regulate water vapour, at least at the large scale.

**Figure 7.10** presents the annual cycle of water vapour from CCMs and HALOE in the lower stratosphere just above the TTL and the cold point (80 hPa). As pointed out by Mote *et al.* (1996), this is the entry point or ‘recording head’ of the stratospheric ‘tape recorder’ circulation. The transport associated with this circulation is discussed

in Chapter 5. Here we focus on the entry point. Most models are able to reproduce the annual cycle of water vapour, with a minimum in NH spring and a maximum in NH fall and winter. There is a wide spread in the ‘entry’ value of water vapour at this level: from 2–6 ppmv, with observations from HALOE closer to 3–4 ppmv. The uncertainties in HALOE observations are discussed in detail in Kley *et al.* (2000), but are less than  $\pm 20\%$  at this level. The shading indicates  $3\sigma$  interannual variability, but is similar to this 20% range. These results are slightly better than CCMVal-1 models (Gettelman *et al.*, 2009) due to a tighter cold point temperature range (Figure 7.3). The multi-model mean indicates that most models shift the water vapour minimum at 80hPa 1–2 months too early. The UMUKCA models fix water vapour in the stratosphere and are not shown. E39CA has too much  $H_2O$ , consistent with a Lagrangian CPT higher than ERA-40 (Section 7.4.3), but CMAM has too little  $H_2O$ , despite also having a higher Lagrangian TCPT.

Some models are clearly outside this range, and some have annual cycles that are shifted more than one month, indicating potential problems in transport and dehydration processes. The outliers include MRI (high  $H_2O$ ), CNRM-ACM (high  $H_2O$ ), LMDZrepro (low  $H_2O$ ), and UMETRAC, with virtually no annual cycle (which may be an analysis or data set problem).

Another method of examining the dehydration process is to look at the relationship between cold point temperature and water vapour just above it. This is a broad way of understanding integrated TTL transport and dehy-



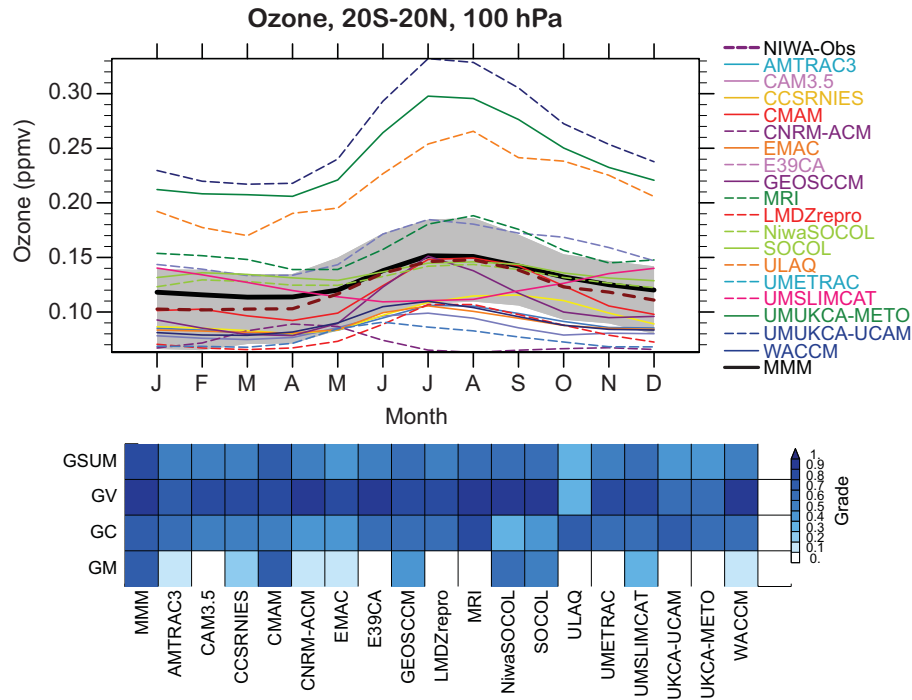


**Figure 7.9:** (Above): Annual cycle of tropical (20°S-20°N) ozone mixing ratio from models and observations. Output and observations are from the period 1980-1999. Gray shaded region is 3σ variability from NIWA observational data set (dashed brown line). (Below): Quantitative metrics summary of 100hPa Ozone for mean (GM), correlation (GC), variance (GV) and the average of all three grades (GSUM).

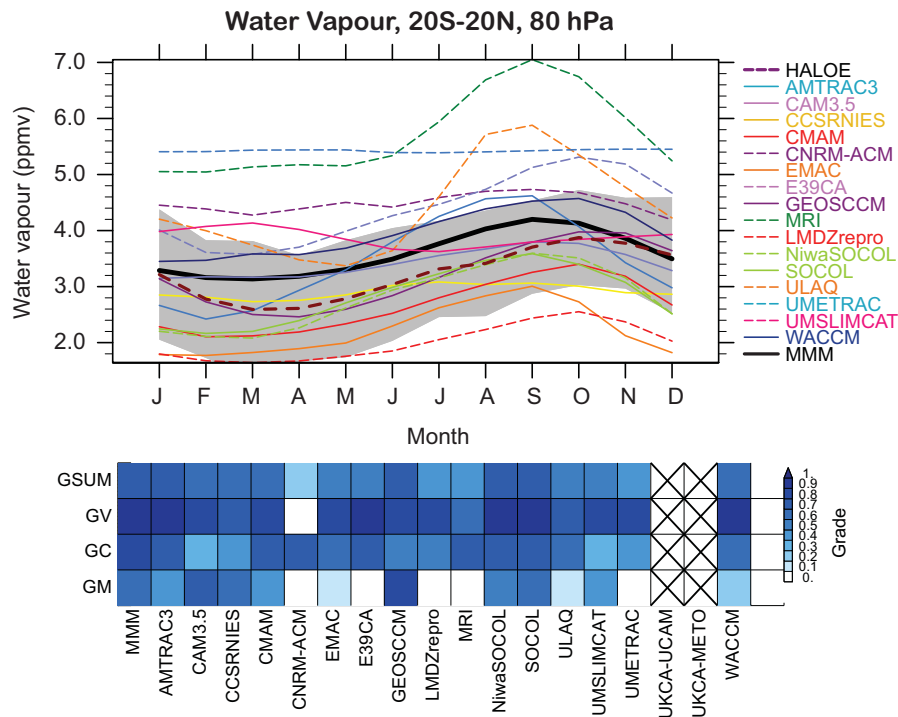


**Figure 7.10:** (Above): Annual cycle of tropical (20°S-20°N) water vapour at 80 hPa from models and observations. Output from the period 1992-2004. Gray shaded region is 3σ variability from HALOE observations over 1992-2004 (brown dashed line). (Below): Quantitative metrics summary of 80hPa H<sub>2</sub>O for mean (GM), correlation (GC), variance (GV) and the average of all three grades (GSUM).

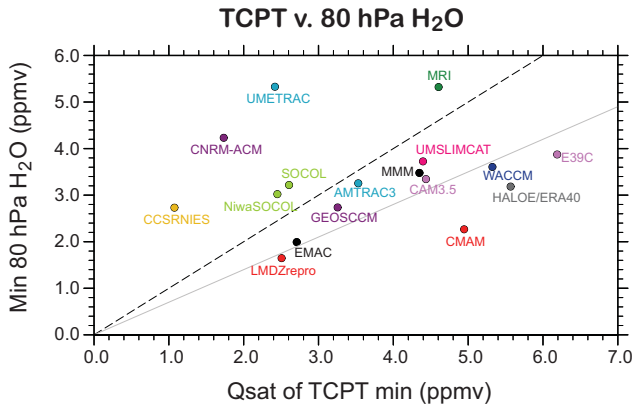


**Figure 7.11:** Correlation of minimum monthly mean water vapour with saturation vapour mixing ratio ( $Q_{\text{sat}}$ ) of the minimum monthly mean TCPT from CCMVal-2 models (1980-1999), the multi-model mean (MMM) and HALOE and ERA-40 observations (HALOE over 1992-2005). The black dashed line is the 1:1 line, indicating 100% saturation. The gray line is the 0.7:1 line, indicating 70% saturation.

dratation in the absence of data for offline Lagrangian cold point calculations as in Section 7.4.3. The TCPT regulates  $\text{H}_2\text{O}$  (Brewer, 1949), so the relationship can be analysed by looking at the ratio of water vapour to the saturation vapour mixing ratio at the cold point ( $Q_{\text{SAT}}(\text{CPT})$ ). An update of this relationship, shown in Gettelman *et al.* (2009), is presented in **Figure 7.11**. For example, the minimum ERA-40 TCPT (Figure 7.11) is about 192 K, which corresponds at 80 hPa to a  $Q_{\text{SAT}}$  of 5.5 ppmv.

Note that the UMUKCA models have very high cold point temperatures (consistent with high ozone at 100hPa and slow transport times), so their water vapour was fixed (and they are not shown). The results indicate that most of the models cluster, similar to the observations ( $\text{H}_2\text{O}$  from HALOE and CPT from ERA-40), near a line that would imply 70% saturation with constant temperatures and transport (which is not the case, hence  $\text{H}_2\text{O}$  is less than implied by TCPT). Three models are near the 1:1 line. MRI is higher than the 1:1 line due to ice-supersaturation permitted in the model. However, three models (CNRM-ACM, CCSRNIES and UMETRAC) have significantly more water vapour than would seem to be justified by their temperatures. This indicates potential problems in fundamental transport, variability and/or condensation processes in the TTL. This is also clear from Figure 7.10.

#### 7.4.6 Intra-seasonal Variability/ Waves

There exists significant sub-seasonal variability in temperature and other parameters around the tropical tropopause (*e.g.*, Tsuda *et al.*, 1994; Fujiwara *et al.*, 2009). This is due to equatorial waves, intra-seasonal oscillations

(ISOs), and other disturbances that are generated by tropical organised convection (*e.g.*, Fujiwara and Takahashi, 2001; Suzuki and Shiotani, 2008). Also, the climatological temperature distribution around the tropical tropopause is in part determined by quasi-stationary disturbances (Highwood and Hoskins, 1998). Therefore, appropriate representation of tropical convection and tropical disturbances is crucial even for stratospheric models, since waves help determine the coldest temperatures, and may affect dehydration in the TTL. For example, with the same minimum  $Q_{\text{sat}}$  in Figure 7.11, larger wave driven temperature variance would reduce  $\text{H}_2\text{O}$ . In this section, the wave activity in temperature at 100 hPa in the tropics is presented for five reanalysis data sets (ERA-40, ERA-Interim, JRA25, NCEP/NCAR (NCEP1), and NCEP-DEO AMIP-II (NCEP2)), and for four CCMs that produced high time frequency winds and temperatures (CCSRNIES, CMAM, MRI, and WACCM), using a zonal-wavenumber-frequency spectral analysis.

All five reanalysis data sets are output four times daily, at a horizontal resolution of  $2.5^\circ$  for ERA-40, NCEP1, and NCEP2,  $1.5^\circ$  for ERA-Interim, and  $1.25^\circ$  for JRA25. CCSRNIES and MRI data are output daily (daily average) at  $\sim 2.8^\circ$  resolution, CMAM data is output four times daily at  $\sim 5.6^\circ$ , and WACCM data is output four times daily at  $2.5^\circ$  by  $\sim 1.895^\circ$ . All data are available for the period between January 1990 and February 2000. All CCM outputs are from the REF-B1 experiment with observed SSTs.

**Figures 7.12** and **7.13** show the zonal-wavenumber-frequency spectrum of temperature at 100 hPa within  $\sim 15^\circ\text{N}$  to  $\sim 15^\circ\text{S}$  for ERA-40, NCEP1, and four CCMs, for symmetric and antisymmetric components, respectively. Analysis is made for several overlapping 92-day segments for all seasons between January 1990 and February 2000. The spectral calculations include a symmetric-antisymmetric decomposition (Wheeler and Kiladis, 1999). The spectrum shown here is normalised by the variance of the original data, and thus the power spectral density is averaged over the latitude region and the period. The background red-noise spectra, against which the statistical significance is evaluated, are estimated for symmetric and antisymmetric components separately (in frequency only) using the auto-regressive-process method (Gilman *et al.*, 1963). Also shown are dispersion curves for theoretical equatorial waves (Matsuno, 1966). Features commonly observed in all data sets are equatorial Kelvin waves (Figure 7.12) and mixed Rossby gravity (MRG) waves (Figure 7.13). ISOs, at frequencies smaller than 0.05 cycle per day, are mostly not statistically significant with respect to the background spectra estimated here; however, the largest power is found in these regions.

**Table 7.2** summarizes the activity for equatorial Kelvin waves, MRG waves, and symmetric eastward-moving ISO. For Kelvin waves, the activity is defined as the

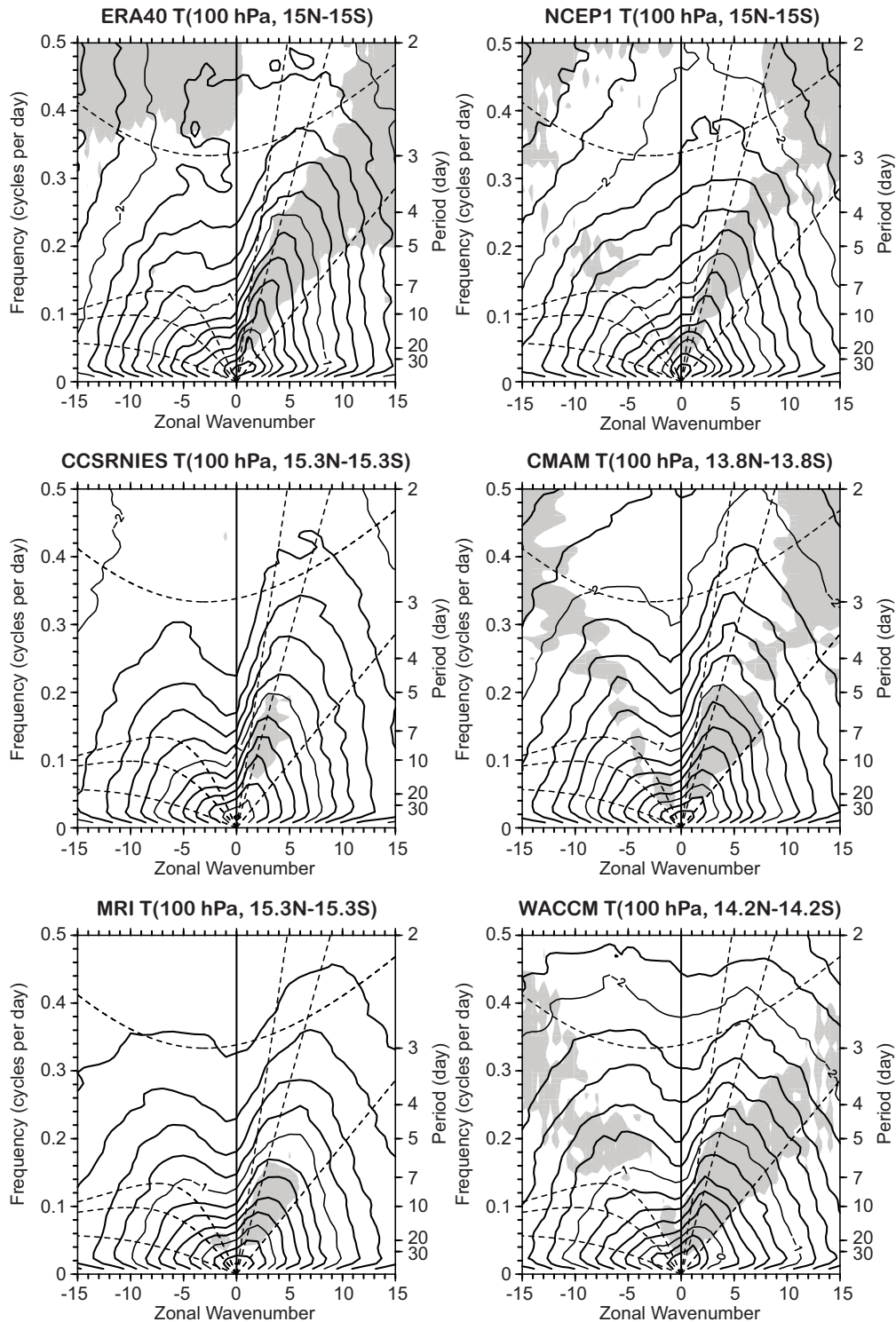


**Figure 7.12:** Zonal-wavenumber-frequency spectrum of temperature at 100 hPa within 15°N-15°S for all seasons between Jan 1990 and Feb 2000 for the symmetric component for ERA-40, NCEP1, CCSRNIES, CMAM, MRI, and WACCM. Contours show the  $\log_{10}$  of power spectral density (interval 0.2). Regions where the ratio to the estimated background spectrum is  $>1.5$  are coloured gray. Dotted curves show the wave dispersion relation at equivalent depth,  $h=8$ , 70, and 240 m for Kelvin waves (positive wavenumbers) and equatorial Rossby waves (negative wavenumbers). The dispersion relation for meridional-mode-number  $n=1$  inertio-gravity waves with  $h=8$  spans all wavenumbers.

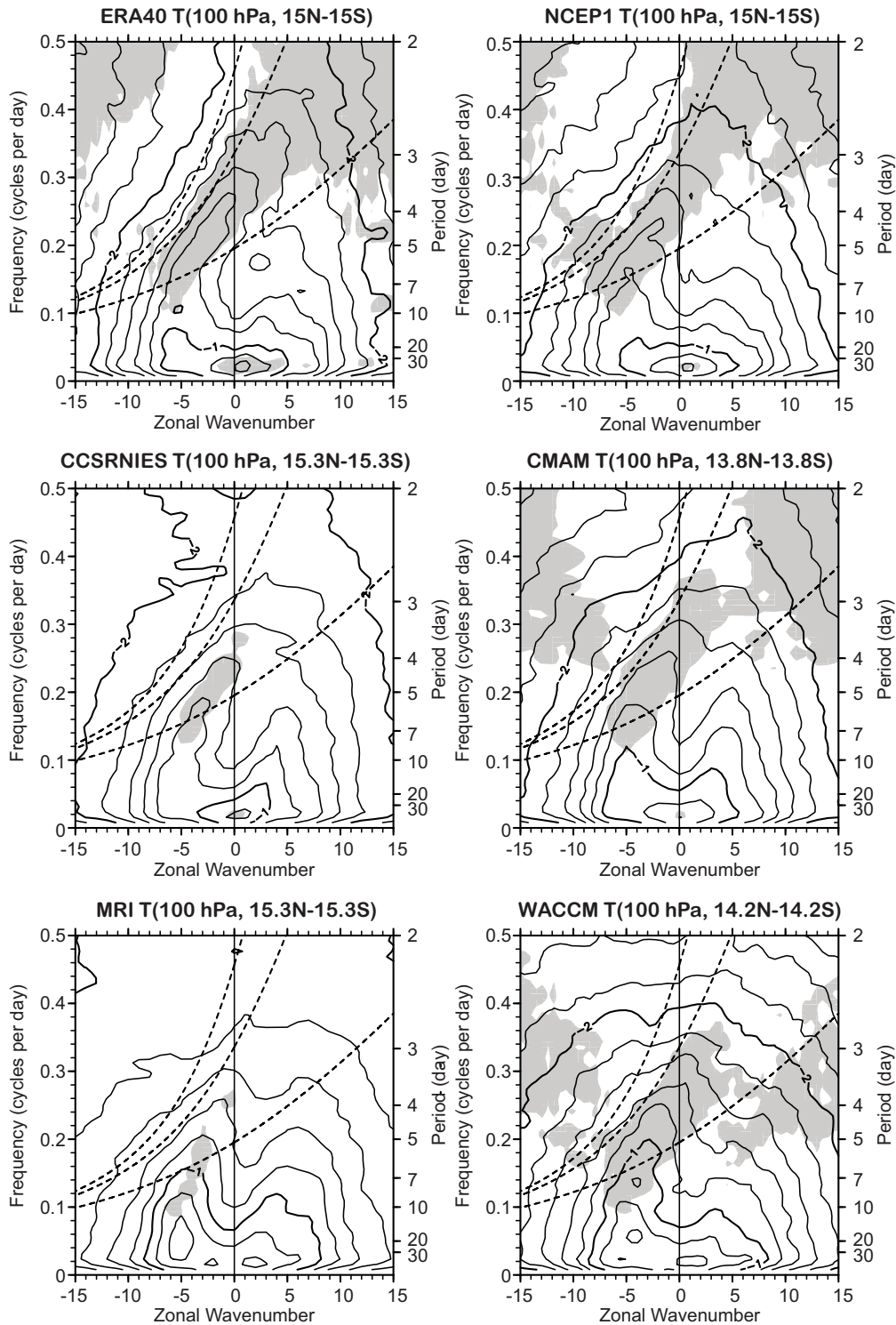


**Figure 7.13:** Same as Figure 7.12 but for the antisymmetric component. Dotted curves show the wave dispersion relation at  $h = 8, 70,$  and  $240$  m for mixed Rossby gravity waves (negative wavenumbers) and  $n=0$  eastward-moving inertio-gravity waves (positive wavenumbers).

integration of power spectral density in the region, zonal wavenumber,  $s = 1$  to  $10$ , frequency,  $f = 0.05$  to  $0.5$  cycles per day, equivalent depth,  $h = 8$  to  $240$  m, and the ratio

to the estimated background spectrum  $\geq 1.5$ . For MRG waves, the activity is defined as the integration in the region,  $s = -10$  to  $0$ ,  $f = 0.1$  to  $0.5$  cycles per day,  $h = 8$  to  $70$

m, and the ratio  $\geq 1.5$ . For the ISO, the activity is defined as the integration in the region,  $s = 1$  to 5, and  $f = 0$  to 0.05; the ratio (the statistical significance) is not considered. Thus, the ISO activity shown here is the upper limit. The activity is then divided by the average activity for five reanalysis data sets for each wave/oscillation.

Results indicate that the five reanalysis data sets have very different wave activities. Fujiwara *et al.* (2009) note that the Kelvin wave amplitudes in the analyses are lower than observed. The Kelvin and MRG wave activities in the ERA reanalyses are 2-3 times greater than those in the NCEP reanalyses; those in JRA25 are close to the average. The ISO activity (the upper limit) is rather similar for the five reanalysis data sets. The wave activities in the four CCMs are generally within the range of those in the reanalysis data. WACCM shows the greatest Kelvin and MRG wave activities, which are comparable to those in the ERA reanalyses. CCSRNIES shows the smallest Kelvin wave activity, and MRI shows the smallest MRG activity. The ISO activity in the CCMs is greater than that in the five reanalysis data sets except for CCSRNIES. Thus the lower range of wave activities is probably too low in these models. The calculation does not explicitly include gravity waves, which may also have significant contributions to temperature variance and dehydration in the TTL.

#### 7.4.7 Vertical Thermal Structure

Recent studies using high-resolution radiosonde data have revealed the presence of a temperature inversion layer, typically a few kilometers deep, located right above the tropopause (Birner *et al.*, 2002; Birner, 2006; Bell and

**Table 7.2:** The wave activity for equatorial Kelvin waves, mixed Rossby gravity (MRG) waves, and symmetric eastward-moving ISO for five reanalysis and four CCM data sets, with respect to the average value for the five reanalysis data sets (0.184 K<sup>2</sup> for Kelvin waves, 0.0311 K<sup>2</sup> for MRG waves, and 0.209 K<sup>2</sup> for the ISO).

	Kelvin waves	MRG waves	ISO
ERA-40	1.46	1.21	1.10
ERA-Interim	1.48	1.28	1.03
JRA25	1.12	0.997	1.22
NCEP1	0.524	0.826	0.859
NCEP2	0.421	0.684	0.786
CCSRNIES	0.344	0.416	0.716
CMAM	1.22	0.799	1.34
MRI	1.04	0.234	1.50
WACCM	1.44	1.43	1.31

Geller, 2008). This so-called ‘‘tropopause inversion layer’’ (TIL) is also characterized by a sharp and strong buoyancy frequency ( $N^2 = -g/\theta d\theta/dz$ ) maximum. The buoyancy frequency is also called the Brunt-Väisälä frequency. The presence of the TIL has been further confirmed by the Global Positional System (GPS) Radio Occultation (RO) data (Randel *et al.*, 2007; Grise *et al.*, 2009); these independent measurements have shown that the TIL is present almost everywhere from the deep tropics to the pole in both hemispheres (Figures 7.14a, d). Although the formation and maintenance mechanisms of the TIL remain to be determined, its presence has potentially important implications for the cross-tropopause exchanges of passive tracers/water vapour and for the dynamical coupling between the stratosphere and troposphere.

The zonal-mean structure of the TIL, simulated by REF-B1 integrations for 9 models with available instantaneous data, is examined and compared with observations. The observed TIL is derived from the COSMIC GPS RO data set (Anthes *et al.*, 2008).

All analyses are performed on the log-pressure coordinate with tropopause pressure ( $p_{TRP}$ ) as a reference level: *i.e.*,  $z = H \ln(p/p_{TRP})$  where  $H$  is a scale height of 8 km. Note that the conventional log-pressure coordinate uses surface pressure for a reference level. At each model grid point (or GPS RO profile) tropopause pressure is first computed using the WMO definition of lapse-rate tropopause. The instantaneous fields of interest, such as temperature and  $N^2$ , are then interpolated onto the tropopause-based  $z$  coordinate using a log-pressure linear interpolation, and are averaged over longitudes for December-January-February (DJF) and June-July-August (JJA). Resulting seasonally-averaged fields in each model are finally interpolated onto 5-degree interval latitudes to construct multi-model mean fields. The COSMIC data are also binned into 5-degree intervals in latitudes.

The observed TIL is computed using both data at full (or raw) levels (Figure 7.14a, d) and data only at CCMVal-2 standard levels (Figure 7.14b, e). CCMVal-2 UTLS standard levels are shown in Figure 7.5. Degraded observations reduce uncertainties associated with model vertical resolution, and allow a more direct comparison of the simulated TIL with observations.

The analysis results for the average of 9 models are summarized in Figure 7.14 in terms of  $N^2$ . We first describe the TIL in the observations. As shown in Figures 7.14a, d, sharp maxima of  $N^2$ , located just above the tropopause ( $z = 0$ ), are distinct in the extra-tropics. They are generally stronger in the summer hemisphere than in the winter hemisphere, but have no hemispheric difference: *i.e.*, the  $N^2$  distribution in the NH summer is quantitatively similar to the one in the SH summer. In contrast, the tropical  $N^2$  profile is only weakly sensitive to season. This is consistent with previous findings (Randel *et al.*, 2007; Grise *et*

al., 2009).

Figures 7.14b, e show the  $N^2$  distribution for degraded GPS RO data. Maximum values of  $N^2$  are substantially weakened. In addition, their locations are somewhat higher than those in the raw data. This strong sensitivity is not surprising as both tropopause pressure and temperature, which directly affect the sharpness of the TIL (Bell and Geller, 2008), are under-estimated in coarse resolution GPS RO data.

The above results suggest that the CCMVal-2 models may not be able to reproduce a quantitative structure of the observed TIL, simply because of coarse resolution in the vertical. Data to perform the TIL analysis was not available for the two highest vertical resolution models (E39CA and EMAC). The simulated TIL (Figures 7.14c, f) is generally weaker and broader than observed using full resolution data (Figures 7.14a, d). The simulations do look more like estimates from the observations using CCMVal vertical

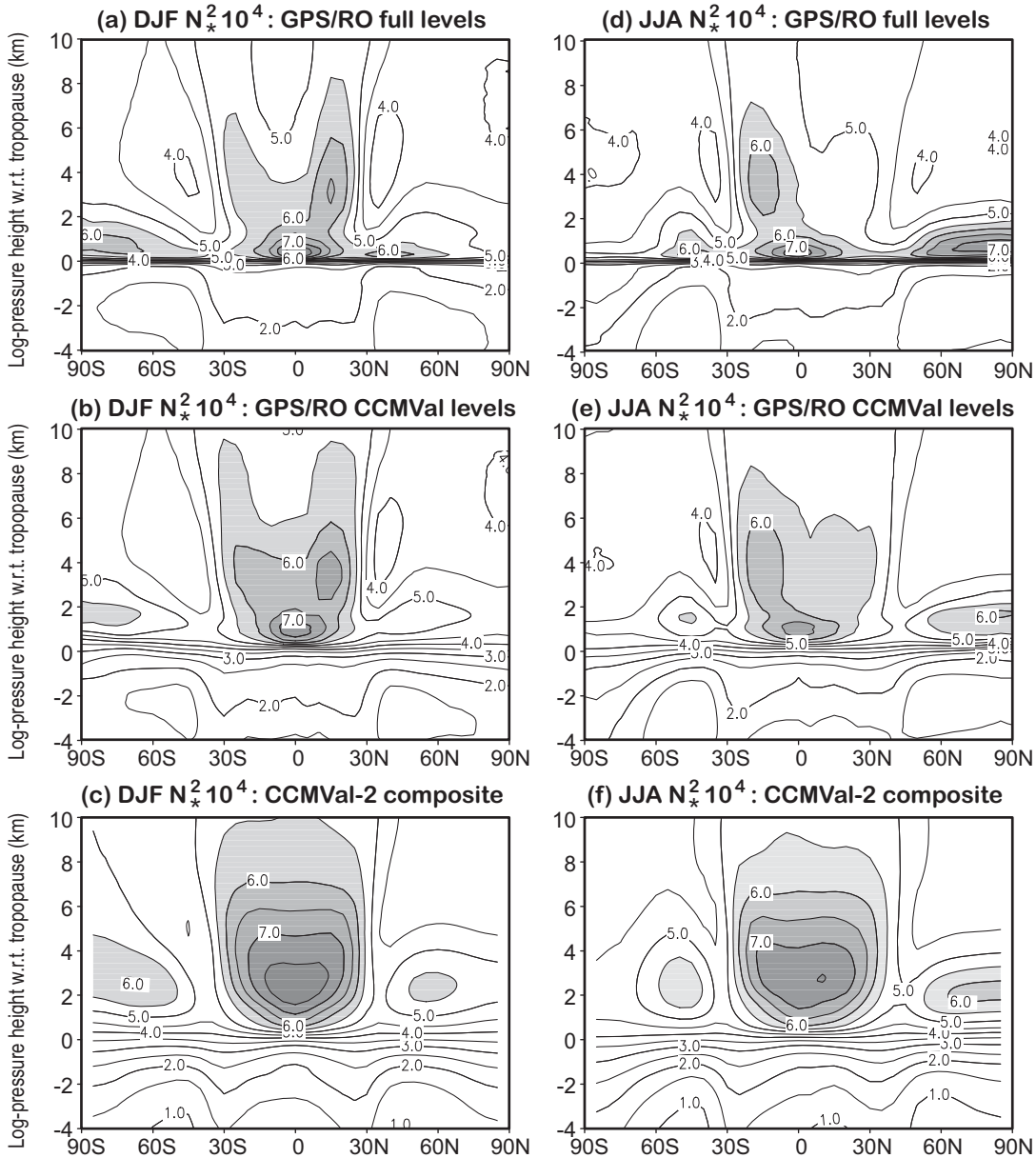


**Figure 7.14:** Zonally-averaged  $N^2 \times 10^4$  as a function of latitudes and log-pressure height on the tropopause based coordinate: (top) COSMIC/FORMOSAT-3 GPS RO data, (middle) COSMIC GPS RO data using only CCMVal-2 standard pressure levels, and (bottom) composite of 9 REF-B1 model integrations. Two seasons are shown separately: (left) December-January-February and (right) June-July-August. Contour intervals are  $0.5 \text{ s}^{-1}$ , and values greater than or equal to  $5.5 \text{ s}^{-1}$  are shaded. Note that zero in y-axis denotes the location of the tropopause.

resolution. (Figures 7.14b, e). Analysis of higher vertical resolution runs from WACCM with 300 m vertical resolution in the UTLS (WACCM-highres) does indicate that at a higher vertical resolution this model has an increased peak  $N^2$  near the tropopause in better agreement with GPS RO observations (Figure 7.15, also Figure 7.19).

**Figure 7.15** illustrates profiles of  $N^2$  from GPS RO observations and simulations in the tropics for 2 seasons from 9 models and WACCM-highres. The CCMVal-2 models under-estimate  $N^2$  in the troposphere and misplace the tropical temperature inversion layer. Simulated  $N^2$  in the tropical lower stratosphere is also much larger than observed by GPS RO, even at degraded resolution. The difference from observations might be caused by underestimated adiabatic cooling from tropical upwelling and/or radiative cooling associated with lower stratospheric  $H_2O$ . Note that WACCM-highres has a larger and sharper peak in  $N^2$ , and the peak is closer to the tropopause than the standard resolution WACCM. In addition, two of the lower vertical resolution models analysed (CCSRNIES and SOCOL) have very broad TIL structures. The discussion on the extra-tropical TIL is continued in Section 7.5.1.4.

## 7.5 The Extra-tropical UTLS

The extra-tropical UTLS is here defined as the region between the free troposphere (6-8 km) and the upper boundary of the tropically controlled transition region (around 22 km, Rosenlof *et al.*, 1997) as illustrated in Figure 7.1. It includes the Lowermost Stratosphere (LMS), the region between the extra-tropical tropopause and the 380 K potential temperature surface (Holton *et al.*, 1995). One main characteristic of the LMS is that isentropes intersect the tropopause, thereby potentially connecting the troposphere and the stratosphere *via* rapid adiabatic motion. The slower diabatic circulation is predominantly downward in the

LMS, which on its own would transport aged stratospheric air into this region. However, meridional mixing from the tropical UTLS transports younger air masses to mid- and high latitudes and ‘rejuvenates’ air as it slowly descends into the LMS (Rosenlof *et al.*, 1997; Bregman *et al.*, 2000; Hegglin and Shepherd, 2007), an effect quantified by Hoor *et al.* (2005) and Bönisch *et al.* (2009) based on SPURT aircraft data, and Levine *et al.* (2007, 2008) using operational analyses of the European Centre for Medium-range Weather Forecasts (ECMWF). The lower boundary of the LMS is defined by the tropopause. Distributions of chemical tracers that are affected by transport exhibit strong spatial gradients across the tropopause in a layer of finite depth referred to as the Extra-tropical Tropopause Transition Layer (ExTL) (Fischer *et al.*, 2000; Zahn *et al.*, 2000; Hoor *et al.*, 2002, 2004; Pan *et al.*, 2004). The ExTL is a global feature with increasing depth towards high latitudes, and has been found to be different for different tracers (Hegglin *et al.*, 2009). The ExTL chemical transition has been interpreted as the result of recurrent wave-breaking events, forced by synoptic-scale baroclinic disturbances, which bring tropospheric and stratospheric air masses with very different chemical and radiative characteristics into close proximity (Shepherd, 2007). Indeed, Berthet *et al.* (2007) found an analogue of the ExTL using large-scale trajectories driven by ECMWF wind fields. Small-scale processes such as three-dimensional turbulence and ultimately molecular diffusion then act to reduce the gradients produced in the tracer fields (Hegglin *et al.*, 2005).

The extra-tropical UTLS is very sensitive to climate change and will cause chemical, radiative and dynamical feedbacks, due to high sensitivity to changes in the UTLS. Changes in the extra-tropical UTLS help determine the stratospheric impact on the troposphere through *e.g.*, the transport of stratospheric ozone into the troposphere or surface UV fluxes. Thus it is important that CCMs are capable

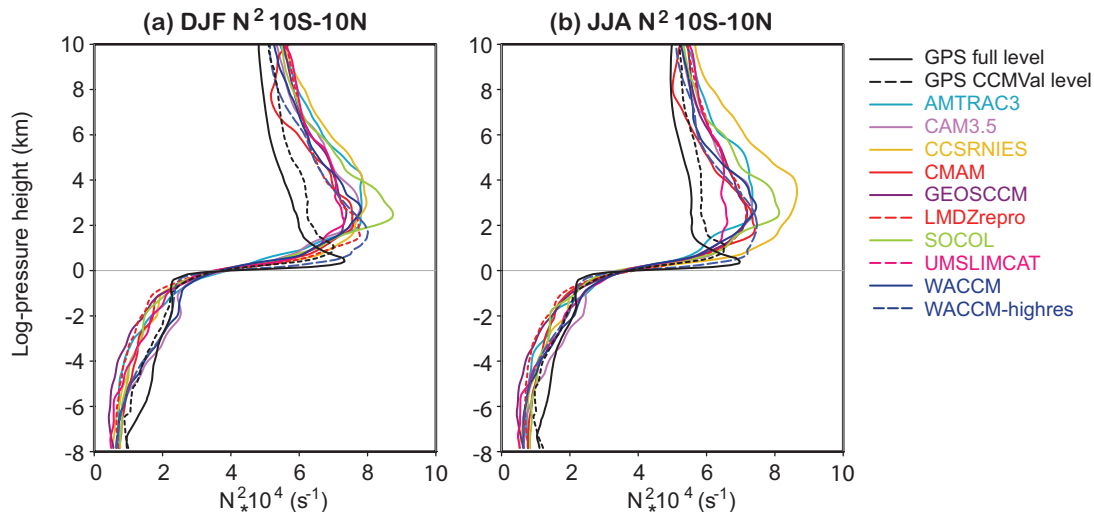


**Figure 7.15:** Vertical profiles of  $N^2$  in each model and observation in the tropics. (A) DJF, (B) JJA.

of resolving chemical and dynamical structures in the extra-tropical UTLS accurately. Here we will investigate the CCMs' capability to reproduce the complex dynamical and chemical structures of the extra-tropical UTLS. Potential long-term changes in these structures will be investigated in Section 7.6.2.

### Detailed description of the extra-tropical UTLS metrics

The following diagnostics are used to obtain performance metrics for the CCMs:

- **Diagnostic 1:** The seasonal zonal-mean zonal wind is used to test the models' realism in representing the latitudinal gradients of the thermal structure.
- **Diagnostic 2:** The seasonal cycle in the LMS mass is a test of the combined radiative-dynamical response to radiative forcing. It can be seen as an integrated measure for the extra-tropical tropopause behaviour, which is a basic measure of the UTLS thermal structure in a model.
- **Diagnostic 3:** The seasonal cycles in  $O_3$ ,  $HNO_3$ , and  $H_2O$  at 100 and 200 hPa are used to test the models' representation of the large-scale transport and mixing properties. This includes the evaluation of the representation of the seasonal relative strength in quasi-horizontal mixing between the tropical latitudes and the extra-tropics within the tropically controlled transition region (380-420 K, or  $\sim 100$  hPa) and across the subtropical jet (340-380 K, or  $\sim 200$  hPa).  $HNO_3$  in addition is a tracer not only influenced by transport, but also by more complex microphysical and chemical processes (a topic that clearly needs to be addressed more thoroughly in the future).
- **Diagnostic 4:** The sharpness of the meridional gradients of long-lived species (here for  $O_3$ ), where long-lived has to be seen in relation to the transport time scales, is a measure of the chemical distinctiveness of the UTLS in latitude, and therefore for the degree of isolation of different regions such as the tropics and the extra-tropics.
- **Diagnostic 5:** Vertical profiles of normalised CO in potential temperature units relative to the tropopause height allows us to separate between transport across the extra-tropical tropopause on short time scales and transport from the tropics and subtropics on longer time scales. It thereby helps to determine the tropospheric influence on the lowermost stratospheric background. The normalisation ensures that the results are dependent purely on transport and mixing processes, and not on the boundary conditions of CO in the troposphere.
- **Diagnostic 6:** A basic test of the models' performance in the UTLS region uses annual and seasonal profiles

of  $H_2O$ , CO, and  $O_3$  in tropopause coordinates at mid-latitudes and northern hemisphere polar regions. This diagnostic is critical for understanding the chemical structure (including sources and sinks) of, and the separation between the UT and LS.

Diagnostics not used in a quantitative way are:

- **Diagnostic 7:** Interannual anomalies in extra-tropical tropopause pressure are a measure of the response of the models to different forcings such as volcanoes, ENSO, *etc.* The anomalies are related to LMS mass.
- **Diagnostic 8:** The tropopause inversion layer (TIL) is a distinctive feature of the thermal structure of the tropopause, which reflects the balance between radiative and dynamical processes.
- **Diagnostic 9:** The depth of the extra-tropical tropopause transition layer (ExTL) and its location relative to the thermal tropopause are used to diagnose the mixing and transport characteristics of the models in the tropopause region.
- **Diagnostic 10:** Ozone probability density functions are used to test the variability of ozone with respect to the tropopause.

## 7.5.1 Dynamical Structure of the Extra-tropical UTLS

### 7.5.1.1 Zonal mean wind

The zonal mean zonal wind field is a very common diagnostic and used to validate the representation of the latitudinal thermal structure of the models, and therefore the basic dynamical state of the models' atmospheres. For this diagnostic, monthly zonal mean wind fields averaged over the period 1979-1999 are compared between the REF-B1 simulations and ERA-40. For further comparison, also NCEP data are included.

**Figure 7.16** and **7.17** (which lists the grade for the mean  $g_m$  and the skill  $S$  calculated using Equations (7.1) and (7.7), respectively, as well as the total grade  $G_{tot}$  calculated using Equation (7.8)) illustrate that the models represent the strength and latitudinal behaviour of the zonal-mean zonal wind in a realistic way. This is to be expected since the models usually tune their gravity wave parameterizations towards getting the observed zonal-mean wind fields correct. ULAQ is the only model that shows clear deficiencies in resolving the latitudinal structure, especially during JJA. This lack of realism is also expressed in the Taylor diagrams by very low (latitude-by-latitude) correlation and skill values, and might be attributable to the very low resolution of the model and its quasi-geostrophic dynamical core. The grades of the mean values of the zonal-mean zonal wind,  $g_m$ , also reveal that SOCOL-models score slightly



lower than the multi-model mean during both DJF and JJA.

The tight correspondence between NCEP and ERA-40 (the skill of NCEP is 0.98), which is tighter than the model spread, indicates good agreement between the two reanalyses, and that the models may still have room for improvement. For example, several models displace the tropospheric ‘eddy-driven’ jet in the SH summer (DJF) when compared to the observations.

The total grading values ( $G_{TOT}$ ) in Figure 7.17 are averaged and listed in the final grading Figure 7.39.

### 7.5.1.2 Mass of the Lowermost Stratosphere

The seasonal cycle in the LMS mass is a basic test of the combined radiative-dynamical response to radiative forcing and represents an integrated measure for the extratropical tropopause behaviour. Stratospheric mass variations due to seasonal tropopause height variations can contribute to stratosphere-troposphere exchange (Appenzeller *et al.*, 1996). This exchange transports ozone (*c.f.* Chapter 10) and reactive nitrogen (besides other species) into the troposphere, where it helps determine the tropospheric ozone budget and hence air quality. Here, we test the realism of the seasonal fluctuations in the total LMS mass by comparing them to the NCEP reanalyses using a method similar to the one of Appenzeller *et al.* (1996). The LMS mass is determined as the fraction of the stratosphere that lies between the thermal tropopause, calculated using the WMO definition, and the 100 hPa pressure surface. The thermal tropopause is derived from monthly zonal mean temperature fields averaged over a time period between

1990 and 1999 using the REF-B1 simulations. The results are shown in **Figure 7.18**.

In the NH, most models show a very high skill (with values larger than 0.9) in reproducing the amplitude and phase of the seasonal cycle in the LMS mass from the NCEP reanalyses. One exception is LMDZrepro which scores lower with a value of 0.62. LMDZrepro captures the structure of the seasonal evolution (expressed in a seasonal correlation of 0.95), but under-estimates its amplitude (expressed in a normalised standard deviation of 0.5). There are also quite a few models that have difficulty in simulating accurate mean values of the LMS mass as shown in **Figure 7.19**. UМУKCA-METO and UМУKCA-UCAM show larger LMS mass values, indicating an average tropopause pressure that is too high. CCSRNIIES, CNRM-ACM, EMAC, NiwaSOCOL, SOCOL, and ULAQ have smaller LMS mass values than expected, indicating generally too low tropopause pressures. The multi-model mean shows both a good mean value and a high skill comparable to those values obtained by the best performing models AMTRAC3, CMAM, GEOSCCM, and E39CA.

In the SH, the models’ overall performance relative to NCEP is worse than in the NH. The skill based on the correlative metrics lies around 20-40% lower than in the NH for all models, with particular deficiencies for CAM3.5, CCSRNIIES, EMAC, GEOSCCM, LMDZrepro, ULAQ, UMSLIMCAT, and WACCM. The Taylor diagram reveals that almost all models exhibit standard deviations that are too large, which shifts them away from the reference point (note the different radial axis scale in the Taylor diagrams in Figure 7.18). The following models have major deficiencies in representing the mean values (see Figure 7.19):

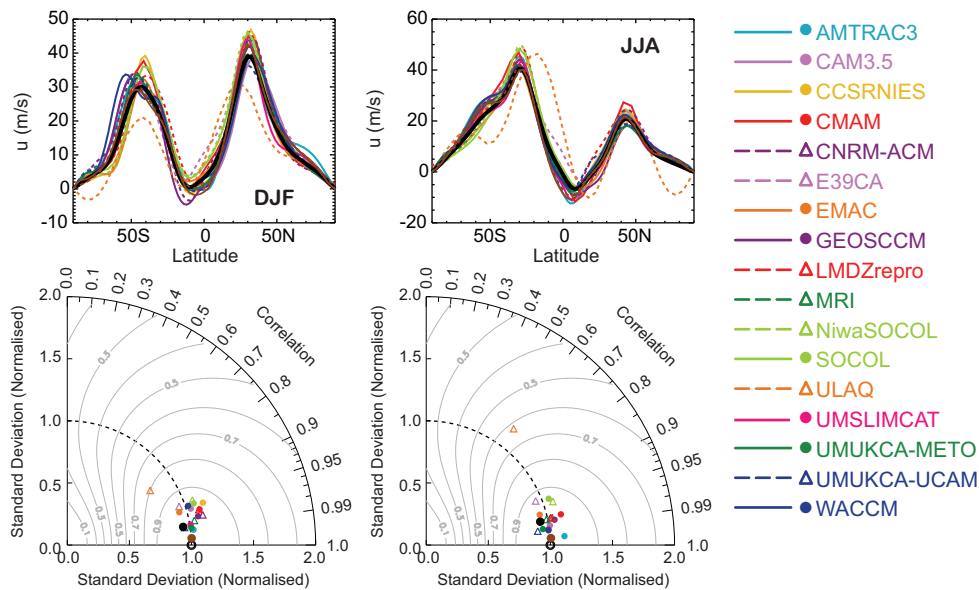


**Figure 7.16:** Zonal-mean zonal wind (upper panels) and corresponding Taylor diagrams (lower panels) at 200 hPa for DJF (left panels) and JJA (right panels). The brown solid line represents ERA-40 data, the brown dashed line and brown dot diagram NCEP data, and the black solid line and dot the multi-model mean.

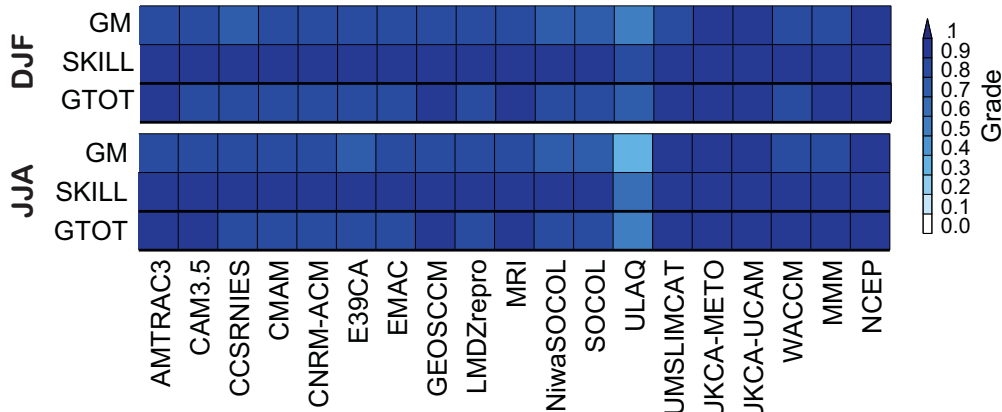


**Figure 7.17:** Metrics for the zonal-mean zonal wind at 200 hPa for DJF (upper) and JJA (lower). MMM indicates the multi-model mean. GM is calculated using Equation (7.1), SKILL (which is equivalent to S) using Equation (7.7), and GTOT using Equation (7.8).

CNRM-ACM and the UMUKCA models.

An acceptable total score which is equal to that of the multi-model mean ( $\geq 0.8$ ) is only reached by E39CA. The difference between the SH and NH can be explained by smaller seasonal variations in the LMS mass in the SH, which is more difficult for the models to capture.

The total grading values ( $G_{TOT}$ ) obtained in Figure 7.19 for the NH and SH are averaged and listed in the final grading Figure 7.39.

### 7.5.1.3 Extra-tropical Tropopause pressure

The extra-tropical tropopause pressure is a basic measure of the thermal structure in a model. We here focus on interannual anomalies in tropopause pressure that yield insight into the models' abilities to respond to forcing of the climate system. The tropopause is calculated using the WMO-definition and averaged over a year and  $40^{\circ}\text{N}$ - $60^{\circ}\text{N}$  and  $40^{\circ}\text{S}$ - $60^{\circ}\text{S}$ , respectively. The analysis is based on monthly mean temperature fields (T3M) from the REF-B1 runs. The models are compared to 5 different analyses, ERA-Interim, ERA-40, NCEP, NCEP2, and JRA25.

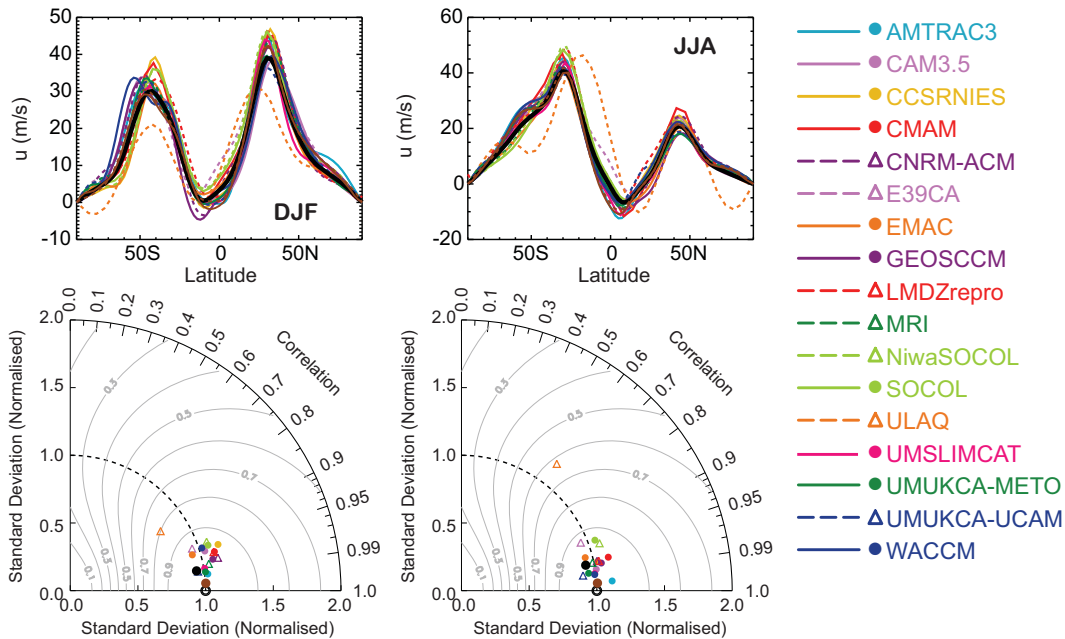


**Figure 7.18:** Seasonal cycle in LMS mass following Appenzeller et al. (1996) (upper panels), and corresponding Taylor diagrams of model performance (lower panels) for NH (left panels) and SH (right panels). Coloured lines, dots and triangles denote models, black solid line and dot the multi-model mean, and brown line and gray shading the NCEP reanalyses  $\pm 1\sigma$  standard deviation.

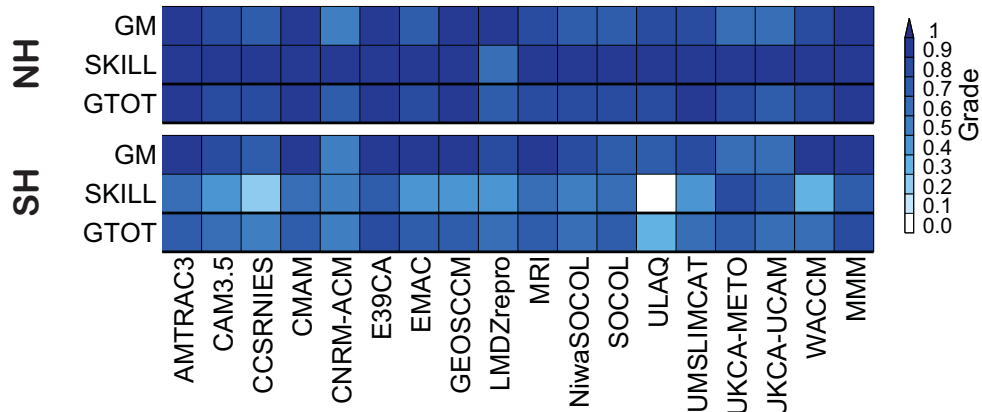


**Table 7.19:** Same as Figure 7.17, but for LMS mass in the NH (upper) and SH (lower).

Although the models seem to reproduce the seasonal cycle in tropopause pressure well in the NH (which can be argued based on the diagnostic for the LMS mass), they show more problems in representing interannual variability. This can be seen from **Figure 7.20**. Similar to the evaluation in the tropics, CNRM-ACM has unrealistic interannual variability and low tropopause pressure. CCSRNIIES, EMAC, ULAQ and WACCM achieve lowest total scores (not shown) due to both too high/low mean values and smaller correlation with the observed variability structure.

In the SH, the models simulate the interannual variability somewhat better, except CNRM-ACM which has large interannual variability and as in the NH a too low tropopause pressure. CCSRNIIES, MRI, ULAQ, and WACCM have a negative bias in the mean tropopause pressure, and ULAQ shows the worst correlative score.

### 7.5.1.4 Extra-tropical Tropopause Inversion Layer

**Figure 7.21** shows the  $N^2$  profiles at two latitude bands, representing the NH TIL in winter and summer (for discussion of full cross-section see Section 7.4.7). It can be seen that maximum values of simulated  $N^2$  are comparable to or larger than those derived from degraded GPS RO data. However, they are always weaker than those computed from full-level GPS RO data unless vertical resolution is sufficiently high (*e.g.*, WACCM-highres). It is also evident that the location of maximum  $N^2$  in the CCMVal-2 models is always higher above the tropopause than in observations. These results are consistent with the findings in the tropics (**Figure 7.15**) and those by Bell and Geller (2008) as discussed in Section 7.4.7.

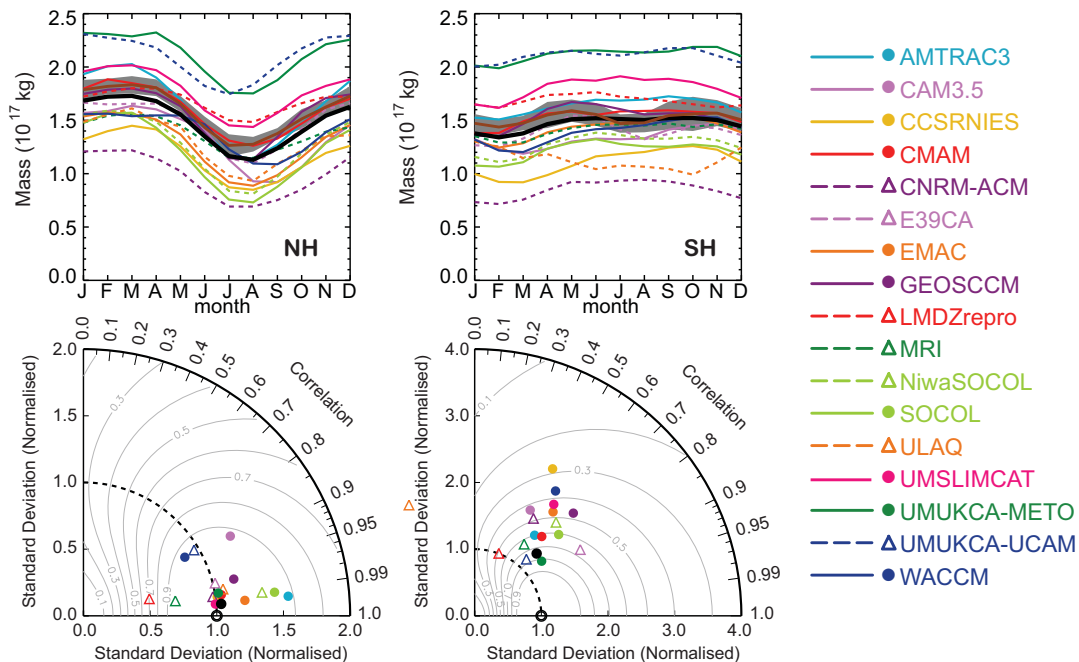


**Figure 7.20:** Extra-tropical tropopause pressure variability for SH (left panel) and NH (right panel).

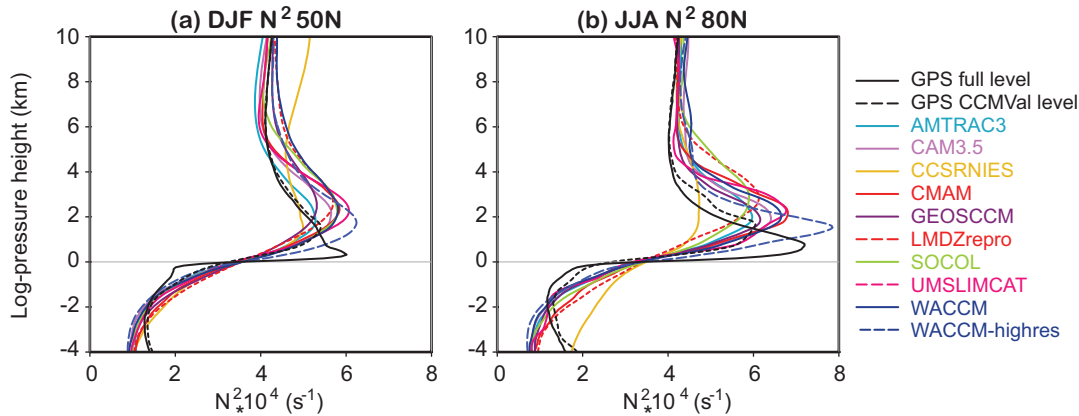


**Figure 7.21:** Vertical profiles of  $N^2$  in models and observation at (a)  $50^\circ\text{N}$  during DJF and (b)  $80^\circ\text{N}$  during JJA.

It should be emphasised that, although the maximum  $N^2$  values of the TIL are somewhat under-estimated, most CCMVal-2 models qualitatively reproduce the seasonal and latitudinal changes observed in the TIL. In fact, the models' simulated TIL is more realistic than that derived from reanalysis data (Birner *et al.*, 2006). This may be because the reanalysis systems are ingesting data that may cause degradation to the structure, either through errors or through coarse vertical resolution (*e.g.*, satellite temperatures).

## 7.5.2 Transport and mixing

The chemical structure of the extra-tropical UTLS and its seasonal evolution is determined by the source/sink characteristics of the various species, together with the relative strength of large-scale and small-scale transport and mixing processes. The tracers we focus on in this report ( $\text{O}_3$ ,  $\text{H}_2\text{O}$ ,  $\text{HNO}_3$ , and  $\text{CO}$ ) are relatively long-lived compared to the transport time scales determining their distributions across the extra-tropical UTLS, therefore, the chemical structure of these tracers can be used to validate the underlying transport processes. While large-scale and small-scale mixing processes are hard to disentangle completely, their relative importance is strongly dependent on the sub-region one is considering.

### 7.5.2.1 Tracer seasonal cycles in the 'background' Lowermost Stratosphere

The large-scale Brewer-Dobson Circulation (BDC), driven by (planetary, gravity, and synoptic-scale) wave-drag in the stratosphere, transports aged stratospheric air into the LMS (Logan, 1999). The breaking of synoptic scale waves above the subtropical jet mixes younger tropical air masses with older higher-latitude air masses. The BDC and synoptic-wave transport exhibit a seasonally varying strength, and determines the chemical background

composition of the LMS (Hoor *et al.*, 2005; Hegglin and Shepherd, 2007). It is crucial for CCMs to capture the relative strength and seasonality of these processes. This is because they determine the distribution of the radiatively active species  $\text{O}_3$  and  $\text{H}_2\text{O}$ , which through radiative heating can alter temperature distributions and thereby winds in the UTLS, and also determine the monthly input of stratospheric ozone into the troposphere. Lowermost stratospheric background  $\text{O}_3$  furthermore determines the impact of aircraft emissions on ozone at these altitudes.  $\text{H}_2\text{O}$  plays an important role as precursor of  $\text{HO}_x$  ( $\text{OH} + \text{HO}_2$ ) which are the dominant radicals for ozone destruction in the LMS.

The models' representation of these large-scale transport and mixing processes, with typical time scales of weeks to a couple of months, is evaluated here using the seasonal cycles in  $\text{O}_3$ ,  $\text{HNO}_3$ , and  $\text{H}_2\text{O}$  at 100 and 200 hPa for latitude bands between  $40^\circ$  and  $60^\circ\text{N/S}$ , respectively. While  $\text{O}_3$  and  $\text{HNO}_3$  are expected to yield about the same seasonal cycles since their sources are mostly stratospheric at these levels,  $\text{H}_2\text{O}$  is a tropospheric tracer (since the contribution of  $\text{CH}_4$  oxidation to total water is small) and gives insight into a possible tropospheric influence as well as the lowest saturation vapour pressure an air parcel has experienced.  $\text{HNO}_3$  is further affected by chemistry and microphysics, which may cause some differences in its seasonal cycle when comparing it to that of  $\text{O}_3$ . The monthly mean zonal-mean tracer fields of the REF-B1 simulations from 2000-2006 are compared to observations obtained by the MIPAS instrument between 2004 and 2008.

The upper two rows in **Figures 7.22** and **7.23** show the results for the 100 hPa level with the corresponding Taylor diagrams in the NH and SH, respectively. In the NH,  $\text{O}_3$  is relatively well represented in all the models despite a tendency to overestimate the mean and the amplitude (*i.e.*, standard deviation) of the seasonal cycle relative to MIPAS observations. Moreover, the Taylor diagram reveals slightly lower correlation values than average for CAM3.5, ULAQ, UMUKCA-UCAM, and WACCM. The seasonal cycle in

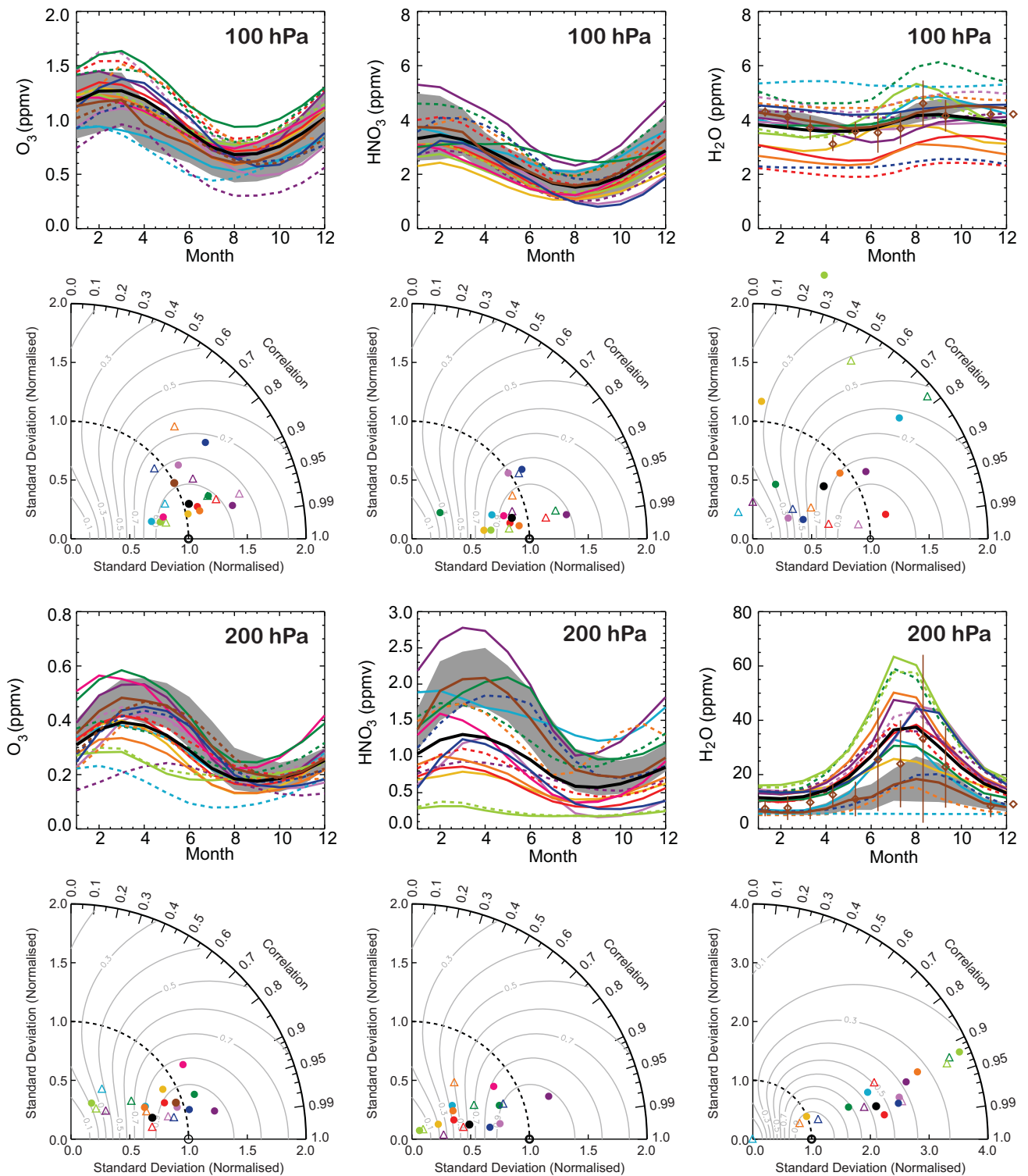


**Figure 7.22:** Seasonal cycles in monthly mean O<sub>3</sub>, HNO<sub>3</sub>, and H<sub>2</sub>O between 40°N and 60°N and corresponding Taylor diagrams at 100 hPa (upper two rows) and 200 hPa (lower two rows) for different models (colour-coded) compared to MIPAS satellite data and their 1 $\sigma$  uncertainty (brown solid lines and gray shading) over the years 2004-2008. For O<sub>3</sub>, MLS data over the years 2004-2008 (brown dashed lines and dots), and for H<sub>2</sub>O, ACE-FTS data (brown diamonds) are shown in addition to the MIPAS data. Black lines and dots indicate the multi-model mean.

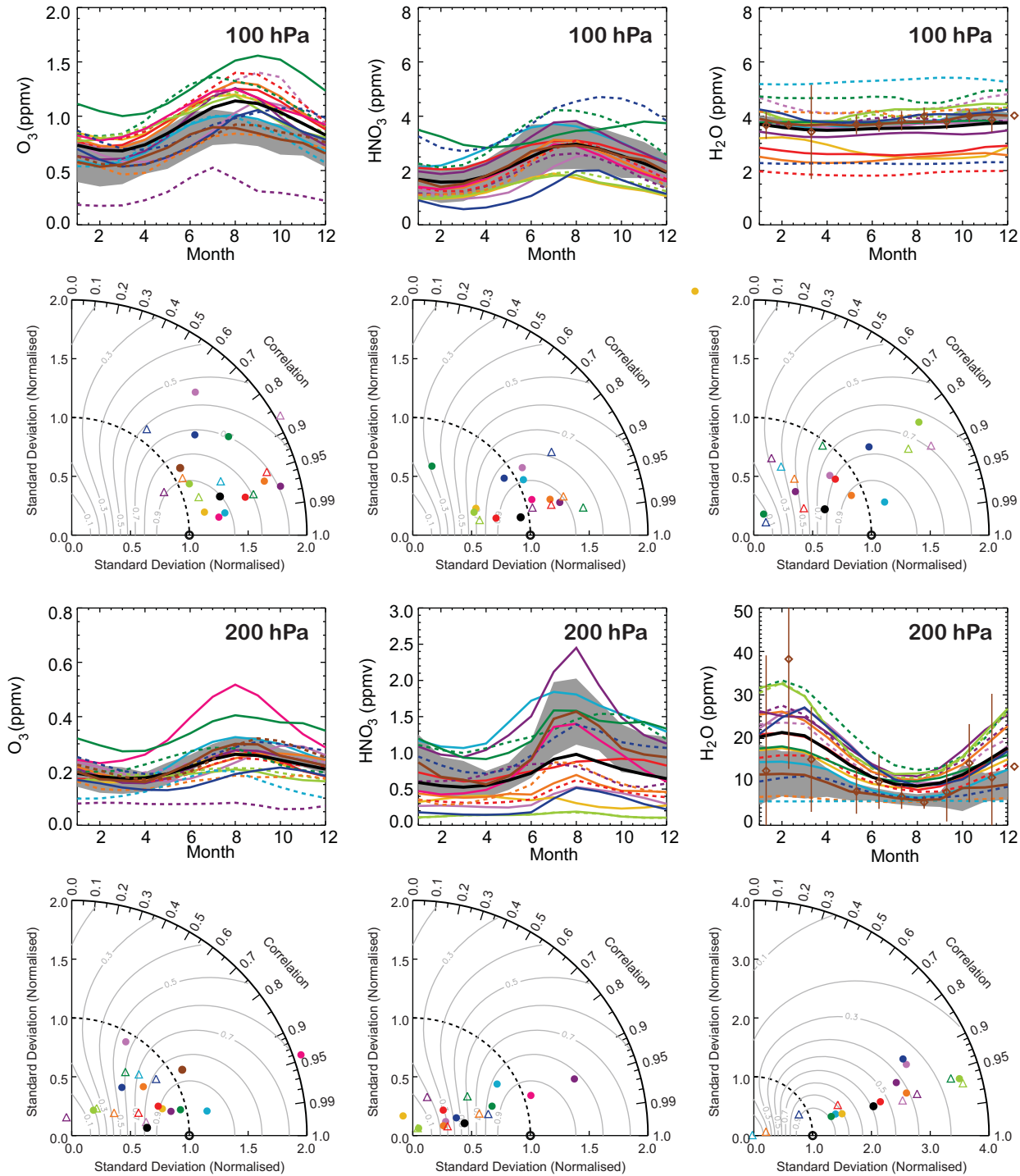


Figure 7.23: Same as Figure 7.22, but for latitudes between 40°S and 60°S.

HNO<sub>3</sub> mostly confirms this behaviour, with the exception of UMUKCA-METO, which exhibits a very low correlation with MIPAS satellite observations. The seasonal cycle in H<sub>2</sub>O is similar to that obtained in the tropics at 80 hPa (see Figure 7.10), pointing toward a strong connection between the tropics and the extra-tropics. The performance of the models therefore strongly depends on their ability

to represent tropical processes such as dehydration (see Section 7.4.5). Indeed, models that score low in the tropical H<sub>2</sub>O diagnostic also score low in this diagnostic. From this, it might be inferred that the slightly too high amplitude in O<sub>3</sub> has its origin in the tropics. This also confirms the finding by Gettelman *et al.* (2009) that most of the CCMVal-1 models have O<sub>3</sub> in the tropics that increases too quickly at and above the tropopause. This discrepancy is improved

in the CCMVal-2 models (see section 7.4.4), but several outliers still exist. The seasonal cycles in the SH generally show smaller amplitudes, reflecting the weaker BDC, and also weaker transport within the tropically controlled transition region. The models generally show the same behaviour, however, overestimating the mean  $O_3$  values. In both the NH and SH at 100 hPa, the multi-model mean reaches grades comparable to the better performing models.

The results for the 200 hPa level are shown in the two lower rows in Figures 7.22 and 7.23. At 200 hPa in the NH, the models' performance seems to decrease compared to the 100 hPa level in almost all the models. The mean values and amplitudes in the  $O_3$  seasonal cycle tend to be lower than those in the observations. The worst scores are obtained by CNRM-ACM, NiwaSOCOL, SOCOL, and UMETRAC, which show too low amplitudes and relatively low correlations in comparison with the MIPAS observations.  $HNO_3$  again shows a consistent behavior with that of  $O_3$  in almost all of the models. The generally low mean values in both  $O_3$  and  $HNO_3$  can be explained by too much

vertical transport across the extra-tropical tropopause. This is reflected also in too large amplitudes in the  $H_2O$  seasonal cycle (as seen in the Taylor diagrams with the standard deviations on the radial axes). Tropospheric influence seems to be particularly high during late summer and autumn. As the analysis is done on fixed pressure levels, the model biases could in principle stem from biases in the tropopause altitude. However, this seems not to be the case. MRI for example shows a too low tropopause, but too strong mixing, while UMSLIMCAT shows a too high tropopause, but not enough mixing. SOCOL and NiwaSOCOL both are too diffusive, possibly due to their semi-Lagrangian transport scheme.

At 200 hPa in the SH, the observed seasonal cycles of all three tracers show smaller amplitudes than in the NH, similar to the finding on the 100 hPa level. The models' means and amplitudes (standard deviations) in  $O_3$  and  $HNO_3$  are shifted to smaller values than expected from the observations. For  $O_3$ , the worst model performance is found for CNRM-ACM, the SOCOL-based models, ULAQ and

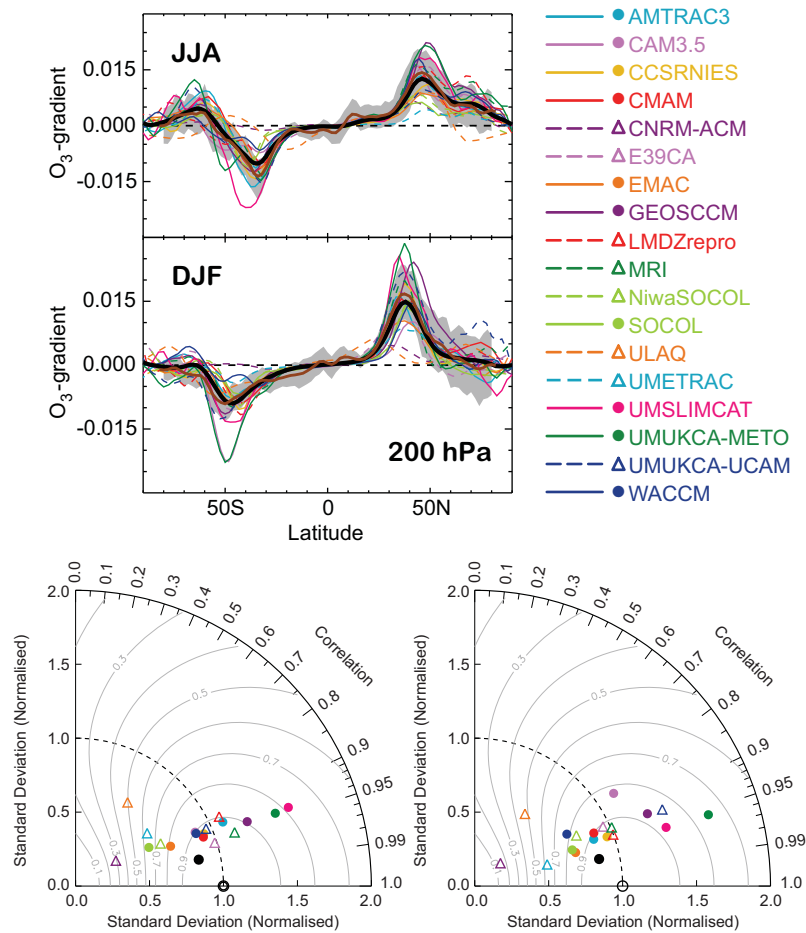


**Figure 7.24:** Meridional gradient in  $O_3$  (ppmv/deg) at 200 hPa and corresponding Taylor diagrams for JJA (upper/left panel) and DJF (lower/right panel). Brown lines indicate MLS data averaged over the years 2004–2008, black thick lines and dots the multi-model mean. The gray region in the top panel indicates 1 $\sigma$  from the observations.

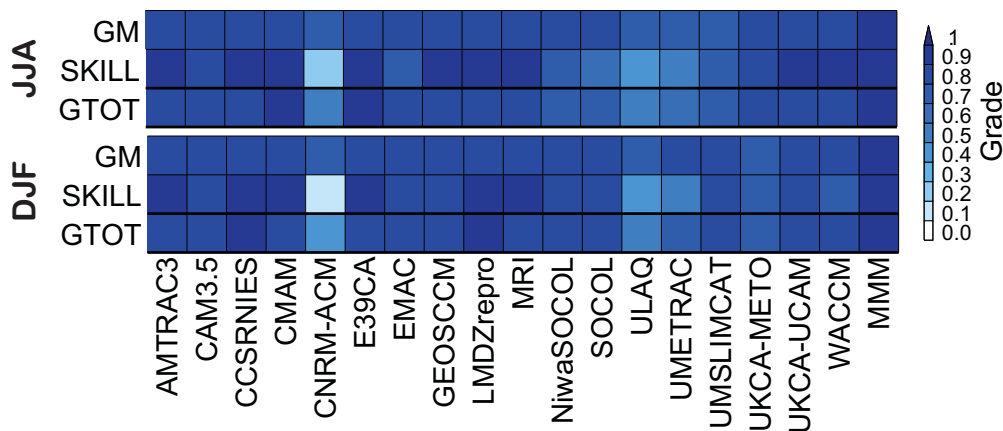


**Figure 7.25:** Same as Figure 7.17 but for meridional gradient in  $O_3$  at 200 hPa for JJA (upper) and DJF (lower).

UMSLIMCAT. Again,  $H_2O$  indicates too strong cross-tropopause transport. Note that there is some evidence that the seasonal cycle in the MIPAS  $H_2O$  exhibits too small amplitude. Comparison with the ACE-FTS measurements indicates that MIPAS might be somewhat low especially during summer on the 200 hPa level and in both hemispheres, an issue which is currently under investigation. However, the large noise and standard deviations in the ACE-FTS data imply that the sampling from the ACE-FTS is not sufficient in determining the seasonal cycle in  $H_2O$  accurately. Additional measurements with higher (spatial and temporal) resolution will be needed to resolve this issue and to gain more confidence in this metric in the future.

For this diagnostic we derive two grades for the models. One grade is based on the  $O_3$  seasonal cycle, and calculated as the average over all mean and skill values obtained for both pressure levels and hemispheres. The other grade is based on the  $H_2O$  seasonal cycle, calculated as the average of all skill values obtained for both pressure levels and hemispheres. We do not include the mean for  $H_2O$ , since the mean is already used as metric in the tropics and we do not expect significant changes due to the  $CH_4$  oxidation. The models' final grades are shown in Figure 7.39.

### 7.5.2.2 Meridional Tracer Gradients

Useful information on mixing barriers and therefore the degree of isolation and chemical distinctness of different regions such as the tropics and the extra-tropics is provided by the sharpness of meridional gradients of long-lived species. Here we use the meridional gradient in  $O_3$  at 200 hPa (which is long-lived in relation to the transport time scales in this region). We use seasonal means for JJA and DJF derived from monthly mean zonal-mean  $O_3$  fields (REF-B1 simulations) from all models and compare them to a multi-year seasonal climatology using MLS data (averaged over 2004-2008).

**Figure 7.24** shows that the models reproduce the

meridional gradients in both seasons (JJA and DJF). Most models are within 1 sigma of the observations (gray). This implies that the models are capable of reproducing the separation between the tropical UT and the extra-tropical LMS. As can be seen in the Taylor diagrams in Figure 7.24 (lower panels) the correlations are mostly higher than 0.9, except for ULAQ and CNRM-ACM, which show correlations between 0.5 and 0.7. There is, however a substantial spread in the models in terms of standard deviations, resulting in somewhat decreased skill (see **Figure 7.25**). Too low variability is shown by ULAQ, CNRM-ACM, NiwaSOCOL and SOCOL, and too high variability by UMUKCA-METO and UMSLIMCAT, although the latter achieves a very high skill of 0.9 due to a high correlation with the observations.

A relation between this diagnostic and the zonal-mean zonal wind would be expected, as the subtropical jet acts as a barrier to transport, and maintains strong gradients across this region as observed in aircraft observations (Ray *et al.*, 1999). This is indeed the case for ULAQ, which shows low grades for both the zonal-mean zonal wind and for the meridional tracer gradient.

### 7.5.2.3 Normalised Vertical Profiles of CO in Tropopause Coordinates

To evaluate the representation of tropospheric influence on the background LMS in the models, and to separate between transport across the extra-tropical tropopause on short time scales and transport from the tropics and subtropics on longer time scales, we use CO with a  $\sim 3$  month lifetime in the LMS. In the middle stratosphere above  $\theta = 500$  K, CO is nearly constant, with an observed background value of 10-15 ppbv (Flocke *et al.*, 1999), due to the chemical equilibrium between methane and CO oxidation. Any excess CO must then originate from the troposphere.

To examine the coupling between the LMS and the extra-tropical troposphere, CO was evaluated in tropo-



pause coordinates, expressed in potential temperature units relative to the 2 PVU surface ( $d\theta$ ) as applied to the SPURT data set (Hoor *et al.*, 2004, 2005). Key results from Hoor *et al.* (2004, 2005) are:

- The coupling to the local troposphere drops below 25% over the lowest 30 K above the tropopause (2 PVU).
- The stronger influence of the sub-tropical troposphere above the extra-tropical tropopause ( $d\theta \geq 30$  K) accounts for the background CO in the LMS, which varies with season.

The largest inter-seasonal differences are found when comparing winter/spring to summer/autumn (Hoor *et al.*, 2005).

For CCMVal-2, instantaneous model output for the year 1995 was sampled within the SPURT measurement domain (30°N-80°N, 20°W-10°E). Data were analysed in layers of 30 K relative to the 2 PVU surface (represented by the centred layer means at -15, 15, 45, and 75 K in **Figure 7.26**). The tropospheric fraction of CO in the stratosphere ( $\text{CO}^*$ ) is determined by  $\text{CO}^* = (\text{CO} - \text{CO}_{\text{strat}}) / (\text{CO}_{\text{trop}} - \text{CO}_{\text{strat}})$ . The stratospheric CO-background ( $\text{CO}_{\text{strat}}$ ) was deduced for each individual model for  $\theta = 500$ -600 K, for  $\text{CO}_{\text{trop}}$  the layer mean for  $d\theta = -30$ -0 K was used. Note, that the normalisation accounts for the varying boundary specifications of CO in the models, which would lead to a degradation of the performance in many models if not accounted for. Models that did not provide instantaneous tropospheric CO were not included in the comparison.

Two properties were tested:

1. The abundance of tropospheric tracer  $\text{CO}^*$  between 30 and 60 K above the tropopause as a measure for tropospheric influence.
2. The decreased coupling to the local tropopause in the lowest 30 K above the dynamical tropopause, and at  $d\theta = 30$ -90 K as represented by the different gradients of  $\text{CO}^*$  in the respective layers.

For the grading, the following properties were used:

1. W1: The abundance of  $\text{CO}^*$  in the  $d\theta = 30$ -60 K layer was compared to the SPURT data. A model was given a grade of 3 if the difference between observations and model was smaller than  $1\sigma$  of the measured inter-annual variability, 2 points for  $\sigma$  between 1 and  $2\sigma$ , 1 point for  $\sigma$  between 2 and 3, and 0 for data outside the  $3\sigma$  level.
2. W2: The vertical gradient of  $\text{CO}^*$  in the  $d\theta = 30$ -90 K region must be much smaller than it is closer to the tropopause (up to  $d\theta = 30$ K) since the decrease in  $\text{CO}^*$  is largest in the lowest layer. Grading was performed by calculating the gradients in  $\text{CO}^*$  between the levels  $d\theta = 45$  and 75 K, and  $d\theta = -15$  and 15 K, respectively, taking the ratio between these two gradients, and comparing the ratios obtained from models

and observations. As in W1, the ratio of the gradient of each model was tested to see if it fell within the uncertainty range of the observed ratio in steps of 1 s.

Thus, high values for both weights indicate a good separation from the extra-tropical troposphere and mainly weak influence from the subtropics (*e.g.*, CAM3.5, CMAM, WACCM, EMAC). Low values for W1 (abundance), but high values for W2 (separation) indicate too much tropospheric tracer  $\text{CO}^*$  in the LMS, but the transition from the local troposphere to the LMS occurs correctly within  $d\theta = 0$ -30 K (*e.g.*, AMTRAC, CCSRNIES). Low values for both W1 and W2 indicate that the coupling to the extra-tropical tropopause extends too deep into the stratosphere (*e.g.*, LMDZrepr0, NiwaSOCOL during winter) leading to an unrealistic tropospheric contribution due to overestimation of transport across the extra-tropical TP. SOCOL, ULAQ, and CCSRNIES do perform well in both metrics during summer, but less so during winter.

In general models tend to transport too much tracer into the LMS in winter as indicated by the low values of W1, and the fact that the multi-model mean lies outside of the 1 sigma range of the observations. However, most

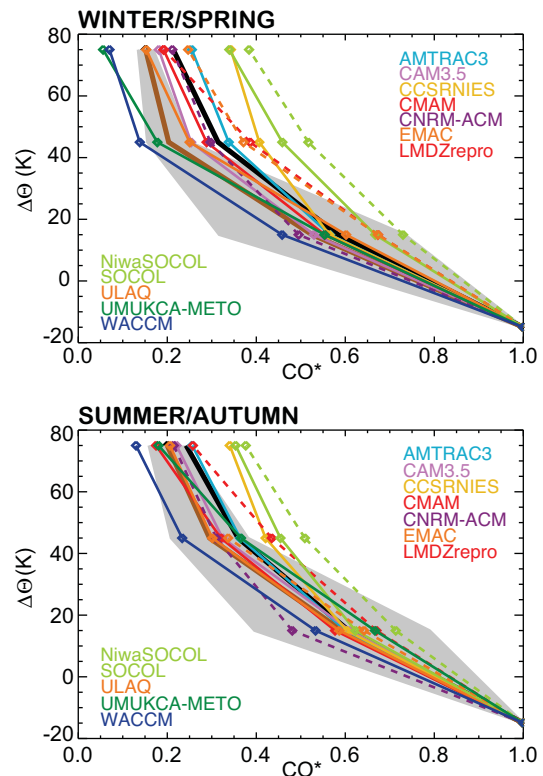


**Figure 7.26:** Profiles of  $\text{CO}^*$  (normalised CO) for winter/spring and summer/autumn in layers of  $d\theta = 30$  K and for the different models. The brown solid line and grey shading shows mean CO ( $\pm 1\sigma$ ) from SPURT aircraft measurements. The black indicates the multi-model mean.

models capture the separation (*i.e.*, the change of gradient) around  $d\theta = 30\text{K}$  well, as indicated by W2. Thus most models are able to separate between transport across the local tropopause in the extra-tropics and processes involving other time scales and source regions. During summer, when tropospheric influence from the subtropics is higher, the models capture this feature. The high summer values of W2 are a result of weaker differences of the vertical gradient through this enhanced transport from the subtropics accompanied with larger variability in the measurements. Most models therefore tend to get the separation between different regimes in the LMS right within the measurements variability.

The best representation of transport and troposphere-stratosphere coupling is seen in CAM3.5, CMAM, CNRM-ACM, EMAC, UМУKCA-METO and WACCM, whereas LMDZrepro and NiwaSOCOL seem to be too diffusive or too permeable across the tropopause, confirming the results of the previous diagnostic using seasonal cycles.

#### 7.5.2.4 Vertical profiles of $\text{O}_3$ , $\text{H}_2\text{O}$ and CO relative to the tropopause height

The vertical structure of  $\text{O}_3$ ,  $\text{H}_2\text{O}$  and CO across the tropopause is evaluated using profiles in tropopause-

referenced relative altitude coordinates (Logan, 1999; Pan *et al.*, 2004, 2007; Hegglin *et al.*, 2006; Considine *et al.*, 2008). Note, that this diagnostic uses absolute values of CO, thereby adding information on the representation of tropospheric CO to the metric of normalised vertical CO profiles discussed in Section 7.5.2.3. In the region of  $\pm 5\text{ km}$  around the tropopause, relative altitudes with respect to the tropopause (RALT) are effective coordinates for separating the tracer variability as a result of chemistry and transport from that caused by the variability of the tropopause height. The diagnostic requires instantaneous model output. For consistency with the coverage of the aircraft data, models are evaluated for the years between 1995 and 2005.

The region of analysis is chosen to be that part of the extra-tropics that is not strongly influenced by the subtropical tropopause break and double tropopauses. The selection criterion is a tropopause height of 325 K or below in winter and spring, and 335 K or below in summer and fall. Additional requirements are that no double tropopause is observed and that the latitude is lower than  $80^\circ\text{N}$  (Tilmes *et al.*, 2010). The profiles selected are largely within  $40^\circ\text{N}$ - $80^\circ\text{N}$ . The LS chemical composition of this region, as discussed in Section 7.5, is largely controlled by the downward branch of the BDC in the stratosphere, with seasonally varying contribution from the isentropic mix-

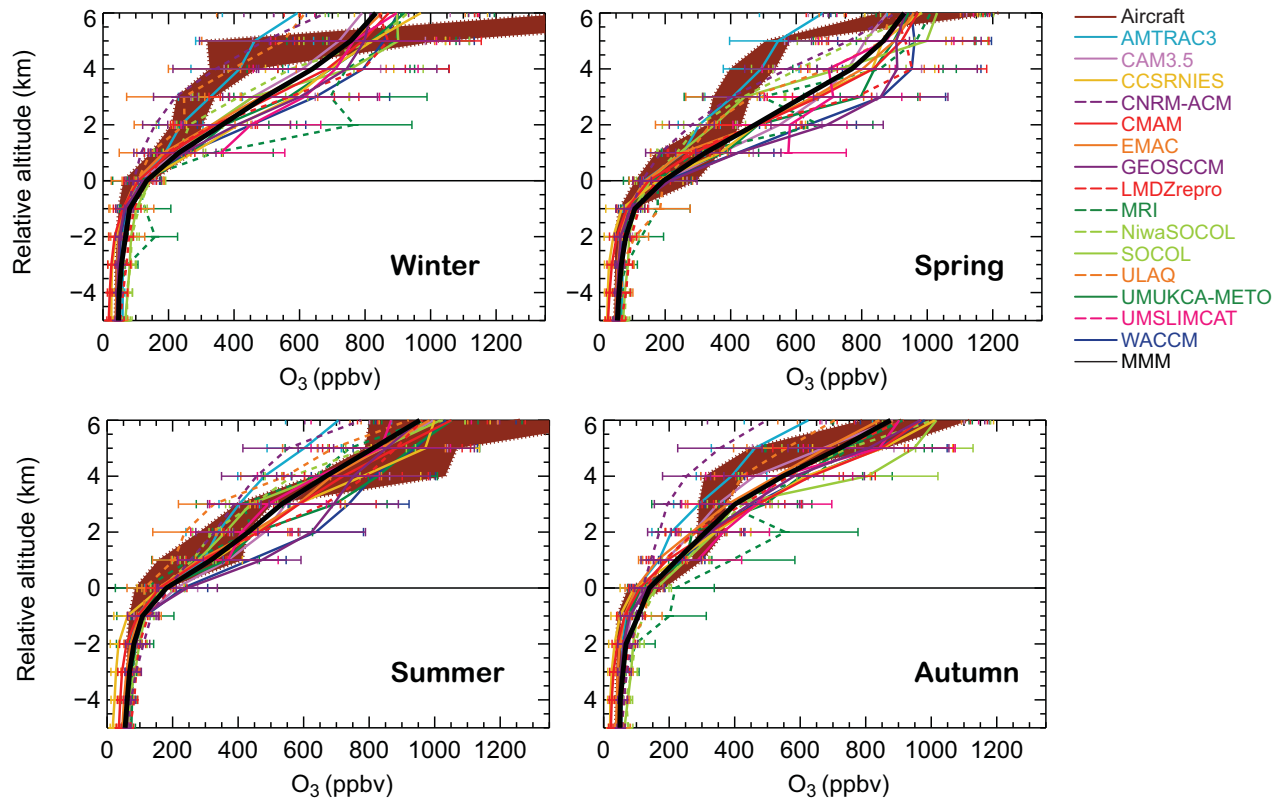


**Figure 7.27:** Ozone profiles in RALT for four seasons. The distribution of the aircraft data is represented by 25-75 percentiles (black shading) and the 5 and 95 percentiles (dotted lines). Models are represented as median (colour lines) and the 25 -75 percentiles (error bars).

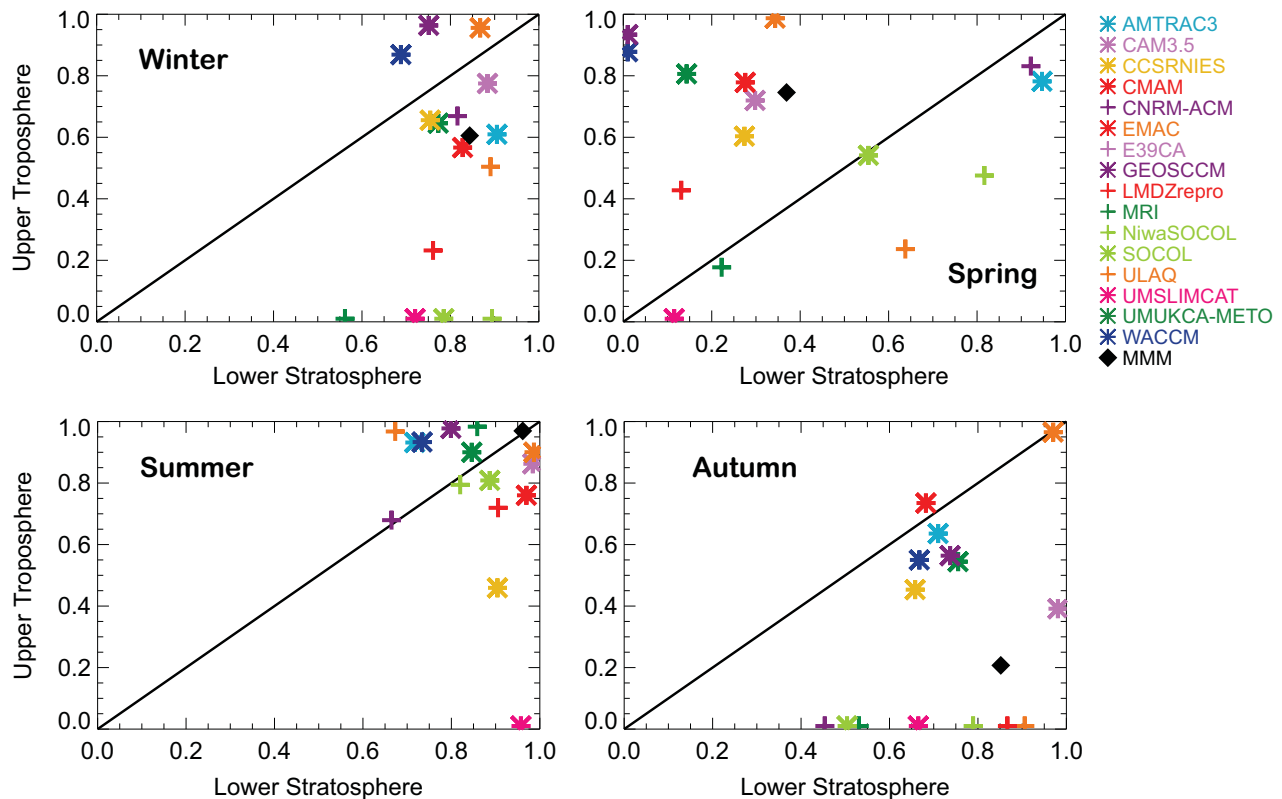


**Figure 7.28:** Grades calculated using simplified metrics (Douglass *et al.*, 1999) for mean ozone values in the upper troposphere (1–4 km below the tropopause) and lower stratosphere (1–5 km above the tropopause) and four seasons.

ing between tropical latitudes and the LMS. The region is therefore well suited for evaluating how well models represent the two competing processes. The vertical structure is examined using  $O_3$ ,  $H_2O$ , and  $CO$ . The  $O_3$  structure is examined for four seasons.  $CO$  and  $H_2O$  structures are examined using the annual mean.

**Figure 7.27** shows the ozone profiles in relative altitudes with respect to the tropopause (RALT) for four seasons. Observations show a seasonality of ozone mixing ratios in the LMS, with lower values in fall and winter, and higher values in summer and spring. **Figure 7.27** can be compared to **Figure 7.22** at two pressure levels. The figures are consistent, but interpretation across coordinates is difficult because the RALT level in **Figure 7.27** varies in pressure throughout the year. In general, all models represent the ozone behaviour well, qualitatively. Quantitatively, in most models ozone increases more rapidly above the tropopause compared to the aircraft climatology, a result that is also consistent with the finding of the diagnostic of the seasonal cycle in  $O_3$  at 100 hPa (see Section 7.5.2.1). The comparison is quantified using the metrics defined by Douglass *et al.* (1999), as described in Section 7.3 with  $n_g$  chosen to be 3. The calculated grades for the UT and LS are given in **Figure 7.28**.

In general, models agree better with observations in

summer, when stratospheric transport processes are weaker compared to other seasons, and photochemical production is more active. Models also do better in the UT in spring. There is a wide spread in model performance during winter and fall.

The annual mean  $CO$  and  $H_2O$  vertical structures and the grading values are shown in **Figure 7.29**. The UT chemical composition, especially  $CO$ , is significantly influenced by the contribution of anthropogenic and fire emissions in the densely populated NH. Most of the models are not representing latitudinal and seasonal variations in  $CO$  emissions, resulting in significant deviations between models and observations in UT  $CO$  distributions (**Figure 7.29**, left column), but good agreement is found for the LS in general. The disagreement in the UT was not identified in the previous metric (Section 7.5.2.3) due to the applied normalisation. (The normalisation is designed on purpose to avoid testing the boundary  $CO$  condition in the troposphere, and therefore to be able to solely focus on transport and mixing effects.)  $H_2O$  is well simulated by the models in both the UT and LS, except for MRI which shows too high values in the LS. The comparison with the ACE-FTS satellite data indicates a good agreement between the two data sets. They agree within their uncertainties. Differences may be due to both, the coarser vertical resolution in the

satellite data and the smaller regional coverage of aircraft observations.

We use the average over the UT and LS grades of  $\text{H}_2\text{O}$  for each model (shown in lower left of Figure 7.29) in Figure 7.39. We do not use the same composite grade for  $\text{O}_3$  and  $\text{CO}$ , since these two species are strongly influenced by the representation of tropospheric chemistry, which is treated in most models in a simplified way.

### 7.5.2.5. Structure of the ExTL

The extra-tropical tropopause transition layer (ExTL) is composed of air masses with partly tropospheric, partly stratospheric characteristics. The representation of the ExTL characterizes how well the models reproduce the tropopause as a chemical transport boundary and the sharpness of the barrier. The transition layer depth is examined using tracer correlations between ozone and water vapour (Pan *et al.*, 2007; Hegglin *et al.*, 2009). A stratospheric branch is identified using a fit to a polynomial function of second order to all data points in the LS ( $\sim$ below 20 km) with  $\text{H}_2\text{O} < 10$  ppmv. Similarly, a tropospheric branch is represented by a linear function derived in fitting all data points with  $\text{O}_3 < 100$  ppbv for both observations and models. Mixed air masses are identified as those points outside the 3 sigma

range of both the stratospheric branch and the tropospheric branch. The observed transition layer is derived using POLARIS aircraft data, which include measurements in spring, summer and fall (Pan *et al.*, 2007). Results of both model and observations are shown in Figure 7.30 (left) as histograms of the fraction of samples in relative altitudes. Model analyses used output for the same seasons.

Two parameters are used to quantify the comparisons: a) the centre of the transition layer, defined as the centre point of the distribution at the half maximum, b) the width of the layer, defined as the width of distribution at the half maximum. These criteria are influenced by the bin size, which was chosen to be 0.5 km for the observations and 0.5 or 1 km for the models depending on which number is closer to their vertical resolution in the UTLS. A comparison of layer width and centre location is shown in Figure 7.30 (right). The transition layer between UT and LS is well manifested in all models, however in all cases the layer is broader, between 2 and 4 km, compared to 1 km derived from observations. Further, the layer centres in the models are shifted upward  $\sim 1$  km in most cases. Uncertainties in tropopause location derived from the relatively coarse vertical resolution models may have contributed to the discrepancies, equivalent to an artifact seen when using low resolution radiosonde observations to deduce tropopause heights (Bell and Geller, 2008).

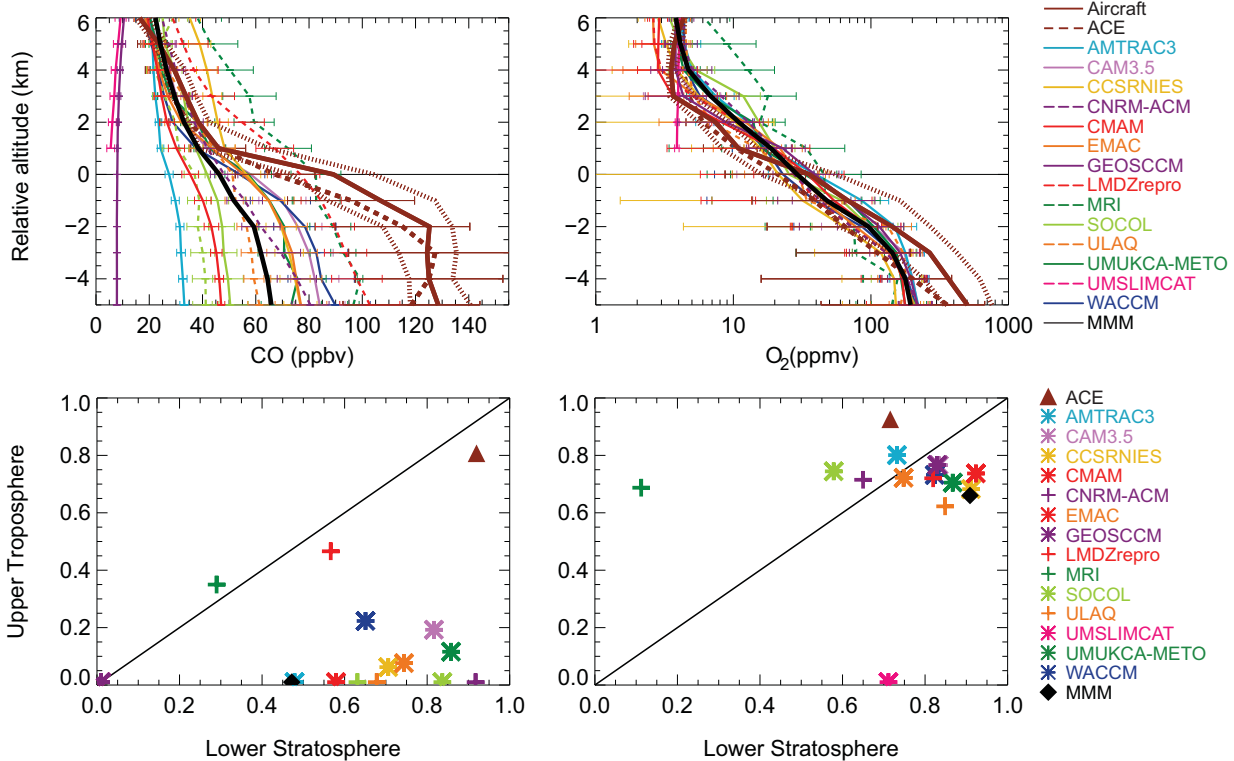


**Figure 7.29:** Top panels as in Figure 7.27 and bottom panels as in Figure 7.28, but for annual means of  $\text{CO}$  (left) and  $\text{H}_2\text{O}$  (right). Also included in the comparison are the annual means of ACE-FTS data for the year 2007 (brown dashed line in the upper panels, brown triangles in the lower panels). The multi-model mean is indicated with a black solid line or diamond, respectively.

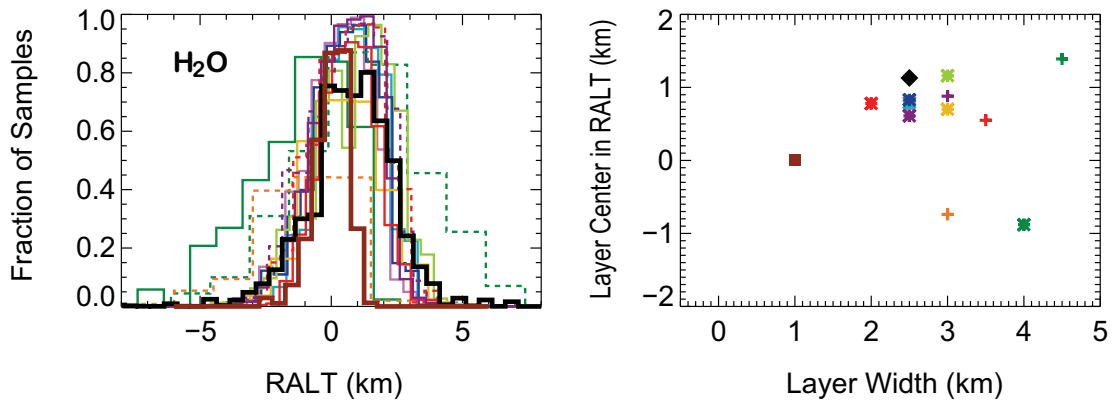


**Figure 7.30:** Left panel: Fraction of air parcels within the mixing layer from models (colours) and the multi-model mean (black) for the year 2000, and from POLARIS observations for 1997 between spring and fall (brown). Right panel: Scatter plot between centre and width of the ExTL. See legends Figure 7.27 and 7.28 for colour coding.

The fact, that models have major difficulties to reproduce this diagnostic, might be at least partly attributable to the limited vertical resolution of the models (see also Section 7.5.1.4). Recent satellite observations from the ACE-FTS, which have an effective resolution similar to the CCMs (around 1 km), show indeed a behaviour similar to that of CMAM and CAM3.5, exhibiting a layer width of 2 km and a layer centre at 1 km above the thermal tropopause. The POLARIS data set on the other hand might not be representative of the ExTL depth in a climatological sense.

### 7.5.5 Variability in UTLS ozone

Correlations between tracers and tropopause heights can be used to examine the tracer sensitivity to tropopause changes in the UTLS and to evaluate transport processes between low latitudes and mid-latitudes related to synoptic waves. Here we provide a representative metric to facilitate evaluating transport and mixing processes in CCMs using conditional probability density functions (PDFs) (Rood *et al.*, 2000) of correlations between ozone and tropopause height at mid-latitudes. Simulations are compared to version (v2.2) of MLS observations between 2004 and 2008.

Whenever tropopause relative altitude is used as the vertical coordinate, it should be kept in mind that a difference in vertical profiles might simply result from time-varying tropopause height levels and consequent changes in reference levels (*i.e.*, zero levels) in the coordinate. In other words, even the same levels in the tropopause-relative-altitude coordinate may contain tracers at different levels of pressure. Our key concern is whether there would be changes in tracer distributions due to the varying tropopause height that would distort the interpretation of changes in distributions due to transport and mixing processes by synoptic waves. To examine the tracer sensitivity

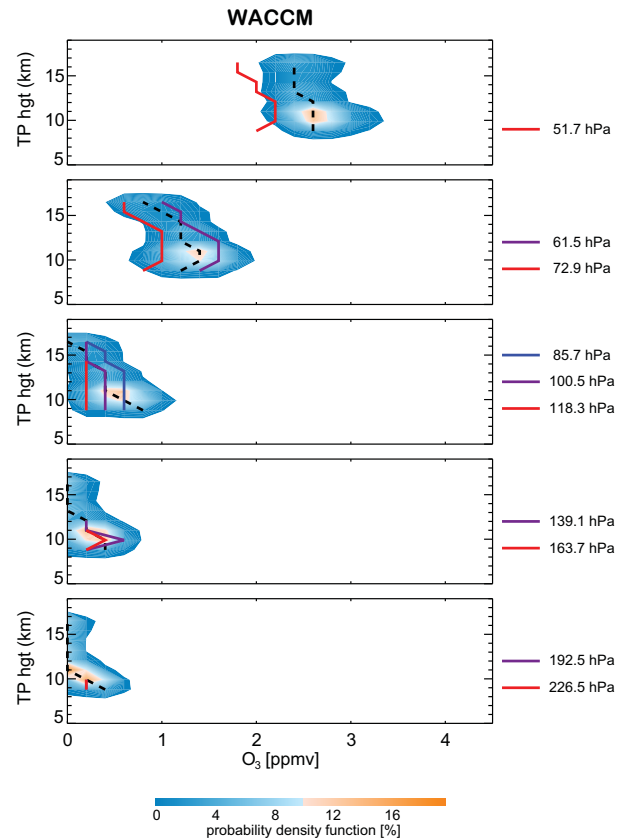


**Figure 7.31:** Example of probability function maps at NH mid-latitudes (40°N to 50°N) during JJA season showing the relationship of O<sub>3</sub> (x-axis) and tropopause heights (y-axis) for MLS (shaded contour) at five isobaric levels (46.4, 68.1, 100, 146.8 and 215.4 hPa, from top to bottom) and WACCM (coloured lines). Lines indicate the maxima in the MLS (dashed) and model (solid) PDFs at each tropopause height for each pressure level.

of models to the tropopause changes at mid-latitudes, two dimensional correlation maps between simulated tropopause heights and ozone ( $O_3$ ) from REF-B0 CCM simulations at five isobaric surfaces (46.4, 68.1, 100, 146.8 and 215.4 hPa) in the UTLS region are compared to maps with MLS observations. An example is shown for WACCM in **Figure 7.31**.

At NH mid-latitudes there are distinguishable changes in the observed vertical profiles of  $O_3$  by varying tropopause heights during the summer. For higher tropopauses,  $O_3$  exhibits lower values throughout the UTLS. The decreased  $O_3$  related to increased tropopause heights is largest at 68.1 hPa. When the tropopause height is above 15 km, 68.1 hPa  $O_3$  is 50% lower than  $O_3$  with a tropopause height below 10 km. Therefore, when tropopause heights are higher, decreased  $O_3$  can be commonly found in both MLS and CCMs.

The PDF representation of model/data comparison is entirely qualitative. To provide a quantitative measure of the performance of the CCMs, the simple metric  $g$  defined in Douglass *et al.* (1999), which is similar to Equation (7.1), is applied to this diagnostic. Here we used  $n_g = 5$ , thereby expanding the range of acceptable performance (larger difference from observed for a given  $g$  value). To calculate  $g$ , simulated  $O_3$  concentrations on the 68 hPa surface were estimated using linear interpolation. Then for each month, we classify all observed and simulated data within a latitude band  $40^\circ\text{N}$ – $50^\circ\text{N}$  into two groups, for high and low tropopause cases. A tropopause height of  $> 14$  km was used to distinguish tropical air masses from air originating at mid-latitudes. In each group, the average and standard deviation of  $O_3$  are calculated. Comparing the difference in each group between MLS and models allows evaluation of models relative to observed data, minimising effects due to different frequency of higher tropopause heights between the real atmosphere and the CCMs. Also the difference in  $O_3$  concentrations between the two groups shows the dependence of tracer concentrations on tropopause heights.

**Figure 7.32** displays the grades ( $g$ -values) derived from the differences between the maximum in the  $O_3$  PDFs of the models and MLS. In winter, most models show good agreement with MLS except UMUKCA-METO, which shows much higher  $O_3$  values (not shown). Overall, models do worse in the summer than winter. The common weakness of the other five models is for high tropopause cases during the summer-time. When the tropopause height is lower than 14 km, models show better agreement with MLS. Therefore, to improve performance of models in the summer, models need to better reproduce  $O_3$  when the tropopause is higher.

To examine the dependence of  $O_3$  on tropopause height, we calculated mean  $O_3$  for low and high tropopause cases separately and subtracted  $O_3$  for high tropopause cases from low tropopause cases. The resulting  $O_3$  difference

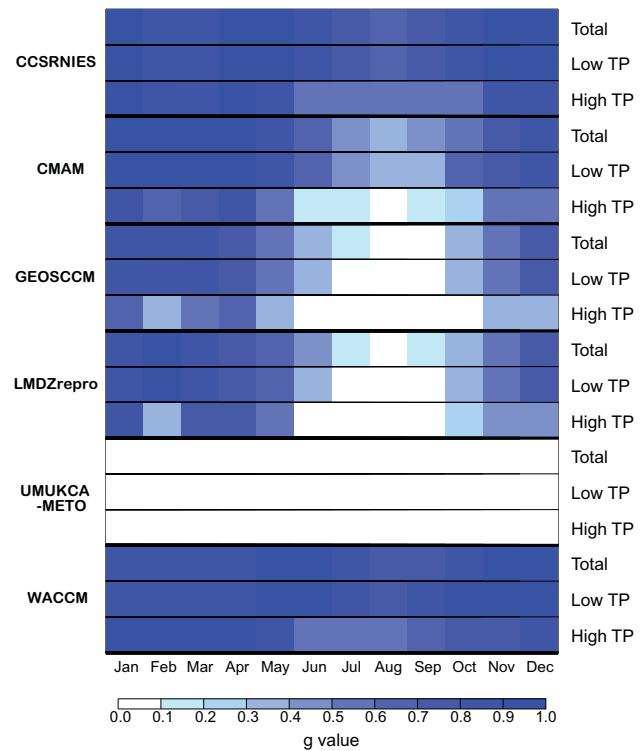


**Figure 7.32:** The temporal variation of the obtained grades ( $g$  values) on 68 hPa isobaric surfaces at mid-latitude ( $40^\circ\text{N}$  –  $50^\circ\text{N}$ ). From top to bottom,  $g$  values (calculated after Douglass *et al.*, 1999) for CCSRNIES, CMAM, GEOSCCM, LMZDrepro, UMUKCA-METO and WACCM. In each model,  $g$  values for all tropopauses, low tropopauses ( $\leq 14$  km) and high tropopauses ( $> 14$  km) are shown separately.

between the high and low tropopause cases has an annual cycle both in the MLS data and the models (**Figure 7.33**). This annual cycle may be related to stronger wave activity and accompanying mixing in the winter and spring. Simulated  $O_3$  is less sensitive to the changes of tropopause heights than in MLS, with smaller simulated  $O_3$  differences between low and high tropopause cases than observed. The smaller differences simulated in the models are likely the main reason for discrepancies shown in **Figure 7.33** and lower overall performance of models in the summer. This is likely a result of more frequent high tropopause cases at mid-latitudes during summer than in other seasons, which is possibly due to a connection with stronger moist-convective events in this season, which is likely under-estimated by the models.

Conventional inter-comparison tools that simply analyse the difference of values between models and observations do not illuminate model performance related to the synoptic wave activity and accompanying changes in tropopause heights. The sensitivity of  $O_3$  at isobaric levels highlights the importance of tropopause heights to simulated tracer distributions at mid-latitudes especially in

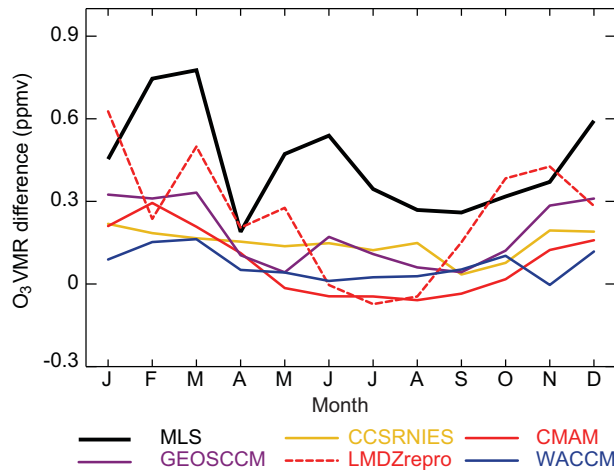


**Figure 7.33:** Time series of  $O_3$  differences ( $O_3$  for low tropopause –  $O_3$  for high tropopause) on 68 hPa isobaric surfaces from MLS observation (black) and five model outputs. The average of  $O_3$  differences is taken at NH mid-latitude ( $40^\circ\text{N} - 50^\circ\text{N}$ ) and is calculated each month.

the summer. Tropopause heights could affect average and variation of tracer fields in the UTLS. Note however that the performance of models is correlated tropopause height variability, not with mean tropopause height.

## 7.6 Trends in the UTLS

The CCMVal model runs for the past and future provide a unique multi-model ensemble to examine trends in the UTLS. UTLS trends for CCMVal-1 models, and for IPCC AR4 models, have recently been analysed by Gettelman *et al.* (2009), Son *et al.* (2009a) and Son *et al.* (2009b). Trends have also been presented for REF-B1 historical simulations in the context of validating the models against observations. Here we present some basic results of future trends in the UTLS from CCMVal-2 models.

### 7.6.1 Tropical Tropopause Trends

We have already shown historical trends for cold point temperature (Figure 7.4) and tropopause pressure (Figure 7.6), along with available data from reanalysis systems and radiosonde observations. These will be discussed further here with the addition of trends for the future (REF-B2) runs. We note that for convenience, future runs were processed using zonal-mean data. As noted by Son *et al.* (2009a) and Gettelman *et al.* (2009), the use of zonal mean temperatures does not significantly affect values or trends of derived tropopause parameters. We have further validated this by using four models and calculating tropopause pressure and cold point temperature using both 2D zonal monthly mean and 3D monthly mean temperatures

(CMAM, CCSRNIIES, MRI and SOCOL). Results indicate that there is less than a  $\pm 10\%$  difference in the magnitude of the trends, and no change in significance.

Tropopause pressure in the models over the historical period is well constrained as noted above. The robustness of the tropopause pressure metric was also noted for CCMVal-1 models by Gettelman *et al.* (2009). Almost all models have historical trends that are close to observations and highly significant. Analyses have trends of  $-0.4$  hPa/decade, and models are slightly higher ( $-0.3$  to  $-0.9$  hPa/decade). The four models with the highest overall on all 4 metrics have a mean trend of  $-0.6$  hPa/decade. Interannual variability is highly correlated with observations, and generally small. Model absolute values of pressure vary, with many close to the observations, and several typically a level above or below. Recall that all analyses and models have been processed onto a relatively high (10-15hPa) resolution vertical grid. There are generally larger decreases in pressure in the subtropics where tropopause gradients are large.

Trends for the future REF-B2 runs are illustrated in **Figure 7.34**. The figure contains multiple ensembles for WACCM and CMAM, illustrating that the trends are quantitatively the same for different ensemble members. There are some large differences in trends in the models. CMAM, UMSLMCAT, UМУKCA-METO and CNRM seem to have trends that are larger ( $-10$  to  $-15$  hPa per century) than other models ( $-5$  hPa/century). Some of the difference in the trends may be due to the resolution of the models in the TTL. The multi-model mean is about  $-7$  hPa per century. This does not appear directly correlated with stratospheric metrics, such as changes in the strength of the BDC. Note that the TCPT and PTP mechanisms are different, as discussed in Section 7.4.2.

Tropical cold point temperature trends are illustrated for the REF-B1 case in Figure 7.6. Models do not show the cooling over the last 25 years seen in NCEP and NCEP2. However, an analysis of the distribution of the trends in space indicates coherent patterns of warming and cooling; in general the patterns represent alterations to the equatorial Kelvin wave and Rossby wave patterns induced by the change in strength of an equatorial heat source (Gill, 1980). The heat source variations are changes in convection. However, different models put these patterns in different locations in the tropics. The overall picture is one of cooling in some regions balancing warming, for little net trend. This indicates that TCPT patterns respond to changes in tropical deep convection. The confidence in analysis systems might be limited by the sparse input data used for constraining the analysis models in the tropics.

Tropical cold point temperature trends for the future (REF-B2) are illustrated in **Figure 7.35**. Most models show a slow increase in minimum temperature of  $0.5$ - $1.0$  K per century. Several models (ULAQ, UМУKCA-METO)

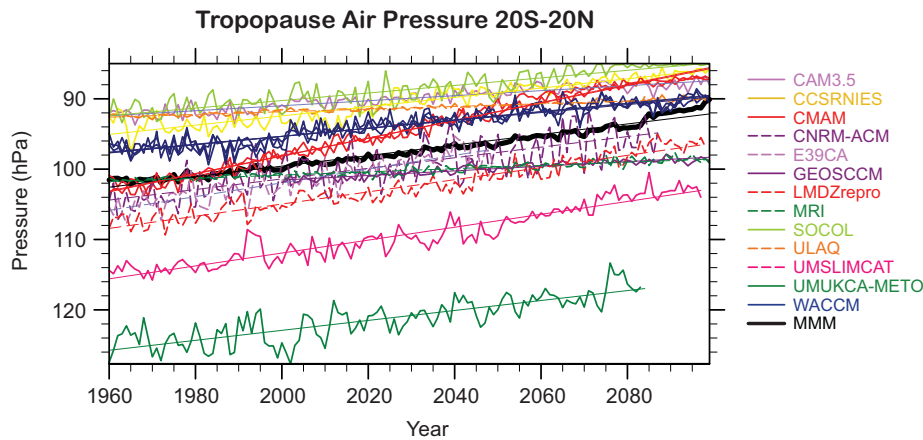


**Figure 7.34:** Lapse Rate Tropopause Pressure time series from 20°S-20°N for future REF-B2 scenarios. Thin lines are linear fits. Multi-model mean (MMM) is the thick black line.

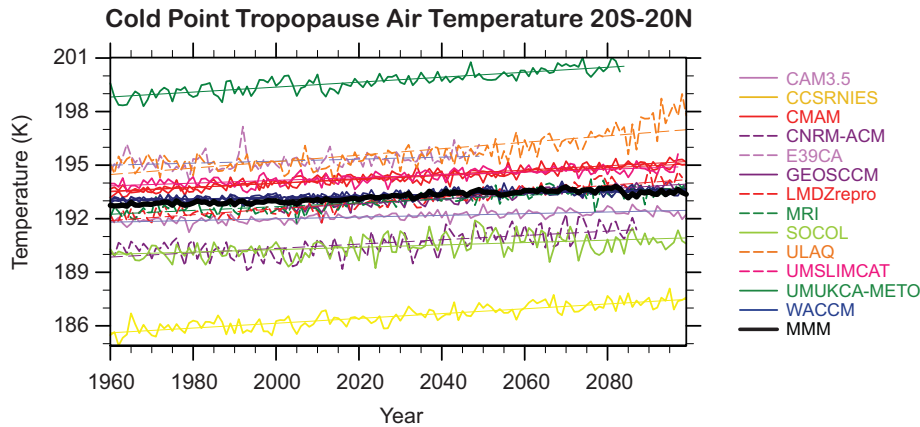


**Figure 7.35:** Cold Point Temperature time series from 20°S-20°N for future REF-B2 scenarios. Thin lines are linear fits. Multi-model mean (MMM) is the thick black line.

have larger trends. This is consistent with water vapour increases (see below).

There exist no consistent observations of water vapour trends over long periods of time. There are indications of long-term increases in water vapour from a variety of records (Kley *et al.*, 2000), and a significant increase in water vapour in the 1990s observed by HALOE, followed by a sharp, step-change decrease after 2000. The overall trend in HALOE H<sub>2</sub>O from 1992-2004 is negative (-0.05 ppmv yr<sup>-1</sup>) and significant at the 99% level. Almost all models also simulate a negative H<sub>2</sub>O trend over this period, with the multi-model mean -0.03 ppmv yr<sup>-1</sup> (but significant only at the 95% level). Recent changes in water vapour over the last decade or so are broadly consistent with changes in the tropical tropopause temperature (see Section 7.4.5 and Randel *et al.*, 2006).

Future changes in water vapour just above the CPT simulated in the models are illustrated in **Figure 7.36**. Also illustrated in Figure 7.36 are multiple ensembles from WACCM (3) and CMAM (2), confirming that their trends are different from each other, but consistent across the same

model ensemble members. Most model trends are from 0.5-1.0 ppmv per century, or nearly 25%. These trends are affected very little by methane oxidation at 80hPa, so that is unlikely to be a cause of these trends. This is consistent with the magnitude of TCPT trends, and temperature trends of 0.5-1 K per century at 193 K translate into 0.5-1 ppmv per century increase in water vapour. Models with larger temperature trends, or a stronger correlation between water vapour and temperature, appear to indicate larger increases in water vapour. This is true for example of ULAQ (large *T* increase) and MRI, CNRM-ACM and CCSRNIIES (strong dependence of H<sub>2</sub>O on *T*). UМУKCA-METO is off-scale in Figure 7.11 (no correlation between H<sub>2</sub>O and *T*) so it is not surprising there is no increase in water vapour. SOCOL indicates a large change in water vapour, without a large change in temperature. Note that the UМУKCA models (fixed water vapour) and GEOSCCM (output problem with water vapour) are not included in the analysis of REF-B2. Water vapour trends are also illustrated in **Figure 7.37**, indicating larger water vapour trends in the upper tropical troposphere at the convective outflow level near 200 hPa.



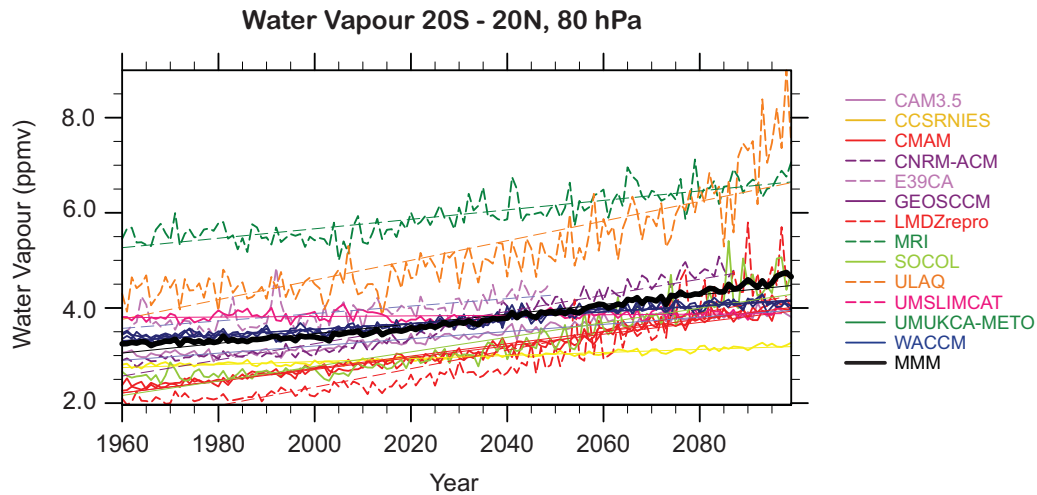


**Figure 7.36:** 80 hPa water vapour time series from 20°S-20°N for future REF-B2 scenarios. Thin lines are linear fits. Multi-model mean (MMM) is the thick black line.

Radiatively active tracers such as  $\text{H}_2\text{O}$  and  $\text{O}_3$  exhibit large gradients across the tropopause. The radiative response to changes in these tracers is therefore expected to be highly sensitive to the detailed structure of the trends of  $\text{H}_2\text{O}$  and  $\text{O}_3$  in the global UTLS. Generally, one expects the trends in absolute (*e.g.*, pressure) coordinates to be af-

ected by tropopause height trends. We will therefore show two sets of trends, in absolute coordinates as well as in tropopause-based coordinates to highlight the sensitivity of trends to the tropopause. Trends are calculated as above, based on the monthly zonal mean output with respect to the tropopause obtained from the T2Mz data.

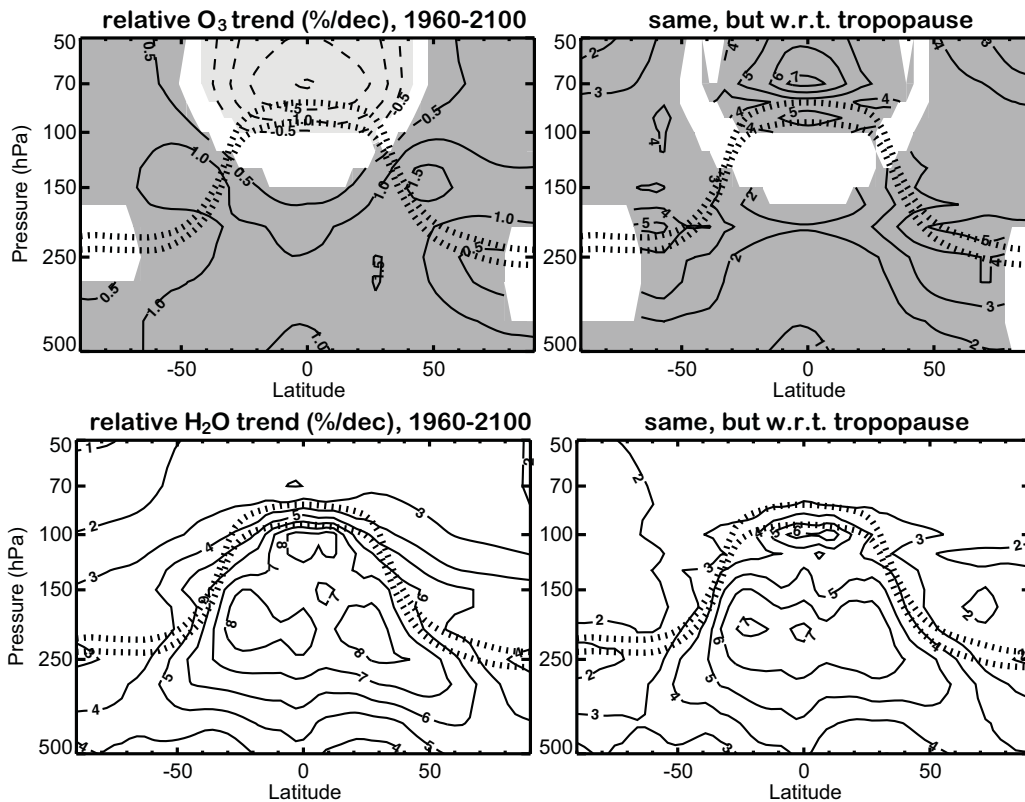


**Figure 7.37:** Trends in  $\text{O}_3$  (upper panels) and  $\text{H}_2\text{O}$  (lower panels) in pressure (left panels) and tropopause coordinates (right panels). Shading indicates the 95% significance level. For  $\text{H}_2\text{O}$ , the calculated trends are significant at the 95% level. Dotted lines in each panel denote the tropopause with the lower line corresponding to the reference period (1960-1980) and the upper line corresponding to the year 2100.

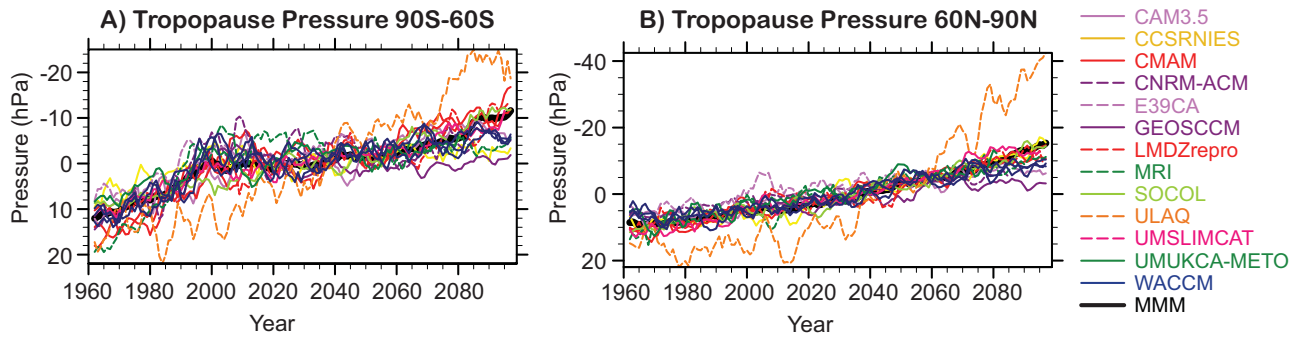


**Figure 7.38:** Northern and Southern Hemisphere extra-tropical tropopause pressure time series from 90°S-60°S (left panel) and 60°N-90°N (right panel) for future REF-B2 scenarios. Multi-model mean (MMM) is the thick black line.

Figure 7.37 shows the multi-model ensemble of annual mean trends of  $O_3$  (top) and  $H_2O$  (bottom) for the period 1960-2100 based on the 9 REF-B2 models with data from 1960-2100. Models included are: CAM3.5, CCSRNIES, CMAM, LMDZrepro, MRI, SOCOL, ULAQ, UMSLIMCAT, and WACCM. The left panels show trends in conventional (absolute) coordinates, whereas the right panels show trends in tropopause-based coordinates. The latter are obtained by first calculating the decadal shift in tropopause pressure followed by shifting the decadal changes of the respective field ( $O_3$  or  $H_2O$ ) to a reference tropopause pressure. The shift in the tropopause is shown on the panels (with the higher altitude tropopause corresponding to 2100). Here, the average over the period 1960-1980 is used as reference state.

$O_3$  trends are negative ( $-2\% \text{ dec}^{-1}$ ) in conventional coordinates in the tropical lower stratosphere. Decreasing  $O_3$  is consistent with a strengthening of the BDC. Moderate increases of around  $0.5\text{-}1.5\% \text{ dec}^{-1}$  are found throughout the upper troposphere and in the extra-tropical lower stratosphere. These results are consistent with Hegglin and Shepherd (2009) and Li *et al.* (2009) in the tropics and mid-latitudes, but differ in the SH polar regions. In tropopause-based coordinates however the trends are strongly positive above the tropopause in both the tropics and extra-tropics ( $4\text{-}5\% \text{ dec}^{-1}$ ). In the tropics the sign is reversed between conventional and tropopause based coordinates. Ozone decreases due to faster upwelling resulting from an enhanced BDC. Thus  $O_3$  decreases at any given pressure level. This may be a direct result of higher tropical SST (Deckert *et al.*, 2008). However, the gradient of ozone around the tropopause increases as the tropopause moves to higher altitudes, so relative to the tropopause,  $O_3$  increases. This trend is larger than the decrease at fixed altitude/pressure due to the strengthened BDC. In the extra-tropical lower stratosphere both contributions are positive (increasing BDC increases ozone), and are therefore amplified in tropopause-based coordinates.

$H_2O$  exhibits strong positive trends in the upper troposphere from a realistic upper troposphere (UT) base state.

The base state has high humidity in tropical convective outflow regions and low humidity in downwelling branches of the Hadley and Walker circulations. In the tropical UT maximum trends of  $\sim 9\% \text{ dec}^{-1}$  are found around 200 hPa. These trends are likely due to increases in temperature associated with anthropogenic greenhouse gas induced warming. In conventional coordinates one also finds rather strong positive changes throughout the extra-tropical LMS (between  $3\text{-}5\% \text{ dec}^{-1}$ ). However, these changes in the LMS are in part caused by the upward tropopause trend: in tropopause-based coordinates the strong positive trend in  $H_2O$  is largely confined to the upper troposphere whereas stratospheric  $H_2O$  shows moderate changes of around  $2\% \text{ dec}^{-1}$  throughout the global lower stratosphere.

## 7.6.2 Extra-tropical Tropopause Trends

Trends in the extra-tropical tropopause pressure for future scenarios are shown over the southern (Figure 7.38, left panel) and northern (in Figure 7.38, right panel) polar caps for REF-B2 simulations from 1960-2100. As in the tropics, tropopause pressure is expected to decrease  $\sim 20$  hPa per century in both hemispheres. The century scale trends are not quantitatively different between hemispheres over the 21<sup>st</sup> century (about 30hPa for the century). However, it is clear that there are differences in the timing of PTP trends between the hemispheres in Figure 7.38: the trends in the SH polar regions are not steady, but are larger from 1960-2000 and lower (flatter) from 2000-2050. As noted by Son *et al.* (2009) in comparing IPCC AR5 models with and without ozone depletion, these differences are due to the effects of ozone depletion (1960-2000) and recovery (2000-2050). Note that the overall trend over 140 years is nearly the same in both hemispheres.

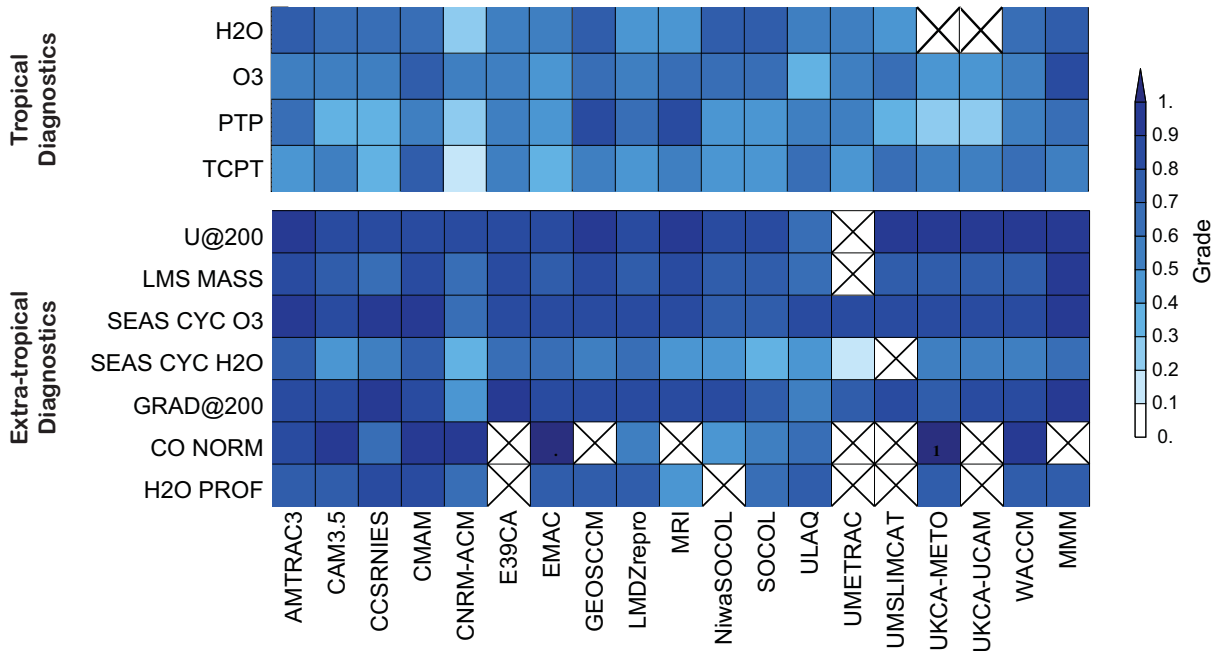


Figure 7.39: Quantitative metrics summary for tropics (upper) and extra-tropics (lower). MMM indicates the multi-model mean.

## 7.7 Summary and Conclusions

### 7.7.1 Quantitative metrics

Figure 7.39 shows the grading obtained for the key diagnostics presented in this chapter, and provides an overall assessment of how well the models performed in the UTLS. The upper panel depicts the grades for the tropical diagnostics, the lower panel grades for the extra-tropical diagnostics as discussed in the specific sections of this chapter, and in a more qualitative way in Section 7.7.2. The grading methodology does not necessarily define an ‘acceptable’ grade. The different methods may yield different scores. The discussion defines what is an acceptable grade based on the uncertainty in the observations, often using the spread of multiple observation data sets. For some metrics this spread is narrow (*e.g.*, U@200 in Figure 7.17, or PTP in Figure 7.6) while for others there is large uncertainty (*e.g.*, TCPT in Figure 7.6). In general tropical grades > 0.5 are considered acceptable, and grades > 0.6 in the extra-tropics are considered acceptable. This difference might reflect the larger database of observations in the extra-tropics, or simply the choice of diagnostics.

### 7.7.2 Qualitative Diagnostics Discussion

#### Tropical Diagnostics

**Tropical Cold Point Temperatures:** The annual cycle of tropical cold point temperatures is well reproduced by most models, as is the amplitude of the annual cycle. There remain some significant biases between models, with the UMETRAC models having warm temperatures, and CNRM-ACM and CCSRNIES having cold temperatures. CNRM-ACM has too large a response to volcanic perturbations, and SOCOL and NiwaSOCOL are also high in this regard. Most models do not have strong trends in CPT over the historical period. Analysis systems also disagree over the satellite period.

**Tropical Tropopause Pressure:** Again, most models get the absolute value of tropical tropopause pressure to the right level (about 100 hPa). The UMETRAC models are below this (120hPa), which is likely the reason for their tropopause temperature warm bias. This may be a function of a slightly different vertical structure in the tropopause region. CNRM-ACM and CCSRNIES are slightly higher, as are the SOCOL models, ULAQ and EMAC. Most models do get consistent trends in tropopause pressure. Again, CNRM-ACM has too large a response to volcanic events. In general model variance is higher than observed inter-annual variance of tropopause pressure. Trends are consistent between models and analysis systems and variability is

highly correlated.

**Tropical Ozone:** 100hPa ozone is generally well reproduced. Most models have less NH summer-time tropical ozone than observations at 100hPa. CNRM-ACM and UMSLIMCAT have the wrong annual cycle. The UMUKCA models are higher throughout the year, as is ULAQ.

**Tropical Water Vapour:** E39CA, CNRM-ACM and MRI are too wet at 80 hPa, and several models (LMDZrepro and EMAC) are too dry, with water vapour below 3 ppmv throughout the year. The annual cycle is not as well reproduced, with many models shifted 1-2 months (or more) early relative to HALOE observations. With respect to the CPT and water vapour correlation, there are 3 models (CCSRNIES, CNRM-ACM and UMETRAC) that are clear outliers: There appears to be more water vapour than the temperatures would permit if transport were occurring similarly to observations. UMUKCA-METO is off-scale due to a very warm CPT.

**Equatorial Wave Activity:** There are huge differences between the analysis systems for the wave diagnostics, and the models examined (CCSRNIES, MRI, CMAM, WACCM) span this range. CCSRNIES appears to have lower wave activity than any of the analysis systems, which are on the low end of observed. Several models have higher ISO activity than the analysis systems (WACCM, CMAM), which is likely similar to observations.

### *Extra-tropical Diagnostics*

**Seasonal zonal-mean zonal wind:** Most models perform well in this diagnostic as well, except ULAQ. This might be due to an insufficient horizontal and vertical resolution in this model and its geostrophic dynamical core.

**Seasonal cycle in LMS mass:** Most models represent well the phase and amplitude of the seasonal cycle in LMS mass, but this is not so for the annual mean value in LMS mass. Overall scores are generally higher for the NH than for the SH. Models scoring high are AMTRAC3, CMAM, E39CA, and GEOSCCM. Models which perform the least well are CCSRNIES, CNRM-ACM, and ULAQ. The diagnostic yields insight into the strength and seasonality of the BDC which will affect stratosphere-troposphere exchange and therefore both UT and LS tracer distributions.

**Seasonal cycles in O<sub>3</sub>, HNO<sub>3</sub>, and H<sub>2</sub>O at 100 and 200 hPa:** Most models perform reasonably well for O<sub>3</sub> in the NH, however the amplitude is generally a little too high at 100 hPa and too low at 200 hPa. The latter finding indicates

that the models exhibit too much transport across the extra-tropical tropopause (in particular CNRM-ACM and the SOCOL-based models). The spread in skill in representing H<sub>2</sub>O is larger than that in O<sub>3</sub>, with models doing better at 100 hPa than at 200 hPa. At 200 hPa, strong tropospheric influence causes too large amplitudes. Note, that there exist some observational uncertainties in H<sub>2</sub>O at the 200 hPa level. Better measurements are needed to gain more confidence in this diagnostic. The spread in skill to represent HNO<sub>3</sub> in the SH at 200 hPa is even larger. UMSLIMCAT shows the best representation of HNO<sub>3</sub>, but most other models have a low correlation with observations and under-estimate the annual cycle amplitude.

**Sharpness of meridional gradients in O<sub>3</sub>:** The results of this metric are largely consistent with the one from the seasonal cycle in O<sub>3</sub> on 200 hPa. Models perform generally well, with some models overestimating (UMSLIMCAT and UMUKCA-METO), and some models (CNRM-ACM and ULAQ) under-estimating the maximum in the gradient.

**Normalised vertical profiles of CO in potential temperature relative to the tropopause height:** Most models perform reasonably well in this diagnostic and are able to separate between transport across the local tropopause in the extra-tropics and processes involving other time scales and source regions, except LMDZrepro, SOCOL, and NiwaSOCOL.

**Vertical profiles of H<sub>2</sub>O, CO, and O<sub>3</sub> in tropopause coordinates:** The models show some difficulties simulating the seasonal mean vertical profiles of the different tracers. Models perform best for H<sub>2</sub>O, possibly because it is least affected by chemistry. CO is represented very poorly, clearly because most models do not include tropospheric chemistry. However, even models including tropospheric chemistry perform rather poorly in this diagnostic (CAM3.5, EMAC, and ULAQ). The lack of a more sophisticated tropospheric chemistry also causes poor UT O<sub>3</sub> distributions.

**Depth of the extra-tropical tropopause transition layer (ExTL):** The models simulated an ExTL that is deeper than observed, and shifted above the thermal tropopause. This might be due to the models' limited vertical resolution as indicated also by the findings of the study by Bell and Geller (2008). CMAM's representation of the ExTL is closest to the observations, which is noteworthy since CMAM has a relatively low horizontal resolution compared to other models. The ratio between vertical and horizontal resolution might matter more. Models that show the most difficulties in reproducing the ExTL are SOCOL, UMUKCA-METO, and CNRM-ACM, which might be

due to too diffusive transport schemes. For the ExTL (as well as for the TIL), it seems difficult to find a model measure that can be usefully compared against observations due to the mismatch between the scale of observations and the scale resolved by models.

### 7.7.3 Qualitative Model Discussion

**Summary:** In the tropics there are 4 models that score at least 0.5 on all metrics and have consistent transport and trends: CMAM, GEOSCCM, E39CA and WACCM. In the extra-tropics, models that score consistently higher than 0.6 are AMTRAC3, CMAM, EMAC, E39C and UMSLIMCAT. Note however, that the latter two are validated only on a subset of the diagnostics.

**AMTRAC3** performs acceptably well on the tropical metrics examined, although slightly lower on TCPT. Summer tropical ozone is a bit low, as with other models. Water vapour annual cycle is shifted a month or two early. In the extra-tropics, AMTRAC3 is one of the better performing models, with scores mostly equal or higher than 0.6.

**CAM3.5** shows generally good performance on tropical metrics. The tropical tropopause is slightly high and cold, but the tropical water vapour annual cycle is one of the best despite this. CAM3.5 also performs relatively well on extra-tropical metrics, with the exception of the metrics for the seasonal cycle in  $H_2O$ , which shows a too large (small) amplitude at 200 (100) hPa, respectively.

**CCSRNIES** has a tropical tropopause pressure is high and tropopause is cold, yet water vapour is reasonable, implying a different transport than observed. CCSRNIES scores lower on some of the tropical metrics as a result. Tropical 100 hPa ozone is relatively good. In the extra-tropics, CCSRNIES performs relatively well, with the exception of exhibiting a too small mass in both the NH and the SH LMS, and a strong shift in the seasonal cycle of  $H_2O$  at 100 hPa. The normalised vertical profiles of CO indicate a good separation from the extra-tropical troposphere, but too large transport from the tropical tropopause.

**CMAM:** Tropical tropopause temperature is well reproduced. CMAM has all tropical metrics over 0.5. However, there are very large trends in tropical tropopause pressure for the REF-B2 simulations. In the extra-tropics, CMAM is one of the best performing models, with scores mostly above 0.6, and it also shows the best representation of the ExTL. CMAM performs less well for  $HNO_3$  in the SH.

**CNRM-ACM** exhibits some significant problems with tropical transport. The tropopause is cold and high, with

more water vapour than would be implied by the temperatures. The tropopause response to volcanic events is very large, and the secular trend is also larger than other models due to problems with volcanic aerosol heating. Future trends are also relatively large in water vapour compared to other models, and not consistent with temperatures. Also in the extra-tropics, CNRM-ACM shows major deficiencies in both the dynamical and the transport and mixing diagnostics. Extra-tropical tropopause pressure is too low, which is also reflected in too small values for the LMS mass in both hemispheres. These deficiencies go along with too low  $HNO_3$  in the SH, and too high  $H_2O$  in the NH at 200 hPa.

**E39CA** performs well on tropical diagnostics with a score of 0.5 on all grades. The tropical tropopause pressure variability is larger than observed, and tropical ozone is lower than observed. In the extra-tropics, E39CA in one of the best scoring models, however some critical diagnostics are missing. E39CA got only one low score of 0.5 for the amplitude in the seasonal cycle of  $H_2O$  in the NH at 200 hPa, which is too large.

**EMAC:** The tropical tropopause is colder and higher, resulting in less water vapour in the stratosphere than observed. Transport appears to be correct, though without much of an annual cycle. The seasonal cycle in ozone at 100 hPa is relatively well represented. In the extra-tropics EMAC performs relatively well, especially for the metrics based on the mean  $O_3$  values in the UT and LS, the metric for CO in  $d\theta/dz$ , and the latitudinal  $O_3$  gradient.

**GEOSCCM** tropical metrics are good, with generally all at 0.5 or higher. The tropical tropopause is slightly colder than observed, but with reasonable water vapour just above the tropical tropopause. Water vapour cannot be analysed for the REF-B2 run in the lower stratosphere, due to problems with the REF-B2 run. In the extra-tropics GEOSCCM is one of the better performing models, however, the amplitude in the NH  $H_2O$  seasonal cycle at 200 hPa of the REF-B1 run is too large indicating too large tropospheric influence.

**LMDZrepro** exhibits relatively low temperatures and tropical water vapour. The transport and condensation processes appear to be reasonable, but water vapour is low. Ozone is low at 100hPa as well. LMDZrepro performs reasonably well in the extra-tropics, with reasonable seasonal cycle and meridional gradient in  $O_3$  at 200 hPa, while the model achieves lower scores in the metrics testing tropospheric influence such as normalised CO in  $d\theta/dz$ , the ExTL depth, or the seasonal cycle in  $H_2O$  at 200 hPa.

**MRI:** The tropical tropopause temperatures are reasona-

ble, but water vapour is higher than the temperatures would imply due to the presence of ice supersaturation. Ozone is also higher than observations at 100hPa. MRI performs reasonably well in the extra-tropics, with intermediate to high scores for the dynamical metrics, but relatively low scores for transport and mixing metrics, in particular those testing  $H_2O$ .

**NiwaSOCOL:** The annual cycle of water vapour in the tropics is shifted slightly. The annual cycle of ozone at 100 hPa is very flat (almost no annual cycle), with too much ozone in NH winter. The tropical tropopause is slightly higher than observations (90 hPa), one level up, though the temperatures are reasonable. NiwaSOCOL is one of the lowest performing models in the extra-tropics. Low scores are obtained in the metrics testing the vertical structure of the tracers, indicating too large tropospheric influence. This is also confirmed by the too large amplitude in the seasonal cycle of  $H_2O$  and  $O_3$  on the 200 hPa level. NiwaSOCOL it scores reasonably well in the dynamical metrics.

**SOCOL** shows very similar performance to NiwaSOCOL quantitatively and qualitatively in the tropics. It has very large water vapour trends in REF-B2 scenarios, likely due to large trends in tropical tropopause pressure in the 21<sup>st</sup> century. In the extra-tropics, SOCOL shows similar performance to NiwaSOCOL. The relatively poor performance of NiwaSOCOL and SOCOL in UTLS transport and mixing may stem from the semi-Lagrangian transport scheme, which is known to be overly diffusive. The rather low resolution may enhance the problems due to the transport scheme applied.

**ULAQ** performs acceptably well on tropical metrics except for ozone. Tropical tropopause variability is large. The 100 hPa Ozone annual cycle is large and ozone concentrations are high. Future trends indicate large tropical tropopause temperature and water vapour towards the end of the 21<sup>st</sup> century. ULAQ is the lowest performing model in the extra-tropics, with a major problem in simulating the latitudinal structure of the zonal-mean zonal wind at 200 hPa. This deficiency is potentially the reason for a very low score of 0.5 for the meridional gradient in  $O_3$ . Also, the model scores low in reproducing the seasonal cycle in the LMS mass in the SH. The models very low resolution and the use of a geostrophic dynamical core may be the reason for this behaviour.

**UMSLIMCAT:** The tropical tropopause pressure is slightly lower in altitude than other models, but tropical tropopause temperatures are reasonable. The annual cycle of tropical water vapour at 80 hPa and ozone at 100 hPa does not have the same phase over the annual cycle as observed, though tropopause temperatures do have the

correct phase. This reduces confidence in TTL transport of water vapour and ozone, though minimum temperature and water vapour correlations are reasonable. In the extra-tropics, UMSLIMCAT is among the better performing models. It achieves the highest score in reproducing the seasonal cycle of  $HNO_3$  in the SH and also of  $O_3$  in the NH at 200 hPa, pointing towards a good representation of chemistry in the model.

**UMUKCA-METO** has low (120 hPa) tropopause pressure and hence warm CPTs in the tropics. In addition, water vapour has no annual cycle above the cold point, and is low. Tropical water vapour trends in the REF-B2 run seem inconsistent with tropopause temperature trends. Thus there is no correlation between temperature and water vapour. This might be due to errors in processing or the run. In the extra-tropics, UMUKCA-METO is one of the reasonably performing models. Notable deficiencies are a very high LMS mass in both hemispheres, and in the representation of the vertical structure of  $O_3$  and  $H_2O$ , as well as the ExTL depth. The latter is surprising, since the model seems to score highest in the diagnostic testing the CO in  $d\theta/dz$ , pointing toward a reasonable stratosphere-troposphere exchange.

**UMUKCA-UCAM:** In the tropics, UMUKCA-UCAM is similar in performance to UMUKCA-METO. UMUKCA-UCAM has excessive tropical ozone at 100 hPa. Several diagnostics were not performed due to incorrectly formatted data. In the extra-tropics UMUKCA-UCAM is one of the better performing models, although this might be due to the fact that it is missing some diagnostics. As UMUKCA-METO, it shows too high LMS mass in both hemispheres.

**WACCM** generally has all tropical metrics at or above 0.5. The annual cycle of water vapour is 1-2 months early, but well correlated with temperatures. The 100 hPa ozone annual cycle is a bit flat (less ozone in NH summer). It is one of the best models for CPT. WACCM performs reasonably well in the extra-tropics. The overall model performance is decreased due to a relatively low skill in reproducing the amplitude and phase of the seasonal cycle in  $H_2O$  at both 100 and 200 hPa in the NH.

#### 7.7.4 Overall Summary

In summary, in the tropical UTLS the models are able to reproduce the climatology of tropopause temperature, pressure, water vapour and ozone, with some common deficiencies. This statement includes both the annual cycle, and interannual anomalies. Interannual anomalies of tropopause pressure are reproduced well. The annual cycle of water vapour in the lower stratosphere is shifted early

by a month or more in many models. This indicates likely problems with transport, since tropical cold point temperatures appear to have the correct annual cycle. There is still a large spread in tropical CPTs, but this is smaller than in the CCMVal-1 models. This spread yields a significant spread in stratospheric water vapour, but the transport appears consistent in that models with higher water vapour have higher CPTs, with a few exceptions. Lagrangian cold points can differ substantially from the Eulerian cold point, and biases between models and reanalyses differ. Tropical wave variability is reproduced in the few models examined, but there is also a wide spread in reanalyses. The TIL is found in the tropics in models, but differs from observations. This appears to be partially a function of coarse vertical resolution.

The overall model performance in the extra-tropical UTLS can be summarized as follows: The models score better in metrics testing dynamics (zonal-mean zonal wind and LMS mass) rather than transport and mixing (seasonal cycle of  $O_3$  and  $H_2O$ , meridional gradient in  $O_3$ , normalised and absolute vertical profiles), and better in metrics focusing on the LS (seasonal cycle of  $O_3$  at 100 hPa, meridional gradient in  $O_3$ ) rather than the transition between the troposphere and the stratosphere (seasonal cycle of  $O_3$  and  $H_2O$  at 200 hPa, and normalised and absolute vertical profiles). This may be simply due to the length-scales of the observed chemical and dynamical structures, which are much smaller in the tropopause region than in the stratosphere. In particular the fine-scale structure of the TIL and ExTL cannot be fully resolved due to the models' limited vertical resolution. The results, however, improve substantially if the models are compared with coarser resolution (or degraded) observations. The multi-model mean generally scores higher than any individual model, except for the seasonal cycle of  $H_2O$ . In fact, most models seem to score lower in this latter metric, which is likely due to the uncertainty in the observations. The fact that the multi-model mean scores so well on all diagnostics suggests that there are no significant missing processes in the models, although particular models may have significant deficiencies in the representation of the processes.

These results allow a better understanding of model trends, and raise our confidence in the trends. Decreasing observed tropopause pressure trends are highly correlated with observations, especially in the tropics. Trends in extra-tropical tropopause pressure differ between hemispheres due to ozone depletion and recovery. Observed UTLS trends in tropical tropopause temperature are not consistent between reanalyses. Some models show slight decreases in tropopause temperature (observed in some reanalyses), an encouraging sign. These results provide more confidence in future trends. Trends in multiple ensemble members of individual models are similar to each other. CCMVal-2 models predict decreases in tropopause

pressure in the tropics and extra-tropics, with different extra-tropical behaviour between hemispheres due to ozone recovery. Tropical tropopause temperatures are expected to increase slightly (1 K per century) with a corresponding consistent increase of 0.5ppmv (about 10-20%) in lower stratospheric water vapour. The magnitude of these trends is consistent across the high performing models.

## References

- Anthes, R. A., R. A. Anthes, P. A. Bernhardt, Y. Chen, L. Cucurull, K. F. Dymond, D. Ector, S. B. Healy, S.-P. Ho, D. C. Hunt, Y.-H. Kuo, H. Liu, K. Manning, C. McCormick, T. K. Meehan, W. J. Randel, C. Rocken, W. S. Schreiner, S. V. Sokolovskiy, S. Syndergaard, D. C. Thompson, K. E. Trenberth, T.-K. Wee, N. L. Yen, and Z. Zeng, 2008. The COSMIC/FORMOSAT-3 mission: Early results. *Bull. Amer. Meteor. Soc.*, **89**, 313-333.
- Appenzeller, C., J. R. Holton, K. H. Rosenlof, 1996. Seasonal variation of mass transport across the tropopause, *J. Geophys. Res.*, **101**, 15071-15078, 10.1029/96JD00821.
- Bell, S. W., and M. A. Geller, 2008. Tropopause inversion layer: Seasonal and latitudinal variations and representation in standard radiosonde data and global models, *J. Geophys. Res.*, **113**, doi:10.1029/2007JD009022.
- Bernath, P. F., C. T. McElroy, M. C. Abrams, C. D. Boone, M. Butler, C. Camy-Peyret, M. Carleer, C. Clerbaux, P.-F. Coheur, R. Colin, P. DeCola, M. DeMazière, J. R. Drummond, D. Dufour, W. F. J. Evans, H. Fast, D. Fussen, K. Gilbert, D. E. Jennings, E. J. Llewellyn, R. P. Lowe, E. Mahieu, J. C. McConnell, M. McHugh, S. D. McLeod, R. Michaud, C. Midwinter, R. Nassar, F. Nichitiu, C. Nowlan, C. P. Rinsland, Y. J. Rochon, N. Rowlands, K. Semeniuk, P. Simon, R. Skelton, J. J. Sloan, M.-A. Soucy, K. Strong, P. Tremblay, D. Turnbull, K. A. Walker, I. Walkty, D. A. Wardle, V. Wehrle, R. Zander, and J. Zou, (2005), Atmospheric Chemistry Experiment (ACE): Mission overview, *Geophys. Res. Lett.*, **32**, doi:10.1029/2005GL022386.
- Berthet G., J. G. Esler, P. H. Haynes, 2007. A Lagrangian perspective of the tropopause and the ventilation of the lowermost stratosphere, *J. Geophys. Res.*, **112**, doi:10.1029/2006JD008295.

- Birner, T., A. Dornbrack, and U. Schumann, 2002: How sharp is the tropopause at midlatitudes? *Geophys. Res. Lett.*, **29**, doi:10.1029/2002GL015142.
- Birner, T., D. Sankey, T. G. Shepherd, 2006. The tropopause inversion layer in models and analyses, *Geophys. Res. Lett.*, **33**, doi:10.1029/2006GL026549.
- Birner, T., 2006. Fine-scale structure of the extra-tropical tropopause region, *J. Geophys. Res.*, **111**, doi:10.1029/2005JD006301.
- Bönisch, H., Engel, A., Curtius, J., Birner, Th., and Hoor, P., 2009. Quantifying transport into the lowermost stratosphere using simultaneous in-situ measurements of SF6 and CO2, *Atmos. Chem. Phys.*, **9**, 5905-5919.
- Bonazzola, M., and P. H. Haynes, 2004. A trajectory-based study of the tropopause region, *J. Geophys. Res.*, **109**, doi:10.1029/2003JD004356.
- Boone, C. D., R. Nassar, K. A. Walker, Y. Rochon, S. D. McLeod, C. P. Rinsland, and P. F. Bernath, 2005. Retrievals for the Atmospheric Chemistry Experiment Fourier Transform Spectrometer, *Appl. Opt.*, **44**, 7218–7231.
- Bregman, A., J. Lelieveld, M. M. P. van den Broek, P. C. Siegmund, H. Fischer, and O. Bujok, 2000. N2O and O3 relationship in the lowermost stratosphere: A diagnostic for mixing processes as represented by a three-dimensional chemistry-transport model, *J. Geophys. Res.*, **105**, 17,279–17,290.
- Brewer, A. W., 1949. Evidence for a world circulation provided by the measurements of helium and water vapour distribution in the stratosphere, *Quart. J. Roy. Meteorol. Soc.*, **75**, 351–363.
- Brunner, D., J. Staehelin, H. L. Rogers, M. O. Köhler, J. A. Pyle, D. Hauglustaine, L. Jourdain, T. K. Bernsten, M. Gauss, I. S. A. Isaksen, E. Meijer, P. van Velthoven, G. Pitari, E. Mancini, G. Grewe, and R. Sausen, 2003. An evaluation of the performance of chemistry transport models by comparison with scientific aircraft observations. Part 1: Concepts and overall model performance., *Atmos. Chem. Phys.*, **3**, 1609–1631.
- Brunner, D., J. Staehelin, H. L. Rogers, M. O. Köhler, J. A. Pyle, D. A. Hauglustaine, L. Jourdain, T. K. Bernsten, M. Gauss, I. S. A. Isaksen, E. Meijer, P. van Velthoven, G. Pitari, E. Mancini, V. Grewe, and R. Sausen, 2005. An evaluation of the performance of chemistry transport models - Part 2: Detailed comparison with two selected campaigns, *Atmos. Chem. Phys.*, **5**, 107-129.
- Clerbaux, C., M. George, S. Turquety, K. A. Walker, B. Barret, P. Bernath, C. Boone, T. Borsdorff, J. P. Cammas, V. Catoire, M. Coffey, P.-F. Coheur, M. Deeter, M. De Mazière, J. Drummond, P. Duchatelet, E. Dupuy, R. de Zafra, F. Eddounia, D. P. Edwards, L. Emmons, B. Funke, J. Gille, D. W. T. Griffith, J. Hannigan, F. Hase, M. Höpfner, N. Jones, A. Kagawa, Y. Kasai, I. Kramer, E. Le Flochmoën, N. J. Livesey, M. López-Puertas, M. Luo, E. Mahieu, D. Murtagh, P. Nédélec, A. Pazmino, H. Pumphrey, P. Ricaud, C. P. Rinsland, C. Robert, M. Schneider, C. Senten, G. Stiller, A. Strandberg, K. Strong, R. Sussmann, V. Thouret, J. Urban, and A. Wiacek, 2008. CO measurements from the ACE-FTS satellite instrument: Data analysis and validation using ground-based, airborne and spaceborne observations, *Atmos. Chem. Phys.*, **8**, 2569–2594.
- Considine, D. B., M. Natarajan, T. D. Fairlie, G. S. Lingenfelter, R. B. Pierce, L. Froidevaux, and A. Lambert, 2008. Noncoincident validation of Aura MLS observations using the Langley Research Center Lagrangian chemistry and transport model, *J. Geophys. Res.*, **113**, doi:10.1029/2007JD008770.
- Corti, T., B. P. Luo, Q. Fu, H. Vömel, and T. Peter, 2006. The impact of cirrus clouds on tropical troposphere to stratosphere transport, *Atmos. Chem. Phys.*, **6**, 1725–1747.
- Deckert, R., and M. Dameris, 2008. Higher tropical ssts strengthen the tropical upwelling via deep convection, *Geophys. Res. Lett.*, **35**, doi:10.1029/2008GL033719.
- Douglass, A. R., M. J. Prather, T. M. Hall, S. E. Strahan, P. J. Rasch, L. C. Sparling, L. Coy, and J. M. Rodriguez, 1999. Choosing meteorological input for the global modeling initiative assessment of high-speed aircraft, *J. Geophys. Res.*, **104**, 27 545–27 564.
- Dupuy, E., K. A. Walker, J. Kar, C. D. Boone, C. T. McElroy, P. F. Bernath, J. R. Drummond, R. Skelton, S. D. McLeod, R. C. Hughes, C. R. Nowlan, D. G. Dufour, J. Zou, F. Nichitiu, K. Strong, P. Baron, R. M. Bevilacqua, T. Blumenstock, G. E. Bodeker, T. Borsdorff, A. E. Bourassa, H. Bovensmann, I. S. Boyd, A. Bracher, C. Brogniez, J. P. Burrows, V. Catoire, S. Ceccherini, S. Chabrillat, T. Christensen, M. T.



- Coffey, U. Cortesi, J. Davies, C. De Clercq, D. A. Degenstein, M. De Mazière, P. Demoulin, J. Dodion, B. Firanski, H. Fischer, G. Forbes, L. Froidevaux, D. Fussen, P. Gerard, S. Godin-Beekmann, F. Goutail, J. Granville, D. Griffith, C. S. Haley, J. W. Hannigan, M. Höpfner, J. J. Jin, A. Jones, N. B. Jones, K. Jucks, A. Kagawa, Y. Kasai, T. E. Kerzenmacher, A. Kleinböhl, A. R. Klekociuk, I. Kramer, H. Küllmann, J. Kuttippurath, E. Kyrölä, J.-C. Lambert, N. J. Livesey, E. J. Llewellyn, N. D. Lloyd, E. Mahieu, G. L. Manney, B. T. Marshall, J. C. McConnell, M. P. McCormick, I. S. McDermid, M. McHugh, C. A. McLinden, J. Mellqvist, K. Mizutani, Y. Murayama, D. P. Murtagh, H. Oelhaf, A. Parrish, S. V. Petelina, C. Piccolo, J.-P. Pommereau, C. E. Randall, C. Robert, C. Roth, M. Schneider, C. Senten, T. Steck, A. Strandberg, K. B. Strawbridge, R. Sussmann, D. P. J. Swart, D. W. Tarasick, J. R. Taylor, C. Tétard, L. W. Thomason, A. M. Thompson, M. B. Tully, J. Urban, F. Vanhellemont, C. Vigouroux, T. von Clarmann, P. von der Gathen, C. von Savigny, J. W. Waters, J. C. Witte, M. Wolff, and J. M. Zawodny, 2009. Validation of ozone measurements from the Atmospheric Chemistry Experiment (ACE), *Atmos. Chem. Phys.*, **9**, 287-343.
- Engel, A., H. Bönisch, D. Brunner, H. Fischer, H. Franke, G. Günther, C. Gurk, M. Hegglin, P. Hoor, R. Königstedt, M. Krebsbach, R. Maser, U. Parchatka, T. Peter, D. Schell, C. Schiller, U. Schmidt, N. Spelten, T. Szabo, U. Weers, H. Wernli, T. Wetter, and V. Wirth, 2006. Highly resolved observations of trace gases in the lowermost stratosphere and upper troposphere from the SPURT project: An overview, *Atmos. Chem. Phys.*, **6**, 283–301.
- Eyring, V., N. Butchart, D. W. Waugh, H. Akiyoshi, J. Austin, S. Bekki, G. E. Bodeker, B. A. Boville, C. Brühl, M. P. Chipperfield, E. Cordero, M. Dameris, M. Deushi, V. E. Fioletov, S. M. Frith, R. R. Garcia, A. Gettelman, M. A. Giorgetta, V. Grewe, L. Jourdain, D. E. Kinnison, E. Mancini, E. Manzini, M. Marchand, D. R. Marsh, T. Nagashima, P. A. Newman, J. E. Nielsen, S. Pawson, G. Pitari, D. A. Plummer, E. Rozanov, M. Schraner, T. G. Shepherd, K. Shibata, R. S. Stolarski, H. Struthers, W. Tian, and M. Yoshiki, 2006. Assessment of temperature, trace species, and ozone in chemistry-climate model simulations of the recent past, *J. Geophys. Res.*, **111**, doi:10.1029/2006JD007327.
- Fischer, H., M. Birk, C. Blom, B. Carli, M. Carlotti, T. von Clarmann, L. Delbouille, A. Dudhia, D. Ehhalt, M. Endemann, J. M. Flaud, R. Gessner, A. Kleinert, R. Koopman, J. Langen, M. López-Puertas, P. Mosner, H. Nett, H. Oelhaf, G. Perron, J. Remedios, M. Rindolfi, G. Stiller, and R. Zander, 2008. MIPAS: an instrument for atmospheric and climate research, *Atmos. Chem. Phys.*, **8**, 2151-2188.
- Flocke, F., R. L. Herman, R. J. Salawitch, E. Atlas, C. R. Webster, S. M. Schauffler, R. A. Lueb, R. D. May, E. J. Moyer, K. H. Rosenlof, D. C. Scott, D. R. Blake, and T. P. Bui, 1999. An examination of chemistry and transport processes in the tropical lower stratosphere using observations of long-lived and short-lived compounds obtained during STRAT and POLARIS, *J. Geophys. Res.*, **104**, 26,625–26,642.
- Fueglistaler, S., H. Wernli and T. Peter, 2004. Tropical troposphere-to-stratosphere transport inferred from trajectory calculations, *J. Geophys. Res.*, **109**, doi:10.1029/2003JD004069.
- Fueglistaler, S., and P. H. Haynes, 2005. Control of interannual and longer-term variability of stratospheric water vapor, *J. Geophys. Res.*, **110**, doi:10.1029/2005JD006019.
- Fueglistaler S., A. E. Dessler, T. J. Dunkerton, I. Folkins, Q. Fu, P. W. Mote, 2009. Tropical tropopause layer, *Rev. Geophys.*, **47**, doi:10.1029/2008RG000267.
- Fujiwara, M., and M. Takahashi, 2001. Role of the equatorial Kelvin wave in stratosphere-troposphere exchange in a general circulation model, *J. Geophys. Res.*, **106**, 22,763–22,780.
- Fujiwara, M., S. Iwasaki, A. Shimizu, Y. Inai, M. Shiotani, F. Hasebe, I. Matsui, N. Sugimoto, H. Okamoto, N. Nishi, A. Hamada, T. Sakazaki, and K. Yoneyama, 2009. Cirrus observations in the tropical tropopause layer over the western Pacific, *J. Geophys. Res.*, **114**, doi:10.1029/2008JD011040.
- Gill, A. E., 1980. Some simple solutions for heat-induced tropical circulation, *Quart. J. Roy. Meteorol. Soc.*, **106**, 447–462.
- Gettelman, A. and P. M. F. Forster, 2002. A climatology of the tropical tropopause layer. *J. Met. Soc. Japan*, **80**, 911-924.
- Gettelman, A., P. M. F. Forster, M. Fujiwara, Q. Fu, H.

- Vomel, L. K., Gohar, C., Johanson and M. Ammerman, 2004. The Radiation Balance of the Tropical Tropopause Layer, *J. Geophys. Res.*, **109**, doi:10.1029/2003JD004190.
- Gottelman, A., T. Birner, V. Eyring, H. Akiyoshi, S. Bekki, C. Brühl, M. Dameris, D. E. Kinnison, F. Lefevre, F. Lott, E. Mancini, G. Pitari, D. A. Plummer, E. Rozanov, K. Shibata, A. Stenke, H. Struthers, and W. Tian, 2009. The tropical tropopause 1960-2100. *Atmos. Chem. Phys.*, **9**, 1621-1637.
- Gottelman, A., et al., 2010. Multi-model assessment in the UTLS part II: tropics and trends, submitted to *J. Geophys. Res.*
- Gilman, D. L., F. J. Fuglister, and J. M. Mitchell Jr., 1963. On the power spectrum of "red noise," *J. Atmos. Sci.*, **20**, 182-184.
- Grewe, V., and R. Sausen, 2009. Comment on "quantitative performance metrics for stratospheric-resolving chemistry-climate models" by Waugh and Eyring, *Atmos. Chem. Phys.*, **9**, 9101-9110.
- Grise, K. M., D. W. J. Thompson, and T. Birner, 2009. A global survey of static stability, *J. Clim.*, submitted.
- Hassler, B., G. E. Bodeker, and M. Dameris, 2008. Technical note: A new global database of trace gases and aerosols from multiple sources of high vertical resolution measurements, *Atmos. Chem. Phys.*, **8**, 5403-5421.
- Hatsushika, H., and K. Yamazaki, 2003. Stratospheric drain over Indonesia and dehydration within the tropical tropopause layer diagnosed by air parcel trajectories, *J. Geophys. Res.*, **108**, doi:10.1029/2002/JD002986.
- Hegglin, M. I., D. Brunner, T. Peter, J. Staehelin, V. Wirth, P. Hoor, and H. Fischer, 2005. Determination of eddy-diffusivity in the lowermost stratosphere, *Geophys. Res. Lett.*, **32**, doi:10.1029/2005GL022495.
- Hegglin, M. I., D. Brunner, T. Peter, P. Hoor, H. Fischer, J. Staehelin, M. Krebsbach, C. Schiller, U. Parchatka, and U. Weers, 2006. Measurements of NO, NO<sub>y</sub>, N<sub>2</sub>O, and O<sub>3</sub> during SPURT: implications for transport and chemistry in the lowermost stratosphere, *Atmos. Chem. Phys.*, **6**, 1331-1350.
- Hegglin, M. I., and Shepherd, T. G., 2007. O<sub>3</sub>-N<sub>2</sub>O correlations from the Atmospheric Chemistry Experiment: Revisiting a diagnostic of transport and chemistry in the stratosphere, *J. Geophys. Res.*, **112**, doi:10.1029/2006JD008281.
- Hegglin, M. I., C. D. Boone, G. L. Manney, T. G. Shepherd, K. A. Walker, P. F. Bernath, W. H. Daffer, P. Hoor, and C. Schiller, 2008. Validation of ACE-FTS satellite data in the upper troposphere/lower stratosphere (UTLS) using non-coincident measurements, *Atmos. Chem. Phys.*, **8**, 14831499.
- Hegglin, M. I., C. D. Boone, G. L. Manney, and K. A. Walker, 2009. A global view of the extratropical tropopause transition layer from Atmospheric Chemistry Experiment Fourier Transform Spectrometer O<sub>3</sub>, H<sub>2</sub>O, and CO, *J. Geophys. Res.*, **114**, doi:10.1029/2008JD009984.
- Hegglin, M. I., and T. G. Shepherd, 2009. Large climate-induced changes in UV index and stratosphere-to-troposphere ozone flux, *Nature Geosci.*, **2**, 687-691.
- Hegglin, M. I., et al., 2010. Multi-model assessment in the UTLS: Extra-tropics, *J. Geophys. Res.*, submitted.
- Highwood, E. J., and B. J. Hoskins, 1998. The tropical tropopause, *Quart. J. Roy. Meteorol. Soc.*, **124**, 1579-1604.
- Hints, E. J., E. M. Weinstock, J. G. Anderson, R. D. May, and D. F. Hurst, 1999. On the accuracy of in situ water vapor measurements in the troposphere and lower stratosphere with the Harvard Lyman- $\alpha$  hygrometer, *J. Geophys. Res.*, **104**, 8183-8189.
- Holton, J., P. Haynes, M. McIntyre, A. Douglass, R. Rood, and L. Pfister, 1995. Stratosphere-troposphere exchange. *Rev. Geophys.*, **33**, 403-439.
- Hoor, P., Fischer, H., Lange, L., Lelieveld, J., Brunner, D., 2002. Seasonal variations of a mixing layer in the lowermost stratosphere as identified by the CO-O<sub>3</sub> correlation from in situ measurements, *J. Geophys. Res.*, **107**, doi:10.1029/2000JD000289.
- Hoor, P., Brunner, D., Hegglin, M., Peter, Th., Gurk, C., Wernli, H., Fischer, H., 2004. Seasonality and extent of extra-tropical TST derived from in-situ CO measurements during SPURT, *Atmos. Chem. Phys.*, **4**, 1427 - 1442.
- Hoor, P., H. Fischer, and J. Lelieveld, 2005. Tropical and extra-tropical tropospheric air in the lowermost stratosphere over Europe: A CO-based budget, *Geophys. Res. Lett.*, **32**, doi:10.1029/2004GL022018.
- Houghton, J. T., Y. Ding, D.J. Griggs, M. Noguer, P.J. van der Linden, X. Dai, K. Maskell, and C.A. Johnson, editors. Climate Change 2001: The Scientific

- Basis. Contribution of Working Group I to the Third Assessment Report of the Intergovernmental Panel on Climate Change. Cambridge University Press, Cambridge, UK, 2001.
- Kalnay, E., M. Kanamitsu, R. Kistler, W. Collins, D. Deaven, L. Gandin, M. Iredell, S. Saha, G. White, J. Woolen, Y. Zhu, M. Chelliah, W. Ebisuzaki, W. Higgins, J. Janowiak, K. C. Mo, C. Ropelewski, J. Wang, A. Leetmaa, R. Reynolds, R. Jenne, and D. Joseph, 1996. The NCEP/NCAR 40-year reanalysis project, *Bull. Am. Meteorol. Soc.*, **77**, 437-471.
- Kanamitsu, M., W. Ebisuzaki, J. Wollen, S.-K. Yang, J. J. Hnilo, M. Fiorino, and G. L. Potter, 2002. NCEP-DEO AMIP II reanalysis (R-2), *Bull. Am. Meteorol. Soc.*, **83**, 1631-1643.
- Kley, D., J. M. Russell III, and C. Phillips (Eds.), 2000. SPARC Assessment of Upper Tropospheric and Stratospheric Water Vapour, SPARC Report No 2, WCRP Report 113, WMO/TD-N° 1043.
- Kremser, S., I. Wohltmann, M. Rex, U. Langematz, M. Dameris, M. Kunze, 2009. Water vapor transport in the tropical tropopause region in couple chemistry-climate models and ERA-40 reanalysis data, *Atmos. Chem. Phys.*, **9**, 2679-2694.
- Lee, H., D. Youn, D. J. Wuebbles, K. Patten, *Diagnostic tools for evaluating the quasi-horizontal transport process in chemistry transport models*, *J. Geophys. Res.*, in review.
- Levine, J. G., P. Braesicke, N. R. P. Harris, N. H. Savage, and J. A. Pyle, 2007. Pathways and timescales for troposphere-tostratosphere transport via the tropical tropopause layer and their relevance for very short lived substances, *J. Geophys. Res.*, **112**, doi:10.1029/2005JD006940.
- Levine, J. G., P. Braesicke, N. R. P. Harris, and J. A. Pyle, 2008. Seasonal and inter-annual variations in troposphere-to-stratosphere transport from the tropical tropopause layer, *Atmos. Chem. Phys.*, **8**, 3689-3703.
- Li, F., R. S. Stolarski, and P. A. Newman, 2009. Stratospheric ozone in the post-cfc era, *Atmos. Chem. Phys.*, **9**, 2207-2213.
- Livesey, N. J. et al. (2007), MLS Version 2.2 Level 2 data quality and description document, Tech. Rep. JPL D-33509, Jet Propulsion Laboratory, available at <http://mls.jpl.nasa.gov>
- Livesey, N. J., M. J. Filipiak, L. Froidevaux, W. G. Read, A. Lambert, M. L. Santee, J. H. Jiang, H. C. Pumphrey, J. W. Waters, R. E. Cofield, D. T. Cuddy, W. H. Daffer, B. J. Drouin, R. A. Fuller, R. F. Jarnot, Y. B. Jiang, B. W. Knosp, Q. B. Li, V. S. Perun, M. J. Schwartz, W. V. Snyder, P. C. Stek, R. P. Thurstans, P. A. Wagner, M. Avery, E. V. Browell, J.-P. Cammas, L. E. Christensen, G. S. Diskin, R.-S. Gao, H.-J. Jost, M. Loewenstein, J. D. Lopez, P. Nedelec, G. B. Osterman, G. W. Sachse, and C. R. Webster, 2008. Validation of Aura Microwave Limb Sounder O3 and CO observations in the upper troposphere and lower stratosphere, *J. Geophys. Res.*, **113**, doi:10.1029/2007JD008805.
- Logan, J., 1999. An analysis of ozonesonde data for the lower stratosphere: Recommendations for testing models, *J. Geophys. Res.*, **104**, 16151-16170.
- Matsuno, T., 1966. Quasi-geostrophic motions in the equatorial area, *J. Meteor. Soc. Japan*, **44**, 25-43.
- Milz, M., T. von Clarmann, H. Fischer, N. Glatthor, U. Grabowski, M. Höpfner, S. Kellmann, M. Kiefer, A. Linden, G. Mengistu Tsidu, T. Steck, G. P. Stiller, B. Funke, M. López-Puertas, and M. E. Koukouli, 2005. Water vapor distributions measured with the Michelson Interferometer for Passive Atmospheric Sounding on board Envisat (MIPAS/Envisat), *J. Geophys. Res.*, **110**, doi:10.1029/2005JD005973.
- Milz, M., T. v. Clarmann, P. Bernath, C. Boone, S. A. Buehler, S. Chauhan, B. Deuber, D. G. Feist, B. Funke, N. Glatthor, U. Grabowski, A. Griesfeller, A. Haefele, M. Höpfner, N. Kämpfer, S. Kellmann, A. Linden, S. Müller, H. Nakajima, H. Oelhaf, E. Remsberg, S. Rohs, J. M. Russell III, C. Schiller, G. P. Stiller, T. Sugita, T. Tanaka, H. Vömel, K. Walker, G. Wetzel, T. Yokota, V. Yushkov, and G. Zhang, 2009. Validation of water vapour profiles (version 13) retrieved by the IMK/IAA scientific retrieval processor based on full resolution spectra measured by MIPAS on board Envisat, *Atmos. Meas. Tech.*, **2**, 379-399.
- Milosevich, L. M., A. Paukkunen, H. Vömel, S. J. Oltmans, 2004. Development and Validation of a Time-Lag Correction for Vaisala Radiosonde Humidity Measurements, *J. Atmos. Ocean Tech.*, **21**, 1305-1327.
- Mote, P. W., K. H. Rosenlof, M. E. McIntyre, E. S. Carr, J. C. Gille, J. R. Holton, J. S. Kinnersley, H. C. Pumphrey, J. M. Russell, and J. W. Waters, 1996. An atmospheric tape recorder: The imprint of tropical tro-

- popause temperatures on stratospheric water vapor. *J. Geophys. Res.*, **101**, 3989-4006.
- Newman, P. A., D. W. Fahey, W. H. Brune, and M. J. Kurylo, 1999. Preface to special section: Photochemistry of Ozone Loss in the Arctic Region in Summer (POLARIS), *J. Geophys. Res.*, **104**, 26,481 – 26,495.
- Onogi, K., J. Tsutsui, H. Koide, M. Sakamoto, S. Kobayashi, H. Hatsushika, T. Matsumoto, N. Yamazaki, H. Kamahori, K. Takahashi, S. Kadokura, K. Wada, K. Kato, R. Oyama, T. Ose, N. Mannoji and R. Taira, 2007. The JRA-25 Reanalysis. *J. Meteor. Soc. Japan*, **85**, 369-432.
- Pan, L.L., W. J. Randel, B. L. Gary, M. J. Mahoney, and E. J. Hintsa, 2004. Definitions and sharpness of the extra-tropical tropopause: A trace gas perspective, *J. Geophys. Res.*, **109**, doi:10.1029/2004JD004982.
- Pan, L. L., J. C. Wei, D. E. Kinnison, R. R. Garcia, D. J. Wuebbles, and G. P. Brasseur, 2007. A set of diagnostics for evaluating chemistry-climate models in the extra-tropical tropopause region, *J. Geophys. Res.*, **112**, doi:10.1029/2006JD007792.
- Pawson, S., and M. Fiorino, 1998. A comparison of reanalyses in the tropical stratosphere. Part 1: thermal structure and the annual cycle, *Clim. Dyn.*, **14**, 631–644.
- Proffitt, M. H., and R. J. McLaughlin, 1983. Fast-response dual-beam UV-absorption ozone photometer suitable for use on stratospheric balloons, *Rev. Sci. Instrum.*, **54**, 1719– 1728.
- Randel, W. J., M. L. Chanin, and C. Michaut, SPARC intercomparison of middle atmosphere climatologies, Tech. Rep. WCRP 116, WMO/TD - 1142, SPARC Report 3, SPARC, World Climate Research Program, 2002.
- Randel, W. J., F. Wu, and P. Forster, 2007. The Extratropical Tropopause Inversion Layer: Global Observations with GPS Data, and a Radiative Forcing Mechanism, *J. Atmos. Sci.*, **64**, 4489-4496.
- Randel, W. J., F. Wu, H. Vomel, G. E. Nedoluha, and P. F. Forster, 2006. Decreases in stratospheric water vapor since 2001: links to changes in the tropical tropopause and the Brewer-Dobson circulation. *J. Geophys. Res.*, **111**, doi:10.1029/2005JD006744.
- Ray, E. A., Moore, F. L., Elkins, J. W., Dutton, G. S., Fahey, D. W., Vömel, H., Oltmans, S. J., and Rosenlof, K. H., 1999. Transport into the Northern Hemisphere lowermost stratosphere revealed by in situ tracer measurements, *J. Geophys. Res.*, **104**, 26565–26580.
- Rood R. B., A. Douglass, M. Cerniglia, L. Sparling, and J. Nielsen, 2000. Seasonal variability of middle-latitude ozone in the lowermost stratosphere derived from probability distribution functions, *J. Geophys. Res.*, **105**, 17793-17805.
- Rosenlof, K., A. F. Tuck, K. K. Kelly, J. M. Russell, and M. P. McCormick, 1997. Hemispheric asymmetries in water vapor and inferences about transport in the lower stratosphere, *J. Geophys. Res.*, **102**, 13,213–13,234.
- Russell, J. M., L. L. Gordley, J. H. Park, S. R. Drayson, A. F. Tuck, J. E. Harries, R. J. Cicerone, P. J. Crutzen, and J. E. Frederick, 1993. The Halogen Occultation Experiment, *J. Geophys. Res.*, **98**, 10,777-10,797.
- Schoeberl, M.R., A.R. Douglass, Z.Zhu and S.Pawson, 2003. A comparison of the lower stratospheric age spectra derived from a general circulation model and two data assimilation systems, *J. Geophys. Res.*, **108**, doi:10.1029/2002JD002652.
- Seidel, D. J., and W. J. Randel, 2006. Variability and trends in the global tropopause estimated from radiosonde data. *J. Geophys. Res.*, **111**, doi:10.1029/2006JD007363.
- Shepherd, T. G., 2002. Issues in Stratosphere-troposphere Coupling, *J. Meteor. Soc. Japan*, **80**, 769.
- Shepherd, T. G., 2007. Transport in the Middle Atmosphere, *J. Meteor. Soc. Japan*, **85B**, 165-191.
- Son, S. W., L. M. Polvani, D. W. Waugh, T. Birner, H. Akiyoshi, R. R. Garcia, A. Gettelman, D. A. Plummer, and E. Rozanov, 2009a. The impact of stratospheric ozone recovery on tropopause height trends. *J. Clim.*, **22**, 429-445.
- Son, S. W., N. F. Tandon, L. M. Polvani, and D. W. Waugh, 2009b. Ozone hole and southern hemisphere climate change. *Geophys. Res. Lett.*, **36**, doi:10.1029/2009GL038671.
- Steck, T., T. von Clarmann, H. Fischer, B. Funke, N. Glatthor, U. Grabowski, M. Höpfner, S. Kellmann, M. Kiefer, A. Linden, M. Milz, G. P. Stiller, D. Y. Wang, M. Allaart, Th. Blumenstock, P. von der Gathen, G. Hansen, F. Hase, G. Hochschild, G. Kopp, E. Kyrö, H. Oelhaf, U. Raffalski, A. Redondas Marrero, E. Remsberg, J. Russell III, K. Stebel, W. Steinbrecht, G. Wetzel, M. Yela, and G. Zhang, 2007. Bias deter-

- mination and precision validation of ozone profiles from MIPAS-Envisat retrieved with the IMK-IAA processor, *Atmos. Chem. Phys.*, **7**, 3639-3662.
- Suzuki, J., and M. Shiotani, 2008. Space-time variability of equatorial Kelvin waves and intraseasonal oscillations around the tropical tropopause, *J. Geophys. Res.*, **113**, doi:10.1029/2007JD009456.
- Taylor, K. E., 2001. Summarizing multiple aspects of model performance in a single diagram, *J. Geophys. Res.*, **106**, 7183-7192.
- Tilmes, S., L. Pan, P. Hoor, G. W. Sachse, M. Loewenstein, J. Lopez, C. Webster, L. E. Cristensen, M. Proffitt, R.-S. Gao, G. S. Diskin, M. A. Avery, J. R. Podolske, R. L. Herman, N. Spelten, A. Weinheimer, T. Campus, E. J. Hints, E. M. Weinstock, J. Pittman, M. A. Zondl, M. E. Paige, E. Atlas, 2010. An aircraft based upper troposphere lower stratosphere O<sub>3</sub>, CO and H<sub>2</sub>O climatology for the Northern hemisphere, *J. Geophys. Res.*, doi:10.1029/2009JD012731, in press.
- Tsuda, T., Y. Murayama, H. Wiryosumarto, S. Harijono, and S. Kato, 1994. Radiosonde observations of equatorial atmosphere dynamics over Indonesia: 1. Equatorial waves and diurnal tides, *J. Geophys. Res.*, **99**, 10,491-10,505.
- Uppala, S., D. Dee, S. Kobayashi, P. Berrisford, and A. Simmons, Towards a climate data assimilation system: status update of era-interim, *ECMWF Newsletter*, **115**, 12-18, 2008.
- Uppala, S. M., P. W. Kållberg, A. J. Simmons, U. Andrae, V. da Costa Bechtold, M. Fiorino, K. K. Gibson, J. Haseler, A. Hernandez, G. A. Kelly, X. Li, K. Onogi, S. Saarinen, N. Sokka, R. P. Allan, E. Andersson, K. Arpe, M. A. Balmaseda, A. C. M. Beljaars, L. van de Berg, J. Bidlot, N. Bormann, S. Caires, F. Chevallier, A. Dethof, M. Dragosavac, M. Fisher, M. Fuentes, S. Hagemann, E. Hólm, B.J. Hoskins, L. Isaksen, P. A. E. M. Janssen, R. Jenne, A. P. McNally, J.-F. Mahfouf, J.-J. Morcrette, N. A. Rayner, R.W. Saunders, P. Simon, A. Sterl, K. E. Trenberth, A. Untch, D. Vasiljevic, P. Viterbo, and J. Woollen, 2005. The ERA-40 re-analysis, *Quart. J. Roy. Meteorol. Soc.*, **131**, 2961-3012.
- von Clarmann, T., N. Glatthor, U. Grabowski, M. Höpfner, S. Kellmann, M. Kiefer, A. Linden, G. M. Tsidu, M. Milz, T. Steck, G. P. Stiller, D. Y. Wang, H. Fischer, B. Funke, S. Gil-López, M. López-Puertas, 2003. Retrieval of temperature and tangent altitude pointing from limb emission spectra recorded from space by the Michelson Interferometer for Passive Atmospheric Sounding (MIPAS), *J. Geophys. Res.*, **108**, doi:10.1029/2003JD003602.
- von Clarmann, T., M. Höpfner, S. Kellmann, A. Linden, S. Chauhan, B. Funke, U. Grabowski, N. Glatthor, M. Kiefer, T. Schieferdecker, G. P. Stiller, and S. Versick, 2009. Retrieval of temperature, H<sub>2</sub>O, O<sub>3</sub>, HNO<sub>3</sub>, CH<sub>4</sub>, N<sub>2</sub>O, ClONO<sub>2</sub> and ClO from MIPAS reduced resolution nominal mode limb emission measurements, *Atmos. Meas. Tech.*, **2**, 159-175.
- Wang, D. Y., M. Höpfner, G. Mengistu Tsidu, G. P. Stiller, T. von Clarmann, H. Fischer, T. Blumenstock, N. Glatthor, U. Grabowski, F. Hase, S. Kellmann, A. Linden, M. Milz, H. Oelhaf, M. Schneider, T. Steck, G. Wetzel, M. López-Puertas, B. Funke, M. E. Koukouli, H. Nakajima, T. Sugita, H. Irie, J. Urban, D. Murtagh, M. L. Santee, G. Toon, M. R. Gunson, F. W. Irion, C. D. Boone, K. Walker, and P. F. Bernath, 2007. Validation of nitric acid retrieved by the IMK-IAA processor from MIPAS/ENVISAT measurements, *Atmos. Chem. Phys.*, **7**, 721-738.
- Waters, J. W., Froidevaux, L., Harwood, R.S., Jarnot, R.F., Pickett, H.M., Read, W.G., Siegel, P.H., Co-field, R.E., Filipiak, M.J., Flower, D.A., Holden, J.R., Lau, G.K., Livesey, N.J., Manney, G.L., Pumphrey, H.C., Santee, M.L., Wu, D.L., Cuddy, D.T., Lay, R.R., Loo, M.S., Perun, V.S., Schwartz, M.J., Stek, P.C., Thurstans, R.P., Boyles, M.A., Chandra, K.M., Chavez, M.C., Gun-Shing Chen, Chudasama, B.V., Dodge, R., Fuller, R.A., Girard, M.A., Jiang, J.H., Yibo Jiang, Knosp, B.W., LaBelle, R.C., Lam, J.C., Lee, K.A., Miller, D., Oswald, J.E., Patel, N.C., Pukala, D.M., Quintero, O., Scaff, D.M., Van Snyder, W., Tope, M.C., Wagner, P.A., and Walch, M.J., 2006. The Earth Observing System Microwave Limb Sounder (EOS MLS) on the Aura satellite, *IEEE Trans. Geosci. Remote Sens.*, **44**, 1075-1092.
- Waugh, D. W. and V. Eyring, 2008. Quantitative performance metrics for stratosphere-resolving models. *Atmos. Chem. Phys.*, **8**, 5699-5713.
- Wheeler, M., and G. N. Kiladis, 1999. Convectively coupled equatorial waves: Analysis of clouds and temperature in the wavenumber-frequency domain. *J. Atmos. Sci.*, **56**, 374-399.

- Wohltmann, I., and M. Rex, 2008. Improvement of vertical and residual velocities in pressure or hybrid sigma-pressure coordinates in analysis data in the stratosphere, *Atmos. Chem. Phys.*, **8**, 265-272.
- Zhou, X., M. A. Geller, and M. Zhang, 2001. The cooling trend of the tropical cold point tropopause temperatures and its implications, *J. Geophys. Res.*, **106**, 1511–1522.

# Chapter 8

## Natural Variability of Stratospheric Ozone

**Lead Authors:** Elisa Manzini & Katja Matthes

**Co-Authors:** Christian Blume

Greg Bodeker

Chiara Cagnazzo

Natalia Calvo

Andrew Charlton-Perrez

Anne Douglass

Pier Giuseppe Fogli

Lesley Gray

Junsu Kim

Kuni Kodera

Markus Kunze

Cristina Pena Ortiz

Bill Randel

Thomas Reichler

Gera Stenchikov

Claudia Timmreck

Matt Toohey

Shigeo Yoden